The 8th Annual Conference of Thai Physics Society
Chiang Mai, Thailand

March 21-23, 2013

สมาคมฟิสิกส์ไทย
THAI PHYSICS SOCIETY

NARIT

ThEP CENTER

Siam Photon

PROCEEDINGS

SPC 2013

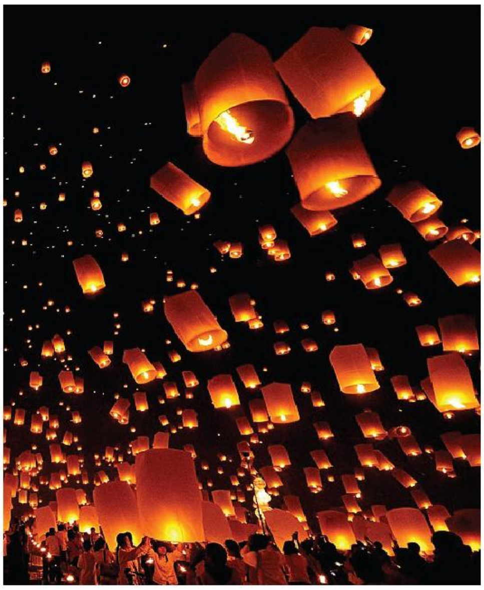

SIAM PHYSICS CONGRESS 2013
MARCH 21-23, 2013
Chiangmai Grandview Hotel, Chiangmai, Thailand

Conference Organizing Committee

Advisory Committee:	Niwes Nantachit	CMU
	Sompol Pongthai	BUU
	Somkit Lertpaithoon	TU
	Boonrucksar Soonthornthum	NARIT
	Thiraphat Vilaithaong	ThEP
	Weerapong Pairsuwan	MOST
Conference Chair:	Vittaya Amornkitbamrung	KKU
Local Organizing Chairs:	Sampan Singharajwarapan	CMU
	Usavadee Tunwaranuruk	BUU
	Pakorn Sermsuk	TU
Executive Secretary:	Prayoon Songsiriritthigul	SLRI
Secretary Team:	Dheerawan Boonyawan	CMU
	Nirun Witit-anun	BUU
	Sayan Pudwat	TU

Members:

Benya Cherdhirunyakorn
Rawat Jaisutti
Jirapa Tangsritrakul
Somyos Kongkarat
Sayan Pudwat
Nopporn Poolyarat
Taewan Pleansaithong
Chumpon Wichitthanakom
Adisak Romputtarn
Kalya Eaiprasertsak
Kamon Aiempanakit
Nuntaporn Kongkajan
Nattapol Narkpathomkul
Sittichork Amnuaypol
Manu FuengFung

Scientific Program Committee

Tawee Chimoye	TU	Pichet Limsuwan	KMUTT
Sukit Limpijumnong	SUT	Rattikorn Yimnirun	SUT
Nason Phonphok	SWU	Udomsilp Pinsook	CU
Mudtorlep Nisoa	WU	Nopporn Poolyarat	TU
Wandee Onreabroy	KMUTT	Sittichork Amnuaypol	TU
Sirapat Pratontep	KMITL	Tanakorn Osotchan	MU
Surasing Chaiyakun	BUU	Nirun Witit-anun	BUU
Siriporn Rojananan	KMUTT	Yutthana Tirawanichakul	PSU
Supub Choopun	CMU	Khamphee Karwan	KU
Thanusit Burinprakhon	KKU	Dheerawan Boonyawan	CMU

Supported by

Thai Physics Society (TPS)
Chiang Mai University (CMU)
Burapha University (BUU)
Thammasat University (TU)
Thailand Center of Excellence in Physics (ThEP)
Synchrotron Light Research Institute (SLRI)
National Astronomical Research Institute of Thailand (NARIT)

Message from the President of Thai Physics Society

On behalf of the Thai Physics Society, we would like to express a warm welcome to the 8th Siam Physics Congress 2013 (SPC2013), which is aimed at providing an academic forum for those with common in Physics, in order to promote the growth of collaboration among Thais and oversea physicists, teachers, students, technologists and young scientists.

This year SPC 2013 is settled on a theme "*Thai Physics Society: on the Road to ASEAN Community*" to match the tourist city in Chiang Mai, which is also a long history. This is a point to glance back to the past development of Physics in Thailand in order to reinforce the present and the future Physics communities. SPC 2013 is organized into three main sessions: Fundamental Physics; Applied Physics, Engineering and Industrial Physics; and Physics Education. This stresses an equal importance of all the three realm of Physics, which are crucial to secure both of radiant future of communities and the advancement of the nation.

This year, we continue to receive a willing supported from the national organizations and international physicists, as well as, from the industrial sectors, with close to 500 participants. We would like to express our graduate to all supported from government and private sector. We would like to thank the co-host organizers, the Faculty of Science, Chiang Mai University, the Faculty of Science, Burapha University, the Faculty of Science, Thammasat University, Thailand Center of Excellence in Physics (ThEP), Synchrotron Light Research Institute (Siam Photon), National Astronomical Research Institute of Thailand (NARIT). SPC 2013 would not be possible without their supports. Last but not least, we are grateful for vital contributions from our distinguished guests, referees, staff and all participants here. Let us the benefit from this conference academically, socially and culturally. I wish you all a memorable time at SPC2013.

Vittaya Amornkitbamrung

Associate Professor Dr. Vittaya Amornkitbamrung
The President of Thai Physics Society

Message from the President of Chiang Mai University (CMU)

On behalf of Chiang Mai University, it is our utmost pleasure to co-host the 8th Siam Physics Congress (SPC2013) together with Burapha University and Thammasat University.

This year, SPC2013 is held in Chiang Mai or the "Rose of the North" city, which houses fascinating indigenous cultural identities that includes diverse dialects, delectable cuisines, distinctive architectures, traditional values, lively festivals, numerous handicraft workshops, northern style massage, and classical dances. Chiang Mai is also blessed with the presence of numerous hill tribes that feature a wealth of unique cultures enhancing Chiang Mai's distinctive diversity, in combination with the riches from the expatriate communities from all over the world.

It is indeed a very good fortune that the theme of Siam Physics Congress this year is "Thai Physics Society: On the Road to ASEAN Community" as Chiang Mai University has been preparing itself to become a part of the ASEAN Community 2015. So far we have academic agreements with six universities in ASEAN countries; Cambodia, Indonesia, Laos, Malaysia, the Philippines, and Vietnam. Therefore, it is an excellent opportunity for physicists, technicians, researchers, scholars, industrial sector representatives and promising students, as well as those interested in the physics world, to exchange information and share their experiences.

On this auspicious occasion, I am convinced that the scientific progress gained from this landmark event will lead to greatness and strengthen collaborations within this research-friendly environment as well as in our society and culture. I would like to take this opportunity to express my sincere appreciation to the organizing teams, sponsors, distinguished speakers, my academic fellows and students for making the SPC2013 possible.

I wish every success to the 8th Siam Physics Congress and sincerely hope that this remarkable event will provide an intellectually inspiring experience to all of you. Please enjoy Chiang Mai, have a pleasant stay and finally a safe journey back home.

N. Nantachit

Associate Professor Niwes Nantachit, M.D.
President, Chiang Mai University

Message from the Rector of Thammasat University (TU)

On behalf of Thammasat University, it is an absolute pleasure to receive an honor from Thai Physics Society to be a co-host of the 8th Siam Physics Congress.

As for the upcoming Asean Economic Community, science and technology development will be important keys for the success of this union. We, Thammasat University, values physics as key fundamental science that will be part of Road to ASEAN. It is our pleasure to co-organize the conference to serve as a forum for physics communities to discuss and exchange scientific progress. Also, this physics congress will serve as an opportunity to develop and strengthen the collaboration among physics communities.

I wish prosperousness and success to the 8th Siam Physics Congress and hope this landmark event will benefit to all of you.

Somkit Lertpaithoon

Professor Dr. Somkit Lertpaithoon
Rector, Thammasat University

Message from the President of Burapha University (BUU)

On behalf of the Burapha University, it is an absolute pleasure to receive an honor to be co-host of the 8th Siam Physics Congress (SPC2013) in conjunction with Thai Physics Society (TPS), the Thailand Center of Excellence in Physics (ThEP), the National Astronomical Research Institute of Thailand (NARIT), the Synchrotron Light Research Institute (SLRI), Chiang Mai University and Thammasat University.

From the past until now, we realize that Physics is one of the most important sciences and harmoniously integrated in every aspect of our society. Physics plays an important role in the future progress of mankind. SPC2013 aims to provide a forum for interactions and dialogues amongst researchers, engineers, academic , industrial and those who are interested in physics to transfer and exchange valuable information.

I am convinced that the scientific progress gained from this landmark event will create ties and strengthen the collaborations to stimulate an active research environment that is relevant to our society. I truly appreciate dedication from corporate sponsors, colleagues, delegates and contributors, especially the dedicated efforts of the SPC2013 collaborative staffs to help ensure the high quality of the conference.

I wish every success to the 8th Siam Physics Congress and anticipate that this important event will provide an intellectually inspiring experience to all of you.

Prof. Sompol Pongthai, MD.
The President of of Burapha University

SIAM PHYSICS CONGRESS 2013
March 21-23, 2013
Chiangmai Grandview Hotel, Chiangmai, Thailand

Conference Overview

The 8th Siam Physics Congress (SPC2013) will be held at the Chiangmai Grandview Hotel, Changpuek, Chiang Mai, Thailand during 21-23 March 2013. The Siam Physics Congress was initiated in 2006 by the Thai Physics Society (TPS). The aim of the congress is to bring together national and international physicists, physics teachers, technologists, young scientists as well as those who are interested in physics from a variety of fields (covering both basic and applied physics research) in order to give them an opportunity to share and exchange their experiences. The Siam Physics Congress incorporates satellite workshops and annual meetings of the Thai Physics Society, the Thailand Center of Excellence in Physics (ThEP), Synchrotron Light Research Institute (SLRI), and the National Astronomical Research Institute of Thailand (NARIT).

Conference Theme

"Thai Physics Society on the Road to ASEAN Community"

Conference Topics

Professionals working in universities, engineering institutions, R&D, academic, governmental, professional organizations, and industries are invited to contribute papers and participate in the conference. An abstract or full paper may be submitted in one of the following areas:

- Accelerators and Synchrotron Radiations (Acc)
- Astronomy, Astrophysics and Cosmology (Astro-Cos)
- Atomic Physics, Quantum Physics, Molecular and Chemical Physics (Atom-QM)
- Optics, Non-linear Optics, Laser Physics, Ultrafast Phenomena (Optic)
- Statistical and Theoretical Physics (Stat-Theo)
- High – energy and Particle Physics (HEP)
- Ion and Plasma Physics (Ion-Plasma)
- Condensed Matter Physics (Con-Mat)
- Nuclear and Radiation Physics (Nu-Rad)
- Biological Physics and Biomedical Engineering (Bio-Phy)
- Environmental Physics, Atmospheric Physics, Geophysics and Renewable Energy (Envi-Energy)
- Instrumentation, Metrology and Standards (Inst-Metro)
- Material Physics, Nanoscale Physics and Nanotechnology (Mat-Nano)
- Magnetic and Semiconductor Devices (Magne-Semi)
- Photonics and Optoelectronics (Photo-Opto)
- Surface, Interface and thin Films (Surf-Films)
- Physics Education : Physics Teaching , Information and Communication Technologies in teaching Physics, and Active learning of Physics (Phy-Edu)

Organizer

Thai Physics Society
Department of Physics, Faculty of Science, Chiang Mai University
Department of Physics, Faculty of Science, Burapha University
Department of Physics, Faculty of Science and Technology, Thammasat University
Website: http://www.spc2013.net/

Language

The official language of the Congress is English.

Poster Sessions

Poster session 1 will be held in the Chiangmai Grandview Convention Center (poster sessions-area) from 8.00 to 18.00 and remove their posters by 18.00 on Friday March 22, 2013. The participants are advised to put up their posters during the 15.00-18.00 on Thursday March 21, 2013.

Poster session 2 will be held in the Chiangmai Grandview Convention Center (poster sessions-area) from 8.00 to 16.00 and remove their posters by 16.00 on Saturday March 23, 2013. The participants are advised to put up their posters during the 18.00-18.30 on Friday March 22, 2013.

Exhibitions

Suppliers of instrumentation, materials, process tools and other products and services will exhibit their products in the Hall Way during the conference.

General Contact of Chiangmai Grandview Hotel

Chiangmai Main Office: 24 Nearby Nimmarnheaminda Rd., Changpuek,Muang, Chiangmai 50300 Thailand
Tel: +66 (0) 53-220-100-9 Fax: +66 (0) 53-221- 602
Bangkok Office: 42/13 Ratchada 42, Ratchadapisake Rd., Chatujak, Bangkok 10900 Thailand
Tel: +66 (0) 2-939-1171-3 Fax: +66 (0) 2-939-1174
http://www.chiangmaigrandview.com/

ตราสัญลักษณ์ Siam Physics Congress 2013 ประกอบด้วย อักษร SPC 2013 โดยที่ อักษร SPC กำหนดเป็นลายไทย สื่อถึงความเป็นไทย ร่วมกับตัวเลข 2013 ที่เป็นเลขอารบิกที่นิยมใช้กันมากที่สุดในโลก ที่บ่งบอกถึงการผสมผสานระหว่างความเป็นไทยกับความเป็นสากล อักษร S ซึ่งมีลักษณะเป็นพญานาคราชและส่วนหางมีลักษณะเป็นถนน ซึ่งพญานาคเป็นเทพแห่งลุ่มน้ำโขงร่วมกับถนน ที่สื่อถึงสายสัมพันธ์วิถีชีวิตของผู้คนในภูมิภาคเอเชียใต้และเอเชียตะวันออกเฉียงใต้ที่มีมายาวนานและพัฒนาความสัมพันธ์อย่างต่อเนื่อง อีกทั้งตามคติศาสนาพราหมณ์ และพุทธศาสนาเชื่อว่านาค คือตัวแทนที่เป็นบันไดสู่จักวาลที่เป็นหนึ่งในศาสตร์ที่สำคัญทางฟิสิกส์ อักษร S ที่เป็นอักษรย่อจาก “Siam” ซึ่งหมายถึงประเทศไทย ที่เป็นผู้ร่วมก่อตั้งหลักของประชาคมอาเซียน และมุ่งมั่นที่จะร่วมพัฒนาประชาคมอาเซียน ซึ่งนำไปสู่แนวคิดในการจัดการประชุมในครั้งนี้ คือ “Thai Physics Society on the Road to ASEAN Community” **สีส้มทอง** ของอักษร SPC เป็นสีผสม ระหว่าง**เหลือง-แดง** ซึ่งเป็นสีประจำมหาวิทยาลัยธรรมศาสตร์ **สีทอง**-เทา ของอักษร S และถนน เป็นสีประจำมหาวิทยาลัยบูรพา และ***สีม่วง*** เป็นสีประจำมหาวิทยาลัยเชียงใหม่ซึ่งเป็นสามเจ้าภาพหลักในการจัดการประชุมวิชาการ SPC2013

The logo of this event includes three capitals letter (S P and C), the number showing the year, and the road connecting with the letter "S". The three letters stand for Siam Physics Congress. The shape of these letters resemble Thai painting especially letter "S" that have the shape of Naga, the serpent king, which is the symbol of power and prosperity that will lead us through the road of bright -future ASEAN Community whom Thailand is a member and also a founder of ASEAN. Moreover, in Hindu, Naga has the great power to give us the key to the universe which relate the astronomy, a field in physic that study the celestial objects. Finally, all colors used in this logo are the combination of symbol color of cohost universities which are Thammasat Universities **(Yellow** and **Red),** Burapa University **(Gold** and **Grey**), and Chiangmai University **(Violet)**.

CONTENTS

Astronomy, Astrophysics, and Cosmology

Orbital Period Change of an Eclipsing Binary System HW Virginis

T. Rangsungnoen[1*]

[1]*Physics and General Science Program, Faculty of Science and Technology,*
Nakhon Ratchasima Rajabhat University, Nakhon Ratchasima, 3000, Thailand.
**Corresponding author. E-mail: kruneng.kk@gmail.com*

Abstract

The aim of this study is to analyse the orbital period change of HW Virginis (Hw Vir). The data gatering were done via CCD (SBIG-ST10-XME) that attached to the 0.5 m - reflecting telescope of Princess Sirindron observatory, Chiang Mai University. The light curves obtained through B, V and R filters were collected and processed via MaxIm DL4 softwere and O-C diagram. Observations were done from January to February 2012. The result has shown that the orbital period of HW Vir was 0.11672 day and continuosly decreased at a rate of 0.000005398307079 sec/year. It new ephemeris of HW Vir was 2445730.55597 + 0.11672E. From the analysis of O-C residual has shown a sine wave pattern.

***Keywords*:** HW Virginis : Eclipsing binary : Period change.

Introduction

HW Vir was discovered as an eclipsing binary by Menzies(1986). The first light curve was published by Menzies & Marang (1986) includes both primary and secondary eclipses and the light curve has shown a striking reflection effect. Wood & Saffer(1999) analyzed parameters of the sdB star using the spectra. Kilkenny et al. (1994) report have shown that orbital period decreasing of HW Vir.

The eclipsing time obtained between 1984 and 1999 were re-analyzed by Cakirli & Devlen (1999) assuming possibing of the orbital period change is the light-time effect. They suggested the period of revolution to be about 19 years around the third body. Wood & saffer(1999), Kilkenny et al. (2000), Kiss et al. (2000) and recently Kilkenny et al. (2003) discussed the O-C diagram for HW Vir has shown that the third body is likely to be brown dwarf. C.Ibanoglu et al.(2004) analyzed orbital period of HW Vir and parameters of the third body. The result has shown that 18.8 years and eccentricity of 0.12 for third body.

However, the aim of this paper has not shown the parameter and characteristic for the third body of HW Vir, but analysis and report of orbital period change of HW Vir.

Observation and Analysis

The data gathering were done via CCD photometer attached by B, V and R filters that connected to the 0.5 m - reflecting telescope of Princess Sirindron Observatory, Chiang Mai University. Observations were done from January to February 2012. The 0bserved data were taken to be sending image reduction process for noise eradicating. Magnitude of HW Vir were measured by MaxIm DL3.0 and MaxIm DL4 softwares respectively. The observed data analysis for time of minimum by the equation of Bob Nelson and it has shown that

$$\mathrm{HJD\ (Min)} = 2445730.5561 + 0.116719E \quad (1)$$

The Time of minimum of HW Vir has shown on table 1.

Table 1: Times of minimum of HW Vir from this Investigation.

HJD (2400000+)	Min	Epoch	O-C
55970.35439	I	87730	0.00139
55970.391347	II	87730	0.001347
55972.3397533	II	87747	0.001753
55972.456427	I	87748	0.001427

Not : Min I is primary eclipse and Min II is secondary eclipse.

From table 1, calculated data for new ephemeris of HW Vir has shown in equation (2)

$$HJD\left(Min\right) = 2445730.55597 + 0.11672E \quad (2)$$

Result and Light curves

From table 1, time of minimum and Epoch of HW Vir calculated by previous authors during the past 25 years and result has shown that O-C diagram on Fig.1

The O-C for each epoch were calculated and the analysis by using a second order polynomial fitting on the O-C curve was shown in equation (3)

$$O-C=\left(-9.98318\times10^{-15}E^{2}\right)+\left(-1.01627\times10^{-7}E\right)+1.12\times10^{-3} \qquad (3)$$

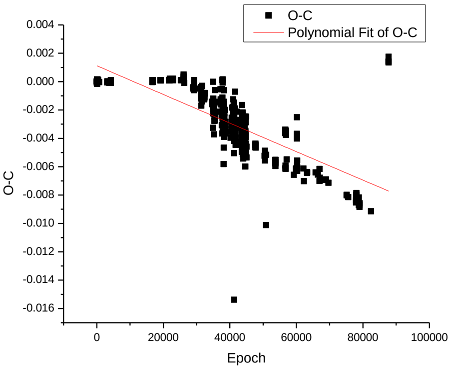

Figure 1. The O-C diagram of HW Vir

The calculated data for orbital period change of HW Vir was 0.11672 day while the orbital period decreased at a rate of 0.000005398307079 sec/year.

Calculated the light curve of polynomial fitting, the result of O-C residual process has shown that a sine wave pattern as shown in Fig.2

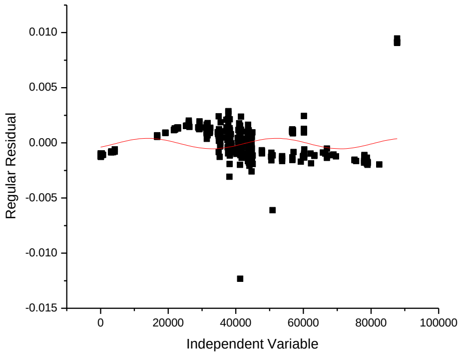

Figure 2. The O-C residual diagram of HW Vir

Conclusions

The aim of this paper has not shown the parameter and characteristic for the third body of HW Vir, but analysis report of orbital period change of HW Vir.

The result has shown that orbital period of an eclipsing binary system HW Vir was 0.11672 day. Comparing to Bob Nelson's data that presented in terms of the orbital period change and its decreased on 0.000005398307079 sec/year or 1.996636 x 10^{-14} day/cycle. The data of light curve has shown that continuousely decreased too. The result has show that new ephemeris of HW Vir on equation (2). However, the data investigation are needed for the better understanding on physical parameter properties and evolution of this binary system.

Acknowledgments

I would like to express sincerely thanks to Nakhon Ratchasima Rajabhat University for granting fund and supporting on this research and wish also to thanks the department of Physics and Materials, faculty of Science, Chiang Mai University for allowed observing times at Princess Sirindron Observatory.

Thanks to Associate Profressor Boonruksar – Soonthornthum, Dr. Pattanapong Jumrusprasert and Mr. Ronnakit Rattanamala for theirs suggestions and kindly helps.

References

1. C. Ibanoglu, O. Cakirli, G. Tas, and S. Evren. "High-speed photometry of the pre-cataclysmic binary HW Virginis and its orbital period change", Astronomy & Astrophysics **414** (2004), 1043 - 1048.
2. D. Kilkenny, F. Marang, and J. W. Menzies, "A Period decreases in the sdB Eclipsing binary System HW virginis" Mon. Not. R. Astron. Soc. 267, 535 – 540 (1994).
3. J. Wood and R. Suffer, "Spectroscopy of the post-common envelope binary HW Virginis" Mon. Not. R. Astron. Soc. 305, 820 – 828, (1999).
4. L. L. Kiss, B. Csak, K. Szatmary, G. Furesz, and K. Sziladi. "Spectrophotometry and period analysis of the sdB eclipsing binary HW Virginis", Astronomy & Astrophysics, arXiv : astro-ph/0010446v1 (2000) 1-7.
5. O. Cakirli and A. Devlen, "UBVR photometry of pre-catacylismic binaries : HW Virginis", Astronomy & Astrophysics, Suppl. Ser. 136 (1999) 27-33.

A Development of Photometry Laboratory by using Digital Single Lens Reflex Camera

P. Hiranrat and C. Ruangsuwan*

Department of Physics, Faculty of Science, Khon Kaen University, Khon Kaen, 40002 Thailand

**Corresponding author. E-mail: chaiyapg@kku.ac.th*

Abstract

This research was aimed to develop the photometry laboratory by using digital single lens reflex camera for measuring apparent magnitude of stars. The astrophotography including Sky images, Dark images, Bias images, and Flat images were taken and combined. The final image was then analyzed to calculate an instrumental apparent magnitude of a star by using IRIS program. An aperture photometry method was used in this research. The diameters of aperture, inner annulus and outer annulus were 10, 13, and 20 pixels, respectively. The apparent magnitudes from the standard catalog II/168 were used for calibrating the instrument apparent magnitude. It was found that the measured visual apparent magnitude contained standard deviation within ± 0.01, which were sufficient for studying variable stars. However, this study was limited to the constellation that is close to zenith or at an altitude of greater than 75 degrees during taken a photograph.

***Keywords*:** Digital SLR, photometry

Introduction

This project was aimed to develop the basic photometry laboratory for an undergraduate physics program or pre-service teacher program. The rapidly improvement of performance of light detector and personal computer causes the astronomical image processing would be interested to be placed in an advance physics laboratory level.

The detectors of conventional digital single lens reflex (DSLR) camera have been fast developed in the past decade. Thus the DSLR cameras are widely used for astrophotography by worldwide amateur astronomers. Many of astronomical images processing software had been developed to serve an astrophotography. In 2009, an International Year of Astronomy (IYA), the American Association of Variable Star Observers (AAVSO) started the project Citizen Sky, the project that welcomes everyone to be a citizen scientist [1]. The DSLR photometry had been promoted as a main tool for studying the light curved of the Epsilon Aurigae, the main target of the Citizen Sky project.

The prize of DSLR cameras was decreasing while it got more performance. Furthermore, many of open-source software for astronomical images processing were continuing developed through the time. Such, the DSLR photometry was very interested to be set as a laboratory for undergraduate students those were interesting to do an astronomy projects.

Our objectives were to do pilot study about DSLR photometry and to develop a laboratory for practical astronomy.

Materials and Methods

Experimental setup

Canon 550D, DSLR camera, with kits lens (18-55mm) was used to shoot a sequence of astrophotography including sky images, dark images, bias images and flat images without using telescope [2]. All photographs were taken in RAW format. A set of images had processed by using IRIS, an open-source astronomical images processing program. The final processed images could be explained by following equation.

$$\text{Final processed image} = \frac{(\text{sky image - Bias image - Dark image})}{\text{Flat image}}$$

The final processed image further separated into red, green and blue. Only green component images were used for verifying instrumental v-apparent magnitude. The instrumental magnitude had calculated by using an aperture photometry method. An instrumental magnitude would be calibrated with standard V magnitude and color index (B-V) in standard catalog II/168 (Mermilliod 1991) [1]. Thus, the v apparent magnitude of target star could be found by using the calibration curve.

Observation

There were twelve constellations had been studied during November 2012, Andromeda, Aquila, Aries, Auriga, Canis Major, Cassiopeia, Cepheus, Cygnus, Gemini, Orion, Sagitta and Triangulum. The location for observation was Khon Kaen University Observatory at Chulabhorn Dam, Chaiya Phum Province, about 140 km west from the city of Khon Kaen. Each constellation, one dim star had been chosen as target star while the others were calibrating stars. One or more constellations had been taken in the same frame by adjusting the focal length of camera's lens to be 50mm. The parameter of camera was set as: shutter speed = 10 seconds, f/3.5 and ISO = 800. There were 15 frames of sky image for each constellation [3]. The sky, bias, dark and flat frame would be analyzed by using IRIS, astronomical images processing software, to verify an instrumental magnitude.

Results and Discussion

Results

The observational results of twelve constellations were analyzed and then created calibration curved for each constellation. For example, the figure 1 shown calibration curve made of the stars in Aries. An aperture size, inner annulus and outer annulus were set to be 10, 13 and 20 pixels respectively. Because this pilot studied aimed to study the precision of DSLR photometry such that all target stars were not variable or binary stars.

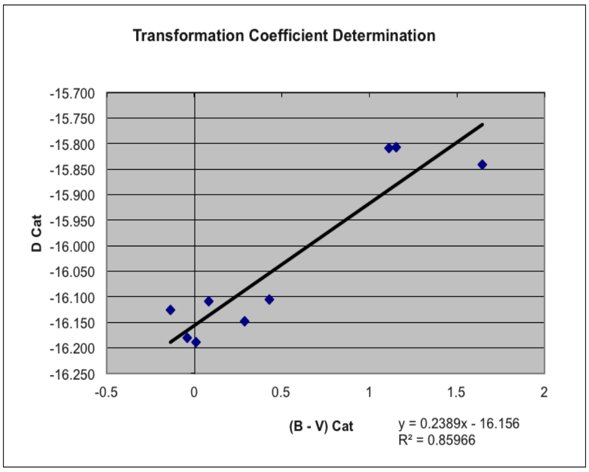

Figure 1. Calibration curve of the stars in Aries

The V apparent magnitudes of selected target stars were calculated and shown in Table 1. It was found that the target stars that had an error with range of ±0.01 were including, δ And, δ Aql, γ Cyg and γ Sge.

In addition, the altitude of constellations those contained an error more than ±0.01 were lower than 75 degrees. It could be disturbed by air mass because there were had high humidity around the reservoir of Chulabhorn Dam. However, this studied was set for developing a photometry laboratory for novice, so that, an air mass could be neglected by observing at high altitude.

Table 1: Standard apparent magnitude compared with experimental apparent magnitude and standard error of the values.

Constellations	**Target stars**	**App Mag (standard)**	**App Mag (Exp)**	**Std Err**
Andromeda	α And	2.073	2.055	0.012
	δ And	3.267	3.252	0.014
Aquila	γ Aql	2.718	2.499	0.012
	δ Aql	3.360	3.402	0.015
Aries	α Ari	2.008	2.073	0.054
	15 Ari	5.701	5.617	0.060
Auriga	λ Aur	4.705	4.690	0.024
	ε Aur	2.084	3.001	0.032
Canis Major	β Cma	1.976	1.493	0.116
	α Cma	-1.449	-1.264	0.037
Cassiopiea	β Cas	2.268	2.091	0.201
	γ Cas	2.483	2.726	0.313
Cepheus	α Cep	2.453	2.463	0.098
	γ Cep	3.212	3.463	0.074
Cygnus	α Cyg	2.868	1.055	0.012
	γ Cyg	2.208	2.066	0.007
Gemini	β Gem	1.143	1.420	0.091
	γ Gem	1.928	1.641	0.100
Orion	γ ori	1.636	1.586	0.106
	κ ori	2.062	1.988	0.113
Sagitta	δ Sge	3.828	3.760	0.014
	γ Sge	3.476	3.443	0.018
Triangulum	α Tri	3.416	3.336	0.088
	β Tri	2.998	3.079	0.069

Conclusions

As a result, the digital single lens reflex camera could be used as photometry tools. It could be set up as an advance physics laboratory level to study the physical properties of stars. However, it was limited to be used for stars at high altitude. The next study would be include air mass and optical limitation of using DSLR in photometry.

References

1. Citizen Sky (2009) Available at: http://www.citizensky.org (Accessed: 8 April 2012).
2. G. D. Roth, "Handbook of Practical Astronomy", London, Springer-Verlag, 2009.
3. R. Berry and J. Burnell, "The Handbook of Astronomical Image Processing", 2nd Edition, Richmond, Willmann-Bell, 2011.

Determination of the Size of the Broad-line Region and the Mass of the Central Black Holes of Active Galactic Nuclei by the Observations at the Crimean Astrophysical Observatory

N. Pulatova[1,2*], S. Sergeev[1], V. Doroshenko[5], S. Klimanov[4],
V. Pronik[1], I. Pronik[1], and I. Vavilova[3]

[1]Crimean Astrophysical Observatory, Nauchny, Crimea, 98409, Ukraine
[2]National Astronomical Research Institute of Thailand, Siripanich Building 191
Huay Kaew Road, Muang District, Chiangmai, 50200, Thailand
[3]Main Astronomical Observatory of the NAS of Ukraine,
27 Akademika Zabolotnoho St., Kyiv, 03680, Ukraine
[4]Central Astronomical Observatory of Pulkovo, Pulkovskoe Shosse 65 196140 St. Petersburg, Russia.
[5]South Station of the Moscow MV Lomonosov State University, Moscow, Russia, P/O Nauchny, 98409 Crimea, Ukraine
**Corresponding author. E-mail:* nadya@mao.kiev.ua

Abstract

The activity in galactic nuclei (AGN) has been studied extensively by many research teams since its discovery. The determination of the size of the so-called “broad-line region” (BLR) and the mass of the central supermassive black hole (SMBH) is one of the most important research area of AGN study. In fact, a lot attention was paid in the last years to this problem and masses of more than 30 SMBH of AGNs were estimated for the first time using the reverberation-mapping method during the long-time international monitoring programs. These data allow us to obtain the “Luminosity – Black Hole Mass” relationship and hence to determine positions of different types of AGNs relatively to the Eddington limit. The Crimean Astrophysical Observatory (CrAO) has traditionally had one of the leading positions in stydying of the AGN phenomenon since the 1960's. The term BLR, which is now widely used, appeared after pioneer works of Crimean astronomers V.Pronik and E.Dibai. Here we present some results of our researches based on the regular optical observations made with the ZTSH (2.6-m) and AZT-8 (0.7-m) telescopes of the CrAO.

Keywords: reverberation-mapping method, AGNs, supermassive black hole

Introduction

Approximately 30% of all galaxies have supermassive black holes (SMBHs) in their nuclei. SMBH manifests itself only by its gravitational field in most cases, but the black hole causes the glow of gas around it allowing to analyze properties of active galactic nuclei (AGN) and to evaluate the SMBH mass (see, for example, review in [16,29]). AGN are the brightest objects in the Universe, with extreme physical conditions (gravitational field of the SMBH, speeds close to the speed of light, high gas temperature, etc.) that cannot be created in an experience on the Earth. This fact makes the investigations connected with AGNs undoubtedly important and actual [5]. Many achievements have been made in understanding the AGN phenomenon of over the last 30 years. At present, the generally accepted model of the nucleus of active galaxy (often called “central engine”) is a system consisted of a SMBH in the center and a dusty and gaseous accretion disk around it. This model explains the existence of the correlation between observed fluxes in the continuum and the broad lines, as well as a delay between them.

The "Mass of the central black hole versus optical AGN luminosity" (“mass-luminosity” for short) correlation is often discussed within the development of different AGN`s models. Therefore the study of this relationship is very urgent problem. Equally important is to clarify the question why the SMBHs in the nuclei of normal galaxies are not active. Comparative analysis of the properties of active and normal galaxies should be done to solve this issue.

Traditionally, CrAO occupies one of the leading positions in the study of AGN properties and conducts its own investigations in this field since the 1960's. The joint efforts of several observatories (from US, Israel, Britain, Canada, Russia, Ukraine (CrAO) and others) provide intensive monitoring of AGNs. As a result, the masses of more than 30 central black holes were estimated by means of the reverberation-mapping technique. CrAO has made a significant contribution to these international projects. Black holes masses were calculated for the first time in two of these AGNs only by CrAO efforts [10,22].

It allowed to improve a general AGN model and SMBH phenomenon, to check the theoretical models, and to describe a distribution of visible/dark matter.

In this paper we give the main results of our past and present research based on the observations at the 2.6-m ZTSH and 0.7-m AZT-8 telescopes (CrAO).

Reverberation-mapping method

Several methods were proposed for determination of the central SMBH mass in AGNs in early studies [1,8,15,28]. However, the most direct method for determination SMBH masses is reverberation-mapping technique [3,14,18,19] which is based is based on the observing the response of the broad emission lines to the continuum changes. High-energy continuum ionizes and heats nuclear gas and produces these lines (the BLR) that stretches up to several hundred gravitational radii from a black hole. In the gravity-dominated motion the mass is related to the distance $c\tau$ and velocity σ_{line} by the following equation:

$$M_{BH} = \frac{f c \tau \sigma_{line}^2}{G}$$

where G is the gravitational constant, c is the speed of light, τ is a delay between the line and continuum flux variations, σ_{line} is the measured line profile dispersion. It was shown that [25]: $f=1.5$ for the spherically symmetrical free-fall motion of gas in the BLR, $f=3$ for Keplerian orbits with random inclinations, and $f=2.0/\sin^2 i$ for the Keplerian disk with the inclination angle i to the line-of-sight. Onken et al. 2004 [17] have calibrated the factor f by comparing the “reverberation” masses and masses obtained by the measurement of the star velocity dispersion in the spherical component of galaxies and it was found to be: $f=5.5\pm1.7$. The value of this coefficient has been updated by [12,27].

Results and Discussion

CrAO conducts its own photometric and spectral monitoring campaign of several AGNs since the 1990's. In particular, the mass of the central black hole and the size of the BLR were calculated by the reverberation-mapping method for Mrk 817 and Mrk 290 within the framework of international cooperation with the US, Canada, and Israel for the first time [10]. Significantly more reliable estimates of the masses and BLR sizes were obtained for NGC 4051, NGC 3227, NGC 3516, and NGC 5548 [2,9,10]. These results play an important role for the determining and interpreting of the "mass-luminosity" and the “BLR size – luminosity” diagrams for AGNs. Furthermore, new results of spectral and photometric monitoring of 3C 390.3 were obtained on the base of observational program in the CrAO during 1992-2007 [23,24]. The time delay was recalculated between flux changes in the Hβ and Hα lines and continuum: 94 ± 6 and 174 ± 16 days respectively. The central black hole mass was estimated through Hβ line $M_{BH}=2*10^9\ M_{sun}$.

In other research the time delay was detected between flux variations in the optical and X-ray bands for several Seyfert galaxies [4,6] for the first time. Additionally, time delay was confirmed between R and I bands relatively to B in the nucleus of NGC 7469 [11] as well as multi-frequency properties for 3C 454.3 were analyzed [30]. Thus, the new evidence was presented in favor of reprocessing model from X-ray radiation into the optical due to Compton scattering in the accretion disk.

We estimated the central black hole mass and found the position of 1E 0754.6+3928 in the “mass-luminosity” diagram using the results of spectroscopic and photometric observations performed at CrAO in 1998–2004 [22]. We classify this object as a narrow-line Seyfert 1 (NLS1) galaxy on formal spectroscopic criteria. The time lag in the Hβ line relative to the continuum flux variations, found from the cross-correlation function centroid, is $\tau_{cent} = 112^{+215}_{-67}$ days. 1E 0754.6+3928 showed very low rms flux variability amplitude in both continuum and Hβ line (~3%) over the observational period. The mass of its central black hole is $M_{BH}=1.05 \times 10^8 M_{sun}$. The position of 1E 0754.6+3928 agrees with the positions of other NLS1 galaxies (Figure 1) and can be explained by an enhanced mass accretion rate on the central source.

The velocity dispersion, sizes of BLR, black hole mass are presented in Table 1.

Table 1: The list of some AGNs for which the SMBH masses and BLR-parameters were obtained with participation of the CrAO.

Galaxy	**σ_{line}, km/s**	**BLR size light days**	**BH mass $*10^7 M_{sun}$**	**Ref**
1E0754	980	112^{+215}_{-67}	10.5	[22]
NGC4051	927	1.75±0.5	0.160±0.05	[9]
NGC5548	1822	6-30[1]	6.54±0.27	[2]
NGC3516	1591	$11.6^{+1}_{-1,5}$	$3.17^{+0.3}_{-0.4}$	[10]
NGC3227	1376	14±3.45	0.76±0.17	[10]
Mrk 817	2025	$14^{+3.41}_{-3.47}$	4.33±1.06	[10]
Mrk 290	1609	$8.72^{+1.2}_{-1}$	2.43±0.37	[10]

[1] For maximum and minimum brightness of the nucleus.

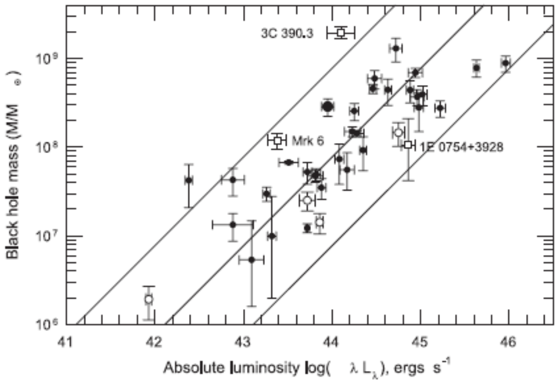

Figure 1. Luminosity-black hole mass diagram, the data for reverberation-mapping are from [20]. With open circles are marked NLS1 type AGNs, with squares are marked the AGNs for which the masses of the central black holes were measured in the CrAO [23,24,25]. The filled circle represent data for 3C 390.3 [23]. L_{Edd}, $0.1L_{Edd}$, $0.01L_{Edd}$ are presented the Eddington limit.

In 2011 a new observational program was initiated in the CrAO that concerns with the determination of SMBH mass of isolated galaxies with active nuclei. The sample of isolated AGNs [7, 21] was compiled from the 2MIG Catalog [13] and contains about 60 galaxies at $z<0.08$. Observations of these objects will allow revealing those AGN's properties which could be explained by the intrinsic physical processes in AGNs, because these objects have no a gravitational influence from neighboring galaxies during 2-3 billion years. This program includes NGC 5231, Mrk 845, Mrk 1018, Mrk 42, UGC 10120, PGC 86291, IC 5287 of the Northern sky (CrAO) and can be extended on the Southern sky thanks to the collaboration with the NARIT.

Conclusions

Crimean Astrophysical Observatory has made a major step towards improving its own instrumental base and methods of data processing and analyzing. Such improvements allow to achieve high levels of data accuracy and reliability. We obtained the updated and reliable estimates of the BLR sizes and central black hole masses for several AGNs.

We believe that our project data are of importance for understanding and further investigation of the AGN phenomenon. They can be used in studying geometry and kinematics of the inner regions of AGNs as well as to improve such fundamental correlations as "mass-luminosity" and "the BLR size-luminosity". These relationships can be used to deduce some essential properties of active nuclei. For example, it was found that the nucleus of 3C390.3, which has wide two-humped profiles of hydrogen lines, is on the upper edge in the "mass-luminosity" diagram. This result may imply that AGNs of such type have extremely low accreting rate (for a given black hole mass).

Our results can be of interest to physicists as well since those extreme physical conditions that exist in the "central engine" of AGN are unattainable in the laboratories on the Earth.

References

1. S. M. V. Aldrovandi, S. M. Viegas, "Supermassive Black Holes and Emission Lines of Active Galaxies and QSOs: Accretion Rate, Black Hole Mass and Photoionization Models", Astronomy and Astrophysics **97** (1981) 122.
2. M. C. Bentz, K. D. Denney, E. M. Cackett, M. Dietrich, J. K. Fogel, H. Ghosh, K. D. Horne, Ch. Kuehn, T. Minezaki, Ch. A. Onken, B. M. Peterson, R. W. Pogge, V. I. Pronik, D. O. Richstone, S. G. Sergeev, *et al.* "NGC 5548 in a low-luminosity state: Implications for the broad-line region", Astrophysical Journal **662** (2007) 205.
3. R. D. Blandford, C. F. McKee, "Reverberation mapping of the emission line regions of Seyfert galaxies and quasars", Astrophysical Journal **255** (1982) 419.
4. E. Breedt I. M. McHardy, P. Arevalo, P. Uttley, S. G. Sergeev, T. Minezaki, Y. Yoshii, Y. Sakata, P. Lira, N. G. Chesnok, 'Twelve years of X-ray and optical variability in the Seyfert galaxy NGC 4051', Monthly Notices of the Royal Astronomical Society **403** (2010) 605.
5. N. G. Chesnok, S. G. Sergeev, I. B. Vavilova, "Photometric and kinematic properties of non-isolated and isolated AGNs", AIP Conf. Proc. **1206** (2010) 328.
6. N. G. Chesnok, S. G. Sergeev, I. B. Vavilova, "Optical and X-ray variability of Seyfert galaxies NGC 5548, NGC 7469, NGC 3227, NGC 4051, NGC 4151, Mrk 509, Mrk 79, and Akn 564 and quasar 1E

0754", Kinematics and Physics of Celestial Bodies **25** (2009) 107.

7. N. G. Chesnok, "General properties of the sample of isolated galaxies with active nuclei", Kosmichna Nauka i Tekhnologiya **16** (2010) 77.
8. E. A. Dibai, Soviet Astronomy **24** (1980) 389. (translated from Astronomicheskii Zhurnal **55**, 677).
9. K. D. Denney, L. C. Watson, B. M. Peterson, R. W. Pogge, D. W. Atlee, M. C. Bentz, J. C. Bird, D. J. Brokofsky, M. L. Comins, M. Dietrich, V. T. Doroshenko, J. D. Eastman, Y. S. Efimov, C. M. Gaskell, C. H. Hedrick, S. A. Klimanov, E. S. Klimek, A. K. Kruse, J. B. Lamb, K. Leighly, T. Minezaki, S. V. Nazarov, E. A. Petersen, P. Peterson, S. Poindexter, Y. Schlesinger, K. J. Sakata, S. G. Sergeev, J. J. Tobin, C. Unterborn, M. Vestergaard, A. E. Watkins, Y. Yoshii, "A Revised Broad-line Region Radius and Black Hole Mass for the Narrow-line Seyfert 1 NGC 4051", Astrophysical Journal **702** (2009) 1353.
10. K. D. Denney, B.M. Peterson, R.W. Pogge, *et al.*, "Reverberation mapping measurements of black hole masses in six local seyfert galaxies", Astrophysical Journal **721** (2010) 715.
11. V. T. Doroshenko, S. G. Sergeev, Ye Vovk, Yu. S. Efimov, S. A. Klimanov, S. V. Nazarov, "X-ray and optical variability of the Seyfert galaxy NGC 7469", Pis`ma v Astronomicheskii zhurnal **36** (2010) 643.
12. A. W. Graham, C. A. Onken, E. Athanassoula, F. Combes, "An expanded Mbh-σ diagram, and a new calibration of active galactic nuclei masses", Monthly Notices of the Royal Astronomical Society **412** (2011) 2211.
13. V.E. Karachentseva, S.N. Mitronova, O.V. Melnyk, I.D. Karachentsev. The Catalog of Isolated Galaxies selected from 2MASS. Astrophysical Bulletin **65** (2010) 1.
14. S. Kaspi, W. N. Brandt, Dan Maoz, H. Netzer, D. P. Schneider, O. Shemmer, "Reverberation Mapping of High-Luminosity Quasars: First Results", Astrophysical Journal **659** (2007) 997.
15. S. A. Lushchenko, M. Maksumov Akademiia Nauk Tadzhikskoi SSR, Doklady **21** (1978) 25.
16. Fulvio Melia, "The Galactic Supermassive Black Hole", Princeton University Press (2007).
17. C. A. Onken, L. Ferrarese, D. Merritt, B. M. Peterson, R. W. Pogge, M. Vestergaard, Amri Wander, "Supermassive Black Holes in Active Galactic Nuclei", Astrophysical Journal **615** (2004) 645.
18. E. Perez, A. Robinson, L. de la Fuente, "The response of the broad emission line region to ionizing continuum variations. III - an atlas of transfer functions", Monthly Notices of the Royal Astronomical Society **256** (1992) 103.
19. B. M. Peterson, "Reverberation Mapping of Active Galactic Nuclei", Publications of the Astronomical Society of the Pacific **105** (1993) 247.
20. B. M. Peterson *et al.*, "Central Masses and Broad-Line Regions Sizes of Active Galactic Nuclei. II. A Homogeneous Analysis of a Large Reverberation-Mapping Database", Astrophysical Journal **613** (2004) 682.
21. N. Pulatova, I. Vavilova, P. Berczik, Statistical study of isolated and non-isolated AGNs in the Local Universe. Proceedings IAU Symposium **290** (2013) 297.
22. S. G. Sergeev, S.A. Klimanov, N.G. Chesnok, V.I. Pronik, "Optical variability of the Active Galactic Nucleus 1E 0754+3928 and reverberation-based mass estimate for the central black hole", Astronomy Letters **33** (2007) 429.
23. S. G. Sergeev, S. A. Klimanov, V. T. Doroshenko, Yu. S. Efimov, S. V. Nazarov, V. I. Pronic, "Variability of the 3C 390.3 nucleus in 2000-2007 and a new estimate of the central black hole mass", Monthly Notices of the Royal Astronomical Society **410** (2011) 1877.
24. S. G. Sergeev, V. I. Pronik, B. M. Peterson, E. A. Sergeeva, W. Zheng, "Variability of the Broad Balmer Emission Lines in 3C 390.3 from 1992 to 2000", Astrophysical Journal **576** (2002) 660.
25. S. G. Sergeev, V. I. Pronik, E. A. Sergeeva, Yu. F. Malkov, "A Link between the Hβ Equivalent Width, Profile Width, BLR Size, and Optical Luminosity from a Small Sample of Well-studied Active Galactic Nuclei", Astronomical Journal **118** (1999) 2658.
26. S. G. Sergeev, S. A. Klimanov, V. T. Doroshenko, Yu. S. Efimov, S. V. Nazarov, V. I. Pronik, "Variability of the 3C 390.3 nucleus in 2000– 2007 and a new estimate of the central black hole mass", Monthly Notices of the Royal Astronomical Society. **410** (2011) 1877.
27. J. H. Woo, T. Treu, A. J. Barth, Sh. A. Wright, L. J. Walsh, M. C. Bentz, P. Martini, V. N. Bennert, G. Canalizo, *et al.*, "The Lick AGN Monitoring Project: The M BH-σ* Relation for Reverberation-mapped Active Galaxies", Astrophysical Journal **716** (2010) 269.
28. A. S. Zentsova Pis`ma v Astronomicheskii Zhurnal **8** (1982) 535.
29. Ya. S. Yatskiv, A. N. Alexandrov, I. B. Vavilova, V. I. Zhdanov *et al.*, "General

Relativity Theory: Tests through Time”, Kyiv, MAO NAS of Ukraine (2005) 288 p.

30. A. E. Vol'vach, L. N. Vol'vach, A. M Kut'kin, N. G. Larionov *et al.* Multi-frequency studies of the non-stationary radiation of the blazar 3C 454.3. Astronomy Reports **55** (2011) 608.

The BIMA Project: I. Project’s Detail and Firtst Report

J. Suherli[1*], H. L. Malasan[1,2], M. Putra[1,2], P. Irawati[3], T. Sarotsakulchai[3], A. Richichi[3],
B. Soonthornthum[3], M.C. Nysewander[4], A.P. LaCluyze[4], and K.M. Ivarsen[4]

[1]Bosscha Observatory, Jalan Peneropongan Bintang, Lembang 40139, Indonesia
[2]National Astronomical Research Institute of Thailand, 191 Siriphanich Bldg., Huay Kaew Rd., Chiang Mai 50200, Thailand
[3]Astronomy Study Program, Bandung Institute of Technology, Labtek III Jalan Ganeca no 10, Bandung 40132, Indonesia
[4]PROMPT-5, Dept. of Physics and Astronomy, UNC-Chapel Hill, NC, USA
**Corresponding author. E-mail: janette@as.itb.ac.id*

Abstract

The Eclipsing Binaries’ Minima Monitoring Project (BIMA) is an observational program started at Bosscha Observatory (Lembang, Indonesia) in June 2012. It is a long term observational project of eclipsing binaries which be done to improve our understanding on this class of objects, specifically to establish the orbital period of each system and its variations. The main purpose of the project is to build an open-database of eclipsing binaries’ minima, collected from observations conducted at Bosscha Observatory and collaborating observatories. So far, the main partner has been the National Astronomical Research Institute of Thailand (NARIT) which joined the project in December 2012. In this paper we present the details of the project and the report for the first semester of activity.

***Keywords*:** Methods, observational, techniques, photometric, stars, binaries, eclipsing, Bosscha Observatory, NARIT

Introduction

The study of eclipsing binaries has been an intriguing field in Astronomy for such a long time. Their vast numbers in the universe and the fundamental stellar properties that can be derived from them have made eclipsing binaries important objects to observe.

In general, the photometric observations of eclipsing binaries have two major goals, which are to determine the time of minimum (TOM), and to obtain the entire light curve [1]. TOM determination is done in order to establish the orbital period and its variation. In many systems, period changes are frequently detected, which indicated by eclipses that occur earlier or later than the expected time (Observed minus Calculated, O-C). These changes may due to the influence of a third body in the system, mass exchange between the components, or even an abrupt single change on the system. Hence, the observations of minimum light timing are important to make a better understanding of the period of eclipsing binary stars.

The advances in instrumentations and observing techniques have brought astronomers into many new and exciting insights about the eclipsing binaries. Since the 1900s, TOM observations have been recorded and various observation methods (visual, photographic plate, photographic, photoelectric, CCD observations) have been used. It is true that the TOM of eclipsing binaries can be determined much more accurately from CCD observations than from the other methods. Hence, CCD observations are prefered in this research.

Since its establishment in 1923, Bosscha Observatory (6°49’28”S and 107°36’56”E) has been continuously active in binary stars observations. Eclipsing **BI**naries’ Mini**ma** (BIMA) Monitoring Project is an observational program that focuses on photometric obsevation of eclipsing binaries, specifically the TOM observations. Essentially, BIMA research program is a continuation from Suherli’s undergraduate thesis research [4]. The main objectives of the project are to calculate the observed TOM of eclipsing binaries and to make an open-database of eclipsing binaries’ minima. BIMA project had started in June 2012 and open for collaboration since. As yet, the main partner of the project has been the National Astronomical Research Institute of Thailand (NARIT) which joined in December 2012.

Instruments

Bosscha Observatory

We used the 0.2 m (8-inch) f/10 Schmidt-

Cassegrain telescope installed at Gunma Astronomical Observatory – Institut Teknologi Bandung Remote Telescope System (GAO-ITB RTS) house, equipped with SBIG ST series CCDs. Alternately, several portable telescopes with similar specifications with previous are available.

NARIT

NARIT has privilege in using the Panchromatic Robotic Optical Monitoring and Polarimetry Telescope (PROMPT) (30°10'03.50"S and 70°48'19.40"E) which being built by the University of North Carolina at Chapel Hill and installed at Cerro Tololo Inter-American Observatory in Chile. We have been using this telescope since late December 2012. In the future, we plan to use the 0.5 m Schmidt-Cassegrain telescope equipped with Apogee CCD located at Thailand National Observatory (TNO) (18°35'32"S and 98°29'12"E).

Eclipsing Binaries on the Project

More than 200 eclipsing binary systems have initially been selected for the BIMA project. The *General Catalogue of Variable Stars* (GCVS) and the *All-Sky Automated Survey* (ASAS) database have largely been used to compile the object list. Some selection criteria had been applied to obtain the list: all those which are brighter than 11th magnitude at maximum and have an amplitude of at least 0.4 magnitude, all those systems with orbital period of less than two days and which have declination ranging from +60 degrees to -60 degrees.

We exclusively focused on eclipsing binary systems which have rather small number of observed TOM.

Calculated Time of Minimum

The predictions of calculated TOMs are essentials in planning the observations of eclipsing binaries. The precise timing allows a system to be observed efficiently, as such, up-to-date ephemerides are important [2]. Using the ephemerides given in Kreiner (2004) for all the systems, the observer can calculate a quite accurate predicted TOM. We use his ephemerides which are provided at `http://www.as.up.krakow.pl`.

In addition to Kreiner ephemerides, we use ephemerides software from David Motl. For several objects which are not in agreement with the GCVS or ASAS period, the observer should first observe the system according to the updated period from literature (if available) and then make a correction to the period based on the observation.

Observations

All the charts for each system have been generated from the American Association of Variable Star Observers (AAVSO)'s online Variable Star Plotter (VSP) page: `http://www.aavso.org/vsp`. The differential photometry method is applied for all BIMA project's observations. Hence, a comparison star and a check star are required. A star of nearly the same color and brightness as the target star is selected as comparison star. The comparison star should be as near to the target star as possible, prefereably within seventeen arc-minutes, which suits the field of view of default CCD camera and telescope combination for this project. A check star with the same criteria as the comparison star should be selected as a test of the nonvariability of the comparison star. Observers can choose the comparison and the check stars which also available from the AAVSO's online VSP service. Otherwise, the comparison and the check stars can be selected by checking the variability of nearby stars using simbad database (`simbad.u-strasbg.fr`).

On each night, there is more predicted TOM than a single observer can hope to cover. Here is the accurate TOM calculation come into play. Generally, priority is given to stars which have fewer observable eclipses and it is suggested that, once the observer has secured two good timings for one object, no more observations of that system should be made that year. This will help to cover an even spread of TOM observations among the objects on the BIMA project.

The observation should cover on average 0.25 to 0.3 times the period of each system, with symmetric amount of time for before and after the predicted TOM. It is important to secure a good series of data on both descending and ascending branches of the light curve, to derive a more accurate timing.

Data Reductions

We performed the standard reduction of CCD images (bias and dark subtraction, flat-fileding) using the Image Reduction and Analysis Facility (IRAF). Then, the instrumental magnitudes of each system from each observation are obtained by applying the aperture photometry method. We used IRAF's apphot package, with batch photometry mode (non-interactive). We also used the IRIS software to recheck the instrumental magnitudes.

After calculating the magnitude difference, the light curve is build with HJD (Heliocentric Julian Date) as x-axis and delta instrumental magnitude as y-axis. Then the observed TOM is determined using the Kwee – van Woerden method [3].

Preliminary Results

Up to mid-February 2013, we have observed 32 eclipsing binaries in several filters, and V filter for most systems. We acquired the data from Bosscha Observatory since 2010 and PROMPT since

December 2012. The summary of the object we have is presented in the Table 1.

Table 1 : List of objects acquaired up to mid-February 2013 and details on observation date and location.

Object		Observation Date(s)	Observation Location
AB	And	Aug 8th 2012	Bosscha Observatory, ID
AH	Pup	Jan 6th, 7th, 8th 2013	PROMPT, CL
AN	Pup	Jan 8th, 10th, 24th, 28th 2013	PROMPT, CL
AO	Vel	Feb 8th, 15th, 16th 2013	PROMPT, CL
AR	CMa	Jan 5th, 6th, 12th, 13th, 20th, 26th, 27th 2013	PROMPT, CL
CS	Pup	Jan 12th, 16th, 20th, 2013	PROMPT, CL
CT	Cet	Nov 11th 2012	Bosscha Observatory, ID
ER	Ori	Oct 10th, 13th 2012	Bosscha Observatory, ID
FR	Ori	Oct 13th 2012	Bosscha Observatory, ID
GU	Ori	Oct 18th 2012	Bosscha Observatory, ID
HM	Pup	Jan 8th, 21st, 26th, Feb 17th 2013	PROMPT, CL
HS	Aqr	Sept 21st 2012	Bosscha Observatory, ID
KX	Pup	Jan 17th 2013	PROMPT, CL
LT	Pup	Jan 10th, 11th, 28th, 29th 2013	PROMPT, CL
MR	Del	Jul 26th, Aug 10th 2012	Bosscha Observatory, ID
TT	Hor	Feb 5th, 11th, 15th, 19th 2013	PROMPT, CL
TU	CMa	Dec 31st 2012, Jan 6th, 7th, 10th, 11th, 23rd, 25th 29th 2013	PROMPT, CL
UU	Aqr	Jul 19th, Sept 10th 2012	Bosscha Observatory, ID
V1073	Cyg	Aug 11th 2012	Bosscha Observatory, ID
V1363	Ori	Sept 13th, Oct 13th 2012	Bosscha Observatory, ID
V1847	Ori	Oct 14th 2012	Bosscha Observatory, ID
V337	Aql	Sept 16th 2012	Bosscha Observatory, ID
V343	Ori	Oct 12th 2012	Bosscha Observatory, ID
V392	Ori	Oct 18th 2012	Bosscha Observatory, ID
V395	And	Jul 21st, Aug 10th 2012	Bosscha Observatory, ID
V417	Aql	Aug 8th 2012	Bosscha Observatory, ID
V566	Oph	Jul 21st 2012	Bosscha Observatory, ID
V579	Pup	Jan 4th, 5th, 16th, 30th, 31st 2013	PROMPT, CL
V701	Sco	Sept 13th 2012	Bosscha Observatory, ID
V857	Her	May 16th, 27th, Jun 18th 2012	Bosscha Observatory, ID
V899	Her	Apr 25th, May 3rd, 4th, 12th 2011, Mar 29th, Apr 24th, May 16th, Jul 19th, 30th, Aug 8th, 2012	Bosscha Observatory, ID
WW	Eri	Nov 4th 2012	Bosscha Observatory, ID

Reporting Observations

A page at the official Bosscha Observatory webpage: `http:bosscha.itb.ac.id` will be launched in mid-2013. The TOM data will be accessible by public and a query form addressed to the primary investigator of BIMA project will be available.

The TOMs of various eclipsing binary systems, if possible, will be published in appropriate journal as a collection of minima.

Conclusions

TOM observation is very important for investigating the behaviour of any eclipsing binaries' orbital period. A plot between observed and calculated TOM residual against the time (O-C diagram) is used to indicate whether the period of certain system is right, is too short or is too long, is decreasing or increasing, is varying sinusoidally or otherwise.

BIMA project is an observational program started at Bosscha Observatory, Indonesia, as a continuation of Suherli's undergraduate thesis research. The project aims for a collection of TOMs that can be accessible by anyone and optimising the utilisation of small aperture telescopes. The project is hoped to cover 200 systems and more in the next few years.

Acknowledgments

The authors would like to deeply thank all the observers at Bosscha Observatory who actively participated in the observations of BIMA project.

References

1. Henden, Arne A. and Ronald H. Kaitchuck, "Astronomical Photometry", New York, Van Nostrand Reinhold Company Inc., 1982.
2. Kreiner, J. M., "Up-to-Date Linear Elements of Eclipsing Binaries", Acta Astronomica Vol.**54** (2004), 207-210.
3. Kwee, K. K., H. van Woerden, "A Method for Computing Accurately the Epoch of Minimum of an Eclipsing Variable", Bulletin of The Astronomical Institutes of The Netherlands vVl. **XII** Num.464 (1956), 327-330
4. Suherli, Janette, 2011, "New O-C Diagram Analysis of V899 Herculis Multiple Stellar System", B.Sc. thesis, Institut Teknologi Bandung, Indonesia.

Orbital Period Change and Evolution of a Binary System FZ Orionis

K. Homsantia, B. Choonhkit*, and T. Rangsungnoen
Physics and General Science Program, Science and technology Faculty,

Nakhon Ratchasima Rajabhat University, Nakhon Ratchasima,Thailand,30000
**Corresponding author. E-mail: Boonyarit_20jt@hotmail.com*

Abstract

The aims of Orbital period change study of a Binary System of FZ Orionis, and it's evolution. Observation were done via Richey - Chertian diffraction telescope 0.5 m connect to CCD Photometry by BVR system at Sirindhorn observatory. The results was three time of minimum by 1st Pirmary eclipe and 2nd Secondary eclipe, The O-C characteristic were increase paraboric variation. The result has show that obtiant orbital period change is 4.8416×10^{-19} sec/year or 0.39998 day,The O-C light curve had show that a third body on this system and it's sin wave pattern. The firth results of WD program has show that 0.14 ratio, 68.24 ± 0.359 degree of inclination, and second data parameter has show that 0.14 ratio, 67.33 degree of inclination. Finaly, an analysis characteristic for FZ Orionis is W Uma type and its evolution were Close binary system.

Keywords: binary system, third body, contact binary system, semi - detached binary system

Introduction

The FZ Orionis binary star system is an eclipsing close binary system that the study is very little. Hoffmeister (1934) FZ Orionis is variable star. Kippenhahn (1953) have revealed the orbital period change of FZ Orionis is BetaLyrae (EB) system with a period of 1.59 day Figer and Le Brogne show that FZ Orionis is W Uma with a period of 0.399986 day. El –Bassuny and Alawy (1993) an orbital period change of FZ Orionis is continuously decreased at a rate of -2.6×10^{-5} day/year. ShengbangQian (2003) From the analysis of physical parameters and model, it was found that FZ Orionis have orbital period change continuously decreased at a rate of 5.1×10^{-7} day/year.

Materials and Methods

Observation of FZ Orionis were done at Sirindhorn Observatory, chiang Mai University Using a 0.5-meter reflecting telescope with CCD photometric system in B,V, and R wavelength bands. Observations were done from 12 February 2012 to 14 February 2012. The observed data were taken to be sent to the image reduction process for noise eradicating. Magnitude of FZ Orionis were measured by Maxlm DL4 softwares respectively. The observed data were takan to analyse the time of minmum by the equation of Bob Nelson and A. Liakos, P. Niarchos;

$$\text{MinI} = \text{JD Hel } 2444024.4668 + 0.39998E \quad (1)$$

Calculate equation (1) for ephimeris equation, that

$$\text{Min} = \text{HJD}_0 + \text{PE} \quad (2)$$

Take the resulted data to add in MinI and Epoch of Bob Nelson and A. Liakos, P. Niarchos data by origin pro8.0 software to gain a new diagram of MinI and epoch relation. Calculate phase from;

$$phase = \frac{HJD_0 - HJD}{E} \quad (3)$$

The phase and magnitude data from the observed light curve, calculate orbital period change rating of FZ Orionis by

$$\frac{dP}{dE} = 2a \quad (4)$$

Take the observed data minus the calculated data to gain the result of the O-C diagram and O-C residual.

Results and Discussion

The result has shown that time of minimum of FZ Orionis in secoundary eclipsing : MinI = 2455970.19873, primary eclipsing : MinII = 2455971.19929 and secoundary eclipsing : MinIII = 2455972.1999 and epoch =29868.6 respectively. Take MinI, MinII and MinIII and epoch to add in Bob Nelson and A. Liakos, P. Niarchos data that show in fig.1.

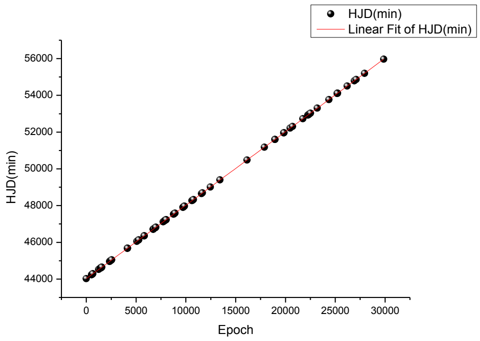

Fig.1 Relation of time of minimum and epoch for FZ Orionis

For the calculated data, orbital period of FZ Orionis binary system: FZ Orionis was 0.39998 day while the orbital period change of FZ Orionis from Bob Nelson and A. Liakos, P. Niarchos data (O) and calculated data (C) werw determined from the O-C diagram is show in fig.2.

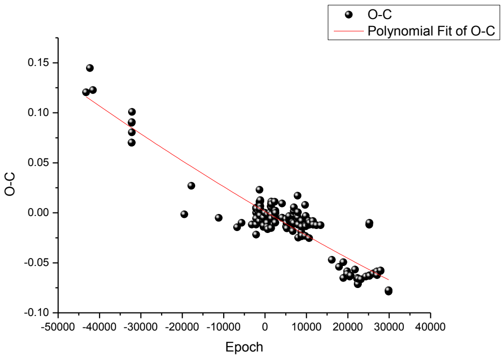

Fig.2 Graph of O-C and epoch relation

The data of light curve after the O-C residual process has a sine wave pattern as show in fig.3.

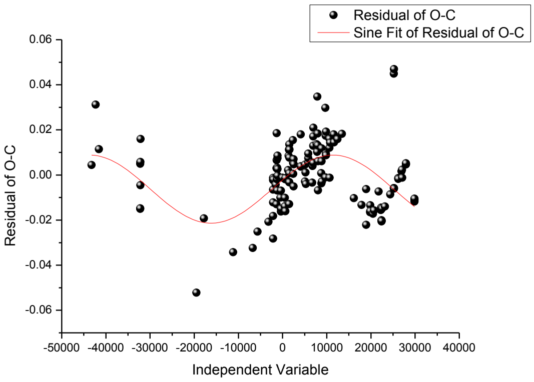

Fig.3 O-C residual of a W Uma binary system: FZ Orionis

From fig.3 this pattern may possibly caused by the existence of the third body on this W Uma binary system: FZ Orionis. Calculation of phase from observed data and magnitude from the light curve, the result has shown that light curve obtained through B,V and R filters were 0.5,0.5,and 0.5-depth respectively (fig.4-6)

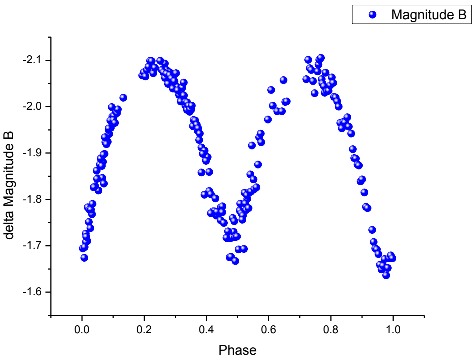

Fig.4 Observational light curve of FZ Orionis in B wavelength band

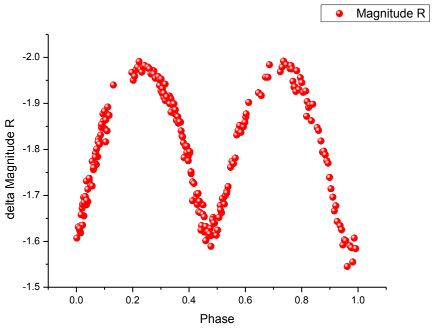

Fig.5 Observational light curve of FZ Orionis in R wavelength band

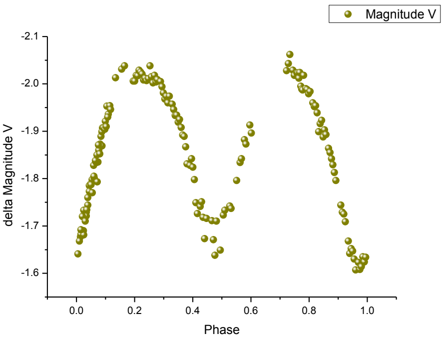

Fig.6 Observational light curve of FZ Orionis in V wavelength band

Photometric solutions

Wilson-Devinney program with DC code (mode 3 as W Uma-Type) was used to calculate physical parameters of FZ Orionis . some fixed parameters used in the calculation was taken from A. Liakos, P. Niarchos (2010)as T_1= 6108 K, Ω_2 = 0.15 ,g_1=0.32, A_1=0.50,A_2=0.50, x_{1v}=0.57 x_{2v}= 0.41 Several values of mass ratio q = 0.2,0.3,0.4,0.5,0.6,0.7,0.8,and 0.9 were used in calculations. The best solution of FZ Orionis is show in table1 and its surface potential and configuration are constructed using Binary Marker 3.0 program and are show in fig.7 and fig.8

Table 1: The best solution of FZ Orionis

parameters	**Best Solution**
$q = (m_2/m_1)$	0.147605 ± 0.0025
i (degree)	68.24 ± 0.359
T (K)	$6108 \pm 0.0010 \quad 5703 \pm 0.0015$
Ω	$2.123151 \pm 0.01 \quad 2.123151 \pm 0.01$
Ω_{in}	2.123151
Ω_{out}	2.123722
$L_{1B} / (L_{1B} + L_{2B})$	0.6371 ± 0.0001
$L_{1V} / (L_{1V} + L_{2V})$	0.6353 ± 0.0001
$L_{1R} / (L_{1R} + L_{2R})$	0.6356 ± 0.0001
$A_1 = A_2$	0.5, 0.5
$g_1 = g_2$	0.32, 0.32
r (pole)	$0.502173 \pm 0.2223 \quad 0.205597 \pm 0.0053$
r (side)	$0.549204 \pm 0.3749 \quad 0.212889 \pm 0.0062$
r (back)	$0.568151 \pm 0.5797 \quad 0.238542 \pm 0.0107$
$\sum$ *input* value	0.068198
$\sum$ *predict*	0.068197

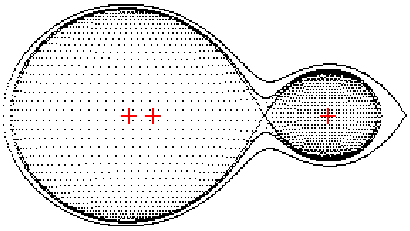

Fig.7 The surface potential of FZ Orionis.

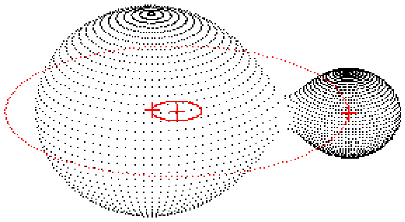

Fig.8 The configuration of FZ Orionis.

Conclusions

Orbital Period Change and Evolution of a Binary System FZ Orionis : was 0.39998 day Comparing to Bob Nelson and A. Liakos, P. Niarchos is data that presented in terms of the orbital period change, FZ Orionis has 1.01478×10^{-11} day/cycle. The data of light curve after the O-C residual process has a sine wave pattern, that means, may possibly caused by the existence of the third body nearby this W Uma binary system : The light curve has show that W Uma binary system: FZ Orionis was semi-detached type.

Acknowledgments

The author would like to sincerely thanks to Sirindhorn Observatory, Chiang Mai University, Thailand I would also like to thanks Mr.Thanawat Rangsungnoen, As well, thanks to Mr.Ronnakit Rattanamalar, Thanks Dr. Pattanapong Jumrusprasert, for kindly helps.

References

1. C. Hoffmeister, Astron Nachr., 253, 196, 1934
2. Liakos, P. Niarchos.(2006).The Light-Time Effect in the W UMa – type eclipsing binary FZ Ori. Astronomy and Mechanics : National & Kapodistrian University of Athens.
3. Byboth, K.N., Markworth, N.L., Bruton, W.B, 2004, IBVS, No 5554.
4. Konkoly. (2004) . Photometric Analyses of the Contact Binaries FZ Orionis and AH Tauri. Department of Physics and Astronomy. Stephen F : Austin State University, Nacogdoches.
5. Zakirov. (2009). Close Binary Systems in Multiple Stars:III. Eclipsing Variables with. LITE effect : National University of Uzbekistan.
6. Mas-Hesse, J.M. et al. (2003). An Optical Monitoring Camera for INTEGRAL. [online]. Available: http://www.aanda.org.
7. Wen-Cong Ghen and Xiang-Dong Li. (2006). Orbital evoluation of Algol Binaries

YZ Phe: PROMPT Data and Future Evolution

P. Irawati[1*], T. Sarotsakulchai[1], J. Suherli[2], A. Richichi[1], B. Soonthornthum[1],
M.C. Nysewander[3], A.P. LaCluyze[3], and K.M. Ivarsen[3]

[1]*National Astronomical Research Institute of Thailand, 191 Siriphanich Bldg., Huay Kaew Rd., Chiang Mai 50200, Thailand*
[2]*Bosscha Observatory, Faculty of Mathematics and Natural Sciences, Institut Teknologi Bandung,Lembang, Bandung, Indonesia*
[3]*PROMPT-5, Dept. of Physics and Astronomy, UNC-Chapel Hill, NC, USA*
**Corresponding author. E-mail: puji.irawati@narit.or.th*

Abstract

We present our observations of the eclipsing binary YZ Phe in the visual band from the robotic PROMPT-5 telescope at the Cerro Tololo Inter-American Observatory. We acquired an almost complete phase of the light curve during three nights of observation in September-October 2012. The light curve of YZ Phe shows a 5.63 hrs period as previously reported, however we notice that the previous ephemeris data for this star need to be updated. The variation in ephemeris data might indicate a change in the orbital period due to angular momentum loss. Further observations are planned to investigate this issue. We also report our investigation on the possible evolutionary scenario of YZ Phe using the recent version of the TWIN stellar evolution code.

***Keywords*:** Eclipsing binaries, photometry, stellar evolution

Introduction

Eclipsing binaries are binary star in which the orbital plane of the two stars is nearly in the line of sight. These objects are easily recognized from the appearance of two minima in their light curves. There are three types of eclipsing binaries according to the shape their light curves: Algol type (EA), β-Lyrae type (EB), and W-UMa type (EW). Algol type eclipsing binaries have detached components of two extreme spectral classes and the light curves show a clearly defined eclipses with one deep minimum and one shallow minimum. The β-Lyrae type has a semi-detached configuration where the one or both stars has almost filled up their Roche-lobe. Therefore the stars in these systems have ellipsoidal shape. The light curve of the EB type eclipsing binary shows a curvy pattern and minima with different depths, although not so extreme like the EA type. The last type is the W-UMa type or the contact system. Both component in this system have filled their Roche-lobe and touch each other through its first Lagrange point, L_1. The stars in EW system would have similar spectral classes and a strongly curved light curve with almost equal depths for the minima.

The eclipsing binary YZ Phe belongs to the W-UMa type system. This star has a 5.6 hrs orbital period and known as one of the shortest eclipsing binaries to date. YZ Phe was discovered as a variable star by Hoffmeister [1] and classified as an eclipsing binary of Algol type. This star is located in the southern hemisphere with RA (J2000) = $01^h\,42^m\,26^s$ and δ (J2000) = $-45°\,57'\,04''$. Later, Gessner and Meinunger [2] find that YZ Phe is actually a W UMa star. The first estimated true period of YZ Phe comes from Jones [3] who performed a complete UBVRI photoelectric observations covering the primary eclipse and derived a ~0.225d period. Kilkenny and Marang [4] and Samec and Terrell [5] reported similar period of 0.23472d from the light curve analysis of simultaneous BVRI observations. Furthermore, Samec and Terrell find that YZ Phe consists of two early K spectral-type dwarf stars with mass ratio of ~0.4.

In this article we report our V band observations of YZ Phe from the Panchromatic Robotic Optical Monitoring and Polarimetry Telescopes (PROMPT). We also investigate the evolution scenario of this system using a recent stellar evolution code by Peter Eggleton [6].

Observations and Data Reduction

Optical observations

We obtain the photometry data of YZ Phe using 0.41cm PROMPT-5 telescope at Cerro Tololo Inter-American Observatory in Chile. The observations was done on 27 and 29 September and 01October 2012 with a 1k×1k Apogee U47 CCD camera in V filter. The U42 CCD camera has 13×13 μm pixel size and total imaging area of 13.3×13.3 mm. The field of view of this telescope is 10′×10′ with pixel scale 0.59″ per pixel. We take 60-seconds exposure for all science and the corresponding calibration images. Bias subtraction, dark image correction and flat fielding were performed through the Skynet pipelines for PROMPT images while the aperture photometry is done using IRAF *apphot* package.

The finding chart of our target star, YZ Phe, is shown in Figure 1. We choose 2MASS stars J01422428-4554060 as the comparison and J01420982-4553468 as check star. Table 1 lists the coordinate and magnitude of the stars used in our photometric analysis.

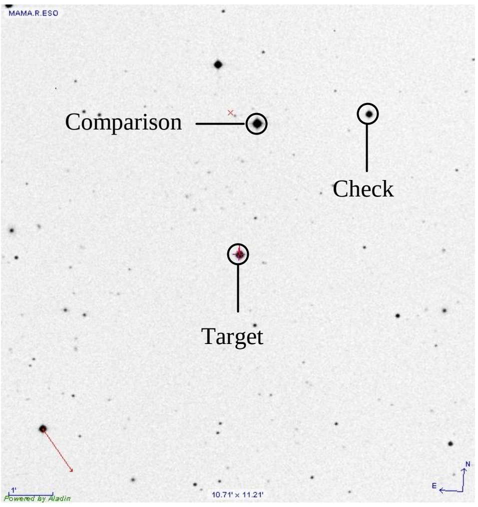

Figure 1. Finding chart of YZ Phe from ESO digitized sky survey in R filter with the field of view of 10.71′×11.21′. The target, comparison, and check stars are marked with circle.

Table 1: Coordinates and magnitudes of the YZ Phe, comparison, and check stars

Star	**RA**	**Dec**	**B**	**V**
YZ Phe	01 42 26	-45 57 04	-	12.70*
J01422428	01 42 24	-45 54 06	12.35	11.72
J01420982	01 42 10	-45 53 47	14.06	13.42

*maximum brightness in visual [7]

The weather is stable during the observations although we notice that there were some technical problems occurred in the night of 29 September and 01 October. The problems caused the change of image orientation in the CCD which happened during the observation. In the observation of 01 October, the images were also shifted to the north so that the check star is out of the CCD frame. However, these technical difficulties did not affect the quality of the data.

Aperture photometry

Before analyzing the photometric data, we examine the images using the *imexamine* package to make sure that the images are free from any image distortion. We exclude the data if the ellipticity (or the roundness) of the stars in the images are larger than 0.15. We present the folded light curve of YZ Phe in Figure 2.

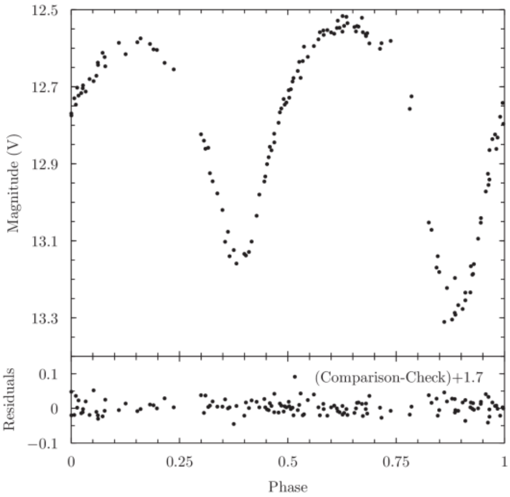

Figure 2. The light curve of YZ Phe in V band (top panel) and the residuals calculated from the magnitude variations of the comparison and check stars (bottom panel).

The light curve shows two minima with similar depth. We calculate the magnitude by averaging the variations to the comparison and check stars. The residuals come from the difference in the observed (instrumental) magnitude of the comparison and check stars to their real visual magnitudes.

It is also seen in the light curve that the phase of the primary and secondary minimum are shifted by 0.1. We will discuss this problem in the Result and Discussion section.

Evolution of YZ Phe

We investigate the evolution scenario of YZ Phe using the TWIN stellar evolution code for binaries from Eggleton [6]. The code was first introduced in 1971 [8] and it has been developed during the past four decades. The recent version of the code is able to follow the evolution of the two components simultaneously. This will allow us to trace the changes in the stellar structure and orbital parameter of both stars in detail.

The TWIN code needs severals initial values as the inputs: the stellar masses, the mass ratio and the orbital period of the progenitor (initial) systems. We take the values needed from the present value of YZ Phe system, assuming that the mass of the star in the system has not change much since its formation. We take this assumption because both stars in YZ Phe system are low mass stars (≤1 Msun) which needs more than 10 Gyr to evolve into the red giant phase.

We take the binary paramaters needed as the input from [5] where the mass ratio ($q = M_2/M_1$) is

0.402 and the present orbital period is 0.2347. Recent study by Stepien and Gazeas [8] proposed that the low mass contact binaries of W-UMa type should have progenitor systems with primary initial mass 0.9 – 1.1 M_{sun} and total initial mass 1.3 -1.6 M_{sun}. The initial period to form these binaries should be between 1.5 to 2.5 day.

We adopt those values and we evolve several models by varying the initial primary mass and the initial orbital period. The initial progenitor system which give the best result is the system with initial primary mass 1.02 Msun, initial secondary mass 0.43 Msun and initial orbital period of 2.0 d. Figure 3 shows the change in masses (top panel) and orbital period (bottom panel) of this model. The stars are in contact at the age of 4.25 Gyr and at this point the mass transfer start from the primary to the secondary. The orbital period decreasing slowly and reaches 0.28 d at the end of the evolution. The mass transfer and orbital period decrease suggest that this system is very likely will experience a merger. The evolution stops when mass transfer occurs because the code could not follow the rapid changes into a merger phase.

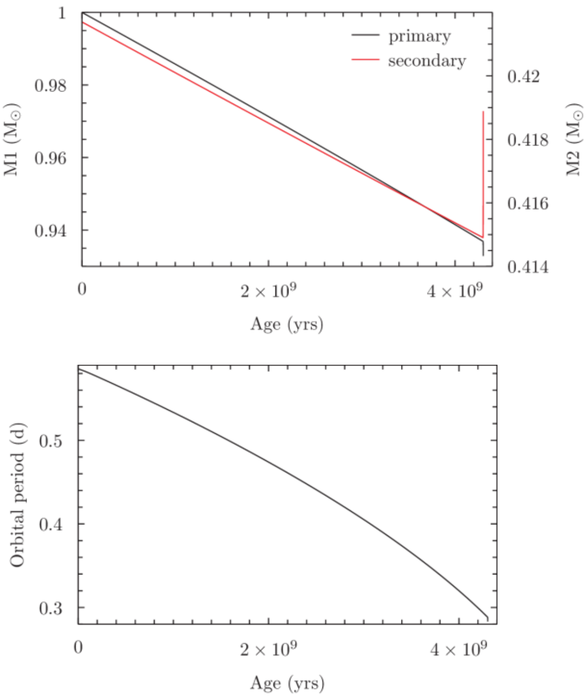

Figure 3. The plot of masses (top) and orbital period (below) of our best model (1.02+0.43, 2d).

This model shows a good agreement with the proposed evolutionary model of contact binary by [8]. They also mentioned that the contact binaries will continuously losing mass and angular momentum which will lead into a merger.

The present geometry model of YZ Phe from the Binary Maker 3 software is shown in Figure 4 (taken from http://ebola.eastern.edu). The two stars are in contact so that they share the same envelope. Therefore both stars will have a similar spectral type.

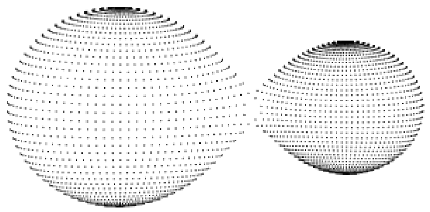

Figure . The geometry model of YZ Phe generated using Binary Maker 3.

Results and Discussion

Our analysis of the visual light curve of YZ Phe shows that the both primary and secondary minima are shifted by 0.1 phase, as shown in Figure 2. The ephemeris we used to calculate the phase is the ephemeris from Kreiner [9]:

$$HJD = 2452500.0721 + E \times 0.23472702 \qquad (1)$$

The shift indicates that this ephemeris is inaccurate to predict the eclipse of YZ Phe at the present time. This may also suggest that the orbital period of YZ Phe has changed since the last ephemeris measurement. Contact binaries with orbital periods shorter than 1 day have high angular momentum loss due to the chromospheric-coronal activity (magnetized wind). Therefore, it is very likely that the YZ Phe system experienced orbit shrinkage due to this effect. However, our observations were very limited and we do not have enough data to show any indication of orbital period change. We are planning to do more observations in future to investigate this possibility.

Acknowledgments

The authors acknowledge the PROMPT telescope and the Skynet team member who provided us the observation times and the science data.

References

1. C. Hoffmeister, “Veraenderliche Sterne am Sudhimmel”, Veroeff. Sternwarte Sonneberg **6** (1963) 1
2. H. Gessner and I. Meinunger, “Veranderliche Sterne am Sudimmer. Teil V”,Veroeff. Sternwarte Sonneberg **8** (1975) 247
3. S. Jones, “A note on the period of the W UMa star YZ Phoenicis”, IAU Inform. Bull. Var. Stars **3296** (1989) 1
4. D. Kilkenny and F. Marang, “On the period of the W UMa star YZ Phoenicis”, IAU Inform. Bull. Var. Stars **3438** (1990) 1
5. R. Samec and D. Terrell, “YZ Phoenicis : photometric study of a W UMa binary near

the short-period limit", Publ. Astron. Soc. Pac. **107** (1995) 427

6. P.P. Eggleton and L. Kiseleva-Eggleton, "The evolution of cool algols", Astrophysical Journal **575** (2002) 461
7. N.N. Samus, V.P. Goranskii, O.V. Durlevich, and 6 co-authors, "An Electronic Version of the Second Volume of the General Catalogue of Variable Stars with Improved Coordinates", Astronomy Letters **26** (2003) 468
8. K. Stepien and K. Gazeas, "Evolution of Low Mass Contact Binaries", Acta Astronomica **62** (2012) 153
9. J. M. Kreiner, "Up-to-Date Linear Elements of Eclipsing Binaries", Acta Astronomica 54 (2004) 207

Photometry of Asteroid

C. Sakulsampansri

Benchamaratrangsarit school 222 Chumpon Road T.Namueang A.Mueang, Chachoengsao,24000
**Corresponding author. E-mail: karn.tukky@hotmail.com*

Abstract

This project studies the variability in apparent magnitude of an asteroid. The apparent magnitude of an asteroid is monitored over time, and a light curve is constructed. The light curve then can tell us about the rotation period of the asteroid, as well as some physical characteristic about the spin and the shape of the asteroid. This project chooses to study Phaedra asteroid by a photograph taken by a telescope PROMPT (Panchromatic Robotic Optical Monitoring and Polarimetry Telescopes) in Chile. Images are taken in filter R and then used to determine the brightness and the light curve of the asteroid .The resulting light curve is fragmented and thus pose a problem in determining the full variable period. However, it has found that the asteroid varies in apparent magnitude and was a variable period longer than 1.608 hours. The variability in magnitude suggests that the asteroid has a rough shape with uneven surfaces.

Keywords**:** Magnitude, Light curve, Phaedra
This research was supported by National Astronomical Research Institute of Thailand (NARIT)

Introduction

There are many interesting objects in the sky such as stars, planets, comets, the researcher was interested about Phaedra. Over 200,000 asteroids have already been discovered to date. They are all of different size. Sizes of asteroids are smaller than planets but larger than meteors. It is believed that asteroids were formed from an accretion of planetesimal in the asteroid belt in early stages of solar system development. Most asteroids are asymmetric in shape, but look like ordinary stars when seen through most telescopes. The majority of the asteroids orbit between Mars and Jupiter in an area called "The Asteroid Belt". The largest asteroid : Ceres, was the first dwarf planet discovered in the solar system.

Phaedra, was the 174th asteroid discovered by JC Watson in 1877 with orbital period around the sun at 4.83 years, with inclination 12.13° and perihelion at 2.443 AU. It had apparent magnitude around 8.5 with period of rotation around 5.75 hours with albedo around 0.149. The researcher is interested in studying the transition period or the period of rotation of asteroids Phaedra shaped and surfaces of asteroids Phaedra.

Objective

To find the periodic variation of the asteroid Phaedra with photography using filter R and scientific data analysis process.

Scope of the project

Variation in brightness of asteroid 174 Phaedra period from September 7, 2012 - January 15, 2013.

Materials and Methods

1. Find a candidate among the catalog from http://www.dur.ac.uk/physics.astrolab/a_lightcurve.html. Determine the coordinate of the asteroid using http://ssd.jpl.nasa.gov/horizons.cgi. Find a rough rotation period from http://spiff.rit.edu/richmond/parallax/phot/LCSUMPUB.TXT.
2. Take images of Phaedra using R filters with exposure time 120 seconds.
3. Use blinking techniques to determine the location of the asteroid
4. Use photometry to measure the apparent magnitude of the asteroid
5. Determined magnitude from formula

$$m_1 - m_2 = -2.5\log\left(\frac{f_1}{f_2}\right)$$

6. Construct a light curve.

Results and Discussion

When we plot the brightness of the asteroid as a function of time, we get the following light curve:

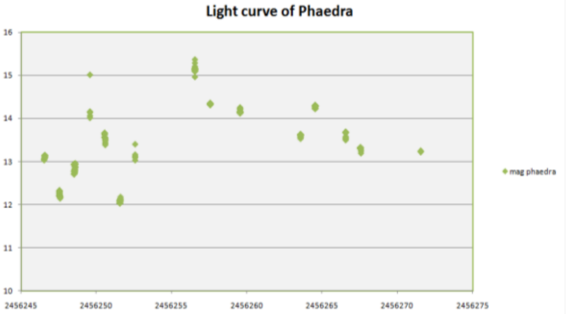

Figure 1. Light curve of Phaedra

X-axis is Julian Date, Y-axis is the magnitude of Phaedra

Conclusion

The graph shows that the light curve is not continuous. This is due to methodological error which cause the overall brightness to fluctuate. However, it can still be seen that the brightness of Phaedra varies, with a variable period of at least greater than 1.608 hours (from the data base ; http://spiff.rit.edu/richmond/parallax/phot/LCSUMPUB.TXT 5.75 hours), indicating that the asteroid is not spherical in shape.

Benefits

Such an approach can be used to determine the brightness of the stars, moon, and other data collection methods to be used in other applications.

Problems and suggestions

As the asteroid is moving quickly, the photographs are not in the same position all the time. This makes it difficult to perform photometry consistently. As a result, the overall brightness of Phaedra measured vary from session to session. Possibly due to the weather and the stars used to calculate the brightness of the asteroid and not the actual brightness of the asteroid.

Acknowledgments

This project has been successfully by Aj.Choochart Paenoi the adviser. Dr. Wiphu Rujopakarn, Mr. Matipon Tangmatitham, Mr. Chanakan Santikunaporn and Miss Pranita Sappankum for suggestions. This project supported by Benchamaratrangsarit school and National Astronomical Research Institute of Thailand (NARIT)

Reference

1. Boonrucksar Soonthornthum. **Astrophysics.** First Published. Chiang Mai: NARIT IPST, **2007.**
2. The institute for the Promotion of Teaching Science and Technology, institute. **Base on Basic Education Core Curriculum Science Science 6 Mathayom 3 Book 2.** First Published. Bankok: OTEP Lat Phrao,**2011.**
3. The institute for the Promotion of Teaching Science and Technology, institute. **Base on Basic Education Core Curriculum Science The Earth the Spsce and the Astronomy for students to focus on science Mathayom 4 - 6.** Second Published. Bankok: OTEP Lat Phrao,**2011.**
4. http://www.dur.ac.uk/physics.astrolab/a_lightcurve.html
5. http://ssd.jpl.nasa.gov/horizons.cgi
6. http://spiff.rit.edu/richmond/parallax/phot/LCSUMPUB.TXT
7. http://www.skynet.unc.edu/
8. http://sv.wikipedia.org/wiki/174_Phaedra

The Important of 'Radio-Quietness' for Radio Astronomy

R. Umar[1,2*], Z.Z. Abidin[1], Z.A. Ibrahim[1], N. Gasiprong[3], K. Asanok[4], S. Nammahachak[5], S. Aukkaravittayapun[6], P. Somboopon[6], A. Prasit[6], N. Prasert[6], and Z. S. Hamidi[7]

[1]Department of Physics, University of Malaya, 50603, Kuala Lumpur, Malaysia,
[2]Astronomy Unit, Universiti Sultan Zainal Abidin, 21300, Kuala Terengganu, Malaysia,
[3]Department of Physics, Ubon Rajathanee University, 34190, Ubon Ratchathani, Thailand,
[4]Department of Physics, Khon Kaen University, 40002, Khon Kaen, Thailand,
[5]Department of Physics, Udon Thani Rajabhat University, 41000, Udon Thani, Thailand
[6]National Astronomical Research Institute of Thailand (NARIT), Ministry of Science and Technology, 50200, Chiang Mai, Thailand
[7]Faculty of Applied Sciences, University Teknologi Mara, 40450, Shah Alam, Kuala Lumpur, Malaysia
**Corresponding author. E-mail: roslan@unisza.edu.my*

Abstract

The Study of Radio Quiet Zone (RQZ) in Malaysia and Thailand Most of radio observatories are located in isolated areas. Since radio sources from the universe is very weak, astronomer need to suppress, remove or avoid radio frequency interference (RFI) from active spectrum users and radio noise produced by human made (telecommunication, mobile phone and microwave oven). There are many observatories around the world are surrounded by a RQZ. RQZ can be set up using public or state laws. A RQZ normally consists of two areas: an exclusive area in which totally radio emissions are forbidden, with restrictions for residents and business developments, and a larger (radius is above 100 km) coordinating area where the power of radio transmission limits to threshold levels. In this paper, we report the importance of the usage of RQZ in order to identify the areas were suitable for RQZ. There are many factors need to consider to address his problem for example mobile phone and TV transmitters. To identify the best site for radio astronomer, RFI mapping could be a best technique. We will also use other information gathered from on-site RFI level measurements on selected 'best' areas generated by the RFI mapping. Then, after identifying best site we travel to the site selected to view the profile of RFI level. The intention is to find the best site for the purpose of establishing first radio quiet zones for radio telescope in Malaysia and Thailand.

Keywords: Radio Quiet Zone (RQZ), Radio Astronomy Interference (RFI) and Radio Telescope.

Introduction

The radio astronomy service is the only entirely passive radiocommunication service defined by the ITU-R [1]. Radio astronomy uses extremely sensitive radio dish to detect very weak signals of cosmic origin. Therefore, it is highly vulnerable to interference by unwanted emissions from other services in nearby or even distant spectrum bands. To avoid or minimize such interference radio astronomy antennas is usually placed in remote locations. Nowadays, with the ever expanding use of the radio spectrum by both the radio astronomer and the communications industry. To establish any radio astronomical observation, the first action is to initially identify all the possible RFI in the targeted site. Human-made RFI are still one of the main enemies in the selection of suitable sites for radio astronomy observation and the installation of new radio telescopes sources. We astronomers have an educational role in making others active radio spectrum users as well as the general public to aware of the high sensitivity of radio telescopes and the consequent need for protection of the Radio Astronomy Service [1] [2]. RFI can come from the ground (near the observatory and) or space. We can run away from ground interference but not from space interferences.

The use of the electromagnetic spectrum is increased in last decades. For radio astronomer especially having equipped with radio astronomical observatories, especially those who are working with large radio dish, establish a radio frequency to protected zones in their neighborhood. For example, the proposed biggest radio astronomy research project in the world, Square Kilometer Array (SKA). It is requested different Radio Quiet Zone (RQZs) for its core, central arrays and outer stations respectively [3]. The radio interference threshold level is normally defined at a value of 10 dB less than the radio telescope noise. Based on this value, the ITU (International Telecommunication Union) regulations concerning the radio astronomy service have assigned different threshold levels for interfering radio sources for spectral line or continuum observations [1].

Radio Quiet Zone (RQZ)

To protect radio astronomy services the RQZ should be proposed. For example a radio-quiet zone can be set up locally using state or national law to restrict housing and industrial developments in the neighborhood of a radio observatory and to restrict the use of electrical equipment. The largest and best known such radio-quiet zone in Green Bank and located in West Virginia in US. Another RQZ is the Mid-West RQZ in Western Australia, located at very remote area whereas the population density is about 0.9 ppl/km^2[2]. Figure 2 shows the pattern of interferences level for the low population density in Australia. For the future large facilities such as the SKA project will require a new type of international radio-quiet zone to gain access to much more of the spectrum than the officially allocated bands, and to receive protection from transmitters on satellites [5].

The size of a RQZ is largely determined by transmission losses, which can be divided into free-space loss and diffraction loss [4]. The area that is within the specified distance is called the buffer zone, which serves the purpose of keeping real-world features distant from one another. Buffer zones are often set up to protect the radio astronomy observatory and its environment from interference with unwanted signals. Most of the radio observatories in Europe have 1–3 km RQZ [6]. Zone-2 and Zone-3, respectively, represent a conservation area within 20 and 30 km. Broadcasting transmitters using radio astronomy frequencies in this area are prohibited. Zone-4, which can be defined as the “Coordination Area” has an approximately 100-km diameter. The size of an RQZ with a radius of z^0 from a radio astronomy service facility must follow the following expression[5]:

$$Pt - L\,(d = z^0) \le Pr \tag{1}$$

Where *Pt(dBW)* is the effective radiated power of an interfering source, defined as the power radiated by the transmitting antenna in the direction to the radio astronomy observatory, *Pr(dBW)* is the interference threshold level assigned by the ITU, *L (dB)* is the transmission loss as a function of distance *(d)* and frequency, among which the transmission loss is the most critical.

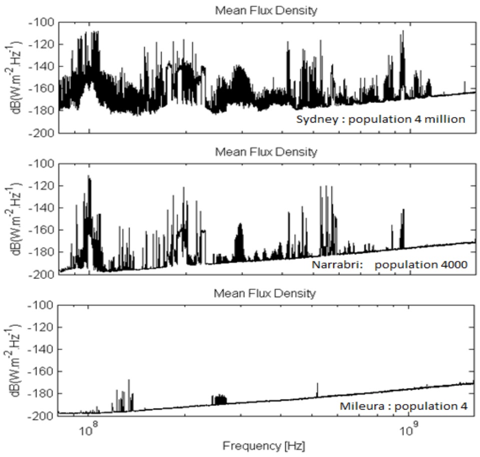

Figure 1. Population density in selected sites in Australia [2].

Materials and Methods

RFI Measurement Protocol for Candidate SKA site was studied and will be practiced in this research [7]. A discone antenna specified for 1420 MHz was built as shown in Figure 2. This instrument connected to a low noise amplifier (LNA) 28dB gain. Spectrum analyzer Protek 3290N (frequency up to 2.9 GHz) using Belden cables connected to an antenna. Observation for the pre-trip will take in one hour with an interval of 15 minutes in 24 hour observation at selected sites [8]. Data will transfer to the laptop for analysis. The results measured RFI value of selected sites were plotted. Both sites selected in Malaysia namely Universisti Pendidikan Sultan Idris (UPSI) and Universiti Malaya (UM). Meanwhile in Thailand we survey RFI at two sites which is Ubon Ratchathani (UB) and Chiang Mai (CM). In Thailand both sites were suggested by the National Astronomical Research Institute of Thailand (NARIT). In Malaysia, UM considers as a control site and UPSI was proposed due to count our shielding and quite low in RFI level.

Figure 2. The Discone antenna used [9]

Table 1: Selected site survey [10]

Sites	Latitude/ Longitude	Pop. Density (peoples /km^2)
UR	105°27’ 37.8” E/ 15°22’ 34.5’’N	110
CM	98°32. 92.5’ E/ 18°29.288’ N	91.5
UM	101°39.445” E/ 03°0.443’’N	7000
UPSI	101°’32’77 ”E/ 3°’44’44.6”N	70

Results and Discussion

In order to study RFI in both countries we ploted 3 spectrogram for all spectrums (0-2.8GHz) and 3D RFI profile to see the different view as shown in figure 3-6. Figure 3 shows that average highest peaks located around window 250MHz-1800MHz. In Figure 4, we can see that RFI profile drop or decrease with time at some point. Figure 5 also presents a lot of signals since UM located near to Kuala Lumpur city center. We also monitor the interferences at another site in Malaysia namely UPSI. This site was proposed by two universities under UPSI-UM project. Meanwhile we also plotted 2D RFI profile for everysites to identify window 1300-1500MHz as shown in Figure 7-10. In UB of Figure 7 show one significant single peak at frequency about 1440MHz and -82.99dBm. Big spike about 1328.75MHz and -69.86dBm existed in CM as shown in Figure 8. Figure 9 in UM also presents a significant peak at 1335MHz and -73.05MHz. Figure 10 in UPSI shows a one significant signal at 1360MHz and -86.49dB. In order to compare RFI signal to the ITU threshold level for hydrogen line, we took an example a spike 1360MHz and -86.49dBm at UPSI. The Free Space Power Loss (FSPL) formula could be used to find the threshold level. Formula defined,

$$FSPL=20\log 4\pi df/c \qquad (2)$$

Which is proportional to the square of the frequency of the radio signal (*f=1420MHz*) and to the square of the distance between the transmitter and receiver *(d)*. Distance during RFI measurements between the antenna and the device (*d=5m*) gives a contribution the power level of -50.53301dBm. The power of the RFI seen as the antenna focus will be: -86.49+(-50.5) = -136.99dBm=-166.99dBW. Being the signal band narrower than the resolution bandwidth used in the spectrum analyzer, no further normalization has to be applied in spectral observation. Therefore, for spectral line observation, the RFI power generate by signal radio is expected to exceed the ITU-R RA.769-2 threshold level (-215dBW) by about 48.01dBW.

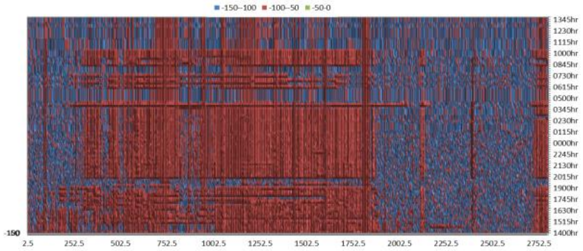

Figure 3: Spectrogram for wide band (0-2.8GHz) in Ubon.

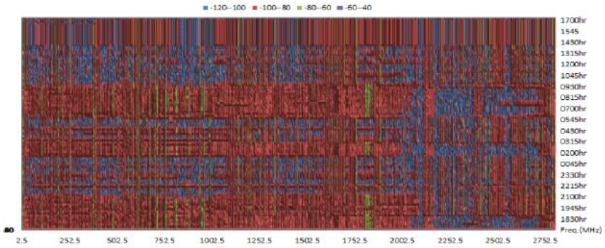

Figure 4: Spectrogram for wide band (0-2.8GHz) in Chiang Mai

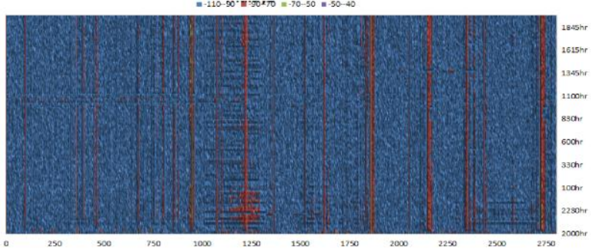

Figure 5 : Spectrogram for wide band (0-2.8GHz) in UM

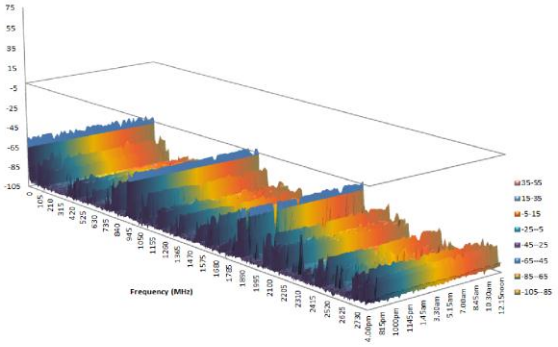

Figure 6 : 3D RFI profile for 0-2.8GHz MHz in UPSI

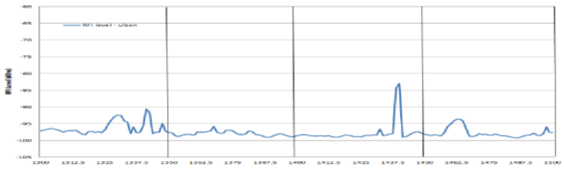

Figure 7 : RFI profile for 1300-1500MHz in Ubon

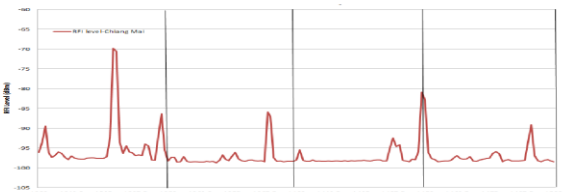

Figure 8 : RFI profile for 1300-1500MHz in CM

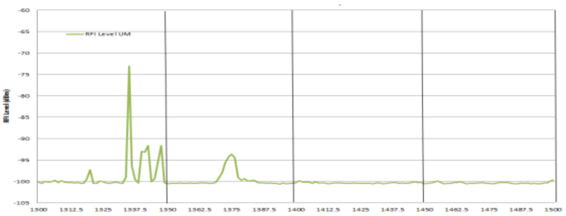

Figure 9 : RFI profile for 0-2.8GHz MHz in UM

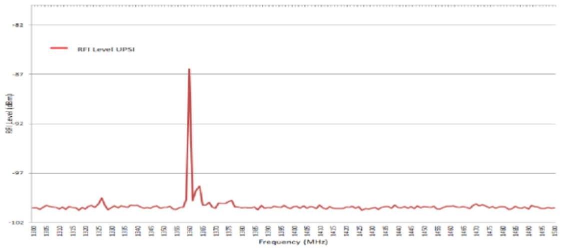

Figure 10 : RFI profile for 1300-1500MHz MHz in UPSI

Conclusions

From the observed spectra we can conclude that CM have relatively strong RFI compare to UB. In order to determine the prime candidate sites, we need to considerd and identified others parameter such as population density mobile phone transmitter, contour and rain drop for example At frequencies about 10 GHz and above, atmospheric effects are dominant factors in selecting a site for radio astronomy observation. However, below approximately 2 GHz, RFI is the strongest consideration. In Europe a radio telescope that can effectively be used The VLBI network, 30–40 meters in diameter dish equipped with at least 1.4–32 GHz broadband receivers and capable of measuring polarization will be constructed [5]. In the future, we may consider the new parameter and different sites in Malaysia and Thailand. We also could be consider others technique to find an appropriate location with RFI-free in order to construct the RQZ and a radio telescope for radio astronomers.

Acknowledgments

The main author would like to thank the University of Malaya for their funding of the IPPP project (PPP PV025 2011A). Thanks a lot to National Astronomical Research, Institute of Thailand (NARIT), Ministry of Science and Technology, Thailand for the financial support and also the assistance of NARIT staffs especially Aukkaravittayapun and Nikom. The authors also thank to Dr Kitiyanee Asanok from Department of Physics, Faculty of Science, Khon Kaen University, Thailand and Dr Nipon Gasiprong from Department of Physics, Faculty of Science, University Ubon Ratchatahni, Thailand for their guidance and encouragement (Figure 3). Special thanks are also reserved for the UniSZA for supporting of the first author. The authors would like to thank the members of the University of Malaya’s Radio Cosmology Research Lab for their support and advice.

Figure 3: RFI team in Thailand

References

1. Cohen, J., T. Spoelstra, et al. (2005). CRAF Handbook for Radio Astronomy, European Science Foundation.
2. DeBoer, D. R., R. G. Gough, et al. (2009). "Australian SKA pathfinder: A high-dynamic range wide-field of view survey telescope." Proceedings of the IEEE **97**(8): 1507-1521.
3. Spectrum, C. o. S. U. o. t. R., & Frequencies, C. o. R. (2010). Spectrum Management for Science in the 21st Century: Natl Academy Pr.
4. Peng, B. and W. Han (2009). "Estimating the size of a radio quiet zone for the radio astronomy service." Experimental Astronomy **27**(1): 109-120.
5. Cohen, R. (2003). "Strategies for Protecting Radio Astronomy." Organizations and Strategies in Astronomy: 59-74.
6. Küçük, I., I. Üler, et al. (2012). "Site selection for a radio astronomy observatory in Turkey: atmospherical, meteorological, and radio frequency analyses." Experimental Astronomy: 1-26.
7. Ambrosini, R., R. Beresford, et al. (2003). "RFI Measurement Protocol for Candidate SKA Site." SKA Memo Series.
8. Abidin, Z. Z., Bahari Ramadzan Syed Adnan, S., & Ibrahim, Z. A. (2010). RFI profiles of prime candidate sites for the first radio astronomical telescope in Malaysia. New Astronomy, 15(3), 307-312.
9. Abidin, Z. Z., Ibrahim, Z. A., Adnan, S. B. R. S., & Anuar, N. K. (2009). Investigation of radio astronomical windows between 1 MHz and 2060 MHz in Universiti Malaya, Malaysia. New Astronomy, 14(6), 579-583.
10. Umar, R., Z. Z. Abidin, et al. (2012). Population density effect on radio frequency interference

(RFI) in radio astronomy. AIP Conference Proceedings.

Spectroscope from Office Supply

J. Wongphecauxsorn[1*] and P. Songpongs[2]

[1]*Department of Physics and Materials Science, Faculty of Science, Chiangmai University 239 Huay Keaw Road, Muang Chiangmai 50200*
[2]*Department of Physics Faculty of Science Chulalongkorn University,* 6th floor MHMK, Phayathai Rd., Patumwan, Bangkok 10330
**Corresponding author. E-mail: Jompoj.bjstp@gmail.com*

Abstract

Spectroscope available in market is too expensive to use for school student’s project. In this research, it is focus on a low price, but effective spectroscope that use designed from office supplies. Paper carton, DVD disc and CD disc was assembled together. A Canon 550D DSLR camera was used as a detector for solar spectrum imaging. The analysis of solar spectra from CD-disc spectroscope and DVD-disc spectroscope show that solar spectrum is blackbody spectrum with the effective temperature of 5300 K and 5400 respectively. However, absorption line cannot be detected. This might be because the resolving power of this spectroscope is not high.

Keywords**:** Transmissions Spectroscope, CD, DVD

Introduction

When the element heated until flame. The element will release the energy in heat and light. The different element will release different wavelength light. On the other hand. Knowing the wavelength can tell us about the element of light source. Spectroscope is the instrument use for dispersion light and measure the wavelength. The spectroscope is used in many filed of science. Gemology use in authentication of jewelry. Astronomy use in authentication of element in the star (Sirawit, 2007) and measure the radial velocity. However, using spectroscope is high cost and nowadays spectroscope can make from CD-discs. So, its cost savings. This experiment study the efficiency of spectroscope that make from CD-dish, DVD-dish, and Grating.

Materials and Methods

1. Study the responding of Canon 550D to wavelengths

Make the spectroscope from CDs. Then, take photos of He and H lamp. Select the wavelength 447.15 nm and 587.56 nm from He spectrum with relative intensity 100 and 1,000 respectively and 486.13 nm and 656.5 nm from H spectrum with relative intensity 80 and 300 respectively in manual mode with speed shutter 30 second. After that, measured the intensity with Salsaj 2.0 and divide with relative intensity.

2. Study the spectrum from CDs, DVDs, and Grating Spectroscope.

Take the H spectrum with CDs , DVDs , and Grating spectroscope in manual mode speed shutter 10 second

3. Calculate temperature of The Sun from Wien's displacement law.

Take the Sun’s spectrum with speed shutter 1 second. Measured the intensity of spectrum with Salsaj 2.0.Then. Calculate the Sun’s temperature compare with true Sun temperature.

Results and Discussion

1. The responding of Canon 550D to wavelengths

Make the spectroscope from CDs. Then, take photos of He and H lamp. Select the wavelength 447.15 nm and 587.56 nm from He spectrum with relative intensity 100 and 1,000 respectively and 486.13 nm and 656.5 nm from H spectrum with relative intensity 80 and 300 respectively in manual mode with speed shutter 30 second. After that, measured the intensity with Salsaj 2.0 and divide with relative intensity. This experiment has shown the result like this The responding of Canon 550D to wavelengths can be fitted to parabolic graph.

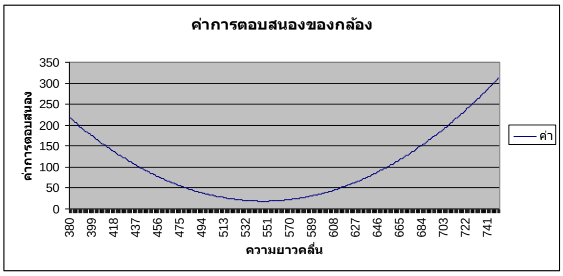

Figure 1. The responding graph

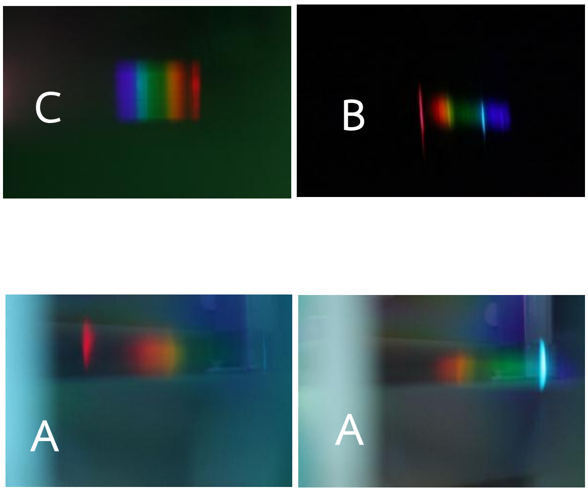

Figure 2. H spectrum
A) H Spectrum from DVDs
B) H Spectrum from CDs
C) H Spectrum from Grating

2. The spectrum from CDs, DVDs, and Grating Spectroscope.

Make the spectroscoTake the H spectrum with CDs, DVDs , and Grating spectroscope in manual mode speed shutter 10 second. This experiment has shown the result like this

3. Temperature of the Sun from Wien's displacement law.

Take the Sun’s spectrum with speed shutter 1 second. Measured the intensity of spectrum with Salsaj 2.0.Then. Calculate the Sun’s temperature compare with true Sun temperature. This experiment has shown the result like this.

Conclusions

550D is the most powerless when responding to wavelength 547 nm and the spectrum form Grating is the highness resolving power. Moreover, it is easy to take a spectrum. The spectrum from CDs is lower resolving power than Grating. However, it is easy to take a spectrum from CDs .Finally, DVDs with high dispersion angle. It is difficult to take spectrum from DVDs. We can calculate the Sun’s temperature is 5,300 K from CDs and DVDs and 5,400 K from Grating.

Acknowledgments

This project cannot been done without Assist. Prof. Pong Songpongs the adviser. Wiphu Rujopakarn and Aj. Dr. Siramas Komonjinda for suggestion in Astronomical method. Aj. Chochart Paenoi and Benchamarajrungsarit Science Department for supporting place for study. This work was supported by National Science and Technology Development Agency (NSTDA)

Type	Max wavelength (nm)		Temperature	
Grating	540	-6	5,400 K	100
CDs	550	4	5,300 K	0
DVDs	550	4	5,300 K	0
Average		546 nm		5,300 K

References

1. The Classification of Stellar Spectra Available from:ww.science.cmu.ac.th/.../4CLASSSTELLARSPECTRA.PDF
2. “การอบรมเชิงปฏิบัติการเทคนิค”, Near Infrared Spectroscopy, Available from: http://www.kapi.ku.ac.th/index.php?option=com_content&task=view&id=66&Itemid=45
3. Anonymous, สเปคโตรสโคปอย่างง่าย Available from: http://sci4 fun.com/spectroscope/spectroscope.html
4. Carroll&Ostlie, an introduction to modern astrophysics, Pearson Education Indochina LTD, 2007.
5. Canon Thailand,Canon 500D Available from: http://www.canon.co.th/p/TH/248-กล้องดิจิตอลซิงเกิ้ลเลนส์/597-EOS/1164-EOS-500D
6. Chaychai, สนุกกับสเปคโตรสโคป2007 Available from:www.vcharkarn.com/uploads/44/44745.doc

7. Edmond Scientific Co,Fun with Optics.,1989.
8. EZ Contributors, CD-ROM, Availablefrom:http://sci4fun.com/spectroscope/spectroscope.html
9. Krittipong,NATURE OF LIGHT,Available from:www.mwit.ac.th/~kitipong/.../NATURE%20OF%20LIGHT.doc
10. R.M. MacKay, Planck Radiation Laws, Available from: http://serc.carleton.edu/introgeo/mathstatmodels/examples/PlanckXL.html
11. Sirawit, การพัฒนาระบบสเปกโตรสโคปโดยใช้เกรตติงเพื่อศึกษาสเปกตรัมของดาวฤกษ์, 2551

Jupiter's Atmosphere Analysis via the Amateur Radio Telescope

T. Worakitwatana[*], Y. Pholphakwean, and P. Jumrusprasert
Physics and General Science Program Science and technology Nakhon Ratchasima Ratjabhat University, Nakhon Ratchasima, Thailand, 30000
**Corresponding author. E-mail: witerlove_13@hotmail.com*

Abstract

The Jupiter's atmosphere was analyzed via the 20.1 MHz radio wave that emitted from the Jupiter due to the turbulence at its great red spot and its IO satellite. The 20.1 MHz radio wave signals were detected via the Jove NASA dipole antenna system which located on the top of NRRU Science Center Building from 20 to 23 August 2012. Data were collected and analyzed via the RadioSkyPipe and Jupiter Pro softwares. The results were shown that there were 15 dominantly observable signals in the three days of data collection. The maximum amplitude of the signal was able to detected on 20 August 2012 at 05.41 am. for 16 seconds with the equivalent antenna temperature of 76 kK. While the minimum amplitude of the signal was detected on 21 August 2012 at 03.00 am. for 14.10 minutes with the equivalent antenna temperature of 32-34kK These results were presented that there were quite often of the intermediate and strong turbulences in the Jupiter's atmosphere at this data collection period.

Keywords: emissions, radio wave, radio telescope for Jove Nasa

Introduction

Human use of the electromagnetic spectrum and in daily life for a long time. Take advantage of the many life forms. Waves are derived from nature. And we humans invented the electromagnetic waves in the frequency with which we see and not see. From radio, television, microwave, infrared, ultraviolet, X-rays, gamma rays, etc., so the waves. It is very useful in the telecommunications and medical.

There is also a fictitious radio waves from outer space sent to the distant planet infested waves within the Earth in the year 2474 Karl Jansky detects radio frequency interference young engineer of the world. Confirmed the discovery of radio signals detected from space in the constellation Sagittarius. The study concluded that Radio Astronomy can be observed deep in the universe beyond the scope of conventional telescopes recognized. We can use radio waves to transmit data over the space. As humans, we discovered radio waves from outer space to detect this signal. Cause the camera to detect waves from outer space. Radio telescope camera was initially built in the year 2480 by the United States Grote Reber. Plate size diameter of 31 feet, which has better performance than conventional telescopes. Optical telescopes because it can not use it in the air with haze from radio telescopes. Detect radio signals from space by the graphics or sound in all weather conditions. Amateur astronomers in the present study, a radio telescope to detect signals from space objects, the Tsar Hercules airplane electric remote. Even the stars near the sun in the solar system, Jupiter is a source of radio waves, which are then sent to Earth from space. Check if the radio telescope. Variability of the atmosphere, it will not.

Therefore, researchers are interested in studying and researching the atmosphere of Jupiter, the nearest star. Using radio telescopes. To know the physical data of Jupiter. And is able to know the state of the atmosphere of Saturn's distance and made aware of the problems of the world, the waves may have an impact on us as well.

Materials and Methods

The research using the tool a simple radio reception radio waves a telescope of Jupiter at 20.1 MHz as a device that is designed by Jove Nasa the project, an organization of the United States. Space exploration and research to study much more about astronomy. Overall he is a member of Jove Nasa.

Preliminary preparation.

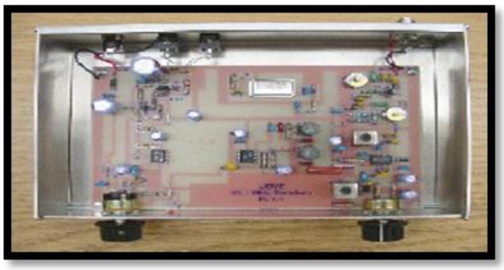

1. Create circuit radio waves receiver in the form of Jove Nasa.

Figures 1. Receiver form Jove Nasa.

2. Created a radio waves receiver half wave length. The frequency of 20.1 Mhz radio waves antenna mounted on PVC. By created dipole antenna up all the second set of images.

Figures 2. Dipole antenna.

3. Steps installing a simple radio a telescope. Generated to detect radio waves signals from Jupiter. The following equipment.

1. radio waves receivers.
2. Noise filter.
3. Connectors.
4. Dipole antenna.
5. Computer.

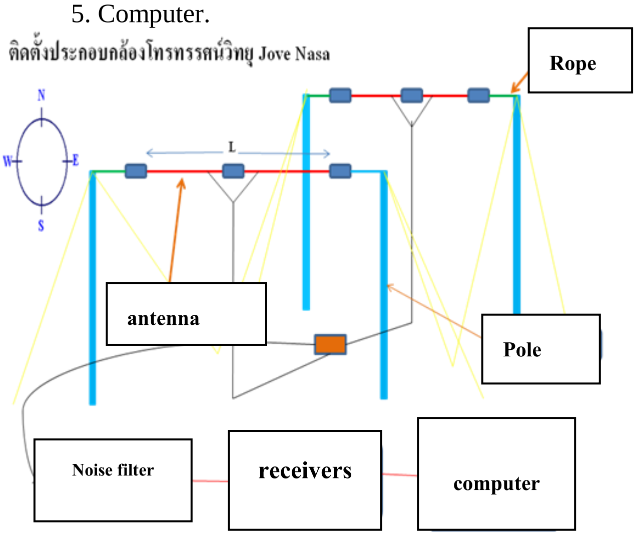

Figures 3. Diagram all materials of Jove Nasa.

The installing consists of the steps shown above. The antenna is to cut through the fall of Jupiter to get a good signal. The researchers installed on the roof of the building.

4. The connection following steps.

The antenna is connected to the second set with a noise filter. Before the introduction of cable to connect the of Receivers to the amplifier again. Before connecting the machine to the standby display of computer.

5. Steps data collection.

Computer by installing the Radio Sky Pipe is a tool that can collect data in a computer using sound card. Analog to digital converter can be used to help analyze the Radio Sky Pipe. The research program was used to analyze the radio signal is captured and stored for the analysis graph. You can view the signal in real time while the storm surge. By looking through the Radio Sky Pipe Pro.

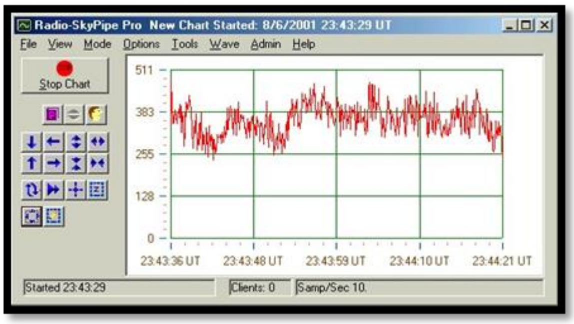

Figures 4. Sky Pipe program.

5. Analysis of data.

Observation that data Analysis of is as follows.

1. Bring photo from observations of the radio Sky Pipe analyzed image with the gradient of the graph of a graph. Characteristics that are indicative of storm radio waves on Jupiter and the sun, the waves, the relationship of the detector signal.2. Import photos from storage to detect motion of the stars relative to the signal detected from the collected information primarily to provide a clear signal that the graph is provided in a manner that is. the storm surge caused by the fluctuations of the stars of planet detection. According to the statistical data of the storm radio waves from other research that has been collected over a period of several years.

Results and Discussion

The data research save the result and analysis radio wave of the signal from Jupiter. Through the program. Radio-SkyPipe 2.4data will displayed as a graph of the frequency 20.1 MHz radio waves on Jupiter's radiation. Variability and the Liberation radio waves telescope Radio Jove Nasa sent to the following.

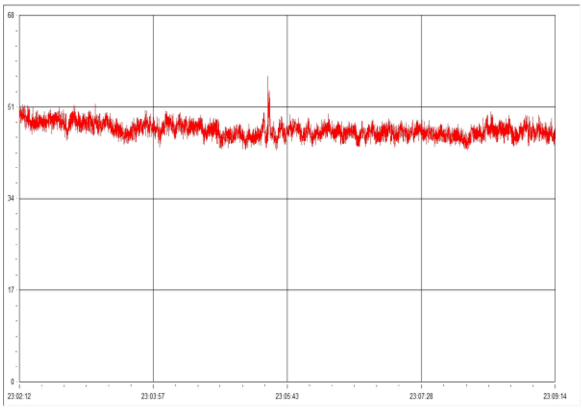

Figures 5. radio waves signals on August 20, 2555.

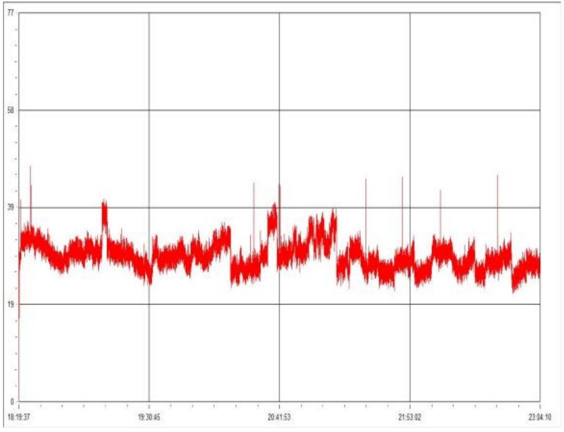

Figure 6. radio waves signals on August 21, 2555.

Detect radio waves on August 20, 2555 by Level of background signal in the antenna temperature by 50 K has the spread in the atmosphere. All times Jupiter's four times the level of severe most the receiving. Started when time. 05:41:40-05:41:56 born period of 16 seconds in 76 kK.

Date August 21, 2555 by radio waves to detect the level of background signals in the antenna temperature On average 30 K and explosion in the atmosphere of Jupiter, by clearly displaying all 8 times 7 is Started most severely time. 06:10:00 to 06:10:08 pm born 8 seconds at a time 49kK.

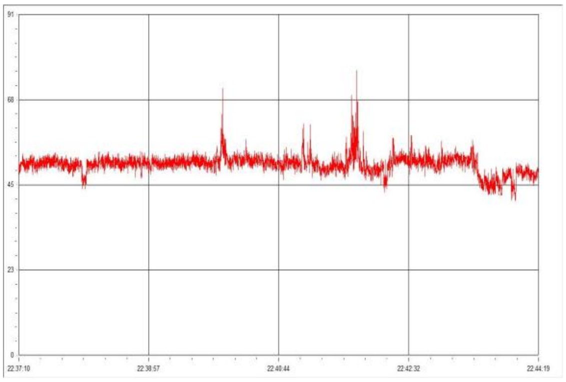

Figure 7. radio waves signals on August 22, 2555.

Detect radio waves Date August 22, 2555 by Background signal level. has radio waves reception in the variability 24kK Jupiter has less violence, but if the temperature of the antenna of the antenna temperature is not very high average 37kK.

The signal detection of radio waves from Jupiter radio telescope by a simple dipole form of Jove Nasa during the period from 20-23 August 2555 clearly detect Have radio waves emissions coming and the time to will be. radiation frequencies lot in the range of 03:00 to 06:00 between this period with the steepness of the graph at high. And a rising pinnacles. Able to observe and detect signals are clearly. That appears on the Radio Sky pipe Pro makes researchers know whether it condition on Jupiter's atmosphere are the variability over time. The detection of all the research I know that the stars Have often variation of atmospheric conditions and Have several levels of violence in. Radio Jove Nasa telescope simple by detected.

Conclusions

Detection of radio waves from Jupiter using radio telescopes of Jove Nasa signal in the frequency range 20.1 MHz to install rooftop. Science Center. Radio Sky pipe Pro using data collection and recording. To detect radio waves from Jupiter will detect the signal variations caused by the atmosphere of Jupiter, explosion, lightning, and the start time of the blast wave from the 20-23 August 2555. between 3:00 to 6:00 pm at the start of a steep wave graph on the Radio Sky pipe Pro has detected radio emissions from the obvious. 3 days to detect signals. The most serious is the third antenna temperature measured Ahmadinejad's start time 05:41:40-05:41:56 PM August 20, Duration 16 seconds at 76 K at a low intensity level is 4 times of the day. August 21 beginning at 3:00:00 to 3:14:10. For the longest period of 3 days is 14 minutes 10 seconds and detect a radio frequency receiver includes three days of intense radiation striking a total of 15 times.

Acknowledgments

This research was accomplished. By the Grace of many teachers. The transfer of business consulting advice to be useful to researchers. In both the academic and activities. Authors thank Dr. Pong shining noble Development Consultant for the helpful advice. And extremely valuable.

Vajra Master poet wishes to thank Martin make consultations. And a generous range of accessories, the radio telescope.

I thank Thanawat nest mound to make the guidance counselor. Research on the analysis of wave conditions Jupiter.

Director and staff Science Center. Nakhon Ratchasima Rajabhat University. Nakhon Ratchasima. The property offers generous storage in the research.

Researchers want to thank all the parents, relatives. And others involved in research and encouragement always. The research was done well.

References

1. Kurosaki Ichigo 0.2010 E Shibuya. Jupiter (25 July 2554).
2. Katie James, Manchester 2010. Wave radio. (Online).(29 July 2554).

3. Katie James Norman (2010). Radio telescope. (System). Sources(online). (29 July 2554).
4. Fansico Reyas. (1995). Observations of Jupiter Jove Nasa radio (online). (29 July 2554).
5. Franklin .(1995). Internet radio burst detected from Jupiter. (Online). (25 July 2554).
6. Han Z Flipper Shaykh: 1608. The telescope. (online). (25 July 2554).
7. Jove Nasa .2012. Antenna. (Online). Sources. (25 July 2554).
8. Roberts French 0.2552. Use a telescope to study the release of radio stars. (Online). (25 July 2554).

Non-perturbative Ghost of the Homogeneous and Isotropic Universe in Massive Gravity

A. D. Felice[1*], A. E. Gümrükçüoğlu[2], and S. Mukohyama[2]

[1]*ThEP's CRL, NEP, The Institute for Fundamental Study,*
Naresuan University, Phitsanulok 65000, Thailand and
Thailand Center of Excellence in Physics, Ministry of Education, Bangkok 10400, Thailand
[2]*Kavli Institute for the Physics and Mathematics of the Universe, Todai Institutes for*
Advanced Study, University of Tokyo, 5-1-5 Kashiwanoha, Kashiwa, Chiba 277-8583, Japan

Abstract

We show that the homogeneous and isotropic solutions of massive gravity are unstable due to the presence of a non-perturbative scalar ghost. We reach this conclusions by studying the propagating modes on a Bianchi type-I manifold. We study the kinetic terms and the masses of these modes, as the the background approaches the homogeneous and isotropic configuration. In this limit at least one ghost always exists and its frequency tends to vanish for large scales.

Introduction

The concept of the mass has been central in many areas of physics. Gravitation is not an exception, and it is one of the simplest but yet unanswered questions whether the graviton, a spin-2 particle that mediates gravity, can have a nonvanishing mass or not. This question is relevant not only from a theoretical but also from a phenomenological viewpoint, since a nonzero graviton mass may lead to late-time acceleration of the universe and thus may be considered as an alternative to dark energy.

Recently Refs.[1, 2] proposed the first example of a fully nonlinear massive gravity theory, where the so called Boulware-Deser (BD) ghost [3], which had been one of the major obstacles against a stable nonlinear gravity theory with a nonvanishing graviton mass, is removed by construction. Due to the theoretical and phenomenological motivations mentioned above, this theory has been attracting significant interest.

The first homogeneous and isotropic Friedmann-Lemaître-Robertson-Walker (FLRW) solution for this theory was presented in [4] for Minkowski fiducial metric and then extended to more general fiducial metrics in [5]. The analysis of linear perturbations in this general setup was carried out also in [5]. Although a massive spin-2 particle generically has 5 propagating degrees of freedom, it was found that the number of degrees of freedom in the gravity sector was 2, same as in general relativity (GR). This is due to the vanishing of the kinetic terms for the expected additional degrees[1] 1 Backgrounds with additional symmetries which remove the extra degrees were introduced in [7].. This feature may extend to other setups: Ref. [6] obtained a vanishing kinetic term on spherically symmetric inhomogeneous backgrounds.

The goal of the present paper is to determine the fate of the extra degrees of freedom. We find that in the nonlinear massive gravity, all cosmological solutions that respect homogeneity and isotropy have a ghost, i.e. an excitation with a wrong sign kinetic term. Therefore, the universe in this theory should have either inhomogeneities [8] or anisotropy [9]. We note that the ghost mode found in the present paper is among five degrees of freedom of the massive spin-2 field and thus, is not the BD ghost.

The model and the background

Imposing the absence of the BD ghost, the massive gravity action, in vacuum, can be constructed as [2]

$$S = \frac{M_{\rm Pl}^2}{2}\int d^4x\,\sqrt{-g}[R-2\Lambda+2m_g^2\mathcal{L}_{\rm MG}]\,, \qquad (1)$$

with $\mathcal{L}_{\rm MG} = \mathcal{L}_2 + \alpha_3\,\mathcal{L}_3 + \alpha_4\,\mathcal{L}_4$, where

$$\mathcal{L}_2 = \tfrac{1}{2}([\mathcal{K}]^2 - [\mathcal{K}^2]),$$
$$\mathcal{L}_3 = \tfrac{1}{6}([\mathcal{K}]^3 - 3[\mathcal{K}][\mathcal{K}^2] + 2[\mathcal{K}^3]),$$
$$\mathcal{L}_4 = \tfrac{1}{24}([\mathcal{K}]^4 - 6[\mathcal{K}]^2[\mathcal{K}^2] + 3[\mathcal{K}^2]^2 + 8[\mathcal{K}][\mathcal{K}^3] - 6[\mathcal{K}^4]),$$

the square brackets denote the trace operation, and

$$\mathcal{K}^\mu{}_\nu = \delta^\mu{}_\nu - \left(\sqrt{g^{-1}f}\right)^\mu{}_\nu\,. \qquad (2)$$

Here, $g_{\mu\nu}$ and $f_{\mu\nu}$ are physical and fiducial metrics, respectively. Since we are interested in the stability of the gravity sector only, it is sufficient to consider a vacuum configuration, with a cosmological constant Λ.

The physical metric is chosen to be the simplest anisotropic extension of FLRW, namely, the axisymmetric Bianchi type–I metric

$$ds^2 = -N^2dt^2 + a^2(e^{4\sigma}\,dx^2 + e^{-2\sigma}\,\delta_{ij}\,dy^i\,dy^j)\,, \quad (3)$$

where *N*, *a*, and σ are functions of the time variable *t*. In the rest of the paper, Greek indices span the space-time coordinates, while the indices *i*, *j* = 2, 3 correspond to the coordinates on the *y*–*z* plane, with $y^2 = y$, $y^3 = z$. Since our goal is to obtain the stability conditions of this metric in the isotropic limit, the whole system in this limit needs to reduce to the general cosmological solutions given in [4, 5]. For this reason, we consider a fiducial metric to be in the flat FLRW form,

$$f_{\mu\nu} = -n^2\partial_\mu\phi^0\partial_\nu\phi^0 + \alpha^2(\partial_\mu\phi^1\partial_\nu\phi^1 + \delta_{ij}\partial_\mu\phi^i\partial_\nu\phi^j), \quad (4)$$

where both *n* and α are functions of the time-Stückelberg field ϕ^0.

The equations of motion for the background can be calculated by varying the action with respect to the Stückelberg fields and the metric. As a result, we obtain three independent equations as

$$3\left(H^2 - \Sigma^2\right) - \Lambda = m_g^2\left[-(3\,\gamma_1 - 3\,\gamma_2 + \gamma_3) + \gamma_1\,(2\,e^{\sigma} + \right.$$
$$\frac{3\dot{\Sigma}}{N} + 9H\Sigma = m_g^2(e^{-2\,\sigma} - e^{\sigma})X\left[\gamma_1 - \gamma_2(e^{\sigma} + r)X + \gamma_3\,r\right.$$
$$J_\phi^{(x)}\,(H + 2\Sigma - H_f\,e^{-2\sigma}X) + 2J_\phi^{(y)}\,(H - \Sigma - H_f e^{\sigma}X) = 0\,, \quad (5)$$

where

$$J_\phi^{(x)} \equiv \gamma_1 - 2\,\gamma_2\,e^{\sigma}\,X + \gamma_3\,e^{2\sigma}\,X^2\,,$$
$$J_\phi^{(y)} \equiv \gamma_1 - \gamma_2\,(e^{-2\sigma} + e^{\sigma})\,X + \gamma_3\,e^{-\sigma}\,X^2\,, \quad (6)$$

and

$$\gamma_1 \equiv 3 + 3\,\alpha_3 + \alpha_4\,,\ \gamma_2 \equiv 1 + 2\,\alpha_3 + \alpha_4\,,\ \gamma_3 \equiv \alpha_3 + \alpha_4$$
$$H \equiv \dot{a}/(aN)\,,\ H_f \equiv \dot{\alpha}/(\alpha n)\,,\ \Sigma \equiv \dot{\sigma}/N\,,$$
$$X \equiv \alpha/a\,,\ r \equiv an/(\alpha N). \quad (7)$$

We note that, in the isotropic limit $(\sigma, \Sigma \to 0)$, we have $J_\phi^{(x)} = J_\phi^{(y)}$, so that the Stückelberg equation of motion, Eq. (5), at leading order, gives

$$\gamma_1 - 2\,\gamma_2\,X + \gamma_3\,X^2 \simeq 0\,, \quad (8)$$

that is $X \to$ *constant*, which corresponds to the FLRW result found in [5]. In the same limit, we can also see that $H \to$ *constant*, as expected.

Even modes

Let us now consider the perturbations which transform as 2D scalars under a spatial rotation in the *y*–*z* plane (also referred as even modes). Then, the perturbed metric for the even sector can be written as [10]

$$\begin{aligned} ds^2 = &-N^2(1+2\Phi)dt^2 + 2aNdt[e^{2\sigma}\partial_x\chi dx + e^{-\sigma}\partial_i B dy^i] \\ &+ a^2e^{4\sigma}(1+\psi)dx^2 + 2a^2e^{\sigma}\partial_x\partial_i\beta dx dy^i \\ &+ a^2e^{-2\sigma}[\delta_{ij}(1+\tau) + \partial_i\partial_j E]dy^i dy^j\,, \end{aligned} \quad (9)$$

while the even-type perturbations of Stückelberg fields read

$$\phi^0 = t + \pi^0\,,\ \phi^1 = x + \partial_x\pi^1\,,\ \phi^i = y^i + \partial^i\pi\,. \quad (10)$$

We can then define gauge invariant combinations as follows

$$\begin{aligned} \hat{\Phi} &= \Phi - \frac{1}{2\,N}\partial_t\left(\frac{\tau}{H-\Sigma}\right)\,, \\ \hat{\chi} &= \chi + \frac{\tau\,e^{-2\sigma}}{2a(H-\Sigma)} - \frac{ae^{2\sigma}}{N}\partial_t\left[e^{-3\sigma}\left(\beta - \frac{e^{-3\sigma}}{2}E\right)\right]\,, \\ \hat{B} &= B + \frac{e^{\sigma}}{2\,a\,(H-\Sigma)}\,\tau - \frac{a\,e^{-\sigma}}{2\,N}\,\dot{E}\,, \\ \hat{\psi} &= \psi - \frac{H + 2\,\Sigma}{H - \Sigma}\,\tau - e^{-3\,\sigma}\,\partial_x^2\,(2\,\beta - e^{-3\,\sigma}\,E)\,, \\ \hat{\tau}_\pi &= \pi^0 - \frac{\tau}{2\,N\,(H-\Sigma)}\,, \\ \hat{\beta}_\pi &= \pi^1 - e^{-3\,\sigma}\left(\beta - \frac{e^{-3\,\sigma}}{2}\,E\right)\,, \\ \hat{E}_\pi &= \pi - \frac{1}{2}\,E\,. \end{aligned} \quad (11)$$

The first four definitions do not refer to the Stückelberg perturbations and are thus already present in GR [11]. However, the additional three degrees arise from the breaking of general coordinate invariance by the non zero expectation value of the Stückelberg fields.

In order to find the behavior of the perturbations, we proceed as usual by expanding the action at second order in the perturbation fields, then by employing the Fourier plane-wave decompositions, as in $\exp[i(k_L x + k_i y^i)]$. The degrees of freedom arising from the $g_{0\mu}$ perturbations, namely $\hat{\Phi}$, $\hat{B}$ and $\hat{\chi}$, are nondynamical, thus can be integrated out. Furthermore, the kinetic term for the $\hat{\tau}_\pi$ is proportional to the background equations of motion, so that this degree of freedom is also nondynamical. We interpret this field as the would-be BD ghost, which is eliminated in this theory by construction.

In the massless theory (i.e. GR), using the constraint equations also removes the degrees $\hat{\beta}_\pi$, $\hat{E}_\pi$, leaving only $\hat{\psi}$ in the action, which becomes one of two gravity wave polarizations in the isotropic limit. However, in our case, due to the nonzero mass of the graviton, these two degrees of freedom are dynamical, in general.

Thus, the Lagrangian for even-type perturbations in vacuum has three physical propagating modes, $\mathcal{V}_a$, (a = 1, 2, 3). Assuming small deviation from FLRW, with $|\sigma| \ll 1$ and $|\Sigma/H| \ll 1$, we study the kinetic matrix $\mathcal{K}_{ab}$

$$S^{(2)}_{\rm even} \ni \frac{M_p^2}{2} \int N\, dt\, dk_L\, d^2k_T\, a^3 \left(\frac{\dot{\mathcal{V}}_a^\star}{N} \mathcal{K}_{ab} \frac{\dot{\mathcal{V}}_b}{N} \right) . \qquad (12)$$

Thanks to the 2D rotational symmetry on the y–z plane, the action depends on $k_T \equiv \sqrt{k_2^2 + k_3^2}$, instead of the individual components. The eigenvalues of $\mathcal{K}_{ab}$, at leading order in small anisotropy expansion, are

$$\kappa_1 \simeq \frac{p_T^4}{8\, p^4} \,, \; \kappa_2 \simeq -\frac{2a^4 M_{\rm GW}^2 p_L^2}{1-r^2} \sigma \,, \; \kappa_3 \simeq -\frac{p_T^2}{2\, p_L^2}\, \kappa_2 \,, \quad (13)$$

where we defined $M_{GW}{}^2 \equiv m_g{}^2(1 - r)X^2(\gamma_2 - \gamma_3 X)$, and introduced the physical momenta

$$p_L \equiv \frac{k_L}{ae^{2\sigma}} \simeq \frac{k_L}{a} \,, \; p_T \equiv \frac{k_T}{ae^{-\sigma}} \simeq \frac{k_T}{a} \,, \; p^2 \equiv p_L^2 + p_T^2 \,. \quad (14)$$

The kinetic term κ_1 which is the only eigenvalue that does not vanish in isotropic limit corresponds to one of the gravity wave polarizations in FLRW. Once small but nonvanishing anisotropy is introduced, two additional even modes acquire nonzero kinetic terms at quadratic order. More importantly, from (13), we see that κ_2 and κ_3 have opposite signs, regardless of the parameters of the theory. Thus, we conclude that in the isotropic limit, one of the new degrees is always a ghost. Assuming that $\sigma(1 - r) > 0$ (which turns out to be the condition for stability in the odd sector, as we show later), the ghost mode is associated with the eigenvalue $\kappa_2 < 0$.

We conclude the discussion of the even modes by presenting their dispersion relations. We first make a field redefinition into new field basis fields W_a defined such that the kinetic action can be written as

$$S^{(2)}_{\rm even} \ni \frac{1}{2} \int N\, dt\, dk_L d^2k_T a^3 \left(\frac{\dot{\mathcal{W}}_a^\star}{N} \eta_{ab} \frac{\dot{\mathcal{W}}_b}{N} \right) , \quad (15)$$

where η_{ab} = *diag*(1,−1,1). The mass spectrum can be determined either by studying the equation for the frequency-discriminant, or equivalently, by performing a Lorentz transformation to diagonalize the frequency matrix. Eventually, we find

$$\begin{aligned} \omega_1^2 &\simeq p^2 + M_{\rm GW}^2 \,, \\ \omega_2^2 &\simeq -\frac{1-r^2}{24\sigma} \left[\sqrt{(10p^2 + p_T^2)^2 - 8p_L^2 p_T^2} - (2p^2 + 3p_T^2) \right] , \\ \omega_3^2 &\simeq -\omega_2^2 + \frac{1-r^2}{12\sigma} \left(2p^2 + 3p_T^2 \right) , \end{aligned} \qquad (16)$$

with $\omega_2{}^2\omega_3{}^2 < 0$ in general, and $\omega_2{}^2 < 0$ by assuming $\sigma(1 - r) > 0$. We note that the dispersion relation corresponding to the ghost, $\omega_2{}^2$, becomes smaller at larger scales. Therefore, at sufficiently large scales, this mode cannot be integrated out from the low energy effective theory. This feature makes the FLRW background unstable for massive gravity. As a consequence, the homogeneous and isotropic cosmology cannot be accommodated in the nonlinear massive gravity theory.

Odd modes

Let us now discuss the odd sector (i.e. the divergence-less part of the modes which transform as 2D vectors under a rotation in the y–z plane). The perturbed metric we consider is

$$\begin{aligned} ds^2 = &-N^2dt^2 + 2ae^{-\sigma} N v_i dt dy^i + 2a^2 e^\sigma \partial_x \lambda_i dx dy^i \\ &+ a^2 e^{4\sigma} dx^2 + a^2 e^{-2\sigma} (\delta_{ij} + \partial_{(i} h_{j)}) dy^i dy^j \,, \end{aligned} \quad (17)$$

where $\partial_{(i}h_{j)} \equiv (\partial_i h_j + \partial_i h_j)/2$ and $\partial^i v_i = \partial^i \lambda_i = \partial^i h_i = 0$. For the Stückelberg fields, we consider instead

$$\phi^0 = t \,, \, \phi^1 = x \,, \, \phi^i = y^i + \pi^i \,, \qquad (18)$$

where $\partial_i \pi^i = 0$. Since the vectors are defined on the 2D y–z plane, the transverse condition can be used to reduce each of these vectors to a single degree of freedom

$$v_i = \epsilon_i{}^j \partial_j v, \;\; \lambda_i = \epsilon_i{}^j \partial_j \lambda, \;\; h_i = \epsilon_i{}^j \partial_j h, \;\; \pi_i = \epsilon_i{}^j \partial_j \pi_{\rm odd},$$

where ϵ_i^j is a unit anti-symmetric tensor with $\epsilon_2{}^3 = -\epsilon_3{}^2 = 1$. Also for the odd modes we can introduce gauge invariant combinations as follows

$$\begin{aligned} \hat{v} &= v - \frac{a\, e^{-2\,\sigma}}{2\, N}\, \dot{h} \,, \\ \hat{\lambda} &= \lambda - \frac{e^{-3\,\sigma}}{2}\, h \,, \\ \hat{h}_\pi &= \pi_{\rm odd} - \frac{1}{2}\, h \,. \end{aligned} \qquad (19)$$

Using these fields, the second-order resulting action depends on the three perturbations ($\hat{\upsilon}$, $\hat{\lambda}$, $\hat{h}_\pi$). Among these, $\hat{\upsilon}$ does not have any time derivatives and can be removed by solving its own constraint equation. In General Relativity, this operation also removes $\hat{h}_\pi$ and the final action can be written in terms of $\hat{\lambda}$ only. However, in this nonlinear theory of massive gravity, we expect the field $\hat{h}_\pi$ to remain in the action as an extra degree of freedom coming from the Stückelberg sector.

After a further field redefinition,

$$\mathcal{Q}_1 \equiv -e^{3\sigma}\,\hat{\lambda}\,, \qquad \mathcal{Q}_2 \equiv \frac{2\,e^{3\sigma}\,p_L^2}{p^2}\,\hat{\lambda} - 2\,\hat{h}_\pi\,, \qquad (20)$$

the quadratic action, for small anisotropy, takes the following form

$$S^{(2)}_{\rm odd} \simeq \frac{M_{\rm Pl}^2}{2}\int N\,dt\,dk_L\,d^2k_T\,a^3\left[K_{11}\,\frac{|\dot{\mathcal{Q}}_1|^2}{N^2} - \Omega_{11}^2\,|\mathcal{Q}_1|^2 + K_{22}\,\frac{|\dot{\mathcal{Q}}_2|^2}{N^2} - \Omega_{22}^2\,|\mathcal{Q}_2|^2\right], \qquad (21)$$

where the two modes decouple at leading order in the small anisotropy expansion, with coefficients

$$K_{11} = \frac{a^4\,p_L^2\,p_T^4}{2\,p^2}\,, \quad K_{22} = \frac{a^4\,p_T^2\,M_{GW}^2}{4\,(1-r^2)}\,\sigma\,,$$
$$\frac{\Omega_{11}^2}{K_{11}} = p^2 + M_{\rm GW}^2\,, \quad \frac{\Omega_{22}^2}{K_{22}} = c_{\rm odd}^2\,p^2\,, \qquad (22)$$

and $c_{odd}^2 = (1 - r^2)/(2\sigma)$. Thus, at leading order, we identify the mode $\mathcal{Q}_1$ with one of the gravity wave polarizations in the FLRW background [5]. The extra degree of freedom $\mathcal{Q}_2$ is massless and has sound speed c_{odd}. In order for this mode to be stable, we require the kinetic term for $\mathcal{Q}_2$ to be positive, that is

$$(1-r)\,\sigma > 0\,. \qquad (23)$$

In this case, also c_{odd}^2 becomes positive, and the odd mode $\mathcal{Q}_2$ is, in general, free from ghost instabilities.

Conclusions

In the search for a theory which could explain the dark energy enigma, the nonlinear massive gravity, recently introduced in [1], has raised lots of interest among both theoretical and experimental physicists, thanks to its implications in our understanding of fundamental forces, if it is theoretically consistent and observationally viable.

This theory admits homogeneous and isotropic solutions, and it has been shown in [5] that, out of the five modes which would be typically expected in this theory, only two actually propagate at the linearized level. Therefore, it is of interest to investigate the reason for this unexpected feature.

We propose here that this phenomenon is due to the high symmetry structure of the FLRW background. Accordingly, we have studied the small anisotropy limit of the Bianchi–I manifold and found that there is always a ghost mode in the even sector, with a propagation speed that diverges in the isotropic limit. Furthermore, this mode does not have a mass gap; its frequency tends to zero for small values of the momentum. Therefore, at sufficiently large scales, the frequency cannot be considered as large compared to the ultraviolet cutoff of the theory. As a consequence, the ghost mode cannot be integrated out in general, and the almost-isotropic background becomes unstable under production of negative energy quanta.

Although our analysis is linear, the terms in the quadratic action with coefficients proportional to the small anisotropy can be interpreted as the leading order nonlinear perturbations in a pure FLRW universe. The presence of a mode with negative kinetic term indicates that a homogeneous and isotropic universe in nonlinear massive gravity is unstable.

Our conclusion about ghost instability is far more general than it appears 2 2 Partially massless gravity [12] may evade our conclusion but it is a different theory. Also, nonlinear completion is not known., despite the simplicity of the analysis presented above. This is because, whenever a quadratic kinetic term vanishes, the leading kinetic term is generically cubic and thus can easily become negative, signaling the existence of ghost at the nonlinear level. Moreover, the other type of homogeneous and isotropic solutions (in the non-self-accelerating branch) suffer from ghost instability already at the linearized level [13], as expected from the classical work of Higuchi [14]. Therefore, all homogeneous and isotropic backgrounds, as well as most (if not all) of known spherically-symmetric inhomogeneous solutions, are unstable.

Acknowledgments

In acknowledgement yThe work of A.E.G. and S.M. was supported by the World Premier International Research Center Initiative (WPI Initiative), MEXT, Japan. S.M. also acknowledges the support by Grant-in-Aid for Scientific Research 24540256 and 21111006, and by Japan-Russia Research Cooperative Program. The authors are grateful to Yukawa Institute for warm hospitality during the workshop YITP-W-11-26, when this project was initiated.

References

9. C. de Rham, G. Gabadadze, Phys. Rev. **D82**, 044020 (2010). [arXiv:1007.0443 [hep-th]].
10. C. de Rham, G. Gabadadze and A. J. Tolley, Phys. Rev. Lett. **106**, 231101 (2011) [arXiv:1011.1232 [hep-th]].
11. D. G. Boulware and S. Deser, Phys. Rev. D **6**, 3368 (1972).
12. A. E. Gumrukcuoglu, C. Lin and S. Mukohyama, JCAP **1111**, 030 (2011) [arXiv:1109.3845 [hep-th]].
13. A. E. Gumrukcuoglu, C. Lin and S. Mukohyama, JCAP **1203**, 006 (2012) [arXiv:1111.4107 [hep-th]].

14. P. Gratia, W. Hu and M. Wyman, Phys. Rev. D **86**, 061504 (2012) [arXiv:1205.4241 [hep-th]].
15. G. Tasinato, K. Koyama and G. Niz, JHEP **1207**, 062 (2012) [arXiv:1204.5880 [hep-th]].
16. G. D’Amico, C. de Rham, S. Dubovsky, G. Gabadadze, D. Pirtskhalava and A. J. Tolley, Phys. Rev. D **84**, 124046 (2011) [arXiv:1108.5231 [hep-th]].
17. A. E. Gumrukcuoglu, C. Lin and S. Mukohyama, *to appear in Phys. Lett. B*, arXiv:1206.2723 [hep-th].
18. A. E. Gumrukcuoglu, C. R. Contaldi and M. Peloso, JCAP **0711**, 005 (2007) [arXiv:0707.4179 [astro-ph]]; A. De Felice and T. Tanaka, Prog. Theor. Phys. **124**, 503 (2010) [arXiv:1006.4399 [astro-ph.CO]].
19. B. Himmetoglu, C. R. Contaldi and M. Peloso, Phys. Rev. Lett. **102**, 111301 (2009) [arXiv:0809.2779 [astro-ph]].
20. C. de Rham and S. Renaux-Petel, arXiv:1206.3482 [hep-th].
21. M. Fasiello and A. J. Tolley, arXiv:1206.3852 [hep-th].
22. A. Higuchi, Nucl. Phys. B **282**, 397 (1987).

Accelerators and Synchrotron Radiations

Optimization of Lattice Parameters for Infrared Free-Electron Lasers at Chiang Mai University

S. Suphakul[1,2*], S. Rimjaem[1,2], and C. Thongbai[1,2]

[1]*Department of Physics and Materials Science, Faculty of Science,*
Chiang Mai University, Chiang Mai 50200, Thailand
[2]*Thailand Center of Excellence in Physics, CHE, Bangkok 10400, Thailand*
**E-mail: sikharin.sup@gmail.com*

Abstract

The linear accelerator system at the Plasma and Beam Physics (PBP) Research Facility, Chiang Mai University (CMU), is under studying for an upgrade to be the injector system for an infrared free-electron laser (IR FEL). The current PBP accelerator system consists of an S-band thermionic cathode RF-gun, a bunch compressor in a form of alpha-magnet and a SLAC-type linear accelerating structure. A 180° achromat section will be installed downstream the linac to manipulate the longitudinal bunch length. The numerical simulation code "ELEGANT" has been used to optimize the lattice parameters to provide the electron beam properties suitable for the FEL. The results of optimized lattice parameters and electron beam properties are presented in this contribution.

Keywords: Beam dynamics, Infrared free-electron laser, FEL injector

Introduction

The Infrared Free-electron Lasers (IR FEL) facility at Chiang Mai University has been developed under the plan of a new research facility establishment of the Thailand Center of Excellence in Physics. The facility focuses on the production and utilization of the mid- and far-infrared radiation (MIR and FIR) based on femto-second electron pulses and free-electron lasers technology [1]. As shown in Fig. 1, the facility considered in this paper consists of a thermionic cathode RF-gun as an electron source [2], a magnetic bunch compressor in a form of an alpha-magnet [3], a 3-m SLAC-type S-band linear accelerator (linac), a 180° achromat section a planar type undulator and an optical resonator.

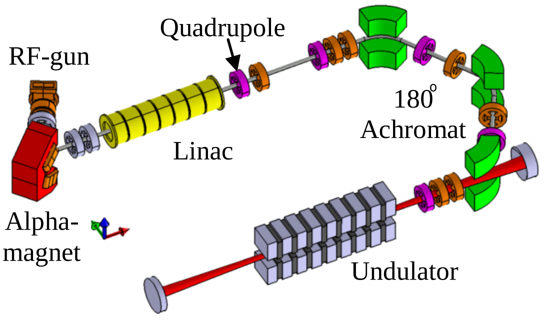

Figure 1. Schematic view of planned IR-FEL at CMU.

The first three components of the existing PBP-CMU linac system are planned for both coherent THz transition radiation from femto-second electron pulses and free-electron lasers. Details of the current PBP-CMU linac system were reported in [4]. The 180° achromat section is a new component which is under detailed consideration. Therefore, we adopt the magnet lattice of the Kyoto University Free-Electron Lasers (KU-FEL) for initial optimization in this study. The achromat section consists of three 60° deflecting angle dipole magnets and two sets of doublet quadrupole magnets. Details of KU-FEL achromat system have been described in [5]. Through the achromat, the electron bunch length shortens and the peak current becomes higher for a given bunch charge.

This study investigates and optimizes the electron beam parameters suitable for the IR FEL project at CMU by modifying the PBP-CMU linac driving condition and considering the bunch compression in the 180° achromat. To investigate the beam dynamics, the computer code PARMELA [6] and ELEGANT [7] have been used for simulations of multi-particle beam dynamics and optimization of the electron beam lattice parameters.

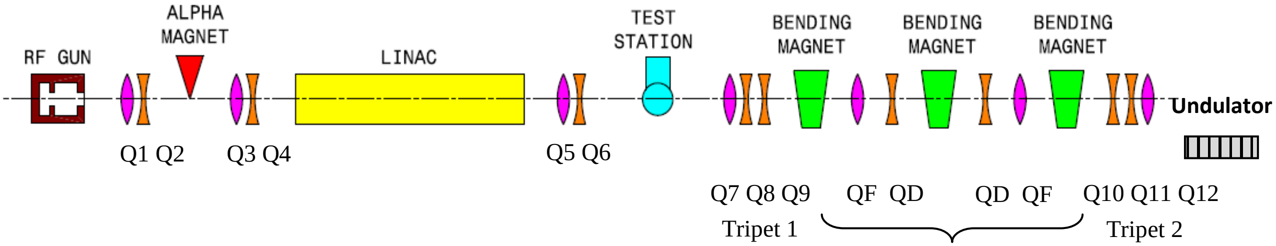

Figure 2. Planned schematic diagram of the injector system for an IR-FEL at CMU

Lattice Optimization

Generally, electron beams for FEL must have high peak current, small emittance, and low energy spread in order to generate intense coherent FEL light in an undulator. To achieve this, the optimization conditions along the beam line must be carefully defined. In this study, we focus on optimization of beam transverse properties by adjusting quadrupole focusing element.

RF gun

The accelerating field gradients of both half- and full-cell cavities of RF gun were adjusted to produce an electron bunch with low energy spread, especially at the head of the bunch, which will be used for FEL lasing. With the field ratio of 1:2 and the accelerating field of 35/70 MV/m, the RF-gun provides the 12,764 particles exiting with low energy spread at the head of the bunch. The particle distributions at the RF-gun exit are shown in Fig. 3, 4.

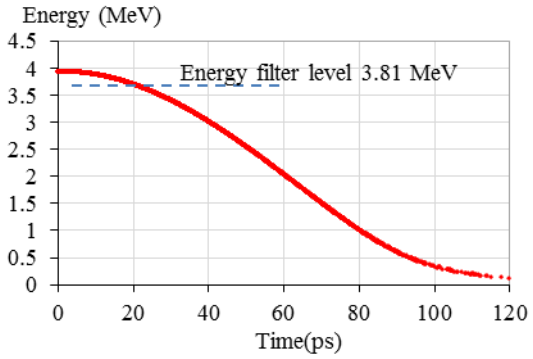

Figure 3. Particle distributions in longitudinal phase space at the RF gun exit.

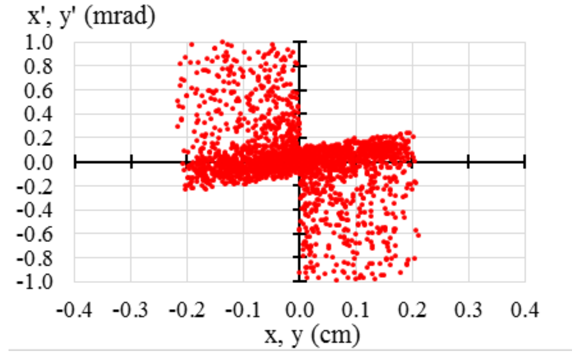

Figure 4. Particle distributions in transverse phase space at the RF gun exit.

Alpha magnet

The alpha magnet is a magnetic bunch compressor equipped with the energy slits inside to filter out the low energy particles. In this study, alpha magnet gradient was set at 400 G/cm. and the energy slits were set to remove particle with energy lower than 3.81 MeV. Because the electron bunches exiting from RF gun have flat energy at the head of the bunch. So the bunch compression due to the alpha-magnet can be neglected in this study.

Linac

The electrons are accelerated by gaining the energy from the RF wave which propagates inside the linac. Since the electron bunch which is compressible by 180° achromat magnetic bunch compressor must have lower energy at the head and higher energy at the tail of bunch. So the electron bunches have to be accelerated with an off-crest phase in the linac. In this study, the RF phase was fixed of 60 deg. and accelerating voltage were adjusted to have electron energy about 15 MeV at the head of electron bunch.

However, the electrons gain different energy along the bunch due to sinusoidal shape of the RF wave. So the increasing of energy spread of electron bunch exiting the linac has to be compromised with the desired electron bunch length.

180° Achromat

The 180° achromat magnetic bunch compres-sor is a triple bend type equipped with 2 sets of quadrupole doublet (see Fig.2 QF and QD). Inside the achromat, different electron energy travels in different path or called “dispersive system”. In this system, the electron bunch length can be manipulated by adjusting the QF and QD strength. The QF and QD have to carefully optimize to have both desire bunch length and zero dispersion at the exit of achromat.

Focusing element

The quardrupole is used for focusing beam to control the transverse beam properties. For PBP CMU injector system, we require the minimum beam size at test station and undulator waist. The transverse beam conditions in each position along the beam line are listed in Table 1., where β is the betatron function, α is the alpha function, σ is the beam size, η is the dispersion function and subscribe x,y mean axis x, y respectively.

Table1: Beam optimization condition in each position of beam line for an IR FEL at CMU.

Position	**Conditions**	**Optimized Quadrupole**
1) Linac entrance	$\beta_x = \beta_y$ $\alpha_x, \alpha_y = 0$	Q1, Q2, Q3, Q4
2) Test station	$\sigma_x, \sigma_y = 0$	Q5, Q6
3) Achromat exit	$\eta_x, \eta_{xp} = 0$	QF, QD
4) Tripet2 entrance	$\beta_x = \beta_y$	Q7, Q8, Q9
5) Undulator waist	$\sigma_x, \sigma_y = 0$	Q10, Q11, Q12

Computer Code

The computer code PARMELA or the "Phase And Radial Motion in Electron Linear Accelerator" code has been used for simulations of multi-particle beam dynamics of the RF-gun. The number of macro particle 30,000 particles per 2856 MHz are assumed to be emitted uniformly from the cathode with current of 2.9 A. One particle represents a charge of 33.85 fC equivalent to 2.12x10^5 electrons.

From the RF-gun exit to undulator waist, the numerical simulation code "ELEGANT" or "ELEctron Generation And Tracking" has been used to optimize the lattice parameters and tracking particle trough the beam line. The ELEGANT is a 6-dimensional phase space tracking code using transport matrices up to 3rd order. The particle distributions exiting from the RF gun which were simulated by PARMELA were converted and imported to ELEGANT by using SDDS toolkit. The SDDS or "Self Describing Data Set" are group of the programs using for pre- and post processing of input and output of ELEGANT i.e. converting input/output to other programs, text or graphical outputs etc**.**

Results

The optimized quadrupole strengths are listed in table 2. The quadrupole Q8 and Q10 can be removed because the optimized strength is of 0 m^{-2}. The large beam size in x axis is of 1.8 cm at the inside of the alpha-magnet and of 1.22 cm. at the focusing quadrupole of the achromat. The beam size at the test station is of 0.138 mm in the x axis and of 0.234 mm in the y axis. And the beam size at the undulator waist is of 0.223 mm and 0.201 mm in the x and y axis respectively. The maximum dispersion is of 0.433 m at focusing quadrupole of the achromat. The beam size and dispersion function are shown in Fig. 5, 6.

Table 2: Results of optimized quadrupole strength for an IR FEL at CMU. (F – Focusing, D – Defocusing)

Quadrupole/Type	**Eff length(m)**	**Strength(m^{-2})**
Q1 / F	0.077	26.90
Q2 / D	0.077	-43.64
Q3 / F	0.077	38.23
Q4 / D	0.077	-33.35
Q5 / F	0.077	20.80
Q6 / D	0.077	-21.17
Q7 / F (Triplet 1)	0.1	38.22
Q8 / - (Triplet 1)	0.1	0
Q9 / D (Triplet 1)	0.1	-25.04
Q10 / D (Triplet 2)	0.1	0
Q11 / D (Triplet 2)	0.1	-43.36
Q12 / F (Triplet 2)	0.1	83.27

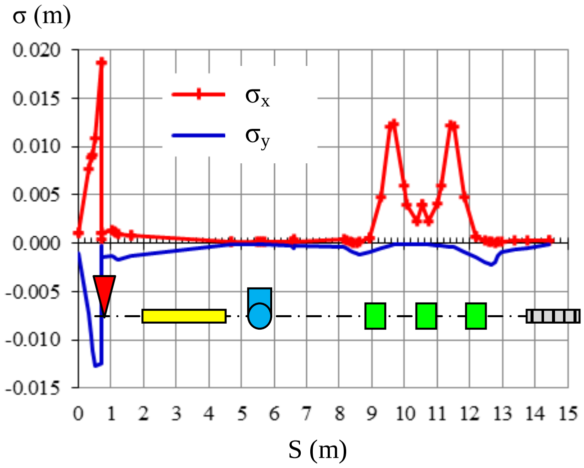

Figure 5. Beam size of optimized beam line for an IR FEL at CMU.

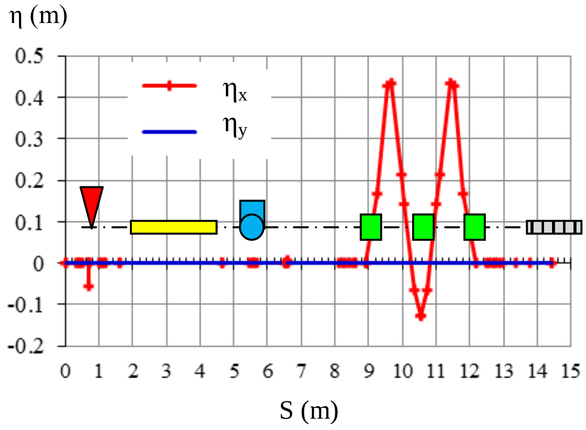

Figure 6. Dispersion functions of optimized beam line for an IR FEL at CMU.

Conclusions

The transverse beam dynamics of the injector system for an IR FEL at CMU has been investigated and optimized by numerical simulation. The optimization conditions which were defined (Table 2.) can provide the small beam size at test station and undulator waist (0.138 mm. x 0.234 mm., 0.223 mm. x 0.201 mm. respectively) and the beam have no dispersion after exiting the 180^o achromat.

For the next study, we will optimize both transverse and longitudinal beam properties simultaneously. The RF phase of the linac will be varied and the 180^o achromat will be re-optimized to investigate the minimum bunch length.

Acknowledgments

Authors would like to acknowledge the support from the Thailand center of Excellence in Physics and the Department of Physics and Materials Science, Chiang Mai University.

References

[1] T.Vilaithong et al., Journal of the Korean Physical Society 59 (2011) 2.
[2] S. Rimjaem, “Generation of Far Infra-red Radiation from Relativistic Electron Beam”, Ph.D. Thesis, Chiang Mai University, 2006.
[3] J. Saisut et al., Nucl. Instr. and Meth. A 637 (2011) S99-S106.
[4] C. Thongbai et al., Nucl. Instr. and Meth. A 587 (2008) 130-135
[5] H. Zen et al., ”Numerical study on the optimum cavity voltage of RF gun and bunch compression experiment in KU-FEL”, in proceeding of the 2007 Free-Electron Laser Conference, Novosibirsk, Russia, WEPPH07.
[6] L.M. Young and J.H. Billen, “PARMELA,” LANL Technical Note LA-UR-96-1835, 2002.
[7] M. Borland, APS LS–287 (2000).

X-ray Photoelectron Spectroscopy Studies of Nitrogen and Sulfur Ions in Aqueous Solutions

W. Pokapanich[1,*], O. Björneholm[2], and G. Öhrwall[3]

[1]Faculty of Liberal Arts and Science,
Nakhon Phanom University, Muang District, Nakhon Phanom, 48000 Thailand
[2]Department of Physics and Astronomy,
Uppsala University, Box 516, SE-751 20 Uppsala, Sweden
[3]MAX-lab, Lund University, P.O. Box 118, SE-221 00 Lund, Sweden
**Corresponding author. E-mail: wandared.pokapanich@npu.ac.th*

Abstract

X-ray photoelectron spectroscopy has been used extensively to investigate the geometric and electronic structure of solid materials and gases, and recently the methods have become more accessible for investigations of liquids. This progress in electron spectroscopy has been possible by combining synchrotron radiation and a liquid micro-jet setup. Liquid micro-jet is a new innovation and its characteristic; small size of the jet reduces the vapour pressure. Together with combining liquid nitrogen in cold trap makes the experiment smoothly. This work, we performed using such a setup to study aqueous ammonium sulfate and ammonium bisulfate. Dilute and nearly saturated solutions were explored; 0.4 and 4.0 M for ammonium sulfate as well as 0.6 and 6.0 M for ammonium bisulfate. Both aqueous ammonium solutions, the N 1s photoelectron spectra were identical. Moreover, no concentration dependence could be observed. Furthermore, the binding energies of the S 2p core-level photoelectron spectra in aqueous ammonium bisulfate are shifted 0.2 eV higher than the case of aqueous ammonium sulfate for both concentrations. The result attributed that bisulfate ion has stronger interaction with the surrounded water molecules than sulfate ion. This has implications for several aspects of physical and chemistry, as well as biology. Moreover, it can be applied to agriculture due to high consumption of sulfate compounds, as well as an impact of acid rain.

Keywords: X-ray, photoelectron, aqueous, nitrogen, sulfur

Introduction

Ammonium sulfate [$(NH_4)_2SO_4$] is intensively used in agricultural as fertilizers. However, if over consumption, nitrogen and sulfur can be accumulated in plants and soil causes several diseases and plant deflection. Ammonium bisulfate [$(NH_4)HSO_4$] is also a fertilizer substance. It is highly acidic and causes acid rain. This work investigated the effect of solvated nitrogen and sulfur ions with different concentrations; dilute and nearly saturation by using liquid micro-jet setup, based photoelectron spectroscopy.

X-ray photoelectron spectroscopy (XPS) is a powerful tool where this process is used to probe matter, both gas and solid [1, 2], recently it is available to probe liquid samples [3, 4]. The XPS process arises when a photon interacts with a core level of the sample, leading to ionization of one of these inner electrons [5]. This work, the solvated N 1s and S 2p XPS were explored.

Experimental details

Aqueous ammonium sulfate and ammonium bisulfate were prepared by mixing high purity salts (< 99.0%, Sigma Aldrich) with deionized water to obtain nearly saturated and low concentrations; 4 and 0.4 M (Molar) for ammonium sulfate as well as 6 and 0.6 M for ammonium bisulfate. The experiments were performed at the Swedish synchrotron radiation facility MAX-lab, at the undulator-based soft x-ray beamline I411 [6, 7], equipped with a Scienta R4000 electron spectrometer, mounted at magic angle 54.7◦ for reducing angular effects. The spectra were obtained using a 15 micron liquid jet which is shown in Figure 1, injected into a differentially pumped vacuum chamber. The propagation of the jet was perpendicular to the direction of the photon beam and the spectrometer.

Figure 1. The nozzle with 15 micron in diameter has been used in liquid jet setup.

Typical working pressures were in the 10^{-5} mbar range in the differential pumping stage and in the 10^{-6} mbar range in the analyzer chamber. The experimental setup has been described in more detail elsewhere [8].

The S 2p and N 1s photoelectron spectra were recorded with the photon energy 250 eV and 480 eV, respectively. The experimental resolution in both case was 240 meV. The fitting parameters were in all cases the vertical energies and Gaussian widths of each peak as well as a linear background. Moreover, all spectra have been calibrated against the X state of liquid-phase water [9].

Results and Discussion

Figure 2 shows the N 1s photoelectron spectra of aqueous ammonium sulfate and ammonium bisulfate obtained with photon energy of 480 eV. The N 1s components show a single peak which locates at 406.7 eV binding energy and the width is 1.2 eV. The N 1s XPS spectra were identical for all cases and no significant concentration effect was found. Therefore, we attributed that there is no influence of ammonium ion (NH_4^+) in aqueous ammonium solutions.

Comparing the binding energy of N 1s between aqueous and solid ammonium sulfate which reported by Ref. [10], the N 1s in aqueous solutions is higher than the case of crystal 5.4 eV. However, solvated N 1s is lower than atomic nitrogen 3.2 eV [11].

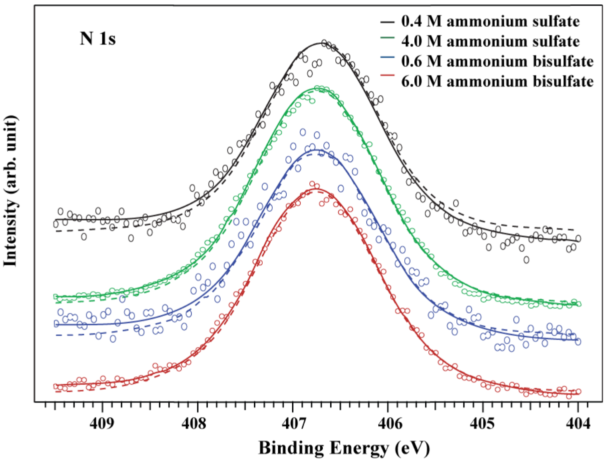

Figure 2. The N 1s photoelectron spectra of aqueous ammonium sulfate and ammonium bisulfate are presented. Circles are experimental data points. The dashed line shows the N 1s component. And the thin solid lines show the sum of the lineshapes. The colors; black and red represent 0.4 and 4.0 M for ammonium sulfate respectively. As well as the colors; blue and red represent 0.6 and 6.0 M for ammonium bisulfate respectively.

The core level S 2p XPS spectra of aqueous ammonium sulfate and bisulfate are presented in figure 3(a) and 3(b), respectively. Dilute and nearly saturation solutions were varied, however no concentration effect could be observed. In addition, the sulfate and bisulfate features are distinguishable by their core levels.

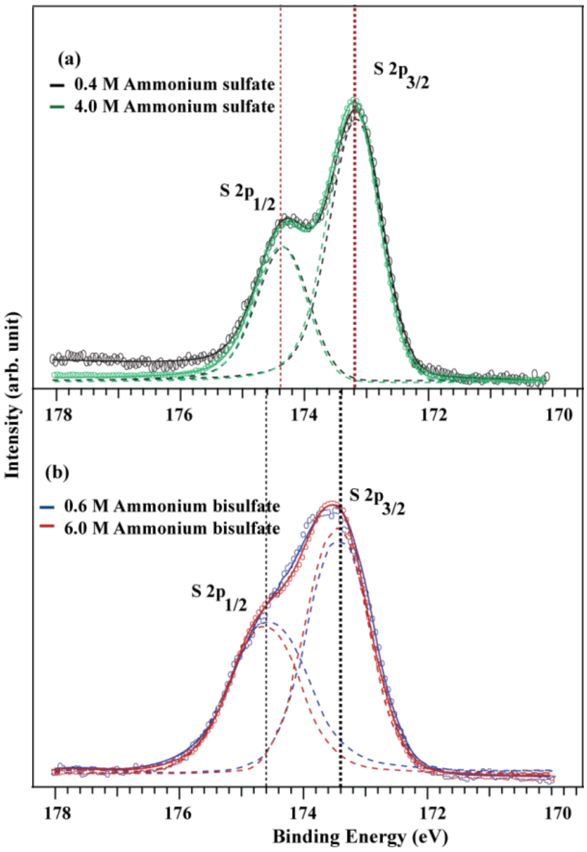

Figure 3. The S 2p photoelectron spectra of aqueous ammonium sulfate and ammonium bisulfate are shown in figure (a) and (b), respectively. Circles are experimental data points. The dashed lines show the S $2p_{3/2}$ components at lower binding energy and S $2p_{1/2}$ components at higher binding energy. And the thin solid lines show the sum of the lineshapes. The colors; black and red represent 0.4 and 4.0 M for ammonium sulfate respectively. As well as the colors; blue and red represent 0.6 and 6.0 M for ammonium bisulfate respectively. The vertical thin dot lines represent the binding energies of S $2p_{3/2}$ components, and the ticker dot lines represent the binding energies of S $2p_{1/2}$ components.

In the case of aqueous ammonium sulfate, the two distinguished components are detected at binding energies 173.2 and 174.4 eV for S $2p_{3/2}$ and $2p_{1/2}$ respectively. The energy splitting is 1.2 eV. For solid ammonium sulfate, the binding energies of S $2p_{3/2}$ were reported at 168.0 and 168.6 eV in Ref. [12] and [13] respectively. They were lower than the liquid phase 5.2 and 5.8 eV. The comparison of different core level binding energies of solvated sulfate ion in aqueous ammonium sulfate to sulfate atomic level, the S $2p_{3/2}$ and $2p_{1/2}$ were 10.7 and 10.8 eV respectively [11].

Figure 3(b) represents S $2p_{3/2}$ and $2p_{1/2}$ in aqueous ammonium bisulfate which the binding energies are detected at 173.4 and 174.6 eV respectively. Moreover the energy splitting between the S $2p_{3/2}$ and $2p_{1/2}$ is 1.2 eV, equally to the case of aqueous ammonium sulfate. However, the core level binding energies are shifted to higher binding energy than aqueous ammonium sulfate 0.2 eV. Therefore, we concluded that HSO_4^- from aqueous ammonium bisulfate is prevailing conduct and effected by the intra-atomic interaction in the ions; H-O-S, which agreed with Ref. [13] and has stronger interaction with the surrounded water molecules than SO_4^{2-} ions from aqueous ammonium sulfate.

Conclusions

Dilute and nearly saturated aqueous ammonium sulfate and ammonium bisulfate were investigated by using liquid micro-jet setup based photoelectron spectroscopy. However, no concentration effect could be observed in all solutions. The N 1s core level spectra were identical for all cases and no significant difference was found. This means no influence of solvated ammonium ion (NH_4^+) in aqueous ammonium sulfate and ammonium bisulfate. The S 2p core level in aqueous ammonium bisulfate is shifted to higher binding energy than aqueous ammonium sulfate 0.2 eV because the intra-atomic interaction effects (H-O-S) and HSO_4^- ions is more pronounced than SO_4^{2-} ions. It is valuable to explore the effect of nitrogen and sulfur in aqueous solution, as well as to investigate the acidifying effect on soil because they are widely used in agricultural applications.

Acknowledgments

This work has been financially supported by Higher Education Research Promotion and National Research University Project of Thailand (HERP-NRU) from The Office of the Higher Education Commission. We also thank Dr. Johan Söderström and Dr. Niklas Ottosson for their encouragement, as well as the MAX lab staff for their helpful assistance during the experiments.

References

1. S. Hüfner. Photoelectron spectroscopy. Springer Verlag, Berlin, 1995.
2. D. W. Turner, C. Baker, A. D. Baker, and C. R. Brundle. Molecular Photoelectron Spectroscopy. Wiley-Interscence, London, 1970.
3. R. Weber, B. Winter, P. M. Schmidt, W. Widdra, I. V. Hertel, M. Dittmar and M. Faubel, J. Phys. Chem. B 108 4729 (2004).
4. B. Winter, R. Weber, W. Widdra, M. Dittmar, M. Faubel and I. V. Hertel, J. Phys. Chem. A 108 2625 (2004).
5. K. Siegbahn, C. Nordling, A. Fahlman, R. Nordberg, K. Hamrin, J. Hedman, G. Johansson, T. Bergmark, S. E. Karlsson, I. Lindgren, and B. Lindberg, editors. ESCA-atomic, molecular, and solid state structure studied by mean of electron spectroscopy. Almqvist och Wiksells, Uppsala, 1967.
6. M. Bässler, J. O. Forsell, O. Björneholm, R. Feifel, M. Jurvansuu, S. Aksela, S. Sundin, S. L.
Sorensen, R. Nyholm, A. Ausmees, et al., J. Electron Spectrosc. Relat. Phenom. 101-103, 953 (1999).
7. M. Bässler, A. Ausmees, M. Jurvansuu, R. Feifel, J. O. Forsell, P. T. Fonseca, A. Kivimäki, S. Sundin, S. L. Sorensen, R. Nyholm, et al., J. Nucl. Instrum. Methods Phs Res. A 469, 382 (2001).R. Saito, G. Dresselhaus, and M. S. Dresselhaus, “Physical Properties of Carbon Nanotubes”, London, Imperial College Press, 1998.
8. H. Bergersen, R. R. T. Marinho, W. Pokapanich, A. Lindblad, O. Bj¨orneholm, L. J. Sæthre, and G. ¨Ohrwall, J. Phys. Condens. Matter 19, 326101 (2007).
9. L. Karlsson, L. Mattsson, R. Jadrny, R. G. Albridge, S. Pinchas, T. Bergmark and K. Siegbahn, J. Chem. Phys. 62 4745 (1975).
10. W. E. Swartz and R. A. Alfonso, J. Electron Spectrosc. Relat. Phenom. 4, 351 (1974).
11. Y. Ralchenko, A. E. Kramida, and J. Reader, NIST Atomic Spectra Database, version 3.1.5; NIST ASD Team, National Institute of Standards and Technology: Gaithersburg, MD, 2008.
12. X.-R. Yu, F. Liu, Z.-Y. Wang, and Y. Chen, J. Electron Spectrosc. Relat. Phenom. 50, 159 (1990).
13. M. Wahlqvist, A. Shchukarev, J. Electron Spectrosc. Relat. Phenom. 156–158, 310–314(2007).

Atomic Physics, Quantum Physics, and Molecular Physics

Influence of Acidity on Spiral Waves in a Bubble-Free Belousov-Zhabotinsky Reaction with Pyrogallol

Jiraporn Luengviriya[1] and Chaiya Luengviriya[2*]

[1]*Department of Industrial Physics and Medical Instrumentation, King Mongkut's University of Technology North Bangkok, 1518 Pibulsongkram Road, Bangkok 10800, Thailand*

[2]*Department of Physics, Kasetsart University, 50 Phaholyothin Road, Jatujak, Bangkok 10900, Thailand*

[*]*Corresponding author. E-mail: fscicyl@ku.ac.th*

Abstract

Spiral waves are ubiquitously observed in a variety of the physical and biological systems ranging from superconductors, superfluids, CO-oxidation on platinum surfaces, cell aggregation of slime mould, and arrhythmia in cardiac tissues. Such spiral waves are uniquely explained by a reaction-diffusion mechanism. Due to both its easy preparation and the convenient detection, the excitable chemical Belousov-Zhabotinsky (BZ) reaction is employed to study spiral waves in experiments. In this article, we present a study on the influence of initial concentration of H_2SO_4 ($[H_2SO_4]$) on the dynamics of spiral waves in a thin layer of the BZ reaction with pyrogallol. This reaction has an advantage over the classical BZ reaction with malonic acid, as it is a bubble-free reaction. We found that the spiral tip, i.e. the organizing center, moved along so-called meandering trajectories with three or four outward petals. In addition, the area occupied by the spiral tip decreased when $[H_2SO_4]$ was increased. A further investigation on the dynamics far from the organizing center was performed by measuring properties of propagating fronts. An increase of $[H_2SO_4]$ resulted in a decrease of the wavelength and the wave period simultaneously. In contrast, the wave speed grew with $[H_2SO_4]$. Since disturbances by the byproduct CO_2 bubbles are avoided and the wave velocity is sufficiently low, the results are expected to present a suitable guideline for further investigations on propagating excitation waves in two- and three-dimensional excitable media, especially, observations of wave instabilities in three-dimensional systems using optical tomography.

***Keywords*: excitable medium, self-organization, meander, tip trajectory.

Introduction

Spiral waves have been observed in different systems such as superconductors [1], superfluids [2], CO-oxidation on platinum surfaces [3], and cell aggregation of slime mould [4]. In the heart, such spiral waves of electrical excitation and their instabilities concern cardiac tachycardia and life-threatening fibrillations [5–7]. The dynamics of spiral waves have been often studied in the Belousov-Zhabotinsky (BZ) reaction as a convenient laboratory model [8, 9]. Depending on the initial concentrations of reagents, the spiral tip may either rotate simply on a circular path or it may meander, involving a more complicated path of motion [10–15]. However, the classical BZ reaction, with malonic acid as organic substrate, produces CO_2 bubbles which disturb the propagation of waves and their observation [16, 17].

In this article, we present a study on dynamics of spiral waves in a bubble-free BZ reaction, in which pyrogallol (1,2,3-trihydroxybenzene) is utilized as substrate [18–24]. We study the effect of the initial concentration of H_2SO_4 on dynamics of the organizing center as well as the properties of propagating fronts in a thin layer of solution.

Materials and Methods

The bubble-free BZ solutions were prepared from $NaBrO_3$, H_2SO_4, pyrogallol and ferroin, all purchased from Merck. Stock solutions of $NaBrO_3$ (1 M) and pyrogallol (1 M) were freshly prepared by dissolving powder in deionized water (conductivity ~ 0.056 $\mu S\ cm^{-1}$), whereas stock solutions of H_2SO_4 (2.5 M) and ferroin (25 mM) were commercially available.

To prevent any hydrodynamic perturbation, the reaction was embedded in a 1.0% w/w agarose gel (Sigma). Appropriate volumes of the stock solutions were mixed and diluted in deionized water to form BZ solutions with different initial concentrations of reagents: $[H_2SO_4]$ was varied between 100 mM and 400 mM, where $[NaBrO_3]$=150 mM, [pyrogallol]=20 mM, and [ferroin]=0.625 mM in all cases. We investigated the dynamics of spiral waves in a uniform thin layer of the BZ reaction in a flat reactor constructed from transparent plexiglas plates [15]. The medium volume was 100×100×1.0 mm^3.

An isolated spiral wave was initiated at about the middle of the medium by the following procedure: The reactor was oriented vertically and 5 ml of BZ solution were filled into the reactor forming the first layer of 5 cm height. Then, we waited until the gel was formed. Wave fronts were initiated by immersion of a silver wire of 0.5 mm diameter close to the left edge of the reactor. Note that the silver wire locally reduces [Br$^-$], which is the inhibitor of the system, by forming AgBr. Next, we waited until one open end of the wave front reached the edge of the reactor and the other open end was located near the middle of the reactor. Another 5 ml of the BZ medium were added to the reactor as the second layer. Shortly after filling the second layer, the open end of the wave front started to curl in and began to form an isolated spiral wave in the BZ system.

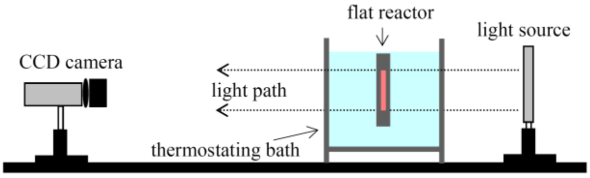

Figure 1. Experimental setup.

The dynamics of the spiral wave was observed in a spectrophotometric setup, as shown in Fig. 1. The reactor was placed into a transparent plexiglas bath thermostated at a temperature 24±0.1°C. The bath was set between a white light source and a colour CCD camera (Super-HAD, Sony). To trace the spiral tip precisely, the images of the medium were recorded every second with a resolution of 0.025, 0.033, or 0.050 mm pixel^{-1}.

For analysis, the color images were converted to 8-bit gray scale ones. The contrast of the images was further enhanced by background subtraction and histogram stretching. The background was calculated as the temporal average of all images. The wavelength was measured as the distance between two adjacent fronts. The period was the duration which it took a wave front to travel for a distance of one wavelength. The speed of the wave front was calculated as the ratio between wavelength and period.

The spiral tip was defined as the intersection of contour lines (0.6×amplitude) of two subsequent images with a time interval of 5 seconds (Fig. 2a) as proposed in [25]. A temporal set of the tip positions was plotted to show the tip trajectory (Fig. 2b).

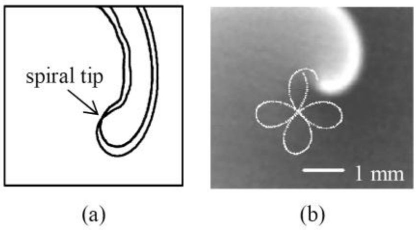

Figure 2. Analysis of spiral tip motion. (a) Definition of the spiral tip. (b) Plot of a spiral tip trajectory.

Results and Discussion

Our fresh prepared BZ solutions had red color due to the reduced state of ferroin. Our results showed that the dynamics of these BZ media depended on the initial concentration of H_2SO_4. For moderate concentrations [H_2SO_4]=150–300 mM, the BZ media exhibited propagating spiral waves. The spiral tip (the organizing center of the wave structure) moved along well-known meandering trajectories often found in different excitable media [10–15]. We observed two types: 3-petal and 4-petal forms of meandering trajectories, as shown in Fig. 3. Note that these paths did not remain unchanged. They might slowly translate or/and rotate as commonly found in other systems.

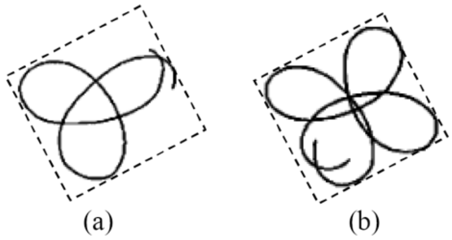

Figure 3. Spiral tip trajectories with (a) 3-petal and (b) 4-petal forms. Dashed rectangles indicate occupying areas of the spiral tip.

Table 1 summarized dynamics of the spiral tip at different [H_2SO_4]. For low concentration 150 mM, the spiral meandered with 3-petal. As the concentration increased, the trajectory form changed to 4-petal. However, it took the 3-petal shape when the concentration was increased to 275 and 300 mM.

The fate of spiral waves in excitable media generally depends on the motion of the spiral tip. The spiral waves are terminated when the tip strongly meanders and ultimately hit the boundary of the media. To study strength of meandering, we measured the occupying area where the spiral tip located (see Fig. 3). As shown in Table 1, this area monotonously decreased when [H_2SO_4] was increased. In addition, it was independent to the form of trajectory.

Table 1: Form and occupying area of the tip trajectory of spiral waves at different [H_2SO_4].

[H_2SO_4] (mM)	**form**	**occupying area (mm^2)**
100–125	no wave	no wave
150	3-petal	6.622
175	4-petal	2.85
200	4-petal	2.59
225	4-petal	1.56
250	4-petal	1.44
275	3-petal	1.21
300	3-petal	1.00

325–400	no wave	no wave

For very low concentrations ([H_2SO_4]≤125 mM), the media were unexcitable. Its color stayed red all time and waves can not be triggered by a silver wire (marked as “no wave” in Table 1 and 2). However, a spiral wave cannot propagate in case of very high concentrations ([H_2SO_4]≥325 mM, “no wave” in Table 1 and 2). Even though waves can be initiated, they can survive for a short time. Then the whole media changed rapidly from red to blue. In this case, the systems were in a so-called stable oxidized state as reported recently in our article [26].

Dynamics of the media far from the spiral tip were investigated via measurements of the properties of wave fronts which emitted from the organizing center. As shown in Table 2, when [H_2SO_4] was increased from 150 mM to 300 mM, both the wavelength and the wave period of the fronts decreased, however, the wave speed grew. The meandering motion of the organizing center which acted as a non-stationary source and caused the Doppler effect. The local properties of wave fronts fluctuated in the course of time. The average values in Table 2 are presented together with the standard deviations.

Table 2: Properties of propagating fronts at different [H_2SO_4]. λ: wavelength, *T*: wave period, and *v*: speed.

[H_2SO_4] (mM)	**λ (mm)**	***T* (min)**	***v* (mm min^{-1})**
100–125	no wave	no wave	no wave
150	8.99±0.86	7.81±1.15	1.16±0.09
175	6.65±0.36	5.55±0.52	1.20±0.06
200	6.03±0.73	4.29±0.77	1.43±0.21
225	5.79±0.56	3.92±0.68	1.50±0.16
250	5.83±0.75	3.62±0.50	1.62±0.07
275	5.98±0.68	3.69±0.27	1.63±0.22
300	5.79±0.75	3.38±0.67	1.76±0.37
325–400	no wave	no wave	no wave

Conclusions

We have studied the influence of [H_2SO_4] on dynamics of spiral waves in the BZ reaction with pyrogallol. For concentration [H_2SO_4] = 150–300 mM, the BZ media supported meandering spiral waves. The spiral tip moved along a 3-petal or 4-petal path whose occupying area decreased when [H_2SO_4] was increased. Far from the spiral tip, the front properties were measured. When [H_2SO_4] became higher, the wavelength and the wave period decreased, while the wave speed increased.

Advantages of the media in this investigation are that they do not produce CO_2 bubbles and they also support slow wave propagation. These properties make the present media suitable for further investigations on propagating excitation waves in 2D and 3D excitable media, especially, observations of wave instabilities in 3D media using optical tomography [16, 17].

Acknowledgments

We thank the Faculty of Science and the Research and Development Institute (KURDI), Kasetsart University; the Faculty of Applied Science, King Mongkut’s University of Technology North Bangkok and the Thailand Research Fund for financial support.

References

1. P.G. de Gennes, *Superconductivity of Metals and Alloys* (Benjamin, New York, 1966).
2. R. Blaauwgeers, V.B. Eitsov, M. Krusius, J.J. Ruohlo, R. Schanen, G.E. Volovik. Double-quantum vortex in superfluid 3He-A, *Nature* (London) **404**:471-473, 2000.
3. S. Nettesheim, A. von Oertzen, H.H. Rotermund, and G. Ertl. Reaction-diffusion patterns in the catalytic CO-oxidation on Pt (110): Front propagation and spiral waves. *J. Chem. Phys*., **98**:9977-9985, 1993.
4. F. Siegert and C.J. Weijer. Digital image processing of optical density wave propagation in Dictyostelium discoideum. *J. Cell Sci*, **93**:325-335, 1989.
5. A.T. Winfree. Electrical turbulence in three-dimensional heart muscle. *Science*, **266**:1003-1006, 1994.
6. R.A. Gray, A.M. Pertsov, and J. Jalife. Spatial and temporal organization during cardiac fibrillation. *Nature* (*London*), **392**:75-78, 1998.
7. F. Fenton, E.M. Cherry, H M. Hastings, and S.J. Evans. Multiple mechanisms of spiral wave breakup in a model of cardiac electrical activity. *Chaos*, **12**:852-892, 2002.
8. A.M. Zhabotinsky. Periodic process of the oxidation of malonic acid in solution (study of the kinetics of Belosouv's reaction). *Biofizika*, **9**:306-311, 1964.
9. A.T. Winfree. Spiral waves of chemical activity. *Science*, **175**:634-636, 1972.
10. S.C. Müller, T. Plesser, and B. Hess. The structure of the core of the spiral wave in the Belousov-Zhabotinsky reaction. *Science*, **230**:661-663, 1985.
11. T. Plesser, S.C. Müller, and B. Hess. Spiral wave dynamics as a function of proton concentration in the ferroin-catalyzed Belousov-Zhabotinsky reaction. *J. Phys. Chem*., **94**:7501-7507, 1990.

12. G.S. Skinner and H.L. Swinney. Periodic to quasiperiodic transition of chemical spiral rotation. *Physica D*, **48**:1-16, 1991.
13. Zs. Nagy-Ungvarai, J. Ungvarai, and S.C. Müller. Complexity in spiral wave dynamics. *Chaos*, **3**:15-19, 1993.
14. G. Li, Q. Ouyang, V. Petrov, and H.L. Swinney. Transition from simple rotating chemical spirals to meandering and traveling spirals. *Phys. Rev. Lett*., **77**:2105-2108, 1996.
15. C. Luengviriya, U. Storb, M.J.B. Hauser, and S.C. Müller. An elegant method to study an isolated spiral wave in a thin layer of a batch Belousov-Zhabotinsky reaction under oxygen-free conditions. *Phys. Chem. Chem. Phys*., **8**:1425-1429, 2006.
16. U. Storb, C.R. Neto, M. Bär, and S.C. Müller. A tomographic study of desynchronization and complex dynamics of scroll waves in an excitable chemical reaction with a gradient. *Phys. Chem. Chem. Phys*., **5**:2344-2353, 2003.
17. C. Luengviriya, U. Storb, G. Lindner, S.C. Müller, M. Bär, and M.J.B. Hauser. Scroll wave instabilities in an excitable chemical medium. *Phys. Rev. Lett.*, **100**:148302, 2008.
18. E. Körös, M. Orbán and I. Habon, Chemical oscillations during the uncatalyzed reaction of aromatic compounds with bromate 3: Effect of one-electron redox couples on uncatalyzed bromate oscillators, *J. Phys. Chem.*, **84**:559-560, 1980.
19. C.C.D. Giles, P. Ibison, J. Liu and S.K. Scott, Uncatalysed Belousov-Zhabotinskii reaction with pyrogallol: Experimental behaviour in a flow reactor and the influence of ferroin as catalyst, *J. Chem. Soc. Faraday Trans.*, **88:**917-924, 1992.
20. M. Orbán, K. Kurin-Csörgei, A. M. Zhabotinsky and I. R. Epstein, New indicators for visualizing pattern formation in uncatalyzed bromate oscillatory systems, *J. Am. Chem. Soc.*, **120**:1146-1150, 1998.
21. A. K. Dutt, Complex dynamical behaviour from coupling between a catalyzed Belousov-Zhabotinskii-like reaction and its uncatalyzed oscillatory component in a flow reactor, *J. Phys. Chem. B*, **106:**11069-11072, 2002.
22. V. Sridevi and R. Ramaswamy. Propagating waves and pattern formation in a reaction-diffusion system with pyrogallol as substrate. *Chem. Lett. (Chem. Soc. Jpn.)*, **5**:459-460, 1998.
23. M. Pornprompanya, S.C. Müller, and H. Ševčíková. Pulse waves under an electric field in the Belousov-Zhabotinsky reaction with pyrogallol as substrate. *Phys. Chem. Chem. Phys.*, **4**:3370-3375, 2002.
24. M. Pornprompanya, H. Ševčíková, and S.C. Müller. Multiple reversals of pulse waves in an excitable medium resulting from switching the polarity of dc electric field. *Chem. Phys. Lett.*, **375**:364-368, 2003.
25. S. Grill, V. S. Zykov, and S.C. Müller. Spiral wave dynamics under pulsatory modulation of excitability. *J. Phys. Chem*., **100**:19082-19088, 1996.
26. C. Luengviriya, J. Luengviriya, M. Sutthiopad, P. Porjai, B. Tomapatanaget, and S. C. Müller. Excitability of the ferroin-catalyzed Belousov-Zhabotinsky reaction with pyrogallol. *Chem. Phys. Lett.*, **561**:170-174, 2013.

Biological Physics and Biomedical Engineering

The Study of Structure and Dynamics of Water Molecules around POPE Phospholipid Bilayer using Molecular Dynamics Method

Somyot Srikongrug[1] and Chalermpol Kanchanawarin[2,3*]

[1]*Department of Physics, Faculty of Science and Technology,*
Rambhai Barni Rajabhat University, Chanthaburi 22000, Thailand
[2]*Theoretical and Computational Biophysics Laboratory, Department of Physics,*
Faculty of Science, Kasetsart University, Bangkok 10900, Thailand
[3]*Thailand Center of Excellence in Physics (ThEP),*
Commission Higher on Education, Bangkok 10400, Thailand

**Corresponding author. E-mail: fscicpk@ku.ac.th*

Abstract

Water is a very essential part of biological membrane. It controls membrane structure as well as forming the membrane surrounding. Simulations and experiments from other research groups have suggested that diffusion of water molecules near a lipid bilayer is affected the membrane surface charges making these water molecules move slower than those in the bulk. To investigate this finding in finer atomic details, we performed simulations to study the structure and dynamics of water molecules around phospholipids bilayer POPE using Molecular Dynamics Methods. Our results show that the diffusion coefficient of water molecules near the membrane surface decrease rapidly up to 50% as they reach the hydrophilic region of the lipid bilayer. This is clearly due to the charges and dipoles of the lipid headgroups. This implies a possibility that water molecules may form a strong and long-lived two-dimensional hydrogen bonded network at the membrane surface which probably allow faster proton transport towards membrane proteins.

Keywords: Molecular Dynamics, POPE lipid, Lipid Bilayer, TIP3P water, Diffusion

Introduction

Water is a very essential part of biological membrane. It involve in both structural and functional roles of biological membrane such as formation of membrane bilayers or liposomes, transport of ions and protons, as well as forming membrane environment. Evidences from both experiments and simulations have suggested that the dynamics of water molecules near biological membrane are affected by membrane surface charges. The dynamics of water molecules near the phospholipids bilayer surface has been investigated by molecular dynamics simulations. The simulations show that diffusion of water molecules varies with the distance from the membrane [1]. Another study compared the effects of lipid bilayers POPC, POPE and POPG on water dynamics, showing that the headgroups of POPC and POPG bilayers affect the rotational motion of water more than that of POPE [2]. The effect of membrane bilayer on the translational and rotational diffusion of water extends far from the surface by a distance of about 7 Å [3].

In this study, we aim to make a detailed understanding at atom scales on how the diffusion and orientation of water molecules are affected by POPE bilayer using molecular dynamics simulations.

Materials and Methods

We setup a membrane-water system of POPE (1-palmitoyl-2-oleoyl-glycero-phosphoethanolamine) lipids surrounded by water. The atomic structure of the POPE membrane bilayer with 72 lipids on each layer was constructed from CHARMM–GUI membrane building server [4]. Water layers of thickness 30 Å modeled using TIP3P [5] were added on each side of the membrane. To simplify the system and analysis, we did not add ions to the system. The final system consisted of 144 POPE lipids and 9,284 TIP3P water molecules and had 45,825 atoms in a rectangle of size 67.35×67.35×100 Å^3.

MD simulations of the membrane system were performed using NAMD 2.6 program [6] running on a computer cluster using twenty-four 2.3 GHz AMD Opteron CPUs at 1.33 ns per day. All atomic parameters for the force and energy calculations were obtained from CHARMM27 force fields [7]. MD simulations were performed using periodic boundary conditions. Temperature and pressure were controlled using Lengevin temperature control with a damping constant of 5.0 per ps and Langevin piston control [8] with an oscillation period of 200 fs and a damping time of 100 fs. van der Waals interactions were calculated every time step using a 13 Å cutoff distance and a switching function. An integration time step of 2 fs was used to enable multiple time-stepping algorithm to be used in the calculations of the long range electrostatic interactions which was done using the particle mesh Ewald method [9,10].

The MD simulations were performed in four parts. First, the membrane-water system was energy-minimized for 10,000 steps. Second, it was heated to increase the temperature from 0 K to 310 K for 0.12 ns. Third, the system was equilibrated at pressure 1 atm and temperature 310 K for 2 ns. Fourth, the system was further equilibrated at pressure 1 atm and temperature 310 K for 20 ns.

Analysis was done using VMD program [11] for visualizing the membrane-water system on a 3D-stereo graphics workstation. Atomic coordinates of the system was taken every picosecond from the last nanosecond of the fourth MD simulation to make a 1,000 frame trajectory used for analysis. For each frame, the system was divided and analyzed sequentially as a thin rectangular layer with a thickness of 4 Å along the z axis perpendicular to the membrane plane. The next rectangular layer was formed and analyzed by shifting the previous layer along the z-axis by 0.2 Å. For each rectangular layer, we calculated (over all trajectory frames) the average values of the number density of different types of atoms in the system, the diffusion coefficient and the total electric dipole moment of all the water molecules in each layer. This was done for 460 layers from the top to the bottom part of the membrane-water system.

Results and Discussion

The system of POPE bilayer in water at the end of the 20 ns MD simulation equilibrated at temperature 310 K and pressure 1 atm is shown in Figure 1. It forms a planar bilayer with a thickness of about 40 Å as can be estimated from the distance between the two peaks of phosphorus-atom layers in the number density profile of the bilayer shown in Figure 2. Water molecules can be found as far as about 10 Å below the phosphorus atom layers. Beyond that it is a non-polar region of the bilayer where water cannot form hydrogen bonds with.

The diffusion coefficients of the water molecules shown in Figure 3 show that water molecules move slower in all three directions as they get closer towards the membrane surface. The diffusion coefficients start to decrease at the distance about 30 Å from both sides of the membrane surfaces. Within 20 Å, they can decrease to about one half of its bulk value (from 4.3×10^{-5} cm^2s^{-1} to 2×10^{-5} cm^2s^{-1}). Just before these water molecules move beyond the polar regions containing oxygen atoms of the membrane, the diffusion coefficients start to increase and then peak at the maxima of the number densities of hydrogen and carbon atoms and then decrease abruptly towards zero within about 4 Å distance from the peaks.

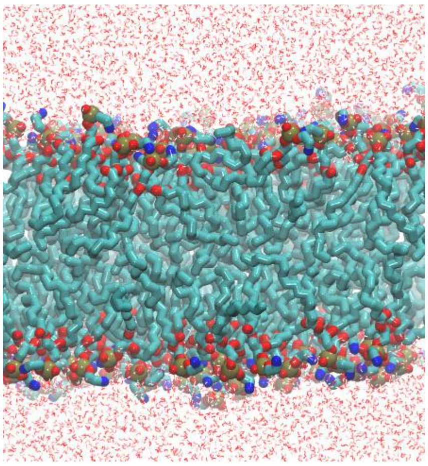

Figure 1. POPE bilayer in water at the end of 20 ns simulation (side view). POPE molecules are drawn as tubes. Water molecules are drawn as red lines. Phosphorus atoms are drawn as golden spheres. Carbon, oxygen atoms nitrogen atoms are colored in cyan, red and blue respectively. Hydrogen atoms on POPE are not shown to reduce complexity of the figure.

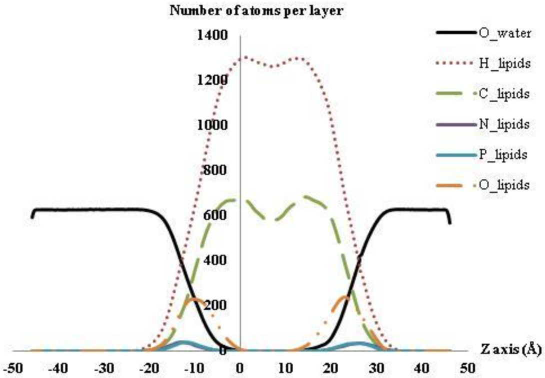

Figure 2. The number density profile of various atoms in POPE-bilayer. The thickness of the membrane can be estimated from the distance between two peaks of phosphorus atoms colored in blue.

To explain the decrease in the values of the diffusion coefficients of water molecules near membrane surface we need to see how the electric dipoles of POPE lipids affect the surrounding water molecules. This can be seen by calculating the total electric dipole and its components in x, y and z-directions of water molecule at various distances along the z-axes as shown in Figure 4. It can be seen that mainly there are strong dipole moments of water molecules along the z-axis (green solid line, but not along the x- and y-axes) peaks at positions z = -15 and +28 Å where the electric dipole moments of lipids formed by positively charged PE (phosphatidyl-ethanolamine) head group and negatively charged phosphate groups are located. This suggests that the decrease in water diffusion coefficients may come directly from the strong electrical attraction between the two charged groups on the polar heads of POPE lipids and the surrounding water molecules.

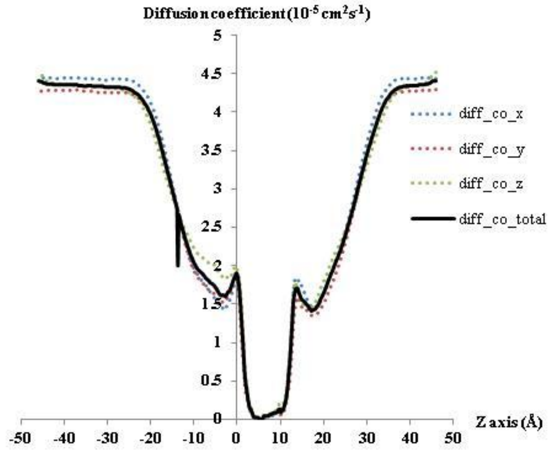

Figure 3. Diffusion coefficient of water molecules along x, y, and z directions at various positions along the z-axis.

Another feature that may explain the further decrease and the later increase in water diffusion coefficients is the two flipping of total dipole moment along the z axis (green solid line) of water molecules below the strong dipole peaks between z = -10 and 0 Å; and between z = +14 and +23 Å in Figure 4. The water dipole flipping possibly comes from the strong attraction of the phosphate groups (at z = -13 and +27 Å) in those regions. This causes further decrease in water diffusion coefficients. As we move deeper towards the membrane center, the flipped dipole moments become smaller and disappear between z = +3 and +14 Å. This is possibly due to the lack of polar groups in the region and the negatively charged oxygen atoms on glycerol parts of the lipids that counteract with the negatively charged phosphate groups. The later increase in the values of water diffusion coefficients may be explained from increase in mobility of water molecules around glycerol parts of the lipids due to much less electrostatic interactions in this region.

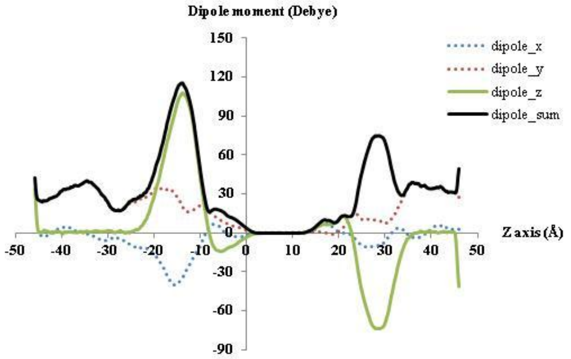

Figure 4. Total electric dipole moment and its components along x, y and z axes of water molecules (magnitude) in rectangular layers of 4 Å thickness along z axis.

The strong reduction in water molecule mobility near membrane surfaces has very important implications in various biological processes that involve water molecules such as proton transfer from bulk water to membrane proteins. Protons are often involved in transport of electrical energy and charges in biological systems. For example, in ATP synthesis protons are transported from water to a membrane protein, called ATP synthase, which converts the electrical energy of proton motion to chemical energy stored in chemical bond of a molecule called ATP. Some experimental evidence suggested that proton transport by 3-dimensional diffusion from bulk water to the protein is lower and not consistent with the ATP synthesis rate measured. It has been suggested that protons may not comes from the 3D bulk water but diffuse along the 2D plane of the membrane-water interface instead. Our results support this idea in that as water molecules near the membrane surface moves slower, they can form a 2D network of hydrogen bonds that last longer. This allows protons to be transported faster along the 2D hydrogen bonded network of water molecules at the membrane-water interface.

Conclusions

In this study, we performed a 22 ns molecular dynamics simulation of a POPE bilayer-water system without ions. We observe very strong decrease in diffusion of water molecules near the POPE bilayer surface and found that the reduced mobility of water molecules comes mainly from the charges and the dipole moment on the polar part of POPE lipids. The result could imply that water molecules may form a strong and long-lived two-dimensional hydrogen bonded network at the membrane surface which probably allow faster proton transport towards membrane proteins.

Acknowledgments

This work is supported by Kasetsart University Research and Development Institute (KURDI) Grant No. Por-Tor(Dor)158.55. S.S. is grateful for scholarship and financial supports from Rambhai Barni Rajabhat University. C.K. is grateful for support from Thailand Center of Excellence in Physics (ThEP). Both authors would like to thank the Department of Physics, Faculty of Science, Kasetsart University for computational facilities and supports.

References

1. O.Chara, A.N. McCarty, C.G. Ferara and E.R. Caffarena. “Water behavior in the neighborhood of hydrophilic and hydrophobic membranes : Lessons from molecular dynamics simulations”, Physica A. **388** (2009), 4551-4599.
2. T. Ro′g, K. Murzyn and M.P. Gierula. “The dynamics of water at the phospholipids Bilayer surface a molecular dynamic simulation study”, Chemical Physics Letters. **352**(2005), 323-327.
3. W. Zhao. “Molecular modeling of charged membrane systems”, Ph.D. Thesis, Helsinki University. 2006.
4. J. Sunhwan, J.B. Lim, J.B. Klauda and W. Im. “CHARMM-GUI Membrane Builder for Mixed Bilayers and Its Application to Yeast Membranes”, Biophysical Journal. **97**(2009), 50-58.
5. W. L. Jorgensen, J. Chandrasekhar, J. D. Madura, R. W. Impey and M. L. Klein. “Comparison of simple potential functions for simulating lipid water”, J. Chem. Phys. **79**(1983), 926-935.
6. J. C. Phillips, R. Braun, W. Wang, J. Gumbart, E. Tajkhorshid, E. Villa, C. Chipot, R. D. Skeel, L. Kale′ and K. Schulten. “Scalable Molecular Dynamics with NAMD”, J. Comput. Chem. **26**(2005), 1781-1802.
7. A. D. MacKerell, Jr., D. Bashford, M. Bellott, R. L. Dunbrack, J. D. Evanseck, M. J. Field, S. Fischer, J. Gao, H. Guo, S. Ha, D. Joseph-McCarthy, L. Kuchnir, K. Kuczera, F. T. K. Lau, C. Mattos, S. Michnick, T. Ngo, D. T. Nguyen, B. Prodhom, W. E. Reiher, III, B. Roux, M. Schlenkrich, J.C. Smith, R. Stote, J. Straub, M. Watanabe, J. Wio′rkiewicz-Kuczera, D. Yin and M. Karplus. “All-Atom Empirical Potential for Molecular Modeling and Dynamics Studies of Proteins”, J. Phys. Chem. B. **102**(1998), 3586-3616.
8. S. E. Feller, Y. Zhang and R. W. Pastor. “Constant pressure molecular dynamics simulation:The Langevin piston method”, J. Chem. Phys. **103**(1995), 4613-4621.
9. T. Daarden, D. York and L. Pedersen. “Particle mesh Ewald:An Nlog(N) method for Ewald sums in large systems”, J. Chem. Phys. **98**(1993), 10089-10092.
10. U. Essmann, L. Perera, M. L. Berkowitz, T. Darden, H. Lee and L. G. Pedersen. “A smooth particle mesh Ewald method”, J. Chem. Phys. **103**(1995), 8577-8593.
11. W. Humphrey, A. Dalke and K. Schulten. “VMD:Visual Molecular Dynamics”, J. Mol. Graphics. **14**(1996), 33-38.

Surface Modification of Polystyrene Dishes with Sericin by Plasma Grafting Polymerization

J. Nuandee[1]*, W. Wongkham[2] and D. Boonyawan[1]

[1] *Plasma-Bio and Clean Energy Laboratory, Department of Physics and Materials Science, Faculty of Science, Chiang Mai University, Chiang Mai 50200, Thailand*
[2] *Department of Biology, Faculty of Science, Chiang Mai University, Chiang Mai 50200, Thailand*
**Corresponding author. E-mail: jompak_nuanee@hotmail.com*

Abstract

During Culture, most mammalian cells require serum or culture medium containing serum replacement but also contaminated with virus. This research aims to use silk sericin instead of using serum because it is low cost and free of alien cell contamination. However, sericin quickly releases to culture media which effect cell attachment and cell proliferation rate. In this study we coated sericin on polystyrene by plasma grafting technique lead to sericin and polystyrene bound with covalent bond and also perform cross-link between sericin. So, it can slow down the release rate of sericin in cell culture. For the plasma process, we utilize Plasma-enhanced chemical vapor deposition by using capacitively coupled plasma discharge (CCP) reactor.We observed protein adsorption on treated culture dishes using UV visible technique. The optical intensity of treated sample was 8% improved at 280 nm wavelength. It was found that the release rate of sericin to decrease when plasma grafting had performed.

***Keywords*:** Sericin, Cell Culture , Polystyrene , Plasma modification

Introduction

Polystyrene (PS) is widely used as biomaterials for cell culture because of it potential biocompatibility and biodegradability, non-toxicity with cell, high transmittance in the visible range, low production cost, easily processed[1]. However, PS surfaces are not optimal for cell adhesion because PS surfaces are hydrophobic and do not provide a suitable environment for cell growth. In cell culture can seen that cells grow very well on a hydrophillic surface than on hydrophobic surface. Therefore, many researchers have developed various kinds of methods to modify hydrophobic surface to improve the cell the cell adhesion on surface. These include bulk modification of the chemical structure, plasma treatment or plasma polymerization, and coating or grafting adhesive protein that mediate cellular attachment[2].

Plasma is a highly unusual and reactive chemical environment in which many plasma-surface reactions occur. The high-density of ionized and excited species in the plasma can change the surface properties of normally inert materials such as polymer[3]. In particular, the plasma polymerization is the method of choice for modifying polymer surfaces for cell culture. It provided a unique and powerful method for modification of polymeric materials. The major effects observed in plasma treatment of polymer surfaces are cleaning of organic contamination, micro-etching, cross-linking, increases the surface energy and associated adhesion to other materials[4]. The most important feature of the plasma technique is that the surface properties of the treated material can be modified without changing their intrinsic bulk properties[5].

Sericin is an important bio-material, which can be used in cell culture, because it shows good biocompatiblity, biodegradation, non-toxicity, oxidation resistance, antibacterial properties, UV resistance, etc. Sericin is a water-soluble natural protein constituting 25%-30% of silk[6]. Sericin is a macromolecular globular protein having molecular mass of 10 to 310 kDa. Sericin consists of 18 amino acids, most of which have strongly polar side groups such as hydroxyl, carboxyl, and amino groups (Sarovart et al., 2003). Sericin is also especially rich in aspartic acid (~19%) as well as serine (~32%) (Wu et al., 2006). The protein can be cross-linked, copolymerized, and blended with other macromolecular materials to produce materials of improved properties[7].

Since, sericin easy to dissolve by water which effected cell attachment and cell proliferation rate. The aim of this study is to slow down the release rate of sericin in cell culture on the PS surface dish by using plasma grafting polymerization technique to increase adhesion on PS surface dishs and cross-linking. UV-Visible spectroscopy was performed to examined the releasing rate of sericin by the absorbance spectra of protein in PBS. The functional group and adhesion on the surface of sericin were analyzed using Fourier transform infrared spectroscopy (FTIR). The atomic force microscope (AFM) was used to study the morphology of the surface of the modified polystyrene dish. The efficiency of cell attachment and proliferation will be tested by biological technique.

Material and method

Material

Polystyrene dish were purchased from SPL Lifesciences Co.Ltd (Korea). Sericin (Bombyx mori) was purchased in powder from Thailand Institute of Nuclear Technology (Public Organization) (Thailand).

Method

Preparation of sericin solutions

The sericin solutions were prepared by dissolving 0.1 g sericin powder in deionized water at 80ºC and stirring for 60 minutes to form solutions of 5% (w/v) concentration.

Preparation of plasma grafting sericin

The PS dish were exposed to Argon plasma in capacitively coupled plasma discharge reactor. The RF power at 13.56 MHz was coupled to the chamber via a manual impedance matching network. A Pirani gauge and digital controller monitored pressures. A base presure of typically 8 mtorr was achieved using a rotary vacuum pump. A constant flow rate of argon gas at 1 mtorr and 100 W RF power for 10 minute were used in all experiments. After exposure to the plasma the PS dish were graft with sericin solution at 100 µl and keep in dry.

Surface Characterization

Contact anglemeter: contact angle were measured using Contact Angle Meter using sessile drop and single fiber wilhelmy methods at 20 µl droplet of doubly distilled water. Samples (PS untreated and treated Argon plasma) were cut into 3 cm diameter. The valves of contact angle were taken as average values at different place.

FTIR: The infrared spectra of the modified and unmodified polystyrene dish were recorded using ThermoFisher scientific. The spectra were recorded in the absorption mode within the wavenumber range 4000-400 cm^{-1}. Samples(unmodified PS and modified PS with sericin) were cut into 1.4 cm diameter for determination.

AFM: The surface topography and roughness of samples were studied in tipping mode. The samples were cut into 1.4 cm diameter for determination. Measurements were done with 30 × 30 µm^2 scan area at room temperature.

UV-Visible: The release rate of sericin was examined using UNICAM UV 500 Type 9423 UV530EEE. The spectra was recorded in the absorption mode within the wavelength rang 200 - 350 nm. Samples (modified PS with sericin and unmodified PS with sericin) were dissolves by PBS at 5 ml for 24 hours.

Result and Discussion

Contact Angle

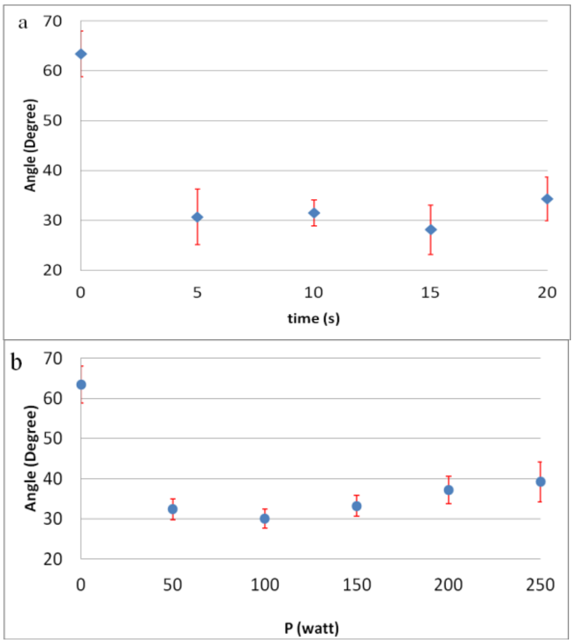

Fig. 1 Water contact angle on PS as a function of (a) exposure times (RF power: 100 W), (b) RF power (plasma duration: 10 min)

Fig.1 show the changes of the contact angles of water on PS as a function of (a) exposure times, (b) RF power by argon plasma. The contact angles of water on PS modified samples were reduced to 30.1º from 63º of unmodified sample. As shown Fig. 1(a), the contact angles are not much change with exposure times. However, at 10 minutes is optimized for argon plasma because it had minimum error bar. As shown in Fig. 1(b), the minimum contact angle was 30.1º at RF power 100 W, which lower than RF power 150 and 200 W due to PS gets too high energy caused loss structure function. From this result, we can conclude that the condition of capacitively coupled plasma discharge reactor was used in RF power 100 W for 10 min.

UV-visible spectroscopy

Sericin is one of a protein synthesized by silkworm. Generally, proteins absorb near-ultraviolet region. In this experiment, sericin be expected also the absorption at 280 nm. As Shown in Fig. 2, the absorption band at 280 nm of the samples of modified PS with sericin were decreased as much as 8% compare to the samples of unmodified PS with sericin. These results indicate that the release rate of sericin on PS dish to decrease when modified PS dish by using Argon plasma because of plasma induces a chemical reaction between sericin and PS structure.

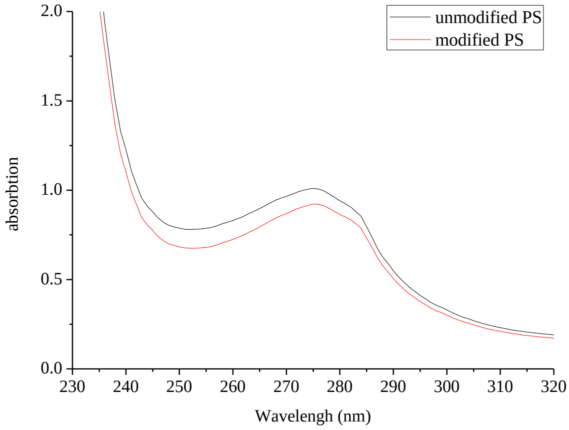

Fig. 2, UV-VIS spectra of unmodified PS with sericin and modified PS with sericin

Fourier transform infrared spectroscopy

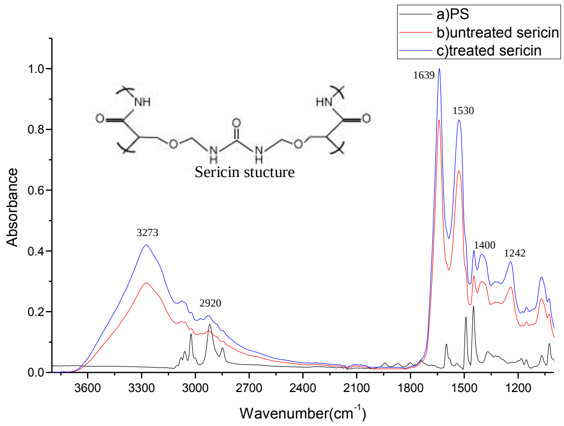

Fig. 3 FTIR spectra of PS, unmodified PS with sericin and modified PS with sericin

FTIR spectra of unmodified PS, unmodified PS with sericin and modified PS with sericin. The FTIR spectra of sericin can be shown in Fig. 3, The broad peak centered around 3273 cm^{-1} is assigned to the stretching frequencies of the hydroxyl groups of sericin and peak at 2920 cm^{-1} is assigned to C–H asymmetrical stretching. For a protein bands can be seen at 1639 cm^{-1}(amide I), 1530 cm^{-1}(amide II) and 1242 cm^{-1}(amide III) is assigned corresponding to C=O, N-H, and C-N stretching, respectively. And the peak at 1400 cm^{-1} is observed corresponding to OH groups of serine. As shown in Fig. 3, the relative intensity of the band between unmodified PS with sericin and modified PS with sericin is seem similar. However, the chemical reaction between sericin and PS can be affirmed by using the results from UV-Visible spectroscopy.

Conclusion

The PS with sericin coatings prepared by plasma grafting polymerization techniques with Argon gas was found enhanced the adhesion between sericin and PS. The results of UV-Visible indicated that the PS surface induces a chemical reaction between sericin and PS structure. It can be concluded that plasma grafting polymerization techniques is promising for decreasing the release rate of sericin on PS dishs.

Acknowledgements

This work was financially supported by Plasma and Clean Energy Laboratory, Department of Physics and materials science, Faculty of Science, Chiang Mai University. And we also acknowledge Thailand Center of Excellence in Physics (ThEP) for providing scholarships for the author.

References

1. W. Hu, E. K. F. Yim, R. M. Reano, K. W. Leong, and S. W. Pang (2005). Effects of nanoimprinted patterns in tissue-culture polystyrene on cell behavior. J Vac Sci Technol A. November; 23(6): 2984–2989.
2. Choi, S. C., Choi, W. K., Jung, H. J., Park, J. G., Chung, B. C., Yoo, Y. S., & Koh, S. K. (1999). Relation between hydrophilicity and cell culturing on polystyrene Petri dish modified by ion-assisted reaction. Journal of applied polymer science, 73(1), 41-46.
3. P.K. Chu, J.Y. Chen, L.P. Wang, N. Huang (2002). Plasma-surface modification of biomaterials. Materials Science and Engineering R 36 143–206.
4. G.H. Ryu, W.S. Yang, H.W. Roh, I.S. Lee, J.K. Kim, G.H. Lee, D.H. Lee, B.J. Park, M.S. Lee, J.C. Park. (2005). Plasma surface modification of poly(D,L-lactic-co-glycolic acid) (65/35) film for tissue engineering. Surface and Coatings Technology 193(1-3), 60-64.
5. I. A. Rusu, G. Popa, S. O. Saied, J. L. Sullivan (2005). Argon rf plasma treatment of pet films for silicon films adhesion improvement. Journal of Optoelectronics and Advanced Materials.
6. G. Genç, G. Narin, O. Bayraktar, Spray drying as a method of producing silk sericin powders, Journal of Achievements in Materials and Manufacturing Engineering 37/1 (2009) 78-86.
7. Wu J-H, Wang Z, Xu S-Y (2007). Preparation and characterization of sericin powder extracted from silk industry waste water. Food Chem 103: 1255-1262.

Scaffold Preparation from Silk Fibroin on Polystyrene Dish by Plasma Grafting Polymerization

A. Kanjai[1*], W. Wongkham[2], D. Boonyawan[1]

[1]*Plasma - Bio and Clean Energy Laboratory, Department of Physics and materials science,*
Faculty of Science, Chiang Mai University, Suthep Road, Chiang Mai 50200, Thailand
[2]*Department of Biology, Faculty of science Faculty of Science,*
Chiang Mai University, Suthep Road, Chiang Mai 50200, Thailand
**Corresponding author. E-mail: Aekkarach.k@gmail.com*

Abstract

This research aims to modify surface of polystyrene dish, utilized in cell culture. According to the low efficiency of cell attachment and proliferation on commercial polystyrene dish, scaffold with porous structure on the polystyrene dish is required to improve the cell attachment and proliferation efficiency on the dish. The scaffold with porous structure will be fabricated from solution of powdered silk fibroin by plasma grafting polymerization technique. The plasma is produced by a capacitively coupled discharge reactor (CCP) at low pressure 100 mTorr. The variation of the power generator, plasma treatment time, and the cycle of coating on the dish are studied. The proper treatment time and power of generator are 10 minutes and 100 watts, respectively. Argon plasma treatment of PS surface yielded decreased water-contact angles relative to untreated surface so that plasma can change the property of surface from hydrophobic to hydrophilic. It was revealed that the scaffold prepared in this study had uniformly distributed pores and high porosity. Representative UV-vis absorption spectra increase with the number of scaffold layers. The treated dish has lower spectra absorbance than the untreated dish which means the efficiency of grafting between the scaffold and treated surface is better than the untreated surface. Also the peak of amino acid with aromatic ring, named phanyalanine at 280 nm affirmed the success of grafting between fibroin and polystyrene.

Keywords**:** polystyrene, plasma treatment, silk fibroin, cell culture

Introduction

Several kinds of polymer have been utilized in cell culture application. Among many polymers, polystyrene (PS) has generally been used as a disposable culture dish due to the following properties; its optical transparency in visible range, excellent stamina and non-toxicity. PS, however, has a low surface energy and is classified as a nonspecific adsorbent of biological molecules. Moreover, this also results in its poor wettability by water and to very low adsorptive and adhesive properties with cells. To simplify animal cell growth on the PS dishes, the surface of the dishes has been treated by either γ-irradiation, chemical modification, or plasma discharge to generate hydrophilic groups such as ether, carbonyl, and carboxylic groups [1, 2, 3].

Surface modification has been obtained by plasma polymerization techniques. Without altering their bulk properties [3], plasma polymerization techniques furnish a unique and powerful method for modification of polymeric materials. At atomic level, polymerization is also plausible when adequate energy is supplied to destroy the bonds on the polymer. The plasma polymerization is commonly pinhole-free, high cross-linked and strongly bound to the surface [4]. Argon plasma has been applied in many ways, for example, pretreatment for grafting or crosslinking of surface macromolecules, removal of contaminants on the surface, and ablation of material from the surface in order to remove a weak boundary layer and increase surface roughness for better adhesion [5].

Silkworm silk fibroin has been commercially used for decades as biomedical sutures and for centuries in textile production. Silkworm silk from Bombyx mori is primarily composed of two protein components; fibroin and sericin. Fibroin is a structural protein of silk fibers while sericin is a water-soluble glue-like protein that binds fibroin fibers together. Connected by a disulfide link, silk fibroin consists of heavy and light chain polypeptides of ~350 and 25 kDa, respectively. Fibroin is a protein dominated in composition by the amino acids glycine, alanine and serine which form antiparallel β-sheets in the spun fibers, leading to the stability and mechanical features of the fibers. Silk fibroin provides an important set of material options for biomaterials and scaffolds for tissue engineering due to the impressive mechanical properties, biocompatibility and biodegradability [6].

For tissue engineering, an ideal scaffold material is one of many important components. The scaffold provides mechanical stability and maintains a three-dimensional space for the formation of new cells with appropriate structure. Scaffold should support cell attachment, migration, cell-cell interaction, cell proliferations and differentiation. Highly porous scaffolds are desirable because cells can easily penetrate the pores and fill the scaffolds [7, 8].

This study aims to create scaffold from solution of powdered silk fibroin on the PS surface by plasma grafting polymerization technique. A scanning electron microscope (SEM) and an atomic force microscope (AFM) will be used to investigate the morphology of the surface of the modified polystyrene. The releasing rate of scaffold will be measured by the absorbance spectra of protein in PBS from UV-Visible spectroscopy. The chemical bonding of the surface will also be examined with the Fourier transform infrared spectroscopy (FTIR). Finally, the efficiency of cell attachment and proliferation will be determined by biological assay.

Materials and Methods

Materials

Commercial materials used in the present study were obtained as follows: 35×10 mm culture polystyrene dishes from SPL Lifesciences Co.Ltd (Korea); Bombyx mori silk fibroin powder from Thailand Institute of Nuclear Technology (Public Organization) (Thailand); Hexafluoroisopropanol (HFIP) from Sigma-Aldrich (Singapore). All other reagents were of the highest grade available.

Preparation of scaffold from silk fibroin on PS surfaces by plasma grafting polymerization

The sterilized pure PS Petri-dishes were used as substrate in the argon plasma treatment without cleaning because the Petri-dishes could be contaminated by the cleaning process which could affect the results of cell culturing. For the surface modification, the Petri-dishes were exposed to argon plasma in the cylindrical chamber. The RF power at 13.56 MHz was coupled to the chamber via a manual impedance matching network using circular disc-shaped parallel electrodes which are separated by a distance of 10 centimeters. A base pressure of typically 8.3×10^{-3} Torr was achieved using a rotary vacuum pump. The argon pressure during plasma treatment was set at 100 mTorr with a range of RF powers from 50 to 250 watts and treatment times from 5 to 20 minutes. After plasma was produced, a 2.5% w/v of fibroin solution dissolved in HFIP in the amount of 100 microlitres was added to each treated dish and then incubated at room temperature for 24 h.

Contact angle measurement

In order to examine the effect of plasma treatment on the hydrophilicity of PS dishes, the dish surface was characterized by static water contact angle measurements using the sessile drop method. For the sessile drop measurement, a water droplet of approximately 20 μl was placed on the dry surface of each dish. The contact angle of water onto the dish was detected at room temperature using a contact angle analyzer equipped with a special optical system and a device camera.

UV-Vissible Spectroscopy

To monitor the releasing rate of fibroin scaffold from the PS surface, UV-Visible Spectroscopy were used. After scaffolds were fabricated on the PS surface, 5 ml of phosphate-buffered saline (PBS) were added to each modified dish and then left the dishes for 24 h. Then suck up the PBS to quartz cuvette and measure the absorbance spectra of protein in PBS solution from UV-Visible spectroscopy.

Surface analysis

The Petri-dishes were cut into circular shaped with 1 centimeter diameter. The surface topographies of the untreated and treated dishes were identified by atomic force microscopy (AFM) in tapping mode. And the morphologies of the scaffolds were observed by scanning electron microscope (SEM). The cut dishes were mounted and sputter-coated with gold using an ion coater and then observed at accelerating voltage of 15 kV.

Fourier Transform Infrared Spectroscopy (FTIR)

The surface chemical composition of modified dish was investigated by a Fourier transform infrared spectroscopy. Polarized absorbance spectra of fibrils were recorded using a spectrometer in the spectroscopic range between 400 and 4000 cm^{-1} with a resolution of 4.0 cm^{-1}. The measurement was carried out at room temperature.

Results and Discussion

1. Contact angle

The water contact angle was measured to determine the effect of argon plasma treatment on the hydrophilicity of PS dish surfaces. As shown in Figure 1 (A), the plasma pressure and exposure time were fixed at 100 mTorr and 10 minutes, respectively and the powers were varied from 50 to 250 watts. The untreated PS is hydrophobic, but became hydrophilic when treated with the argon plasma. The water contact angle of the surfaces before plasma treatment was $63.4\pm1.3^\circ$, which was significantly decreased to $32.4\pm0.8^\circ$ and $30.1\pm0.7^\circ$ after plasma treatment at the powers of 50 and 100 watts, respectively. At the powers of 150, 200 and 250 watts, the water contact angle was slightly increased when the powers increased. These results suggest that the highest hydrophilicity surface occurred at 100 watts of power. In Figure 1 (B), the plasma pressure and power of generator were fixed at 100 mTorr and 100 watts, respectively and the exposure time were varied from 5 to 20 minutes. The lowest value of contact angle occurred at 10 minutes of exposure time, prolonged treatment after 10 minutes correlated with higher contact angles. These results can be concluded that the proper treatment time and power of generator are 10 minutes and 100 watts, respectively at 100 mTorr of plasma pressure.

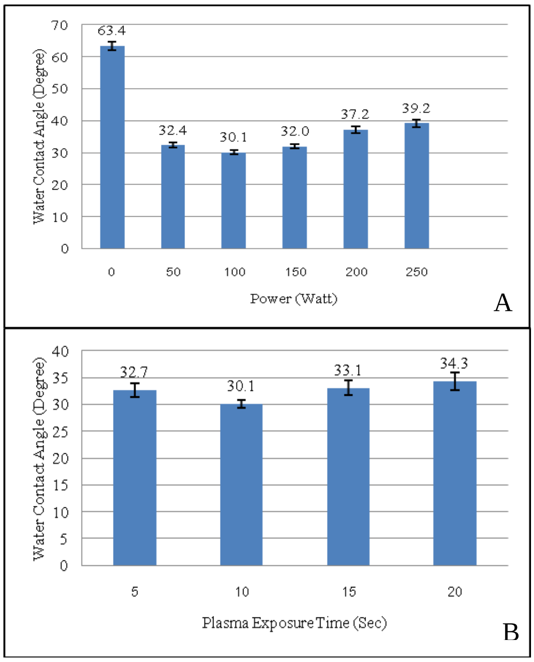

Fig.1 Contact angles of PS surfaces. (A): effect of RF power (plasma pressure: 100 mTorr and plasma exposure time: 10 minutes) (B): effect of plasma exposure time (plasma pressure: 100 mTorr and RF power: 100 watts)

It is well-known that the surface hydrophilicity of a polymer plays an important role in homogeneous cell seeding and predominant cell growth onto it. In our previous report, it has already been shown that argon plasma treatment provided remarkably enhanced cell affinity for the polymer surface [5].

2. UV-Visible Spectroscopy

To monitor the releasing rate of fibroin scaffold from the PS surface, UV-Visible Spectroscopy was employed. Representative UV-Vis absorption spectra of protein in PBS can be shown in Figure 2. The curves, from bottom to top, correspond to adsorption of treated dish with 1 layer of scaffold, untreated dish with 1 layer of scaffold, treated dish with 2 layers of scaffolds and untreated dish with 2 layers of scaffolds, respectively. From the figure 2, higher absorbance means higher releasing rate of scaffold. From the comparison of absorbance between the treated dish and untreated dish resulted that the untreated dish had higher releasing rate than the treated dish. Energy transfer from the argon plasma to PS surface caused ablation of hydrogen or chain scission. Moreover, free radicals occurred on the surface as ready to construct covalent bonds with the elements from coated fibroin solution such as oxygen, hydrogen, or nitrogen. After that chemical functional groups, e.g. amine, carboxyl, carbonyl, were formed on the modified surface. These functional groups are very important for growth of cells. Strength of covalent bonds affected scaffold releasing rate from the PS surface. The high strength of covalent bond leads the low scaffold releasing rate and vice versa.

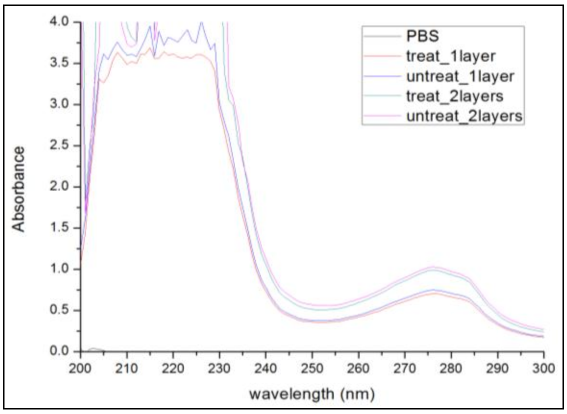

Fig.2 UV-Vis absorption spectra of protein in PBS. The curves, from bottom to top, correspond to adsorption of treated dish with 1 layer of scaffold, untreated dish with 1 layer of scaffold, treated dish with 2 layers of scaffold and untreated dish with 2 layers of scaffold, respectively.

As shown in Figure 2, the maximal absorption wavelength was at ~280 nm which assigned to aromatic amino acid absorption wavelength. It can be implied that amino group from fibroin can successfully bond with aromatic ring on the PS surface.

3. Scanning Electron Microscope (SEM)

The surface morphology of scaffolds was observed under a scanning electron microscope. As shown in Fig.3, it was revealed that the scaffold prepared in this study had uniformly distributed pores and high porosity, seen by naked eyes. These properties may be more suitable for cell growth because there is not only larger space in which the seeded cells live, but cell migration is also easier.

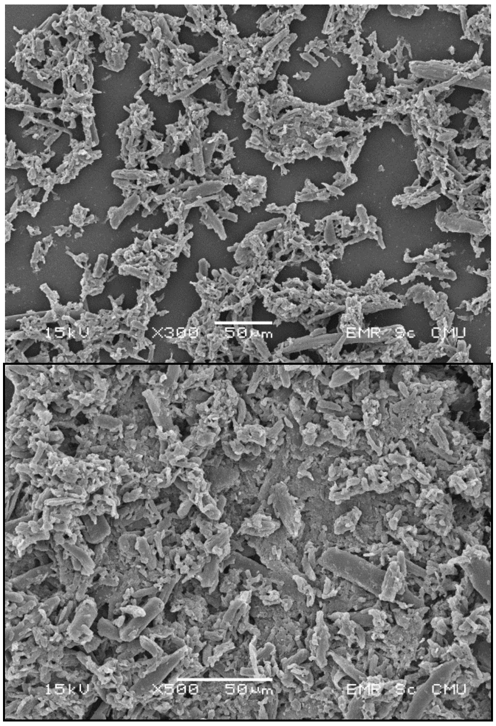

Fig.3 Scanning electron micrographs at different magnifications showing morphologies of scaffold on the PS surfaces. Original magnification: (A) ×300; (B) ×500

4. Fourier Transform Infrared Spectroscopy

FTIR was performed to investigate the chemical reaction between fibroin and the surface of PS. Figure 4. shows the absorbance spectra of untreated PS, untreated PS+ fibroin, treated PS + fibroin. In the case of untreated PS, the C−H located at the range of 2850 - 3150 cm^{-1} appeared. Moreover, IR spectra shows broad peaks of aromatic C=C at the range of 1475 - 1600 cm^{-1}, which indicated main structure of PS, a long chain hydrocarbon contains elements carbon and hydrogen. The peaks around 1026 – 1182 cm^{-1} , 1742 snd 1800 cm^{-1} also reveal the C−O and C=O, respectively. Oxygen appeared on the surface may come from the manufacturing process. In the case untreated PS + fibroin and treated PS + fibroin, the N−H peaks occurred at 3069 – 3272 cm^{-1} while the C−H peaks at 2926 and 2970 is reduced from the untreated PS. The protein conformation was determined by identifying the peak positions of amide I, II and III corresponding to C=O, N−H and C−N stretching, respectively. As shown in Figure 4, all scaffold exhibited amide I and amide II peaks at 1624 and 1511 cm^{-1} and amide III peak at 1229 cm^{-1}. The peaks around 650 – 1000 cm^{-1} also revealed the C−H. From this result, it could be explained that the C=C, C−C or C−H chains in the polymer are broken by energetic plasma bombardment, and the induced unstable chain react with the atoms from fibroin, such as O, N and H.

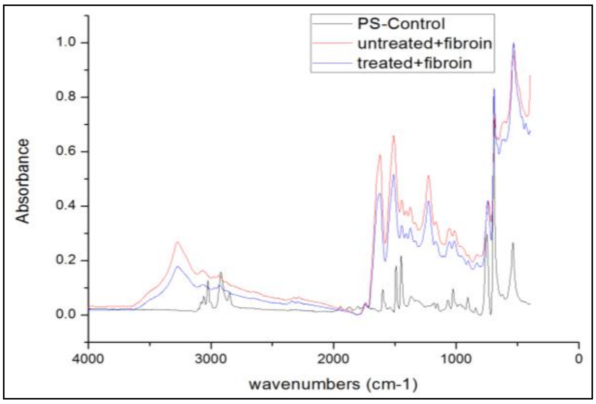

Figure 4. the absorbance spectra of untreated PS, untreated PS+ fibroin, treated PS + fibroin.

Conclusions

Wettability of water on PS was improved by argon plasma treatment. Plasma can change the property of surface from hydrophobic to hydrophilic. It was revealed that the scaffold had uniformly distributed pores and high porosity. Representative UV-vis absorption spectra increased with the number of scaffold layers. The treated dish had lower spectra absorbance than the untreated dish which means the efficiency of grafting between the scaffold and treated surface was better than the untreated surface. Also the peak of amino acid with aromatic ring, named phanyalanine at 280 nm affirmed the success of grafting between fibroin and polystyrene. From FTIR results, The C=C, C−C and C−H chains in the polymer are broken by energetic plasma bombardment, and the induced unstable chain react with the atoms from fibroin such as O, N and H. Then the formation of new bonds, such as C−N, N−H, and C=O will be occurred.

Acknowledgments

This work was financially supported by Plasma and Clean Energy Laboratory, Department of Physics and materials science, Faculty of Science, Chiang Mai University. And we also acknowledge Thailand Center of Excellence in Physics (ThEP) for providing scholarships for the author.

References

1. L Sasai, Y., Matsuzaki, N., Kondo, S., Yamauchi, Y., & Kuzuya, M. Surface modification of polystyrene dishes using plasma techniques to enhance cell adhesion and proliferation.
2. Choi, S. C., Choi, W. K., Jung, H. J., Park, J. G., Chung, B. C., Yoo, Y. S., & Koh, S. K. (1999). Relation between hydrophilicity and cell culturing on polystyrene Petri dish modified by ion-assisted reaction. *Journal of applied polymer science*, *73*(1), 41-46
3. Sipehia, R. (1990). The enhanced attachment and growth of endothelial cells on anhydrous

ammonia gaseous plasma modified surfaces of polystyrene and poly (tetrafluoroethylene). *Artificial Cells, Blood Substitutes and Biotechnology*,*18*(3), 437-446.

4. Gilliam, M. A. (2006). *A plasma polymerization investigation and low temperature cascade arc plasma for polymeric surface modification* (Doctoral dissertation, University of Missouri).
5. Jin, S. C., Baek, H. S., Woo, Y. I., Lee, M. H., Kim, J. S., Park, J. C., ... & Han, I. H. (2009). Beneficial effects of microwave-induced argon plasma treatment on cellular behaviors of articular chondrocytes onto nanofibrous silk fibroin mesh. *Macromolecular Research*, *17*(9), 703-708.
6. Kim, U. J., Park, J., Joo Kim, H., Wada, M., & Kaplan, D. L. (2005). Three-dimensional aqueous-derived biomaterial scaffolds from silk fibroin.*Biomaterials*, *26*(15), 2775-2785.
7. Zhao, Y., Chen, J., Chou, A. H., Li, G., & LeGeros, R. Z. (2009). Nonwoven silk fibroin net/nano-hydroxyapatite scaffold: Preparation and characterization.*Journal of Biomedical Materials Research Part A*, *91*(4), 1140-1149.
8. Wang, Y., Kim, H. J., Vunjak-Novakovic, G., & Kaplan, D. L. (2006). Stem cell-based tissue engineering with silk biomaterials. *Biomaterials*, *27*(36), 6064-6082.

Roughness Reduction of PCB-based Master Mold for PDMS-based MCE Fabrication

M. Jitvisate_[1*], R. Pinchaipat [1], T. Luangpairod [1], K. Singkarat [1,2],
M. W. Rhodes [2], N. Pussadee [1,2], and S. Singkarat [1,2]

[1]Plasma and Beam Physics Research Facility, Department of Physics and Materials Science, Faculty of Science, Chiang Mai University, Chiang Mai 50200, Thailand
[2]Thailand Center of Excellence in Physics, CHE, 328 Si Ayuthaya Road,
Bangkok 10400, Thailand
**Corresponding author, E-mail: mjitvisate@gmail.com*

Abstract

A few years ago, the technique referred to as Etched Wiring Board Technique (EWBT) was introduced by our group for producing a PDMS-based microfluidic chip master mold. It is based on an ordinary printed circuit board (PCB) so this technique is simple, fast and inexpensive. However, roughness on the surface of the PCB substrate and on the edges of copper ridges after a wet etching cause certain problems to a PDMS replica in relationship to the qualities of laminar flow in the microchannel, bonding with glass slides and hydrophilic properties of the 4 walls of the channel of a microfluidic chip. Here we proposed a procedure to overcome these problems simultaneously. The thin layer of PMMA film that has been spin coated on the etched-PCB mold can smooth the edges of both the copper ridges and surface of the PCB substrate. From SEM images, the edges of the microchannel and surface of the PDMS stamp have been significantly improved, although the channel is shallower. After only a brief irradiation with oxygen plasma, both PDMS stamp and cover glass in contact have created a strong bonding with each other and at the same time every wall of the microchannel becomes hydrophilic. The microchip has successfully been applied as a Microchip Capillary Electrophoresis (MCE) device.

***Keywords*:** Master mold, PDMS-based microfluidic chip, Etched-PCB mold, PMMA

Introduction

Poly(dimethylsiloxane) (PDMS) has been widely used as a stamp material in microfluidic chip fabrication for Lab-on-Chip and micro total analysis system (µTAS) due to its beneficial properties. PDMS is inexpensive and easy to modify. It has a wide range of optical transparency ranging from visible band down to 230 nm, so that several detection techniques are possible. The flexibility is one of the important characteristics that permit an integration fabrication such as integrated detection electrodes. The material is chemically inert, non-hygroscopic, isotropic and homogeneous and durable in the sense that stamps can be used many times over several months without degradation [1, 2]. More on surface property, it can be bonded with itself or other surfaces. Irreversible bonding can occur if the surfaces are Si-based. Oxygen plasma plays an important role in forming a O-Si-O covalent bond for a strong bonding [3]. However, PDMS itself has a hydrophobic nature [4]. This property is inferior in many experiments such as in microchip electrophoresis separation.

In soft lithography, the PDMS stamp is cast from a master mold. There are several methods available for the production of the master mold. One of the simplest and cheapest methods has been proposed by our group since 2007 [5]. The method, edge wiring board technique (EWBT), makes master a mold out of an ordinary printed circuit board (PCB). However, despite those advantages, there are disadvantages relating to surface roughness of the resin substrate and edge roughness of the copper ridges. Moreover, for Microchip-based Capillary Electrophoresis (MCE) which a double-T microchannel configuration with total length in the order of 5 cm is normally used, a hydrophilic channel is required for improving buffer loading and an electro-osmotic flow (EOF) [6].

To economically overcome these obstacles, first of all, the surface roughness of the PCB substrate of the master mold has to be reduced. By this way, the PDMS stamp surface is smooth enough so that, after a brief oxygen plasma treatment, it can be permanently sealed by a bare glass slide through contact bonding and its microchannel surfaces are transformed from being hydrophobic to hydrophilic [7, 8].

By this research, the solution to the mentioned obstacles, i.e., the roughness of PCB master molds and the hydrophobicity of PDMS surfaces, has been proven. Herein, details of experimental methods and results are described.

Materials and Methods

Master mold fabrication

The PCB-based master mold was constructed by adapting the traditional electronic circuit patterning method, which is described briefly in Fig. 1. The commercial grade PCBs and other materials used in this work such as a photoresist film, etching solution, etc, were bought from a local electronic shop. Generally, the thickness of its copper cladding is 30 μm and the thickness of the resin substrate is 1 mm. The microchannel network was transferred from mask pattern, printed on silk screen film, to PCB by using photoresist film and UV exposure as shown in steps (a) to (c). In step (d), the unirradiated photoresist was dissolved by sodium hydroxide solution. After etching by ferric chloride solution, as shown in step (e), the copper ridge pattern for making microchannel network was created.

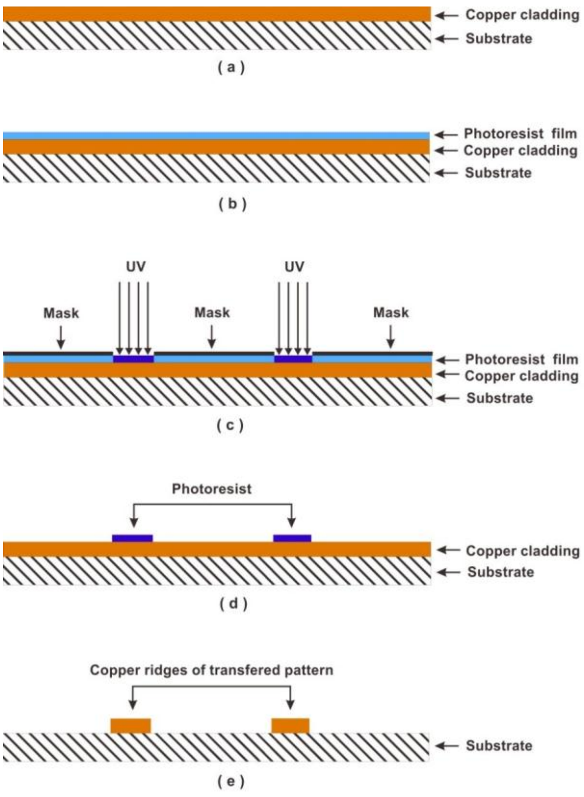

Figure 1. PCB-based master mold fabrication process (see text).

Chemicals

All chemicals used in the experiment were laboratory-grade substances. PMMA beads of MW ≈ 540,000 was purchased from Scientific Polymer Products (New York, USA). The anisol (C_7H_8O), which was used as a solvent for the PMMA beads, was bought from Sigma-Aldrich (Germany). The PDMS was prepared from Sylgard 184 Silicone Elastomer Kit, purchased from Dow Corning (Michigan, USA).

Coating process

As shown in Fig. 2, after the PCB had been etched, its top surface was coated with PMMA viscous solution by using a self-made spin coater. The 11% w/w PMMA viscous solution was prepared by dissolving the PMMA beads in the anisol solvent, stirred well overnight at room temperature in a closed container. The viscous solution of PMMA was poured onto the mold’s surface, then spin coated at 2000 rpm for 45 seconds. The coating process is completed with baking using a hot plate at 160˚C for 2 minutes to remove the solvent and harden the PMMA coated layer. Our investigation had covered up to 3 layers of coating.

Microfluidic chip fabrication

The PDMS microfluidic chips were fabricated by casting technique in which the viscous solution of PDMS was poured on top of the PMMA coated master mold and then cure at 70˚C on the hot plate for 2 hours. After the PDMS had been solidified, the polymer was peeled off the master mold. Next, both a PDMS stamp and clean glass slide were exposed to oxygen plasma of 50 W power for 60 seconds by the in-house built plasma generator. After this step, the treated PDMS stamp was press bonded to the treated glass surface for 15 minutes to ensure good bonding between both surfaces. At this point, a microfluidic device with a hydrophilic microchannel at all 4 walls has been completely fabricated. In order to prevent hydrophobic recovery, the whole microchannel was filled with de-ionized (DI) water when not in use.

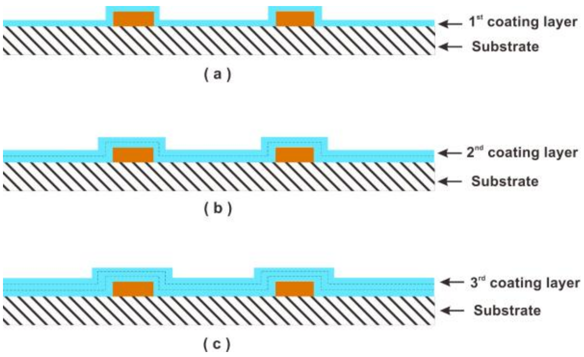

Figure 2. Illustration of the 1-layer, 2-layer and 3-layer PMMA coatings on the same PCB-based master mold.

Results and Discussion

Roughness reduction

As clearly seen from Fig. 3, even by the naked eye, the surface of PDMS stamp from each mold has significantly been improved. The transparency of each slab increases as more PMMA layers are coated on the master mold surface. This is one of the evidences indicating that the master mold surface can become smoother by the PMMA coating. In addition, SEM images of PDMS stamps, as shown in Fig. 4, confirm that both surfaces of PCB substrate and channel walls of the coated samples were much smoother compared with the uncoated one. However, the depth of the channel was affected by the coated layers. To study this consequence, the microchannels on the PDMS stamps were cut across and the cross-sectional viewed in order to measure the channel depth through the microscope. The results are shown in Table 1. It can be seen that the channel is shallower as more layers were added on the mold. It also shows that edges of the microchannel are not sharp but has been rounded-off by the PMMA coated layer. In conclusion, we may not have a sharp rectangular microchannel chip but will have a smooth surface channel which is more important for the MCE applications [6].
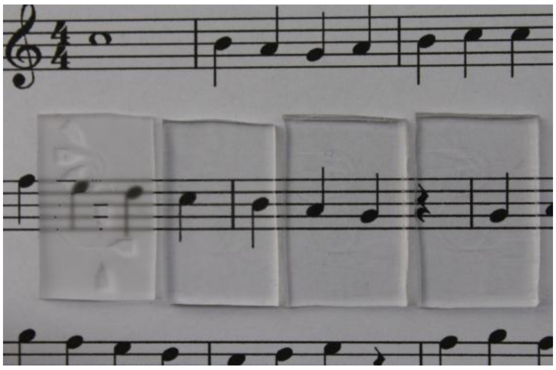
Figure 3. Photo of 4 PDMS slabs that were peeled off, from left to right, the uncoated, 1-layer coating, 2-layer coating, and 3-layer coating master molds. The improvement in transparency of each slab is clearly shown.

Table 1: The average microchannel depth of the PDMS stamps replicated from each coated mold.

Master mold	Average channel depth (µm)
Uncoated	31.73
1-layer coating	26.51
2-layer coating	23.33
3-layer coating	18.58

PDMS / glass interface bonding strength

The bonding strength investigation was performed by tearing off the PDMS slabs from the glass cover by force. In every try, the PDMS bulk was ruptured rather than breaking the bonding at the interface except for the uncoated one. This shows that the two parts have been irreversibly bonded. The results emphasize that the oxygen plasma can be used for PDMS-glass bonding in the case that the contact surfaces are smooth enough. The hydophilicity of the microchannel can be observed simply by filling DI water to any end of the microchannel. The water will fill the entire network almost instantaneously without any bubble and without using any external driving force.

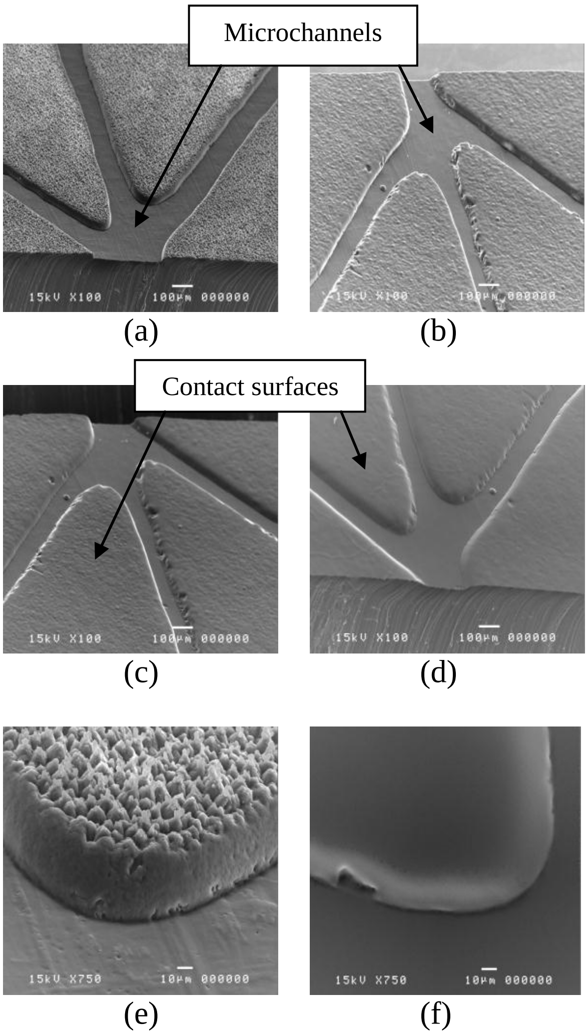

Figure 4. SEM images of PDMS stamps fabricated from uncoated (a), 1-layer coating (b), 2-layer coating (c), and 3-layer coating (d) master molds. The (e) and (f) are closed-up images showing the texture of the PDMS surfaces from the uncoated and 3-layer coating master molds, respectively.

Conclusions

In summary, the technique for PCB-based master mold surface roughness reduction by spin coating thin layers of PMMA on the top of the mold was invented by our group. The proposed process can solve the hydrophobicity and plasma bonding problems of PDMS-based microfluidic chip simultaneously. The surface of the mold was smoothened as PMMA thin layers were coated which can be observed from SEM images of PDMS stamp surfaces. The microfluidic devices with hydrophilic channel sealed with glass slide can be fabricated using oxygen plasma bonding technique. The interface bonding is irreversible and the bonded PDMS device can withstand any inner pressure level of every MCE applications.

Acknowledgments

This work is supported by the Development and Promotion of Science and Technology Talented Project (DPST) and the Thailand Center of Excellence in Physics (ThEP Center).

References

1. M. J. Madou, Fundamentals of Microfabrication, 2nd Edition, CRC Press, Florida, 2002, pp. 63-64.
2. J. Han, J. H. Lee, S. Chung, and S. J. Kim, “Poly(dimethylsiloxane)-Based Protein Preconcentration Using a Nanogap Generated by Junction Gap Breakdown”, Anal. Chem., 2007, 79, 6868-6873.
3. S. Bhattacharya, A. Datta, J. M. Berg, and S. Gangopadhyay, “Studies on Surface Wettability of Poly(Dimethyl) Siloxane (PDMS) and Glass Under Oxygen-Plasma Treatment and Correlation With Bond Strength”, JMEMS, Vol. 3, No. 3, 2005, 590-597.
4. S. K. Sia and G. M. Whitesides, “Microfluidic Devices Fabricated in Poly(dimethylsiloxane) for Biological Studies”, Electrophoresis, 2003, 24, 3563-3576.
5. R. Pinchaipat, “Effect of Pressure on Flow Rate in Microfluidic Chip Fabricated by an Etched Wiring Board Technique”, M. Sc. Thesis, Graduate School, Chiang Mai University, 2011.
6. C. S. Henry, J. A. Vickers, and M. M. Caulum, “Generation of Hydrophilic Poly(dimethylsiloxane) for High-Performance Microchip Electrophoresis”, Anal. Chem., 2006, 78, 7446-7452.
7. J. Zhou, D. A. Khodakov, A. V. Ellis, and N. H. Voelcker, “Surface Modification of PDMS-based Microfluidic Devices”, Electrophoresis, 2012, 33, 89-104.
8. N. T. Nguyen, S. H. Tan, and T. G. Kang, “Oxygen Plasma Treatment for Reducing Hydrophobicity of a Sealed Polydimethylsiloxane Microchannel”, Biomicrofluidic 4, 2012, 032204.

Electric properties of oil containing in oil palm mesocarp

Julsamhang S.[1], Jitbun P.[2], Jampa N.[3], Kongchana P.[4], and Sudsiri (J.) Ch.[5*]

[1] *Faculty of Sciences and Industrial Technology, Prince of Songkla University Surat-thani Campus, Muang District, Surat-thani Province, 84100 Thailand*
[2] *Faculty of Sciences and Industrial Technology, Prince of Songkla University Surat-thani Campus, Muang District, Surat-thani Province, 84100 Thailand*
[3] *Sciences Laboratory and Equipments Center, Prince of Songkla University Surat-thani Campus, Muang District, Surat-thani Province, 84100 Thailand*
[4] *Sciences Laboratory and Equipments Center, Prince of Songkla University Surat-thani Campus, Muang District, Surat-thani Province, 84100 Thailand*
[5] *Faculty of Sciences and Industrial Technology, Prince of Songkla University Surat-thani Campus, Muang District, Surat-thani Province, 84100 Thailand*
**Corresponding author. E-mail: jutipornc@gmail.com, jutiporn.s@psu.ac.th*

Abstract

In this work, we compared amount of oil in oil palm fruits to the electric properties i.e. conductance and capacitance of the fruits. Three varieties of oil palm with different ages and different colors were investigated. Conductance and capacitance were measured using an RCL meter. To record the electric parameters, two electrodes with a constant space between them were inserted into the fruit. After the electric measurement, the fruit was pressed to measure the amount of oil in the fruit. We found that the unripe fruits from the three varieties had average oil contents in the range 0.05-4.0 g. The capacitance was in the range 0.02-0.05 μF and the resistance was in the range of 25.0-78.0 kΩ. Ripe oil palm fruits contain 1.4-4.0 g of oil for all varieties. The resistances and capacitances of ripe fruits were in the range of 0.01-0.03 μF and 40.0-136.0 kΩ respectively. The results showed that the amount of oil in palm oil fruit is correlated with their electric parameters. The method can be applied by oil palm growers to monitor the development of their crop so that the oil palm fruits can be harvested at the appropriate time.

Keywords**:** Oil Palm, Electric Properties, Oil Parameters

Introduction

Oil palm is widely cropped in Thailand since it is used in a wide variety of ways by the local population. The primary purpose until now has been the extraction of palm oil (from the flesh of the oil palm fruit) and palm kernel oil (from its kernel or seed) for the production of edible and industrial oils. More recently, the second major objective has emerged: the production of biodiesel from crude palm oil. In general, to harvest oil palm fruits, their colour is observed and assumptions made about amount of oil they contain. As the palm fruit ripens, the color changes from black to reddish orange and the oil content increases in the process. When the oil content reaches the maximum, the fruit becomes loose and falls to the ground. However, color changes can also be caused by external factors such as weather, temperature, other environmental factors and handling of the harvest handling. Mere appearance of the oil palm seeds is not a reliable indicator of oil content. A better monitoring method than simple observation is needed.

To overcome this problem, electrical properties of oil palm seeds were studied in order to develop a rapid and non destructive assessment method to characterize the state of ripening of oil palm seeds. Behavior of the electrical properties of materials is related to their dielectric properties. The dielectric constant of material, which correlates well with certain properties of the products such as moisture content and ripeness, were studied by different researchers over the past years [1-3]. Several important factors greatly influence the dielectric properties of materials. Some of these factors are related to the nature of the material (composition, structure), while others are associated with the conditions when electro heating is applied (temperature, frequency), and others are involved with the age or maturity stage of the seeds or other food material [4].

The dielectric properties of fruits and vegetables have been investigated in several studies. For oil palm, however, no useful characteristics of this type have previously been found to have a reliable correlation with quality. The objective of the present work was to identify ripening parameters of oil palm fruits, and to quantify the relationship between color changes, electrical conductivity and amount of oil contained in the fruit. The close relationship between the electric properties and oil contents in the mesocarp gives us simple to measure parameters to gauge the mesocarp ripeness and the harvesting time.

Materials and Methods

Materials

Oil palm fruits obtained from a private orchard were picked at ambient temperature and then weighed using an electronic balance to group them based on their weight. The experiment was carried out on fresh and ripening fruit of three varieties of oil palm. The three varieties used in this study were: (1) Gotta-Rica, (2) Suratthani1 and (3) AVROS pisifera. The measurements of all parameters were done when the fruits were still in fresh condition.

Measurement

The dielectric properties of the oil palm seeds of a range of stages of maturity were measured. The resistance and capacitance of the seeds were measured by using a LCR meter. The samples of oil palm were placed between two plate conductive electrodes, as the dielectric material. After the measurement, the mesocarp of each fruit was peeled and oil palm was extracted. The amount of oil was compared to the measured electrical parameters. Each LCR measurement was repeated three times and then the average was calculated.

Results and Discussion

Amount of oil content in oil palm mesocarp at different age (unripe fruits and ripening fruits) are shown in Table 1. Both groups provide different electric parameters and amount of oil content in the mesocarp. The unripe fruits give a less amount of oil, are higher in electric capacitance and lower in electric resistance than the ripening fruits. For all three cultivars, a constant of electric capacitance for ripening and ripe fruits could be calculated.

In unripe fruits, the capacitance of the fluid in the mesocarp is clearly higher than that of the ripening fruit. The capacitance varied from about 0.02 μF to about 0.04 μF depending on the cultivar. The resistance varied from 25 kΩ to the 50 kΩ dependent on the cultivar.

In the ripening groups, for all cultivars, the capacitance is constant in the range from about 0.01 μF to 0.03 μF. An increase in electric resistance was observed. The mean values vary in the three oil palm varieties used in the study but in each case there is a clear difference between unripe and ripe fruits.

Table1: Comparison of amount of oil in mesocarp to electric capacitance (C) and resistance (R). The data were averaged from 30 fruits.

oil palm cultivar	**C (μF)**	**R (kΩ)**	**amount of oil (g)**
1			
unripe fruits	0.02-0.04	40.5-63.5	3.20-3.90
ripening fruits	0.01-0.03	94.0-136.0	4.0-6.5
2			
unripe fruits	0.02-0.05	25.0-50.0	0.60-2.30
ripening fruits	0.01-0.03	50.0-65.0	1.37-3.50
3			
unripe fruits	0.02-0.04	25.0-61.0	0.05-0.60
ripening fruits	0.01-0.03	40.0-78.0	1.50-3.40

During ripening, extensive changes may occur in the composition of the cell contents such as electrical conductance and capacitance [25]. Electrical conductance values expressed the ability of charge movement in the material and depended on the number of ions or free electrons of the material. Capacitance describes the ability of capacitors to store energy and electrical charge. The presence of a dielectric material in capacitors causes an increase in the capacitance value. Increase in the amount of oil is accompanied by increasing resistance and decreasing in capacitance. The results agree with work of Sirikulrat et al. [5] who demonstrated that the relative permittivity of fresh soybean decreases as the bean matures. An increase in internal fruit resistance may be related to decreased concentration of mobile ions in fluid content in mesocarp.

The high correlation between electric capacitance and resistance and amount of oil in oil palm fruits indicates that the electrical parameters could be suitable as an index of amount of oil in oil palm fruit. It was found that the changes of the electrical parameters of oil palm fruits were closely related to the ripening and amount of oil.

Conclusions

In this work, electric capacitance and resistance were used as an index to predict amount of oil content in oil palm mesocarp. This paper studied the ability of this method to predict the amount of oil during ripening period. Results showed that this technique, which is based on dielectric property, was able to assess changes in the amount oil in oil palm fruits during ripening period. The results showed that the amount of oil in palm oil fruit is correlated with their electric parameters. The method can be applied by oil palm growers to monitor the development of their crop so that the oil palm fruits can be harvested at the appropriate time. We feel that a simple LCR instrument could be developed for use by farmers to monitor their oil palm crop.

Acknowledgments

The authors are grateful to the Prince of Songkla University for their providing the laboratory equipment and financial support for this work.

References

1. M. Soltani, R. Alimardani, and M. Omid, “Use of dielectric properties in quality measurement of agricultural products”, Nature and Science, 9 (2011) , no 4, pp 57-61.
2. M. Soltani, R. Alimardani, and M. Omid, “Evaluating banana ripening status from measuring dielectric properties”, Journal of Food Engineering 105 (2011) 625.
3. S.O. Nelson, “Dielectric spectroscopy of fresh fruit and vegetable tissues from 10 to 1800 MHz”, Journal of Microwave Power and Electromagnetic Energy 40(2005) 31.
4. M.E. Sosa-Morales, L. Valerio-Junco, A. López-Malo, H. S. García, “Dielectric properties of foods: Reported data in the 21st century and their potential applications”, LWT - Food Science and Technology 43 (2010) 1169.
5. K. Sirikulrat and N. Sirikulat, “Dielectric properties of different maturity soybean”, KMITL Sci. J 8 (2008) 12.

Immobilization of Sericin onto a-C Layer for Serum-free hBM-MSCs Culture by PECVD

Somruthai Tunma[1,2], Kyoung-Nam Kim[3], Jeon-Geon Han[4] and Dheerawan Boonyawan[2,5*]

[1]The Graduate School, Chiang Mai University, [2]Thailand Center of Excellence in Physics (ThEP), 239 Huay Kaew Road, Muang District, Chiang Mai, 50200, Thailand
[3]Research Center for Orofacial Hard Tissue Regeneration, College of Dentistry, Yonsei University, 50 Yonsei-ro, Seodaemun-gu, Seoul 120-752, Republic of Korea
[4]Center for Advanced Plasma Surface Technology, Sungkyunkwan University, 300 Chunchun-dong, Jangan-gu, Suwon 440-746, Republic of Korea
[5]Department of Physics and Materials Science, Faculty of Science, Chiang Mai University, 239 Huay Kaew Road, Muang District, Chiang Mai, 50200, Thailand
**Corresponding author. E-mail: dheerawan.b@cmu.ac.th*

Abstract

In this study, we focused on sericin hydrolysates, originating from silkworm, used for human bone marrow mesenchymal stem cells (hBM-MSCs) serum-free culture. Silk sericin protein was absorbed onto various substrates spontaneously, however, it will be removed immediately from the surface when exposed to the culture media. We reported that the effect of a covalent linkage between bioactive protein molecules and polystyrene dish surface via a carbon intermediate layer can slow down the release rate of protein molecules into the phosphate buffer saline (PBS) solution. Films of amorphous carbon (a-C) and functionalized carbon were deposited on PS culture dish surfaces using a dc magnetron sputtering system and RF PECVD system which were used as intermediate layers. We found that a-C based-films can increase the hydrophlilicity and biocompatibility of polystyrene (PS) dish, especially a-C films and a-C:N_2 films which show the good attachment of human bone marrow-derived mesenchymal stem cells (hBM-MSCs) at 24 hrs. For the UV-vis absorbance, all of carbon modified-PS dishes showed the less release rate of sericin molecules into PBS solution than PS control. This revealed that functionalized carbon can be enhanced of specific binding property with given molecules. The carbon-coated PS dishes grafting with sericin protein were used in serum-free condition. We also found that hBM-MSCs have higher % of proliferated cells at day 7 for the modified dishes with carbon films and coated with sericin than the PS control coated with sericin.

Keywords: amorphous carbon layer, sericin, serum-free conditions, covalent grafting, hBM-MSCs

Introduction

Nowadays, *In vitro* mammalian cell culture for cell therapy, mammal-derived factors including fetal bovine serum (FBS) are often used as a source of nutrients and growth factors in the media which cause the concern about the risk of zoonosis such as abnormal prions and various viruses [1]. Therefore, serum- and mammal-free culture is strongly required. We focused on sericin hydrolysates, a protein extracted from the glue of cocoons, with the alternative strategy of being used as supplemented in the culture media. Silk proteins were added to culture media used as serum free media for cell culture [1]. In comparison with bovine serum albumin (BSA), sericin had an equivalent effect on the proliferation of the hybridomas with BSA and the activity of sericin was not affected by autoclaving. Commonly, sericin protein absorbed onto various substrates spontaneously, however, sericin itself is water soluble.In the case of cell culture application, their immediately removal from the surface when exposed to the culture media and could not support the cell growth for a prolonged time.

The tissue culture polystyrene (TCPS), as a standard *in vitro* cell culture substrates, is unsuitable for serum free cell culture medium since it normally occur in a poor and insufficiently reproducible manner. Therefore, surface modifications are required to optimize cell adhesion and accelerate the cell proliferation. Amorphous carbon (a-C) is now being attractive in biological applications because it can be prepared relatively inexpensively for a wide variety of low-cost precursors. It is typically biocompatible and quite chemically stable under nonoxidizing conditions. Moreover, it has low density, high thermal conductivity, good electrical conductivity, mechanical stability and is non cytotoxic [2]. Of prominent features of the carbon film including a high specific-area, porous carbon is a more binding activemolecule and more resistant to structural change by hydrolytic effects in aqueous environments.

This review therefore selectively focuses on a new method of immobilization bioactive compounds onto polymer surface via deposited-carbon films. The objective of this study is to investigate and discuss the interaction between PS surface - Intermediate layer - Silk coating and attempt to control and slow down the release rate of coated-silk molecules by chemical bond between protein molecules and PS surface.

Materials and Methods

Physical vapor deposition (PVD) sputtering system and Plasma-enhanced chemical vapor deposition (PECVD) system

Commercialized TCPS dishes (Nunclon®, Denmark; Cat#153066), 35 mm in diameter, were used as the material model in this study. The bottom part of each dish was used in this experiment as modified PS dish with amorphous carbon-based intermediate layer.

To manipulate the amorphous carbon-based films, we used a DC magnetron sputtering system (Center for Advanced Plasma Surface Technology; CAPST, Sungkynkwan University, Korea) attached to a high vacuum chamber (base pressure 2.0×10^{-5} Torr) using a 4-inches diameter high purity carbon target cathode and argon (purity 99.999%) gas as a sputter gas. The a-C films deposited onto the PS bottom part was used for the SiO_x deposition as a-C:SiO_x films and was used for the nitrogen plasma treatment as a-C:N_2 films by using a RF plasma-enhanced chemical vapor deposition (PECVD) system. Table 1 lists the sputtering deposition parameters.

To functionalize the carbon film surfaces with SiO_x plasma using octamethylcyclotetrasiloxane (OMCTS) as a precursor and oxygen as a carrier gas,we used oxygen plasma treated onto SiO_x films to improve the hydrophilic and used as the a-C:SiO_x films. In case of a-C:N_2 films, we used nitrogen plasma treated onto a-C films.

Table 1: Sputtering parameters

Parameters	Conditions
Base pressure	About 2.0×10^{-5} Torr
Sputtering pressure; 1) a-C_1	1.2×10^{-1} Torr
2) a-C_2	1.3×10^{-1} Torr
DC power	0.8 kW
Sputter time	10 min

The sericin release rate detection using Ultraviolet (UV) absorption

1. Immobilization method

Sericin powder (Thailand Institute of Nuclear Technology; TINT) was dissolved in DI water and stirred at 60-70 ˚C for 30 min. 100 µl of sericin solution was kept and immersed it into each PS dish, let dry in air for 24 h. After that, 7 ml of phosphate buffer saline (PBS) solution was poured into each sericin coated-PS dish and taken an immersed time for 1, 3 and 7 days (n=4 for each time).

2. Measurement the UV absorbance of the released-sericin solution.

UV spectra of the released-sericin solution were taken on a UV-VIS-NIR spectrophotometer (UV-3600, Shimadzu,Tokyo, Japan). Start with kept 3 mll of released-sericin solution and transferred it to the quartz cuvette with a 1-mm pathlength and scanned with the scanning range was recorded between 190 - 450 nm.

Cell behavior study

Cell culture and seeding

The human bone marrow-derived mesenchymal stem cells (hBM-MSCs) were purchased from Lonza group Ltd., Switzerland. The cells were cultured on 75 cm^2 PS cultured flasks (SPL®, Korea; Cat#70025) in DMEM (Dulbecco’s modified Eagle’s medium) (Gibco, USA) containing 20% (v/v) FBS (fetal bovine serum) (Gibco, USA) and 1% penicillin/streptomycin (Pen Strep, Gibco, California, USA) for serum condition and FBS omitted for serum-free condition. Cultures were maintained at 37˚C, 5% CO_2 and 95% relative humidity. The culture medium was refreshed every 2 days before achieving 80% cell-population confluence.

Cell attachment efficiency and proliferation assay

Attachment efficiency and proliferation assay of hBM-MSCs were quantitatively evaluated by using the WST-1 reagent (Roche, USA). Cells were plated at a density of 1×10^4 cells per well. According to the manufacture’s instruction, 150 µl of WST-1 solution was added to each dish and incubated at 37˚C for 4 h. The colorimetric optical density (OD) of liquid in each dish was obtained by spectrophotometry at 450 nm using Epoch (Biotek, USA). The proliferation assay was analyzed using the OD_{450} value from each PS dish sample at day 1 and day 7 in comparison to the control at day 1, which was presented as percentage of attached and proliferated cells. A higher percentage of cell attachment and proliferation corresponded to a higher number of viable cells.

Materials and Methods

Surface characterization

The surface hydrophilicity of modified PS dish was improved by amorphous carbon (a-C) deposition and was significantly improved by using SiO_x deposition and nitrogen plasma treatment. A different a-C films; vary of DC power and Ar pressure, had lower contact angle of less than 50° (compared with 82° for the PS-control) and a-C:N_2 films had lower contact angle of 25°.A-C:SiO_x films had a great lower contact angle of less than 10°, indicating good spreading of water on the material surface and low hydrophobicity of the material surface (Table 2). The deposited of SiO_x+O_2 treatment and nitrogen treatment resulted in more polar groups (oxidized structures e.g. carbonyl, carboxyl and ester groups and Si-O, NH_2) being grafted onto the PS surface during the plasma process. Nonpolar molecules are exhibited by London forces because of the correlated movements of the electrons in interacting molecules. These forces reveal weak intermolecular forces. If the material is too hydrophobic, molecules of extracellular matrix (ECM) are absorbed in a denatured and rigid state. This geometrical appearance is unsuitable for binding to cells, since specific sites on these molecules are less accessible to cell adhesion receptors, e.g. integrin. The polar component of surface energy consists of all other interactions due to non-London forces. Polar molecules interact through dipole-dipole intermolecular forces and hydrogen bonds. On hydrophilic surfaces, cells adhered in higher numbers to more hydrophilic materials and were spread over a large area. At the same time, ECM proteins were adsorbed in a more flexible form, which allows them to be rearranged by the cells and thus provides access for cell adhesion receptors to the adhesion motifs on these molecules.

Table 2 showed the a-C_1 and a-C_2 films thickness of approximately 35 nm and 25 nm, respectively (sputter time: 10 min) were measured by surface profiler Alpha-step IQ. The a-C_2:N_2 film thickness was about 110 nm (sputter time: 10 min and N_2 treatment time: 1 min). In the case of a-C:SiO_x films, the thickness were 157 nm for a-C_1:SiO_x film, 95 nm for a-C_2:SiO_x film (sputter time: 10 min and SiO_x treatment time: 1 min and O_2 treatment 1 min). It was also shown that SiO_x deposition and nitrogen plasma treatment can increase the film thickness and the hydrophilic of carbon films.

Table 2: Films thickness and contact angle.

Modified-PS	**Film thickness**	**Contact angle (°) ± SD**
PS control	-	82 ± 1.4
PS + a-C_1	35	43 ± 2.5
PS + a-C_2	25	46 ± 2.0
PS + a-C_1:SiO_x	157	14 ± 2.0
PS + a-C_2:SiO_x	94	19 ± 2.0
PS + a-C_2:N_2	110	25 ± 1.5

The release rate detection of sericin molecules into PBS solution.

For the release rate detection of released-sericin solution, it was found that all of sericin coating onto modified-PS culture dishes had lower released rate of sericin compounds into the PBS solution than PS control for the immersed time at day 1 (Figure 1a), day 3 (Figure 1b) and day 7 (Figure 1c). It was implied that the covalent bonds interaction between the a-C_1, a-C_2 as intermediate layer on PS surfaces and sericin coatings can slow down the release rate of sericin compound into the immersed-solution, due to the porous and pore structures and the reactivity functional groups surfaces. This supports the idea that carbon material is more attractive for protein adsorption due to their inherent stability and surface properties such as high surface area.

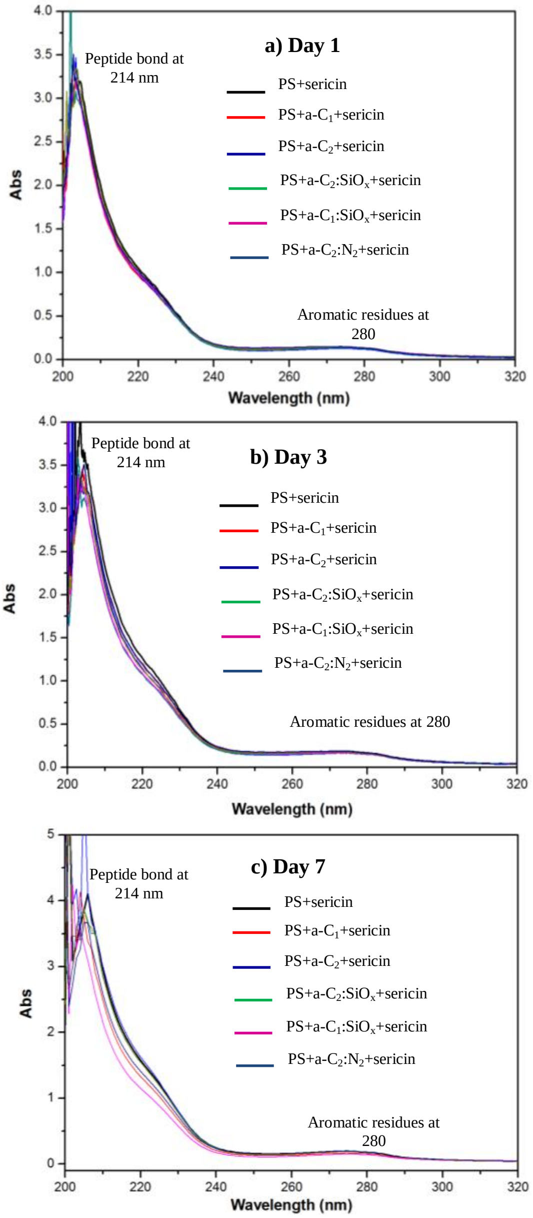

Figure 1. UV absorption spectrum of the released-sericin solution.

Cell behavior study

Cellular behavior on any biomaterial is an important indication to determine its biocompatibility. The whole process of adhesion and spreading of cells after contacting with biomaterials consists of cell attachment, filopodia growth, cytoplasmic webbing and flattening cell mass, and the ruffling peripheral cytoplasm, which progress in a sequential fashion.

Cell behavior experiments were performed over 7 days using hBM-MSCs. Less adhesion was observed on the three groups of a-C:Si-O_x-based (silica surface) films as shown in Fig. 10. The cells were also appeared rounded which indicated the incomplete attachment of hBM-MSC with ragged cytoplasmic boundary. The silica surface has the strong electrostatic attraction between surface silanol groups and the surface charge of non-prosthetic residues of protein molecules may alter the damage to the coherent structure and the native state of the protein [3]. Moreover, silica has the weak stability upon prolonged exposure to aqueous solutions which remains a major problem in the case of cell culture. It might be concluded that the biological activity and stability of the sericin protein may change upon interaction with a silica surface.

Figure 2 shows the proliferation pattern of hBM-MSCs at day 1 and day 7 with the 5% sericin coatings,the 5%FBS and without FBS conditions. It was shown that PS control dish with 10%FBS has the highest % of proliferated cells at day 7 whereas at day 1, nodifference were detected. It was possible that sericin protein and FBS effect on cell attachment in the same way. The carbon-based with sericin-coated surfaces have the higher proliferation rate with the mixed of 5% FBS and sericin coatings and the without FBS than the PS control coated with sericin at day 7 especially, in the case of a-C_2 surface. However, PS dishes with the mixture of 5% FBS and sericin showed the higher proliferated cells than the used of only sericin in the same condition.

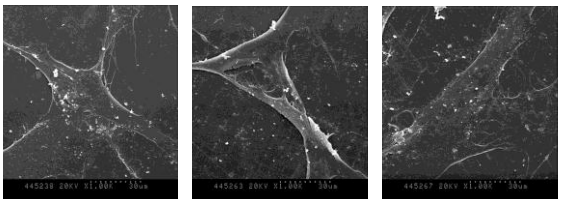

Figure 2. Examples of SEM micrographs of attached hBM-MSCs in serum-free condition.

Conclusions

In this study, amorphous carbon based films were used as intermediate layers for covalent grafting between sericin protein and PS surface and also were successfully slow down the release rate of sericin molecules into PBS solution. The Si-O and nitrogen-functional groups great affect to the hydrophilic property of surface more than the roughness of a-C based films. The Si-O groups also influence to surface by made the smooth surface of carbon film and disfavor with hBM-MSCs adhererance. The stability of carbon based films with sericin grafting which is more resistant to structural change by hydrolytic effects in aqueous environments and biocompatibility could used in hBM-MSCs culture with serum-free condition. Amorphous carbon material is attractive material for biomolecules adsorption due to its high specific surface area and rough structure and lead to an increase in the total amount of sericin protein absorbed and has the significantly proliferated-cells number at a prolonged time.

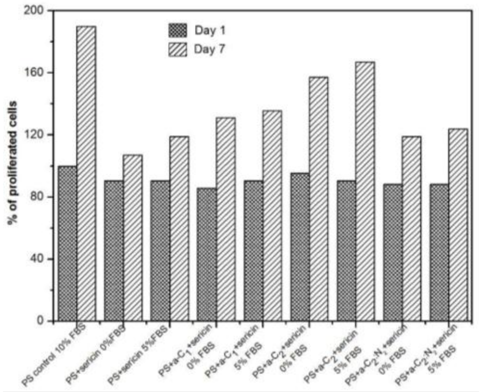

Figure 3. Cell proliferation patterns of hBM-MSCs on PS surfaces when cultured in serum-free condition at day 1 and 7.

Acknowledgments

We thank the Graduate School Chiang Mai University, Thailand Center of Excellence in Physics (ThEP), Center for Advanced Plasma Surface Technology (CAPST), College of Dentistry at Yonsei University and Kwangwoon University for financial and scholarship support.

References

1. W. Sato, K. Fukumoto, K. Yanagihara, M. Sasaki, Y. Kunitomi and S. Terada, “Mitogenic effect of sericin on mammalian cells” BioMed Central Proceedings **5(l 8)** (2011), 121.
2. S.E. Rodil, R. Olivares, H. Arzate and S. Muhl, “Properties of carbon films and their biocompatibility using in-vitro tests”, Diamond and Related Materials **12** (2003), 931.
3. M. Vijayaraj, R. Cadiou, K. Anselme, C. Ghimbeu, C. Vix-Guterl, H. Orikasa, T. Kyotani and S. Ittisanronnachai,“The influence of surface chemistry and pore size in the adsorption of proteins on nanostructured carbon materials” Advanced Functional Material **20** (2010), 2489.

Effect of Electromagnetic Fields on oil Palm Germination

Sudsiri Ch.[1*], Jampa N.[2], and Kongchana P.[3]

[1]*Faculty of Sciences and Industrial Technology, Prince of Songkla University Surat-thani Campus, Muang District, Surat-thani Province, 84100 Thailand*
[2]*Sciences Laboratory and Equipments Center, Prince of Songkla University Surat-thani Campus, Muang District, Surat-thani Province, 84100 Thailand*
[3] *Sciences Laboratory and Equipments Center, Prince of Songkla University Surat-thani Campus, Muang District, Surat-thani Province, 84100 Thailand*
**Corresponding author. E-mail: jutipornc@gmail.com, jutiporn.s@psu.ac.th*

Abstract

Oil palm has widely been grown in Southern Thailand. Nowadays, it has been become an important economic plant. The oil from different varieties are used for bio-energy and industrial uses and also for human consumption. However, production of young oil palm trees is still limited and the plants are expensive because it takes up to 8 months for germination to occur and the germination percentage is only about 60 %. The slow germination rate and the high failure rate leads to additional costs because it makes disease control much more difficult. Electromagnetic Fields (EMFs) are known to increase overall percentage germination and shortens the incubation time of several plant species. We therefore present a physical method to stimulate oil palm germination by treating seeds with EMF. Oil palm seeds were exposed to EMF fields of 100mT to 250 mT and compared to controls. The treatments also were done for different period of times varying from 30 min to 5 hrs. The treated seeds were placed in germinators and sprayed with magnetically treated water. Germination percentages improved on seeds exposed to EMF and the time before germination decreased compared to the controls. The seeds which were exposed to EMFs at of 200 mT for 4 hrs started initial primary root at 8 days after magnetic treatment. There was 30% germination after 8 days incubation and 100% germination after 35 days. The results indicated that electromagnetic fields significantly shorten the time taken for oil palm seeds to germinate and greatly increases the proportion of seeds that do germinate. It reduces germination time of oil palm seeds from 8 months to 8 days and provides very high percentage of germination.

Keywords: Oil Palm Germination, Electromagnetic Fields on Plants, Plant Enhancement

Introduction

During the evolution process, all living organisms experienced the action of the Earths magnetic field (geo-magnetic, GMF), which is a natural component of the air environment. In general, the living systems are beings influenced by the Earth's magnetism. The processes of life take place in an electromagnetic context result from an interactive conjunction between the vital magnetism and geomagnetic field which is an important global component of the average outside. All living organisms evolved in the presence of a natural GMF; determining the influence that magnetic fields might have on organisms is now the subject of an increasingly large research effort. Magnetic and electromagnetic treatments are being used in agriculture, as a non invasive technique, to improve the germination of seeds and increase crops and yields. It is thought that plants might respond to magnetic fields by showing greater growth and productivity. At the cellular level, a wide range of physiological effects can be observed. Magnetic fields have been reported to exert a positive effect on the germination of seeds. [1-2]. Extensive research has revealed that the effects of magnetic treatments depend not only on the magnetic field strength and exposure period [3-4], but also on the physiological condition of the organism involved, and on the reigning environmental conditions [4]. Basic stimulating doses (based on magnetic field strength and exposure period) must therefore be established under controlled conditions before using them with plants to be grown in the field [5].

In previous studies, several authors have found that magnetic treatment produces a biostimulation on initial growth stages and an early sprouting of several seeds [6]). Carbonell *et al*. [2] concluded that a stationary magnetic field acts as a noninvasive external stimulant for germination of rice seeds.

In this study the germination of oil palm seeds magnetically treated have been evaluated. We object to determine the optimal range of magnetic field intensities and suitable time period for increasing germination rate of oil palm and generally finding the effect of magnetic field on plant in different aspects.

Materials and Methods

Biological material

Agricultural species of oil palm seeds harvested from a single yield have been chosen to compose the samples (each sample contains 50 seeds). The seeds have been divided into two portions as follows:

A-The first group, is the control group.

B-The second group, called magnetically treated groups, has been subdivided into four groups.

Seeds in each group have been preliminarily soaked in distilled water for 2 h. The procedure of study was conducted. The magnetic treatment was provided as doses (D), varying the exposure time t and the magnetic field induction (B) with magnetic induction values B_1 =50 mT, B_2 = 100mT B_3 =100 mT, B_4 = 200mT and B_5 = 250mT. The doses D_1-D_{30} were obtained by exposing the seeds to each magnetic field induction for different time, as follows: 1-Exposure to 50 mT: D_1 (t=30min), D_2 (t=1 hr), D_3 (t=2 hr), D_4 (t=3), D_5 (t=4h), D_6 (t=5h). 2-Exposure to 100 mT: D_7 (t=30min), D_8 (t=1 hr), D_9 (t=2 hr), D_{10} (t=3), D_{11} (t=4h), D_{12} (t=5h). 3-Exposure to 150 mT: D_{13} (t=30min), D_{14} (t=1 hr), D_{15} (t=2 hr), D_{16} (t=3), D_{17} (t=4h), D_{18} (t=5h). 4-Exposure to 200 mT: D_{19} (t=30min), D_{20} (t=1 hr), D_{21} (t=2 hr), D_{22} (t=3), D_{23} (t=4h), D_{24} (t=5h). 5-Exposure to 250 mT: D_{25} (t=30min), D_{26} (t=1 hr), D_{27} (t=2 hr), D_{28} (t=3), D_{29} (t=4h), D_{30} (t=5h). Magnetic induction was measured using teslameter with Hall probe, having 10^{-4} T accuracy. All groups were let to germinate on watered paper support in a Petri dish at room temperature at 35 °C in darkness. The humidity on watered paper support in a Petri dish was controlled to not more than 80 %. All seeds in each group were labeled with numbers according to exposing time and randomly located to carry out the germination. All groups were supplied daily with magnetically treated water. The daily germination was registered for a period of 35 days. Germination percentages of seeds as a ratio of the number of germinated to the total number of seeds is determined. When the sprouts is observed, their length were measured. The experiments were distributed in 3 replicate.

Magnetic field generator

Exposure to EMFs was performed by a locally designed EMF generator. The electrical power was provided by a 220 V, AC power supply with variable voltages and currents. This system consisted of one coil, cylindrical in form, made of iron with 12 cm in diameter and 50 cm in length. The number of turns is 1000 of 0.5mm copper wire, which were in two layers. A fan was employed to avoid the increase of temperature (22 + 1±C). Calibration of the system as well as tests for the accuracy and uniformity of EMFs (60 Hz) were performed by a tesla meter with a probe type of hall sound.

Results and Discussion

The oil palm seeds were exposed to magnetic field ranging from 50 mT to 250 mT at different period of time varied from 30 min to 5 hr. In Figures 1-3, germination percentages of the seeds exposed to selected magnetic field strength at 50 mT, 150mT and 250 mT are shown. The fastest early growth of the seeds was observed on day 5th in group of D_{29}. The highest germination percentage for each treatment was obtained from the group of D_5, D_{11}, D_{17}, D_{23} and D_{29} and shown in Figure 4. It can be noticed that all seed treatments yielded a higher germination percentage compared with the control. Sprouts of oil palm at day 35th were illustrated in Figure5.

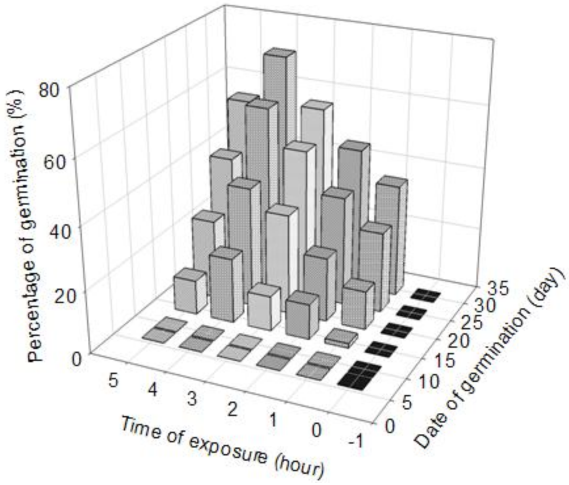

Figure 1 Germination percentages of oil palm seeds exposed to magnetic field of 50 mT at different period of time. The data were averaged from 3 replications.

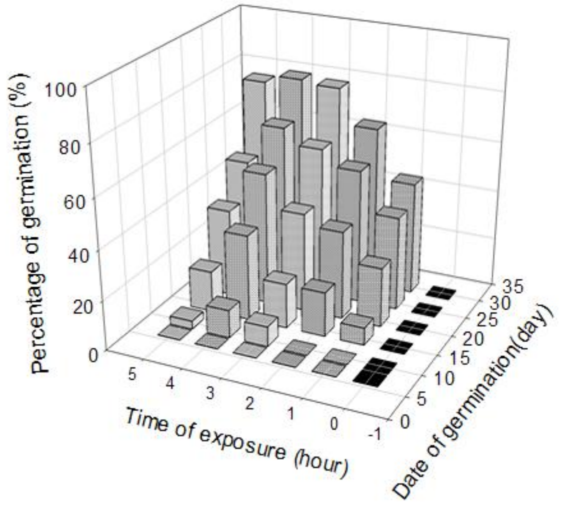

Figure 2 Germination percentages of oil palm seeds exposed to magnetic field of 100 mT at different

period of time. The data were averaged from 3 replications.

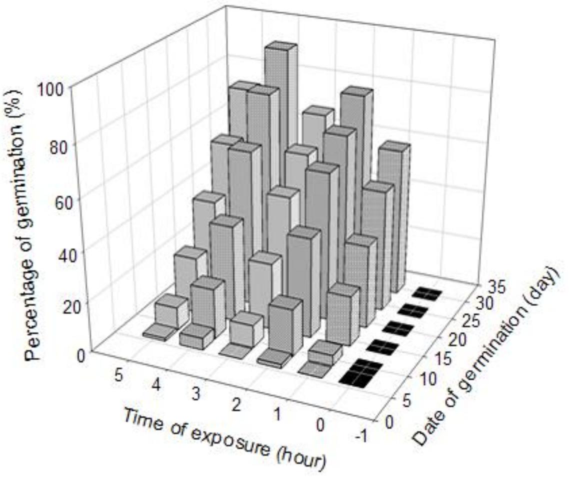

Figure 3 Germination percentages of oil palm seeds exposed to magnetic field of 150 mT at different period of time. The data were averaged from 3 replications.

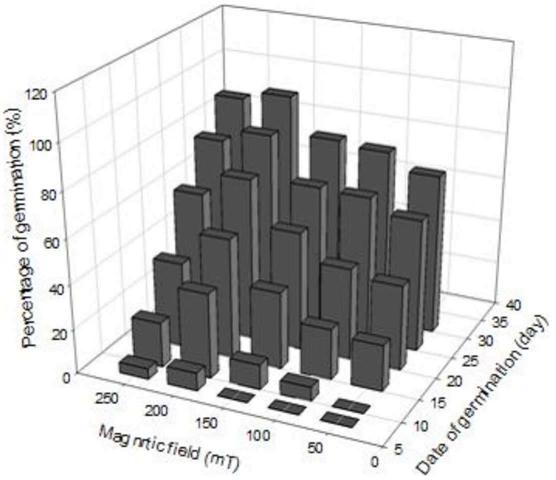

Figure 4 Maximum germination percentages of oil palm seeds exposed to magnetic field for 4 hours at different fields.

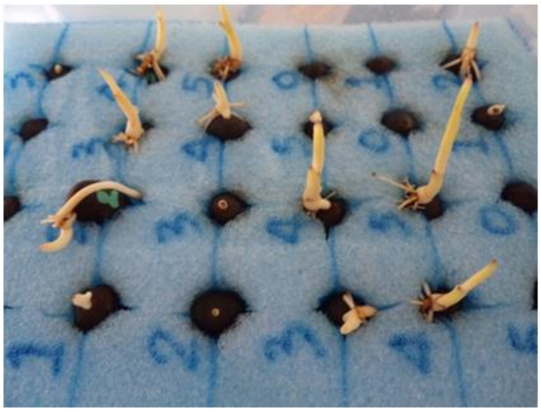

Figure 5 Oil palm sprouts at day 35th of germination. The numbers present in the figure mean the period of magnetic exposure.

Results illustrate a visible increase in the number of germinated seeds. The seeds under the influence of MTW germinated faster in comparison to the control. The stimulatory effect of the application of different magnetic doses on the germination is in agreement with that obtained by other researchers. Florez et al. [7] observed an increase for initial growth stages and an early sprouting of rice and maize seeds exposed to 125 and 250 mT stationary magnetic fields. Martinez et al. [8, 9] observed similar effects on wheat and barley seeds magnetically treated. Alexander and Doijode [1] reported that pregermination treatment improved the germination and seedling. Vigor of low viability rice and onion seeds. Kavi [10] found that seeds exposed to a magnetic field absorbed more moisture. Carbonell et al. [2] found that magnetic treatment produced a biostimulation of the germination. The mechanisms at work when plant and other living systems are exposed to a magnetic field are not well known yet, but several theories have been proposed, including biochemical changes or altered enzyme activities by Phirke et al. [11]. Garcia and Arza [12] carried out an experimental study on water absorption by lettuce seeds previously treated in a stationary magnetic field of 1-10 mT; they reported an increase in water uptake rate due to the applied magnetic field, which may be the explanation for increase in the germination speed of treated.

Conclusions

1. Results obtained for oil palm seeds allow to conclude that magnetic treatment improves the germination percentage of plants. It can be recommended to farmers for improving plant performance and the yield.
2. The best treatment in this experimental setting with Magnetic field induction 200 mT has been achieved at exposure time 4 hr for the parameters measured on the 35th day.
3. The influence of magnetic field is not well defined. Different plants could be sensitive to different combination of B and exposure time, thus further investigations of the nature of magnetic field stimulation are needed.

Acknowledgments

The authors thank the Prince Songkla University, Suratthani, Thailand to provide an opportunity to complete this project.

References

1. M.P. Alexander and S.D. Doijode, “Electromagnetic field a novel tool to increase germination and seedling vigour of conserved onion (*Allium cepa* L.) and rice (*Oryza sativa*, L.) seeds with low viability”, Plant Genetic Resources Newsletter 104 (1995) 1.
2. M.V. Carbonell, E. Martinez, and J.M. Amaya, 2000. “Stimulation of germination in rice (*Oryza sativa* L.) by a static magnetic field”, Electro Magnetobiol. 19 (2000) 121.
3. E. Wittekind, D. Broers, G. Kraepelin, and I. Lamprecht, “Influence of non-thermic AC magnetic fields on spore germination in a dimorphic fungus” Radiat Environ Biophys 143 (1990) 29.
4. J.C. Weaver, “Combined environmental exposures to chemicals and transient magnetic fields: a hypothesis for possible human health hazards”, Proc. Bioelectromagnetics Society 16th Annual Meeting 12-16 June (1993). Copenhagen, Denmark, 19.
5. M. Jristova, 1986. “Irradiation techniques in agriculture and food industry”, Center for Nuclear Energy University of Havana 87-113.
6. J.M. Amaya, M.V. Carbonell, E. Martínez, and A. Raya, 1996. “Effect of stationary magnetic field on growth and germination of seeds”, Agricultura 773 (1996) 1049.
7. M. Florez, M. V. Carbonell, and E. Martınez. “Exposure of maize seeds to stationary magnetic fields: Effects on germination and early growth”, Environmental and Experimental Botany 59 (2007) 68.
8. E. Martinez, M. V. Carbonell, and M. Florez. “Magnetic biostimulation of initial growth stages of wheat (*Triticum aestivum*. L)”, Electromagnetobiol. Med. 21(2002) 43.
9. E. Martinez, M. V. Carbonell and J. M Amaya. “A static magnetic field of 125 mT stimulates the initial growth stages of barley (*Hordeum vulgare* L.)”, Electromagnetobiol. 19 (2000) 271.
10. P.S. Kavi, “The effect of magnetic treatment of soybean seed on its moisture absorbing capacity”, Sci. Cult. 43 (1997) 405.
11. P. S. Phirke, A. B Kubde and S. P. Umbakar. “The influence of magnetic field on plant growth”, Seed Sci. Technol. 24 (1996) 375.
12. F. Garcia, and L.I. Arza. “Influence of stationary magnetic field on water relations in lettuce seeds. Part I: theoretical considerations”, Bioelectromagnetics 22 (2001) 589.

Enhancement of oil Palm trees by Magnetically treated Water

Sriplong C.[1], Sriplong C.[2], Jampa N.[3], Kongchana P., and Sudsiri Ch.[5*]

[1] *Faculty of Sciences and Industrial Technology, Prince of Songkla University Surat-thani Campus, Muang District, Surat-thani Province, 84100 Thailand*
[2] *Faculty of Sciences and Industrial Technology, Prince of Songkla University Surat-thani Campus, Muang District, Surat-thani Province, 84100 Thailand*
[3] *Sciences Laboratory and Equipments Center, Prince of Songkla University Surat-thani Campus, Muang District, Surat-thani Province, 84100 Thailand*
[4] *Sciences Laboratory and Equipments Center, Prince of Songkla University Surat-thani Campus, Muang District, Surat-thani Province, 84100 Thailand*
[5] *Faculty of Sciences and Industrial Technology, Prince of Songkla University Surat-thani Campus, Muang District, Surat-thani Province, 84100 Thailand*
**Corresponding author. E-mail: jutipornc@gmail.com, jutiporn.s@psu.ac.th*

Abstract

Oil palm planting has become a very important agriculture especially in Southern Thailand. Because its oil production has been used as human consumption and is now developed as bio-energy used for some vehicles therefore oil palm has become a very important economical plant which has been promoted to crop widely. However, since a nursing time of young oil palm trees needs more than 2 years, rare of young oil palm trees which caused high price has still caused a problem to agriculturist. In addition, some young trees weak and unable to grow. This work we therefore present physics method to enhance oil palm seedling. Magnetically treated water (MTW) was applied to young oil palm nursery. Oil palm seedlings which were electromagnetically germinated were divided into two groups and transferred into soil pot with same basic nutrition. Both groups were planted at nature environments. Light intensity at 1200 Lux was controlled. The first group was watered every day by MTW whereas the second group was applied by normal water and act as control. Sprout Heights of both groups were daily recorded. We found that oil palm seedlings which were watered by MTW grew faster than control. Larger and longer leafs than those of control also were observed. Our results conclude that MTW is able to stimulate plants growth and reduce their nursing time.

Keywords: Oil Palm, Plants Enhancement, Magnetically treated Water

Introduction

Biological stimulation plays an important role in optimizing crops in terms of the maximization of yield, promotion of plant growth. The main advantage of using electromagnetic stimulation methods over traditional chemical processes is the absence of toxic residues. Then, Murphy, (1942) [1] reported changes in seed germination due to a magnetic field. Exposure of seeds to magnetic field for a short time was found to help in accelerated sprouting and growth of the seedlings [2]. They reported the enhancement of plant growth under magnetic conditions. Savostin, (1930) [3] observed increase in the rate of wheat seedling elongation under magnetic conditions. Aladjadjiyan, (2000) [4] detected that seed exposure to a 150 mT magnetic field stimulated shoot development and led to increase of the germination, fresh weight and shoot length of maize plants. Studies indicated that suitable magnetic treatment increased the absorption and assimilation of nutrients.

Magnetically treated water (MTW) has been noted to increase crop production and drastically decrease plant disease incidence, and in some cases to improve the taste of agricultural products. The effects of MTW on biological materials have widely been studied [5-7]. It has been reported to stimulate the growth of seedlings, increase of height, size and number of leaves. Results show that MTW is more easily absorbed by the seed tissue and in this way it can stimulate internal metabolic processes which are conducive to germination.

Oil palm (*Elaeis guineensis*) is widely cropped in Thailand since it is used in a wide variety of ways by the local population. Unfortunately, the seedling of young oil palm tress takes more than one year and growing percentage rarely exceeds 60 %. This is insufficient for agriculturist and caused high-priced young oil palm trees. Any improvement, even be it small, in the growing efficiency would therefore be of great socio-economic importance for palm-crop.

In the work, the use of MTW obtained from extremely low frequency magnetic field treatment to stimulate the seedling process of young oil palm tree will be investigated.

Materials and Methods

Magnetic field generator

The device for the treatment of irrigation water has been created according to our own magnetic equipment in laboratory conditions. Exposure to EMFs was performed by a locally designed EMF generator. The electrical power was provided by a 220 V, AC power supply with variable voltages and currents. This system consisted of one coil, cylindrical in form, made of iron with 12 cm in diameter and 15 cm in length. The number of turns is 500 of 0.5mm copper wire. A fan was employed to avoid the increase of temperature (37 ^{o}C). Calibration of the system as well as tests for the accuracy and uniformity of EMFs (50 Hz) were performed by a tesla meter with a probe type of hall sound.

Preparation of oil palm seeds

The oil palm seeds which harvested from the same yield in order to minimize the genophond variation and three tests are implemented. In each test, oil palm of the same weight and similar appearance are selected and grouped in fifties. Each group of 50 seeds was soaked in normal water for 2h. The seeds of two groups were exposed to magnetic field of 200 mT for 4 h. Another was served as control. This experiment was conducted with three replications.

Selection of seed samples

We established three seed treatments in the experiments, as well as a control sample as a comparison pattern. The treatments were the following:

1) The seeds with no magnetic exposure were initially imbibed of 2 h in normal water and irrigation with normal water at the moment of germinating. We will refer to this treatment as control samples.

2) The seeds with no magnetic exposure were initially imbibed of 2 h in normal water and irrigation with MTW at the moment of germinating. We will refer to this treatment as MTW.

Seed germination

All seeds were transferred to a Petri dish with two sheets of absorbent paper (serviette). A single sheet of serviette was used to cover the seeds. For one such set of experiment, two Petri dishes were prepared and labeled as either N for sprinkling on top to soak the serviette with normal water or M which served as magnetically treated water. Humidity on the paper sheet is control to not more than 70 %. The seeds were allowed to germinate in dark room at room temperature about 30^{o}C. The number of germinated seeds was recorded daily for the time necessary to achieve the final number or percentage of germinated seeds. Seeds were observed daily for up to 35 days and considered seedling when the sprout was approximately 1 cm long or more.

Selection of young tree samples

A number of 25 seed for each seed treatment was divided into two groups to establish four young tree treatments in the experiments. The treatments were the following:

a) Irrigating with normal water at the moment of germinating and watering with normal water during the seedling.

b) Irrigating with normal water at the moment of germinating and watering with normal MTW .

c) Irrigation with MTW at the moment of germinating and watering with normal water.

d) Irrigation with MTW at the moment of germinating and watering with MTW.

All young trees were grow in soil which initial nutrition are known at nature conditions i.e. light intensity of about 1200 Lux, temperature of about 30 degree. Each sample was watered one time with 30 ml of water (the kind of water depended on the seed treatment) at the moment of seedling.

Results and Discussion

Germination percentages of three tests were shown in Figure 1. First test, the seeds were sprayed with magnetic water, started early growth at 7th day with germination percentage of about 5 % and reaches to 98 % at 35th day. Second test, normal water is applied, provided early growth at 9th day. The germination percentage reaches maximum at 93 % at the day of 35th.

Results illustrate a visible increase in the number of germinated seeds. The seeds under the influence of MTW germinated faster in comparison to the control samples. All seed treatments yielded a better germination response in time and in number of germinated seeds than the control samples.

The seeds from the first and the second test were transferred in to the known nutrition soil. Length of the sprouts was started to record as a high of young trees and shown in Figure 2. As shown, the average sprout length of the oil palm with magnetic water sprayed was the greatest of all three groups, and those of the oil palm grown spayed with normal water were the least. Therefore, it is clear that magnetic water has an enhancing effect on the growth of oil palm. At the day of 21st of the germination, young oil palm seeds under effect of magnetic water grow as shown in Figure 3.

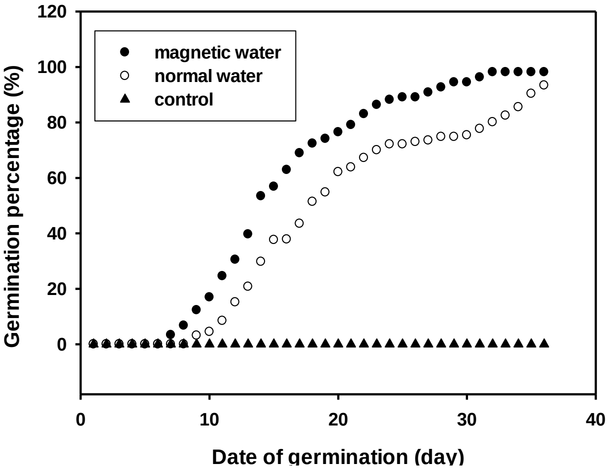

Figure 1. Germination percentages of seeds sprayed with normal water (empty circles) and magnetic water (full circles) compared to the control. Data are means of 3 replications experiments.

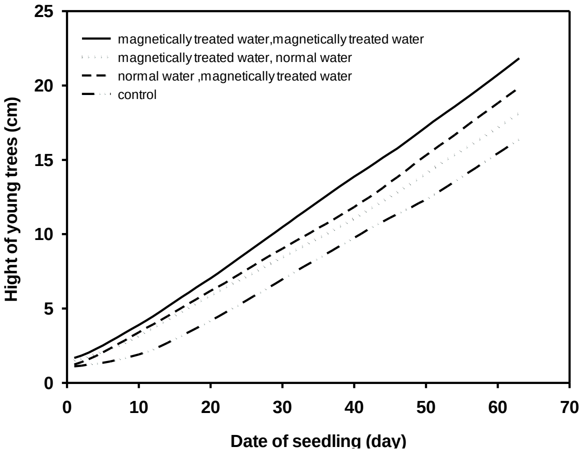

Figure 2. Heights of young oil palm trees at seedling date of 60 days. Data are means of 3 replications experiments.

The stimulatory effect of the application on the oil palm seedling is in agreement with that obtained by other researchers [8-10]. They reported that magnetically treated water used for crop irrigation resulted into better germination percentages, larger growth and better yields of tomatoes, wheat, cucumbers and carrots.

The behavior was hypothesized that magnetizing causes physical and chemical changes of natural water parameters, resulting in improvement of filtration and dissolving properties of water. According to experiments done by Henkenius and Retseck, (1992) [11], magnetic treated water also stimulates the growth of seedlings through increased height, weight and number of leaves.

Figure 3. Oil palm seeds germination at a period of 21 days grow under magnetic field effect

Correct explanation of the interaction of MTW and biological systems is a very complex issue nowadays and most experiences are only in practice, anyway some experimental results have pointed to some hypothesis. Some studies have shown that when normal water is exposed to magnetic fields some of its physical and chemical properties are changed, such as: surface tension, conductivity, solubility of salts, refractive index and pH, which has been shown by Smikhina, (1981) [12] , and Srebrenik *et al.*, (1993) [13], Yakovlev and Kolobenkov, (1976) [14].

Conclusions

1. Magnetically treated water largely influences the germinating and seedling growth. In general the best results were found for the cases of MTW with initial imbibition and at the moment of seedling.
2. The basic mechanism consisted in the change in the physical and chemical properties of water under the influence of magnetic field, such as: surface tension, solubility of salts, which allowed the MTW water to be better incorporated to the inner parts of the cells, thus increasing the probability of germination and seedling.
3. Those simple and basic experiments could lead to a better understanding of the influence of MTW on the germination process and in this respect create scientific bases of upcoming technologies.

Acknowledgments

The authors thank the Prince Songkla University, Suratthani, Thailand to provide an opportunity to complete this project.

References

1. J.D. Murphy, “The influence of magnetic field on seed germination”, Am. J. Bot. 29 (1942) 15.
2. L.Yinan, L.Yuan, Y. Yongquing, L. Chunyang, 2005. “Effect of seed pretreatment by magnetic field on the sensitivity of cucumber (*Cucumis sativus*) seedlings to ultraviolet-B radiation”, Environ. Exp. Botany 54 (2005) 286.
3. P.W. Savostin, “Magnetic growth relations in plant”, Planta 12 (1930) 327.
4. A. Aladjadjiyan, “Study of influence of magnetic field on some biological characteristics of *zea mays*”, J.Central Eur. Agric. 3(2002) 89.
5. C.K. Chou, “Thirty-five years in bioelectromagnetics research”, Bioelectromagnetics 3 (2007) 28.
6. B. Tenuzzo, A. Chionna, E. Panzarini, R. Lanubile, P. Tarantino, B. Di Jeso, M. Dwikat , and L. Dini, 2006. “Biological effects of 6 mT static magnetic fields: A comparative study in different cell types”, Bioelectromagnetics 560 (2006) 27.
7. G. Trebbi, F. Borghini, L. Lazzarato, P. Torrigiani, G. Lorenzo, and L. Betti, “Extremely low frequency weak magnetic fields enhance resistance of tobacco plants to tobacco mosaic virus and elicit stress-related biochemical activities”, Bioelectromagnetics 214 (2007) 28.
8. K. Namba, A. Sasao, and S. Shibusawa, “Effect of magnetic field on germination and plant growth”, Acta Horticulture 399 (1995) 143.
9. S. Nargis and C.P. Thiagarajan, “Effect of magnetic treatment on physiological and biochemical features of tomato seeds. South Indian Horticulture”, 44(1996) 159.
10. M. H. Hilal and M.M. Hilal, “Application of magnetic technologies in dessert agriculture, Seed germination and seedling emergence of some crops in a saline calcareous soil” Egyptian Journal of Soil Science 40 (2000) 413.
11. M. Henkenius and G. Retseck, **“**Magnetic water treatment”, Popular Mechanics J., 6 (1992) 70.
12. L.P. Smikhina, “Change in the refractive index of water on magnetic treatment”, Colloid J., (1992) 401.
13. S. Srebrenik, S. Nadiv, and L.J. Lin, “Magnetic treatment of water – a theoretical quantum model”, Magn. Electr. Separation 5 (1993) 71.
14. N.P. Yakovlev and K.Y. Kolobenkov, “Irrigation with magnetized water and the yield (Experiments with cereals and vegetables”, Viestnik Nauki, 20 (1976) 101.

Condensed Matter Physics

Effect of Ball Milling Time on Particles Size of $Ca_3Co_4O_{9+\delta}$

N. Prasoetsopha[1*], S. Pinitsoontorn[2], T. Khamwanna[2], K. Kurosaki[3], and S. Yamanaka[3]

[1]*Materials Science and Nanotechnology Program, Faculty of Science, Khon Kaen University, Khon Kaen, 40002, Thailand*
[2]*Department of Physics, Faculty of Science, Khon Kaen University, Khon Kaen, 40002, Thailand*
[3]*Division of Sustainable Energy and Environment Engineering, Graduate School of Engineering, Osaka University, Suita, Osaka, 565-0871, Japan*
**Corresponding author. E-mail: butsciku@hotmail.com*

Abstract

Thermoelectric (TE) materials can directly convert heat to electricity or vice versa. The misfit-layered $Ca_3Co_4O_{9+\delta}$ is one of the most promising TE oxide materials due to its high figure-of-merit (*ZT*) close to 1.0. In this work, polycrystalline $Ca_3Co_4O_{9+\delta}$ ceramics were prepared by a simple thermal hydro-decomposition method. The influence of ball milling time on particle size was investigated. The ball milling process exploited tungsten carbine balls with diameter of 1.6 mm, the ball per powder ratio of 10:1, the rotating speed of 300 rpm, the milling time of 2.5 - 20 h with acetone as dispersion media. The crystal structure and crystallite size were characterized by x-ray diffraction. The single phase of every cobaltite sample was obtained. The particle size and morphology were observed by a field emission scanning electron microscope (FESEM). The particle size was observed to be about 1 µm before ball milling and was reduced down to 200 nm after milling. The ball milled particles were fabricated to form a bulk ceramics using a spark plasma sintering (SPS) technique. However, second phases were found for the bulk ceramics. Seebeck coefficient, resistivity and thermal conductivity of the milled sample is higher than that of the unmilled sample. The highest *ZT* value of the unmilled and milled samples are 0.11 and 0.10, respectively, at 773 K.

Keywords: $Ca_3Co_4O_9$, ball mill, Thermoelectric, Thermal hydro-decomposition

Introduction

Thermoelectric (TE) materials can directly convert heat to electricity or vice versa. Recently, TE materials have attracted many groups of researchers because they are noiseless, have no moving part, and are environmental friendly. Several kinds of TE materials such as alloys, skutterudite, oxides have been investigated [1, 2, 3, 4]. The thermoelectric efficiency are defined as a dimensionless figure-of-merit, $ZT= S^2T/\rho\kappa$ where $Z, T, S, \rho,$ and κ are the figure-of-merit, the absolute temperature, the Seebeck coefficient (or so called thermopower), the electrical resistivity and the total thermal conductivity, respectively. In practice, $ZT \geq 1.0$ is required. The dependence of three parameters; $S, \rho,$ and κ, makes it difficult to improve TE properties. However, many research attempted to solve this challenging problem by many means, for examples, doping with other elements [5, 6, 7], improving fabrication process [8, 9], or making composites [10].

The misfit-layered $Ca_3Co_4O_{9+\delta}$ is one of the most promising TE oxide materials due to its non-toxicity, high oxidation resistance, high Seebeck coefficient, and low resistivity [11]. The single crystal $Ca_3Co_4O_{9+\delta}$ showed the highest *ZT* of 0.87 at 973 K [12]. Although the single crystal provides a high density and good TE properties but it is very difficult to fabricate in a large quantity. Therefore, polycrystalline $Ca_3Co_4O_{9+\delta}$, though lower *ZT* than the single crystal counterpart, is a more suitable choice for a practical use. One of the methods to improve TE properties of polycrystalline $Ca_3Co_4O_{9+\delta}$ is doping with other elements. Partially substituted of several metals either for Ca or Co were investigated, for examples, Ga [13], Ti [14], Fe [6, 15], Cu [6], Mn [6], or Y [7].

Furthermore, nanostructures are a novel approach to enhance TE properties due to a reduction of thermal conductivity. It is hypothesized that nanostructures can scatter phonon strongly so that they can reduce the total thermal conductivity. Yin et al. compared thermoelectric properties of $Ca_3Co_4O_{9+\delta}$ between the nanocrystals prepared by electrospinning and the conventional crystals prepared by a sol-gel method. TE properties were enhanced by nanocrystalline particles [16].

In this work, polycrystalline $Ca_3Co_4O_{9+\delta}$ were synthesized by a simple thermal hydro-decomposition method. The effect of ball milling time on particle size was investigated. Then, the TE properties of bulk ceramics prepared, from unmilled and milled samples, by a spark plasma sintering were studied.

Materials and Methods

Misfit-layered $Ca_3Co_4O_{9+\delta}$ polycrystals were synthesized by a simple thermal hydro-decomposition method [17]. Calcium and cobalt acetates in a stoichiometric ratio were employed as starting ingredients. The starting materials were dissolved in deionized (DI) water. After completely dissolved, the mixed solution was heated up to 1053 K and held at that temperature for 6 h in a furnace under normal atmosphere. The obtained product was grounded and calcined for second time at 1123 K for 24 h. The calcined powder was subjected to a ball milling process using tungsten carbine balls with diameter of 1.6 mm, a ball per powder ratio of 10:1, a rotating speed of 300 rpm, a milling time of 2.5 - 20 h with acetone as dispersion media. The bulk ceramic of the milled powders was fabricated by a spark plasma sintering technique.

The $Ca_3Co_4O_{9+\delta}$ samples were characterized by x-ray diffraction (XRD) using an x-ray diffractometer with Cu-Kα radiation (Rigaku, UltimaIV). The morphology and the chemical composition at the pressed surface and the fractured surface of the samples were evaluated by a field emission scanning electron microscope (FESEM, JEOL, JSM 6500F) and energy dispersive x-ray spectroscopy (EDS), respectively. The sintered pellet was cut and polished for thermoelectric and transport properties measurement. The resistivity and Seebeck coefficient were measured by using ZEM-3 (Ulvac-Riko) in a temperature range of 423-773 K. The thermal conductivity was calculated by $\kappa = DC_pd$, where D is the thermal diffusivity (measured using a laser flash technique, NETZSCH, LFA457), C_p is the heat capacity (estimated from the Dulong-Petit model, $C_p = 3nR$, where n is the number of atoms per formula unit and R is the gas constant) and d is density of the sample which were determined by using their mass and dimensions.

The crystallite sizes and lattice strain were calculated based on Scherrer's equation as follows:

$$d = \frac{0.9\lambda}{B\cos\theta} \qquad (1)$$

$$B\cos\theta = \frac{0.9\lambda}{d} + \eta\sin\theta \qquad (2)$$

where d, λ, B, θ and η are the crystalline size, x-ray wavelength, line broadening at half the maximum intensity, Bragg angle, and lattice strain, respectively.

Results and Discussion

Phase Identification and Morphology

Figure 1 shows the XRD pattern of unmilled powder, milled power, and sintered $Ca_3Co_4O_{9+\delta}$ samples. The unmilled and milled samples show the single phase of $Ca_3Co_4O_{9+\delta}$ according to JCPDS card No. 21-0139. The intensities of the XRD peaks of the milled samples decrease with increasing milling time. This is probably due to a reduction in crystallite size (See in Table 1). Moreover, the lattice strains of the milled samples increased with increasing milling time. The longer milling time induce a larger number of defects in the crystal structure which causes higher lattice strain. Highly dense bulk ceramics can be obtained after spark plasma sintering (SPS), 4.42 and 4.12 g/cm^3 for the unmilled and milled samples, respectively. However, the second phase of Co_3O_4 was observed from the bulk ceramics prepared from the milled powder. The impact of ball milling might create a small inhomogeneity distribution of Ca, Co and O but cannot be detected by XRD. When we applied the SPS process, such inhomogeneity was driven a by thermodynamic process, by the aid of heat and pressure, to from a more stable second phase which was detected in the XRD spectrum as shown in Figure 1.

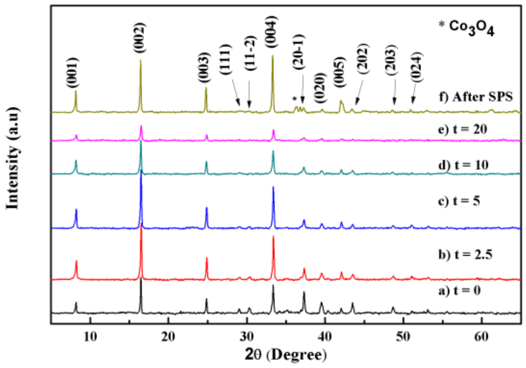

Figure 1. XRD pattern of $Ca_3Co_4O_{9+\delta}$ with various ball milling times: a) t = 0 h, b) t = 2.5 h, c) t = 5 h, d) t = 10 h, e) t = 20 h and f) SPS bulk ceramics from milled powder with t = 2.5 h.

Table 1: Effect of milling time on particle size, crystallite size and lattice strain of $Ca_3Co_4O_{9+\delta}$ powders

Time, h	Particle Size, nm	Crystallite Size, nm	Lattice Strain, %
0	838	632	0.50
2.5	535	404	0.71
5	321	192	0.71
10	226	177	1.40
20	208	85	3.61

Figure 2 shows the SEM micrographs of the samples. The particle size of the sample was decreased from 1 μm (unmilled sample) to 200 nm (milled sample) by ball milling for 20 h as shown in Figure 2 a) and 2 e), respectively. This implies that the ball milling process can be used to reduce the particle size of $Ca_3Co_4O_{9+\delta}$. Not only the particle size was decreased but the crystallite sizes, based on the calculation of the Scherrer's equation, were also decreased with increasing milling time. Nevertheless, the SPS sample after milling of 2.5 h exhibits impurity phase as can be seen at the fractured surface of the ceramic (black arrow of Figure 2 f). This result is in an agreement with the XRD pattern (Figure 1), the surface morphology and the EDS data (Figure 3).

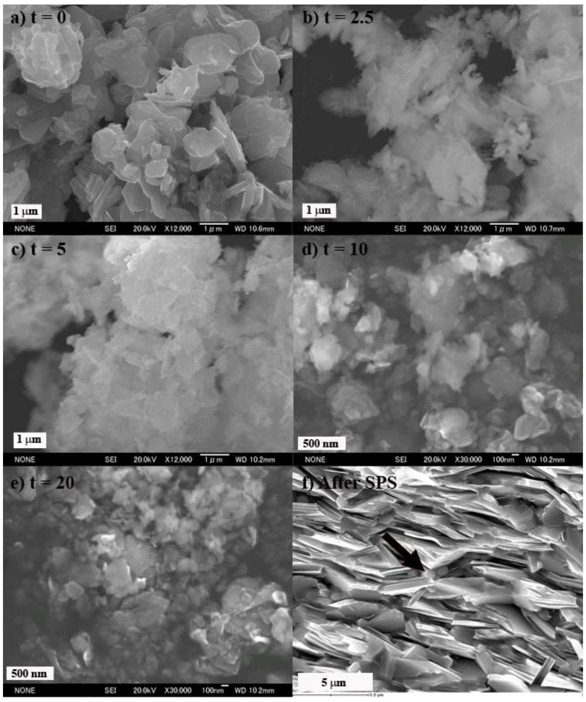

Figure 2. SEM micrograph of; non-milled and milled $Ca_3Co_4O_{9+\delta}$ particles with various ball milling times (a-e): a) t=0, b) t=2.5, c) t=5, d)=10, e) t=20 h; and fracture surface of f) t=2.5h after SPS. The black arrow indicates the impurity phase.

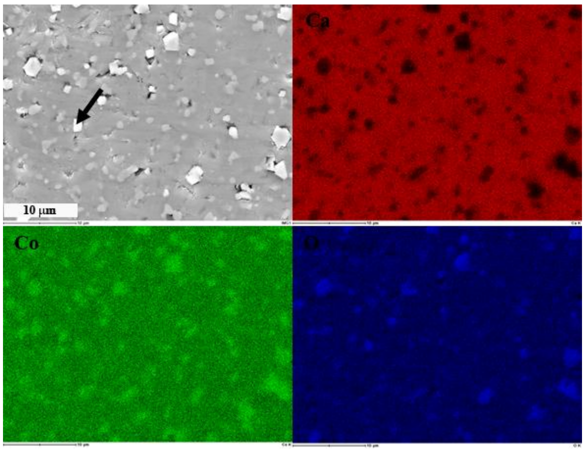

Figure 3. SEM micrograph of the pressed surface and the corresponding EDS mapping of the $Ca_3Co_4O_{9+\delta}$ ceramic. The black arrow points at the second phase.

Figure 3 shows SEM and EDS mapping of the SPS ceramics. The impurity phase is obvious observed on the surface of bulk ceramic. Not only the loss of Ca is illustrated but also the rich of Co and O are observed by EDS mapping. Moreover, the point analysis at the area of the second phase exhibits the Ca:Co:O ratios of 7:25:67, which is significantly different from the ratio of the $Ca_3Co_4O_{9+\delta}$ phase.

Thermoelectric Properties

Figure 4 shows temperature dependence of Seebeck coefficient (S), resistivity (ρ), and thermal conductivity (κ). The Seebeck coefficients of the unmilled and milled samples increase with increasing temperature. The S of the milled samples is higher than that of the unmilled samples. Hence, the ball milling process can be used to improve S. On the other hand, the resistivity of both samples decrease with increasing temperature. The ρ of the milled sample is higher than that of the unmilled samples. The higher ρ of the milled samples may be a result of a reduction in crystallite size which would enhance electron scattering at grain boundaries, and thus an increase in ρ.

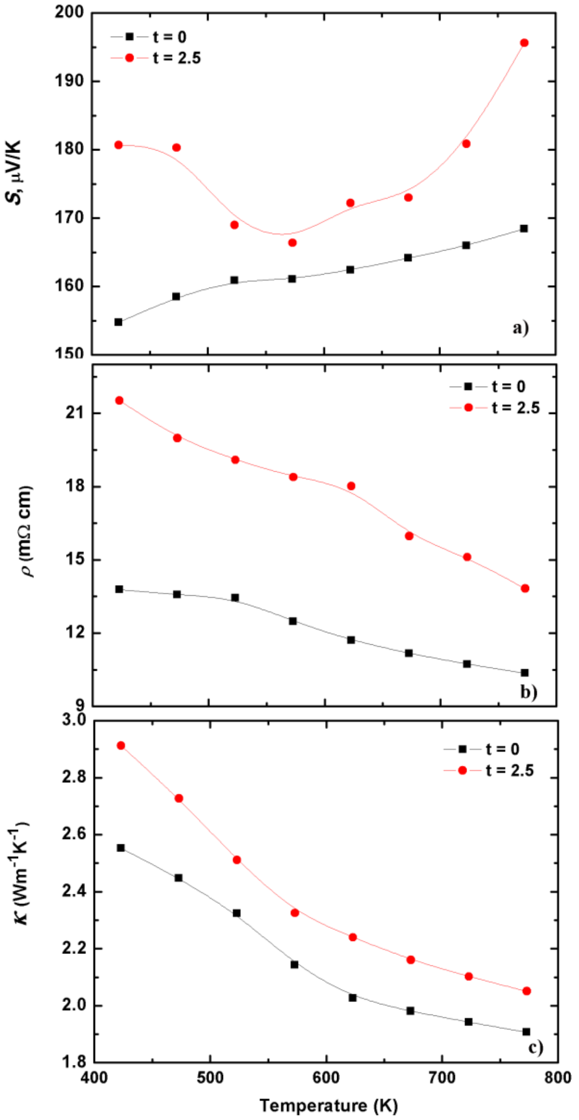

Figure 4 Temperature dependence of unmilled and 2.5 h milled $Ca_3Co_4O_{9+\delta}$: a) Seebeck coefficient, b) resistivity, and c) thermal conductivity.

The thermal conductivity of the milled sample is higher than that of the unmilled sample. Usually, the materials with smaller grain size should have the lower thermal conductivity due to the stronger scattering of electrons at grain boundary. However, in $Ca_3Co_4O_{9+\delta}$ the major contribution of κ is from phonon [16]. Thus, the difference in grain size does not have a significant effect on the κ. The reason for the higher κ of the milled sample may probably due to a presence of the second phase. Combining S, ρ, and κ, the ZT values of the unmilled and milled samples are calculated to be 0.11 and 0.10, respectively, at 773 K.

Conclusions

The reduction of particle size of $Ca_3Co_4O_{9+\delta}$ was achieved by a ball milling technique. For milling time of 20 h, the nanoparticle size of 200 nm was obtained. The bulk ceramic prepared from the milled powders of 2.5 h showed some impurity phase after the SPS process. The Seebeck coefficient, the resistivity and the thermal conductivity of the milled samples were increased. The highest ZT of the milled sample is 0.10, respectively, at 773 K.

Acknowledgments

The authors would like to thank the financial supports from Graduate School and Faculty of Science, Khon Kaen University. This work was also supported by the Higher Education Research Promotion and National Research University Project of Thailand, Office of the Higher Education Commission, through the Advanced Functional Materials Cluster of Khon Kaen University.

References

1. T. M. Tritt and M. Subramanian, **“**Thermoelectric Materials, Phenomena, and Applications: A Bird’s Eye View**”**, MRS Bulletin **31** (2006), 188.
2. G. J. Snyder and E. S. Toberer, **“**Complex Thermoelectric Materials**”**, Nature Materials **7** (2008), 105.
3. K. Koumoto, I. Terasaki and R. Funahashi, **“**Complex Oxide Materials for Potential Thermoelectric Applications**”**, MRS Bulletin **31** (2006), 206.
4. H. Ohta, K. Sugirua and K. Koumoto, **“**Recent Progress in Oxide Thermoelectric Materials: p-type $Ca_3Co_4O_9$ and n-type $SrTiO_3^-$**”**, Inorganic Chemistry **47** (2008), 8429.
5. J. Pei, G. Chenh, D. Q. Lu and P. S. L. N. Zhou, **“**Synthesis and High Temperature Thermoelectric Properties of $Ca_{3.0-x-y}Nd_xNa_yCo_4O_{9+\delta}$**”**, Solid State Communications **146** (2008), 283.
6. Y. Wang, Y. Sui, P. Ren, L. Wang, X. Wang, W. Su and H. Fan, **“**Strongly Correlated Properties and Enhanced Thermoelectric Response in $Ca_3Co_{4-x}M_xO_9$ (M=Fe, Mn, and Cu)**”**, Chemistry of Materials **22** (2010), 1155-1163.
7. H. Q. Liu, Y. Song, S. N. Zhang, X. B. Zhao and F. P. Wang, **“**Thermoelectric Properties of $Ca_{3-x}Y_xCo_4O_{9+\delta}$ Ceramics**”**, Journal of Physics and Chemistry of Solids **70** (2009), 600.
8. C. Yuankui, C. Chuan and L. Xiang, **“**Effect on the Properties of Different Preparation Processes in $Ca_3Co_4O_9$ Thermoelectric Material**”**, International Conference on Electrical and Control Engineering (2010), 4672.
9. J. G. Noudem, D. Kenfaui, D. Chateigner and M. Gomina, **“**Toward the Enhancement of Thermoelectric Properties of Lamellar $Ca_3Co_4O_9$ by Edge-free Spark Plasma Texturing**”**, Scripta Materialia **66** (2012), 258.
10. P.-H. Xiang, Y. Kinemuchi, H. Kaga and K. Watari, **“**Fabrication and Thermoelectric Properties of $Ca_3Co_4O_9$/Ag Composites**”**, Journal of Alloys and Compounds **454** (2008), 364.
11. A. C. Masset, C. Michel, A. Maignan, M. Hervieu, O. Toulemonde, F. Studer, B. Raveau and J. Hejtmanek, **“**Misfit-layered Cobaltite with an Anisotropic Giant Magnetoresistance: $Ca_3Co_4O_9$**”**, Physical Review B **62** (2000), 166.
12. M. Shikano and R. Funahashi, **“**Electrical and Thermal Properties of Single-crystalline $(Ca_2Coo_3)_{0.7}CoO_2$ with a $Ca_3Co_4O_9$ Structure**”**, Applied Physics Letters **82** (2003), 1851 -1853.
13. N. Nong, N. Pryds, S. Linderoth and M. Ohtaki, **“**Enhancement of the Thermoelectric Performance of p-type Layered Oxide $Ca_3Co_{4-x}Ga_xO_{9+\delta}$ Through Heavy Doping and Metallic Nanoinclusions**”**, Advanced Materials **23** (2011), 2484.
14. L. Xu, F. Li and Y. Wang, **“**High-Temperature Transport and Thermoelectric Properties of $Ca_3Co_{4-x}Ti_xO_9$**”**, Journal of Alloys and Compounds **501** (2010), 115.
15. C. Liu, L. Huang and J. Wang, **“**Improvement of Thermoelectric Characteristics of Fe-doped Misfit-layered $Ca_3Co_{4-x}Fe_xO_{9+\delta}$ (x = 0, 0.05, 0.1, and 0.2)**”**, Applied Physics Letters **89** (2006), 204102.
16. T. Yin, D. Liu, Y. Ou, F. Ma, S. Xie, J.-F. Li and J. Li, **“**Nanocrystalline Thermoelectric $Ca_3Co_4O_9$ Ceramics by Sol-gel Based Electrospinning and Spark Plasma Sintering**”**, Journal of Physical Chemistry **114** (2010), 10061.
17. S. Daengsakul, C. Mongkolkachit, C. Thomas, S. Siri, I. Thomas, V. Amornkitbamrung and S. Maensiri, **“**A Simple Thermal Decomposition Synthesis, Magnetic Properties, and Cytotoxicity of $La_{0.7}Sr_{0.3}MnO_3$ Nanoparticles**”**, Applied Physics A-Materials Science & Processing **96** (2009), 691.

Environmental Physics, Geophysics, and Renewable Energy

A New Type of Green Jewelry Product from Glass-Ceramics Composite

A. Kiratisin*, B. Phichaikamjornwut, K. Wongpreedee, and D. Bootkul

Department of General Science, Faculty of Science, Gems and Jewelry division,
Srinakharinwirot University, 114 Sukhumvit 23, Bangkok 10110, Thailand
**Corresponding author. E-mail: amonmat@*swu.ac.th

Abstract

The purpose of this research was to produce glass-ceramic from recycled glass and kaolin clay addition. The recycled glass of soda lime silica glass (SLSG) was used as main raw material and kaolin clays as reinforce filler. The glass powders were prepared by crushing to a particles size distribution 100-200 μm. The SLSG powder were then mixed with the kaolin clay according to the ratio of SLSG to kaolin clay of 75:25 wt.%, 80:20 wt.% 85:15 wt.% 90:10 wt.% and 95:5 wt.%. The glass ceramic samples were fabricated using uniaxial pressing and cold isostatic pressing with constant pressure at 1500 PSI. Temperature processing was conducted at different temperatures at 850°C and 1,000°C with 4 hrs holding time. There are several changes in terms of shape, color and appearance after the firing process. Temperature 1,000°C with 90:10 wt.% ratio of SLSG to kaolin clay is the best result in term of color and appearance to produce new glass-ceramic material for Turquoise costume jewelry applications

Keyword: Glass-ceramic, soda lime glass, kaolin, turquoise fashion jewelry

Introduction

Glass-ceramics are composite materials produced through controlled crystallization of base glass called "controlled crystallization". The most conventional definition of glass is an amorphous material possessing under the glass transition behavior. [1-3] In the case of crystal as figure 1, transition from liquid to solidified crystal occurs at the melting temperature, T_m. On the other hand, a glass material takes the supercooled state below the Tm, and shows the transition to glass in the temperature range where the viscosity of glass increases.

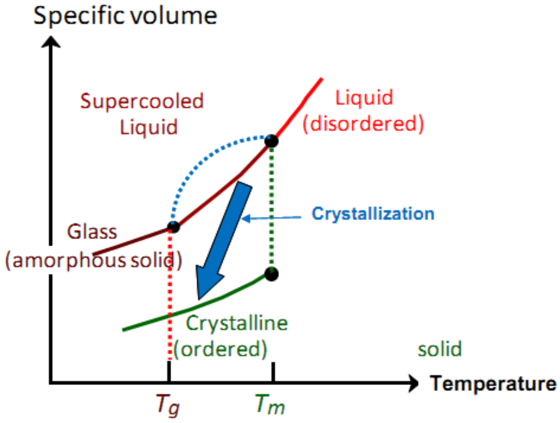

Figure 1. A volume difference between crystal and glass.

Temperature at which transition from supercooled liquid to glass occurs is mentioned

as the glass transition temperature, T_g. In the temperature region, some physical parameters of glass material show "some steep" change. Since the T_g is a fictive temperature that depends on the fabrication process, a glass can take several values of T_g depending on the cooling rate.

Materials and Methods

The sample preparation was starting with powder preparation which includes sieving, mixing and weighing process of the mixture powder of SLSG and kaolin clay. As shown in figure 2, the green samples produced after Cold Isostatic Pressing (CIP). The sample result of powder after producing from pressing process is in cylindrical shape or pellets form with a diameter of 30 mm.

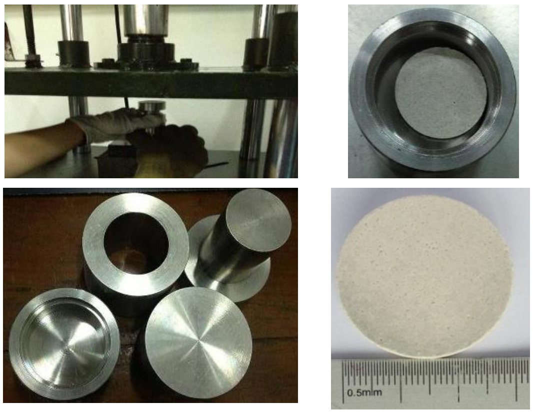

Figure 2. The green sample after CIP process.

Results and Discussion

Table 1 shows the result of sample color for each temperature with different SLSG to kaolin clay ratio. At 850°C, it can be observed that the sintering process is in its initial stage. The best mixing ratio is 90:10 wt.% ratio of SLSG to kaolin clay at 1000 °C because the presence of kaolin clay helps the uniformity of the green body. This may be explained by the high viscosity of the SiO_2 rich melting the constituent [4-5].

Table 1 Glass-ceramic samples at temperature 850 °C (left) and 1000 °C (right) using different SLSG:kaolin ratio.

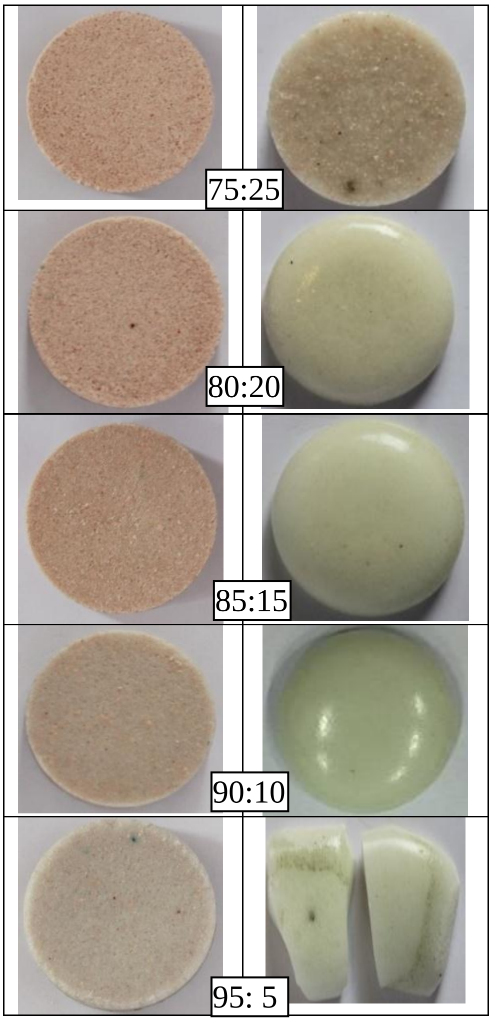

Firing temperature plays an important role during this study because the glass ceramic produced give various results of physical and mechanical properties. The observations on microstructure gives a lot of information about surface of glass ceramic produced to identify the existence of a positive effect in terms of crystal growth and the negative effects terms of open and closed porosity and cracks. Through the study, the bulk density had increased with the increasing of temperature but had decreased with the increasing of SLSG to kaolin clay weight ratio. The appropriate temperature for this study is at 1000°C because at this temperature had the best result of physical and mechanical properties. When the amount of kaolin clay had increased produced a very bad surface finish. While at 90:10 wt.% ratio of SLSG to kaolin clay produced a very good surface finish. Overall, the sintering temperature and addition of kaolin clay provide different effects on each of the samples, but most result, in the event of increasing temperatures, the values such as the porosity, density measurement and water absorption will decrease.

Table 2: Characterization of produced from flint glass with the addition of CuO

Color appearance	CuO (ppm)	Colors	Tone	Saturation
	0.002 0.004 0.006	Very slightly green blue: VslgB	4 : Medium Light	4: Moderately strong
	0.008 0.010 0.012	Very slightly green blue: VslgB	5: Medium	4: Moderately strong
	0.014 0.016 0.018 0.020	Very slightly green blue: VslgB	6: Medium dark	3: Very slightly grayish

Ordinary soda-lime glass appears colorless to the naked eye. Metals and metal oxides can be added to glass during its manufacture to change its color which can enhance its aesthetic appeal. Such a small concentrations of copper oxide (2 to 3%) used for produces a deep blue green color [6]. All glasses were completely melted at 1000^{o}C. This melting temperature still remaining very small bubbles. The additions of copper powder affects to color and are appearance of glasses. Consideration Cu^{2+} which provides a convenient means of changing the color of the flint glasses from colorless to blue. When CuO was increased from 0.0-0.02 ppm the colors were changed from clear glass to bluish-green glasses as shown in table 2. Silicate glass is an amorphous material in the form of $(SiO_4)^4$-. CuO shifted the Cu^{2+} ion in glasses from the network-modifying to network-forming positions. Cu^{2+} ion as the network-modifying broke the Si-O-Si bonds and replaced Si^{4+} into the network producing a blue glass [6]. The results of the green glass show same effects manner as flint glasses. Rare earth metals are not as sensitive to the base glass composition. They also have sharper absorption bands as compared to the transition metals. The coloring substance can also be a chromophore consisting of ions of two or more elements. When a glass is colored by metal ions, the color is due to electron transitions associated with the transition elements or rare earth metals. The color originates from ligand field splittings of d- or f-electron orbitals. The color can also differ depending on which base glass is used and whether the ions are part of the glass structure as a network former or network modifier.

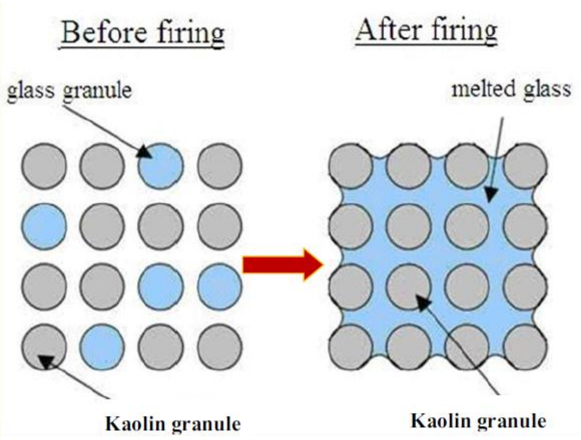

Figure 3. Firing process of SLSG and Kaolin.

The investigations discussed in this research demonstrate the potential of turning soda lime glass wastes into useful glass-ceramic products. According to table 2 in case of glass-ceramic color displayed distinct depending on the glass body color. The soda lime glass from flint color combination of kaolin without copper powder is shown in figure 4a. The blue green samples displayed some green color concentrations forming an original of copper powder adding when processing of glass-ceramic (figure 4b). The deep blue color appeared to be superimposed on the blue base of natural turquoise pieces; this gave an overall blue-green coloration to the specimen (figure 4c and 4d).

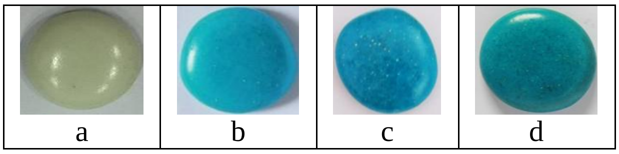

Figure 4 Glass-ceramic products flint glass without copper powder (a) flint glass with 0.5% copper powder (b) flint glass with 1% copper powder (c) and flint glass with 2% copper powder (d).

Figure 5 after cutting for jewelry shape.

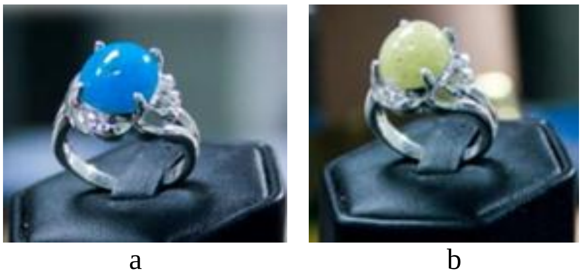

Figure 6. All the turquoise jewelry fashion prototype set.

Additional, pilot plants as Turquoise gem quality have been successfully operated for the manufacture of these glass-ceramics. Figure 6 shows product from recycle soda lime glass/kaolin composite provide properties as 1.7-1.9 refractive Index, density 2.8-2.9 g/cm^3 and 8 hardness on Moh's scale.

Conclusions

The present new ways of recycling silicate waste, whereby the production of glass-ceramics will become a viable for a new design and an alternative of fashion jewelry. Soda Lime Silica Glass (SLSG) with the addition of kaolin clay as a filler at a various weight ratio successfully produced a new material of glass ceramic produced from recycled glass. Preparation of glass ceramic by using Cold Isostatic Pressing (CIP) method is the suitable method in order to produce more compact and uniform glass ceramic materials. The glass ceramic produced from the sintering process provide a various changes in term of color, shape and appearance. The best result happen at 1000°C with 90:10 wt.% ratio of SLSG to kaolin clay because the cylindrical shape are compact and flat. The effects of firing temperature and weight ratio of SLSG to kaolin clay produced a different physical, microstructure, phase and mechanical properties.

Acknowledgments

This research was supported by a grant from the Faculty of Science, Srinakharinwirot University. Also Dr Saweat Intarasiri from Plasma and Beam Physics Research Facility, Department of Physics and Materials Science, Faculty of Science, Chiang Mai University for his PIXE characterization.

References

1. Holand W and Beall G H, Glass-Ceramic Technology, Wiley-Blackwell (2002)
2. Strnad Z, Glass-Ceramic Materials in Glass science and technology V.8 (1986) Czechoslovakia: Elsevier Science Publishing Company, Inc.
3. Douglas, R. W. (1972) A history of glassmaking. Henley-on-Thames: G T Foulis & Co Ltd. ISBN 0854291172.
4. Pannhorst, W., Glass-ceramics: State-of-the-Art, J. Non-Cryst. Solids 219 (1997) 198-204.
5. Beall, G. H., Design and Properties of Glass-Ceramics, Ann. Review Mater. Sci. 22 (1992) 91-119.
6. McMillan, P. F. (2004) "Polyamorphic transformations in liquids and glasses". J. Mater. Chem. 14: 1506–1512.

Application of Airborne Gamma-ray Spectrometric Data to Study Weathering of Rocks in Songkhla Province

M. Boonya[1] and T. Bhongsuwan[1,2,*]

[1]*Department of Physics, Faculty of Science, Prince of Songkla University, Hatyai, Songkhla, 90112, Thailand*
[2]*Geophysics Research Center, Prince of Songkla University, Hatyai, 90112, Thailand*
**Corresponding author. E-mail: tripop.b@psu.ac.th*

Abstract

Airborne gamma-ray spectrometric survey measures the abundance of natural gamma ray emitted from potassium (K), uranium (U) series and thorium (Th) series in the top of the earth's surface. Gamma ray emitted from the ground surface relates to the mineralogy and geochemistry of bedrock and weathered materials. Airborne gamma-ray spectrometric method can be used to study weathering of rocks. The weathering is disintegration or alteration of rocks and minerals by chemical and physical processes those relate to environmental condition at or near the earth's surface. The weathering process modifies the distribution and concentration of radioelements from initial bedrock concentration. The concentration of potassium generally decreases with increasing the weathering of rocks because potassium is highly soluble and leaches from weathering profile, whereas the concentration of uranium and thorium in weathered rocks depends on complexities of dissolution and precipitation process of each radioelement. The weathering data of rocks in Songkhla Province obtained from analyzing airborne gamma-ray spectrometric data and digital elevation model are compared with geological, erosion and landslide hazard maps. Data processing and interpretation are currently being carried out.

***Keywords*:** Airborne gamma-ray spectrometry, Weathering, Radioelements, Songkhla Province

Introduction

Airborne gamma-ray spectrometric survey is one of aerial geophysical methods by measuring abundance of natural gamma ray emitted from potassium (K), Uranium (U) series and thorium (Th) series in the top of the earth's surface. The abundance of gamma ray emitted from the ground surface relates to geochemistry and mineralogy of bedrock and weathered materials. Airborne gamma-ray spectrometric survey has been used in many applications, such as detecting mineral deposits, geological mapping tool and environmental applications. The objective of this work is using airborne gamma-ray spectrometric data to study the weathering of rocks. Studying the weathering of rocks is beneficial because the weathering is one of important factors affecting the occurrence of landslide apart from rainfall and deforestation. Nowadays, the landslide is an important disaster destroying a lot of lives and building. Consequently, the weathering data of rocks covering a wide area are useful to further study the landslide hazard area.

Radioactivity is common phenomena of natural geological materials. Radioactivity occurred in three types that are named alpha particle, beta particle and gamma ray. Alpha and beta particles cannot move though soils, rocks and air. Therefore, there is only gamma ray that can be detected by airborne radiometric survey. Generally, there are many natural radioisotopes. However, there are only radioisotopes of potassium, uranium series and thorium series that can produce sufficient gamma ray to be measured by gamma-ray spectrometry. Potassium measurement is direct estimate from abundance of ^{40}K. Uranium and Thorium measurement are indirect estimate through daughter radioisotopes, ^{214}Bi and ^{208}Tl respectively.

Potassium is a major component of the earth's crust (~2.5%) [Wilford, Bierwierth and Craig, 1997] and is mainly found in rock-forming minerals such as K-feldspar and mica. The abundance of potassium is high in felsic rock but low in mafic and ultramafic rocks. Uranium and thorium are a minor component of the earth's crust (~3 and ~12 ppm respectively) [Wilford, Bierwierth and Craig, 1997]. The abundance of uranium and thorium is high in accessory and resistant minerals such as monazite, xenotime and zircon but low in rock-forming minerals.

Weathering is breaking down or alteration of rocks and minerals by chemical and physical processes that relate to environmental conditions at or near the earth's surface. The weathering of rocks can be separated in two major types which consist of physical weathering and chemical weathering. The physical weathering is disintegration of rocks into smaller pieces by mechanical process without a change in mineral and chemical composition of rocks. The chemical weathering is alteration in composition by chemical reaction of minerals with elements in water and air. Factors influencing the weathering intensity of rock consist of parent material, external climate, topography, biotic potential and time. During weathering, potassium concentration generally decreases with increasing the weathering because potassium has high solubility. In contrast, Thorium has low solubility and solubility of uranium depends on valence state of uranium ion. Therefore, the concentration variation of uranium and thorium during weathering is complicated. Uranium and thorium are released from rocks during weathering but can be adsorbed by clay oxide of Fe and Al in weathering profile.

Materials and Methods

Study Area

Study area is Songkhla Province. Songkhla is an east coastal province in southern Thailand which covers an area of 7,393.889 km^2. This area is located in 6°17′-7°56′ N latitude and 100°1′-101°6′ E longitude. Landform in the north part mainly is alluvial plain, the east part is coastal plain and the west and the south parts are mountains and plateau. Songkhla has been influenced by tropical monsoons which include the northeast monsoon and the southwest monsoon. Therefore, Songkhla has only two seasons. The hot season is from February to July. The rainy season is from October to January. Figure 1 shows geological map of Songkhla [DMR, 2007]. Songkhla is mostly covered by Quaternary sediments. The found oldest rock occurs in Cambrian period. Sedimentary and metamorphic rocks are found having many types. Moreover, igneous rock found in this area is granite occurring in Triassic period.

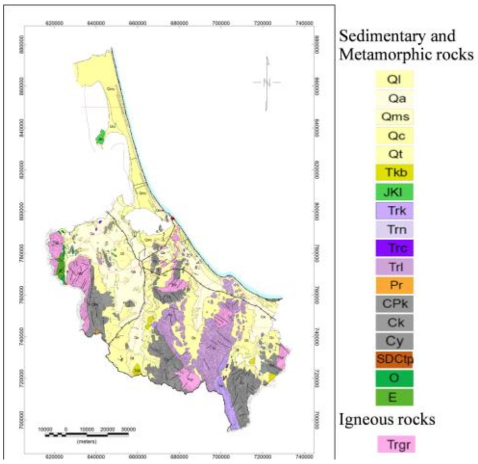

Figure 1. Geological map of Songkhla Province.

Data sets

This work studied the weathering of rocks by using airborne gamma-ray spectrometric data. The data consist of K, eU and eTh. These data were derived from surveying in 1984-1989 which cover most area of Thailand under handing of the Department of Mineral and Resources. Potassium is expressed in percent while uranium and thorium are in parts per million. The digital elevation model (DEM) was also used in this work. DEM was derived from The Shuttle Radar Topography Mission (SRTM) elevation data collected in 2000. Figure 2 shows all data sets that were used.

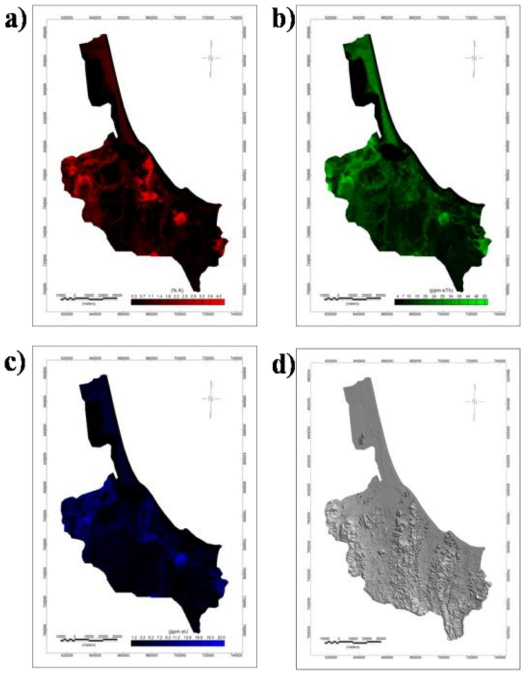

Figure 2. a) Potassium map, b) Thorium map, c) Uranium map and d) DEM.

Weathering intensity of rocks

This work used the weathering intensity index (WII) [Wilford, 2012] to assess weathering intensity of rocks in study area. The WII formula was generated by analyzing correlation between airborne gamma-ray spectrometric data and DEM with weathering class for the Australian continent in 2012. The weathering class is levels of rocks-weathering intensity from field investigations which separated into six levels. The WII formula is shown below.

$$WII = 6.751 + -0.851K + -1.319\,Relief + 2.682\,Th/K + -2.590\,Dose \qquad (1)$$

The dose rate was calculated by using the formula 13.078 K (%) + 5.67 U (ppm) + 2.49 Th (ppm) [IAEA, 2003] and is expressed in nanoGrays per hour (nGy/h). The relief surface was generated from DEM analysis by calculating the difference between the lowest and the highest elevations within a 270 m radius.

Results and Discussion

The abundance of radioelements corresponds with geological features and landscape process (figure 1, 2 and 3). Figure 3 is ternary map (RGB = K, Th and U). Granite mountain zones apparently show high concentration of K, Th and U, whereas other zones of sedimentary and metamorphic rocks show lower concentration. Moreover, the ternary map can show channel as a result of transportation and deposition from granitic mountain.

Area of special interest is granite mountain zones. Main component of granite are quartz and feldspar. Feldspar is easily weathered by hydrolysis reaction. Besides, granite zones are higher steep than other zones. Therefore, these zones have high risks in occurrence of landslide.

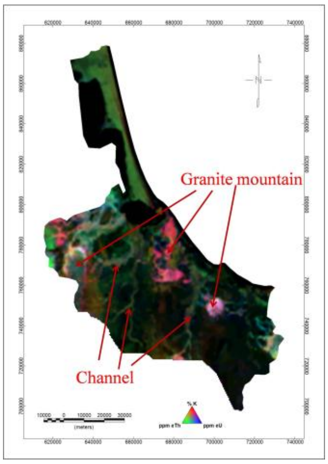

Figure 3. Ternary map.

The WII image for Songkhla shown in Figure 4 was calculated by using equation 1. The WII values can be used to indicate weathering intensity of rocks. Values of the WII increase with increasing weathering of rocks.

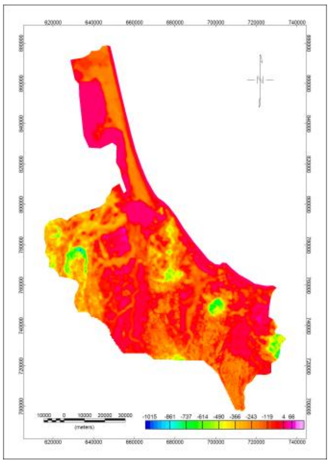

Figure 4. WII image.

The WII image in Songkhla indicates that the WII values in low plain areas are higher than mountain zones. In plain areas, there is much time for rocks to weather. In contrast, mountain zones have more slopes. Weathering of rocks in these zones is more difficult. Moreover, weathered rocks in these zones may be eroded from the origin by agents such as wind and water. Therefore, the WII values in mountain areas are lower.

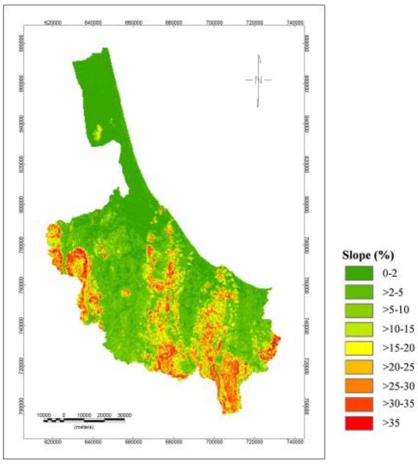

Figure 5. Slope image derived from DEM.

Slope image for Songkhla shown in Figure 5 was calculated from DEM data. Levels of slope were separated into nine levels. The slope levels correspond with WII values. High levels of slope correlate with low WII values, whereas lower levels correlate with higher WII values. The levels of slope affect weathering intensity of rocks and erosion rate.

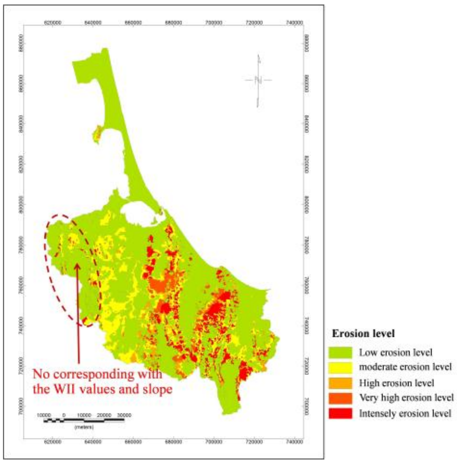

Figure 6. erosion map.

Figure 6 shows erosion map [LDD, 2002]. Erosion levels are separated into five levels. Most of erosion map corresponds with the WII values. High erosion levels correlate with low WII values, whereas lower levels correlate with higher WII values. However, some zones are not correlated. For example, the WII values of the granite mountain area in west Songkhla are not correlated with erosion levels. This area is mountainous that there are both high and low slope. The erosion map shows low levels in this area, whereas the WII image shows low values in steep zones and higher value in more flat zones.

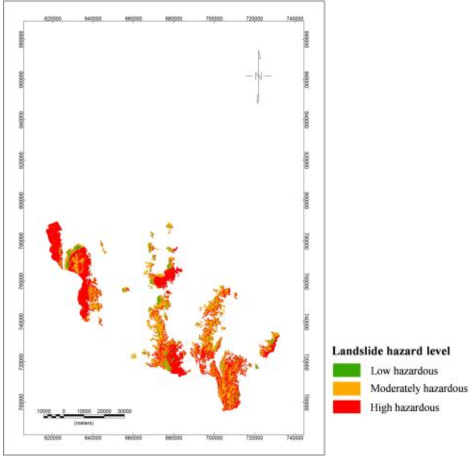

Figure 7. Landslide hazard map.

Figure 7 shows landslide hazard map [DMR, 2004]. This map shows risks in occurrence of landslide which separated into three levels. This map indicates that landslide hazard areas mostly are near the granite mountain, whereas other zones have no risk although there are the high WII values. In the risk zones, high values of the WII indicate high risks in occurrence of landslide, whereas lower values indicate lower risks.
High values of the WII in mountainous zone are result of high weathering intensity of rock and thick layer of weathered rocks. In contrast, low values may be result of low weathering intensity of rocks or high erosion rate.

Conclusions

The airborne gamma-ray spectrometric data can be used to assess weathering intensity of rocks. Particularly, potassium content systematically decreases with increasing the weathering of rocks. This work indicates possibility of applying the WII in order to assess weathering intensity of rock in Songkhla area. The WII values correlate with geological map, slope image derived from DEM, erosion map and landslide hazard map. However, this index might be adjusted for this area because of difference in geology and climate between Thailand and Australia.

Acknowledgments

The authors would like to thank the Graduate School, Prince of Songkhla University for the financial support. We greatly thank the Department of Mineral Resources for providing the airborne radiometric map and geological map. We are also thankful the GEO-Informatics Research Center of Natural Resource and Environment for providing the necessary GIS data. We also thank the Department of physics, Faculty of Science and the Geophysics Research Center, Prince of Songkhla University for many supports.

References

13. J.R. Wilford, P.N. Bierwierth and M.A. Craig, “Application of airborne gamma-ray spectrometry in soil/regolith mapping and applied geomorphology”, AGSO Journal of Australian Geology & Geophysics **17(2)** (1997), 201-216.
14. J. Wilford, “A weathering intensity index for the Australian continent using airborne gamma-ray spectrometry and digital terrain analysis”, Geoderma **183-184** (2012), 124-142.
15. IAEA, Guidelines for radioelement mapping using gamma ray spectrometry data, IAEA-TECDOC-1363, Vienna, 2003.
16. B.L. Dickson and K.M. Scott, “Interpretation of areal gamma-ray surveys - adding the geochemical factors”, AGSO Journal of Australian Geology & Geophysics **17(2)** (1997), 187-200.
17. L.S. Chan, P.W. Wong and Q.F. Chen, “Abundances of radioelements (K,U,Th) in weathered igneous rocks in Hong Kong”, Journal of Geophysics and Engineering **4** (2007), 285-292.
18. Q.F. Chen and L.S. Chan, “In-situ gamma-ray spectrometric study of weathered volcanic rocks in Hong Kong”, Earth Surface Processes and Landforms **27** (2002), 613-625.
19. B.R.S. Minty, “Fundamentals of airborne gamma-ray spectrometry”, AGSO Journal of Australian Geology & Geophysics **17(2)** (1997), 39-50.
20. J. Wilford and B. Minty, “The use of airborne gamma-ray imagery for mapping soils and understanding landscape processes”, Developments in Soil Science **31** (2007), 207-220.
21. J. Ehlen, “Above the weathering front: contrasting approaches to the study and classification of weathered mantle”, Geomorphology **65** (2005), 7-21.
22. DMR, Geological map of Songkhla Province, 1:250,000 scale, Department of Minerals Resources, Bangkok, 2007.
23. DMR, Landslide hazard map of Songkhla Province, 1:1,000,000 scale, Geohazard Section, Environmental Geology Division, Department of Minerals Resources, Bangkok, 2004.
24. LDD, Erosion map of Songkhla Province, Land Development Department, Bangkok, 2002.

Comparison of Performance between the Digester and the Biogas Reactor to Produce Biogas

S. Pannakham*, R. Sewongsa, N. Kaewkongnog, and P. Jumrusprasert

Physics and General Science Progam, Nakhon Ratchasima Rajabhat University
Nakhon Ratchasima , Thailand. 30000
**Corresponding Author: E-Mail:sukanya_bfc@hotmail.com*

Abstract

The biogas digester and reactor were built to test and compare theirs performance of gas production. The site of experiment locates at Ban Kung Klang, Kok Krong subdistric, Kangkraw District, Chaiyaphum. The 50 kg of pig stool and 50 l of water were put and mixed together into each biogas producer. Both of biogas digester and reactor were controlled to have 30 days of HRT each. Then the data of biogas : pressure, temperature and pH were collected. The results were presented that the average and maximum pressures of biogas digester and reactor were 413.89 N/m^2/543.30 N/m^2 and 842.22 N/m^2 /1030.00 N/m^2 respectively. Whereas, the average and maximum temperatures of biogas digester and reactor were 36.0 ^0C / 37.6 ^0C and 38.9 ^0C / 43.6 ^0C respectively. While, the average and maximum pH of biogas digester and reactor were 6.67 / 7.7 and 6.67 / 7.7 respectively. In summary, the gas production performance of biogas reactor was 50.85% better than the biogas digester. The temperature and pH of both producers were illustrated that they had suitable condition for biogas production.

Keywords: Biogas, biogas digester, biogas reactor, pressure, temperature and pH

Introduction

According to the rapid and continuity growth of economic, the demand of energy use is increasing so many ways such as for a household, business and big industrial companies, it caused a lack of energy and caused a lot of pollution.

The pollution caused by energy consumption and the amount of wastes is increasing. The wastes generated from municipal such solid waste, agriculture and food industry effect on pollutions: soil, water and air which effected to health and mind of human. Waste will change into gas that contributes to global warming. The gas formed by this process mainly consists of carbon dioxide and methane.

Biogas production is a way to save money in the household and another sectors. This study aims to build the anaerobic system biogas digester and reactor. We have set up this study at Ban Kung Klang, Kok Krong subdistric, Kangkraw District, Chaiyaphum. The study compared the performance between pig stool - biogas digester and reactor used to produce biogas.

Materials and Methods

To study the performance of the biogas digester and reactor, it consists of five steps;

Step 1: Study the documents and related researchs.

Step 2: Design the biogas digester and reactor to test the biogas production. Analyze the probability of the biogas produced in order to compare the performance.

1) Design a pig stool digester using PVC bags in a deep clarifier with the cylinder shape which radius (r) of 27.5 centimeters and the length of 150 centimeters.

2) Design the three biogas reactor tanks of 150 liters and 200 liters,

- The first tank for 150 liters of pig stool which will contain the waste and overflow pipe and rubber pipe connecting the tank to the second tank.
- The second tank for 200 liters storage tank for biogas obtained with water contained within the tank.
- The third tank for 150 liters tank which will float down to collect the biogas.

Step 3: Invent the biogas digester and reactor following the design in Step 2.

Step 4: Experimental biogas digester and reactor.

1) Mix pig stool together.

2) Add water into the mix of pig stool in both biogas digester and reactor; the ratio is pig stool weighing 50 kg per 50 liters of water.

3) Mix together thoroughly and close the valve of the reactor digester tightly and leave them for 5 days before the first experimental data collecting. Experimental period from the start to the end is 30 days 3 times repeatly

Step 5: Collect data and analyze results.

1) Compare the biogas pressure in graph from the data collecting in 30 days period.

2) Comparison of the performance of the system pressure of the reactor and digester to produce biogas.

Results and discussion

We have tested the pressure and another parameters of the digester and reactor. The experimental results show the following graphs.

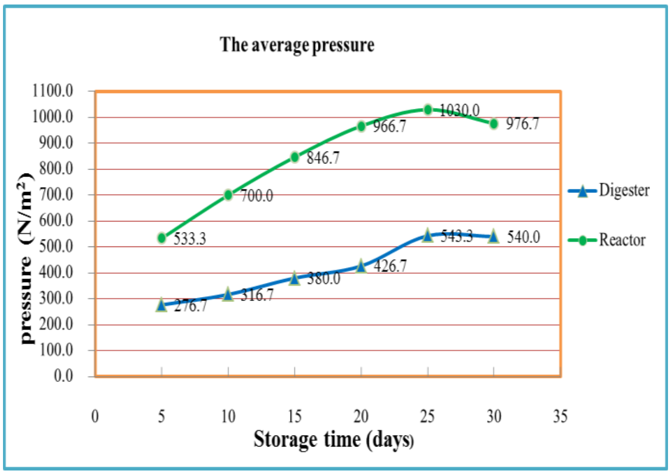

Figure 1. The average pressure (N/m^2) of biogas within the biogas digester and reactor; measurement taken 5 days to 1 time.

Figure1 has shown that the average of pressure in the reactor is higher than biogas digester. The pressure of the reactor has a maximum of 1030.0 N/m^2 during a period of 25 days whereas from the digester gas pressure is highest at 543.3 N/m^2 during a period of 25 days.

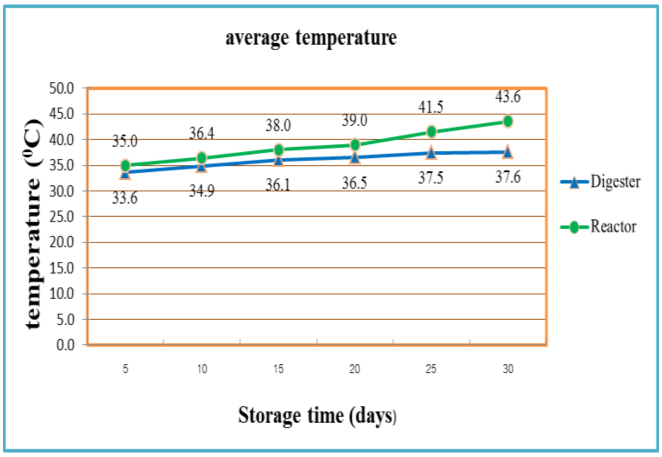

Figure 2. The average temperature (^0C) within the biogas digester and reactor; measurements taken 5 days to 1 time.

Figure2 has presented that the temperature in the biogas digester is lower than the reactor. During the storage period to 5,10,15,20 days the temperature difference had increased gradually. Biogas digester temperatures lowest at 33.6 ^0C and the highest at 37.6 ^0C while in the Mesophilic the reactor temperature lowest at 35.0 ^0C and the highest temperature at 43.6 ^0C. the temperature is not high up to 48-57 ^0C during the Thermophilic.

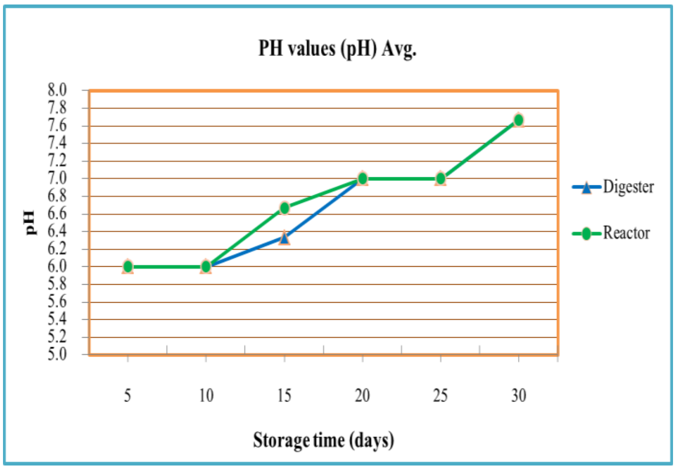

Figure 3. The average pH of the biogas digester and reactor; measurement taken 5 days to 1 time.

Figure 3 has shown that the experimental results show that the acid-base (pH) of the biogas digester and reactor during fermentation and storage period of 15 days. The average pH is slightly different. The retention period of 5,10,20,25,30 days didn't cause any difference to the pH. It close to the pH optimum base which is an important factor in the control of the biogas anaerobic fermentation system. The system performance will work perfectly in pH 6.6 – 7. 6 and will perform at it best when pH at 7.0- 7.2 and will decrease dramatically when pH is lower than 6.2. This is due to hazardous conditions, microbial methane generated as microbial volatile organic acids are used to catch and stop the growth of microorganisms.

Conclusion

1.) The average pressure of the biogas digester was 413.89 N/m^2 and the maximum pressure at 543.30 N/m^2. The average pressure of the reactor was 842.22 N/m^2 with the maximum pressure at1030.00 N/m^2 .We found that the biogas was increasing in the storage period of 15-25 days and then gradually decreasing at the end. The performance of average pressure in the reactor was higher than biogas digester at about 50.85%, so that the reactor can be produced for use in the household with better performance than biogas digester.

2.) The average temperature of the biogas digester was 36.0 ^{0}C the maximum temperature was 37.6 ^{0}C and the reactor's temperature at 38.9^{0}C the maximum temperature was 43.6 ^{0}C. The average temperature of the biogas digester and reactor during Mesophilic is also the optimal.

3.) The average pH of biogas digester was 6.67 with a pH up to 7.7 and the reactor is a pH averaged 6.72 with a pH maximum of 7.7 We found that the pH is in the proper range and were not significantly different.

Acknowledgments

I would like to thank to the supporters and my parent and also my classmates who help assisting me through the project.

References

1. Jintana J. (2552). Biogas production from pineapple peel and Pulp by a 2 steps of fermentation. Bachelor of Science. King Mongkut's University of Technology North Bangkok.
2. Jeerasamai D. (2551). Study of biogas production from volatile organic acid in the two steps tanks. Bachelor of Science. Phranakhon Rajabhat University. R. Saito, G. Dresselhaus, and M. S. Dresselhaus, “Physical Properties of Carbon Nanotubes”, London, Imperial College Press, 1998.
3. Kayun K., (2545). Development of production, biogas from pig stool in a two-stage reactor, The flow of water.Master of Engineer. King Mongkut's University of Technology Thonburi.
4. Mongkol D., (2537). Studies to produce biogas from farvm waste to cattle and pigs by type of fermentation medium and UASB procedure, Master of Science, Kasetsart University.
5. Pimjai N., (2552). Biogas production from pineapple peel and Pulp in a tubular flow reactor. Bachelor of science, King Mongkut's University of Technology North Bangkok.
6. Sastra S., (2551). The type of reactor performance and biogas production from palm oil mill sludge. Master of Science, King Mongkut's University of Technology Thonburi.

Determination the Velocity of Gas and the Transferring Heat in Thermosyphon Heat Pipe by Simulation Method

D. Ngamrungroj[1], S. Duangchan[1], S. Wangnipparnto[2], and K. Honglertkongsakul[3*]

[1]Department of Social and Applied Science, The College of Industrial Technology, King Mongkut's University of Technology North Bangkok, Bangkok, 10800, Thailand
[2]Electrical Engineering Department, Pathumwan Institute of Technology, Bangkok, 10330, Thailand
[3]Department of Physics, Faculty of Science, Burapha University, Chonburi, 20131, Thailand
**Corresponding author. E-mail: kanchaya_h@hotmail.com*

Abstract

The velocity of gas and the transferring heat in the thermosyphon heat pipe can be calculated by using simulation method. In the simulation method, all thermosyphon heat pipes were made from copper tube at different diameters and lengths in the range of 0.02-0.10 m and 0.50-1.00 m, respectively. In this work, water was selected as the working fluid, which was contained 40% by volume of tube at pressure of 50 mbar. The simulation results showed that the velocity of gas at the end of pipe decreased with increasing of diameter size of thermosyphon heat pipe, corresponding to decreasing of heat transfer. The length of heat pipe had little effect on the velocity of gas and the transferring heat in Thermosyphon heat pipe. All of these results can be used to be the preliminary result for finding the most efficient heat pipe.

***Keywords*:** Thermosyphon, Heat Pipe and velocity

Introduction

Heat pipe has been used in several applications due to their property, which can exchange of heat between two regions. These two regions are not necessary obtained more different temperature. Heat pipe is commonly used in a wide range of applications such as air-conditioning, refrigeration, power plant as well as personal computer [1-3].

There are several types of heat pipe, such as U-shaped heat pipe, standard heat pipe, rotary heat pipe, loop heat pipe, electrohydrodynamic heat pipe, osmotic heat pipe and thermosyphon heat pipe. Each of types of heat pipe will be used in difference works.

For thermosyphon heat pipe is the popular one heat pipe that has been used in several application because it is easy to construct and to use. It is only the tube, which contains the working fluid under less than 500 mbar pressure. Moreover, this pipe is simple heat pipe for study and use to experiment for find characteristic of heat pipe.

Thermosyphon heat pipe can separate to be three sections: evaporator section, adiabatic section and condenser section, as is shown in figure 1. Generally, the basic idea of heat pipe is based on an evaporation process and the condensation process. At the evaporation section, the working fluid is evaporated to be vapor by addition of heat at this section. This vapor is transferred to condenser section by passing the adiabatic section without exchanging of heat. When the vapor arrived to condenser section, it will be condensed to be fluid and this fluid will flow down to evaporation section again. This process will occur to be cycle.

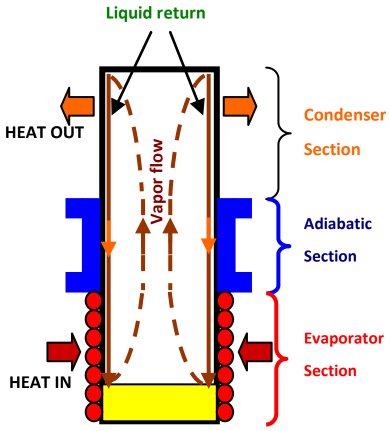

Figure 1. Configuration of Thermosyphon Heat pipe.

In recently years, many researchers attempt to improve the performance of the heat transfer by using the heat transfer enhancement techniques such as addition of external power, employ special surface geometries. While there is a little research explain to the simulation method, which can gain to the heat transfer result [4, 5]. Therefore; if we can obtain the performance of the heat transfer in heat pipe from simulation method, it helps to reduce the cost of construction the heat pipe. In this work, we have an objective to study the velocity of gas in heat pipe from using simulation method. This velocity of gas will be studied and compared with heat transfer results.

Materials and Methods

Thermosyphon Heat Pipe

The copper-thermosyphon heat pipe with 0.02 m diameter and 0.30 m length was constructed. The water was selected to be the working fluid, which was contained 40% by volume of tube at pressure of 50 mbar. Adiabatic section was the position on the heat pipe from 0.12 m to 0.22 m. The temperature of heat source was controlled at 60^{o}C at position 0.03 m on the heat pipe in evaporator section. The temperature on the heat pipe surface was measured by 10 thermocouples, which were placed every 0.03 m from heat source on the heat pipe surface.

Simulation Method

The velocity of gas in the thermosyphon heat pipe can be calculated by using the numerical of the steady Navier-stokes Equation [6-8]. The Steady Navier-Stokes equations are express as:

$$
\begin{aligned}
&-\nu\Delta u + (u\cdot\nabla)u + \nabla P = f \ in\ \Omega \\
&\nabla\cdot u = 0 \ in\ \Omega \\
&u = 0 \ on\ \Gamma_{\omega}, u = g_{in} \ on\ \Gamma_{in}, \\
&\left(\nu\frac{\partial u}{\partial\hat{n}} - p\hat{n}\right) = 0 \ on\ \Gamma_{out} \qquad (1)
\end{aligned}
$$

where Ω is a domain occupied by fluid of constant density, u is the fluid velocity, p is the pressure, f is a force field, ν is a kinematic viscosity and n the normal unit vector to the domain boundary.

The density of gas in heat pipe can be calculated by equation:

$$PV = nRT \qquad (2)$$

When ρ is the density of gas, R is the gas constant (=8.314 J/mol K), T is the temperature (we used 298 K in this case) and M is the Molecular weight (we used the molecular weight of Nitrogen gas)

Results and Discussion

The temperature on the heat pipe surface is shown in figure 1. The heat transfer on the heat pipe from an experiment will be compared with the velocity of gas in the heat pipe from using the numerical method of the Navier-stokes Equation, as is shown in figure 2.

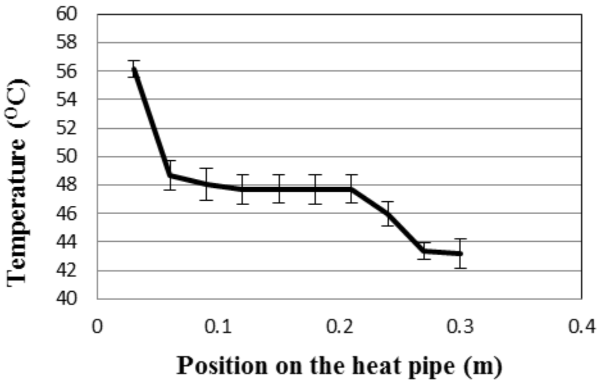

Figure 1 : The temperature on the surface of heat pipe form experimental.

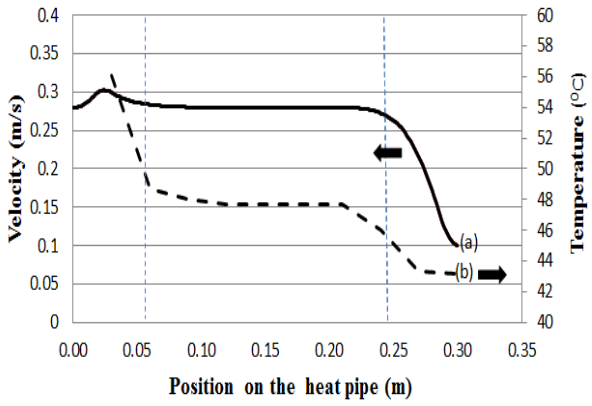

Figure 2 : The position on the heat pipe versus (a) the velocity of gas in the heat pipe from the simulation method (b) the temperature on the surface of heat pipe from the experimental.

In figure 1 showed that the temperature decreased with increasing position on the heat pipe, and temperature on the heat pipe surface in adiabatic section quite to be constant. In figure 2 showed that temperature on the heat pipe corresponds with velocity of gas in the heat pipe by being the initial velocity equal 0.28 m/s. This results can be used to predict the heat transfer on others heat pipe.

Figure 3 and Figure 4 show the position on the heat pipe versus the velocity of gas with different diameter sizes of thermosyphon heat pipe at 0.50 m and 0.80 m length of heat pipe respectively. It was found that the heat pipe with 0.02 m diameter showed highest velocity of gas at the end of pipe and heat pipe with 0.06 m diameter had higher velocity of gas at the end of pipe than heat pipe with 0.10 m diameter.

This means that the heat pipe with 0.02 m diameter showed the highest heat transfer, and heat pipe with 0.06 m diameter had more heat transfer than heat pipe with 0.10 m diameter. This is because at larger diameter of heat pipe the molecules of gas will loss energy by collisions with wall of heat pipe, leading to the lower heat transfer.

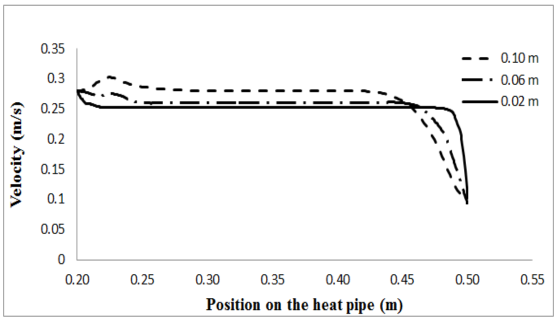

Figure 3 : The position on the heat pipe versus the velocity of gas with 0.50 m length of heat pipe at different diameter sizes of heat pipe such as 0.02, 0.06 and 0.10 m.

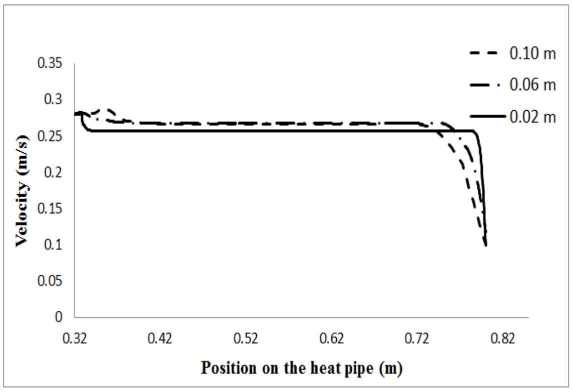

Figure 4 : The position on the heat pipe versus the velocity of gas with 0.80 m length of heat pipe at different diameter sizes of heat pipe such as 0.02, 0.06 and 0.10 m.

Figure 5 and Figure 6 show the distance from working fluid level versus the velocity of gas with different lengths of thermosyphon heat pipe at 0.06 m and 0.10 m diameter of heat pipe respectively. It was found that at constant diameter of heat pipe, the velocity of gas had almost constant with increasing the length of heat pipe. This means that the length of heat pipe had a little effect on heat transfer. This is because the molecules of gas have not lost energy in adiabatic section, leading to the almost constant heat transfer.

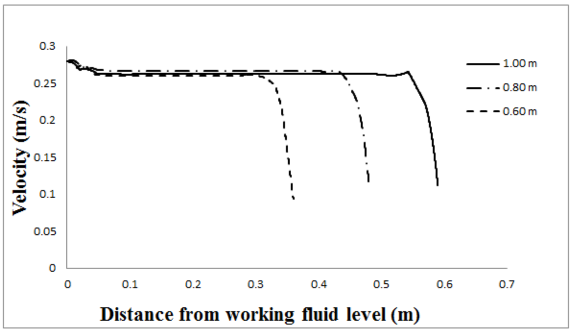

Figure 5 : The position on the heat pipe versus the velocity of gas with 0.06 m diameter of heat pipe at different lengths of heat pipe such as 0.60, 0.80 and 1.00 m.

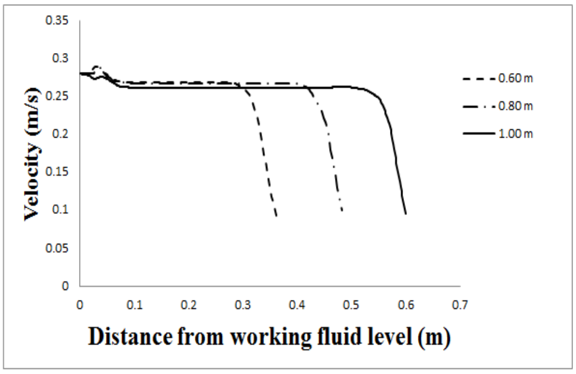

Figure 6 : The position on the heat pipe versus the velocity of gas with 0.10 m diameter of heat pipe at different lengths of heat pipe such as 0.60, 0.80 and 1.00 m.

Conclusions

The simulation results showed that the velocity of gas at the end of pipe decreased with increasing of diameter size of thermosyphon heat pipe, corresponding to decreasing of heat transfer. The length of heat pipe had little effect on the velocity of gas and the transferring heat in Thermosyphon heat pipe. All of these results can be used to be the preliminary result for finding the most efficient heat pipe.

References

1. R. E. Critoph, “The use of thermosyphon heat pipes to improve the performance of a carbon-ammonia adsorption refrigerator”, International Journal of Environmentally Conscious Design & Manufacturing, **9** (2000), 3.
2. M. Lotfi, R. Ghasemzadeh and A. Kargar, “Reduction of CO_2 Productionin Industry by Using Thermosyphon Heat Exchangers”, Ecology and Environmental Sciences (2011), 452.

3. M. Karthikeyan, S. Vaidyanathan and B. sivaraman, “Thermal Performance of a Two Phase Closed Thermosyphon Using Aqueous Solution”, International Journal of Engineering Science and Technology **2(5)** (2010), 913.
4. C. Harley, A. Faghri, “Complete transient two-dimensional analysis of two-phase closed thermosyphons including the falling condensate film”, Transactions of the ASME **116** (1994), 418.
5. J. G. Reed, C. L. Tien, “Modeling of the two-phase closed thermosyphon”, Transactions of the ASME **109** (1987), 722.
6. G. P. Galdi., “An Introduction to the Mathematical Theory of the Navier-Stokes Equations”, Volume II: Nonlinear Steady Problem. Springer-Verlag, New York, 1994.
7. C. Canuto, M.Y. Hussaini, A. Quarteroni, T.A. Zang. Spectral Methods:Evolution to Complex Geometries and Applications to Fluid Dynamics.Springer, Heildeberg, 2007.
8. V. Girault, P.A. Raviart. Finite Element Methods for Navier-Stokes Equa-tions. Springer-Verlag, Berlin, 1986.

Monitoring of Volatile Organic Compound Diffusion in One Dimension with Electronic Nose Array

A. Seeda[1*], K. rachu[1], and S. Pratontep[1,2]

[1]College of Nanotechnology, KMITL, Chalongkrung Rd. Ladkrabang, Bangkok Thailand 10520
[2]Thailand Center of Excellence in Physics, CHE, 328 Si Ayutthaya Rd., Bangkok
10400, Thailand
**Corresponding Author. E-mail: ryblack9@gmail.com*

Abstract

Today rapid technological and industrial advances face environmental challenges, particularly in petrochemical industries, in which leakages of volatile organic compounds (VOC) are becoming a major issue. Here we demonstrate the use of an array of artificial or electronic noses in monitoring one-dimensional diffusion of VOC, namely acetone, toluene and their mixture. Three electronic noses comprising the same set of commercial gas sensors were placed in a 5 meter long tunnel (40 cm x 45 cm cross section) in order to measure diffusion of the VOC with nearly one-dimensional diffusion conditions. The electronic nose system was able to distinguish the faster diffusion rate (in the order of 1 m/min) of acetone than that of toluene. In the VOC mixture some temporal separation of acetone and toluene has been identified by the electronic nose array, which failed in the case of a single type of gas sensors. Temporal changes in the characteristics of the VOC mixture are discussed.

***Keywords*:** volatile organic compounds, diffusion, Electronic nose

Introduction

The current technological and industrial development have been expanding at an unprecedented rate over the past decades. Pollutions in both urban and rural areas are becoming a limiting factor for further development. In particular, air pollution is one of the most demanding problems to tackle. A current method to detect chemical contamination in air is very high cost, time-consuming and limited to only a fraction of chemical species in real atmosphere [1].

An electronics nose (E-nose) is a device that comprises many different types of chemical sensors and is able to classify various odor types by pattern recognition algorithms, such as the Principal Component Analysis (PCA) [2,3]. In general, E-nose is applied to identify volatile compounds from solid or liquid samples, such as food and beverages [4,5]. The use of E-nose in air quality monitoring is limited [6]. The type of gas sensors employed for E-nose is usually Metal Oxide Semiconductor (MOS) gas sensors, which are mostly only partially specific to certain chemical groups. Despite their low cost, MOS gas sensors are not favored for real environmental monitoring with stringent standards. However, the information on air quality required by industries and communities is often simpler, such as to the source odor and the direction of odor diffusion.

Here we explore a use of an array of electronic noses in monitoring a one-dimension diffusion of a mixture of volatile organic compounds (VOC). Two common VOCs have been selected, namely acetone and toluene, because of their widespread use in many industries. The VOC diffusion has been monitored in a five-meter long tunnel. The response patterns of the e-nose are classified by PCA. The type of VOCs as identified by PCA as a function of time has been studied. The accuracy of such method will be discussed.

Materials and Methods

The in-house Electronic nose systems comprised commercial metal oxide gas sensors (TGS825, TGS830, TGS2600, TGS2610, TGS2602) and a temperature-humidity sensor (SHT15). The sensor housing was made of stainless steel to minimize odor absorption. The data collection was obtained via a microcontroller and a data acquisition unit, which stores the data on an SD memory The air sample intake was initiated by an inlet fan for 3 seconds and the sensor voltages were recorded for 20 seconds. The ambient temperature and humidity were also measured throughout.

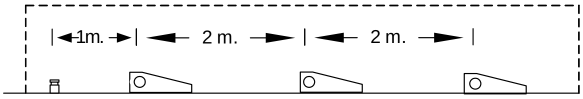

Figure 1. VOC diffusion tunnel.

In the diffusion experiment, three electronic noses with the same set of sensors were positioned along the 5-meter tunnel as shown in Fig. 1, at the distance of 1.0, 3.0 and 5.0 m from the vapour source. The time references for all E-noses were set by the GPS signal. Vapour diffusion measurements were obtained separately on three samples: acetone (C_3H_6O), toluene (C_7H_8) and a 50%w/w mixture of acetone and toluene. The samples were stored in air-tight bottles and exposed for 30 seconds to start the experiment. The weight loss of the samples were recorded. The measurements were continued for 30 min. The data on the SD card were then taken for analysis by the Labview-based program for PCA pattern classification.

Results and Discussion

The different gas sensors will respond variably to VOCs. The TGS825 gas sensor, with characteristic responses to many VOCs. Figure 2 displays thes respond signals of the E-nose at the 1m position acetone, toluene and a 50%w/w mixture of acetone and toluene. The results show that the vapours reach the first E-nose within the first two minutes. Their arrivals do not seem to differ significantly in time. The total diffusion spread lasted just over ten minutes. Their main differences can be seen in the response level. The sensor voltages for acetone are higher than those of toluene. This may be explained by the high vapour pressure of acetone (2.40 kPa) than toluene (2.9 kPa) [7]. Surprisingly for the mixed solvents, the response level seems higher than both individuals The weight loss of the samples after the experiment were recorded as 37.2 mg for acetone, 10.8 mg for toluene, and 25.4 mg for the mixture. The ambient temperature and the relative humidity were 31 ^{o}C and 64%, respectively. The smaller weight loss for the mixed solution than that of acetone seems to contradict the highest signals of the mixed solvents. The only explanation is that the TGS825 may be more sensitive to toluene than acetone. This is supported by the signal voltage levels of toluene at half that of acetone, whereas the weight loss of toluene is a third and the toluene molecular weight nearly twice that of acetone. This should be equivalent to a molar concentration ratio between acetone and toluene of 6:1.

Figure 3 illustrates the TGS825 response of the three different test vapours on the three E-noses. For all the vapours, the profiles of the temporal response of the sensors seem to be characteristics of the diffusion transport. The spread of the patterns increases as a function of the distance from the source. The diffusion rates of the three vapour types are in the order of minutes per metre. Interestingly, the rates do not differ greatly. Acetone may diffuse slightly faster than toluene. According to Graham's law [8], the rate of diffusion R should be dependent on the molecular mass M as

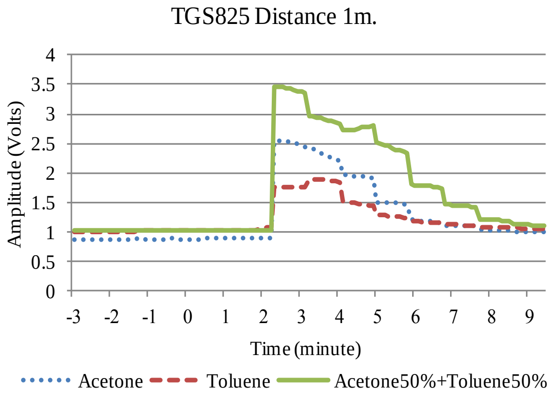

Figure 2. TGS825 gas sensor responses of E-nose at the 1m position to acetone, toluene and a 50%w/w mixture of acetone and toluene**.**

$$R \propto \frac{1}{\sqrt{M}}. \qquad (1)$$

However, the law is only applied for gas diffusion in void. The vapour diffusion in this case occurs in ambient. The proper diffusion relations should concerns a mixture of two gases, namely air and solvent vapour. The Chapman-Enskog theory [9] suggests that for a mixture with low concentration of one specie (<10%) the diffusion constant D should be dependent on molecular mass M_1 and M_2 of Gas 1and Gas 2, respectively, as

$$D \propto \sqrt{\frac{1}{M_1} + \frac{1}{M_2}}. \qquad (2)$$

The diffusion constant D determine the diffusion flux J according to Fick's laws of diffusion [9],

$$J = -D\frac{\partial n}{\partial x}$$

where $\frac{\partial n}{\partial x}$ is the concentration gradient.

Since the molecular mass of air i.e. nitrogen is much less than those of acetone and toluene. The diffusion constant of acetone in

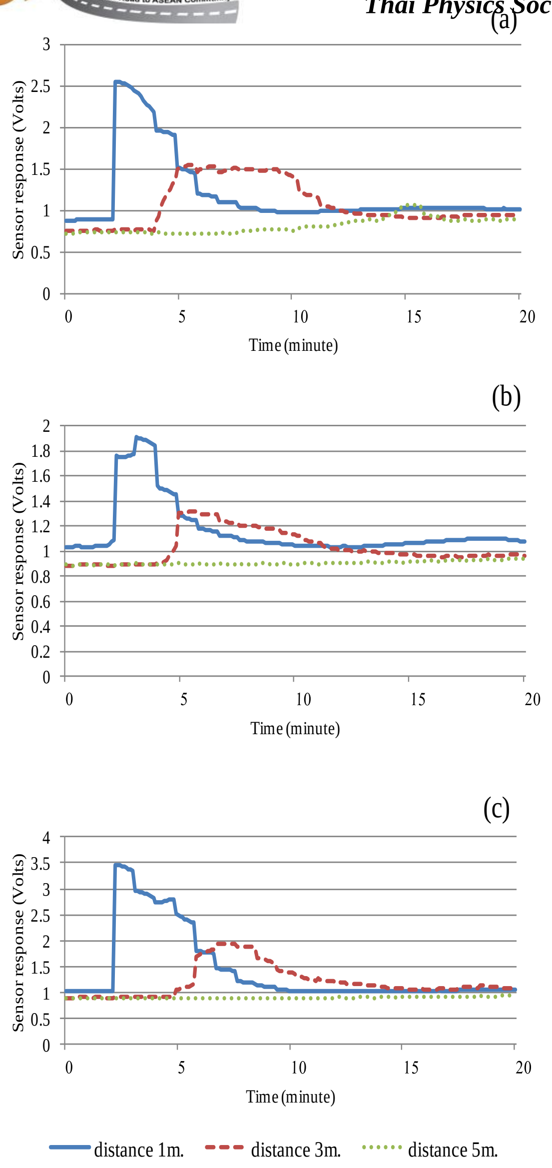

Figure 3. TGS825 responses from the E-noses with the distance from the vapour source of 1.0 m, 3.0 m and 5.0 m, for (a) acetone, (b) toluene, and (c) a 50% w/w mixture of acetone and toluene..

air should not differ much from that of toluene. This should explain why the evolution of the profiles in Fig. 3 does not show significant differences for the three vapour types.

The use of a single gas sensor in analyzing mixed vapours may not be sufficient, as indicated by the results. For a further analysis of the vapour diffusion, the PCA technique has been employed in combining responses from the five gas sensors in classifying the type of vapour. Figure 4 shows a PCA score plot of the vapour classification of a reference ambient air, acetone and toluene. The obtained PCA conversion matrix was then applied to the vapour mixture data at different times to calculate their position on this PCA map.

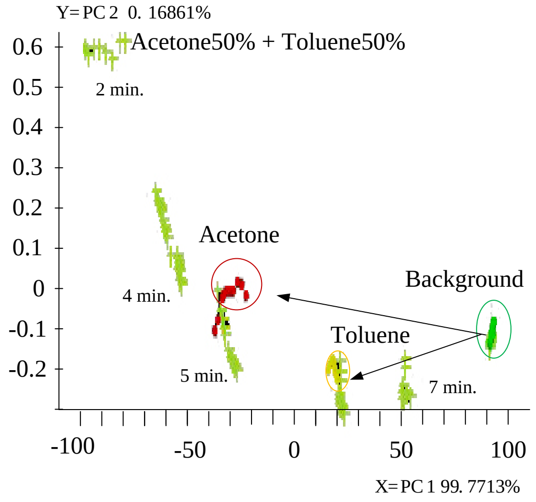

Figure 4 PCA score plot of the vapour classification of a reference ambient air, acetone and toluene from the E-nose at the 1m position. The location of the mixed vapour data at different times were calculated from the obtained PCA conversion matrix.

The first Principal Component (PC1) contains most of the variance (99.8%) from the input data set, since the PCA method ranks the PC in terms of their importance. This PC1 should correspond mainly to the concentration level of the vapours, starting from zero around the background point and going to toluene and higher concentration of acetone to the left, respectively. Note that in this case the plot is akin to the polar coordinate, whereby the background acts as a centre. The PC2, which accounts to only 0.17% of the variance, should correspond to the type of vapour i.e. either acetone or toluene. The arrows are indicative of the vector directions that should relate to the vapour type. As the mixed vapour started to diffuse pass the 1m E-nose, the results indicate that pattern changes from the acetone side to more of the toluene side within about 7 min. However, it is worth noting that the initial pattern of the mixture is rather isolated from both acetone and toluene. Its vector direction also differs significantly. This is normally indicative of a new type rather than a mixture between the two solvents. Thus analyses of the mixture of vapours using an array of electronic noses are able to provide more detailed information than the use of a single gas sensor. However, an accurate fractional quantification of the vapour species requires further investigation.

Conclusions

The use of an array of electronic noses has been demonstrated to monitor diffusion of volatile organic compounds and their mixture in one dimension. Their advantage over monitoring with a single type of gas sensors is clearly illustrated. However, the quantification of the vapour composition remains problematic. Future work will explore a more accurate fractional quantification method and applications to a wider range of chemical vapour. In addition, vapour diffusion at large scale will be a subject of further interest.

Acknowledgments

We acknowledge the support of IRPC public company ltd, UBE industrial ltd. and Environmental Research and Training Centre, the Ministry of Natural Resources and Environment. We thank Advance Embedded Solution company for usage of measuring instrument and electronic circuit assembly.

References

1. Alphus Dan Wilson, "Review of Electronic-nose Technologies and Algorithms to Detect Hazardous Chemicals in the Environment", Procedia Technology 1 (2012) , 453.
2. S.Fuchs,P.Strobel,M.Siadat and M.Lumbreras, "Evaluation of unpleasant odor with a portable electronic nose", Materials Scienceand Engineering C 28 (2008),949.
3. HuichunYua,JunWanga,HongXiao and MiaoLiu, "Quality grade identification of green tea using the eigenvalues ofPCA based on the E-nose signals", Sensorsand Actuators B140 (2009),378
4. N.ElBarbri, E.Llobet, N.ElBariand, B.Bouchikhi, X.Correig, "Application of aportable electronic nose system to assess the freshness of Moroccansardines", Materials Scienceand Engineering C28 (2008), 666.
5. Zhi-biao Shi, Tao Yu, Qun Zhao, Yang Li and Yu-bin Lan, "Comparison of Algorithms for an Electronic Nose in Identifying Liquors", Journal of Bionic Engineering 5 (2008) ,253.
6. A.-C.Romain, D.Godefroid, and J.Nicolas, "Monitoring the exhaust air of acompost pile with an e-nose and comparison with GC–MS data", Sensors and Actuators B106 (2005),317
7. C. Reichardt, Solvents and Solvent Effects in Organic Chemistry, Wiley-VCH Publishers, 3rd ed., 2003.
8. S.S. Zumdahl. Chemical Principals. Boston: Houghton Mifflin Harcourt Publishing Company, 2008, p.164.
9. E.L. Cussler. Diffusion: Mass Transfer in Fluid Systems, New York: Cambridge University Press, 2nd ed., 1997.

Solar Radiation over Thailand and Some ASEAN Countries: Ground-based Measurement Approach

S. Janjai*, R. Wattan, S. Pattarapanitchai, I. Masiri,
S. Buntoung, W. Promsen, and J. Laksanaboonsong,

Solar Energy Research Laboratory, Department of Physics, Faculty of Science,
Silpakorn University, Nakhon Pathom 73000, Thailand
**Corresponding author. E-mail: serm@su.ac.th*

Abstract

In this work, surface solar radiation over Thailand and some ASEAN countries was investigated. In order to obtain solar radiation data for this investigation, solar radiation monitoring stations were established in Thailand, Laos, Cambodia and Myanmar. Solar radiation data for the period of 2-10 years from these stations were analyzed. The seasonal variation of solar radiation at these stations was investigated. It is found that the incident solar radiation on these countries is strongly influenced by tropical monsoons. In addition, the amount of solar radiation indicates that these countries have relatively high solar energy potential.

Keywords: solar radiation, measurements, ASEAN countries

Introduction

Information of the amount of solar radiation incident on the earth's surface is of importance for solar energy applications [1]. For example, it is required for designing solar energy applications. For example, it is required for designing solar energy conversion systems, such solar systems, solar water heaters and solar crop dryers [2]. In general, the amount of the incident solar radiation varies with time, location and atmospheric opacity. In order to obtain information for such applications, solar radiation monitoring stations are normally established to measure the amount of surface solar radiation on a long-term basis. In many countries, the stations were established in the form of a national network. Due to the importance of solar radiation measurement, Solar Energy Research Laboratory of Silpakorn University established the first solar monitoring station at Silpakorn University in Nakhon Pathom in 1981. In 1994 additional 3 stations were established at Chiang Mai, Ubon Ratchathani and Songkhla. Both global and diffuse radiation is routinely measured at these stations. For Nakhon Pathom station, direct radiation is also monitored. These stations have been operated until now. To respond to more demands of solar radiation data, Department of Alternative Energy and Development (DEDE) under the collaboration project with Silpakorn University established 38 solar monitoring stations during 2002-2006. Global radiation is measured at these stations. In 2007, DEDE together with Silpakorn University set up the equipment for measuring direct radiation at 8 existing stations. Silpakorn University and DEDE under the collaboration projects between Thailand and neighboring countries also established solar monitoring stations in Laos, Cambodia and Myanmar (Figure 1). Global radiation is measured at these stations. In this work, solar radiation data obtained from all stations established in these countries are preliminarily analyzed and the results are reported.

Measurement

Global solar radiation of the stations of Silpakorn University at Chiang Mai, Ubon Ratchathani and Songkhla is measured using Kipp&Zonen pyranometers (model CM21) whereas pyranometer produced by the same company (model CM11) is employed for monitoring global radiation at Nakhon Pathom. Diffuse radiation at these four stations is measured by Kipp&Zonen pyranometer (model CM11) equipped with shade rings (model CM121) fabricated by the same company. The direct radiation at Nakhon Pathom is measured employing a pyrheliometer produced by Eppley (model NIP).

For all stations of DEDE, global radiation is measured using Kipp&Zonen pyranometers (model CM11). Direct radiation at the stations of DEDE is monitored employing pyrheliometers fabricated by Kipp&Zonen (model CH1) and equipped with automatic sun trackers of the same company (model 2AP).

For the stations in Laos, Cambodia and Myanmar, global radiation is measured using pyranometers produced by Kipp&Zonen (model CMP11)

Voltages signals from pyranometers and Cambodia are recorded using Yokogawa (model DC100) data loggers whereas Campbell data loggers (model CR1000) are used to record the voltage signals from the solar radiation measuring devices for the measurement in Myanmar. For all stations in these four countries the voltage signals are captured every second and averaged over a time period of 10 minutes. The averaged data are recorded in the memory of the data loggers and downloaded at the end of every month. They are then sent to Solar Energy Research Laboratory, Silpakorn University. At the Laboratory, the voltage signals are converted pyrheliometers of the stations in Thailand, Laos and into solar irradiance using the calibration factors of these radiation measuring devices. The 10-minute average of solar irradiance is then integrated over a period of one hour and one day to obtain hourly and daily radiation, respectively. All radiation measuring devices are calibrated once a year by employing travelling standard measuring devices whose responsivities are traceable to the world standard of the World Radiation Center.

Details of the stations and the periods of data used in this study are shown in Table 1.

Table 1: Details of the stations and the periods of data used in this study

No.	Stations	Latitude (Degree)	Longitude (Degree)	Period of data
	Thailand			
	- Global radiation			
	Northern region			
1	Chiang Rai	20.08	99.88	Jan, 2003 – Dec, 2012
2	Mae Hong Son	19.43	97.96	Jan, 2003 – Dec, 2012
3	Doi Intanon (Mae Klang)	18.40	98.67	Jan, 2005 – Dec, 2012
4	Doi Intanon	18.54	98.52	Jan, 2005 – Dec, 2012
5	Doi Intanon (Radar)	18.59	98.48	Jan, 2006 – Dec, 2012
6	Nan	18.72	100.75	Jan, 2003 – Dec, 2012
7	Chiang Mai (DEDE*)	18.83	98.88	Jan, 2003 – Dec, 2012
8	Chiang Mai (SU^{+})	18.78	98.98	Jan, 2003 – Dec, 2012
9	Mae Sa Riang	18.17	97.93	Jan, 2005 – Dec, 2012
10	Phrae	18.06	100.06	Jan, 2005 – Dec, 2012
11	Tak	16.80	98.90	Jan, 2003 – Dec, 2012
	Northeastern region			
12	Loei	17.40	101.00	Jan, 2005 – Dec, 2012
13	Nong Khai	17.87	102.72	Jan, 2003 – Dec, 2012
14	Khon Kaen	16.45	102.78	Jan, 2003 – Dec, 2012
15	Nakhon Panom	16.97	104.73	Jan, 2003 – Dec, 2012
16	Surin	14.88	103.50	Jan, 2003 – Dec, 2012
17	Ubon Ratchathani (DEDE*)	15.28	105.14	Jan, 2003 – Dec, 2012
18	Ubon Ratchathani (SU^{+})	15.25	104.87	Jan, 2003 – Dec, 2012
19	Nakhon Ratchasima	14.97	102.08	Jan, 2003 – Dec, 2012
20	Roi Et	16.07	103.00	Jan, 2005 – Dec, 2012
	Central region			
21	Phitsanulok	16.78	100.27	Jan, 2003 – Dec, 2012
22	Phetchabun	16.43	101.15	Jan, 2003 – Dec, 2012
23	Nakhon Sawan	15.67	100.12	Jan, 2003 – Dec, 2012
24	Lopuuri	14.83	100.62	Jan, 2003 – Dec, 2012
25	Bangkok	13.75	100.52	Jan, 2003 – Dec, 2012
26	Nakhon Pathom (SU^{+})	13.82	100.04	Jan, 2003 – Dec, 2012
27	Kanchanaburi (Muang)	14.02	99.53	Jan, 2005 – Dec, 2012
28	Kanchanaburi (Thong Pha Phum)	14.73	98.63	Jan, 2003 – Dec, 2012
29	Sa Kaeo (Aranyaprathet)	13.70	102.00	Jan, 2005 – Dec, 2012
30	Trat	11.77	102.88	Jan, 2005 – Dec, 2012

31	Prachinburi	13.97	101.70	Jan, 2003 – Dec, 2012
32	Chonburi	13.37	100.97	Jan, 2005 – Dec, 2012
33	Prachuap Khiri Khan	11.83	99.83	Jan, 2003 – Dec, 2012
	Southern region			
34	Chumphon	10.40	99.18	Jan, 2005 – Dec, 2012
35	Ranong	9.98	98.62	Jan, 2003 – Dec, 2012
36	Surat Thani (Samui)	9.47	100.05	Jan, 2003 – Dec, 2012
37	Surat Thani (Punpin)	9.13	99.15	Jan, 2005 – Dec, 2012
38	Phuket	8.13	98.30	Jan, 2003 – Dec, 2012
39	Trang	7.52	99.62	Jan, 2005 – Dec, 2012
40	Songkhla (DEDE*)	6.92	100.43	Jan, 2003 – Dec, 2012
41	Songkhla (SU$^+$)	7.20	100.60	Jan, 2003 – Dec, 2012
42	Narathiwat	6.40	101.82	Jan, 2003 – Dec, 2012
	- Diffuse radiation			
43	Chiang Mai (SU$^+$)	18.78	98.98	Jan, 2003 – Dec, 2012
44	Nakhon Pathom (SU$^+$)	13.82	100.04	Jan, 2003 – Dec, 2012
45	Ubon Ratchathani (SU$^+$)	15.25	104.87	Jan, 2003 – Dec, 2012
46	Songkhla (SU$^+$)	7.20	100.60	Jan, 2003 – Dec, 2012
	- Direct radiation			
47	Chiang Mai (SU$^+$)	18.78	98.98	Jan, 2008- Dec, 2012
48	Nakhon Pathom(SU$^{+)}$	13.82	100.04	May, 2003 – Dec, 2012
49	Ubon Ratchathani (SU$^+$)	15.25	104.87	June, 2008 – Dec, 2012
50	Songkhla (SU$^+$)	7.20	100.60	Jan, 2008 – Dec, 2012
51	Prachuap Khiri Khan	11.83	99.83	Jan,2009 – Dec,2010, Sep, 2011 – Dec, 2012
52	Nakhon Ratchasima	14.97	102.08	Oct, 2007 – Nov, 2007, Jan,2008-Jun,2010, Apr,2011 – Dec, 2012
53	Nakhon Sawan	15.67	100.12	Oct, 2007- Nov,2011, Jun,2012-Dec,2012
54	Lopburi	14.83	100.62	Apr, 2009 – Feb,2011, Apr, 2011 – Nov, 2012
55	Bangkok	13.75	100.52	Nov,2007 – Dec, 2012
	Laos			
56	Vientiane	17.97	102.57	Jun, 2006 – Dec, 2010
57	Luangprabang	19.89	102.16	Jun-2006 – Aug, 2010
58	Samnua	20.42	104.07	May, 2006 – Dec, 2010
59	Thakhek	17.40	104.81	Jun, 2006 – Dec,2010
60	Pakxe	15.13	105.79	Jun, 2006 – Aug,2010
	Cambodia			
61	Kampong Thom	12.68	104.88	Sep, 2007 – Dec, 2009
62	Phnom Penh	11.55	104.83	Sep, 2007 – Dec, 2009
63	Kampot	10.70	104.28	Sep, 2007 – Mar, 2011
64	Sihanou Ville	10.67	103.63	Sep, 2007, Sep, 2010
65	Siem Reap	13.87	103.85	Aug, 2007 – Aug, 2010
	Myanmar			
66	Yangon	16.87	96.002	Aug, 2008 – Jun, 2011
67	Napyidaw	19.60	96.216	Aug, 2008 – Aug, 2011
68	Meiktila	20.880	95.880	Aug, 2008 – Jul, 2011
69	Mandalay	21.980	96.080	Jul, 2008- Aug, 2011
70	Shwebo	22.580	95.72	Feb, 2008 - Jul,2009

*DEDE Station of Department of Alternative Energy Development and Efficiency
$^+$SU Station of Silpakorn University

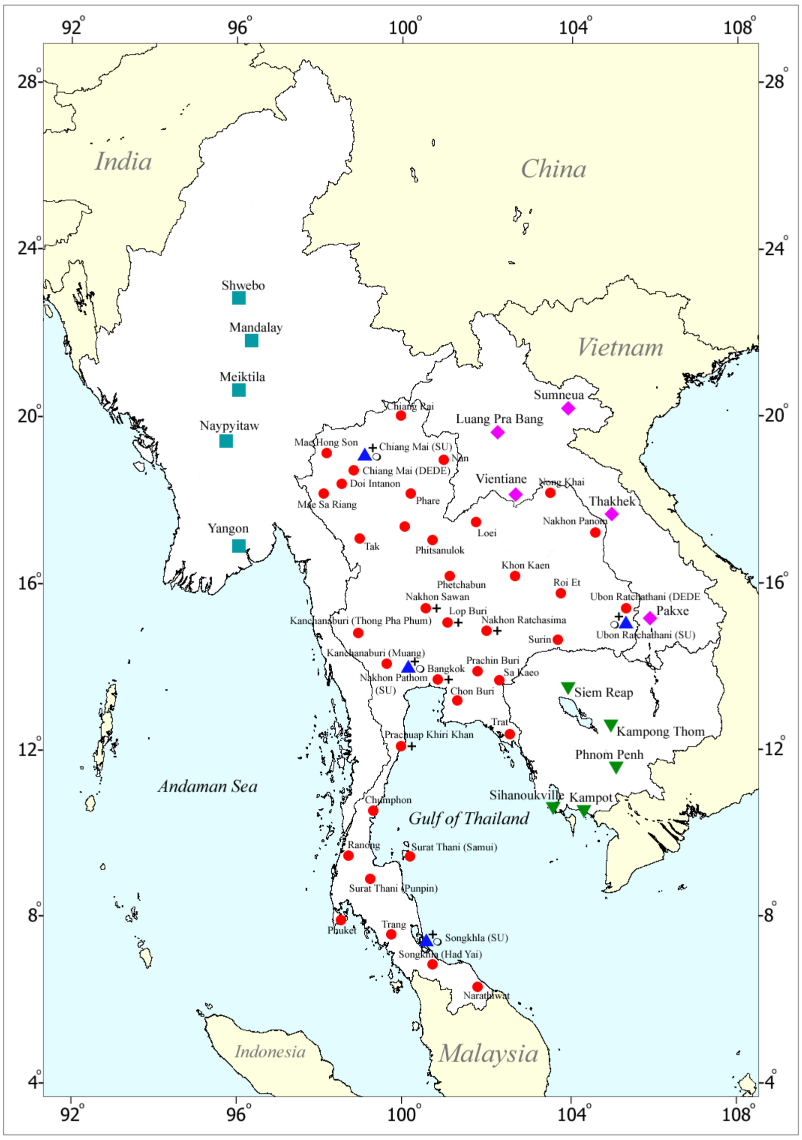

Figure 1 Positions of solar monitoring stations in Thailand (●,▲,+,○), Laos (♦), Cambodia (▼) and Myanmar (■).

● Department of Alternative Energy Development and Efficiency (DEDE) (Global radiation)

▲ Silpakorn University (SU) (global radiation) + direct radiation ○ diffuse radiation

Data analysis

Prior to the analysis of solar radiation data, the data are subjected to a quality control. They are manually checked for instrument or data processing errors. Data which violated physical law are eliminated. These include negative global or diffuse radiation during daytime, diffuse irradiance exceeding global irradiance, and others. A table of correction factors supplied by Kipp&Zonen is also used to correct the effect of the shade ring on the diffuse radiation. After this quality control, long-term daily averaged global, diffuse and direct radiation is calculated. The ratio of diffuse to global radiation is also computed. The seasonal variation of the amount of global, diffuse and direct radiation and the ratio of diffuse to global radiation are investigated and the results are revealed in the next section.

Results and discussion

Radiation in Thailand

- Global radiation

The seasonal variation of global radiation is basic information for utilization of solar energy as it demonstrates the levels of solar radiation received by the earth's surface year round. These levels of radiation are a prerequisite information prior to the installation for solar energy systems which used global radiation as energy source such a PV-power plant. Based on the analysis of solar radiation measured at solar monitoring stations under this investigation, the seasonal variations of global radiation in Thailand, Lao, Cambodia and Myanmar are shown in Figure 2, 6, 7 and 8, respectively.

Thailand can be divided into 4 main regions, namely the north, the northeast, the south and the central region. From Figure 2, it is observed that solar radiation at most stations in the north, the northeast and the central region increases from January to reach the maximum in April and then decreases with some fluctuations to the end of the year. The increase from January to the peak in April is mainly caused by the northward movement of the apparent sun path with the decrease of the incident angle of solar radiation on the ground. Cloudiness is not a dominant factor affecting surface solar radiation. This is because this period corresponds to the dry season with the majority of clear days. The decrease of solar radiation after the peak is mainly due to cloudiness caused by the southwest monsoon whose onset normally occurs in May and it continues blowing until August or October. It brings moisture from Indian Ocean to the country, causing cloudy skies and rainfall in most parts of the country. Normally, October is the transitional period from the southwest monsoon to the northeast monsoon. The northeast monsoon brings cold and dry air from Siberia to Thailand. Although this monsoon causes clear skies in the north, northeast and the central region solar radiation in these regions is still relatively low. This is because the apparent sun path moves southward, causing higher incident angle of solar radiation on the ground, and lowing surface radiation.

From Figure 2 it is also noticed that the seasonal variation of solar radiation at most stations in the south has a distinct pattern, compared to that of the other regions. In the south, solar radiation is relatively high during the period of February to April due to the favorable incident angle of solar radiation caused by the position of apparent sun path in this period. For most stations in the south, solar radiation decrease to the minimum at the end of the year. This is due to the fact that the southwest monsoon brings clouds and rain to the region during May to October like in the north, northeast and the central region. In addition, for the period of November to December, the northeast monsoon which blow across the Gulf of Thailand also brings clouds and rain to the region, resulting in lower radiation, compared to radiation in the other regions.

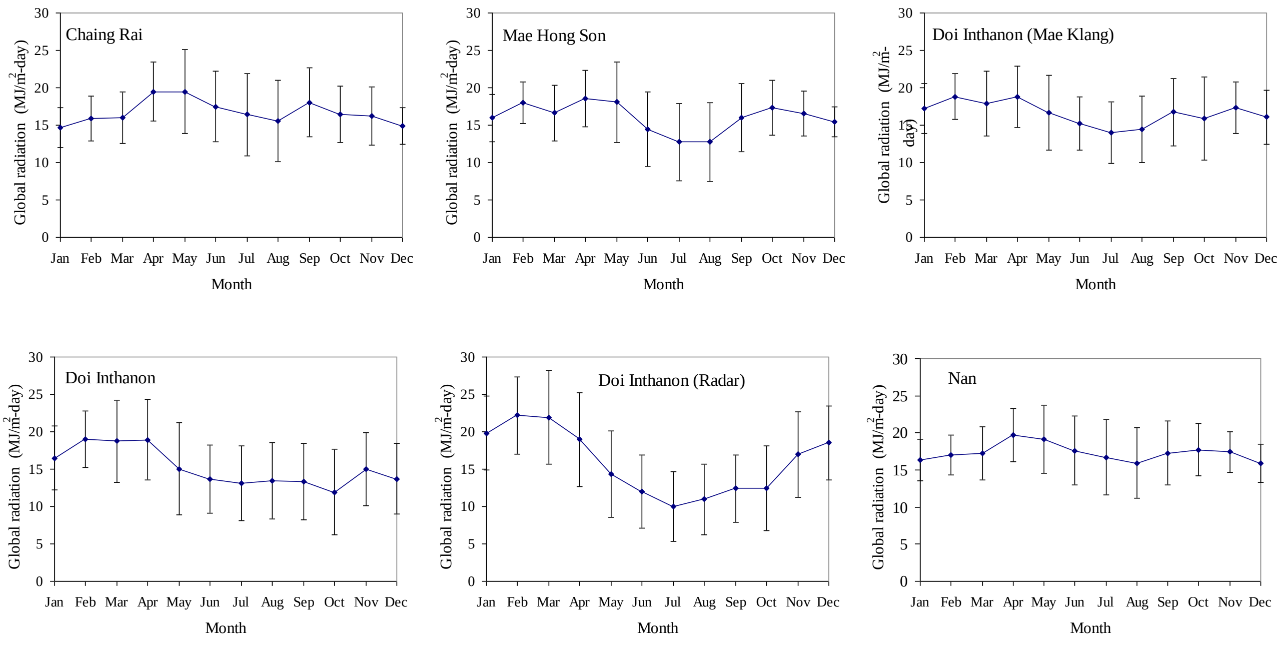

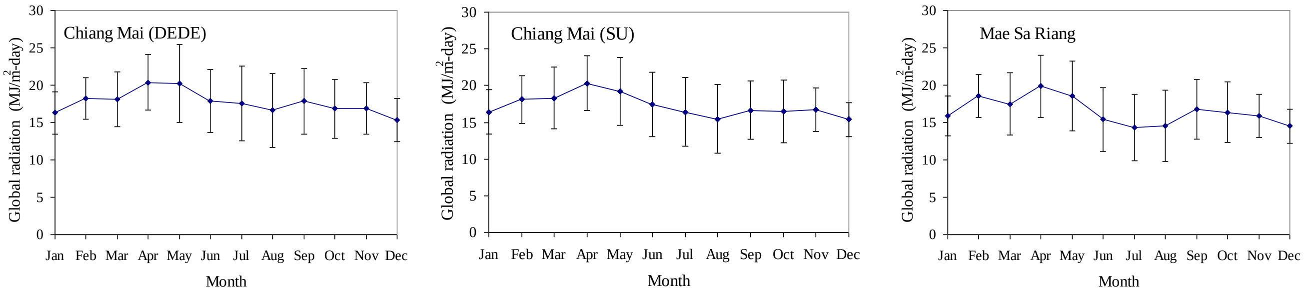

Figure 2. Seasonal variation of global radiation in Thailand

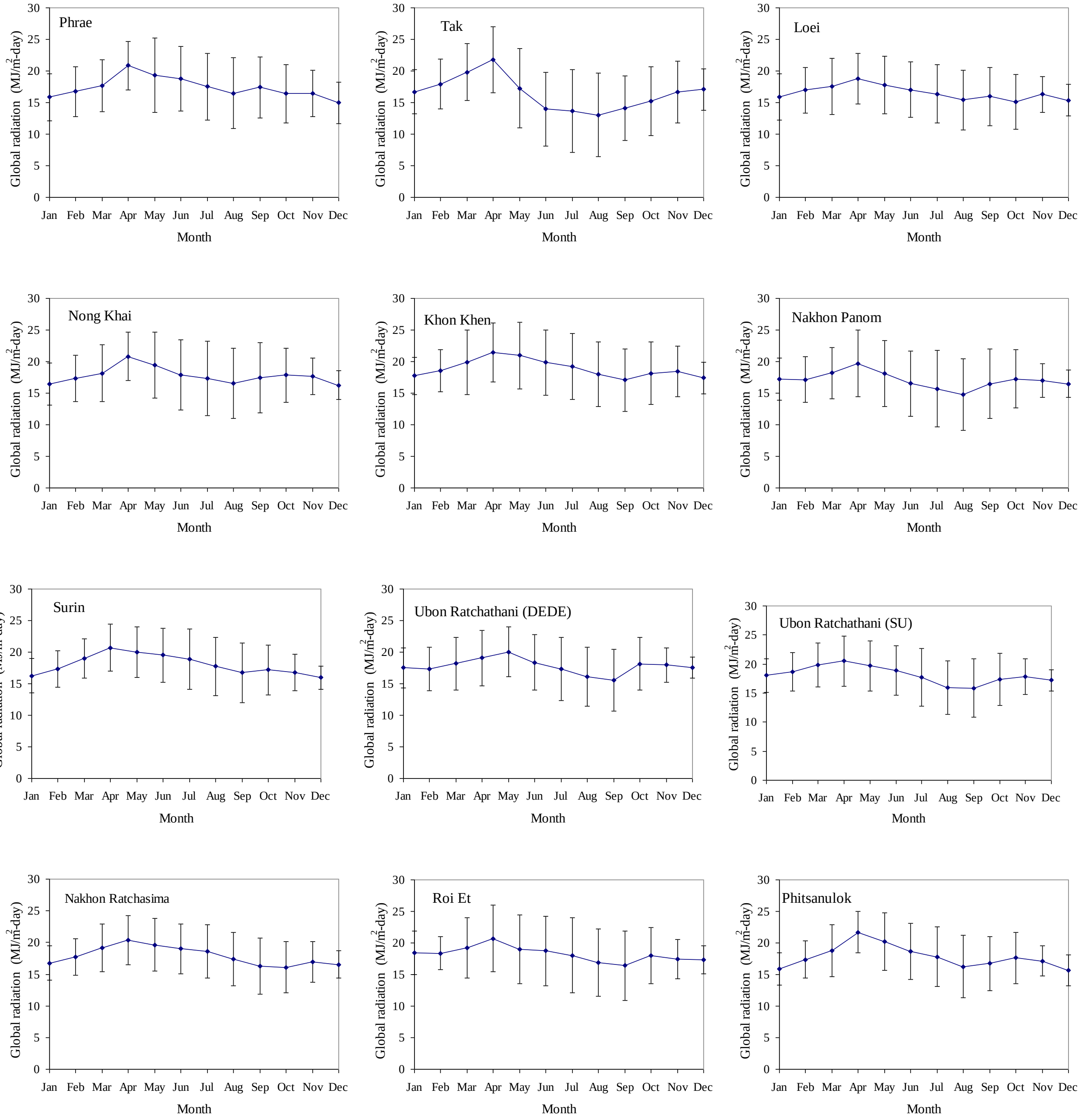

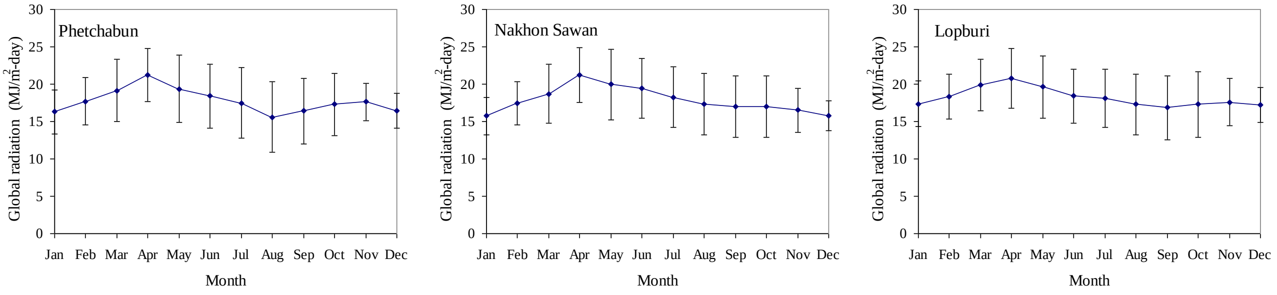

Figure 2. (Cont.)

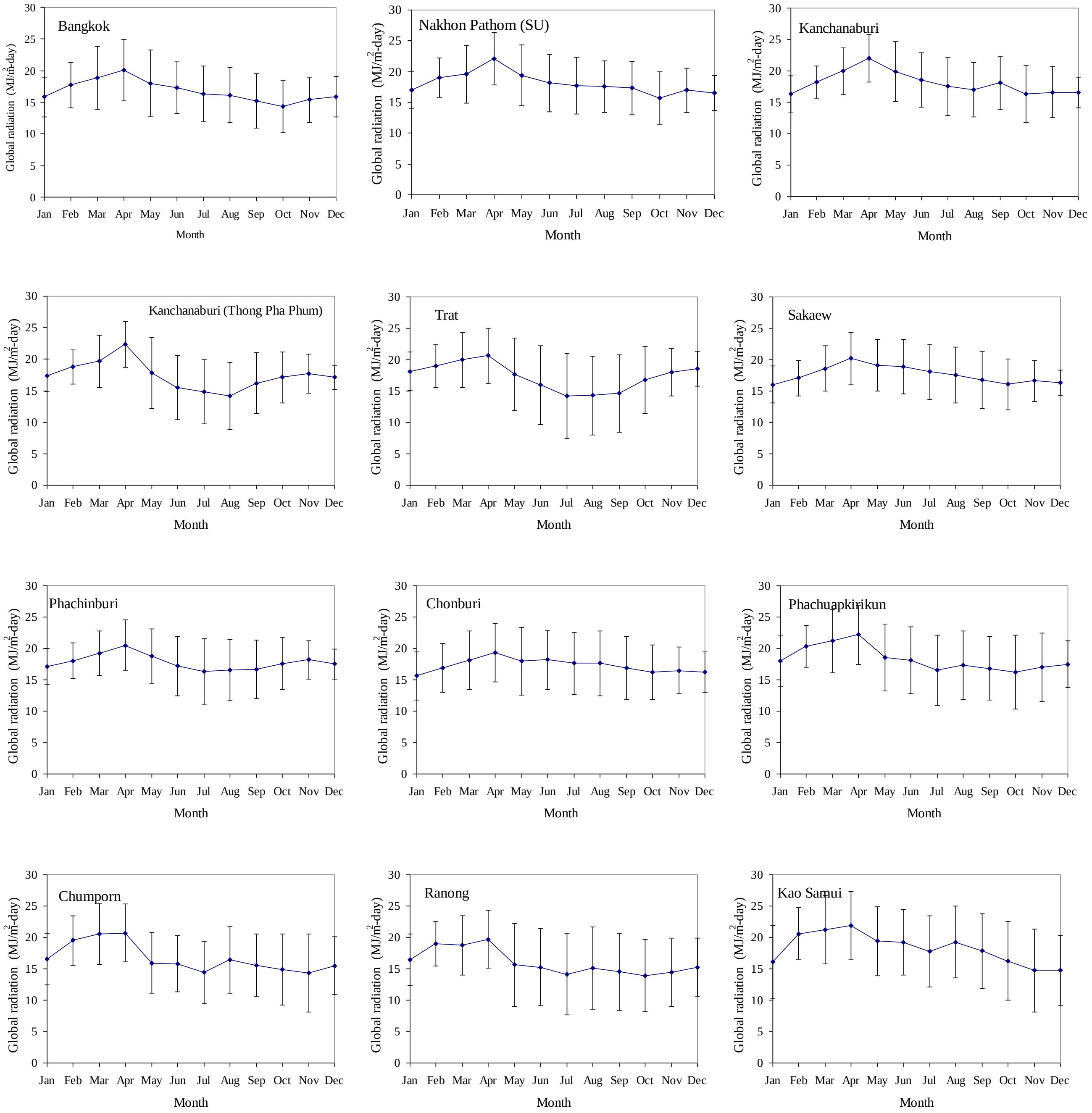

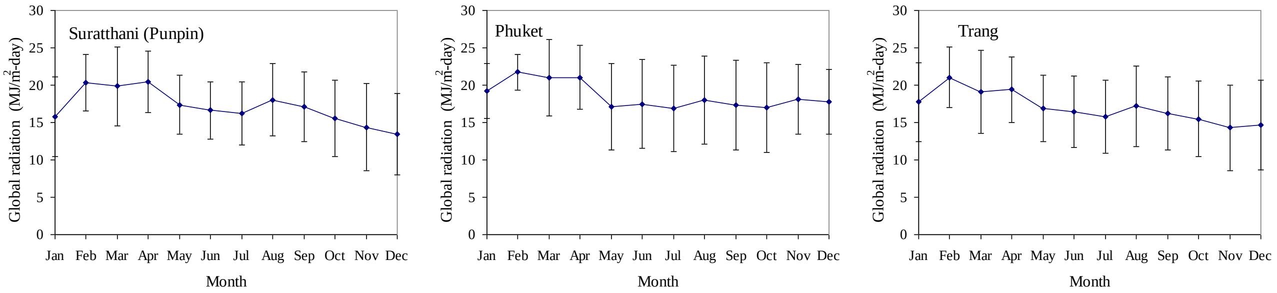

Figure 2. (Cont.)

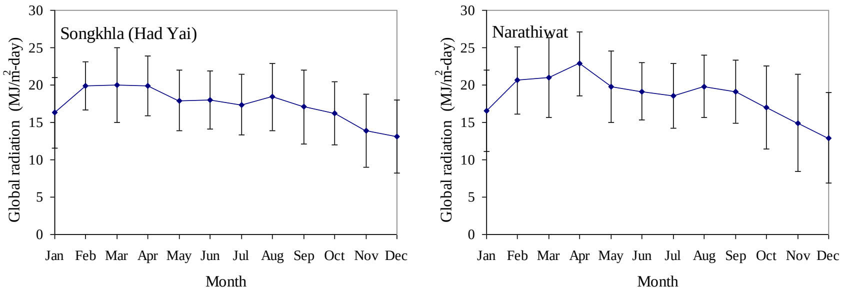

Figure 2. (Cont.)

- Diffuse radiation

Diffuse radiation is generated by the scattering of solar radiation due to aerosols, clouds and multiple reflections between the atmosphere and the ground. The information on diffuse radiation is important for daylighting applications [3]. It is also used to convert global radiation on horizontal surface to global radiation on inclined surface. The number of the stations, where diffuse radiation is routinely measured, is very limited. This is because the measurement of diffuse radiation requires daily adjustment of shade ring or the use of a solar tracker with high equipment cost. In Thailand, there are only four stations belonging to Silpakorn University where diffuse radiation is routinely monitored. These stations are located in Chiang Mai, Ubon Ratchathani, Nakhon Pathom and Songkhla. The seasonal variation of long-term average daily radiation is shown in Figure 3.

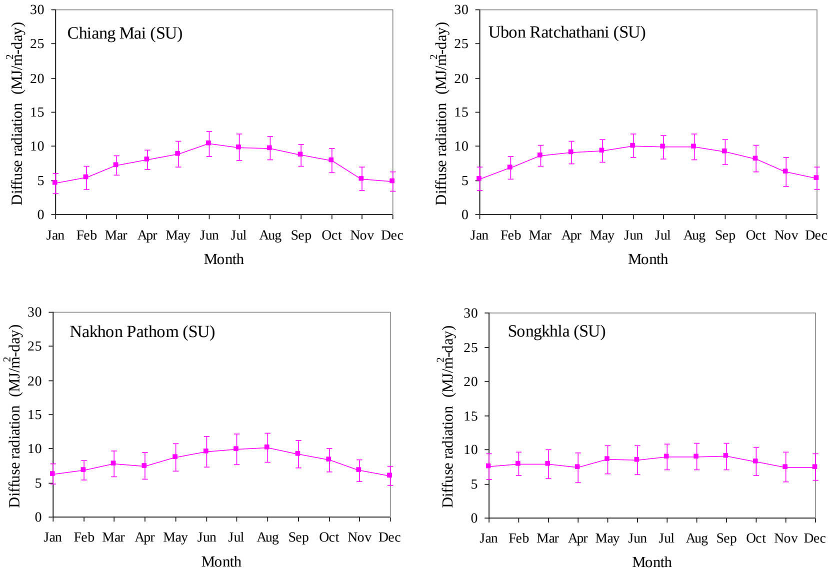

Figure 3. Seasonal variation of diffuse radiation at Chiang Mai, Ubon Ratchathani, Nakhon Pathom and Songkhla.

From Figure 3, it is noticed that the seasonal variation of diffuse radiation at Chiang Mai, Ubon

Ratchathani and Nakhon Pathom has similar pattern. According to this pattern, diffuse radiation increases from January to the peak in June or July and gradually decreases to the end of the year. The period of high diffuse radiation corresponds to the rainy season (May-October). This is because high cloudiness in this period results in high scattering of solar radiation, causing high diffuse radiation. For Songkhla, diffuse radiation is constantly high year round. This is due to the fact that Songkhla is located in the south with the long period of rainy season (May-December) and diffuse radiation is constantly created by clouds in this season. In addition, biomass burning aerosols produced in the dry season (January-April) is also created diffuse radiation in this period of the year.

- Direct radiation

Direct radiation is of importance for concentrating solar energy systems such as solar thermal power plants [4]. This is because these systems use only direct radiation as energy source. The equipment to measure direct radiation is expensive because it requires a sun tracker to point the radiation sensors toward the sun all days. Therefore, direct radiation is not widely measured in a country. In Thailand, there are only 9 stations where direct radiation is routinely monitored. In this work, seasonal variation of direct radiation at 9 stations in Thailand is analyzed and the results are depicted in Figure 4.

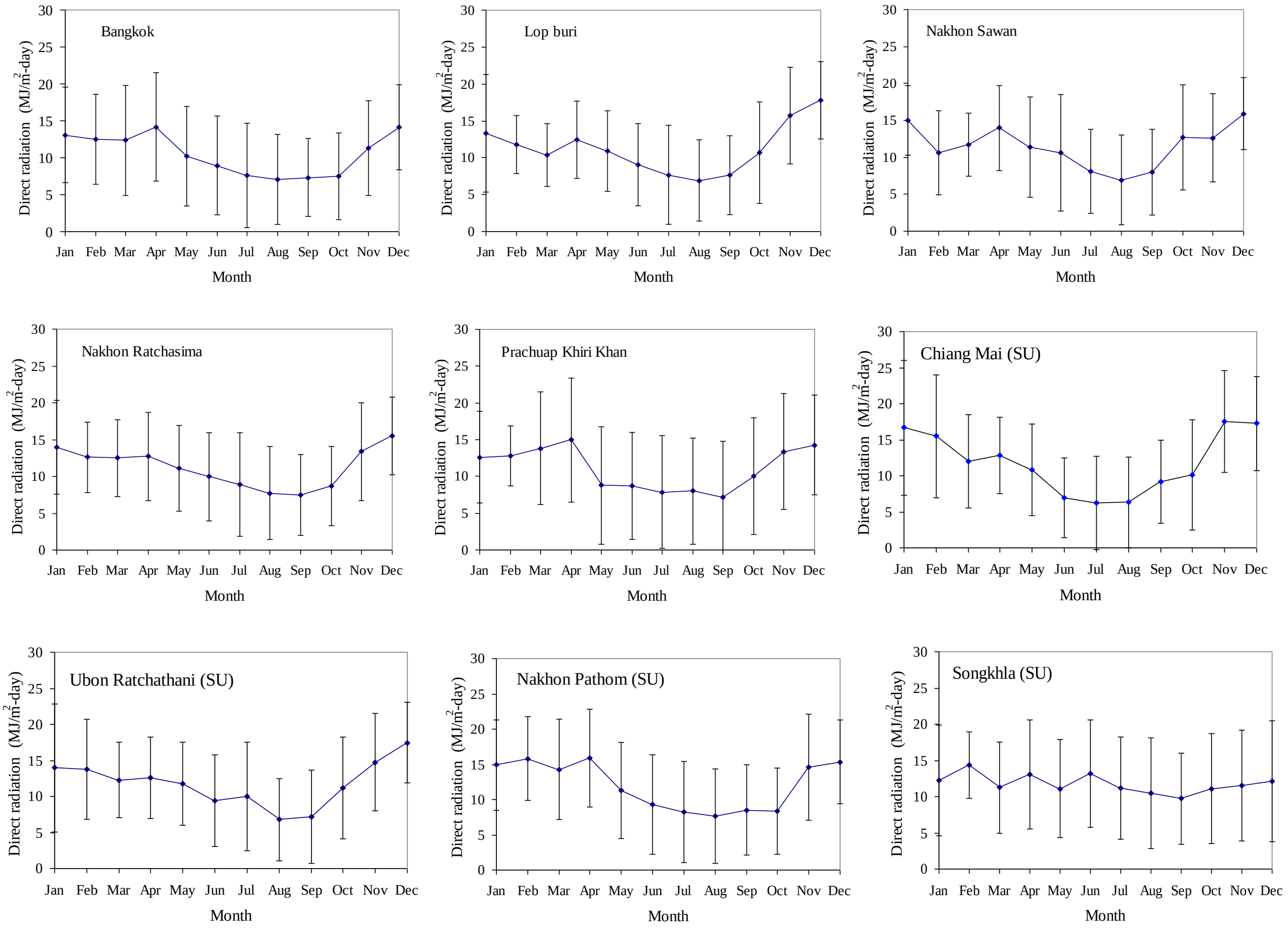
Bangkok
Lop buri
Nakhon Sawan
Nakhon Ratchasima
Prachuap Khiri Khan
Chiang Mai (SU)
Ubon Ratchathani (SU)
Nakhon Pathom (SU)
Songkhla (SU)

Figure 4. Seasonal variation of direct variation in Thailand

Results from Figure 4 show that seasonal variation of direct radiation at Bangkok, Lopburi, Nakhon Sawan, Nakhon Ratchasima, Pracuap Khiri Khan, Chiang Mai, Ubon Ratchathani and Nakhon Pathom has similar pattern. Direct radiation at most of these stations decrease from January to the minimum in August or September with some fluctuations. Then it gradually increases to the end of the year. This is due to the fact that direct radiation is mainly affected by clouds and high cloudiness in the rainy season causes low direct radiation in this season. For the case of Songkhla, the variation of direct radiation is not prominent. Although, the rainy season in the south is about 8 months, it is likely that the occurrence of rain in a day is not continuous with some periods of bright sunshine, causing relatively high direct radiation, even in the wet season.

- Ratio of diffuse to global radiation

The ratio of diffuse to global radiation indicates the energetic quality of solar radiation. For example, solar radiation with high ratio of diffuse to global radiation has low energy potential for solar concentrating applications, even global radiation is high. In this study, the ratios at Chiang Mai, Ubon Ratchathani, Nakhon Pathom and Songkhla are investigated and the result is shown in Figure 5.

From Figure 5, it is noticed that the ratios of diffuse to global radiation at Chiang Mai, Ubon Ratchathani and Nakhon Pathom are high during the wet season (May-October) due to high cloudiness where as the ratio at Songkhla is almost constant year round. The yearly average values of the ratio for Chiang Mai, Ubon Ratchathani, Nakhon Pathom and Songkhla are 0.44, 0.46, 0.45 and 0.43, respectively.

Radiation in Laos, Cambodia and Myanmar

Although, only global radiation is measured in these countries and the data period is relatively short, the results from the analysis reveal the trend of the seasonal variation as shown in Figure 6-8.

The results show that seasonal variation of solar radiation at most stations in these countries are similar with that in Thailand. Solar radiation in these countries increases from January to the peak in April or May and decreases with some fluctuations to the end of the year due to the influence of the change of the sun path, the monsoons and local geographical features.

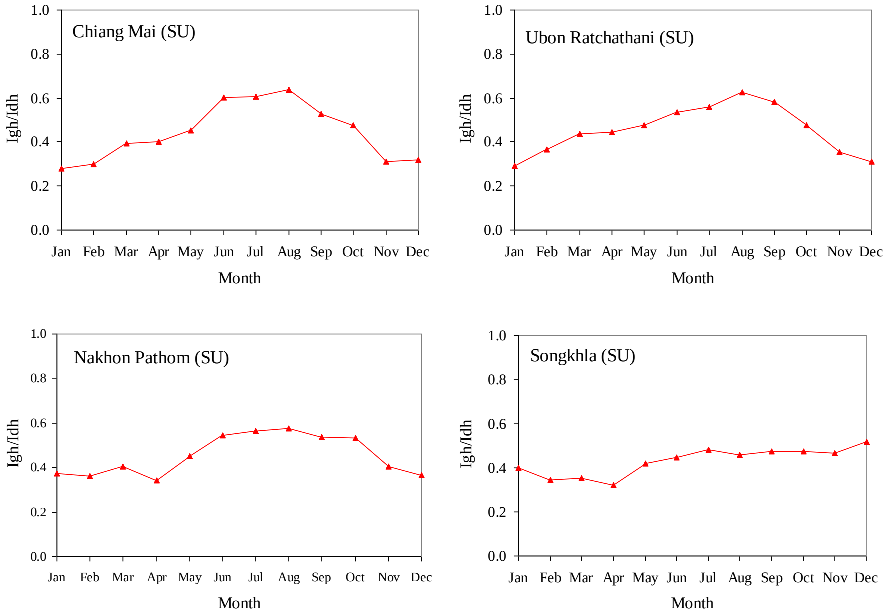

Figure 5. Ratio of diffuse to global radiation at four stations in Thailand

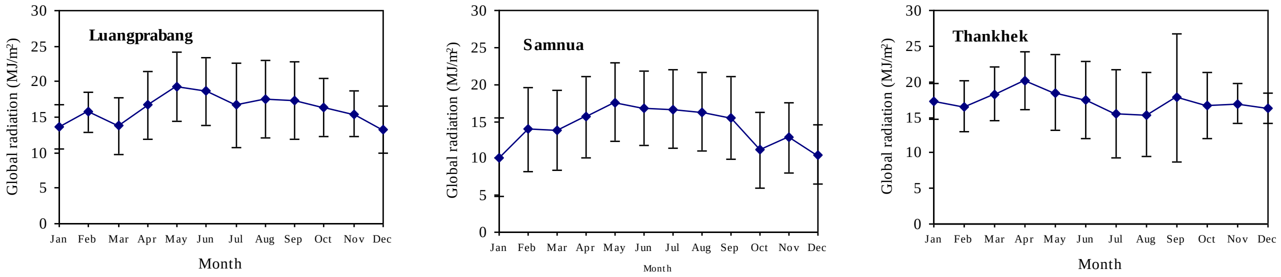

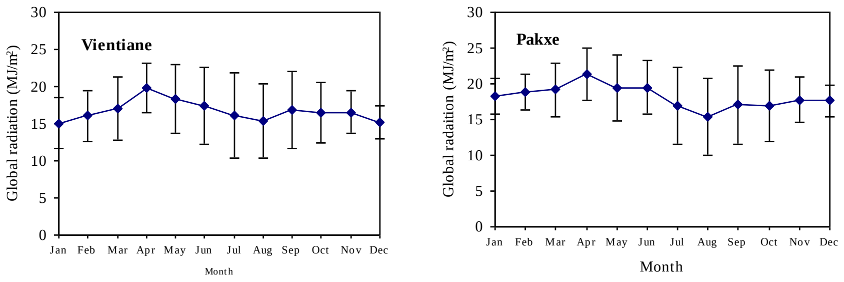

Figure 6. Global radiations in Laos

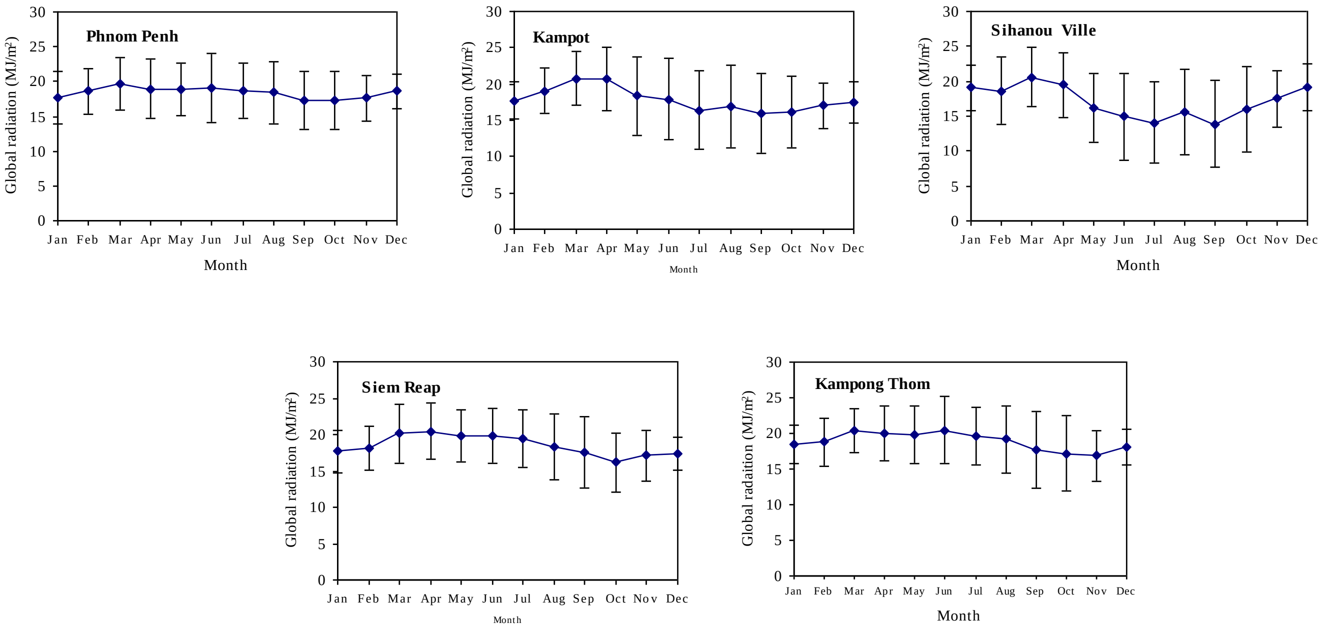

Figure 7. Global radiation in Cambodia

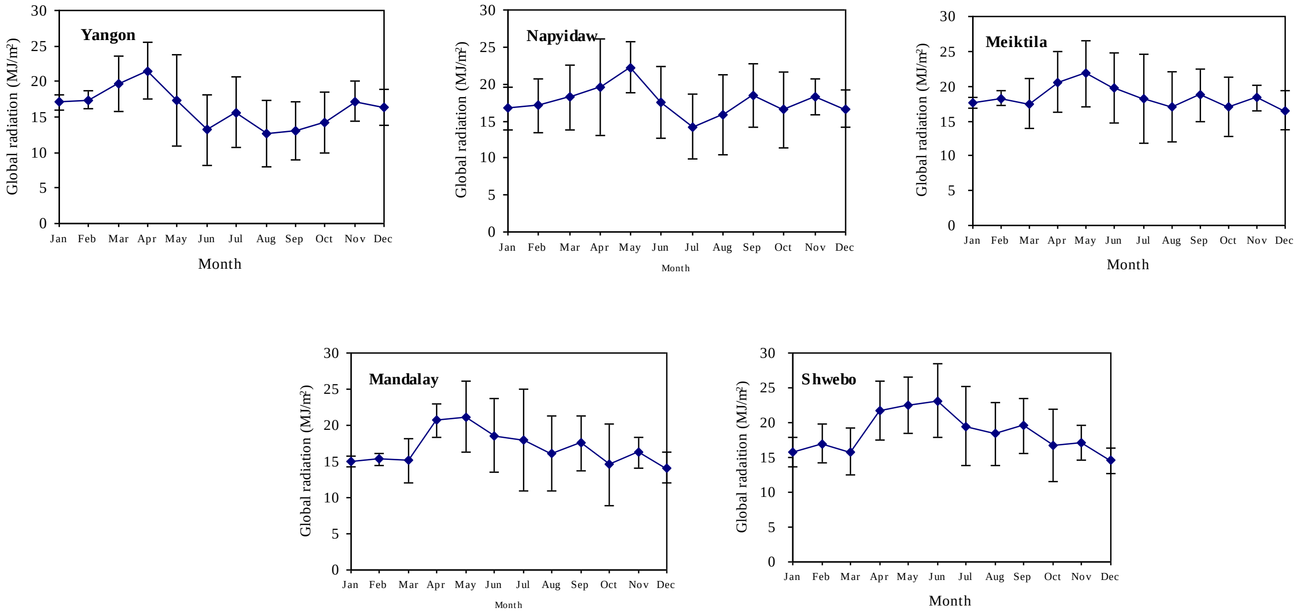

Figure 8. Global radiation in Myanmar

Variation with latitude

In general, the latitude of the stations plays and important role in the amount of solar radiation incident on the earth's surface because the incident angle of solar radiation depends strongly on the latitude. In this work, monthly average daily global radiation from all stations in Thailand, Laos, Cambodia and Myanmar is plotted against the latitude and the results are shown in Figure 9.

From Figure 9, it is noticed that global radiation in these countries varies systematically with latitude and the variation depends on the month, mainly due to the change of the sun path.

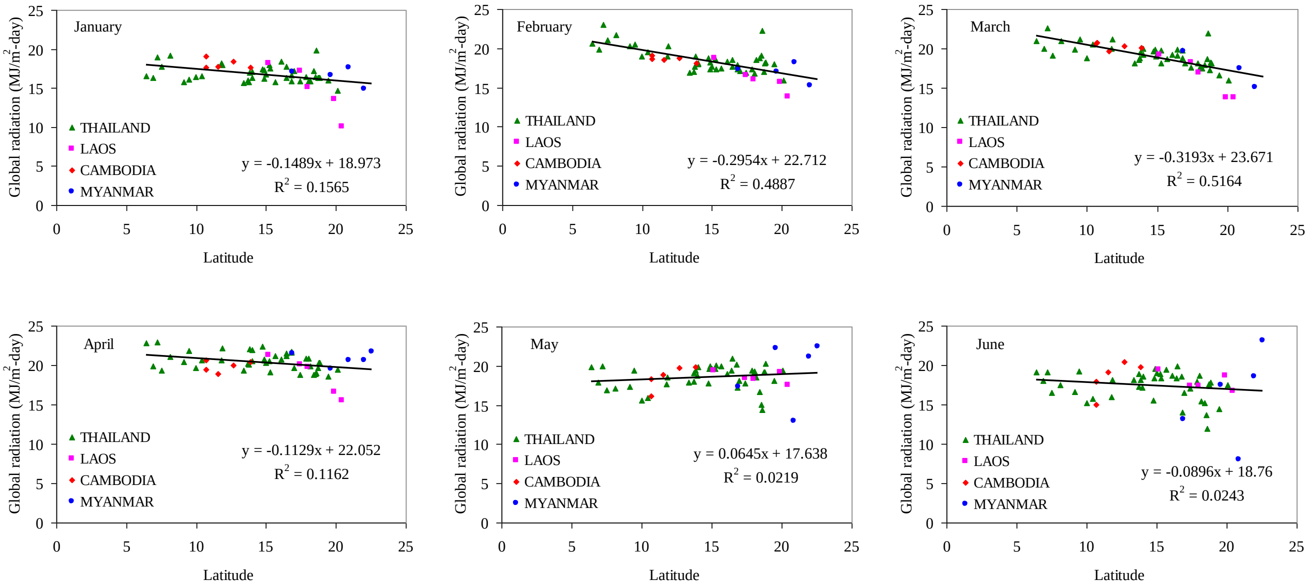

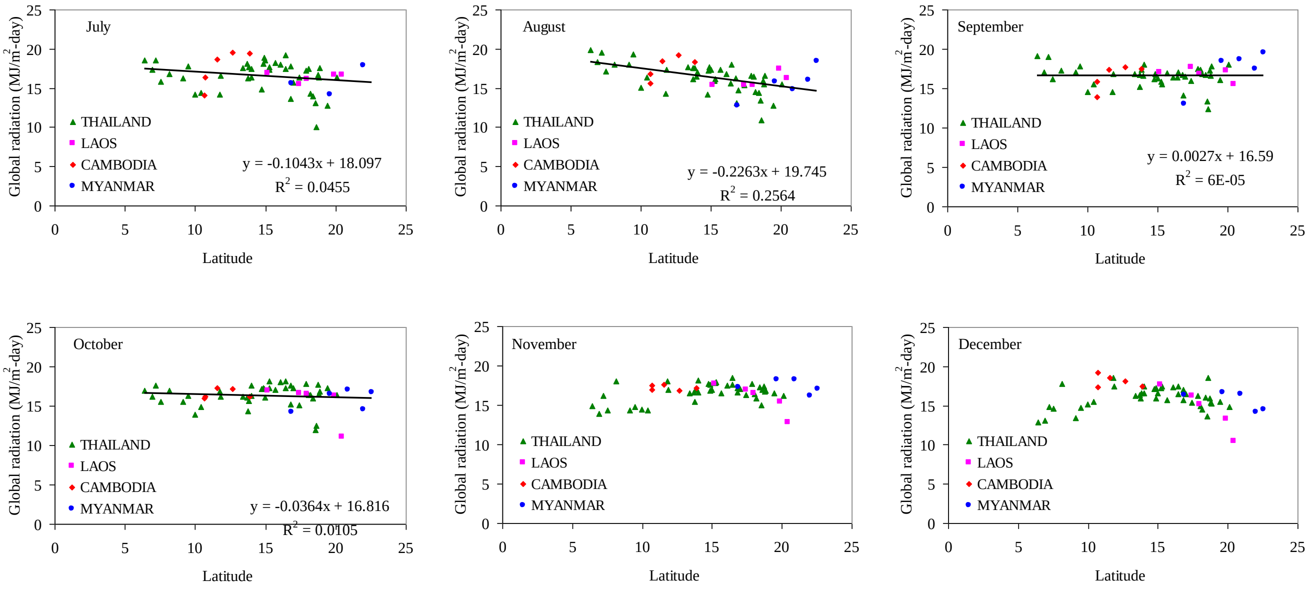

Figure 9 Variation of monthly average daily global radiation with latitude

Conclusions

Solar radiation monitoring stations have been established in Thailand, Laos, Cambodia and Myanmar. Global, diffuse and direct radiation in Thailand have been analyzed. The seasonal variations of global, diffuse and direct radiation at the stations in the north, northeast and the central region have similar pattern which is different from the south, due to the differences in the influence of the monsoons. The ratio of diffuse to global radiation in the four regions of the country are relatively high. For the case of Laos, Cambodia and Myanmar, the seasonal variation of global radiation at most stations is similar to the variation in most parts of Thailand. Global radiation at most stations in these four countries varies systematically with latitude. Finally, the level of solar radiation in these countries indicates that the countries have relatively high solar energy potential.

References

1. M. Iqbal, “An Introduction to Solar Radiation”, New York, Academic Press, 1983.
2. S. Janjai, “A greenhouse type solar dryer for small-scale dried food industries: Development and dissemination”, International Journal of Energy and Environment 3(3) (2012) 383-398.
3. S. Janjai, R. Wattan, M. Nunez, “A statistical approach for estimating diffuse illuminance on vertical surfaces”, Building and Environment 44 (2009) 2097-2105.
4. S. Janjai, J. Laksanaboonsong, T. Seesaard, “Potential application of concentrating solar power systems for the generation of electricity in Thailand”, Applied Energy 88 (2011) 4960–4967.

Acknowledgments

The authors would like to thank the Department of Alternative Energy Development and Efficiency of Thailand for inviting Silpakorn University to carry out all radiation projects. The authors also thank the Department of Electricity of Laos, Ministry of Industry, Mines and Energy of Cambodia and the Department of Meteorology and Hydrology of Myanmar for supporting the radiation projects in these countries.

High–energy and Particle Physics

Probing the Medium Effects of Hadrons by the Azimuthal Distributions of K^+ Mesons in Relativistic Heavy-ion Collisions

O. Ketsungnoen[1*], P. Srisawad[1], A. Harfield[1], Y. –M. Zheng[2], A. Limphirat[3], and Y. Yan[3]

[1] *Faculty of Science, Naresuan University, 65000 Phitsanulok Thailand.*
[2] *China Institute of Atomic Energy, P.O. Box 275(18),102413 Beijing, China.*
[3] *School of Physics, Suranaree University of Technology, 3000 Nakhon Ratchasima, Thailand.*
**Corresponding author. E-mail: nattanicha9@gmail.com*

Abstract

We investigated the in-medium kaon potential and nuclear equation of state by the azimuthal distribution of π^+ and K^+ mesons in heavy ion collision. We used quantum molecular dynamics (QMD) models based on covariant kaon dynamics to simulate ${}^{197}_{79}Au + {}^{197}_{79}Au$ collisions at 1.50 A GeV and ${}^{58}_{28}Ni + {}^{58}_{28}Ni$ collisions at 1.93 A GeV, analyzed the azimuthal distributions of K^+ mesons, and compared to the KaoS data. Calculated results with in-medium π^+N and K^+N potential can reasonably describe the features of the KaoS data. These indicate that the azimuthal distribution is one of sensitive probes to extract information on in-medium properties of hadrons at high densities.

Keywords: Azimuthal distributions, in-medium potential, nuclear equation of state, quantum molecular dynamics, covariant kaon dynamics.

Introduction

Relativistic heavy-ion collisions provide a unique opportunity to study both the behavior of nuclear matter at high densities as well as the properties of hadrons in nuclear matter. In particular, strange mesons are considered to be sensitive to in-medium modifications. Theory predicts a repulsive K^+N potential and an attractive K^-N potential in dense matter [1]. It is suggested that the latter effect leads to a condensate of K^- mesons in the interior of the neutron stars, causing dramatic consequences for the neutron star stability [2].

Microscopic transport calculations simulating heavy-ion collisions predict measurable consequences of the in-medium modification of strange mesons. A repulsive K^+N potential would repel the K^+ mesons from the bulk of the nucleons and therefore causes a preferred out-of-plane emission of the K^+ mesons at midrapidity and a directed flow opposite to the nucleons at target and projectile rapidity. These effects were found in experiments [3,4].

The K^+ mesons are expected to be repelled from the nucleons and hence the kaon emission pattern should be anticorrelated with the collective motion of the nucleons. Indirect evidence for such a behavior comes from a measurement of the average K^+ momentum in the event plane in ${}^{58}_{28}Ni + {}^{58}_{28}Ni$ collisions at 1.93*A* GeV: the directed in-plane flow found for protons and lambdas near target rapidity is absent for kaons. This finding was attributed to a repulsive K^+N potential which compensates the effect of the directed nucleon flow.

In this paper we present microscopic transport calculations simulating the azimuthal distributions of K$^+$ mesons in nucleus-nucleus collisions. We have calculated two systems: ${}^{58}_{28}Ni + {}^{58}_{28}Ni$ at 1.93 A GeV and ${}^{197}_{79}Au + {}^{197}_{79}Au$ at 1.50 A GeV.

Quantum Molecular Dynamics

In the quantum molecular dynamics (QMD) model each nucleon is represented by a coherent state of the form. (we set $\hbar$, c =1)

$$\varphi(\mathbf{r},\mathbf{p_0},t)=\left[\frac{1}{(2\pi L)^{3/4}}\exp\left[\mathbf{ip_0}.\right](\mathbf{r}-\mathbf{r_0})-\frac{(\mathbf{r}-\mathbf{r_0})^2}{4L}\right] \tag{1}$$

where $\mathbf{r_0}$ is the time dependent center of the Gaussian wave packet in coordinate space. The width L is kept constant. One uses Wigner density instead of working with wave function. Then, the Wigner density reads

$$\begin{aligned} f(\mathbf{r},\mathbf{p},t) &= \frac{1}{(2\pi)^3}\int e^{-i\mathbf{p}.\mathbf{r}_{12}}\varphi\left(\frac{\mathbf{r}+\mathbf{r}_{12}}{2},t\right)\varphi^*\left(\frac{\mathbf{r}-\mathbf{r}_{12}}{2},t\right)d^3\mathbf{r}_{12} \\ &= \frac{1}{\pi^3}\exp\left[\frac{(\mathbf{r}-\mathbf{r}_{12})^2}{2L}-(\mathbf{p}-\mathbf{p_0})^2.2L\right] \end{aligned} \tag{2}$$

The N-body Wigner density is the direct product of the Wigner densities of N coherent states

$$f^N(\mathbf{r}_1,...,\mathbf{r}_N;\mathbf{p}_1,...,\mathbf{p}_{N;t}) = \prod_{i=1}^{N} \frac{1}{(\pi)^3} e^{-(\mathbf{r}_i-\mathbf{r}_{io})^2/2L-(\mathbf{p}_i-\mathbf{p}_{io})^2.2L} \quad (3)$$

The Wigner representation of our Gaussian wave packets obeys the uncertainty relation $\Delta r_x \Delta p_x = \hbar/2$. The density in coordinate space is given by the momentum integral over the Wigner density.

$$\rho(\mathbf{r}) = \sum_{i=1}^{N} \int \delta(\mathbf{r}-\mathbf{r}_i) f^N(\mathbf{r}_1,...,\mathbf{r}_N,...;\mathbf{p}_1,...\mathbf{p}_N;t) d^3\mathbf{p}_1...d^3\mathbf{p}_N...d^3\mathbf{r}_1...d^3\mathbf{r}_N$$

$$= \sum_{i=1}^{N} \frac{1}{(2\pi L)^{3/2}} \exp\left[\frac{(\mathbf{r}-\mathbf{r}_{i0})^2}{2L}\right] \quad (4)$$

The next step is to determine the local potential $U(r)$ generated by all the other nucleons at the centers of the Gaussian. Finally the momenta of all particles are chosen randomly, the time evolution of the N-body distribution is determined by the motion of the centroids of the Gaussian $(\mathbf{r}_{i0}, \mathbf{p}_{i0})$, which are propagated by the Poisson brackets

$$\dot{\mathbf{p}}_{i0} = \left\{\mathbf{p}_{i0}, \sum_j H_j\right\} = \{\mathbf{p}_{i0}, T_i + U_i\} \quad (5)$$

$$\dot{\mathbf{r}}_{i0} = \left\{\mathbf{r}_{i0}, \sum_j H_j\right\} = \{\mathbf{r}_{i0}, T_i + U_i\} \quad (6)$$

These differential equations are solved using an Eulerian integration routine with a fixed time step Δt

$$\mathbf{p}_{i0}(n+1) = \mathbf{p}_{i0}(n) - \nabla_{\mathbf{r}_{i0}} U_i(n+\tfrac{1}{2})\Delta t \quad (7)$$

and

$$\mathbf{r}_{i0}(n+1/2) = \mathbf{r}_{i0}(n-1/2) + \frac{\mathbf{p}_{i0}(n)}{\left[\mathbf{p}_{i0}^2(n) + m_i^2\right]^{1/2}}\Delta t + \nabla_{i0} U_i(n-1/2)\Delta t \quad (8)$$

H is the nuclear Hamiltonian

$$H = \sum_i \sqrt{p_{i0}^2 + m_i^2} + \frac{1}{2}\sum_{i \neq j} (U_{ij}^{str} + U_{ij}^{cou}) \quad (9)$$

Here U_{ij}^{str} is the nuclear mean field. U_{ij}^{cou} is the Coulomb interaction. The strength of the nuclear compression is quoted normally in terms of the incompressibility constant (K). A soft equation of state (EOS) is represented by a value of K = 200 MeV, which a hard EOS is represented by a value of K = 380 MeV.

Results and Discussion

We consider Fig 1. the result of the QMD calculations based on covariant kon dynamics [5] for $^{58}_{28}Ni + ^{58}_{28}Ni$ collisions at 1.98 A GeV at impact parameter 3.8 < b < 6.5 were performed with the Kaon Spectrometer (KaoS) [6] (solid circle). Corresponding calculations are performed with the hard equation of state (EOS). The solid line and dashed line represent results of calculations with and without in medium potential, respectively. Figure 2. shows a comparison of the K^+ data of $^{58}_{28}Ni + ^{58}_{28}Ni$ at 1.98 A GeV with QMD model at impact parameter 3.8< b < 6.5 were performed with the KaoS (solid circle). Corresponding calculations are performed with the soft EOS. The dashed and solid lines represent results of calculations with and without in medium potential, respectively.The azimuthal distributions of the K^+ mesons from $^{197}_{79}Au + ^{197}_{79}Au$ reactions at 1.5 A GeV with QMD model calculations in Fig. 3 the dashed and solid lines represent results of calculations without and with in-medium potentials, respectively**.** Both calculations take into account kaons nucleon rescattering (by soft EOS). The experiments were performed with (KaoS) (solid circle).

The model calculations have been made exactly according to experimental conditions selecting the corresponding laboratory angles and laboratory momenta. It is seen clearly again from these figures that theoretical results with in-medium K^+ potential can reasonably describe KaoS data.

We use $v_1 = \left\langle \frac{p_x}{p_t} \right\rangle$ and $v_2 = \left\langle \frac{p_x^2 - p_y^2}{p_x^2 + p_y^2} \right\rangle$ to calculate the direct and elliptic flow of $K+$ mesons, which are shown in Table 1 for $^{197}_{97}Au + ^{197}_{97}Au$ collisions at 1.5 A GeV and Table 2 for $^{58}_{28}Ni + ^{58}_{28}Ni$ collisions at 1.93 A GeV,respectively. Here, one sees from the tables that calculated v_1 and v_2 with in-medium K^+ potential are in agreement with data.

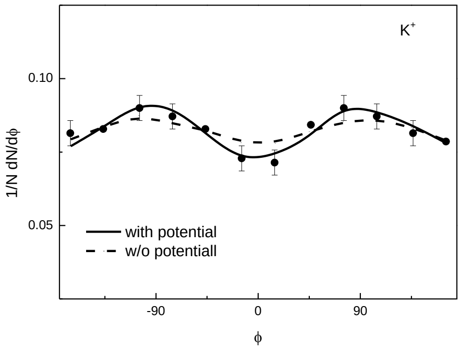

Fig. 1 Azimuthal distribution of K^+ mesons for semi-central $^{58}_{28}Ni + ^{58}_{28}Ni$ reactions at 1.93 A GeV. The data are corrected for the resolution of the reaction plane and refer to impart parameter of 3.8 < b < 6.5 fm, rapidites of 0.3 < y/y_{beam} < 0.7, and momenta of 0.2 < p_t < 0.8 GeV/c. The lines represent results of QMD calculations for without (solid line) and with an in-medium potential (dashed line) . Both calculations take into account kaons nucleon rescattering (by hard EOS)

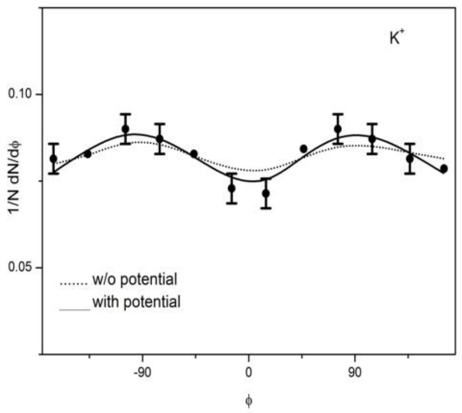

Fig. 2 Azimuthal distribution of K$^+$ mesons for semi-central $^{58}_{28}Ni+^{58}_{28}Ni$ reactions at 1.93 A GeV. The data are corrected for the resolution of the reaction plane and refer to impart parameter of 3.8 < b < 6.5 fm, rapidites of 0.3 < y/y$_{beam}$ < 0.7, and momenta of 0.2 < p$_t$ < 0.8 GeV/c. The lines represent results of QMD calculations for without (dashed line) and with an in-medium potential (solid line) . Both calculations take into account kaons nucleon rescattering (by soft EOS)

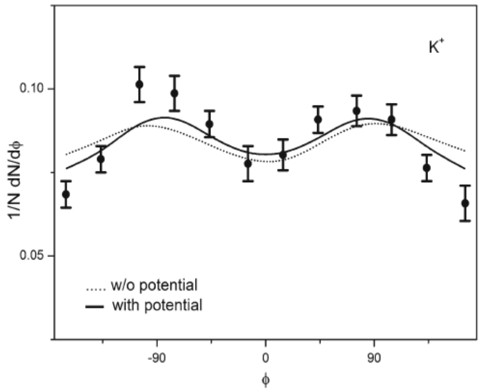

Fig. 3 Azimuthal distribution of K$^+$ mesons for semi-central $^{197}_{79}Au+^{197}_{79}Au$ reactions at 1.50 A GeV. The data are corrected for the resolution of the reaction plane and refer to impart parameter of 5.9 < b < 10.2 fm, rapidites of 0.3 < y/y$_{beam}$ < 0.7, and momenta of 0.2 < p$_t$ < 0.8 GeV/c. The lines represent results of QMD calculations for without (dashed line) and with an in-medium potential (solid line). Both calculations take into account kaon nucleon rescattering (by soft EOS)

Table 1: The direct flow and elliptic flow of K^+ mesons in $^{197}_{97}Au+^{197}_{97}Au$ collisions at 1.50 *A GeV*

First	**Data**	**Claculation with *K*$^+$*N* potential / without *K*$^+$*N* potential**
Direct flow (n_1)	0.04± 0.01	-0.041± 0.002 / -0.008± 0.0013
Elliptic flow (v_2)	-0.09± 0.03	-0.042± 0.01 / -0.03± 0.0013

Table 2: The direct flow and elliptic flow of K^+ mesons in $^{58}_{28}Ni+^{58}_{28}Ni$ collisions at 1.93 *A GeV*

First	**Data**	**Claculation with *K*$^+$*N* potential / without *K*$^+$*N* potential**
Direct flow (n_1)	-0.01± 0.01	-0.013± 0.002 / -0.006± 0.001
Elliptic flow (v_2)	-0.05± 0.03	-0.04± 0.002 / -0.02± 0.001

Conclusions

We have analyzed the azimuthal emission patterns of K$^+$ mesons to simulate $^{197}_{79}Au+^{197}_{79}Au$ collisions at 1.50 A GeV and $^{58}_{28}Ni+^{58}_{28}Ni$ collisions at 1.93 A GeV , and compared to the KaoS data. We used quantum molecular dynamics (QMD) models based on covariant kaons dynamics. These distributions are rather flat and the sensitivity on the K$^+$N potential. This means that the azimuthal distribution of K$^+$ mesons is one of sensitive probes to extract information on the in-medium properties of strange at high densities.

Acknowledgments

This work was supported in part by the Thiland Center of Excellence in Physics (ThEP) and Faculty of Science, Naresuan University.

References

1. Schaffner, J., Bondorf, J. and Mishustin, I. N. (1997). In-medium kaon production at the mean-filed level. Nuclear Physics A, 625(1-2), **325.**
2. Brown, G. E., Lee, C. H., Rho, M. and Thorsson, V. (1994). From kaon-nuclear interactions to kaon condensation. Nuclear Physics A, 567(4), **937**.
3. Aichelin, J. (1990). Quantum molecular dynamics a dynamical microscopic n-body approach to investigate fragment formation and the nuclear equation of state in heavy ion collisions. Phys. Rep. **202**, 233.
4. Senger, P., et al. (1993). The kaon spectrometer at SIS. Nucl. Instrum. Methods Phys. Res. **327**, 393.
5. Uhlig, F., et al.(2005). Observation of different azimuthal emission pattern of *K*+ and of *K*− meson in heavy-ion collision at 1–2 A GeV. Phys. Rev. Lett. **95**, 012301.
6. Zheng, Y.M., et al. (2004). Covariant kaon dynamics and kaon flow in heavy ion collisions. Phys. Rev. C. **69**, 034907

Uncharged and Non-rotating Black Holes in Higher Dimensions

T. Ngampitipan[1*] and P. Boonserm[2]

[1]Department of Physics, Faculty of Science, Chulalongkorn University, Bangkok 10330, Thailand
[2]Department of Mathematics and Computer Science, Faculty of Science, Chulalongkorn University, Bangkok 10330, Thailand
**Corresponding author. E-mail: tritos.ngampitipan@gmail.com*

Abstract

The simplest type of black hole known to science is the Schwarzschild black hole because it has no charge or rotation. In this paper, Schwarzschild black holes are considered in higher dimensions. The rigorous bounds on the greybody factors for these black holes are derived using the 2×2 transfer matrices. The results show that the greybody factors decrease as the number of dimensions increase.

***Keywords*:** Greybody factors, higher dimensions, black holes, the 2×2 transfer matrices

Introduction

Classically, a black hole is a region in spacetime in which the gravitational field is so strong that anything, even light, cannot escape. From quantum point of view, however, a black hole could emit radiation. This radiation is known as Hawking radiation, a phenomenon discovered by Stephen Hawking in 1974 [1]. If particles are created from vacuum near a black hole horizon, one particle can move out of the black hole and appear to an observer as Hawking radiation. Due to the curvature of spacetime around a black hole, Hawking radiation is modified. How much the spectrum is modified by can be measured using the so-called "greybody factor".

The greybody factors have widely been studied in the literatures [2-7]. Moreover, there is one interesting technique, called the 2×2 transfer matrix, which is used to obtain a rigorous bound on the greybody factors [8-10]. The bounds of the greybody factors of the four-dimensional Schwarzschild black holes have been derived through the application of this method [11]. In this paper, we derive the bounds of the greybody factors of the Schwarzschild-Tangherlini black holes using the 2×2 transfer matrix.

The Schwarzschild-Tangherlini black holes

The Schwarzschild-Tangherlini black holes are the generalized four-dimensional Schwarzschild black holes in higher dimensions. The Schwarzschild-Tangherlini metric in *d* dimensions is given by [7]

$$ds^2 = -\left[1-\left(\frac{r_0}{r}\right)^{d-3}\right]dt^2 + \left[1-\left(\frac{r_0}{r}\right)^{d-3}\right]^{-1} dr^2$$

$$+r^2 d\Omega_{d-2}^2, \tag{1}$$

where the Schwarzschild radius r_0 in *d* dimensions is given by

$$r_0 = \frac{16\pi GM}{(d-2)\Omega_{d-2}}, \tag{2}$$

with

$$\Omega_{d-2} = \frac{2\pi^{(d-1)/2}}{\Gamma\left(\frac{d-1}{2}\right)}. \tag{3}$$

If a particle emitted from the black hole is a massless uncharged scalar field, with energy ω^2 and angular momentum *l*, its equation of motion is the Klein-Gordon equation

$$\nabla^{\mu}\partial_{\mu}\Phi = 0, \tag{4}$$

where ∇^{μ} is the covariant derivative. By separating the variables

$$\Phi = e^{i\omega t}\varphi(r)Y_{lm}(\theta,\phi), \tag{5}$$

the radial equation is the Schrödinger like equation [12-13]

$$\left[\frac{d^2}{dr_*^2} + \omega^2 - V(r)\right] r^{(d-2)/2}\varphi = 0, \tag{6}$$

where

$$dr_* = \frac{1}{f(r)}dr \tag{7}$$

and

$$V(r) = \frac{(d-2)(d-4)}{4}\frac{f^2(r)}{r^2} + \frac{(d-2)}{2}\frac{f(r)\partial_r f(r)}{r}$$

$$+l(l+d-3)\frac{f(r)}{r^2}, \tag{8}$$

with

$$f(r)=1-\left(\frac{r_0}{r}\right)^{d-3}. \tag{9}$$

From Figure 1, the Schwarzschild-Tangherlini potential is plotted with l = 3 and GM = 2 in various dimensions.

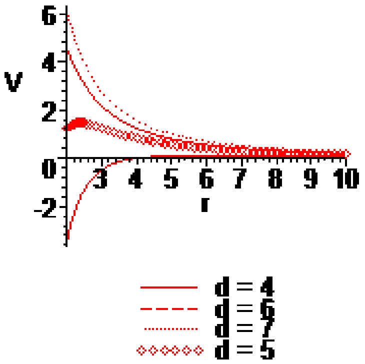

Figure 1. The Schwarzschild-Tangherlini potential with l = 3 and GM = 2 in various dimensions.

In accordance with general relativity, since the gravitational field around a black hole is strong, the emitted particle, which appears to an observer as radiation, is incidental to the potential barrier given by equation (8). Part of the radiation will be reflected back into the black hole and the rest will be transmitted out of the black hole. The greybody factor is thus defined as the transmission probability.

Using the analysis of [8-10], lower bounds on the transmission probabilities are given by

$$T \geq \operatorname{sech}^2\left(\int_{-\infty}^{\infty}\vartheta dr_*\right), \tag{10}$$

where

$$\vartheta=\frac{\sqrt{(h')^2+\left(\omega^2-V-h^2\right)^2}}{2h}, \tag{11}$$

for some positive function h. The lower bound on the transmission probability for $h = \omega$ is

$$T \geq \operatorname{sech}^2\left[\frac{(d-2)(d-3)+4l(l+d-3)}{8\omega r_0}\right]. \tag{12}$$

If d = 4, this bound is reduced to

$$T \geq \operatorname{sech}^2\left[\frac{2l(l+1)+1}{8GM\omega}\right], \tag{13}$$

which is exactly the bound for the four-dimensional Schwarzschild black holes emitting spinless particles [11, 13]. Figure 2 and 3 show the plot between the bounds of the transmission coefficients and the energy of the emitted particle in various dimensions. The graphs are plotted by setting l = 3 in figure 2 and l = 10 in figure 3 with GM = 2 in both figures. The line d = 4 corresponds to the four-dimensional Schwarzschild black hole. If energies of the emitted particles increase, the greybody factors also increase. Figure 4 shows the plot between the bounds of the greybody factors and the dimensions. The results indicate that the greybody factors decrease when the number of spacetime dimensions increase. Figure 5 shows the plot between the bounds of the greybody factors and angular momenta of the emitted particles. The results state that if the angular momenta increase, the greybody factors decrease. Higher dimensions and angular momenta could cause the emitted particles to penetrate through the potential barriers with more difficulty.

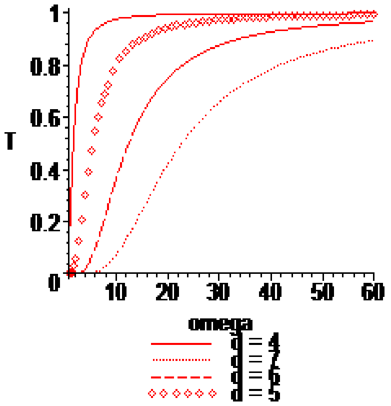

Figure 2. The bound of the greybody factor of the Schwarzschild-Tangherlini black hole with l = 3 and GM = 2 in various dimensions.

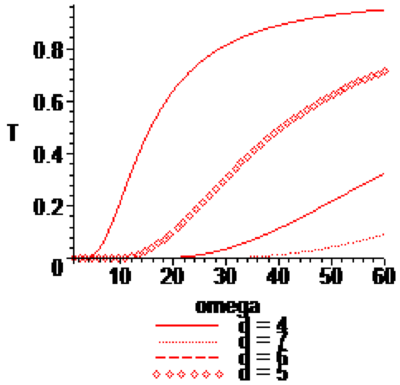

Figure 3. The bound of the greybody factor of the Schwarzschild-Tangherlini black hole with l = 10 and GM = 2 in various dimensions.

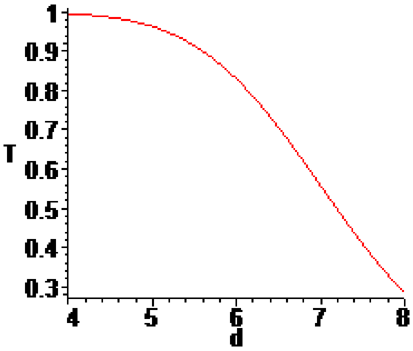

Figure 4. Dependence of the greybody factor bound on the number of dimensions for the Schwarzschild-Tangherlini black hole, with l = 3 and GM = 2.

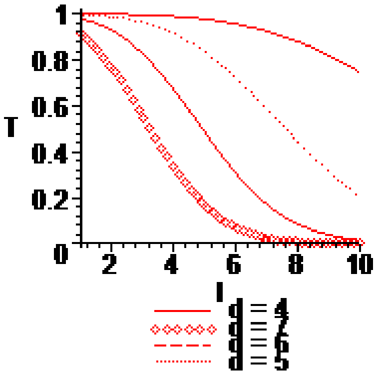

Figure 5. Dependence of the greybody factor bound on angular momenta of the emitted particles for the Schwarzschild-Tangherlini black hole, with GM = 2 in various dimensions.

Conclusions

In this paper, we obtained the bounds on the greybody factors using the 2×2 transfer matrix for the Schwarzschild-Tangherlini black holes. It is found that the greybody factors depend on the spacetime dimension, as well as the energy and the angular momentum of the emitted particles. Higher dimensions could result in the generation of stronger potentials, which would consequently lead to the diminution of the greybody factors.

Acknowledgments

This research was supported by a grant, for the professional development of new academic staffs, from the Ratchadapisek Somphot Fund at Chulalongkorn University, by Thailand Toray Science Foundation (TTSF), and by the Research Strategic plan program (A1B1), Faculty of Science, Chulalongkorn University. PB was additionally supported by a scholarship from the Royal Government of Thailand. TN was additionally supported by a scholarship from the Development and Promotion of Science and Technology talent project (DPST). TN gives special thanks to Dr. Auttakit Chatrabuti for his invaluable advice. We also thank Prof. Matt Visser for his extremely helpful suggestions and comments.

References

1. S. Hawking, “Particle creation by black holes”, Communications in Mathematical Physics **43** (1975), 199.
2. M. Parikh and F. Wilczek, “Hawking radiation as tunneling”, Physical Review Letter **85** (2000), 5042 hep-th/9907001.
3. C. Fleming, “Hawking radiation as tunneling”, (2005).
4. P. Lange, “Calculation of Hawking radiation as quantum mechanical tunneling”, Thesis, Uppsala Universitet, 2007.
5. S. Fernando, “Greybody factors of charged dilaton black holes in 2 + 1 dimensions”, General Relativity and Gravitation **37** (2005), 461.
6. W. Kim and J. Oh, “Greybody factor and Hawking radiation of charged dilatonic black holes”, Journal of the Korean Physical Society **52** (2008) 986.
7. J. Escobedo, “Greybody Factors Hawking Radiation in Disguise”, Master's Thesis, University of Amsterdam, 2008.
8. M. Visser, “Some general bounds for 1-D scattering”, Physical Review A **59** (1999), 427 [arXiv: quant-ph/9901030].
9. P. Boonserm and M. Visser, “Bounding the Bogoliubov coefficients”, Annals of Physics **323** (2008), 2779 [arXiv: 0801.0610 [quant-ph]].
10. P. Boonserm, “Rigorous Bounds on Transmission, Reflection, and Bogoliubov Coefficients”, Ph. D. Thesis, Victoria University of Wellington, 2009 [arXiv: 0907.0045 [math-ph]].
11. P. Boonserm and M. Visser, “Bounding the greybody factors for Schwarzschild black holes”, Physical. Review D **78** (2008) 101502 [arXiv: 0806.2209 [gr-qc]].
12. J. Natario, “Greybody factors for *d*-dimensional black holes”, Talk at Universidade do Porto, 2008.
13. T. Ngampitipan and P. Boonserm, “Bounding the greybody factors for non-rotating black holes”, [arXiv: 1211.4070 [math-ph]]

VHbb Analysis with CMS

E. Simili[1,2*], B. Asavapibhop [1,2], and N. Suwonjandee [1,2]

[1] *Particle Physics Research Laboratory, Department of Physics, Faculty of Science, Chulalongkorn University, Bangkok 10330, Thailand*

[2] *Thailand Center of Excellence in Physics, Commission Higher on Education, Ministry of Education, Bangkok 10400, Thailand*

[†] *Supported in part by the Special Task Force for Activating Research (STAR) Project, Ratchadaphiseksomphot Endowment Fund, Chulalongkorn University*

[*] *Corresponding author. E-mail: pepposub@gmail.com*

Abstract

The observation of a new particle with a mass of about 125 GeV, announced in July 2012 by the ATLAS and CMS collaborations, has given hopes to the HEP community as the long sought Higgs boson, last missing ingredient of the Standard Model of Particle Physics, might have been discovered at last. The Compact Muon Solenoid experiment (CMS) is a general purpose detector installed at the Large Hadron Collider (LHC) at CERN. During the years 2011 and 2012, the CMS detector has collected over 17 inverse femto-barns of proton-proton collisions (5 fb^{-1} at $\sqrt{s}$=7 TeV and 12 fb^{-1} at $\sqrt{s}$=8 TeV). These data are currently been analyzed to further characterize the recently discovered Higgs boson candidate. For a Higgs mass of about 125 GeV, the dominant decay mode should be into $b\bar{b}$, however such decay has not yet been observed experimentally due to overwhelming backgrounds. A promising channel to search for $H\rightarrow b\bar{b}$ is the VHbb channel, where the Higgs boson is produced via ‘Higgs-Strahlung’ process (a virtual W or Z boson with sufficient energy can then emit a Higgs) and recoils with large momentum transverse to the beam-line, to finally decay into a $b\bar{b}$ pair (b-jets). The presence of a vector boson in the final state highly suppresses the large QCD background and also provides an efficient trigger path when the vector boson decays to charged leptons (e, μ). Recent developments in τ lepton reconstruction and vector boson invariant mass determination made it feasible to extend the VHbb analysis to both leptonic (e, μ) and hadronic (jets) decays of the τ lepton. The current VHbb results are summarized and the novel VHbb final states are presented, with particular focus on HZ, with H decaying to b-quarks and Z decaying to tau electron and hadronic tau.

Keywords: Higgs, CMS, LHC, VHbb, Tau

Introduction

The Higgs Boson is the last missing ingredient of the Standard Model (SM) of particle physics, and is essential for the internal consistency of the whole theory. Its existence was postulated in 1964 by Peter Higgs and others [1] as the mechanism for which the gauge vector bosons of the weak interaction ($W^{+/-}$ and Z^0) acquire their mass through electroweak symmetry breaking while the photon stays massless. At energies high enough that electroweak symmetry is unbroken, all elementary particles are massless, but at a critical temperature the symmetry is spontaneously broken and the gauge bosons acquire their masses. Fermions, such as leptons and quarks, also acquire mass by interacting with the Higgs field, but in a slightly different way than gauge bosons.

In other words, elementary particles acquire their mass by interacting with the Higgs field that permeates the entire space. The Higgs boson is an excited quantum of the Higgs field. As the other 19 free parameters of the SM, the mass of the boson is not predicted by the theory and has to be measured experimentally.

On the 4th of July 2012, both ATLAS and CMS have publicly announced the observation of a new particle, showing an excess of events at a mass of about 125-126 GeV in the two-photons and in the four leptons channels, with a statistical significance above the background of over 5σ [2,3]. The new particle is consistent with the Standard Model Higgs boson, however its properties have to be further investigated before the Higgs label can be attached to it.

For a Higgs boson mass of about 125 GeV, the dominant decay mode should be into $b\bar{b}$. However, because of the large backgrounds, there is no direct evidence for such decay yet, which is indeed crucial to determine the nature of the Higgs boson.

VHbb Analysis with CMS

The Standard Model predicts a number of possible mechanisms for the production and subsequent decay of the Higgs boson.

The main SM mechanism for Higgs production at the LHC is Gluon Fusion, with a cross section σ~17 pb (for m_H=125 GeV) [4], however the detection of a

Higgs boson decaying to $b\bar{b}$ in this production channel is almost impossible due to the overwhelming QCD background at the LHC. The next most abundant production mechanism is Vector Boson Fusion (VBF), with a total cross section σ~1.3 pb [5]. This process can result in a final state with 2 b-quarks and a vector boson (σ_{VHbb}~1.02 pb [6]).

In 2008, a new method has been proposed [7] to search for a SM Higgs Boson decaying into $b\bar{b}$, in events where the Higgs is produced in association with a Z or a W. The presence of a vector boson highly suppresses the QCD background and also provides an efficient trigger path when the vector boson decays into leptons (see Fig. 1).

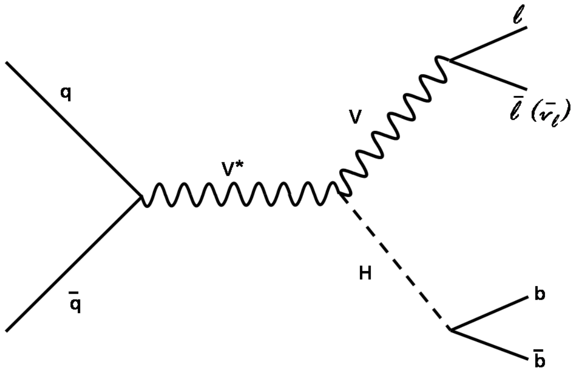

Figure 1. Generic Feynman diagram for a VHbb final state, consisting of two bottom quarks and two leptons (or lepton plus neutrino, or two neutrinos).

Preliminary results from CMS show that, in a region of phase space where the Higgs is boosted, the analysis sensitivity for these production channel (with $H \to b\bar{b}$) is significant [8].

The VHbb analysis searches for a SM Higgs boson in the $pp \to VH$ production mode, where V is a vector boson (either $W^{+/-}$ or Z^0) that decays leptonically, while the Higgs boson decays into $b\bar{b}$.

The Compact Muon Solenoid experiment

The Compact Muon Solenoid experiment is a general purpose detector installed at the Large Hadron Collider at CERN.

It is composed of concentric shells of different types of detector, immersed in a strong magnetic field oriented along the beam axis (B~3.8 T). The arrangement is optimized to provide good tracking and particle identification over the full azimuth and over a large pseudo-rapidity window ($|\eta| < 3$). Fig. 2 shows an expanded view of the CMS detector, a detailed description of the experiment and its sub-detector systems can be found in the reference [9].

During the years 2011 and 2012, CMS has collected over 17 inverse femto-barns of proton-proton collisions (about 5 fb^{-1} at $\sqrt{s}$=7 TeV and 12 fb^{-1} at $\sqrt{s}$=8 TeV). These data are currently under investigation by the various physics analysis groups in order to finalize the ongoing searches.

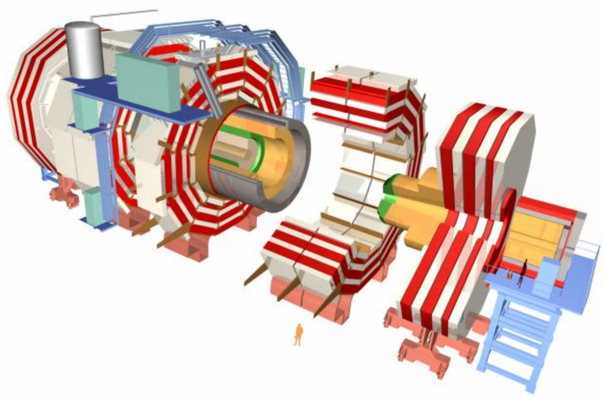

Figure 2. Expanded view of the CMS detector. The LHC beams travel in opposite directions along the central axis of the cylinder, colliding in the middle of the detector [9].

Signal and Background Simulation

The main background arise from single vector bosons associated with jets or di-boson production, from single-top or $t\bar{t}$ events, and from QCD processes involving multiple jets. These processes overwhelm the signal by orders of magnitude, therefore a careful tuning of the analysis parameters is crucial to acquire a decent sensitivity over the background.

Simulations are produced within the CMSSW software framework [10], where various event generators (PYTHIA, POWHEG, HERWIG, MADGRAPH) are interfaced to a detailed CMS detector response simulation modeled with GEANT4 [11].

The pile-up scenario (number of simultaneous collision within the same "trigger") is tuned to the average pp interaction per bunch crossing during each LHC run. For 2011 data, the average pile-up is about 10, while 2012 data have an average pile-up of ~ 20-25 due to the higher luminosity [12].

Event Reconstruction and Analysis

A number of triggers are combined to select events that are consistent with the VHbb signal hypothesis in each sub-channel [13]. Several isolated lepton triggers are applied, together with tight lepton identification and different p_T thresholds for each channel, missing transverse energy requirements are also applied to account for the neutrinos involved in some of the processes.

The analysis strategy begins by identifying the vector boson from its decay products (charged lepton(s) and/or missing transverse energy in case of $Z \to \nu\nu$) [13,14]. The $H \to b\bar{b}$ decay is reconstructed as two separate jets clustered using the anti-k_T algorithm [15], with a cone radius of 0.5. The Combined Secondary Vertex algorithm [16] is used to identify b-jet candidates.

All objects are reconstructed using the particle-flow algorithm [17], which best combines the various sub-detectors' signal into a consistent hypothesis of track, jet, primary or secondary vertex and missing transverse energy.

Event Selection/Cut Optimization

Beside the trigger selection (see Ch. 3 of [13]), a number of kinematic and topological cuts are applied in order to maximize the signal yield with respect to the reducible background in the Higgs mass window: 110 < m_H < 135 GeV [13,14].

The optimization of the analysis is achieved by mean of Monte Carlo simulations: for a given Higgs mass hypothesis, the expected signal and main backgrounds are simulated and fully reconstructed with CMSSW [10]. The events are then analyzed using the VHbb package and a Figure of Merit (a certain function that quantifies the visibility of the signal over the background) is drawn with respect of the relevant cut-variable.

A set of pre-selection cuts is applied to enforce basic kinematic requirements, as well as track isolation and fit quality requirements. Several other discriminating variables are calculated from event and track observables, such as p_T balance, b-tagging, opening angle between vector and Higgs boson, etc.

In a preliminary stage the optimization is done by “cut & count” (i.e., cuts are applied in steps while counting the number of passing candidates). Final results are then produced using a Boosted Decision Tree (BDT), which further improves the optimization and also accounts for existing correlations between cut variables (a multivariate analysis tool is used at this stage [18]).

For a detailed list of the discriminating variables and applied cuts see the references [13,14].

Results and Discussion

Published results only include 2011 data and are limited to five VHbb final states or sub-channels [13]. Preliminary results on the same sub-channels are publicly available for 2012 data and combined [14].

Since recently, a few additional final states have been included in the VHbb analysis. The study of these novel channels is still in progress.

Published Results

Published and preliminary VHbb results are limited to the following five sub-channels: W(μν)H, W(eν)H, Z(μμ)H, Z(ee)H and Z(νν)H, with all the Higgs decaying to $b\bar{b}$.

Due to the small cross section of the VHbb process compared to other SM reactions, a large component of irreducible background will always dominate the signal for about one order of magnitude in the best case. Therefore, the signal is observed as a small excess of events within the Higgs mass window (110-135 GeV) in the di-jet invariant mass plot (m_{jj}).

Cumulative results from all the VHbb sub-channels listed above do not show a significant excess, therefore only upper limits can be drawn. Fig. 3 shows the expected and observed 95% Confidence Level upper limit (CL) for a Higgs boson with mass m_H. Observed data, background-only and signal + background expectations are plotted. The 1 and 2 σ limits for the background-only hypothesis are also shown [14].

Combining 2011 and 2012 data, the excess of observed events at m_{jj}=125 GeV is ~2.2 σ away from the background-only hypothesis. The excess is consistent with the Standard Model prediction for a Higgs boson with that mass [14].

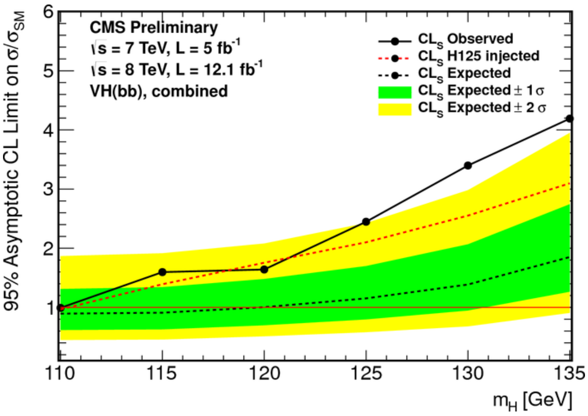

Figure 3. Expected and observed 95% Confidence Level upper limits for the VHbb production of a Higgs boson with mass m_H. This plot shows the combined results of 2011 and 2012 data from all five VHbb sub-channels mentioned in the text (see [14]).

Ongoing efforts

The VHbb analysis has been extended to include channels with τ lepton(s) from the vector boson.

Tau leptons are short lived particles with mean lifetime $t_\tau = 2.9\times10^{-13}$ sec. ($c\cdot t_\tau$ = 87.11 μm), therefore they are not directly observed with the CMS tracker, but their decay product(s) can be used to reconstruct the secondary vertex of the τ decay. Taus decay leptonically into muons ($\tau\rightarrow\mu+\bar{\nu}_\tau+\nu_\mu$) or electrons ($\tau\rightarrow e+\bar{\nu}_\tau+\nu_e$) about 35% of the times, and hadronically ($\tau\rightarrow$hadrons$+\bar{\nu}_\tau$) the remaining 65% [19].

The novel VHbb sub-channels are chosen to be orthogonal to the existing ones (i.e., they do not produce the same final state particles). They are the following: W($\tau_h\nu$)H, Z(τ(e)τ(μ))H, Z(τ(μ)τ_h)H, Z(τ(e)τ_h)H, with all the Higgs decaying to $b\bar{b}$.

The study of these channels is made possible thanks to improved algorithms for the reconstruction of hadronic τ decays, such as the Hadron Plus Stript (HPS) algorithm [20,21], and through the use of a likelihood method to determine the mass of the vector boson decaying into τ(s) [22]. This method combines the information on the visible products and missing transverse energy with knowledge about the kinematic of either hadronic or leptonic τ decays, and it can reconstruct the invariant mass of the vector boson when the reaction involves one or more neutrinos which escape undetected.

Fig. 4 shows the pseudo-Feynman diagram of one of these novel sub-channels included in the VHbb analysis: $Z(\tau(e)\tau_h)\ H(b\bar{b})$.

This channel is particularly challenging due to the weak signature of the of the Z^0 boson (with only one charged lepton in the final state) and to the large irreducible background from more copious SM processes.

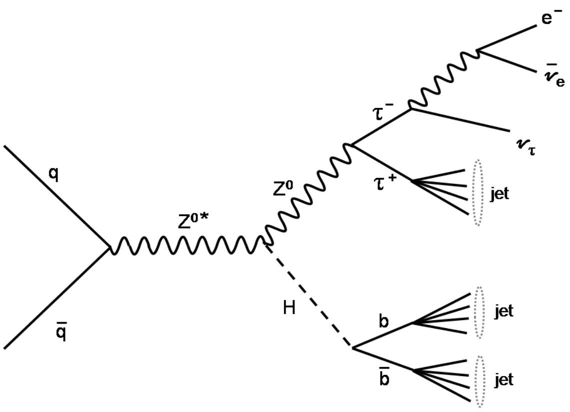

Figure 4. Intuitive diagram of the production and decay of a novel VHbb channel, with hadronic tau and tau electron in the final state: $Z \longrightarrow \tau(e)\tau_h$, $H \longrightarrow b\bar{b}$.

Conclusions

So far there are no significant excesses of events in the VHbb signal region, therefore there is no direct evidence of the decay $H \rightarrow b\bar{b}$.

Combined VHbb results from 2011 and 2012 data are still to be finalized, but they are ~2.2 standard deviations away from the SM background and are consistent with a SM Higgs boson of mass 125 GeV.

Acknowledgments

I would like to thank the CMS collaboration, and in particular the VHbb analysis group at KU-UNL.

References

1. P.W. Higgs, "*Broken symmetry and the mass of gauge vector mesons*", **Phys. Rev. Lett. 13** (1964) p.508.
2. CMS Collaboration, *"Observation of a new boson at a mass of 125 GeV with the CMS experiment at the LHC"*, **Phys. Lett. B 716** (2012) p.30–61.
3. ATLAS Collaboration, *"Observation of a new particle in the search for the Standard Model Higgs boson with the ATLAS detector at the LHC"*, **Phys. Lett. B 716** (2012) p.1-29.
4. LHC Higgs Cross Section Working Group Collaboration, *"Handbook of LHC Higgs cross sections: 1. Inclusive Observables"*, CERN Report **CERN-2011-002** (2011).
5. P. Bolzoni et al., *"Higgs production via vector-boson fusion at NNLO in QCD"*, **Phys. Rev. Lett. 105** (2010) 011801.
6. S. L. Glashow, D. V. Nanopoulos, and A. Yildiz, *"Associated production of Higgs bosons and Z particles"*, **Phys. Rev. D 18** (1978) p.1724.
7. J.M.Butterworth, *et al.*, "*Jet substructure as a new Higgs search channel at the LHC*", **Phys. Rev. Lett. 100** (2008) p.242001.
8. CMS Collaboration, "*Search for SM Higgs boson decaying to Bottom Quarks and Produced in Association with a W or a Z Boson*", **HIG-11-012** (2011).
9. CMS Collaboration, "*The CMS experiment at the CERN LHC*", **JINST 3 S08004** (2008).
10. CMS Collaboration, "*The CMS Offline SW Guide*", https://twiki.cern.ch/twiki/bin/view/CMSPublic/SWGuide.
11. S.Agostinelli, *et al.*, "*Geant 4: A Simulation Toolkit*", **Nucl. Inst. Meth. A506** (2003), p.250.
12. CMS Collaboration, *"Public CMS Luminosity Information"*, **https://twiki.cern.ch/twiki/bin/view/CMSPublic/LumiPublicResults** (2013).
13. The CMS Collaboration, *"Search for the standard model Higgs boson decaying to bottom quarks in pp collisions at $\sqrt{s}$=7TeV"*, **CERN-PH-EP/2012-040** (2012).
14. CMS VHbb, *"Search for the standard model Higgs boson produced in association with W or Z bosons, and decaying to bottom quarks"*, **https://twiki.cern.ch/twiki/bin/view/CMSPublic/Hig12044TWiki** (2012) preliminary.
15. M.Cacciari, G.P.Salam, G.Soyez, "*The anti-*k_T *jet clustering algorithm*", **JHEP04** (2008).
16. C.Weiser, "*A Combined Secondary Vertex Based B-Tagging Algorithm in CMS*", **CERN-CMS-NOTE-2006-014** (2006).
17. CMS Collaboration, *"Particle–Flow Event Reconstruction in CMS and Performance for Jets, Taus, and E_T^{miss}"*, CMS Physics Analysis Summary **CMS-PAS-PFT-09-001** (2009).
18. A. Hoecker et al., *"TMVA - toolkit for multivariate data analysis"*, **arXiv:0703039**, (2007).
19. Particle Data Group Collaboration, *"Review of Particle Physics"*, **Phys. Rev. D 86** (2012).
20. CMS Collaboration, *"Search For Neutral MSSM Higgs Boson Production via Decays to Tau Pairs in pp Collisions at $\sqrt{s}$=7TeV"*, **CMS-PAS-HIG-10-002** (2010).
21. CMS Collaboration, *"Study of the di-tau spectrum using muon-tau and electron-tau final states with CMS detector at $\sqrt{s}$=7TeV"*, **CMS AN-2010/387** (2010).
22. J. Conway, E. K. Friis, and C. Veelken, *"Likelihood based Mass Reconstruction in Events containing Tau Leptons"*, **CMS AN AN-11-165** (2011).

Instrumentation, Metrology and Standards

Bread Baking Aroma Analysis by an Intelligent Electronic Nose System for Future Robotic Chef

K. Timsorn[1], C. Khunarak[2], P. Nipakul[1], T. Pogfay[3], and C. Wongchoosuk[1,*]

[1]*Department of Physics, Faculty of Science, Kasetsart University, Bangkok, 10900 Thailand*
[2]*Materials Science and Engineering Programme, Faculty of Science, Mahidol University, Bangkok, 10400 Thailand*
[3]*Nanoelectronics and MEMS Laboratory, National Electronics and Computer Technology Center, Klong Luang, Pathumthani, 12120 Thailand*
**Corresponding author. E-mail: Chatchawal.w@ku.ac.th*

Abstract

Electronic nose (E-nose) is an instrument that can be used to detect and distinguish volatile organic compounds (VOCs) with high accuracy and fast operating time. The E-nose can be applied to various fields such as food analysis, medicine, environmental control, and industrial processes. Combined with robot technologies (robotic chef), the E-nose may be installed and used to detect food aromas during cooking process. In this work, we have developed the E-nose for robotic chef noses. An example of application for robotic chef noses has been demonstrated in case of bread baking aromas detection. The bread baking process has been varied at four different baking temperatures of 40, 60, 80, and 100 °C and four different baking time of 5, 10, 15, and 20 minutes. The percentage changes of sensor resistance and principal component analysis (PCA) method have been employed to analyze the data. The results show that the E-nose can detect bread baking aromas and clearly classify the bread with baking process at different conditions. This study will be useful for robotic chef noses in various food quality applications in near future.

Keywords**:** E-nose, food quality control, PCA method, robotic chef

Introduction

Electronic nose (E-nose) is an olfactory sensing system that mimics mammalian nose for detection of volatile organic compounds (VOCs) [1]. Presently, E-nose systems have continually been developed to apply in different engineering and industrial areas including food quality analysis, medicine and environmental control etc. In case of food industries applications, the E-nose can be used for detecting the food spoilage [2], identifying the state of freshness [3,4] and monitoring the toxic contamination in beverage [5]. The performance of E-nose is directly related to the different responses of sensors [6]. One of the challenges for the practical food application of E-nose is to detect and distinguish food aromas during cooking processes. If this purpose can be done, the E-nose may be used as a sensing part in robotic chef.

In this work, we have constructed an E-nose and used for the detection of bread baking aromas at four different baking temperatures and four different baking times. Eight metal oxide semiconductor gas sensors were used as sensing part of the E-nose Percentage changes of sensor responses and principal component analysis (PCA) method have been employed to analyze the data.

Materials and Methods

Bread baking preparation

Fresh bread purchased from a market in Bangkok was baked at four different baking temperatures; 40, 60, 80 and 100 ºC, and four different baking times; 5, 10, 15 and 20 minutes. Then, the baked bread was cut into samples with weight about 1-2 g. The samples were placed in the sample bottle for E-nose analysis.

E-nose system

The schematic diagram of E-nose system is shown in Fig. 1. It consists of three main components; (I) valves and air pump with mass flow controller,(II) sensor array, and (III) data acquisition (DAQ) & computer. For sensor array, the eight commercial Taguchi gas sensors (TGS) were used as sensing part as listed in Table 1.

Starting, a pump will suck clean air into a mass flow controller. The mass flow controller was used to control air flow rate. In this experiment, the air flow rate was set at 2 L/min. The solenoid valves were used to select the path of aroma molecule delivery. The zero air in the reference bottle was sucked into sensor array chamber for 5 minutes in order to be a reference line and clear bread baking aromas in sensor chamber. When the sensor responses reached to the resistance baseline, valve 2 was closed and valve 3 was opened. Bread baking aromas in the sample bottle were sucked into sensor array for 1 minute. Then, the resistances of sensors were recorded every 1 minute as a function of time via DAQ for subsequent analysis.

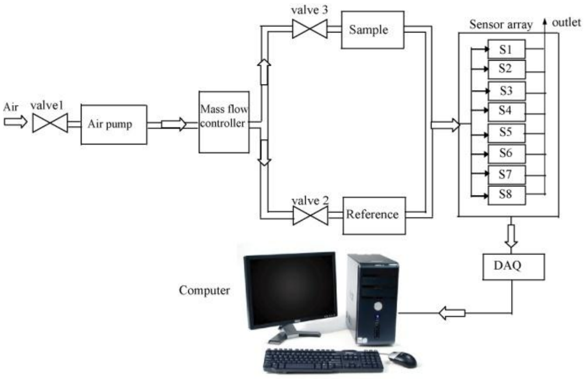

Figure 1. Schematic diagram of E-nose system.

Table 1: Lists of sensor array

Sensor number	Sensor name	Sensing type
S1	TGS 821	Hydrogen
S2	TGS 822	Organic Solvent Vapors
S3	TGS 825	Hydrogen Sulfide
S4	TGS 826	Ammonia
S5	TGS 2600	Air Contaminants
S6	TGS 2602	Air Contaminants
S7	TGS 2610	LP gas
S8	TGS 2620	Solvent Vapors

Principal component analysis (PCA)

The principal component analysis (PCA) [7,8] was employed for recognition and discrimination of bread baking aromas from measurements of the E-nose system. In principles, PCA process contains five following steps: (I) Get data from matrix, (II) Normalize the data matrix by the mean subtraction, (III) Calculate the covariance matrix, and determine eigenvectors and eigenvalues of the covariance matrix. The calculated eigenvectors must be unit eigenvectors. (IV) Rearrange the eigenvectors and eigenvalues. The eigenvectors are ordered by eigenvalues from highest to lowest. And (V) Obtain the PCA result by matrix multiplication and transpose. The obtained new dataset with orthogonal linear transformation are usually plotted in two or three dimensions containing the most relevant of the data set.

Results and Discussion

The resistance changes of each sensor are displayed in Fig. 2. We can be seen that these curves differ from each other in the form of curve shapes and maximum value of resistance changes depending on the type of each sensor. This result shows that all sensors are sensitive to bread baking aromas. The resistances of all sensors decrease when the bread baking aromas are introduced into sensor chamber. It implies that most deoxidizing gases can emit from the bread baking.

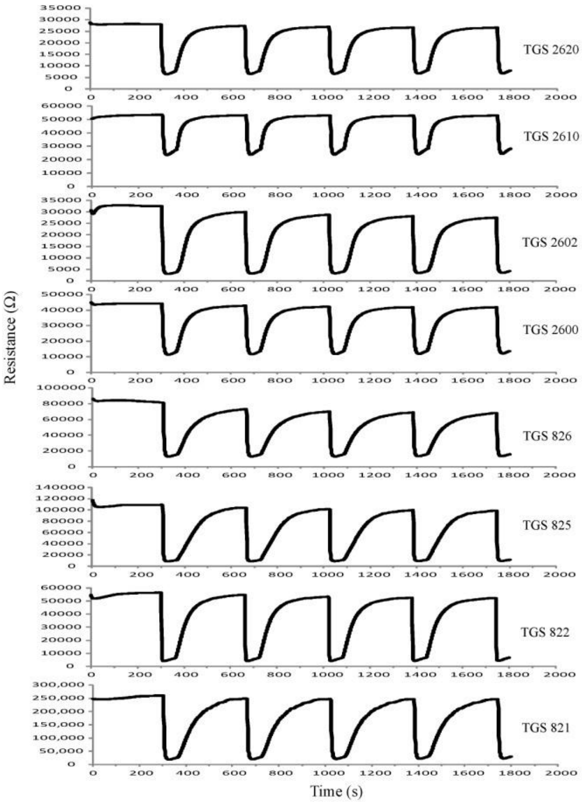

Figure 2. Resistance changes of each sensor as a function of time.

The percentages of sensor responses can be obtained from following equation;

$$\text{Sensor reponse (\%)} = \frac{R_0 - R_{Sens}}{R_0} \times 100 \qquad (1)$$

where R_0 is the value of resistance baseline and R_{Sens} is the value of sensitive resistance.

Fig. 3 shows the three dimensional plot of the percentages of sensor responses at different baking temperatures for baking time of 15 min. We can obviously observe that all sensors exhibit high response to the bread baking aromas in the range of

60-95% at all baking temperatures. At baking temperature of 60 ºC, all sensors show the highest response. It refers that more VOCs can emits at this temperature. If baking temperature is so high, some VOCs can be lost.

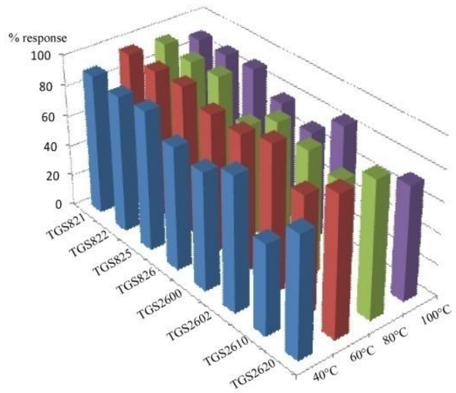

Figure 3. 3D plot of the percentages of sensor response at different baking temperatures.

All data sets were introduced into PCA. Fig. 4 shows the PCA plot of bread baking aromas at different baking temperatures. It can be observed that the PCA plot clearly discriminates the bread baking aromas to four clusters related to different baking temperatures and time. The best result occurs at baking time of 15 min. From results, it suggests that baking time of 15 min can well generate the unique pattern of bread baking aromas at a function of baking temperatures.

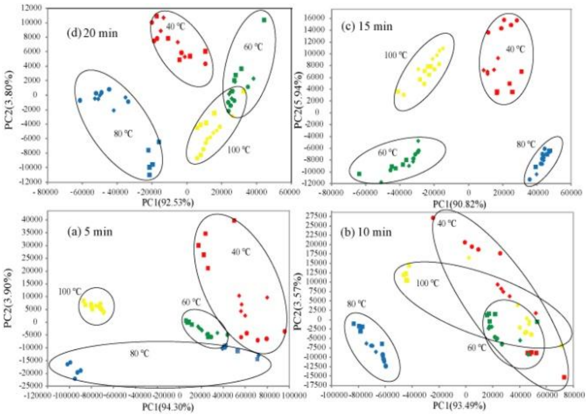

Figure 4. PCA plot of bread baking aromas at (a) 5 min, (b) 10 min, (c) 15 min, and (d) 20 min of baking time with different baking temperatures.

Conclusions

In this work, an E-nose has been developed for food application during cooking processes. An example has been demonstrated in term of bread baking aromas detection and classification. The TGS sensor array shows high response to bread baking aromas in the range of 60-95%. With condition of bread baking time at 15 min and baking temperature of 60 ºC, the bread product can generate a unique pattern of aroma. Combined with PCA method, our E-nose can classify bread baking aromas at the different bread baking conditions. It is hoped that our E-nose will be installed in robotic chef for real-time monitoring food aroma during cooking processes in near future.

Acknowledgments

Preproposal Research Fund (PRF) from Faculty of Science, Kasetsart University and TRF-CHE-KU Research Grant for New Scholar (MRG 5580229) are gratefully acknowledged for supports of this research.

References

1. S. Sankaran, L. R. Khot and S. Panigrahi, “Biology and Application of Olfactory Sensing System: A Review”, Sensors and Actuators B: Chemical **171-172** (2012) 1-17.
2. I.A. Casalinuovo, D. D. Pierro, M. Coletta and P. D. Francesco, "Application of Electronic Noses for Disease Diagnosis and Food Spoilage Detection", Sensors **6** (2006) 1428-1439.
3. N. E. Barbri, A. Amari, M. Vinaixa, B. Bouchikhi, X. Correig, E. Llobet, "Building of a metal oxide gas sensor-based electronic nose to assess the freshness of sardines under cold storage", Sensors and Actuators B: Chemical **128** (2007) 235–244.
4. H. Guohua, W. Yuling, Y. Dandan, D. Wenwen, Z. Linshan and W. Lvye, “Study of Peach Fressness Predictive Method Based on Electronic Nose”, Food Control **28** (2012) 25-32.
5. C. Wongchoosuk, A. Wisitsoraat, A. Tuantranont, T. Kerdcharoen, “Portable electronic nose based on carbon nanotube-SnO$_2$ gas sensors and its application for detection of methanol contamination in whiskeys, Sensors and Actuators B: Chemical 147 (2010) 392-399.
6. A. Ponzoni, A. Depari, M. Falasconi, E. Comini, A. Flammini, D. Marioli, A. Taroni and G. Sberveg, “Bread Baking Aromas Detection by Low-Cost Electronic Nose”, Sensors and Actuators B **130** (2008) 100-104.
7. H. Yu, J. Wang, H. Xiao and M. Liu, “Quality Grade Identification of Green Tea Using The Eigen Values of PCA Based on The E-Nose Signals”, Sensors and Actuators B **140** (2009) 378-382.
8. S. Capone, M. Epifani, F. Quaranta, P. Siciliano, A. Taurino and L. Vasanelli, “Monitoring of Rancidity of Milk by Means of An Electronic Nose and A Dynamic PCA Analysis”, Sensors and Actuators B **78** (2001) 174-179.

Determination of Size of Source Effect for 650nm Standard Radiation Thermometer with Indirect Method at National Institute Metrology (Thailand)

N. Noulkhow*

Radiation Thermometry Laboratory, Thermometry Metrology Department,
National Institute of Metrology (Thailand), Pathumthani, 12120 Thailand
**Corresponding author. E-mail: narudom@nimt.or.th*

Abstract

A 650nm standard radiation thermometer is used as the standard thermometer for the calibration of radiance temperature in the temperature range of 960 °C to 2 500 °C by comparison method at the radiation thermometry Laboratory in National Institute of Metrology (Thailand), NIMT. However, due to the scattering and diffraction from the radiation within the imperfection of the field of view (FOV) defined optical system of the radiation thermometer, the sized of source effect (SSE) is shown to be the systematic error in the calibration. Therefore, the SSE has to be determined for more accurate calibration results. A new facility for the SSE determination of the radiation thermometer with an indirect method was developed this work. In-house made acrylic black spot sheets are used as the obscured black spots while an integrating sphere illuminated by two halogen lamps has been used as the radiation source for this method. Therefore, the SSE is determined from the changing of output signals from the radiation thermometer when the sizes of obscured black spots in front of the radiation source are varied. The. The results from these determinations show an agreement with the SSE determination by the indirect method from National Metrology Institute of Japan (NMIJ).

Keywords: size of source effect (SSE), standard radiation thermometer, indirect method, integrating sphere, National Institute of Metrology (Thailand

Introduction

At the radiation thermometry laboratory in NIMT, the 650 nm Standard Radiation Thermometer has been used as the standard thermometer for the calibration of a radiation thermometer in the high temperature range of 960 °C to 2 500 °C by comparison method using the variable temperature blackbodies (VBBs) with the cavity aperture size of 50 mm and 25 mm. However, the temperature scale of this standard radiation thermometer was realized by silver and copper fixed point blackbodies which have the cavity aperture size only 6 mm. Although the temperatures of the VBBs are set at the same temperature of the fixed point blackbodies, the temperature readings from the 650 nm standard radiation thermometer can be different due to the variation of the radiation temperature source sizes. This phenomenon is called “Size-of-Source Effect”, and affects to the accuracy of the radiation thermometer calibration.

There are three methods for the determination SSE[1], i.e., a direct method[2], an indirect method[2] and a scanning method[3]. In the previous work at NIMT, the SSE of the 650 nm standard radiation thermometer has been investigated by the direct method using an integrating sphere illuminated with halogen lamp as the radiation temperature source and the monitor detector for correction of the measurement signal. The results show the agreement between the results determined by direct method in NIMT and results from the determination by indirect method in National Metrology Institute of Japan (NMIJ), however the different is still 0.08%[4]. Due to the existing of the instruments in laboratory, the SSE determination by the indirect method is employed in this work in order to improve the results. The integrating sphere with halogen lamps is still used as the radiation temperature source and a series of black spot sheets are additional used in this work.

Materials and Methods

The SSE determination by the indirect method in this work has been done by obtain the changing of output signals from the 650 nm standard radiation thermometer when the sizes of obscured black spots in front of the radiation source are varied. The new series of in-house made acrylic black spot sheets are used as the obscured black spots in this work with the diameters of 6 mm, 9 mm, 12 mm, 18 mm, 25 mm, 36 mm, 48 mm, and 60 mm respectively. These are almost the same sizes as the black spots used for the SSE determination at NMIJ (NMIJ used the 72 mm black spot instead of 60 mm black spot). The SSE is obtained at the distances between the standard radiation thermometer and the radiation temperature source are 49 cm and 70 cm similar to the SSE determination distances at NMIJ. The 9.75 inches PTFE integrating sphere with the circular exit opening of 3 inche illuminated with two 250 watt halogen lamps has been used as the radiation temperature source. A precision DC power supply is used for the precision control of the power supply for both halogen lamps and two DC ventilators are used as cooling system for the halogen lamps.

The 650 nm standard radiation thermometer has been mounted on a set of slide table that allow precisely move of the standard thermometer in X, Y, and Z axes. With this set of the slide table the distance between the 650 nm standard radiation and the radiation temperature source can be varied from 49 cm to 70 cm and the optical axis of 650 nm standard radiation is still the same along the variation.

Two nanovoltsmeters are used for reading the output signals from the 650 nm standard radiation thermometer and monitoring the stability of the detector temperature inside the 650 nm standard radiation thermometer. The output signals and the detector temperature of this standard radiation thermometer are recorded by a computer with a LabVIEW program.

The schematic diagram and the photography of the setting up of the SSE determination in this work are illustrated in figure 1 and figure 2 respectively.

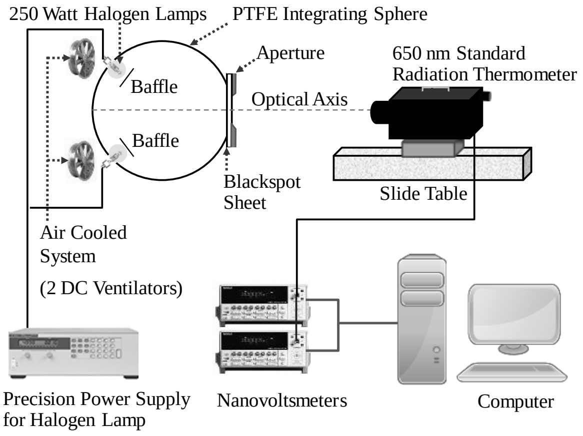

Figure 1. The schematic diagram of the setting up of the SSE determination by indirect method using in this work

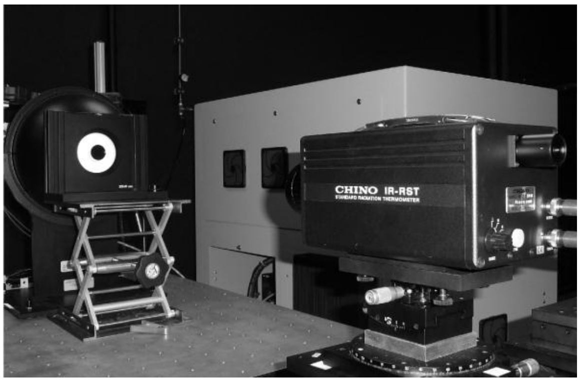

Figure 2. The photography of the setting up of the SSE determination by indirect method using in this work

The SSE determination by the indirect method for the aperture diameter d compared to the reference diameter d_{ref}, $SSE(d,d_{\mathrm{ref}})$, is defined as the ratio of the signal of the black spot (V_{black}) and the bright area (V_{bright}) between the aperture and the black spot[5], given below.

$$SSE\left(d,d_{ref}\right)=\frac{V_{Black}}{V_{Bright}} \qquad (1)$$

The image of the aperture, the bright are and the black spot for the SSE determination by indirect method is shown in figure 3.

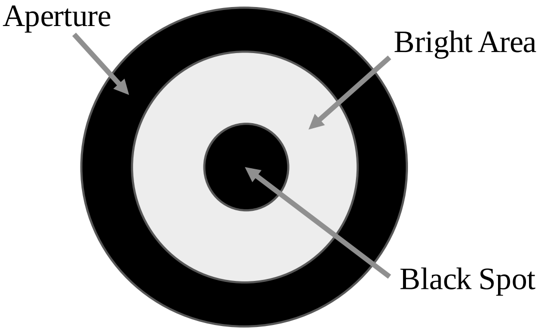

Figure 3. The target image including the aperture and black spot of the SSE determination by indirect method.

The diameter of the black spot is d and was varied from the smallest diameter size of 6 mm to the largest diameter size of 60 mm. The diameter of the bright is 70 mm (the 70 mm diameter aperture is applied), while the reference diameter d_{ref} is 6 mm. The SSE can be obtain as following equation,

$$\begin{aligned} SSE\left(d,d_{ref}\right) &= SSE\left(70,d_{ref}\right)-SSE\left(70,d\right) \\ &= SSE\left(70,6\right)-SSE\left(70,d\right) \qquad (2) \end{aligned}$$

Results and Discussion

The SSE determinations by the indirect method in this work have been done at the temperature of the radiance temperature source is approximately 1 085 ^{o}C corresponding to the freezing of copper therefore the 650 nm standard radiation thermometer can detect the real signal from the measurement. The SSE are determined at the aperture size of 70 mm and the reference black spot size of 6 mm with the variation of the black spot diameter size, the SSE can be obtained at SSE(6,6), SSE(9,6), SSE(12,6), SSE(18,6), SSE(25,6), SSE(36,6), SSE(48,6) and SSE(60,6) which are the SSE when the diameter of the radiance temperature source has been changed from 6 mm to 6 mm, 9 mm, 12 mm, 18 mm, 25 mm, 36 mm, 48 mm and 60 mm, respectively. The results of the SSE determinations by the indirect method at NIMT while the distance between the radiance temperature source and the standard radiation thermometer have been set at 49 cm and 70 cm are presented in Table 1.

Table 1: The SSE determination by the indirect method in NIMT at the measurement distance of 49 cm and 70 cm.

Size of Source	SSE at the measurement distance of	
	49 cm	70 cm
6 mm	0.000%	0.000%
9 mm	0.023%	0.032%
12 mm	0.032%	0.042%
18 mm	0.048%	0.069%
25 mm	0.057%	0.076%
36 mm	0.065%	0.082%
48 mm	0.075%	0.091%
60 mm	0.076%	0.102%

The results of the SSE determination in previous work has been shown in the figure 4 while the comparison of the SSE determination results by the direct method in the previous work with the result determined by the indirect method in this work is illustrated in the figure 5. The results show that the trend of the SSE from the determinations by the difference method are going in almost same way. However the values of the SSE are shown to be significantly different. Moreover, the results of the SSE determination by the indirect method in this work compared with the results of the SSE obtained by the indirect method at NMIJ are given in the figure 6.

Although the results from the SSE determination by direct method in previous work trend to be similar with the result of SSE obtained with the indirect method in this work and at NMIJ (see the figure 4 and figure 5), the results from the figure 6 show a better agreement of the SSE determination by the indirect method from NIMT and NMIJ.

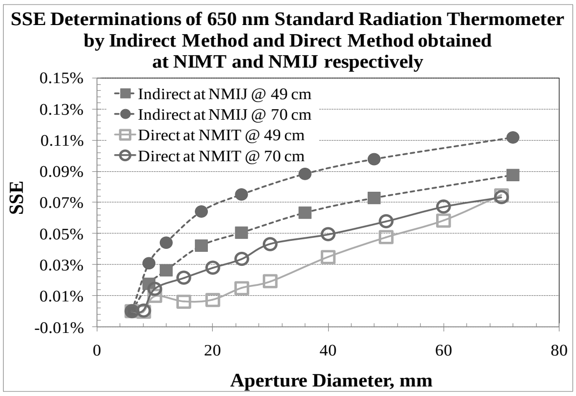

Figure 4. SSE determination results of the 650 nm standard radiation thermometer. The solid line series are the SSE determined by the direct method at NMIT and the dot line series are the SSE measured by the indirect method at NIMJ

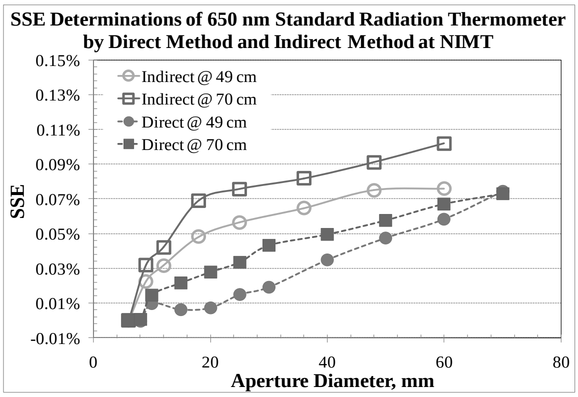

Figure 5. SSE determination results of the 650 nm standard radiation thermometer measured at NIMT. The dot line series are the SSE obtained with the direct method in previous work while the solid line series are the SSE determined by the indirect method in this work.

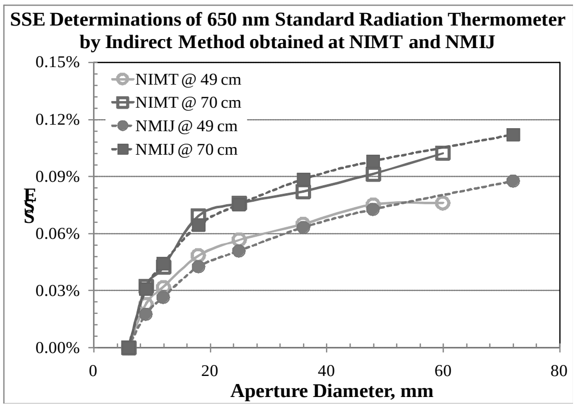

Figure 6. SSE determination results of the 650 nm standard radiation thermometer obtained with indirect method. The solid line series are the SSE determined

at NIMT in this work when the dot line series are the SSE measured at NMIJ.

The results of the SSE determination in this work do not only have the same tendency as the SSE results measured at NMIJ but also show the close proximity from both the measurement results.

Conclusions

The results from the SSE determination by indirect method in this work show a very good agreement with the SSE determination results obtained at NMIJ with the same method. Although the calibration facility and staff are different, the results from the SSE determination of the same standard radiation thermometer are shown that the different are within 0.008% which are 10 times better than the results from the previous work. This new facility for the SSE determination by the indirect method will be used for investigated the SSE of other standard radiation thermometers calibrated at NIMT.

Acknowledgments

First of all, I would like to thank Mr. Rattapon Kongchana for the construction of the black spot sheet set. Many thank to Dr. Sakda Somkun for the fruitful discussion in this paper. For the data recording, the LabView Program from Mr. Phichet Wongnut is very helpful for this work. Finally, a special thank to Mr. Uthai Norranim for his support and comments.

References

1. F. Sakuma, L. Ma , "Uncertainty estimation of Size-of-Source Effect measurement for 650 nm Radiation Thermometers" XIX IMEKO World Congress, 1481-1486, 2009
2. G. Machin, R. Sergienko, "A Comparative Study of Size-of-Source Effect (SSE) Determination Techniques" Proc. of TEMPMEKO '01, Vol. 8, 155-160, 2001
3. M. Bart, E. W. M. van der Ham. and P. Saunders, "A New Method to Determine the Size-of-Source Effect" Int. J Thermophys. Vol.28 2111–2117, 2007
4. N. Noulkhow, "Size-of-Source Effect determination for 650 nm standard radiation thermometer by direct method", 38th Congress on Science and Technology of Thailand (Full paper), B_B0042, 2012.
5. L. Ma and F. Sakuma, "Improvement of Size of Source Effect Measurement of Standard Radiation Thermometers", SICE Annual Conference 2007,1743-1748, 200

Developing Magneto–optical Kerr Effect Measurement Setup by using a Home–made Electromagnet and a Moving Permanent Magnet for Investigating the Magnetic Properties of Nickel and Metal–Phthalocyanine Films

P. Srisawet*, A. Sinsarp, K. Tivakornsasithorn, and T. Osotchan

Department of Physics, Faculty of Science, Mahidol University, 272 Rama VI Road, Ratchatathewi Bangkok 10400, Thailand
**Corresponding author. E-mail: lukgolf_g1@hotmail.com*

Abstract

The interaction between polarized light on magnetized media under external magnetic field can be investigated by magneto-optical Kerr effect (MOKE). In this work, we study the polar and longitudinal MOKE measurements by using either home–made electromagnet or movable permanent magnet for generating an external applied magnetic field. The external magnetic fields are applied ether perpendicular or parallel to thin film samples. The home–made electromagnet is constructed with coil diameter and length of 8.6 and 9.1 cm, respectively, using copper wire with 4,500 turns and the measured coil resistance equals 70.4 Ω. The magnetic field strength can reach 1,110 Gauss at the applied current of 2.84 A. For another type of applied magnetic field, a 5x5x2 cm^3 NdFeB permanent magnet with the magnetic field strength of 1,700 Gauss (measured at 10 mm far from the magnet surface) is also used. This magnetic field can be varied by movable this permanent magnet utilizing a stepping motor. The MOKE measurement setup consists of a low-cost diode laser at wavelength of 654 nm, two polarizers, a photoelastic modulator (PEM), a lock–in amplifier and a photo-detector. The linear polarized light reflected from the surface of the sample is modulated by PEM with λ/4 retardation at frequency of 42 kHz. The nickel thin film prepared by electro-deposition technique is used to examine MOKE under two types of magnetic sources. We observe the MOKE of the nickel thin film in both types of magnetic source. One of disadvantage of using the electromagnet is the generated heat at high current while the lack of field uniformity and vibration from moving motor are those for permanent magnet. The MOKE results are confirmed by our home-built vibrating sample magnetometer in both of in – plane and out of plane directions. These results indicate that the saturated field and coercive field occur at about 600 and 170 Gauss, respectively for out of plane mode while for in–plane mode the magnetization is not saturated at our maximum field of 1,500 Gauss. The MOKE setup has been developed to investigate the magnetic properties of metal phthalocyanine films such as, NiTsPc, FeTsPc, CuPc, etc.

***Keywords*:** Magneto-optical Kerr effect (MOKE), electromagnet, permanent magnet

Introduction

The interaction between polarized light and magnetized media under external magnetic field can be investigated by magneto-optical Kerr effect (MOKE). The MOKE was first observed by John Kerr in 1877 [1-2]. The plane of polarization of light reflected from sample is rotated due to the interaction with the magnetization of the sample. The amount of rotation, called Kerr rotation, is proportional to the magnetization of the sample.

Three different geometries in MOKE experiment setup are shown in Figure 1. For polar mode (P-MOKE), the applied magnetic field is parallel to the plane of incidence and normal to the sample surface. For longitudinal mode (L–MOKE), the applied magnetic field is parallel to both the plane of incidence and the sample surface. For transverse mode (T–MOKE), the applied magnetic field is normal to the plane of incidence and parallel to the sample surface.

The MOKE setup is a very useful technique for investigating the magnetic properties of thin film of various materials such as metals and organic compounds. In this work, the generating magnetic field for MOKE technique is designed by using a home-made electromagnet and a movable permanent magnet for studying magnetic materials.

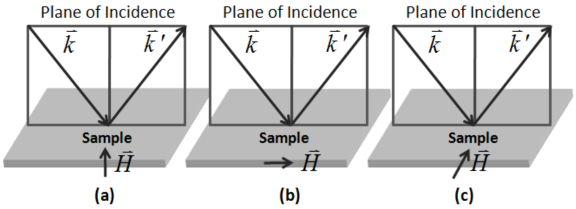

Figure 1. Three geometries of MOKE measurements: (a) polar, (b) longitudinal and (c) transverse modes.

The application of MOKE to study surface magnetism was introduced by E.R. Moog and S.D. Barder in 1985 by surface magneto-optical Kerr effect (SMOKE) [3]. The first system was used to study ultrathin Fe film growth on Au(100) substrates. The magnetic properties of organic thin films have been investigated by magnetic circular dichroism (MCD) and magneto-optical Kerr effect (MOKE) techniques [2-3]. The films of metal phthalocyanine (MPc, M = Ni, Fe, Co and Mn) are one of those films with wide interest. A MPc molecule consists of a metal atom M as a center of the molecule surrounded by a ring structure composed of nitrogen, carbon and hydrogen [5]. The MPc thin films have been extensively investigated theoretically and experimentally due to their potential applications in future electronics, such as gas sensor devices [4] and data-storage devices [6].

In this work, we develop the MOKE measurement apparatus with polar and longitudinal modes using either a home–made electromagnet or a movable permanent magnet as an external magnetic field generator. The MOKE setup has been developed to investigate the magnetic properties of both metal and organic thin films.

Materials and Methods

Nickel and FePc thin films are used as samples during the development of the MOKE setup. Nickel thin films are prepared by electro-deposition technique. The FePc thin films are fabricated using layer by layer (LBL) technique [7].

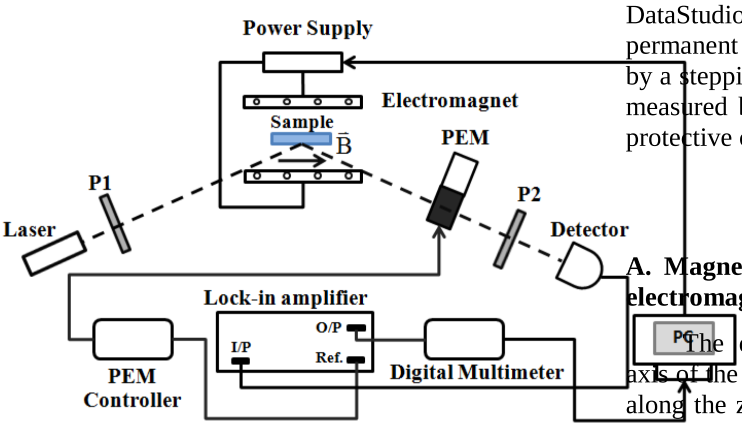

Figure 2. Schematic diagram setup for longitudinal MOKE measurement.

The schematic diagram of the MOKE measurement setup with longitudinal mode is shown in Figure 2. A diode laser is use as a light source with the wavelength of 654 nm and the power of 1 mW. The light beam is linearly polarized by polarizer P1, reaches and reflected from the sample, passes through a photoelastic modulator (PEM-90^{TM} model, Hinds Instrument, Inc.) and polarizer P2, respectively, and finally reaches a detector (DET210 high speed silicon detector, Thorlab, Inc.). The PEM modulates the light beam with λ/4 retardation at the frequency of 42 kHz. The signal detected by the detector is connected to a lock-in amplifier (5610B two phase Lock –in Amplifier, NF Corporation), which is using the reference signal from the PEM controller. The orientation of the magnet can be changed between applying the magnetic parallel to the film for longitudinal mode and perpendicular to the film for polar mode.

The calculation of the Kerr signal, θ_K , is based on the previous study in reference 3. The optic axis of the analyzing polarizer P2 is rotated to the orientation which the minimum intensity of light detected by the detector, then rotated more by a small angle δ (5° or 8°) then fixed. The Kerr signal is then given by

$$\theta_K = \frac{\delta}{2}\frac{I - I_0}{I_0} \qquad (1)$$

where I and I_0 are the intensities with and without applied magnetic field, respectively.

The home–made electromagnet is a coil with 4,500 turns of copper wire. The coil dimensions are 8.6 cm in diameter and 9.1 cm in length. The electrical resistance of the coil is measured to be 70.4 Ω. The magnetic field strength of the home-made electromagnet is measured using a magnetic field sensor (CI-6510A model, PACSO scientific). The sensor was connected directly to an analog channel on the ScienceWorkshop 500 interface (CI-6400 model, PACSO scientific) and controlled with a computer via DataStudio program. The position of the NdFeB permanent magnet (size of 5x5x2 cm^3) is controlled by a stepping motor and the magnetic field strength is measured by a Hall probe (13610.02 tangential with protective cap model, PHYWE Systeme GmbH).

Results and Discussion

A. Magnetic field distribution of the home-made electromagnet

The distribution of component along the coil axis of the magnetic field as a function of the position along the z- axis of our home-made electromagnet is shown in Figure 3. The magnetic field strength is not uniform along the coil axis. However, the uniformity is better around the center of the coil than the around the edges. The magnetic field strength is controlled by an electrical d.c. power supply. The maximum voltage of 200 V can be applied to the coil generating the current of 2.84 A, resulting in the maximum magnetic field strength of 110 and 50 mT at the center and the edge of the coil, respectively.

The stability of the magnetic field strength generated by the coil was investigated. The magnetic field strength at the center of the coil produced from using the maximum applied voltage of 200 V decreases linearly from 110 mT to 98 mT after operating for 10 minutes. It is considered due to the decrease of applied current from the increase of the resistance of the coil resulted from the heat generated.

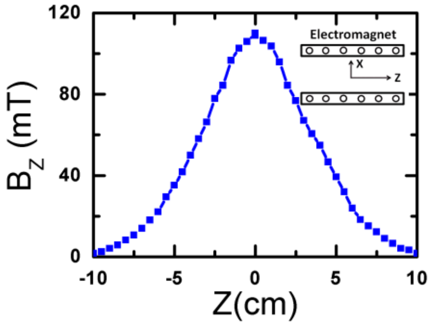

Figure 3. Magnetic field distribution along z-axis of home-made electromagnet.

B. Magnetic field distribution of the movable permanent magnet

The magnetic field strength distributions of a movable permanent magnet are shown in Figure 4. Figures 4 (a) and 4 (b) shows the contour plots of the magnetic field strength components perpendicular to the surface and parallel to the surface, respectively, near the surface (z = 2 mm) of the permanent magnet In the area near the center of the magnet, the magnetic field component perpendicular to the magnet surface is dominated and the uniformity of the magnetic field strength is moderated. In the area near the edges of the magnet, the magnetic field is non-uniform.

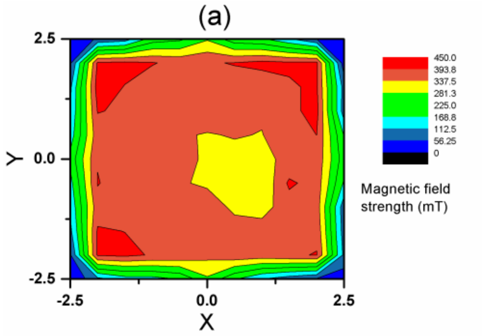

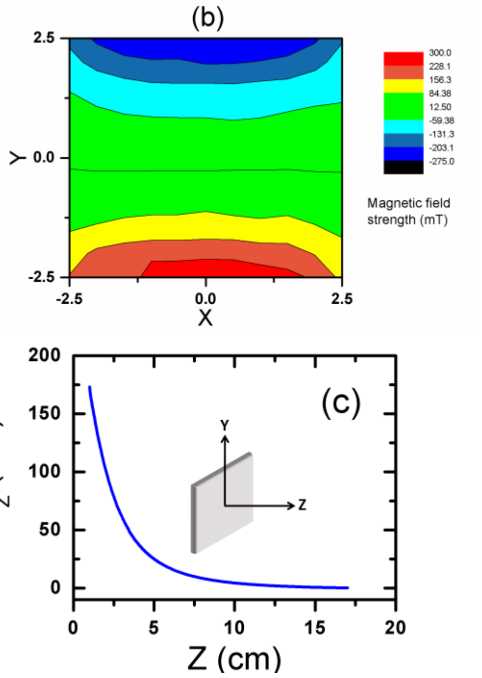

Figure 4. Two-dimensional contour plot of magnetic field (a) perpendicular (b) parallel to magnet surface and (c) magnetic field distribution as a function of z distance from permanent magnet.

Figure 4 (c) shows the dependence of the perpendicular to the surface component of the magnetic field strength on the distance *z* from the magnet surface. This relation is used as a calibration of the magnetic field strength applied to the sample during the MOKE measurement.

C. Magneto-optical Kerr effect of nickel and MPc thin films

The Kerr signals of electrodeposited Ni thin film under applied magnetic field are shown in Figure 5. For MOKE measured in the longitudinal mode using the home-made electromagnet, as shown in Figure 5(a), the Kerr signal increases linearly with magnetic field. The Kerr signal is not saturated at our maximum applied magnetic field of 110 mT. In addition, the result of the second scan (L2) slightly shifts from the first scan (L1). It is considered to be due to the shift of actual magnetic field strength from the calibration due to heat generated during the scan.

For MOKE measured in the polar mode using a movable permanent magnet, as shown in Figure 5(b), the Kerr signal of electrodeposited Ni thin film

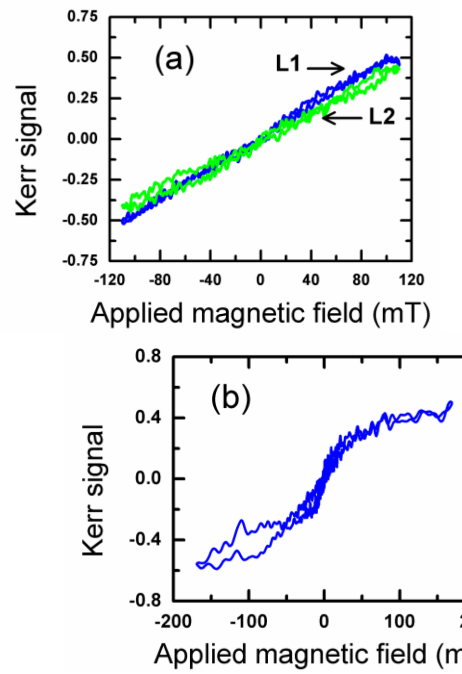

Figure 5. Kerr signals of electrodeposited Ni thin film for; (a) longitudinal mode by home-made electromagnet and (b) polar mode by a moving permanent magnet.

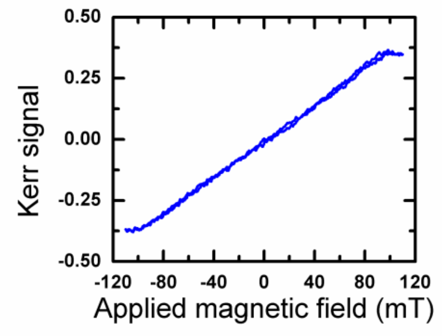

Figure 6. Kerr signal of FePc thin film in longitudinal mode.

increase with magnetic field. The slope of the curve decrease gradually with magnetic field indicating the tendency to be saturated of the magnetization of the film under the magnetic field. The results imply that the magnetic easy axis of the Ni films is out-of-plane. This is in agreement with that films energetically prefer growing along the [111] direction of the bulk nickel and this direction is the magnetic easy axis of the bulk nickel. However, the results are very noisy. It is considered to be due to the vibration of the system from the movement of the permanent magnet during the measurement.

The Kerr signal of FePc thin film measured in longitudinal mode using a home-made electromagnet is shown in Figure 6. The Kerr signal increases linearly with magnetic field. In general, organic materials are not magnetic materials. Very small magnetic properties are induced by week magnetic field as in our study. The result indicates that our MOKE setup is sensitive enough to measure the magnetic properties of organic thin films.

Conclusions

We developed the MOKE measurement setup using a home-made electromagnet and a movable permanent magnet. The system is sensitive enough to measure the magnetic properties of the metal and organic thin films. The magnetic field strength of the home-made electromagnet is more uniform than that of the permanent magnet. Disadvantage of using the home-made electromagnet is the heat generated at high current while the lack of field uniformity and vibration from moving drive are disadvantages of the permanent magnet.

Acknowledgments

This work was partially supported by National Nanotechnology Center, National Science and Technology Development Agency, Mahidol University.

References

1. J. L, Erskine and E. A. Stern, "Magneto-optic Kerr Effect in Ni, Co, and Fe", Physical Review Letter **30** (1973), 1329.
2. S. D. Bader and E. R. Moog, “Magnetic properties of novel epitaxial films”, Journal of Applied Physics. **61** (1987), 3729.
3. Z. Q. Qui, and S. D. Bader, “Surface magneto-optic Kerr effect”, Review of Scientific Instruments **71** (2000), 1243.
4. J. J. R. Hampton, J-L M-Albertos, and H. D. Abruña, “Development of a versatile SMOKE system with electrochemical Applications”, Review of Scientific Instruments **73** (2002), 3108.
5. M. Fronk, B. Bräuer, J. Kortus, O. G. Schmidt, D. R. T. Zahn, and G. Salvan, “Determination of the Voigt constant of phthalocyanines by magneto-optical Kerr-effect spectroscopy”, Physical Review B **79** (2009), 235305.
6. J.S. Tsay, H.Y. Nieh , Y.D. Yao, Y.T. Chen, W.C. Cheng, “Magnetic phases of Co/Ge(1 1 1) studied using surface magneto-optic Kerr effect”, Surface Science **566–568** (2004), 226–230.
7. A. Thangprasert, P. Pasitsuparoad, A. Dangtip S. and T. Osotchan, “Electrochemical Detection of Dopamine by Electrostatic Self-Assembly Nanostructure Electrode of Nickel Tetrasulfonated Phthalocyanine”, FAOBMB Congress 2012, Bangkok, Thailand.

Rotary Encoder Calibration System

W. Samit[1,*], K. Vacharanukul[2], T. Watanabe[3], and T. KaewKongka[1]

[1] *Department of Physics, Faculty of Science, Chulalongkorn University, Bangkok 10330, Thailand*
[2]*Dimensional Department, National Institute of Metrology (Thailand), Pathumthani 12120, Thailand*
[3]*Dimensional Department, AIST Tsukuba Central 3, Umezono 1-1-1 Tsukuba Ibaraki 305-8563, Japan*
**Corresponding author. e-mail: watcharin@nimt.or.th*

Abstract

Rotary encoder is an angle measuring instrument. It is widely used in various instruments and machines especially in the industrial segment such as printers, CNC machines, theodolites and servo motors. At the moment, rotary encoder cannot be evaluated in Thailand because there is no approved calibration system. This leads to a questionable performance of the encoder in the instruments and machines. We have developed the self-calibration angle system to solve this problem. It consists of three rotary encoders arranging in specific configuration. The measurement principle of a rotary encoder (figure 1) is based on the Equal-Division-Averaged (EDA) Method. The system provides the uncertainty of measurement of 0.15 arc second. The system can be used to validate and to evaluate rotary encoders.

***Keywords*:** Self-calibration, rotary encoder, angle standard

Introduction

We developed rotary encoder calibration system for various purposes in angle metrology instruments. This calibration system can self calibrate with accuracy about 0.15 arc second and more useful when compare the old model which stalled in angular laboratory, National Institute of Metrology (Thailand).

Materials and Methods

Principle of multi combination encoder, SelfA

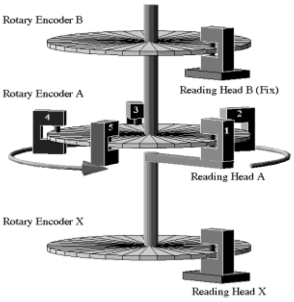

Figure 1. Diagram of self-calibration angle system

Several sensors are setting around the one scale disc with the same interval. One of sensor is chosen main head, A_1. When the scale rotate one revolution angle signal deviation between main head, A_1 and other head, A_j carried out be $\delta_{i,(1,j)}$. Where i ($i = 1,2,\ldots, N_G$) represent graduation line number, N_G is total graduation line on scale disc. j ($j = 1,2,\ldots, N_H$) represent sensor head number, N_H is total number of sensor heads.

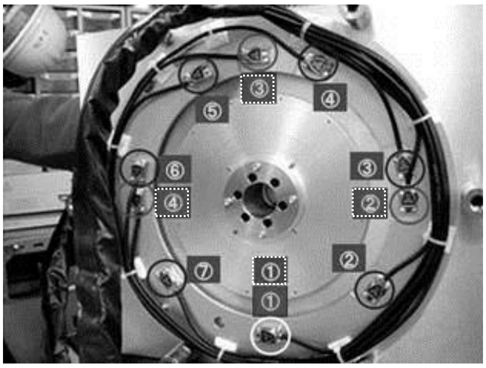

Figure 2. Diagram of SelfA

Table 1: Compare Specification between self-calibration angle system and SelfA

Specification	**Self-Calibration Angle System**	**SelfA**
Accuracy	0.05″	0.15″
Encoder Plate	3	1
Reading Head	7	10
Measuring Axis	Vertical	Vertical & Horizontal

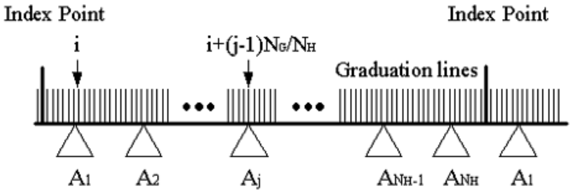

Figure 2. Position relation between a rotary encoder scale and sensor heads of self-calibration rotary encoder

When main head, A_i detect the scale i at the same time another sensor head, A_j detect scale $i+(j-1)N_G/N_H$ angle deviation between two position represent $\delta_{i,(1,j)}$ can be written as follows:

$$\delta_{i(1,j)} = a_i - a_{i+(j-1)N_G/N_H} \qquad (1)$$

The average of angle deviation, μ_i between each sensor, j from sensor head, i can be express with the following formula

$$\mu_i = \frac{1}{N_H}\sum_{j=1}^{N_H}\delta_{i(1,j)} = a_i - \frac{1}{N_H}\sum_{j=1}^{N_H} a_{i+(j-1)N_G/N_H} \qquad (2)$$

From the law of fourier series we can prove by mathematic about arbitrary periodic curve,
"An arbitrary periodic curve of 2π can be expressed by the Fourier series, and when n-number of curves with a phase shift of 2π/n at a time are averaged, the averaged curve shows the sum of an integral multiple of n-order Fourier components of the original curve."

Following this law the average of angle deviation, μ_i is calibration curve of rotary encoder but in equation(2) not include N_H order of fourier component, $\frac{1}{N_H}\sum_{j=1}^{N_H} a_{i+(j-1)N_G/N_H}$

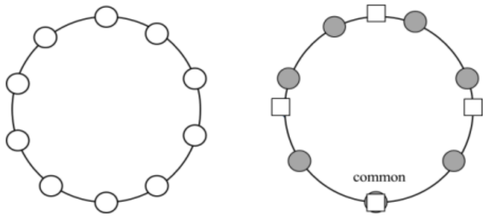

Figure 3. Multi-combination between 4 sensors set and 7 sensors set of selfA system

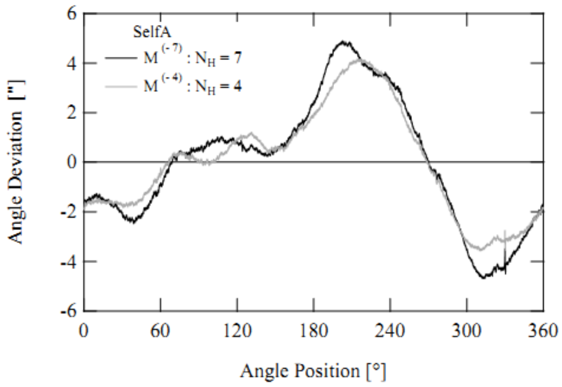

Figure 4. Self calibration result of 4 sensors set, $M^{(-4)}$ and 7 sensors set, $M^{(-7)}$

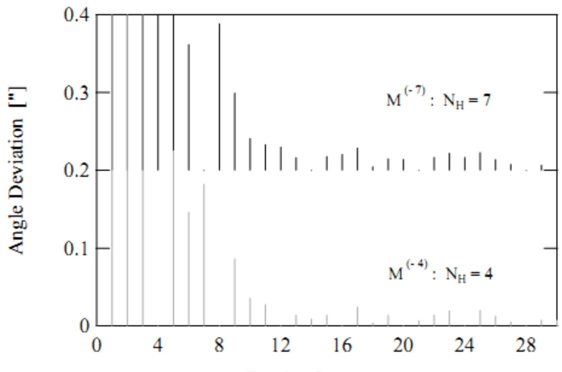

Figure 5. Fourier component of 4 sensors set, $M^{(-4)}$ and 7 sensors set, $M^{(-7)}$

Calibration results of 4 sensors set not have 4th component and 7 sensors set not have 7th component. We purpose compensate lack of each result to another one. How ever this method still lacks every 28th components from least common multiple (L.C.M) rule.

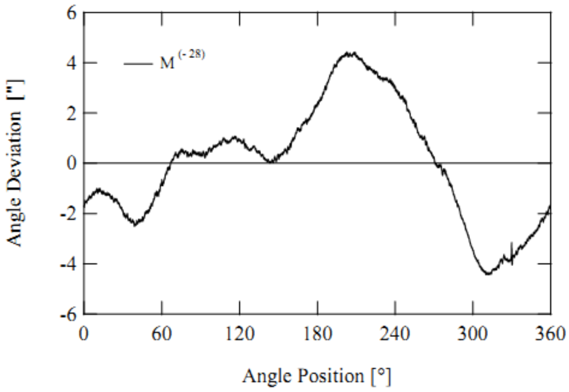

Figure 6. Combination of calibration result of 4 and 7 sensors set, $M^{(-28)}$

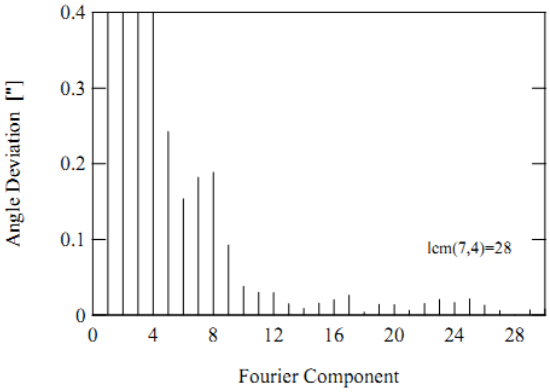

Figure 7. Fourier component of combination between 4 and 7 sensors set, $M^{(-28)}$

Phase shifted combination method

When analysis combination of calibration result we use fourier transform and inverse fourier transform. We purpose phase shifted combination method which more simple explanation. When create 7 shifted curve of 4 sensors set, $M^{(-4)}$ with same interval of 2π/7and average as shown in Figure 8.

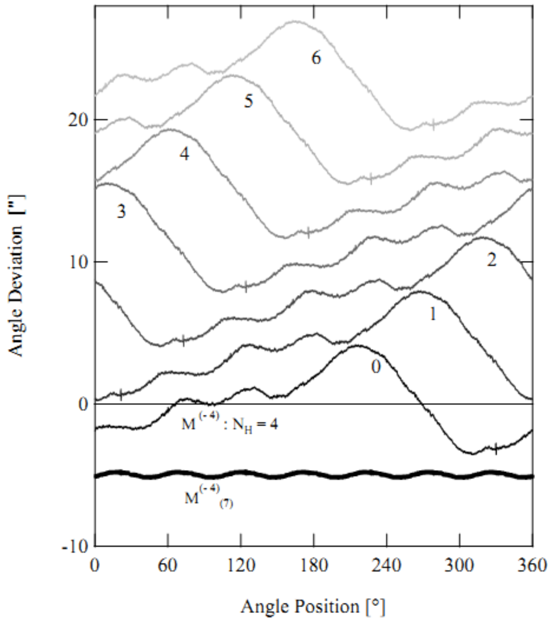

Fi

Figure 8. 7 shifted curve and average of $M^{(-4)}$

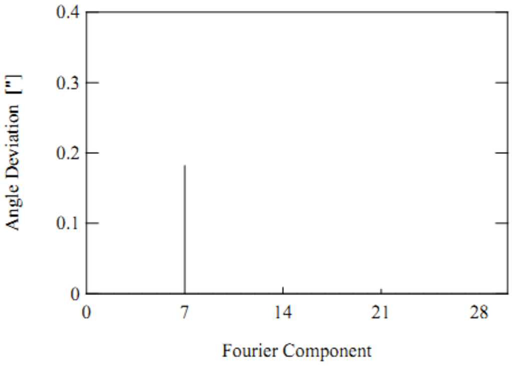

Figu

Figure 9. Fourier component of average $M^{(-4)}$

According to law of fourier series the average curve in Figure 8 have only 7th fourier component. We add result of 7 sensors set, $M^{(-7)}$ in Figure 4 with average curve in Figure 8 and create new formula

$$M^{(-28)} = M^{(-7)} + M^{(-4)}{}_7 \tag{3}$$

Experiment and Results

Rotary table built-in MC-selfA encoder

We developed the Rotary table built-in MC-selfA, figure 10 shows the picture of the selfA47-table.This table uses an air bearing (AB-80: CANON), 10 pieces of sensor heads (SMD-01: SEIKO NPC CORPORATION) are arranged as shown in fig. 3 (right side). This SMD-01 is a high-precision optical encoder that employs a diffraction image projection method. It incorporates an OEIC (Opto-Electric Integrated Circuit) and LED light source in a single package. Miniature clear-mold package size is (5.3 X 4.3 X 1.68 mm), and its resolution is 20 μm pitch pattern scale. The rotary scale disc (KOSHIBU PRECISION CO., LTD) has 18000 graduation lines and its scale pitch is 20 μm and angle interval corresponds 72”. The work table of the selfA47-table is controlled by servo motor control.

Figure 10. The selfA system

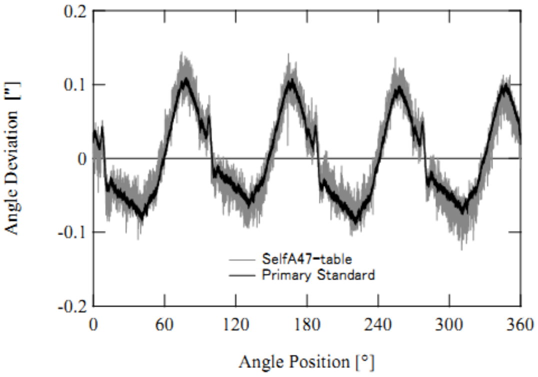

Figure 11. Calibration result of RON905 rotary encoder by selfA47 and primary standard

Conclusions

The selfA is useful angle calibration system when compare with self calibration angle system however selfA still have weak point that lack of frequency component data at the same number of sensors we purpose prove this problem by multi combination of selfA because this method can evaluate higher frequency component with small number of sensors and calibration results curve have much higher accuracy.

Acknowledgments

This research is support from Grant for Industrial Technology Research (Japan), National Institute of Metrology (Thailand) and Chulalongkorn University

References

1. T. Watanabe, H. Fujimoto, K. Nakayama, T. Masuda and M. Kajitani, Automatic High Precision Calibration System for Angular encoder, Proc. of SPIE 5190 (2003), **400–409**.
2. T. Watanabe, H. Fujimoto, T. Masuda, Self-Calibration Rotary encoder, 7th Int., Sym, Meas., Techol. Intellig. Instrum. (2005), **240–245**.
3. T. Masuda and M. Kajitani, An Automatic Calibration System for Angular encoders, Precision Engineering 11 (2) (1989), **95–100**.

Establishment of Thailand National Measurement Standard for Infrared Ear Thermometer

A. Manoi* and U. Norranim

National Institute of Metrology (Thailand), 3/4-5 Moo 3 Klong 5 Klong Luang, Phathumthani, 12120 Thailand
**Corresponding author. E-mail: athikom@nimt.or.th*

Abstract

To support testing/calibration of Infrared Ear Thermometer (IRET) within Thailand, National Institute of Metrology (Thailand) has been established the national measurement standard for IRET. The measurement system composed of two main parts which are a heat source, blackbody furnace, and a temperature measurement system, i.e., standard platinum resistance thermometer which can be traceable to national temperature standard. The blackbody was designed as recommendation in the Japanese industrial standard (JIS) T 4207:2005 - Infrared ear thermometers which has the effective emissivity at least 0.9995. The measurement uncertainty of the blackbody furnace was estimated less than 50 mK for 35 ^{o}C to 42 ^{o}C temperature range. This system capability complies with the ISO 80601-2-56, Medical electrical equipment – part 2-56: Particular requirements for basic safety and essential performance of clinical thermometers for body temperature measurement.

Keywords**:** Infrared ear thermometer, calibration, national measurement standard.

Introduction

For clinical screening and medical diagnosis, one of the most vital parameters apart from blood pressure and heart rate is body temperature. The temperature can be measured by using contact thermometer, i.e. clinical mercury-in-glass thermometers or clinical electrical thermometers. The thermometers rely on conductive heat transfer between body site and the thermometers. Therefore, thermal equilibrium between body sites and the thermometers is required taking time normally more than 1 minute for the measurement. This is the drawback of the thermometers especially when using with infant or children. Also, mercury-in-glass thermometer has problems of glass breakage and toxicity of the material. To reduce measuring time and avoid using of poisonous material, infrared ear thermometer (IRET), one type of non-contact thermometers, is used instead of contact thermometers. IRET determines subject's temperature by means of detecting the intensity of thermal radiation emitting from ear canal which has emissivity close to unity. At present, IRET has been widely used in Thailand both in household and infirmary. To assess conformity of the instrument, calibration or testing of the device is necessary and also traceability system to national standard is required.

National Institute of Metrology (Thailand), NIMT, is responsible to establish and maintain national standard to support measurement activities in Thailand, and link the traceability to international measurement system. Thus, to support measurement of IRET to be traceable to national temperature scale, the national measurement standard for infrared ear thermometer which is a blackbody furnace has been established. Its performance has been verified and present in this publication.

Thailand Measurement Standard for Infrared Ear Thermometer

Thailand national measurement standard for IRET is a blackbody furnace manufactured by Chino cooperation Co., Ltd. The system composes of two main parts which are temperature controlled bath, including a cavity, and a temperature measurement system which is a standard platinum resistance thermometer (SPRT) and read out unit. The SPRT was positioned at the cavity bottom and was calibrated according to the international temperature scale 1990 (ITS-90) from the triple point of water (0.01 ^{o}C) to the freezing point of Zn (419.527 ^{o}C). The uncertainty of SPRT calibration is less than 5 mK. Cavity of the blackbody furnace was made from copper designed following as recommendation in the Japanese industrial standard (JIS) T 4207:2005 - Infrared ear thermometers illustrated in Figure 1. Inside cavity wall was coated by special blackbody coating resulting in effective emissivity value of 0.9995±0.0005. The cavity was fully immersed horizontally in the temperature controlled bath. For the bath, the working temperature range is from 30 ^{o}C to 50 ^{o}C. Distilled water is used as a medium. For bath performances, stability and temperature distribution, i.e. uniformity, was investigated by measuring temperature variation within 2 hrs and maximum temperature difference between temperature at cavity bottom and any position along side of cavity, respectively. The measurement standard was maintained in controlled temperature and humidity room. The room temperature was 23±2 ^{o}C and room relative humidity was 55%±10%.

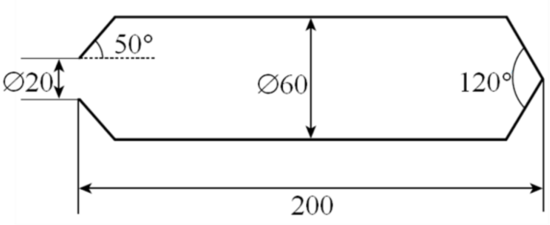

Figure 1. Dimension of the cavity used (unit in mm) [1].

Results and Discussion

Stabilities of the blackbody furnace were measured at 35.5 ^{o}C, 37.0 ^{o}C, and 41.5 ^{o}C which normally are the measuring points for IRET calibration. The results were 2 mK, 2mK and 3 mK respectively. Uniformity represented a source of uncertainty due to blackbody emissivity (non-isothermal case) was found to be less than 4 mK. Uncertainty of the temperature measurement of the blackbody furnace including stability and effect of temperature distribution of cavity wall described above was estimated to be 11 mK for all three measuring points. Measurement uncertainty sources of the blackbody furnace are shown in table 1. Effect of heat loss inside cavity was estimated as same as in [1]. For uncertainty due to effective emissivity of isothermal cavity, the values were estimated following MSL Technical Guild 22 [2] by adjusting emissivity of the blackbody to the maximum and minimum of possible value. On the same hand, effect of change in ambient temperature was estimate by varying ambient temperature from 21 ^{o}C to 25 ^{o}C. The results in the table 1 were evaluated for commercial IRET which has 8 μm to 14 μm operating spectral wavelength.

The results indicate that uncertainty of the national measurement standard for IRET is less than 50 mK which complies with the ISO 80601-2-56, Medical electrical equipment – part 2-56: Particular requirements for basic safety and essential performance of clinical thermometers for body temperature measurement. The measurement system established here is suitable to be measurement standard for calibration of working standard blackbody radiator for secondary calibration laboratory which requires uncertainty of the measurement less than 70 mK. Traceability of the national measurement standard for IRET is shown in Figure 2.

Table 1: Uncertainty budget of the national measurement standard for IRET

Component of uncertainty	Temperature of Blackbody furnace (mK)		
	35.5 ^{o}C	37.0 ^{o}C	41.5 ^{o}C
Calibration of SPRT	5		
Temperature measurement (incl. stability and uniformity)	11		
Heat loss inside cavity	1		
Effective emissivity of isothermal cavity	12	13	17
Effect of change in ambient temperature	2		
Calibration of indicator (incl. drift)	2		
Drift of SPRT	2		
Combined standard uncertainty	17	18	21
Extended uncertainty (95% confidence level)	34	36	42

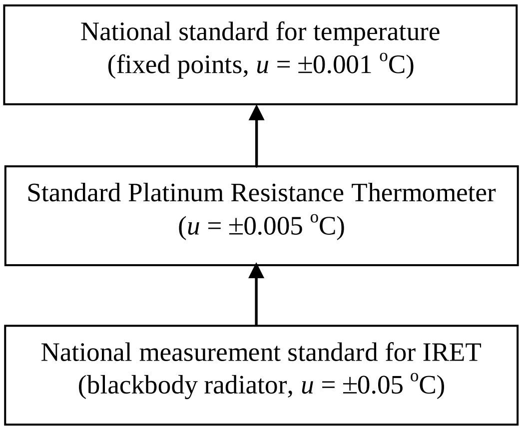

Figure 2. Traceability for national measurement standard for IRET with its uncertainty (u) at 95% confidence level.

To be confidence in the capability of national standard, Thailand national blackbody standard for IRET was compared with the national measurement standard of Japan at National Metrology Institute of Japan (NMIJ), AIST. Radiance temperature difference between two national standards was found within 10 mK [3] illustrating good agreement between two national radiance temperature scale.

Conclusions

NIMT has established national measurement Standard for IRET with uncertainty less than 50 mK for temperature range from 35.5 °C to 41.5 °C. The standard can be used to transfer national radiance temperature scale from NIMT to working standard in secondary calibration laboratory.

References

1. J. Ishii, "Improving the reliability of temperature measurements taken with clinical infrared ear thermometer", Synthesiology-English edition **1** (2008) 47.
2. Measurement Standards Laboratory of New Zealand, "Technical guild 22 – calibration of low-temperature infrared thermometer", http://msl.irl.cri.nz.
3. A. Manoi, U. Norranim, A. Kaneko, and J. Ishii, "Bilateral comparison of blackbody for clinical infrared ear thermometer between NIMT and NMIJ" to be published in proceeding of the symposium on temperature and thermal measurements in industry and science, Oct 2013.

Eutectic Fixed Point Cells for High Temperature Measurement in an Application of AEC Product: Iron and Steel

O. Ongrai[*] and U. Norranim

National Institute of Metrology (Thailand), Klongluang, Pathumtani, 12120 Thailand
**Corresponding author. E-mail: oijai@nimt.or.th*

Abstract

The accurate temperature measurement and control is essential to maintain high quality of products and efficiency of industrial operation process. An example of high temperature measurement and control is in fabrication process of iron and steels which are one of the key products for Asian Economic Community (AEC). For this high temperature range (above 1000 °C), thermocouples are the most extensively used. Currently, the accurate of high temperature measurement is limited by an achievement of low calibration uncertainty. The best way of thermocouple calibration is by using the metal fixed point temperature assigned on the International Temperature Scale 1990 (ITS-90) which has the highest temperature at the freezing point of the copper (1085 °C). In this paper, the measurement of the melting point of a cobalt carbon (Co-C) eutectic fixed point cell for high temperature measurement above 1085 °C is realized by using the Pt/Pd thermocouples. The results show that the reproducibility of the Co-C eutectic fixed point cell at 1324 °C can be achieved within 50 mK.

Keywords: Temperature measurement, ITS-90, Eutectic fixed point, Thermocouple, metal fabrication.

Introduction

Iron and steels are one of the key products for Asian Economic Community (AEC). Manufacturing iron and steel, an alloy of iron, have advances over the past decade to provide reliable clean material with precision properties and performance. The melting temperature ranges of iron and steel are important to manufacturers because the success fabrication depends on the correct selection of solidification temperature. The melting point of iron is reported approximately 1535°C and the melting point of steel depends on its type (almost 90% carbon steel) is varied from 1320°C to 1530°C [1]. Fabrication processes such as casting, annealing and extrusion of iron and steel are usually performed at high temperature above 1000 °C. For this high temperature range, thermocouple are the most extensively used temperature sensors because of their simplicity, low cost, robustness and wide temperature range used up to 2300 °C.

The eutectic fixed point

The best way for thermocouple calibration is by using the metal fixed point temperature assigned on the International Temperature Scale 1990 (ITS-90) which has the highest temperature at the freezing point of the copper (1085 °C). However, there is considerable need to ensure the reliability of higher temperatures than fixed points specified in ITS-90 [2], additional high temperature fixed points with well known thermodynamic temperatures will give an improvement to practical temperature measurement. Pure metal fixed points such as the freezing point of palladium (1554.8 °C), platinum (1768.2 °C) and rhodium (1963 °C) have been recommended above the freezing temperature of copper as secondary reference points [3]. In principle, any pure metals that have melting point higher than copper could be used as high-temperature fixed points. However, the problem is the lack of a suitable material to contain the molten pure metal for example ceramics are too fragile to make a crucible, and the contamination between the metal and its crucible. Therefore, Yamada (1999) proposed that metal-carbon eutectic alloys, in graphite crucibles, could be used as fixed points instead of pure metals for a solution to the fragile crucible and contamination problems [4].

In this paper, we present the measurement of the melting point of a cobalt carbon (Co-C) eutectic fixed point cell by using the Pt/Pd thermocouples [5,6]. It is thus of significant interest to examine the effect of exposing the thermocouple to such treatment in temperature range used in iron and steel fabrication.

The stability of the Pt/Pd thermocouple under test at Co-C fixed points after exposure to 1350 °C at intervals over a period of 500 hours is presented. This paper is arranged as follows. First, the construction of the thermocouples and fixed point is explained.Second, the measurement results of the Pt/Pd thermocouple at Co-C fixed point cell is described, and finally the results of the stability is presented and disscused.

Construction of Thermocouple

The Pt/Pd thermocouple was constructed using high purity metal wires of 0.5 mm diameter and 2000 mm length. The purities of the Pt and Pd wires were 99.997% and 99.97% respectively. The Pt wire was annealed electrically in air for 10 h at approximately 1300 °C and the Pd wire was annealed electrically at the same temperature for 10 h before cooling to ambient temperature by switching off the current. The purposes of annealing the thermocouple are to produce a homogenous structure, remove the strain from cold work handling during assembly, equilibrate the point defects and remove the contaminants.

The annealed thermocouple wires were inserted gently into twin bore high purity alumina insulating tubes. The twin bore tube was used to support the wires and insulate the bare wires before reaching the measurement junction. The wires were inserted into the alumina insulator tube, and 1000 mm from the measuring junction of the thermocouple was annealed at 1100 °C in a horizontal furnace for a further 1 h to remove cold work introduced during assembly. The measuring junction was formed by welding the two thermoelements together. The thermoelements emerging from the alumina insulator were insulated with flexible Teflon tubes and connected to a pair of Cu wires of diameter 0.3 mm to form the reference junction. Figure 1 shows the Pt/Pd thermocouple after assembly.

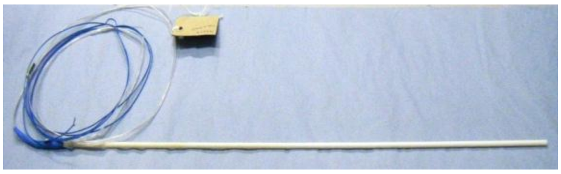

Figure 1. The noble standard Pt/Pd thermocouple after assembly.

The Eutectic Fixed Point and Furnace

The primary calibration services of the noble thermocouples by National Measurement Institutes are usually performed by using a series of fixed points: the freezing points of tin (231.928 °C), zinc (419.527 °C) and copper (1084.62 °C) for range up to 1100 °C. For the range up to 1500 °C, the calibration employs the melting point of the cobalt-carbon eutectic (1324 °C) and the palladium-carbon eutectic (1492 °C). Figure 2 shows the standard fixed point crucible and cross section showing the ingot material and thermometer re-entrant well. The fixed point material is contained in a graphite crucible. The Graphite cap to the crucible incorporates the thermometer re-entrant well. The furnace must provide a uniform-temperature zone for maintaining the fixed point temperatures to be able to be closely controlled of melting and freezing cycle. The fixed point graphite crucibles are protected from oxidation by enclosure in a ceramic or silica tube (depending on temperature), as in Figure 3. The fixed point assembly has a graphite equalizer block with many layers of thermally insulating by graphite felt and radiation baffles. To protect the thermometer from graphite, an alumina tube is inserted to the fixed point crucible to be a thermometer well. The assembly is purged and filled of inert gas (Ar) to prevent oxidation of the graphite [7].

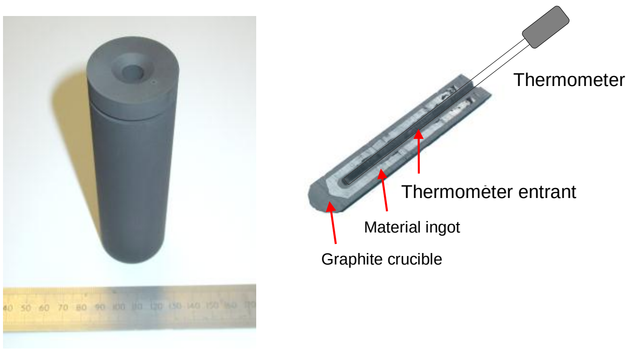

Figure 2. The standard fixed point crucible (left) and the cross section with thermometer (right)

The typical fixed point furnace is a three-heater zone tube furnace shown in Figure 3. The inner tube of the furnace must be adequate to accommodate the cell assembly, which is 80 mm in diameter and 750 mm long. The temperature uniformity of the furnace needs to be well within the few degrees over the length of the crucible. The temperature profile of the three zone fixed point furnace suitable to maintain the Co-C eutectic cell is shown in Figure 4. The measurements were performed by withdrawing a reference thermocouple in steps from the bottom of the fixed point cell up through the thermometer well.

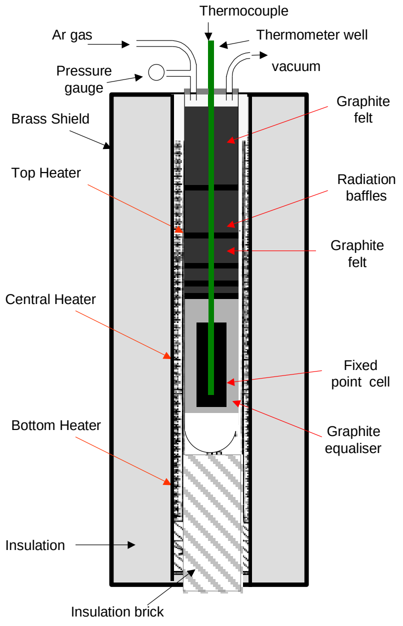

Figure 3.The three zone fixed point furnace with the fixed point cell construction.

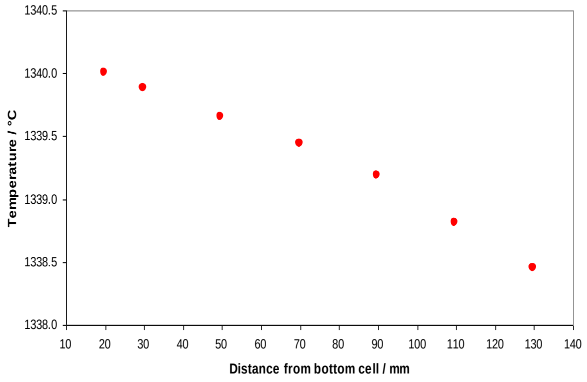

Figure 4. The temperature profile of a furnace that is suitable for the use with a Co-C eutectic fixed point cell. The axial uniformity of this furnace is within 1.5 °C.

Measurement Results and Discussion

To initiate the melting point, the furnace temperature is slowly raised with temp rate 2.5 °C/min to about 10 °C below the melting temperature of the Co-C metal eutectic. It is held at this temperature for at least 1 hr to ensure thermal equilibrium has been established. After 1 hr, the thermocouple output versus time shows thermal equilibrium between the thermocouple and the furnace. Then, the temperature of the furnace is increased to about 20 °C above the fixed-point melting temperature. By recording the thermocouple output versus time (e.g. in Figure 5), as the furnace temperature increases, a melting plateau is observed.

Once the melt has been completed, the furnace is set to about 20 °C below the freeze temperature. The temperature of the fixed point cell will fall below the freeze temperature (supercooling), followed by recalescence. Then the thermocouple output will indicate a freeze plateau. After the freeze completed, the cell is cooled down to the furnace temperature as shown in Figure 5.

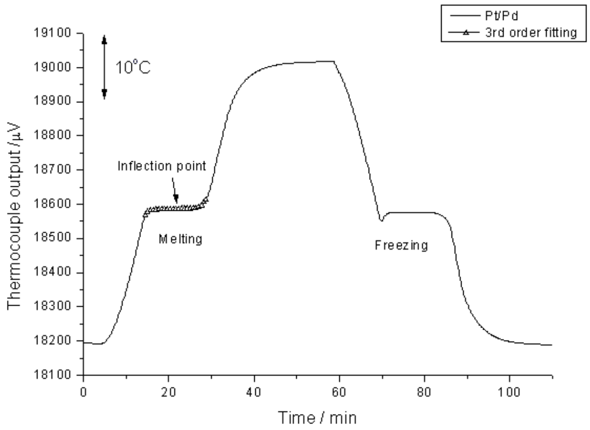

Figure 5. A representative curve of the melting of a Co-C eutectic cell measured with a Pt/Pd thermocouple.

For the realization of the melting point of the eutectic fixed point temperature, the inflection point is used in the melting curve [8]. The unique value of the thermocouple emf at the inflection point is then compared with the standard reference emf function of the Pt/Pd thermocouple at the assigned fixed point temperature [9]. The measured thermocouple emf values at the melting point of Co-C for this Pt/Pd thermocouple was 18589 $\pm$ 2 µV.

To evaluate the thermocouple stability such treatment in temperature range used in iron and steel fabrication, the exposed temperature for the thermocouples was selected to be 1350 °C, and was applied using a horizontal single-zone tube furnace. The output of the Pt/Pd thermocouple was measured at the melting point of the Co-C eutectic before ageing, and again every 100 h during the ageing process. The stability of the Pt/Pd thermocouple measured at the melting point of Co-C is shown in Figure 6.

The emf values of the Pt/Pd thermocouple at the Co-C melting point drifted upward before getting stable. After the first ageing step of 100 h, a drift in the emf of about 1.5 µV (64 mK) was observed. During further ageing, from 200 h to 500 h, the Pt/Pd thermocouple retained its stability within about 0.8 µV (34 mK). This data showed that the stability of this Pt/Pd thermocouple at the Co-C eutectic fixed point is comparable to that of other Pt/Pd thermocouples e.g. reported in [6].

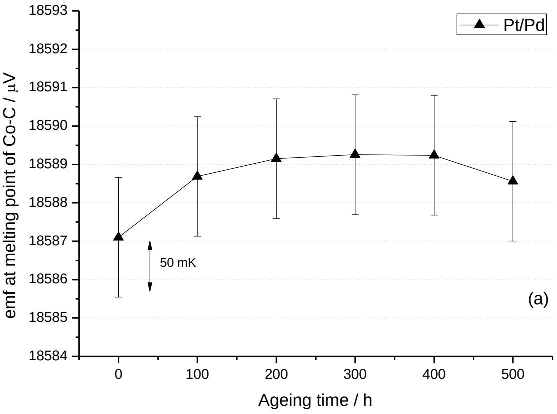

Figure 6. The thermoelectric stability of the Pt/Pd thermocouple at the melting point of Co-C as a function of ageing time at 1350 °C, with measurement uncertainty (*k*=1).

Conclusions

The measurement of the melting point of a cobalt carbon (Co-C) eutectic fixed point cell for high temperature measurement above 1085 °C was realized by using the Pt/Pd thermocouples. A Pt/Pd thermocouple was constructed for a study of its thermoelectric stability at regular intervals during a 500 h ageing program at 1350 °C. The stability was measured every 100 h at the Co-C eutectic fixed points. The results show that the reproducibility of the Co-C eutectic fixed point cell after the thermocouple first ageing step of 100 h can be achieved within 50 mK. These results show that the performance of the Pt/Pd thermocouple has good stability to the high temperature thermal environment. Moreover, the implementation of high temperature eutectic fixed points for thermocouples calibration could lead to an improvement in high temperature measurement for iron and steel fabrication.

Acknowledgments

We are grateful to Prof. Graham Machin and Dr. Jonathan Pearce for providing the opportunity and resources to carry out this work at National Physical Laboratory (NPL), UK.

References

1. R. E. Smallman and A. H. W. Ngan, *Physical Metallurgy and Advance Materials*, 7 ed. Oxford: Butterworth-Heinemann, 2007.
2. H. Preston-Thomas, "The International Temperature Scale of 1990 (ITS-90)," *Metrologia* **27**(1990) 3.
3. R. E. Bedford, G. Bonnier, H. Maas, and F. Pavese, "Recommended values of temperature on the International Temperature Scale of 1990 for a selected set of secondary reference points," *Metrologia* **33**(1996) 133.
4. Y. Yamada, H. Sakate, F. Sakuma, and A. Ono, "Radiometric observation of melting and freezing plateaus for a series of metal-carbon eutectic points in the range 1330 °C to 1950 °C," *Metrologia* **36** (1999) 207.
5. F. Edler, R. Morice, and J. Pearce, "Construction and investigation of Pt/Pd thermocouples in the framework of the EUROMET Project 857," *Int. J. Thermophys.* **29** (2008) 199.
6. J. V. Pearce, H. Ogura, M. Izuchi, and G. Machin, "Evaluation of the Pd-C eutectic fixed point and the Pt/Pd thermocouple," *Metrologia* **46** (2009) 473.
7. J. V. Pearce, G. Machin, T. Ford, and S. Wardle, "Optimizing heat treatment of gas turbine blades with a Co-C fixed point for improved in-service thermocouples," *Int. J. Thermophys.* **29** (2008), 222.
8. E. R. Woolliams, G. Machin, D. H. Lowe, and R. Winkler, "Metal (carbide)–carbon eutectics for thermometry and radiometry: a review of the first seven years," *Metrologia* **43** (2006) R11.
9. ASTM,"E1751-00Guidefor Temperature Electromotive Force (EMF) Tables for Non-Letter Designated Thermocouple Combinations," in ASTM st rds section 14 Vol.14.03 Temperature Measurement, Conshohocken, PA: ASTM International, 2005.

Harmonics in Thai Classical Instrument: Cha-Kae

P. Anusasananan[1*], K. Deenourpanao[2], S. Suwanarat[1], and N. Thangprasert[1]

[1]Department of Physics, Faculty of Science,
Ramkhamhaeng University, Bangkok 10240, Thailand
[2] The Demonstration School of Ramkhamhaeng University,
Faculty of Education, Ramkhamhaeng University, Bangkok 10240, Thailand
[*]E-mail: suksan_rang@hotmail.com

Abstract

In this research we determine the harmonics in a Thai classical instrument; Cha-Kae, using Fourier analysis. The musical timbre of a steady tone is also determined by calculating the decay of each harmonics presented in a series. The result shows that a sound from Cha-Kae is made up from many frequencies, which included the fundamental and several harmonics. As an example, a sound spectrum of the note C (middle) played on a first string of Cha-Kae consists of one dominant frequency (228 Hz) with the loudness of -16 dB. and several frequencies 461, 688, 1147.5, 1377.5, 1604, 1835, 2070, 2311 Hz, etc. with less amplitude -18, -24, -27, -29, -30, -34, -26, -31 dB respectively. The ratio between these frequencies and the lowest frequency are much closed to a whole number. This set of frequencies is called harmonic series. So the fundamental or the 1st harmonics is 228 Hz, the 2nd harmonics is 461 Hz, the 3rd harmonic is 688 Hz, and so on. The difference between nearby harmonics is constant and equals to the fundamental frequencies (228 Hz). The waveform produces by Cha-Kae contains richness of musical tones, as the result of the superposition of various harmonics. From the calculation of the decay in each harmonics we observed that the plucking action gives it a sudden attack characterized by a rapid rise to its peak amplitude. The decay time is less than 1 second for almost every harmonics except the first three harmonics which is continued until 2 seconds. The relative amplitudes and the decay of the various harmonics primarily determine a tone color or timbre of the sound. An understanding of harmonics can be very helpful in better understanding what's happening in a Cha-Kae and allows a musician to manipulate it to make its sound the way he wants.

Keywords: Cha-Kae, Fourier analysis, harmonic, fundamental frequencies, decay time.

Introduction

Cha-Kae is a musical instrument that is based on a harmonic oscillator (string) which oscillates at numerous frequencies simultaneously. At these resonant frequencies, waves travel in both directions along the string, adding and canceling each other to form standing waves. These frequencies are mostly limited to integer multiples, or harmonics, of the lowest frequency. Any complex tone is a combination of several simple periodic waves or partials, each with its own frequency of vibration, amplitude and phase. A struck string on Cha-Kae produces many frequencies which include the lowest partial (the fundamental frequency), which is the one created by vibration oven the full length of the string, and several harmonics [1,2]. This phenomenon is in contrast to a percussive musical instrument that the combination of frequencies does not form a harmonic series.

The harmonic series is a series containing only frequency components whose frequencies are whole number multiples of the fundamental frequency, In other words. If f is the fundamental frequency, then a harmonic spectrum has the from {…, -2f, -f, 0, f, 2f, …}. The first eight harmonics of the note C is shown in figure 1.

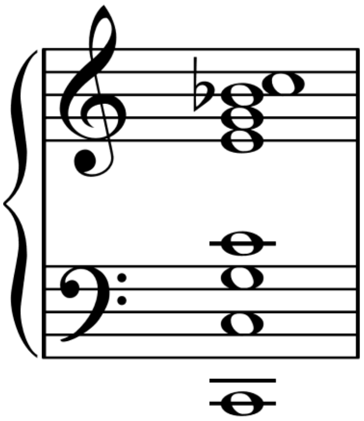

Figure 1. First eight harmonics on C.

Materials and Methods

We first recorded the sound from Cha-Kae using a hi-speed recorder and saved as a wav file on the computer. Then we characterize a periodic waveform in terms of harmonics using Fourier analysis. Switching from a time to a frequency plot can make the harmonic content more evidence. Most computer programs use a simplified version of Fourier analysis called the Fast Fourier Transform (FFT) [3,4]. We also calculated the decay of each harmonics presented in a series.

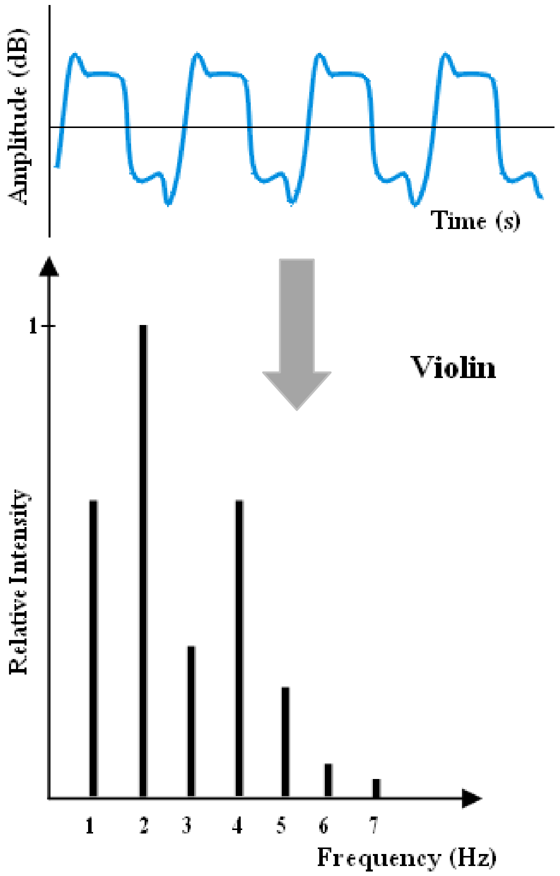

Figure 2. A Fourier transform converts a time domain into the frequency domain.

Results and Discussion

A waveform of the note C (middle) played on a first string of Cha-Kae is shown in figure 3. The x-axis represents time (in second) and the y-axis represents amplitude of the sound (in dB). It shows one cycle of waveform that can easily be seen to be symmetric with positive peak amplitude excursions equal to the magnitude of the negative peak amplitude excursions.

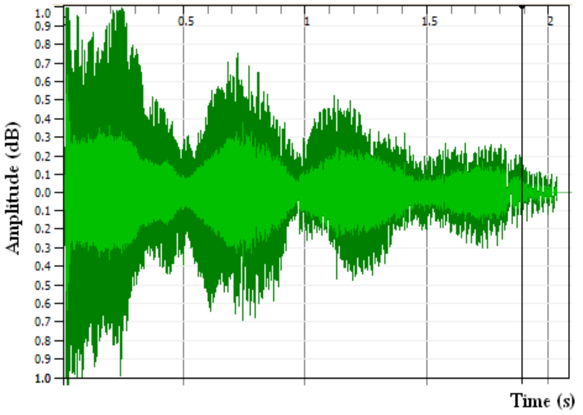

Figure 3. A wave-form of the note C (middle) played on a first string of Cha-Kae.

The figure above also shows the attack and decay of a Cha-Kae string. The plucking action gives it a sudden attack characterized by a rapid rise to its peak amplitude. The decay is about 2 second long and gradual by comparison. The up/down patters is a result from the interference of various harmonics present in the sound.

A spectrogram of the note C (middle) is shown in figure 4. The x-axis represents time (in second), the y-axis represents frequencies of the sound (in Hz.) and a color value represents the relative power at each time and frequency. The Fourier transforms converts

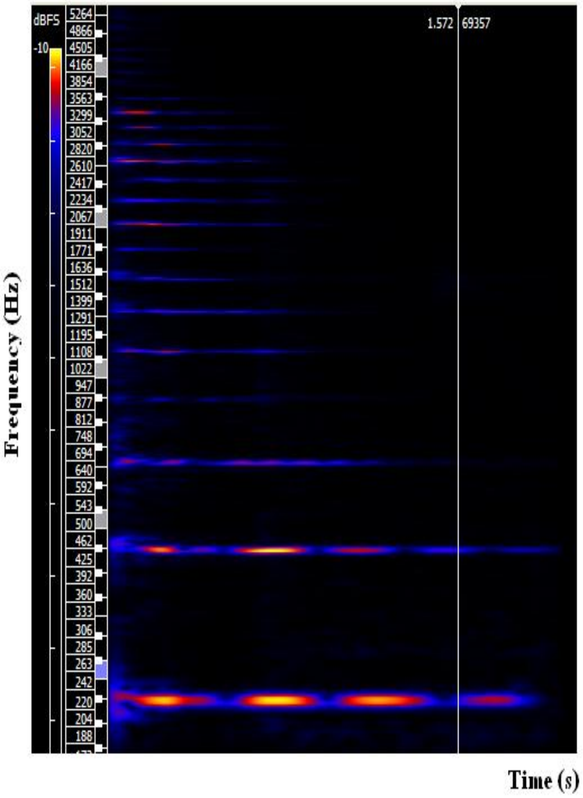

Figure 4. A sound spectrum of the note C (middle) played on a first string.

a time domain waveform into a frequency spectrum. As we seen from the figure, note C is not a simple pure tone (or one frequency), it is made up from several different frequencies or partials. The lowest frequency is 228 Hz, with the highest loudness of -16 dB. Another frequencies are 461, 688, 902, 1147.5, 1377.5, 1604, 1835, 2070, 2311 Hz. etc, with less amplitude -18, -24, -27, -29, -30, -34, -26, -31 dB respectively. The ratio between these frequencies and the lowest frequency (288 Hz) are 2.02, 3.01, 3.95, 5.03, 6.04, 7.03, 8.04, 9.07, 10.13, etc, These ratios are very closed to the integer 2, 3, 4, 5, 6, 7, 8, 9, 10, etc. Since a harmonics is a set of partials that are whole number multiples of a common fundamental frequency, these frequencies form a harmonic series. In our case the fundamental or the 1st harmonics is 228 Hz, the 2nd harmonics is 461 Hz, the 3rd harmonics is 688 Hz. and so on as show in figure 5.

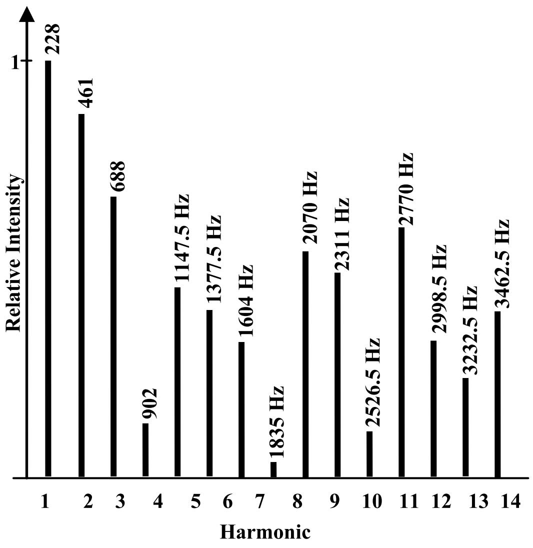

Figure 5. A spectrum diagram summaries the frequency and the amplitude of the wave visually. The horizontal position of the line represents the frequency and its height represents the amplitude.

The decay times for the note C is plotted in figure 6. As can be seen, the decay times vary drastically among the various harmonics. The most prominent harmonics are the fundamental (228 Hz), the 2nd harmonics (461 Hz) and the 3rd harmonics (688 Hz). The fundamental starts at a highest amplitude, drops and grows four times before dying out at two seconds. The 2nd harmonic starts moderately loud, grow and drop in the same manner as the fundamental. The 3rd harmonics starts at low intensity, grows and decays, and grows to maximum intensity at 0.7 second and then decays again until the intensity go to zero at 1.8 second. The decay times of another harmonics are less than 1 second. This means that after 1 second the sound will consist mainly of the first three harmonics shortly after the attack, since the higher harmonics will fade away very quickly. The relative amplitudes and the decay of the various harmonics determine the musical timbre of a tone.

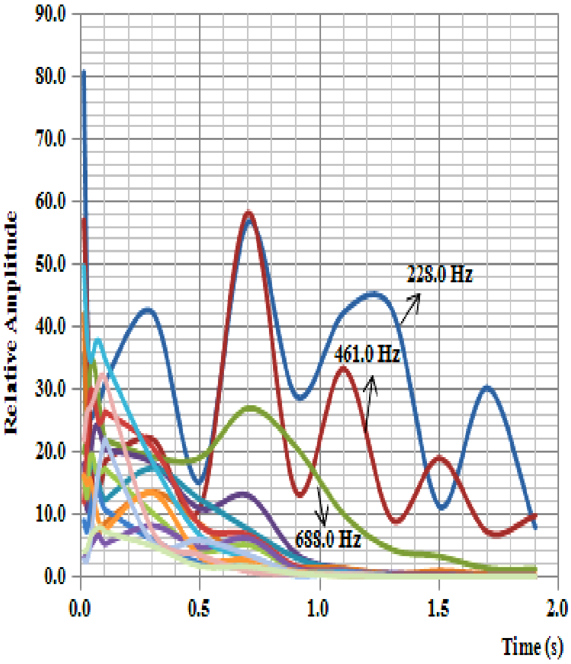

Figure 6. Decay times for the harmonics from note C from Cha-Kae.

Conclusions

A sound from Cha-Kae is made up from many frequencies, which included the fundamental and several harmonics. A sound spectrum of the note C consists of a fundamental (288 Hz.) and several

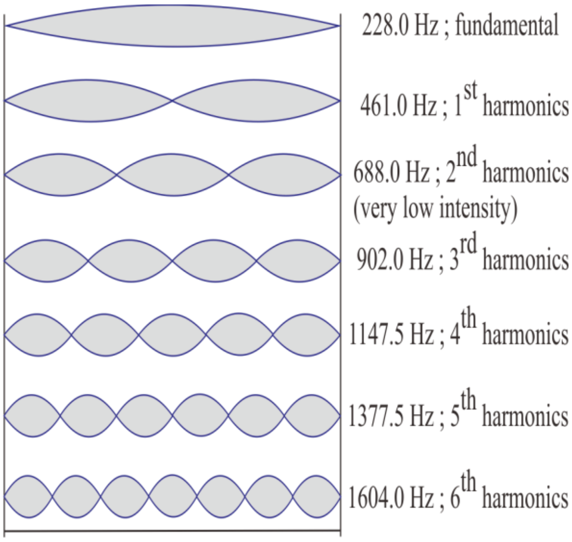

Figure 8. Harmonics series of the note C from Cha-Kae.

harmonics (461, 688, 1147.5, 1377.5, 1604, 1835, 2070, 2311 Hz, etc.) The difference between consecutive harmonics is constant (228 Hz) and equal to the fundamental (228 Hz) as shown in figure 8 Since pitch is a psychological reaction, our ears respond to sound nonlinearly. We perceive higher harmonics as closer together than lower ones. The second harmonic sounds an octave higher. The third harmonic, three times the frequency of the fundamental sounds a perfect fifth above the second. The fourth harmonic vibrates at four times the frequency of the fundamentals and sounds a perfect fourth above the third (two octaves above the fundamental). Double the harmonic number means double the frequency (which sounds an octave higher). Human ears tend to group an integer multiples of a fundamental frequency or the harmonics into a single sensation. Listener perceives them together as a tone color or timbre and assigns a pitch to the sound based on the fundamental frequency. An understanding of harmonics, together with the frequencies of all notes on the scale of Cha-Kae [5], can be very useful in better understanding what's happening in a Cha-Kae and allows the musicians to make its sound the way they want.

Acknowledgments

Thank you Ramkhamhaeng University for supporting this research.

References

1. Ellis, Alexander J., The Musical Scales of Various Nations, Journal, Society of Arts, 1885.
2. Seelig, Paul, Siamesische Musik, Bandoeng: Editions Matatani, 1932.
3. Terras Audrey, Fouries analysis on finite group and applications, Cambridge University Press, 1999.
4. S. Haykin, Aduances in Spectrum Analysis and Array Processing, Prentice Hall, 1991.
5. Suksan Suwanarat, Kornsuang Deenourpanao, Panatcha Anusasananan and Nipon Thangprasert, Analysis of the musical scale in Cha-Kae using Fourier method, Science Research Conference, University of Phayao, 2013.

Interpolation Equation for Calibration Results of Thermo-Hygrometers

T. Sinhaneti*, P. Phuauntharo, and T. Keawprasert

National Institute of Metrology Thailand, 3/4-5 Moo 3 Klonghar Klong Luang,
Pathum Thani, 12120 Thailand
**Corresponding author. E-mail: thasorn@nimt.or.th*

Abstract

Most of commercial thermo-hygrometers applied the linear equation as its calibration equation for both relative humidity and temperature, so three calibration points for each parameter are required for the thermo-hygrometer calibration by their manufacturer. Meanwhile calibration laboratories calibrate thermo-hygrometers in terms of correction at points. As a result, it is rather difficult for users to apply any calibration results for a whole range since the instrument's behavior is non-linear and sensitive to temperature. In this paper, two selected types of high accuracy thermo-hygrometer were intensively calibrated for their relative humidity corrections throughout the relative humidity range of 30 % to 80 % at different temperatures of 15 °C to 30 °C. For each type, the resulting corrections were evaluated by fitting to different polynomial equations to determine its best interpolation equation. It was found that the quadratic polynomial equation of two variables for the relative humidity with the linear function of temperature is accurate enough to use as an interpolation equation for these two types of thermo-hygrometers. Moreover, for one type of them, the quadratic polynomial equation of two variables both for relative humidity and temperature is very accurate, yielding the residual error of lower than 0.1% for relative humidity. From this result, this type of thermo-hygrometer and its best appropriate interpolation equation will be implemented for the next inter-laboratory comparison in humidity measurement among calibration laboratories in Thailand.

***Keywords*:** Thermo-hygrometer, calibration, interpolation equation

Introduction

Presently thermo-hygrometers are widely used in many applications especially for environment control and industrial process control. For traditional application, a narrow operating temperature range is enough, while a wide range is required for industry. Normally thermo-hygrometer manufacturers require sensors which their response is linear for relative humidity measurement so that a linear equation can be used as their calibration equation. Moreover, relative humidity at a given temperature is defined as the ratio between the actual partial vapor pressure to the saturation vapor pressure of the air temperature [1]. That is the air temperature is a main factor affecting to the accuracy of thermo-hygrometers, including non-linearity, thermal radiation, hysteresis, contamination and condensation.

A main task of this work is to study the relationship between the thermo-hygrometer output and the actual relative humidity at any temperatures. The aim is to find out an appropriate interpolate equation which can describe the behavior of thermo-hygrometer. It is expected that the resulting equation will be used to determine correction values of relative humidity at any temperatures accurately.

Problem

Fig. 1 show measurement results of a thermo-hygrometer in terms of relative humidity correction for the range of 40% to 80% at different temperatures. It can be clearly seen that the correction values at any relative humidity are changed by the air temperature. Moreover the non-linearity can be found at the results of 40%, 50% and 60% since the manufacture use a linear equation as its calibration equation.

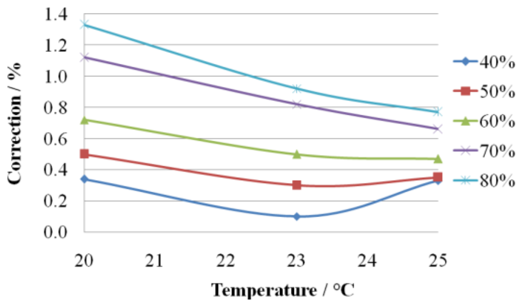

Figure 1. Corrections at difference temperatures

For properly use, thermo-hygrometers must be used at same temperature on certificate of calibration to avoid such a problem. Moreover 3 calibration points for each parameter (temperature and relative humidity) are not enough for a whole range calibration.

Methodology

In this work, two types of high accuracy thermo-hygrometer were selected in this work. Firstly these thermo-hygrometers were intensively calibrated for their correction covering their measuring range as much as possible. A dew-point hygrometer and a platinum resistance thermometer were used as reference thermometers to calibrate the test thermo-hygrometers by comparison method in a 4.5 ft^2 climatic chamber. An accuracy of the used dew-point hygrometer and the PRT is traceable to NIMT national standard in humidity and temperature respectively. The climatic chamber used to generate humid air was characterized for its stability and uniformity for a whole operation range.

The calibration for each item was started from the lowest temperature to the highest temperature. For each temperature, at least 5 calibration points in the relative humidity range from 30% to 80% are required. Measuring relative humidity of thermo-hygrometer, and the relative humidity and the air temperature measured by the dew-point hygrometer and the PRT were the main parameters which must be recorded in this measurement.

Next the correction values at the calibration points $H(R,t)$ can be calculated by subtracting the actual relative humidity value obtaining from the reference thermometers (R_{STD}) with the reading value of the test thermo-hygrometer (R_{UUC}.) as follows

$$H(R,t) = R_{\mathrm{STD}}(t) - R_{\mathrm{UUC}}(t) \qquad (1).$$

After that, the resulting corrections were fitted to different polynomial function both for the relative humidity and the air temperature using the regression method. Finally the resulting interpolation equation was used to estimate correction values at any relative humidity and temperature in order to compare to the measuring correction values.

Results and Discussion

Measurement results of one sensor for each type are shown and analyzed. Here the first type and the other one are defined as sensor A and sensor B respectively. From the method mentioned above, it was found that the polynomial function of the two variables in Equation (2) to be sufficiently accurate for both of them.

$$\begin{aligned} H(R,t) &= b_0 + b_1R + b_2R^2 + b_3t + b_4Rt + b_5R^2t \\ &\quad + b_6t^2 + b_7Rt^2 \qquad (2), \end{aligned}$$

where $H(R,t)$ is resulting correction of the test thermo-hygrometer at the relative humidity R and the air temperature t measured by the dew-point thermometer and the PRT. The b_{i} parameter is fitting coefficient calculated from the measurements results of R and t.

Figure 2 shows the measured correction values of the sensor A in comparison to estimate correction values calculated from the interpolate equation above.

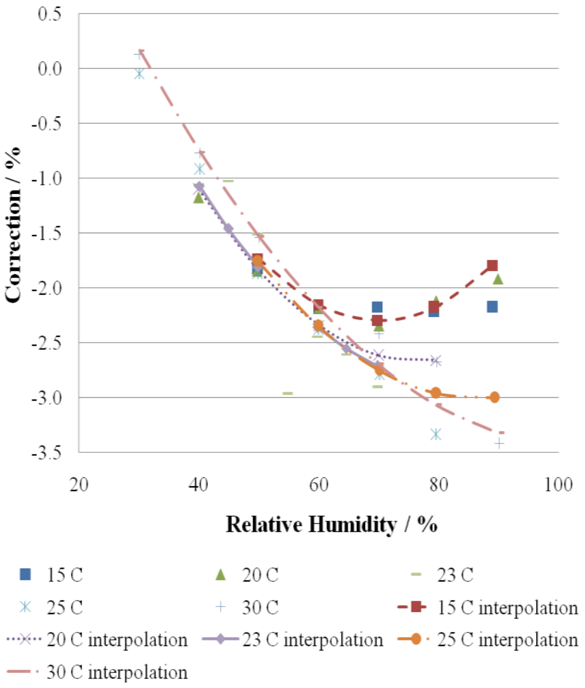

Figure 2. Measured correction and estimate correction calculated from the interpolate equation for sensor A

From the measurement result of the sensor A, the non-linearity behavior can be clearly observed at low temperatures.

Figure 3 shows residual errors of within ±0.6% from the measured value for the whole relative humidity range. It seems the residual errors increases with increasing relative humidity.

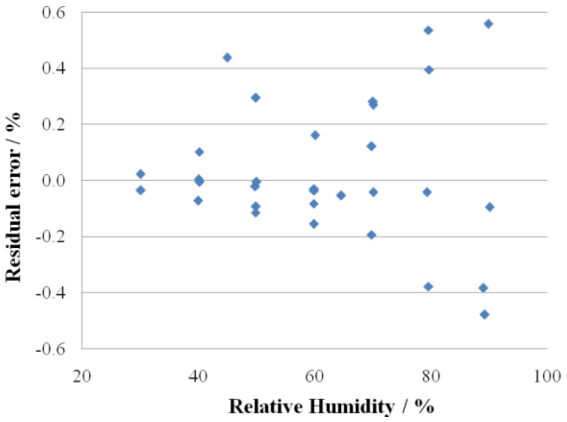

Figure 3. Residual error from the measured value for the thermo-hygrometer sensor A

For the sensor A, a poor fitting result was found with the r^2 of lower than 0.9. Even increasing the order of the polynomial function, the measurement results are still unable to fit accurately.

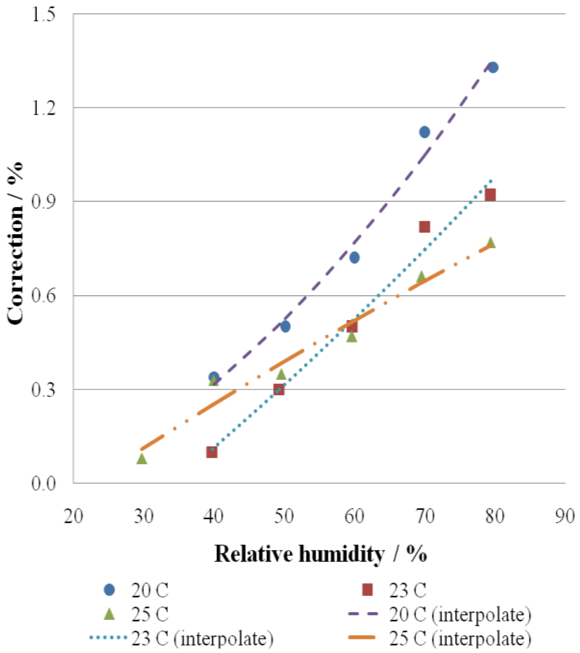

Figure 4. Measured correction and estimate correction calculated from the interpolate equation for sensor B

Figure 4 shows the measured correction values of the sensor B and its estimate correction values calculated from the interpolate equation in Equation 2. For the sensor B, a good fitting result was found for its measurement results with r^2 of greater than 0.99. Furthermore, this sensor seems to response to relative humidity linearly for all test temperatures.

For the sensor B, the associate residual errors from the measuring value are not larger than $\underline{+}0.1\%$ for the whole range of 30% to 80%. The advantage of applying this interpolate equation for the calibration results is that the calibrated thermo-hygrometer can be used at any temperatures cover the whole calibration range with much lower error. At this stage, the maximum of residual error is considered as an uncertainty for the whole range calibration.

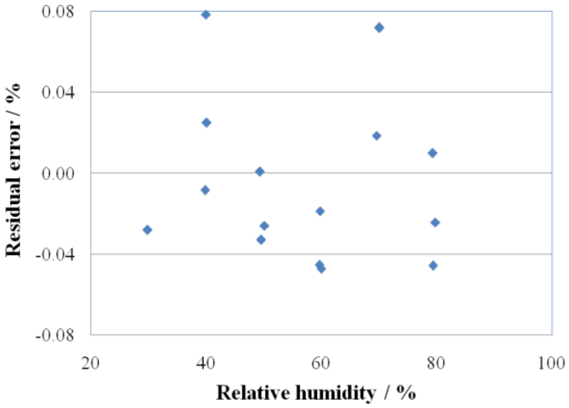

Figure 5. Residual error from the measured value for the thermo-hygrometer sensor B

Even a good agreement was found for this type of thermo-hygrometer, it should be noted that this is the results from one sample of this type. In fact, more than two sensors for each type must be investigated to ensure their behavior. Therefore an ultimate goal of the subsequent work is to identify the characteristic of frequently used types of thermo-hygrometer.

Conclusions

Two types of high accurate thermo-hygrometer were investigated to find out the sufficiently general interpolation equation for each type. With the quadratic polynomial equation of two variables for relative humidity and temperature, a good agreement between the measured values and the estimate values was found for the calibration result of one sensor. As a result, this type of thermo-hygrometer and its appropriate interpolation equation are already implemented for the in progress inter-laboratory comparison in humidity measurement of Thailand.

Reference

1. J. W. Lovell-Smith and H. Pearson, “On the concept of relative humidity”, Metrologia **43** (2006), 129-134.

Resistance Thermometer Bridges used for the Standard Platinum Resistance Thermometers Calibration

C. Yaokulbodee[1*], U. Norranim[1], and S. Chollalarp[2]

[1] *Thermometry Metrology Department, National Institute of Metrology (Thailand), Pathumthani 12120, Thailand*
[2] *Department of Physics, Faculty of Science, Siam University*
38 Petkasem Road; Phasicharoen; Bangkae Bangkok 10160, Thailand
**Corresponding author. E-mail: charuayrat@nimt.or.th*

Abstract

The resistance thermometer bridges are the devices used by National Institute of Metrology (Thailand) for the standard platinum resistance thermometers (SPRTs) calibration. Performance of thermometer bridges is significant to determination of uncertainties of the SPRTs calibration. This paper presents the effects from using the different bridges, AC bridge and DC bridge. The results of the different bridges are summarized.

***Keywords*:** Resistance thermometer bridges, Standard platinum resistance thermometer calibration

Introduction

The International Temperature Scale of 1990 (ITS-90) defines temperatures from Triple point of equilibrium of hydrogen (13.8033 K) to Freezing point of silver (1234.93 K) of Standard Platinum Resistance Thermometers (SPRTs) calibration [1]. The performance of the resistance ratio bridges estimation of the uncertainties arising from the resistance measurement. It is necessary to accurately measure the resistance ratio with the resistance thermometer bridges.

Normally, National Institute of Metrology (Thailand), NIMT, use DC bridge model MI 6010 for the calibration of SPRT. AC and DC Bridge are used a similar principle of measurement. The measured resistor Rx, the resistance of SPRT, is compared to Rs, AC/DC standard resistor, the result of measurement is a ratio n;

$$n = Rx/Rs$$

A bridge circuit is a type of electrical circuit in which two circuit branches (usually in parallel with each other) are "bridged" by a third branch connected between the first two branches at some intermediate point along them. The bridge was originally developed for laboratory measurement purposes and one of the intermediate bridging points is often adjustable when so used. Bridge circuits now find many applications, both linear and non-linear, including in instrumentation, filtering and power conversion [2].

Measurement system

The resistance thermometer bridges used in this study consist of one AC bridge (ASL model F900) and one DC bridge (model MI 6010).

AC bridge ASL model F900 is based on measuring the resistance with alternating current [3]. The current flows through the AC/DC standard resistor compare with the SPRTs. The maximum ratio of this bridge is 1.299999999. The ASL F900 bridge are shown in Figure 1.

Figure 1. The AC bridge ASL model F900.

DC bridge model MI 6010 is based on measuring the resistance with direct current [4]. The current flows through the AC/DC standard resistor and the resistance thermometer are adjusted in the inverse ratio. The maximum ratio of the bridge is 13.00000000. The DC bridge are shown in Figure 2.

Both resistance thermometer bridges were placed inside the primary thermometry laboratory. AC/DC standard resistors, 25 Ω, were placed inside the oil bath with temperature stability of ± 1°C. This measurement we have used standard platinum resistance thermometer (SPRT) having resistances of 25 Ω at the triple point of water (0.01°C), Tinsley model 5187SA quartz sheath thermometer. The Water Triple Point cell was used in this measurement.

Figure 2. The DC bridge MI 6010.

We Placed the Standard Platinum Resistance Thermometer in the thermometer well of water triple point cell, shown in Figure 3. The SPRT and AC/DC standard resistors were connected directly to the AC bridges. After finished the first measurement, we move the cable connectors to MI 6010 DC bridge.

All measurements were performed on the same fixed point cell plateau of triple point of water cell. The measurements are reported using the two currents, which are 1 mA and √2 mA, and recorded for 250 readings with reversal time of current 20 seconds per reading. The performance was evaluated by observing the standard deviation of the resistance readings one and half hour of measurement. An operating frequency of the AC bridge is 75 Hz.

Measurement setup was investigated. All devices in the laboratory were switched on as normal use. Electric devices emit amount of electromagnetic interference. Especially critical are some power supplies for laptop computers, computer monitor, UPS, etc. Computer monitor was placed near the thermometer bridge.

Figure 3. The SPRT in the water triple point cell.

Results

The measurement results of SPRTs with ASL F900 AC bridge are shown in Figure 4.

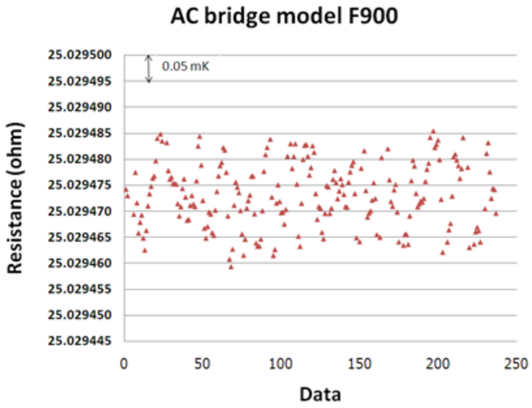

Figure 4. Resistance measurement of SPRT with the ASL F900 AC bridge in the triple point of water cell.

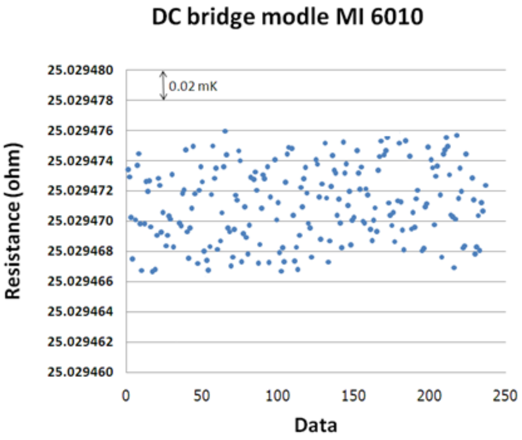

Figure 5. Resistance measurement of SPRTs with the MI 6010 DC bridge in the triple point of water cell.

The average values of all measurements, DC bridge and AC bridge, are shown in Figure 6. There was a lot of noise in the measurements. Many researches with interference sources were conducted on the thermometer bridge [5]. AC bridges are more susceptible to electromagnetic interference from electronic devices and interference from the power supply voltage.

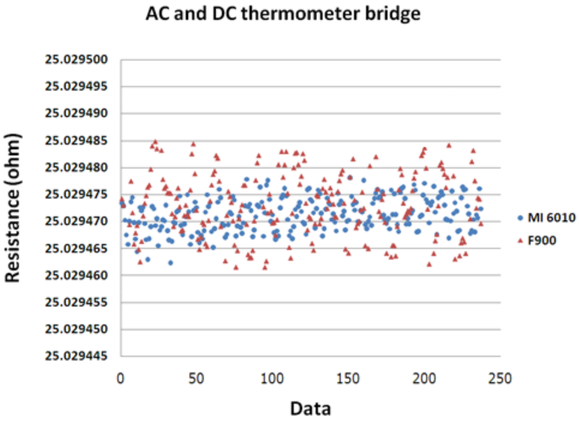

Figure 6. Comparison resistance measurement of SPRT with AC bridge and DC bridge in the triple point of water cell.

Conclusions

Many laboratories have not had as much success with AC bridges, seeing noise closer to 50 µK. We have gotten better results in NIMT's laboratory with DC bridge, which give us noise within 20 µK, compared to about 50 µK for our AC ASL F900 bridge. Again, this may only be because we're using AC furnaces and haven't taken as much care to reduce interference and reactance [6].

Future plan will include the difference frequency of AC bridge.

Acknowledgments

This work was supported by the National Institute of Metrology (Thailand).

References

1. The International Temperature Scale of 1990 (ITS-90), Metrologia. 1990, Vol.37: 3-10.
2. http://en.wikipedia.org/wiki/Bridge_circuit
3. ASL, F900 Precision Thermometer Bridge, Operator's Handbook.
4. Measurement International, Model 6010, Operator's Handbook.
5. Valentin Batagelg, Jovan Bojkovski, "Noise and Interference in Thermometry Resistance Bridges", XIX IMEKO World Congress Fundamental and Applied Metrology (2009), Lisbon, Portugal.
6. http://www.fluke.eu/comx/showproduct.aspx?localeThen&product=CSTORM&pid=756

Spectral Domain Optical Tomography Techniques for Nondestructive Metrology of Layered Materials

P. Meemon

School of Laser Technology and Photonics, Institute of Science,
Suranaree University of Technology, Nakhon Ratchasima, Thailand 30000
Corresponding author. E-mail: panomsak@sut.ac.th

Abstract

Optical Coherence Tomography (OCT) is an optical imaging technology that based on principle of low coherence interferometry. It is capable of nondestructive and noninvasive depth sectioning of the sample at high resolution (less than 10 microns), high speed (more than 100 frames/second), and high sensitivity (down to 10^{-6} reflectivity). The ability to perform noninvasive 3D imaging at micrometer resolution attracts vast applications in bio-imaging and medical imaging fields for over 20 years. Furthermore, OCT also finds application for nondestructive characterization of non-biological samples, such as ancient paintings, semiconductors, and material metrology. This work reports application of three dimensional OCT imaging for metrology of layered polymeric materials. As an example, 3D metrology of layered polymeric components with discrete gradient refractive index (GRIN) is demonstrated. Advantages of the polymeric GRIN lens are reduced size, light weight, aberration corrected, easy-mounting yet highly robust optical systems compared to conventional lenses. Nevertheless, the fabrication of the layered polymeric GRIN optics is quite different from the conventional lens fabrication. As a result, most of conventional metrologies fail to correctly characterize such materials. The design and fabrication of this new type of GRIN optics require new approach of nondestructive metrology techniques to inspect the samples across the manufacturing stages, e.g. from nanofilms to sheets to preforms to diamond turning and pollishing. In this work, we have investigated the capability of OCT, particularly the frequency domain OCT (FD-OCT), to nondestructively characterize layered polymeric GRIN materials. Several techniques for high-resolution sub-surfaces topography as well as thickness topography of layered polymeric GRIN samples were developed. The results correlated well with light microscope observance, however caused no surface damage in comparison, which confirms the potential of FD-OCT for fast and nondestructive metrology of the layered polymeric GRIN across the manufacture processes.

Keywords: optical coherence tomography, 3D imaging, nondestructive metrology, optical metrology, thickness topography, surface profilometry, spectrometer design

Introduction

Optical Coherence Tomography conventionally builds on the principle of white light interferometry developed by Albert Michelson. In addition, Low-Coherence Interferometry (LCI) extended white light interferometry to the near infrared spectrum. The technique was extended in the early 90s as a non-invasive tomographic technique [1], referred broadly as OCT in the current literature, for biomedical imaging of the eye as well as highly scattering media such as the coronary artery and the human skin. OCT has the potential for unprecedented imaging depth and resolution comparable to other noninvasive medical imaging modalities.

Furthermore, recent advancement in Frequency Domain OCT (FD-OCT) has enabled high speed and high sensitivity depth-resolved 3D imaging of samples [2, 3]. FD-OCT utilizes the principle of light interference in the frequency domain [4], where reflected light from different depths inside the sample relative to the position of the reference reflector are encoded as different modulation frequencies on the detected spectrum at the interferometer exit. As a result, the full depth profile of the sample can be obtained through the Fourier transform of the spectral interference pattern captured at the output of the interferometer without scanning the reference reflector. This mechanism dramatically improves imaging speed of OCT, allowing 3D imaging of a sample in real time [5, 6].

In recent years, there has been an ever-growing interest in exploring novel, highly efficient optical materials to develop compact and effective optical components. One of the most fast-moving directions of interest has been focused on the gradient refractive index (GRIN) optics, which allow for reduced size, light weight, easy-mounting yet highly robust optical systems compared to conventional optical set-ups. One of the breakthroughs is a process to produce nanolayered polymer film based GRIN optics with an unparalleled control of the internal refractive index distribution has been previously described [7, 8]. This process, based on multilayer co-extrusion polymer film processing [9, 10], is capable of producing polymer films comprised of a plurality of layer thicknesses constrained in individual layer thicknesses below the quarter-wavelength of visible light.

Nevertheless, the design and fabrication of such high-performance GRIN optics require nondestructive metrology techniques to inspect the samples. In this paper, we demonstrate the capability of OCT to nondestructively characterize layered polymeric GRIN materials. Using our new developing system and techniques of FD-OCT [11, 12], high-resolution 3D imaging, sub-surface interface topography and layer thickness metrology of a few typical layered polymeric GRIN samples are demonstrated.

Materials and Methods

Polymeric GRIN samples used in this development were fabricated by manufacture site at PolymerPlus, USA. For 3D imaging of the layered polymeric GRIN materials, we primarily used a Fourier-domain swept-source OCT (SS-OCT) system with central wavelength at 1.33 µm and bandwidth of 158 nm. The axial optical resolution of the system is approximately 8 µm and the effective frequency sweep rate of the light source is 45 kHz. The system configuration and specification is detailed elsewhere [11, 13, 14]. The system was built on Mach-Zehnder interferometer as illustrated in Figure 1. Light from the source is split by a fiber coupler (80/20) and then delivered to a sample and reference arms of the interferometer. Light in the sample arm is focused into a sample through the focusing optics. Backscattered light from the sample is then collected and recombined with light from the reference arm at another fiber coupler (50/50). The interference signal is detected by a balanced photodetector and processed by a personal computer to construct a cross-sectional image of the sample.

Fourier transform of each interference spectrum yields an entire sample reflectivity profile along the incident beam path. Combining with lateral scanning of the sample beam, 2-dimensional (2D) and 3-dimentional (3D) cross-sectional images can be obtained. The maximum sensitivity of the system was measured to be about 98 dB. The imaging depth range was about 1 mm as determined by -10 dB sensitivity fall-off. For a typical lateral imaging field of view (FOV) of 10x10 mm^2, 500x500 depth scans were acquired with lateral sampling resolution of 20 µm. Each depth scan consisted of 500 sampling points with sampling resolution of about 1.9 µm, and therefore covered depth range of approximately 0.9 mm.

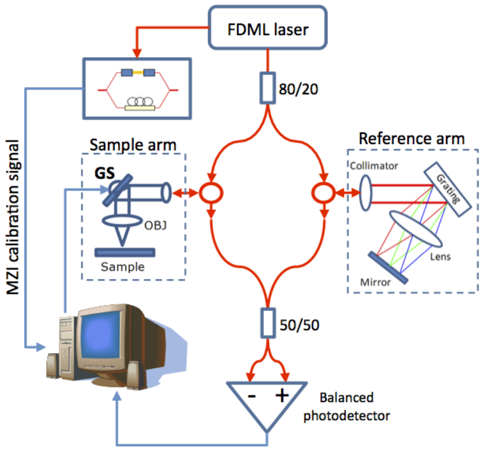

Figure 1 System layout

Based on the 3D imaging data, topography of the internal layer interfaces of the layered polymeric GRIN samples can be achieved. In our work, we detected the axial positions of the intensity peaks of every depth scan to find the depth locations of layer interfaces. By applying peak detection algorithm to all depth scans across the entire lateral FOV, we segmented layer interfaces within the 3D imaging volume for topographic mapping. After interface mapping, the optical thickness of one or more layers can also be obtained by computing the depth position difference between interfaces. It should be noted that the axial quantities directly offered by OCT are measured in terms of group optical path length (OPL), or the physical quantities multiplied by group refractive index (n_g). This is due to the low-coherence interferometry nature of OCT.

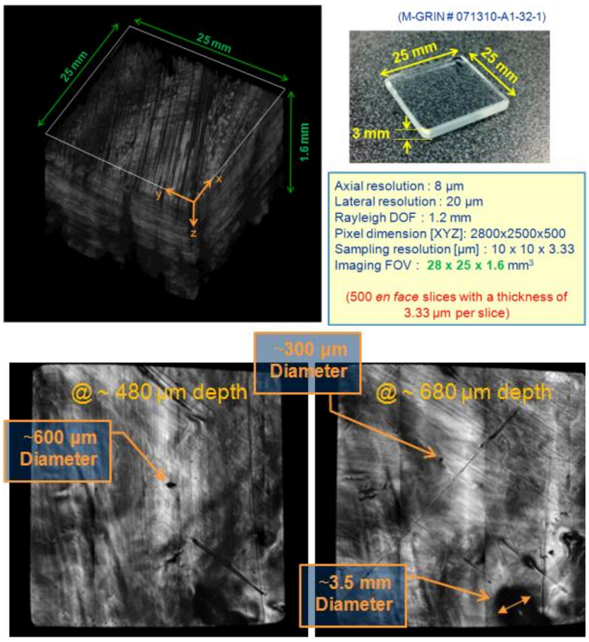

Axial resolution : 8 µm
Lateral resolution : 20 µm
Rayleigh DOF : 1.2 mm
Pixel dimension [XYZ]: 2800x2500x500
Sampling resolution [µm] : 10 x 10 x 3.33
Imaging FOV : 28 x 25 x 1.6 mm^3

(500 *en face* slices with a thickness of 3.33 µm per slice)

Figure 2. Nondestructive 3D tomographic imaging of a layered GRIN polymer, showing microscopic detail of its internal structure.

The 3D imaging data of the layered polymeric GRIN samples enables micron-scale 3D viewing of their internal structures and details. From the imaging data, the depth locations and spatial dimensions of sub-surface defects can be precisely quantified. Figure 2 shows a screen capture of the reconstructed 3D image of a GRIN sample and a few examples of its *en face* images at different depths. A number of line and particle defects can be clearly resolved from the images and accurately located in 3D. The non-destructive 3D visualization and quantification of defects provided by OCT imaging allows for valuable feedback to the manufacturing process for pre-screening and quality control of the materials.

Figure 3 shows an example of layer interface topography and subsequent transverse optical thickness topography results. The thickness topography was based on subtraction of the interface topography of two distinct layers. From thickness topography of each internal layer, a histogram distribution of sub-surface thickness variation across the sample was computed. The thickness distribution histogram associated to each plot of thickness topography in Figure 3 (bottom part) indicates the transverse thickness inhomogeneity of the sample. The capability of OCT for layer thickness topography allows us to diagnose the problematic samples and guide improvement directions for manufacturing process.

Figure 4 shows layer thickness profile over depth of an iso-index sample computed from OCT data. It appears that the layer thickness decreases from the edge towards the middle of the sample. The metrology results provided by OCT indicates that the sample was under-compressed near the edges and over-compressed in the middle prompted the manufacturer to inspect their coextrution operation. The existence of this non-uniform compression was verified by destructive test under the normal light microscope [15].

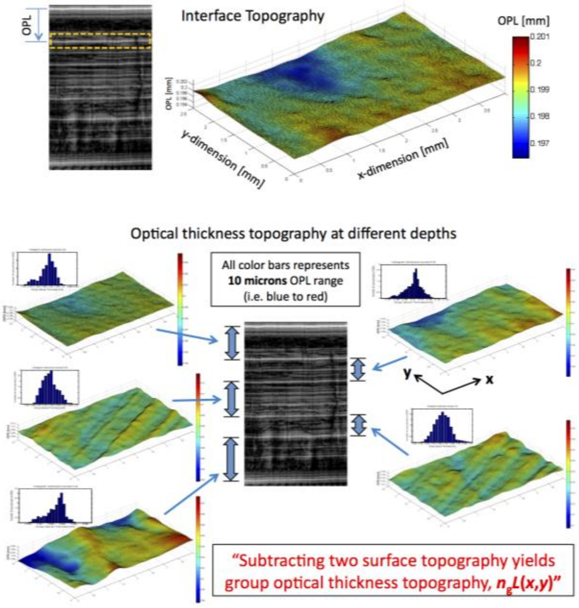

Figure 3. Topography of internal film interfaces (top) and optical thickness (bottom) of a layered GRIN polymer. The top topography is an example of topography of internal interfaces and corresponding reconstructed *en face* images at the interfaces denoted by an orange dash box; The bottom part shows cross sectional image of the layered GRIN polymer and corresponding topography of the optical thickness denoted by the arrows. Histogram distribution plot associated with each thickness topography, reveals transverse thickness inhomogeneity.

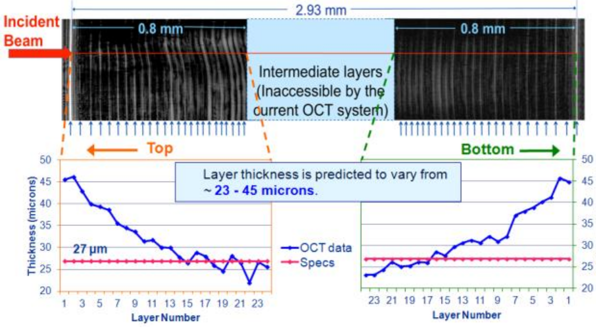

Figure 4. Films thickness profile as a function of layer number from the top surface (left plot) and from the bottom surface (right plot)

Conclusions

In conclusion, OCT has been proven to be a useful technique for metrology across the fabrication processes of the polymeric layered material. OCT-based metrology provides potential advantages for microscopic level of material characterization, such as nondestructive 3D visualization of materials micro-structures, high sensitivity to extremely small refractive index variation, and high speed imaging that would enable for in-line metrology for industrial applications. The potential useful of these developing techniques for microscopic metrology of other types of material is under investigation. Given these promising features of OCT for material characterization applications, a new high speed spectrometer-based FD-OCT system (Figure 5) is now designed and built at Suranaree University of Technology, Nakhon Ratchasima, Thailand. The system was designed to be capable of less than 6 μm depth resolution and high speed 3D imaging of sample (e.g. more than 100 frames per second) over large imaging field of view (e.g. 25 mm x 25 mm laterally and 2-5 mm axially).

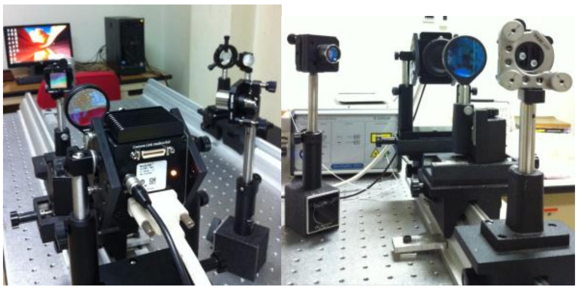

Figure 5. New spectrometer-based FD-OCT at the Laboratory of Laser Technology and Photonics at Suranaree University of Technology (Nakhon Ratchasima, Thailand).

Acknowledgments

The original OCT system and techniques were developed at Optical Diagnostics and Applications Laboratory at the Institute of Optics, University of Rochester as part of Manufacturable GRIN project supported by the Defense Advanced Research Projects Agency (DARPA) (USA). We thank PolymerPlus (USA) for providing the layered polymeric GRIN samples. The new FD-OCT system is supported by Suranaree University of Technology and by the Higher Education Research Promotion and National Research University Project of Thailand, Office of the Higher Education Commission.

References

1. D. Huang, E. A. Swanson, C. P. Lin, J. S. Schuman, W. G. Stinson, W. Chang, M. R. Hee, T. Flotte, K. Gregory, C. A. Puliafito, and J. G. Fujimoto, "Optical coherence tomography," Science **254**, 1178-1181 (1991).
2. A. F. Fercher, C. K. Hitzenberger, G. Kamp, and S. Y. El-Zaiat, "Measurement of intraocular distances by backscattering spectral interferometry," Optics Communications **117**, 43-48 (1995).
3. M. Choma, M. Sarunic, C. Yang, and J. Izatt, "Sensitivity advantage of swept source and Fourier domain optical coherence tomography," Optics Express **11**, 2183-2189 (2003).
4. M. Born and E. Wolf, *Principles of Optics, seventh expanded edition*, Cambridge, England (Cambridge University Press, 1999).
5. B. Potsaid, I. Gorczynska, V. J. Srinivasan, Y. Chen, J. Jiang, A. Cable, and J. G. Fujimoto, "Ultrahigh speed Spectral/Fourier domain OCT ophthalmic imaging at 70,000 to 312,500 axial scans per second," Optics Express **16**, 15149-15169 (2008).
6. L. An, P. Li, T. T. Shen, and R. Wang, "High speed spectral domain optical coherence tomography for retinal imaging at 500,000 A-lines per second," Biomedical optics express **2**, 2770-2783 (2011).
7. G. Beadie, J. S. Shirk, A. Rosenberg, P. A. Lane, E. Fleet, A. Kamdar, Y. Jin, M. Ponting, T. Kazmierczak, Y. Yang, A. Hiltner, and E. Baer, "Optical properties of a bio-inspired gradient refractive index polymer lens," Opt. Express **16**, 11540-11547 (2008).
8. Y. Jin, H. Tai, A. Hiltner, E. Baer, and J. S. Shirk, "New class of bioinspired lenses with a gradient refractive index," J. of Appl. Poly. Sci. **103**, 1834-1841 (2007).
9. M. Ponting, T. M. Burt, L. S. T. J. Korley, J. Andrews, A. Hiltner, and E. Baer, "Gradient multilayer films by forced assembly coextrusion," Ind. Eng. Chem. Res. **49**, 12111-12118 (2010).
10. M. Ponting, A. Hiltner, and E. Baer, "Polymer nanostructures by forced assembly: process, structure, and properties," Macromol. Symp. **294**, 19-32 (2010).
11. P. Meemon, "Development of Optical Coherence Tomography for Tissue Diagnostics," Dissertation (University of Central Florida, Orlando, 2010).
12. P. Meemon, S. Murali, K. Lee, and J. P. Rolland, "Gabor Domain Optical Coherence Microscopy," in *Frontiers in Optics*, OSA Technical Digest (CD) (Optical Society of America, 2008), paper FWW4.
13. P. Meemon and J. P. Rolland, "Swept-source based, single-shot, multi-detectable velocity range Doppler optical coherence tomography," Biomedical Optics Express **1**, 955-966 (2010).
14. K. S. Lee, P. Meemon, W. Dallas, K. Hsu, and J. P. Rolland, "Dual detection full range frequency domain optical coherence tomography," Optics letters **35**, 1058-1060 (2010).
15. J. Yao, P. Meemon, K.-S. Lee, K. Xu, and J. P. Rolland, "Nondestructive metrology of layered polymeric optical materials using optical coherence tomography," in *SPIE Optical Engineering+ Applications*, (International Society for Optics and Photonics, 2012), **8493**, 849307-(1-8).

The Study of a Resonance in a Spring Pendulum by Experiment and Numerical Analysis

S. Suwanarat*, P. Anusasananan, and N. Thangprasert

Department of Physics, Faculty of Science,
Ramkhamhaeng University, Bangkok 10240, Thailand
**Corresponding author. E-mail: suksanwork@gmail.com*

Abstract

The purpose of this research is to study a resonance in a spring pendulum both by the experiment and by the numerical computation. First, we build the spring pendulum system which consists of the spring pendulum, the data acquisition system and the software to collect and save the experimental data into the microcomputer for further analysis. Second, we write a program to solve the equations of motion for a spring pendulum using Runge-Kutta method. From our apparatus we can observe the resonance in the spring pendulum clearly by using these parameters; k = spring constant = 0.9155 N/m , M = mass of a bob = 0.0200539 kg, L = length of pendulum = 0.8572 m, r = elongation from equilibrium = 0.0142 m and θ = initial angle = 3°. The spring pendulum can oscillate in two ways: vertically, with elasticity of the spring acting as a restoring force and horizontally with gravity as the restoring force. The resonance in the spring pendulum happens when the frequency of the vertical oscillation is twice that of the horizontal oscillation. The result from our numerical calculation is exactly the same as from the experiment as we used the same parameter. The apparatus created in our laboratory together with the application program can be used as an educational and research tool for students and scientist.

***Keywords*:** Runge-Kutta method**,** resonance**,** spring pendulum, data acquisition system**.**

Introduction

The spring pendulum comprises of a bob suspended by a light elastic spring which may stretch but not bend as shown in figure 1. The bob is free to move in a vertical plane. Friction is neglected. The oscillations of this system are of two types, distinguished by their physical restoring mechanisms, spring oscillation and pendulum oscillation.

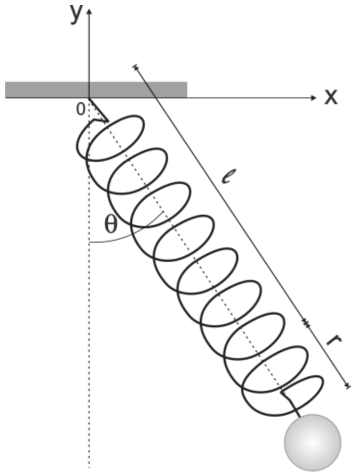

Figure 1. Spring pendulum.

A Lagrangian approach is implemented to deduce the equations of motion of the spring pendulum system. We define the elongation r(t) and the angle θ(t) as two generated coordinates. The kinetic and potential energies of this dynamical system are:

$$KE = \frac{1}{2}m\left[\dot{r}^2 + (\ell + r)^2\dot{\theta}^2\right]$$

$$PE = \frac{1}{2}kr^2 + mg(\ell + r)(1 - \cos\theta) - mgr$$

Where ℓ is equilibrium length of the pendulum, m is mass of the bob, ℓ + r(t) is the length of the spring and θ(t) is the angle of the spring.

The equations of motion can be derived from the Lagrange equations, the results are:

$$\ddot{r} = (\ell + r)\dot{\theta}^2 + g\cos\theta - \omega_r^2 r\ ,$$

and $\ddot{\theta} = -\dfrac{2}{\ell + r}\dot{r}\dot{\theta} - \omega_\theta^2 \sin\theta\ ,$

where $\omega_r = \sqrt{\dfrac{k}{m}}$ and $\omega_\theta = \sqrt{\dfrac{g}{\ell + r}}$.

The resulting equations of motion may be solved numerically [1, 3, 4].

Materials and Methods

The steps involved in this experiment are:

1. Design, develop and construct the spring pendulum system consists of a fixed base (30x30 cm), a long shaft (150 cm) and a spring pendulum.
2. Design, develop and construct the data acquisition system consists of phototransistor sensor, signal conditioning and decoder in order to get the data from the experiment.
3. Assembly the data acquisition system with the spring pendulum system.
4. Develop the computer program to receive the signal from usb port of the computer
5. Analyze the data stored on the computer by plotting a) the graph between angular position and time b) the phase space diagram which is a graph between angular velocity and angular position.
6. Change the parameter r, ℓ , m and k until we find a small spring oscillation and a resonance phenomenon.
7. Write a program to solve the equations of motion using Runge-Kutta method and using the same parameter as in the experiment.
8. Compare the experimental result with the numerical calculations.

Results and Discussion

In this research we first design, develop and build the spring pendulum system. The fixed base used to mount an optical wheel and the spring pendulum, is a 1.5 cm thickness and 30x30 cm wide. It’s weight 12 kg is enough to support the system during the experiment.

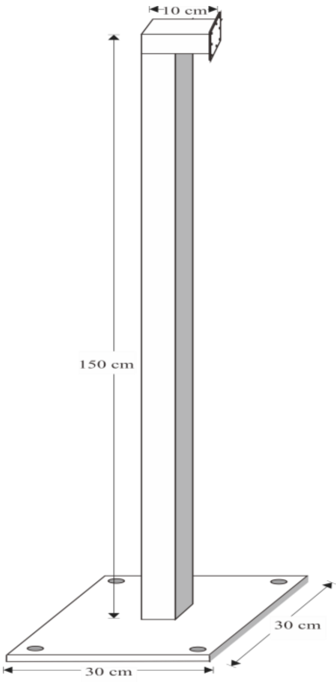

Figure 1. Fixed base 30x30 cm wide.

Then we design, develop and build the sensor, the decoder and the computer program to get the experimental data onto the computer. An optical encoder wheel which is used for reading angular displacement is fixed to axis of the spring pendulum. The encoder wheel has an angular resolution of about ± 0.09 degree and the maximum sample rate of 1000 samples/sec. The optical encoder used to read the angular position as a function of time. The data is stored on the computer for further analysis.

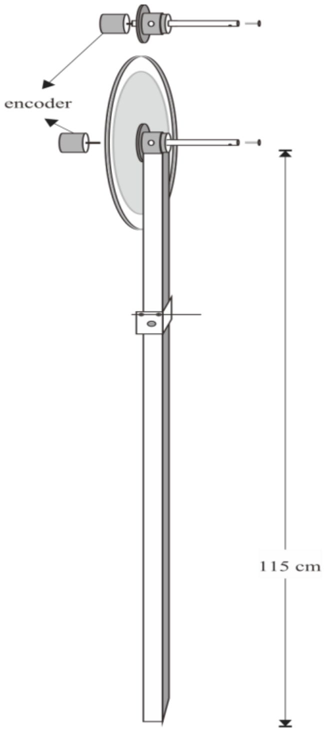

Figure 2. Optical encoder wheel.

A. Experimental results

Case I Non-resonant system behavior

In case that k=1000 N/m, m=0.2 kg, ℓ =0.1548 m , r= 0 m and $\theta = 7^{o}$ the spring pendulum acts like a simple pendulum as we can observed from the angular position-time curve in figure 3.

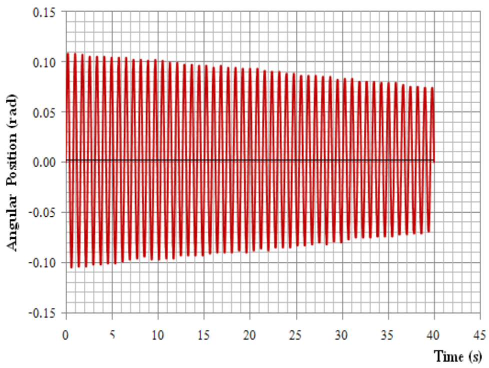

Figure 3. Time-series plot between amplitude and time.

From the data in the range 0-40 second, we fitted the amplitude with the non-linear regression equation. We obtain

$$Y=0.109789\times e^{\left(-x/107.124\right)}\times\sin\left(2\pi\left(\frac{t}{0.790954}\right)+6.21658\right)$$

When we compare the parameters involved with the damped harmonic oscillator equation

$$Y=Ae^{\left(-\gamma.t\right)}\sin\left(\left(\frac{2\pi t}{T}\right)+\phi\right)$$

We get the period of oscillation T=0.790954 second. After we substitute time into the above equation, we obtain the graph exactly as from the experiment as shown in figure 4.

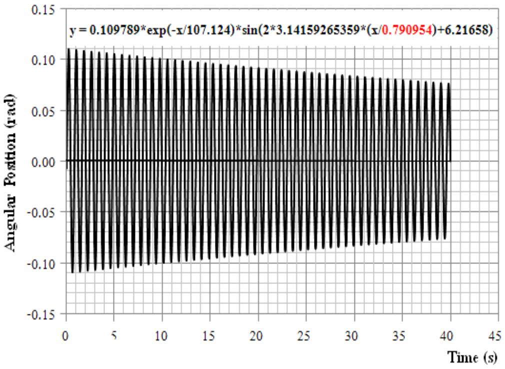

Figure 4. The graph calculated from the regression equation

Case II Resonant system behavior

In case that k=0.9155 N/m, m=0.0200539 kg, ℓ =0.8572 m , r= 0.142 m and θ = 3°, the resonance phenomenon of the spring pendulum appeared as shown in figure 5. The spring pendulum can oscillate in two ways: vertically, with elasticity of the spring acting as a restoring force and horizontally with gravity as the restoring force. The resonance happened when the ratio of the frequency of oscillation of the spring is twice that of the horizontal oscillation. There are two modes of oscillation, the bouncing mode as a result from destructive interference and the swinging modes as a result from constructive interference.

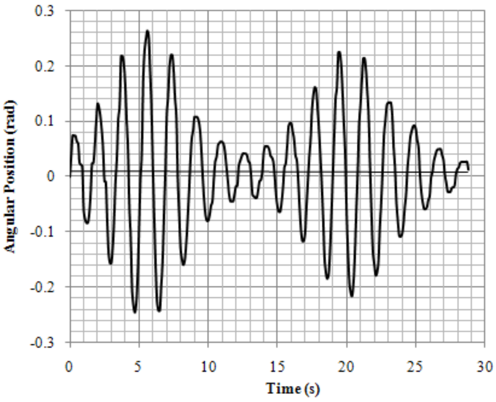

(a)

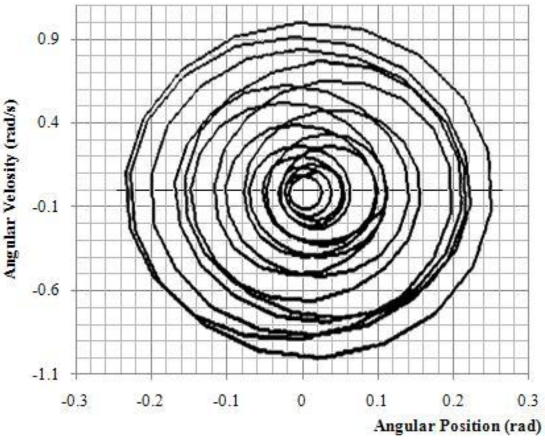

(b)

Figure 5. Resonance phenomenon.

A spring with length ℓ will oscillate vertically according to the equation of motion:

$$m\ddot{z}+k(z-\ell)=mg\,,$$

where z is the vertical position with z=0 at the top of the unstretch spring, $\ddot{z}$ is the second derivative in time, m is the mass attached to the spring, k is the spring constant and g is the gravitational acceleration. The solution of the above equation is $z(t) = A\cos\theta(\omega_s t) + (\ell + mg/k)$. For the initial position z_0, the spring oscillates with amplitude $A = z_0 - \ell - mg/k$ about the equilibrium point $\ell + mg/k$. For a massless spring, the angular frequency $\omega_S=\sqrt{k/m}$.

A pendulum with length ℓ oscillates according to the equation of motion:

$$I\ddot{\theta}+mg\ell\sin\theta=0$$

For simple pendulum, $I = m\ell^2$, and for small angles, sin θ ≈ θ. The solution of this equation is $\theta(t) = \theta_0\cos(\omega_p t)$, where $\omega_p=\sqrt{mg\ell/I}=\sqrt{g/\ell}$.

When the resonance occurs, it is observed that the period of the pendulum, T_p, is equal to twice the spring-like period, T_s: $2T_s= T_p$,when, for a mass less spring and a simple pendulum.

$$T_S=2\pi\sqrt{m/k}\,,\ T_p=2\pi\sqrt{\ell/g}$$

For the resonance to occurs, the unstretched length ℓ_S must be stretched to a length $\ell = 4mg/k$ [1, 2].

B. Numerical calculation

The linear analysis of this mechanical system is straightforward. Spring pendulum such as this one exhibit complex dynamical behavior including chaos and resonance. When non-linear effects are included there is coupling between the two types of motion, and analytical methods are incapable of providing the solution. To obtain insight into the characteristics of the motion in this case we must turn to numerical calculation. The equations of motion are integrated to obtain the position of the spring pendulum as a function of time using Runge-Kutta method.

In this numerical calculation, we used exactly the same parameters as in the experiment. The results from our numerical calculation agree quite well with the results from the experiment. This shows a high accuracy of our experimental system that can measure and store up to 60,000 points in 1 minute.

Case I Non-resonant system behavior

In case that k=1000 N/m, m=0.2 kg, ℓ =0.1548 m , r= 0 m and $\theta = 7^{o}$ the spring pendulum acts like a simple pendulum with friction. The angular position time curve is shown in figure 6.

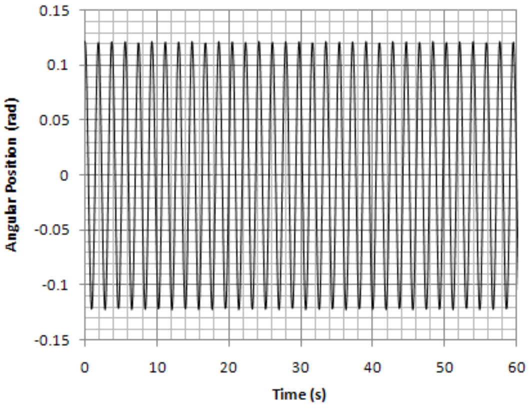

Figure 6. Time-series plot between amplitude and time from numerical computation.

Case II Resonant system behavior

In case that k=0.9155 N/m, m=0.0200539 kg, ℓ =0.8572 m , r= 0.142 m and $\theta = 3^{o}$, the resonance phenomenon of the spring pendulum appeared. The angular position curve is shown in figure 7 and the phase space diagram is shown in figure 8.

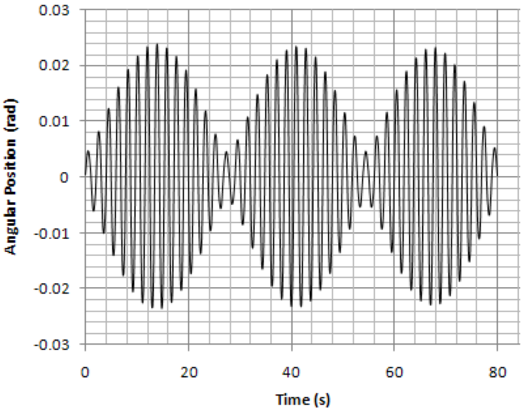

Figure 7. Time-series plot between amplitude and time from numerical calculation.

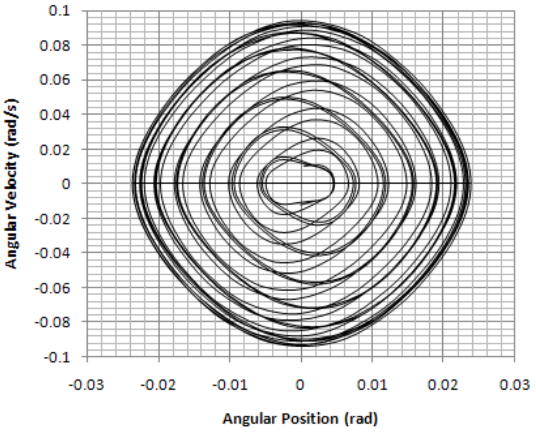

Figure 8. Phase space diagram as calculated from numerical analysis.

Conclusions

In this research we study a resonance in a spring pendulum both by the experiment and by the numerical computation. We first build the spring pendulum to do the experiment and then we write a program to solve the equations of motion of a spring pendulum using numerical analysis. The results from our experiment agree quite well with the result from numerical calculation. The apparatus developed in our laboratory together with the software can be very useful in other physics experiments. Our numerical analysis is worth in many systems that can not set up the apparatus to do the real experiment. The complexity between the numerical analysis and the real experiment makes this experiment a very useful tool to simulate the thinking process of a physicist.

Acknowledgments

Thank you Department of Physics, Faculty of Science, Ramkhamhaeng University for supporting this research.

References

1. Daniel R. Stump, Solving classical mechanics problems by numerical integration of Hamilton's equations, Am. J. Phys.54 (12), 1985.
2. J. P. van der Weele , E. de Kleine, "The order-chaos-order sequence in the spring pendulum", Elsevier Science Physics A 228 (1996) 245-272.
3. S.V. Kuznetsov, "The Motion of the Elastic Pendulum", Regular and chaotic dynamics, V. 4, No.3, 1999.
4. Siva Srinivas Kolukula , "Spring Pendulum". From:http://www.mathworks.com/matlabcentral/ fileexchange/33168-springpendulum

The Study of Mini-Tin Fixed Point Cell

P. Wongnut*, P. Phanphanit, and U. Norranim

National Institute of Metrology (Thailand), 3/4-5 Moo 3, Klong 5,
Klong Luang, Pathumthani 12120 Thailand
**Corresponding author. E-mail: phichet@nimt.or.th*

Abstract

There are many temperature calibration laboratories in Thailand; however, there is a few of them could provide calibration with primary standard instruments (The Fixed-point cells corresponding to ITS-90). This is due to highly expensive price of a set of the fixed point cells. If the temperature calibration laboratories could have their own set of fixed point cells, it will reduce their calibration uncertainty. As a result, the calibrated thermometers will be more accurate, increasing the quality of measurement of the industrial thermometers. Therefore, as being a National Institute of Metrology (Thailand), we decided to study and invent the fixed point cells (Ga (29.7646 °C), Sn (231.928 °C) and Zn (419.527 °C) fixed point cells) to cover the temperature range of 0 °C to 420 °C, which is the most common range used by industrial sections. First of all, Tin fixed point is of our interest because Tin material is available commercially in Thailand. Since this research is to support the industrial section, the Tin cell is reduced in size in order to be practical with existing temperature sources, for example, temperature baths and blocks in the calibration laboratories. A Tin purity, certified by the supplier, is greater than or equal to 99.999% and its crucible is made of graphite ISO 63, which is also available in Thailand. The protection tube is made of stainless steel. The diameter of the cell is 45 mm and its height is 235 mm. The mini-Tin cell is characterized for its important properties: freezing temperature plateau, reproducibility, and stability. It was found that the mean freezing temperature of the mini Tin cell is 4.0 mK higher than our reference cell. The freezing plateau is approximately 5 hours with a reproducibility of 1.0 mK and a stability of better than 2.7 mK.

Keywords: Tin fixed point cell, freezing plateau, freezing temperature

Introduction

Temperature and its measurement system have been involved in many subject areas, for example, food industrial, automotive industrial and public health. In present, National Institute of Metrology (Primary Laboratory) is an organization, who maintains the national standard of temperature and transfers the standard value to secondary laboratories. Then the standard value will be transferred to industrial section by thermometers calibration. However, all secondary laboratories could not provide all calibration services to the industrial section due to a lack of primary standard instrument, which are considerably expensive.

Therefore, the National Institute of Metrology (Thailand), department of Thermometry Metrology has studied and developed the mini fixed-point cells from material available in Thailand. This is to support the secondary laboratories to establish the primary standard with an affordable price for testing and calibration. As a result of this, a capability of temperature measurement will be improved to be more reliable with a higher accuracy.

The mini Tin fixed-point cell has been designed in order to be practical with existing temperature sources of the secondary laboratories. Firstly, the mini Tin fixed-point cell is of interest because Tin material is commercially available in Thailand. In general, the temperature baths are 50 mm or more in diameter and 300 mm in depth; thus, the mini Tin fixed-point cell is required to be smaller than 50 mm in diameter and shorter than 300 mm in height.

Materials and Methods

Material

The mini Tin fixed-point cell is designed to be 235 mm in height and 45 mm in diameter. It has been made of material available in Thailand and its structure is shown in figure 1. There are 3 components; 1. The crucible is made from Graphite ISO-63, 2. The protection tube is made from stainless steel 304 and 3. The Tin material has a purity of 99.999% and a weight of 174.45 g. The total height of Tin is approximately 90 mm.

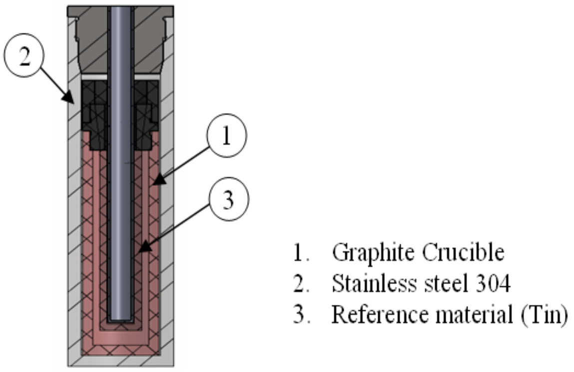

Figure 1. The structure of mini Tin fixed-point cell

The equipments used in the experiment are thermometry Bridge Model F700 (manufacturer: ASL), standard platinum resistance thermometer Model 909 (manufacturer: Isotech), and the silicone oil bath Model 6022 (manufacturer: Hart scientific). The pressure in the cell was monitored by a pressure indicator and the data were collected and saved by computer with Labview program.

Method

First of all, the effect of the bath temperature setting on the temperature of the mini Tin fixed-point cell was investigated in order to be able to choose the appropriate setting temperature throughout the experiment. To investigate this effect, the cell has been realized many times by varying the setting temperature for melting state from 232.5 ˚C to 236 ˚C and keeping the setting temperature for freezing state fixed. Then the temperatures of the mini Tin fixed-point cell were observed. Moreover, the setting temperature was kept constant for melting state and was varied from 231.3 ˚C to 231.7 ˚C for the freezing state. Figure 2 illustrates the correlation between the mini Tin fixed-point temperature and the liquid bath setting temperature.

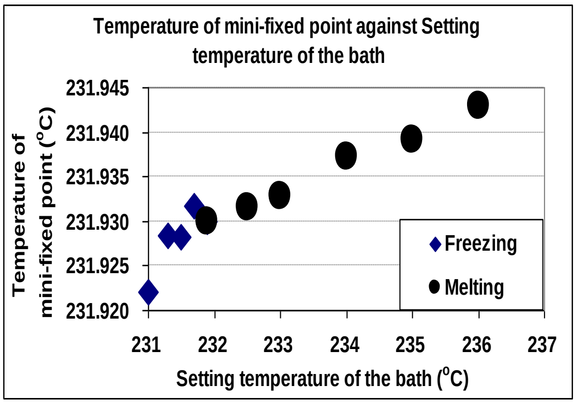

Figure 2. The correlation between temperature of the mini Tin fixed-point cell and the setting temperature of the bath.

As can be seen from figure 2, the setting temperature of the bath could affect the temperature of the mini Tin fixed-point cell, the higher the setting temperature, the larger the deviation observed for melting state. For the setting temperature of the freezing state, the lower the temperature set, the larger the deviation occurred. This is due to the heat transfer at the top of the SPRT, which was not immersed in the cell. The most appropriate temperature to be set is 231.7 ˚C because this setting temperature results in the least deviation from the theoretical value. Additionally, this temperature will slightly affect the temperature of the mini Tin fixed-point cell and give the longest Tin freezing curve.

The oil bath had been set at 228 ˚C for 3 hours (pre-condition) and then the setting temperature was increased to be 235 ˚C at least for 14 hours in order to completely melt the cell. The temperature of the oil bath had been decreased to 229 ˚C until the Tin material reached its recalescence and then the oil bath temperature was increased to 231.7 ˚C to maintain the freezing state of the mini Tin fixed-point cell. Figure 3 shows the melting and the freezing curve of the cell. As can be seen from figure 3, the melting plateau was approximately 20 minutes at 231.98 ˚C and the recalescence was observed at 229.4 ˚C. The freezing plateau was approximately 8 hours at 231.93 ˚C.

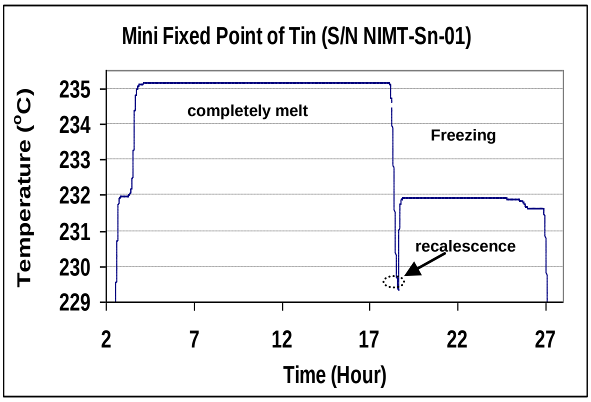

Figure 3. The melting and freezing curve of the mini Tin fixed-point cell.

Results and Discussion

From the experiment, the average freezing point of the mini Tin fixed-point cell from three repeated realizations is found to be 231.932 ˚C, which is 4 mK higher than the temperature of the reference Tin fixed-point cell. This deviation of the mini Tin fixed-point cell from the reference cell could be because the purity of the Tin material has been decreased due to the contamination from contacting the Graphite crucible. The mini Tin fixed-point cell has a reproducibility of approximately 1 mK and a stability of less than 2.7 mK for 5 hours as shown in figure 4.

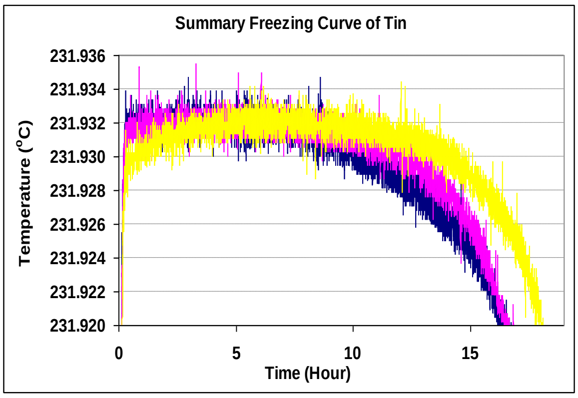

Figure 4. The freezing curves of three repeated realizations of the mini Tin fixed-point cell.

Conclusions

It can be concluded that the mini Tin fixed-point cell has sufficiently good characteristics and it can be used as the primary standard. It is also suitable for using in the secondary laboratories in order to improve their capability of calibration.

References

1. Supplementary Information for The International Temperature Scale of 1990 (1997 reprinting of the first edition).
2. ASTM E1502-98 (Reapproved 2003), Standard Guide for Use of Freezing-Point Cells for Reference Temperatures.
3. Uncertainties in the Realisation of the SPRT Subranges of the ITS-90. CCT-WG3

The Study of Self-heating Errors on 100 Ω Platinum Resistance Thermometers

P. Phanphanit* and U. Norranim

National Institute of Metrology (Thailand),3/4-5 Klong Luang, Pathumthani12120 Thailand
**Corresponding author. E-mail: phattharawadee@nimt.or.th*

Abstract

Platinum resistance thermometers (PRTs) are widely used in many fields of industrials because it is significantly accurate compared with other types of thermometers. Although the PRTs are very accurate, there are few errors occurred in PRT measurement, for example, errors due to an immersion depth, a long term drift and a self-heating. In this study, self-heating error is of interest for the PRTs. Self heating is the phenomenon that caused by the power dissipated and accumulated in the element, resulting in the increase of element temperature to be higher than the surrounding temperature. As a result of this, there will be an error from the self-heating, which is always happened and very difficult to avoid in the measurement results. In this research, the self-heating errors of the 100 ohm PRTs are investigated. Three parameters that could affect the self-heating error are studied: sensing currents, measured temperatures and probe dimensions. The ratio of the couple current used to obtain the self heating error is $1:\sqrt{2}$ and the sensing currents are varied from 0.5 mA to 2 mA. The measured temperatures are 0 °C, 23 °C, 150°C and 300 °C. In this study, there are 5 different types of 100 ohm PRTs. It was found that the higher the sensing current, the larger the self-heating error occurs. However, the sensing current of 0.5 mA resulted in instable measurements, whereas the current of 1 mA caused the least self-heating error (less than 10 mK at 300 °C) with sufficiently stable results. The measured temperature and the probe dimension were found to have less effect on the self-heating errors. Additionally, the medium where the PRT is immersed has been shown up to be more influential in the self-heating errors. From the study, the medium with less thermal conductivity caused more self-heating error.

Keywords Self heating error, Platinum resistance thermometer

Introduction

Platinum Resistance Thermometers (PRTs) are devices used to measure temperature by correlating resistance with temperature; the change in resistance is depending on the temperature, the higher the temperature, the larger the resistance. To measure the resistance, the electrical current is required to pass through the sensing element and the voltage drop across the resistance is observed to obtain the resistance.

PRTs are widely used in many fields of industrial due to low cost, compared with Standard Platinum Resistance Thermometers (SPRTs). Additionally, they have relatively high accuracy, compared with other type of thermometers: thermocouple, digital thermometer, and liquid in glass thermometers. Although they are very accurate, there are a few errors occur in the PRTs measurement. One of the major causes to the errors is the self-heating effect. The self-heating effect is a well known phenomenon that occurs when sensing current heats up the PRTs sensor, [1, 2]. As a result of this, the reading temperature is slightly higher than the actual temperature. For a very high accuracy measurement, SPRTs, the self-heating errors is typically 0.2 – 3 mK , [3], and for PRTs 100 Ω, it can be up to 50 mK, depending on many factors, [1, 4, 5].

In this paper, the self-heating background is presented and the factors influencing the self-heating errors are investigated on the 5 different types of PRTs 100 Ω in order to estimate and reduce the self-heating errors by obtaining the optimal conditions for PRTs 100 Ω measurements.

Self-Heating Background

Self-heating effect occurs when the sensing current dissipates power and increases the temperature of the sensing element. The self-heating error is directly proportional to the square of the sensing current. The current, I, dissipates power, P, the self-heating error can be directly calculated in term of temperature by the following equation, [6];

$$\Delta T_{SH} = \Pr = I^2 Rr \qquad (1)$$

ΔT_{SH} is the self-heating error, R is the resistance and r is the thermal resistance, which can be divided into two parts; one is the thermal resistance from the PRTs coil to the sheath and the other one is the thermal resistance from the sheath surface to the ambient. Therefore, the thermal resistance is dependent on the PRT Design and the medium in which the PRT is immersed. However, these two thermal resistances are very difficult to obtain; the two currents method is introduced, [7].

To obtain the self-heating error, two different currents are used to measure temperatures and the self-heating error can be calculated accurately to better than 1% for PRTs 100 Ω from the following equation, [4];

$$\Delta T_{SH1} = (T_2 - T_1)[I_1^2/(I_2^2 - I_1^2)] \qquad (2)$$

ΔT_{SH1} is the self-heating error at current I_1 and T_1 and T_2 are the temperature at I_1 and I_2 , respectively. The most commonly currents used are 1 mA and $\sqrt{2}$ mA because they make equation (2) very simple and the optimal uncertainty of the self-heating error is at a certain pair of currents; 1.5 mA and 2.5 mA, [7]. The self-heating effect is always happened and it cannot be eliminated; however it could be correct with some uncertainty by using equation (2).

Factors Influencing Self-Heating Error

There are many factors that could affect the self-heating error; PRT design, sensing current and surrounding medium; therefore, if the optimal conditions of these factors can be obtained, then the self-heating error could be reduced.

PRT Design

The different PRT designs could result in different self-heating error. If the PRT has a large surface area of the sensing element, the heat generated can be dissipated more to the surrounding medium than the PRT with a small surface area. Additionally, the size of the sheathing could also affect the error; the smaller the sheathing, the larger the error occurs.

Sensing Current

As can be seen from equations (1) and (2), the temperature error due to the self-heating effect is increased with the square of the current; thus the sensing current needs to be considered when using the PRT. The conventional current used is typically 1 mA for PRT 100 Ω, recommended by the manufacturer.

Surrounding Medium

A medium, in which the PRT is immersed, also plays an important role in the self-heating phenomenon. The highly thermal conductivity medium could help more heat to be dissipated. In addition, the self-heating error decreases with the increase of the flow rate of the moving medium, [6]. However, the temperature of the medium could also affect the error because it will alter the properties of the medium.

Results and Discussion

Experiment

In an investigation, there are 5 different types of PRT 100 Ω; Table 1 shows details of each probe used.

Table 1: Details of each PRT 100 Ω

Model	Length	Diameter
5626	38 cm	6.40 mm
5627	30 cm	6.40 mm
STS100A500	50 cm	4.00 mm
Pt 100	53 cm	5.95 mm
TS32A	49.5 cm	3.20 mm

There are three parameters that had been studied in this research; sensing currents, measured temperature and probe dimensions. The ratio of the couple currents used to obtain the self-heating errors is 1:√2 and the sensing currents were varied from 0.5 mA to 2 mA by 0.5 mA each step. The measured temperatures are 0 ˚C, 23 ˚C, 150 ˚C and 300 ˚C. These measured temperatures could not be done by using one temperature source. Therefore, the alcohol bath was used to set the temperature of 0˚C and 23 ˚C. For higher temperatures, the oil bath and the dry block were used to set the measured temperatures of 150 ˚C and 300 ˚C, respectively. Then the self-heating errors are calculated based on equation (2) and the results are presented and discussed in next section.

Result and Discussion

First of all, the sensing currents were varied at each measured temperature. All PRT models result in the same trends of the self-heating errors; therefore, only the results of PRT model STS100A500 were presented. Figure 1 illustrates the self-heating errors of PRTs 100 Ω model STS100 A500 against the measured temperature for various sensing currents.

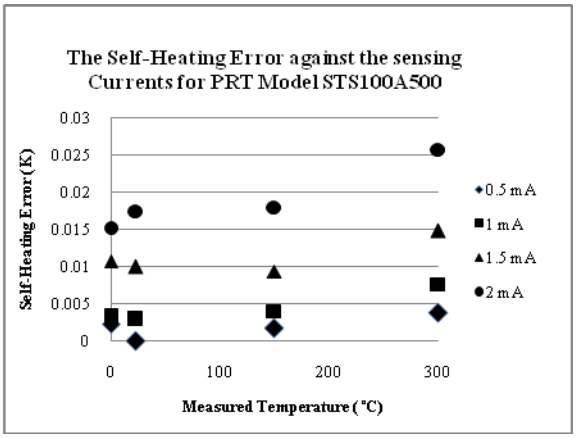

Figure 1. The self-heating error against the sensing current for PRT Model STS100A500 with various sensing currents.

As can be seen from Figure 1, at each sensing current the self-heating error at the measured temperature of 300 ˚C are the highest. In addition, the self-heating error increases with the sensing current. However, at low currents (0.5 mA and 1 mA) the measured temperature has less effect, comparing with the high currents (1.5 mA and 2 mA) as can be seen from the slopes of the graphs. When plotting the self-heating errors against the currents as shown in Figure 2, it could confirm that sensing current has strong effect on the self-heating errors as the slopes of all graphs are very deep.

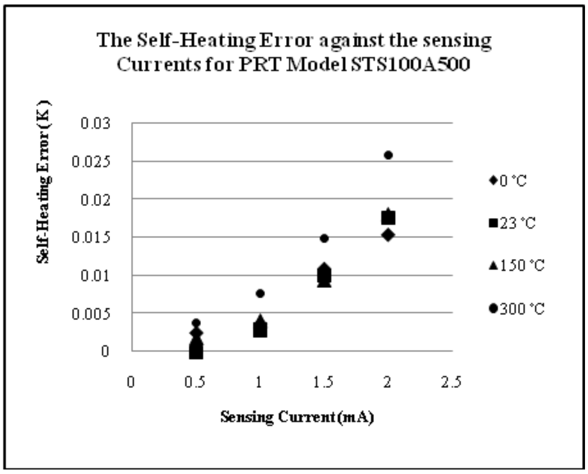

Figure 2. The self-heating error against the sensing current for PRT Model STS100A500 with various measured temperature.

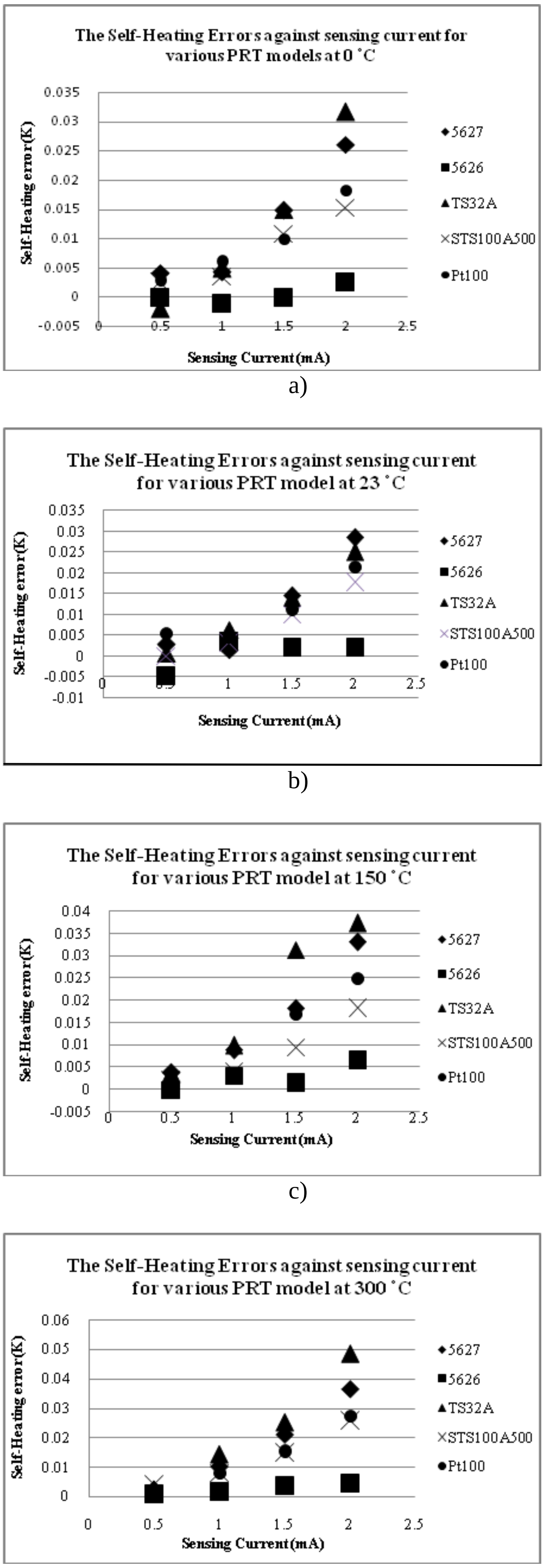

a)

b)

c)

d)

Figure 3(a-d). The self-heating errors against the sensing currents for various PRT models.

As can be seen from Figure 3(a-d), at the sensing current of 0.5 mA the results are very instable since there is no trend for the self-heating errors. This is corresponding to the result of the study of V. Batagelj that the low currents result in a high standard deviation of the measurement [7]. Additionally, apart from 0.5 mA, the self-heating error is the least at 1 mA current and the values of the self-heating errors are within 10 mK for every measured temperature. The highest self-heating errors occur at 2 mA current and 300 ˚C, the values are between 5 mK to 50 mK. The probe dimension has less effect on the self-heating errors for the low currents since there is no particular trend observed and the self-heating errors are not significantly different from each other. When the current is increased up to 2 mA, the effect can be seen more clearly. However, this is still not caused by the probe dimension because the self-heating errors are increased with neither increase nor decrease of both diameter and length.

The measured temperatures do not affect the self-heating errors as can be seen in figure 3(a-c) that the results are slightly different for the measured temperatures of 0 ˚C to 150 ˚C, the self-heating errors are between 5 mK to 30 mK. However, at 300 ˚C the self-heating errors are considerably larger than those in the other three temperatures, the values of the errors become 10 mK to 50 mK. Since the media in temperature sources are different, the thermal property of the media are considered and presented in Table 2.

Table 2: Thermal property of the medium at 25 ˚C in temperature source [8].

Medium	**Thermal conductivity (W/(m·K))**
Alcohol	0.17
Silicone Oil	0.1
Air	0.024

Alcohol has the highest thermal conductivity; thus, it should cause the least self-heating errors. However, the self-heating errors in oil bath are close to the self-heating error in the alcohol bath; this could be because the self-heating error is also dependent on the flow rate of the medium, which is not investigated in this research. The silicone oil at 150 ˚C might have a larger flow rate than the alcohol at 0˚C or at 150 ˚C the thermal properties of silicone oil might be altered. Not only air has the lowest thermal conductivity, but air is also not moving; as a result of this, the self-heating errors in the dry block at 300 ˚C are significantly higher than those at other measure temperatures.

Conclusions

It can be concluded that the sensing current has a strong effect on the self-heating errors of the PRTs 100 Ω; the larger the current used, the higher the self-heating error occurs. Although the lowest current used was 0.5 mA, but the current of 1 mA is more appropriate to be used because it gives the lowest self-heating errors with more stable results. The measured temperature and the probe dimension slightly affect the self-heating errors. The more important factor to be considered is the medium used, which has also shown the strong effect on the self-heating errors.

Acknowledgments

We would like to thank National Institute of Metrology (Thailand), who provides me all equipments and facilities to complete the experiment in this research.

References

1. V. Batagelj, J. Bojkovski, and I. Pusnik, “Optimizing the Uncertainty due to the Self-Heat of Platinum resistance Thermometers in Practical Use”, Proceedings, XVII IMEKO World Congress, 2003.
2. H. E. Sostman, and J. P. Tavener, “Fundamentals of Thermometry part V - Industrial (Use) Platinum Resistance Thermometers”.
3. V. Batagelj, J. Bojkovski, and J. Drnovsek, “Methods of reducing the uncertainty of the self-heating correction of a standard platinum resistance thermometer in Temperature Measurements of the Highest Accuracy”, Measurement Science and Technology, 2003.
4. C. M. Sutton, “In situ Measurement of Resistance Thermometer Self-Heating and Response Time”, Measurement Science and Technology, 1994.
5. H. E. Sostman, “Fundamentals of Thermometry part III - The Standard Platinum Resistance Thermometer”.
6. J. V. Nicholas, and D. R. White, “Traceable Temperatures An Introduction to Tempearature Measurement and Calibration”, John Wiley & Sons Ltd, 1994.
7. V. Batagelj, J. Bojkovski, J. Drnovsek, and I. Pusnik, “ Influence of SPRT Self-Heating on Measurement Uncertainty in Fixed Point Calibration and Calibration by Comparison”, Temperature: Its Measurement and Control in Science and Industry, Volume 7, 2003.
8. www.engineeringtoolbox.com.

Ion and Plasma Physics

From Electric Birth through Micro-nova to Streaming Demise of the Plasma Focus-Knowledge and Applications

S Lee[1,2,3*] and S H Saw[1,2]

[1]*INTI International University, 71800 Nilai, Malaysia.*
[2]*Institute for Plasma Focus Studies, 32 Oakpark Drive, Chadstone, 3148 Australia.*
[3]*Physics Department, University of Malaya, Malaysia.*
**Corresponding author. E-mail:* leesing@optusnet.com.au

Abstract

The plasma focus is a copious source of multiple radiation and highly energetic particles: hard and soft x-rays, electromagnetic radiation, fusion neutrons, relativistic electron beams, fast ion beams and highly energetic plasma streams with shock fronts exceeding Mach 1000. All these complex interactive radiation and particle streams are generated from a device which typically could be table-top located. It is a triumph of modern science and technology that we can now present a complete picture of the plasma focus in the lifetime of its dynamic evolution. That lifetime typically occupies all of 10 microseconds; from the time a spark starts the electric current which rises to 100 kA within a microsecond, driving a shock wave to Mach 100 straight down the coaxial tube; to the radial compression phase when increasing electromagnetic forces doubles the speed of the hot plasma shock waves; before the final focusing action; squeezing the plasma into a superheated highly dense 'pinch' with temperatures exceeding that of the centre of the sun. From this minute cauldron of hot dense matter comes forth the rich explosion of multiple radiation and energetic particles and beams. In a typical device this "micro-nova" lasts less than 0.1 microsecond. This paper uses sequences of detailed nanosecond-exposure pictures to show the evolution of the plasma pinch, conveying the idea of the very high speeds and hence high temperatures involved. Although detailed knowledge of many specific areas within the lifetime of the plasma focus is still lacking so that the microscopic view in many areas need to be filled in; yet there is a satisfactory picture of the whole processes linking the plasma focus as it evolves from stage to stage. Particularly exciting are the many applications that have been demonstrated using the multiple radiation and energetic particles for micro-lithography, micro-machining, advanced materials manipulation and fabrication down to nano-levels. Work is on-going for materials interrogation and identification with security implications; and generation of complex radiation and particle pulses of relevance to nuclear fusion reactors. Numerical experiments gain valuable insights that guide future developments and applications, suggesting new devices for compression and yield enhancements. An integrated hardware and numerical experiment package can also be profitably developed to train manpower and generate applications for the dawning of the Fusion Age.

1. Introduction

The Plasma Focus is a compact powerful pulsed source of multi-radiation [1]. Even a small table-top sized 3 kJ plasma focus produces an intense burst of radiation with extremely high powers. For example when operated in neon, the x-ray emission power peaks at 10^9 W over a period of nanoseconds. Powerful ion beams are emitted typically carrying 10^{15} 100 keV ions per kJ of discharged energy. When operated in deuterium the neutron burst produces rates of neutron typically 10^{15} neutrons per second over burst durations of tens of nanosecond. The emission comes from a point source making these devices among the most powerful laboratory pulsed radiation sources in the world. These sources are plasma-based.

When matter is heated to a high enough temperature, it ionizes and becomes plasma. It emits electromagnetic radiation. The spectrum depends on the temperature and the material. The higher the temperature and the denser the matter, the more intense is the radiation. Beams of electrons and ions may also be emitted. If the material is deuterium, nuclear fusion may take place if the density and temperature are high enough. In that case neutrons are also emitted. Typically the temperatures are above several million K and compressed densities above atmospheric density starting with a gas a hundredth of an atmospheric density.

One way of achieving such highly heated material is by means of an electrical discharge through gases. As the gas is heated, it expands, lowering the density and making it difficult to heat further. Thus it is necessary to compress the gas whilst heating it, in order to achieve sufficiently intense conditions. An electrical discharge between two electrodes produces a constricting magnetic field which pinches the column. In order to 'pinch', or hold together, a column of gas at about atmospheric density at a temperature of 1 million K, a rather large pressure has to be exerted by the pinching magnetic field. Thus an electric current of at least hundreds of kA are required even for a column of small radius of say 1 mm. Moreover the dynamic process requires that the current rises very rapidly, typically in under 0.1 μs in order to have a sufficiently hot and dense pinch. Such a pinch is known as a super-fast super-dense pinch; and requires special MA fast-rise (ns) pulsed-lines. These lines may be powered by capacitor banks, and suffer the disadvantage of conversion losses and high cost due to the high technology pulse-shaping line, in addition to the capacitor banks.

A superior method of producing the super-dense and super-hot pinch is to use the plasma focus. Not only does this device produce superior densities and temperatures, moreover its method of operation does away with the extra layer of technology required by the expensive and inefficient pulse-shaping line. A simple capacitor discharge is sufficient to power the plasma focus.

2. The plasma focus

The plasma focus is divided into two sections. The first is a pre-pinch (axial) section. The function of this section is primarily to delay the pinch until the capacitor discharge (rising in a damped sinusoidal fashion) approaches its maximum current. This is done by driving a current sheet down an axial (acceleration) section until the capacitor current approaches its peak. Then the current sheet is allowed to undergo transition into a radial compression phase. Thus the pinch starts and occurs at the top of the current pulse. This is equivalent to driving the pinch with a super-fast rising current; without necessitating the fast line technology. Moreover the intensity which is achieved is superior to the line driven pinch.

The two-phase mechanism of the plasma focus [2] is depicted in Figure 1. The inner electrode (anode) is separated from the outer concentric cathode by an insulating backwall (see Figure 2). The electrodes are enclosed in a chamber, evacuated and typically filled with gas at about 1/100 of atmospheric pressure. When the capacitor voltage is switched onto the tube, breakdown occurs axisymmetrically between the anode and cathode across the backwall. The 'sheet' of current lifts off the backwall as the current rises to a sufficient value.

Axial phase: The self-magnetic force of the current then pushes the current sheet, accelerating it supersonically down the tube. This is very similar to the mechanism of a linear motor. The speed of the current sheet, the length of the tube and the rise time of the capacitor discharge are matched so that the current sheet reaches the end of the axial section just as the discharge reaches its peak value. This phase typically lasts 1-3 μs for a plasma focus of several kJ.

Radial Phase: The part of the current sheet in sliding contact with the anode then 'slips' off the end 'face' of the anode forming a cylinder of current, which is then pinched inwards. Imploding inwards at higher and higher speeds, the shock front coalesces on-axis and a super-dense, super-hot plasma column is pinched onto the axis (see Figure 2). This column stays super-hot and super-dense for typically ten ns for a small focus. The column then breaks up and explodes. For a small plasma focus of several kJ, the most intense emission phase lasts for the order of several ns. The radiation source is spot-like (1mm diameter) when viewed end-on.

3. The Pinch phase of the plasma focus

3.1 A filtered photo of the million K pinch

Figure 3 shows a photograph of the INTI PF [4,5] pinch taken with an ordinary digital camera. The long-exposure allows light from all the phases of the PF device to be incident on the recording CCD. But the combination of filters allows only the brightest part of the discharge dynamics to be shown; hence the pinch (the brightest part of the column) is recorded. The more diffuse part of the column at the right edge of the photo is the post-pinch plasma stream.

3.2 Nanosecond shadowgraphs of the plasma focus pinch and post-pinch

To capture time-resolved images of the focus pinch an exposure time of 1 ns is necessary to freeze the motion to less than 0.3 mm (since the highest speed of the current sheet is expected to be around 30 cm/μs (or 0.3 mm/ns). A collimated laser beam with an exposure time of 1 ns is shone through the plasma focus (side-on) and the shadow of the moving plasma is cast onto a recording CCD. The plasma self light is filtered away. The time of the laser pulse is adjustable. A composite sequence of shots is obtained [6] as shown in Figure 4. The time of the image is recorded on top of the image with t=0 being the time when the plasma focus pinch is judged to be at its most compressed state.

From this sequence the average speed of implosion from a=8mm (t=-30 ns) to a~0.5 mm (t=0) is found to be 0.25 mm/ns or 25 cm/μs. The peak speed is more as the current sheet is accelerating as it speeds inwards. Taking the speed of 25 cm/μs, due to the equipartition of energy in a shock the on-axis temperature is immediately found to be 1.5x10^6K; and on shock

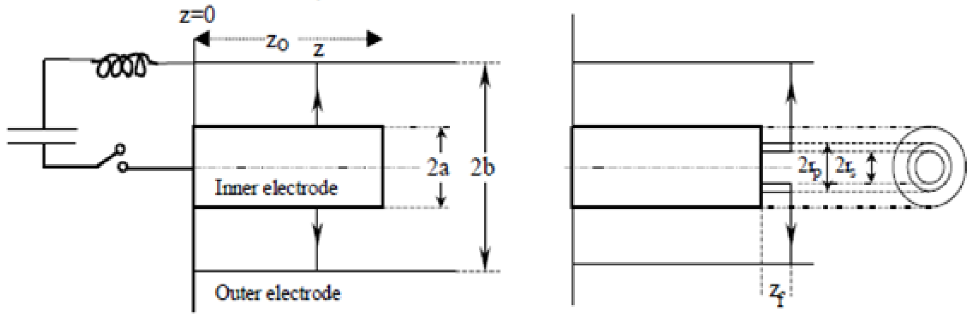

Figure 1. Schematic of the axial and radial phases. The left section depicts the axial phase, the right section the radial phase. In the left section, *z* is the effective position of the current sheath-shock front structure. In the right section r_s is the position of the inward moving shock front driven by the piston at position r_p. Between r_s and r_p is the radially imploding slug, elongating with a length z_f. The capacitor, static inductance and switch powering the plasma focus is shown for the axial phase schematic only.

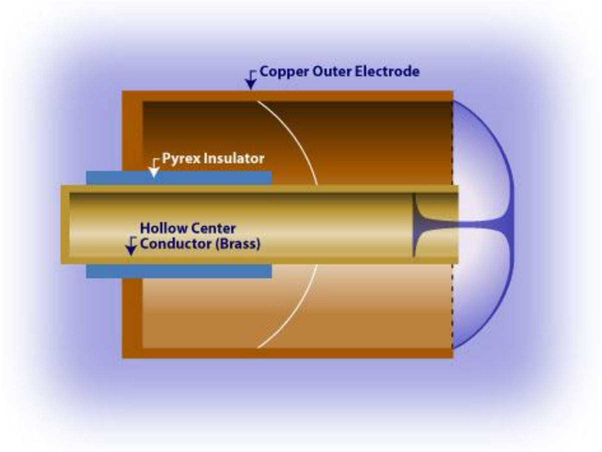

Figure 2. Dense plasma focus device. Image from Glenn Millam. Source: Focus Fusion Society [3]

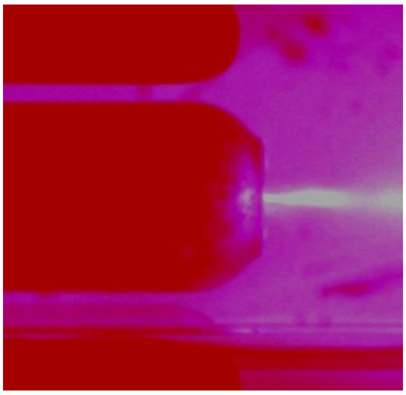

Figure 3. A still photo of the million C plasma pinch produced in the INTI PF (taken by Paul Lee) Using suitably chosen filters, the most intense optical radiation is shown, which turns out to be the pinch; all other phases of dynamics, being less optically intense, are filtered away.

causing the column to reach a temperature of 3x10^6K. The instability break-up of the column is seen in the last 2 frames.

In Figure. 5 the anode is shown pointing upwards (whereas in Figure 4 the anode is pointing left to right). The sequence [6] follows that of the inward implosion and instability break-up of the pinch. This post-focus sequence shows that 14 ns after the break-up (shown in the sequence of Fig 4) a fast shock wave is shot out from the focus region traversing 9 mm in 22 ns or 40 cm/μs.

Fig 6 shows a sequence of shadowgraphs taken at a much later time from 0.65 μs (t=+650 ns) to 1.75 μs. Measurements [7] show that this copper jet comes from material sputtered from the anode by the electron beam. This copper jet travels much more slowly at 2 cm/μs containing ¼ mg of copper carrying 50 J of kinetic energy.

The radiations from the plasma focus are produced for the 3 kJ PF from -5ns to +26 ns (Fig 4). First the soft x-rays which is characteristic of the gas (particularly in gases from nitrogen upwards in atomic number) start to be emitted just before t=0; the ion beams emitted in a downstream direction and the electron beam in the opposite direction towards the anode; and the neutrons (from deuterium pinches) are emitted just after t=0; as are the hard x-rays. The high speed axial shock waves (Fig 5) carrying considerable energy and the associated post-pinch plasma streaming and then the slower jet from anode sputtered materials (see Fig 6) constitute the final products of the plasma focus phenomenon. The use and control of these 'streaming death' products are proving of importance for plasma focus materials modification, fabrication and deposition as thin films.

3.3 From electrical birth through micro-nova to streaming demise of the Plasma Focus

The above images reveal detailed dynamics of the radial phases of the 3 kJ plasma focus, from the compression to the pinch and instability break-up to the subsequent fast plasma streaming, these processes taking just over 100 ns extending another microsecond or s

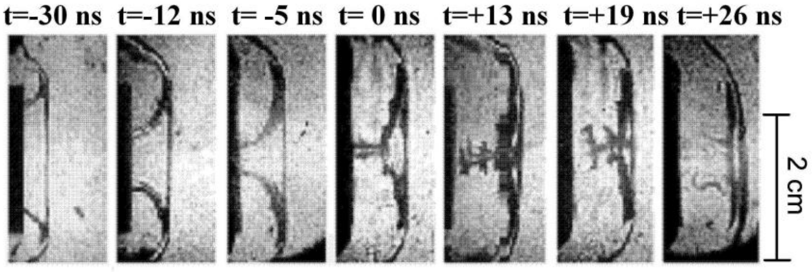

Figure 4. A composite sequence [6] of the radial implosion dynamics of the plasma focus (anode shown pointing sideways- left to right)

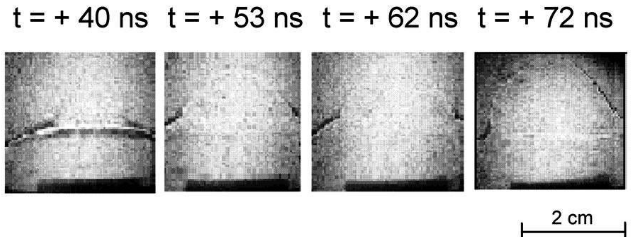

Figure 5. A sequence showing post focus axial shock waves blown out from the pinch [6] (anode shown pointing up)

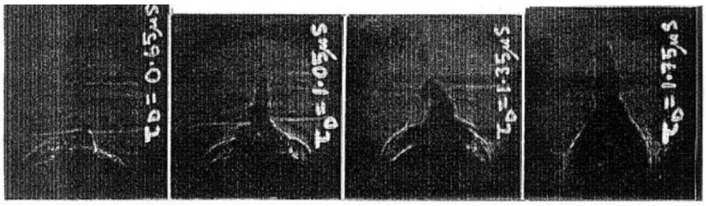

Figure 6. Composite sequence [7] showing anode-sputtered copper plasma jet occurring at a later time (anode shown pointing up)

Many other diagnostics are used to find more information for all the phases of the plasma focus. At the same time a comprehensive and complete numerical experiment code is available to be configured to run as any plasma focus in the world. This code [8] needs only one measurement from the selected plasma focus namely the current waveform. With this current waveform fitted to the computed waveform the code outputs all the dynamics from axial to radial phase and pinch phase giving speeds, times and dimensions of the pinch, condition of the plasma, radiation and neutron yields, and the numbers and energetics of the ion beam, electron beams, post-pinch fast plasma stream and the anode-sputtered copper jet. An example is shown in Figure 7 of the simplest measurement requiring only a current coil. All the information of that plasma focus shot – from electrical birth (start of axial phase) through the pinch (end of radial phase) to the streaming death- is contained in the current waveform and to some extent in the voltage waveform, also shown in Figure 7.

4. Research towards applications

The small group of plasma focus experts gathered here today to review the research conducted in our the following ss. The list is not exhaustive but is a useful guide. More details will be added as our conference proceeds.

1. Microelectronics lithography towards nano-scale using focus SXR, EUV and electrons
2. Micro-machining
3. Surface modification and alloying, deposition of advanced materials: superconducting films, fullerenes, DLC films, TiN, ZrAlON, nanostructured magnetic CoPt thin films
4. Surface damage for materials testing in high-radiation and energy flux environment
5. Diagnostic systems of commercial/industrial value: CCD-based imaging, multi-frame ns laser shadowgraphy, pin-hole and aperture coded imaging systems, neutron detectors, diamond and diode x-ray spectrometer, vacuum uv spectrometer, ccd-based electron energy analyser, Faraday cups, mega-amp current measurement, pulsed magnetic field measurement, templated

SXR spectrometry, water-window radiation for biological applications; neutron activation and gamma ray spectroscopy'

6. Pulsed power technology; capacitor discharge, Pulsed power for plasma, optical and lighting systems, triggering technology, repetitive systems, circuit manipulation technology such as current-steps for enhancing performance and compressions; powerful multi-radiation sources with applications in materials and medical applications
7. Plasma focus design; complete package integrating hardware, diagnostics and software.
8. Fusion technology and fusion education, related to plasma focus training courses

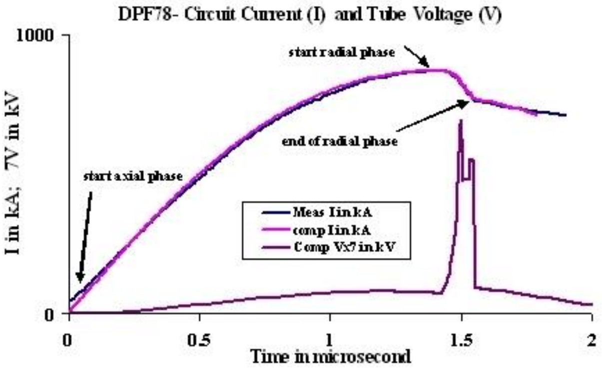

Figure 7. Computed current waveform fitted to the measured current waveform. Indicated on the current trace are the start and end of axial phase, start and end of radial phase. This fitting of the computed current calibrates the code configured as the DPF78 for this figure. The code then outputs realistic dynamics, lifetime and dimensions of the pinch and yields and energetics for this shot.

5. Conclusion: Presenting some products

5.1 Micro-lithography and micro-machining towards nano-scale

Figure 8. shows the NX2 (2 kJ, 400 kA, 16 shots per second, 300 W neon SXR per shot, 10 minute burst duration) in its original set-up for micro-lithography. Figure 8(a) is a schematic of the 1-tonne (1.4 m high) structure with the focus chamber surrounded by the capacitor bank and raised above the ground on pillars made up of ALE chargers, gas distributors and trigger sub- systems.The lithography assembly is suspended below (behind) the focus electrodes platform see also Figure 8(d) which shows clearly the extraction of the neon SXR though the rear of the anode.

Figure 8(b) shows some details of the water-cooled anode and cathode structures. Figure 8(c) shows the m-high beamline for monitoring the SXR mounted above the plasma focus chamber. Figure 8(d) shows the details of the lithography beamline 1=hollow anode; 2= cathode; 3=focus pinch; 4= SXR beam extracted with a diverging angle; 5= magnets for deflecting electron beam; 6= holder with 3 in-line apertures extracting the SXR beam but reducing the shock/blast waves from the discharge; 7= berylium window; 8= SXR mask with pattern to be lithographed; 9= SXR resist on which lithograph pattern is formed; 10= substrate holding the SXR resist. Figure 8(e) shows 6 small squares in two rows. The top row are test structures replicated in resist of PMMA495. The left square of the second row is the SXR lithography test mask consisting of 200 nm gold features placed on a supporting100 nm membrane of Si3N4. The other two squares are test structures replicated in ERP40 positive resist. Figure 8(f) shows details of two sub-micron replicated lithographed structures.

The NX2 is also used in repetitive mode for the related application of micro-machining, producing sub-micron high aspect ratio trenches; very well defined and with a much greater depth than the width. Figure 9 is a SEM image of a 100 nm trench micro-machined with neon SXR.

5.2 Materials deposition and advanced materials fabrication

A simple set-up for depositing thin films is shown in Figure 10. The centre of the anode is inserted with a cylinder of chromium and argon may be used as the operating gas. The electron beam from the pinch impacts on the chromium producing a post pinch chromium jet which moves to the sample, coating it within 20-30 shots. The shutter is opened for the process to begin only when the device is focussing strongly. For coating a sample surface with TiN the chromium is replaced with titanium, and nitrogen is used as the operating gas. After the pinch the fast nitrogen plasma stream impacts the sample followed microseconds later by the anode-sputtered titanium plasma.

Figure 11. shows the NX2 set-up for fabricating advanced nano-materials. In this set-up 100 nm agglomerates of FeCo are deposited consisting of grains typically 20 nm across. This material has potential for the next generation of ultra-high density of magnetic data storage. Other possible candidates are nano-structured materials like CoPt and FePt which are are also deposited.

5.3 A world-class product: Integrating a proven hardware package with a proven numerical experiments package: Developing the most powerful training and research system for the dawning of the Fusion Age.

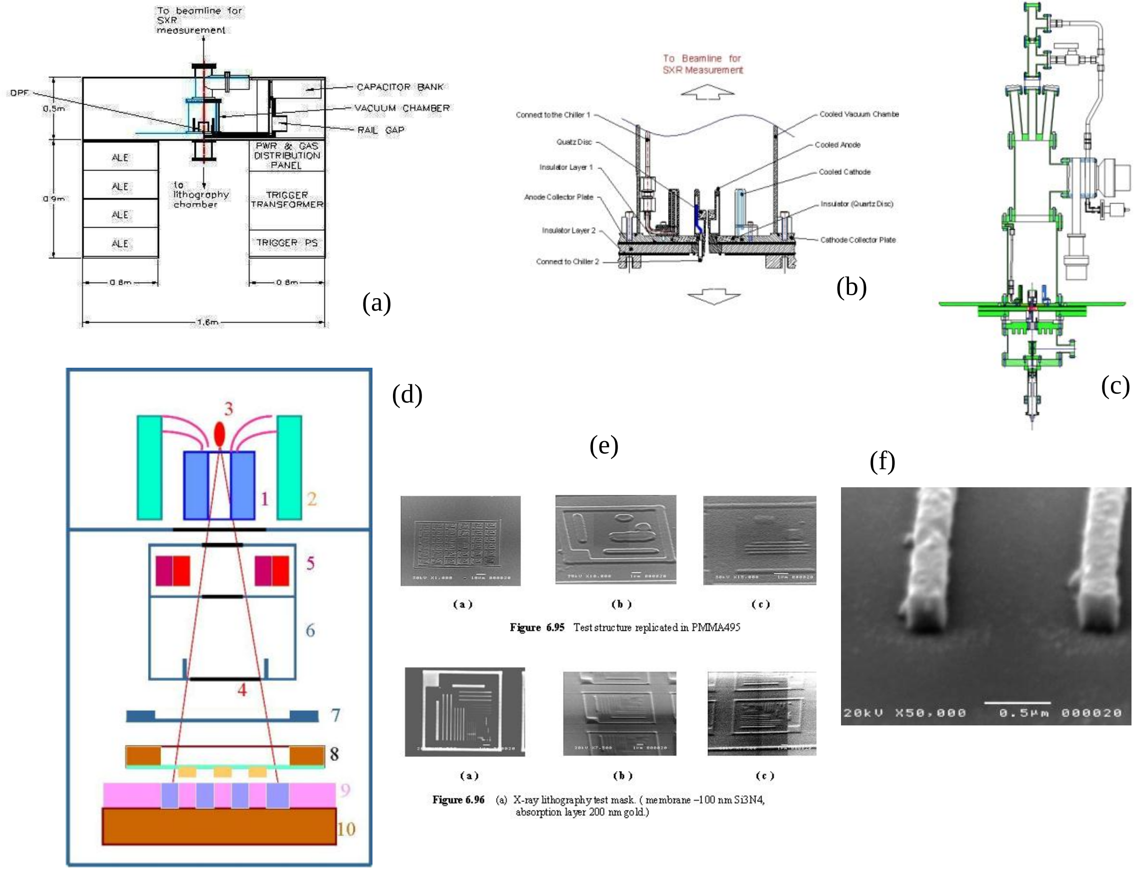

Figure 8. NX2 (Singapore) Lithographic machine, duplicated test structures and sub-micron lines [9]

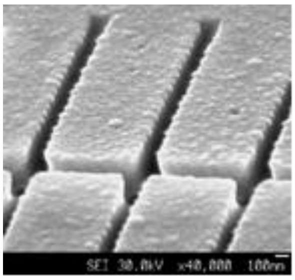

Figure 9. The NX2 producing micro-machined samples [9].

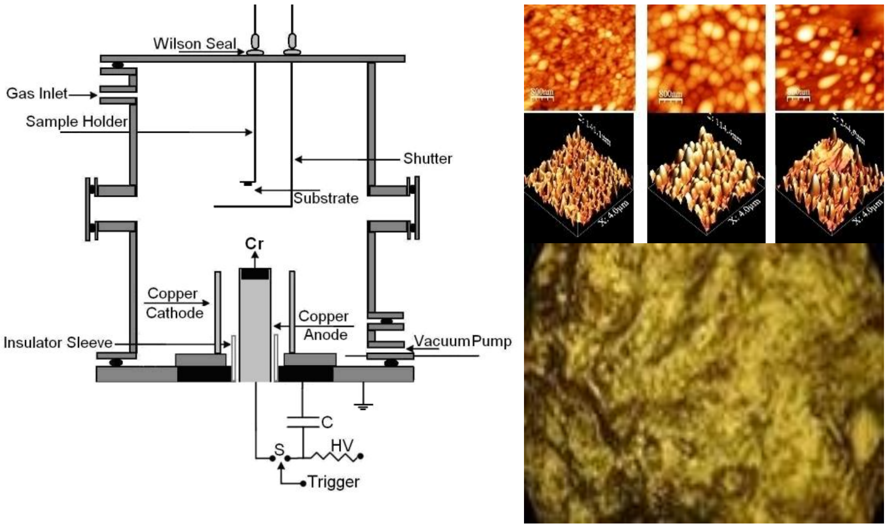

Figure 10. 2 kJ plasma focus for thin film deposition [10]; and samples of deposited chromium (Right side, top 2 rows) & TiN films (right side, bottom image)

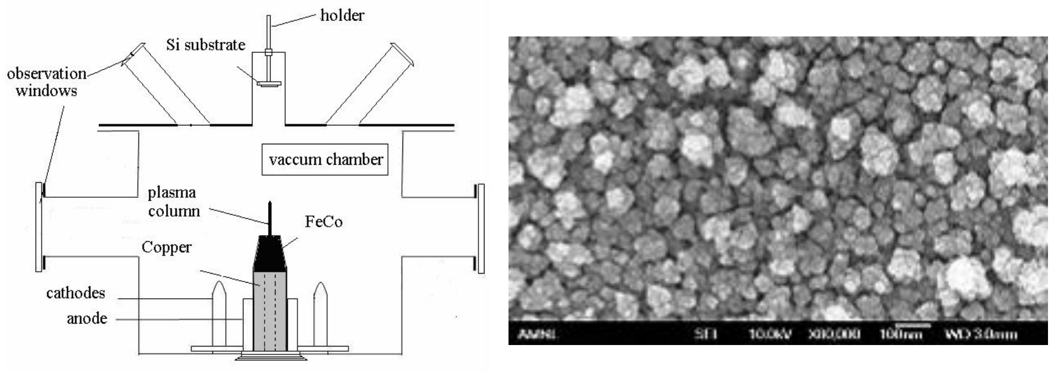

Figure 11. NX2 set-up for depositing thin films; deposited thin films with 100nm FeCo agglomerates [11]

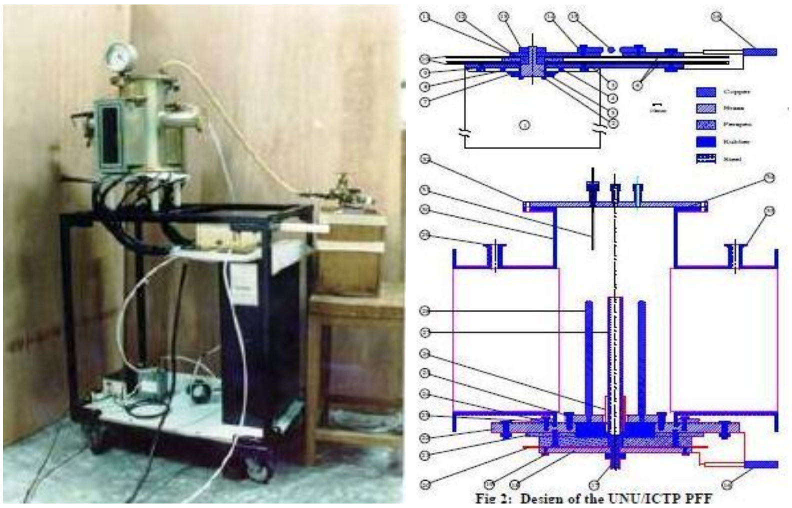

Figure 12. The trolley based UNU/ICTP PFF 3 kJ plasma focus training and research system [12]

UNU Fellow Widdi Usada assembling his UNU/ICTP PFF   Parts of several UNU/ICTP PFF'

Dr Walter Shearer of UNU with UNU Fellows Zakaullah and Dr Eissa   UNU Fellows Warnate and Dr Smith with 1 set (in crates) of UNU/ICTP PFF

Figure 13. Building on a tradition (shown in this pictoral record) [12-14] the small plasma focus is ready to be developed into the world’s most effective training and research package when integrated with the Lee model code [2.8] with emphasis on dynamics, radiation and materials applications.

Figure 12 shows the UNU/ICTP PFF 3 kJ system, already acknowledged as a very successful training and research package. It is ready to be updated technologically and then integrated to the Lee Model code with emphasis on dynamics, radiation and materials applications.

It will draw on the spirit and tradition of the UNU/ICTP PFF (shown in the pictoral record of Fig 13) and the Lee model code. It will be the world's most effective training and research package developed to help meet the needs of scientific and engineering manpower for the inevitable dawning of the Fusion Energy Age [15].

References

1. A Bernard, H Bruzzone, P Choi, H Chuaqui, V Gribkov, J Herrera, K Hirano, A Krejci, S Lee, C Luo, F Mezzetti, M Sadowski, H Schmidt, K Ware, C S Wong, V Zoita *Scientific Status of Plasma focus Research*. J Moscow Physical Society, 8, 93-170 (1998).
2. S Lee *Plasma focus model yielding trajectory and structure*. In Radiations in Plasmas, McNamara, B., Ed.; World Scientific, Singapore: Volume II, pp. 978–987 (1984).
3. Glenn Millam Focus Fusion Society
4. S H Saw, S Lee, F Roy, PL Chong, V Vengadeswaran, ASM Sidik, YW Leong & A Singh-In-situ determination of the static inductance and resistance of a plasma focus capacitor bank– Rev Sci Instruments 81, 053505 (2010).
5. S Lee, S H Saw, R S Rawat, P Lee, R Verma, A.Talebitaher, S M Hassan, A E Abdou, Mohamed Ismail, Amgad Mohamed, H Torreblanca, Sh Al Hawat, M Akel, P L Chong, F Roy, A Singh, D Wong, K Devi. *Measurement and Processing of Fast Pulsed Discharge Current in Plasma Focus Machines*- J Fusion Energy DOI: 10.1007/s10894-011-9456-6 Online First™ 28 July 2011
6. Muhammad Shahid Rafique. *Compression Dynamics and Radiation Emission from a Deuterium Plasma Focus* PhD thesis Nanyang Technological University, Singapore (2000).
7. S. Lee, Harith Ahmad, T.Y. Tou, K.H. Kwek and C.S. Wong. *Dynamics of REB-sputtered copper plasma jets*. J. Fiz. Mal., Malaysia 6: 23-28 (1985)
8. S Lee Radiative Dense Plasma Focus Computation Package:RADP http://www.plasmafocus.net/IPFS/modelpackage/File1RADPF.htm (2012). http://www.intimal.edu.my/school/fas/UFLF/File1RADPF.htm (2019).
9. **G.X.Zhang.** ***Plasma Soft x-ray source for Microelectronics lithography*****. PhD thesis, Nanyang Technological University Singapore (1999).**
10. **M. Ghoranneviss*, S. Javadi, M. Habibi, Z. Abdolahi, S. Lee, S.H. Saw *Investigation of Structural Properties of Chromium Thin Films Prepared by Plasma Focus Device* (submitted for publication)**
11. **R S Rawat, Z Ahang, J J Lin, Z Y Pan and P Lee *Application of Plasma Focus Device for Deposition of Nanostructured Magnetic Thin Films and Ion-irradiation Induced Nanostructuring of PLAD Grown Magnetic Thin Films* Proceedings of International Workshop On Plasma Computations & Applications Ed S H Saw et al 23-32 (2008)**
12. **S.Lee, S.P.Moo, C.S.Wong, A.C.Chew. Twelve Years of UNU/ICTP PFF- A Review. IC/98/231, CTP Preprint, International Centre for Theoretical Physics, Trieste, Italy (1998), 101 pages.**
13. S.Lee, T.Y.Tou, S.P.Moo, M.A.Eissa, A.V.Gholap, K.H.Kwek, S.Mulyodrono, A.J. Smith, Suryadi, W.Usala, M. Zakaullah. A simple facility for the teaching of plasma dynamics and plasma nuclear fusion. Amer J. Phys., USA, 1988, 56: 62-68.
14. S Lee and S H Saw. J Fusion energy 30, 398-403 (2011)
15. Sing Lee & Chiow San *Wong Initiating andStrengthening Plasma Research in Developing Countries* Physics Today pg 31-36 May 2006

Numerical Experiments of Ion Beams from Plasma Focus

S H Saw[1,2] and S Lee[1,2,3]

[1]*INTI International University, 71800 Nilai, Malaysia.*
[2]*Institute for Plasma Focus Studies, 32 Oakpark Drive, Chadstone, 3148 Australia.*
[3]*Physics Department, University of Malaya, Malaysia.*
**Corresponding author. E-mail: sorheoh.saw@newinti.edu.my*

Abstract

A recent paper derived benchmarks for deuteron beam fluence and flux based on neutron yield data assuming a beam-gas target mechanism [S Lee and S H Saw, Phys. Plasmas **19**, 112703 (2012)]. In our latest work we start from first principles and derive the flux of the ion beam of any gas with mass number M and effective charge number Z_{eff}**.** The flux equation is then linked to the Lee Model code which computes the properties of the plasma focus pinch. In this manner the properties of the fast ion beams (FIB) at the pinch exit of any Mather-type plasma focus operating in any gas are computed. The results show that whilst fluence, flux, ion number and ion current decrease from the lightest to the heaviest gas, the energy fluence, energy flux and damage factors are relatively constant throughout the range of gases H_2 to Ne but increase for the 3 high-Z gases Ar, Kr and Xe due to the susceptibility of their pinches to radiative collapse. The FIB energy has a range of 4-9% E_0.

I. Introduction

A recent survey[1] of ion beam measurements in plasma focus devices showed a wide range of experimental methods producing results (using mostly inappropriate, even confusing units) which are neither correlated among the various methods and machines nor show any discernible scaling or trend. That paper suggested that since the ion beam exits the focus pinch as a narrow beam with little divergence, the exit beam is best characterized by the yield of ion number per unit cross-section per shot or the fluence per shot. To compute the fluence that paper noted that D-D neutron yield and scaling were already successfully computed by means of a beam-gas target neutron generating mechanism[2-6] in the Lee Model code[7]. Since the deuteron fluence was already implicit in the neutron yield equation, it was a natural step to deduce the deuteron fluence equation, incorporate it in the Lee Model code and hence compute the fluence and other ion beam properties. This was done for a number of machines. The main results[1] were that: deuteron number fluence (ions m^{-2}) and energy fluence (J m^{-2}) computed as 2.4-7.8x10^{20} and 2.2-33x10^{6} respectively were independent of storange energy E_0 from 0.4 – 486 kJ. Typical inductance machines (33-55 nH) produce 1.2-2 x 10^{15} ions per kJ carrying 1.3-4 % E_0 at mean ion energy 50-205 keV. Thus that paper defined appropriate ion properties and established reference numbers for these properties for the case of deuterons.

A natural next question is: What are the corresponding reference numbers for ions produced in plasma focus devices operated in other gases? This question is not only of basic importance to provide reference numbers for measurements but may also help in the selection of gases for materials application such as damage studies where gases with high ion beam damage factor and power flow may be important; or in materials fabrication where uniformity may require a gas having a lower damage factor whilst having higher values of fast plasma stream energy with a bigger radial distribution.

The plasma focus dynamics may be divided in two major phases[7-11] the axial and the radial. In the axial phase a current sheath is driven down the coaxial channel between the anode and concentric cylindrical cathode in the direction from left to right in Fig 1[12]. At the end of the axial phase the radial phase begins in which a cylindrical current sheath is driven radially inwards preceded by a shock wave. When the shock wave goes on-axis a stagnated pinch column is formed with the boundary of the stagnated region moving outwards. This boundary may be characterised as a reflected shock wave moving radially outwards separating a radially inward region of doubly shocked gas of higher density and temperature from the outer region of inward streaming plasma which is driven by the radially inward moving radial current sheath (piston). When the outwardly moving reflected shock meets the incoming piston the focus pinch phase begins in which the pinch boundary moves slowly either inwards or outwards depending on the relative strengths of the magnetic pressure exerted by the piston and the increased hydrostatic pressure of the stagnated pinch. The radiation from the dense hot pinch plasma may become sufficient to affect the plasma dynamics in terms of radiation cooling and radiation collapse[13] in the case of high Z gases such as Ar, Kr or Xe. From experimental observations it has been suggested[14] that Ar (Z=18) is the transition gas in the sense that for gases with Z<18 the pinching proceeds as a column whereas for gases with Z>18 the pinching breaks the column up into a line of densely collapsed hot spots. We return to this point later in the paper when it becomes pertinent to our results. The dynamics of the current sheath causes large temporal changes of inductance dL/dt and consequential rate of change of currents dI/dt. Large electric fields are induced. These and the extreme conditions of the pinch lead to observed plasma disruptions. Besides electromagnetic radiations from the focus, particles are also emitted: generally ion beams in the axial direction away from the anode and relativistic electrons (REB) towards the anode. In this paper we focus on the ion beams. We use the mechanism proposed by Gribkov et al[2]. A beam of fast deuteron ions is produced by diode action in a thin layer close to the anode (see Fig 1[12]) , with plasma disruptions in the pinch generating the necessary high voltages. These disruptions also terminate the quasi-static nature of the pinch so that the duration of the pinch may be related to the transit time of relevant small disturbances across the pinch column[7].

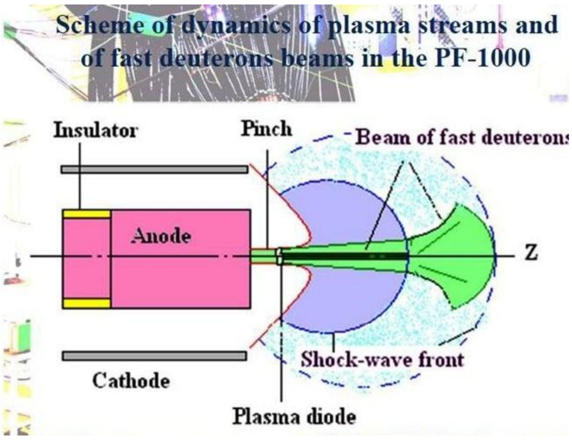

Figure 1. Schematic[12] of the post- pinch FIB (fast ion beam illustrated here with deuterons) and FPS (fast plasma stream) indicated by the post-pinch shock wave.

During the radial compression phase, energy is imparted to the plasma and stored in the increasing inductance of the pinch column. Some of this accumulating energy is emitted as radiation, primarily line radiation in the case of high Z gases and also provided to the ion and REB. The remnant energy may be considered to manifest in the fast plasam stream (FPS).

II. The Method

A. The ion beam flux and fluence equations

We now proceed to estimate the flux of the ion beam.
We write the ion beam flux as $J_b = n_b v_b$ where
n_b= number of beam ions N_b divided by volume of plasma traversed and
v_b = effective speed of the beam ions.
All quantities are expressed in SI units, except where otherwise stated.
Note that $n_b v_b$ has units of ions per $m^{-2}\ s^{-1}$.
We derive n_b from pinch inductive energy considerations. We derive v_b from the accelerating voltage taken as the diode voltage U. The flux equation is derived as:

$$\text{Flux}=J_b=2.75\text{x}10^{15}(f_e/[MZ_{eff}]^{1/2})\{(\ln[b/r_p])/(r_p^{2})\}(I_{pinch}^{2})/U^{1/2} \quad \text{ions } m^{-2}s^{-1} \qquad (1)$$

Where M=ion mass, Z_{eff} = average effective charge of the ion in the pinch, b= cathode radius, r_p =pinch radius and I_{pinch} =pinch current.
The parameter f_e is the fraction of energy converted into beam energy from the inductive energy of the pinch. By analyzing neutron yield data[1,3,4] and pinch dimensional and temporal relationships[15] we estimate a value of f_e =0.14.

In this manner starting from first principles we have derived exactly the same equation as we did using empirical formula calibrated at a 0.5MJ point of neutron yield.
In this derivation from first principles we need only one additional condition: f_e =0.14. and the approximate scaling: $\tau = 10^{-6}\ z_p$. This condition f_e =0.14 is equivalent to ion beam energy of 3%-6% E_0 in the case when the pinch inductive energy holds 20% -40% of $E_{0.}$ Our extensive study of high performance low inductance plasma focus classified[16] as Type 1 shows that this estimate of f_e is consistent with data.
We summarise the assumptions:

1. Ion beam flux $\mathbf{J_b}$ is $n_b v_b$ with units of ions $m^{-2}\ s^{-1}$.
2. Ion beam is produced by diode mechanism[2].
3. The beam is produced uniformly across the whole cross-section of the pinch
4. The beam speed is characterized by an average value v_b.
5. The beam energy is a fraction f_e of the pinch inductive energy, taken as 0.14 in the first instance; to be adjusted as numerical experiments indicate.
6. The beam ion energy is derived from the diode voltage U
7. The diode voltage U is proportional to the maximum induced voltage V_{max}; with $U=3V_{max}$; a relationship obtained from data fitting in extensive earlier numerical experiments[3,4] .

The value of the ion flux is deduced in each situation (specific machine using specific gas) by computing the values of Z_{eff}, $r_{p,}$ I_{pinch} and U by configuring the Lee Model code with the parameters of the specific machine and specific gas. The code and the procedure are discussed in more detail in the next section.

B. The Lee Model code

The code[7] couples the electrical circuit with PF dynamics, thermodynamics and radiation. It is energy-, charge- and mass- consistent. It was described in 1983[8] and used in the design and interpretation of experiments[9,10,17,18]. An improved 5-phase code incorporating finite small disturbance speed[19], radiation and radiation-coupled dynamics was used[20,21], and was web-published[22] in 2000 and 2005[23]. Plasma self- absorption was included[22] in 2007. It has been used extensively as a complementary facility in several machines, for example: UNU/ICTP PFF[17,18,20,21], NX2[21,24], NX1[21], DENA[25]. It has also been used in other machines for design and interpretation including sub-kJ PF machines[26], FNII[27] and the UBA hard x-ray source[28]. Information computed includes axial and radial dynamics[17] and pinch properties[15], SXR emission characteristics and yield[20,21,24,29-34], design of machines[15,17,21,24,26], optimization of machines[3-6,17,26] and adaptation to Filippov-type DENA[25]. Speed-enhanced PF[10] was facilitated. Plasma Focus neutron yield calculations[3-6], current and neutron yield limitations[4-6], neutron saturation[5,6], radiative collapse [13], current-stepped PF[35] and extraction of diagnostic data[34-39] and anomalous resistance data[16,40] from current signals have been studied using the code[7]. As already pointed out in the introduction the Model code has recently been used to produce land-mark reference numbers for deuteron beam number and energy fluence and flux and scaling trends for these with plasma focus storage energy[1]. The present paper extends the beam ion calculations to include all gases.

C. Procedure used in the numerical experiments

We use the NX2[21] for these numerical experiments to study the number and energy flux and fluence in various gases including hydrogen, deuterium, helium, nitrogen, neon, argon, krypton and xenon. This gives us a good range in terms of mass and charge numbers. We configure the NX2 as follows:

Capacitor bank parameters: L_0=20 nH; C_0=28 mF, r_0=2.3 mOhm

Tube parameters: b=4.1 cm; a=1.9 cm, z_0=5 cm

Operating parameters: V_0=14 kV; P_0= appropriate range of pressures.

The parameters are: L_0=static inductance defined as inductance of discharge circuit without any plasma dynamics (for example with the bank short-circuited at the input to the plasma focus tube), C_0=bank capacitance, r_0=short circuited resistance of the discharge circuit; b=cathode radius, a=anode radius, z_0=effective anode length; V_0=bank charging voltage and P_0=operating pressure, with a range of pressures chosen so that the plasma focus axial run-down time covers a range which encompasses at least from 0.5 to to 1.3 of the short-circuit rise time which is approximately $(L_0/C_0)^{0.5}$. This range is chosen so that the matched condition with the strongest energy transfer into the plasma focus pinch is well covered within the range and also to ensure that the range also covers conditions of high enough pressures that the focus pinch is almost not ocurring as defined by the condition that the reflected shock is barely able to reach the rapidly decelerating magnetic piston.

For each shot the dynamics is computed and displayed by the code which also calculates and displays the ion beam properties. For H_2, D_2, He, N_2 and Ne the procedure is relatively simple even though Ne already exhibits enhanced compression due to radiative cooling.

For Ar, Kr and Xe, the radiation yield (almost wholly the line yield) is so severe that the radiative collapse has to be adjusted in terms of minimum radius of compression rmin (defined by the radius ratio rmin/a) and time of the pinch so that the remnant fast plasma stream energy remains at least minimally positive. This adjustment involves studying the line yield, the ion beam energy and the FPS energy as well as the value of fe point by point. The final results contain a range a degree of uncertainty in the sense that each strong radiative collapse point could be adjusted a little differently (by 10% or so) in distribution of energies. However extensive number of runs show that despite the uncertainty of the few strong radiative collapse points for each gas the total picture of energy distributions with pressure is clear and unambiguous.

We need to point out here that we model the pinch radiative collapse as a collapse of the pinch as a whole column whereas experimental observations[14] indicate that Ar is the transition gas below which (lighter gases) the pinch compresses as a column whilst for heavier gases (Kr and Xe) the compression breaks up into a line of hot spots. Our numerical experiments indicate from energy considerations that when the compression breaks up into hot spots the electric current does not all flow through the hot spots but there is a substantial flow of current in a far less compressed column in which the line of hot spots is 'embedded'; so that the total effect in terms of energy transfer and inductance is less severe than indicated by our collapse- as- a- column modelling.

III. Results and Discussions

A. Discharge current and general dynamics

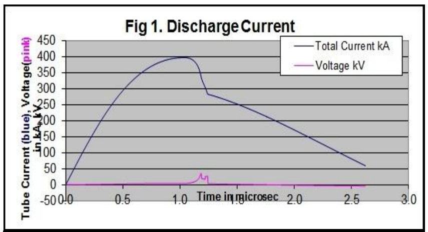
Fig 1. Discharge Current

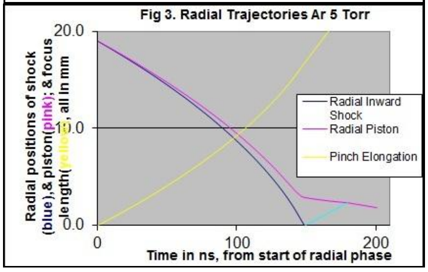
Fig 3. Radial Trajectories Ar 5 Torr

Figure 2. NX2 Ne 3 Torr (a) Typical discharge current (b) Radial trajectories

Figure 2(a) shows the plasma focus discharge current computed for the NX2 and fitted to the measured discharge current in order to obtain the model parameters f_m, f_c, f_{mr} and f_{cr}[32,33,41]. Figure 2(b) shows the computed radial trajectories of the radially inward shock wave, the reflected radially outward shock wave, the piston trajectory and the pinch length elongation trajectory.

B. Radius ratios for various gases

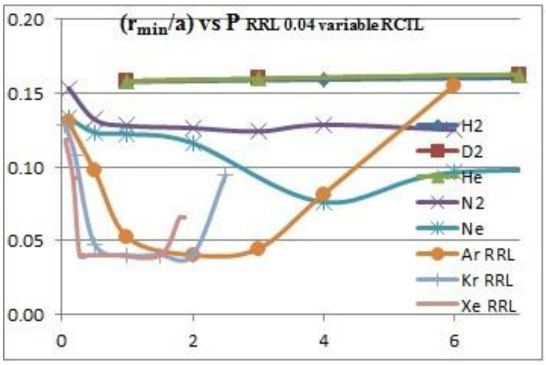

Figure 3. Radius ratio vs P for different gases

The range of pressures appropriate for operating the gases in the numerical experiments is widest for the lightest gas H_2 which may be operated from 1 Torr up to 70 Torr still producing a weak pinch. For D_2 and He the range reduces to 1- 40 Torr; for Ne we successfully ran numerical experiments from 0.1 to 10 Torr; for N_2 from 0.1 toTorr and for Xe it is 0.05 to 1.8 Torr.

Figure 3 illustrates the different compression of the plasma focus pinch for different gases. In H_2, D_2 and He the radius ratio stays above 0.15 the 3 graphs staying together up to 10 Torr towards 0.2 in the cases of D_2 and He and 0.18 for H_2. The higher pressures are not shown in Fig 3. For N_2 the radius ratio drops from 0.15 to a value about 0.13 over its useful range of operation. Ne shows signs of enhanced cvompressionsbetween 3 to 5 Torr indicated by the enhanced compression (smaller radius ratio down to a minimum of 0.08 at 4 Torr. Ar shows strong radiative collapse with a radius ratio of 0.04 (a cut-off value designed to make the energy distribution adjustments feasible and not too involved a process) over a narrow range of pressure around 2.0 Torr. Kr from 0.5-2 Torr whilst Xe over 0.3 to 1.5 Torr, these latter being a large proportion of their range of operation.

C. Ion Beam Flux for various gases

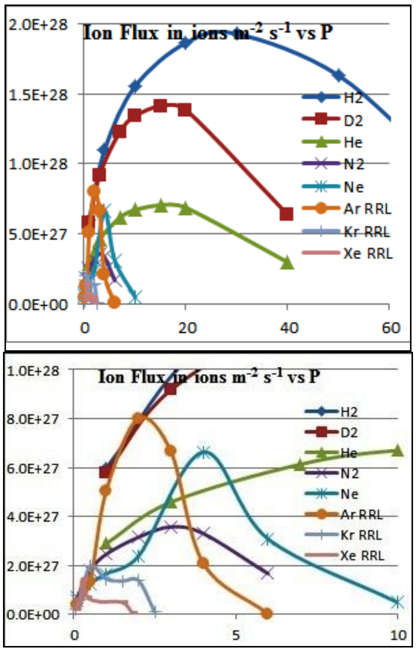

Figure 4. (4a) Flux vs Pressure, various gases and (4b) Flux, expanded scale

Figure 4a shows the flux in ions m^{-2} s^{-1} for the various gases investigated. The H_2 curve starts at low pressures with a value of 6x10^{27} at 1 Torr and rises to a peak of 1.9x10^{28} at 25 Torr. A detailed study of the results shows that 25 Torr is the pressure where the magnetic piston work is optimised corresponding to best energy matching for the NX2 operationn in H_2. The flux then drops gradually and reaches a value below 10^{28} at 70 Torr. The D_2 and He curve show the same trend with lower peak flux values of 1.4x10^{28} and 7x10^{27} respectively at 15 Torr and with a reduced pressure range. N_2 shows the same trend peaking at 3.6x10^{27} at 3 Torr. Ne shows an accentuated peak of 6.6x10^{27}, the peak of the accentuated hump appearing at 4 Torr Fig (4b) corresponding to observed radiative enhanced compression at 4 Torr (Fig 3). Ar flux is even more obvious in displaying the effect of radiative collapse peaking at a highly accentuated 8x10^{27} at 2 Torr. For Kr although the radiative compression is even greater than Ar, the flux is fairly flat at 1.4x10^{27} in the pressure range of good energy transfer into the pinch in the region of 1 Torr. The accentuating effect on the flux being more than made up by the much greater energy per ion due to the greatly increased mass numbers of 84. The competing effects are more complicated than our first discussion here and will become clearer as we discuss the other properties. Xe shows the same flat flux curve as Kr with a flat central value around 6x10^{2}6. Thus we observe that the beam ion flux drops as the mass number of the ions, with accentuating factors provided by radiatively enhanced compression.

D. Ion Beam Fluence for various gases

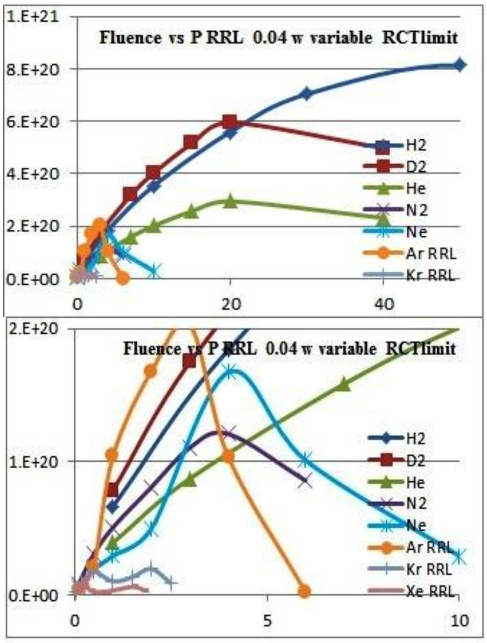

Figure 5. (5a) Fluence vs Pressure, various gases and (5b) Fluence, expanded scale

Figure 5a shows the fluence in ions m^{-2} for the various gases investigated. The shape of the curves and the trend with gases are very similar to the flux discussed in the previous section the fluence being the flux multiplied by the estimated duration of the ion beam pulse duration. The peak values of the fluence (ions m^{-2}) range from 8x10^{20} for H2 to 6x10^{18} for Xe; again with clearly radiation enhanced values of 2x10^{20} and 1.7x10^{20} for Ar and Ne respectively. The values for each gas are placed in Table 1 for comparison of the main ion beam properties.

E. Beam ion number per kJ

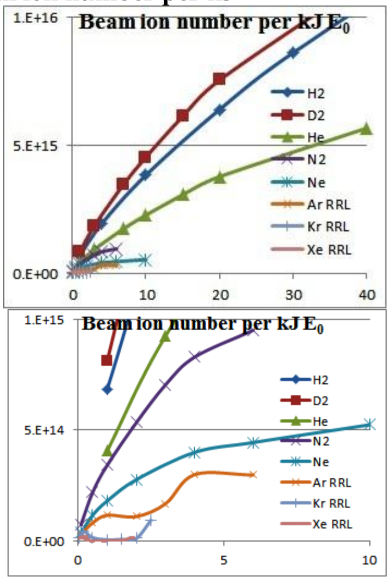

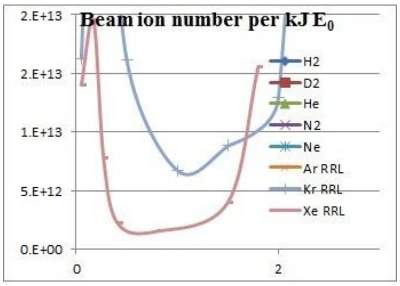

Figure 6. Beam ion number per kJ as a function of pressure in various gases (a) range up to 40 Torr (b) expanded showing up to 10 Torr (c) up to 3 Torr to show Kr and Xe graphs

Figure 6 a-c show that the beam ion number per kJ range from about 10^{16} for the lightest gases to 1.5x10^{12} for Xe in the radaitive enhanced regime.

F. Beam energy in the various gases

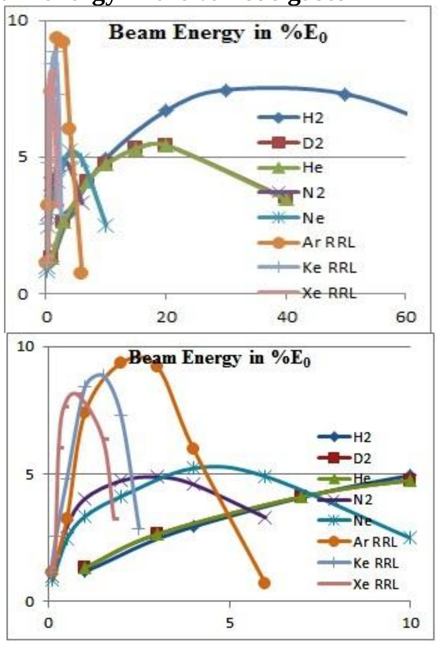

Figure 7. Beam energy as % E_0 in the various gases

The results of the numerical experiments show that although the beam ion number is the lowest (see Fig 6) for the heaviest gases Ar Kr and Xe, yet these beams also carry the largest amounts of energy at 8-9% E_0 compared to around 5-8% for the other gases. This is because the energy per ion more than compensate for the low numbers.

G. Damage factor

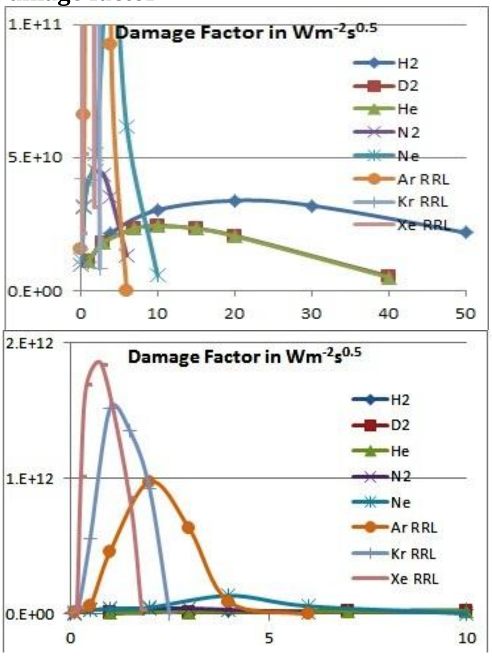

Figure 10. Damage Factor (a) showing the lighter gases (b) the heavier gases

The damage factor defined as power flow density multiplied by (pulse duration)$^{0.5}$. This quantity is considered to be important for assessing the utility of a beam for damage simulation of plasma-facing wall materials in fusion test reactors.

H. Tabulation of ion beam properties in various gases for comparison

The above results and some others are tabulated for comparison in Table 1.

IV Conclusion

In this paper we deduce the flux equation of ion beams in plasma focus for any gas using experimental data from the case of deuterons to obtain a calibration constant for energy fraction. We configure the Lee Model code as the NX2 using best estimated average model mass and current factors obtained from fitting the computed current traces of several gases with experimentally measured current traces. The flux equation is incorporated into the code and the number and energy flux and fluence from different gases are computed together with other relevant properties. The results portray the properties of the ion beam at the pinch exit. They indicate that the ion fluence range from 7x10^{20} for the lightest gas H2 decreasing through the heavier gases until a value of 1.7x10^{20} for Ar and decreases further dramatically to 0.03 x10^{20} for Xe. The very small fluence value of Xe is due to the very large energy of the Xe ion, estimated to have average charge state Z_{eff} of 28 and accelerated by exceedingly large electric fields induced in the radiative collapse. The ion number goes from 86x10^{14} per kJ for H_2, decreases to 2.8x10^{14} per kJ for Ne and then to 0.02 x10^{14} for Xe. The beam energy drops slightly from 7.5 % of E_0 for H_2 to 4.1% of E_0 for Ne and then increases to 9% for Ar and 7.6 % for Xe. The damage factor is highest for Xe at 170x10^{10} $Wm^{-2}s^{0.5}$ dropping to 100x10^{10} for Ar and to 2-5x10^{10} for the lighter gases. The results for Kr and Xe and to a lesser extent in Ar are very much affected by the way the radiative collapse is modelled whilst those of the other gases from H2 to Ne are not affected by radiative collapse.

Acknowledgement

This work is partly carried out within the framework of IAEA Research Contract No: 16934 of CRP F1.30.13 (Investigations of Materials under High Repetition and Intense Fusion-relevant Pulses).

References

[1] S Lee and S H Saw, Phys. Plasmas **19**, 112703 (2012); http://dx.doi.org/10.1063/1.4766744

[2] V A Gribkov, A Banaszak, B Bienkowska, A V Dubrovsky, I Ivanova-Stanik, L Jakubowski,L Karpinski, R A Miklaszewski, M Paduch, M J Sadowski, M Scholz, A Szydlowski and K Tomaszewski, J. Phys. D: Appl. Phys. **40,** 3592–3607 (2007)

[3] S Lee and S H Saw, J Fusion Energy, **27,** 292-295 (2008)

[4] S. Lee and S H Saw, Appl. Phys. Lett., **92,** 021503 (2008)

[5] S Lee. Plasma Physics Controlled Fusion, **50** 10500 (2008)

[6] S Lee. Appl. Phys. Lett. **95** 151503 (2009)

[7] S Lee, Radiative Dense Plasma Focus Computation Package: **RADPF.** http://www.plasmafocus.net; http://www.intimal.edu.my/school/fas/UFLF/(archival websites)

[8] S Lee in *Radiation in Plasmas* Vol II, Ed B McNamara, Procs of Spring College in Plasma Physics (1983) ICTP, Trieste, p. 978-987, ISBN 9971-966-37-9, Published byWorld Scientific Publishing Co, Singapore (1984)

[9] T.Y.Tou, S.Lee & K.H.Kwek. IEEE Trans Plasma Sci **17**, 311-315 (1989)

[10] A Serban and S Lee, Plasma Sources Sci and Tehnology, **6**, 78 (1997)

[11] S H Saw, P C K Lee, R S Rawat, S Lee, IEEE Trans Plasma Sci, **37**, 1276-1282 (2009)

[12] V A Gribkov, Presentation at IAEA. Dec 2012

[13] S Lee, S. H. Saw and Jalil Ali, J Fusion Energy DOI: 10.1007/s10894-012-9522- 8 First Online 26 Feb (2012)

[14] F N Beg, I Ross, A Lorenz, J F Worley, A E Dangor and M G Haines, J Appl Phys **88**, 3225-3230 (2000)

[15] S Lee & A Serban, IEEE Trans Plasma Sci **24**, 1101-1105 (1996)

[16] S Lee, S H Saw, A E Abdou and H Torreblanca, J Fusion Energy **30**, 277-282 (2011)

[17]S Lee, T.Y. Tou, S.P. Moo, M.A. Elissa, A.V. Gholap, K.H. Kwek, S. Mulyodrono, A.J. Smith, Suryadi, W.Usala & M. Zakaullah. Amer J Phys **56**, 62 (1988)

[18] SP Moo, CK Chakrabarty, S Lee - IEEE Trans Plasma Sci 19, 515-519 (1991)

[19]D E Potter, Phys Fluids **14**, 1911 (1971)

[20]M H Liu, X P Feng, SV Springham & S Lee, IEEE Trans Plasma Sci. **26**, 135 (1998)

[21]S Lee, P.Lee, G.Zhang, X.Feng, V.A.Gribkov, M.Liu, A.Serban & T.Wong. IEEE Trans Plasma Sci, **26**, 1119 (1998)

[22]S.Lee in
http://ckplee.home.nie.edu.sg/plasmaphysics/
(archival website) (2012)

[23]S. Lee in ICTP Open Access Archive: http://eprints.ictp.it/85/ (2005)

[24]D.Wong, P.Lee, T.Zhang, A.Patran, T.L.Tan, R.S.Rawat & S.Lee. Plasma Sources, Sci & Tech 16, 116 (2007)

[25]V. Siahpoush, M.A.Tafreshi, S. Sobhanian, & S. Khorram. Plasma Phys & Controlled Fusion **47**, 1065 (2005)

[26]L. Soto, P. Silva, J. Moreno, G. Silvester, M. Zambra, C. Pavez, L. Altamirano, H. Bruzzone, M. Barbaglia, Y. Sidelnikov & W. Kies. Brazilian J Phys 34, 1814 (2004)

[27]H.Acuna, F.Castillo, J.Herrera & A.Postal. International conf on Plasma Sci, 3-5 June 1996, conf record Pg127

[28]C.Moreno, V.Raspa, L.Sigaut & R.Vieytes, Applied Phys Letters 89(2006)

[29]S. Lee, R S Rawat, P Lee and S H Saw, J. Appl. Phys. **106,** 023309 (2009)

[30]S. H. Saw and S. Lee, Energy and Power Engineering, **2** (1), 65-72 (2010)

[31]M. Akel, Sh Al-Hawat, S H Saw and S Lee, J Fusion Energy, **29**, 3, 223-231 (2010)

[32]Sh. Al-Hawat, M. Akel, S H Saw, S Lee, J Fusion Energy, **31**, 13 – 20, (2012)

[33]M. Akel , S. Lee, S. H. Saw, IEEE Trans Plasma Sci **40,** 3290 – 3297; DOI:
http://dx.doi.org/10.1109/tps.2012.2220863

[34]S Lee, S H Saw, R S Rawat, P Lee, A.Talebitaher, A E Abdou, P L Chong, F Roy,
A Singh, D Wong and K Devi, IEEE Trans Plasma Sci **39**, 3196-3202 (2011)

[35]S Lee and S H Saw, J Fusion Energy DOI: 10.1007/s10894-012-9506-8 First Online 31 January (2012)

[36] S Lee, S H Saw, P C K Lee, R S Rawat and H Schmidt, Appl Phys Lett **92**, 111501 (2008)

[37]S H Saw, S Lee, F Roy, PL Chong, V Vengadeswaran, ASM Sidik, YW Leong & A
Singh, Rev Sci Instruments, **81**, 053505 (2010)

[38] S Lee, S H Saw, R S Rawat, P Lee, R Verma, A.Talebitaher, S M Hassan, A E Abdou,
Mohamed Ismail, Amgad Mohamed, H Torreblanca, Sh Al Hawat, M Akel, P L Chong, F
Roy, A Singh, D Wong and K Devi, J Fusion Energy **31**,198–204 (2012)

[39]S.Lee, S.H.Saw, L..Soto, S V Springham, S P Moo, Plasma Phys and Control. Fusion, **51** 075006 (11pp) (2009)

[40]F M Aghamir and R A Behbahani, J. Plasma Physics: doi:10.1017/S0022377812000438 in press (2012)

[41] S.P. Chow, S. Lee and B.C. Tan, J Plasma Phys, **8** 21-31 (1972).

Table 1: NX2 Properties and computed Ion beam characteristics in a number of gases

NX2	**H2**	**D2**	**He**	**N2**	**Ne**	**Ar**	**Kr**	**Xe**
Pressure (Torr) matched	30	15	15	2	3	2	0.5	0.41
I_{peak} (kA)	397	397	397	395	382	406	390	394
z_p (cm)	2.8	2.8	2.8	2.8	2.8	3.0	2.4	2.3
r_p (cm)	0.33	0.32	0.31	0.24	0.22	0.08	0.08	0.08
□ (ns)	37	37	37	26	21	21	9	5
Z_{eff}	1	1	2	6.4	8.5	11.5	24	28
Ion Fluence ($x10^{20}$ m^{-2})	**7.0**	**5.2**	**2.6**	**0.8**	**0.8**	**1.7**	**0.15**	**0.03**
Ion Flux ($x10^{27}m^{-2}s^{-1}$)	19	14	7	3.2	5.0	8.0	1.9	0.7
Mean ion energy (keV)	54	54	108	553	927	5250	18601	215664
FIB Energy (%E_0)	7.5	5.3	5.3	4.7	4.1	9.3	4.8	7.6
Dam Fr ($x10^{10}Wm^{-2}s^{0.5}$)	**3.2**	**2.3**	**2.3**	**4.5**	**5.1**	**98**	**55**	**170**
Ion Number/kJ ($x10^{14}$)	86	61	31	5.3	2.8	1.1	0.16	0.02

Characterization of Red Spinel by PIXE

B. Srisataporn[1*], D. Bootkul[1,4], S. Intarasiri[2,4], and S. Singkarat[3,4]

[1]*Department of General Science, Faculty of Science, Gems and Jewelry division, Srinakharinwirot University, 114 Sukhumvit 23, Bangkok 10110, Thailand*
[2]*Science and Technology Research Institute, Chiang Mai University,* 239 *Huay Kaew Rd, T. Suthep, A. Muang, Chiang Mai 50200, Thailand*
[3]*Plasma and Beam Physics Research Facility, Department of Physics and Materials Science, Faculty of Science, Chiang Mai University,* 239 *Huay Kaew Rd, T. Suthep, A. Muang, Chiang Mai 50200, Thailand*
[4]*Thailand Center of Excellence in Physics, CHE, 328 Si Ayutthaya Road, Bangkok, 10400, Thailand*
**Corresponding author. E-mail:* meaw_mercury@hotmail.com

Abstract

Natural spinels are found in colors equal to those of fine rubies or sapphires. The most valuable one is known as ruby spinel. Recently, the demands of bright red spinel as a substitution for ruby was increasing. There are only a few publications on spinel chemical composition available. The paper presents ion beam technique as a new way to characterize the chemical composition of natural red spinels from Mokok source. In Thailand, ion beam technology has been recently applied for gemstone analysis, particularly, the Proton Induced X-ray Emission (PIXE) which is an effective and nondestructive technique to quantify trace elements analysis in ppm level. Chemical analysis by PIXE technique showed the major trace element such as chromium (Cr), iron (Fe) and minor trace elements are titanium (Ti), vanadium (V), zinc (Zn) and gallium (Ga). The amounts and combination of trace elements affect the optical properties such as clarity, color, hue, tone and saturation. Through this experiment was successful examined its effect of red spinel for gem quality. UV-Vis spectroscopy technique results provide absorption spectra of natural spinel, which is appearing origin dependent. The color in red spinel is also related to the contents of chromium and iron in individual samples. The investigations discussed of high chromium content is the parameter of beauty in a gemstone need, causes dominant red color whereby correlates with the absorption spectrum.

***Keywords*:** Spinel, Trace Elements, UV-Vis absorption, Ion Beam Analysis

Introduction

Natural spinels occur in various shades of color such as red, blue, green, yellow, brown, black or even colorless resemble to those found in ruby and sapphire [1]. The structure of spinel is mainly magnesium-aluminum-oxide ($MgAl_2O_4$) [2]. They are generally indicated by the formula AB_2O_4, where “A” is a divalent element such as Mg, Fe, Zn, Mn, Ni, Co, V, and Cu, and “B” a trivalent element such as Al, Fe, and Cr with reciprocal diadochal exchange. Pure spinel is colorless which contain ideal composition of 28% MgO and 71.8% Al_2O_3. The presence of trace elements such as chromium, vanadium, iron and cobalt produce many different shades of color. Most appreciated in the gemstone market are red spinels. However, the beautiful rich reds spinels are very rare; they can be found in a range of pastel shades blended with brown, orange and purple. There are only a few publications on spinel composition available, therefore, the objective of this study is to characterize the physical properties and chemical composition of some natural spinels by using ion beam technique.

Materials and Methods

The samples used in this study are 24 natural spinels from Myanmar having assorted color including red-orange (24 samples). All samples were cut and polished into two parallel faces. The physical and gemological properties such as refractive index, specific gravity were studied and also features using sterozoom microscope (70X). The chemical analysis was carried out by PIXE. PIXE is powerful, fast and relatively simple analytical technique that can be used to identify and quantify trace elements [3]. It is non destructive character and its capability to determine simultaneously major and trace elements. The experiment was examined its effect on the absorption spectra of Cr^{3+} in natural spinel, which is appearing origin dependent, by UV-Vis spectroscopy.

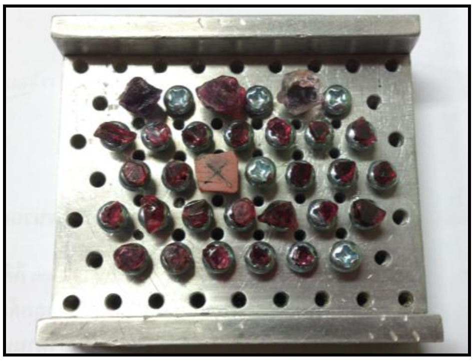

Figure 1. Sample holder.

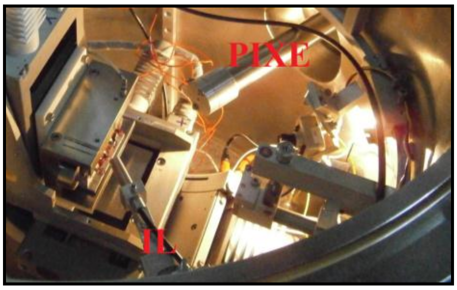

Figure 2. Ion beam analysis chamber of PIXE.

Results and Discussion

Gemological properties of all samples were summarized in Table 1.

Table 1. Gemological properties of spinels from Myanmar.

Properties	Results
Refractive Index	1.705 - 1.720
Specific Gravity	3.50 - 3.69
Long Wave UV	Moderate - Strong Red
Short Wave UV	Weak Red - Inert
Color	red orange
Tone	Light - Dark
Saturate	very slightly grayish - strong

Chemical analysis by PIXE for trace element analysis is an excellent tool for this purpose. Showing that major trace elements are chromium (Cr), iron (Fe) and minor trace elements such as titanium (Ti), vanadium (V), zinc (Zn), and gallium (Ga) as seen in table 2.

Table 2. The trace elements concentration of the red spinel from Myanmar.

Trace elements	Min-max (Wt%)
Mg	16.45 – 20.69
Al	73.39 – 79.15
Ti	0.01 – 0.40
V	0.02 – 0.75
Cr	0.58 – 3.38
Fe	0.16 – 3.23
Zn	0.08 – 2.81
Ga	0 - 0.06

UV-Vis spectroscopy can be used to study the mechanisms of coloration caused by transition metal in gemstones [3]. The crystal field transition (d-d) for Cr^{3+} (in octahedral coordination) bands centered at approximately 390-403 and 538-540 nanometer dominating the absorption spectra of red spinels. The crystal field transition (d-d) for Fe^{3+} (in octahedral coordination) bands centered at approximately 286-299 and 303-325 nanometer. The red color in spinel from Myanmar is related to the contents of Cr^{3+} and Fe^{3+} substitution of Al^{3+} (in octahedral coordination) in individual samples. High chromium content causes dominant red color that correlates with the absorption spectrum. Iron content causes brown color. When both chromium and iron are present, the absorption spectra are intermediate between the mixed colors. Dominant color shows higher absorption by the corresponding element. Example of UV-Vis measurement is demonstrated in Figure 3-5.

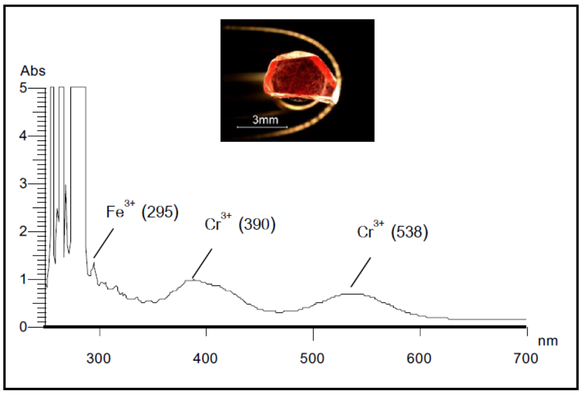

Figure 3. UV-Vis spectra of Browish red spinel.

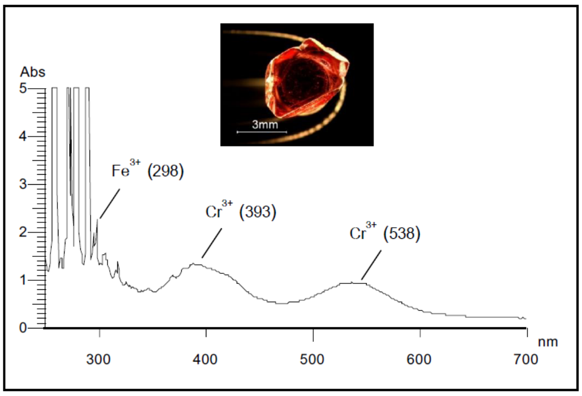

Figure 4. UV-Vis spectra of red orange spinel.

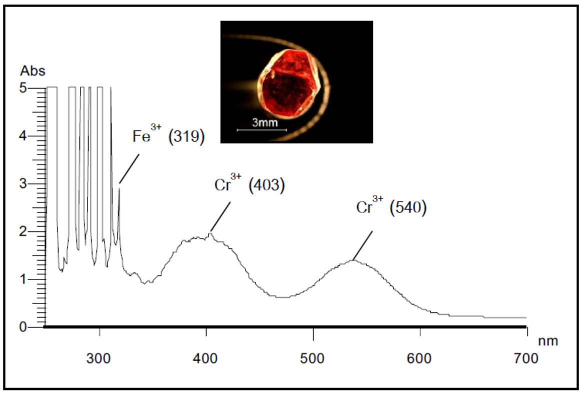

Figure 5. UV-Vis spectra of red spinel with its shades and variations.

As concern the changes in intensity of Fe^{3+} ions and UV-Vis absorption spectral characteristics from figure 6. Therefore, this leads to the intensity of the orange and yellow tints in the color of the samples. The color also depending on the Cr^{3+} ions intensity these red spinels can become more saturated.

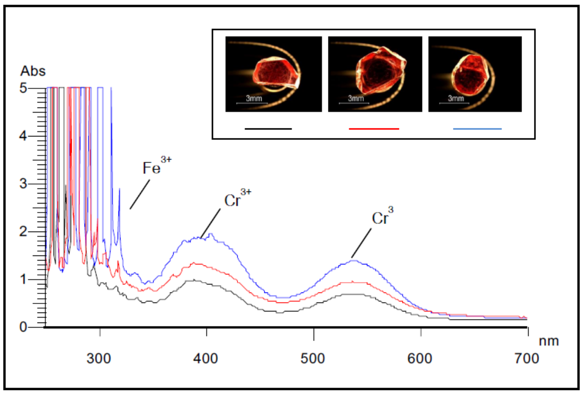

Figure 6. Comparison UV-Vis spectra of red spinels.

Table 3 presents data on the dependence of the rationale Cr/Fe of the color of samples. Also when ratio Cr/Fe increases then color changes in a certain way: Browish red, Red orange and Red.

Table 3. The trace elements concentration rational of the red spinels from PIXE.

Color of samples	Cr (Wt %)	Fe (Wt %)	Rational Cr/Fe
Brownish red	1.88	3.23	0.58
Red orange	1.26	1.07	1.17
Red	3.38	0.37	9.13

Conclusions

All spinel samples from Myanmar the gemological properties showed specific gravities range from 3.50 to 3.69, refractive indices range from 1.705 to 1.720 and inert to weak red in short-wave ultraviolet radiation, moderate to strong red fluorescence in long wave ultraviolet radiation. Chemical analysis by PIXE technique showed the major trace element analysis showing that major trace elements are chromium (Cr), iron (Fe) and minor trace elements are titanium (Ti), vanadium (V), zinc (Zn), and gallium (Ga). UV-Vis spectra of red spinels, show absorption bands of Cr^{3+} at 390-403 and 538-540 nanometer, show absorption bands of Fe^{3+} at 286-299 and 303-325 nanometer.

Acknowledgments

This work was supported by Thailand Center of Excellence in Physics (ThEP Center), Department of General Science, Faculty of Science, Srinakharinwirot University Faculty of Science, Chiang Mai University.

References

1. C. Hurlbut, and RC. Kammerling, Gemology. 2nd ed., New York: Jonh Wiley & Son, 1991.
2. N. Daneu, A. Recnik, T. Yamazaki, and T. Dolenec, Phys Chem Minerals (2007) 34:233-247.
3. D. Bootkul, S. Intarasiri, T. Kamwanna, U. Tippawan, and S. Singkarat, Proceedings of the 6th Annual Conference of the Thai Physics Society (2011) 264-267.

4. N. Bunnag, and P. Thanasuthipitak, Chiang Mai Journal of Science (2003) 30:69-79.

Correlation between PIXE and IL Techniques in Corundum

T. Chulapakorn[1*], S. Intarasiri[2], D. Bootkul[3], and S. Singkarat[4]

[1]Plasma and Beam Physics Research Facility, Department of Physics and Materials Science, Faculty of Science, Chiang Mai University, Chiang Mai 50200, Thailand
[2]Science and Technology Research Institute, Chiang Mai University, Chiang Mai 50200, Thailand
[3]Department of General Science (Gemology & Jewelry), Faculty of Science, Srinakharinwirot University 10400, Thailand
[4]Thailand Center of Excellence in Physics, Commission on Higher Education, 328 Si Ayutthaya Road, Bangkok 10400, Thailand
** Corresponding authors. E-mail: wizmacho@gmail.com*

Abstract

Particle-induced X-ray emission (PIXE) and ionoluminescence (IL) are the ion beam analysis techniques for investigating the trace elements of various materials. The former is the common method, which use of finding out an amount of trace element in the matter, and the latter is used for observing the luminescent character in the matter. It is worth to note that a 2 MeV proton beam from a 1.7 MV tandem accelerator was used for these analysis. On the behalf in this research, a number of clear and transparent corundum, dull white sapphires, were investigated by the mentioned techniques. After that, both PIXE and IL results show the correlation which depend upon the concentration of many trace elements. Basically, a luminescence peak at 692 nm which relate to the Cr^{3+} luminescence is obviously observed in spite of the low content of Cr. The result, additionally, is benefit for verifying a few existence of Cr^{3+} in corundum. Although it is not enough to produce any color, the further ion beam modification can be applied by using these results.

***Keywords*:** PIXE, IL, corundum, Cr^{3+}

Introduction

Corundum is the valuable gemstone which having been found worldwide. Aluminum oxide, Al_2O_3, is a major composition in the hexagonal structure, which is very clear if it is without other impurities [1]. However, natural corundum is found that occur in many colors on account of originally different elements, structures, and their quantity. The visual appeal and characteristics of corundum is determined by many variables including: brilliance, color, fire (light dispersion), and luster. Considering, ions of certain elements are high absorbent of some specific wavelengths of light, i.e. these are called chromospheres, which possess strong pigmenting capabilities. Moreover, it is an allochromatic mineral to which referring color varies based on the presence of impurities in their composition and on defects in their structure [2]. In this case, dull white sapphire comprise of either coloration or discoloration element in a few concentrations. Because the red color in sapphire is caused by the substitution of Cr^{3+} to Al^{3+} in the six surrounded oxygen ions, the lack of the Cr^{3+} is normally degraded the saturation of color [3]. In other words, the insufficient amount of chromium is caused to produce the red color; thus, a white color exists instead.

Ion beam analysis (IBA), as a non-destructive analytical method, is an alternative technique for characterization of gemstones. Particle-induced X-ray emission (PIXE) is a sensitive analytical technique which can be used to identify trace elements in a gemstone. Ionoluminescence (IL) likewise is a highly sensitive method for detecting optical phenomenon in the matter. Not only PIXE has been made use of a few trace element investigations, but IL also has been used to determine luminescence process of rubies and sapphires [4-7]. Next, we investigate luminescence of corundum and checked the data with the above-mentioned research. Due to the lack of relation information between PIXE and IL of corundum, we have tried to fulfill this vacancy. Fortunately, our research facility has the Tandem accelerator for detecting the previous mentioned analysis which is the only one in Thailand. The objective of this research is to find out the correlation between the quantitative analysis by PIXE technique and the qualitative analysis by IL technique. Particularly, both

Cr^{3+} concentration and luminescence are the main points for this research.

Experimental procedures

Six natural corundum, dull white sapphires from Sri Lanka, were chosen for this investigation. All of them had cleaned to remove silicate and calcite prior to the following processes. The process can be done by filling the 48% hydrofluoric acid into the plastic bottle which submerged the sapphires. Next, we left the sapphires in the acid about 24 hours in a fume hood of good ventilation and after this return the acid to other bottle. Then, the water was filled into the bottle to clear out the acid. Afterwards, stains and small particles on the gems' surfaces were cleaned by dispersing with ethyl alcohol in an ultrasonic bath. These methods are necessary for the further investigation. Generally, the samples were closely observed and recorded at 10x magnification through an optical microscope. Subsequently, samples were attached on a small bolt with a piece of carbon tape and then skewed it onto the sample holder. Certainly, samples had been adjusted till the level was horizontal, then, inserted the sample holder into the control system which placed in the analysis chamber.

For IBA analysis, the elemental compositions of the gemstone samples were analyzed by PIXE and IL techniques with a 2 MeV proton beam generated from a Cs-sputter ion source using the 1.7 MV tandem accelerator system at Chiang Mai University [8]. The beam was collimated to ~1 mm diameter, and the beam current at the sample was kept below 10 nA. Base pressure in the vacuum chamber was about 1×10^{-5} torr.

Prior to the PIXE experiment, the high-voltage supply for the detector is slowly adjusted to -500 V, and wait at least 30 minutes to let the system stable. The other associated systems such as preamplifier supply and amplifier supply also turn on the same way as was mentioned. The analysis chamber has an aperture of 1 mm-diameter for collimating the ion beam at the entrance of the chamber. During measurement, energetic protons collide and penetrate into the sample at a depth of ~15 μm (calculated by SRIM code) and induce characteristic X-ray emissions in all directions. The X-rays were detected by a Si(Li) detector placed at 120^{o} to the beam direction. An ORTEC multichannel analyzer card connected to a personal computer was used for data accumulation and acquisition. The ion beam current was approximately measured at the small bolt placed nearby the scintillation plate and verified the matching of channel number and X-ray energy. The measurement time depend on the ion current, density of sample, and the distance to detector, however, it consumes normally about 600 – 900 seconds. An electron shower generated by an electron gun was applied to reduce the bremsstrahlung effect caused by the charging-up phenomena. The data was accumulated by the Maestro software and evaluated by GUPIXWIN software which reported element concentration as parts per million by weight (ppm). Trace element concentrations were calculated using GUPIXWIN software and were reported as parts per million (ppm).

For IL, the preparation and incident ion is quite similar to the PIXE technique. However, a fiber optic light guide, placed at about $200^{\mathbf{o}}$ to the beam direction, was used to lead the emitted light to the spectrometer outside the analysis chamber. Next, the spectrometer and personal computer were located close to the analysis chamber to analyze the luminescence spectra by using an Ocean Optics spectrometer. In order to clarify any emission peak, each spectrum was recorded to 300-3,000 ms. For qualitative analysis, IL spectra were measured and compared with another spectra by normalized accumulation time. This method can be used for identifying the ion-induced luminescence mechanism, leading to an explanation of the color differences, which was the qualitative data by fitting with the OriginPro software compared with the trace element quantitative analysis.

The emission spectra acquired by the IL technique will be collected and analyzed in relating to the Cr^{3+} concentration which can be preliminary observed by the color appearance. Consequently, the intensity of the Cr^{3+} luminescence peak is compared to the quantitative data by PIXE technique in order to find out the correlation between the two ion beam analysis techniques.

Results and Discussion

Six dull white sapphires, labeled the number including 1, 2, 3, 12, 14, and 15, were characterized with PIXE technique as shown the amount of trace elements in Table 1. The table confirms that Al is the main composition in the sapphire, and other elements are overshadowed compared with the main element.

By the way, IL spectra were spectacularly analyzed, which normalized by averaging the accumulation time equals to 300 ms prior to analysis. Our measurements exemplify that an emission peak of chromium, as shown in Figure 1, is clearly seen at a wavelength of ~692 nm. By Ligand field theory [9], this peak is the splitting of energy in the d-orbital in Cr^{3+} together with the surrounding O^{2-} ions. In fact, this peak is an electron transition from ^2E (first excited state) to $^4A_2$ (ground state) with emission of~1.79 eV. In addition to the main peak, the spectra show dwarf peaks at 657.5 nm and 667.5 nm caused by electron transition from $^2T_1$ (second excited state) to $^4A_2$ [10]. There are also the lines at 702.6 nm and 704.6 nm so-called n-line which are an effect of paired Cr^{3+} [11]. Finally, the side band at 711.7 nm is caused by molecular vibration [12]. It is worth mentioning that some sapphires appear the broad peaks centered at 330, and 420 nm. These belong to

Dull white sapphire (code)	Al	K	Ca	Ti	V	Cr	Fe	Zn	Ga
G1	526164	49	250	402	7	106	390	25	35
G2	525593	25	137	254	17	31	3700	21	131
G3	526896	59	326	148	29	33	592	33	35
G12	526058	121	1412	149	17	52	2619	164	108
G14	527621	37	442	197	6	21	551	48	34
G15	525937	118	564	257	20	22	462	217	44

Table 1. The concentration in part per million (ppm) of six dull white sapphires analyzed by PIXE technique

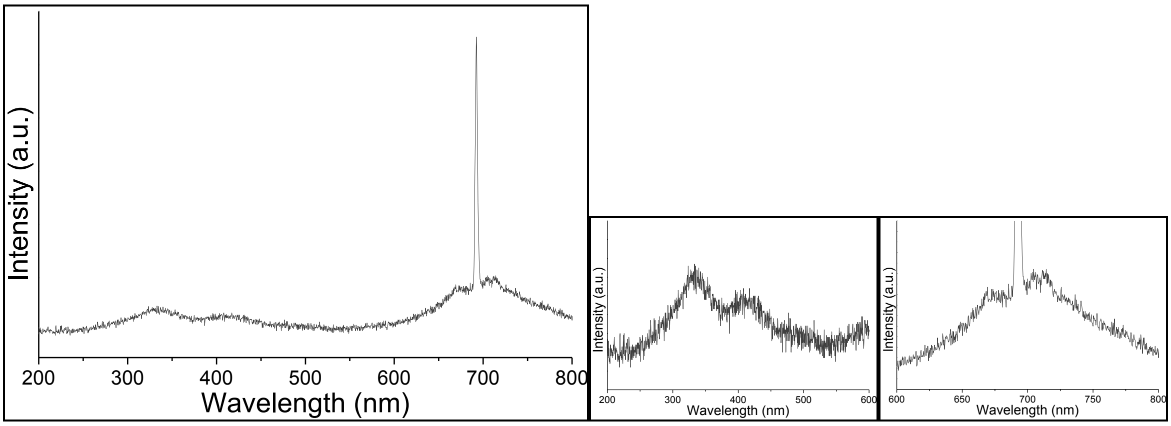

Figure 1. IL spectrum of dull white sapphire in overall regions (a), 200–600 nm (b) and 600–800 nm (c).

the F^+-center [13] and F_2-center [14], respectively, which relate to the imperfection in the crystal lattice of sapphires. In other words, these color center luminescence peaks are also observed in the highly existence of calcium because Ca leads to distort the octahedral structure of Cr_2O_3, which induce ultimately the color center. These results indicate that ion beam luminescence is not only a very sensitive method for detecting Cr inclusion through substitution of Cr^{3+} in an alumina matrix, but also indicating the single crystal property of the sapphire.

For correlation between PIXE and IL results, each IL spectra of sapphire was normalized, as mentioned earlier, and plot in the relation between the maximum luminescent intensities and the ratio of Ca/Cr concentrations is shown in Figure 2. It is clear that the amount of Ca is the reason why the luminescence of sapphires is less than others despite the higher chromium concentration. The calcium also acquires the kinetic energy of incident ion so that not produce any direct emission in the visible region, i.e., this element also complete the energy which lead to the less probability for Cr^{3+} luminescence. In addition, the trend line likewise indicates that the luminescent tendency of sapphire is inverse proportional to the ratio of Ca/Cr concentration. In other words, one sapphire which contains much calcium leads to inhibit the luminescent characteristic of chromium.

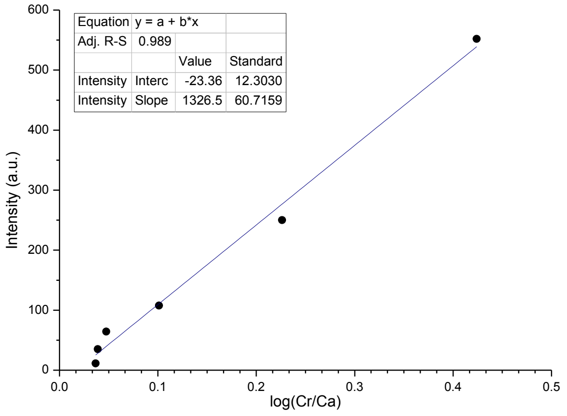

Figure 2. The plot relation between Cr3+ luminescence intensity and the logarithm of ratio of Cr/Ca concentrations.

The second interesting for the low luminescence in spite of as same as Cr^{3+} concentration, G2 with G3, and G14 with G15, may have caused by the effect of low iron concentration in the sapphire. As illustrated in Table 1, the iron concentration in G2 is more than G3, which likely appear in G14 superior to G15, and have more luminescence intensity than another. It can be stated that the iron ion (Fe^{3+}) may be a co-activator for the luminescence by Cr^{3+} [15]. Alternatively, the kinetic energy of incident ion can be transferred to the Fe_2O_3 inside the matter; furthermore, the luminescence of Fe^{3+} occur in the infrared region (>

800 nm) [16], which not observed in this experiment. Then, the Stoke shift effect may be the reason why the emission energy from Fe^{3+} is able to re-activate the neighbor Cr_2O_3 such more luminescence that appear in the common mechanism as stated earlier. It seems that the iron concentration effect is less significant than the calcium concentration, for instance, the more concentration of either Cr^{3+} or Fe^{3+} in G12 are limited by the high concentration of calcium as shown in Table 1.

Conclusions

It is clear that the PIXE analysis can be analyzed an amount of trace element which benefit to correlate with the luminescence spectra of sapphire by IL technique. Even if this investigated sapphire does not appear any color, dull white sapphire, the luminescence of Cr^{3+} which normally found in red sapphire or ruby can be slightly observed. The observation express that there are no difference between the luminescence of this sapphire compared with ruby or other coloration sapphire.

As a result, the different emission peak centered at 692 nm of Cr^{3+} is mainly inhibited by the presence of an amount of calcium element in the matter. It may offer that the low of co-activator, Fe^{3+}, is slightly responsible for the Cr^{3+}-emission; however, it has rather a dominantly influence on the corresponding chromium concentration in each sapphire. Moreover, the correlation between IL and PIXE data show a good trend line in order to predict the luminescent mechanism for this discoloration sapphire.

It is worth mentioning that the particle-induced X-ray emission and ion beam induced-luminescence technique is advantageous and alternative for primarily investigating the discoloration sapphire. Additionally, these data can be implied to select the sapphire for further enhancing sapphire such as more clarity, enrich the color.

Acknowledgments

T. Chulapakorn would like to acknowledge the Development and Promotion of Science and Technology Talents Project for his scholarship. He also thanks C. Thongleum for operation of the 1.7-MV Tandem accelerator. This work was advocated the subsidy in part by the International Atomic Energy Agency (IAEA), the National Research Council of Thailand, The Graduate School of Chiang Mai University, and the Thailand Center of Excellence in Physics. All sapphires were provided by the Division of Material Science (Gems and Jewelry), Department of General Science, Faculty of Science, Srinakharinwirot University, and by S. Srisupawattana.

References

1. P.G. Read, "Gemmology", 3rd ed., Oxford, UK: Elsevier Ltd., 2005.
2. T. Themelis, "The Heat Treatment of Ruby and Sapphire", California: Gemlab Inc., 1992.
3. K. Nassau, "The origins of color in minerals", American Mineralogist **63** (1978), 220.
4. T. Osipowicz, T.S. Tay, I. Orlic, S.M. Tang, and F. Watt, "Nuclear microscopy of rubies: trace elements and inclusions", Nuclear Instruments and Methods in Physics Research B **104** (1995), 590–594.
5. T. Calligaro, J.P. Poirot, and G. Querré, "Trace element fingerprinting of jewellery rubies by external beam PIXE", Nuclear Instruments and Methods in Physics Research B **150** (1999), 628–634.
6. A.A. Bettiol, K.W. Nugent, and D.N. Jamieson, "The characterisation of high-grade synthetic quartz, corundum and spinel using ionoluminescence (IL)", Nuclear Instruments and Methods in Physics Research B **130** (1997), 734–739.
7. H. Calvo del Castillo, J.L. Ruvalcaba, and T. Calderón, "Some new trends in the ionoluminescence of minerals", Analytical and Bioanalytical Chemistry **387** (2007), 869–870.
8. T. Kamwanna, U. Tippawan, S. Intarasiri, and S. Singkarat, "The combined PIXE and IL investigations of gemstones", Thai Journal of Physics **6** (2010), 232–236.
9. K. Nassau, "The Physics and Chemistry of Color", New York: John Wiley & Sons, 2001.
10. M. Milos, S. Kairouani, S. Rabaste, and A. Hauser, "Energy migration within the ^2E state of Cr^{3+}", Coordination Chemistry Reviews **252** (2008), 2540–2551.
11. A. Inouye, S. Nagata, K. Toh, B. Tsuchiya, S. Yamamoto, and T. Shikama, "Luminescence of Cr-doped alumina induced by charged particle irradiation", Journal of Nuclear Materials **367-370** (2007), 1112–1116.
12. L.C. Cossolino and A.R. Zanatta, "Influence of chromium concentration on the optical-electronic properties of ruby microstructures", Journal of Physics D: Applied Physics **43** (2010), 015302–015310.
13. A. Moroño and E.R. Hodgson, "On the origin of the F^+ centre radioluminescence in sapphire", Journal of Nuclear Materials **249** (1997), 128–132.
14. K.H. Lee and J.H. Crawford, Jr., "Luminescence of the F center in sapphire", Physical Review B **19** (1979), 3217–3221.
15. H. Calvo del Castillo, N. Deprez, T. Dupuis, F. Mathis, A. Deneckere, P. Vandenabeele, T. Calderón, and D. Strivay, "Towards the differentiation of non-treated and treated corundum minerals by ion-beam-induced luminescence and other complementary

techniques", Analytical and Bioanalytical Chemistry **394** (2009), 1055.

16. D.S. McClure, "Optical spectra of transition-metal ions in corundum", Journal of Chemical Physics **36** (1962), 2769.

Design and Construction the Atmospheric Plasma System

K. Honglertkongsakul[1, 2*], J. Pongsopa[3], Dusit Ngamrungroj[4],
N. Witit-anun[1,2], and S. Chaiyakun[1,2]

[1]Plasma for Surface Sciences Research Laboratory (PSS), Department of Physics, Faculty of Science,
Burapha University, Chonburi, 20131, Thailand
[2]Thailand Center of Excellence in Physics, (ThEP), CHE,
Ministry of Education, Bangkok 10400, Thailand
[3]Faculty of Science and technology, Suan Dusit Rajabhat University,
Bangkok, 10700, Thailand
[4]Department of Social and Applied Science, The College of Industrial Technology, King Mongkut's
University of Technology North Bangkok, Bangkok, 10800, Thailand
**Corresponding author. E-mail: kanchaya@buu.ac.th*

Abstract

The dielectric barrier discharge (DBD) plasma system was designed and constructed at atmospheric pressure air for studying the breakdown voltage. The discharge was generated by applying high voltage alternative current (AC) source across the copper electrodes. High voltage AC source can be applied of frequency 50 Hz and potential difference in range of 0-15 kV. Transparent sheet was selected to be the dielectric barrier and was placed in front of copper electrode with two different configurations such as single dielectric barrier and double dielectric barrier. In this work, we studied both discharging with transparent sheet and discharging without transparent sheet. The gap between two copper electrodes will be adjusted for measuring the breakdown voltage, which can be obtained by using digital oscilloscope. It was found that the breakdown voltage increased with increasing the gap between two copper electrodes. The electron temperature of this constructed DBD plasma system was measured and reported by using optical emission spectrometer. It was found that electron temperature was in the range of 3-8 eV.

***Keywords*:** Dielectric barrier discharge, atmospheric plasma, breakdown voltage, electron temperature

Introduction

Due to the vacuum unit in plasma system has quite more expensive, therefore; the atmospheric plasma system exhibits to be the alternative in plasma system for reduction in vacuum unit. Nowadays, atmospheric plasma system became to main operation in plasma process with surface modification in short period [1-4]. There are several plasma systems can generate plasma at atmospheric pressure, such as plasma jet, plasma needle, plasma torch and dielectric barrier discharge (DBD) [5, 6]. To compare these atmospheric plasma systems, DBD has been attracted high attention with using both laboratory experiment and large industrial. Moreover, DBD system can be obtained in a much simpler way than other systems due to their merits of small dimension, low cost as well as easy circuit in electric power supply.

The characteristic of DBD system is the non-equilibrium plasma. In non-equilibrium plasma, free electrons obtain energy from an applied electric field and loss energy by collisions with neutral gas molecules. This transfer energy between free electrons and gas molecules leads to new species formation, such as ions, atoms, free radicals as well as metastable species. Moreover, non-equilibrium plasma can generally be obtained at atmospheric pressure with reduction of the discharge size and working at low excitation frequency. Therefore non-equilibrium plasma is suitable for various applications, such as polymer treatment, material modification, material processing as well as substrates cleaning [1-4].

However, the breakdown voltage and the electron temperature in DBD system should have known in order to get well controlled treatment, modification as well as cleaning. The high voltage probe and the optical emission spectroscopy (OES) have been commonly used to obtain the breakdown voltage and the electron temperature; respectively [7-9].

In this work, DBD plasma system was designed and constructed at atmospheric pressure air by 50 Hz of high voltage alternative current (AC) source. Transparent sheet was selected to be the dielectric barrier. The gap between two copper electrodes will be adjusted for measuring the breakdown voltage. The electron temperature of this DBD plasma system was measured by OES.

Materials and Methods

DBD system

The DBD plasma system was designed and constructed at atmospheric pressure air by applying high voltage alternative current (AC) source across the electrodes and dielectric sheet. These electrodes made from the copper plate with 6×9 cm sizes. High voltage AC source was generated at frequency 50 Hz with potential difference in range of 0-15 kV by connecting the variac with a neon transformer, which used to be step up transformer. The resistor with 20 Ω and 200 watts was used to be load in the circuit.

The transparent sheet was selected to be the dielectric barrier. This sheet was placed in front of copper electrode with two different configurations such as single dielectric barrier and double dielectric barrier. In this work, we studied both discharging with transparent sheet and discharging without transparent sheet.

All configuration view of electrodes in atmospheric plasma system is also shown in figure 1.

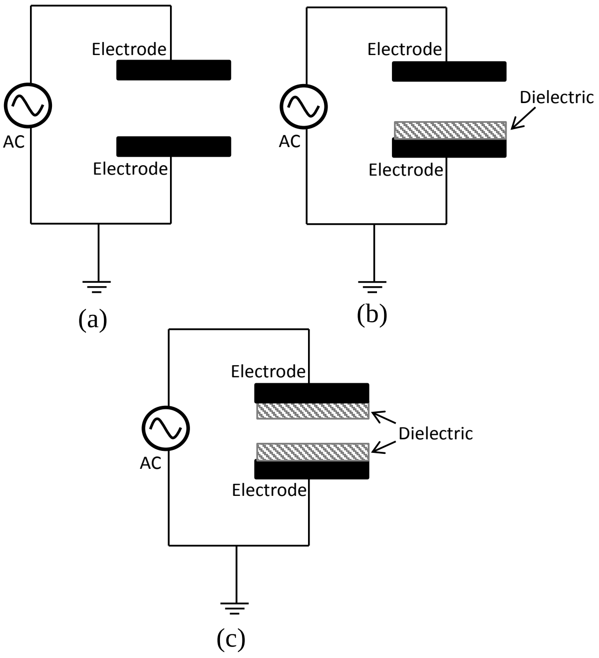

Figure 1. All configuration view of electrodes (a) without dielectric barrier, (b) single dielectric barrier and (c) double dielectric barrier in atmospheric plasma system.

Characteristics

The relation of breakdown voltage to gap between two copper electrodes was measured by high voltage probe. The electron temperature of this constructed DBD atmospheric plasma system was measured and reported by using OES in the range between 200 and 1,100 nm. A miniature fiber optic spectrometer (USB2000, Ocean Optic Inc.) was used in this measurement. The spatial distribution of reactive species was measured at different gaps between two copper electrodes. For elemental analysis OES, it is important that plasma should be in local thermodynamic equilibrium (LTE).

Results and Discussions

Breakdown voltage

The breakdown voltage versus the gap between two copper electrodes is also shown in figure 2. It was found that the breakdown voltage increased with increasing the gap between two copper electrodes in all configurations of electrodes in atmospheric plasma system. This is because at larger gap the energy of the particles transiting in the discharge gap increased. This energy will be proportional to the applied voltage and the charge of the particles, leading to the higher breakdown voltage.

While electrode with double dielectric barrier showed the highest breakdown voltage and electrode with single dielectric barrier had more breakdown voltage than electrode without dielectric barrier. This is because the increasing amount of dielectric barrier had more the dielectric strength; hence the transport current in the discharge gap will occur when the electric field had high enough, leading to the higher breakdown voltage.

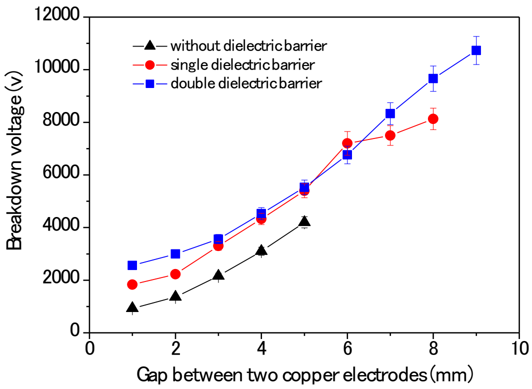

Figure 2. Plot of the breakdown voltage versus the gap between two copper electrodes.

Electron temperature

An example of optical emission spectrum of DBD plasma system from 200 nm to 1,100 nm is shown in figure 3. The main intensive nitrogen lines were found in the region between 300 and 425 nm because the nitrogen is the main composition of air. Spectroscopic data of specific emissions nitrogen lines present in the atmospheric pressure air were listed in Table 1. This spectroscopic data were taken from the atomic database of NIST [10].

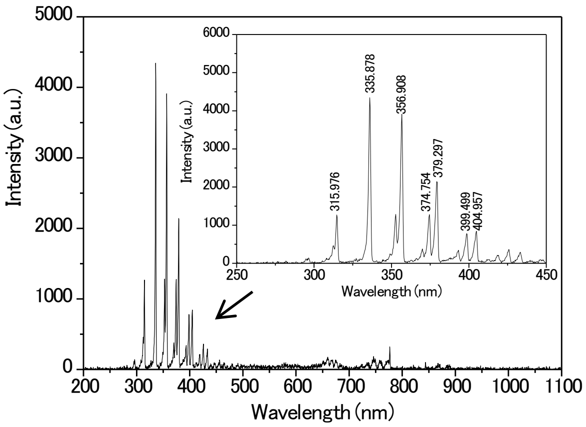

Figure 3. Example of optical emission spectrum of DBD plasma system from 200 nm to 1,100 nm.

Table 1: Spectroscopic data of specific emissions lines present in the DBD plasma system [10].

Species	λ [nm]	g_i-g_k	E_i-E_k [eV]	A_{ki} ($\times 10^8$) [s^{-1}]
N-V	315.976	2-2	84.1-88.0	1.030
N-III	335.878	2-2	35.6-39.3	0.305
N-IV	374.754	3-5	58.6-62.0	0.992
N-III	379.297	8-6	38.4-41.7	0.103
N-II	399.499	3-5	18.5-21.6	1.220
N-IV	405.776	3-5	50.2-53.2	0.662

Where λ is the emission spectrum wavelength. E_i and E_k is the energy level in the lower level and upper level; respectively. g_i and g_k is the statistical weight in the lower level and upper level; respectively. And A_{ki} is the Einstein transition probability for spontaneous emission from level k to level i.

To interpret the optical emission spectra, the energy level populations of nitrogen plasma species under LTE condition were given by the Boltzmann distribution law. The intensity measurement of a spectral line occurring between the upper energy level and low energy level of nitrogen plasma species in ionization stage Z [11, 12], is given as

$$I_z = \frac{hc}{4\pi\lambda_{ki,z}} A_{ki,z} \frac{g_{k,z} n_o}{P_z} \exp\left(-\frac{E_{k,z}}{k_B T}\right) \quad (1)$$

where h is Planck's constant. c is the speed of light. $A_{ki,z}$ is the transition probability. $\lambda_{ki,z}$ is the transition line wavelength. k_B is the Boltzmann constant. $g_{k,z}$ is the statistical weight of the upper level. $E_{k,z}$ is the energy of the upper level. P_z is the partition function and n_o is the total number density of atom in the ground state.

However, the absolute intensity, the partition function and the number density must to determine in an equation 1. To avoid these difficult, the method based on the relative intensity ratio of two nitrogen lines will be used in this work. The intensity ratio of two lines of the same species of ionization stage Z is express as

$$\frac{I_1}{I_2} = \left(\frac{\lambda_{nm,z}}{\lambda_{ki,z}}\right)\left(\frac{A_{ki,z}}{A_{nm,z}}\right)\left(\frac{g_{k,z}}{g_{n,z}}\right) exp\left(-\frac{E_{k,z}-E_{n,z}}{k_B T}\right) \quad (2)$$

Where I_1 and I_2 are the line intensity from the k-i and n-m transition; respectively [11, 13].

In this work, the intensity ratio of two N-III lines at 335.878 and 379.297 nm was chosen for finding the electron temperature. The electron temperature versus the gap between two copper electrodes is shown Fig. 4.

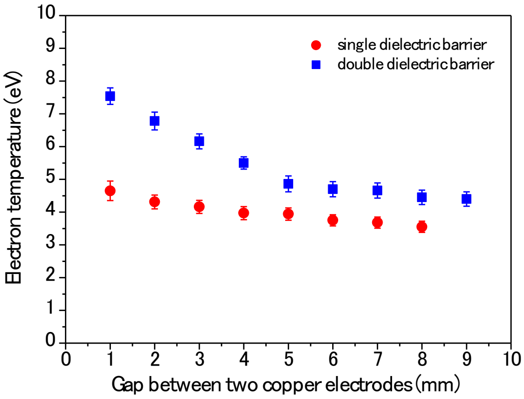

Figure 4. Plot of an electron temperature versus the gap between two copper electrodes.

This figure shows that the electron temperature was in the range 3-8 eV, depending upon the gap between two copper electrodes. It was found that the electron temperature decrease with increasing gap between two copper electrodes. This is because at lower gap the electrons had higher average kinetic energy, because they had not lost much energy due to collisions with other atoms. With increasing gap, the electrons have more collisions and lose more kinetic energy, hence decreasing electron temperature. These results are similar to results in other reports [8].

Conclusions

The DBD atmospheric plasma system was designed and constructed by high voltage AC source with 50 Hz frequency and 0-15 kV potential difference. Transparent sheet was used to be the dielectric barrier in front of copper electrode. The breakdown voltage measurement indicates that the breakdown voltage increased with increasing the gap between two copper electrodes and increasing amount of dielectric barrier. The analysis of OES indicates that electron temperature in DBD atmospheric plasma system was found in the range of 3-8 eV. The electron temperature decreased with increasing gap between two copper electrodes but the electron temperature increased with increasing amount of dielectric barrier. Therefore, both the breakdown voltage and the electron temperature depended on the gap between two copper electrodes and amount of dielectric barrier.

Acknowledgments

This present work was partially supported by Faculty of Science of Burapha University.

References

1. A. Chirokov, A. Gutsol and A. Fridman, “Atmospheric Pressure Plasma of Dielectric Barrier Discharges”, Pure and Applied chemistry **77** (2005) 487.
2. U. Kogelschatz, B. Eliasson and W. Egli, “Dielectric-Barrier Discharges. Principle and Applications”, Journal de Physique IV **7** (1997) C4-47.
3. P. Deeyai, P. Jitsomboonmit, W. Soonthonchaikul, M. Suphantharika, and S. Dangtip, “Effect of Atmospheric Argon Plasma on Morphology of Tapioca Starch Granule”, Journal of the Microscopy Society of Thailand **24(2)** (2010) 112.
4. H. Ayan, D. Staack, G. Fridman, A. Gutsol, Y. Mukhin, A. Starikovskii, A. Fridman and G. Friedman, “Application of Nanosecond-Pulsed Dielectric Barrier Discharge for Biomedical Treatment of Topographically Non-Uniform Surfaces”, Journal of the Microscopy Society of Thailand **24(2)** (2010) 112.
5. M. D. Ionita, M. Teodoresch, T. Acsente, M. Bazavan, E. R. Ionota and G. Dinescu, “Remote Surface Modification of Polymeric Foils by Expanding Atmospheric Pressure”, Romanian Journal of Physics **56** (2011) 132.
6. E. Stoffels, A. J. Flikweert, W. W. Stoffels and G. M. W. Kroesen, “Plasma Needle: A Non-Destructive Atmospheric Plasma Source for Fine Surface Treatment of (Bio)Materials”, Plasma Sources Science and Technology **11** (2002) 383.
7. V. Nehra, A. Kumar and H. K. Dwivedi, “Atmospheric Non-Thermal Plasma Sources”, International Journal of Engineering **2** (2012) 53.
8. N. Estrada, R. Valdivia and J. Pacheco, “Chemical and Electrical Diagnostic of Two Configurations of Dielectric Barrier Discharges Applied to Nitric Oxides Degradation”, Superficies y Vacio **24(3)** (2011) 88.
9. R. Shrestha, R. B. Tyata and D. P. Subedi, “Estimation of Electron Temperature in Atmospheric Pressure Dielectric Barrier Discharge Using Line Intensity Ratio Method”, Kathmandu University Journal of Science, Engineering and Technology **8** (2012) 37.
10. NIST Atomic Spcetra Database on http://www.nist.gov.
11. V. K. Unnikrishnan, K. Alti, V. B. Kartha, C . Santhosh, G. P. Gupta and B. M. Suri, “Measurement of Plasma Temperature and Electron Density in Laser-Induced Copper Plasma by Time Resolved Spectroscopy of Neutral Atom and Ion Emissions”, Journal of. Physics. **74** (2010) 983-993.
12. N. Zhang, F. Sun, L. Zhu, M.P. Planche, H. Liao, C. Dong and C. Coddet, “Electron Temperature and Density of the Plasma Measurement by Optical Emission Spectroscopy in VLPPS Conditions”, Journal of Thermal Spray Technology **20(6)** (2011) 1321-1327.
13. A. Sarani, A. Y. Nikiforov and C. Leys, “Atmospheric Pressure Plasma Jet in Ar and Ar/H_2O Mixtures: Optical Emission Spectroscopy and Temperature Measurements”, Physics of Plasma **17** (2010) 063504.

Review on Ion Beam Treatment of Gemstones in Thailand

D. Bootkul[1,4*], S. Intarasiri[2,4], U. Tippawan[3,4], and S. Singkarat[3,4]

[1]Department of General Science, Faculty of Science, Srinakharinwirot University,
Bangkok 10110, Thailand
[2]Science and Technology Research Institute, Chiang Mai University, Chiang Mai 50200, Thailand
[3]PBP Research Facility, Department of Physics and Materials Science, Faculty of Science,
Chiang Mai University, Chiang Mai 50200, Thailand
[4]Thailand Center of Excellence in Physics, Commission on Higher Education,
328 Si Ayutthaya Road, Bangkok 10400, Thailand
**Corresponding author. E-mail: mo_duangkhae@hotmail.com*

Abstract

Gemstones generally are naturally-occurring-crystalline forms of mineral, which are desirable for their beauty, rarity and durability that are valuable enough to be enjoyed for generations. However, the best quality gem materials usually are rare in nature. Therefore, individuals continue to strive for methods to treat lower-quality materials to enhance their appearance and thereby their marketability. Heat treatment is the most popular technique commercially used for the improvement of quality of gemstones. However, the treatment is time consuming and is not an efficient process to bring about desirable changes in the properties of the stones. Heavy ion beams are a good candidate of irradiating gemstones, for they are able to bring about both heating effect and introduction of defects, impurities and charges for modification of the optical properties, as well as treat individually different gems. In the past ion implantation has been investigated from the point of view of improving the optical and mechanical properties of sapphires for the application on optics, optoelectronics, photonics and tooling. Many studies have dealt with understanding basic and applied aspects of ion beam modifications of sapphire but not many have focused on developing industry-ready technology. Plasma and Beam Physics Research Facility (PBP), Chiang Mai University, Thailand, can facilitate various ion beam facilities and has engaged into the gemstone industry since 2007. Advanced techniques in plasma and particle beam are utilized for modification of various gems materials, such as corundum, spinel, tourmaline and garnet, with respect to optical enhancement. The treatment has shown to be able to modify color, unify inclusions, increase transmittance and improve luster of gems, thus value adding. Hence it is the purpose of this presentation to give a review of what have been accomplished for gemstone enhancement from such facilities.

Keywords: Gemstone, corundum, ion implantation, chromophoric elements, luster

Introduction

A gemstone is the naturally occurring crystalline form of a mineral, which is desirable for its beauty, valuable in its rarity and durable enough to be enjoyed for generations. Although new occurrences of natural gemstones are found from time to time in many parts of the world, these localities combined with historically important gem deposits have not always provided the best quality material in sufficient amounts to meet the current demand for gemstones among consumers. Besides the relatively small amount of high quality gem material typically produced at a given mining locality, there is also recovered a much larger percentage of lower quality material (for example, with poorer size, color or clarity) that has little market value. Therefore, individuals continue to strive to develop methods to treat this lower-quality material in the laboratory to enhance its appearance and thereby its marketability for gem purposes.

Heat treatment is the most popular technique commercially used for the improvement of quality of gemstones [1]. Heat treatment mainly [2,3] modifies color, unifies inclusions, increases transmittance and improves luster. However, heat treatment is expensive and is not an efficient process to bring about desirable changes in the properties of gem stones. For example, it involves annealing at 1000 ^{o}C and above for periods ranging from few hours to few months depending on the type of gemstones. Different types of gemstones cannot be treated simultaneously. Alternative treatments are exposing the gemstones to energetic particle beams and laser beams. Laser beams do not produce localized heating, whereas low mass particles such as electrons produce localized but yield poor coloration. Neutron irradiation makes gemstones radioactive. Heavy ion beams are a good candidate of irradiating gemstones, for they are able to bring about both heating effect and introduction of defects, impurities and charges for modification of the optical properties [4], as well as treat individually different gems.

In the past ion implantation on sapphires has been investigated from the point of view of improving their optical and mechanical properties [5–10] for the application on optics, optoelectronics, photonics and tooling [11,12]. Many studies have dealt with understanding basic and applied aspects of ion beam modifications of sapphire but not many have focused on developing industry-ready technology. The present work aims at developing heavy ion beam irradiation process for enhancing the quality of gemstones and thus increasing their market values.

Materials and Methods

A variety of gemstones used for this study are rubies, sapphires, topazes, spinel and garnets from Thailand, Myanmar (Burma), and Africa. The untreated samples vary in sizes from a few mm to almost 1 cm in specific diameters. The ion implantation was carried out by using various ion beam facilities at Chiang Mai University, including a 150-kV mass-analyzed heavy ion implanter (Figure 1), a 20-kV multicusp high-intensity plasma source ion implanter, and a 25-kV negative ion implanter attached to the Tandem accelerator. The target holders were designed with special considerations, aiming at avoiding sputtering contamination on the gem surface as much as possible, which was able to fit any shape of gem samples to the holder. Argon, oxygen and nitrogen ions at energy between 20 - 100 keV were implanted to the gem specimens with beam currents of 0.1 to a few mA to implant from 10^{17} to a few 10^{19} ions/cm^2. The operating pressures in the target chambers were about 10^{-3}-10^{-4} Pa. The target temperatures during ion implantation were measured using an infrared thermometer to be stabilized at about 200-600 ^{o}C, depending on the size of sample and the ion implantation conditions. No post treatments were deliberately done on the ion-implanted gems. The ion beam-treated specimens were observed under either gemologist-professional binocular microscopes (Zeiss, Germany) or directly the natural lights. The measurement by PIXE and IL were also taken into account. The grades of the gemstones were judged by authorized gemological professionals.

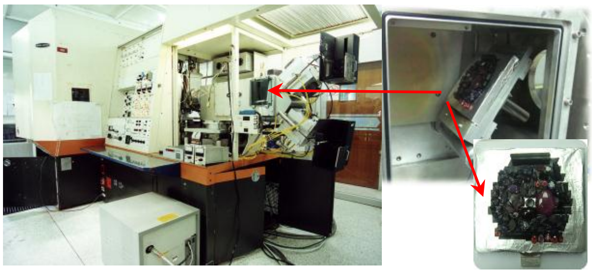

Figure 1. 150-kV mass analyzed heavy ion implanter and its target holder.

Results and Discussion

In a normal sapphire, the high concentration of titanium [Ti^{4+}] and iron [Fe^{2+}] will produce blue color in sapphire. Bluish or purplish core or inclusions in ruby are typically attributed to high concentrations of iron and titanium in the same way as the coloration of blue sapphire [13]. As shown in Figure 2, the O-ion implantation gives a positive effect by reduce purplish tint and make the stones brighter in red and improve its clarity. The oxygen ion would be involved in the charge transfer following the process of $4Fe^{2+} + O^{2} \rightarrow 4Fe^{3+} + 2O^{2-}$. Thus, the blue color blended with red in ruby is reduced. In case of natural blue sapphire, the greenish tint in core (due to the yellow or orange coloration) could be reduced by N-ion implantation and the stone turned purer blue after treatment (Figure 3). These results show that appropriate type of ion should be selected for different kinds of impurity to enhance ruby and sapphire.

The different varieties of gemstones, including rubies, sapphires, and garnets were subjected to treated by plasma beams and are illustrated in Figure 4. The oxygen plasma ion implantation can turn yellow sapphire at its one end and colorless at the center into more intense yellow. Also its clarity and luster are slightly improved from originally slightly brownish tint and somewhat lower saturation.

Ion beam technique can also eliminate the micro-inclusions of red spinel by locally heating of ion beams as seen in Figures 5. This heating can be explained by thermal spike model [14], in which the penetrating ions releases energy in a cylindrical volume around their paths and the energy is converted into heat. At the end, the color of spinel turns to be more intense red.

Other interesting example is the color change of green tourmaline by nitrogen ion treatment as seen in Figure 6.

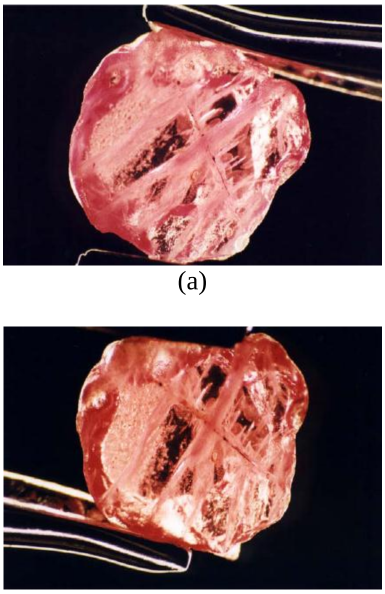
(a)

(b)

Figure 2. Comparison of natural ruby for (a) before, and (b) after O-ions implantation.

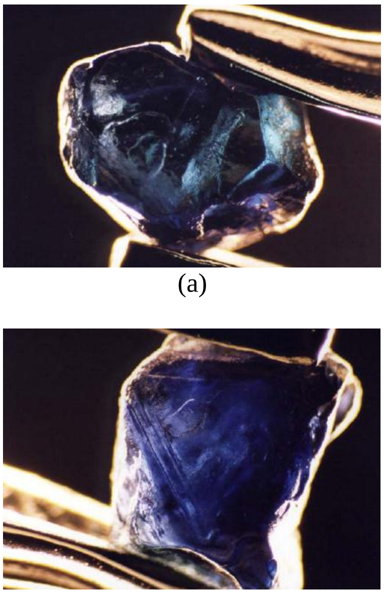
(a)

(b)

Figure 3. Comparison of natural blue sapphire for (a) before, and (b) after N-ions implantation.

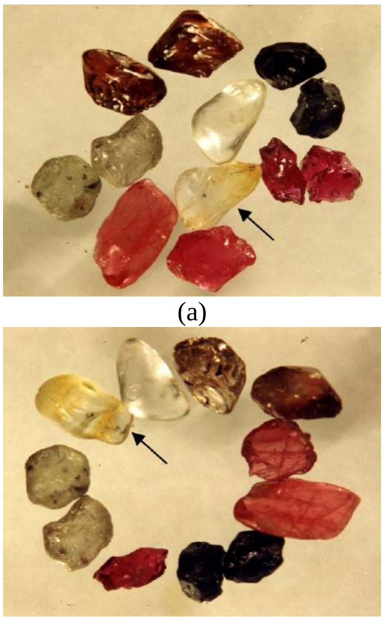
(a)

(b)

Figure 4. Demonstration of (a) untreated natural gemstones and (b) after treated with O-plasma.

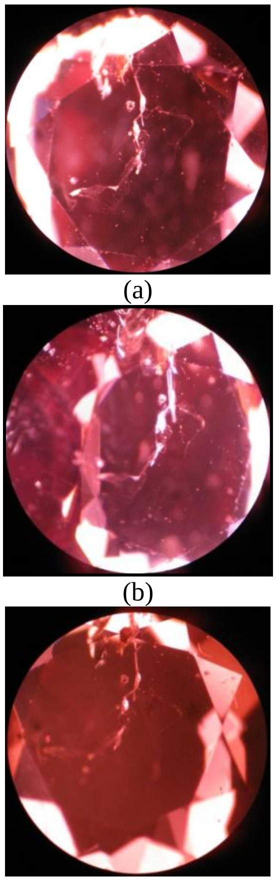
(a)

(b)

(c)

Figure 5. Demonstration of (a) untreated natural red spinel and (b) after 1st and (c) 2nd treatments by ion beam techniques.

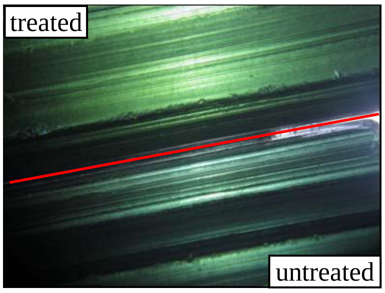

Figure 6. Color enhancement of green tourmaline by ion beam techniques.

In case of applying the technique for gems market we focus our work to 2 objects, namely inducing of purple sapphire by nitrogen beams (Figure 7) and improving of white sapphire for diamond replacement (Figure 8). For these purposes, violet sapphires are induced from low quality pink sapphire and brilliant white sapphires are converted from low quality dull white sapphire.

Figure 7. Violet sapphire (right) induced from low quality pink sapphire (left) by ion beam techniques.

Figure 8. Low quality dull-white sapphires (middle) can turn into more brilliant (left-right) by ion beam treatment.

Conclusions

This overview has demonstrated that by using ion beam treatments, the color of the ion implanted gemstone is viewed as more lively and brilliant. For example, brighter red, better clarity and luster after oxygen-ion implantation in rubies or more vivid blue and less green after nitrogen-ion implantation. Inclusions in red spinel can be reduced, resulting in better clarity and luster. The striking results are the changing of the dull, opaque, white sapphire to be the brilliant, transparent white sapphires for diamond replacement and the inducement of violet sapphire from low quality pink sapphire. These modifications lead to quality improvement of gemstones and thus the added values.

Acknowledgments

The authors would like to express their gratitude to the Thailand Center of Excellence in Physics (ThEP Center) and the National Research Council of Thailand (NRCT) for funding.

References

1. P. G. Read, Gemmology, Butterworth-Heinemann Ltd., Oxford, 1995.
2. T. Themelis, The Heat Treatment of Ruby and Sapphire, Gemlab Inc., USA, 1992.
3. R.W. Hughes, Ruby and Sapphire, RWH Publishing, Boulder, Colorado, USA, 1997.
4. K. Nassau, Am. Mineral. **63** (1978) 219
5. G.W. Arnold, G.B. Kreft, C.B. Norris, Appl. Phys. Lett. **25** (1974) 540.
6. C.J. McHargue, P.S. Sklad, J.C. McCallum, C.W. White, A. Perez, E. Abonneau, G. Marest, Nucl. Instr. Methods **B46** (1990) 74.
7. K. Sickafus, N. Yu, R. Devanathan, M. Nastasi, Nucl. Instr. Methods **B106** (1995) 573.
8. Y. Aoki, N.T. My, S. Yamamoto, H. Naramoto, Nucl. Instr. Methods **B114** (1996) 276.
9. J.N. Mitchell, R. Devanathan, N. Yu, K.E. Sickafus, C.J. Wetteland, V. Gopalan, M.A. Nastasi, K.J. McClellan, Nucl. Instr. Methods **B141** (1998) 461.
10. N.K. Huang, B. Tsuchiya, K. Neubeck, S. Yamamoto, K. Narumi, Y. Aoki, H. Abe, A. Miyashita, H. Ohno, H. Naramoto, Nucl. Instr. Methods **B143** (1998) 479.
11. Y. Saito, H. Horie, S. Suganomata, Nucl. Instr. Methods **B59/60** (1991) 1173.
12. M. Ikeyama, M. Tazawa, H. Morikawa, A. Chayahara, in: J.S. Williams, R.G. Elliman, M.C. Ridgway (Eds.), Proc. of the 9th Int. Conf. on Ion Beam Modification of Materials, Canberra, Australia, Feb. 5–10, 1995, North-Holland, Elsevier Science B.V., Amsterdam, 1996, p. 1077.
13. R.W. Hughes, Ruby & sapphire. RWH Publishing, 1997; Fallbrook http://www.ruby-sapphire.com (2008).
14. G.H. Vineyard, Radiation Effects **29** (1976) 245.

Material Physics, Nanoscale Physics and Nanotechnology

Characterization of Cu-Zn Oxide Compounds Synthesized by Co-precipitation Process

K. Phiwdang[1*], N. Thaweesang[2], W. Techitdheera[2], and W. Pecharapa[1,3]

[1] *College of Nanotechnology, King Mongkut's Institute of Technology Ladkrabang, Ladkrabang, Bangkok, 10520 Thailand*
[2] *Department of Applied Physics, Faculty of Science, King Mongkut's Institute of Technology Ladkrabang, Ladkrabang , Bangkok, 10520 Thailand*
[3]*ThEP Center, CHE,328 Siayuthtaya Rd., Bangkok 10400,Thailand*
**Corresponding author. E-mail: pd.kankanit@gmail.com*

Abstract

A series of Cu-Zn oxide compounds were prepared via co-precipitation process using copper chloride ($CuCl_2{\cdot}2H_2O$) and zinc chloride ($ZnCl_2{\cdot}2H_2O$) as starting precursors. The compounds were synthesized with various molar ratio of copper-zinc (1:9 , 3:7, 5:5, 7:3, 9:1) combination with annealing at 600 °C for 2 h. As-synthesized samples were characterized by X-ray diffraction (XRD),transmission electron microscope(TEM), scanning electron microscope (SEM) and Fourier transform infrared (FTIR) spectroscopy. For XRD results, diffraction peaks of the compounds are well-defined and reveal the well-crystalline characteristic of the samples. TEM and SEM results show different morphologies of CuO, ZnO and Cu-Zn oxide compounds appearing in rod, flower and quasi spherical shapes, respectively.. The presence of functional groups and chemical bonding of the compounds is affirmed by FTIR results. FTIR results additionally indicate the existence of mixture phases of ZnO and CuO in the compounds which were obtained by facile precipitation process.

Keywords: copper oxide, zinc oxide, precipitation process, compounds

Introduction

Metal oxide semiconductors are materials that attract great attention because of their excellent physical properties for example, electricity and magnetism and optics. In this regard, copper oxide (CuO) material, in particular in form of low dimensional nanostructure has been extensively studied because of its narrow band gap 1.2 eV and feasibility in various applications such as catalysis [1], antimicrobial activity [2] , solar energy conversion [3] and gas sensor [4]. Meanwhile, zinc oxide (ZnO) is in great interest for practical applications owing to its fascinating properties including wide direct band gap of 3.37 eV with high exciton binding energy of 60 meV and strong chemical-thermal stability [5]. Because of prominent properties, ZnO can be used in various fields of applications such as sensor [6], varistor [7] and electrical device [8]. Moreover, both semiconductor materials are rather cheap, environmental friendly and similar physical-chemical properties comparing to other metal oxide materials. Up-to now, various structures with exceptional morphologies of these compounds can be obtained by different preparation methods, for example, solid state reaction method, wet impregnation method, sol-gel based method and precipitation method. For large scale production, the precipitation process is highly considered because of simple and low-cost process, safe system, environmental friendly, low temperature process and decreased time of production [9-12]. Nevertheless, few researches have been found regarding to the synthesis of the Cu-Zn oxide low-dimension nanostructure compounds.

The main objective of this work is to synthesize copper-zinc oxide compound via precipitation process and investigate the effect of the Cu:Zn ratio on structural properties of the compounds. The as-synthesized samples were extensively characterized by transmission electron microscopy, X-ray diffractometer, Fourier transform infrared spectroscopy and scanning electron microscopy.

Materials and Methods

In typical procedure to synthesize a series of material, copper chloride ($CuCl_2{\cdot}2H_2O$) and zinc chloride ($ZnCl_2{\cdot}2H_2O$) were used as precursors of Cu and Zn sources, respectively. Cu-Zn oxide were prepared with various molar ratio of Cu:Zn as followed; 3:7, 5:5 and 7:3. First, mixed precursors were dissolved in 100 ml deionized water by magnetic stirring. NaOH solution (1.0 M) was slowly dropped under vigorous stirring until pH reached to 12 and kept at room temperature for 2 h. The precipitated products were filtered and washed several times by water until pH reached to 7 and washed twice by absolute ethanol, then dried in an oven at 80 °C for 24 h. After that, the as-prepared precipitations were calcined at 600 °C for 2 h. Finally, after-calcined powders of Cu-Zn oxide compounds were obtained.

Morphologies and crystallite structure of the samples were investigated transmission electron microscopy (TEM, operated at 200 kV) and scanning electron microscope (SEM) and X-Ray Diffraction (XRD) technique, respectively. Chemical bonding information was investigated by Fourier transform infrared spectroscopy in range of 400-4000 cm^{-1}.

Results and Discussion

Figure 1 shows the XRD patterns of the pure CuO, ZnO and Cu-Zn 0xide compounds with various molar ratio of copper-zinc (3:7, 5:5, 7:3). XRD pattern of all samples were nicely indexed to the characteristic peaks of CuO and ZnO without unknown phase. The asterisk (*) marked in Figure 1 is attributed to CuO phase. The peaks in Figure 1(a) are indexed to the monoclinic phase of copper oxide. The characteristic peaks located at 2θ= 35.47°, 38.97° and 48. 74° are assigned to (002), (200) and $(\bar{2}02)$ plane of CuO phase [13]. The presence of hexagonal wurtzite of zinc oxide phases are shown in Figure 1(b)[5]. For Cu-Zn oxide compounds in figure(c)–(e), their XRD peaks exhibit the mixed phase of copper oxide and zinc oxide for all samples. The intensity of peaks indicated the crystallinity of particles. are varied with variation in Cu:Zn ratio owing to effect of different molar ratio of copper and zinc oxide from precursor. The peaks intensity of CuO is sharp and intense with increasing of Cu content but conversely decreasing peak intensity of ZnO.

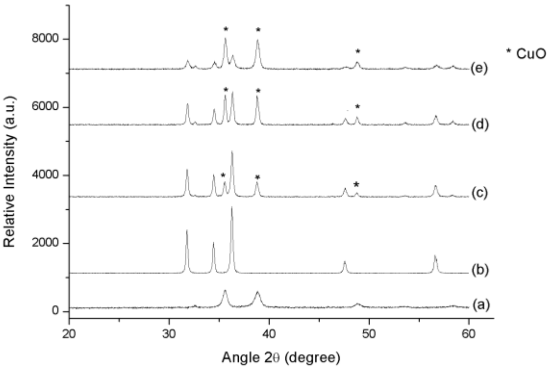

Figure 1. X-Ray diffraction patterns of (a) pure CuO, (b) pure ZnO, Cu-Zn oxide compounds with Cu:Zn ratio of (c) 3:7, (d) 5:5 and (e) 7:3.

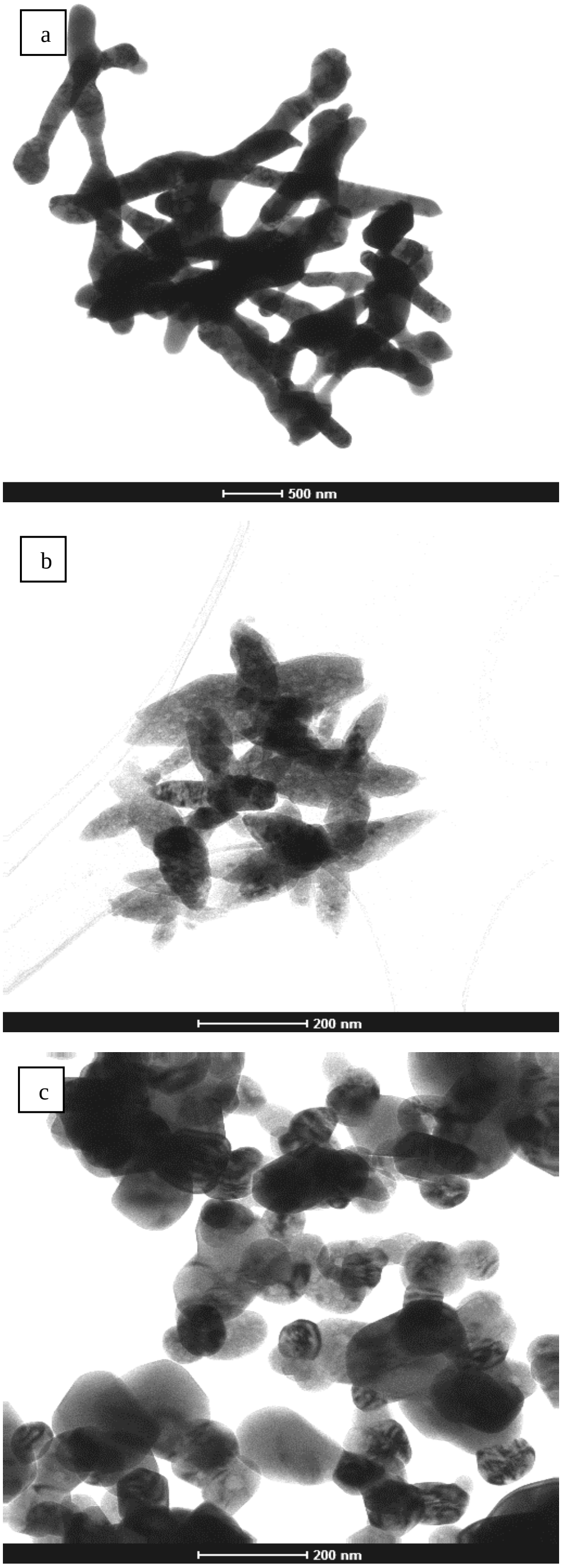

Figure 2. TEM images of (a) pure CuO, (b) pure ZnO, (c) Cu-Zn oxide compounds with Cu:Zn ratio of 5:5.

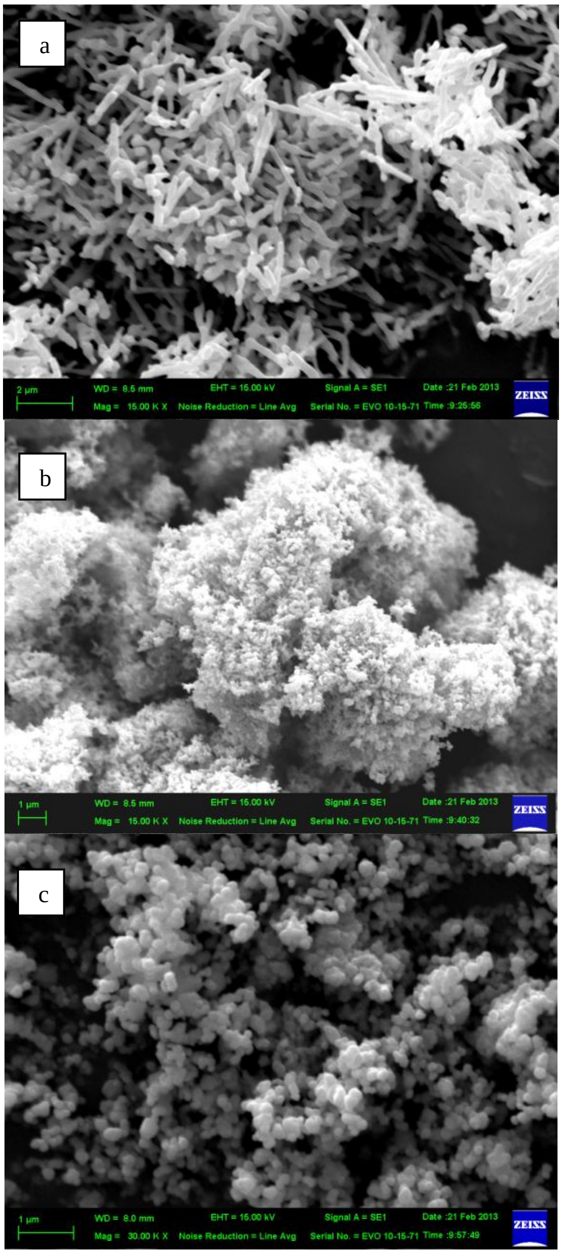

Figure 3. SEM of (a) pure CuO, (b) pure ZnO, (c) Cu-Zn oxide compounds with Cu:Zn ratio of 5:5.

Figure 2(a) and (b) represent typical TEM images of both pure CuO and ZnO, respectively. It is revealed that structure of as-synthesized CuO and ZnO are in nanorod-like and flower-like or spear-like structure with diameter less than 100 nm. As observed in Figure 2(C), unlike pure compound, the Cu-Zn oxide compound with Cu:Zn molar ratio of 5:5 shows the formation of quasi-spherical nanostructure whose size is less than 200 nm. The variation of particle size in the Cu-Zn oxide compound noticed in the TEM image may originate from thermal-induced agglomeration of CuO and ZnO particles after calcination.

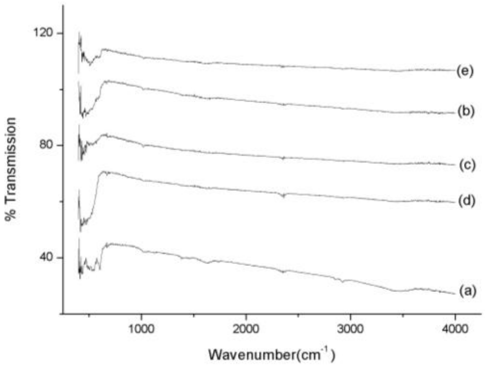

Figure 4. FTIR spectra (a) pure CuO, (b) pure ZnO, Cu-Zn oxide compounds with Cu:Zn ratio of (c) 3:7, (d) 5:5 and (e) 7:3.

SEM images of pure CuO, pure ZnO and Cu-Zn oxide compounds with Cu:Zn ratio at 5:5 are shown in Figure 3. Fig. 3 (a) shows the morphology of uniform CuO blunted-rod structure whose length is approximately 2 μm with high length to diameter aspect ratio. In the case of pure ZnO (Fig. 3(b)), it is seen that the cluster of ZnO comprises ZnO fluffy nanospear-like particles with uniform size distribution. Surprisingly, as seen in Fig. 3(c), the shape and morphology of as-synthesized Cu-Zn oxide compounds change significantly to be small cluster of uniform quasi-spherical nanoparticles with greater size than pure ZnO. It is acknowledged from TEM and SEM results that the atomic ratio of Cu/Zn has strong influence on the formation, morphology and shape of this oxide compound. Further study and investigation on this matter is underway so that the better understanding of the involved mechanisms can be clarified.

The chemical bonding of these compounds was evaluated by FTIR spectroscopy recorded in range of 4000-400 cm^{-1}.The FTIR spectra of pure CuO, ZnO and Cu-Zn oxide compounds are shown in Figure 2. The spectra of all samples exhibit the same features without strange extra band, indicating the good formation of metal oxide compound. Furthermore, as observed in Fig. 4(a), center of prominent absorption bands can be observed in the vicinity of 600 cm^{-1} which are related to the vibration of Cu-O bond. The absorption band at 470 cm^{-1} as noticed in Fig. 4(b) is attributed to typical Zn-O stretching mode. Meanwhile, the FTIR spectra of all Cu-Zn oxide compounds show the large absorption bands in the range of 400-600 cm^{-1} corresponding to various metal bonding. In Fig. 4(c) center of board peak at 440 cm^{-1} is assigned to Zn-O bond due to high molar ratio of Zn:Cu. As the Cu:Zn molar ratio increases, additional peak appeared at 620 cm^{-1} that is ascribed to Cu-O bending vibrations significantly increases as seen in Fig. 3(d-e). Moreover, no existence of OH group of H_2O is noticeable, indicating the complete dehydration at high temperature. Thus, FTIR result suggests that the good formation of this Cu-Zn oxide compound can be obtained by this precipitation process and post thermal treatment at moderate temperature [14-15].

Conclusions

A series of Cu-Zn oxide compounds with various molar ratios of copper and zinc have been successfully prepared via co-precipitation process. Diffraction peaks of the compounds samples are distinct resulting to well-crystalline forming between CuO and ZnO in the compound. SEM and TEM results revealed that spherical structure of Cu-Zn oxide compounds is obtained that different from the morphology of rod-like CuO and flower-like ZnO due to the agglomeration during the process and optimized annealing temperature. Chemical bonding results additionally indicate the existence of mixture phases of ZnO and CuO.

Acknowledgments

This work has been financially supported by the National Nanotechnology Center (NANOTEC), NSTDA, Ministry of Science and Technology Thailand, through its program of Center of Excellence Network. This work has been also partially supported by Nation Research Council of Thailand (NRCT). Authors would like to express deep thank to Rajamangala University of Technology Thanyaburi (RMUTT) for XRD measurement**.**

References

1. J. Cao, Y. Wang, T. Ma, Y. Liu and Z.Yuan, "Synthesis of porous hematite nanorods loaded with CuO nanocrystals as catalysts for CO oxidation" Journal of Natural Gas Chemistry, **20** (2011) 669-676.
2. M. S. Hassan , T. Amna , O. Yang , M. H. El-Newehy , S. S. Al-Deyab and M.S. Khil, "Smart copper oxide nanocrystals: Synthesis, characterization, electrochemical and potent antibacterial activity" Colloids and Surfaces B: Biointerfaces, **97** (2012) 201– 206.
3. J. Kaneshiro, N. Gaillard, R. Rocheleau and E. Miller, "Advances in copper-chalcopyrite thin films for solar energy conversion" Solar Energy Materials & Solar Cells, **94** (2009) 12-16.
4. D. H. Yoon, J. H. Yu and G. M. ChoiR, "CO gas sensing properties of ZnO–CuO composite" Sensors and Actuators B, **46** (1998) 15–23.
5. S.Singhal, J.Kaur, T.Namgyal and R.Sharma, "Cu-doped ZnO nanoparticles: Synthesis, structural and electrical properties" Physica B, **407** (2012) 1223–1226.
6. C.M. Changa, M.H. Hona and I.C. Leu, "Preparation of ZnO nanorod arrays with tailored defect-related characterisitcs and their effect on the ethanol gas sensing performance" Sensors and Actuators B ,**151** (2010) 15–20.
7. J. Li, G. Chenn and Ch.Yuan, "Microstructure and electrical properties of rare-earth doped ZnO-based" Ceramics International, **39** (2013) 2231–2237.
8. L. Cheng, L.Y. Zheng, L. Meng, G.R. Li ,Y. Gu, F.P.Zhang , R.Q. Chu and Zh.J. Xu, "Electrical properties of Al2O3-doped ZnO varistors prepared by sol–gel process for device miniaturization" Ceramics International ,**38S** (2012) S457–S461.
9. C.C. Vidyasagar, Y. A. Naik, T.G. Venkatesh and R. Viswanatha, "Solid-state synthesis and effect of temperature on optical properties of Cu–ZnO, Cu–CdO and CuO nanoparticles" Powder Technology, **214** (2011) 337–343.
10. P. Sathishkumara, R. Sweenaa, J.J. Wub and S. Anandan, "Synthesis of CuO-ZnO nano-photocatalyst for visible light assisted degradation of a textile dye in aqueous solution" Chemical Engineering Journal, **171** (2011) 136–140.
11. A. Nalbant, Ö. Ertek and I. Okur, "Producing CuO and ZnO composite thin films using the spin coating method on microscope glasses" Materials Science and Engineering B, **178** (2013) 368– 374.
12. L. He, H. Cheng, G. Liang, Y. Yu and F. Zhao, "Effect of structure of CuO/ZnO/Al2O3 composites on catalytic performance for hydrogenation of fatty acid ester" Applied Catalysis A: General, **452** (2013) 88– 93.
13. R. Wua, Z. Maa, Z. Gua and Y. Yanga, "Preparation and characterization of CuO nanoparticles with different morphology through a simple quick-precipitation method in DMAC–water mixed solvent" Journal of Alloys and Compounds **504** (2010) 45–49.
14. M. Y. Ghotbi , N. Bagheri and S.K. Sadrnezhaad, "Nanocrystalline copper doped zinc oxide produced from copper doped zinc hydroxide nitrate as a layered precursor" Advanced Powder Technology, **23**(2012) 279–283.
15. D.P. Dubal, D.S. Dhawale, R.R. Salunkhe, V.S. Jamdade and C.D. Lokhande, "Fabrication of copper oxide multilayer nanosheets for supercapacitor application" Journal of Alloys and Compounds, **492** (2010), 26–30.

Dielectric Relaxation and Microstructures of PtO_2-doped $CaCu_3Ti_4O_{12}$ Electroceramics

W. Makcharoen

College of Data Storage Innovation, King Mongkut's Institute of Technology Ladkrabang, Bangkok 10520, Thailand
Corresponding author. E-mail: warmak77@hotmail.com

Abstract

$CaCu_3Ti_4O_{12}$ (CCTO) is a ceramic compound with a high dielectric constant, but it has a high loss tangent at room temperature. In this work, the Influences of PtO_2 doping on the dielectric properties of $CaCu_3Ti_4O_{12}$ (CCTO) ceramics were investigate. The ceramics CCTO and PtO_2 doping CCTO were prepared by a solid-state reaction method. The samples were studied by X- ray diffraction (XRD), scanning electron microscopy (SEM) and dielectric properties have been measured as a function of temperature and frequency range 100 Hz– 500 kHz. The XRD shows the CCTO structure does not changes after doping with platinum. The results show that PtO_2 doped can reduce the mean grain sizes of CCTO, but the dielectric constant still remained a height. The samples of 2.0 mol% Pt-doped have exhibited high dielectric constant of about 22,000 and the loss tangent about 0.7 at room temperature and frequency at 10 kHz. The reduced of the loss tangent could be interpreted with the internal barrier layer capacitor model (IBLC)

***Keywords*:** CCTO, Dielectric properties, Perovskites, IBLC

Introduction

The high dielectric material $CaCu_3Ti_4O_{12}$ (CCTO), discovered by Subramanian et al. [1], exhibits high dielectric constant over 10000 at room temperature $CaCu_3Ti_4O$ (CCTO) has attracted a significant amount of attention base on the dielectric properties [1-3]. The dielectric constant is almost temperature independent from 200 K to 400 K, with low frequency dielectric constant of CCTO can be as high as 95000 in single crystals, and 12000 in sintered pellets [4, 5]. For the ceramic [4] and the thin-film [6] samples at room temperature, the typical value of tan δ is about 0.2 at 10 kHz. The dielectric materials are widely used in electrical components such as capacitors as well as switching and sensing devices [3]. The CCTO has a complex cubic perovskite like the structure with a lattice parameter, a$\sim$7.393 Å [7]. The explanation of high dielectric constant of CCTO was proposed in the terms of local dipole moments associated with off-center displacement of Ti ions [1]. Change in dielectric constant of CCTO has been wildly related to its microstructure [8]. It is also reported that electrical properties of CCTO depends on many factors such as processing conditions, doping, and chemical stoichiometry. The partial substitution of divalent Ca^{2+} by the trivalent La^{3+} was carried out, in order to increase the conductivity of the grains [9].The loss angle can be reduced by adding of some elements such as platinum oxide (PtO_2) [10]. L. Avalle et al. [11] reported that dielectric constant in TiO_2 thin film was improved by doping PtO_2. In this work, study on CCTO samples with the substitutions of Ti ions by Pt ions. The CCTO ceramics were fabricated via a solid-state reaction. The properties of the obtained ceramics were investigated with the aim of improving its dielectric properties. The characterization of the samples was carried out using x-ray diffraction (XRD) and scanning electron microscopy (SEM). Physical properties such as density, dielectric constant and loss tangent were also investigated.

Materials and Methods

The undoped $CaCu_3Ti_4O_{12}$ (CCTO) powder was prepared by the mixed-oxide route. High purity (> 99.9%) $CaCO_3$ (Riedel-de Haen), CuO (Aldrich) and TiO_2 (Riedel-de Haen) powders were weighed in an appropriate ratio, fully mixed by vibratory milling machine for 10 hour using yttria-stabilized zirconia balls in the ethanol media. After being dried, the powders were calcined at the 900^{o}C for 2 hour to form the CCTO powder. For the doping study, PtO_2 powders at various concentrations were mixed to CCTO at the calcinations stage (1.0 and 2.0 mol %). The calcined powder was granulated using polyvinyl alcohol (PVA) 3% binder and formed under a uniaxial pressure of 1,500 kg/cm^2 into discs, typically 10 mm in the diameter and 1.5 mm in the thickness. The discs were sintered in the air at 1,000^{o}C in a step of

5^{o}C/min (with soaking time of 4 hour). During sintered oxygen gas was fed into the furnace at the rate of 100 c.c./min. The discs were polished to produce the flat uniform surfaces. The characterization of the samples was carried out using x-ray diffraction (XRD) (using Bruker D8 Discover) at room temperature using CuK$_{\alpha}$ radiation as the x-ray source and scanning electron microscopy (SEM) (using JEOL JSM-5910LV). The silver paste was used as the electrical contact. The painted samples were dried at 700 ^{o}C for 20 minutes. The dielectric constants and loss tangents against the temperature were measured at the frequency of 100 Hz - 500 kHz (using Agilent 4284A LCR meter). In the other physical properties such as density, shrinkage were intensively studied.

Results and Discussion

Fig. 1 illustrates the XRD patterns for the undoped CCTO and PtO$_2$ doped CCTO ceramics. All of the diffraction peaks were corresponds to the known peaks of the standard CCTO, indexed from the data in the Inorganic Crystal Structure Database (ICSD) file No.032002. All of the samples exhibited a phase-pure perovskite within the detection limit of the XRD equipment. The crystal symmetry of the samples at room temperature was determined to be the cubic. In addition, the density and the shrinkage slightly increased with the concentration (Fig.2), suggesting that the doping oxide slightly promoted the densification.

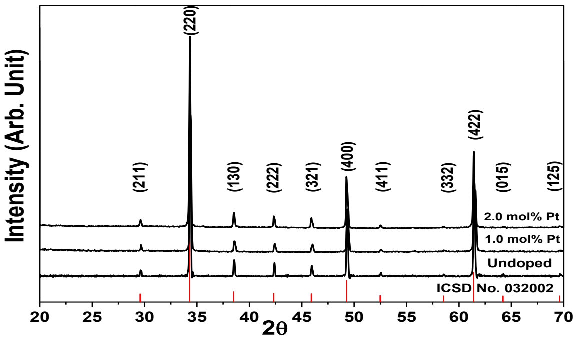

Figure 1. XRD patterns of pure and doped CCTO: undoped CCTO, 1.0 mol% Pt doped CCTO and 2.0 mol% Pt doped CCTO.

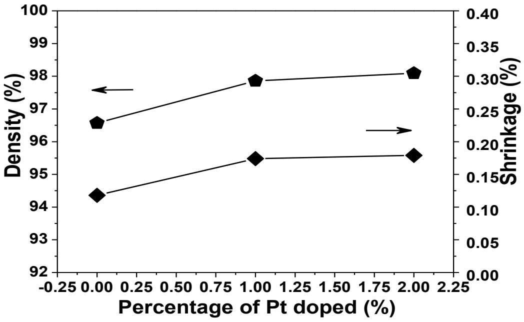

Figure 2. The density and the shrinkage of CCTO as a function of doping the concentration.

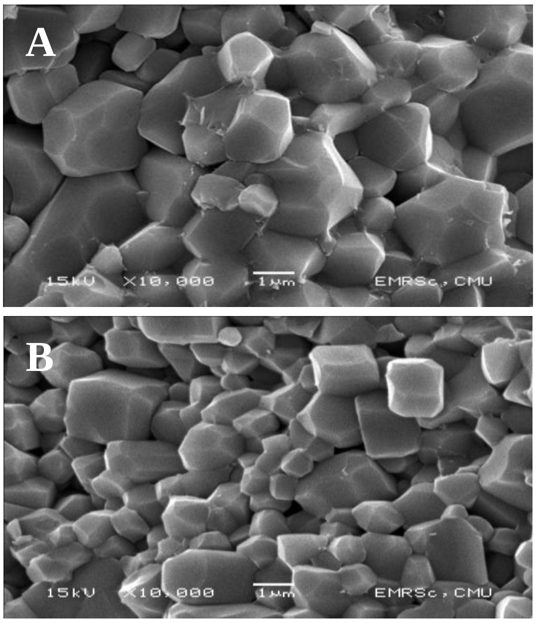

Figure 3. Fracture surfaces of selected the samples: (A) the crack of undoped CCTO ceramics and (B) the crack of 2.0 mol% Pt doped CCTO ceramics.

Fig. 3 illustrates SEM images of the fracture surfaces of an undoped and a doped sample. The partial intergranular fracture was observed for the unmodified sample. After doping, the doped samples exhibited a non-uniform in grain size. The morphology of PtO$_2$ doped CCTO sample consists of some huge grains (3–5 μm), surrounded by small ones (~0.5 μm). The fracture mode changed to mainly intra-granular for the doped samples, suggesting a higher strengthening of the grain boundaries. These results indicate a rearrangement of the gain boundary structure take place due to the effect of the addition. A slightly decrease in the grain size was observed after doping: grain size slightly decreased from 5 μm for unmodified sample to 1 μm for the 2.0 mol% sample. It is believe that some amount of Pt ions may go into the CCTO lattices. However, the existence of the small grains, suggested that partial Pt ions which could not go into the lattices and it produced the grain growth inhibition.

Fig. 4 illustrates the temperature dependences on the dielectric constant and the loss tangent at a various frequencies of the undoped CCTO and 2.0 mol% Pt doped CCTO ceramic samples. For the unmodified CCTO, the dielectric constant exhibited a stronger dielectric-frequency dependent while the doped samples showed a weaker dielectric-frequency dependent. It should be noted that at the high frequency, all of the samples showed a dielectric independent of the temperature. The dielectric constant at room temperature and at 10 kHz decreased from 35,000 for the unmodified sample to 22,000 for the 2.0 mol% Pt doped sample. However, the doping improved in the loss tangent performance (Fig.4 (D)). The loss tangent at room temperature and at 10 kHz decreased from 0.15 for the unmodified sample to 0.07 for the 2.0 mol% Pt doped sample while at 100 kHz, it decreased from 0.1 for the unmodified sample to 0.025 for the 2.0 mol% Pt doped sample. However, the lowest loss tangent was 0.01 at 500 kHz and at ~55 ^{o}C.

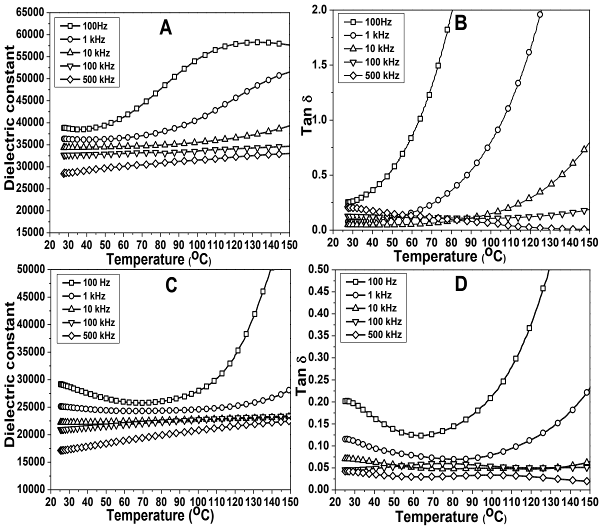

Figure 4. The dielectric constant and the loss tangent as a function temperature of the samples: (A) the dielectric constant of undoped CCTO samples, (B) the dielectric loss of an undoped CCTO samples, (C) the dielectric constant of 2.0 mol% Pt doped CCTO samples and (D) the dielectric loss of 2.0 mol% Pt doped CCTO samples.

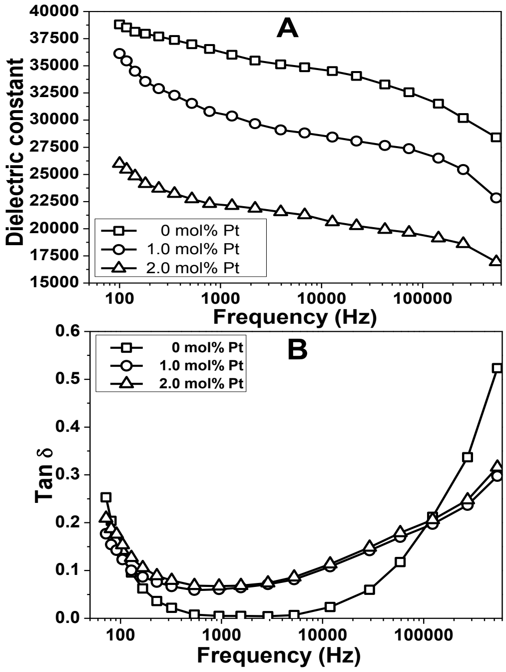

Figure 5. The dielectric properties of the samples as a function of frequency: (A) dielectric constant and (B) The loss tangent.

Fig.5 shows the dielectric constant and the loss tangent as a function of a frequency at room temperature. The dielectric constant decreased with a frequency. A similar result was observed for the work done by Kwon *et al*.[12]. With the increasing frequency in doping produced a lower in loss tangent. However, at a lower frequency and a higher frequency, a higher loss tangent was observed. From the internal barrier layer capacitor model (IBLC), the equivalent circuit of CCTO system can be consisted of two parallel RC elements connected in the series. The two parallel RC circuits represent to the semiconducting bulk grain (which consists of grain resistor (R_g) and grain capacitor (C_g)) and insulating grain boundary (which consists of a grain boundary resistor (R_{gb})) and grain boundary capacitor (C_{gb})). In case $R_{gb} >> R_g$ and $C_{gb} \sim C >> C_g$ and $\omega R_b C_b << 1$, the loss tangent can be expressed as [13,14]:

$$\tan\delta = \frac{1}{\omega R_{gb} C} + \omega R_g C \qquad (1)$$

The first term is dominated at the low frequency, therefore the loss tangent decreased with the increasing frequency. However, at high frequency, the second term has a strong effect. Thus, the loss tangent increased with the frequency. This feature also consists with our result (Fig. 5).

The characteristic of the grain (bulk grain and grain boundary) may be an important factor that effects on the dielectric properties of the samples. It is believed that the PtO_2 addition resulted in a reduction in total resistance of the grain boundary [11]. These may be cased a reduction in conductivity as a result of the lowered loss tangent. Further, the decrease in grain size may be a reason for the reduction of in dielectric constant for the present work. However, the microstructure of a doped samples showed some small grains or a doped samples had a large grain size distribution. Therefore, the grain size distribution may be another factor to control the dielectric constant. From Fig.3, it should be noted that there were some small grains placed between the large gains. Therefore, believe that these small grains may have more effective effects than the large grains.

Conclusions

The pure and PtO_2 doped CCTO ceramics were prepared by a conventional solid-state reaction technique. Although the dopants produced the reduction in the dielectric constant, the dielectric constant after doping still high especially for Pt doping. However, the better loss tangent performance was observed after doping. The loss tangent – frequency characteristic at room temperature was agreed with the IBLC model. The significant change in the microstructure of the Pt doped samples shows a strong temperate and a frequency independent that are a proposed from the change in the microstructure can be related to the change in the dielectric properties.

Acknowledgments

This work was supported by College of Data Storage Innovation, King Mongkut's Institute of Technology Ladkrabang.

References

1. M. A. Subramanian, D. Li, N. Duan, B. A. Reisner, and A. W. Sleight, “High dielectric constant in $ACu_3Ti_4O_{12}$ and $ACu_3Ti_3FeO_{12}$ phases”, J. Solid State Chem. 151 (2000) 323-5.
2. A. P. Ramirez, M. A. Subramanian, M. Gardel, G. Blumberg, D. Li, T. Vogt, and S. M. Shapiro, “Giant dielectric constant response in a copper-titanate”, Solid State Commun. 115 (2000) 217-220.
3. Hammoud AN, Myers IT. “Proceedings of the Annual Report Conference on electrical insulation and dielectric phenomena”. 1989. p. 459.
4. D. C. Sinclair, T. B. Adams, F. D. Morrison, and A. R. West, “$CaCu_3Ti_4O_{12}$: One-step internal barrier layer capacitor”, Appl. Phys. Lett. 80 (2002) 2153.
5. Y. Lin, Y. B. Chen, T. Garret, S. W. Liu, C. L. Chen, L. Chen, R. P. Bontchev, A. Jacobson, J. C. Jiang, E. I. Meletis, J. Horowitz, and H.-D. Wu, “Epitaxial growth of dielectric $CaCu_3Ti_4O_{12}$ thin films on (001) $LaAlO_3$ by pulsed laser deposition”, *Appl. Phys. Lett.* **81** (2002) 631.
6. W. Si, E. M. Cruz, P. D. Johnson, P. W. Barnes, P. Woodward, and A. P. Ramirez, “Epitaxial thin films of the giant-dielectric-constant material $CaCu_3Ti_4O_{12}$ grown by pulsed-laser deposition”, *Appl. Phys. Lett.* **81** (2002) 2056.
7. B. Bochu, M.N. Deschizeaux, J.C. Joubert, “Synthèse et caractérisation d'une série de titanates pérowskites isotypes de $[CaCu_3](Mn_4)O_{12}$”, J. Solid State Chem. **29**, (1979) 291-298.
8. Y. Lin, Y.B. Chen, T. Garret, S.W. Liu, C.L. Chen, L. Chen, R.P. Bontchev, A. Jacobson, J.C. Jiang, E.I. Meletis, J. Horwitz, H.D. Wu, “Epitaxial growth of dielectric $CaCu_3Ti_4O_{12}$ thin films on (001) $LaAlO_3$ by pulsed laser deposition”, Appl. Phys. Lett. 81 (2002) 631-633.
9. B. A. Strukov and A. P. Levanyuk, ‘‘Ferroelectric Phenomena in Crystals: Physical Foundations”, Chapter 1, Springer (1998).
10. R.C. Buchanan 1986, “Ceramics materials for electronics, Processing, Properties and Applications” (New York:Marcel Dekker) p.110.
11. L. Avalle, E. Santos, E. Leiva, V.A. Macagno, “Characterization of TiO2 films modified by platinum doping”, Thin Solid Films, Volume 219, Issues 1–2 (1992) 7-17.
12. S. Kwon, C.-C. Huang, E. A. Patterson, D. P. Cann, “The effect of Cr_2O_3, Nb_2O_5 and ZrO_2 doping on the dielectric properties of $CaCu_3Ti_4O_{12}$”, materials letters, 62 (2008)633-636.
13. D.C. Sinclair, T.B. Adams, F.D. Morrison, A.R. West, “$CaCu_3Ti_4O_{12}$: One-step internal barrier layer capacitor”, Appl. Phys. Lett.80, (2002) 2153.
14. L. Feng, X. Tang, Y. Yan1 X. Chen, Z. Jiao, and G. Cao, “Decrease of dielectric loss in $CaCu_3Ti_4O_{12}$ ceramics by La doping”, Phys. Stat. Sol. (a) 203, 4, (2006) R22– R24.

Dithieno-pyrroles Derivative Organic Dye forDye-sensitized SolarCells

P. Thanakit[1,2], P. Chittratan[1,2], W. Jarernboon[1,2], S. Pratontep[1,2],
and D. Sae-Tang Phromyothin[1,2*]

[1]*Collage of Nanotechnology, King Mongkut's Institute of Technology Ladkrabang,*
Chalongkrung Rd., Ladkrabang, Bangkok 10520, Thailand

[2]*Thailand Center of Excellence in Physics, CHE, 328 Si Ayutthaya Rd., Bangkok 10400, Thailand*

[*]*Corresponding author. E-mail: ksdarine@kmitl.ac.th*

Abstract

A novel organic compound based on dithieno[3,2-b;2’,3’-d]pyrrole (DTP) was synthesized by a palladium(0)-catalyzed Buchwald-Hartwig reaction and used as donor materials for dye sensitized solar cell. The dye molecule consists of cyanoacrylic acid and benzyl group as acceptor and linker, respectively. The compound was characterized with nuclear magnetic resonance (NMR) and UV-Visible spectroscopy. The results of the synthesis organic dye for dye sensitized solar cell were obtained V_{oc} as 0.58 V, J_{sc} as 3.47 mA/cm^2, Fill Factor as 0.54 and the conversion efficiency 1.10%. The optimized structural electronic properties of dyes have been investigated by using the density functional theory (TD-DFT/cam-B3LYP/6-31G(d)) method of calculation.

Keywords**:** Organic dyes, dye-sensitized solar cells, dithieno-pyrroles (DTP)

Introduction

Dye-sensitized solar cells (DSSCs) have attracted significant attention as an alternative to the conversional solar cell due to their ability design of structures, low cost synthesis and process compliance with environmental issues. Since1991 Gräzel and co-workers have developed high efficient DSSC based on ruthenium complexes inorganic dyes[1]. Although ruthenium complexes have higher molar extinction coefficients, efficiency and better stability but ruthenium is metal and hard to purify from the synthetic mixture and high cost of dye limit their development. Thus, the ruthenium complexes dyes should be replaced by metal-free organic dyes. Normally, organic dyes systems consist of an electron donor (D), π-spacer (π) and electron acceptor (A). Most of organic dyes include carbazoledyes [7,11], fluorine dyes[9,11], triphenylamine dyes[2-6], coumarin dyes[12-14], indolin dyes[15] and porphyrin dyes[16-17], etc.

In this study, the novel organic dye containing DTP was designed and synthesized as an electron donor and cyanoacrylic acid as an electron acceptor bridged by aromatic system.The compound was characterized with nuclear magnetic resonance (NMR), fourier transform infrared spectroscopy (FTIR) and UV-Visible spectroscopy.The photovoltaic properties were measured to electron acceptor on the performance of the DSSCs. The optimized structures electronic properties of dyes have been investigated by using the density functional theory (TD-DFT/cam-B3LYP/6-31G(d)) method of calculation.

Materials and Methods

Experimental Detail

Material

Synthesis of N-(methyl)thieno[3,2-b:2’,3’-d]pyyrole(DTP)[18-20]. 3,3’-Dibromo-2,2’-bithiophene (6.18 mmol, 1.0017 g) and 2-methylbuthyl amine(6.18 mmol, 0.2881 g) were dissolved in toluene under N_2. BINAP (0.620 mmol, 0.1955 g), NaOt-Bu (14.8 mmol, 0.7215 g) and Pd_2dba_3 (0.155 mmol, 0.0954 g) were added.After stirring for 7 hr. at 110°C, the reaction mixture was cooled and extracted with water and ethyl acetate, respectively.

Synthesis of 2,6-diBromo-N-(methyl)thieno[3,2-b:2’,3’-d]pyyrole(DTP-2Br)[18-20]**.**DTP (1 mmol, 0.1 g) was dissolved in glacial acetic acid and $CHCl_3$ under N_2.N-bromosuccinimide (2.2 mmol, 0.1986 g) was dissolved and stirred for 4hr at 0 °C to RT. The reaction mixture was cooled and extracted with water and ethyl acetate, respectively. The organic layer was dried over anhydrous sodium sulphate and removed solvent under reduced pressure. The residue was purified by column chromatography using hexane: CH_2Cl_2.

Synthesis of N-(methyl)thieno[3,2-b:2’,3’-d]pyyrole-2,6-aldehyde (DTP-P)[21]. DTP-Br (5 mmol, 0.1014 g) was dissolved in toluene under N_2. 4-formylphenylboronic acid (10 mmol, 0.0884 g), TBAB (0.6 g) and K_2CO_3 (30 ml) were added. The mixture was stirred for 0.5 hr at RT under N_2 then tetrakis(triphenylphosphine)palladium (0.1 g) and heat to 90°Cfor 24 hr. The organic layer was dried over anhydrous sodium sulphate and removed solvent under reduced pressure. The residue was purified by column chromatography using CH_2Cl_2: ethyl acetate.

Synthesis of N-(methyl)thieno[3,2-b:2',3'-d]pyyrole-2,6-cyanoacrylic (DTP-C)[21]. DTP-P (0.48 mmol, 0.0417 g) and cyanoacetic acid (0.94 mmol, 0.0447 g) was dissolved in acetonitrile under N_2 and then piperidine (20 drop) was added. The mixture was refluxed and stirred for 20 hr under $N_2$and then removed solvent under reduced pressure. The residue was purified by column chromatography using CH_2Cl_2: ethyl acetate.

Methods

Devices fabrication

The working electrode preparation

The TiO_2 films (using PST-18NR; particle size 18 nm as transparent layer and PST-400C as the scattering layer) were coated on a conductive fluorine-doped tin oxide glass (FTO, 15 Ω/sq) in area 0.25 cm^2 (0.5x0.5 cm) by screen printing technique and then annealed at 325 ^{o}C for 10 min, 375^{o}Cfor 10 min, 450^{o}C for 15 min and 500^{o}C for 30 min. After cooling down, the electrodes were immersed in the 0.5 mM of DTP-C dye solution using acetonitrite as the solvent for 24 hr.

The counter electrode preparation

The Pt films were prepared by screen printing technique using the mixture of $HPtCl_4.5H_2O$ with ethyl cellulose and terpineol as the Pt paste and then annealed at 325 ^{o}c for 10 min, 375^{o}C for 10 min, 450^{o}C for 15 min and 500^{o}C for 30 min and then cooling down.

DSSC assembly

The working electrode and counter electrode were assembled in the sandwich structure. The both electrodes were separated by a paraffin thin sheet for preventing the short circuit and leaking of electrolyte. The electrolyte consisting of 0.05 M I_2, 0.5 M LiI, 0.5 M TBP, 0.5 M EMII in 3-methoxypropiolnitrile was filled into the cells by capillary force.

DSSC measurement

The J-V characteristic curves was measured using Kiethley 2400 electrometer under AM 1.5 solar simulator (16s-002,SolarLight Co.Ltd., USA). The incident light intensity was 100 mW cm^{-2} calibrated with a standard Si solar cell.

Computational Detail

The structures of donor-acceptor conjugated compound comprise the electron donor molecule and acceptor molecule were studied the photophysical properties using density functional theory (DFT) and time dependent DFT with B3LYP/6-31G(d,p) method. All calculations were performed using Gaussain09 program.

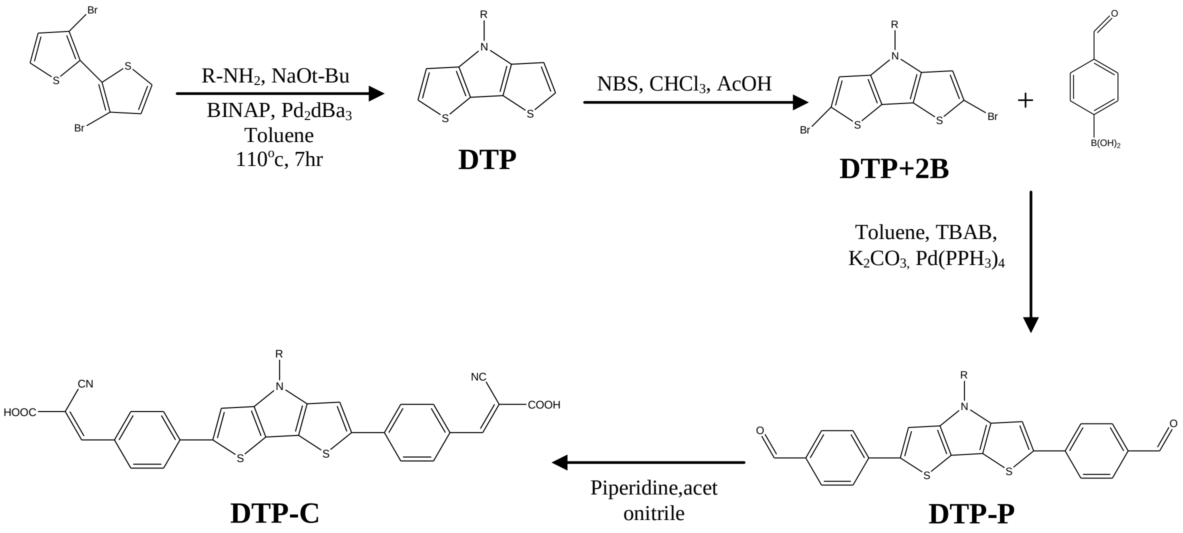

Scheme 1 The synthesis of DTP-C

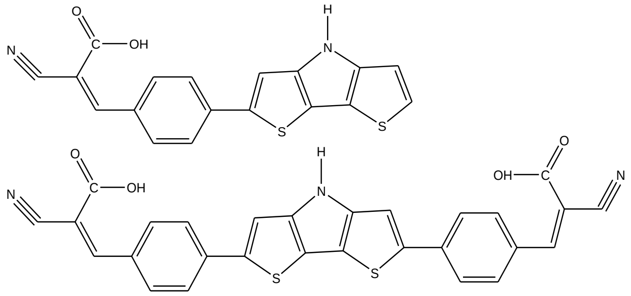

Figure 1. The studied structure of dye-sensitized.

Results and Discussion

Synthesis

As shown in **scheme 1**, the organic dye DTP-C which contained aromatic linker with DTP as an electron donor and cyanoarylic acid as an electron acceptor moiety was performed. DTP moiety were synthesized by a palladium(0)-catalyzed Buchwald-Hartwig reaction after that there was coupled with 4-formylphenylboronic acid via Suzuki reaction with tetrakis(triphenylphosphine) palladium(0) (Pd(PPh$_3$)$_4$) as the catalyst, followed by conversion of the aldehyde moiety to cyanoacetic acid through Knoevenagel reaction in the present piperidine. DTP-C was characterized the structure of dye in each step of reaction by nuclear magnetic resonance (NMR) and the functional group of dye by fourier transform infrared spectroscopy (FTIR).

^{1}H NMR of DTP-C (CDCl$_3$):δ 10.00(s, 1H, -aromatic-C=CHO), 7.90 (s, 1H, - aromatic-CH=C), 7.76 (m, 4H, aromatic-CHO), 7.39 (d, 2H, aromatic-dithieno), 7.26 (s, 1H, dithieno)

Fig 2 FTIR spectra :at 1,614.23 cm^{-1}as C=C stretch of aromatic, 1,723.24 cm^{-1} as C=O stretch of carboxylic acid, 2,257.67 cm^{-1} as C=N, 2,862.67 and 2,932.40 cm^{-1} as CH stretch and 3,414.84 cm^{-1} as OH stretch.

Optical property

Fig. 3 shows the UV-visible spectra of the DTP-C dye measured in DMF solution. The absorption spectrum of DTP-C in DMF solution displays at 260-380 nm. The absorption maximum at 320 nm corresponds to the π-π* electron transition.

Figure 2. FTIR of DTP-C

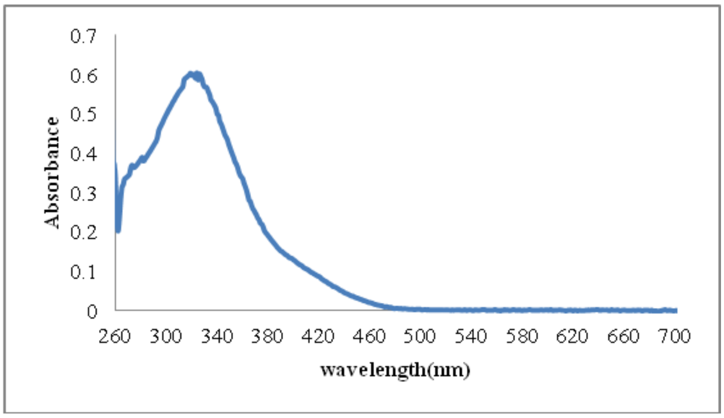

Figure 3. Absorption spectra of DSSCs based on DTP-C

Table 1 Photovoltaic performance of DSSCs based on DTP-C

Dyes	J_{sc} (mA/cm^2)	V_{oc} (V)	Fill Factor	Efficiency (%)
DTP-C	3.47 ± 0.08	0.58 ± 0.01	0.54± 0.02	1.10 ± 0.04

Photovoltaic performance of DSSCs based on the dye

Dye-sensitized solar cells were fabricated with the DTP-C and TiO_2. The cells had an effective area 0.25 cm^2 and the electrolytes were used composed of I_2, LiI in 3-mothixypionitrite solution. The device performance statistics under standard global AM 1.5 solar condition are presented in Table 1 with the photocurrent-voltage (*J*-*V*) curve of DSSC the devices using DTP-C as the photo sensitizer. The cells exhibited the short-circuit photocurrent density (J_{sc}), open-circuit voltage (V_{oc}) and fill factor (FF) of the devices are in the range of 3.47±0.08 mA cm^{-2}, 0.58±0.01 V and 0.54±0.02, corresponding to an efficiency of 1.10±0.04 %

Theoretical calculation

Density functional theory (DFT) calculations were performed by Gaussian09 program. The optimized structures electronic properties of DTP-C have been investigated by using the B3LYP method with 6-31G (d) basis set.Molecular-orbital calculations were shown in Fig3which the highest occupied molecular orbitals (HOMO) of DTP-C were delocalized by DTP as electron-donor and the lowest unoccupied molecular orbitals (LUMO) by cyanoacrylic acid as an electron-acceptor through aromatic ring.

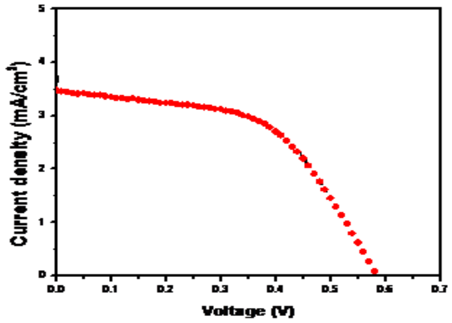

Figure 3. *J-V* curves of DSSCs based on DTP-C

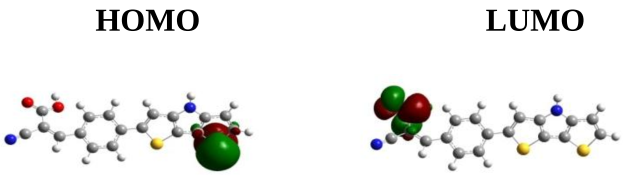

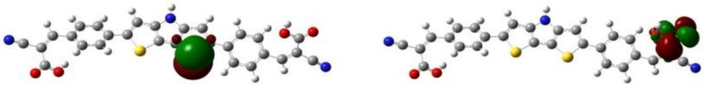

Figure 3. Frontier molecular orbital profiles of DTP-C at the B3LYP/6-31G(d) level.

The HOMO were delocalized over the π-spacer system to the LUMO which comparison of the number of cyanoacrylic acid (single or double) were found that di-cyanoacrylic acid electron will transfer to only one part of cyanoacrylic acid.

Conclusions

In summary, DTP as an electron donor in the application of solar cells was studied by computational methodology: density functional theory (DFT) and time-dependent(DFT) with B3LYP/6-31G(d,p) method and synthesis organic dye-sensitized. The dye based on DTP-C was characterized the structure in each step of reaction by nuclear magnetic resonance (NMR)and the functional group by fourier transfer infrared spectroscopy (FTIR). The optical property of DTP-C exhibited the excite state at 320 nm. The conversion efficiency reaches in the range of 1.10±0.04%.

Acknowledgments

The authors would like to thank the computational resources at the Laboratory for Computational & Applied Chemistry (LCAC), Kasetsart University, Thailand and the large scale simulation research laboratory of NECTEC, Thailand.

References

1. B. O`Regan, M. Gräzel: NatureVol.253 (1991), p.737-740
2. D. Kuang, P. comte, S.M. Zakeeruddin, D.P. Hagberg, K.M. Karlsson, L. Sun, M.K. Nazeeruddin, M.Gratzel:Solar energyVol. 85 (2011), p. 1189-1194
3. D.H. Lee, M.J. Lee, H.M. Song, B.J. Song, K.D. Seo, M. Pastore, C. Anselmi, S. Fantacci, F.D. Angelis, M.K. Nazeeruddin, M. Graetzel, H.K. Kim:Dyes and PigmentVol.91 (2011), p. 192-198
4. X. Cheng, S. Sun, M. Liang, Y. Shi, Z. Sun, S. Xue:Dyes and PigmentsVol.92 (2012), p. 1292-1299

5. L. Zhou, C. Jia, Z. Wan, Z. Li, J. Bai, L. Zhang, J. Zhang: Dyes and PigmentsVol.95 (2012), p. 743-750
6. J.K. Lee, S.M. Lee, S.B. Lee, K.H. Kim, S.E. Cho, S.I. Jang, S.H. Park, W.P. Hwang, M.H. Seo, M. R. Kim: Current Applied PhysicsVol. 11 (2011), p. s140-s146
7. M. Liang, Z.Y. Wang, L. Zhang, H.Y. Han, Z. Sun, S. Xue:Renewable EnergyVol.36 (2011), p. 2711-2716
8. X. Cheng, M. Liang, S. Sun, Y. Shi, Z. Ma, Z. Sun, S. Xue:TetrahedronVol. 68 (2012), p. 5375-5385
9. P. Singh, A Baheti, K.R. Thomas, C.P. Lee, K.C. Ho:Dyes and Pigments Vol.95(2012),p. 523-533
10. S. Kajiyama, Y. Uemura, H. Miura, K. Hara, N. Koumura: Dyes and Pigments Vol. 92(2012), p. 1250-1256
11. L.F. Lai, C.L. Ho, Y.C. Chen, W.J. Wu, F.R. Dai, C.H. Chui, S.P. Huang, K.P. Guo, J.T. Lin, H. Tian, S.H. Yang, W.Y. Wong:Dyes and PigmentsVol.96 (2013), p. 516-524
12. K.D. Seo, I.T. Choi, Y.G. Park, S. Kang, J.Y. Lee, H.K. Kim:Dyes and Pigments Vol.94(2012), p. 469-474
13. K.D. Seo, H.M. Song, M.I. Lee, M.K. NaZeeruddin, M. Graetzel, et al:Dye Pigments Vol.90 (2011), p. 304-310
14. K. Hara, Z.S. Wang, T. Sato, A. Furube, R. Katoh, H. Sugihara, et al: J. Phys Chem Vol. 109 (2005), p. 15476-15482
15. T. Horiuchi, H. Miura, S. Uchida:J Photochem Photobiol A Chem Vol.164 (2004), p. 29-34
16. H. Imahori, T. Umeyama, S. Ito: Acc Chem Res Vol. 42 (2009), p. 1809-1818
17. M.J. Lee, K.D. Seo, H.M. Song, H.S. Kang, H.K. Kim, et al:Tetrahedron Vol. 52 (2011), p. 3879-3882
18. K.R. Radke, K. Ogawa, S.C. Rasmussen:Organic LettersVol.7 (2005), p. 5253-5256
19. S.A. Odom, K. Lancaster, L. Beverina, K.M. Lefler, N.J. Thompson, V. Coropceanu, J.-L. Brédas, S.R. Marder, S. Barlow: Chemistry – A European JournalVol. 13 (2007), p. 9637-9646
20. G. Koeckelberghs, L.D. Cremer, W. Vanormelingen, W. Dehaen, T. Verbiest, A. Persoons, C. Samyn: TetrahedronVol. 61 (2005), p. 687-691
21. X.-q. Zhang, Z.-g. Chi, B.-j. Xu, H.-y. Li, W. Zhou, X.-f. Li, Y. Zhang, S.-w. Liu, J.-r. Xu: Journal of Fluorescence Vol.21 (2011), p.133-140

Effect of Annealing Temperature on Physical Properties of Sisal Fibers from Hupkapong, Phetchaburi Province

P. Kiewaram* and N. Pattanaboonmee

Department of Physics, Faculty of Science King Mongkut's University of Technology
Thonburi(KMUTT) 126 PhachaUthit Road, BangMod, ThungKhru , Bangkok 10140 Thailand
**Corresponding author. E-mail: pk_physics@hotmail.com*

Abstract

Sisal fibers extracted from the leaves of Agavasisalana plants (2-3 years old) from Hupkapong,Phetchaburi Province were tested at different temperatures for study of the variation of mass, modulus and the stability of chemicals. The variations of mass were analyzed by thermogravimetric analysis. Modulus and the stability of chemicals were analyzed by Modulus measurement. The thermogravimetric curve of sisal fiber shows a weight loss in the temperature range of 60-100 °C, which is due to the loss of adsorbed water in the fiber and a fast rate of fiber degradation in the range of 255-370 °C. Modulus and the stability of chemicals values of sisal fibers decreased with increase in temperature.

***Keywords*:**Sisal fibres/ Modulus /thermogravimetric analysis(TGA)

Introduction

Sisal fiber, one of the most widely used natural fibers, is very strong fibers [1]. Sisal fiber is hard fiber extracted from leaves of the sisal plant (Agave sisalana). The sisal plant is a monocotyledon, widely grown in tropical and sub-tropical countries, North and South America, Africa, the West Indies and the South East Asia. Tanzania and Brazil are two main producing countries [2]. Nowadays, It has been an increasing demand for natural fiber reinforced thermoplastic composite in a many variety of industrial applications [3,4].

In Hupkapong,Phetchaburi Province, Sisal fibers made for materials of handicraft such as handbag, hat, shoes and others. They made socio-economical valve for residents in Hupkapong, Phetchaburi Province. Sisal fiber is Lignocellulosicfibers composed of cellulose, hemicelluloses and lignin as major constituents so this made sisal fiber is special fibersfor reinforcement for use in composites on account of its low cost, low density, high specific strength [5,6].The processing methods for extracted sisal fibers have dried for sunlight. In this work, it will be presented a study of the effects of temperature on the mass variation, modulus and chemical durability of the fibers were tested. The variation of mass was examined by thermogravimetric analysis. Modulus and the chemical stability were characterized by Modulus measurement.

Materials and Methods

2.1 Young's modulus apparatus

The apparatus was designed and built for modulus measurement. The equipment contains two aluminium rods attached by two scale bars and two binder clips for fastening the specimen. The whole system was mounted vertically to the heavy wooden base.

Figure 1. Optical image of an individual sisal fiber.

2.2 Sample preparation

Sisal pants (*Agave sisalana*) were obtained from Hupkapong, Phetchaburi province as shown in Figure 2a. Fibers were extracted from 2-3 year old leaves of the *Agave sisalana*by using decorticating machine (Figure 2b). Optical image of an individual fiber is shown in Figure 1.

(a) (b)

Figure 2.The Sisal (*Agave sisalana*) pants (a) and fibers (b) from Hupkapong, Phetchaburi Province.

2.3 Fiber strength measurement

The fibers with diameter of 0.030- 0.050 mm^2 and length of 15 cm were selected for the measurement. The specimens were divided into 3 groups; non heating and heating at 50°C and 100°C in an oven. In order to test the chemical stability of the fibers, non-heat-treated and 100°C heat treated fibers were soaked in vinegar and detergent solution with pH of 3 and 12, respectively for 30 mins. The stress and strain of specimens for all groups was measured before and after soaked in different pH solution. The slope of graph between stress and strainwas calculated to determine the Young's Modulus of sisal fibers. Thermogravimetric analysis(TGA) was carried out on a Shimadzu TGA-50 instrument. Dynamic TG scans were conducted in a temperature range from 30 to 495°C and heating rate of 10° C min^{-1}. The experiments were carried out under nitrogen atmosphere at a flow rate of 20 mL min^{-1}for TGA measurements, samples with approximately 5 – 6 mg, respectively, of raw sisal fiber and its constituents were used.

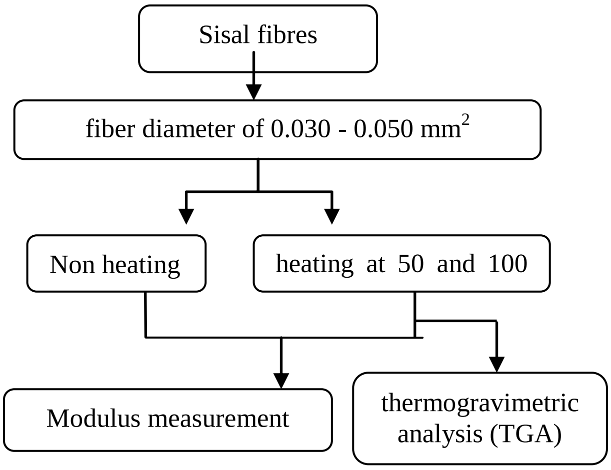

Figure 3. This chart showed procedure of this experiment

Results and Discussion

According toYoung's Modulus measurement of sisal fibers, the slope of graph between stress and strain of sisal fibers, Young's Modulus values of the sample which annealing at 50 and 100 °Care lower than that of not annealing as showed in figure 3. This results indicated that Young's Modulus valves decreased after annealed at various temperature and decreased even more when annealing temperature increased.

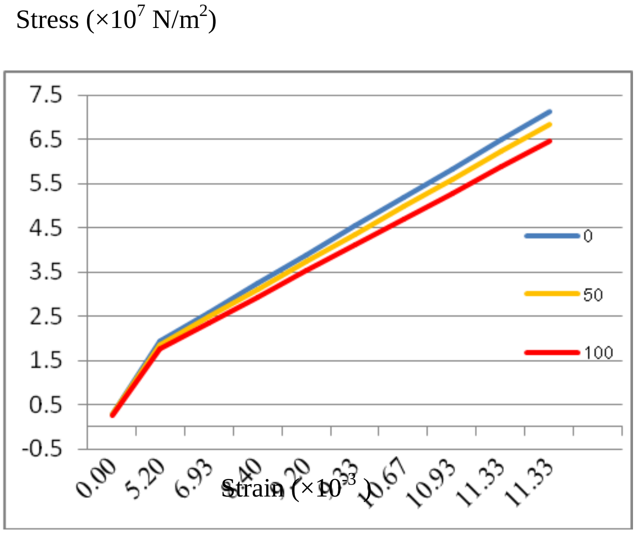

Figure 3. Graph between stress and strain of non-heating and heating at 50°C and 100°C sisal fibers

The percent of Young's Modulusdecreasing of sisal fibers after soak in acid and basis solution were showed in Table 1. The percent of Young's Modulus decreasing of annealed sisal fibers at 100 °C after soak in acid increased from 10.53% to 25.54% and increased from 1.28% to 8.16% after soak in basic. These results indicate that annealing process has the effect to the durability of sisal fibers for against the acid and basic. Much more effect to the durability of acid due to the percent of Young's Modulus decreasing much more increased than other.

The average of the most weight that the sisal fibers can be received showed in Table 2. The most weight that the sample can be receive of the annealed sisal fibers decreasing from 283.55 g(raw sisal) to 231.44 g (sisal fibers at 100°C) be equal to 18.37% . The effect to the durability of sisal fibers for against the acid and basic of raw sisal fiber decreasing from 283.55 g(raw sisal) to 159.58 g (pH 3) and 195.52 g(pH12).The effect to the durability of the sisal fibers annealing at 100 °C for against the acid and basic decreasing from 231.44 g(annealing at 100 °C) to 139.59 g (pH 3) and 183.55 g(pH12).

Table 1: comparison of average modulus values of the sisal fibers under different treatment conditions.

Type of treated sisal fibers	Average modulus values(N/m)	Percentage of decreasing
Non heating	7.03×10^{7}	
Heating 50 °C	6.76×10^{7}	
Heating 100 °C	6.37×10^{7}	
Non heating pH3	6.29×10^{7}	10.53%
Heating 100 °C, pH3	4.74×10^{7}	25.59%
Non heating pH12	7.12×10^{7}	1.28%
Heating 100 °C, pH12	5.85×10^{7}	8.16%

Table 2: related between kind of sisal fibers and the most weight that the sample can be received.

Type of treated sisal fibers	the average of the most weight that the sample can be received (g)
Non heating	283.55
Heating 50 °C	243.53
Heating 100 °C	231.44
Non heating pH3	159.58
Heating 100 °C, pH3	139.59
Non heating pH12	195.52
Heating 100 °C, pH12	183.55

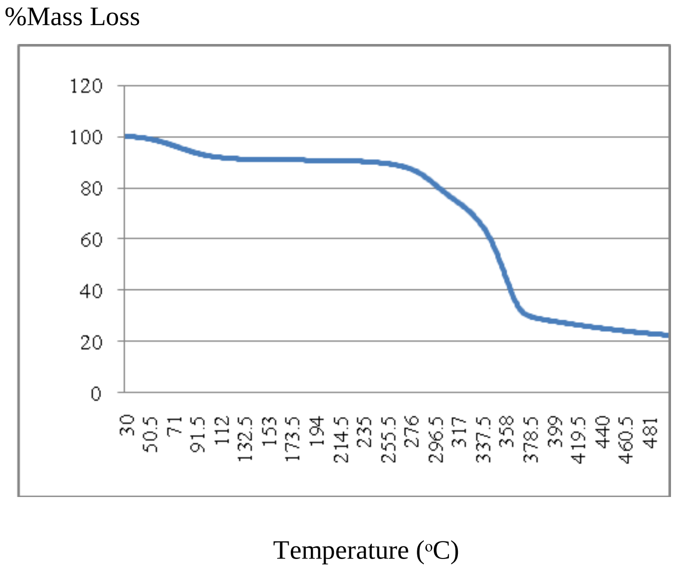

Figure 4. Thermogravimetriccurve of sisal fiber.

The thermogravimetric curve of sisal fiber shows a weight loss in the temperature range of 60-100 °C had decreased in 10 % of mass, which is due to the loss of adsorbed water in the fiber and a fast rate of fiber degradation in the range of 255-370 °C had rapidly decreased in 70 % of mass and after 375 °C, sisal fibers had decreased continuously.

Conclusions

In this work,The effects of temperature on the mass variation, modulus and chemical durability of the sisal fibers from Hupkapong,Phetchaburi Province represent that modulus and the chemical durability in acidic and basic conditions of sisal fibers decreased with increasing temperature and the most weight can be receive decreased with increasing temperature.Thermogravimetric analysis showed the variation of mass changed at two phases in temperature showed that the variation of structure and elements at two phases in temperatures.

Acknowledgments

This research project would not have been possible without the support of many people. My first and sincere appreciation goes to, Dr. NakarinPattanaboonmee who was abundantly helpful, support and guidance. Deepest gratitude is also due to the members of the supervisory committee, Dr. Jittra Ketkeaw and Assoc. Prof. Dr. Supanee Limsuwan without whose knowledge and assistance this study would not have been successful. My greatest appreciation and friendship goes to my friend, Honey , Sastra, Piyawadee and Manus, who was always a great support in all my struggles and frustrations in my workand I would like to express my deep gratitude and respect to my family; for their understanding & endless love, through the duration of her studies.

References

1. Chand,N. and Hashmi, S.A.R.,1993,“Mechanical properties of sisal fibre at elevated temperatures”,Journal of Materials Science, Vol. 28, pp. 6724-6728.
2. Li, Y.,Mai. Y.W. and Ye, L., 2000,“Sisal fibre and its composites: a review of recent development”, Composites Science and Technology,Vol. 60, pp. 2037–2055.
3. Singha, A.S. and Thakur, V.K., 2008,“Mechanical properties of natural fibre reinforced polymer composites”, Indian Academy of Sciences,Vol. 31, pp. 791–799.
4. Chanddramohan, D.andMarimuthu, K., 2011,“Tensile and Hardness Tests on Natural Fiber Reinforced Polymer Composite Material” ,International journal of advanced engineering science and technologies, Vol. 6, pp. 097 – 104.

5. Martin, A.R.,Martins, M.A., Odilon, R.R.F. and Mattoso, H.C.,2010,“Studies on the thermal properties of sisal fiber and its constituents”,ThermochimicaActa, Vol. 506, pp. 14–19.
6. Belaadi,A.,Bezazi,A.,BourchakM.andScarpaF., 2012, “Tensile static and fatigue behavior of sisal fibres”, Materials & Design,Vol.46 ,pp.76-83.
7. Naga Prasad naiad,V.,2011, “ Compressive & impact properties of sisal/glass fiber reinforced hybrid composites”,International Journal of Fiber and Textile Research, Vol.1(1) ,pp. 11-14.
8. Ahmed, B., Abderrezak, B., Mostefa, B. and Fabrizio, S.,2012, “Tensile static and fatigue behaviour of sisal fibres”, Materials and Design.
9. Reem Sabah M., Mohamed A. and Mohannad Sale H., 2012,“ A Study On Mechanical, Thermal andMorphological Properties Of Natural Fibre/Epoxy Composite” , Journal of Purity, Utility Reaction and Environment, Vol.1 No.5,pp. 237-266.
10. Duangkae Butkul, Production of Natural Fiber Polymer Composites. 2011, 5th SWU Academic and Research Conference. 2011, SWU 1188. 17-18 March 2011.

Effect of Carburizing on the Surface Mechanical Properties of Ti-5Al-2.5Sn and Ti-10V-2Fe-3Al.

A. Thongon[*] and C. Boonruang

Department of Physics and Materials Science, Faculty of Science, Chiang Mai University,
Chiang Mai 50200, Thailand.
**Corresponding author. E-mail: mai_atcha@hotmail.com*

Abstract

The specimens of Ti-5Al-2.5Sn and Ti-10V-2Fe-3Al alloys with the diameter of 20 mm and the thickness of 1.5 mm were prepared. The specimens were carburized via current heating technique using the electrical powers of 40-180 W for 30 min. The microstructure and chemical composition of the specimens were examined by SEM, EDS and XRD. The Vickers hardness test was performed. The carburizing temperature, carbon content and TiC formation are increased as the applied electrical power increases. TiC was formed on Ti-5Al-2.5Sn and Ti-10V-2Fe-3Al carburized at 120 W and above. Hardness of the alloys carburized at 180 W was decreased in comparison with that of 160 W due to the spallation of the TiC and high porosity of the surface.

***Keywords*:** carburizing, current heating technique, titanium carbide

Introduction

Since titanium was firstly synthesized in the late 1940, titanium and titanium alloys have been developed and widely used leading to the rapid growth of the titanium industry at the present time. Titanium and titanium alloys have a high strength, high corrosion resistance and low density [1-9]. Ti-5Al-2.5Sn is categorized as alpha alloy (α-Ti). The alloys in this group contain the element such as aluminium and have the HCP structure [1-5]. The alloy has high strength and resistance to oxidation at temperatures in the range of 316-593 °C, has high resistance to corrosion and has good welding properties [1,3]. Ti-10V-2Fe-3Al is categorized as beta alloy (β-Ti). The alloys in this group contain the elements such as vanadium, molybdenum, iron and chromium and have the BCC structure [1-5]. The alloy has very high strength and hardenability. It could have the ductile-to-brittle transition and not suitable for low temperature applications [3].

However, titanium alloys have an important limitation. The surface properties are poor at high temperature. Therefore, it is necessary to improve their surface in order to increase the strength, wear resistance and corrosion resistance which would extend the life of equipments and parts [1-5].

Carburizing via a new diffusion coating technique, the current heating technique, could improve the surface properties of titanium and titanium alloys [10-11]. The advantages of this technique are easy, cheap, low power consumption and causes very low contamination to the environment [11-12].

Materials and Methods

Two titanium alloys were used in this study. Their compositions are shown in Table 1.

Table 1 Composition of titanium alloys.

compositions	Ti-5Al-2.5Sn	Ti-10V-2Fe-3Al
Al	5	3
Sn	2.5	-
V	-	10
C	0.08	-
Fe	0.05	2
N	0.05	0.05
O	0.02	0.13
H	0.02	0.015
Ti	Bal.	Bal.

The specimens with a diameter of 20 mm and a thickness of about 1.5 mm were polished down to 0.05 µm alumina suspension and cleaned with acetone. After that, the specimen was placed amidst the 20 µm graphite powder within a glass tube with the inner-diameter of 25 mm and the thickness of 2 mm. The specimen and graphite were subsequently packed by compression with the pressure of 10.3 kPa. After that, the package was placed on the lower-copper electrode in the chamber and the electrical contact with the upper-copper electrode was done as the chamber lid on the top was closed as shown in Figure 1. The chamber was evacuated by a rotary pump and the argon gas was subsequently flowed into the chamber with the rate of 50 ml/min. In the carburizing, the electric current was flowed through the package with the constant electrical power of 40, 80, 120, 140, 160 and 180 W for 30 min.

The microstructure, chemical composition and surface morphology of the specimens were examined by scanning electron microscope (SEM), energy dispersive X-ray spectroscopy (EDS) and X-ray diffractometer (XRD) and the Vickers hardness test was performed.

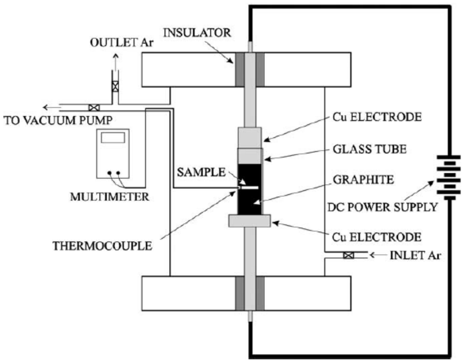

Figure 1. Schematic diagram of current heating apparatus used for carburizing [10-12].

Results and Discussion

3.1 Temperature

The temperature of the alloys carburized at 40 - 180 W is shown in Figure 2. The temperature increased with increasing applied electrical power. In the first 5 min of carburizing, the temperature increased rapidly. After that, the temperature gradually increased slowly until the end of the process. The temperature has an effect on the diffusion of carbon. The diffusion coefficient of the carbon in the alloys increased exponentially with the increasing temperature as described by Arrhenius equation [11, 13-14]:

$$D = D_0 \exp\left(\frac{-Q}{RT}\right)$$

where D is the diffusion coefficient, D_0 is a pre-exponential term, Q is the activation energy , R is the universal gas constant and T is absolute temperature, respectively.

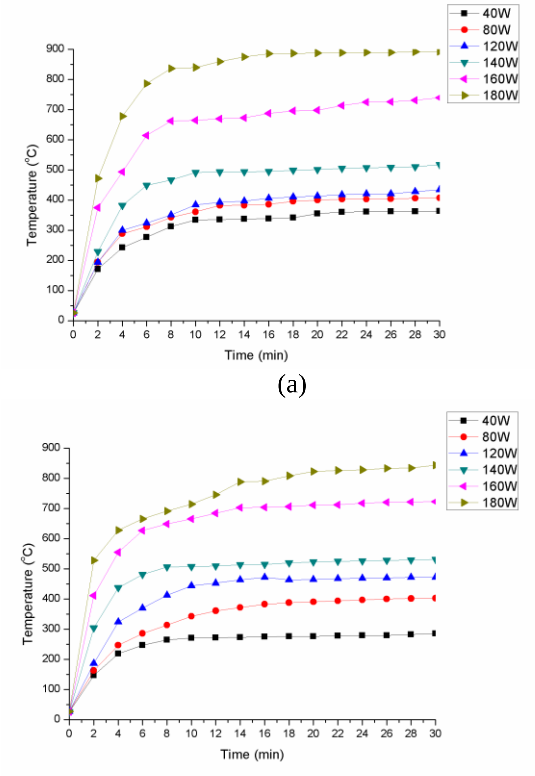

(a)

(b)

Figure 2. Plot of temperature as a function of time in carburizing of (a) Ti-5Al-2.5Sn and (b) Ti-10V-2Fe-3Al.

3.2 EDS

Chemical compositions of the alloys examined by EDS are shown in Figure 3 and 4. It's shown that the carbon-peak intensity of the untreated specimen is low in comparison with the carburized specimen reflecting the diffusion of carbon into the specimen during carburizing. The relative intensity of carbon spectrum, with that of titanium, is increased as the applied electrical power increased reflecting the increase in carbon content resulting from the increasing carburizing temperature.

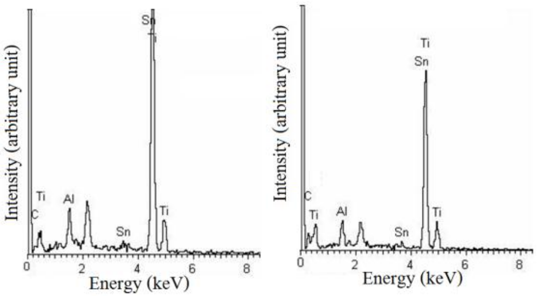

(a) (b)

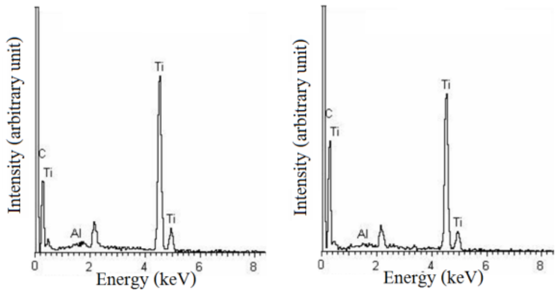

(c) (d)

Figure 3. EDS spectra for (a) untreated Ti-5Al-2.5Sn and the alloy carburized at (b) 80 W, (c) 160 W and (d) 180 W.

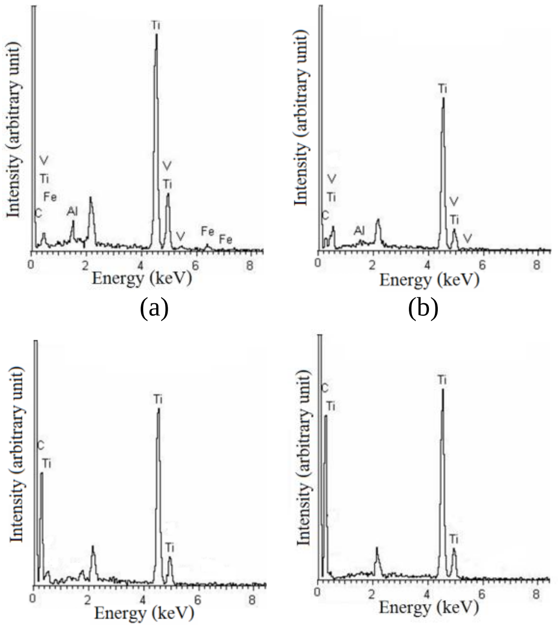

(a) (b)

(c) (d)

Figure 4. EDS spectra for (a) untreated Ti-10V-2Fe-3Al and the alloy carburized at (b) 80 W, (c) 160 W and (d) 180 W.

3.3 XRD

XRD patterns for untreated Ti-5Al-2.5Sn and Ti-10V-2Fe-3Al and the alloys carburized at the electrical powers of 80, 120 and 160 W are shown in Figure 5 and 6. It is obvious that the pattern of Ti in the untreated Ti-5Al-2.5Sn is different from that of Ti-10V-2Fe-3Al because their microstructures are HCP and BCC, respectively.

The results show that TiC was formed in Ti-5Al-2.5Sn and Ti-10V-2Fe-3Al carburized at 120 W and above. There's no detection of TiC in the alloys carburized at 80 W. TiC might be not formed or its formation might be too low to be detected. The intensity of Ti peaks in the patterns of 160 W is very small in comparison with that of 120 W, or not detected, resulting from the increase in the formation of TiC with the increasing applied electrical power.

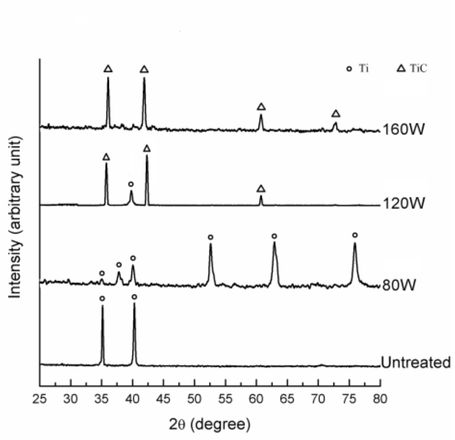

Figure 5. XRD patterns for untreated Ti-5Al-2.5Sn and the alloy carburized at the electrical powers of 80, 120 and 160 W.

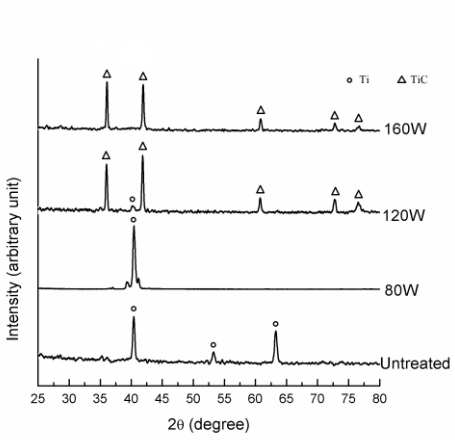

Figure 6. XRD patterns for untreated Ti-10V-2Fe-3Al and the alloy carburized at the electrical powers of 80, 120 and 160 W.

3.4 SEM

Surface morphology of untreated Ti-5Al-2.5Sn and Ti-10V-2Fe-3Al and the alloys carburized at 80, 160 and 180 W is shown in Figure 7 and 8. The surface morphology of the alloys carburized at 40 - 120 W is resembled. There's a little amount of formation of the compound that could be TiC. The surface morphology of the alloys carburized at 140 - 160 W is resembled as well. It is obvious that there's the formation of TiC, with slightly-equiaxed grain and low porosity, covering on the surface. The surface morphology of the alloys carburized at 180 W is quite different from the others. There're the flake-like grain with the larger size and the higher porosity in comparison with that of 160 W.

The cross-sectional images for untreated Ti-5Al-2.5Sn and Ti-10V-2Fe-3Al and the alloys carburized at 160 W are shown in Figure 9. The images show the formation of the TiC film, with the thickness of 30 – 50 μm, on the surface of the alloys carburized at 160 W. The result is consistent with Arrhenius equation and the results of EDS and XRD. As the temperature increased; large amount of carbon could diffuse into the alloys leading to large amount of formation of TiC.

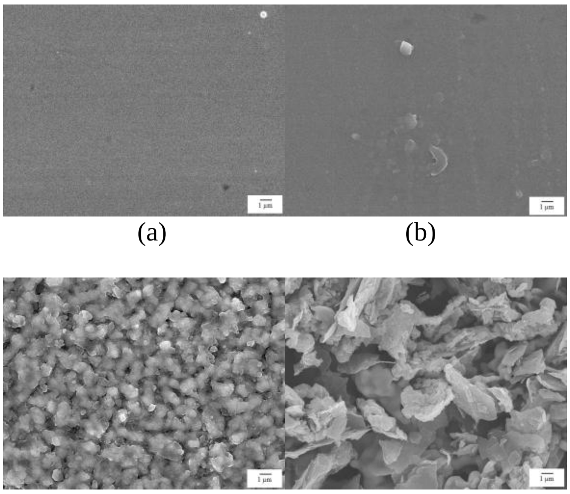
(a) (b)
(c) (d)

Figure 7. SEM micrographs of (a) the untreated Ti-5Al-2.5Sn and the alloy carburized at (b) 80W, (c) 160W and (d) 180W.

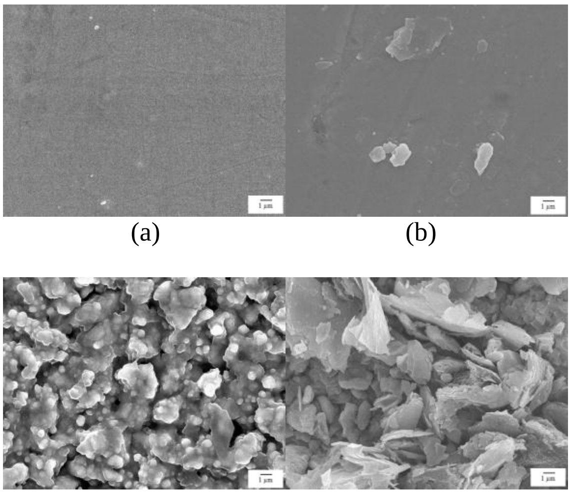
(a) (b)
(c) (d)

Figure 8. SEM micrographs of (a) the untreated Ti-10V-2Fe-3Al and the alloy carburized at (b) 80W, (c) 160W and (d) 180W.

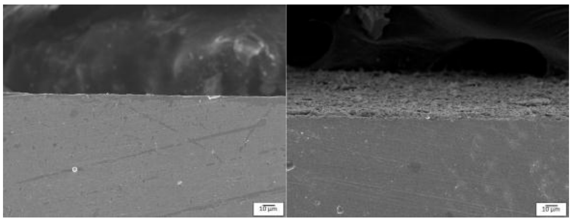
(a) (b)

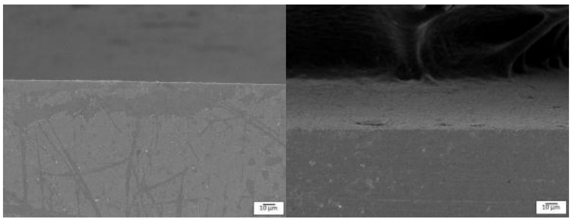
(c) (d)

Figure 9. Cross-sectional images of (a) the untreated Ti-5Al-2.5Sn, (b) the alloy carburized at 160W and (c) the untreated Ti-10V-2Fe-3Al and (d) the alloy carburized at 160W.

3.5 Hardness

The hardness of untreated Ti-5Al-2.5Sn, Ti-10V-2Fe-3Al and the carburized alloys is shown in Figure 10. The hardness of carburized alloys is higher than that of the untreated alloys. For Ti-5Al-2.5Sn, the hardness increases from 310.54 ± 15.53 kg/mm^2, for the untreated alloy, to the highest at 651.36 ± 32.57 kg/mm^2 for the alloy carburized at 160W and then decreases to 498.1 ± 24.90 kg/mm^2 for that of 180 W. For Ti-10V-2Fe-3Al, the hardness increases from 358.04 ± 17.90 kg/mm^2, for the untreated alloy, to the highest at 541.68 ± 27.084 kg/mm^2 for the alloy carburized at 160W and then decreases to 440.32 ± 22.02 kg/mm^2 for that of 180 W.

The increase of the hardness with the increasing applied electrical power caused by the formation of TiC. The result is consistent with the XRD result in that TiC was detected at 120 W and the hardness of the alloys carburized at 120 W is significantly higher than that of the lower powers. Because TiC is hard and brittle, it would be flaked when it largely formed on the alloy surface. Therefore, the surface of alloys carburized at 180 W would flake when the hardness indentation was done leading to the decrease in the hardness. The result is consistent with that of SEM.

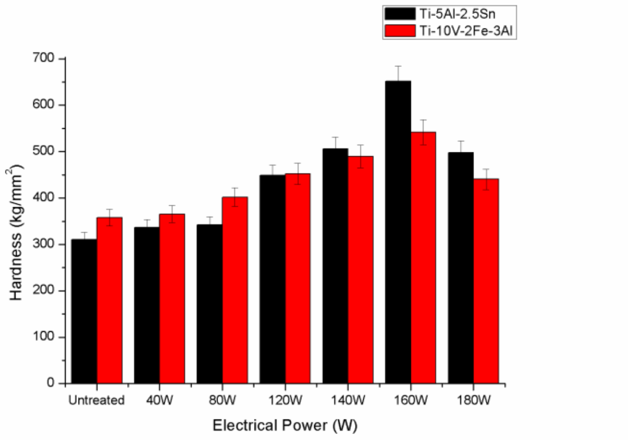

Figure 10. The plot of hardness of Ti-5Al-2.5Sn and Ti-10V-2Fe-3Al as a function of applied electrical power.

Conclusions

The carburizing temperature, carbon content and TiC formation are increased as the applied electrical power increases. TiC was formed on Ti-5Al-2.5Sn and Ti-10V-2Fe-3Al carburized at 120 W and above. Hardness of the alloys carburized at 180 W was decreased in comparison with that of 160 W due to the spallation of the TiC and high porosity of the surface.

Acknowledgments

This research is financial supported by The Faculty of Science and the Graduate School, Chiang Mai University.

References

1. ASM International the Materials Information Society, “Materials Properties Handbook: Titanium Alloys”, (1994), 1-857.

2. M.J. Jr. Donachie, “Titanium Alloy Guide” RMI Titanium Company An RTI International Metal, (1988), 1-17.

3. G. Lütjering, JC. Williams, and A. Gysler, “Microstructure and Mechanical Properties of Titanium Alloys”, World Scientific., (2000), 1-77.
4. A. Zhecheva, W. Sha, S. Malinov, and A. Long. “Enhancing the Microstructure and Properties of Titanium Alloys through Nitriding and other Surface Engineering Methods”, Surface & Coatings Technology, **200** (2005), 2192– 2207.
5. X. Liu, P. K. Chu, and C. Ding, “Surface modification of titanium, titanium alloys, and related materials for biomedical applications”, Materials Science and Engineering R, **47** (2004), 49-121.
6. S. Niyomwas, “Synthesis and Characterization of TiC and TiC-Al_2O_3 Composite from Wood Dust by Self-Propagating High Temperature Synthesis”, Energy Procedia., **9** (2011), 522-531.
7. S. Izman, M. R. Abdul-Kadir, M. Anwar, E.M. Nazim, R. Rosliza, A. Shah and M.A. Hassan, “Surface Modification Techniques for Biomedical Grade of Titanium Alloys: Oxidation, Carburization and Ion Implantation Processes” Titanium Alloys – Towards Achieving Enhanced Properties for Diversified Applications., (2012), 201-222.
8. K. Matsuura and M. Kudoh, “Carbo-nitride Coating Treatment of Titanium by a Diffusional Method”, Key Engineering Materials, **280-283** (2005), 1847-1850.
9. Y. Luo, S. Ge, H. Liu, and Z. Jin, “Microstructure analysis and wear behavior of titanium cermet femoral head with hard TiC layer”, Journal of Biomechanics., **42** (2009), 2708–2711.
10. C. Boonruang, and S. Thongtem, “Fast Processing Technique for TiC Coatings on Titanium”, Chiang Mai J. Sci., **37 No.2** (2010), 206–212.
11. C. Boonruang, and S. Thongtem, “Surface Modification of TiAl Alloy Via Current Heating Technique”, Appl. Surf. Sci., **256** (2009), 484–488.
12. C. Boonruang, W. Kumpangkeaw, K. Sopunna, N. Chomsaeng, and S. Narksitipan, “Effect of Carburizing via Current Heating Technique on the Near-Surface Microstructure of AISI 1020 Steel”, Chiang Mai J. Sci, **39 No.2** (2012), 254-262.
13. American Society for Metals. “Carburizing and Carbonitriding”, (1977), 1-215.
14. Askeland, R. Donald, “The Science and Engineering of Materials” SI ed, (1988), 93-117.

Effect of Grain Size on Nanostructure Ferroelectric Films using Effective Medium Theory

J. Thongsri

College of Data Storage Innovation, King Mongkut's Institute of Technology Ladkrabang, Bangkok, 10520, Thailand
Corresponding author. E-mail: Thongsri_j@hotmail.com

Abstract

Based on the effective medium theory, the temperature dependence of effective dielectric permittivity $(\varepsilon_e(T))$ of a nanostructured ferroelectric film consisting of cylindrical ferroelectric grains has been theoretically investigated as a function of core radius and the thickness of a nonferroelectric dead layer (DL) in inhomogeneous grains. The results show the increase in $\varepsilon_e(T)$ with increasing the core radius and the decrease in $\varepsilon_e(T)$ with increasing the DL thickness.

Keywords: Effective Medium Theory, Ferroelectric Film, Dielectric Permittivity

Introduction

(Ba,Sr)TiO$_3$ (BST) thin film is a leading candidate to be applied as the dielectric material in high-density dynamic random-access memory because it provides high dielectric constant. Obviously, the dielectric constant of ferroelectric thin film depends on the thickness. Since the thickness of the film is reduced to ten of nanometers as device requirement, the dielectric constant is suppressed significantly. This phenomenon is referred to as the effect of grain size that makes the ferroelectric thin film less attractive. In order to explain the size effect, the assuming existence of "dead layer" (DL) was proposed [1], which was confirmed by the preparation of BST thin film based on the series capacitor model [2]. The obtained thin film revealed that each grain has the ferroelectric core surrounded by the nonferroelectric surface dead layer, which affects the effective permittivity of thin film. Therefore, it is useful to study the effect of grain size on ferroelectric thin film.

Based on the average field method, Vendik et al. theoretically studied the dependence of effective dielectric permittivity of a nanostructure ferroelectric film on the thickness of DL and the spherical and elliptical grain sizes [3,4]. The effective permittivity shows the similar trend that reported in the experiment [5].

The effective medium theory (EMT) originally proposed by Hashin [6] in the study of the effective properties of spherical two-phase composite materials. Previously, we used the EMT to model a two-phase strongly nonlinear dielectric composite and predicted the effective nonlinear coefficient [7]. The obtained results are in agreement with the experimental results confirming the reliability of the EMT.

In this article, we apply the EMT to model the ferroelectric film having cylindrical grains in two dimensions. The temperature dependence of effective permittivity has been theoretically investigated as a function of grain size and the thickness of DL.

Methodology

In the EMT model, the ferroelectric film is considered to be composed of cylindrical gains. Each grain has a ferroelectric core with radius a, surrounded by a concentric nonferroelectric shell with radius b, while the others are replaced by a homogeneous medium. The permittivity of the core, the shell, and the effective medium are ε_c,ε_s and ε_e, respectively. Figure 1 shows a grain modeled in the EMT with the shell thickness t $(b = a + t)$.

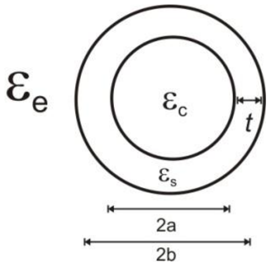

Figure 1. Schematic diagram of a grain modeled in the EMT.

To determine the effective permittivity of ferroelectric film (ε_e), the solution of Laplace equation in the cylindrical coordinate is given by

$$\phi_c(r,\theta) = Ar\cos\theta, \qquad 0 \le r \le a \qquad (1)$$

$$\phi_s(r,\theta) = (Br + \frac{C}{r})\cos\theta, \qquad a \le r \le b \qquad (2)$$

$$\phi_e(r,\theta) = \left(-r+\frac{D}{r}\right)\cos\theta, \qquad b \le r < \infty \qquad (3)$$

where, ϕ is the electric potential and the subscripts c, s and e, referred to core, shell and effective medium, respectively.

The constants A, B, C and D in equations (1)-(3) are determined by using the boundary conditions of the continuity at the core and shell surfaces, which gives

$$A = \frac{-4b^2\varepsilon_s\varepsilon_e E_0}{v_c(\varepsilon_c-\varepsilon_s)(\varepsilon_s-\varepsilon_e)+(\varepsilon_c+\varepsilon_s)(\varepsilon_s+\varepsilon_e)}, \qquad (4)$$

where E_0 is the external electric field and $v_c = a^2/b^2$

The effective permittivity of the medium volume V, is defined by [6]

$$\varepsilon_e\langle E\rangle = v_c\varepsilon_c\langle E_c\rangle + v_s\varepsilon_s\langle E_s\rangle, \qquad (5)$$

where $\langle E\rangle = (1/V)\int_V |E|\,dV$. v_c and v_s are the volume packing fraction of the core and the shell, respectively, restricted by $v_s = 1 - v_c$.

It is true that volume average of electric field inside the medium is uniform throughout [6] with the solution $\langle E\rangle = E_0$. This leads to

$$v_c\langle E_c\rangle + v_s\langle E_s\rangle = E_0. \qquad (6)$$

Using equations (5) and (6), we get

$$\varepsilon_e E_0 = \varepsilon_s E_0 + v_c(\varepsilon_c - \varepsilon_s)\langle E_c\rangle. \qquad (7)$$

Calculating the volume average of electric filed inside the core, we obtain $\langle E_c\rangle = -A$. Substituting the expressions (4) into (7), the effective permittivity of ferroelectric film can be rearranged to

$$\varepsilon_e = \varepsilon_s\left[1+\frac{v_c}{\frac{\varepsilon_s}{\varepsilon_c-\varepsilon_s}+\frac{v_s}{2}}\right]. \qquad (9)$$

This equation is familiar in the study of effective linear coefficient of cylindrical two-phase composite materials [6]. Alternative expression of ε_e is given by

$$\varepsilon_e = \varepsilon_s\left[\frac{\varepsilon_c(b^2+a^2)+\varepsilon_s(b^2-a^2)}{\varepsilon_c(b^2-a^2)+\varepsilon_s(b^2+a^2)}\right]. \qquad (10)$$

Replacing $b = a + t$ into equation (10) and neglecting the second power of small value t with the approximation $b^2 \cong a^2 + 2at$, the effective permittivity of ferroelectric film is determined as the function of the grain size (a) and the thickness of dead layer (t):

$$\varepsilon_e = \varepsilon_c\left(1+\frac{t}{a}+\frac{\varepsilon_s}{\varepsilon_c}\frac{t}{a}\right)\Big/\left(1+\frac{t}{a}+\frac{\varepsilon_c}{\varepsilon_s}\frac{t}{a}\right). \qquad (11)$$

Results and Discussion

To investigate the temperature dependence, figure 2 shows the permittivity of a homogeneous ferroelectric film of $Ba_{0.65}Sr_{0.35}TiO_3$ (BST) with the

structural quality factor of based on the phenomeno

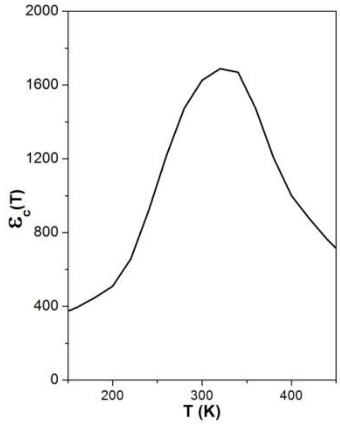

Figure 2. The temperature dependence of the permittivity of ferroelectric core (ε_c) based on phenomenological model [5].

The shell exhibits nonferroelectric properties when the thickness (t) is about 3 nm and permittivity of DL (ε_s) is around order of 40 [2], which is assumed to be temperature dependent. Using the permittivity reported in figure 2 as the property of core and that of DL mentioned in reference [2] as property of shell, the effective permittivities of ferroelectric film are determined and reported in figures 3 and 4.

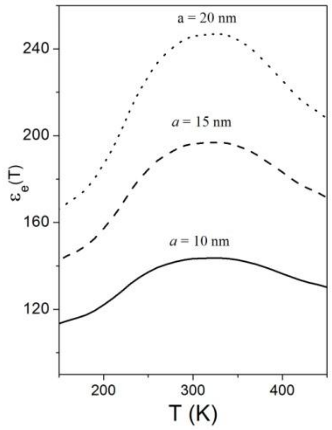

Figure 3. The temperature dependence of effective permittivity $(\varepsilon_e(T))$ of ferroelectric film for the DL thickness $t = 3$ nm with the core radius (a) as parameter.

Figures 3 reveals the increase in effective permittivity with increasing the core radius for the DL thickness of

$t = 3$ nm. The higher the core radius, the more the effective permittivity is observed.

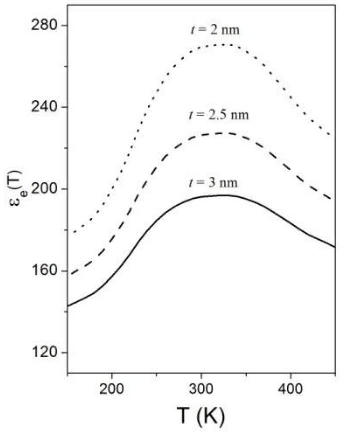

Figure 4. The temperature dependence of effective permittivity $(\varepsilon_e(T))$ of ferroelectric film for the core radius $a = 15$ nm with the DL thickness (t) as parameter.

In figure 4, the temperature dependence of effective permittivity $(\varepsilon_e(T))$ for the core radius $a = 15$ nm with the DL thickness (t) as parameter, is reported. It shows the increase in $\varepsilon_e(T)$ with decreasing the DL thickness. Since the permittivity of the shell with the DL thickness t is less than that of the core, decrease t enhances ε_e of ferroelectric film.

The results of $\varepsilon_c(T)$ of monocrystalline ferroelectric film in figure 2 are compared with those presented in figures 3 and 4. It can be analyzed that the existence of DL reduces the effective permittivity of the ferroelectric film.

Moreover, we also applied the EMT to investigate the temperature dependence of effective permittivity $(\varepsilon_e(T))$ in the study of effective permittivity of a nanostructure ferroelectric film consisting of the spherical grains. The obtained results are consistent with those reported in references 3 using average field method since the electric fields inside the ferroelectric film are uniform.

Conclusions

In this work, the effective medium theory is used to model the ferroelectric film possessing cylindrical grains, and then the effective permittivity (ε_e) is investigated in two dimensions. The temperature dependence of effective permittivity $(\varepsilon_e(T))$ is determined as a function of grain size (a) and the thickness of DL (t). The result shows the increase in ε_e with increasing the core radius for the DL thickness $t = 3$ nm using the core radius as parameter. Moreover, for the core radius $a = 15$ nm with the DL thickness as parameter, the result reveals the increase in $\varepsilon_e(T)$ with decreasing the DL thickness. It can be analyzed that the existence of DL reduces the effective permittivity of the ferroelectric film. This result can be applied as fundamental information for improving and characterizing the ferroelectric film.

Acknowledgments

The sincere thanks is given to College of Data Storage Innovation, King Mongkut's Institute of Technology Ladkrabang, Thailand, for the financial support of this work.

References

1. B. T. Lee, and C. S. Hwang, “Influences of Interfacial Intrinsic Low-Dielectric Layers on the Dielectric Properties of Sputter (Ba,Sr)TiO_3 thin films”, Applied Physics Letters **77** (2000), 124.
2. B. Chen, H. Yang, L. Zhao, J. Miao, B. Xu, X. G. Qiu, and B. R. Zhao, “Thickness and Dielectric Constant of Dead Layer in Pt/($Ba_{0.7}Sr_{0.3}$)TiO_3/$YBa_2Cu_3O_{7-x}$Capacitor”, Applied Physics Letters **84** (2004), 583.
3. O.G. Vendik, N. Yu. Medvedeva, and S. P. Zubko, “Size Effect in Nanostructured Ferroelectric Films”, Technical Physics Letters **33** (2007) 8.
4. O.G. Vendik, N. Yu. Medvedeva, and S. P. Zubko, “Effective Permittivity of a Nanostructured Film Consisting of Elliptic Ferroelectric Grains”, Technical Physics Letters **34** (2008) 323.
5. O. G. Vendik, and S. P. Zubko, “Modeling the Dielectric Response of Incipient Ferroelectrics”, Journal of Applied Physics **82** (1997) 4475.
6. Z. Hashin, “Assessment of the Self Consistent Scheme Approximation: Conductivity of Particulate Composites”, Journal of Composite Materials **2** (1968) 284.
7. J. Thongsee, and M. Natenapit, “Effective nonlinear coefficients of strongly nonlinear dielectric composites”, Journal of Applied Physics **101** (2007) 024103.

Effect of Plasma Treatment on Copper Substrate using for Carbon Nanotubes Synthesis

C. Suttichart[1], W. Thamjaree[2*], D. Boonyawan, and W. Nhuapeng

Department of Physics and Materials Science, Faculty of Science, Chiang Mai University, Chiang Mai 50200 , Thailand
[*]Corresponding author. E-mail: th_wandee@hotmail.com

Abstract

In this research , improvement of copper substrate for carbon nanotubes growth was carried out by low pressure plasma treatment technique which is using plasma energy at frequency of 13.56 MHz , electric power of 50W and gas pressure 100 mT. The gas mixture gases of 10%Ar + 90%N_2 was used as the working gas and the substrates were treated for 10 min. Thereafter , the treated copper substrates were then used for synthesizing the carbon nanotubes by Alcohol Catalytic Chemical Vapor Deposition (ACVD) technique. The effects of plasma treatment on the copper surface was determined by Contact Angle test which using Sessile Drop model. It was found that the plasma treatment affected the contact angle of copper surface. The contact angle of treated sample is lower than that of untreated sample which exhibits the hydrophilic and more surface energy. Moreover, microstructures of samples were examined by using Scanning Electron Microscopy (SEM). From the result , it was found that the copper substrate which treated by 10%Ar + 90%N_2 gases showed better characteristic of carbon nanotubes.

***Keywords*:** Plasma treatment, carbon nanotubes, alcohol catalytic chemical vapor deposition

Introduction

Carbon nanotubes have been well-know over the past 15 years. First discovered by Iijima in 1991[1] . He was studying the synthesis of fullerenes by electric arc discharge technique. Iijima observed were so called multi-walled carbon nanotubes ($MWNT_S$) [2] . Extensive research have been investigated for many different technical application [3] . Potential technical applications in the areas of molecular electronic devices [4-8] , nanocomposites [9-12] , and electron field emission have been proposed or explored [13-17]

CNT_S can be synthesized by various techniques such as arc discharge , laser ablation and chemical vapor deposition (CVD) [18, 19]. The CVD method has attracted much attention because of the advantage that the growth of CNT_S can be achieved with high purity , high yield , vertical alignment and low coat. Ethanol , known as a very promising candidate of a low raw materials cost by using alcohol source. From these facts , several research groups have used ethanol as the carbon source to produce single -walled carbon nanotubes ($SWNT_S$) and $MWNT_S$ by various CVD methods [20-24].

Synthesis of carbon nanotubes directly on conducting substrates such as copper, nickel and cobalt. At the same time , the growth of CNT_S directly on metallic substrate also resolves the problem of adhesion of nanotubes layer [25, 26]. In recent years , copper alloy has been increasingly used as a major substrate materials due to its good thermal and electrical performance , good manufacturability and low cost. However , the formation of copper oxide and contaminants [27, 28].

Plasma cleaning has been used for many years as a pretreatment prior to coating processes. These chemical and physical processes can remove oxide and contaminants from the surface which can be from “natural” or “technological” origin. Natural contaminants come from exposure of surface to the ambient atmosphere and mostly contain oxygen , carbon and hydrogen-containing species. Oxide growing on metal and other surface , adsorbed water and various organic [29]. Plasma cleaning , employing hydrogen as reactive gas , has been used for many years. The idea behind the utilization of the plasma is the creation of a very reactive gas environment , often enclosed in a vacuum system [30].

In this study , we reported the improvement of copper substrate for carbon nanotubes growth were carry out low pressure plasma treatment technique. The characteristic and microstructure of

CNTs was examined and compared with that of CNTs from conventional technique

Materials and Methods

The copper sheet (1×1×0.05 cm) was cleaned with CH_3COCH_3 (Acetone , ACI Labscan). The plasma treatment under the following conditions in table 1. Thereafter , the sample surface was examined contact angle by Sessile drop mode.

Table 1: Experimental condition for plasma treatment

Gas	*10%Ar + 90%N$_2$*
Base pressure (Torr)	$1.9×10^{-2}$
Volume (Torr)	10%Ar = $2.50×10^{-2}$ 90%N_2= $7.29×10^{-2}$
Frequency (MHz)	13.56
Electric power (walt)	50
Gas pressure (mmTorr)	100
Plasma treatment time (min)	10

The synthesis of CNTs was showed in Fig 1.

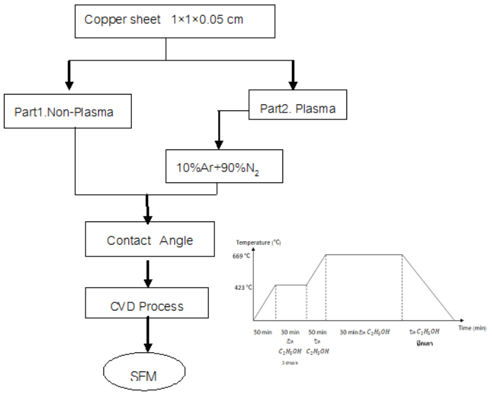

Figure 1. The schematic diagram of CVD set up for the synthesis of CNT.

Firstly , Nickel oxide powder (NiO, commercial grade) was weighted 0.1 g and mixed with Ethanol (C_2H_5OH 99.8% , Merck). The set up sample was put into the furnace tube. Ethanol vapor was then introduced into the furnace after heated up to 450 °C for 50 min and let it flow into system for 30 min. Ethanol was then stopped to heat the furnace up to 700°C for 50 min and thereafter ethanol was let to flow again for 3 hours.

The microstructure of obtained product was analyzed using a SEM technique (Scanning electron microscope, JEOL JSM-6335F). Moreover, the percent yield was estimate from equation.

$$\text{Carbon yield (wt \%)} = \text{WCNTs} / W_C \times 100 \qquad [18]$$

Where W_{CNTs} is the weight of CNTs (g), W_C is the approximate of weight of NiO(g)

Results and Discussion

3.1 Effect of contact angle by Sessile drop model of copper substrate before CVD process.

Experimental conditions for plasma treatment	
Non-plasma treatment	10%Ar+90%N_2

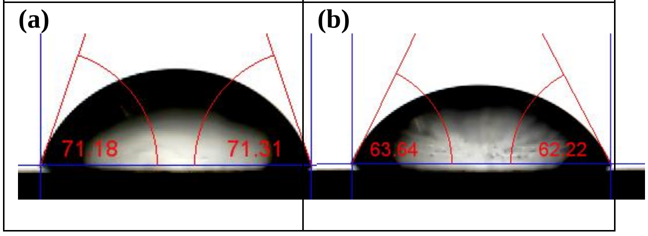

Figure 2. The image of contact angle of the Cu substrate.

(a) Non – plasma treatment.
(b) 10%Ar + 90%N_2 plasma treatment.

The average contact angle of water on the Cu substrate about 61.239 ± 1.238 degree. It was observed the contact angle plasma treatment was decrease when compared with that of non-plasma sample. It may be due to plasma treatment has effect to change the surface energy of the sample.

Table 2. The average contact angle (Degree) of copper substrate.

Contact angle (Degree)			
Non-plasma treatment		10%Ar+90%N_2	
Left	Right	Left	Right
71.18	71.31	63.64	62.22
74.40	72.67	58.55	59.47
80.63	79.02	66.50	65.01
80.71	81.47	52.17	53.62
77.92	77.74	65.33	66.33
68.951 ± 0.846		61.239 ± 1.238	

Fig 2. and table 2 showed difference contact angle by Sessile drop model of copper substrate non-plasma treatment , 10%Ar+90%N_2 and 10%Ar+90%H_2 plasma treatment before CVD process. From the result could be found that.

3.2 Effect of plasma treatment on the synthesis of carbon nanotubes on copper substrate according to the condition.

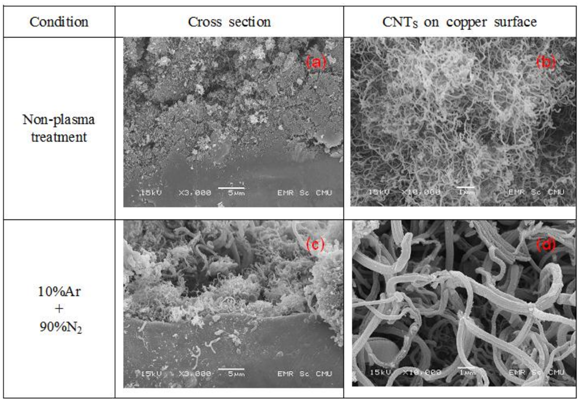

Figure 3. SEM micrographs of CNTS on synthesis copper substrate.
(a) Non-plasma treatment Cu substrate.
(b) CNTs on non-plasma Cu substrate.
(c) Plasma treatment (10%Ar + 90%N_2) Cu substrate.
(d) CNTs on plasma treatment Cu substrate.

The SEM micrograph of samples was show in Fig 3. It could be found the smooth and long nanotubes could be obtained from the sample.

Quantity of obtained nanotubes was much more than that of non-treat sample. Moreover , the average diameter of CNTs was in the range of 70-235 nm which shown in Table 2.

Table 2. The average diameter of CNT_S depending on the plasma treatment condition.

No.	Diameter of CNT_S variation in plasma treatment condition (nm)	
	Non-plasma	**10%Ar+90%N_2**
Scale	100	100
1	53	70
2	71	76
3	34	118
4	59	96
5	96	91
6	42	82
7	71	77
8	44	82
9	104	82
10	78	117
11	102	110
12	63	92
13	57	102
14	55	117
15	63	102
16	106	234
17	84	155
18	76	70
19	36	126
20	56	112
Averages diameter(nm)	**34 - 106**	**70 - 235**

Conclusions

The plasma treatment has affected to copper substrate surface. Comparison SEM image and contact angle of Sessile drop on copper substrate variation in plasma treatment condition. It could be found that the plasma treatment had effect to the contact angle of Cu substrate sample which had effect to characteristic quantity and size of CNTs when compared with that of non-treat Cu substrate sample.

Acknowledgments

The author would like to thank the National Research University Project under Thailand 's offices of the Higher Commission for financial support. We also wish to thank the Composites and Reinforcement Nanocomposites Unit , Department of Physics and Materials Science , Faculty of Science , Chiang Mai University for greatfully support.

References

1. S.Iijima, Nature (London), 1991. **354**: p. 56-58.
2. S.Iijima and T.Ichihashi, Nature (London), 1993. **363**: p. 603-605.
3. Daraio, C., V.F. Nesterenko, and J.F. Aubuchon, *Dynamic Nanofragmentation of Carbon Nanotubes.* Nano Letters, 2004. **4[10]**: p. 1915-1918.
4. Kong, J., et al., *Nanotubes molecular wire as chemical sensors.* Science, 2000. **287**: p. 622-625.
5. Drycke, V., et al., *Carbon Nanotubes Inter-and Intramolecular Logic Gates.* Nano Letters, 2001. **1**: p. 453-456.
6. Collins, P.C., M.S. Arnold, and P. Avouris, *Engineering Carbon Nanotubes and circuits using electrical breakdown.* Science, 2001. **292**: p. 706-709.
7. Bachtold, A., et al., *Logic Circuits with Carbon Nanotubes Transistors.* Science, 2001. **294**: p. 1317-1320.
8. Avouris, P., et al., *Carbon nanotube transistors and logic circuits.* Physica B: Condensed Matter, 2002. **323**(1–4): p. 6-14.

9. Geng, H.Z., et al., *Fabrication and Properties of Composites of Poly(ethylene oxide) and Functionalized Carbon Nanotubes* Advanced Materials, 2002. **14**: p. 1387-1390.
10. Cadek, M., et al., *Morphological and Mechanical Properties of Carbon Nanotube Reinforced Semi-crystalline and Amorphous Polymer Composites.* Applied Physics Letters, 2002. **81**: p. 5123-5125.
11. Biercuk, M.J., et al., *Carbon nanotubes composite for thermal management.* Applied Physics Letters, 2002. **80**: p. 2676-2769.
12. Bhattacharyya, A.R., et al., *Crystallization and orientation studies in polypropylene/single wall carbon nanotube composite.* Polymer, 2003. **44**(8): p. 2373-2377.
13. Zhu, W., et al., *Large current density from carbon nanotube field emitters.* Applied Physics Letters, 1999. **75**: p. 873-875.
14. Saito, Y. and S. Uemura, *Field emission from carbon nanotubes and its application to electron sources.* Carbon, 2000. **38**(2): p. 169-182.
15. Musatov, A.L., et al., *Field electron emission from nanotube carbon layers grown by CVD process.* Applied Surface Science, 2001. **183**(1–2): p. 111-119.
16. Chernozatonskii, L.A., et al., *Carbon crooked nanotube layers of polyethylene: Synthesis, structure and electron emission.* Carbon, 1998. **36**(5–6): p. 713-715.
17. Saito, Y., et al., *Field emission of carbon nanotubes and its application as electron sources of ultra-high luminance light-source devices.* Physica B: Condensed Matter, 2002. **323**: p. 30-37.
18. Thongtem, S., et al., *Growth of carbon nanoflowers on glass slides using sparked iron as a catalyst.* Materials Science and Engineering: A, 2006. **423**(1–2): p. 209-213.
19. Dillon, A.C., et al., *Continuous Hot Wire Chemical Vapor Deposition of High-Density Carbon Multiwall Nanotubes.* Nano Letters, 2003. **3**: p. 1425-1429.
20. Chiashi, S., et al., *Cold wall CVD generation of single-walled carbon nanotubes and in situ Raman scattering measurements of the growth stage.* Chemical Physics Letters, 2004. **386**(1–3): p. 89-94.
21. Okamoto, A. and H. Shinohara, *Control of diameter distribution of single-walled carbon nanotubes using the zeolite-CCVD method at atmospheric pressure.* Carbon, 2005. **43**(2): p. 431-436.
22. Nishide, D., et al., *Growth of single-wall carbon nanotubes from ethanol vapor on cobalt particles produced by pulsed laser vaporization.* Chemical Physics Letters, 2004. **392**(4–6): p. 309-313.
23. Maruyama, S., et al., *Low-temperature synthesis of high-purity single-walled carbon nanotubes from alcohol.* Chemical Physics Letters, 2002. **360**(3–4): p. 229-234.
24. Okazaki, T. and H. Shinohara, *Synthesis and characterization of single-wall carbon nanotubes by hot-filament assisted chemical vapor deposition.* Chemical Physics Letters, 2003. **376**(5–6): p. 606-611.
25. Du, C. and N. Pan, *CVD growth of carbon nanotubes directly on nickel substrate.* Materials Letters, 2005. **59**(13): p. 1678-1682.
26. Park, D., Y. Hoon Kim, and J. Kee Lee, *Synthesis of carbon nanotubes on metallic substrates by a sequential combination of PECVD and thermal CVD.* Carbon, 2003. **41**(5): p. 1025-1029.
27. Hsieh, J.H., et al., *Plasma cleaning of copper leadframe with Ar and Ar/H2 gases.* Surface and Coatings Technology, 1999. **112**(1–3): p. 245-249.
28. Nishimura, A., S. Kawai, and G. Murakumi, *Effect of Lead Frame Materials on Plastic-Encapsulated IC Package Cracking Under Temparature Cycling* IEEE Trans. Comp. Hybrids., 1989. **12**: p. 639-645.
29. Belkind, A. and S. Gershman, *Plasma Cleaning of Surface.* Vacuu Technology and Coating, 2008.
30. *Korner, N., et al., Hydrogen plasma chemical cleaning of metallic substrates and silicon wafers. Surface and Coatings Technology, 1995.* ***76–77, Part 2****(0): p. 731-737.*

Effect of Reactive Gas-timing on Physical and Chemical Corrosion Property of Ta_2O_5 Thin Film Grown by R.F. Magnetron Sputtering

N. Khemasiri[1,5], S. Porntheeraphat[2 *], D. Phromyothin[1], W. Bunjongpru[1,3],
S. Pratontep[1], and J. Nukeaw[1,4,5]

[1]College of Nanotechnology, King Mongkut's Institute of Technology Ladkrabang, Chalongkrung Rd., Ladkrabang, Bangkok 10520, Thailand
[2]Photonic Technology Laboratory, National Electronics and Computer technology Center, National Science and Technology Development Agency, Patumthani 12120, Thailand
[3]Thai Microelectronic Center, National Electronics and Computer technology Center, National Science and Technology Development Agency, Chacheungsao 14000, Thailand
[4]ThEP Center, CHE, 328 Si Ayutthaya Rd., Bangkok 10400, Thailand
[5]Nanotec-KMITL Center of Excellence on Nanoelectronic Devices, Chalongkrung Rd., Ladkrabang, Bangkok 10520, Thailand
**Corresponding author. E-mail: Tonnam@nectec.or.th*

Abstract

Thetantalum oxide (Ta_2O_5) thin films with thickness of 200 nm have been prepared on p-type silicon (100) wafer and quartz substrates by reactive r.f magnetron sputtering with our patented technique called "reactive gas-timing" without any substrate heating or post annealing. The reactive gas-timing as an on-off time-sequence control between argon and oxygen plasma (Ar:O) during sputtering process of 2:5 and 2:1 sec was used. X-ray diffraction (XRD), Atomic Force Microscope (AFM), UV-Visible spectrometer (UV-Vis), Potentiostat and Galvanometer were carried out to determine the crystallization, surface morphology, optical and chemical corrosion properties, respectively. The XRD result shows amorphous phase of the sputtered 200 nm Ta_2O_5 thin film. The very smooth surfaces with very low roughness of the deposited Ta_2O_5 thin films are revealed from AFM. The gas-timing sequence of Ar:O = 2:5 sec yielded a sputtered film to more less roughness than 2:1 sec. UV-Vis spectrum shows that the prepared Ta_2O_5 thin films have more than 90% of transparent and the absorption edge at 300 nm. The gas-timing sequence of Ar:O = 2:5 sec affected a sputtered film to higher transparent than 2:1 sec. The chemical corrosion measurement demonstrates a high anti-corrosion efficiency of the sputtered-Ta_2O_5 thin films. All sputtered-Ta_2O_5 samples were set as working electrode that was immersed in 1M of NaOH, HCl and H_2SO_4 electrolyte, respectively. The experiment results revealed that the reactive gas-timing technique plays the importance role on the corrosion property of Ta_2O_5 thin film. The Ta_2O_5 thin film grown with Ar:O gas-timing sequence of 2:5 sec has a better corrosive resistance than 2:1 sec, especially in NaOH electrolyte.

Keywords: Tantalum oxide (Ta_2O_5), reactive gas-timing, RF magnetron sputtering

Introduction

Many wonderful features of tantalum oxide (Ta_2O_5) have been interested in many applications such as anti-chemical corrosion layer[1]. Bioimplant, photocatalyic[2], solar cell, capacitor, electrochromic devices[3], biosensor, pH sensing membrane[4] due to the stability in chemical and thermal, high dielectric constant, high reflective index, wide energy gap and biocompatibility material which depends on deposition condition and process. Included corrosion resistance makes an advantage for tantalum oxide than other sensitive membrane material as silicon nitride (Si_3N_4), silicon oxide (SiO_2) and silicon carbide (SiC) especially, in strong alkali solution.

Various technique and system were carried out to prepare Ta_2O_5 thin film as chemical vapor deposition (CVD)[5], pulsed laser deposition (PLD)[6], atomic layer deposition (ALD)[7], cathodic arc deposition[8], D.C. magnetron sputtering[9]. In this work Ta_2O_5 films were deposited by r.f. magnetron sputtering with our patented call reactive gas-timing technique (US200900226065) which successfully deposited indium nitride (InN) at room temperature with a high crystalline quality[10]. Furthermore the reactive gas-timing technique can vary composition in the films.

However technique the r.f. magnetron sputtering parameter such as r.f. generator power, base pressure, substrate glancing angle, target to substrate distance and gas flow rate can be adjusted to improve microstructure, electrical, chemical and optical properties. In this work we focus on the chemical corrosion property of the Ta_2O_5 films sputtered by r.f. magnetron sputtering included reactive gas-timing technique. The physical properties of the sputtered films were characterized by the X-ray diffraction (XRD), the atomic force microscope (AFM), the Uv-visible spectrophotometer (Uv-vis). The sputtered films with 2 cm^2 surface area were immersed in various corrosive electrolytes for determination corrosion resistance by potentiostat and galvanometer.

Experiment

Tantalum Oxide thin films deposition and characterization

Tantalum Oxide films deposited on Quartz and glass slide substrates by reactive gas-timing magnetron sputtering of Tantalum metal target with 99.95% purity; Krut. J. The substrates were ultrasonically cleaned in acetone, Isopropanol alcohol and Di water, respectively to remove an organic stain and else on substrate’s surface and then re-hydrated in oven at 100 degree Celsius for 15 minutes. The chamber was pumped down to $2x10^{-6}$mBar by cooperated between rotary pump and diffusion pump. Before sputtering process Tantalum target was pre-sputtered in argon plasma in 15 minutes at 120W for removing oxide-contaminated on metal surface. The fixed gas-timing sequentially on-off between argon and oxygen fed into the chamber (show in figure 1) controlled by external program the other parameter shows in table 1.The crystallinity, optical property and surface morphology characterization was examined by X-ray diffractometer(Bruker, D8 Advance using Cu Ka with the radiation wavelength 0.154056 nanometer), UV-Vis spectrophotometer with a single beam (Thermo electron corporation, Heliosa) and Atomic force Microscope (Seiko, SPA-400)

Table 1: RF Magnetron Sputteringparameters for deposition Ta_2O_5 films

Parameters	**Conditions**
Target	*Tantalum (Ta) 99.95%*
RF Generator Power	*200 W*
Base Pressure	*$2x10^{-6}$mBar*
Gas-timing (Ar : O_2)	*2 : 1 , 2 : 5 second*
Argon flow rate	*8 sccm*
Oxygen flow rate	*6.5 sccm*
Film Thickness	*200 nm*

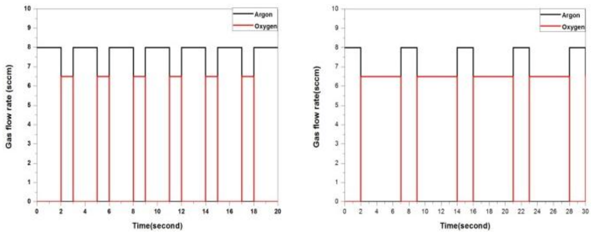

A B

Figure1.shows a diagram of argon-oxygen timing;
A. 2 : 1 sec and B. 2 : 5 sec

Chemical corrosion Test

To investigate the chemical corrosion of oxide films in various electrolytes, Poteniostat and Galvanometer (Autolab PGSTAT 302) was performed. Platinum wire and Ag/AgCl electrode served as the counter electrode and reference electrode, respectively. The tantalum oxide thin filmswhich 2 cm^2 surface area used as the working electrode. The electrodes were immersed in to the corrosive electrolyte using NaOH, HCl and H_2SO_4 , respectively.

The system was controlled by NOVA 1.6 version that voltage bias from -1 V. to 0 V. at 0.05 volt step resolution. The measure period was 90 minute after immersed in 50 ml of corrosive electrolyte. All experiments were carried out at 25 degree Celsius.

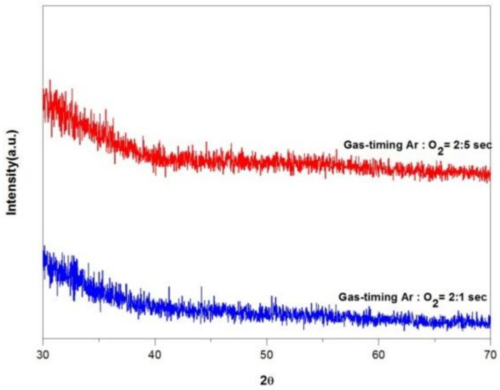

Figure 2. Shows XRD patterns of gas-timing sputterd Ta_2O_5 films; Ar : O_2 = 2:1 and 2:5 sec

Results and discussion

Crystallization

Well-known and basic technique have been usually used to indentify and determine the crystallization of films is X-ray driffractrometer. Form figure 1 shows no any presented peak in scanned range 30^0 to 70^0 refers to all films are amorphous[11]. According to our conditions has been deposited at low temperature without any heated whereas polycrystalline of Ta_2O_5; orthorohmbic and hexagonal structure requires at high temperature around 500 deegree celsius up.S.V. JagadeeshChandra and Chel-JongChoi have reported a transition from amorphous to orthorohmbic structure Ta_2O_5 by post-annealing at least 673 degree kelvin[12]. Hsyi-En Cheng and Chien-Tang Mao have reported polycrystalline Ta_2O_5 by substrate treatment at least 400 degree celsius [13]

Surface Morphology

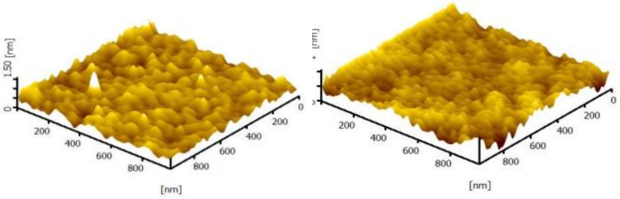

A B

Figure 3. shows surface morphology of gas-timing sputterd Ta_2O_5 films; A. 2:1 secand B. 2:5 sec.

In figure 2 demostrates the surface morphology of the sputtered films with 1 μm^2 scaned area. The smooth surface and crackless spot was shown with the root mean square roughness(RMS) 0.6307 nm and 0.107 nm of the 2:1 and 2:5 sec sputtered films, respectively. Smooth feature of the sputtered Ta_2O_5 films may cause by the amorphous orientation of the films as result is agreeable to previous XRD patterns showed the films are amorphous. Shih-jehJimmyWu et all have reported the roughness of amorphous Ta_2O_5 films at 0.547 nm deposited by r.f. magnetron sputtering system [14]. According to decrease of the roughness from 0.6307 nm to 0.107 nm and particle size trend to smaller with increasing oxygen timing from 1 sec to 5 sec, respectively.

Optical property

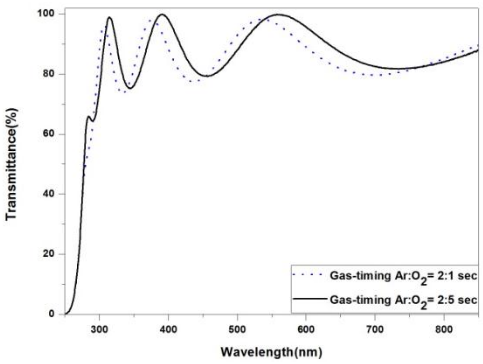

Figure4. shows the transmittance of gas-timing sputtered Ta_2O_5 films

Figure 3 shows the optical property of the sputtered Ta_2O_5 films deposited at different oxygen gas-timing sequence was measured at wavelength range from 250 to 850 nm. The green-yellow light reflected films have the transmittance close to 95% to 98%. Considering to the sputtered films at 2:5 sec ratio is transparent than sputtered 2:1sec ratio films cause by surface roughness and oxygen vacancies. Referred to AFM image the sputtered 2:5 sec films are lower surface roughness around 0.1015 nm which lower roughness can reduce the scattered visible light consequently the transmittance gets higher. According to sputtering conditions, at increasing oxygen timing the films completely forms to Ta_2O_5 with lower oxygen vacancies result to lower point defect that reduces light absorption in the film which makes the higher transmittance.

Chemical Corrosion

Effect of NaOH concentrations

The corrosion potential was determined in 2 divisions. Firstly, comparision the corrosive tolorance of 2:1 sec sputterd Ta_2O_5 film and 2:5 sec sputterd Ta_2O_5 film in alkali electrolyte. Secondly, an concentrated effect of 1M and 5M NaOH.

The corrosion potential of 2:1 second sputterd Ta_2O_5 film exhibited -261.69 mV and -121.61 mV whereas 2:5 sec sputterd Ta_2O_5 film shown -202.71 mV and-150.54 mV in 1M and 5M NaOH, respectively. Compared the corrosive resistance of 2:5 second sputtered film can tolarable corroded better than at 2:1 second sputtered film as a result of surface area. According to AFM image 2:5 second sputtered film is smoother surface makes low surface area in corrosive electrolyte which surface area is an important factor of chemical reaction.

In cause of various concentration, the corrosion potential decreases when increasing NaOH concentration owing to high concentration reveal to low ion mobility so detected ion decreased.

An effect of corrosive electrolytes

Gas-timing 2:1 sec Ta_2O_5		Gas-timing 2:5 sec Ta_2O_5	
Electrolyte	Potential(mV)	Electrolyte	Potential(mV)
NaOH	-261.69	NaOH	-202.71
H_2SO_4	-53.78	H_2SO_4	-53.25
HCl	-133.47	HCl	-82.60

Table2. The corrosive potential in 1M corrosive electrolyte

In Table 2 exhibits the corrosive potential in 1M of various corrosive electrolytes NaOH, H_2SO_4 and HCl. The corrosion potential of sputtered Ta_2O_5 films with 2:1 sec ratio is -261.69 mV, -53.78 mV and -133.47 mV ,whereas the corrosion potential of the sputtered Ta_2O_5 films with 2:5 sec ratio are -202.71 mV, -53.25 mV and -82.60 mV (vs Ag/AgCl) in NaOH, H_2SO_4, and HCl, respectively. We classified to determine in 2 factors; Firstly, a comparison of the corrosive tendency in difference corrosive electrolytes according to NaOH and H_2SO_4 demonstrates the corrosive potential in alkali is more negative than in acid. It was indicated that the sputtered films could be tolerably corrosion in strong acid better than strong alkali that are corresponded to literature. Secondly in strong acid exhibits the nearby corrosive potential of both the sputtered films in H_2SO_4 electrolyte. It could be implied that gas-timing ratio is not affected to the corrosion in H_2SO_4. Where the corrosive potential in HCl electrolyte of both the sputtered films is similarly higher than in H_2SO_4 electrolyte which due to Cl^- ion had an effect to tantalum atom as Takanori Hino et al have reported the effect of Cl^- ion on pitting corrosion of Ta_2O_5 films[15].

Conclusions

This article is displayed the effect of the gas-timing control of reactive gas (Ar:O) during the sputtering process on the properties of Ta_2O_5 thin films. The sputtered Ta_2O_5 as amorphous thin films grown at Ar:O gas-timing sequence of 2:5 sec was revealed the higher smooth surface, transparent and corrosive resistance than at 2:1 sec. It can imply that the reactive gas-timing technique plays the importance role in thin film sputtering process as shown in our experiment.

Acknowledgment

This work has partially been supported by the National nanotechnology Center (NANOTEC), NSTDA, Ministry of Science and Technology, Thailand, through its program of Center of Excellence Network.

References

1. Y.-S. Sun, J.-H.Chang, and H.-H. Huang, “Corrosion resistance and biocompatibility of titanium surface coated with amorphous tantalum pentoxide,” *Thin Solid Films*, vol. 2011, no. 6.
2. K. J. Kumar, N. R. C. Raju, and A. Subrahmanyam, “Properties of pulsed reactive DC magnetron sputtered tantalum oxide (Ta2O5) thin films for photocatalysis,” *Surface and Coatings Technology*, vol. 205, Supplement 2, no. 0, pp. S261–S264, Jul. 2011.
3. S.-C. Wang, K.-Y.Liu, and J.-L. Huang, “Tantalum oxide film prepared by reactive magnetron sputtering deposition for all-solid-state electrochromic device,” *Thin Solid Films*, vol. 520, no. 5, pp. 1454–1459, Dec. 2011.
4. T. Mikolajick, R. Kühnhold, and H. Ryssel, “The pH-sensing properties of tantalum pentoxide films fabricated by metal organic low pressure chemical vapor deposition,” *Sensors and Actuators B: Chemical*, vol. 44, no. 1–3, pp. 262–267, Oct. 1997.
5. N. Ndiege, V. Subramanian, M. A. Shannon, and R. I. Masel, “Rapid synthesis of tantalum oxide dielectric films by microwave microwave-assisted atmospheric chemical vapor deposition,” *Thin Solid Films*, vol. 516, no. 23, pp. 8307–8314, Oct. 2008.
6. X. He, J. Wu, X. Li, X. Gao, L. Wu, L. Zhao, X. Gan, and F. Zhuge, “Characterization of high quality tantalum pentoxide film synthesized by oxygen plasma enhanced pulsed laser deposition,” *Thin Solid Films*, vol. 518, no. 1, pp. 94–98, Nov. 2009.
7. A. Lintanf-Salaün, A. Mantoux, E. Djurado, and E. Blanquet, “Atomic layer deposition of tantalum oxide thin films for their use as diffusion barriers in microelectronic devices,” *Microelectronic Engineering*, vol. 87, no. 3, pp. 373–378, Mar. 2010.
8. B. Díaz, J. Światowska, V. Maurice, M. Pisarek, A. Seyeux, S. Zanna, S. Tervakangas, J. Kolehmainen, and P. Marcus, “Chromium and tantalum oxide nanocoatings prepared by filtered cathodic arc deposition for corrosion protection of carbon steel,” *Surface and Coatings Technology*, vol. 206, no. 19–20, pp. 3903–3910, May 2012.
9. S. V. J. Chandra, S. Uthanna, and G. M. Rao, “Effect of substrate temperature on the structural, optical and electrical properties of dc magnetron sputtered tantalum oxide films,” *Applied Surface Science*, vol. 254, no. 7, pp. 1953–1960, Jan. 2008.
10. S. Porntheeraphat and J. Nukeaw, “Photomodulated reflectance study on optical property of InN thin films grown by reactive gas-timing rf magnetron sputtering,” *Applied Surface Science*, vol. 254, no. 23, pp. 7851–7854, Sep. 2008.
11. O. A. Azim, M. M. Abdel-Aziz, and I. S. Yahia, “Structure and optical analysis of Ta2O5 deposited on infrasil substrate,” *Applied Surface Science*, vol. 255, no. 9, pp. 4829–4835, Feb. 2009.
12. S. V. Jagadeesh Chandra, C.-J. Choi, S. Uthanna, and G. Mohan Rao, “Structural and electrical properties of radio frequency magnetron sputtered tantalum oxide films: Influence of post-deposition annealing,” *Materials Science in Semiconductor Processing*, vol. 13, no. 4, pp. 245–251, Dec. 2010.
13. H.-E. Cheng and C.-T. Mao, “The effect of substrate temperature on the physical properties of tantalum oxide thin films grown by reactive radio-frequency sputtering,” *Materials Research Bulletin*, vol. 38, no. 14, pp. 1841–1849, Nov. 2003.
14. S. J. Wu, B. Houng, and B. Huang, “Effect of growth and annealing temperatures on crystallization of tantalum pentoxide thin film prepared by RF magnetron sputtering method,” *Journal of Alloys and Compounds*, vol. 475, no. 1–2, pp. 488–493, May 2009.
15. T. Hino, M. Nishida, and T. Araki, “Effect of Droplets on Corrosion Resistance of Tantalum

Oxide Films Fabricated by PLD," *Journal of Laser Micro/Nanoengineering*

Effect of Surfactant on Prepared Polystyrene-iron Oxide Composite Nanoparticles

T. Rutirawut[*], A. Sinsarp, K. Tivakornsasithorn, T. Srikhirin, and T. Osotchan

Capability Building Unit for Nanoscience and Nanotechnology and Department of Physics, Faculty of Science, Mahidol University, 272 Rama VI Road Ratchathewi Bangkok 10400, Thailand
[*]*Corresponding author. E-mail: teerapat.ruti@gmail.com*

Abstract

Fabricating metal or metal oxide into a polymer nanoparticle has been attracted in recent years as a simplified method to modify their physical and chemical properties. This research focuses on synthesizing ferromagnetic iron oxide powder and then encapsulating with nonmagnetic polymer nanoparticles. The co-precipitation method of ferric ($FeCl_36H_2O$) and ferrous ($FeCl_34H_2O$) was used to prepare the iron oxide powder in water based solution. Sodium dodecyl benzene sulfonate (SDBS), using as a surfactant, and oleic acid (OA) were added to modify the surface of iron oxide powder to be compatible with polystyrene (PS) in the nano-encapsulating process. X-Ray Diffraction (XRD) pattern were analyzed to determine the crystal structure of iron oxide nanoparticles. The XRD pattern shows d-spacing close to those of both magnetite (Fe_3O_4) and maghemite (γ-Fe_2O_3). However, the relative diffraction intensity between peaks of d=2.52 Å and d=1.48 Å indicates that the maghemite is dominated in our samples. The PS-iron oxide composite nanoparticles are synthesized by emulsion polymerization of styrene and methyl methacrylate at the temperature of 70°C. The particles size and morphology were observed by Transmission Electron Microscopy. The iron oxide powder has a diameter of 2- 15 nm with irregular shape. The PS-iron oxide nanoparticles have a diameter in the range of 160-400 nm. Only encapsulate in the nanoparticles with diameter above 220 nm showed iron oxide incorporate in the nanoparticles. Furthermore, the sequence of adding surfactant in surface modification step played a major role on achieving two distinct morphologies types of composite nanoparticle. The iron oxide powder was attached on a polystyrene nanoparticle surface if the SDBS and OA were mixed first. In case of the SDBS was firstly added, the iron oxide nanoparticles occur as clumps within the polystyrene nanoparticles. The permanent magnet was used to sort the magnetic composite nanoparticles out from nonmagnetic particles. The nonmagnetic nanoparticles have a narrow diameter range of 160-180 nm and can also be compressed to show the photonic crystal effect in a liquid phase.

Keywords: Composite nanoparticles, co-precipitation, polymerization, surfactant, iron oxide

Introduction

A process for the synthesis of magnetic colloids for controllable PCs was reported by Asher et al. [1]. The polystyrene (PS)-iron oxide composite colloidal particles synthesized by the emulsion polymerization were highly charged, monodisperse and superparamagnetic at room temperature. For building magnetic controllable photonic crystals (PCs) with wide tuning ranges, instant response with low applied magnetic field, the magnetic controllable PCs with high magnetic content were developed by Yin et al. [2]. They developed a high-temperature hydrolysis reaction process for the synthesis of superparamagnetic colloidal nanocrystal clusters (CNCs) uniform consist of three-dimension aggregate of iron oxide nanocrystals, with average diameter tunable from ~30 nm to 180 nm [3-5]. Each cluster composed of many interconnected iron oxide nanocrystals of ~10 nm. Due to the high-temperature hydrolysis method in preparing magnetic CNCs needed very careful control reaction conditions [6], a simple method for producing magnetic colloids was reported by Liu et al. [7]. The oleic acid (OA) emulsion droplets containing OA-capped iron oxide colloidal nanoparticles were developed by emulsion droplet showed superparamagnetic behavior with high magnetic loading fraction. The superparamagnetic iron oxide core nanoparticles were prepared by using chemical co-precipitation reaction. The OA-capped iron oxide emulsion was synthesized by mixing of OA and iron oxide nanoparticles in deionized water.

Materials and Methods

Synthesis of iron oxide nanoparticles

The iron oxide nanoparticles can be prepared by the co-precipitation of ferric ($FeCl_36H_2O$) and ferrous ($FeCl_34H_2O$) in 1.0 M ammonium hydroxide solution (NH_4OH). A 10.8 g portion of $FeCl_36H_2O$ and 4.0 g $FeCl_34H_2O$ are dissolved in 50 ml of deionized water. The resulting solution is poured with vigorous stirring into 500 ml of a 1.0 M NH_4OH solution. These iron oxide precipitated colloid is transferred to 500 ml of a 1.0 M tetra methyl ammonium hydroxide (TMAOH) by collecting with a permanent magnet. After that, 6.3 g of oleic acid (OA) liquid and 1.0 g of sodium dodecyl benzene sulfonate (SDBS) are added to modify the iron oxide colloid surface.

Synthesis of PS-iron oxide nanoparticles

PS-iron oxide composite colloids are synthesized by emulsion polymerization of styrene (St) and methyl methacrylate (MMA) by using a reaction vessel that contained a reflux condenser. The reaction vessel containg 180 mL of deionized water and 20 mL of the above nanosize iron oxide is deoxygenated for 30 min. A 3.0 mL portion of MMA and 30 mL of St are added. A nitrogen atmosphere and a stirring rate of 350 rpm are maintained throughout the polymerization. The temperature of reaction vessel is increased to 70°C when a 0.2 g of sodium styrene sulfonate (NaSS) is added to be as a surfactant and 2.0 g of ammonium persulfate (APS) is added to initiate the polymerization. The polymerization process is achieved for 5 h.

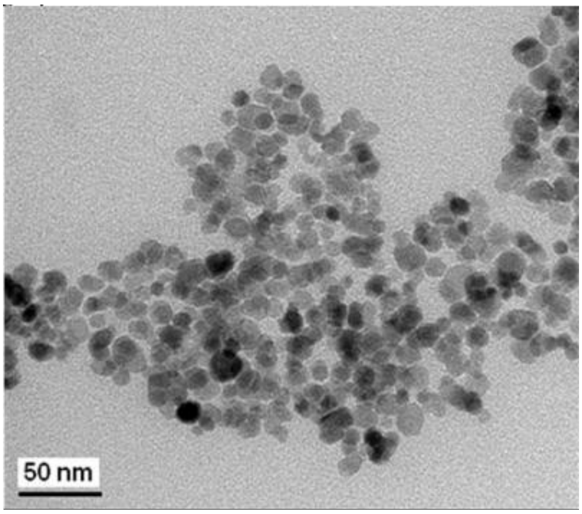

Figure 1. TEM image of synthesized iron oxide nanoparticles by OA and SDBS surfactants with diameter varies from 2-15 nm

Characterization of nanosize iron oxide and PS-iron oxide composite nanoparticles

Morphology and size of the nanoparticles are characterized by using a transmission electron microscope (TEM) operated at 120 kV. The nanoparticles dispersed in water cast onto a Formvar-coated copper grid at room temperature. Crystal structure is measured on a Bruker D8 Advance X-ray Diffractometer (XRD) with a $Cu_{K\alpha}$ radiation (λ=15402 Å). The data are collected from 2θ = 20-70° at a scan rate of 0.05 per step and 10 s per point.

Results and Discussion

The particles size and morphology were observed by Transmission Electron Microscopy. The iron oxide powder has a diameter of 2- 15 nm with irregular shape.

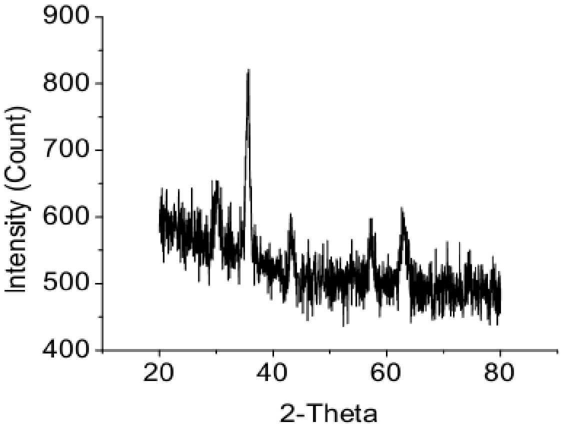

Figure 2. XRD pattern of synthesized iron oxide nanoparticles. XRD peaks of magnetite and maghemite occur at d=2.52 Å (2θ=35.7^o) and d=1.48 Å (2θ=62.8^o), respectively.

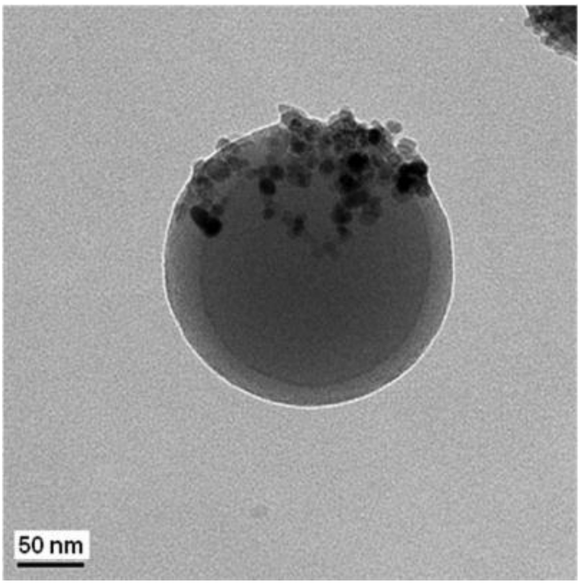

Figure 3. TEM image of synthesized PS-iron oxide composite nanoparticles by firstly mixing OA and SDBS surfactants then adding to the iron oxide nanoparticle before polymerization. This indicates that the iron oxide distributes only on surface of PS nanoparticles.

X-Ray Diffraction (XRD) pattern were analyzed to determine the crystal structure of iron oxide nanoparticles. The XRD pattern shows d-spacing close to those of both magnetite (Fe_3O_4) and maghemite (γ-Fe_2O_3). However, the relative diffraction intensity between peaks of d=2.52 Å and d=1.48 Å indicates that the maghemite is dominated in our samples.

The PS-iron oxide nanoparticles have a diameter in the range of 160-400 nm. Only encapsulate in the nanoparticles with diameter above 220 nm showed iron oxide incorporate in the nanoparticles. Furthermore, the sequence of adding surfactant in surface modification step played a major role on achieving two distinct morphologies types of composite nanoparticle. The iron oxide powder was attached on a polystyrene nanoparticle surface if the SDBS and OA were mixed first. In case of the SDBS was firstly added, the iron oxide nanoparticles occur as clumps within the polystyrene nanoparticles.

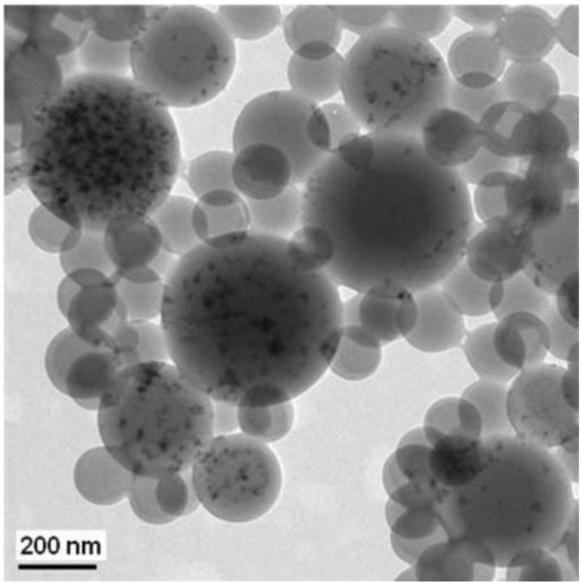

Figure 4. TEM image of synthesized PS-iron oxide composite nanoparticles by firstly adding SDBS surfactant then later adding OA surfactant to the iron oxide nanoparticle before polymerization. It indicates that iron oxide is corporate inside PS nanoparticle.

Conclusions

The synthesized iron oxide powder has a diameter of 2- 15 nm with irregular shape. The PS-iron oxide nanoparticles have a diameter in the range of 160-400 nm. The permanent magnet was used to sort the magnetic composite nanoparticles out from nonmagnetic particles. The nonmagnetic nanoparticles have a narrow diameter range of 160-180 nm and can also be compressed to show the PC effect in a liquid phase.

Only encapsulate in the nanoparticles with diameter above 220 nm showed iron oxide incorporate in the nanoparticles. The two distinct morphologies types of composite nanoparticle were found with the different sequence of adding surfactant in surface modification step. The iron oxide powder was attached on a polystyrene nanoparticle surface if the SDBS and OA were mixed first. In case of the SDBS was firstly added, the iron oxide nanoparticles occur as clumps within the polystyrene nanoparticles.

Acknowledgments

This work was partially support by National Nanotecnolygy Center, National Science and Technology Development Agency, Mahidol University. One of the author would like to acknowledge the Development and Promotion of Science and Technology Talents Project (DPST) for scholarship.

References

1. X. L. Xu, G. Friedman, K. D. Humfeld, S. A. Majetich, S. A. Asher, “Synthesis and Utilization of Monodisperse Superparamagnetic Colloidal Particles for Magnetically Controllable Photonic Crystals”, Chem. Mater. **14** (2002) 1249.
2. J. Ge, Y. Hu, Y. Yin, “Highly Tunable Superparamagnetic Colloidal Photonic Crystals”, Angew. Chem. Int. Ed. **46** (2007) 7428.
3. J. Ge, Y. Hu, M. Biasini, W. P. Beyermann, Y. Yin, “Superparamagnetic Magnetite Colloidal Nanocrystal Clusters”, Angew. Chem. **119** (2007) 4420.
4. J. Ge, Y. Yin, “Magnetically Tunable Colloidal Photonic Structures in Alkanol Solutions”, Adv. Mater. **20** (2008) 3485.
5. J. Ge, L. He, J. Goebl, Y. Yin, “Assembly of Magnetically Tunable Photonic Crystals in Nonpolar Solvents”, J. Am. Chem. Soc. **131** (2009) 3484.

6. Xia H., Zhang L., Chen Q.D., Guo L., Fang H.H., Li X.B., “Band-Gap-Controllable Photonic Crystals Consisting of Magnetic Nanocrystal Clusters in a Solidified Polymer Matrix”, J. Phys. Chem. C **113** (2009) 18542.

7. H. Xia, B. Xu, H. Zhang, L. Zhang a, X. Liu, “Tunable Photonic Crystals from Emulsion Containing Magnetic Nanoparticles”, Mater. Lett. **66** (2012) 29-32.

Fabrication and Characterization Anodized Titania Nanotubes for Enhancing Hydrogen Generation

B. Samran[1], P. Krongkitsiri [2], T. Saipin[3], S. Wantawee[1], S. Budngam[1],
and U. Tipparach[1*]

[1]Department of Physics, Ubon Ratchathani University, Ubon Ratchathani 34190 Thailand
[2]Department of Science and Mathematics, Faculty of Industry and Technology, Rajamangala University of Technology Isan, Phangkon, Sakonnakon, 47160, Thailand
[3]Department of Arts and Sciences, Ubon Ratchathani Technical College, Mueang District, Ubon Ratchathani Province 34000 Thailand
**Corresponding author. E-mail: ut007@hotmail.com*

Abstract

Titania nanotubes (TiO_2 NTs) photoanodes were fabricated by means of anodization method. The electrolytes were the mixtures of oxalic acid ($H_2C_2O_4$), ammonium fluoride (NH_4F), and sodium sulphate(VI) (Na_2SO_4) with different pHs. A constant dc power supply at 20 V was used as anodic voltage. The samples were annealed at 450 °C for 2 hours. The resultant products were characterized by Scanning Electron Microscopy (SEM) and X-ray diffraction (XRD) to determine their microstructure. TiO_2 NTs with diameter of 100 nm were obtained when the electrolyte consisting of 0.08 M oxalic acid, 0.5 wt% NH_4F, and 1.0 wt% Na_2SO_4 with pH 3 was used. Without external applied potential, the maximum photocurrent density was 2.77 mA/cm^2 under illumination of 100 mW/cm^2.

Keywords: Titania nanotubes, TiO_2, anodization, Hydrogen production, renewable energy

Introduction

Direct conversion of sunlight to chemical energy in the form of hydrogen to be used as a renewable energy is an ultimate goal of scientific and technological interests which solutions may be feasible importance as a renewable source of sustainable and environmentally energy for next generations. Photoelectrolysis of water to produce hydrogen (H_2) has attracted attention due to the depletion of fossil fuels and global warming. The photocatalytic evolution of H_2 and O_2 from water occurs when a photocatalytic agent with appropriate band gap is illuminated by sufficiently energetic light. Honda and Fujishima [1] demonstrated the process of electrochemical photolysis of water using semiconductor TiO_2 as a working anode. Since then, a large number of semiconductor materials have been employed for photoanodes, also called working anodes for hydrogen production. All of semiconductor materials, TiO_2 and modified structure TiO_2 are widely used because they are highly photocatalytic, stable, abundant, and environmentally safe [2].

The scientific principles for the hydrogen generation were established by Bockris and Uosaki in Bockris and Uosaki in 1976 [3], Bockris in 1980 [4], Bockris in 2003 [5], Bockris et al. in 1981 [6], Gerischer in 1977 [7], and Chandra in 1985 [8] and reviewed by numerous literatures e.g., by Linsebigler et al. in 1995 [9], Bak et al. in 2002 [10], and Nowotny et al. in 2007 [11]. Recently, most of efforts have been focused on nanostructured titania such as nanoparticles [12], nanoflims [13], and nanotubes [14-15] to increase water photo-splitting efficiency due to their high surface-to-volume ratios and size-dependent properties in hoping to increase energy conversion efficiecy. Nanostructured Titania may be synthesized by many methods [12-16] such as sol-gel, and anodization. Anodization has been one of the most popular in making Titania nanotubes (TiO_2 NTs). We have recently prepared mesoporous of TiO_2 electrodes by anodization [17]. It is believed that ability to control the structures of TiO_2 NTs can be expected to positively impact a variety of important technologies and the structures of TiO_2 NTs depend largely on many preparation parameters such as temperature, electrolytes, and anodic voltages. In this paper, we present the effect of electrolytes on the structures and photoelectrochemical properties of TiO_2 NTs for hydrogen production.

Materials and Methods

TiO_2 NTs were grown by anodization method at room temperature. Titanium sheet with 0.25 mm thick, 99.7% purity purchased from Sigma Aldrich were firstly polished by various abrasive papers. After polishing, polished Ti substrates were ultrasonically cleaned in the mixture of acetone and ethanol. The mixed electrolytes consisting of 1/12 M $C_2O_4H_2{\cdot}2H_2O$, 0.5 wt% NH_4F, and 1.0 wt% Na_2SO_4 with different pH values (3, 5, and 7) were used. The pH of the mixed electrolytes were adjusted by adding appropriate amount of 1 M H_2SO_4, or 1 M NaOH. Titanium substrate samples were anodized using home-made housing for the substrate. The system consists of a two-electrode configuration with a piece of highly pure platinum counter electrode. The configuration of the set up is shown in Fig. 1. This set up allows only one face of titaniun substrates contact with the electrolyte. The anodization process was carried on under a constant dc potential 20 V for 2 hrs. Then, anodized Ti substrates were rained by distilled water and dried in the flow of N_2 gas. All substrates were annealed at 450 ˚C for 2 hrs to obtain anatase crystalline phases of TiO_2 [13-16,]. The current and anodization time data were collected computer-controlled apparatus equipped by LabVIEW programming. To investigate the surface morphology and microstructure of TiO_2 NTs, all samples were characterized by SEM and XRD techniques. The determine optical bandgap and photocatalytic activity for water splitting of TiO_2 NTs the sample were characterized by UV-Vis and I-V curve measurement.

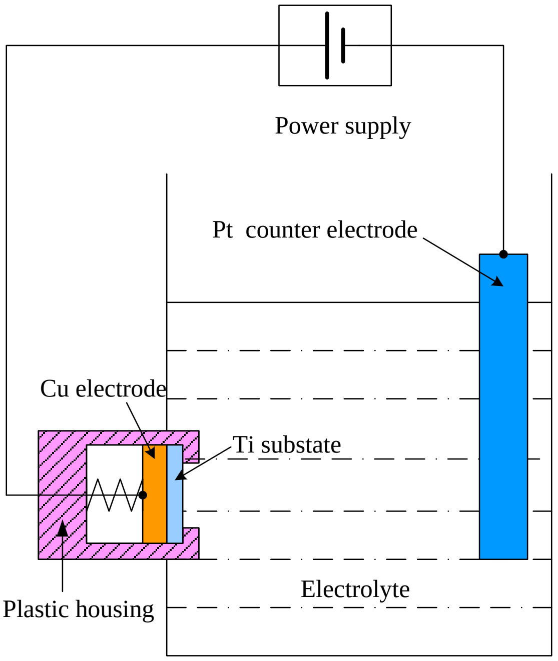

Figure 1. Experimental equipment diagram of one-face anodization for TiO_2 NTs

Results and Discussion

XRD patterns of Ti sheet and post annealed TiO_2 NTs are shown in Fig. 2. The XRD patterns show that the phases of TiO_2 NTs are anatase. The anatase (101) peak shows prominently when the anodization was carried out in the electrolyte with pH 3. The SEM images of post-annealed TiO_2 NTs grown in the different pH electrolytes are shown in Fig. 3. The morphology of the TiO_2 was found to be influenced by pH of the anodizing electrolyte. The prepared samples with the anodization in pH 5 and pH 7 electrolytes were the titania films with anatase phase.

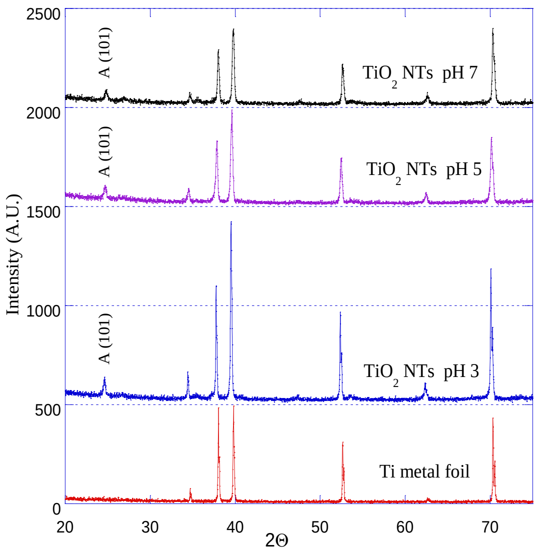

Figure 2. XRD patterns of post annealed TiO_2 NTs grown in the electrolytes with different pHs

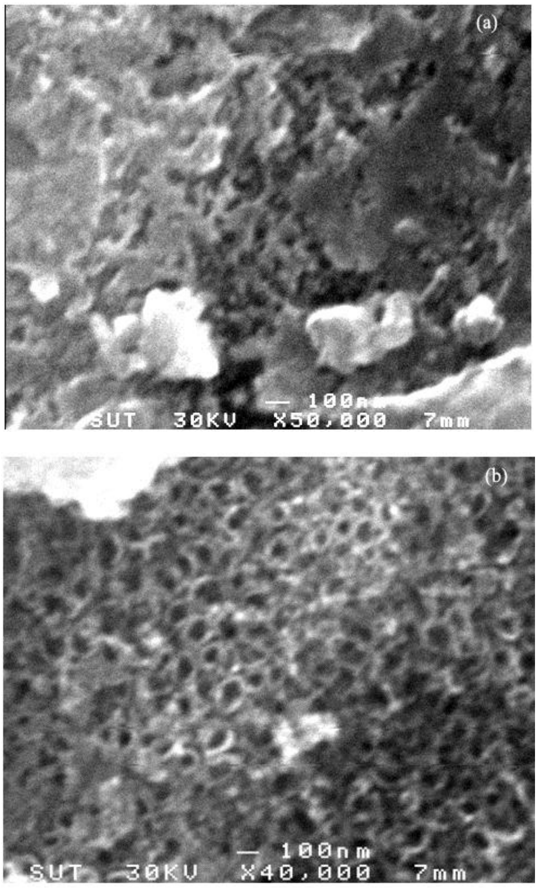

Figure 3. SEM images of TiO_2 NTs grown in the different pH electrolytes (a) pH 5 and (b) pH 3

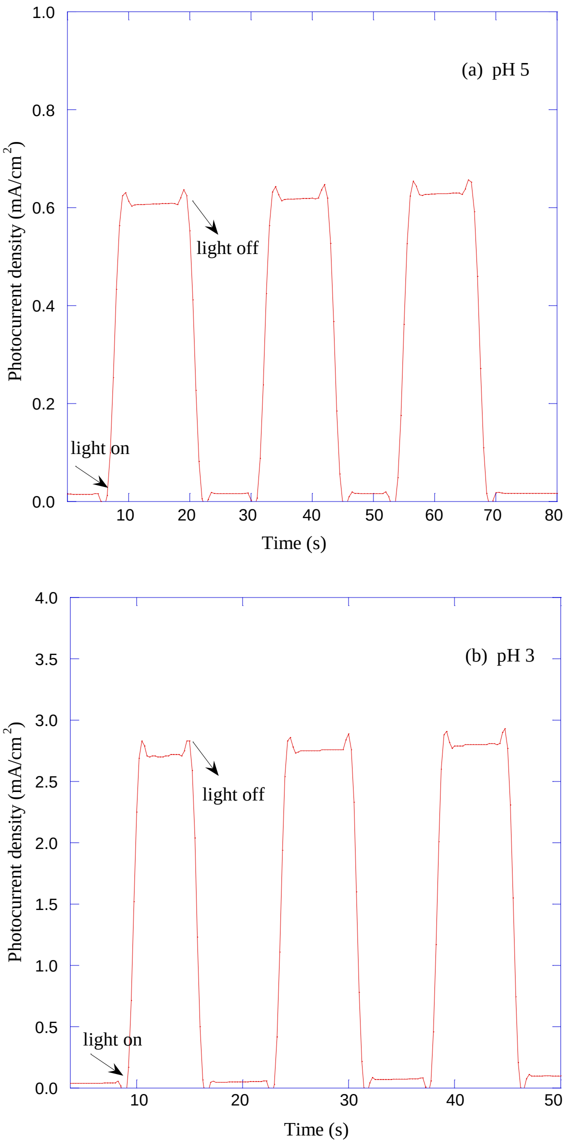

Figure 4. Photocurrent densities as a function of time under interrupted illumination of light of TiO_2 NTs working electrodes anodized in the different pH electrolytes (a) pH 7 and (b) pH 3

The TiO_2 NTs were not observed while the samples with anodization in pH 3 electrolyte showed clearly titania nanotubes (TiO_2 NTs) with diameters of about 100 nm.

Photoconversion efficiency of TiO_2 NTs was measured by a standard three-electrode cell at room temperature under the illumination of 100 mW/cm^2 in a 1 M KOH solution. The photocurrent response measurement was tested without external applied potential to investigate the photo-induced charge separation efficiency of the prepared photanodes and are shown in Fig. 4. When the light was turned on and irradiated the photoanode, the photocurrent rose up and kept constant during the light was on while the light was turned off, the photocurrent abruptly disappeared. This evident showed that the current came from the illumination. The photoconversion efficiency of water electrolysis was calculated based on the following relations [17-18],

$$\eta(\%) = \left(\frac{J\times E^0_{rev}}{I_0}\right)\times 100,$$

where J is the photocurrent density, $j\times E^0_{rev}$ is the total power output and I_0 is the power density of incident light and E^0_{rev} is the standard reversible potential which is 1.23V. The photocurrent densities of the photoanode prepared with pH 5 and pH 3 electrolytes after switchs were turned on were 0.60 mA/cm^2 and 2.77 mA/cm^2, respectively coresponding with the photocoversion efficiencies of 0.7 % and 3.4 %, respectively.

This photoconversion efficiency (3.4 %) of TiO_2 NTs photoanode is larger than that (0.8%) of nano-TiO_2 film photoanode made by sol-gel dip coating [13, 19]. The increase of photoconversion efficiency may be resulted from the fact that the surface areas of TiO_2 NTs are larger than those of nano-TiO_2 films due to the agglomeration of the small spherical crystals of nano TiO_2 crystals by nature [13]. Another reason may be due to the reduction of TiO_2 NTs optical bandgap energy because nitrogen from NH_4F used for making the electrolyte may incorporate the structure of TiO_2 NTs. It is well known that N-doped TiO_2 lowers the bandgap energy of TiO_2 [20, 21] leading to increase the utilization of sunlight spectrums and also increase photoactivity. This may be possible to identify the existence of nitrogen in the structure of TiO_2 NTs by X-ray photoelectron spectroscopy (XPS)**.**

Conclusions

We have synthesized TiO_2 NTs on titanium foils by anodization method in the mixtures of oxalic acid ($H_2C_2O_4$), ammonium fluoride (NH_4F), and sodium sulphate(VI) (Na_2SO_4) with different pHs. The post anodization process was carried out by anneaing in air at 450 °C for 2 hrs. The best condition for growing TiO_2 NTs was the electrolyte with pH 3. In this condition, the diameter of prepared TiO_2 NTs was about 100 nm. The phase of prepared TiO_2 NTs was predominantly anatase. The photocurrent response indicated that the photocurrent was the contribution of light irradiation on photoanode. The hydrogen can be produced with overall the photoconversion efficiency of 3.4 %.

Acknowledgments

The authors thank National Research Council of

Thailand (NRCT) and Thailand Research Fund (TRF) for funding. Sangworn Wantawee and Buagun Samran would like to thank Faculty of Science Ubon Ratchathani University for partially financial supports. One of the authors, Pacharee Krongkitsiri, would like to thank Department of Science and Mathematics, Faculty of Industry and Technology, Rajamangala University of Technology Isan, Phangkon, Sakonnakon Province for financial support and scholarship.

References

1. A. Fujishima and K. Honda, "Electrochemical photolysis of water at a semiconductor electron", Nature **238** (1972), 37.
2. M. Ni, K.H. Leung, Y.C. Leung, and K. Sumathy, "A review and recent developments in photocatalytic water splitting using TiO_2 for hydrogen production", Renewable and Sustainable Energy Reviews **11** (2007), 401.
3. J.O'M. Bockris, and K. Uosaki, "Photo-production of Hydrogen: Potential Dependence of the Quantum Efficiency as a Function of Wavelength", Energy **1** (1976), 143.
4. J.O'M. Bockris, in "Energy Options Real Economics and the Solar-Hydrogen System", Sydney, Australia & New Zealand Book Company, 1980.
5. J.O'M. Bockris, "On hydrogen futures: toward a sustainable energy system", International Journal of Hydrogen Energy, **28** (2003) 131.
6. J.O'M. Bockris, K. Uosaki, and H. Kita, "Modern Electrochemistry 2B", Applied Physics **52** (1981), 808.
7. H. Gerischer, in: The electrochemical cell, Edited by A. Heller (Ed.), The Electrochemical Society, Inc., Princeton, NJ 1977.
8. S. Chandra, "Photoelectrochemical solar cells", New York, Gordon & Breach, 1985.
9. A. L. Linsebigle, L. Guangquan and T. John, "Photocatalysis on TiO_2 Surface: Principles, Mechanisms, and Selected results", Chemical Reviews **95** (1995), 735.
10. T. Bak, J. Nowotny, M. Rekas, and C.C. Sorrell, "Photo-electrochemical hydrogen generation from water using solar energy", Hydrogen Energy **27** (2002), 991.
11. J. Nowotny, T. Bak, M.K. Nowotny, and L.R. Sheppard, "Titanium dioxide for solar-hydrogen I. fanctional properties", Hydrogen Energy **32** (2007), 2609.
12. X. Chen and B. Clemens, "Photoelectron Spectroscopic Investigation of Nitrogen doped Titania Nanoparticles", Physical Chemistry B **108** (2004), 15446.
13. U. Tipparach, P. Wongwanwatthana, T. Sompan, T. Saipin, and P. Krongkitsiri, "Preparation and Characterization of Nano-TiO_2 Thin Films by Sol-gel Dip-coating Method" CMU, J. Nat. Sci. Special Issue on Nanotechnology **7** (2008), 129.
14. O. K. Varghese, M. Paulose, and A. Craig, "Long vertically aligned titania nanotubes on transparent conducting oxide for highly efficient solar cells", Nature Nanotechnology **4** (2009), 592.
15. D. Wang, L. Ying, B. Yu, F. Zhou, and W. Liu, "Highly flexible coaxial monohybrids made from porous TiO_2 nanotubes", Chemistry Mater **21** (2009), 1198.
16. Y. Wang, Y. Wu, Y. Qin, G. Xu, X. Hu, J. Cui, H. Zheng, Y. Hong, and X. Zhang, "Rapid anodic oxidation of highly ordered TiO_2 nanotube arrays", Alloys and Compounds **509** (2011), L157.
17. Nelson A. Kelly, Thomas L. Gibson, "Design and characterization of a robust photoelectron-chemical device to generate hydrogen using solar water splitting", International Journal of Hydrogen Energy, **31**, 1658, 2006.
18. L. X. Sang, Z. Y. Zhang, G. Bai, D. Chun, and M. Chong-fang, "A photoelectro chemical investigation of the hydrogen devolving doped TiO_2 nanotube arrays electrode", international journal of hydrogen energy **37** (2012), 854.
19. P. Wongwanwattana, P. Krongkitsiri, P. Limsuwan, and U. Tipparach, "Fabrication and photocatalysis of nanostructured TiO2 for solar hydrogen production", Ceramics International **38S** (2012), S517.
20. Q. Wang, X. Yang, X. Wang, M. Huang, and J. Hou, "Synthesis of N-doped TiO2 mesosponge by solvothermal transformation of anodic TiO2 nanotubes and enhanced photoelectrochemical performance", Electrochimica Acta **62** (2012), 158.
21. S. Zhou, J. Lv, L.K. Guo, G.Q. Xu, D.M. Wang, Z.X. Zheng, and Y.C. Wu, "Preparation and photocatalytic properties of N-doped nano-TiO2/muscovite composites", Applied Surface Science **258** (2012), 6136.

Fabrication and Mechanical Properties of Nanocomposites between Carbon Nanotubes/Carbon Fiber/Epoxy Resin

S. Nanthachompoo, W. Thamjaree, and W. Nhuapeng*

Department of Physics and Materials Science, Faculty of Science, Chiang Mai University, Chiang Mai 50200 , Thailand
**Corresponding author. E-mail: nhuapeng@yahoo.com*

Abstract

In this research, fabrication and mechanical properties of nanocomposites between carbon nanotubes (CNTs)/carbon fiber and epoxy resin was studied. The CNTs was prepared via chemical vapor deposition technique. To fabricate the nanocomposites, CNTs was mixed with epoxy resin and then molded with carbon fiber in the tube shape using hand lay-up technique. Physical and mechanical properties of composite samples such as density, compressive strength and were measured. From the results, it could be found that density of sample with 4 vol% of CNTs was 1.2504 g/cm^3 which was lighter than that of bicycle steel (7.6034 g/cm^3). The compressive strength of samples was in the range of 2.0-2.7 Ton whereas the compressive strength of bicycle steel was about 2.0 Ton. Furthermore, microstructure of nanocomposite samples was determined using scanning electron microscope technique (SEM).

***Keywords*:** Carbon fiber, Carbon nanotubes, Epoxy resin, Nanocomposites

Introduction

In the present days, synthesis fiber have used in many roles for various applications. Carbon fiber is one of synthesis fiber which is very popular in many industries, especially vehicle parts. Bicycle frame made from carbon fiber is well-known and accepted in light weight, high strength and durability.

Generally, bicycle frame made from various types of fabrication to produce high performance bicycle parts. Therefore, there are many works try to improve the starting materials and processing of carbon fiber to obtain the better properties of bicycle parts.

In this work, the authors attempted to fabricate the bicycle part from carbon nanotube/carbon fiber and epoxy resin composites using hand lay-up technique. Mechanical properties such as density and compressive strength were examined using scanning electron microscopy technique (SEM).

Materials and Methods

Carbon fiber which used in this work is a commercially plain carbon fiber (diameter 0.005-0.010 mm), supplied by Union Science CO., Ltd. The polymer matrix epoxy resin 852 and hardener 7278 are mixed in the ratio of 100:27 supplied by Union Science CO., Ltd. To fabricate composite specimen, carbon nanotube synthesized by CVD technique (density about 2.1 g/cm^3) was added and mixed into epoxy resin for 4 Vol%. The specimen was molded using hand lay-up technique which three layers of fiber woven was plies to the pipe shape. The specimen was then let in room temperature for 1 day to settle. Composites specimens were then examined the mechanical properties such as, compressive strength and densities. The microstructure of composites was also determined using SEM technique.

Results and Discussion

Table 1: Densities of specimens

Specimen	Densities (g/cm^3)
Epoxy resin	1.1322
Epoxy resin + Carbon Fiber	1.2489
Epoxy resin + Carbon Fiber + CNTs	1.2504
Iron	7.6034

Table 1. Showed density of composites specimen compared with those of neat epoxy resin and iron. The results showed that density of composites specimens were lower than that of epoxy resin and lower than that of iron about 6 times. Besides, it was also found that adding CNTs into carbon fiber/epoxy resin composites was not significantly changed in density of the specimen.

Compressive strength

Figure 1., showed the compressive strength of the composites specimens. It could be seen that composites between carbon fiber and epoxy resin contained with CNTs exhibit higher compressive strength when compared with that of non-containing CNTs specimen. The non-containing CNTs specimens showed some small crack around the centre of pipe at the load of 20000 N. And the specimen began propagation to large crack at the higher load.

The composites specimen containing with 4 Vol% of CNTs started to damage and failure in the range of load about 25000-27000 N. Adding CNTs particles have effect to failure behavior of composites specimen. Because the nanoparticle could adsorb shear load which similar to microfiber. Moreover, the external load was transmitted through matrix via reinforcement. When load was overload, the specimens tried to release the overload by micro-cracking which corresponding to the results and the previous work [1-7]. Specimens containing carbon nanotube which performed compressive strength more than that of non-containing carbon nanotube specimen and iron parts about 13% and 25.5%, respectively, and then iron inhibited compressive strength higher specimen non carbon nanotube at 14.4%. It was a good point of composites upon metal in weight at some volume.

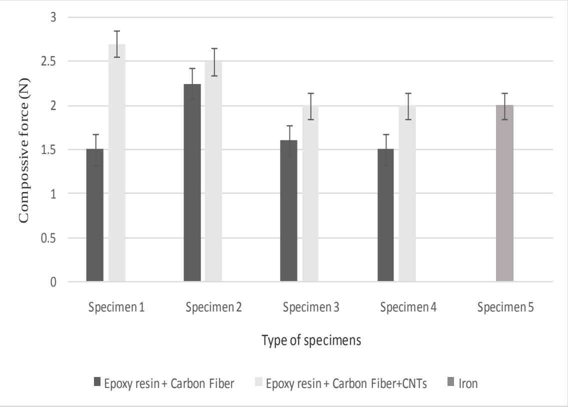

Fig 1. Increasing in effective compressive strength of specimens containing carbon nanotube compared specimens non containing carbon nanotube and iron.

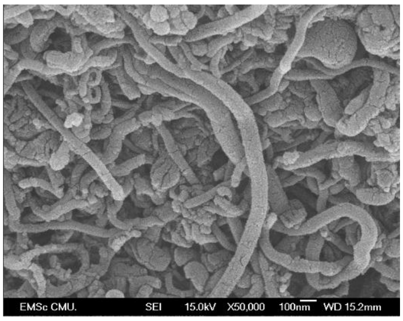

Fig 2. SEM picture of carbon nanotube.

Fig 3. Show failure behavior of specimen due to overload.

Table 2. EDX data of CNTs.

Element	Weight%	Atomic%
C K	97.93	99.57
Ni K	2.07	0.43
Totals	100.00	

Conclusions

The effect of containing carbon nanotube on the compressive strength of composites specimen was investigated unidirectional axial load. The mechanical properties of carbon nanotube was found to improve compressive strength and reduction porous in microstructure whereas it was not changed in density.

The comparison of experimental result with specimen containing carbon nanotube and other specimens indicated that these compressive strength can be enhanced by filling carbon nanotube particle for 4Vol%.

Acknowledgments

The author would like to thank the National Research University Project under Thailand‘s offices of the Higher Commission for financial support. We also wish to thank the Composites and Reinforcement Nanocomposites Unit, Department of Physics and Materials Science, Faculty of Science, Chiang Mai University of great fully support.

References

[1] L. Ci, J. Suhr, V. Pushparaj, X. Zhang, and P. M. Ajayan "Continuous Carbon Nanotube Reinforced Composites" , Received May 4, 2008; Revised Manuscript Received June 12, 2008

[2] Sunny S. Wicks *, Roberto Guzman de Villoria, Brian L. Wardle "Interlaminar and Intralaminar reinforcement of composite laminates with aligned carbon nanotubes" , Composites Science and Technology 70 (2010) 20–28.

[3] L. S. Schadler, S. C. Giannaris, and P. M. Ajayan "Load transfer in carbon nanotube epoxy composites" , Appl. Phys. Lett. 73, 3842 (1998); doi: 10.1063/1.12291.

[4] J. A. Bennett and R. J. Young "The effect of fibre–matrix adhesion upon crack bridging in fibre reinforced composites", Composites Part A 29A (1998) 1071–1081

[5] A.-M. Harte and N. A. Fleck "Deformation and failure mechanisms of braided composite tube in compression and torsion", Acta mater. 48 (2000) 1259±1271.

[6] Behnam Ashrafi a, Jingwen Guan b, Vahid Mirjalili , Yunfa Zhang , Li Chun , Pascal Hubert ,Benoit Simard , Christopher T. Kingston , Orson Bourne , Andrew Johnston "Enhancement of mechanical performance of epoxy/carbon fiber laminate composites using single-walled carbon nanotubes", Composites Science and Technology 71 (2011) 1569–1578.

[7] Yu-xin He, Qi Li a, Tapas Kuila , Nam Hoon Kim, Tongwu Jiang, Kin-tak Lau, Joong Hee Lee "Micro-crack behavior of carbon fiber reinforced thermoplastic modified epoxy composites for cryogenic applications" , Composites: Part B 44 (2013) 533–539.

Fabrication and Mechanical Properties of Ceramics Nanoparticles/Carbon Nanotubes/Rubber Composites

K. Janyakunmongkol , W. Nhuapeng[*], and W. Thamjaree

Department of Physics and Materials Science, Faculty of Science, Chiang Mai University, Chiang Mai 50200 , Thailand
**Corresponding author. E-mail: nhuapeng@yahoo.com*

Abstract

In this work, mechanical properties of 0-3 nanocomposite materials between silicon carbide nano wires (SiCNWs), carbon nanotubes (CNTs) and natural rubber were studied. The SiCNWs and CNTs were used as reinforcement fiber whereas natural rubber was used as matrix phase. The current heating technique (CHT) and chemical vapor deposition technique (CVD) were used to synthesis the nano wires and nanotubes phase, respectively. The volume fraction of reinforcement was varied from 0-10%. To fabricate nanocomposites samples, the nanophases were mixed into natural rubber matrix and molded. Mechanical properties of the samples, for example, hardness, tensile strength, elongation and wear test were examined. From the results, it could be found that nanocomposites with volume fraction of 10% exhibited the maximum hardness (50.6 shore A). The maximum tensile strength and elongation of the samples were obtained from 4% volume fraction sample which were 17.6 MPa and 1.6000%, respectively. Moreover, microstructure of samples was investigated by using scanning electron microscopy (SEM).

***Keywords*:**SiCNWs, CNTs, Nanocomposites

Introduction

Energy consumption of most humans is mainly dependent on nonrenewable energy. Because electricity generating with renewable energy is high cost. At present, the problem of energy especially petroleum is a problem that all parties both public and private sectors provide important. Therefore, oil is the main power or energy that we use in daily life which is limited and disappears to be possible in the future.

For this reason, researcher and inventors tried to improve over the engine to reduce using oil. The concept of this study is that reducing the energy to drive the optimization of fuel consumption in vehicles. Which have able to reduce petroleum consumption. As a result, the researchers have the idea to produce high performance tires with rolling resistance by filling nano particle into the rubber for apply in automotive industry.

In 1990, the company Rhodia Silica [1] had been synthesis of silicon oxide with a high surface area and mixing with the tire. The results showed that adding silicon oxide could prevent the loss of energy of the tires and reduce rolling resistance to 25% and reduced CO_2 by 5%. Moreover, it was also found that the rubber-containing silicon oxide exhibited the working life more than that of pure carbon rubber to 10%.

Advanced Fillers & Pigments Business Unit of Degussa Corporation, a company that develops thetruck tires. Found the chemical properties of the rubber components of the tire in general. Including the 30% of reinforcing filler in rubber couldpromote the property of the rubber such as adhesion, resistance to wear and tear. The carbon black was the popular filler which was adding in rubber for various quantities [2-3].

Research Group of the Degussa [2] discovered that the particle size of the additives could reduce the rolling resistance of truck tires by up to 20 percent, which reduced emissions carbon dioxide and indirect environmental benefits. It also reduced the emission of volatile organic compounds or VOC (volatile organic compound) to 80 percent during the manufacturing process of rubber.

Beside, Gupta et.al. [4] studied the energy absorption of composite materials between rubber and glass particles. They reviewed that the materials could withstand the pressure up to 40% of the damage on the work piece. It was also found that the specimens prepared with fracture strain increased without resulting in decreased strength.

Furthermore, Brinke et.al. [5] studied the effect of the addition of silica into the rubber applying for tire products. It was found that the addition of silica in the rubbercould produce a low rolling resistance tire and more energy-efficient vehicles.

For these reasons, this research to fabricate and study the mechanical property of composite materials between carbon nanotubes, silicon carbide nano wires and natural rubber.

Materials and Methods

Fabrication of nanocomposites

CNTs (synthesized from CVD technique) and SiCNWs (synthesized from CHT technique) were weight in the different ratios (1-10%) and mixed together by using ball milling technique for 3 hours.

The mixture was then weighed by volume percentage beaker. The 50 ml of ionized water was then added into the beaker. And the mixture was sonicated by using ultrasonic device for 2 hours until nanoparticle was well dispersion in the water and water turn to be black. The mixture was then mixes with natural rubber and molded by hand lay-up technique. Composites sample was let into room temperature for 1 day to settle. Mechanical properties and microstructure of the samples was examined.

Characterization Methods

The tensile strength was measured using Universal Testing Machine (CAT No. 2603-080). The durometer shore hardness scale (SHORE A)was using for examining the hardness of materials. Finally study microstructure with Scanning Electron Microscopy (JEOL JSM-5910LV).

Results and Discussion

Table 1 showed the density of composites samples. From the result, it could be found that density of the sample were in the range of 0.9697 g/cm^3. It could be observed that the density of the composites was higher when compare with that of neat samples (natural rubber). It was the effect of density of nanofiller which added into the rubber matrix.

Table 1. The density of nanocomposites

% CNTs+SiCNWs	Density
0	0.9281
1	0.9563
2	0.9339
3	0.9718
4	0.9541
5	0.9623
6	0.9882
7	0.9945
8	0.9869
9	0.9855
10	1.0058

The tensile strength results of the samples were shown in Fig 1. It was found that tensile strength of sample was increased with the increasing of quantities of nanofiller. The maximum tensile strength obtained from 4 vol% of CNTs+SiCNWs sample. When the quantities of nanofiller were higher than 4 vol%, the tensile strength of sample exhibited the decreasing trend. This was may be due to the agglomeration of CNTs and SiCNWs nanoparticles.

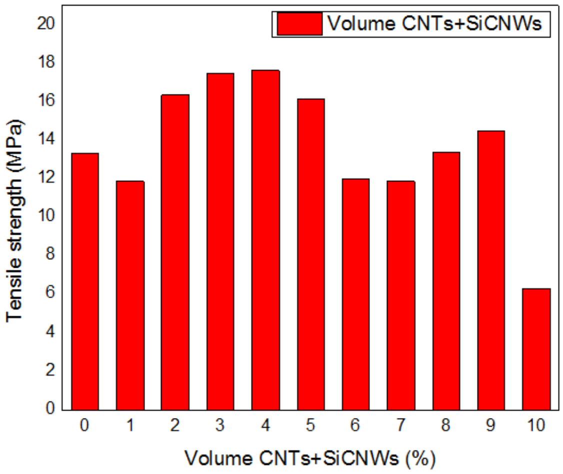

Figure 1. Tensile strength of nanocomposites.

Thereafter, hardness of the samples was determined using the durometer shore hardness scale (SHORE A). The result was showed in Table 2. It was found that hardness of the samples increased with the increasing of nanofiller. Hardness (Type A) were in the range of 42.9 – 50.6.

Table 2. Hardness of nanocomposites materials

% CNTs+SiCNWs	Hardness (Type A)
0	42.9
1	44.8
2	46.8
3	47.7
4	47.8
5	48.2
6	49.1
7	49.4
8	49.5
9	49.7
10	50.6

Figure 2 showed SEM micrographs of nanocompsites samples. It could be seen that the adding nanofiller had effect to the morphology of natural rubber (Fig.2(a)). The nanofiller was dispersed and distributed to the rubber matrix (Fig.2(b)). When the quantity of nanofiller had increased, the agglomeration of nanofiller could obtain (Fig.2(c)) which could be effect to mechanical property of nanocomposites sample. Hardness of nanocomposites was increased with increasing of nanoparticle quantity.

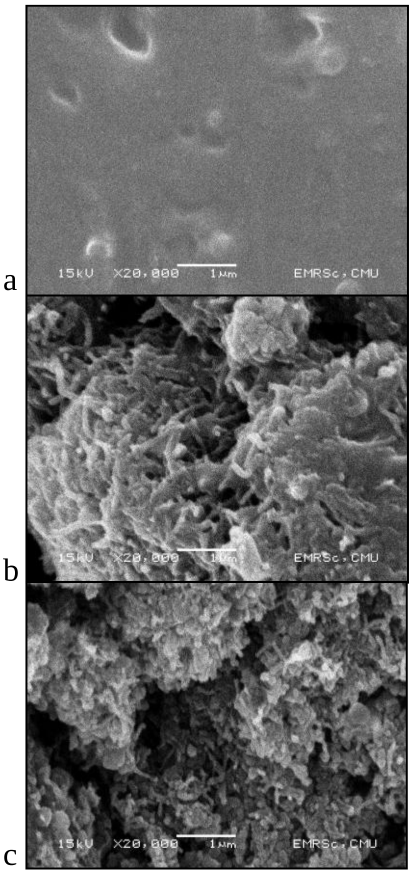

Figure 2. SEM Micrographs of nanocomposites sample (a) neat sample, (b) 4 vol% CNTs+SiCNWs and (c) 7 vol% CNTs+SiCNWs

Conclusions

The nanocomposites between CNTs, SiCNWs and natural rubber was fabricated. Density of the sample were in the range of 0.9697 g/cm^3. Adding the nanofiller had effect to the tensile strength of nanocomposites. The maximum tensile strength obtained from 4 vol% CNTs/SiCNWs sample which exhibited the tensile strength of 17.63 MPa. Furthermore, the microstructure of the sample reviewed the distribution of nanofiller in the natural rubber.

Acknowledgments

The author would like to thank the National Research Project Management (NRPM) for funding. The Composites and Reinforcement Nano composites Unit, Department of Physics and Materials Science, Faculty of Science and the Graduate School of Chiang Mai University for facilities and gratefully knowledge.

References

1. Rhodia: “New silica from Rhodia further im-proves tyre rolling resistance”, Additives for polymers, 4(2008) 3-4
2. R. Gehm, Rolling with Degussta Tire Fillers, Materials Innovations, June 2006, 42-46
3. Tires and Passenger Vehicle Fuel Economy: Informing Consumers, Improving Performance Special Report 286, National Academy of Sciences, Transportation Research Board, Retrieved on 2007-08-11
4. N. Gupta, R. Maharsia, H. Dwayne Jerro. Enhancement of energy absorption characteristics of hollow glass particle filled composites by rubber addition, Mats. Sci. Eng. A. 395 (2005). 233-240.
5. J.W. Brinke, S.C. Debnath, L.A.E.M. Reuvekamp, J.W.M. Noordermeer. “Mechanistic aspects of the role of coupling agents in silica-rubber composites”, Comp. Sci. Tech. 63(2003) 1165-1174.

Fabrication of Flexible Graphene-PEDOT/PSS Gas Sensor by Ink-jet Printing Technique

Y. Seekaew[1], S. Lokavee[2], D. Phokharatkul[3], T. Kerdcharoen[4], and C. Wongchoosuk[1,*]

[1]*Department of Physics, Faculty of Science, Kasetsart University, Bangkok 10900, Thailand*
[2]*Materials Science and Engineering Programme, Faculty of science, Mahidol University, Bangkok 10400, Thailand*
[3]*Nanoelectronics and MEMS Laboratory, National Electronics and Computer Technology Center, Klong Luang, Pathumthani 12120, Thailand*
[4]*Department of Physics, Faculty of Science, Mahidol University, Bangkok 10400, Thailand*
[*] *Corresponding author. E-mail: chatchawal.w@ku.ac.th*

Abstract

Graphene has emerged as a highly important material for applications in nanoelectronics, solar cells, and gas sensors due to its unique two-dimensional honeycomb lattice carbon nanostructure and electronic properties. In this work, we have fabricated graphene-PEDOT/PSS gas sensor using ink-jet printing method for NH_3 detection. In preparation of electronic ink, graphene (0.1 mg) were dispersed in PEDOT/PSS (40 ml). The interdigitated electrodes made from patterned silver conductive paint were deposited on a flexible substrate (Transparency film). The graphene-PEDOT/PSS was deposited on interdigitated electrodes by ink-jet printing technique. Surface morphology of graphene-PEDOT/PSS was characterized by atomic force microscopy (AFM). The fabricated flexible graphene-PEDOT/PSS gas sensor was measured in test chamber at room temperature. Ammonia (NH_3), ethanol, and acetone were used to test graphene-PEDOT/PSS sensing behavior with gas concentrations between 100-1000 ppm. From results, graphene-PEDOT/PSS gas sensor shows a strong response to NH_3 and much weaker responses to ethanol and acetone at room temperature. The sensor response (R/R_0) to NH_3, acetone, and ethanol at 1000 ppm concentration is 1.3977, 1.0155, and 1.0078, respectively. It can be concluded that the flexible graphene-PEDOT/PSS gas sensor prepared by our ink-jet printing technique exhibits high sensitivity and selectivity to NH_3 at room temperature.

Keywords: Ink-jet printing technique, graphene gas sensor, PEDOT/PSS, NH_3 sensor, printed electronics

Introduction

Graphene has emerged as a highly important material for applications in nanoelectronics, solar cells, and gas sensors due to its unique two-dimensional honeycomb lattice carbon nanostructure and electronic properties [1]. Poly(3,4-ethylenedioxythiophene)/poly(styrenesulfonate) or PEDOT:PSS is a polymer mixture of two ionomers. The PEDOT/PSS has received increasing attention as possible transparent and conductive materials because of their efficacious electronic properties and potential applications in flexible electronic devices [2]. Although, several researches have been studied the mixture between graphene and PEDOT/PSS materials, it has never been used to apply in flexible gas sensing application. So, this research have interested for application in gas sensor devices. In fabrication of gas sensor, it can be fabricated by several techniques such as reactive sputtering [3], chemical vapor deposition [4], and screen printing [5]. Although these techniques have been successfully applied in the fabrication of gas sensor, some of the techniques have disadvantages such as high cost, complicated and long-time operations. Very recently, a promising method for gas sensor preparation was proposed by using ink-jet printing technique that can make controlled deposition of functional materials with suitable geometer on various substrates [6-8]. Because of its many unique advantages such as low temperature processing, and low-cost, ink-jet printing has become a potential solution in material and device preparation. In this work, we have fabricated graphene-PEDOT/PSS gas sensor by using ink-jet printing method on flexible substrate (Transparency film) based on an electronic ink formula for ammonia (NH_3) detection. Atomic force microscopy (AFM) was used to investigate the surface morphology of sensing film.

Materials and Methods

In preparation of the electronic ink, graphene material (0.1 mg) was dispersed in dimethyl sulfoxide (DMSO) of 5 ml. The graphene solution was thoroughly stirred for 30 min at room temperature. Then, graphene solution was dissolved in the PEDOT/PSS of 40 ml. The final solution was thoroughly sonicated for 30 min at room temperature (see Fig. 1a).

(a) Prepared electronic ink. **(b) Interdigitated electrodes fabrication.**

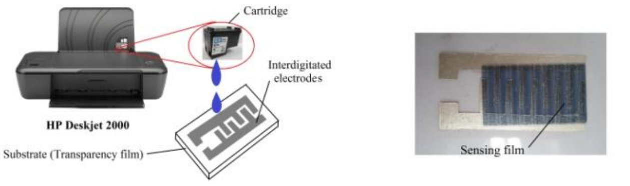

(c) Ink-jet printing. **(d) Graphene-PEDOT/PSS gas sensor.**

Figure 1. Gas sensor fabrication steps.

The interdigitated electrodes made from patterned silver conductive paint were deposited on a flexible substrate (Transparency film) (see Fig. 1b). A flexible gas sensor was fabricated by using modified HP deskjet 2000 j210 printer with a resolution (BW) of 1200×1200 dpi. The cartridge was refilled with the prepared electronic ink. The graphene-PEDOT/PSS was deposited on interdigitated electrodes by ink-jet printing technique (see Fig. 1c). The fabricated flexible graphene-PEDOT/PSS gas sensor is displayed in Fig. 1d. NH_3, ethanol, and acetone were used to test graphene-PEDOT/PSS sensing behavior with gas concentrations between 100-1000 ppm at room temperature.

Results and Discussion

Surface morphology of graphene-PEDOT/PSS sensing film by AFM is shown in Fig. 2. From AFM image, it indicates that the film surface is well uniform and only tiny defects are presented with a scan size area of 2 µm x 2 µm. The surface of inkjet printed film is rather smooth. However, it is hard to clearly see the graphene structure on PEDOT/PSS due to limited availability of AFM. Further investigation on graphene-PEDOT/PSS formation mechanism will be studied in future.

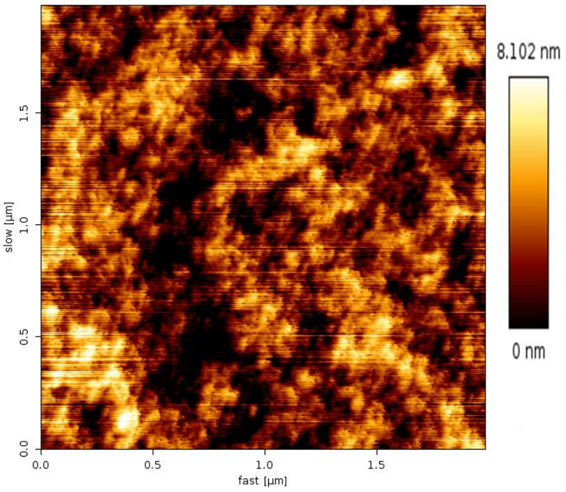

Figure 2. AFM image of an ink-jet printing film of graphene-PEDOT on substrate (Transparency film).

The sensor response (S) of the gas sensor is defined as $S = R/R_0$ where R_0 and R are the resistance of the gas sensor in pure air and test gas, respectively. Figure 3 shows the sensing behavior of the graphene-PEDOT/PSS gas sensor to NH_3 vapor under a concentration 1000 ppm, 500 ppm, and 100 ppm at room temperature.

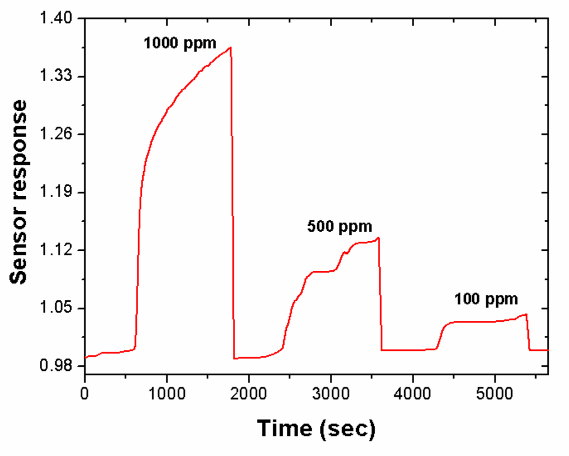

Figure 3. Gas sensor response to NH_3 gas at room temperature.

It can be observed that the response of gas sensor increases when graphene-PEDOT/PSS is exposed to NH_3 gas. It can be seen that the different concentration affects on response of gas sensor as a power-law relationship. To study the sensitivity and selectivity of the graphene-PEDOT/PSS gas sensor, its sensing response to various gas vapors is plotted in Fig. 4.

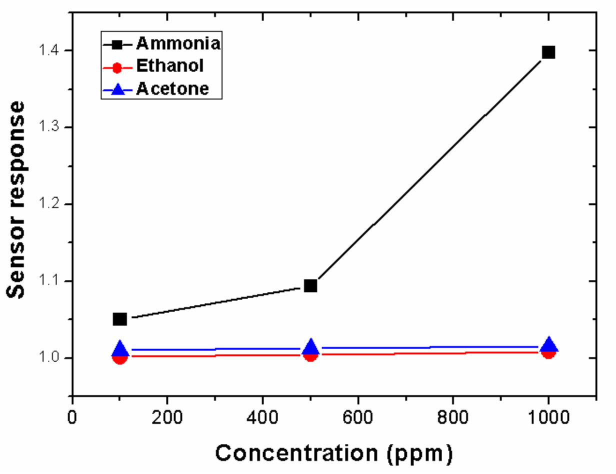

Figure 4. Sensing response of the gas sensor to NH_3, acetone, and, ethanol at room temperature.

From Fig. 4, graphene-PEDOT/PSS gas sensor shows a strong response to NH_3 and much weaker responses to acetone and ethanol at room temperature. The sensor response to NH_3, acetone, and ethanol at 1000 ppm concentration is 1.3977, 1.0155, and 1.0078, respectively. So, It can be concluded that the flexible graphene-PEDOT/PSS gas sensor prepared by our ink-jet printing technique exhibits high sensitivity and selectivity to NH_3 at room temperature.

Conclusions

The flexible graphene-PEDOT/PSS gas sensor has been successfully fabricated by using ink-jet printing technique with high homogeneous surface sensing film morphology. The results indicate that graphene-PEDOT/PSS gas sensor shows a strong response to NH_3 and much weaker responses to ethanol and acetone at room temperature. It is hoped that this research will be useful for development and manufacture of future sensing wearable electronics technology.

Acknowledgments

This work was supported by Kasetsart University Research and Development Institute (KURDI). Y.S. acknowledges M.Sc. Scholarship for International Publication from the Graduate School, Kasetsart University.

References

1. G.Ko, H.-Y. Kim, J. Ahn, Y.-M. Park, K.-Y. Lee, and J. Kim, “Graphene-based nitrogen dioxide gas sensors”, Current Applied Physics **10** (2010), 1002.
2. Yanfei Xu, Yan Wang, Jiajie Liang, Yi Huang, Yanfeng Ma, Xiangjian Wan, and Yongsheng Chen, “A Hybrid Material of Graphene and Poly (3,4-ethyldioxythiophene) with High Conductivity, Flexibility, and Transparency”, Nano Research **2** (2009), 343.
3. D.Mutschall, K. Holzner, and E.Obermeier, “Sputtered Molybedeum Oxide Thin Films for NH_3 Detection”, Sensors and Actuators B: Chemical **36** (1996) 320.
4. C. Cantalini L. Valentini, I. Armentano, L. Lozzi, J.M. Kenny, and S. Santucci, “Sensitivity to NO_2 and cross-sensitivity analysis to NH_3, ethanol and humidity of carbon nanotubes thin film prepared by PECVD”, Sensors and Actuators B: Chemical **95** (2003) 195.
5. B. Ismail, M. Abaab, and B. Rezig., “Structural and electrical properties of ZnO films prepared by screen printing technique”, Thin Solid Films **383** (2001) 92.
6. M. Singh, H.M. Haverinen, P. Dhagat, and G.E. Jabbour., “Inkjet Printing-Process and Its Applications”, Advanced Materials **22** (2010) 673.
7. Y. Seekaew, S. Lokavee, S. Chomkokard, T. Kerdcharoen, C. Wongchoosuk, "Effect of Thickness on Ethanol Gas Sensor Prepared by Ink-jet Printing Techique", Proceeding of the 38th Congress on Science and Technology of Thailand (STT-38), 2012.
8. C.Wongchoosuk, P. Jangtawee, P. Lokavee, S. Udomrat, P. Sudkeaw, and T.Kerdcharoen., “Novel Flexible NH3 Gas Sensor Prepared By Ink-Jet Printing Technique”, Advanced Materials Research **506** (2012)39.

F-doped SnO_2 Nanopowders Synthesized by Ultrasonic-assisted Co-precipitation Method

R. Noonuruk, W. Mekprasart, C. Kahattha, N. Vittayakorn, W. Techitdheera,
and W. Pecharapa*

College of Nanotechnology, King Mongkut's Institute of Technology Ladkrabang,
Bangkok, 10520, Thailand
Thailand and Center of Excellence in Physics (ThEP Center), CHE, 328 SiAyutthaya RD,
Bangkok, 10400, Thailand
**Corresponding author. E-mail: kpewisan@gmail.com*

Abstract

F-doped SnO_2 nanopowders were synthesized by ultrasonic-assisted precipitation process using tin chloride ($SnCl_4$) as a tin source, ammonium fluoride (NH_4F) as a fluorine dopant source. The fluoride composition was varied from 0 to 20 mol%. The precursor was prepared using both sources dissolved in deionized water and kept under sonication in ultrasonic bath. The aqueous ammonia was added dropwise into the solution with operating time of 2 h. The as-precipitated products were dried at 80 ºC and then calcined at 400 ºC for 2 h. The physical properties of nanoparticles with/without fluoride dopant were characterized by X-ray diffraction, scanning electron microscope and transmission electron microscope. Obtained results indicate significant effects of ultrasonic radiation on particle size distribution, uniformity and reduction of agglomeration due to cavitations in solution restrained aggregation of particles during operated precipitation process. The results reveal that ultrasonic-assisted method can efficiently synthesize tetragonal F-doped SnO_2 nanopowders with small particle size of 10-13 nm.

Keywords: F-doped SnO_2 powder, Ultrasonic-assisted, Precipitation

Introduction

Tin Oxide (SnO_2) has attracted considerable attentions due to their distinguished characteristic such as special mechanical, chemical stability, environmental and good thermal properties [1]. Typically, SnO_2 is an n-type semiconductor with wide energy gap (3.67 eV) as tetragonal structure (a=b=4.737Å and c=3.18 Å) related to rutile structure. Due to promising properties of SnO_2, it has been utilized in wide range of applications such as gas sensors [2], transparent conducting electrodes [3], and optical electronic devices [4]. However, low optical and electrical performance has occurred by the stoichiometric SnO_2 due to its low intrinsic carrier density and mobility. The concentration of charge carriers in SnO_2 can be increased by extrinsic dopant [5]. The most common dopants used for increasing the conductivity and optical properties of SnO_2 are In, Sb, F and Mo [6]. The non-stoichiometric structure of SnO_2 can create oxygen vacancies generating free electrons to promote higher conductivity in the samples [7]. In recent years, many processes have been developed to the synthesis of SnO_2 in form of low dimensional nanostructure leading to the improvement in physical, optical, catalytic and electric properties [8]. Furthermore, effective size of the particles down to nano scale regime can drastically increase large specific surface areas. Up to now, several methods including sol-gel methods [9], precipitation [10], solvothermal [11] and hydrothermal methods [12] have been conducted and proposed on the preparation of fascinating SnO_2 nanostructure. Among these techniques, the precipitation method has considerable benefits over the others such as simple synthesis process, low energy consumption and simplicity of solution concentration [13]. Moreover, in this study, ultrasonic radiation was supplemented during in precipitation process because it is able to provide high frequency clean energy to prevent the agglomeration [14]. This present paper reports the synthesis of F-doped SnO_2 nanoparticles using ultrasonic-assisted co-precipitation process. The crystalline and surface morphology of nanoparticles with/without F-dopant were characterized by X-ray diffraction (XRD) and transmission electron microscope (TEM).

Materials and Methods

F-doped SnO_2 nanopowders were synthesized by ultrasonic-assisted precipitation process using ultrasonic bath as a mixing device. In experiment, analytical grade chemical reagents were used without further purification. Tin chloride ($SnCl_4$) and ammonium fluoride (NH_4F) were used as a tin and fluorine dopant source, respectively. The composition of fluoride was varied from 0 to 20 mol%. 0.2 M of $SnCl_4$ and NH_4F was dissolved in deionized water under sonication in ultrasonic bath operated at 120 W with frequency of 40 kHz. The suspension was sonicated at 60 ºC for 20 min until homogeneous solution was obtained. Then, aqueous ammonia was dropped into solution within operating time of 2 h. The gelatinous precipitated product was washed several times with deionized water and ethanol via centrifugation to remove chlorine ions. Finally, the as-synthesized products were dried in oven at 80 ºC and then calcined at 400 ºC for 2 h.

The crystalline structure and surface morphology of nanopaticles with/without F-dopant were characterized by X-ray diffraction and transmission electron microscope. XRD (LabX, XRD-6000) operated at 40 kV and 30mA over a 2θ in range of 20-80º using Cu-$K\alpha$ radiation. The diffraction patterns were recorded with a scanning speed 2º/min. The size, shape and crystal structure of F-doped SnO_2 were observed by TEM (FEI, TECNAI $G^2$20) operated at 200 kV. Before TEM analyses, the samples was suspended in ethanol and dropped on a carbon-film coated copper grid.

Results and Discussion

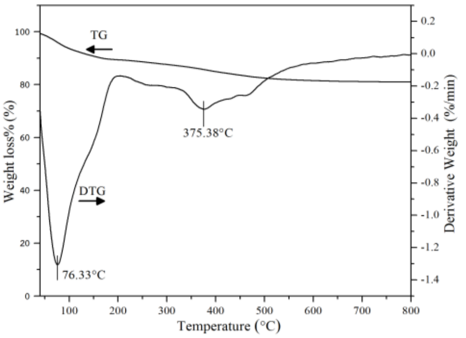

Figure 1. TG/DTA curves of as-synthesized SnO_2 nanopowders.

The thermal behaviors of as-synthesized precipitates of SnO_2 powders are shown in Fig.1. The TG/DTA curves of as-synthesized precipitates detected at around 70 ºC and 230 ºC are assigned to the removal of absorbed water and alcohol and the decomposition of NH_4^+ in the powder according to the Eq.1[15],

$$SnCl_4 + 4NH_4OH \rightarrow Sn(OH)_4 + 4NH_4Cl. \qquad (1)$$

The noticeable peak position about 375 ºC of sample prepared under ultrasonic bath may be attributed to the dehydroxylation and phase transformation of the as-precipitated product according to the Eq. 2 [16],

$$Sn(OH)_4 \rightarrow SnO_2 + 2H_2O. \qquad (2)$$

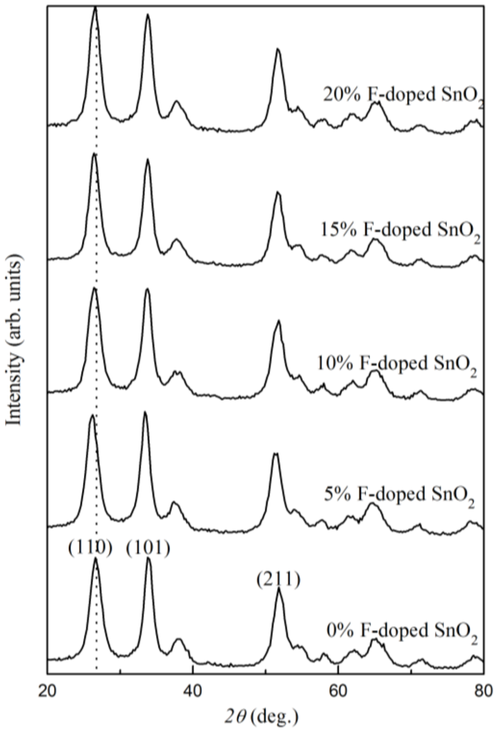

Figure 2. XRD patterns of F-doped SnO_2 nanopowders with different fluorine content of 0-20 mol%.

The XRD patterns of F-doped SnO_2 nanopowders with different fluorine doping content of 0-20 mol% are illustrated in Fig 2. All diffraction peaks of samples show the major peak of (110), (101) and (211) plane orientation corresponding to polycrystalline phase of tetragonal SnO_2 crystal structure [17]. The XRD patterns of all samples reveal only diffraction peak of pure SnO_2 without another impurity phase. It is noticeable that major peak position of F-doped SnO_2 powders shifts slightly toward the lower diffraction angles due to the prolongation of d-spacing [18] caused by the dopant. Because the ionic radius of fluorine ion (1.33 Å) is close to oxygen ion (1.32 Å). When doping, the good substitution of oxygen sites by fluorine ions can result to the alternation of d-spacing of the structure [19]. In addition, average crystallite sizes of the F-doped SnO_2 nanopowders were calculated by well-known Scherrer's equation as follows:

$$D = \frac{0.9\lambda}{\beta\cos\theta}, \qquad (3)$$

where λ is the X-ray's wavelength (0.154 nm), β is the peak width at half-maximum (FWHM),θ is the diffracted angle of the corresponding peak. The crystallite size of all samples are obtained from the FWHM of the (100) peak and summarized in Table1. The crystallite size of nanopowders slightly varies in the range of 10.2-11.2 nm by fluoride incorporation.

Fig. 3 (a) and (b) show EDX analysis of undoped and F-doped SnO_2, respectively. In Fig. 3(a), the major elements found in EDX result are Sn and O. The existence of Cu is resulted from the Cu grid used in TEM and EDX measurement. Meanwhile the EDX result of F-doped sample as seen in Fig. 3(b) indicates the existence of fluorine in SnO_2 nanopowder. TEM images and selected area electron diffraction (SAED) patterns of undoped and F-doped SnO_2 nanoparticles are illustrated in Fig.4. The TEM images of SnO_2 nanoparticles exhibit excellent dispersion with less agglomeration and uniformity of particle size in the range of 10-13 nm. It is suggested that the good dispersion of the particles is obtained by the aid of ultrasonic energy supplied during synthesis. The SAED of F-doped SnO_2 nanoparticles exhibits several strong halo rings confirming to polycrystalline structure and the brightest inner ring attributes to the (110) plane of SnO_2 structure. The halo ring has reciprocal relation with space between crystallite planes (d-spacing) [20]. The d-spacing of undoped and F-doped SnO_2 nanopowder was calculated from halo ring of (110) plane and found to be 0.33 nm and 0.39 nm, respectively. The particles size and d-spacing of samples obtained from TEM images are in harmony with XRD results. This feature is probably caused by the substitution of oxygen sites by fluorine ions.

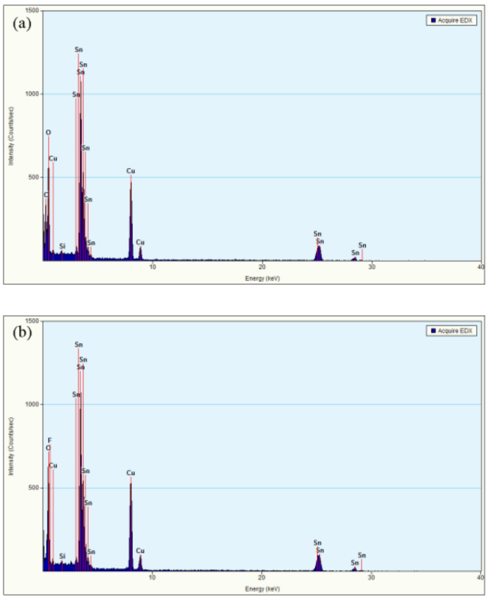

Figure 3. EDX analysis of (a) undoped and (b) F-doped SnO_2 nanopowders.

Table 1
crystallite sizes of the F-doped SnO_2 nanopowders

F contents (mol%)	crystallite size (nm)
0	10.2
5	10.1
10	9.8
15	11.2
20	11.0

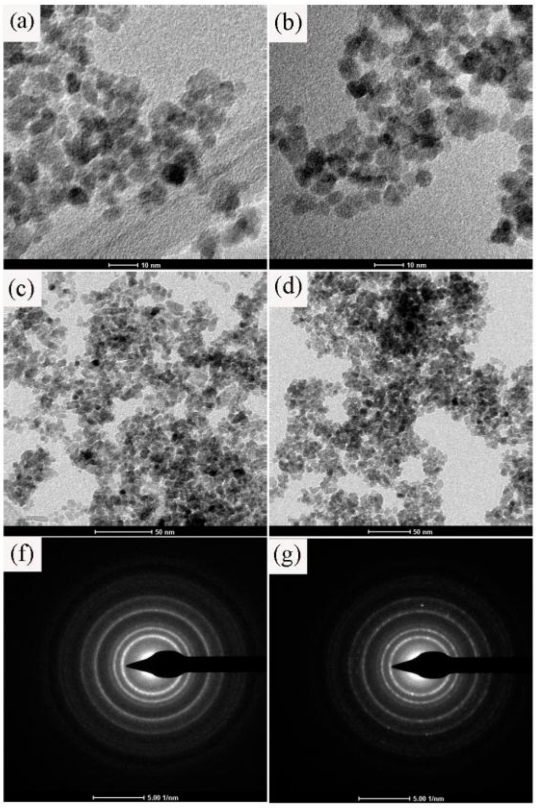

Figure 4. TEM images and SAED patterns of (a,c,f) undoped and (b,d,g) F-doped SnO_2 nanopowder.

Conclusions

F-doped SnO_2 nanoparticles were synthesized by ultrasonic-assisted precipitation method. TG result reveals the phase transformation from $Sn(OH)_4$ to SnO_2 can be taken at 375 °C. The well-dispersed SnO_2 nanoparticles with uniform size in the range of 10-13 nm can be prepared by the assistance of ultrasonic irradiation. The XRD and TEM results exhibit that the observable change of d-spacing and particle size caused by the substitution of oxygen sites by fluorine ions.

Acknowledgments

This work has partially been supported by the National Nanotechnology Center (NANOTEC), NSTDA, Ministry of Science and Technology, Thailand, through its program of Center of Excellence Network. Authors would like to express deep thank to Nation Research Council of Thailand (NRCT) for XRD measurement and King Mongkut's Institute of Technology Ladkrabang Research Fund (KMITL) for financially support.

References

1. A.R. Babar, S.S. Shinde, A.V. Moholkar and K.Y. Rajpure, “Electrical and dielectric properties of co-precipitated nanocrystalline tin oxide”, Journal of Alloys and Compounds **505** (2010) 743.
2. C.H. Han, S.D. Han, I. Singh and T. Toupance, “Micro-bead of nano-crystalline F-doped SnO_2 as a sensitive hydrogen gas sensor”, Sensors and Actuators B **190** (2005) 264.
3. H.J. Jeon, M.K. Jeon, M. Kang, S.G. Lee, Y.L. Lee, Y.K. Hong, B.H. Choi, “Synthesis and characterization of antimony-doped tin oxide (ATO) with nanometer-sized particles and their sonductivities”, Materials Letters **59** (2005) 1801.
4. A.R. Babar, S.S. Shinde, A.V. Moholkar, C.H. Bhosale, J.H. Kim and K.Y. Rajpure, “Structural and optoelectronic properties of antimony incorporated tin oxide thin films”, Journal of Alloys and Compounds **505** (2010) 416.
5. X. Zhong, B. Yang, X. Zhang, J. Jia and G. Yi, “Effect of calcing temperature and time on the characteristics of Sb-doped SnO_2 nanoparticles synehesized by the sol-gel method”, Particuology **10** (2012) 365.
6. L.S. Wang, H.F. Lu, R.Y. Hong and W.G. Feng, “Synthesis and electrical resistivity analysis of ATO-coated talc” Powder Technology **224** (2012) 124.
7. J. Montero, C. Guillén and J. Herrero, “Dischange power dependence of structural, optical and electrical properties of DC sputtered antimony doped tin oxide (ATO) films”, Solar Energy Material & Solar cells **95** (2011) 2113.
8. T. Krishnakumar, R. Jayaprakash, N. Pinna, A.R. Phani, M. Passacantando and S. Santucci, “Structural, optical and electrical characterization of antimony-substituted tin oxide nanoparticles”, Journal of Physics and Chemistry of Solids **70** (2009) 993
9. H. Mahmoudi Chenari, L. Weinhardt, N.S. Rodriguez Lastra, M.A. Ernst, F. Reinert, M.M. Golzan and A. Hassanzadeh, “Structural properties and x-ray photoelectron spectroscopic study of SnO_2 nanoparticles”, Materials Letters **85** (2012) 168
10. K.C. Song and Y. kang, “Preparation of high surface area tin oxide powders by a homogeneous precipitation method”, Materials Letters **42** (2000) 283.
11. J.S Lee and S.C Choi, “Solvent effect on synthesis of indium tin oxide nano-powders by a solvothemal process”, Journal of the European Ceramic Society **25** (2005) 3307.
12. L.M. Fang, X.T. Zu, Z.J. Li, S. Zhu, C.M. Liu, W.L. Zhou and L.M. Wang, “Synthesis and characteristics of Fe^{3+}-doped SnO_2 nanoparticles via sol-gel-calcination or sol-gel-hydrothermal route”, Journal of Alloys and Compounds **454** (2008) 261.
13. Y. Liu and C. Cao, “Enhanced electrochemical performance of nano-size $LiFePO_4/C$ synthesized by an ultrasonic-assisted co-precipitation method”, Electrochimica Acta 55 (2010) 4694.
14. J.F Huang, X.R. Zeng, L.Y. Cao, N.B. Xiong, “Preparation of Y_2BaCuO_5 nanoparticles by a co-precipitation process with the aid of ultrasonic irradiation”, Journal of materials processing teghnology **209** (2009) 2963.
15. S. Xiaolan, L. Dongfeng, Z. Yimeng, D. Yi, L. Mei, W. Shunkui, H. Xi and Q. Yixin, “Grain Growth Kinetics of SnO_2 nanocrystals Synthesized by Precipitation Method”, Journal of Wuhan University of Technology-Mater, Sci.Ed. (2010) 929.
16. S.Mosadegh Sedghi, Y. Mortazavi and A. Khodadadi, “Low temperature CO and CH_4 dual selective gas sensor using SnO_2 quantum dots prepared by sonochemical method”, Sensor and Actuator B **145** (2010) 7.
17. S. Wu, S. Yuan, L. Shi, Y. Zhao and J. Fang, “Preparation, characterization and electrical properties of fluorine-doped tin dioxide nanocrystals”, Journal of Colloid and Interface Science **346** (2010) 12.
18. Y. Kim, S.P. Kim, S.D. Kim and S.E. Kim, “Nitrogen-doped transparent tin oxide thin films deposited by sputtering”, Current Applied Physic **11** (2011) S139.
19. H. Kim, R.C.Y. Auyenung and A. Piqué, “Transparent conducting F-doped SnO_2 thin films grown by pulsed laser deposition”, Thin Solid Films **516** (2008) 5052.
20. A. Hassanzadeh, B. Moazzez, H. Haghgooie, M. Nasseri, M. Maqsood Golzan and H. Sedghi, Synthesis of SnO_2 nanopowders by a sol-gel process using proponol-isopropanol mixture, Central European Journal of Chemistry **6(4)** (2008) 651.

Heavy Metal Detection by Fluorescent Spectroscopy with Fluorescent-modified Magnetic Nanoparticle

R. Puingam[1,2,3], T.Chodjarusawad[1], Y. Wanna[1], G. Tumcharern[2], A. Chindaduang[2],
S. porntheerapat[4], J. nukeaw[1,3], and S. Pratontep[1,3*]

[1]*College of Nanotechnology, King Mongkut's Institute of Technology Ladkrabang, Bangkok 10520, Thailand*
[2]*National Nanotechnology Center (NANOTEC), 111 Thailand Science Park, Pahol-Yothin Rd, Klong Luang, Pathumthani 12120, Thailand*
[3]*Thailand Center of Excellence in Physics, CHE, 328 Si Ayutthaya Rd. Bangkok 10400, Thailand*
[4]*Photonic Technology Laboratory, National Electronic and Computer technology Center, National Science and Technology Development Agency, Patumthani 12120, Thailand*
**Corresponding author. E-mail: kpsirapat@gmail.com*

Abstract

Superparamagnetic (Fe_3O_4) nanoparticles have been modified by N-(Rhodamine 6G)lactam-Tris(2-aminoethyl)amine as heavy metallic sensing materials via fluorescent monitoring within a PDMS/glass microchamber. The magnetic nanoparticles grafted with PEG-bis-amine were functionalized to add fluorescent properties by attaching Fe_3O_4@PEG-GA and N-(Rhodamine 6G)lactam-Tris(2-aminoethyl)-amine in the glutaraldehyde (GA) shell. The prepared fluorescent magnetic nanoparticles were characterized by transmission electron microscopy (TEM), UV–Visible spectroscopy and Fourier transform infrared spectroscopy (FT-IR). The fluorescent responses were examined by a portable fluorescent spectroscopy with an excitation from a 500 nm ultra bright light emitting diode (LED). The nanoparticle sensor exhibits good selectivity and good sensitivity to some heavy metals in aqueous solution (pH = 7.0), particularly mercury salt.

Keywords: superparamagnetic nanoparticles, fluorescence, heavy metal

Introduction

A rapid detection of various metals such as Pb Cu Cd and Hg contaminations in environment is in great demand. In the recent years, many researchers have developed devices and methods for such detection. Traditional methods such as mass spectrometry and atomic absorption spectrometry have been used for the detection of these heavy metal ions [1]. However, the methods have limitation such as high quantity and expert requirements for standard operation. On the other hand, fluorescence spectroscopy offers rapid and nondestructive qualitative and quantitative detection of metal ions [2, 3]. Fluorescence chemosensors are of increasing interest, as detecting heavy metal ions because of their high sensitivity and selectivity. Especially, Rhodamine derivatives are well-known substances in both in academic research and industrial uses, which also have high fluorescence quantum yield [4, 5]. There has been much interest to develop chemosensors by a turn-on mechanism of non-fluorescent rhodamine derivatives, which produce fluorescence upon the addition of analytes, including heavy metal ions such as Hg [6,7]. Recently, we functionalized magnetic core shell Fe3O4@SiO2 nanoparticles by Rhodamine-based fluorescence, which has been designed for separation or sensing of metal ions [8]. In addition, a micro-chamber analysis system, with low fluid volume consumption, has been demonstrated for microfluidic fluorescent detection [9].

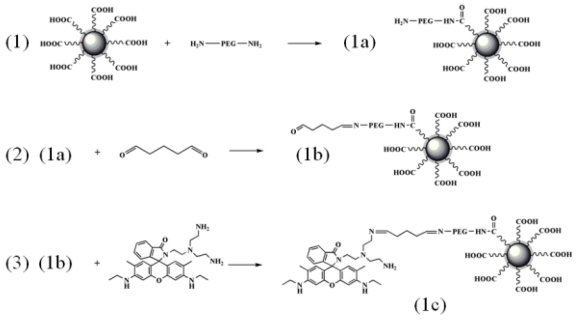

Scheme 1. Structural illustration of Fe_3O_4/PEG-NH_2 (1a), its coupling with glutaraldehyde (1b), and Fe_3O_4/PEG-GA/Rhodamine6G-CLT-TAEA (1c)

This study presents the use of surface-modified magnetic nanoparticles for detecting heavy metal ions by a turn-on fluorescence technique in a microfluidic system. Our interest arises from the possibility of combining magnetic nanoparticle and fluorescent properties by entrapping Fe3O4 and Rhodamine 6G (Rh6G) in the glutaraldehy (GA) shell, using a simple and feasible method (Scheme 1). The composite nanoparticles entrapped in microchamber show enhanced fluorescence emission under the presence of various metal ions in water. The sensitivity and selectivity of the nanoparticles are investigated.

Materials and Methods

FluidMAG magnetic nanoparticles (MNP), Glycol bis(amine) (EGDMA, Sigma Aldrich, MW2,000), 1-ethyl-3-(3-dimethyllaminopropyl) carbodiimide hydrochloride (EDC, MW191.7), N-Hydroxyl succinimide ester (NHS, MW 115.1), Glutaric dialdehyde(25 wt.% solution in water, MW 100.12), Silver(I) trifluoromethanesulfonate CAS No. 2923-28-6 (M_w = 256.94), Iron(II) trifluoromethanesulfonate CAS No. 59163-91-6 (M_w = 353.99), Mercury(II) trifluoromethanesulfonate CAS No. 49540-00-3 (M_w = 498.71), Cobalt(II) acetate tetrahydrate CAS No. 6147-53-1 (M_w = 249.09) and Lead(II) acetate trihydrate CAS No. 6080-56-4 (M_w = 379.33) were purchased form Sigma-Aldrich, Inc. (USA). Deionized water was used to prepare all aqueous solution. 2-morpholinoethane sulfonic acid (MES), Methanol (MeOH,HPLC grade) was purchased form J.T.Bake(USA). Rhodamine 6G-CLT-TAEA was synthesized at the National Nanotechnology Center (NANOTEC)

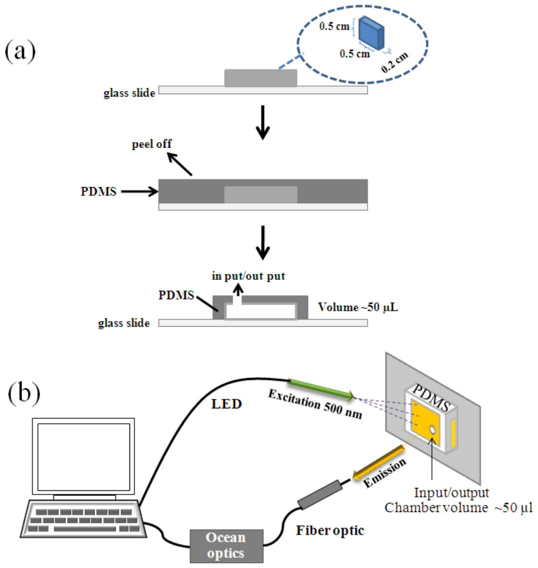

Figure 1. (a) Fabrication process of PDMS chamber. (b) Design for fluorescence detection by a mini fluorescent spectroscopy.

Preparation of Fe_3O_4/PEG-NH_2 : FluidMAG (5 mg) was dispersed in a vial with 100 µl of a 25 mM 2-morpholinoethane sulfonic acid (MES, pH 6). EDC and NHS were dissolved in 200 µL of a 25 mM 2-morpholinoethane sulfonic acid (MES, pH 6) to a concentration of 3.2 M and 1.6 M, respectively. The solutions were then mixed with the MNP solution and sonicated for 30 min at room temperature. Then 0.0064 g of poly(ethylene glycol) bis(amine) was dissolved in 500 µL of 25 mM 2-morpholinoethane sulfonic acid (MES, pH 6). This solution was added to the mixture and sonicate for another 30 min. After the reaction, the grafted MNPs were precipitated by centrifugation at 10000 rpm, washed with water three times and stored in water.

Preparation of Fe_3O_4/PEG-NH_2-GA: Fe3O4- PEG (2.5 mg) was added to a solution of 5 % GA 50 µl, The mixture was prepared and sonicated 30 min at room temperature. The modified Fe_3O_4 nanoparticles were precipitated by centrifugation at 10000 rpm, and washed with water three times.

Preparation of Fe_3O_4/PEG-GA/Rhodamine6G-CLT-TAEA : A solution Rhodamine6G-CLT-TAEA (1 mg) in methanol, and the mixture was prepared and sonicated 30 min at room temperature. The product was precipitated by centrifugation at 10000 rpm, and washed several times with methanol and DI water. Finally, the product was redispersed in deionized water. The morphology and size of the MNPS were characterized by the high resolution transmission electron microscopy (TEM, Jem-2020 200 keV, Jeol). The functional group structures were determined by the Fourier transform infrared spectroscopy (FTIR) (Perkin-Elmer).

Microchamber: Figure 1 shows a fabrication process of Polydimethylsiloxane(PDMS) microchamber though a microscale molding technique. The pattern used was a small piece of glass of size 0.5 cm x 0.5 cm x 0.2 cm, centrally transfixed on glass slide. PDMS liquid was poured onto the mold, then cured and peeled off from the pattern. After alcohol cleaning process, this PDMS plug was treated with oxygen plasma (Harrick Plasma) for 1 min, then bonded to a glass slide to form an enclosed micro-chamber system. The fluorescence spectroscopy was obtained using a near 90^o geometry with a fixed excitation at 500 nm (LED). The emission spectra were collected by the HR4000CG-UV-NIR Ocean Optics spectrometer (Fig. 1b).

Results and Discussion

Characteristics of FluidMAG/ PEG-Glutaral/Rhodamine6G-CLT-TAEA

Fourier Transform infrared (FT-IR) technique was used to identify various functionalgroups grafting on MNPs. The successful conjugation as in 2b, 1c and 1d of Scheme 1 have been obtained. For all samples,

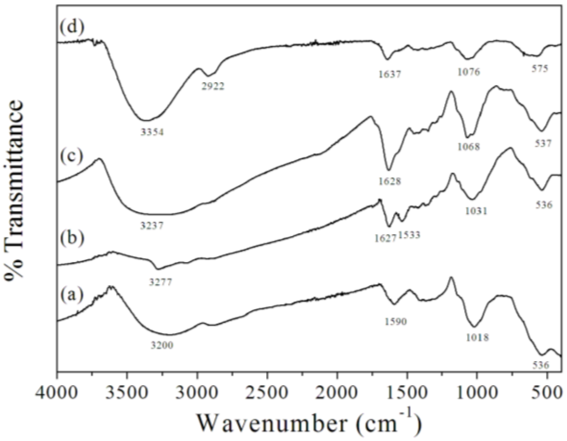

Figure 2. FT-IR spectra of Fe_3O_4 (a), Fe_3O_4/PEG-NH_2 (b), Fe_3O_4/PEG-NH_2-GA (c), and Fe_3O_4/PEG-GA/Rhodamine6G-CLT-TAEA (d)

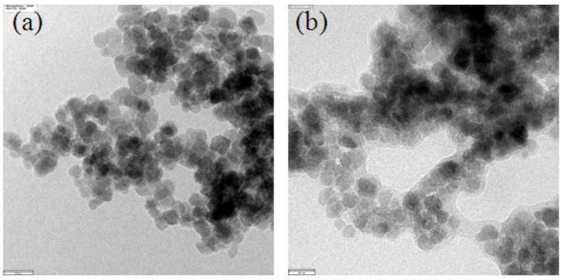

Figure 3. TEM images of (a) Fe_3O_4 and (b) Fe_3O_4/PEG -GA/Rhodamine6G-CLT-TAEA.

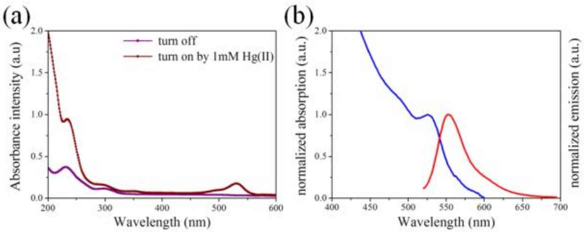

Figure 4. Absorption spectra of Rhodamine6G-CLT-TAEA in water (a). Absorption spectra (blue line) and emission spectra (red line, excitation wavelength = 500 nm) of Fe_3O_4/PEG-GA/Rhodamine6G-CLT-TAEA in water (b)

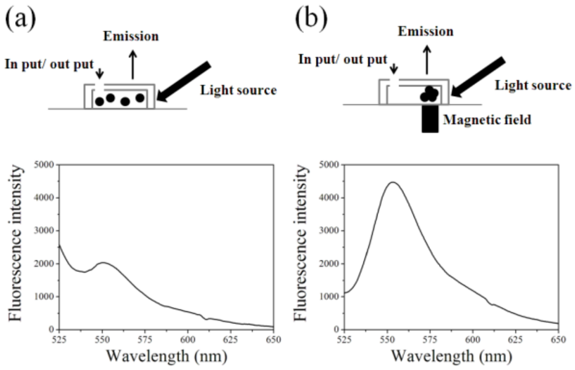

Figure 5. Schematics for enhanced fluorescence detection using magnetic nanoparticles.

the peaks at 536 cm^{-1} correspond to the vibration of the Fe–O stretching. The magnetic nanoparticles grafted with PEG bis(amine) display the peaks at 3069 cm^{-1} and 3277 cm^{-1}, relating to primary and secondary amine stretching, respectively [10]. The absorption bands around 1627 and 1533 cm^{-1} can be attributed to amine I and amine II stretching [11]. The C-N stretching is at 1250-1020 cm^{-1}. For the Fe_3O_4/PEG-NH_2-GA at 3237 cm^{-1} can be attributed to the O-H stretching. The bands at 1628 cm^{-1} can be assigned to the stretching of C=N groups [11]. In the FT-IR spectrum in Fig. 2(d) the peaks around 3354 cm^{-1} relate to $–NH_2$ group and the ν_{lactam}(C=O) vibration occurs at 1637 cm^{-1} . The two bands around 2,922 cm^{-1} and 2,867 cm^{-1} can be assigned to the stretching vibration of $–CH_3$ and $–CH_2$- groups respectively. Overall, the FT-IR results indicate successful cross-linked PEG bis(amine) with GA and Rhodamine6G-CLT-TAEA.

Transmission Electron Microscopy

TEM images show that no significant change in the morphology of the MNPs occurs during the surface replacement reaction (Figure 2.). The mean diameter of the Fe_3O_4 particles determined from TEM micrographs is approximately 10 nm, with a spherical shape as shown in fig 2(a). The grafted Fe_3O_4 has a well defined coating layer seen in Figure 2(b).

Optical and fluorescent spectroscopy

Figure 3(a) provides details of the optical absorption before and after addition of Hg^{2+}. In absorption (black line), peaks are found at 234 and 302 nm. Upon the addition of the Hg^{2+}, a new absorption band at 534 nm appears, which induces a clear color change from colorless to pink. The absorption and emission spectra of the Fe_3O_4/PEG-GA/ Rhodamine6G-CLT-TAEA after an addition of Hg^{2+} exhibits peaks at 525 nm and 554 nm, respectively (Figure 3(b)).

Microchamber experiments

Figure 5 show peak fluorescence before (a) and after fix location of magnetic nanoparticles by magnetic field (b). Fluorescence detection (excitation 500 nm) enhancement of a 0.1 mg of Fe_3O_4/PEG-GA/Rhodamine6G-CLT-TAEA resulting from fix location in microchamber after addition of $50x10^{-5}$ M Hg(II) by fiber optic and mini spectroscopy.

The fluorescence spectra of Fe_3O_4/PEG-GA/Rhoda mine6G-CLT-TAEA 0.1 mg (Scheme 1, 1d) with various concentrations were recorded, as shown in Figure 6. Upon the addition of $5\text{-}50x10^{-5}$ M of Hg^{2+} in water, the optical spectra were recorded within 5 minutes of the addition of Hg^{2+}, is shown in Fig 6a. Plotting (I-Io) and wavelength (nm) will result in straight line as in Figure 6b.

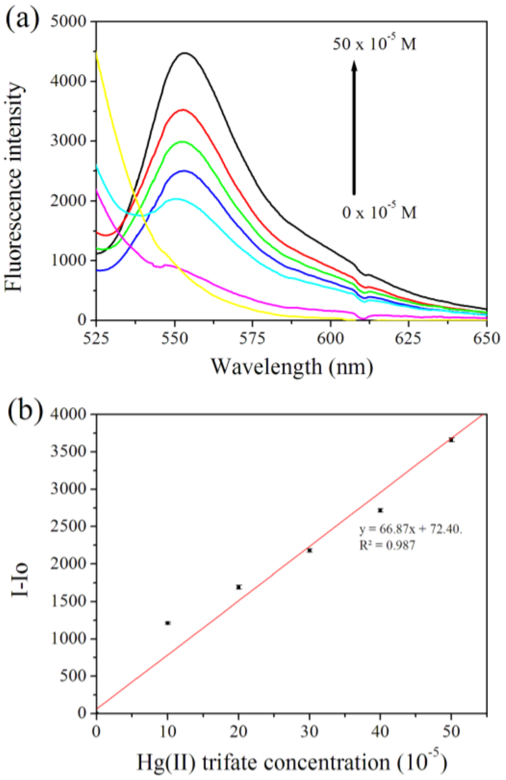

Figure 6. Fluorescent emission (excitation at 500 nm) changes of and Fe$_3$O$_4$/PEG-GA/Rhodamine6G-CLT-TAEA (0.1 mg) upon the addition of Hg^{2+} in water.

A fluorescence changes of Fe$_3$O$_4$/PEG-GA/Rhodamine6G-CLT-TAEA as a result of others metal ions, including 1 Ag(I), 2Fe(II), 3Hg(II) trifate, 4 Co(II), 5 Pb(II), were also measured. Fluorescence spectra of a 0.1 mg of Fe$_3$O$_4$/PEG-GA/Rhodamine6G-CLT-TAEA in water pH 7.0, recorded within 5 minutes of the addition of metals ions, good selectivity and good sensitivity observed for Hg(II) over other ions show in Figure 7.

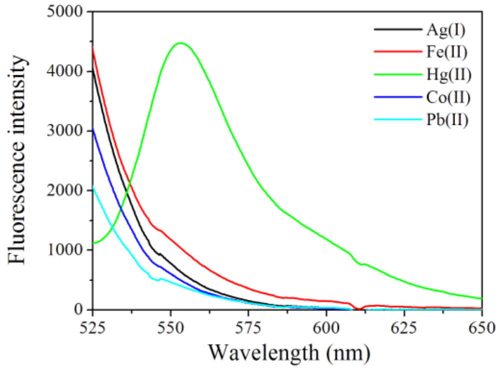

Figure 7. Fluorescent changes of Fe$_3$O$_4$/PEG-GA/Rhodamine6G-CLT-TAEA (0.1 mg/ml) after addition of metal ions.

Conclusions

In summary, we have synthesized a MNP of Fe$_3$O$_4$/ PEG-GA/Rhodamine6G-CLT-TAEA which act as a fluorescent sensor for Hg^{2+} in water. The composite nanoparticles could be used in a microchamber of application to show enhanced fluorescence emission and the presence of various metal ions in water. It is suggested that this method can selectively and sensitively bind to Hg(II), measured of the fluorescence and its application in microchamber by a portable optical spectroscopy.

Acknowledgments

This work supported from the CHE grant no. 2554A11802202 and the National Nanotechnology Center (NANOTEC) NSTDA.

References

1. L. Balcerzak, “Sample digestion Method for the Determination of Traces of Precious Metal by Spectrometric Techniques”, Analytical science 18(2002), 737-750.
2. R. Koteeswari, P. Ashokkumar, E.J.P. Malar, T. Ramakrishnan and P. Ramamurthy , “Highly selective, sensitive and quantitative detection of Hg^{2}+ in aqueous medium under broad pH range”, Chem. Commun 47(2011), 7695-7697
3. H. Prestel, A. Gahr, R. Niessner, “Detection of heavy metals in water by fluorescence spectroscopy” Fresenius J Anal Chem 368(2000) , 182–191
4. Y.K. Yang, K.J. Yook, and J. Tae, “A Rhodamine-Based Fluorescent and Colorimetric Chemodosimeter for the Rapid Detection of Hg^{2+}” American Chemical Society (2005), 127.
5. Y. Wang, *et.al.* “A Novel Chemosensor Based on Rhodamine Derivative for Colorimetric and Fluorometric Detection of Cu^{2+} in Aqueous Solution” Springer-Verlag 22(2012), 799-805.
6. S. Shim and J. Tae, “Rhodamine Cyclen-based Fluorescent Chemosensor for the Detection of Cd2+”, Bull. Korean Chem. Soc. 2011,
7. J. Huang, Y. Xu, and X. Qian, “A Rhodamine-Based Hg2+ Sensor with High Selectivity and Sensitivity in Aqueous Solution: ANS2-Containing Receptor” J. Org. Chem. 74(2009), 2167–2170.
8. X. Peng, Y. Wang, X. Tang and W Liu, “Functionalized magnetic coreeshell Fe3O4@SiO2nanoparticles as selectivity-enhanced chemosensor for Hg(II)”, Dyes and Pigments 91(2011), 26-32.
9. S. Kou, *et.al.* “Microfluidic Detection of Multiple Heavy Metal Ions Using Fluorescent Chemosensors” Bull.Korean Chem.Soc. 30(2009), 1173-1176.
10. B. Hoffmann, *et.al.*“Glutaraldehyde and oxidised dextran as crosslinker reagents for chitosan-based scaffolds for cartilage tissue engineering” Mater Med (2009), 1495-1503.

11. R. Obeid and C. Scholz, “Synthesis and Self-Assembly of Well-Defined Poly(amino acid) End-Capped Poly(ethylene glycol) and Poly(2-methyl-2-oxazoline)” Biomacromolecules 12(2011), 3797−3804.

Light Yield Non-proportionality and Energy Resolution of $Lu_{0.7}Y_{0.3}AlO_3$:Ce and $Bi_4Ge_3O_{12}$ Scintillators

A. Phunpueok[1]*, V. Thongpool[1], K. Bandholnopparat[1], S. Yoo-Kong[2],
and W. Chewpraditkul[2]

[1]*Division of Physics, Faculty of Science and Technology, Rajamangala University of Technology Thanyaburi, Pathumthani 12110, Thailand*
[2]*Department of Physics, Faculty of Science, King Mongkut's University of Technology Thonburi, Bangkok 10140, Thailand*
**Corresponding author. E-mail: aumaum18@hotmail.com*

Abstract

In the last decade, many efforts were devoted to the development of new heavy scintillators for medical imaging, especially, perovskite type based on ceriumed-doped crystals. The scintillation response of two difference sizes of the new Ce-doped lutetium-yttrium aluminum perovskite ($Lu_{0.7}Y_{0.3}AlO_3$:Ce, LuYAP:Ce) crystals were investigated and compared to bismuth germanate ($Bi_4Ge_3O_{12}$:BGO) crystal. The light yield and energy resolution were measured using photomultiplier tube (XP5200B PMT) readout. For 662 keV gamma rays (^{137}Cs source), the small LuYAP:Ce showed the light yield of 10,900 ph/MeV, which is higher than that of 8,900 and 8,500 ph/MeV obtained for BGO and big LuYAP:Ce, respectively. The energy resolution of 7.4 % obtained with small LuYAP:Ce is better than that of 9.0 and 8.9 % obtained with big LuYAP:Ce and BGO, respectively. The light yield non-proportionality and energy resolution versus gamma energy were measured and the intrinsic resolution of the crystals was calculated. Over the energy range from 22.1 to 1,274.5 keV, the non-proportionality of about 19 % for small LuYAP:Ce is better than that of about 21 and 38 % for big LuYAP:Ce and BGO, respectively. The photofraction was determined for all tested crystals and compared with the cross-sections ratio calculated using WinXCOM program.

Keywords**:** BGO, light yield non-proportionality, LuYAP:Ce, scintillators

Introduction

Inorganic scintillators play an important role in detection and spectroscopy of energetic photons and nuclear particles. Important requirements for the scintillation crystals used in these applications include high light yield, fast response time, high stopping power, good energy resolution, good proportionality of light yield, minimal afterglow and low production costs. Good reviews on development of inorganic-scintillators and inorganic scintillation detectors have been published by Moszynski [1], van Eijk [2], and recently by Lecoq et al. [3]. The phenomenon of non-proportionality response and its relation with energy resolution have been studied for many alkali halide scintillators [4] and oxide based scintillators[5]. The scintillation response of alkali halides decreases as the photon energy increases, whereas oxide based scintillators in general show an increasing scintillation response with increasing photon energy, which levels at higher energies.

The aims of this work are to perform a further study of light yield non-proportionality and energy resolution of $Bi_4Ge_3O_{12}$(BGO) and two difference sizes of $Lu_{0.7}Y_{0.3}AlO_3$:Ce (LuYAP:Ce) crystals covering energies from 22.1 to 1,274.5 keV. From the obtained data on photoelectron yield versus the energy of gamma rays and corresponding energy resolution, the light yield non-proportionality and the intrinsic energy resolution of tested crystals were calculated. The estimated photofraction for all tested crystals at 662 keV gamma peak will also be discussed.

Materials and Methods

Two difference size of the new cerium-doped crystals, LuYAP:Ce, with the dimensions of 10x10x5 and 10x10x2 mm^3 supplied by Opto Materials S.r.l. (Italy) were studied and compared to BGO crystal with the dimension of 7x7x1 mm^3 supplied by Shonan Institute of Technology (Fujisawa, Japan).

The crystals were optically coupled to a Photonis XP5200B photomultiplier tube using silicone grease. All measurements were made using standard NIM level electronics. The sources were positioned along the cylindrical axis of the scintillator and the PMT. The signal from the PMT anode was passed to a

CANBERRA2005 preamplifier and was sent to a Tennelec TC243 spectroscopy amplifier. A shaping time constant of 4 µs was used with crystals. The energy spectra were recorded using a Tukan 8k [6] PC-based multichannel analyzer (MCA)[7].

The photoelectron yield, expressed as a number of photoelectrons per MeV (phe/MeV) for each gamma peak, was measured by Bertolaccini method [8]. In this method the numbers of photoelectrons are measured by comparing the position of a full energy peak of gamma rays detected in the crystals with that of the single photoelectron peak from the photocathode, which determines the gain of PMT.

The measurements of photoelectron yield and energy resolution were carried out for a series of gamma rays emitted by different radioactive sources (^{109}Cd, ^{241}Am, ^{133}Ba, ^{51}Cr, ^{137}Cs, ^{58}Co, and ^{22}Na) in the energy range between 22.1 and 1,274.5 keV. For each gamma peak, the full width at half maximum (FWHM) and centroid of the full energy peak were obtained from Gaussian fitting software of Tukan MCA.

Results and Discussion

Photoelectron Yield and Energy Resolution

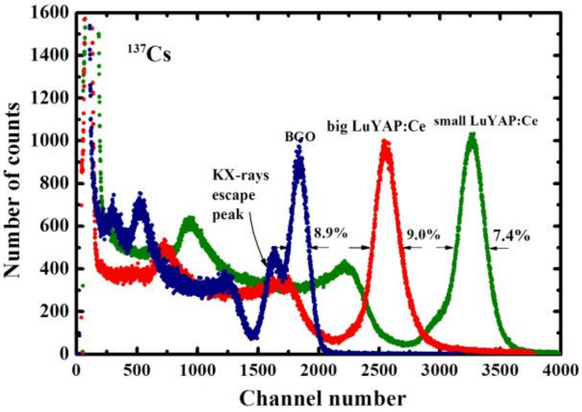

Figure 1. Pulse Height Spectra of Gamma Rays from ^{137}Cs(662 keV) Source as Measured with BGO, Big LuYAP:Ce and Small LuYAP:Ce.

Fig 1. presents the energy spectra of 662 keV gamma rays from a ^{137}Cs source measured with BGO and both LuYAP:Ce detectors. It is seen that small LuYAP:Ce gives better energy resolution than big LuYAP:Ce. The energy resolution of 7.4% obtained with small LuYAP:Ce is much better than the value of 8.9 and 9.0% obtained with BGO and big LuYAP:Ce, respectively. The energy resolution of 7.4 % for the tested small LuYAP:Ce crystal in this study is comparable to small samples observed by Kuntner et al.[9, 10] for LuYAP:Ce crystal (2x2x10 mm^3) supplied by Bogoroditsk Techno-Chemical Plant (Russia). Note a higher photofraction in the spectrum measured with BGO, as would be expected due to a higher effective atomic number of the BGO crystal.

Table 1 summarizes comparative measurements of photoelectron yield, light yield and energy resolution at 662 keV gamma rays for the tested crystals coupled to the Photonis XP5200B PMT, as measured at 4 µs shaping time constant in the spectroscopy amplifier. The small LuYAP:Ce showed a photoelectron yield of 3,250 phe/MeV corresponding to about 10,900 Photon/MeV (ph/MeV), while big LuYAP:Ce showed 2,520 phe/MeV corresponding to about 8,500 ph/MeV, at the PMT photocathode quantum efficiency (QE) of 29.8% for peak emission of 375 nm. The BGO showed a photoelectron yield of 1,840 phe/MeV. This value corresponds to about 8,900 ph/MeV at a QE of 20.7% for peak emission of 480 nm. Note a significantly higher light yield of 10,900 ph/MeV for the small LuYAP:Ce crystal, by about 130%, compared with a smaller sized sample (2x2x10 mm^3) in Ref. [9]. This result shows an improvement of light output for the tested crystal. The different thickness (2 vs 5 mm) of the crystals shall affect the absorption of emitted light decreasing the light yield (3,250 vs 2,520 phe/MeV) of the LuYAP:Ce crystals.

Table 1: Photoelectron Yield, Light Yield and Energy Resolution at 662 keV Gamma Rays for Tested Crystals as Measured with the Photonis XP5200B PMT.

Crystal	Photoelectron Yield [phe/MeV]	Light Yield [ph/MeV]	Energy Resolution [%]
Small LuYAP	3250±160	10900±1100	7.4±0.4
Big LuYAP	2520±130	8500±900	9.0±0.5
BGO	1840±90	8900±900	8.9±0.4

The energy resolution (ΔE/E) of a full energy peak measured with a scintillator coupled to a photomultiplier can be written as [11]

$$(\Delta E/E)^2 = (\delta_{sc})^2 + (\delta_p)^2 + (\delta_{st})^2, \qquad (1)$$

where δ_{sc} is the intrinsic resolution of the crystal, δ_p is the transfer resolution and δ_{st} is the statistical contribution of the PMT to the resolution.

The statistical uncertainty of the signal from the PMT can be described as

$$\delta_{st} = 2.355 \times 1/N^{1/2} \times (1 + \varepsilon)^{1/2}, \qquad (2)$$

where N is the number of the photoelectrons and ε is the variance of the electron multiplier gain, and equals to 0.1 for an XP5200B PMT. The transfer component depends on the quality of optical coupling of the crystal and PMT, homogeneity of quantum efficiency of the photocathode and efficiency of photoelectron collection at the first dynode. The transfer component is negligible compared to the other components of the energy resolution, particularly in the dedicated experiments [11]. The intrinsic resolution of a crystal is mainly associated with the non-proportional response of the scintillator [11] and many effects such as inhomogeneities in the scintillator which can cause local variations in the scintillation light output and non-uniform reflectivity of the reflecting cover of the crystal. Overall energy resolution and PMT resolution can be determined experimentally. If δ_p is negligible, intrinsic resolution δ_{sc} of a crystal can be written as follows

$$(\delta_{sc})^2 = (\Delta E/E)^2 - (\delta_{st})^2. \qquad (3)$$

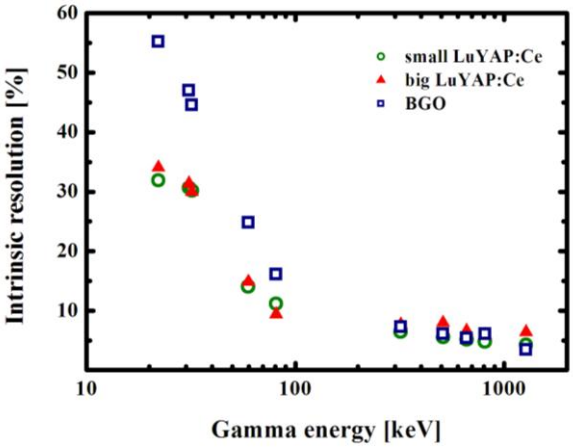

Figure 2. Intrinsic Resolution of BGO and both LuYAP:Ce Crystals.

Fig. 2 presents a direct comparison of the intrinsic resolution for all tested crystals. The intrinsic resolution of small LuYAP:Ce crystal is better than that of BGO and big LuYAP:Ce crystals in the energy range below 80 keV, which is, reflected by a better proportionality of the light yield (see Fig. 3).

Table 2: Analysis of the 662 keV Energy Resolution for BGO and both LuYAP:Ce Crystals.

Crystal	N [electron]	$\Delta E/E$ [%]	δ_{st} [%]	δ_{sc} [%]
small LuYAP	2150±220	7.4±0.4	5.3±0.3	5.2±0.3
Big LuYAP	1670±170	9.0±0.5	6.1±0.3	6.7±0.3
BGO	1220±120	8.9±0.4	7.1±0.4	5.4±0.3

To better understand the energy resolution of tested crystals in gamma ray spectrometry, the contribution of various components to the overall energy resolution was analyzed for 662 keV photopeak, and the results are presented in Table 2. The second column gives N, the number of photoelectrons produced in the PMT. The third column gives $\Delta E/E$, the overall energy resolution at 662 keV photopeak. The PMT contribution (δ_{st}) was calculated using Eq.(2). From the values of $\Delta E/E$ and δ_{st} , the intrinsic resolution (δ_{sc}) was calculated using Eq.(3).

The superior energy resolution of small LuYAP:Ce as compared to BGO is mainly due to a small contribution of both δ_{st} and δ_{sc} , which seems to follow a high light output (almost a factor of two) and good proportionality of the light yield, respectively, for small LuYAP:Ce crystal. For the superior energy resolution of small LuYAP:Ce as compared to big LuYAP:Ce is mainly due to a small contribution of both δ_{st} and δ_{sc} , which seems to follow a high light output (about 1.3 times) and good proportionality of the light yield, respectively, for small LuYAP:Ce crystal.

Non-proportionality of the Light Yield

Light yield non-proportionality as a function of energy can be one of the important reasons for degradation in energy resolution of scintillators [12]. The non-proportionality is defined here as the ratio of photoelectron yield measured for photopeaks at specific gamma ray energy relative to the yield at 662 keV gamma peak.

Fig. 3 presents the light yield non-proportionality characteristics of BGO and both LuYAP:Ce crystals in the energy range of 22.1 to 1,274.5 keV. BGO is clearly poorer than both LuYAP:Ce in terms of light yield proportionality. To better understand, the degree of non-proportionality (σ_{np}) proposed by Dorenbos [13] was calculated with this energy range, we obtain a value of 0.10 for small LuYAP:Ce, 0.12 for big LuYAP:Ce and 0.19 for BGO. The degree of non-proportionality of both tested LuYAP:Ce crystals is lower than the value of 0.15 measured with small sample (2x2x8 mm^3) in Ref.[14], reflecting in lower intrinsic resolution for both tested LuYAP:Ce.

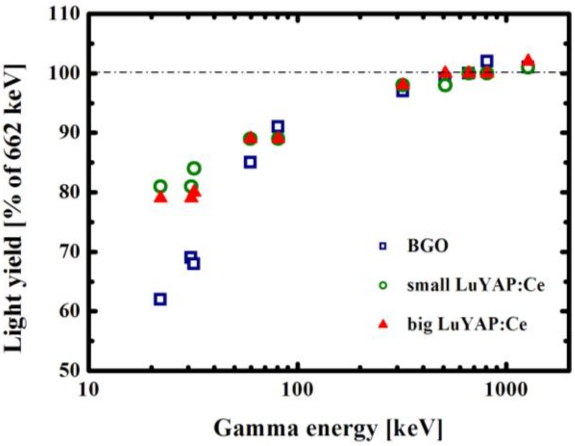

Figure 3. Non-proportionality of the Light Yield of BGO and both LuYAP:Ce Crystals.

Photofraction

The photofraction is defined here as the ratio of counts under the photopeak to the total counts of the spectrum as measured at a specific gamma ray energy. The photofraction for BGO and both LuYAP:Ce at 662 keV gamma peak is collected in Table 3. For a comparison, the ratio of the cross-sections for the photoelectric effect to the total one calculated using WinXCom program [15] are given too. The data indicate that big LuYAP:Ce shows much higher photofraction than small LuYAP:Ce due to higher volume (0.5 vs 0.2 cm^3) of the big crystal. The BGO shows much higher photofraction than small LuYAP:Ce due to higher effective atomic number (74 vs 60) although lower volume (0.049 vs 0.2 cm^3) of the BGO in a same trend with the cross-section ratio (σ-ratio) obtained from WinXCom program.

Table 3: Photofraction at 662 keV Gamma Peak for all Tested Crystals.

Crystal	**Z_{eff}**	**Volume [cm^3]**	**Photofraction [%]**	**σ-ratio [%]**
small LuYAP	60	0.200	23.4±2.3	20.5
big LuYAP	60	0.500	28.7±2.9	20.5
BGO	74	0.049	28.2±2.8	30.8

Conclusions

In this work, the scintillation properties of BGO and two difference sizes of LuYAP:Ce crystals were studied and compared in gamma ray spectrometry. The energy resolution of small LuYAP:Ce is superior than that of BGO and big LuYAP:Ce due to a high light output and small contribution from its intrinsic resolution, reflecting a better proportionality of light yield between 22.1 and 1,274.5 keV. This study demonstrates that the contribution from the non-proportional response of the scintillator is strong correlated with the intrinsic resolution of the scintillators. Moreover, inhomogeneities of Ce-doped and some defects in the LuYAP:Ce crystal could affect the energy resolution, and the crystalline quality of this sample could be further improved. In conclusion, the main advantages of BGO and LuYAP:Ce are high photofraction due to its high effective atomic number and density which make them very promising scintillator for medical imaging.

Acknowledgments

This work was supported by Faculty of Science and Technology, Rajamangala University of Technology Thanyaburi and King Mongkut's University of Technology Thonburi under The National Research University Project.

References

1. M. Moszynski, "Inorganic Scintillation Detectors in γ-ray Spectrometry", Nucl. Instrum. Methods Phys. Res.A **505** (2003)101.
2. C.W.E. van Eijk, "Inorganic-scintillator Development", Nucl. Instrum. Methods Phys. Res.A **460** (2001)1.
3. P. Lecoq, A. Annenkov, A. Gektin, M. Korzhik, and C. Pedrini, "Inorganic Scintillators for Detector Systems", the Netherlands, Springer, 2006.
4. J.D. Valentine, B.D. Rooney, and J. Li, "The Light Yield Nonproportionality Component of Scintillator Energy Resolution", IEEE Trans. Nucl. Sci. **45**(1998) 512.
5. E.P. Sysoeva, O.V. Zelenskaya, and E.V. Sysoeva, "The Nonproportional Response of Single Crystalline Oxide Scintillators", IEEE Trans. Nucl. Sci. **43** (1996) 1282.
6. Z. Guzik, S. Borsuk, K. Traczyk, and M. Plominski, "Enhanced 8k pulse height analyzer and multichannel scaler (TUKAN) with PCI or USB interfaces", IEEE Trans. Nucl. Sci. **53** (2006) 231
7. J. R. Anglin and W. Ketterle, "Bose-Einstein Condensation of Atomic Gases", Nature **476** (2002) 211.
8. M. Bertolaccini, S. Cova, and C. Bussolatti, "A Technique for Absolute Measurement of the Effective Photoelectron Per keV Yield in Scintillation Counters", in Proc. Nuclear Electronics Symp., Versailles, France, 1968.
9. C. Kuntner, E. Auffray, P. Lecoq, C. Pizzolotto, and M. Schneegans, "Intrinsic energy resolution and light output of the $Lu_{0.7}Y_{0.3}AP$:Ce scintillator", Nucl. Instrum. Methods Phys. Res. A **493** (2002) 131.
10. C. Kuntner, E. Auffray, D. Bellotto, C. Dujardin, N. Grumbach, I.A. Kamenskikh, P. Lecoq, H. Mojzisova, C. Pedrini, and M. Schneegans, "Advances in the scintillation performance of LuYAP:Ce single crystals", Nucl. Instrum. Methods Phys. Res. A **537** (2005) 295.
11. M. Moszynski, J. Zalipska, M. Balcerzyk, M. Kapusta, W. Mengeshe, and J.D. Valentine, "Intrinsic energy resolution of NaI(Tl)", Nucl. Instrum. Methods Phys. Res.A **484** (2002) 259.
12. P. Dorenbos, J.T.M. Haas, and C.W.E. van Eijk, "Non-proportionality in the Scintillation Response and Energy Resolution Obtainable with Scintillation Crystals", IEEE Trans. Nucl. Sci. **42** (1995) 2190.
13. P. Dorenbos, "Light output and energy resolution of Ce^{3+}-dopedscintillators", Nucl.

Instrum. Methods Phys. Res. A **486** (2002) 208.

14. J. Trummer, E. Auffray, P. Lecoq, A. Petrosya, and P. Sempere-Roldan, “Comparison of LuAP and LuYAP crystal properties from statistically significant batches produced with two different growth methods”, Nucl. Instrum. Methods Phys. Res. A **551** (2005) 339.
15. L. Gerward, N. Guilbert, K.B. Jensen, and H. Levring, “WinXCom – a program for calculating X-ray attenuation coefficients”, Rad. Phys. And Chem. **71** (2004)653.

Mechanical Properties of Bamboo *(Thyrsostachys Siamensis Gamble)*/ Vetiver *(Vetiveria Zizanioides)* Fibers/Epoxy Resin Hybrid Biocomposites

P. Penpokai, W. Thamjaree[*], and Wim Nhuapeng

Department of Physics and Materials Science, Faculty of Science, Chiang Mai University, Chiang Mai 50200 , Thailand
**Corresponding autho E-mail: th_wandee@hotmail.com*

Abstract

In this work, mechanical properties of bamboo ***(Thyrsostachys Siamensis Gamble)*** /vetiver ***(Vetiveria Zizanioides)*** fibers reinforced epoxy resin biocomposite were studied. The composites samples were fabricated via hand lay-up technique. Firstly, bamboo reinforcement fiber was prepared in the length of 10 mm and added into resin for 12% by weight whereas the vetiver fiber was added in different ratio (2, 4, 6,8,10 and 12 % by weight). Mechanical properties, such as tensile strength and impact strength were examined. From the results, it could be seen that the hybrid biocomposites with 2% by weight of vetiver exhibited the highest tensile strength and impact strength. Furthermore, microstructure of the samples was also examined using Scanning Electron microscopy (SEM). The micrographs revealed the good adhesion between fiber reinforcement and polymer matrix which promote mechanical properties of hybrid biocomposites.

Keywords: Hybrid biocomposites, Mechanical properties, Tensile testing, Impact test

Introduction

Engineered wood has started from the customers using natural materials; the popular natural material is wood. Additionally, they are also recycling the splat, spill, wood-fiber, and thin wood to bond together by adhesives types to make the wood composites. It is most effective and worthy. Today wood is a limited resource. Therefore, the wood composite is used to compensate natural wood. The wood composite has been popular in furniture industrial.

Particleboard (chipboard) is the wood composite that been developed in USA and Europe in 1930 due to insufficiency of natural wood. Germany is the first country that can produce and distribute since 1941. Particleboard is made from a small piece of wood or other material that containing lignin and cellulose such as husk, straw, sawdust, nut-shell, and jute the technology have been developed until now. However, in this study, a bamboo (Thyrsostachys Siamensis Gamble) fiber known in Thailand as Phai Luak fiber and a vetiver (Vetiveria Zizanioides) fiber used as a material to reinforce a polymer matrix in epoxy composites [1].

Bamboo fiber is one of the most attractive candidates as a strengthening natural fiber [2]. It has several advantages, such as (1) the environmental load is small, because it is grows rapidly, thus it is easy to regenerate after cutting, and (2) the bamboo fiber has relatively high strength compared with other natural fibers such as jute and cotton.

Vetiver (Vetiveria Zizanioides) is a tropical plant that grows naturally. They can be founded in the general area of Thailand. The study of properties of vetiver shown that the tensile strength was 247-723 MPa, and the elongation at break was 1.6-2.4% So, these properties of vetiver are interesting to study and apply [3].

Nowadays, the environmental problems and resource insufficiency are important problems. Therefore, in this research the bamboo and vetiver are chosen to be the sources of fibers for producing reinforced composite and investigate the effects of vetiver quantity on mechanical properties of composite between bamboo fibers, vetiver fibers and epoxy resin.

Materials and Methods

In this work, the main studies were carried out to investigate how volume of vetiver fiber reinforced composite affects tensile strength and impact strength. This section presents experimental using the preparation of composites from raw materials. Firstly, the bamboo fibers were collected from the San Kamphaeng Village, San Kamphaeng District, Chiang Mai Province, Thailand and the vetiver fibers were collected from the group of Royal Vetiver, Ban Sang Village, Amphoe Mae Rim, Chiang Mai Province, Thailand. Bamboo fibers were carefully extracted from the bundles with a penknife technique and vetiver fibers were extracted from sieve ASTM number 80 (sieve opening 180 µm). The two years old bamboos were used in the work and the vetiver one year old. A diameter of bamboo fiber was in the range of 250-300 µm and vetiver fiber was in the range of 150-180 µm. Secondly, the bamboo fibers and vetiver fibers were immersed in NaOH solution (NaOH 97% RCI Labscan AR1171-P1KG, 0.25M) for 60 min [4]. Thereafter, fibers were rinsed with deionized water until rinsed solution reached neutral (pH7). The fibers were then dried at room temperature for 5 days. After that, composites containing 12% by weight of bamboo fibers and vetiver fibers in difference quantity that 2, 4, 6, 8, 10, and 12% by weight wrer fabricated. A matrix was created by mixing epoxy resin (Thai Epoxy Resin Ltd,.Thailand) with its hardener in the ratio 100:27 by volume. The density of the matrix is 1.176 g/cm^3. The mixture was poured into the rubber mould in the dog-bone shape it was 130 mm in length, 25 mm in width and 1 mm in thickness with a gage length of 33 mm and in the rectangular shape, it was 55 mm in length, 10 mm in width and 10 mm in thickness. They are noted that Mylar films were put at the upper and the lower of the sample in order to obtain a smooth surface.

Finally, the composite samples were left to settle at the room temperature for one day and then removed from the mould. Tensile strength of the sample was measured by the Hounsfield mechanical testing machine using a cross-head speed of 50 mm/min and 250 mm extensometer. Impact strength was measured by the Impact testing machine. The microstructure of composites sample was investigated by scanning electron microscope (SEM).

Results and Discussion

Figure 1 show the variation in tensile strength of composite with the change in volume of the vetiver fibers (in the range 2-12% by weight). In general the thermoset composites showed an increasing trend in their mechanical properties with the volume fibers [5]. However, the optimal condition is at a vetiver volume of 2% by weight (54.57 MPa). The vetiver volume from 4 to 12% by weight decreasing tendency in tensile strength has been attributed to two situations: namely, the existence of defects, such as voids, and weak interface bonding between matrix and reinforcement [6].

Moreover, the elongations at break (ε) of composite decrease with increasing vetiver contents shows in Figure2. The percent elongation at break of the composites is lower than that of the matrix. This could be affected of low fracture strain and the poor adhesion between the matrix and the fibers [6 and 7].

In addition, the decreased impact strength a higher vetiver volume content could be attributed to poor adhesion between the fiber and the matrix, which promotes micro crack formation at the interface. A higher volume content result in more void formation during processing, which leads to micro crack formation under loading and therefore reduces the impact strength show in the Figure 3 which similar to [6].

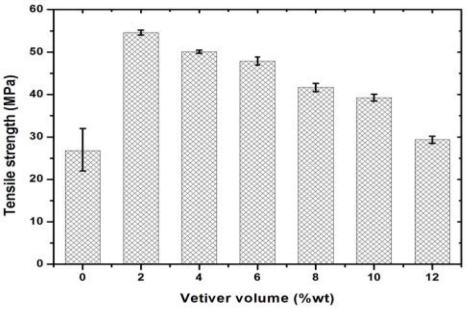

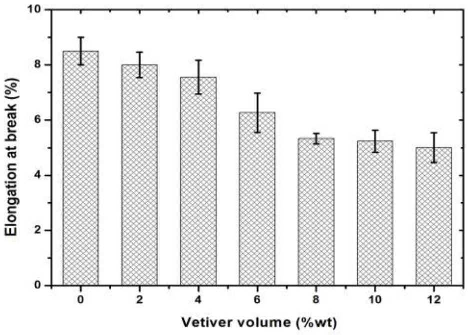

Figure 1.Tensile strength of Bamboo and Vetiver reinforced epoxy composite with vetiver volume.

Figure 2.Elongation percentage at break of Bamboo and Vetiver reinforced epoxy composite with vetiver volume.

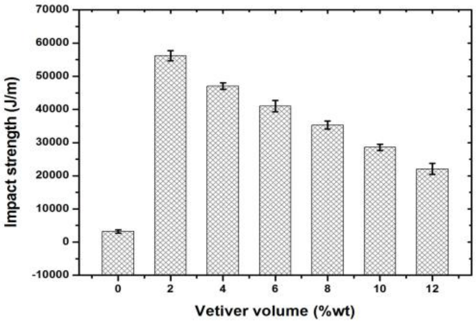

Figure 3.Impact strength of Bamboo and Vetiver reinforced epoxy composite with vetiver volume.

The SEM micrograph of the failure surfaces was used for direct observation of composite structure, and particularly to examine the resin fiber interface. The net result of SEM is that the nature of the differing interactions such as the physical mixing of matrix and sizing resins and the nature of chemisorptions at the fiber surface give rise to an interphase region as opposed to a distinct interface between fiber and matrix [8]. The role of the matrix in the fiber-reinforced composite is transfer the load to the stiff fiber through shear stress at the interface.

In Figure 4, it is showed that 2 % by weight in vetiver volume of composite have a good adhesion between matrix and fiber. The load acting on the matrix has been transferred to the reinforcement via the interface [9]. Thus, reinforcement must be strongly bonded to the matrix if their high strength and stiffness are to be imparted to the composite. It is also noticed that the fiber failed by tearing instead of the interfacial failure is observed. There are traces of matrix is still adhered to the fiber. This can indicate that the adhesion between fiber and matrix was not lost and the failure process was dominated by the matrix material properties.

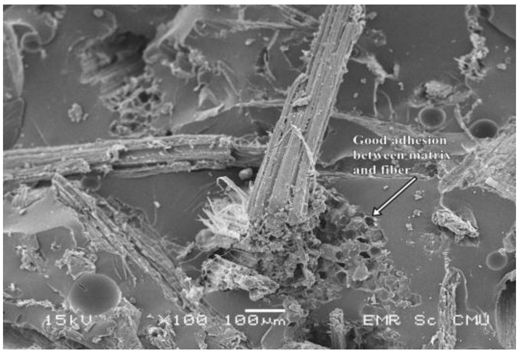

Figure 4. SEM of fracture surface of hybrid composites 2 % by weight of vetiver.

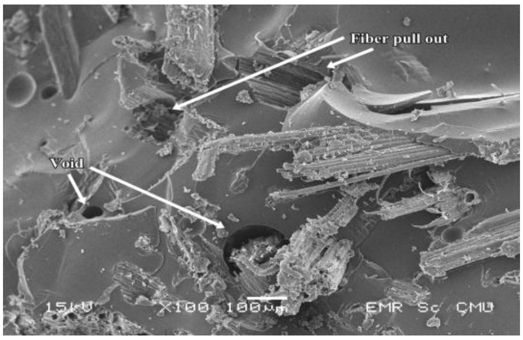

Figure 5. SEM of fracture surface of hybrid composites 12 % by weight of vetiver.

Figure 5, it is shown that there is a small gap between fiber and matrix which means a poor adhesion or interfacial bonding for 2 mm in length. The void and small gap formed was probably caused by incomplete wettability or bonding between matrix resin and fiber during the fabrication of composites [10].

Conclusions

In this work, the tensile properties of bamboo and vetiver fibers reinforced epoxy composite have been measured. Based on the result, it was found that the tensile strength, elongation at break, and impact strength showed a decreasing trend as the vetiver volume was increased. The optimum of vetiver volume in epoxy resin to obtain the highest tensile strength, elongation at break, and impact strength was found at hybrid biocomposites with 2% by weight. It was also found the void, and small gap, vetiver volume and interfacial adhesion between fiber-matrix can affect the mechanical properties of the composite.

Acknowledgments

The authors would like to thank the National Research Project Management (NRPM) for funding. The Composites and Reinforcement Nano composites Unit, Department of Physics and Materials Science, Faculty of Science and the Graduate School of Chiang Mai University for facilities and greatfully knowledge.

References

1. Kalaycioglu H,and Nemli G. “Producing composite particleboard from kenak” (Hibiscus cannabinus L.) stalks, Ind.Crops Props.2006;24:177-180.
2. Okubo K., Fujii T., “Eco-composites using bamboo and other natural fibers and their mechanical properties”, Proc. of International W orkshop on Green Composites, 17-21 (2002).
3. Ruksakulpiwat Y. et al. “Vetiver–polypropylene composites: Physical and mechanical properties”, Nakhon Ratchasima 30000, Thailand. 2007; (38) 590–601.
4. Kongkeaw P., Nhuapeng W., Thamjaree W ., “The influence of alkaline treatment on tensile properties of short bamboo (Thyrsostachys Siamensis Gamble) fiber reinforced epoxy resin composites”, The 2nd CMU Graduate Research Conference 2, 264-269 (2010).
5. Yupaporn Ruksakulpiwat, Jatuporn Sridee, Nitinat Suppakarn, and Wimonlak Sutapun, “Improvement of impact property of natural fiber–polypropylene composite by using natural rubber and EPDM rubber”, Composites: Part B 40 (2009) 619–622.
6. Moe Moe Thwe and Kin Liao, “ffects of environmental aging on the mechanical properties of bamboo±glass ®ber reinforced polymer matrix hybrid composites”, Composites: Part A 33 (2002) 43-52.
7. Chumsamrong P., Sutapun W ., Kiaw-on S., Tonuloon W., “Influence of alkali treated rossells fibers on the tensile properties of unsaturated polyester resin”, 31st Congress on Science and Technology, 2005.

8. Jones F.R., “Interphase formation and control in fiber composite material”, J. Engineering Materials 37, 116-117 (1996).
9. Mathews F.L., Rawlings R.D., “Composites Materials Engineering and Science”, Chapman and Hall, London 1999.
10. Arib R.M.N., Sapuan S.M., Ahmad M.M.H.M., Paridah M.T., Khairul Zaman H.M.D., “Mechanical properties of pineapple leaf fibre reinforced polypropylene composite”, Materials & Design 27, 391-396 (2006).

Microstructure and Mechanical Properties of 6063 Aluminium Alloy Subjected to Equal Channel Angular Pressing

T. Gulroung, T. Chairuangsri, and C. Banjongprasert*

Department of Physics and Materials Science, Faculty of Science, Chiang Mai University,
Chiang Mai 50200, Thailand
**Corresponding author.E-mail:chaiyasit_au@yahoo.com*

Abstract

In this study, microstructure and mechanical properties of an aged aluminium alloy (Al 6063 alloy) processed by Equal Channel Angular Pressing (ECAP) have been investigated. Al 6063 alloy was ECAPed with 1 and 2 passes at room temperature. After ECAPed the samples were aged at five different ageing temperatures (100˚C, 125˚C, 150˚C, 175˚C and 200˚C). The microstructure of the aged samples was examined by optical microscope (OM), scanning electron microscope (SEM) with energy dispersive X-ray spectroscopy (EDS) analysis. The hardness of the aged samples was measured by Vickers hardness tests. The results show that the hardness of ECAPed samples was higher than that of solution heat treated samples. For aged samples, the hardness increased with an increase of the aging temperature and aging time due to a higher volume fraction of precipitates.

Keywords: Aluminium alloy, Equal Channel Angular Pressing, Heat treatment

Introduction

Nowadays, Aluminium alloys have been wide used in a variety of industries ranging from household products to aerospace component. Due to the increasing price of crude oil the automobile industry has recently focused on reducing car weights. One of the strategies is to implement more aluminium alloy in a car. However, to increase the use of aluminum alloys extensive research and development will be required. One problem in the development of this research. The strength of the material without the need to reduce the size of the samples. The Severe plastic deformation (SPD) is the solution of this problem is the material is deformed but not reduce the size of the samples. This process is much like ; Equal channel angular pressing (ECAP), High pressure torsion (HPT), Accumulative roll bonding (ARB) and Groove pressing etc.[1-2].

Equal channel angular pressing (ECAP) is a technique using severe plastic deformation to produce ultrafine - grained alloys in a range of tens of nanometers several microns [3-4]. ECAP is performed by pressing a samples through a die that has two channels which intersect at an angle. The sample experiences covert shear deformation at the intersection without any precipitous change in the cross section area because the die does not allow lateral expansion. Depending on the rotation of the samples, different deformation routes can be applied. Route A designated for no rotation of the samples; route B_A designated for 90˚ counter clockwise on even number of passes and clockwise on odd number of passes; route B_c designated for 90° counter clockwise after every pass; route C is rotated 180° after every pass . This technique can be applied to almost every commercial alloys results in extremely fine-scale microstructure without defects [5-6].

Materials and Methods

In order to evaluate the effect of the initial microstructure on the properties, a set of cylindrical samples in form of rod (with a diameter 20 mm and a length 100 mm) of commercial Al 6063 T5 alloy in two different conditions was ECAPed followed by aging heat treatments.

For the ECAP processing, samples of 20 mm in diameter and 100 mm in length were machined from the solution treated rod. A split die was used to avoid stress concentration at the corners and to facilitate easy removal of the ECAPed specimen. The ECAP die is cylindrical with a channel angle (ϕ) of 100˚ and curvature of the outer corner (ψ) is 20˚ in figure 1. The lubricant was a Mo_2S (WD-40) lubricants.

Two different ageing and ECAP processes were carried out to investigate the inter-relationship between the solution treatment and the subsequent ageing after ECAPed: For the first and second group specimens was anneal at 530˚C for 2 h before ECAP 1-2 pass. In first group after ECAP 1-2 pass was aged at the temperatures of 100˚C, 125˚C, 150˚C, 175˚C and 200˚C for different times. After that in second group after ECAP 1-2 pass was solution treated for 1 h at 520˚C quenching in water on room temperature and aged at 125˚C, 150˚C, 175˚C with different ageing time. Samples were investigated along X and Y planes as illustrated in figure 1.

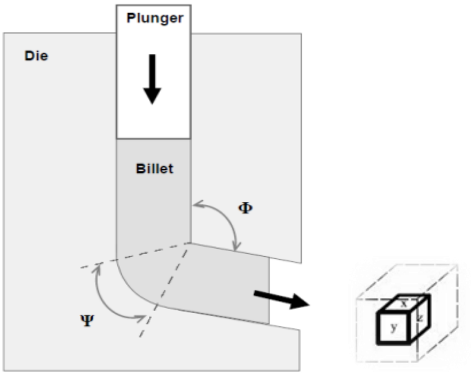

Figure 1. Cyindrical ECAP die with a channel angle (ϕ) and curvature of the outer corner (ψ) [7].

In order to investigate the ageing characteristics and mechanical properties of ECAPed samples, SMV-1000 vickers-hardness and scanning electron microscope (SEM) FP2022/31 and energy dispersive spectroscopy (EDS) were used.

Results and Discussion

Microstructure

- Optical microscope (OM)

Figure 2 shows the distortion of grains due to the shear stresses during ECAPed with an equivalent true strain of 0.899 from one pass. The distortion increased with an increase of number of passes. This was due to an increase of accumulated shear strain from 0.899 to 1.798 calculated from equation 1.

$$\varepsilon_n = \frac{N}{\sqrt{3}}\left[2\cot\left(\frac{\phi}{2}+\frac{\psi}{2}\right)+\psi\,\mathrm{cos}\,ec\left(\frac{\phi}{2}+\frac{\psi}{2}\right)\right] \quad (1)$$

Therefore, for any given value of ϕ and ψ, the accumulated strain can be estimated from Eq. 1 for a multi-pass ECAP process [8]. The angle ϕ plays a significant role in determining the amount of plastic strain induced in the sample per ECAP pass.

- Scanning electron microscope (SEM) and Energy dispersive spectroscopy (EDS)

SEM image shows that the microstructure was composed of precipitation of bright phases. The EDS result revealed that contained: Al, Fe and Si corresponding to AlFeSi, which was a common precipitate in this alloy as shown in figure 3 [9].For smaller precipitates it is necessary to use the transmission electron microscope (TEM) to characterize fine scale precipitates , such as Mg_2Si (β) with an average diameter of 1-5 nm[10].

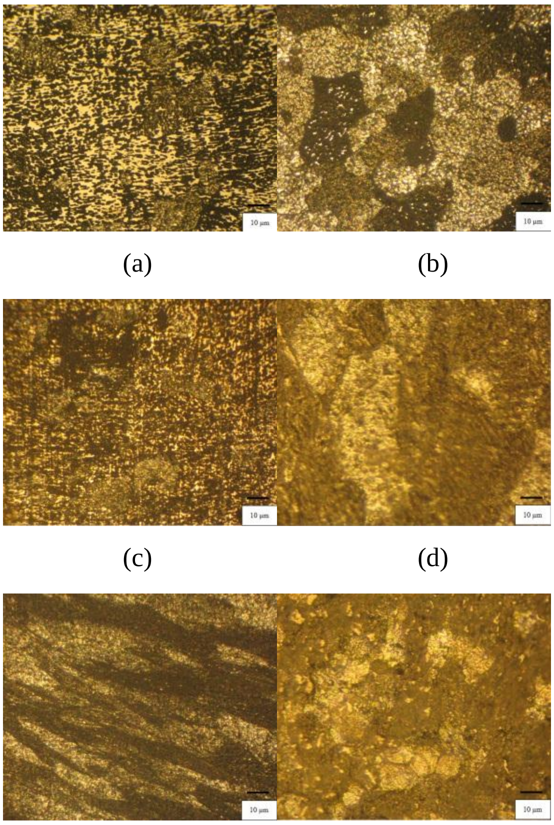

(a) (b)

(c) (d)

(e) (f)

Figure 2. OM images, (a) Al 6063 plane X, (b) Al 6063 plane Y, (c) 1-pass plane X, (d) 1-pass plane Y, (e) 2-pass plane X, (f) 2-pass plane Y.

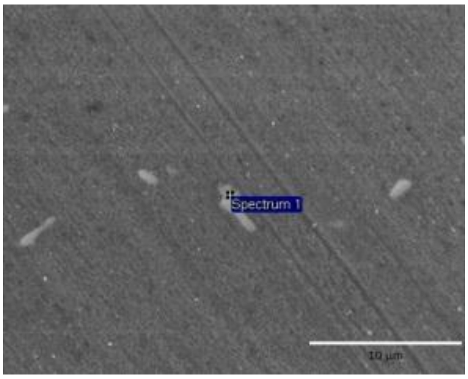

(a)

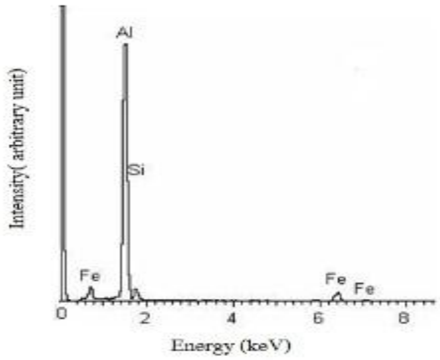

(b)

Figure 3. (a) SEM image and (b) EDS graph of 2 passes (solution heat treated - aged at 175 ˚C for 24h)

Hardness test

In the first condition, appropriate temperatures and times for peak aging were 73 Hv in 125 ˚C at 8 hours on X plane and 74 Hv in 125 ˚C at 16 hours on Y plane and second conditions, for peak aging were 98 Hv in 150 ˚C at 48 hours on X plane, 102 Hv in 150 ˚C at 48 hours on Y plane respectively in figure 4,5.

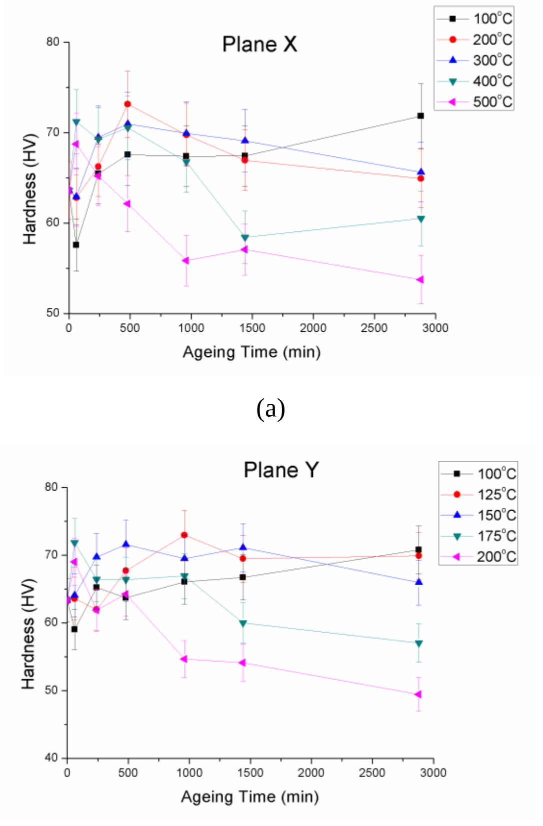

(a)

(b)

Figure 4. Aging curve in the first group, (a) 1-pass plane X, (b) 1-pass plane Y.

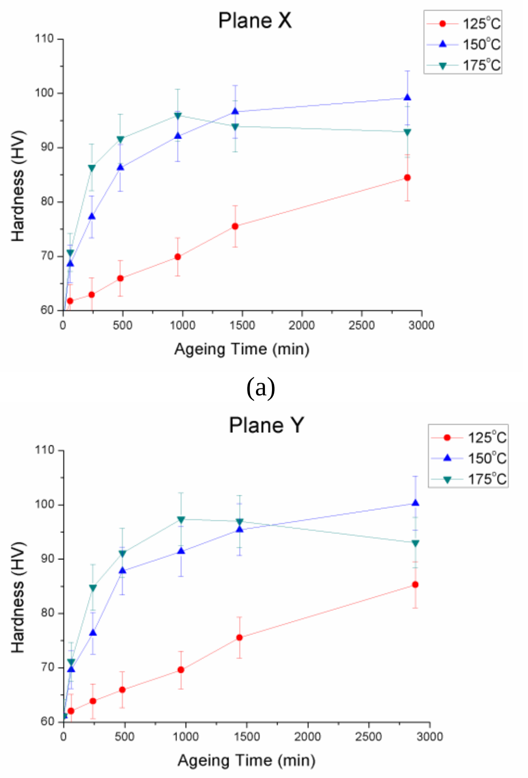

(a)

(b)

Figure 5. Aging curve in the second group, (a) 2-pass plane X, (b) 2-pass plane Y.

The results show the hardness was higher than that of group 1. It was belived that solutionization (group 2) resulted in a uniform distribution of solute atom so that complete ageing could be occurred while ageing without (group 1) solutionization could lead to incomplete ageing and lower hardness, Moreover the X and Y planes hardness in both condition was slightly different because each plane had differrent degree of retained strain due to inhomogeneous applied shear stresses.

Figure 6 shows that ECAP could improve hardness from annealed sample. Moreover higher hardness can be achieved from ECAPed samples after an appropriate ageing condition and this was better than commercially 6063 Al alloy.

It was reported that in the age-hardening process of Al–Si–Mg alloy, GP zones (Mg–Si-vacancy co-clusters), metastable phase, β' and stable phase β can effectively strengthen the alloy and lead to the ageing peaks. The aged sample may had this Mg_2Si precipitate which enhance the hardness and this is yet to be confirmed by further works. [11].

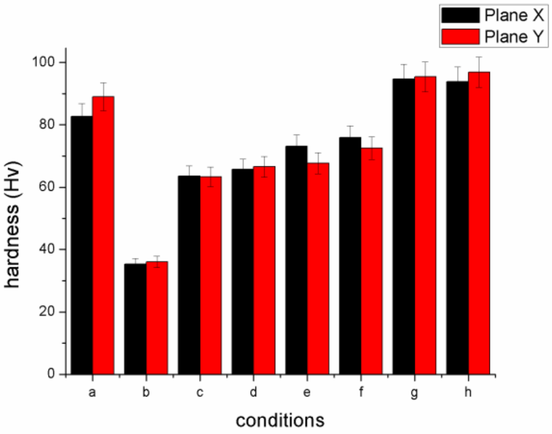

Figure 6. bar chart compared between the samples hardness certain to study the effect of ECAP process (a: commercial 6063, b: anneal, c: 1-pass, d: 2 pass, e: 1-pass-ageing 125 ˚C 8 h, f: 2-pass-ageing 125 ˚C 8h, g: 1-pass-solution heat treated-ageing 175 ˚C 24h, h: 2-pass-solution heat treated-ageing 175 ˚C 24h)

Conclusions

As a result of this study, the hardness of the ECAPed samples was found to be higher than that of the samples. For aged samples, the hardness increased with an increase of the solution temperature and aging time due to a higher volume fraction of precipitates. This is probably the result of effects of grain refinement, developing textures, and recrystallization on mechanical property of ECAPed and aged samples.

Acknowledgments

The authors would like to gratefully acknowledge the Thailand Research Fund (TRF) and the Commission on Higher Education (CHE) Grant (MRG5580181); and the Department of Physics and Materials Science, Faculty of Science, Chiang Mai University

References

1. ASM HANDBOOK, “Properties and Selection: Nonferrous Alloys and Special- Pupose Materials”, **2** (1990).
2. M Saravanan, R.M. Pillai, B.C. Pai, M Brahmakumar and K.R. Ravi, “Equal channel angular pressing of pure aluminium—an analysis” Bulletin Material Science, **29** (2006), 679–684.
3. R.Z. Valiev, A.V. Korznikov, and R.R. Mulyukov, “Structure and properties of ultrafine-grained materials produced by severe plastic deformation”, Materials Science and Engineering, **168** (1993), 141–148.
4. Z. Horita, and T. Fujinami, “Equal-channel angular pressing of commercial aluminium alloys: grain refinement, thermal stability and tensile properties”, Metallurgical and Materials Transactions, **31** (2000), 691–701.
5. *V.M. Segal*, “Materials processed by simple shear”, Materials Science and Engineering, **197** (1995), 157–164.
6. M. Furukawa, Y. Iwahashi, Z. Horita, M. Nemoto, and T.G. Langdon, “The shearing characteristics associated with equal-channel angular pressing”, Materials Science and Engineering, **257** (1998), 328–332.
7. Su Chun Wei , “Mechanical properties and microstructure of magnesium alloy from severe plastic deformation”, PhD thesis University of Singapore, (2006)
8. Y. Iwahashi, Z. Horita, M. Nemoto, and T.G. Langdon, “An investigation of microstructural evolution during equal-channel angular pressing”, Acta Materialia., **45** (1997), 4733–4741.
9. J. M. Gómez de Salazar, A Ureña , E. Villauriz , S. Manzanedo, and I. Barrena, “TIG and MIG welding of 6061 and 7020 aluminium alloys microstructural studies and mechanical properties”, Welding International, **13:4** (2010), 293-295.
10. H. J. Roven, M. Liu, and J. C. Werenskiold “Dynamic precipitation during severe plastic deformation of an Al–Mg–Si aluminium alloy”, Materials Science and Engineering, **483–484** (2008), 54–58.
11. R. Z. Valiev, and T. G. Langdon, “Principles of equal-channel angular pressing as a processing tool for grain refinement”, Progress in Materials Science, **51** (2006), 881–981.
12. M. Vaseghi, T. A. Karimi, JH. Yoo, SH. Joo, and HS. Kim, “Adiabatic shear banding in an Al–Mg–Si alloy processed by equal channel angular pressing”, Material. Science. Forum, **7** (2010), 654–656.

Modification of Used Atomic Force Microscope Cantilever by Carbon Nanotube Attachment and its Imaging Performance

Y. Maneerat[1*], P. Dulyaseree[2], S. Pratontep[2,3] and W. Wongwiriyapan[2,3]

[1]*College of Data Storage Innovation, King Mongkut's Institute of Technology Ladkrabang, Chalongkrung Rd, Ladkrabang, Bangkok 10520 Thailand*
[2]*College of Nanotechnology, King Mongkut's Institute of Technology Ladkrabang, Chalongkrung Rd, Ladkrabang, Bangkok 10520 Thailand*
[3]*Nanotec-KMITL Center of Excellence on Nanoelectronic Devices, Chalongkrung Rd, Ladkrabang, Bangkok 10520 Thailand*
**Corresponding author. E-mail: Yuwapan.Maneerat@Seagate.com*

Abstract

Modification of used atomic force microscope (AFM) cantilever by carbon nanotube (CNT) attachment and its imaging performance was demonstrated. CNTs were directly grown on apex of used AFM cantilever by Ni catalyst-assisted chemical vapor deposition (CVD) using ethanol as carbon source. To obtain CNTs protruding from the apex of the pyramid shape of cantilever, the optimum CVD was operated at growth temperature of 850^{0}C for 20 min. Field-emission electron microscope, transmission electron microscope and Raman spectroscopy were utilized for the synthesized CNT characterization. For imaging performance test, silicon dioxide coated with a uniform layer of platinum which is AFM standard sample, was used as a test sample. Surpassing new and used AFM cantilevers, imaging obtained from CNT-modified AFM cantilever showed high-resolution imaging in both lateral and vertical resolution.

***Keywords*:** Carbon nanotube, Chemical vapor deposition, Atomic force microscope, Cantilever

Introduction

Atomic force microscope (AFM) is an important tool for matter imaging, measuring, and manipulating. Recently, with the development of nanotechnology, carbon nanotube (CNT) is considered as an ideal structure probe used for scanning probe microscopes due to its excellent structural, mechanical, and electrical properties [1]. The key advantages of CNT over conventional microfabricated Si cantilever include high lateral imaging resolution due to tip sharpness, high imaging consistency over prolonged operation, and high durability and long lifetime due to its excellent mechanical stiffness and high resilience against mechanical damage [1]. To fabricate the CNT cantilever, CNT will be attached to the apex of the pyramid shape of cantilever by bonding CNT using an acrylic adhesive [2] or growing CNT directly on the cantilever apex by chemical vapor deposition (CVD) [3-6]. Direct growth provides a good mechanical contact between CNT and the cantilever body. From previous reports, CNT cantilevers mostly demonstrate on the new Si cantilever. However, in term of performance cost, modification of used AFM cantilever for imaging improvement is a challenge.

In this study, the used cantilever was used as a platform for CNT attachment by direct growth method of Ni catalyst-assisted CVD using ethanol as carbon source. Surpassing new and used AFM cantilevers, imaging obtained from CNT-modified AFM cantilever showed high-resolution imaging in both lateral and vertical resolution.

Materials and Methods

AFM cantilever which could not be longer used for imaging scanning, used cantilever, was modified by attachment of CNT on its apex. Attachment of CNT was conducted by direct growth of CNT on the pyramid shape of the cantilever using Ni catalyst-assisted CVD. Ni catalyst layers were deposited on the cantilever using electroplating technique. Next, Ni catalyst layer-deposited AFM cantilever was set into a quartz tube reactor for CVD process. Detailed

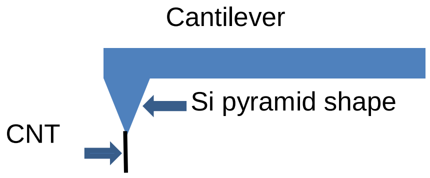

Figure 1 Schematic view of CNT-modified cantilever

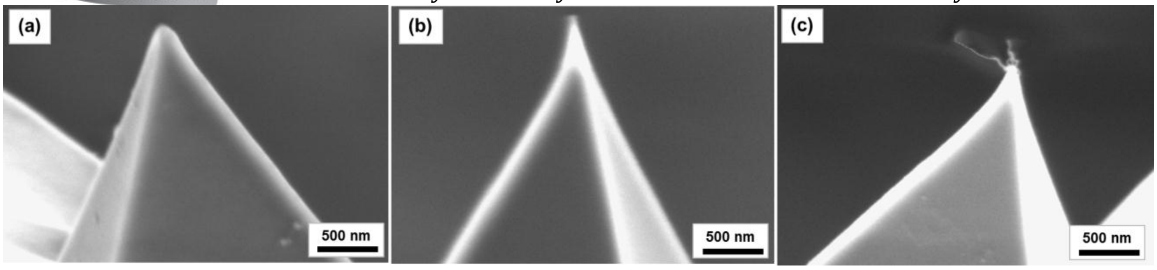

Figure 2 FESEM images of (a) reused, (b) new and (c) CNT-modified cantilevers

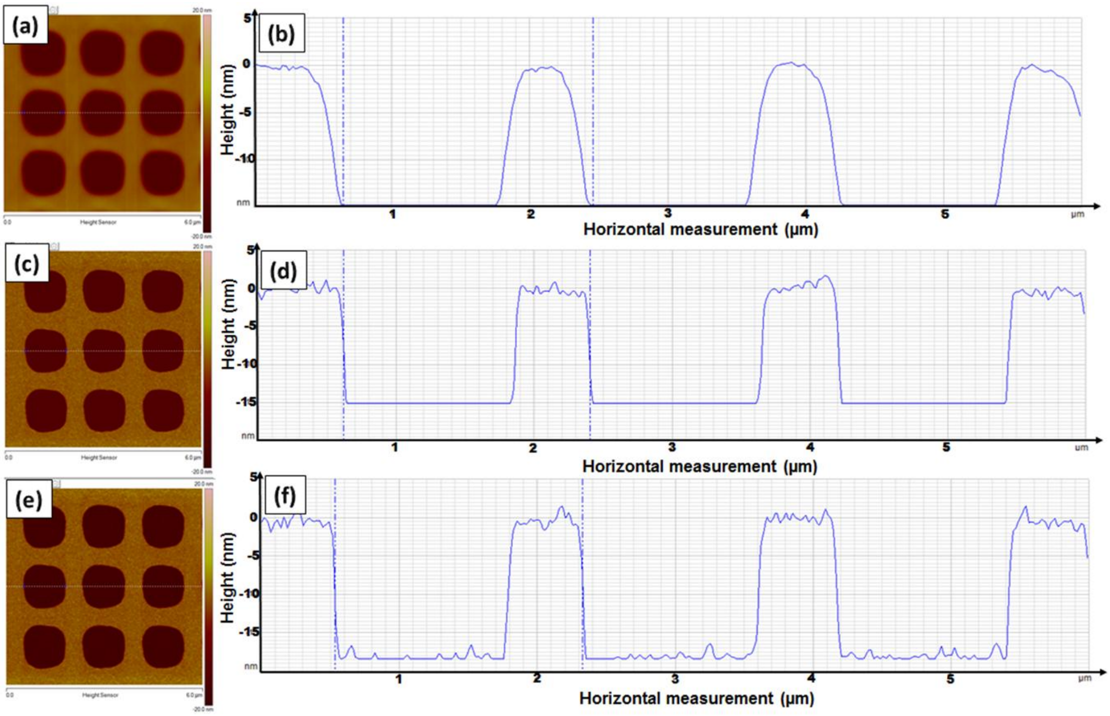

Figure 3 AFM images and its line profile using (a), (b) reused, (c), (d) new and (e), (f) CNT-modified AFM tips, respectively. Scan area is 6µm x 6 µm.

Table 1:Average of mean height, mean pitch and angle of AFM image scanned by different cantilevers

	Mean Height, Z (nm)	Mean Pitch, X (µm)	Mean Pitch, Y (µm)	Angle (degree)
Standard sample	18.400± 3.300	1.799± 0.023	1.799± 0.023	90.00º
Used cantilever	14.632± 0.185	1.817± 0.023	1.830± 0.016	97.61º ± 1.37
New AFM cantilever	15.148± 0.269	1.804± 0.017	1.830± 0.014	93.62º ± 2.23
CNT-Modified cantilever	18.568± 0.315	1.803± 0.013	1.822± 0.015	92.02º ± 1.63

experiment is described elsewhere [7]. Shortly, the quartz tube was filled with Ar gas at a flow rate of 500 sccm until the temperature reached to 850ºC. Ethanol vapor (99.99%) was switched into the furnace by Ar bubbling at a flow rate of 125 sccm for 20 min. Field-emission electron microscope (FESEM, FEI, Sirion NPGS V9), high resolution transmission electron microscope (HRTEM, FEI, Tecnai G2 20) and Raman spectroscopy (Thermo Scientific, DXR Smart Raman) were utilized for the synthesized CNTs characterization.

For AFM imaging performance test, the CNT-modified cantilever was used to scan silicon dioxide coated with a uniform layer of platinum which is AFM standard sample (VLSI standard sample, STS2-180P). Atomic force microscopy (BRUKER, Dimension Icon) was utilized for AFM imaging in tapping mode. For comparison, new and used cantilevers were also employed for imaging scanning.

Results and Discussion

Figure 1 shows a schematic view of CNT-modified cantilever. Figures 2(a)-(c) show FESEM images of used, new and CNT-modified cantilevers, respectively. The curvature radius of each cantilever apex was different. Used cantilever had the dull apex with a curvature radius of 145 nm, while new cantilever had the relatively sharp apex with a curvature radius of 58 nm. For CNT-modified cantilever, CNTs with a thin tubular structure were protruded from apex of cantilever with a length of approximately 465 nm. The curvature radius of the used cantilever before CNT modification was approximately 87 nm.

For HRTEM observation, it is hardly to directly observe the structure of CNT protruded from cantilever apex. To obtain the trend of the resultant CNTs, CNTs on cantilever was removed to Cu grid and characterized. Thus, not only the CNTs at the apex, but also CNTs at the cantilever body were observed. It was found that the resultant CNTs consisted of multi-graphene layers, implying multi-walled carbon nanotube (MWCNT) structure. Diameters of MWNTs were approximately estimated to be with a diameter of 17.29±0.59 nm (data not shown).

In order to demonstrate the imaging performance of the CNT-modified cantilever, silicon dioxide coated with a uniform layer of platinum (VLSI Standard sample, STS2-180P) which is AFM standard sample was used as a test sample. The specification of the stand sample was shown in Table 1. Its mean height, mean pitch (x,y) and angle are 18.400±3.300 nm, 1.799 µm±0.023 µm and 90º, respectively. For imaging scanning, each cantilever was scanned under the same AFM operation setting at a scan rate of 1 kHz, set point of 250 mV, scan size of 6 µm x 6 µm, samples/line of 512 and scan angle of 90º. Scanning was conducted for 2 times for each cantilever. Figures 4(a)-4(f) show AFM images of standard sample and its line profile obtained from used, new and CNT-modified AFM tip, respectively. From figures 4(a), 4(c) and 4(e), it can be obviously seen that the imaging from new and CNT-modified cantilever was clear, while the imaging from used cantilever was vague. Average of mean height, mean pitch and angle of each image were measured from its line profile of 9 pitches and were summary in Table 1. Line profile of the image obtained from CNT-modified cantilever showing relatively same specification as that of standard sample, while that of used and new cantilevers showed the small difference in mean height, implying that surpassing not only used cantilever but also new cantilever, the CNT-modified cantilever showed better resolution imaging in both lateral and vertical resolution. After imaging, the CNT-modified cantilever was observed by FESEM again. The CNT still attached on the cantilever, showing its good mechanical contact with cantilever (data not shown).

Conclusions

The used AFM cantilever was modified by attachment of CNT. CNT was synthesized by CVD method using ethanol as carbon source. After optimum CVD condition, MWNTs were attached at the apex of pyramid shape of cantilever. Silicon dioxide coated with a uniform layer of platinum which is AFM standard sample was used as a sample for AFM imaging. Surpassing new and used AFM cantilevers, imaging obtained from CNT-modified cantilever showed high-resolution imaging in both lateral and vertical resolution. These results show a potential reuse of used cantilever which will have advantages in terms of AFM performance and cost.

Acknowledgments

The author would like to acknowledge HGSA Failure Analysis Laboratory, Seagate (Thailand) Co., Ltd. (KORAT) for the AFM facilities, used cantilevers and AFM standard sample supports. This work has partially supported by the National Nanotechnology Center (NANOTEC), NSTDA, Ministry of Science and Technology, Thailand, through its program of Center of Excellence Network. We also acknowledge the financial support through Master Degree Program Development in HDD Engineering Technology, NSTDA-KMITL-SEAGATE. We thank to Assoc. Prof. Dr. Vittaya Amornkitbamrun and Ms. Phikun Ratphonsan, KhonKaen University for their partly assistance in HRTEM observation.

References

1. M. S. Dresselhaus, G. Dresselhaus and Ph. Avouris, “Carbon Nanotubes; Synthesis, Structure, Properties, and Application”, Springer, Berlin, (2001).
2. H. Dai, J. H. Hafner, A. G. Rinzler, D. T. Colbert and R. E. Smalley, “Nanotubes as Nanoprobes in Scanning Probe Microscopy”, Nature **384** (1996) 147.
3. J. H. Hafner, C. L. Cheung and C. M. Lieber, “ Growth of Nanotubes for Probe Microscopy Tips”, Nature **398** (1999) 761.
4. C. L. Cheung, J. H. Hafner, T. W. Odom, K. Kim, and C. M. Lieber, “Growth and Fabrication with Single-Walled Carbon Nanotube Probe Microscopy Tips” Applied Physics Letters, **76** (2000), 3136.
5. Y. Erhan, W. Qian, Robert J. Chen, W. Dunwei and D. Hongjie, “Wafer scale production of carbon nanotubes scanning probe tips for atomic force microscopy”, Applied Physics Letters, **80** (2002), 2225.
6. K. Takagahara, Y. Takei, E. Iwase, K. Matsumoto, and I. Shimoyama, “Batch Fabrication of Carbon Nanotubes at AFM Probe Tips and AFM Imaging”, Proceedings of Micro

Electro Mechanical Systems, 2008, IEEE 21st International Conference on (2008), 713.

7. P. Dulyaseree, W. Wongwiriyapan, W. Jarernboon, W. Bunjongpru, S. Sopitpan, . Porntheeraphat, S. Ichikawa and J. Nukeaw, “Effect of Support Layers on Growth of Carbon Nanomaterials by Alcohol Catalytic Chemical Vapor Deposition”, Journal of the Microscopy Society of Thailand **5** (2012), accepted

Optical pH Sensor Using Alizarin Yellow R Immobilized on Hydrolyzed Cellulose Acetate Membrane

Panya Khakhlong[1] and Mayuree Hansupanusorn[1*]

[1]*Department of Physics, Faculty of Science, King Mongkut's University of Technology Thonburi,*
126 Pracha Uthit Rd., Bang Mod, Thung Khru, Bangkok 10140, Thailand

**Corresponding author. E-mail: mayuree.kit@kmutt.ac.th*

Abstract

Optical pH sensing material was prepared using alizarin yellow R (AY) immobilized onto a hydrolyzed cellulose acetate (CA) membrane. Used photographic film was color-bleached with sodium hypochlorite and hydrolyzed with sodium hydroxide to obtain the hydrolyzed membrane. AY was immobilized onto the hydrolyzed membrane from methanol solution. AY was strongly fixed on the CA membrane and not washable by water. UV-visible spectrometer was used to measure the absorption intensity of the immobilized dye (at wavelength 382 nm) as a function of solution pH (7 - 14). It was found that a linear correlation (between pH and absorption intensity) was obtained at pH = 8 – 12, with a response time of less than 4 min. At pH > 12, the sensing membrane cannot be used due to the formation of white precipitates on the CA membrane.

Keywords: Optical pH sensor, Hydrolyzed cellulose acetate membrane, Alizarin yellow R

Introduction

Developments of pH sensors have grown rapidly because so many chemical process, biological process, and practical applications such as clinical analysis, environmental analysis and process control are dependent on pH [1, 2]. Measuring methods for pH values can be divided into 5 categories: pH indicator reagents, pH test strips, hydrogen electrode, glass electrode, metal electrodes and optical pH sensor [1].

Most optical pH sensors are usually based on acid–base indicators. The pH indicator dyes can be immobilized on the surface of supporting materials (such as polymeric or sol-gel) to obtain the pH sensor membrane. The diffusion of acid/base solutions into the sensor membrane causes the change of absorbance or luminescence of certain indicator molecules.

The construction of an optical pH sensor based on several dyes immobilization of transparent cellulose acetate (CA) was described [2-4]. CA membrane was prepared from used photographic film whose original color layer was bleached out. Suitable type of indicator dye can be chosen such that the membrane sensor can effectively measure pH at high and low pH ranges, where common pH electrodes encounter alkaline and acid errors [3-5]. In addition, the mixing of multiple indicator dyes (with different pK_a or pK_b values) on the same sensor membrane can be done to extend the working detection range [2-3].

Our previous work was performed on the immobilization of various indicator dyes (methyl orange, phenolphthalein, thymol blue, bromothymol blue, and alizarin yellow R) onto the hydrolyzed CA membrane obtained from used photographic film. It was found that alizarin yellow R (AY) gave the best result. AY was strongly fixed onto the membrane and not washable by water. Thus, AY immobilized CA membrane was selected as a sensing material for development of optical pH sensor. This paper involves the study of UV-Vis absorption behavior of immobilized AY as a function of pH and sensor characteristics of the immobilized CA membrane.

Experimental

Reagents

All reagents used in this work were of analytical grade. AY was purchased from Sigma-Aldrich. 0.1% w/v solution of AY was prepared by dissolving AY in methanol. Commercial sodium hypochlorite was used as a bleaching agent. 0.1 M sodium hydroxide was used for hydrolyzing CA membrane. All aqueous solutions were prepared with deionized water.

Instrumentation

An AvaSpec-2048 portable fiber optic spectrometer from Avantes was used for recording absorbance and UV-Vis spectra. Setup for the spectrometric measurements was shown in Figure 1. A Metrohm 744 digital pH-meter was used for measuring pH value.

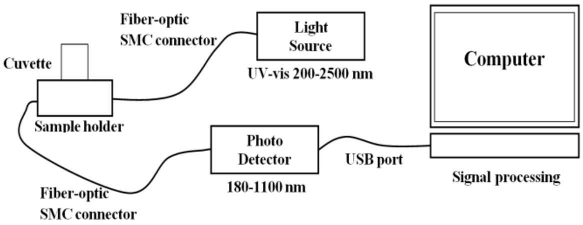

Figure 1. Set-up of measuring system

Preparation of AY-immobilized CA membrane

The transparent CA membrane was prepared from used photographic film. Used film strip was cut into a rectangular shape (1 x 6 cm^2). The used film was treated with commercial sodium hypochlorite for 24 h in order to remove the colored gelatinous layers. The obtained film was then treated with 0.1 M sodium hydroxide solution for 2 h to obtain the hydrolyzed membrane. This hydrolyzing step causes removal of the acetyl groups and increase of the membrane porosity. The hydrolyzed film was rinsed a few times with water and kept in distilled water for 24 h prior to use. Dye immobilization was performed by immersing the hydrolyzed film in a 0.1% w/v AY solution for 1 h. The immobilized film was washed several times with water to remove loosely trapped dyes and kept in distilled water when not in use.

Optical properties of the immobilized membrane

Acid-based behaviors of AY in solution and AY immobilized films were studied by spectrometric measurements. A strip of immobilized film was placed inside a quartz cuvette where a solution with a desirable pH was previously filled. Solutions with various pH from 7.0-14.0 was adjusted by addition of 1 M sodium hydroxide solution into a solution initially at pH 7.0. All of the solution pH was measured by the digital pH meter. The absorption spectra were taken using a cuvette filled with water as blank.

Results and Discussion

Optical property of AY indicator in solution

Effect of pH on the AY in methanol solution and AY immobilized on the hydrolyzed CA membranes was studied in the solution pH between 7 and 14. The basic pH range was used because AY indicator changes color from yellow to red at pH around 10-12. The spectral change, thus, corresponds to an acid-base equilibrium of the indicators.

The absorption spectra of AY in methanol solution as a function pH are shown in Figure 2. Two absorption maxima at 367 and 490 nm can be seen from the spectra. Peak at 367 nm corresponds to the yellow form while that at 490 nm represents the red form. At pH < 10, solution color was yellow and only the peak at 367 nm (yellow form) was found. When the pH got higher, solution color gradually changed from yellow to red as the yellow peak was decreasing in intensity while a new peak at 490 nm (red form) was emerging. At pH > 10, the yellow peak disappeared and only the red peak remained. Plot of peak intensity at 367 and 490 nm against solution pH (in Figure 3) showed the reversible yellow-red transition with the equilibrium pH (end-point of indicator) ~ 11-12. The presence of characteristic *isobestic* point (region where all of the spectrum lines are intercept) at around 410 nm indicates the fully reversible, equilibrium between protonated (yellow) and deprotonated (red) forms of this pH indicator [5].

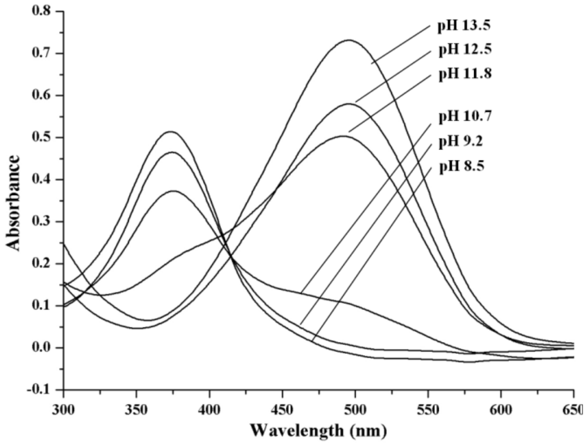

Figure 2. Absorption spectra of AY in methanol solution

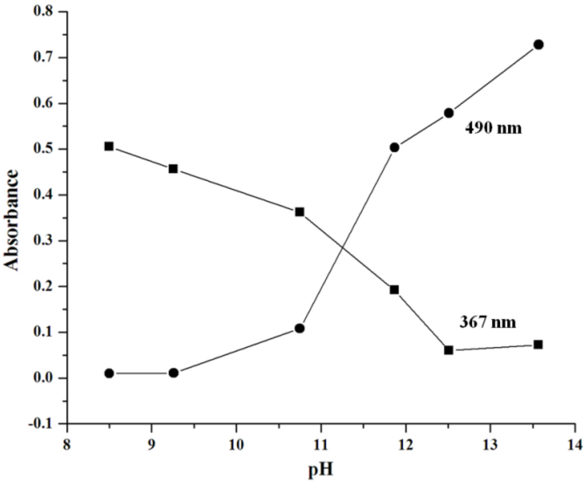

Figure 3. Effect of pH on absorbance of AY solution at 367 nm (yellow form) and 490 nm (red form)

Optical property of immobilized AY in hydrolyzed CA film

After immobilization, colorless CA film turned yellow. It was found that the yellowish AY color was strongly fixed on the CA membrane and not washable by water. After treating with basic pH from 8 to 13, it was observed that the film color was almost unchanged (remained yellow, with slightly stronger color at higher pH). Absorption spectra of AY immobilized onto hydrolyzed CA film as a function pH are shown in Figure 4.

Two obvious differences were found in the spectra of immobilized AY, as compared to those of the AY solution. First, spectra of the immobilized AY only showed one absorption maxima at 382 nm (yellow form) and its yellow peak was also red-shift (from 367 nm to 382 nm). Second, peak intensity of the yellow form was increasing as higher pH while intensity of the solution peak was decreasing as the solution color changes from yellow to red.

The above results indicated that the immobilized AY molecules should form strong interactions (possibly chemical bonding) to the CA surface in such the way that their structural conformations were fixed in a restricted yellow form. The structural restriction of the immobilized form gives rise to the marked differences in both optical property and acid-base reactivity as compared to the dissolved form in the solution. The strong interactions are also contributed to the good film-dying property and stability of the immobilizing film.

Since the film color does not change when exposed to different solution pH, the AY immobilized film cannot be used as a pH sensor in the conventional fashion. Nevertheless, it was observed that color intensity of the immobilized film increases with solution pH and the change is reversible. This intensity change could be useful as pH sensor signal, as oppose to the color change found in most indicator dye systems.

Figure 5 shows a plot between peak intensity of the immobilized yellow form at 382 nm and solution pH. The good linear relation (with an R^2 value of 0.9982) was found in the pH range between 8 to12.

It was found that absorption intensity increases drastically when the solution pH > 12. It was also observed

A small amount of white deposits was also observed in the CA membrane. These deposits remained on the film and reversibility of the film signal was lost. Therefore AY immobilized CA film can be useful as pH sensing material only when solution pH is less than 12.

Sensor response of the AY-immobilized CA film

To determine the response time, the immobilized film was placed in a solution pH 7 for a few minutes to get equilibrium intensity. Then, pre-determined amount of NaOH solution was quickly added and stirred to get a solution pH = 12 and peak intensity was monitored as a function of time until signal reaches equilibrium values.

As seen in Figure 6, the absorption intensity reaches equilibrium within about 5 minutes and the response time from 0% to 95% of the steady state signal is about 3 minutes. Note that several experiments were done and found that the 95% response time was less than 4 minutes

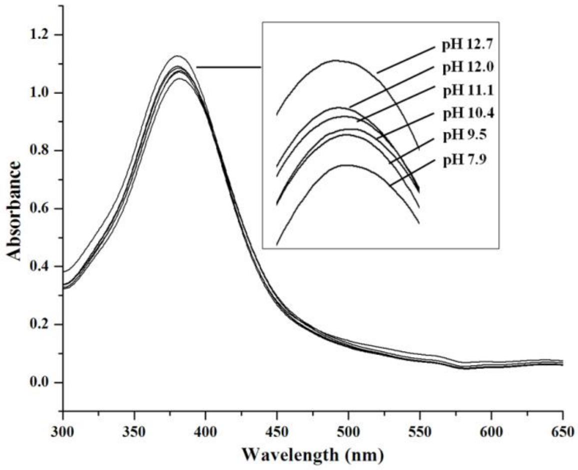

Figure 4. Absorption spectra of immobilized AY on hydrolyzed CA film

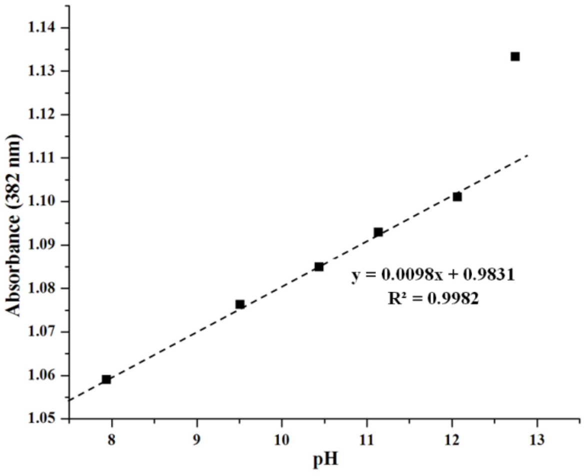

Figure 5. Plot of absorbance at 382 nm of the immobilized membrane against solution pH, showing a linear relation in the pH range of 8-12

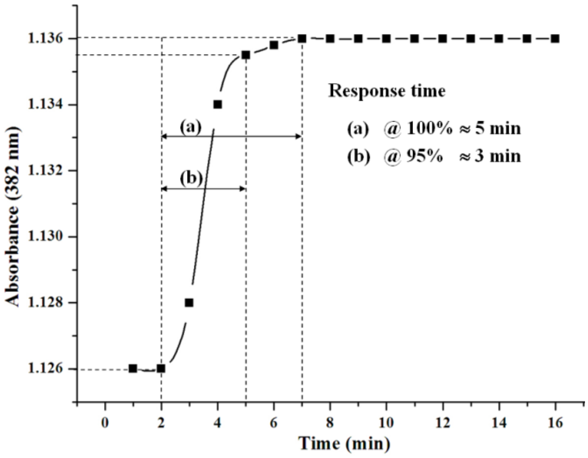

Figure 6. Response time for AY immobilized CA film when solution was change from pH = 7 to 12

Conclusions

A used cellulose acetate film was used as a matrix for immobilization of AY dye. It was found that optical property of the immobilized dye was different from its dissolved form in solution. While the color of the immobilized dye was not unchanged, its color intensity was linearly changed with pH. The AY-immobilized CA film can be useful as a sensor material with a pH working range from pH 8 to 12 and a response time (95% signal) of less than 4 minutes. The sensing membrane cannot be used at pH > 12 due to the formation of white precipitates on the CA membrane.

Acknowledgments

This work was partially supported by the Graduate Financial Support Grant (2012-2013) from the Faculty of Science, KMUTT.

References

1. M. Yuqing, C. Jianrong, and F. Keming, “New Technology for the Detection of pH”, Journal of Biochemical and Biophysical Methods **63** (2005) 1.
2. M. Noroozifar, M. K. Motlagh, S. Bahmanzadeh, and S. Boroon, “A Novel Optical Membrane with Extended Detection Range of pH, Turkish Journal of Chemistry **34** (2010) 719.
3. A. Safavi and M. Bagheri, “Novel Optical pH Sensor for High and Low pH Values”, Sensors and Actuators **B 90** (2003) 143.
4. S. Rouhani and S. Salimi, “Optical pH Sensor Based on Quinizarin for Alkaline pH Regions”, 2008, Progress in Color, Colorants and Coatings **1** (2008) 11.
5. P. Hashemi and M. M. Abolghasemi, “Preparation of a Novel Optical Sensor for Low pH Values using Agarose Membranes as Support”, Sensors and Actuators **B 115** (2006) 49

Physical properties of Calcine $Ba(Zr_xTi_{1-x})O_3$ Powders via Sol-Gel Process

N. Binhayeeniyi[1*], A. Jehsu[1] and S. Nawae[1]

[1]*Faculty of Science and Technology, Princess of Naradhiwas University, Muang, Narathiwat 96000 Thailand*

**Corresponding author. E-mail: nawal.binhayeeniyi@gmail.com*

Abstract

This work presents the physical properties of the Barium zirconate titanate calcined powders which were prepared via sol-gel process. Various compositions, i.e., $Ba(Zr_{0.03}Ti_{0.97})O_3$, $Ba(Zr_{0.05}Ti_{0.95})O_3$ and $Ba(Zr_{0.08}Ti_{0.92})O_3$ were selected to study their physical properties. We employed the chemical solution deposition to produce the sol which were later used as the starting material in dry to powder. The calcined powders were characterized polycrystalline perovskite phase in different compositions. The lattice constants were also studied by XRD patterns. The particle sizes of the calcined BZT powder were analyzed by laser particle size analyzer.

***Keywords*:** Sol-Gel Process, $Ba(Zr_xTi_{1-x})O_3$, Lead free ceramic**,** Laser particle size analyzer

Introduction

Barium zirconate titanate or $Ba(Zr_xTi_{1-x}$,BZT) plays an importance role due to the benefit of it, environmental friendly. These materials derived from two solid-solution systems which are Barium zirconate ($BaZrO_3$) and Barium titanate ($BaTiO_3$). [1-2]. The BZT ceramics is ferroelectric when the Zr content is less than 10 mol % and become paraelectric when it is as high as 27 mol % [1-2]. For the BZT powder, many researchers [1-5] have reported that the lattice symmetry changes from tetragonal to orthorhombic when Zr increased from 0 to 0.06. If the fractional content is 0.06-0.20, the rhombohedral phase is obtained and it becomes cubic at 0.20. This work systematically investigated the crystallographic phases, the XRD patterns, the lattice constant and particle size of the BZT materials.

Materials and Methods

In the sol-gel route [3] the barium acetate: $[Ba(CH_3COO)_2]$, zirconium propoxide : $[C_{12}H_{28}O_4Zr]$, and titanium isopropoxide: $[C_{12}H_{28}O_4Ti]$ were the starting materials. Acetic acid, 2-Methanol and ethylene glycol were the solvent. In the BZT powder preparation, the gel was kept in an oven until dried and calcined at 1,100 °C for 2 hours. The particle sizes were analyzed by laser particle size techniques. The crystalline were determined by using a X-Ray Diffractometer (XRD). The lattice constant a and c obtained from XRD patterns.

Results and Discussion

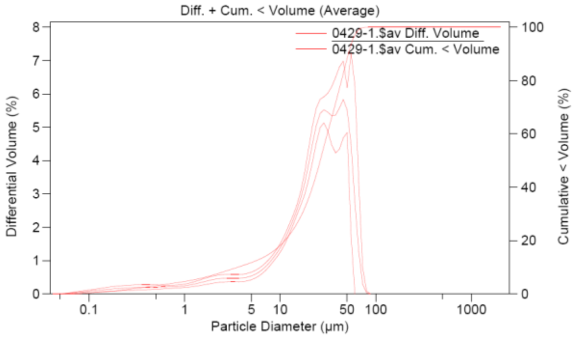

Figure 1. Particle size distribution of the $Ba(Zr_{0.03}Ti_{0.97})O_3$ calcined powder.

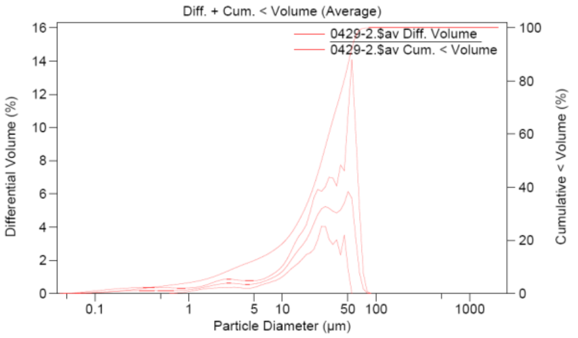

Figure 2. Particle size distribution of the $Ba(Zr_{0.05}Ti_{0.95})O_3$ calcined powder.

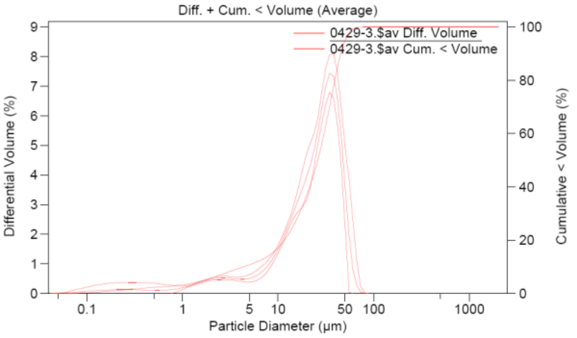

Figure 3. Particle size distribution of the Ba($Zr_{0.08}Ti_{0.92}$)O_3 calcined powder.

The ultrasonic dispersing in distill water was selected to reduce the agglomeration of the powder before testing with the laser particle size analyzer (Beckman Coulter LS 230). An average particle size were 27.49±17.13 µm, 27.74±17.69 µm and 25.72±14.80 µm, respectively. A small portion of the powder with particle size smaller than 1 µm could be observed for all compositions. A board peak distribution ranged from 10 to 100 µm. Because there were the agglomeration of the powder after calcinations as displayed in Figure 1-3.

X-ray diffractometer (Philips X'pert MPD) with Ni filtered CuKα radiation was used to distinguish the phases of the Ba(Zr_xTi_{1-x})O_3 samples. The patterns were recorded at a scan rate of 0.2° per min from 20° to 60° for phase and crystalline analyses as shown in Figure 4. The crystalline can be calculated from using A(peak) divided by A(total) as displayed in Table 1.

Table 1: The crystalline of the calcined Ba(Zr_xTi_{1-x})O_3 powders.

Samples	A(peak)	A(total)	% Crystallinity
Ba($Zr_{0.03}$ $Ti_{0.97}$)O_3	195952.40	295348.00	66.35
Ba($Zr_{0.05}$ $Ti_{0.95}$)O_3	202470.70	303445.00	66.72
Ba($Zr_{0.08}$ $Ti_{0.92}$)O_3	1993663.30	301274.00	64.28

The crystallographic data from the XRD results indicated that the calcination at 1,100 °C for 2 hours. All of composition have the crystallinity more than 60%.

The BZT powders calcined at 1,100 °C for 2 hours were XRD analyzed as displayed in Figure 4. An average crystalline size as shown in Table 2. The 2θ peak shifts to the left indicate the increasing of lattice parameter and successful Zr^{4+} ion (86 pm) substitution to the Ti^{4+} ion (74.5 pm) lattice sites [1, 2, 6, 7,].

The lattice parameter a and c obtained from XRD pattern summarized all the calculated lattice constants of the BZT powders as shown in Figure 5. The results indicated that the lattice constants increased with the zirconium content due to the ionic radius [7]. This result conformed to the report by Qi et al. (2006) [8].

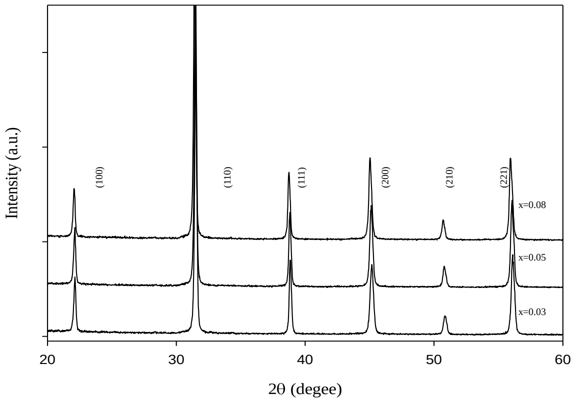

Figure 4. XRD patterns of the Ba(Zr_xTi_{1-x})O_3 powders calcined at 1,100 °C for 2 hours.

Table 2: The crystalline of the calcined Ba(Zr_xTi_{1-x})O_3 powders obtained from XRD results in Figure 4.

Samples	XRD Crystalline size (nm)
Ba($Zr_{0.03}$ $Ti_{0.97}$)O_3	39.60
Ba($Zr_{0.05}$ $Ti_{0.95}$)O_3	43.18
Ba($Zr_{0.08}$ $Ti_{0.92}$)O_3	64.76

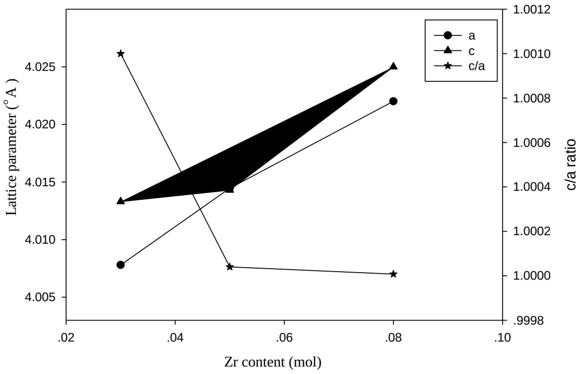

Figure 5. The lattice parameter c and a of the Ba(Zr_xTi_{1-x})O_3 powders calcined at 1,100 °C for 2 hours and c/a ratio (left hand size coordinate) versus Zr content.

Conclusions

The barium zirconate titanate calcined powders, Ba($Zr_{0.03}Ti_{0.97}$)O_3, Ba($Zr_{0.05}Ti_{0.95}$)O_3 and Ba($Zr_{0.08}Ti_{0.92}$)O_3 were prepared via sol-gel process. An average particle size were 27.49±17.13 µm, 27.74±17.69 µm and 25.72±14.80 µm, respectively. All of composition showed the crystalline more than 60%. The calcined powders were polycrystalline perovskite phase. The lattice constants increased with the zirconium content.

Acknowledgments

The authors would like to thank Nation Research Council of Thailand and Faculty of Science and Technology, Princess of Naradhiwas University, Thailand.

References

1. Z. Yu, R. Guo, and A. S. Bhalla, “Orientation dependence of the ferroelectric and piezoelectric behavior of Ba(Ti_{1-x} Zr_x)O_3 single crystals”, Applied Physics Letter **77**(2000) 1535-1537.
2. Z.Yu, C. Ang, R. Guo, and A. S. Bhalla, “Piezoelectric and strain properties of Ba(Ti_{1-x} Zr_x)O_3 ceramics”, Journal of Applied Physics **92**(2002) 1489-1493.
3. Z. Jiwei, Y. Xi, Z. Liangying, S. Bo, and H. Chen, “Orientation control and dielectric properties of sol–gel deposited Ba (Ti, Zr)O_3 thin films”, Journal of Crystal Growth **262**(2004), 341-347.
4. A. Dixit, S. B. Majumder, R. S. Katiyar, And A. S. Bhalla, “Relaxor behavior in sol–gel-derived $BaZr_{(0.40)}Ti_{(0.60)}O_3$ thin films”, Applied Physic Letter 82(2003) 2679-2681.
5. A. Dixit, S. B. Majumder, R. S. Katiyar, and A. S. Bhalla, “Dielectric and tunable properties of $BaZr_xTi_{1-x}O_3$ thin films”, Ferroelectric Letters, **32**(2005) 131-137.
6. N. Binhayeeniyi, P. Sukvisut, C. Thanachayanont, and S. Muensit, “Physical and electromechanical properties of barium zirconium titanate synthesized at low-sintering temperature”, Materials Letters **64**(2010) 305–308.
7. C. Thanachayanont, V. Yordsri, S. Kijamnajsuk, N. Binhayeeniyi, S. Muensit, “Microstructural investigation of sol–gel BZT powders”, Materials Letters **82**(2012) 205–207.
8. J. Q. Qi, Y. Wang, W. P. Chen, L. T. Li, and H. L. W. Chan, “Perovskite barium zirconate titanate nanoparticles directly synthesized from solutions”, Journal of Nanoparticle Research **8**(2006) 959-996.

Preparation and Wettability Behavior of Thai Silk Sericin/ Polyvinyl Alcohol (PVA) Blending Film

Voranuch Thongpool[1,*], Akapong Phunpueok[1], Tukkamon Vijakthanawudhi[1],
Naris Barnthip[1] and Pichet Limsuwan[2,3]
[1]*Division of Physics, Rajamangala University of Technology Thanyaburi,*
Pathumthani12110, Thailand
[2]*Department of Physics, King Mongkut's University of Technology Thonburi,*
Bangkok 10140, Thailand
[3]*Thailand Center of Excellence in Physics, CHE, Ministry of Education,*
Bangkok 10400, Thailand
**Corresponding author. E-mail: nuchphysics@gmail.com*

Abstract

Silk is a natural polymer, produced by silkworm *Bombyx mori*. Silk fibers are composed of sericin and fibroin proteins. Sericin has unique properties in biomedical applications. In this study, Thai silk sericin/polyvinyl alcohol (PVA) blending films were prepared at various PVA concentrations. The result found that, the prepared films were yellow, transparent and flexible. Time-dependent variations of the contact angles of wetting fluids on surfaces of prepared film have been observed. It was found that contact angles decreased with contact time. For this reason, it can be concluded that the Thai silk sericin/polyvinyl alcohol (PVA) blending films can be a key feature in the development of a drug delivery materials.

Keywords: Sericin; Polyvinyl alcohol, Thai silk, Drug delivery

Introduction

Silk is a natural protein fiber from silkworm cocoon, *Bombyx mori*. The proteins of silk are composed mainly of fibroin and sericin. Sericin is extracted from silk cocoons during degumming process. Sericin is a waste of textile industry, leading to environmental contamination because chemicals used in the degumming process have a high oxygen demand [1].

Non-textile benefits of sericin have been reported such as skin care, food antioxidant, anticonagulating agent, antiwrinkle and anticancer drugs [2], [3]. In tissue engineering, sericin has been always neglected because it has weak structural properties, high water solubility and difficult to fabricate [3]. However, sericin consists of serine and aspatic acids with strong polar side chain therefore, it can be co-polymerized or blended with other polymers to improve its properties [4, 5].

Polyvinyl alcohol (PVA) was prepared by hydrolyzing polyvinyl acetate in ethanol with potassium hydroxide. PVA shows biocompatibility with human body, thus it is applied for controlled delivery system of drugs, contact lens, artificial skins and biosensor [6].

In this study, the sericin protein was extracted from Thai silk cocoon. Thai silk sericin/ PVA blending films with various concentrations of PVA were prepared and studied wettability behavior. The wettability behavior of the films was studied by investigating contact angle of water droplet on surfaces of the film at different time. The wettability behavior can be used to evaluate the potential in drug delivery application of the films.

Materials and Methods

Preparation of silk sericin solution

Silk cocoons were supplied from Nan Thailand. The cocoons were cut into small pieces. The 2 g of cocoons were mixed with 20 ml of deionized water. The sample was boiled at 100°C for 30 min. After that, the sericin solution was characterized by FTIR (Perkin Elmer, 2000) and UV-visible (Jasco, V570) spectroscopy.

Preparation of silk sericin/PVA film

The Thai silk sericin/ PVA blending films were prepared by molding method. In brief, the PVA powders and silk sericin solution were blended together at 80°C with different concentrations (0.15%w/v- 0.55%w/v). The silk sericin/PVA blending solutions were poured into the plastic mold and dried in the oven at 37°C for about 2 days. The overall preparation of film is shown in Fig 1.

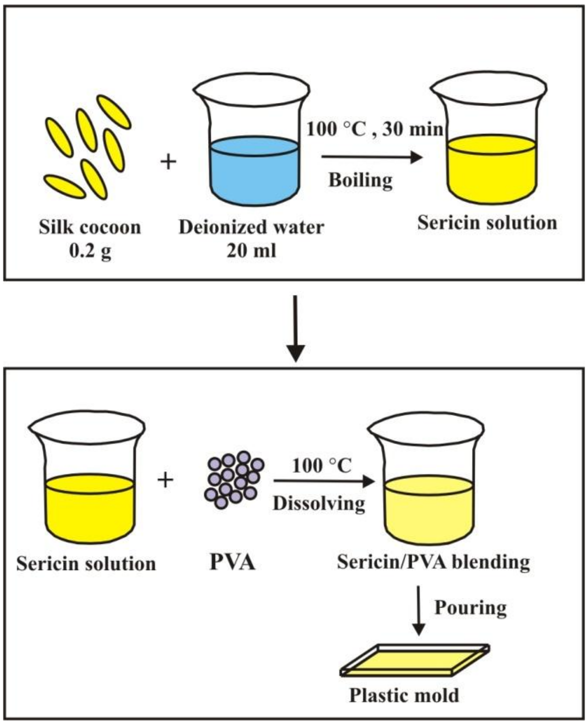

Figure 1. Schematic of the extraction of sericin solution and the preparation of sericin/PVA blending film

Wettability determination

The wettability behavior of solid by liquid is determined by contact angle, where is formed by a liquid at the three boundary intersection between liquid, gas and solid as shown in Fig. 2.

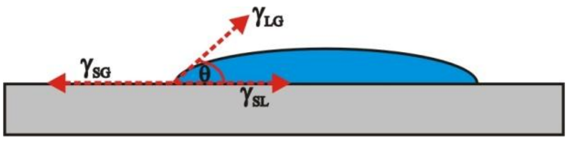

Figure 2. Schematic of the contact angle and interfeacial tensions of three surfaces at the three boundary intersections

The most important relation regarding the contact angle is the Young equation [7, 8] that relates to the contact angle (θ), liquid-gas surface tension (γ_{LG}), solid-gas surface tension (γ_{SG}) and solid-liquid surface tension (γ_{SL}).

$$\gamma_{LG}\cos\theta=\gamma_{SG}-Y_{SL}$$

The wettability behavior of the Thai silk sericin/ PVA blending film was determined using sessile drop technique. The sessile drop technique was used to measure the contact angle. Fig. 3 shows the contact angle measurement setup. All parts, except the sample holder, were kept stable and fixed on the optical bench. The sample holder can be translated. The time-dependent contact angle measurement was analyzed in the case of 8μL drop of deionized water on the film surface at room temperature and monitored the drop shape as a function of time. The photographs of water droplet were taken with the web camera. The contact angles were measured by Image J, free software using the contact angle plugin.

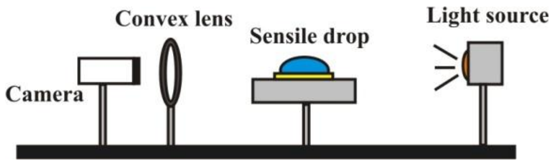

Figure 3. The measurement of liquid sessile drop contact angles

Results and Discussion

The sericin solution was deep yellow. The functional group of sericin solution was characterized by FITR spectroscopy. From Fig. 4, there are three different types of distinguishable vibration peaks associated with protein amide: amide I (1650 cm^{-1}) and amide II (1530 cm^{-1}) [3,4].

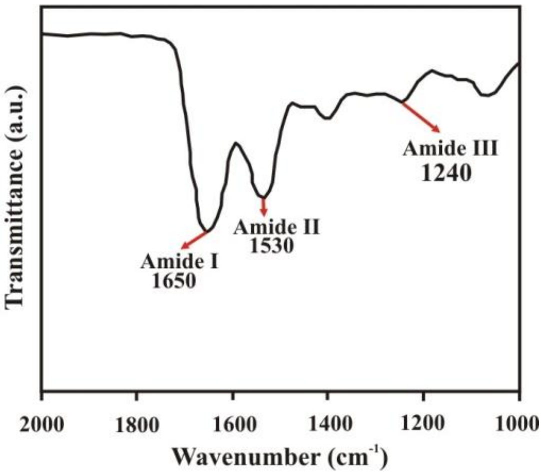

Figure 4. FTIR spectrum of sericin solution

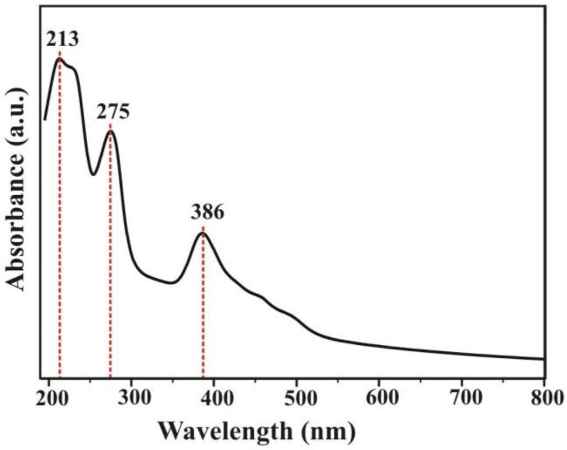

Figure 5. UV-vis spectrum of sericin solution

Sericin solution shows three distinct absorption bands at 213, 275 and 386 nm. The first and second bands appear due to the presence of peptide bond and aromatic ring, respectively. The last band could be significant for visible radiation [9].

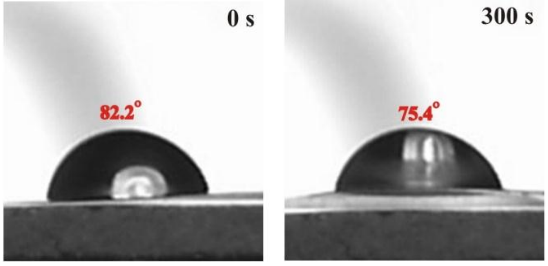

(a) 0.15%w/v PVA

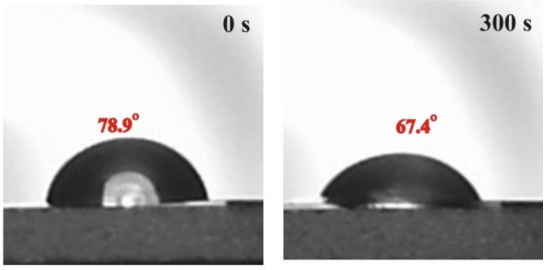

(b) 0.25%w/v PVA

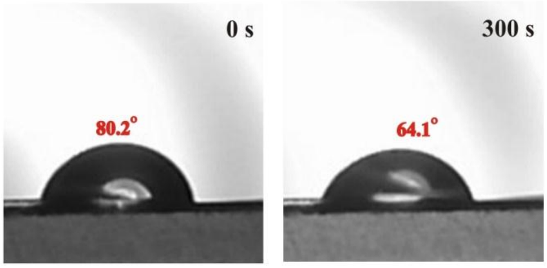

(c) 0.35%w/v PVA

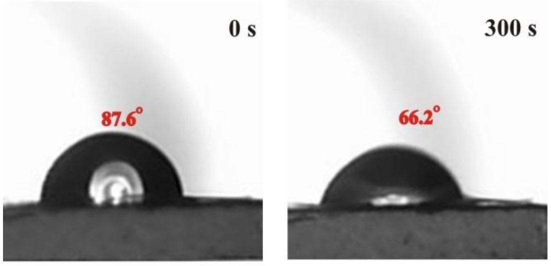

(d) 0.45%w/v PVA

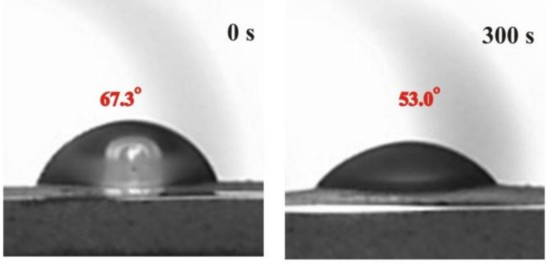

(e) 0.55%w/v PVA

Fig. 6 Photographs of contact angle for (a) 0.15%w/v, (b) 0.25%w/v, (c) 0.35%w/v, (d) 0.45%w/v and (e) 0.55%w/v when taken at 0 and 300 seconds

The prepared Thai silk sericin/ PVA blending films were smooth, transparent and flexible. From Fig. 6, it can be observed that the contact angle of each sample was not constant; instead it was initially decreasing over the contact time. In addition, the contact angles of prepared film significantly decreased with the amount of PVA. At PVA concentration of 0.55%w/v, the contact angle is minimal approximately at 67.3 degrees. The reduction of the contact angle is caused by an increase in hydrophilic groups (OH) at the surface of the film [6]. In addition, the contact angle of the films prepared in all conditions is less than 90 degrees typically refering to the wettability behavior of the film surface which is very high.

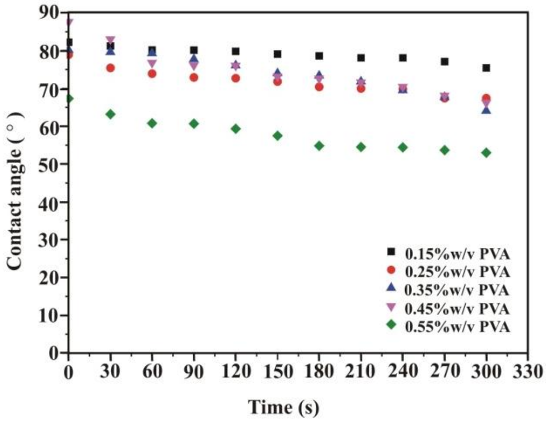

Figure 7. The evolution of contact angle of deionized water on the film surface at various times

Fig. 7 shows the evolution of contact angle of deionized water on the film surface, which depends on contacting time. It can be seen that, the reduction rate of the contact angle of the films which were prepared in all condition is different. At the PVA concentration of 0.45%w/v, the contact angle is mostly decreased.

Conclusions

Sericin/PVA blending films were successfully prepared. The prepared film showed high wettability. The concentration of PVA affected the reduction rated of the contact angles of the prepared film. The results can be used as a guide in the development of drug delivery materials. For the drug delivery of the prepared films are in the process of research.

Acknowledgments

This work was supported by Division of Physics, Faculty of Science and Technology, Rajamangala University of Technology Thanyaburi and King Mongkut’s University of Technology Thonburi under The National Research University Project.

References

1. S.C. Kundu, B.C. Dash, R. Dash and D.L. Kaplan, “Natural Protective Glue Protein, Sericin Bioengineerung by Silkworms: Protential for Biomedical and Biotechnological Applications”, Progress in Polymer Science **33** (2008), 998.
2. B.B. Madal, A.S. Anjana, S. Priya and S.C. Kundu, “Novel Silk Sericin/ Gelatin 3-D Scaffolds and 2-D Film: Fabrication and Characterization for Potential Tissue Engineering Application”, Acta Biomaterials **5** (2009) 3007.
3. B.C. Dash, B.B. Mandal and S.C. Kundul, “Silk Gland Sericin Protein Membranes: Fabrication and Characterization for Potential Biotechnological Applications”, Journal of Biotechnology **144** (2009) 321.
4. P. Aramwit, T. Siritientong, S. Kanokpanont and T. Srichana, “Formulation and Characterization of Silk Sericin-PVA Scafoold Crosslink with Genipin”, International Journal of Biological Macromolecules **47** (2010) 668.
5. M.L. Gimenes, L. Liu and X. Feng, “Sericin/Poly(vinyl alocohol) Blend Membranes for Pervaporation Separation of Ethanol/Water Mixtures”, Journal of Membrane Science **295** (2007) 71.
6. C.D. Nechifor, C.L. Ciobanu, D.O. Dorohoi and C. Ciobanu, “Polymetric Films Properties of Poly(vinyl alcohol) and Poly(hydroxyl urethane) in Different Concentration”, U.P.B Scientific Bulletin Series A **71** (2009) 97.
7. X. Zhao, Q. Zhang and D. Chen, “Enhanced Mechanical Properties of Graphene-Based Poly(vinyl alcohol) Composites”, Macromolecules 43 (2010) 2357.
8. C.A. Miller and P. Neogi, “Interfacial Phenomena Equilibrium and Dynamic Effects”, CRC Press, 2007.
9. J.H. Wu, Z. Wang and S.Y. Xu, “Preparation and Characterization of Sericin Powder Extracted from Silk Industry Wastewater” , Food Chemistry **103(4)** (2007) 1255.

PVP assisted N-doped TiO_2 Nanofibers prepared by Electrospinning Process

S. Suphankij[1*], W. Mekprasart[1] and W. Pecharapa[1]

[1] *College of Nanotechnology, King Mongkut's Institute of Technology Ladkrabang, Chalongkrung Rd., Ladkrabang Bangkok 10520, Thailand.*
**Corresponding author. E-mail:* sineenart.sup@gmail.com

Abstract

N-doped TiO_2 nanofibers were successfully prepared using conventional electrospinning process. The starting precursor was prepared from titanium (IV) isopropoxide (TIP) dissolved in Ethanol and ammonium acetate (CH_3COONH_4) as nitrogen sources. The different percent weight ratio of poly vinyl pyrrolidone (PVP) and TIP was introduced into the precursor. The nanofibers can be obtained using electrospinning process at applied voltage of 10 kV with feeding rate 1 ml/h and distance between a needle tip and collector of 15 cm. As-spun products were calcined at 500 °C for 2 h. Thermal decomposition and structural properties of TiO_2 nanofibers were investigated by Thermogravimetric and Differential Thermal Analysis (TG-DTA), X-ray diffraction (XRD) and field emission scanning electron microscope (FE-SEM). XRD results reveal the mixture of anatase and rutile phase of TiO_2 after calcinations. FE-SEM results suggest that the PVP content has significant influences on the uniformity, smoothness and size of the fibers and the optimized condition of loading PVP content at 8 wt% is notified. UV-visible spectroscopy (UV-Vis) results indicated significant absorption enhancement in visible region of N-doped TiO_2 nanofibers comparing to TiO_2 nanofibers.

***Keywords*:** N-doped titanium dioxide, Electrospinning, nanofiber

Introduction

For decades, titanium dioxide (TiO_2) has been recognized as a versatile metal oxide extensively utilized in various diversity of applications such as photo degradation of organic and inorganic in waste water, environmental purifiers, hydrogen generation, air purification and many other applications [1-4]. Typically, TiO_2 has wide bandgap energy of 3.2 eV for anatase and 3.0 eV for rutile phase resulting in good absorptivity in ultraviolet (UV) region with wavelength lower than 387 nm but not in visible regimes which are main solar spectrum. It is also known that high recombination of activated electron-hole pair of TiO_2 is its major drawback that causes the restriction of practical applications, in particular, solar harvesting aspect. Thus, the pioneered works and researches focusing on the effort to increase its performance efficiency have been devoted. One effective and practical method can be attained by doping with non-metal such as C, F, S and N [5-8] that can efficiently reduce the recombination rate of photo-generated electron-hole pairs and extend the light absorption of TiO_2 to longer wavelengths.

N-doped TiO_2 with specific morphologies can be synthesized and prepared by various methods such as sol-gel based technique, thermal treatment, hydrolysis-precipitation method, hydrothermal method and electrospinning [8-12]. It is found that electrospinning process has considerable advantages over the others such as simplicity of equipment and arrangement, continuity of production, controllability of size, porosity and high surface to volume ratio and adjustability of process conditions [12].

The main objective in this work is focused on the synthesis of N-doped TiO_2 nanofibers by electrospinning process with the assistance of poly vinyl pyrrolidone (PVP) as a fiber template. The influence of PVP loading contents on its physical properties is investigated.

Materials and Methods

Materials

Titanium (IV) isopropoxide (TiP; 97%) and poly (vinyl pyrrolidone) (PVP; Mw 1,300,000) was purchased from Sigma Aldrich. Ammonium Acetate (CH_3COONH_4), Absolute ethanol (99.5%) and acetic acid was purchased from Ajax Finechem, RCI Labscan and Merck, respectively. All reagents were used in the preparation TiO_2 nanofibers with differentpercent weight ratio of PVP: TiP and ammonium acetate was assigned as a nitrogen source.

Methods

N-doped TiO_2 nanofibers (NFs) were prepared by electrospinning using TiP as the Ti source, CH_3COONH_4 as N source and PVP as the fiber template polymer. First, polymer solution was prepared by dissolving 0.49 g of PVP in 6 mL of ethanol and stirred until transparent solution was reached. Next, N-doped Ti precursor was prepared by dissolving 0.3 g of CH_3COONH_4 in 3 mL of ethanol and stirred until dissolved completely and followed by 1.2 g of TiP and 2 mL of acetic acid mixed in solution and stirred for 12 min. Subsequently, two solution was mixed and stirred for another 10 min and was used as starting precursor for electrospinning. The solution was loaded into a 10 mL syringe. Distance between a needle tip and collector was fixed at 15 cm with feeding rate of 1.0 mL/h and applied voltage at 10 kV. As-spun undoped TiO_2 and N-doped TiO_2 NFs were then calcined at 500 °C for 2 h.

Results and Discussion

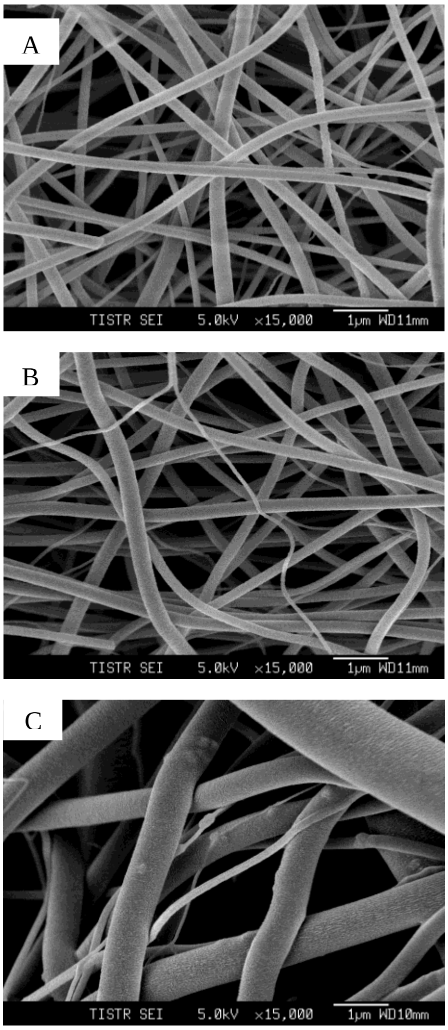

Figure 1. FE-SEM images of electrospun TiO_2 nanofibers using different percent weight of PVP (A) 8 wt%, (B) 10 wt% and (C) 12 wt%.

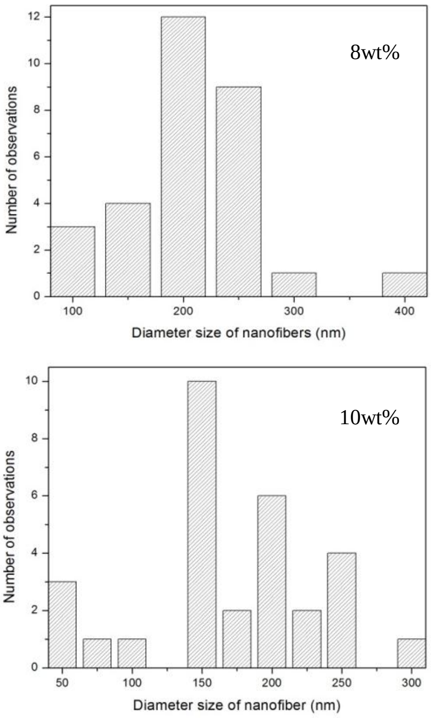

Figure 2. Diameter distribution of electrospun TiO_2 nanofibers using different percent weight of PVP 8 wt% and 10 wt%, respectively.

The morphologies of as-synthesized TiO_2 NFs with different percent weight of PVP 8, 10 and 12 wt% are shown in Fig.1(A), 1(B) and 1(C), respectively. The results exhibit that the TiO_2 NFs are uniform both in diameter and length with smooth surfaces. However, as seen in Fig.1(C), it is informed that the continuity of TiO_2 NFs and smoothness of its surface tends to decrease as PVP concentration advances to 10 wt%. It can be deduced that PVP loading concentration in the precursor has significant effect on morphology, shape and size of the fibers due to the variation in the viscosity of the precursor [12]. The diameter distribution of NFs prepared with various percent weight of PVP is represented in Fig. 2. The diameter of TiO_2 NFs is found to increases from 175 to 200 nm with increasing PVP loading.

The result of TG-DTA curve reflecting to thermal decomposition of electrospun TiO_2 nanofibers is shown in Fig.3. Three main weight losses from 0 °C to 900 °C was found in the TG-DTA curve. First step, 15 wt% weight loss from 0 °C to 100 °C is attributed to ethanol and water removal from precursor. The second and third weigh losses from 250 °C to 350 °C are expected to the decomposition of PVP chain until degradation of PVP by dehydration from 350 °C to 450 °C [12]. No further change is observed in the TG-DTA curve at elevated temperature from 500 °C to 900 °C, indicating the formation of TiO_2 at this temperature range.

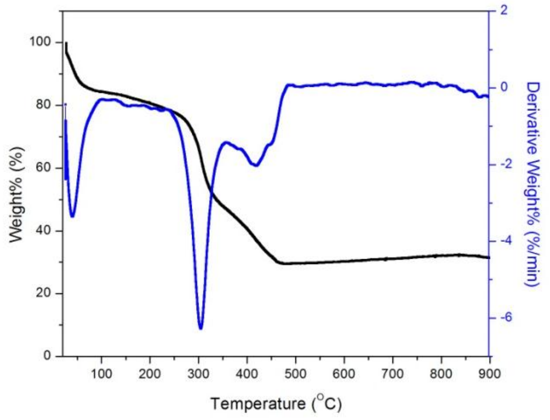

Figure 3. TG-DTA curve of electrospun TiO_2 nanofibers.

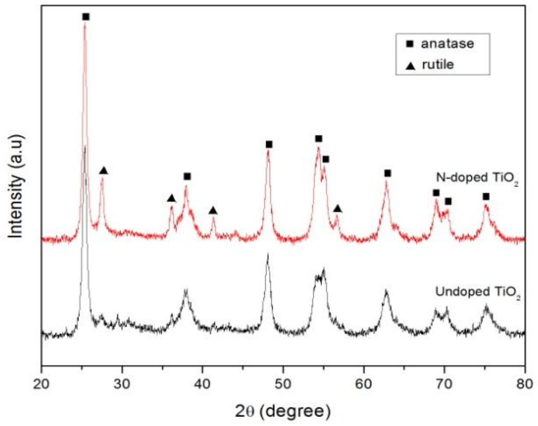

Figure 4. The XRD patterns of N-doped TiO_2 and undoped TiO_2 nanofibers

The X-ray diffraction (XRD) patterns of N-doped TiO_2 and undoped TiO_2 NFs calcined at 500 °C for 2 h are illustrated in Fig. 4. N-doped TiO_2 and undoped TiO_2 NFs show main diffraction peak at $2\theta = 25.5^{o}$ that assigns to (1 0 1) plane of anatase phase. Other peaks designated by solid square are ascribed to anatase phase. Meanwhile, the diffraction peaks of undoped TiO_2 NFs possess both anatase and rutile phase(assigned by solid triangle). This feature may be due to reduction in phase transformation temperature causing by the contribution of nitrogen doping.

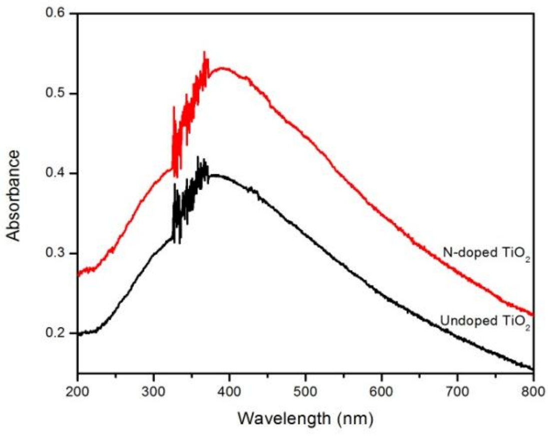

Figure 5. Absorption spectra of N-doped TiO_2 and undoped TiO_2 nanofibers.

The absorption spectra of N-doped TiO_2 and undoped TiO_2 NFs after calcinations are illustrated in Fig. 5. The absorption spectrum of undoped show absorption edge in vicinity of 390-400 nm meanwhile the spectrum of the doped sample exhibits an observable red-shift in absorption edge extending to 400-450 nm. It is suggested that nitrogen doping into TiO_2 matrix results to the enhancement in its absorptivity in visible region leading to more practicable utilization in wide applications.

Conclusions

In summary, N-doped TiO_2 nanofibers were successfully prepared by electrospinning. TG-DTA result informs the thermal behavior and temperature range of the formation of TiO_2. XRD results indicates the formation of N-doped TiO_2 and undoped TiO_2 NFs with different phases after calcinations at 500°C. It is acknowledged from SEM images that as-synthesized NFs have good uniformity and size distribution and concentration of PVP used as fibers template has significant influence on the fiber structures. Furthermore, the optical absorptivity of the fiber can be ameliorated, extending to longer wavelength, by nitrogen doping into TiO_2 matrix.

Acknowledgments

This work has been financially supported by the National Nanotechnology Center (NANOTEC), NSTDA, Ministry of Science and Technology Thailand, through its program of Center of Excellence Network. This work has been also partially supported by Nation Research Council of Thailand (NRCT).

References

1. W. Mekprasart and W. Pecharapa, “Synthesis and characterization of nitrogen-doped TiO_2 and its photocatalytic activity enhancement under visible light”, Energy Procedia **9** (2011), 509-514.
2. J. Ananpattarachai, P. Kajitvichyanukul and S. Seraphin, “Visible light absorption ability and photocatalytic oxidation activity of various interstitial N-doped TiO_2 prepared from different nitrogen dopants”, Journal of Hazardous Materials **168** (2009) 253-261.
3. S. Chainarong, L. Sikong, S. Pavasupree and S. Niyomwas, “Synthesis and Characterization of Nitrogen-doped TiO_2 Nanomaterials for Photocatalytic Activities under Visible Light”, Energy Procedia **9** (2011) 418-427.

4. S. Zhou, J. Lv, L.K. Guo, G.Q. Xu, D.M. Wang, Z.X. Zheng and Y.C. Wu, “Preparation and photocatalytic properties of N-doped nano-TiO_2/muscovite composites” Applied Surface Science **258** (2012) 6136-6141.
5. S. Sakthavel and H. Kisch, “Daylight Photocatalysis by Carbon-Modified Titanium Dioxide” Angrewandte Chemie International Edition **42** (2003) 4908-4911.
6. T. Yamaki, T. Umebayashi, T. Sumita, S. Yamamoto, M. Maekawa, A. Kawasuso and H. Itoh, “Fluorine-doping in titanium dioxide by ion implantation technique” Nuclear Instruments and Methods in Physics Research B **206** (2003) 254-258.
7. Y. Liu, J. Liu, Y. Lin, Y. Zhang and Y. Wei, “Simple fabrication and photocatalytic activity of S-doped TiO_2 under low power LED visible light irradiation” Ceramics International **35** (2009) 3061-3065.
8. X. Cheng, X. Yu and Z. Xing, “Characterization and mechanism analysis of N-doped TiO_2 with visible light response and its enhanced visible activity” Applied Surface Science **258** (2012) 3244-3248.
9. C. Cantau, T. Pigot, J.C. Dupin and S. Lacombe, “N-doped TiO2 by low temperature synthesis: Stability, photo-reactivity and singlet oxygen formation in the visible range” Journal of Photochemistry and Photobiology A: Chemistry **216** (2010) 201-208.
10. Y. Wang, C. Feng, M. Zhang, J. Yang and Z. Zhang, “Enhanced visible light photocatalytic activity of N-doped TiO2 in relation to single-electron-trapped oxygen vacancy and doped-nitrogen” Applied Catalysis B: Environmental **100** (2010) 84-90.
11. A. Simpraditpon, T. Wirunmongkol, S. Pavasupree and W. Pecharapa, “Simple hydrothermal preparation of nanofibers from a natural ilmenite mineral” Ceramics International **29** (2013) 2497-2502.
12. J.S. Lee, Y.I. Lee, H. Song, D.H. Jang and Y.H. Choa, “Synthesis and characterization of TiO_2 nanowires with controlled porosity and microstructure using electrospinning method” Current Applied Physics **11** (2011) S210-S214.

Structural and optical properties of copper phthalocyanine thin film prepared by solution process

B. Tunhoo[1,2*], P. Keeratithiwakorn[1,2], P. Nimorn[3],O. Thearpanpong[3], K. Onlaor[1,2],
and T. Thiwawong[1, 2]
[1]*Electronics and Control System for Nanodevice Research Laboratory, College of Nanotechnology, King Mongkut's Institute of Technology Ladkrabang, Chalongkrung Road, Bangkok 10520, Thailand*
[2]*Thailand Center of Excellence in Physics, Commission on Higher Education, Ministry of Education, 328 Si Ayutthaya Road, bangkok 10400, Thailand*
[3]*Department of Industrial Physics and Medical Instrumentation, Faculty of Science, King Mongkut's University of Technology North Bangkok, Piboonsongkram Road, Bangkok 10800, Thailand*
**Corresponding author. E-mail: ktbencha@gmail.com*

Abstract

Metallophthalocyanines are the key functional materials for organic semiconductor devices. In this work, copper phthalocyanine (CuP) thin films were prepared by spin coat CuPc solution on the glass substrate. The influence of annealing temperature on properties of copper phthalocyanine thin films was investigated by X-ray diffraction and UV-VIS spectrophotometer. The crystalline size can be calculated from X-ray diffraction spectra. Phase transformation of α-β phases of CuPc thin films due to different anneal temperature was observed. Optical absorption spectra of CuPc films show absorption bands which correspond to the B-band and the Q-band.

Keywords: organic semiconductor, copper phthalocyanine, thin film

Introduction

Phthalocyanine (Pc) is a class of organic semiconductor matrials with alternate single-double bond structure. Metallophthalocyanines (MPcs) are planar phthalocyanine organic molecule associated with one metal atom in the molecule's centre, and typically the central atom is the one in the first row of transition metals such as copper, cobalt, iron, etc. The MPcs are found to exhibit conductive properties. Therefore, an attempt has been made to use the MPcs in optoelectronics devices such as organic light emitting diode[1], organic solar cell [2], etc. Copper phthalocyanine (CuPc) has been most frequently used among MPcs for organic electronics devices. The advantages of CuPc are high thermal stability and chemical stability, moreover CuPc can be easily obtained in large quantity and high purity. CuPc thin films are employed as p-type or hole injection layer in organic semiconductor device. Normally, the crystallographic phases exist in at least two different crystalline phases, the α-phase and β-phase. Therefore, the knowledge of the plane orientation and surface morphology are essential for their successful applications. Strucuture of CuPc shows different crystallographic phases and different morphology, depending on deposition conditions such as type of substrate, substrate temperature etc. In addition, by changing phase composition, structure and morphology of phthalocyanine films it is possible to control the sensitivity and response characteristics of the organic electronic devices [3]. The effect of substrate temperature[4, 5] in the properties of various thin films of MPcs compounds including CuPc, NiPc, VoPc and PbPc have been reported in literature paper. In this work, the influences of annealing temperature on properties of CuPc films were investigated.

Materials and Methods

The CuPc powder used in this work was purchased from Aldrich Chem. Co. (purity >97%) and used without further purification. Prior deposition, glass substrate were cleaned ultrasonically in deionized water, methanol, acetone and isopropanol for 15 min, respectively. CuPc powder was solved in dichloromethane (DCM) and trifluoroacetic acid (TFAA) mixed solvent with ratio of DCM and TFAA was kept at 1:1. The films were fabricated from the solution by spin coating technique on the glass substrate at room temperature with speed of 1000 rpm for 15 s, followed by dry process at 50 °C for 15 min under ambient condition. In order to study the effect of annealing temperature on properties of CuPc films, the CuPc Films were annealed at 150, 200, 250 °C for 3 hours in air. The crystalline structure of CuPc films was studies using X-ray diffraction (XRD) technique (Bruker, D8 Explorer) with Cu K_α radiation source (λ=0.1542 nm). Optical absorption of CuPc thin films was measured using a double-beam UV-VIS spectrophotometer (PG Instrument, T90+) at room termperature.

Results and Discussion

X-ray diffraction patterns of CuPc films at various annealing temperature are shown in Fig.1. Table 1 shows the calculated value of the crystalline size (D), the lattice microstrain (ε) and dislocation density (δ) for CuPc films at different anneal temperature. The crystalline size (D) was calculated using the Scherrer equation [6]

$$D = \frac{k\lambda}{\beta\cos\theta} \tag{1}$$

where β is FWHM, k is constant (with a value of 0.94), λ is wavelength of the X-ray radiation and is the Bragg angle. The dislocation density (δ) defined as the length of dislocation lines per unit value of crystal, that was evaluated using Williamson and Smallman's formula [6],

$$\delta = \frac{1}{D^2} \tag{2}$$

The strain function (ε) in the films was calculated using the relation [6]

$$\varepsilon = \left(\frac{\lambda}{D\cos\theta} - \beta\right)\left(\frac{1}{\tan\theta}\right) \tag{3}$$

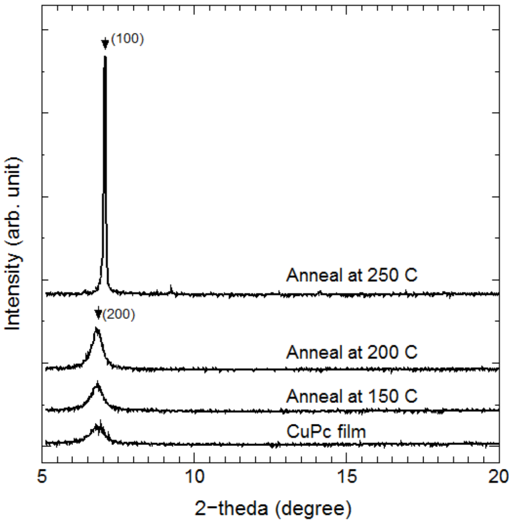

Figure. 1 XRD spectra of CuPc films for various annealing temperature of 150, 200 and 250 °C.

It is found that the film crystallinity increases with increaseing anneal temperature. When the films are coated without post heat treatment, a dominant peak was observed at 2θ= 6.8°, which corresponds to the α-phase monoclinic CuPc in the (200) plane. However, the intensity of peak increases with increasing anneal temperature, whereas the full width at the half maximum (FWHM) decreases with increasing annealing temperature. The decrease in FWHM can be explained by the decrease in the concentration of lattice imperfections, due to the decrease in the internal microstrain within the films, and an increase in the crystalline size. For the annealing temperature about 250 °C, the XRD spectra exhibits the shifted of the diffraction peak at 2θ= 7.1°, which corresponds to the β-phase monoclinic CuPc in the (100) plane and the transformation from metastable α-phase to stable β-phase was observed.

Table 1: Structural parameters (crystalline size, dislocation density and lattice microstrain) of CuPc films at different annealing temperature

Condition	**D (nm)**	**ε (10^{-3}lin^{-2}.m^{-2})**	**δ (10^{14}lin.m^{-2})**
CuPc film	15.7	9.9	40.6
Anneal at 150 °C	18.1	8.6	30.5
Anneal at 200 °C	20.4	7.6	23.9
Anneal at 250 °C	101.6	1.5	0.96

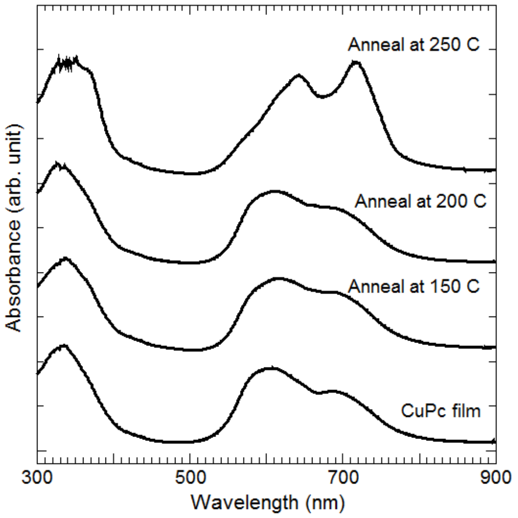

Figure 2. Optical absorption spectra of CuPc films for various annealing temperature of 150, 200 and 250 °C.

Optical absorption spectra of CuPc films, 300-900 nm spectral region was selected which to measure the absorbance spectrum of CuPc thin films. Fig. 2 shows absorption spectra of CuPc films at various annealing temperatures. Normally, organic molecules of MPcs and their derivatives exhibit anomalous optical characteristics because of their unique molecular ring structures. At the CuPc film without post heat treatment, the main peak wavelengths in the absorption spectrum are found at 330 nm and 597 nm and the wavelength of the shoulders appeared around 694 nm. The absorption peaks at 597 nm corresponds to the Q band, where the one at 330 nm corresponds to the B band. The broad absorption bands at 300-400 nm and 600-900 nm are associated with the soret and Q-bands respectively. The Q band high energy maxima observed at wavelength range from 612 nm to 614 nm and the low energy maxima at wavelength ranges from 695 to 697 nm for the films at annealing temperatures of 150 and 200 °C. As the annealing temperature increased, the higher energy maximum peaks were shifted from 614 to 640 nm and decresed gradually compared to the first maximum peak. The intensity of the higher energy maximum peak is larger than that of the second peak and this behavior clearly represents the typical features of the α-phase of CuPc.

As the annealing temperature increased to 250 °C, the higher energy maximum peak was shifted from 614 to 640 nm and the intensity decreased gradually compared to the first maximum peak. The second maximum peak at 640 nm (1.94 eV) becomes smaller than that of the first peak at 717 nm (1.72 eV) and this behaviour represents the stable β-phase of CuPc films. With above results, the phase transformation as reflected in the energy gap structure, from the metastable α-phase to the stable β-phase could be observed to be purely due to the effect of annealing temperature [7]. From the optical absorption spectra, the optical band gaps were determined by the peak energy at low energy maxima. The estimated optical band gap energy values decreased from 1.78 eV (691 nm) to 1.72 eV (717 nm) when the annealing temerpature gradually increased from room temperature to 250 °C.

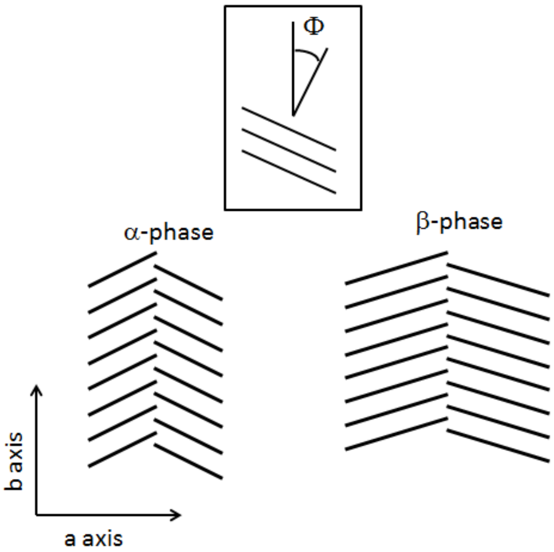

Figure 3. Crystal structures of α-phase and β-phase MPcs.

It has been reported [8-11] about the influence of temperature such as substrate temperature, annealing temperature on physical properties of MPcs. While substrate temperature is increased during evaporation of the MPcs films [8], the spacing of the lattice plane of MPcs in b axis is increased. It suggests that the tilt angle Φ between the stacking of MPcs molecule and the normal axis of the phthalocyanine ring becomes larger as shown in Fig. 3, indicating that the phase transformation has occurred in films. Typically, the α-phase in MPcs is a metastable phase, which can be obtained when a thin film is deposited on an unheated substrate, while the β-phase is the thermodynamically stable phase and it can be prepared at high temperature growth or post-annealing, It has been found that the α-phase can be transformed into the β-phase by a thermal treatment.

Conclusions

CuPc thin films were prepared by the spin coating CuPc solution onto glass substrate. The degree of crystallinity and the size of CuPc grains are found to increase with increasing anneal temperature, whereas the strain and the dislocation density decreased. The CuPc thin films prepared at the room temperature and at low annealing temperatures have the α-phase structure. At the annealing temperature about 250 °C, the orientation of CuPc molecules was arranged to closely the surface of substrate, and the transformation from metastable α-phase to stable β-phase was observed. The increased in annealing temperature leads to increase in crystalline size in the CuPc films, whereas the lattice microstrain and the dislocation density of films are found to decrease. The optical absorption spectra in UV-visible region shows two transition levels in the Q-band and B-band which are corresponding with the optical absorption characteristics of α-phase and β-phase of CuPc films.

Acknowledgments

This work has partially been supported by the National Nanotechnology Center (NANOTEC), NSTDA, Ministry of Science and Technology, Thailand, through its program of Center of Excellence Network.

References

1. A. J. Ikushima, T. Kanno, S. Yoshoda and A. Maeda, “Valence and conduction band edges of metal-phthalocyanines and carrier behavior”, Thin Solid Films **273** (1996), 35–38.
2. J. Y. Kim and A. J. Bard, “Organic donor/acceptor heterojunction photovoltaic devices based on zinc phthalocyanine and a liquid crystalline perylene diimide”, Chemical Physics Letter **383** (2004), 11-15.
3. O. Berger, W. J. Fischer, B. Adolpho, S. Tierbach, “Studies on phase transformations of Cu-phthalocyanine thin films”, Journal of Materials Science **11** (2000), 331-346.
4. Y. L. Lee, W. C. Tsai, J. R. Ma, “Effect of substrate temperature on the film characteristics and gas-sensing properties of copper phthalocyanine films”, Applied Surface Science **173** (2001) 352-361.
5. K. Xiao, Y. Liu, G. Yu, and D. Zhu, “Influence of the substrate temperture during deposition on film characteristic of copper phthalocyanine and

field-effect transistor properties", Applied Physics A: Material Science & Processing **77** (2003) 367-370.
6. K. Onlaor, B. Tunhoo, P. Keeratithiwakorn, T. Thiwawong, J. Nukeaw, "Electrical bistable properties of copper phthalocyanine at different deposition rates", Solid-State Electronics **72** (2012) 60-66.
7. S. Senthilarasu, Y. B. Hahn, S. H. Lee, "Nano structure formation in vacuum evaporated zinc phthalocyanine (ZnPc) thin films", Journal of Material Science **19** (2008), 482-486.
8. B. Tunhoo, and J. Nukeaw, "Structual and optical properties of low temperature evaporated iron phthalocyanine thin films", Materials Research Innovations **13** (2009), 145-148.
9. S. Semthilarasu, Y. B. Hahnm and S. H. Lee, "Structural analysis of zinc phthalocyanine (ZnPc) thin films: X-ray diffraction study", Journal of Applied Physics **102** (2007), 043512.
10. S. Yim, S. Heutz and T. S. Jones, "Structural and morphological modifications in double layer heterostructures containing H_2Pc, perylene-3, 4, 9, 10-tetracarboxylic dianhydride and Alq_3", Journal of Applied Physics **91** (2002) 3632–3636.
11. B. Joseph and C. S. Menon, "Studies on the optical properties and surface morphology of cobalt phthalocyanine thin films", E-Journal Chemistry **5** (2008) 86–92.

Structural Phase Transition of Scandium Trihydride under High Pressure by using *ab initio*

T. Pakornchote[1,2], T. Bovonratanaraks[1,2], and U. Pinsook[1,2*]
[1]*Department of Physics, Faculty of Science, Chulalongkorn University, Bangkok 10330, Thailand*
[2]*ThEP, Commission on Higher Education, 328 Si-Ayutthaya Road, 10400 Bangkok, Thailand*
**Corresponding author. E-mail: Udomsilp.P@chula.ac.th*

Abstract

Scandium trihydride (ScH_3) occurs under pressure higher than 5.3 GPa as a hexagonal close packed (hcp) phase, and then it starts to deform at 28.9 GPa and has a face centered cubic (fcc) phase at 45.9 GPa. The *ab initio* calculations reproduce the experimental results. The enthalpy of fcc is lower than hcp at pressure higer than 22 GPa in the calculations with the exchange-correlation the generalized gradient approximation (GGA), and 26 GPa in the calculation with the local density approximation (LDA). The d-spacing results from the GGA calculations are quite in good agreement with the experiment, but the d-spacing results from LDA are smaller than the experimental results. The intermediate phase is the sliding of some of the $(110)_h$ planes. The energy barrier between the hcp and the fcc phases has been calculated.

Keywords: Structural phase transition, Scandium trihydride, High pressure, *Ab initio*.

Introduction

Metal hydrides change their chemical compositions under high pressure. We are interested in scandium hydride. The experiment shown that the compound becomes scandium hydride at the ambient temperature, and then dihydride and trihydride appear in the x-ray diffraction at 4.1 and 5.3 GPa, respectively. The compound becomes all trihydride at 46 GPa [1]. Thus, these pressure range can force the compound to vary the hydrogen concentration.

The structural phase transitions of ScH_3 have been investigated by using x-ray diffraction and inelastic neutron scattering (INS) [1,2]. The first phase is the hcp structure. Then the hcp starts to deform sluggishly at 28.9 GPa and forms a complete fcc phase at 45.9 GPa. The phase between 28.9-45.9 GPa is the so-called intermediate phase. It could be a long-period stacking structure so as found in YH_3. Yttrium is heavier and in the same group as Sc. YH_3 has the phase transition from hcp to fcc as well, but it occurs at earlier pressure between 11 to 25 GPa [3,4]. The stacking structure of YH_3 has already been investigated [5]. However, the intermediate phase of ScH_3 has never been theoretically investigated before. In this work, we study the hcp to fcc phase transition, and give a possible explanation to the existence of the intermediate phase.

Materials and Methods

The results were calculated by using CASTEP program which is based on *ab initio* calculations [6].

The calculation parameters were well-tested for the convergence, i.e. the energy cutoff is 600 eV, and the k-point separation is 0.04 Å. The exchange-correlation functional are of the generalized gradient approximation (GGA) which is in form of Perdew-Burke-Ernzerhof (PBE) [7] and the local density approximation (LDA) [8]. The results from both functionals are compared with the experimental results. In addition, in high pressure calculations the inner-core electrons can be affected, therefore we use “on the fly” pseudopotential in order to give correction to the inner core. The electron wave functions represent some valence electrons of Sc, i.e. 3d1 4s2 3p6 3s2. The temperature was not treated in this calculation.

Results and Discussion

The hcp and fcc phases were optimized under pressure between 0 - 60 GPa. Their enthalpies were compared in Figure 1. The hcp has lower enthalpy than the fcc at low pressure for both GGA and LDA calculations. The hcp to fcc phase transition starts at 22 GPa from the GGA calculation. Also, in the LDA calculation, the transition pressure is 26 GPa. These calculated transition pressure is a little lower than the experimental result at 28.9 GPa.

From Figure 1, the fcc enthalpy from the LDA calculation exhibits a discrete jump around the pressure of 25 GPa. This is an unusual behavior and needs careful examination. In fact, this jump occurs in the hcp phase. At low pressure, the electrons transfer from p orbital to d orbital as shown in Figure 2. The p orbital gives up 0.02 electrons in every 5 GPa to d orbital as pressure increases upto the pressure of 25 GPa. A sudden jump occur between 25 – 26 GPa, in according to a sudden jump in the electron transfer in the hcp phase using the LDA calculation, see open circles in Figure 2. This behavior causes the discrete hcp volume jump between 25 – 26 GPa, see crosses in Figure 3. As enthalpy H = E + PV, this behavior causes the discrete jump in the enthalpy as well.

There is another discrete volume jump at the phase transition, where the fcc volume is slightly smaller than the hcp volume, as shown in Figure 3. This confirms that this phase transition is a first order phase transition. The hcp and the fcc volumes are compared with the experimental values. The GGA calculation (open circles) gives a better agreement than the LDA calculation (crosses). Furthermore, the volume jump in the LDA calculation in the hcp phase is not seen by the experiment. Thus this behavior must be artificial. Consequently, the LDA calculation might not be an accurate calculation for ScH_3. The GGA calculation is more reliable in this respect.

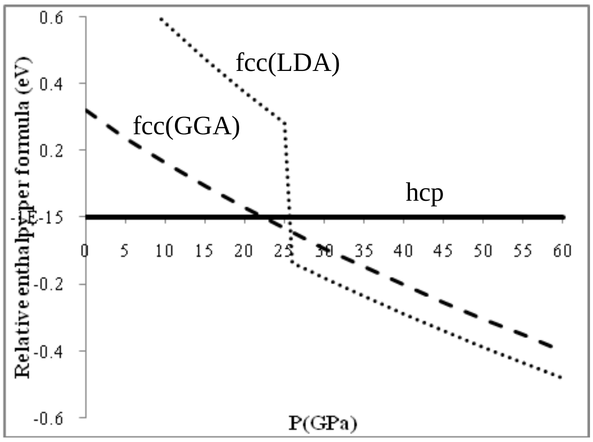

Figure 1. The enthalpy per formula of the hcp and the fcc phases. The hcp enthalpy is set as a reference (solid line). The fcc enthalpy from the GGA (dashed line) and the LDA (dotted line) calculations show that ScH_3 has the transition pressure at 22 GPa and 26 GPa, respectively, compared with 28.9 GPa from the experiment [1].

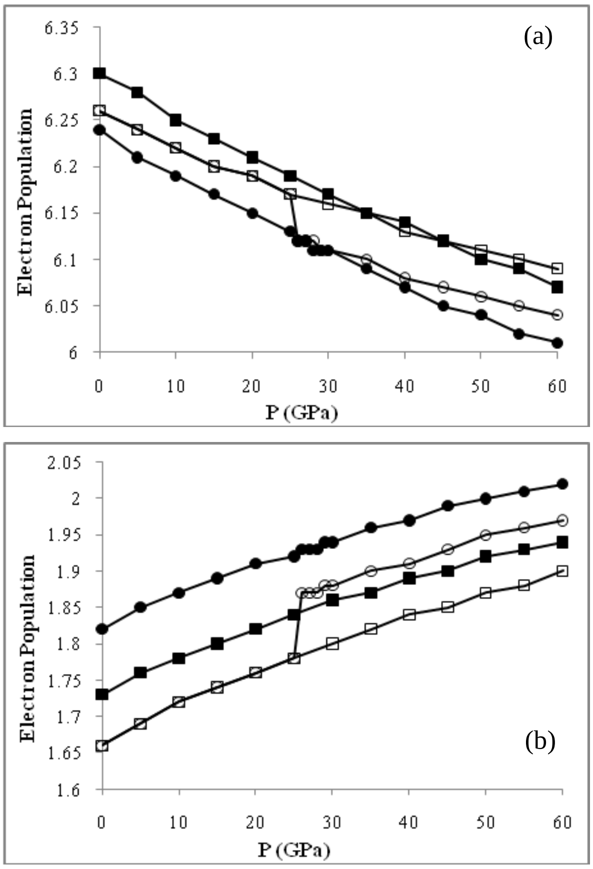

Figure 2. Show the electrons transfer from p orbital to d orbital as pressure increases. The graph composes of the electron population in the hcp phase with the GGA (☐) and LDA (○) calculations, and in the fcc phase with GGA (■) and LDA (●) calculations. (a) The electron population in the p orbital. (b) The electron population in the d orbital. It is clear that p electrons are decreases whereas d electrons are increases, as pressure increases.

Next, the intermediate phase is investigated by using the GGA calculation only. We model the intermediate phase as a distortion of the hcp phase. It deforms from the pattern ABABAB (hcp) to the pattern ABCABC (fcc), where the A, B and C are one of the the $(110)_h$ planes. The experimental results suggested that the hcp deforms by the sluggish sliding of the $(110)_h$ plane. In our calculation, we divide this sliding into arbitrary 7 steps. The barrier of the sliding path is plotted in Figure 4. The 1st step is the hcp phase and the 7th step is the fcc phase. It is most likely that the intermediate phases can be either the 2nd or the 6th step because the energy of these steps are quite low and can be stabilized by the temperature effect. The enthalpy between the 3rd-5th steps is too high, and only decreases slightly as the pressure increases.

Conclusions

The transition pressure was calculated by using *ab initio* with the GGA and the LDA functionals. The hcp to fcc transition occurs at 22 GPa for the GGA calculation, and at 26 GPa for the LDA calculation. These results are a little lower than the experimental results. However, the molar volume from the GGA calculation is good in agreement with the experimental results. The LDA calculation exhibit an artificial jump in the electron transfer. Thus the LDA calculation should not be a good method for the ScH_3 as it cannot accommodate the experimental finding. We propose that the intermediate phase is the distortion of the hcp phase where there is a sluggish sliding of the $(110)_h$ plane, in order to transform the sequence ABABAB (hcp) into ABCABC (fcc). The barrier exhibits some deformation that has relative lower energy, i.e. 2nd and 6th steps. We believe that this deformation could be stabilized by the temperature effect. This could be an explanation for the existence of the intermediate phase of ScH_3.

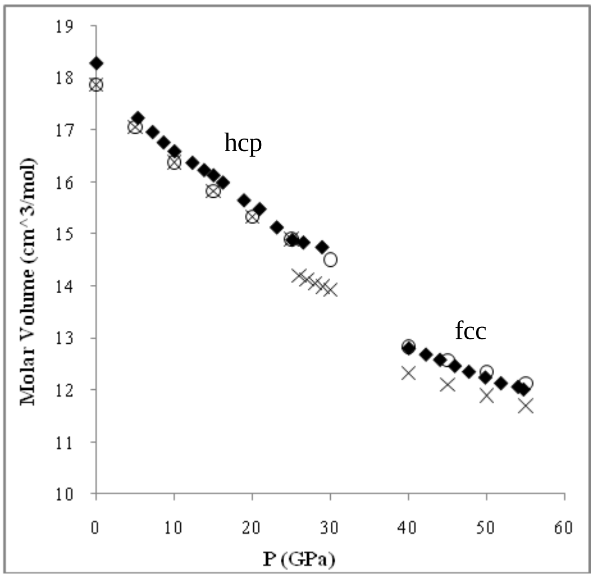

Figure 3. The molar volume as the pressure increases of the hcp phase between 0 - 30 GPa and the fcc phase between 40 - 55 GPa, compared with the experimental results (◆) [1]. The graph shows both the GGA calculation (○), and the LDA calculation (×).

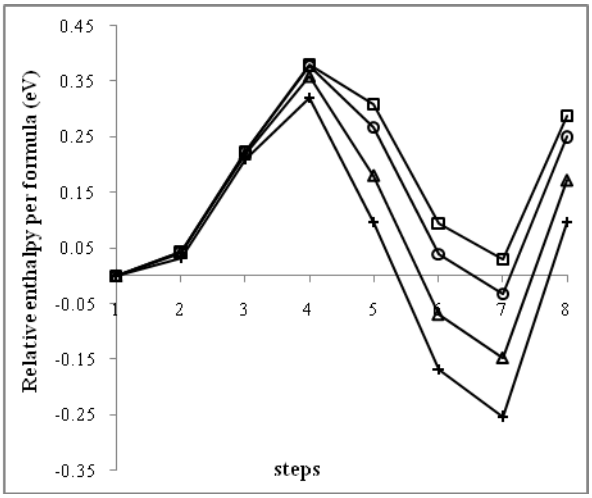

Figure 4. The barrier of the sliding path of the $(110)_h$ plane divided into 7 steps. The 8th step is just another distorted structure. The 1st step is the hcp phase and the 7th step is the fcc phase. The symbols, □, ○, △, +, represent the calculation results at 20, 25, 35, 45 GPa, respectively.

Acknowledgments

The authors would like to thank A. Ohmura and D.Y. Kim for their kind supports of very useful information. This project has been partially supported by special Task Force for Activating Research (STAR), Ratchadaphiseksomphot Endowment Fund and National Research Council of Thailand (NRCT). Computing facilities are supported by Chulalongkorn University Centenary Academic Development Project (CU56-FW10) and A1B1 funding from Faculty of Science, Chulalongkorn University. T.B. acknowledge TRF contract number RSA5580014.

References

1. A. Ohmura, A. Machida, T. Watanuki, K. Aoki, S. Nakano, and K. Takemura, "Pressure-induced structural change from hexagonal to fcc metal lattice in scandium trihydride", J. Alloys Compd. 446, 598 (2007).
2. V. E. Antonov, I. O. Bashkin, V. K. Fedotov, S. S. Khasanov, T. Hansen, A. S. Ivanov, A. I. Kolesnikov and I. Natkaniec, "Crystal structure and lattice dynamics of high-pressure scandium trihydride", Phys. Rev. B 73, 054107 (2006).
3. T. Palasyuk, M. Tkacz, "Hexagonal to cubic phase transition in YH3 under high pressure", Solid State Commun. 133, 477-480 (2005).
4. A. Machida, A. Ohmura, T. Watanuki, T. Ikeda, K. Aoki, S. Nakano, and K. Takemura, "X-ray diffraction investigation of the hexagonal–fcc structural transition in yttrium trihydride under hydrostatic pressure", Solid State Commun. 138, 436-440 (2006).
5. A. Machida, A. Ohmura, T. Watanuki, K. Aoki, and K. Takemura, "Long-period stacking structures in yttrium trihydride at high pressure", Phys. Rev. B 76, 052101 (2007).
6. M. D. Segall, P. J. D. Lindan, M. J. Probert, C. J. Pickard, P. J. Hasnip, S. J. Clark, M. C. Payne, "First-principles simulation: Ideas, illustrations and the CASTEP code", Journal of Physics Condensed Matter, 14 (11), pp. 2717-2744 (2002) .
7. J. P. Perdew, K. Burke, and M. Ernzerhof, "Generalized gradient approximation made simple", Physical Review Letters, 77 (18), pp. 3865-3868 (1996).

8. L. NEDIN, and B. I. LUNDQVIST, “Explicit local exchange-correlation potentials”, J. Phys. C: Solid State Phys. 4 2064 (1917).

Study Microstructure and Electrical Properties of $SrTi_{(1-x)}Sn_xO_3$

P.Khongrattana[1*], A. Muadkongjan[1], N. Tongtae[1], M. Mani[1] and Nikom Choosiri[1]

[1]*Department of Physics, Faculty of Sicence, Thaksin University, Songkhla ,90000 Thailand*
**Corresponding author. E-mail:prachit979@gmail.com*

Abstract

$SrTi_{(1-x)}Sn_xO3$ (x=0.15-0.20) solid solution were prepared by a solid state reaction method. The obtained materials were characterized by x-ray diffraction (XRD) analysis and scanning electron microscopy(SEM) The formation of fully crystalline $SrTiO_3$ was observed in the sintering temperature at 1100 ^oC. With increasing Sn concentration, the grain of $SrTi_{(1-x)}Sn_xO_3$ ceramics increased and maximum dielectric constant first decreased and then increased. At a Sn concentration of x = 0.15 reached its maximum value (159.0).

Keywords: $SrTi_{(1-x)}Sn_xO3$; SEM; dielectric constant

Introduction

Recent technological development in the wireless telecommunication system utilizing microwave dielectric ceramics as resonators, filters and other components have increased interest in designing and engineering of new materials for better performance and miniaturization of the microwave components. Ideal materials for commercial applications as dielectric resonators are required to have dielectric, $\varepsilon_r > 24$, $\tau_f \approx 0$ and high quality factor at microwave frequencies, $Q \times f (\approx 30,000)$. For certain applications, e.g. antennas, the values of τ_f and $Q \times f$ can be compromised to ±10 ppm/^{o}C and > 10,000 GHz respectively; however, ε_r must be high enough to miniaturize the device for incorporation into a handset. Additional, as given by Eq.(1), the use of a high ε_r material is important for reducing the size and weight and hence manufacturing and operational cost of the electronic equipment [1]

$$\lambda_d \alpha \frac{1}{(\varepsilon_r)^{1/2}} \qquad (1)$$

Where λ_d is the wavelength in a dielectric given by $\lambda_d = \lambda_o / (\varepsilon_r)^{1/2}$

Several materials have got their commercial applications as dielectric resonators in handset and base stations but there is still a constant search for materials with ultra low losses, $\tau_f \approx 0$ and high dielectric constants $\varepsilon_r > 50$ [2]

Materials and Methods

Ceramics sample with the composition $SrTi_{1-x}Sn_xO_3$, x = 0.0, 0.15, 0.17, 0.20) were prepared, using starting materials with high purity $SrCO_3$(>99%), SnO_2(>99%) and TiO_2(>99%). Stoichiometic amounts of powders were mixed together and then ball-milled for 24 h, using a nylon jar with agate balls and ethanol as liquid medium, air drying, the mixed powders were calcined at 1,100^{o}C for 4 h in air and pressed into disks with diameter of 15 mm under 100 MPa pressure. The pellets were sintered at 1,300^{o}C for 5 h, and then furnace was cooled down to room temperature.

The crystalline phase of the sintered specimens was revealed by X-ray diffraction (XRD, X 'pert pro MPD, Philips, Netherlands) technique using Cu Kα radiation. The surface microstructure of the sintered specimens was characterized by scanning electron microscopy (SEM, Quanta400, FEI, Czech Republic). The dielectric constant and loss tangent of the ceramics coated with silver electrodes were obtained by Agilent 4284A impedance analyzer over frequency of 200 kHz to 500 kHz at room temperature. Then the samples were measured by Agilent 4284A temperature analyzer in the temperature range from 35^{o}C to 500^{o}C. The dielectric properties were calculated. The equation used for calculation as follow:

$$\varepsilon_r = \frac{Cd}{\varepsilon_0 A} \qquad (2)$$

Results and Discussion

Figure 1 shows the X-ray powder diffraction (XRD) pattern of $SrTi_{1-x}Sn_xO_3$, x = 0.0, 0.15, 0.17, and 0.20) dense ceramics. Except for the peak shift little, the diffraction peaks and their intensities are very similar for the investigated compositions, which indicates the formation of solid solution. All peaks can be assigned to Sr(Ti,Sn)O_3, with cubic perovskite structure, and the result is similar to the previous work [12]

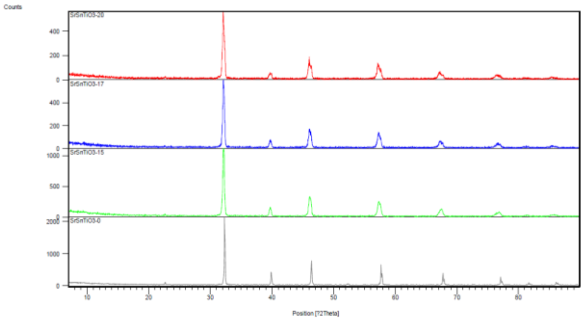

Figure 1. XRD pattern of $SrTi_{1-x}Sn_xO_3$.

Figure 2 the grain sizes obtained in the present work are in the rang 0.2-0.4 micron, the SEM images indicated that the powder particles micrometer in size. The materials show microporous structure and is composed of agglomerated assembles of different grain. The reason for this change is the formation of solid solution of Sr(Ti,Sn)O_3[3]

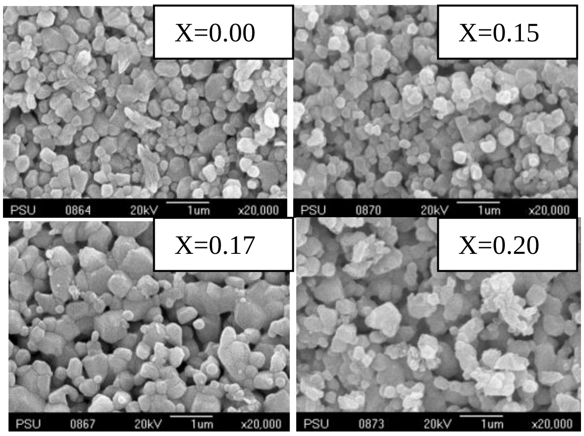

Figure 2. Scanning electron micrographs of $SrTi_{1-x}Sn_xO_3$ synthesized at 1300°C

Figure 3 the temperature dependence of dielectric constant for $SrTi_{1-x}Sn_xO_3$ solid solution at 500 kHz . Dielectric are observed in the temperature range 35-495°C and it is note that the maximum of the dielectric constant reaches reasonable high value.

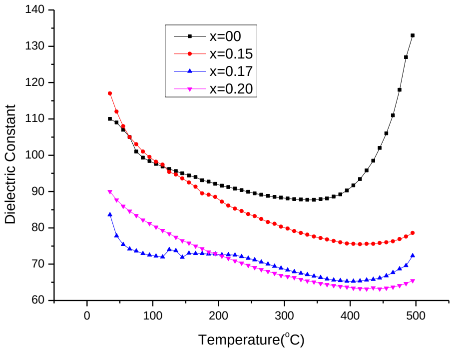

Figure 3. Temperature dependence of dielectric constant of $SrTi_{1-x}Sn_xO_3$ dense ceramics at 500 kHz.

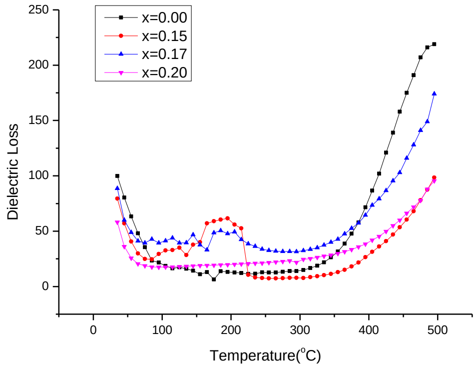

Figure 4. Temperature dependence of dielectric loss of $SrTi_{1-x}Sn_xO_3$ dense ceramics at 500 kHz.

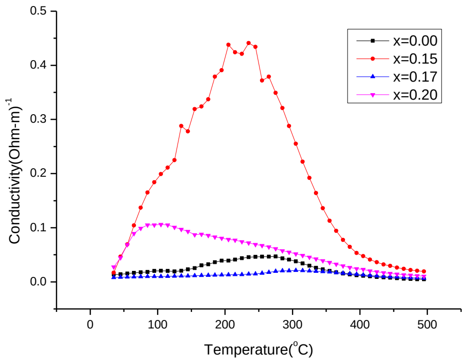

Figure 5. Temperature dependence of conductivity of $SrTi_{1-x}Sn_xO_3$ dense ceramics at 500 kHz.

Conclusions

The present study demonstrates the potential of synthetic approach based on the solid state reaction method to yield phase $SrTiO_3$ and mixed $SrTi_{1-x}Sn_xO_3$ powders at high temperature(1300°C) The morphological characterization of $SrTi_{1-x}Sn_xO_3$ by SEM showed the formation of microcrystalline of nearly uniform. The dielectric constant dependence on temperature confirms the stiffening of polar region dipole correlation in the ferroelectric phase.

References

1. L. Nedelcu, M. I. Toacsan, M.G. Banclu, A Loachim, "Microwave properties of Ba($Zn_{1/3}Ta_{2/3}$)O_3 dielectric resonators", J Alloys. Compd **509**(2011) 477.
2. R. Freer, F. Azouh, "Microstructure Engineering of Microwave Dielectric Ceramics", J. Eur. Ceram. Soc, **28**(2008), 1433.

3. X, Wei X, Yao, “Preparation, Structure and Dielectric Property of Barium Stannate Titanate Ceramics”, Mater. Sci. Eng. B **137**(2007) 184.

Nuclear and Radiation Physics

Assessment and Radioactive Contour Maps of Specific Activities of Natural (^{40}K, ^{226}Ra and ^{232}Th) and Anthropogenic (^{137}Cs) Radionuclides in Surface Soil Samples from Surat Thani Province, Thailand

P. Kessaratikoon[1*], R. Boonkrongcheep[2], S. Benjakul[2], and U. Youngchauy[3]

[1]Nuclear and Material Physics Research Unit, Department of Physics, Faculty of Science, Thaksin University, Muang, Songkhla, 90000,Thailand.
[2]Research Assistant, Nuclear and Material Physics Research Unit, Department of Physics, Faculty of Science, Thaksin University, Muang, Songkhla, 90000, Thailand.
[3]Thailand Institute of Nuclear Technology (Public Organization), 16 Vibhavadi Rangsit Rd, Chatuchak, Bangkok, 10900. Thailand.
[*]Corresponding author. E-mail: prasong_mi@hotmail.com

Abstract

The specific activities of natural (^{40}K, ^{226}Ra and ^{232}Th) and anthropogenic radionuclides (^{137}Cs) in 168 surface soil samples collected from 17 districts in Surat Thani provinces in the southern region of Thailand were measured and analyzed. Experimental results were obtained by using a high-purity germanium (HPGe) detector and gamma spectrometry analysis system. The KCL, IAEA/RGU-1, IAEA/RGTh-1and IAEA/SL-2 radioactive standard sources were used to analyze the concentration of ^{40}K, ^{226}Ra, ^{232}Th and ^{137}Cs in all samples. It was found that the specific activities of ^{40}K, ^{226}Ra, ^{232}Th and ^{137}Cs ranged from 33 – 11,692, 11 – 705, 4 – 301 and 0 – 11 Bq/kg with mean values of 2,119 ± 172, 76 ± 6, 47 ± 5 and 4 ± 2 Bq/kg, respectively. Furthermore, the radiological hazard of absorbed dose rate in air (D), radium equivalent activity (Ra_{eq}), external hazard index (H_{ex}), and annual effective dose rate (AED_{out}) in the area under consideration were also calculated. The experimental results were also compared with research data in the south of Thailand (2009 – 2012), Office of Atoms for Peace (OAP) annual report data and global radioactivity measurement and evaluations. Moreover, the result can be used to create the radioactive contour maps of the investigated area.

***Keywords*:** Specific activity, natural and anthropogenic radionuclides, high-purity germanium (HPGe) detector, radiological hazard, radioactive contour map

Introduction

According to the 2010 National Power Development Plan implemented in March calls for five nuclear power plants to be built in Thailand, each with a capacity of 1 gigawatt (GW). Two 1GW plants will be set up in 2020 and 2021, followed by the rest from 2024-2025. They will start feeding power to the grid in 2020. Surat Thani is one of three provinces (Chumporn and Nahkon Si Thammarat) in the south of Thailand which was chosen to construct the nuclear power plant in this plan. For this reason, the concentration of natural (^{226}Ra, ^{232}Th and ^{40}K) and anthropogenic (^{137}Cs) radionuclides in Surat Thani should be measured and studied before the construction of nuclear power plant.

Surat Thani province with a name that literally means "City of the Good People" is the largest province in the south of Thailand located 685 kilometers from Bangkok. A former capital of the Srivijaya Empire, the province covers an area of approximately 12,891 square kilometers. Surat Thani province borders the Gulf of Thailand to the north and east, Chumphon Province to the north, Nakhon Si Thammarat and Krabi Provinces to the south, Phang-Nga and Ranong Provinces to the west and Nakhon Si Thammarat Province to the east as shown in Fig. 1.

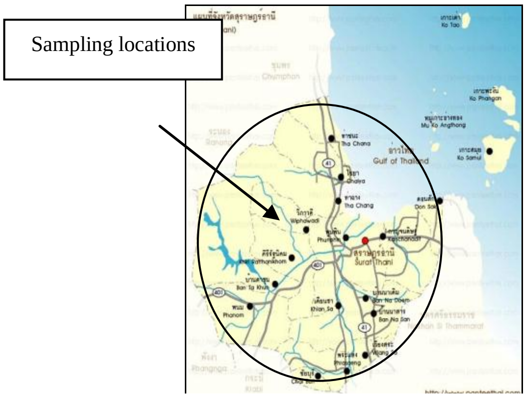

Figure 1. Surat Thani province and sampling locations (http://www.ponteethai.com)

The aim of this paper is to establish reference levels of natural and anthropogenic radioactivity for Surat Thani province (Thailand), through the analysis of absorbed dose rate in air (D), radium equivalent activity (Ra_{eq}), external hazard index (H_{ex}), and annual effective dose rate (AED_{out}) by using high-purity germanium (HPGe) detector and gamma spectrometry analysis system to determine the specific activity of ^{226}Ra, ^{232}Th, ^{40}K and ^{137}Cs in surface soil samples. Moreover, the radioactive contour maps of the investigated area were also created by using the ArcGIS computer program**.**

Materials and Methods

Sample collection and preparation

Surface soil samples (168 samples) were collected from 17 districts (exception on Ko Samui and Ko Pha-ngan districts) of Surat Thani province in the south of Thailand. A map of Surat Thani province and sampling locations is shown in Fig. 1. After collection, each sample was dried up at room temperature and sieved through a 2 mm mesh-sized sieve to remove stone, pebbles and other macro-impurities. All samples were oven dried at a temperature of 100 ^{o}C for 3 hours, before the analysis for removing moisture. The homogenized sample was placed in a 290 cm^3 PVC containers. The container was sealed hermitically and externally using a cellophane tape and kept aside for about a month to ensure equilibrium between ^{226}Ra and its daughters and ^{228}Ra and its daughters before being taken for gamma spectrometric analysis.

Measurement and analysis

The specific activities of natural radionuclides (^{226}Ra, ^{232}Th and ^{40}K) in all beach sand samples were determined by employing a high-purity germanium detector (HPGe, CANBERRA Model GC 2018) and gamma spectrometry analysis system at Nuclear and Material Physics Laboratory, Department of Physics, Faculty of Science, Thaksin University. The detector was enclosed in a massive 10 cm thick lead shielding. Gamma ray radioactive standard sources ^{60}Co, ^{137}Cs and ^{133}Ba were used to calibrate the measurement system up to about 2 MeV. Geometric efficiency for beach sand matrices in the container was determined by an IAEA/RGU-1, IAEA/RGTh-1 and KCL reference material (International Atomic Energy Agency IAEA, Vienna, Austria). The spectra were analyzed using the program GENIE 2000. The specific activity of ^{40}K was determined from its 1460.8 keV γ-line. The specific activities of ^{226}Ra and ^{232}Th were determined by their decay products ^{214}Pb (351.9 keV) and ^{208}Tl (583.2 keV), respectively. The specific activity of ^{137}Cs was also determined from its 661.7 keV γ-line. Counting time interval was 10,800 s. The background spectrum was recorded immediately after or before the sample counting.

Equations and formulae

By using the specific activity values of ^{40}K, ^{226}Ra, and ^{232}Th from this study, the absorbed dose rate (D) in outdoor air at 1 m above the ground is calculated using the conversion factors published in Singh *et al.*, 2005 [14] and is given below

$$D = 0.461C_{Ra} + 0.623C_{Th} + 0.0414C_{K}, \qquad (1)$$

where C_{Ra}, C_{Th} and C_K are the specific activities of ^{226}Ra, ^{232}Th and ^{40}K in Bq/kg, respectively. Furthermore, the radium equivalent activity (Ra_{eq}) is calculated through the following relation:

$$Ra_{eq} = C_{Ra} + 1.43C_{Th} + 0.077C_{K} \qquad (2)$$

Moreover, the external hazard index (H_{ex}) is also evaluated by using the equation which is defined as:

$$H_{ex} = C_{Ra}/370 + C_{Th}/259 + C_{K}/4810 \leq 1 \qquad (3)$$

Using the absorbed dose rates in air (D) obtained from the specific activities of natural nuclides in beach sand, adopting the conversion factor of 0.7 Sv/Gy from absorbed dose in air to effective dose received by adults and considering that people in Thailand, on the average, spent approximately 20% of their time outdoors, the annual effective dose rate (AED_{out}) are calculated using the following equation:

$$AED_{out}\ (mSv/y) = D(nGy/h)\times 8760\ h\times 0.2\times 0.7(Sv/Gy) \times 10^{-6} \qquad (4)$$

All four calculated and average values have been evaluated, presented and compared with the recommended values proposed by UNSCEAR.

Results and Discussion

The range and average values of specific activities of ^{40}K, ^{226}Ra, ^{232}Th and ^{137}Cs in 168 surface soil samples collected from Surat Thani province (Thailand) were calculated and presented in Table 1.

Table 1: Range and average value of specific activities of ^{40}K, ^{226}Ra, ^{232}Th and ^{137}Cs in 168 surface soil samples collected from Surat Thani province (Thailand).

Sampling locations in Surat Thani	**Specific Activities (Bq/kg)**			
	^{40}K	**^{226}Ra**	**^{232}Th**	**^{137}Cs**
Muang	2465 ± 185	57 ± 5	51 ± 5	3 ± 2
Phunphin	1580 ± 162	64 ± 6	39 ± 5	2 ± 1
Don Sak	1998 ± 183	39 ± 5	40 ± 5	3 ± 2
Kanchanadit	3176 ± 253	114 ± 7	**84 ± 6**	4 ± 2
Ban Na doem	1408 ± 136	68 ± 6	40 ± 4	0 ± 0

Ban Na San	4015 ± 244	**156 ± 8**	68 ± 6	6 ± 2
Wiang Sra	2212 ± 185	118 ± 7	65 ± 6	4 ± 2
Kian Sa	524 ± 85	36 ± 4	28 ± 3	4 ± 1
Phrasaeng	639 ± 95	36 ± 4	25 ± 3	0 ± 0
Chaiburi	582 ± 88	29 ± 3	19 ± 3	5 ± 1
Ban Ta Khun	1055 ± 126	40 ± 5	36 ± 7	0 ± 0
Phanom	1895 ± 159	36 ± 4	40 ± 4	2 ± 2
Khiri Rattha-nikhom	2358 ± 193	152 ± 8	67 ± 5	**8 ± 3**
Wipawadi	1386 ± 151	43 ± 4	19 ± 2	0 ± 0
Tha Chana	3543 ± 214	107 ± 7	55 ± 5	3 ± 2
Chaiya	**4169 ± 230**	94 ± 7	70 ± 6	4 ± 2
Tha Chang	3020 ± 233	96 ± 7	60 ± 6	3 ± 2
Ko Samui	-	-	-	-
Ko Pha-ngan	-	-	-	-
Range	**33 – 11692**	**11–705**	**4 – 301**	**0 –11**
Average value	**2119 ± 172**	**76 ± 6**	**47 ± 5**	**4 ± 2**

The average value of the specific activities of ^{40}K, ^{226}Ra, ^{232}Th and ^{137}Cs in 168 surface soil samples collected from Surat Thani province (Thailand) were also compared with research data in the South of Thailand, OAP data and worldwide mean as shown in Table 2.

Table 2: Comparison of the average value of specific activities of ^{40}K, ^{226}Ra, ^{232}Th and ^{137}Cs in 168 surface soil samples collected from Surat Thani province (Thailand) with research data in the South of Thailand, OAP data and worldwide mean.

Data Sources	**Specific Activities (Bq/kg)**			
	^{40}K	**^{226}Ra**	**^{232}Th**	**^{137}Cs**
Songkhla	3562 ± 224	107 ± 7	52 ± 5	3 ± 2
NaKhon Si Thammarat	**4313 ± 148**	109±31	74 ± 4	5 ± 3
Phatthalung	3573 ± 204	136 ± 7	76 ± 5	4 ± 2
Trang	385 ± 23	77 ± 3	84 ± 5	-
Phuket	4092 ± 267	**213±10**	**204 ± 10**	6 ± 3
Satun	4021 ± 247	99 ± 7	64 ± 2	**7 ± 3**
Yala	3608 ± 236	129 ± 7	86 ± 6	5 ± 2
Surat Thani	**2119 ± 172**	**76 ± 6**	**47 ± 5**	**4 ± 2**
South of Thailand	511 ± 7	172 ± 3	211 ± 2	1 ± 1
Thailand Mean (OAP)	400	48	40	-
Worldwide Mean	400	35	30	-

From the result in Table 2, the average specific activities of ^{40}K in Surat Thani is lower than in Songkhla, Nakhon Si Thammarat, Phatthalung, Phuket, Satun and Yala provinces but higher than in Trang province. The average specific activities of ^{226}Ra and ^{232}Th in Surat Thani are lower than in Songkhla, Nakhon Si Thammarat, Phatthalung, Trang, Phuket, Satun and Yala provinces. We can also see that the average specific activities of ^{40}K, ^{226}Ra and ^{232}Th in Surat Thani are always higher than the research data from Thailand and worldwide Means. Moreover, the average specific activities of ^{137}Cs in Surat Thani is higher than the research data from Songkhla province and the south of Thailand, lower than in Nakhon Si Thammarat, Phatthalung, Phuket, Satun and Yala provinces and equal to Phatthalung province. By using the specific activity values of ^{40}K, ^{226}Ra, and ^{232}Th as shown in Table 1, the absorbed dose rates in air (D), the radium equivalent activity (Ra_{eq}), the external hazard index (H_{ex}) and the annual effective dose rate (AED_{out}) can be evaluated by using equation (1) to (4) and presented in Table 3.

Table 3: Gamma absorbed dose rate, radium equivalent activity, external hazard index, and annual effective dose rate of 168 surface soil samples collected from Surat Thani province (Thailand).

Locations	**D (nGy/h)**	**Ra_{eq} (Bq/kg)**	**H_{ex}**	**AED_{out} (mSv/y)**
Muang	160 ± 13	319 ± 27	0.86 ± 0.07	0.20 ± 0.02
Phunphin	116 ± 12	236 ± 25	0.64 ± 0.07	0.14 ± 0.01
Don Sak	126 ± 13	250 ± 26	0.68 ± 0.07	0.15 ± 0.02
Kanchanadit	230 ± 17	468 ± 35	1.26 ± 0.09	0.28 ± 0.02
Ban Na doem	114 ± 11	233 ± 22	0.63 ± 0.06	0.14 ± 0.01
Ban Na San	**281 ± 17**	**562 ± 35**	**1.52 ± 0.09**	**0.34 ± 0.02**
Wiang Sra	186 ± 15	381 ± 30	1.03 ± 0.08	0.23 ± 0.02
Kian Sa	55 ± 7	115 ± 15	0.31 ± 0.04	0.07 ± 0.01
Phrasaeng	58 ± 8	121 ± 16	0.33 ± 0.04	0.07 ± 0.01
Chaiburi	49 ± 7	101 ± 14	0.27 ± 0.04	0.06 ± 0.01
Ban Ta Khun	84 ± 11	173 ± 24	0.47 ± 0.06	0.10 ± 0.01
Phanom	117 ± 11	233 ± 22	0.63 ± 0.06	0.14 ± 0.01
Khiri Rattha nikhom	209 ± 15	429 ± 30	1.16 ± 0.08	0.26 ± 0.02
Wipawadi	70 ± 8	141 ± 15	0.38 ± 0.04	0.09 ± 0.01
Tha Chana	215 ± 14	430 ± 29	1.16 ± 0.08	0.26 ± 0.02
Chaiya	260 ± 16	516 ± 33	1.39 ± 0.09	0.32 ± 0.02
Tha Chang	207 ± 16	414 ± 33	1.12 ± 0.09	0.25 ± 0.02
Ko Samui	-	-	-	-
Ko Pha-ngan	-	-	-	-
Ranges	**12 - 725**	**26 - 1483**	**0.07 - 4.01**	**0.01 - 0.89**
Average Values	**149 ± 13**	**301 ± 25**	**0.81 ± 0.07**	**0.18 ± 0.02**
UNSCEAR (1988, 1993, 2000)	**55**	**370**	**1**	**0.48**

Furthermore, radioactive contour maps (RCM) of specific activities values of ^{40}K, ^{226}Ra, ^{232}Th and ^{137}Cs in 168 surface soil samples collected from Surat Thani province (Thailand) were constructed by using

ArcGIS computer program and shown in Fig. 2 and Fig. 3.

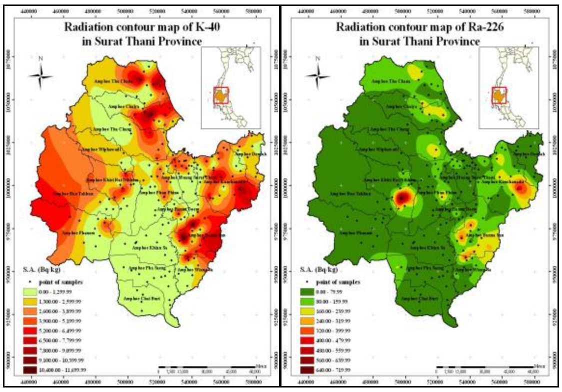

(a) (b)

Figure 2. RCM of specific activities values of ^{40}K (a) and ^{226}Ra (b) in 168 surface soil samples collected from Surat Thani province (Thailand).

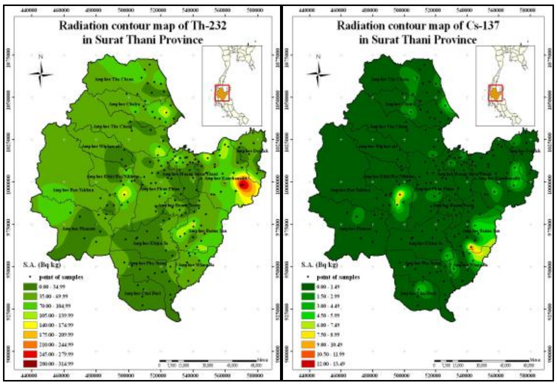

(c) (d)

Figure 3. RCM of specific activities values of ^{232}Th (c) and ^{137}Cs (d) in 168 surface soil samples collected from Surat Thani province (Thailand).

Conclusions

The average value of specific activities of ^{40}K, ^{226}Ra, ^{232}Th and ^{137}Cs in 168 surface soil samples collected from Surat Thani province in the south of Thailand, were 2,119 ± 172, 76 ± 6, 47 ± 5 and 4 ± 2 Bq/kg, respectively. Moreover, all of three natural radionuclides (^{40}K, ^{226}Ra and ^{232}Th) were also used to evaluate the gamma absorbed dose rate in air (D), radium equivalent activity (Ra_{eq}), external hazard index (H_{ex}), and annual effective dose rate (AED_{out}). We can see that the average value of gamma dose rate obtained in this study (149 nGy/h) is about 3 times higher than the world average (55 nGy/h). The average values of radium equivalent activity (301 Bq/kg) is less than 370 Bq/kg, which is acceptable for safe use. The average values of external hazard index obtained in this study was found to be 0.81 which is less than unity. According to the calculated annual effective dose rate with average value 0.18 mSv/y, is lower than the worldwide average value (0.48 mSv/y). This means that the radiation hazard is still insignificant for the population living in the investigated area. According to the radioactive contour maps which were created by using the studied data, we can see that the specific activities values of ^{40}K in this area (especially in the north, the west and the east parts of Surat Thani province) were rather high.

Acknowledgments

The investigation was fully supported by Research and Development Institute Thaksin University (RDITSU). The authors would like to thank Department of Physics, Faculty of Science, Thaksin University for allowing us to use all instruments and radioactive standard sources at Nuclear and Material Physics Laboratory. The authors wish to thank Assoc. Prof. Dr.Tripop Bhongsuwan, Head of Department of Physics, Faculty of Science, Prince of Songkhla University (PSU), Hat Yai Campus for his generous permission to us to use the standard reference materials (IAEA/RGU-1 IAEA/RGTh-1 and KCL) for calculation and analysis in this study. The authors are particularly indebted to some of undergraduate and graduate students for their works and patience in samples collection, measurement and analysis some parts of these data.

References

1. A.K. Mohanty, D. Sengupta, S.K. Das, V. Vijayan and S.K. Saha, “Natural radioactivity in the newly discovered high background radiation area on the eastern coast of Orissa, India”. Radiation Measurements **38**(2004), 153-165.
2. A. Malance, L. Gaidolfi, V. Pessina and G. Dallara, “Distribution of ^{226}Ra, ^{232}Th, and ^{40}K in soils of Rio Grande do Norte, Brazil”. Journal of Environmental Radioactivity **30** (1996), 55–67.
3. A.S. Alencar and A.C. Freitas, “Reference levels of natural radioactivity for the beach sands in a Brazilian southeastern coastal region”. Radiation Measurements **40**(2005), 76-83.
4. C. Ratanasumniang, “Measurement of Specific Activity of Natural and Antropogenic Radionuclides in Soil Samples in Songkhla Province (Thailand)”. Thesis for the master degree of Physics, Thaksin University. 2009.
5. J. Beretka and P. J. Mathew, “Natural radioactivity of Australian building materials,

industrial wastes and by-products”. Health Physics **48**(1985), 87-95.
6. M. Daoh, “Measurement of Specific Activity of Natural (^{40}K, ^{226}Ra and ^{232}Th) and Anthropogenic Radionuclides (^{137}Cs) in Soil from Phathalung Province (Thailand) Using Gamma Ray Spectrometry”. Thesis for the master degree of Physics, Thaksin University, 2010.
7. M. Jahlee, “Quantitative Measurement of Natural and Anthropogenic Radionuclide (^{137}Cs) in Soil Samples from Yala Province, Thailand”. Thesis for the master degree of Physics, Thaksin University, 2012.
8. M. Meena, “Assessment of Natural and Anthropogenic Radioactivities in Soil Samples from Satun Province, Thailand”. Thesis for the master degree of Physics, Thaksin University, 2011.
9. Office of Atoms for Peace (OAP). “OAP Annual Academic Report in 1990-2000”. Ministry of Science and Technology. Office of Atoms for Peace, Bangkok, 1990-2000.
10. P. Kessaratikoon, S. Benjakul and S. Udomsomporn, “Quantitative Analysis of Specific Activity of ^{40}K, ^{226}Ra and ^{232}Th in Soil Samples from the Municipal Area of Muang District in Songkhla Province Using Gamma-Ray Spectrometry”. Thai Journal of Physics **3**(2009), 99-102.
11. R. Boobkrongcheep, ”Specific Activities and Radioactive Contour Maps of Natural (^{40}K, ^{226}Ra and ^{232}Th) and Anthropogenic (^{137}Cs) Radionuclides in Soil Samples in Phuket Province, Thailand”. Thesis for the master degree of Physics, Thaksin University, 2009.
12. R. Veiga, N. Sanches, R.M. Anjos, K. Macario, J. Bastos, M. Iguatemy, J.G. Aguiar, A.H.A. Santos, B. Mosquera, C. Carvalho, M. Baptista Filho and N.K. Umisedo, “Measurement natural radioactivity in Brazilian beach sands”. Radiation Measurements **41**(2005) 189-196.
13. S. Selvasekarapandian, R. Sivakumar, N.M. Manikandan, V. Meenakshisundaram, V.M. Raghunath and V. Gajendran, “Natural radionuclide distribution in soils of Gugalore, India. Applied Radiation and Isotopes **52**(2000), 299-30.
14. S. Singh, A. Rani and R.K. Mahajan, “^{226}Ra, ^{232}Th and ^{40}K analysis in soil samples from some areas of Punjab and Himachal Pradesh, India using gamma ray spectrometry”. Radiation Measurements **39**(2005) 431-439.
15. T. Thongna, “Natural Radioactivity Assessment in Nakhon Si Thammarat Province”. Thesis for the master degree of Physics, Thaksin University, 2009.
16. United Nations Scientific Committee on the Effects of Atomic Radiation, “Sources, effects and risk of ionizing radiation”. UNSCEAR, New York, 1988.
17. United Nations Scientific Committee on the Effects of Atomic Radiation, “Exposure from natural sources of radiation”. UNSCEAR, New York, 1993.
18. United Nations Scientific Committee on the Effects of Atomic Radiation, “Sources, effects and risk of ionizing radiation”. UNSCEAR, New York, 2000.

Comparisons of Transport in Small Tokamak Experiments using Integrated Predictive Modeling Code

J. Promping[1*], R. Picha[1], and Y. Pianroj[2]

[1]*Thailand Institute of Nuclear Technology, Bangkok, Thailand*
[2]*Faculty of Sciences and Industrial Technology, Prince of Songkla University, Suratthani Campus*
**Corresponding author. E-mail: ame026@gmail.com*

Abstract

Small tokamaks have an important role in fusion research. Research on small tokamaks has created a scientific basis for the scaling-up to larger tokamaks. In this paper, self-consistent simulations of a small tokamak are carried out using TASK/TR code, with the same experimental parameters that are used as the initial and boundary conditions. The anomalous core transport in TASK/TR simulations is calculated using either the semi-empirical Mixed Bohm/gyro-Bohm (Mixed B/gB) model or the theory-based current diffusive ballooning mode (CDBM) model. From the preliminary results, they are found that both temperature and density profiles peak near the plasma center. Under the same conditions, the electron temperatures obtained from the simulations using the CDBM model tend to be higher than those from the Mixed B/gB model. But the electron densities from the Mixed B/gB simulations are equal to the CDBM model. In addition, the sensitivity of the results on the plasma parameters, such as temperature, current, density, and stored energy, are investigated.

***Keywords*:** TASK/TR, transport, tokamak, fusion

Introduction

The prediction of plasma performance in a tokamak can be achieved in the nuclear fusion community by using integrated predictive modeling codes to compute the time evolution of plasma profiles such as temperature and density. This task has been done using various integrated predictive modeling codes, for example BALDUR[1], TASK/TR[2], JETTO[3], CRONOS[4] and ASTRA[5]. Cross-comparison between the predictions of different codes is important for the research in order to improve our confidence on these codes predictive capability. Moreover, it is known that plasma performance in a tokamak depends on many parameters. Therefore, the purpose of this paper is to compare plasma performance as the plasma parameters are varied; examples of these quantities are plasma current, heating power and line average density. In this work, TASK/TR code is used because it is readily available with two different core transport models Mixed Bohm/gyro-Bohm (Mixed B/gB) model and Current Diffusive Ballooning Mode (CDBM) model. The neoclassical transport is calculated using NCLASS model.

The simulations are carried out with plasma parameters based on the HL-1M tokamak (China) [6] and include an electron cyclotron resonance heating (ECRH), which allows us to observe the transport behavior. The TASK/TR simulations provide an understanding of plasma behavior in the HL-1M experiment.

This paper is organized as follows: brief descriptions of TASK/TR integrated predictive modeling code, Turbulent Transport Models (Mixed Bohm/gyro-Bohm and CDBM), are given in the next section. Then, experimental observation is described, followed by theresults and discussions..

Simulation Method

Task/TR code

The TASK/TR transport code is based on the diffusive transport equation. The code can calculate temporal evolution of the density and temperature for every species of particles in a plasma core: electrons, deuterium, tritium, thermalized α particles, neutrals, multiple impurities, and the other particles of interest. The code can also deal with a local temporal evolution for the two kinds of beam ion associated with the heating by fast α particle and neutral beam injections. Also, analysis including neutral beam injection, heating current drive, pellet injection, and current ramp up is possible and it can evaluate quantitatively a plasma response to these external actuators since the transport equations include various geometric factors. Furthermore, it is easy to carry out a transport simulation coupled with two-dimensional equilibrium code. The code may incorporate experimental profile data through standard type of data file or data base. The TASK/TR transport code solves the one-dimensional diffusive equation for densities, temperature and a poloidal magnetic flux with respect to the normalized minor radius ρ [7]. The effect of E×B shear stabilization is considered to be important because it allows the plasma to form a transport barrier. Applying this effect appropriately for simulation, the TASK/TR calculates the radial electric field, which is derived by the radial ion force balance. It should be noted that the toroidal velocity used is taken from the experimental data, and every discharge in the profile database does not always contain the toroidal velocity information. Therefore, it can be made up by multiplying the toroidal angular speed by the surface averaged geometrical major radius, both of which are usually included in the database. The poloidal velocity is computed using the NCLASS module. Moreover, the TASK/TR includes various neoclassical transport models to evaluate the transport coefficients, the bootstrap current, the neoclassical resistivity, and the poloidal flow velocity and viscosity. The theory-based turbulent transport models: the CDBM model is included in TASK/TR..

Turbulent transport models

In this work, two turbulent transport models are used: the Mixed B/gB model and CDBM model. Brief descriptions of the models are given as follows.

Mixed Bohm/gyro Bohm

The Mixed B/gB core transport model [8] is an empirical transport model. It was originally a local transport model with Bohm scaling. A transport model is said to be “local” if the transport fluxes (such as heat and particle fluxes) depend entirely on local plasma properties (such as temperatures, densities, and their gradients). A transport model is said to have “Bohm” scaling if the transport diffusivity is proportional to the gyro-radius times thermal velocity over a plasma linear dimension such as major radius. The transport diffusivity in models with Bohm scaling is also a function of the profile shapes (characterized by normalized gradients) and other plasma parameters such as magnetic *q*, which are all assumed fixed in systematic scans in which only the gyro-radius is varied relative to plasma dimensions. The original Mixed B/gB model was subsequently extended to describe ion transport, and a gyro-Bohm term was added in order for simulations to match data from smaller tokamaks, as well as larger machines. Similarly, a transport model is said to have “gyro-Bohm” scaling if the transport diffusivities are proportional to the square of the gyro-radius times thermal velocity over the square of the plasma linear dimension. Usually the Bohm contribution to the JET model dominates over most of the plasma, whereas the gyro-Bohm contribution usually makes its largest contribution in the deep core of the plasma and plays a significant role only in smaller tokamaks with relatively low power and low magnetic field.

CDBM model

The Current Diffusive Ballooning Mode model is based on the theory of self-sustained turbulence due to the ballooning mode [9, 10] driven by the turbulent current diffusivity. Inclusion of the electron viscosity which has often been neglected in a conventional MHD theory allows the electromagnetic fluctuation to enhance electron viscosity and to make instabilities more unstable in a short-wavelength mode. As the fluctuation amplitude increases, however, the stabilizing effect due to the thermal diffusivity and the ion viscosity eventually overcomes the destabilizing effect of the current diffusivity. The saturation level is determined by the balance of these effects, and solving an eigenvalue problem for the ballooning mode [11].

Experimental observation

HL-1M is a small tokamak with circular cross section. HL-1M was operated with the ECRH heating power of 200 kW with off-axis heating scheme. During off-axis ECRH, $B_T = 2.5$ T, $n_e = 1.4\text{x}10^{13}$ cm^{-3}, $I_P = 150$ kA, $P_{EC} = 200$ kW. For the off-axis heating case (heat at plasma edge region), the electron density profiles are found to be flat [6]. The experimental temperatures are plotted in Figure 1. The central peak was observed in both time instances.

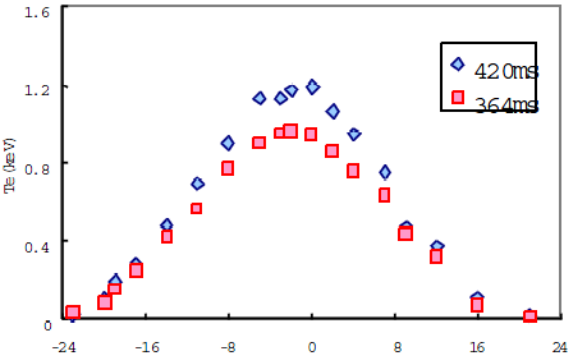

Figure 1. Electron temperature profiles in ECRH stage. $B_T = 2.5$ T, $n_e = 1.4\text{x}10^{13}$ cm^{-3}, $I_P = 150$ kA, P_{EC} = 200 kW

Results and Discussion

The TASK/TR transport code is used to carry out the plasma of the HL-1M experiment with ECRH heating. The engineering parameters used in the simulation are listed in Table 1. The boundary conditions in each simulation are set with the same conditions. In most simulations, the auxiliary heating power of 200 kW, which is assumed to fully heat the electrons, is used.

The temperature profiles and density profiles are shown in Figures 2 and 3. The Mixed B/gB results on the electron temperature fit satisfactorily well to the experimental results, whereas the CDBM results are significantly higher. No transport barriers are observed.

Table 1. Plasma parameters for HL-1M.

Parameter	Physical Description	Values
R (m)	Major radius	1.02
a (m)	Minor radius	0.26
I_p (kA)	Plasma current	150
B_T (T)	Toroidal field	2.5
κ_{95}	Elongation	1.0
ECRH	Electron cyclotron resonant heating	200

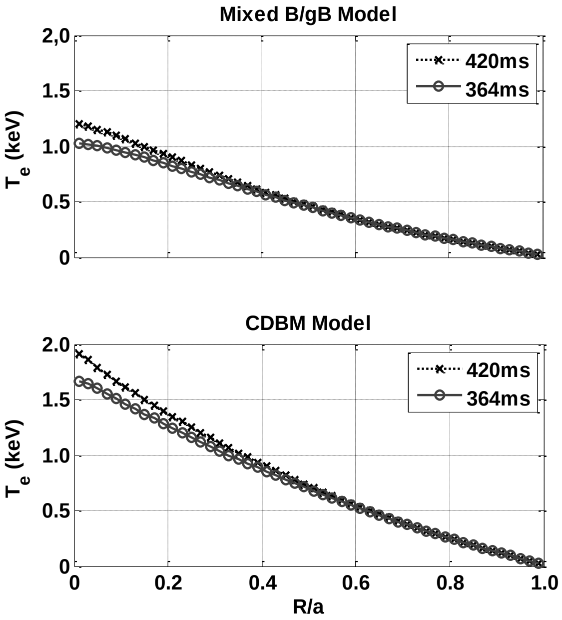

Figure 2. Profiles of electron temperature as a function of normalized minor radius. The cross/dotted line is based on 420ms and the circle/solid line is based on 364ms. This simulation uses Mixed B/gB model (upper) and CDBM model (lower).

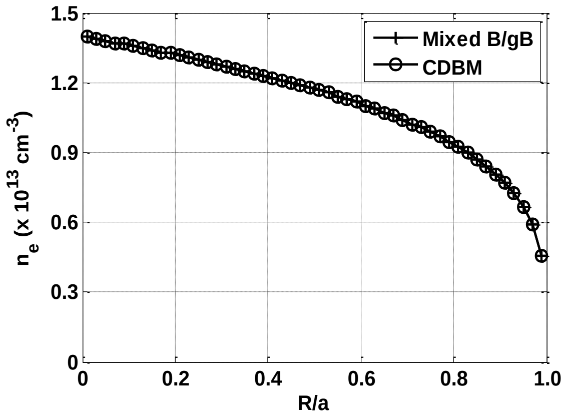

Figure 3. Profiles of electron density as functions of normalized minor radius at time 420ms. The plus sign/data line is based on Mixed B/gB model and the circle/solid line is based on CDBM model.

To summarize the results, the Mixed B/gB model gives the electron temperature at the center $T_e(0)$ = 1.2 keV (420 ms) and 1.03 keV (364 ms). The CDBM model gives the electron temperature at the center $T_e(0)$ = 1.91 keV (420 ms) and 1.67 keV (364 ms). The electron density = 1.4x10^{13} cm^{-3} in both Mixed B/gB and CDBM simulations. The total maximum stored energy is 140 kW in Mixed B/gB and 236 kW in CDBM. The plasma current is 150 keV for both Mixed B/gB and CDBM.

The total stored energy (W_{TOT}) as functions of time are shown in Figure 4. A sharp increase in W_{TOT} is observed in both models, but the magnitude of W_{TOT} is significantly higher in CDBM case than in Mixed B/gB case. In Figure 5 the total electron thermal diffusivity as functions of normalized minor radius is plotted. It can be seen that, similar in both models, the calculated diffusivity is dominant in small regions closed to the edge. The CDBM results are significantly higher. But at the core plasma, the total electron thermal diffusivity from the Mixed B/gB model is higher than the CDBM model. Also the electron temperature from CDBM model is higher than that obtained from Miked B/gB model.

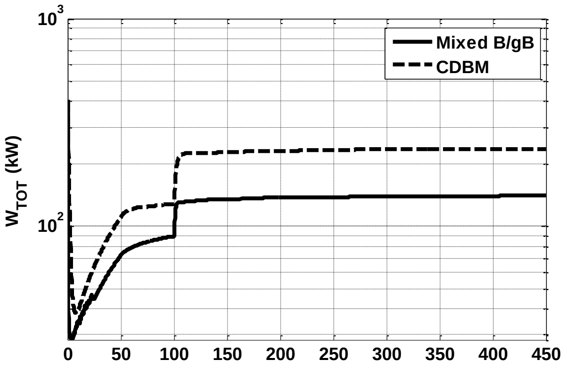

Figure 4. Profiles of total stored energy as functions of time. The solid line is based on Mixed B/gB model and the dashed line is based on CDBM model.

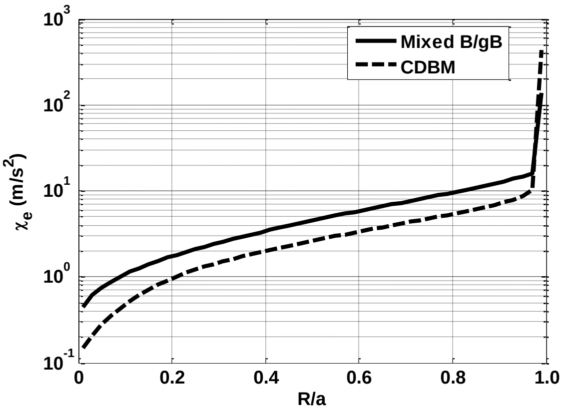

Figure 5. Profiles of the electron thermal diffusivity as functions of normalized minor radius. The solid line is based on Mixed B/gB model and the dashed line is based on CDBM model.

Conclusions

Two turbulent transport models are used to calculate different plasma parameters. The study of the thermal transport during ECRH experiment of plasma in a HL-1M tokamak is carried out using the TASK/TR code. The temperature results are compared to the experimental results from tokamak HL-1M. In general, Mixed B/gB model yields results closer to the experimental results from HL-1M than CDBM does. It is found that the temperatures obtained from both simulations are in the range of experiment results. When ECRH is applied, electron thermal transport increases. Consequently, electron temperature and plasma stored energy increases. It is also found that the Bohm term is the main transport contribution, similar to the results obtained for experiments. The electron density and plasma current results, however, are similar in the two cases. Additional simulations using other tokamaks' settings are in future plan.

Acknowledgments

The author would like to thank Professor A. Fukuyama, from the Department of Nuclear Engineering, Kyoto University, for the introduction of TASK/TR code.

References

1. Singer, C.E., et al. A one-dimensional plasma transport code, Comput. Phys. Common, Vol. 49, pp. 275-398, 1988.
2. Honda, M., Transport simulation of Tokamak plasmas including plasma rotation and radial electric field, Ph.D. Thesis, Nuclear Engineering, Kyoto University, 2007.
3. Genacchi, G. and Taroni, A. JETTO: a free boundary plasma transport code (basic version) Rapporto ENEA RT/TIB, Vol. 5, 1988.
4. Basiuk, V. Artaud, J.F, Imbeaux, F. et al. Simulations of steady-state scenarios for Tore Supra using the CRONOS code, Nuclear Fusion, Vol. 43, pp. 822-830, 2003.
5. Pereverzev G.V, Soldner F.X., Bartiromo R. et al. Transport analysis of lower hybrid current drive plasmas in ASDEX, Nuclear Fusion, Vol. 32, pp. 1023-1036, 1992.
6. Ding, X.T. et al. IAEA-CN-94, 2002; EX/P4-09
7. Honda, M. and Fukuyama, A. Comparison of turbulent transport models of L- and H-mode plasmas, Nuclear Fusion, Vol. 46, pp. 580-593, 2006.
8. Tala, T.J.J., Heikkinen, J.A. and Parail, V.V.. ITB formation in term of ωExB flow shear and magnetic shear on JET, *Plasma Phys*. Control. Fusion, Vol. 43, pp. 507-524, 2001.
9. Itoh, K., Yagi, M., Itoh S I, et al. L-mode confinement medel based on transport-MHD theory in Tokamaks, Plasma *Phys. Control. Fusion*, Vol. 35, pp. 543-549, 1993.
10. Itoh, K., Itoh, S.I., Fukuyama, A., et al. Self-sustained turbulence and L-mode confinement in toroidal plasmas, *Plasma Phys. Control. Fusion*, Vol. 36, pp. 279-306, 1994.
11. Fukuyama, A., Itoh, K., Itoh, S.I., et al. Transport simulation on L-Mode and improved confinement associated with current profile modification, *Plasma Phys. Control. Fusion*, Vol. 37, pp. 611-631, 1995.

Development of a Light Tight Box for Real Time Neutron Imaging in TRR-1/M1

N. Prasing[1], N.l Panapurksa[1], C. Tipayakul[2], R. Picha[2*], W. Ratanatongchai[2], S. Khaweerat[2], S. Wonglee[2], K. Silva[2], and J. Promping[2]

[1]*Faculty of Science, King Mongkut's Institute of Technology Ladkrabang, Ladkrabang, Bangkok, Thailand, 10520*
[2] *Thailand Institute of Nuclear Technology, Ongkharak, Nakorn Nayok, Thailand, 26120*
**Corresponding author. E-mail: aeroppon@gmail.com*

Abstract

Neutron radiography is a non-destructive technique which makes use of a specific property of neutron that can penetrate through object providing non-invasive characterization via imaging. A neutron radiography facility is currently installed in front of the thermal column of the Thailand Research Reactor-1/Modification 1 (TRR-1/M1). We have been using films and reusable neutron imaging plates for neutron radiography. The former needs image developing process and the latter requires neutron imaging plate reading process before obtaining the images, both of which prohibit real time image processing. Thailand Institute of Nuclear Technology (TINT) has a plan to enable a 3-D neutron imaging by adding a light tight box, a rotary table and an image processing system to the current neutron radiography facility. We developed a light tight box as a first step of this project. The principle of this device is as follow. The neutron beam from TRR-1/M1 reaches the neutron sensitive scintillator screen (Gd_2O_2S:Tb) where each neutron triggers a photon cascade. These photons reflect at the mirror and then are captured by a charge-coupled device (CCD)-camera. This device enables a real time neutron imaging which can greatly contribute to the development of a 3-D neutron imaging system in the future.

Keywords: Radiography, nuclear, reactor

Introduction

Reactor neutron radiography is a non-destructive testing method which can be used to study physical information such as shapes and compositions of samples [1].

Located at Thailand Institute of Nuclear Technology (TINT), Thailand Research Reactor-1/Modification 1 (TRR-1/M1) has been employing a neutron radiography facility to probe the internal structures of objects. The images from neutron radiographs and X-ray radiographs have been found to provide complementary information about the samples to each other [2].

However, the current installation has a limited space and fully manual controls. Therefore, there is a plan to renovate the facility and upgrade the system to to have automatic controls and to be able to reconstruct 3-D images.

In this study we designed and constructed a light tight box (dark box) equipped with a radiation conversion screen and a mirror and connected to a camera system which can be remotely controlled. One aim was to build a neutron camera which is cost effective and to test the process before committing to a more permanent installation. Applying different parameters we tried to come up with optimal setups for larger and more complex samples in the future.

Reactor neutron radiography has been widely done around the world [3-4]. The flux is high and safety measures are usually already in place. This is in contrast to a portable system using a radioisotope where shielding can be a challenge [5]. Reactor neutron radiography is a useful technique and not as widely available as X-ray radiography. Therefore, optimizing the facility at TRR-1/M1 will provide a material testing alternative to users, especially from universities and industry.

Materials and Methods

Materials

Samples were exposed to the neutron beam from TRR-1/M1 (setup shown in Figure 1). The 2-MW TRIGA Mark III reactor, which achieved its first criticality on 27 Oct 1962, was being operated in a fuel-saving mode, running only three days a week at about 1 MW power. The reactor has thermal neutron flux at the thermal column of about 8.90×10^{9} cm^{-2} s^{-1} (Jan 2013). The thermal flux at the radiography area is about 4 orders of magnitude smaller. The beam size is 20 cm x 20 cm. These thermal neutrons have energies around 0.025 eV which correspond to de Broglie wavelengths of about 2 angstroms.

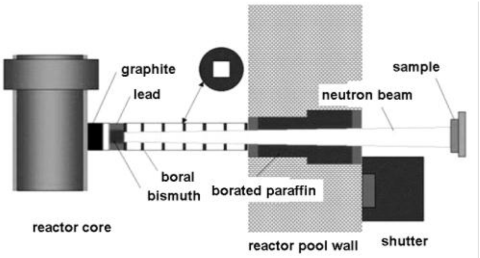

Figure 1. Current neutron radiography facility at TRR-1/M1.

The box (Figure 2) was made of black painted wood. The size of the box was set in consideration of the reactor beam area. The inner dimensions were 34.6 cm^3. The outer dimensions were 40 cm^3. A PVC tube, which was used to mount the camera, was 16 cm in height and 9 cm in radius. A 30.5 cm x 30.5 cm converter screen Gd_2O_2S:Tb (GADOX) was affixed to a 40 cm x 40 cm aluminum plate (0.7 mm thick). The converter screen is directed inward into the box. This Gd_2O_2S:Tb screen captures the neutrons and release green photons (545 nm) into the box. A 38.6 cm x 34.5 cm mirror, which was oriented at 45 degrees, reflects the photons toward a camera (Canon D500 SLR).

Figure 2. The cubic box used as an integrated neutron imaging system.

The current neutron radiography setup uses either a digital imaging plate (phosphor-coated plastic sheet [6]) or film to record images. The plate or film was placed directly behind a converter screen. The images must be developed in a separate facility, either in a dark room (film) or an imaging plate reader. Using the camera allows the images to be captured and investigated right after the exposure. This can help in recording many images in a given time, which is essential in multi-image recording such as 3-D reconstruction. The mirror setup helps reducing the direct neutron dose which can potentially damage the camera.

The camera was connected to a computer via three USB cables (two of them were 10-m extension cables) wired across the reactor hall via a powered USB hub. The long USB line proved to be problematic sometimes, with losses of connection. The camera was mounted to the PVC pipe and stabilized using foam.

Equipment preparation

The camera focus is fixed manually prior to the actual exposure by estimating the distance from the converter to the camera. This focal distance was measured to be 33 cm. The camera ISO was initially set to 100, whereas the focal ratio (F-number) was 4.5.

Conditions

The distance from beam opening was set at 90 cm. The distance was chosen in consideration of the current wall geometry. The exposure time was varied from 60, 120, and 180 s. The shutter was controlled manually via Canon EOS software.

Results and Discussion

To study image brightness and contrast, various exposure times were used. Shown in Figure 3, the samples used for the first test were a rubber figurine with a metallic key inserted and put inside a cylindrical lead container (3-mm thickness).

Figure 3. Samples used in the contrast and brightness analysis.

In the first study, a cylindrical lead container filled with a rubber figurine was used. For quantification of brightness and contrast, ImageJ software v. 1.46 [7] was used to plot the gray value (GV) profiles of different exposure times. The noise was removed thrice by Despeckle adjustment in ImageJ. The plots between the image gray value (brightness) along the line connecting the object to the background (illustrated in Figure 4) for different exposure times are shown in Figure 5. The average gray values for different exposure times are shown in Figure 6. Note that pixel 0 is the starting point, located in the object area, this area ends around pixel 20. Pixels 20-40 cover the background area. High gray values imply high transmission (background), whereas low gray values indicate low transmission (object).

In general, longer exposure time led to higher image brightness and contrast.

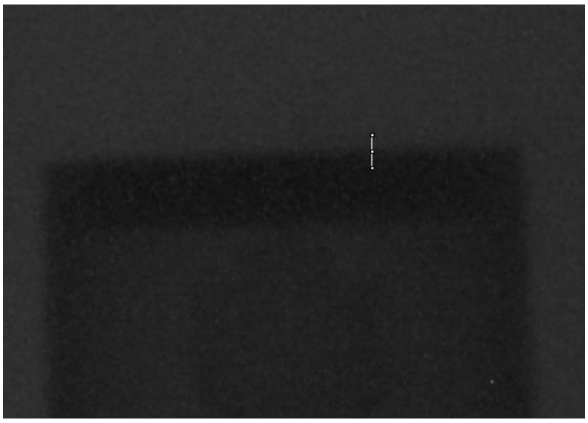

Figure 4. A representative image used to measure contrast.

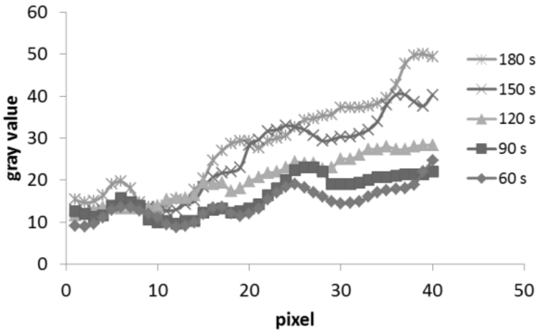

Figure 5. Graphs of the gray value vs pixel location for the different exposure times.

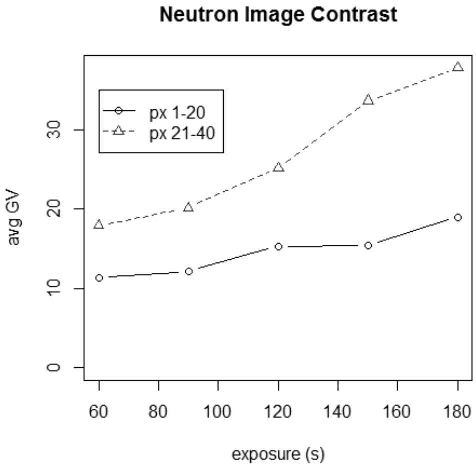

Figure 6. Graphs of the average gray value vs exposure time between the two different pixel areas.

For the second test, we studied the impact of camera ISO on the overall image quality. The higher the ISO number, the more sensitive the camera sensor is to light. A set of children toys (a remote controller, a music box, a toy bug, and a toy car, shown in Figure 7) was tested. The values of the camera ISO and exposure time are listed in Table 1. For the last two cases, we added in a beam purity indicator (BPI), a sensitivity indicator (SI), and a cadmium test strip.

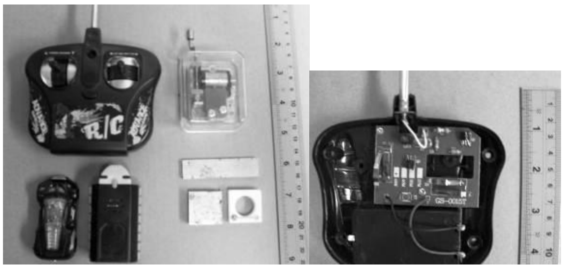

Figure 7. Plastic toys and quality indicators used in the experiment.

Table 2: Conditions for measurement.

	T1	T2	T3	T4
ISO	800	400	200	100
Exposure (s)	30	60	90	150

The resulting images (without noise removal) are shown in Figure 8**.**

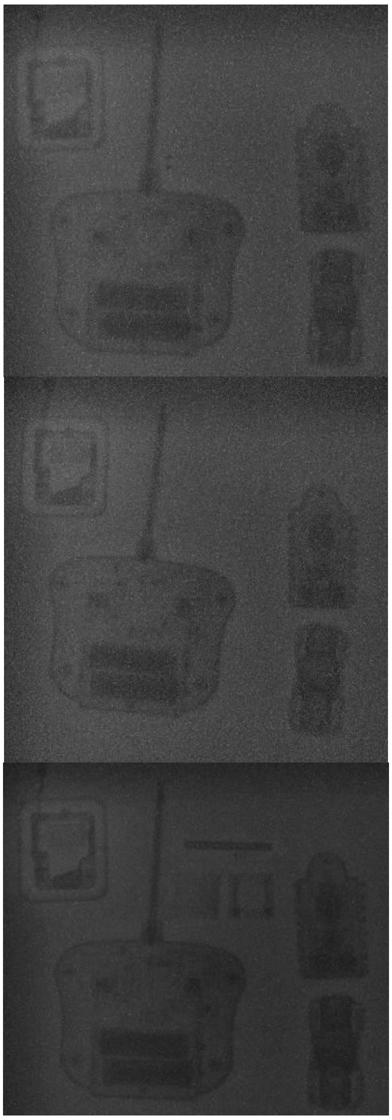

Figure 8. Neutron images of children toys. From top to bottom: T1, T2, T3, and T4.

The cadmium test strip showed that the best resolution achieved was approximately 1 mm. The SI does not give much information. Subjectively, the image qualities of T3 and T4 are comparable.

Looking in the BPI region, the gray value profiles of a line starting from the boron nitride disc to the lead disc were shown in Figure 9. It can be seen that the noise makes it difficult to distinguish between the supposedly bright region (BPI hole) and the supposedly dark regions (the discs).

High-ISO images were brighter but had more noise. To obtain "clean" images, long exposure time and low ISO setting seemed to be the best approach. However, the noise could be quite effectively removed in case a long exposure time is not practical.

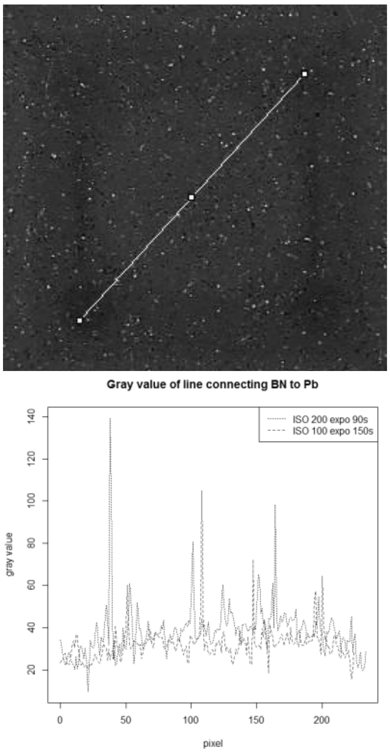

Figure 9. (Top) A line starting from the BN disc (bottom left corner) to the Pb disc (upper right corner). (Bottom) The gray value profiles of the two cases.

Conclusions

An upgrade of the neutron radiography facility at TINT is being planned. A light tight box has been constructed and first images using this setup have been acquired from various samples. Compared to the digital imaging plate, the measurement time scale of the camera system was similar but obtaining the image is faster. Difference of exposure time and ISO led to visible difference in image quality. Problems involving radiation exposure to the equipment, cable connection, and lens focusing were encountered and learned. Further tests of the integrated system will be required before a permanent facility can be installed.

Acknowledgments

The authors thank TINT Reactor Section for facilitating access to the neutron radiography facility as well as beam time for the experiment. The Department of Nuclear Engineering, Chulalongkorn University, kindly provided us important equipment used in this study. The research is partly supported by the International Atomic Energy Agency Coordinated Research Project fund.

References

1. N. Kardjilov, I. Manke, A. Hilger, M. Strobl, and J. Banhard, "Neutron Imaging in Materials Science", Materials Today 14, 6 (2011), 248-256.
2. W. Ratanatongchai and S. Wonglee, "Enhancements of Neutron and X-ray Imaging", in Proc. of the ISTS2012 Conference, 21-24 Nov 2012, Bangkok.
3. A. Dudley et al., "Designs for Neutron Radiography and Computed Tomography at Oak Ridge National Laboratory", JCPDF-International Centre for Diffraction Data (1999) 361-366.
4. B. Tang, H. Huo, S. Zhang, and S. Zhu, "The Neutron Digital Radiography Facility Based CCD in SPRR-300", 9th European Conference on NDT, Sep 2006, Berlin.
5. R. Picha, N. Simaroj, and V. Sangphet, "Designing a Transportable Neutron Radiography System", Kasetsart J. (Nat. Sci.) 42 (2008) 305-310.
6. K. Takahashi, S. Tazaki, J. Miyahara, Y. Karasawa, and N. Niimura, "Imaging Performance of Imaging Plate Neutron Detectors", Nuclear Instruments and Methods in Physics Research Section A 377 (1996) 119-122.
7. ImageJ, http://rsbweb.nih.gov

Development of Flexible Low Energy Gamma Ray Shielding Material Composing of Pre-vulcanized Natural Rubber Latex (PVNRL), Styrene-butadiene Rubber (SBR) and Bismuth

N. Kaotong and D. Wongsawaeng*

Department of Nuclear Engineering, Faculty of Engineering, Chulalongkorn University, Bangkok 10330, Thailand
**Corresponding author. E-mail: doonyapong.w@chula.ac.th*

Abstract

This research developed a flexible low-energy gamma ray shielding material by blending pre-vulcanizable natural rubber latex (PVNRL) and Synthetic rubber SBR in the presence of radiation shielding materials, bismuth powder and bismuth solution. The results indicate that PVNRL/SBR blend, with the blend ratio of 50/50 in the presence of bismuth can shied low-energy gamma rays. The obtained shielding material with 100g of bismuth powder gave 27.7% attenuation of gamma radiation emitted by nuclide ^{137}Cs (662 keV) and 48.9% attenuation of gamma ray generated by nuclide ^{131}I (364 keV). In the presence of 80-ml bismuth solution,obtained 26.6% attenuation of gamma radiation emitted by nuclide ^{137}Cs (662 keV) and 39.4% attenuation of gamma ray generated by nuclide ^{131}I (364 keV).

Keyword: Flexible low energy gamma ray

Introduction

Gamma ray is an electromagnetic wave with the wavelength in the range of 10^{-13} - 10^{-7} m, being shorter than that of X-ray. Shorter wavelength results in higher frequency and, thus, higher energy of the electromagnetic radiation. There are three types of interactions between gamma ray with matter: Photoelectric effect, Compton effect and Pair production. Gamma-emitting radioactive materials are in widespread uses today. In working with ionizing radiation, one must try to minimize the radiation dose received. Therefore, radiation shielding material must exhibit good radiation shielding property and must not weight too heavily. Bismuth is a heavy metal with more electrons orbiting the nucleus than lead, thus gamma ray can interact with more electrons resulting in good radiation shielding properties comparable to lead.

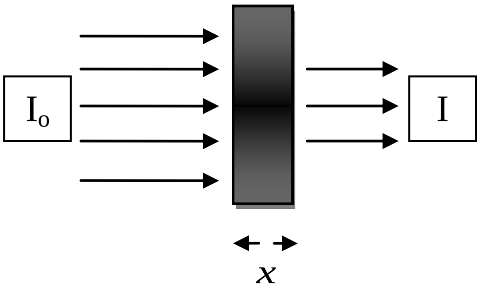

Figure 1. Gamma ray with intensity I_o passes through a matter with thickness x. I is the intensityof gamma ray after passing through the matter.

When gamma ray with intensity I_o passes through a matter with thickness x with the exiting gamma ray intensity of I, the following relationship can be obtained: $I = I_0 e^{-\mu x}$. From the calculated µ value, the HVL (Half Value Layer) and TVL (Tenth Value Layer) parameters can be calculated. HVL and TVL refer to the thickness of the medium that can attenuate gamma radiation to half and 1/10 of the original intensity, respectively. Mathematical relationships are HVL = 0.693/µ and TVL = 2.3/µ.

Experimental Procedure

1. Mix PVNRL and SBR in a beaker with the following volume portions: 0:100, 10:90, 20:80, 30:70, 40:60, 50:50, 60:40, 70:30, 80:20, 90:10 and 0:100. Stir until the mixture becomes homogeneous. Pour the solution onto a mould and let it dry. Setup the gamma ray measurement system by placing the gamma ray source in lead shielding and fixing the gamma ray detector at 25 cm on top of the source. Measure the background gamma radiation with the source removed and measures the emitted gamma ray from the source for 3 times to obtain the average value. Place the shielding material, each with different

blend ratio, between the source and the detector. For each blend ratio, the average value was obtained from 3 runs and results are shown in Figure 2 for Cs-137 source and Figure 3 for I-131 source.

2. Mix the PVNRL and SBR with 50:50 volume ratio for 100 mL in a beaker for 10 minutes, then pour 100 g of bismuth powder into the mixture and stir to achieve homogeneity. Then, pour the mixture onto a mould and let it dry. Setup the gamma ray measurement system as described previously, measure the background gamma radiation with the source removed and measure the emitted gamma ray from the source for 3 times to obtain the average value. Place the bismuth-containing shielding material between the source and the detector and perform 3 runs in order to obtain the average value. Increase the thickness of the shielding material by 0.5 cm at a time. Results are illustrated in Figure 4 for Cs-137 source and Figure 5 for I-131 source.

3. Mix the PVNR and SBR with 50:50 volume ratio for 400 mL in a beaker for 10 minutes, then pour 40 mL (and 80 mL for another set of runs) of bismuth solution into the mixture and stir to achieve homogeneity for 25 minutes. Pour the mixture onto a mould and let it dry. Setup the gamma ray measurement system as described previously, measure the background gamma radiation with the source removed and measure the emitted gamma ray from the source for 3 times to obtain the average value. Place the bismuth-containing shielding material between the source and the detector and perform 3 runs in order to obtain the average value. Increase the thickness of the shielding material by 0.5 cm at a time. Results are shown in Figure 4 for Cs-137 source and Figure 5 for I-131 source.

4. Stack the shielding material on top of one another and place them on an X-ray film. Perform gamma ray photography using **Selenium-75 (Se-75) source for** 15 minutes. Results are illustrated in Figure 6.

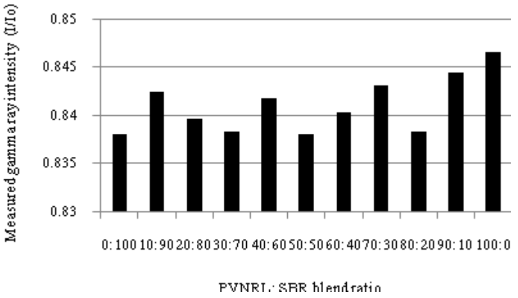

Figure 2. Attenuation of gamma ray from Cs-137 source by shielding material made of PVNRL and SBR blend with various blend ratios

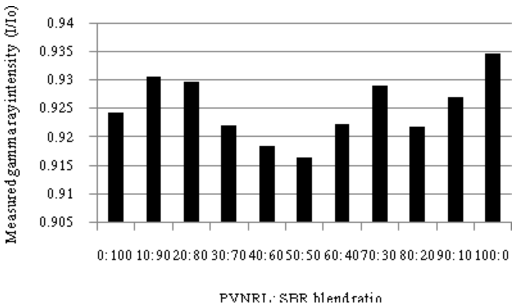

Figure 3. Attenuation of gamma ray from I-131 source by shielding material made of PVNRL and SBR blend with various blend ratios

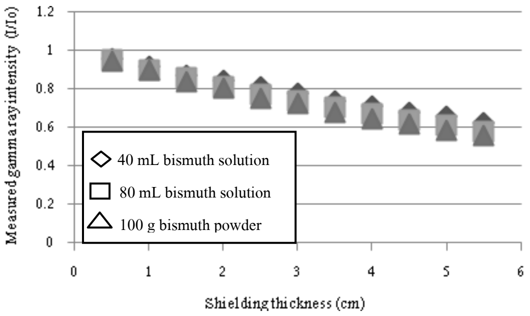

Figure 4. Attenuation of gamma ray from Cs-137 source by shielding material made of PVNRL and SBR (50:50 blend ratio) and different forms of bismuth

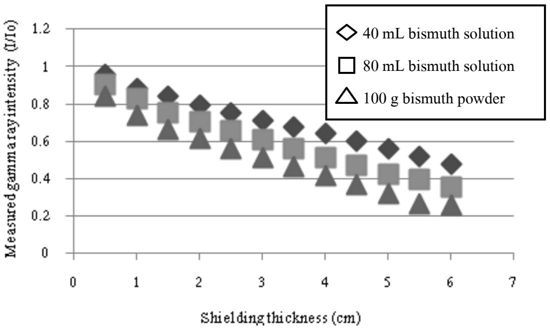

Figure 5. Attenuation of gamma ray from I-131 source by shielding material made of PVNRL and SBR (50:50 blend ratio) and different forms of bismuth

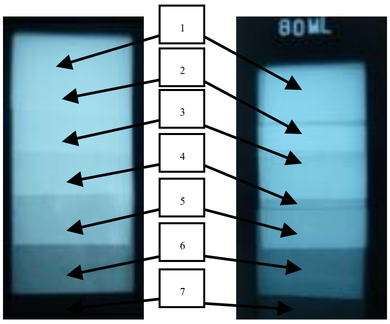

Figure 6. Gamma radiography of (left) PVNRL and SBR blend (50:50 blend ratio) at 100 mL mixed with 100 g of bismuth powder, and (right) PVNRL and SBR blend (50:50 blend ratio) at 400 mL mixed with 80 mL of bismuth solution

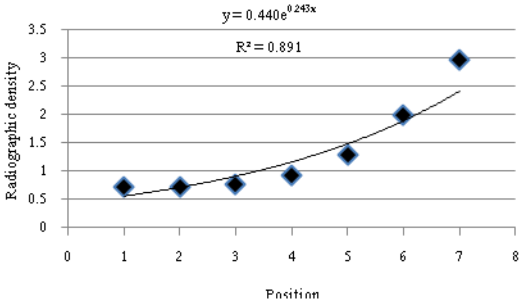

Figure 6. Measured radiographic density according to numbered positions in Figure 6 (left).

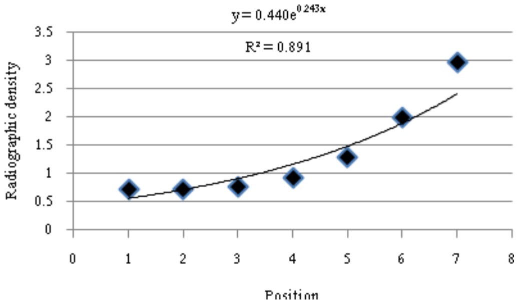

Figure 7. Measured radiographic density according to numbered positions in Figure 6 (right)

Conclusions

This research work developed a flexible low-energy gamma ray shielding material by blending PVNRL and SBR with 50:50 volume ratio for 400 mL with 80 mL of bismuth solution in a magnetic stirrer for 25 minutes. The mixture was poured into a pasture mould to achieve a uniform thickness of 0.5 cm. Results indicated that the attenuation of low-energy gamma ray was a function of shielding thickness. The transmitted gamma radiation from Cs-137 and I-131 sources decreased exponentially with increasing shielding thickness, yielding the following relationships $y = 0.986e^{-0.048x}$ ($R^2 = 0.999$) and $y = 0.990e^{-0.169x}$ ($R^2 = 0.998$), respectively, where x is shielding thickness (cm) and y is the gamma ray attenuation. The most suitable shielding thickness against low-energy gamma radiation was determined to be 3 cm, obtained by stacking 6 pieces of 0.5-cm-thick shielding materials on top of one another. The obtained shielding material with 100 g of bismuth powder in 100 mL of rubber blend can attenuate 27.7% of gamma ray from Cs-137, while it can attenuate 48.9% of gamma ray from I-131. The presence of 80 ml of bismuth solution in 400 mL of rubber blend exhibited 26.6% attenuation of gamma ray from Cs-137 source, and 39.4% attenuation of gamma ray from I-131 source. Thus, it can be concluded that the fabricated flexible and light-weight radiation shielding material exhibited good shielding capability against low-energy gamma ray. Moreover, from radiographic density measurement results, the fabricated shielding material offered uniform gamma ray shielding throughout the material.

References

1. Jackson Heighte ,Jan M.Krol, “Flexible radiation Shielding Material” Natural rubber with gamma radiation shielding materials (tin, bismuth, Antimony,barium, cadmium, silver and lead) in the powder form with various mixing ratios were studied to determine gamma radiation shielding efficiencies., (November, 1986), 455-662.
2. Phongthorn Saeoui. Rubber: the properties and applications. 2nd edition. County: Pearson Education Limited (Thailand), 2548.
3. Nualchavee Roongtanakiat Ph.D., Nuclear science. Bangkok: Kasetsart University Press, 2545.
4. Salag Dhabanand. Chemical plants. Chulalongkorn University Press, .2527.
5. Office of Atoms for Peace. The radiation protection level 1. Ministry of Science. And Technology, 2546.
6. Office of Atoms for Peace. The radiation protection level 2. Ministry of Science. And Technology, 2546.
7. Research rubber tires. Department of Agriculture and the Department of Science Service, 2540.
8. Wikipedia, the Free Encyclopedia. Rubber SBR. Rubber nature bismuth vitriol [Online]: http://th.wikipedia.org. (The day with the information: March 2554).

Focusing for MeV Proton Beam using Tapered Capillary for Micro-PIXE Analysis

S. Jaiyen

Division of Physics, Faculty of Science and Technology, Rajamangala University of Technology Thanyaburi, Klong 6, Thanyaburi, Pathumthani 12110, Thailand
Corresponding author. E-mail: sarawutjaiyen@gmail.com

Abstract

A compact micro-PIXE system using a tapered glass capillary for beam focusing was developed in a beam line of the 1.6-MV tandem accelerator facility at Tokyo Institute of Technology, Japan. A tapered glass capillary of 70 μm in outlet diameter was fabricated from borosilicate glass tube. The elemental compositions of the glaze, paint and substrate layers of the Sangkhalok pottery were investigated by micro-PIXE analysis. The sample was prepared from a piece of the broken pottery and its cross section was carefully polished and cleaned. The layers on the cross section of the pottery were separately irradiated by 2-MeV proton micro-beam focused by the tapered glass capillary. The measured spectra show that the glaze layer contains a large amount of Ca and the brown paint layer contains Ca and Fe.

Keywords: Glass capillary, beam focusing, micro-PIXE, archaeological sample

Introduction

Recently tapered glass capillaries have been attracting much attention as a tool to guide and focus energetic ions with MeV energies. This beam focusing optics uses the elastic scattering of incident ions by atomic nuclei, which is one of the major interaction processes between energetic ions and solid surfaces. Because the micro-beam irradiation devices based on this technique is compact and inexpensive compared to the conventional devices, this technique has been used for various application. Nebiki *et al*. [1] demonstrated for the first time the focusing of 2 MeV helium ions with tapered glass capillaries having outlet diameter of less than 1 μm. They successfully observed a beam focusing effect of the tapered glass capillaries and applied this new technique to in-air-PIXE analysis [2]. This technique has been used for various applications such as nuclear reaction analysis [3], high-contrast X-ray imaging [4], cell surgery [5], in-air RBS [6], in-air STIM [7] and micro-PIXE analysis [2,8].

The particle-induced X-ray emission (PIXE) is a well know technique for material analysis using a few MeV ion beam [9]. Its sensitivity is quite high and multiple elements in a sample can be analyzed simultaneously. Furthermore, only several tens microgram is enough to analyze elements in a sample. The interest in PIXE technique has been recently growing because it can be applied to studies in a wide range of fields such as biology [10], art and archeology [11].

This research aims to reveal the elemental composition of glaze layer, paint layer and substrate of typical Sangkhalok potteries by micro-PIXE analysis based on a glass-capillary-focused proton microprobe.

Materials and Methods

Fabrication of tapered glass capillary

The tapered glass capillary was fabricated from a straight glass tube. As a glass material for the tapered capillary, borosilicate glass was chosen most frequently because of its low softening temperature (~700 °C). To extend a straight glass tube and form a gradually tapered capillary, a commercially available puller was used. By controlling the amount of heat and the pulling force, the tapered glass capillaries having various tapered angles were fabricated. After the pulling process, the tapered capillary typically had an outlet diameter less than 1 μm. To obtain a desired outlet diameter, a micro-forge device was used to cut

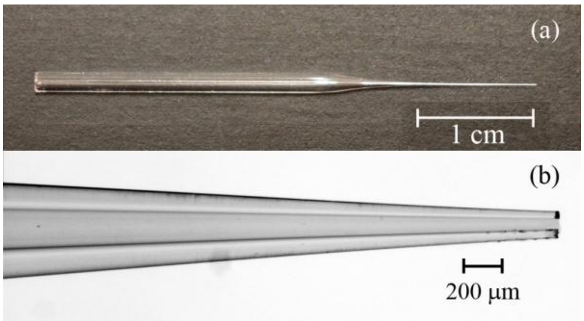

Figure 1. (a) A complete view of tapered glass capillary and (b) photograph of capillary outlet.

the tip of the capillary. Fig. 1(a) shows the complete view of the tapered glass capillary and (b) photograph of capillary outlet.

Archaeological sample

To examine the feasibility of the tapered glass capillary as a compact beam-focusing device for actual micro-PIXE analysis, an archaeological sample was used in this research. This archaeological sample is a piece of “Sangkhalok” pottery, which has been unearthed in Sukhothai province of Thailand. The surface of the sample has paint patterns with brown color on white foundation and transparent glaze coating. The cross section of the sample was carefully polished by fine sandpaper and cleaned by pure water in an ultrasonic bath. To observe the cross section near the pottery surface in more detail, magnified images of the cross section were taken by a CCD camera combined with an optical microscope. From the magnified image shown in Fig. 2, the Sangkhalok pottery has three different layers: an outermost glaze layer, a white foundation layer, and a substrate. Moreover, the outermost layer consists of two parts with different color; one is a brown paint layer corresponding to the surface brown painting and the other is a glaze layer where one can see the white foundation color from the surface. The thicknesses of the glaze and foundation layers were around 250 μm and 200 μm, respectively.

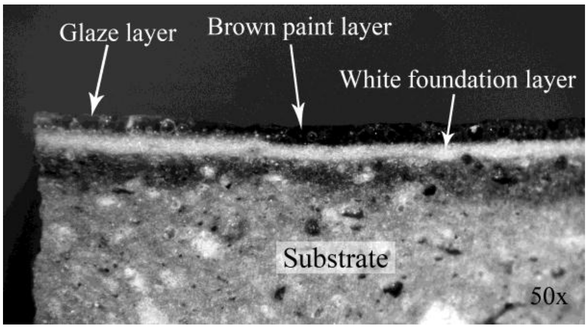

Figure 2. An image on cross section of the Sangkhalok pottery taken by optical microscope.

Experimental setup

Figure 3 shows the experimental setup for micro-PIXE analysis using the ϕ70-μm tapered glass capillary. This experiment was performed in a large vacuum chamber with a pressure less than 10^{-4} Pa. This chamber was installed in a beam line of the 1.6-MV tandem accelerator facility at Tokyo Institute of Technology, Japan. The tapered capillary was mounted on the stainless steel holder and its tilt angles were controlled by two actuators. The capillary head was placed on a two-axis stage, which could align the capillary inlet position with respect to the beam axis. The holder for the archaeological sample was made of aluminum and connected to the two-axis motorized stage. To measure the beam current from the capillary outlet, the Faraday cup was also installed on the sample holder. The carbon sheet was put on the front surface of the sample holder to reduce background X-rays emitted from the sample holder. A small piece of the archaeological sample was fixed on the sample holder using carbon adhesive tape. The distance between the capillary tip and the sample was around 1 mm. A Si-PIN X-ray detector was installed at -135º to measure X-ray emitted from the target. To normalize the X-ray yield, a Si charge particle detector was installed at +135º to measure backscattered proton.

A 2-MeV proton beam was injected into the capillary inlet and a micro beam was extracted from the capillary outlet. The elemental composition in the sample was determined by irradiation the sample by a micro-beam and the energy spectrum of the sample was measured.

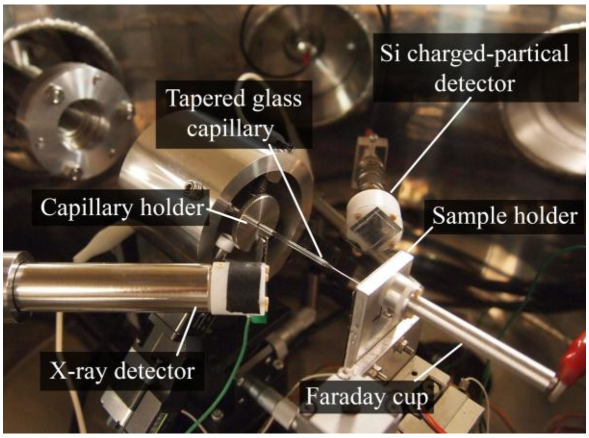

Figure 3. The experimental setup for micro-PIXE analysis using tapered glass capillary.

Results and Discussion

Typical PIXE spectra obtained from the cross section of the Sangkhalok sample are shown in Fig. 4. A 2-MeV proton beam was used and the outlet diameter of the tapered glass capillary was 70 μm. The beam current at the capillary outlet was around 0.3 nA. The X-ray counts were normalized by the scattered proton counts measured by a Si charge-particle detector. The cross section was irradiated at three different positions of the beam spot, on the glaze layer, the brown paint layer, and the substrate, as shown in Fig. 2. The measured spectra show that all of layers contain Si, K, Ca, Ti, Mn, and Fe. However, the ratios of X-ray intensities for these elements are different. The intensity of Ca-K_α for the glaze layer was roughly two times larger than that for the brown paint layer. On the other hand, the intensity of Fe-K_α for the brown paint layer is much higher than that for the glaze layer, whereas that for the substrate is a bit higher than that for the glaze layer. These results indicate that the glaze layer contains a large amount of Ca compounds and the brown layer also contains less amount of it. Thus, the brown layer can be regarded to be a mixture of brown paint and glaze. Moreover, we see that the brown paint layer contains a lot of Fe, which is consistent with the fact that the brown color is made of rust.

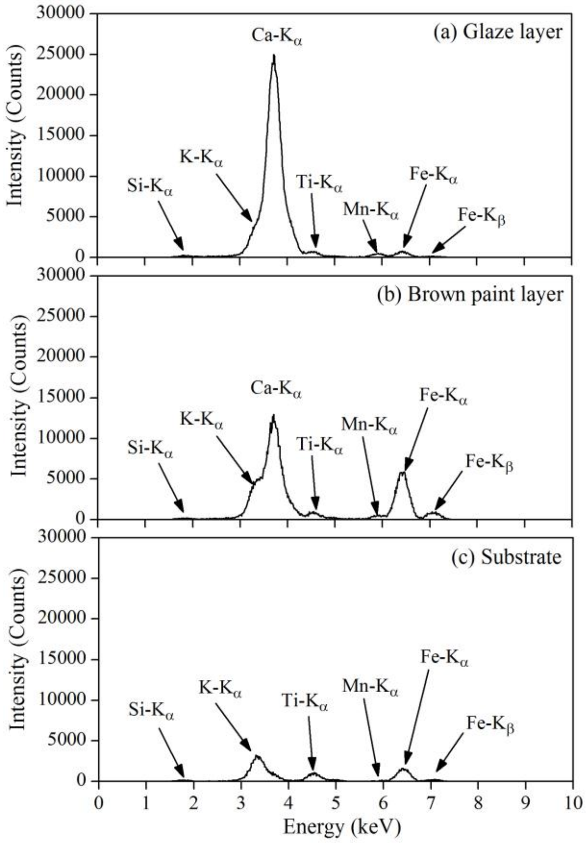

Figure 4. PIXE spectra from the cross section of the Sangkhalok pottery at (a) glaze layer, (b) brown paint layer and (c) substrate.

Conclusions

A compact micro-PIXE system using a tapered glass capillary for beam focusing has been developed. This technique was applied to determine the elemental composition of the archaeological sample. The PIXE spectra of the Sangkhalok were successfully obtained at three different positions (glaze, brown paint and substrate) on the cross section of the pottery by using ϕ70-μm capillary-focused proton beams. The elemental composition of each layer was separately investigated. The glaze layer contains a large amount of Ca. The brown paint layer contains Ca and Fe, which indicates a mixture of brown paint and glaze.

Acknowledgments

The author is deeply grateful to Prof. Yoshiyuki Oguri, Assoc. Prof. Jun Hasegawa and Assoc. Prof. Nares Chankow for their understanding and expert suggestions. I wish to thank Mr. Hitoshi Fukuda for providing assistance in the preparation of the experimental apparatus.

References

1. T. Nebiki, T. Yamamoto, T. Narusawa, M. B. H. Breese, E. J. Teo and F. Watt, “Focusing of MeV ion beam by means of tapered glass capillary optics”, Journal of Vacuum Science and Technology A **21** (2003), 1671.
2. T. Nebiki, M. H. Kabir and T. Narusawa, “In-air PIXE analysis by means of glass capillary optics”, Nuclear Instruments and Methods in Physics Research B **249** (2006), 226.
3. D. Sekiba, H. Yonemura, T. Nebiki, M. Wilde, S. Ogura, H. Yamashita, M. Matsumoto, J. Kasagi, Y. Iwamura, T. Itoh, H. Matsuzaki, T. Narusawa, K. Fukutani, “Development of micro-beam NRA for 3D-mapping of hydrogen distribution in solid: Application of tapered glass capillary to 6 MeV ^{15}N ion”, Nuclear Instruments and Methods in Physics Research B **266** (2008), 4027.
4. J. Hasegawa, S. Shiba, H. Fukuda and Y. Oguri, “A compact micro-beam system using a tapered glass capillary for proton-induced X-ray radiography”, Nuclear Instruments and Methods in Physics Research B **266** (2008), 2125.
5. Y. Iwai, T. Ikeda, T. M. Kojima, Y. Yamazaki, K. Maeshima, N. Imamoto, T. Kobayashi, T. Nebiki, T. Narusawa and G. P. Pokhil, “Ion irradiation in liquid of μm^3 region for cell surgery”, Applied Physics Letters **92** (2008), 023509.
6. K. Ishii, N. Fujita and H. Ogawa, “Development of an in-air RBS technique using a metal capillary”, Nuclear Instruments and Methods in Physics Research B **269** (2011), 1026.
7. M. J. Simon, M. Döbeli, A. M. Müller and H.-A. Synal, “In-air STIM with a capillary microprobe”, Nuclear Instruments and Methods in Physics Research B **273** (2012), 237.
8. J. Hasegawa, S. Jaiyen, C. Polee and Y. Oguri, “Development of a micro-PIXE system using tapered glass capillary optics”, Nuclear Instruments and Methods in Physics Research B **269** (2011), 3087.
9. S. A. E. Johansson, J. L. Campbell and K. G. Malmqvist, “Partical-Induced X-ray Emission Spectrometry (PIXE)”, New York, John Wiley & Sons, 1995.
10. K. Ishii, A. Sugimoto, A. Tanaka, T. Satoh, S. Matsuyama, H. Yamazaki, C. Akama, T. Amartivan, H. Endoh, Y. Oishi, H. Yuki, S. Sugihara, M. Satoh, T. Kamiya, T. Sakai, K. Arakawa, M. Saidoh and S. Oikawa, “Elemental analysis of cellular samples by in-air micro-PIXE”, Nuclear Instruments and Methods in Physics Research B 180 (2001), 448.

11. H. B. Abdelouahed, F. Gharbi, M. Roumié, S. Baccouche, K. B. Romdhane, B. Nsouli and A. Trabelsi, "PIXE analysis of medieval silver coins", Materials Characterization **61** (2010), 59.

Introduction of Probabilistic Method to Nuclear Accident Consequence Assessment using Cost per Severe Accident

K. Silva[*], S. Wonglee, R. Picha, S. Khaweerat, and W. Ratanathongchai

Thailand Institute of Nuclear Technology, 9/9 Moo 7, Saimul, Ongkharak, Nakorn Nayok, Thailand
[*]*Corresponding author. E-mail: kampanart.silva@gmail.com*

Abstract

The 2011 Fukushima accident emphasizes the need to integrate the assessments of health effects, economic, social and environmental impacts of severe accidents in nuclear power plants, in order to perform a comprehensive nuclear accident consequence assessment. Cost per severe accident is selected as an index for this purpose. In preceding studies, the calculations of the cost per severe accident were deterministically performed, which makes it difficult to take into account the uncertainties associated with input parameters and conditions. A probabilistic calculation scheme is introduced in order to systematically consider the uncertainties regarding differences in meteorological conditions and also to broaden the applications of the index. The accident sequences used in the analysis are taken from the results of level 2 seismic probabilistic risk assessment (PRA) of a virtual 1,100 MWe boiling water reactor. The doses to the public and the numbers of people affected by the accident are calculated for 248 representative meteorological sequences using the level 3 PRA code OSCAAR of Japan Atomic Energy Agency (JAEA). They are used as inputs for the estimation of the cost per severe accident. The mean and various percentile values of the cost per severe accident are estimated. Average cost per severe accident and its breakdown are consistent with the deterministic results of preceding studies. Decontamination cost, relocation cost and radiation effect cost are the costs which dominate the cost per severe accident. Use of the cost per severe accident to optimize the radiation protection countermeasures is introduced as its applications. Differences of the results when the mean value and various percentile values are used were discussed.

Keywords: Probabilistic method, cost per severe accident, consequence assessment, nuclear accident, Fukushima accident.

Introduction

On March 11, 2011, the Great East Japan Earthquake (M 9.0) occurred, followed by three huge tsunamis to attack Fukushima Daiichi Nuclear Power Station. They drove the reactors into station blackout (SBO). The reactor cores of the units 1–3 were strongly suspected to have melted. Hundred thousands of people have sheltered and evacuated, and many of them will not be able to return home for several years. This accident revealed an importance of a comprehensive nuclear accident consequence assessment which could help us realize the actual consequences of severe nuclear accidents, and mitigate their impacts.

The authors introduced the cost per severe accident as an index for severe accident consequence assessment of nuclear power plants because it can cover a large scope of consequences including health effects, economic, social and environmental impacts, and it is easy to understand [1-3]. The 'expected values' of sheltered, evacuated, relocated populations and periods, and the collective dose of selected accident sequences were calculated using the level 3 probabilistic risk assessment (PRA) code OSCAAR of Japan Atomic Energy Agency (JAEA) [4,5] were used as inputs, and the cost per severe accident was deterministically calculated. This made the calculation straightforward. On the other hand the evaluator may not be able to capture the whole picture of the evaluation especially when the evaluator of cost per severe accident is not the one who performed the level 3 PRA. Moreover, this made it difficult to take into account the uncertainties associated with input parameters and conditions, e.g. the uncertainties regarding differences in meteorological conditions, the uncertainties of the dose and cost conversion factors.

Problems stated above can be solved by introducing the probabilistic method to the cost per severe accident evaluation. Therefore, the primary objective of this research is to introduce the probabilistic calculation scheme to the nuclear accident consequence assessment in order to systematically consider the uncertainties regarding differences in meteorological conditions. The secondary objective is to demonstrate the use of the probabilistically calculated cost per severe accident to optimize the radiation protection countermeasures, as an example to confirm the applications of the cost per severe accident broadened by the introduction of probabilistic method.

Methodology

Calculation conditions and inputs

Same as in the previous works, a severe accident is assumed to occur in a virtual 1,100 MWe BWR plant which is located at the center of Tokai R&D Center of JAEA, Japan. Dominant sequences of severe accidents are picked up, and containment failure frequencies (CFFs), release times, release durations and release ratios of each radionuclide of each accident sequence are taken from the results of open documents of level 2 PRA [6]. The radiation protection scenario follows the recommendations by International Atomic Energy Agency (IAEA) and International Commission on Radiological Protection (ICRP) [7,8].

Level 3 PRA

The conditions and inputs mentioned above are used to perform level 3 PRA calculations using the OSCAAR code. The code first calculates the dispersion and deposition of the released radionuclides under 248 representative meteorological sequences. Then the acute and chronic exposure doses are estimated considering the reduction regarding the radiation protection counter-measures. At the same time, the sheltered, evacuated and relocated populations and periods, and the weight of the food of which intake being restricted are evaluated. Finally, the collective dose is calculated.

Calculation of cost per severe accident

Outputs of OSCAAR are used as the input data to calculate the cost per severe accident. The cost per severe accident consists of various costs and other consequences converted into monetary values. The former includes costs of sheltering, evacuation, relocation, food intake restriction, decontamination (including waste management), decommissioning, and alternative power source. The latter considers radiation effects, psychological effects and damage by harmful rumors. Appropriate cost conversion factors and equations being used for the calculation are selected from preceding works, documents of electric utilities and regulatory bodies, and documents about the Fukushima accident and the Chernobyl accident. Detailed information about conversion factors and equations can be referred to in the previous works [1-3].

Introduction of probabilistic method

Instead of using expected values like in previous works, the sheltered, evacuated and relocated populations and periods, the weight of the food of which intake is restricted, and the collective dose calculated for 248 representative meteorological sequences along with the probability density functions (PDFs) of each meteorological sequences are organized in Excel worksheets for each accident sequence. Those values are randomly picked up according to the PDFs of the meteorological sequences in order to perform a probabilistic calculation of the cost per severe accident for a considerable number of times. We performed Monte Carlo calculations to figure out the appropriate number of times, and the results are shown in Table 1. ‘50,000’ is selected as the suitable number of times because when the number of times is set to 50,000, the mean of each calculation falls within ±1% of the mean of means with confidence level of 95%. The results of the cost per severe accident and its components are shown in terms of mean values, 5th, 50th, 90th, 95th and 99th percentile values, though the Excel workbook used for the cost per severe accident evaluation can calculate any percentile values defined by the evaluator. After performing the calculations for each accident sequences, the average of the mean values and each percentile values of the cost per severe accident and its components are obtained by weighting the values of each severe accident sequences by its normalized CFF which represents the likelihoods of the accident sequences.

Table 1: Numbers of calculations that the mean of the cost per severe accident falls within ±1% of the mean of means for several number of times per calculation.

Number of times per calculation	**Number of calculations that the mean falls within ±1% of the mean of means (Out of 1,000 times)**
1,000	221
5,000	462
10,000	626
30,000	860
50,000	952

Results and Discussion

Cost per severe accident

The breakdown of the cost per severe accident for the reference case (deterministic calculation [3]), the mean values, and the 5th, 50th, 90th, 95th and 99th percentile values is shown in Figure 1. It is obvious from the figure that the means of the probabilistically calculated cost per severe accident and its components is consistent with the reference case. Decontamination cost, relocation cost and radiation cost are dominant for all cases except for the 5th percentile values. As shown in Figure 2, the cost per severe accident becomes so small for the 5th percentile values case that the constant costs: decommissioning cost, rumors, dominate the whole cost per severe accident. Another trend to be observed is that the relocation costs exceed the decontamination costs in higher percentile values cases which are opposite to the reference case. This may be because all of the cases with higher percentile values are those with extreme meteorological conditions which normally result in a relatively large relocation area. When cities which are densely populated are included into the relocation area, the cost to compensate the relocation of a large number of people would be much higher than the cost to decontaminate the area.

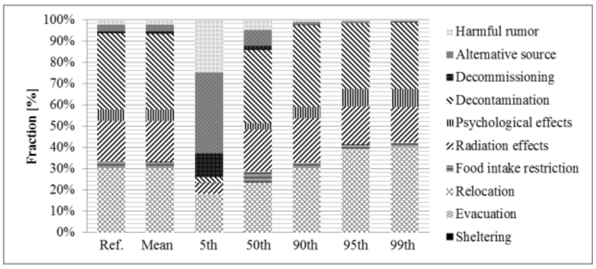

Figure 1. Breakdown of cost per severe accident for each case.

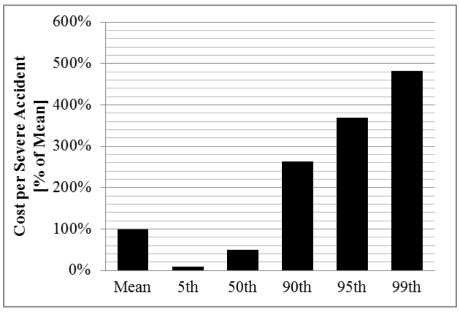

Figure 2. Comparison of the mean and each percentile values of the cost per severe accident.

Optimization of radiation protection counter-measures using cost per severe accident

Countermeasures that can minimize the individual exposure dose have been conventionally selected as the optimum ones. Economic, social and environmental impacts resulted from severe accidents have not been considered. Optimization of radiation protection strategies using the cost per severe accident is introduced in this section as a new option. The dose levels for recommending sheltering, evacuation and relocation, and the dose level for returning home that minimize the average cost per severe accident are investigated. The optimizations of the dose levels for recommending relocation and returning home are alternative source cost and cost regarding harmful presented in this paper as representative results.

Figure 3 shows the relative changes of the mean and each percentile values of the cost per severe accidents from the reference cases when the dose levels for recommending relocation and the dose level for returning home are increased or decreased (Both dose levels are set to 20 mSv/year for reference cases). Here, the reference cases are the cost per severe accidents shown in Figure 2. It can be concluded that the higher dose levels give the smaller cost per severe accidents in all cases, which is not different from the deterministic calculation results. However, the probabilistic method provides a broader view to the evaluator. When the dose for recommending relocation is increased, the decreases of the cost per severe accident in cases with higher percentile values are sharper. On the other hand, the degree of the increase of the cost per severe accident is higher for the smaller percentile values for a slight decrease, while it is lower for a sharp decrease of the dose for returning home.

However, when the dose limit for returning home is reduced to 1 mSv/year, the trend observed in 50th and 95th percentile values are not consistent with other values. This can be described by Figure 4 which shows the distribution of cost per severe accidents when 50,000 calculations are performed for the station blackout accident sequence (TB). Though the graph seems to be close to the log normal distribution, the tail of the graph is very long and high irregularity can be observed especially after the average line. Unlike the percentile values of the log normal distribution, the percentile values selected in this study may not be the representative ones. Further study may be needed on the selection of the percentile values and the way to handle the meteorological data which leads to the results that do not follow any common distributions.

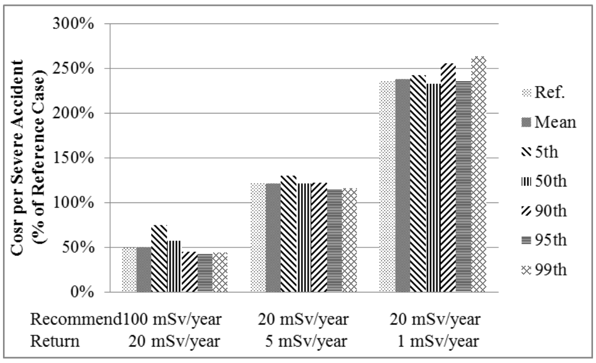

Figure 3. Cost per severe accident when the dose levels for recommending relocation or the dose levels for returning home are increased or decreased.

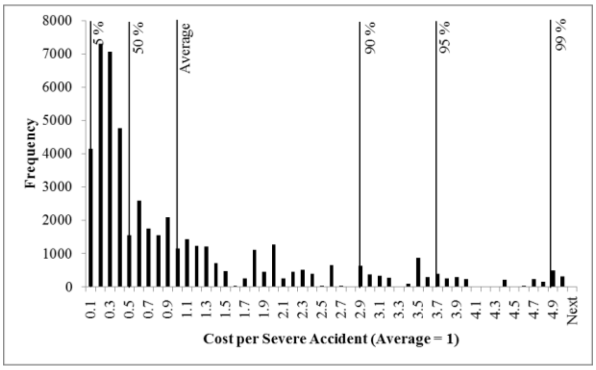

Figure 4. Distribution of cost per severe accidents when 50,000 calculations are performed for the station blackout accident sequence.

In spite of the issues stated above, the introduction of the probabilistic method to the calculation of the cost per severe accident may give a broader view to the evaluator when they use the cost per severe accident to optimize the radiation protection countermeasures as they have all results in their hands: the mean and several percentile values of the cost per severe accident. For example, they may use the 90th, 95th or 99th percentile values when they would like to obtain conservative results, or they may construct a radiation protection plan to employ different countermeasures for different percentile values which represent different meteorological conditions.

Conclusions

Probabilistic calculation scheme is introduced to the calculation of cost per severe accident in order to systematically consider the uncertainties regarding differences in meteorological conditions in the nuclear accident consequence assessment. Average cost per severe accident and its breakdown are consistent with the deterministic results of preceding studies. Also the broadened applications of the probabilistically calculated cost per severe accident were confirmed when using it to optimize the radiation protection countermeasures.

References

1. K. Silva, Y. Ishiwatari, S. Takahara, “Integration of direct/indirect influences of severe accidents for improvements of nuclear safety”, Proceedings of the 2012 20th International Conference on Nuclear Engineering, California, 2012.
2. K. Silva, Y. Ishiwatari, S. Takahara, “Introduction of external cost regarding severe accident as an index of nuclear power plant risk and its relationship with sourceterm”, Proceedings of the 7th Annual Conference of the Thai Physics Society, Ayutthaya, 2012.
3. K. Silva, Y. Ishiwatari, S. Takahara, “Modification of severe accident consequence analysis calculation method of nuclear power plant and considering of effect of discount rate”, Proceedings of the 2012 International Symposium on Technology for Sustainability, Bangkok, 2012.
4. T. Homma, J. Ishikawa, K. Tomita, K. Muramatsu, “Radiological consequence assessments of degraded core accident scenarios derived from a generic level 2 PSA of a BWR”, JAERI-Research-2000-060, JAERI, 2000.
5. T. Homma, K. Tomita, S. Hato, “Uncertainty and sensitivity studies with the probabilistic accident consequence assessment code OSCAAR”, Nuclear Engineering and Technology 37 (2005) 245.
6. J. Ishikawa, K. Muramatsu, T. Sakamoto, “Systematic source term analysis for level 3 PSA of a BWR with Mark-II type containment with THALES-2 code”, JAERI-Research 2005-021, JAERI, 2005.
7. IAEA, “Intervention criteria in a nuclear or radiarion emergency”, Safety Series No.109, Vienna, 2006.
8. ICRP, “The 2007 recommendations of the International Commission on Radiological Protection”, Publication 103, Elsivier, 2007.

Investigation of High Background Radiation by Gamma Spectrometry of Surface Soil in the Chaiya District, Suratthani Province

S. Angkunrat Auisui[1] and Tripob Bhongsuwan[2]*

[1]*Department of Physics, Faculty of Science, Prince of Songkla University, Hat Yai, Songkhla, 90112, Thailand.*
[2]*Department of Physics and Geophysics Research Center, Faculty of Science, Prince of Songkla University, Hat Yai, Songkhla, 90112, Thailand*
**Corresponding author. E-mail: tripop.b@psu.ac.th*

Abstract

The aim of this work is to determine the activity concentration of Ra-226, Th-232 and K-40 in surface soil (0-5 cm depth) collected from Lamet sub-district in Chaiya district, Surat - Thani Province, Southern Thailand. The soil samples were measured using a low background gamma-ray spectrometer with a high purity germanium detector in a low-background lead shield. The activity concentrations of radionuclide Ra-226, Th-232 and K-40 are 15.63±0.69 – 5,493.08±0.11, 11.58±1.14 – 143.17±0.44 and 8.86±1.37 – 932.65±0.71 Bq/kg, with a mean value of 568.86±0.82, 56.52±1.35 and 369.41±5.24 Bq/kg, respectively. The absorbed gamma dose rate due to the naturally occurring radionuclides varies from 14.78±1.08 to 2,618.56±2.74 nGy/hr. The annual external effective dose rate for the region varies from 0.018±0.001 to 3.211±0.003 mSv, with a median value of 0.156±0.001 mSv, comparing with the world average of 0.07 mSv (UNSCEAR, 2000). The estimation of the annual external effective dose rate in the third quartile (Q_3) ranged from 0.31 – 3.21 mSv, which is higher than 75% (Q_3) of all data. The investigated area can be said to have a high background radiation level.

Keywords: soil, high background radiation area, effective dose, Gamma ray spectrometer

Introduction

Naturally occurring radioactive materials (NORM) of terrestrial origin are present in the earth's crust since its origin. There are two sources of natural radiation: cosmic ray from spaces and primordial radionuclides. These primordial radionuclides are typically long lives, with half-life often about hundreds of millions of years. In places on the earth, the natural radioactivity varies only with narrow limits, but in some places there are wide deviations from normal levels because of the abundance of minerals with high radioactivity (UNSCEAR, 2000; Mohanty et al., 2004). The major sources responsible for exposure are naturally occurring radionuclides in the earth's crust (U-238, Th-232 and K-40), which are associated with minerals such as monazites and zircons. Cosmic radiation can also contribute significantly in areas at high altitudes. The distribution of naturally occurring radionuclides, depend on the distribution of rocks from which they originate and processes that concentrate them. Their concentrations in rocks, soil and sand depend on the local geology of each region in the world. Dose by ingestion are mainly due to K-40 and to the U-238 and Th-232 series radionuclides in food and drinking water. The inhalation intake from radon and thoron of U-238 and Th-232 daughters contribute to internal dose. The annual effective dose from natural and artificial source varies locally is due to external exposure from radionuclides in rocks, soils and the buildings (UNSCEAR, 2000).

Wallop (1996) studied airborne radiometric and airborne magnetic data in Surat-Thani Province, which found the anomalies obviously indicate two Hot springs fields. Hot spring systems in Surat-Thani Province are associated with limestone and clastic sedimentary rocks of sandstone and shale. Heat source of hot spring system may be the high heat flow from high heat generating capacity of granite or radiogenetic heat from granitic rock. Hot spring areas are fracture or fault control; they are NW-SE, NE-SW, N-S and E-W trending (Chaturrongkawanich, 2001). Saina et al. (2009) studied activity of Ra-226 in dispersion of hot spring, shallow well water, well water and vegetables in Surat-Thani Province. The result shows that the average activity in hot spring samples value of 1,855±185, 57±36, 49±17 and 4,345±624 mBq/l, respectively. The activity of Ban Khao Nam Ron in Chaiya District is higher than the other areas.

Surat -Thani Province is a significant province in the east of southern Thailand. There has been regarded as the most geothermal areas among the southern province. The general geology of Surat-Thani Province is predominantly composed of sedimentary rock and granitic rock with minor metamorphic rock. The geographical of the study area can be classified to many rocks formations: sandstone, pebbly sandstone, shale, mudstone, pebbly mudstone, chert and limestone of Silurian – Devonian – Carboniferous Periods; limestone, sandstone and shale of Permian Periods; red sandstone siltstone and limestone conglomerate of Triassic – Jurassic Periods; and the youngest Quaternary deposit. The shallow reservoir confines to the unconsolidated Quaternary sediments or gravel beds while the deeper reservoir may be clastic sedimentary rocks of sandstone or limestone. The major faults and fractures mainly in NE – SW, NW – SE, almost N-S and almost E-W directions, are the main conduits for hot water ascending to the surface (Figure.1). Perhaps, the active Khlong Marui fault zone is an indirect heat source of these geothermal areas while the main heat source should be from a subsurface granitic pluton which may be retains heat to raise the thermal gradient or heat flow. Heat is released from the decay of anomalously high contents of radioactive element, i.e., Uranium in granite.

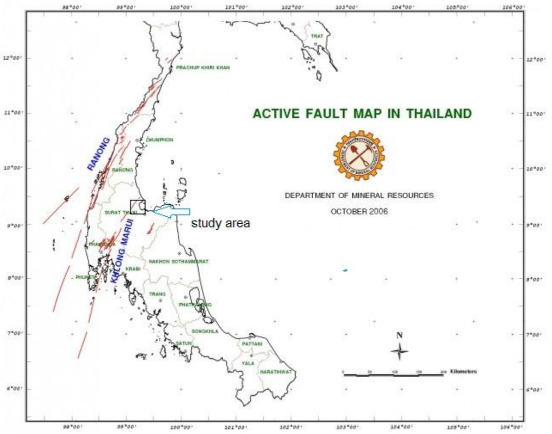

Figure 1. Location of the fault in the vicinity of the study area. (Department of Mineral Resource, 2006)

The objective of this work is to determine the activity concentrations of Ra-226, Th-232 and K-40 in surface soil, sand and rocks samples collected from Lamet sub-district in Chaiya district, Surat - Thani Province, Southern Thailand, which to assessing their contribution to the external effective dose relative to the UNSCEAR data.

Materials and Methods

Physiographic setting

The study area, Lamet Sub-District is a part of the south of Chaiya District (517000-528500 E 1032000-1037700 N), Surat-Thani, Thailand. Landscape of the Lamet Sub-District has 3 parts: the plateau west of the area, the lowlands and the coastal plain of the east. The general geology of Surat-Thani Province is predominantly composed of sedimentary rock and granitic rock with minor metamorphic rock.

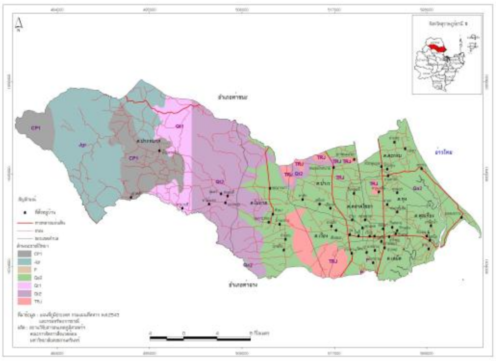

Figure 2. The geology of Chaiya District (517000-528500 E 1032000-1037700 N) is a part of the Surat Thani Province, Thailand.

Sample collection and preparation

Eighteen surface soil samples were collected from Lamet and Tha-Chang sub-district in the northtern region of Surat-Thani (Figure.2). Our sampling points are located around the hot spring, near the coastal plain. The humus layer of soil which contains decayed organic matter was removed using a flat-blade shovel. Soil samples were taken to a depth of about 5 cm. The garbage extraneous material such as plant roots were removed from the soil. The sample of about 1,000 g was then packed in a plastic bag. Two rocks and five sand samples were collected near the soil sampling point. All rock samples were chiseled out of fixed rocks. Approximately 1,000 g material of each rock was collected and packed in a plastic bag.

In the laboratory, all samples were dried in a drying oven at 105 °C for 8 hours. Each soil and rock sample was ground into fine powder. Finally all samples were sieved using a 2 mm mesh screen to obtain a sample for measurement (International Atomic Energy Agency, 1989). Each sieved sample was sealed in a 100 ml cylindrical plastic container. The sealed samples were stored for about 30 day before carrying out gamma analysis to allow Ra-226, Th-232, K-40 and its short-lived progenies to reach equilibrium.

Radioactivity measurements

The activity concentration of soil samples were measured using a Canberra coaxial high purity germanium detector (HPGe, Canberra, USA) with an active volume of 59.9 cm^3. A low background lead shied (Canberra model 747, USA) was used to reduce background gamma-ray in detector chamber. The energy resolution of the 1,332.5 keV line from 60Co was found to be 1.75 keV at full-width of half maximum (FWFM). The data acquisition and analysis were carried out with the use of the Genie 2000 software package (Canberra, USA).

The specific activities of Ra-226, Th-232 and K-40 were averaged from gamma-ray photo peaks at several energies. Gamma-rays from Pb-214 (at 295.2 and 351.9 keV) and Bi-214 (at 609.3, 1120.3 and 1764.3 keV) were used to determine the activity of Ra-226 (also known as the U-238 equivalent). Gamma-rays emitted from Ac-228 (at 338.3, 911.6 and 969.1 keV) were used to determine the average activity of Th-232, whereas potassium (K-40) 1460.0 keV was measured directly by the K-40 isotope.

The IAEA standard reference material (a standard soil of known activity, IAEA CU-2010-03 WWOPT) was used for calibrating the gamma-ray spectrometric system. All the samples were counted for a period of 10800 s.

Dose rate

The absorbed gamma dose rates in air at 1m above the ground surface for the uniform distribution of radionuclides (Th-232, Ra-226 and K-40) were computed on the basis of guidelines provided by UNSCEAR (1993, 2000). The conversion factors used to compute absorbed gamma dose rate (D) in air per unit activity concentration in (1 Bq kg^{-1}) sand corresponds to 0.604 nGyh^{-1} for Th-232, 0.462 nGyh^{-1} for Ra-226, and 0.0417 nGyh^{-1} for K-40.

$$D = (0.462A_{Ra} + 0.604A_{Th} + 0.0417A_{K})\ \text{nGyh}^{-1} \quad (1)$$

where A_{Ra}, A_{Th} and A_{K} are the activity concentration of Ra-226, Th-232 and K-40 in (Bq kg^{-1}), respectively.

To estimate the annual effective dose rates to human body, the conversion coefficient from absorbed dose in air to effective dose (0.7 SvGy^{-1}) and outdoor occupancy factor (0.2) proposed by UNSCEAR (2000) were used. The effective dose rate in units of mSv yr^{-1} was calculated by the following formula:

$$\text{Effective dose rate (mSv yr}^{-1}\text{)}$$

$$=\text{Dose rate (nGyh}^{-1}\text{)} \times 8760\ \text{h} \times 0.2 \times 0.7\ \text{SvGy}^{-1} \times 10^{-6} \quad (2)$$

Results and Discussion

Activity concentrations

The result of activity concentration measurement in the soil, sand and rock samples are shown with their counting errors in Table 1. The activity concentrations of Ra-226 ranged from 15.63±0.69 to 5,493.09±0.11 Bq kg^{-1} in soils and from 20.70±1.78 to70.92±0.81 Bq kg^{-1} in sand and from 115.82±0.57 to 486.46±0.30 Bq kg^{-1} in rocks with mean of 733.66±0.74; 39.75±1.14 and 301.14±0.44 Bq kg^{-1}, respectively. The samples collected at Lamet had Ra-226 activity concentration is higher than the world average value of 35 Bq kg^{-1} (UNSCEAR, 2000). The high concentration of Ra-226 observed in samples can be explained with the associated Permian limestone; Triassic-Jurassic red sandstone; fault and granite shown in Figure. 1.

The activity concentrations of Th-232 ranged from 12.57±1.33 to 143.17±0.44 Bq kg^{-1} in soils and from 12.34±1.73 to 32.47±0.70 Bq kg^{-1} in sand and from 7.34±2.44 to 42.02±3.34 Bq kg^{-1} in rocks with mean of 70.98±1.15 and 18.83±1.33 and 24.68±2.89 Bq kg^{-1}, respectively. The activity concentrations of Th-232 in samples collected from Lamet is more than the world average value of 30 Bq kg^{-1} (UNSCEAR, 2000). The high concentration of Th-232 indicates the presence of thorium bearing minerals in the samples.

The activity concentrations of K-40 ranged from 8.86±1.37 to 785.12±0.85 Bq kg^{-1} in soils and from 80.86±2.64 to 932.65±0.71 Bq kg^{-1} in sand and from 6.83±13.03 to 23.97±16.32 Bq kg^{-1} in rocks with mean of 355.25±5.14 and 519.80±1.44 and 15.40±14.68 Bq kg^{-1}, respectively. The K-40 mean activity concentration in sand is more than another samples and higher than the word average value of 400 Bq kg^{-1} (UNSCEAR, 2000).

Absorbed dose rates in air

The values of absorbed dose rates D in air are listed in Table 1. The absorbed dose rates due to the presence of Ra-226, Th-232 and K-40, in soil samples in the studied area vary from 14.78±1.08 to 2618.56 ± 2.74 nGy h^{-1}with a mean value of 397.84±1.27 nGy h^{-1}, which is much higher than the world average value of 56 nGy h^{-1} (UNSCEAR, 2000).

Annual effective dose equivalent

The annual effective dose rate varies from 0.018±0.001 to 3.211±0.003 mSv y^{-1} with a median values 0.156±0.001 mSv y^{-1}. These values are higher than the world average of 0.070 mSv y^{-1} (UNSCEAR, 2000).

Conclusions

The natural radioactivity and associated radiation dose rate in samples from the Lamet sub-district of Chaiya district, Surat Thani Province were assessed by gamma-ray spectrometer. The average values of the activity concentration of Ra-226, Th-232 and K-40 in different locations are much higher than that proposed by UNSCEAR.

Table 1. The average activity concentration of Ra-226, Th-232 and K-40 of the Lamet sub-district in Chaiya district, Surat – Thani Province in the samples.

Type	**^{226}Ra (Bq kg^{-1})**	**^{232}Th (Bq kg^{-1})**	**^{226}K (Bq kg^{-1})**	**Dose rate (nGyh^{-1})**
Soil (18)	733.66±0.74	70.98±1.15	355.25±5.14	397.84±1.27
Sand (5)	39.75±1.14	18.83±1.33	519.80±1.44	51.73±1.41
Rock (2)	301.14±0.44	24.68±2.89	15.40±14.68	155.10±2.61
Total (25)	560.27±0.80	56.84±1.33	360.98±5.16	313.32±1.43

The median value of annual external effective dose rate estimate of 0.156 mSv from this study is higher than the world average value of 0.07 mSv for outdoor terrestrial radiation of regions with normal background radiation (UNSCEAR, 2000). The values of the annual external effective dose rate in the third quartile (Q_3) ranged from 0.31 – 3.21 mSv, which more than 75% of all data is higher than the world average. The Lamet region in the Surat-Thani Province can be said to have a high background radiation level.

Acknowledgments

The first author is grateful to the Graduate School at the Prince of Songkla University for grant support and thanks the Department of Physics, Faculty of Science, for equipment support and other necessary facilities.

References

1. M.A.Cetiner, H.Gunduz and A.Ilgar, "High Background radiation areas at Canakkale in Turkey", Radiation Physics and Chemistry **80**(2011) 704-709.
2. M.Sohrabi, "World high background natural radiation areas: Need to protect public from radiation exposure", Radiation Measurements (2012) 1-6.
3. A.K.Mohanty, D. Sengupta, S.K. Das, V. Vijayan and S.K. Saha, "Natural radioactivity in the newly discovered high background radiation area on the eastern coast of Orissa, India", Radiation Measurements **38**(2004) 153-156.
4. W.Wallop, " Some airborne geophysical characteristics of geothermal promising areas in Thailand.", Mineral resources development division report. Department of mineral resources, Ministry of Industry 9(1996).
5. P.K.Shetty and Y.Narayana," Variation of radiation level and radionuclide enrichment in high background area.", Journal of Environmental Radioactivity **101**(2010) 1043-1047.
6. P.E. Abiama, P.O.Ateba, G.H.Ben-Bolie, F.H.P.Ekobena and T.El.Khoukhi, "High background radiation investigated by gamma spectrometry of the soil in the southwest region of Cameroon.", Journal of Environmental Radioactivity **101**(2010) 739-743.
7. H.Samavat, M.R.D.Seaward, S.M.R. Aghamiri and F. Reza-Nejad, "Radionuclide concentrations in the diet of residents in a high level natural radiation area in Iran.", Radiation Environment Biophysics **45**(2006) 301-306
8. S.Chaturrongkawanich, "Geothermal resources of Changwat Surat Thani.", Department of Mineral Resources (2001) 1-48.
9. S.Jeasai, T.Bhongsuwan and T.Chittakarn, "Radioisotope Radium-226 and Its Dispersion in Hot Spring area of Suratthani Province.", The 11st Conference on Nuclear Science and Technology Bangkok, Thailand. (2011).
10. International Atomic Energy Agency, 1989. Measurement of radionuclides in food and the environment. IAEA technical report series no. 295, Vienna.
11. UNSCEAR, 2000. The United Nations scientific committee on the effects of atomic radiation, Annex:b Exposures from natural radiation sources, United Nations New York.

The Development of k0-INAA Method for Large Sample at Thai research Reactor-1/Modification 1

S. Wonglee[1*], C. Tippayakul[1], J. Channuie[2], and S. Laoharojanaphand[1]

[1]*Thailand Institute of Nuclear Technology, 16 Vibhavadi Rangsit Road,*
Ladyao, Chatuchak, 10900, Thailand
[2]*Department of Nuclear Engineering, Faculty of Engineering,*
Chulalongkorn University, Wangmai, Pathumwan, 10330, Thailand
[*]*Corresponding author. E-mail: sarinratw@hotmail.com*

Abstract

Thai brown rice with a weight of 1.5 kg was analyzed as a large sample in this research. A sample container was made from polystyrene with the size of approximately 14 cm in diameter and 14 cm in height. The k0-instumental neutron activation analysis (k0-INAA) method was developed to determine the elemental composition and concentration in bulk rice sample. The technique had been firstly performed for large sample in Thailand. The Thai Research Reactor-1/Modification 1 (TRR-1/M1) was used as the neutron source. The thin gold foil was activated with rice sample to determine the absolute neutron flux and the Cu-wires were used to study flux distribution in bulk sample. The average thermal neutron flux in large sample was 8×10^8 n/cm^{2}s. The neutron flux distribution across the blank container for the thermal column facility generally differs within 30% and the difference increases up to approximately 60% when loaded with the rice. The gamma self-shielding effect during gamma measurement was corrected using the Monte Carlo simulation with MCNPX code. The elemental concentration in the bulk rice sample was calculated taking into account the flux depression and gamma efficiency correction using k0-IAEA program. A small rice sample was analyzed by the conventional INAA method for quantitative comparison. The results show that the trace metal elements, Zn and As could be detected only in the bulk rice sample. In addition, the concentrations of Na, K and Br from the k0-INAA method were 10.3, 1122.1 and 50.8 ppm, respectively. From the comparison, we could observe the discrepancies of approximately 2-3 times. However, more research on the validation of k0-INAA method will be performed to identify sources of errors.

Keywords: k0-INAA, k0-IAEA, large sample, rice, monte Carlo.

Introduction

The instrumental neutron activation analysis (INAA) is one of the most sensitive analysis techniques used for the quantitative multi-element determination. The technique can apply to many kinds of samples without special pretreatments and chemical processes. In general, the technique works well for small and homogeneous samples. On the other hand, for bulk sample, it requires sampling from the bulk material. This is a challenge especially for inhomogeneous material. The sampling of the bulk material may not be a good representative of the whole sample. Therefore, k0-INAA method for inhomogeneous large sample has become of interest. This technique is capable of performing analysis without sub-sampling or homogenization of the bulk material. Thus, there is the need to develop the analytical technique for the analysis of inhomogeneous bulk sample.

As we know, Thailand is one of the major rice producers and exporters in the world. Many research works have been conducted to study the elemental composition of Thai rice samples using the conventional INAA method [1, 2]. For INAA, the homogenization of rice sample is crucial for the accuracy and precision of the analysis. A sample and the reference standard are irradiated together. The activity specific to each nuclide of the irradiated sample is compared with that of the irradiated standard. The ratio of the activities is used to calculate the amount of the element. Nevertheless, the standard may not be available for all sample types.

The standardless technique has become of interest as an advanced technique to determine the trace elements in the sample. First, the k0-INAA method has been developed for the large sample in the research to evaluate the elemental concentration in Thai rice. Due to the sample size, the neutron and gamma self-shielding effects during neutron irradiation and gamma measurement should be emphasized. Therefore, the technique to account for flux depression in the sample shall be developed as well as the technique to correct for actual efficiency of the bulk sample. When all techniques are developed, the validation of the technique shall be performed. The last step would be to perform the inter-comparison of a sample. The development of the k0-INAA in Thailand has been initiated under the Coordinated Research Project (CRP) in agreement with IAEA.

Materials and Methods

Neutron distribution in bulk rice sample

The thermal column facility of TRR-1/M1 as shown in Figure 1 (left) was used for this research since the effects from epithermal and fast neutron fluxes can be neglected without serious errors. The average neutron flux of the thermal column facility is approximately 10^9 n/cm^{2}s (at reactor power of 1200 kW). The first experiment was to characterize the neutron distribution in a sample container using Cu wires with diameter of 2 mm and 14 cm in length. A container was made from polystyrene with the size of approximately 14 cm in diameter and 14 cm in height. The Cu monitors were placed around a container and the center as shown in Figure 1 (right). The blank sample container with Cu wires was irradiated for 7 hours and was left to decay for 1 day. To determine the neutron distribution along the axial position, each activated Cu wire was cut into short pieces (approximately 1 cm long) for gamma counting. Gamma energy of 1345 keV from Cu-64 was employed for flux evaluation. With the same method, the brown jasmine rice of a 1.5 kg weight was filled in sample container for studying neutron self-shielding.

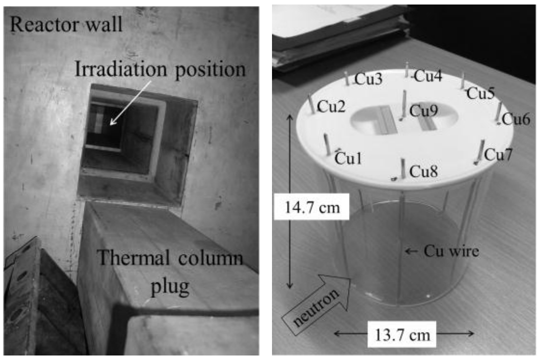

Figure 1. Thermal column facility (left) and the sample container with Cu wires (right).

K0-IAEA program

The k0-IAEA program [3] was used to determine of the concentration of trace elements in the rice sample. Improvements over the conventional k0-INAA technique were to be developed specifically for the larger sample in this research. The program requires some data such as, the gamma background measurement, energy calibration, detection efficiency, irradiation facility and gamma measurement of the irradiated sample. The specifications of the HPGe detector were required by the k0-IAEA program such as crystal diameter, crystal length, dead layer thickness, end cap to crystal length, and so on. The Eu-152 and the Cs-137 standard point sources were used for the energy and efficiency calibration. It is important to note that the k0 procedure should be done by following step-by-step instructions.

Monte Carlo simulation

Due to the large sample size, not only the correction of neutron self-shielding but also the gamma self-shielding was evaluated. The gamma self-shielding effect was corrected using Monte Carlo simulation. The MCNPX code [4] was used for the gamma transport simulation. The HPGe detector and the bulk rice sample were modeled by the MCNPX code as shown in Figure 2 and the “f8” tally card was used to tally the gamma energy deposited in the HPGe crystal. At each energy point, two simulations were performed – the first was the model with the irradiated bulk sample and the second was the model with a point source. Each simulation produces an efficiency value. The correction factor is then defined as following;

$$f_E = \frac{\varepsilon_{v,E}}{\varepsilon_{p,E}} \tag{1}$$

The MCNPX simulations were performed at several energy points to cover the range of detected photo peaks. The correction factors were then used to correct the actual efficiency derived from the efficiency calibration by k0-IAEA program. The corrected efficiency file was then imported to k0-IAEA program to calculate the element concentrations in the rice sample.

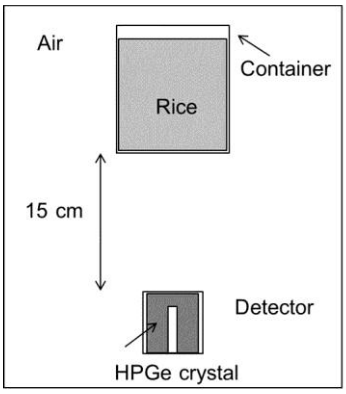

Figure 2. MCNPX model for the efficiency simulation.

Instrumental neutron activation analysis

The brown jasmine rice was prepared as a large sample with a weight of 1.5 kg for determining the elemental concentrations. Due to the characteristic of thermal column facility of TRR-M1/1, the long half-life isotopes were studied. The high purity gold flux monitors (Au) were placed at different locations within the bulk rice sample as shown in Figure 3 for the absolute neutron flux determination. The corrected flux was then input into the k0-IAEA program to simulate the activation of trace elements in rice sample. The bulk sample was irradiated in the facility for 7 hours and was left to decay for 4 days before taking to the gamma counting system. The irradiated sample was positioned at 15 cm from the detector and was measured for 1 hour. The spectrum file was then saved for subsequent use in the k0-IAEA program.

Moreover, all relevant information including the averaged flux and corrected efficiency curve was then input into this program.

At the same time, the small rice sample with a weight of 80 mg was prepared for the quantitative comparison by the conventional INAA technique. The brown rice was ground to power and put in a polyethylene vial with a size of 10 mm in diameter and 10 mm in height. The rice flour 1568a standard reference material (SRM) from National Institute of Standards and Technology (NIST) was prepared to determine the elemental concentrations. The rice flour standard material and small rice samples were irradiated together at A4 facility of TRR-M1/1 for 7 hours and were left to decay for 1 day. The gamma counting configuration for small sample was set the same as that for the bulk sample.

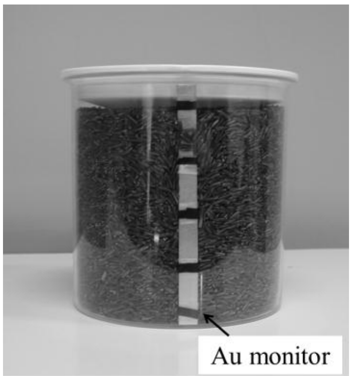

Figure 3. Bulk rice sample with Au monitors.

Results and Discussion

As mentioned above, the lowest position of Au monitor (Figure 3) was located at the same place as the lowest position of the Cu1 wire (Figure 1 (right)). Then we could calculate the absolute neutron flux at each point across the bulk sample as shown in Figure 4. The averaged flux was then calculated to 7.8 x 10^8 n/cm^{2}s. The result shows that the difference between the neutron flux at the front and the back sides of the rice sample was up to approximately 60%. It was obvious that the neutron self-shielding of the bulk rice sample cannot be neglected. Finally, the ratio between the averaged neutron flux to the surface flux directly facing the reactor core was calculated to be 0.70 and it was used for flux correction of the neutron self-shielding effect in the k0-IAEA program.

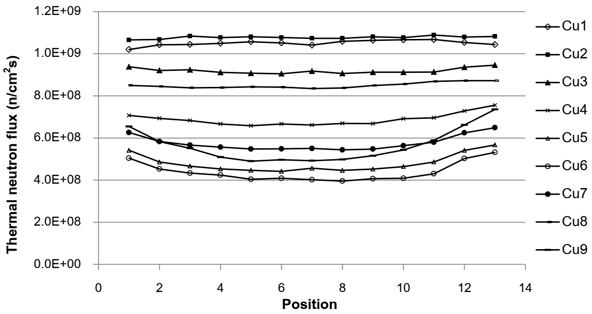

Figure 4. Neutron flux distribution along axial direction in the bulk rice sample.

Subsequently, the k0-IAEA program was used to calculate the elemental concentrations in the rice sample. The gamma measurement information and the neutron irradiation condition were required by the program. The efficiency correction factor as a function of gamma ray energy to correct for gamma self-shielding in the sample during measurement was calculated by the MCNPX code. It is noted that the reference point source was positioned at the bottom of the sample container. The simulation result is shown in Figure 5.

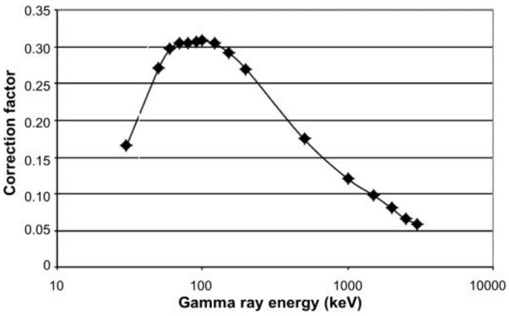

Figure 5. The efficiency correction factor as a function of gamma ray energy.

In addition, an activation analysis by the conventional relative method was performed with the small rice sample. The result of the relative method was to compare with that of the developed k0-INAA technique. The elemental concentration results from the large sample NAA technique which had been developed in this research and the conventional relative method are shown in table 1. The relative method was regarded as the reference in this experiment.

Table 1. The elemental concentrations in a brown rice sample.

Element	**Relative method**	**K0-INAA method**	**Relative error (%)**
Na	2.9 ± 0.2	10.3 ± 0.6	255
K	2418.5 ± 121.1	1122.0 ± 112.2	-54
Br	31.2± 2.1	50.8 ± 0.6	63
Mn	26.6 ± 2.6	-	-
Zn	-	26.3 ± 4.7	-
As	-	0.26 ± 0.06	-

The results show that the differences between the value determined by the relative method and k0-INAA technique are still large. Thus, it was concluded that the large sample NAA technique still need more validation to identify the sources of discrepancies. It shall be noted that although there are still large differences, the large sample NAA technique can detect Zn and As which exist in very small amount in the rice sample. This is a remarkable advantage over the conventional method. After more research on the validation, this technique will be beneficial to the determination of very small amount elements in the rice sample.

Conclusions

The neutron activation analysis technique for large samples was developed in this research. The methodology was selected to be based on the k0-INAA technique. Developments to correct for the neutron self-shielding and gamma self-shielding were conducted throughout the research work. The internal flux monitors were used to determine spatial distribution in the sample and calculated the average neutron flux based on the distribution. For gamma self-shielding during the measurement, the correction factor was performed by Monte Carlo simulation. At the moment, the results still show quite large discrepancies comparing to the small sample comparative NAA. Nevertheless, the technique in general is promising but still requires more research especially for the validation. The important remark from the research is that the methodology is established but needs more elaborations.

Acknowledgments

This research is a part of the coordinated research project (CRP) in the title of the application of large sample neutron activation analysis for inhomogeneous bulk archaeological samples and bulk objects. We would like to thank the IAEA whose support is gratefully acknowledged, and that has sponsored this work. Moreover, we would like to thank the TINT reactor staff for the thermal column facilitation and the radioactive waste disposal division for the gamma spectroscopy.

References

1. S. Laoharojanaphand, W. Dharmavani, A. Busamongkol, R. Pareepart, W. Wimolwattanapun, and W. Chantarachot. “Research and development on activation analysis at the Thailand institute of nuclear technology”, J. Radioanal. Nucl. Chem. **273** (2008) 675.
2. S. Laoharojanaphand, A. Busamongkol, S. Chaiyasith, V. Permnamtip, M. Parengam, and S. Srianujata, “Elemental composition of Thai rice and beans by instrumental neutron activation analysis”, J. Radioanal. Nucl. Chem. **281** (2009) 69.
3. M. Rossbach, M. Blaauw, M.A. Bacchi, and X. Lin, “The K0-IAEA program” J. Radioanal. Nucl. Chem. **274** (2007) 657.
4. J. S. Hendricks, G. W. McKinney, M. L. Fensin, M. R. James, R. C. Johns, J. W. Durkee, J. P. Finch, D. B. Pelowitz, L. S. Waters, M. W. Johnson, and F. X. Gallmeier, “MCNPX 2.6.0 extensions”, Los Alamos National Laboratory, 2008.

Optics, Non-linear Optics, Laser Physics, Ultrafast Phenomena

A Reliable Polarization-analysis Method for Determination of Optical Axes and Phase Retardance of Transparent Birefringent Materials

T. Lertvanithphol* and W. Rakreungdet

Department of Physics, Faculty of Science, King Mongkut's University of Technology Thonburi
126 Prachauthit Rd., Bangmod, ThungKhru, Bangkok, 10140, Thailand,
**Corresponding author. E-mail:lertvanithphol_kmutt@hotmail.com*

Abstract

We investigated the method of analyzing polarization of a laser beam passing through transparent birefringent materials, in order to extract its optical axes and phase retardance. The setup consisted of a He-Ne laser, a calcite polarizer, a birefringence sample, a quarter-wave plate, a calcite analyzer, and a linear-response detector, respectively. The quarter-wave plate was rotated to produce an intensity profile of light reaching the detector. The Jones calculus was used to derive an analytical expression of the intensity profile as a function of the rotating axis of the quarter-wave plate. The experiment result was then fitted with this expression, and the values of optical axes and phase retardance of the sample were extracted. This data fitting allowed the determination to be robust against weak signal and noisy data. The theoretical model was also tested under systematic errors such as wrong settings of axes and tilted angles of quarter-wave plate and analyzer. This method can be applied to further studies of photoelasticity which can then be characterized locally.

Keywords: Birefringence, polarization, Jones calculus

Introduction

Birefringence is the property associated with the difference in refractive indices along orthogonal directions of the materials. It is useful in many applications such as in making optical devices like optical modulators, polarizers, wave plates and retarders, liquid crystals, etc., and in studies of nonlinear processes, photoelasticity, optically active biological substances, etc. [1]. The birefringence can be determined from measurement of the optical axes and the phase delay between orthogonal polarizations. Several measurement techniques have been implemented over the years, such as rotating-wave plate Stoke polarimetry [2], the phase locking [3], the circular-heterodyne interferometry with electro-optics modulation [4], and the Zeeman spectroscopy [5].

In this work we studied the experimental method for extracting parameters associated with birefringence of unknown sample, using the rotating quarter-wave plate (QWP) polarimetry. The mathematical model based on Jones calculus was used to derive an analytical expression which was then used for fitting the signals from the experiment. Independent checks of this method had been implemented to verify validity of the method. The model was also used for exploring systematic errors subject to different optical components in the setup. One of the applications in photoelasticity was demonstrated, in determining localized birefringence of an unknown, transparent sample.

Mathematical Model

Any pure polarizations of light can bedecomposed intoa linear basis, described by two linearly orthogonal polarizations having a certain value of relative phase between them. Generally, one can set polarizations of light and optical axes of relevant optical components to convenient choices of laboratory axes, i.e. horizontal and vertical axes. According Jones calculus [6], the electric fields associated with pure polarizations can be written as:

$$\vec{E} = \begin{bmatrix} E_{0x}e^{i\delta_x} \\ E_{oy}e^{i\delta_y} \end{bmatrix} = \begin{bmatrix} E_{0x} \\ E_{0y}e^{-i\Delta} \end{bmatrix}, \qquad (1)$$

where$E_{0x}$and E_{oy}represent the amplitudes of horizontal and vertical electric-field components of linear polarizations, δ_x and $\delta_y$represent the absolute phases of horizontal and vertical linear polarizations in the laboratory frame, and $\Delta = \delta_x - \delta_y$ is the phase difference between the two polarizations. Materials with nonzero value of the relative phase Δ are referred to as the birefringent materials.

Figure 1 shows the setup of choice in this study, which consists of the polarization generator, the sample of interest, and the polarization analyzer. The polarization generator sets the input polarization with respect to the laboratory frame, e.g. vertical orientation. This known polarization is sent to the sample. Birefringent medium will cause theoutput polarization to deviate from the input polarization. The information regarding the birefringence of the sample can then be obtained by determining the rotated polarization axes and the induced relative phase between the polarizations, with respect to the input polarization.

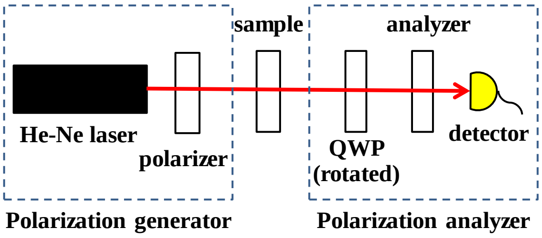

Figure 1.The experimental setup.

If the laboratory, or reference, axis is chosen along the *x* direction, according to the Jones calculus the polarization generator in Figure 1 gives the transfer matrix in forms of,

$$\begin{bmatrix}\cos\alpha & -\sin\alpha\\ \sin\alpha & \cos\alpha\end{bmatrix}\cdot\begin{bmatrix}1 & 0\\ 0 & 0\end{bmatrix}\cdot\begin{bmatrix}\cos\alpha & \sin\alpha\\ -\sin\alpha & \cos\alpha\end{bmatrix},(2)$$

where the matrix in the middle represents the linear polarizer and the rest of the matrices represent the rotation matrices for aligning the optical axis of the polarizer to the reference axis by an angle of α. The sample can add relative phase delay, Δ, to the polarizations along its optical axes, resulting in

$$\begin{bmatrix}\cos\theta & -\sin\theta\\ \sin\theta & \cos\theta\end{bmatrix}\cdot\begin{bmatrix}1 & 0\\ 0 & e^{-i\Delta}\end{bmatrix}\cdot\begin{bmatrix}\cos\theta & \sin\theta\\ -\sin\theta & \cos\theta\end{bmatrix},(3)$$

where the middle matrix represents the birefringent material adding the phase delay between the two polarizations, and the angle of θ represents the orientation angle between the fast axis of the material and the reference axis.

The light after the sample is then sent through the polarization analyzer which consists of a QWP and the polarizer, hereafter the analyzer. If β and γ are respectively the orientation angles of the QWP and the analyzer, with respect to the reference axis, the polarization component along the optical axis of the analyzer can be written as

$$\begin{bmatrix}1 & 0\\ 0 & 0\end{bmatrix}\cdot\begin{bmatrix}\cos\gamma & \sin\gamma\\ -\sin\gamma & \cos\gamma\end{bmatrix}\begin{bmatrix}\cos\beta & -\sin\beta\\ \sin\beta & \cos\beta\end{bmatrix}\cdot\begin{bmatrix}1 & 0\\ 0 & e^{-\frac{i\pi}{2}}\end{bmatrix}\cdot$$
$$\begin{bmatrix}\cos\beta & \sin\beta\\ -\sin\beta & \cos\beta\end{bmatrix}\cdot\begin{bmatrix}\cos\theta & -\sin\theta\\ \sin\theta & \cos\theta\end{bmatrix}\cdot\begin{bmatrix}1 & 0\\ 0 & e^{-i\Delta}\end{bmatrix}\cdot$$
$$\begin{bmatrix}\cos\theta & \sin\theta\\ -\sin\theta & \cos\theta\end{bmatrix}\cdot\begin{bmatrix}\cos\alpha & -\sin\alpha\\ \sin\alpha & \cos\alpha\end{bmatrix}\cdot\begin{bmatrix}1 & 0\\ 0 & 0\end{bmatrix}\cdot\begin{bmatrix}E_{0x}\\ E_{0y}e^{-i\Delta}\end{bmatrix},\qquad(4)$$

where the most right 2x1 matrix represents the polarization of a laser beam. If the angles α and γ are set to 90 and 0 degrees, respectively, the intensity, *I*,at the detector in Figure 1, can be simplified to,

$$I = k[(2\cos\Delta + 2)\sin^2 2\beta - 4\sin 2\theta\sin\Delta\sin 2\beta + (2\cos\Delta - 2)(\cos(4\beta - 4\theta) + \cos 4\theta - 1)],(5)$$

where *k* is a proportional constant. When the optical axis of the QWP is set, β will be known. Thus the intensity in Equation 5 will be only in terms of θ and Δ, which are the parameters representing the birefringence of the sample.

Experiments

The experimental setup followedwhat was shown in Figure 1, with the sample setting up in the transmitting mode. The He-Ne laser at wavelength of 632.8 nmwas used as a laser source. A high-extinction-ratio calcite polarizer with its optical axis aligned in the vertical direction was used to set the polarization of the input light. Different transparent samples were investigated, including materials with known (half-wave plate, HWP) and unknown (Compact-Disc, CD, case) birefringence. The HWP and the QWP were zero-order waveplate at the wavelength of 632.8 nm. The analyzer was the same material as the polarizer. All polarization optics were mounted in the rotation stages with resolutions of 2 degrees. The light intensity after the analyzer was measured by the Si photodetector with a transimpedance amplification of 1,000 and a signal-to-noise ratio of 10,000:1. The signal of rms voltage out of the amplifier was read by a multimeter.

In order to extract the values of θ and Δ, the angle of the optical axis of the QWP with respect to the reference axis, β, was set, and the light intensity after the analyzer was recorded. This procedure was repeated to obtain the intensity profile in terms of β, from 0 to 360 degrees, with a resolution of 10 degrees. This profile was fitted with an analytical expression derived in Equation 5. The free parameters for the fit were *k*, θ, and Δ, and the fitting method was the least-squared fit.

Results and Discussions

Determination of relevant systematic errors

Since α, γ, and β were set to known values in Equation 4, it was important to set these values as correct as possible. To determine systematic errors in setting angles α, γ, and β and to include in our mathematical model, the following procedure was implemented. First angle α was set as vertical as possible, and then referred to as 90 degrees with respect to the horizontal *x*-axis. The analyzer was placed in the setup with its optical axis closed to 0 degree. As its optical axis was varied, the intensity after the analyzer was measured and plotted as shown in Figure 2. The intensity variation was expected to be the square of the sinusoidal function, and thus the signal was fitted with this function. The fitting result suggested that the angle γ should be offset by approximately 0.8 degrees.

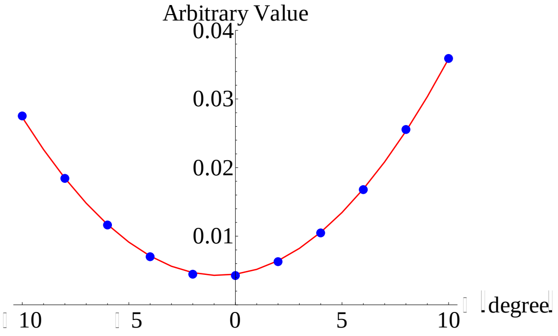

Figure 2. The plot of intensity after the analyzer versus angle γ. The data and the fit were shown in the blue dots and red line, respectively. (Color online).

Then the QWP was placed between the polarizer and analyzer. To find the optical axis of the QWP for setting β, the intensity after the analyzer was recorded as a function of β, as shown in Figure 3. Setting θ and Δ equal zero in Equation 5, and letting $\beta \rightarrow \beta + \beta_0$ with β_0 being the offset angle, the fit result suggested that β_0 was equal to 101.9 degrees. The offset values of γ and β were included as angle constants in Equation 4, which led to some modifications of the analytical expression of Equation 5.

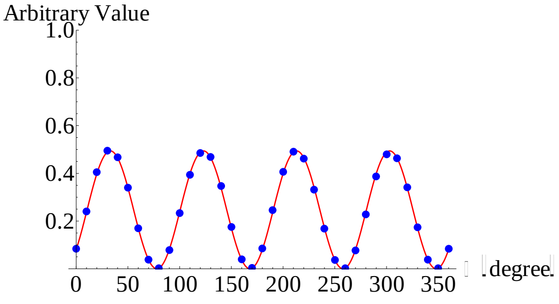

Figure 3. The plot of intensity after the analyzer versus angle β. The data and the fit were shown in the blue dots and red line, respectively.

Validation of the mathematical model

To check the validity of our mathematical model, the HWP was used as the sample. The plot of intensity versus angle β was obtained, as shown in Figure 4. The data were fitted to the corrected expression similar to Equation 5. The extracted values of θ and Δ were 176.2 and 169.7 degrees,agreeing well with known values of 176.2 and 180 degrees,respectively. These corresponded to percent inaccuracy of <0.1% and 5.7%, respectively.

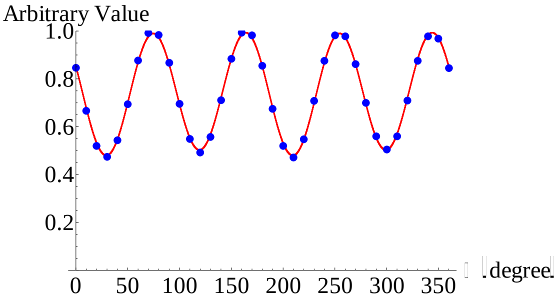

Figure 4. The plot of intensity after the analyzer versus angle β when HWP was used as the sample. The data and the fit were shown in the blue dots and red line, respectively.

It should be noticed that extraction of θ gave a very accurate value while the extraction of Δ gaveapproximately 5% inaccuracy. According to the Poincare-sphere representation [7], the intensity andβ signals were represented by the projection of the Stoke vector on to the equatorialplane and the angle that the $^{\pi}/_{2}$-torque vector was located on the equatorial plane, with respect to the horizontal axis, respectively.The projection of the Stoke vector by the torque vector must repeatitselfevery 180 degree rotation, giving very strong constraint in the fit. This led to accurate extraction of θ in our experiment. On the other hand, the extraction of Δ was associated with how far the Stoke vector was away from the equatorialplane. When the Stoke vector was close to the poles (i.e. circularly polarization),it would not be sensitive to theprojection operation. In this scenario, the projection on the equatorial plane changed little compared to the change of Stoke vector. This led to some inaccuracy in the fit to extract a value of Δ. Our error in our extraction was about 5%. A better signal-to-noise intensity measurement and more data points would reduce inaccuracy in the extraction of Δ.

We have repeated this procedure a number of times, over the course of months, and found the results reproducible and thus reliable.

The θ and Δ measurement of unknown sample

The result with a sample of unknown specimen (i.e. a piece of transparent plastic) was shown in Figure 4. The result yielded values θ and Δ of26.6 and 52.9 degrees,respectively.

Robustness of fit method

As mentioned earlier, optical axes of components must be set and known to reduce systematic errors. The effect of these errors was analyzed by using the simulation from mathematical model.

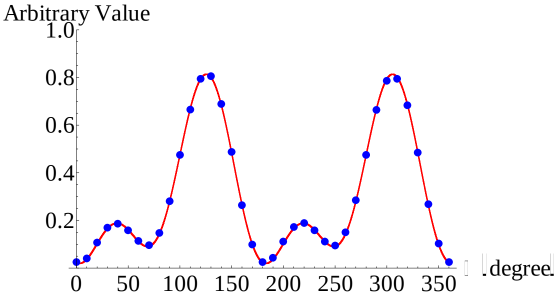

Figure 5. The plot of intensity after the analyzer versus angle β when CD case was used as the sample. The data and the fit were shown in the blue dots and red line, respectively.

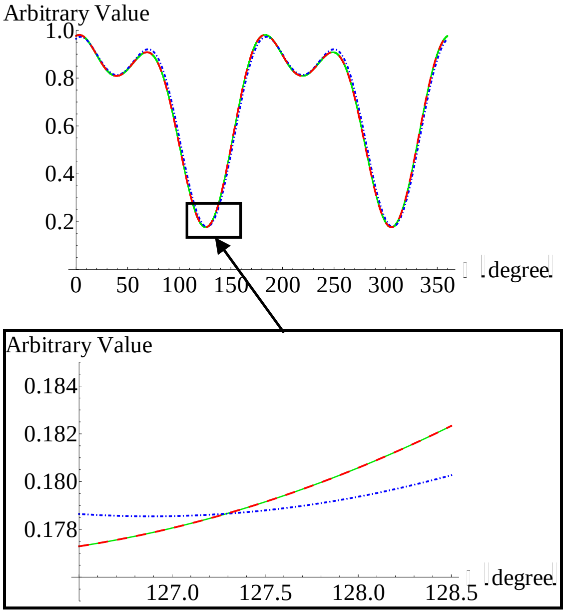

Figure 6. The simulated plot of intensity after the analyzer versus angle β. The simulation in the subject of all correct angle (green solid line), β shifting for 2 degrees (red dash line), and γ shifting for 2 degrees (blue dot dash line) were shown.

The simulated setup was generated in the same configuration as that in Figure 1 and simulated sample was set θ and Δto equal 26.55 and 52.86 degrees, respectively. The +2 degrees was added to shift the rotation angle of linear polarizer and QWP in analyzer part separately. As shown in Figure 6, the +2 degrees that added to linearly part affects to the data more than same value of QWP. However, the θ and Δ values are virtually no difference with setup values after using least-square-fit, the inaccuracy percentages are about 0. This show the robustness of this methodwas not affected from a few systematic errors.

Calculation of θ and Δ in separated areas and way of application

The birefringence property of sample can be determined in the small areas separately. The sample of plastic CD case was divided into 60 small areas, 5mm x 5mm, and calculated θ and Δ of each area by the presented method. After calculation, the data of θ and Δ were used for mapping birefringence property for all area of plastic case. In addition, the case of polarization changing when the input +45 linear polarization passing through this plastic plate was generated and shown in Figure 7. This calculation can be applied to further studies in a branch of photoelasticity.

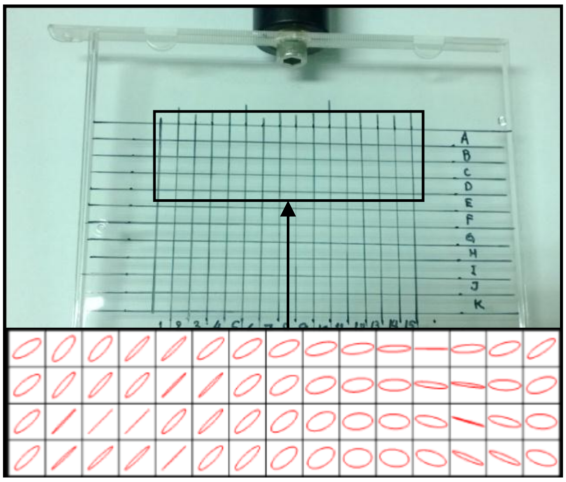

Figure 7. The simulation of output polarization when input +45 linear polarization pass through the sample of CD case.

Conclusions

The transparent birefringence determination by using the setup of rotating quarter wave plate with mathematical model from Jones calculus was presented. The technique for setup measurement, robustness of the method, and the effect of rotation angle misalignment were shown. The sample of CD case was used to determine its birefringence. In addition, the way of application from this method is photoelasticity that can be study more in the future.

Acknowledgements

The authors would like to thank King Mongkut's University of Technology Thonburi, the National Research Council of Thailand, the National Research Council and Science Achievement Scholarship of Thailand, and the Development and Promotion of Science and Technology Talented Project for financial supports.

References

1. Hecht, E., 2002,Optics, Addison-Wesley.
2. Lin, J.-F., 2010, "Measurement of Linear Birefringence Using a Rotating-Wave-Plate Stokes Polarimeter", Optik - International Journal for Light and Electron Optics, Vol. 121, No. 23, pp. 2144-2148.
3. Lo, Y.L., Lee, S.Y., and Lin, J.F., 2004, "The New Circular Polariscope and the Senarmont Setup with Electro-Optic Modulation for Measuring the Optical Linear Birefringent Media Properties", Optics Communications, Vol. 237, No. 4–6, pp. 267-273.
4. Lin, J.-F. and Lo, Y.-L., 2006, "The New Circular Heterodyne Interferometer with Electro-Optic Modulation for Measurement of the Optical Linear Birefringence", Optics Communications, Vol. 260, No. 2, pp. 486-492.
5. Lin, J.-F., Liao, T.-T., Lo, Y.-L., and Lee, S.-Y., 2007, "The Optical Linear Birefringence Measurement Using a Zeeman Laser", Optics Communications, Vol. 274, No. 1, pp. 153-158.
6. Collett, E., 1993, Polarized Light: Fundamentals and Applications, Marcel Dekker.
7. Nagib, N.N. and Khodier, S.A., 2000, "Applications of the Poincaré Sphere in Polarization Metrology", Optics & Laser Technology, Vol. 32, No. 5, pp. 373-377.

Fluorescence Study of Rice

S. Chomdaeng and A. Pattanaporkratana [*]

[1] *Department of Physics, Faculty of Science, Kasetsart University, Bangkok 10900, Thailand*
**Corresponding author. E-mail: fsciacp@ku.ac.th*

Abstract

We studied fluorescence of rice. Different varieties of rice we have studied in this research are commonly used for internal consumption and export of Thailand. There were total of 38 varieties of rice used in the experiment: 9 of these were sticky rice and the rest were paddy rice. Rice husks were peeled away before taking the measurement. A cw 532-nm laser source was focused onto the samples and the scattered light was collected to a spectrometer. Principle Component Analysis (PCA) was used to analyze the fluorescence spectra. An open-source software, Tanagra 1.4, was used to perform the PCA. We discovered that sticky rice typically showed spectra with higher intensities than other varieties of rice. The PCA results showed the rice samples were clearly separated into two groups. This fluorescence technique can be used to distinguish sticky rice from paddy rice in Thailand.

***Keywords*:** Rice, sticky rice, fluorescence, principle component analysis (PCA)

Introduction

Rice is among crops that can make revenue in Thailand. The whole world demand for rice consumption is around 417.7 million tons a year. The market share for rice export of Thailand to all over the world is about 36 percents. In addition, rice is the main food of the population of Thailand, so that it has become the economic crop. There are a number of milled rice and a rice packaging product that can normally be seen at a supermarket or a local shop. As a consequence, rice is the most essential crops which can make a large number of benefits for Thailand.

In milling industry, the need to correctly identify the rice variety is important because different kind of rice has different property and cost. Some cheated farmers mixed high price paddy with a cheaper one, making it hard for the mill to do quality control, costing a lot of problem. The ability to distinguish between different varieties of rice is therefore very crucial.

Many researchers have put a lot of attempt to try to characterize or do quality control on rice. For example, Tang et al. have used Surface enhanced Raman scattering (SERS) to determine content of pesticide in paddy rice[1]. Kim et al. have tried to improve the ability to differentiate geographical origin of rice using Raman spectroscopy[2]. Ellepola et al. have studied conformation of globulin, a protein in rice, using Fourier-transform Raman spectroscopy[3]. In this paper, we have used laser-induced fluorescence method to study varieties of rice commonly grown in Thailand. The result showed that this fluorescence technique can be used to distinguish sticky rice from paddy rice in Thailand.

Materials and Methods

Thirty nine different varieties of rice, commonly grown in Thailand, were selected for the experiment as shown in Table 1: 9 of these were sticky rice and the rest were paddy rice. 5 grains of rice were randomly selected from each of the rice variety to do the experiment. Rice husks were peeled away before taking the measurement.

The experimental setup for the fluorescence measurement is shown in Figure 1. A 532 nm cw solid-state laser (cnilaser, MGL-H-532nm-500mW with 5% stability) is set at 10 mW power and used as the light source. The laser light passes through a laser-line filter (filter 1; Semrock MaxLine Laser-line Filters, LL01-532-12.5) to clean out other laser wavelengths that are not used. The laser is directed through the mirrors and the dichroic mirror (Semrock, LPD01-532RU-25x36x1.1) and focused onto the rice sample by a microscope objective lens (Nikon 4X/0.45, WD 30 mm). The scattered light is collected by the same objective lens and passes through the dichroic mirror, which acts as a long-pass filter, allowing light with wavelength longer than 532 nm to pass. The light then passes through a notch filter (filter 2), which filters the laser light at 532 nm. The light is then focused to a fiber optic spectrometer (Ocean Optics: Maya Pro 2000) by a convex lens.

The fluorescence spectra of all samples are analyzed for similarities by Principle Component Analysis (PCA). PCA is an exploratory statistical tool to find similarities in the samples. It finds the covariance matrix between data vectors and utilizes rotation matrix to project the data into the principal axes where the data are most correlated (eigenvalues of the covariance matrix is highest) at the first few axes (PC-1 and PC-2). In this axes, the samples that are closer in coordinates are said to share similarities. Detailed explanation on PCA can be found out there in statistic textbooks or electronic sources. We use an open source software, Tanagra 1.4, for the Principle Component Analysis.

Table 1: Rice varieties used in the experiment

Name	Code	Gender
RD11	3092	Rice
RD7	18060	Rice
RD27	7125	Rice
RD21	4791	Rice
RD23	19325	Rice
RD13	3093	Rice
RD1	24496	Rice
RD15	22049	Rice
RD25	4793	
Khao Tah Haeng	905	
Khao'JowHawm –		Rice
Phitsanulok 1	23409	Rice
Nahng Sa-gui 19	15833	Rice
Khao Dawk – Mali 105	1	Rice
Peuak Nam 43	1561	Rice
Leb Nok Pattani	21962	Rice
Leuang Pratew 123	1203	Rice
Khao'Jow Hawm- Suphan Buri	23062	Rice
Chai Nat 2	24393	Rice
Gow Ruang 88	972	Rice
Khao Pahk – Maw 148	10613	Rice
Phatthalung	24392	Rice
Nahng Mon S-4	1289	Rice
Look Daeng Pattani	23410	Rice
Puang Rai 2	18444	Rice
Khem Thong	10007	Rice
Phatthalung 60	24414	Rice
Khao'Jow Hawm- Khiong Luang 1	23061	Rice
Pueng Ngen	5369	Rice
Hom Nin	24398	Rice
RD8	22051	Sticky Rice
RD2	22305	Sticky Rice
RD10	21643	Sticky Rice
RD4	21636	Sticky Rice
RD12	21628	Sticky Rice
Hahng Yi 71	7613	Sticky Rice
Muey Nawng 62 M	309	Sticky Rice
Niaw San-pah-towng	622	Sticky Rice
Niaw Ubon 2	23408	Sticky Rice

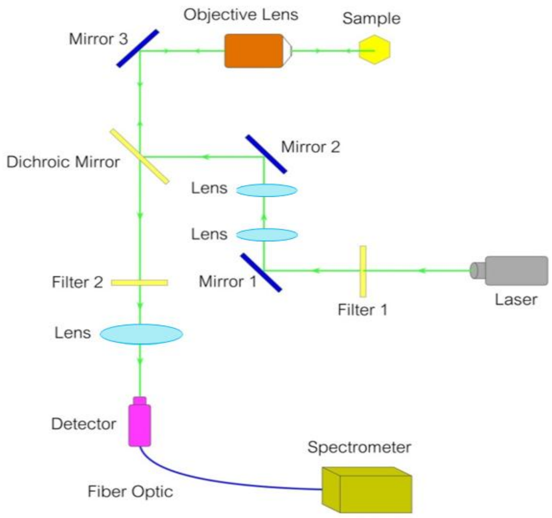

Figure 1. Setup to measure fluorescence of rice.

Results and Discussion

Fluorescence spectra of some rice and sticky rice samples are shown in Figure 2. The wavelengths (x-axes) are in the units of nanometer and the intensities (y-axes) are in arbitrary units. The left column is sticky rice and the right column is paddy rice. Five rice's seeds from the same group of rice are randomly selected to compare similarities. In general the fluorescence spectra of the rice seeds in the same group are similar in shapes and intensities, with the common peak wavelength around 590 nm. From time to time, one out of five of the rice seeds in some group of rice shows an extra peak wavelength at around 670 nm (i.e. Rice 21628, Rice 21643, and Rice 974). However, Rice 309 shows the most intensity variation among the rice seeds within the same group. Some of the rice seed in this group even saturates the spectrometer (black line).

Comparing between different groups of rice, we find that typical value for the peak intensity at 590 nm is around 7,500 counts for paddy rice, and around 30,000 counts for sticky rice: the value for the sticky rice is about 3 times higher than the paddy rice. The only exception is the paddy Rice 24496, which shows comparable intensity value to the sticky rice's. Among the varieties of paddy rice, there are a group of jasmine rice and regular rice. We cannot detect any difference in fluorescence spectra among them using the 532 nm excitation wavelength in our experiment.

It is clear that the spectra intensity can be used to differentiate between the group of sticky rice and paddy rice. The sticky rice samples usually have higher spectral intensity than the paddy rice.

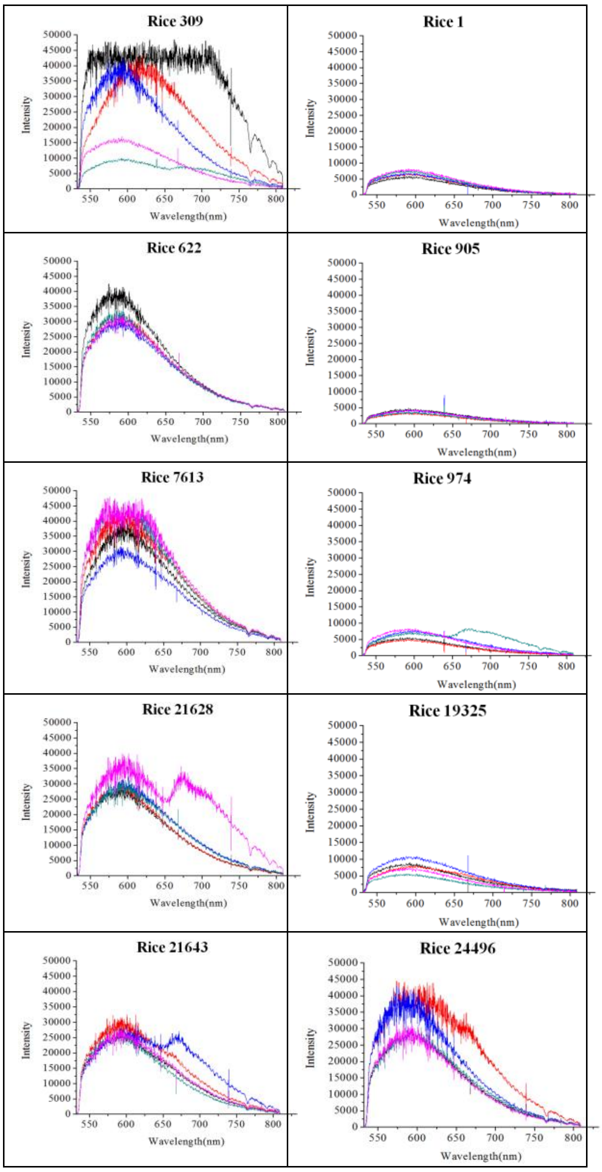

Figure 2. Fluorescence spectra of some rice samples. The wavelengths (x-axes) are in the units of nanometer and the intensities (y-axes) are in arbitrary units. The left column is sticky rice and the right column is paddy rice.

The fluorescence spectra of the rice and sticky rice samples in Figure 2 are analyzed by PCA and the corresponding loading score plots of the principle axes PC-1 versus PC-2 are shown in Figure 3. In Figure 3a, the whole measured spectra are analyzed, while in Figure 3b, only spectra up until wavelength 646 nm are analyzed. The reason for this is we want to get rid of the unusual extra peak at 670 nm and compare this result with Figure 3a (the uncut version). The symbols representing sticky rice are shown black in color, and the symbols representing paddy rice are shown by colors that are not black.

The PCA results shown in Figure 3a and 3b are very similar. They show that the rice samples were clearly separated into two groups as shown in red and blue circles. The samples in the red circle are mostly paddy rice (shown by colorful symbols), while the samples in the blue circle are mostly sticky rice (shown by black symbols). This means that we can identify sticky rice or paddy rice by either analyzing the whole spectra as in Figure 3a or analyzing only a range of wavelength centered around the 590-nm peak as in Figure 3b. This can help reduce some computational time when lots of samples are analyzed.

The paddy rice samples are mostly distributed on the negative side of the PC-1 axis, while the sticky rice samples are mostly lying on the positive side. However, both groups of rice are randomly distributed along the PC-2 axis. This means the PC-1 is the most important axis that can distinguish the sticky rice from the paddy rice, and this axis should correspond to the spectral intensity.

Out of the 39 varieties, total of 195 rice samples used in the experiment, there are 12 rice samples that are mixed in the wrong group. For example, all 5 samples of paddy Rice 24496 are mixed in the sticky rice group. This is due to the high spectral intensity of the rice as seen in Figure 2. There are four rice samples, one rice sample from each variety, from paddy Rice 22049, Rice 23062, Rice 19325, and Rice 5369, that get mixed in the sticky rice group. There are also three rice samples from sticky Rice 309, Rice 21643, and Rice 23408, that get mixed in the paddy rice group.

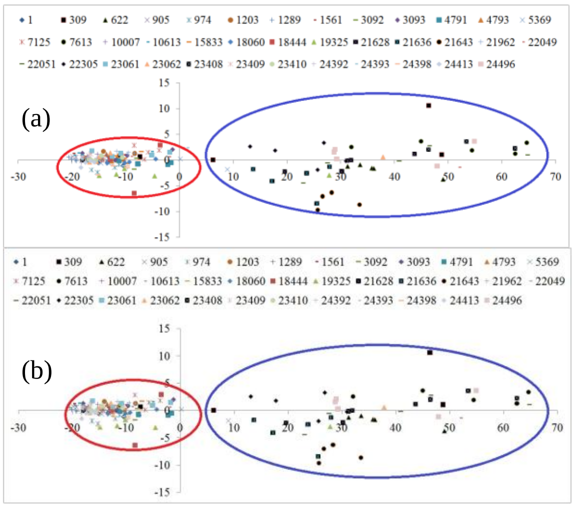

Figure 3. PCA analysis of (a) PCA result with the whole spectral range analyzed, and (b) the PCA result with only spectral wavelength up to 646 nm analyzed. The sticky rice samples are shown in

black color and the paddy rice sample are shown by colors that are not black. See text for details.

Conclusions

Principle Component Analysis (PCA) was used to analyze the fluorescence spectra of the rice grains, when excited by the 532-nm laser. The results showed that fluorescence spectra of. The PCA results showed that the spectral intensity can be used to differentiate sticky rice from paddy rice.

Acknowledgments

We would like to thank the Rice department of Thailand to kindly supported the rice samples.

This work is supported by Faculty of Science, Kasetsart University, National Research Council of Thailand, and Kasetsart University Research and Development Institute.

References

8. T. Tang, D. Fang, Q. Li, P. Cao, J. Geng, T. Sui, X. Wang, J. Iqbal, and Y. Du, “Determination of Tricyclazole Content in Paddy Rice by Surface Enhanced Raman Spectroscopy”, Journal of Food Science **77** (2012), 105-109.
9. Y. Kim, S. Lee, H. Chung, H. Choi, and K. Cha, “Improving Raman spectroscopic differentiation of the geographical origin of rice by simultaneous illumination over a wide sample area”, J. Raman Spectrosc **40** (2009), 191-196.
10. S.W. Ellepola, S.-M. Choi, D.L.Phillips, and C.- Y. Ma, “Raman spectroscopic study of rice globulin”, Journal of Cereal Science **43** (2006), 85-93.

Optimization of Transverse Shift inside a Near-field Talbot Interferometer

S. Deachapunya* and S. Srisuphaphon

Department of Physics, Faculty of Science, Burapha University, Chonburi, 20131, Thailand
**Corresponding author. E-mail: sarayut@buu.ac.th*

Abstract

The Talbot interferometry is a near-field diffraction which is explained by the Fresnel diffraction. A diffraction grating, illuminated by a coherent light source can produce a series of periodic patterns behind the grating which are often called optical carpets. We here show the optimization of sensitivity of transverse shift inside Talbot interferometer as a function of grating constant and opening fraction of the grating. We summarize that the sensitivity of the transverse shift is increased dramatically at smaller grating constants while no effect for different opening fractions. The advantage of extremely high sensitivity in nanometer scale of Talbot interferometry compared to far-field diffractions such as Young double slit experiment can be suggested as a new type of inertial sensing applications such as displacement sensor, spectrometer, and vibration sensor.

Keywords**:** Talbot effect, optical near-field effect, Optical carpet

Introduction

The Talbot effect, which is an optical near-field effect, was discovered by Henry Fox Talbot since 1836 [1]. He reported that a diffraction grating illuminated by a collimated light generates a periodic interference pattern which has the periodicity as same as the grating itself when the observed screen located at a certain distance behind the grating so called *Talbot length* (L_T). This effect can be explained clearly by Fresnel diffraction [2,3].

Many studies and applications of Talbot effect have been carried out so far. In light optics, the Talbot effect was used for making surface profiles of transparent objects [4], for measuring temperature profiles [5], for displacement sensors [6]. In quantum optics, The Talbot effect has been used to study quantum mechanics, i.e. superposition principle with electron [7], atom in space domain [8], atom in time domain [9], as well as molecules [10, 11].

Here, we report on the realization of transverse shift of the interference pattern in the Talbot interferometer. The transverse displacement due to an external perturbation can explicitly cause the interference shift. The sensitivity of fringe shift will be optimized presently with the characteristic parameters of the grating, i.e. grating constant or period (d), and opening fraction (f). The sensitivity in the scale of nanometer will be obtained in our scheme. A new type of inertial sensing applications can be invented based on this near-field Talbot interferometric technique. The sensor can be simple, low-cost, portable, even the sensitivity is in the unprecedented range.

Materials and Methods

Here, we explain briefly the Talbot effect. The detail of theory is shown elsewhere [3]. Assuming a plane wave with the wave number $k = 2\pi/\lambda$ propagating along z axis falls onto a diffraction grating at z=0 (Fig. 1). The grating has the periodic modulation in the x direction so the incident wave can be represented by $\psi = exp\{i\, k_\theta\, x\}$, where $k_\theta = k\, sin\theta$ is the projection of the incident wave vector onto the x-axis. According to the Talbot effect we can set $\theta = 0$. While the time dependence in the wave function can be omitted in case of static grating.

Behind the grating at z=0 the wave will be transformed by the grating to be,

$$\psi(x, z = +0) = T(x)\, exp\{i\, k_\theta\, x\} \qquad (1)$$

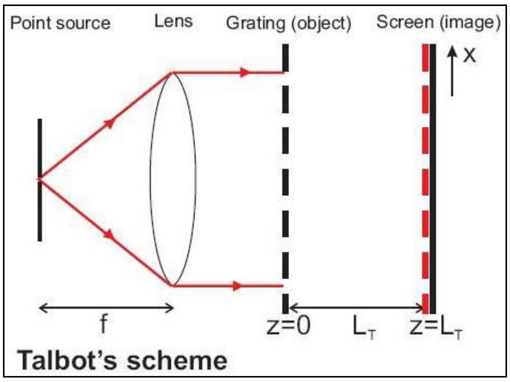

Figure 1. The idea of Talbot effect.

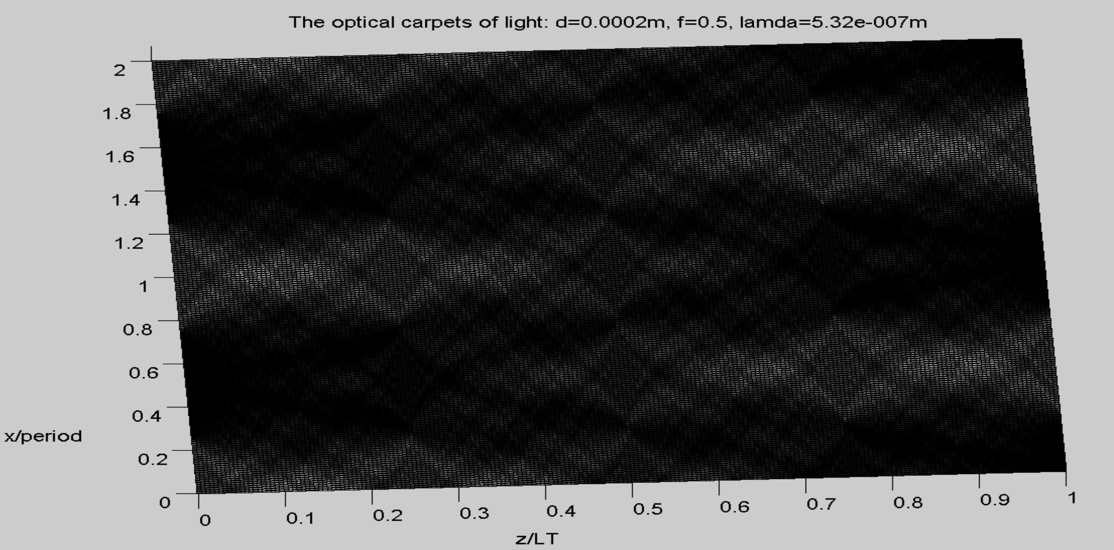

Figure 2. Theoretical simulation of carpet of light according to Eq. (4): the grating period is 200 μm, the opening fraction is 0.5, and the laser wavelength is 532 nm.

Here, the grating transmission function $T(x)$ is given by

$$T(x) = \sum_n A_n \, exp\{i \frac{2\pi n x}{d}\} \qquad (2)$$

where d is the grating period and A_n represents the components of the Fourier decomposition of the periodic for the grating. For grating with an opening fraction f the Fourier components are given by

$$A_n = \frac{sin(n\pi f)}{n\pi} \qquad (3)$$

where $n = 0, \pm 1, \pm 2, \ldots$. When the wave propagates for a distance z behind the grating it acquires an additional phase $exp\{i\sqrt{k^2 - k_\perp^2}\, z\}$, where $k_\perp$ is the wave vector parallel to the x-axis. With the paraxial approximation ($k >> k_\perp$) the wave function is reduced to

$$\psi(x,z) = \sum_n A_n \, exp\{ink_d x - \frac{in^2 \pi z}{L_T}\} \qquad (4)$$

where $k_d = 2\pi / d$ and $L_T = d^2 / \lambda$ is the Talbot length. In this work, we want to study the transverse shift over the interferogram. We therefore replace the screen shown in Fig. 1 by a second grating as a mask grating and a photodiode for intensity detection behind the mask therefore the corresponding intensity with the mask can be express as

$$\begin{aligned} I(x,z) &= \psi^*(x,z)\psi(x,z) \\ &= \sum_{n,m} M(x-\delta) A_n A_m \, exp\{i(n-m)k_d x - i\frac{(n^2 - m^2)\pi z}{L_T}\} \end{aligned} \qquad (5)$$

The function $M(x)$ is the step function corresponding to the mask,

$$M(x) = \begin{cases} 1 \; ; jd - \frac{fd}{2} < x < jd + \frac{fd}{2}, \\ 0 \; ; \text{otherwise} \end{cases} \qquad (6)$$

where $j = 0, \pm 1, \pm 2, ..$ and δ is the transverse shift between the two gratings.

Results and Discussion

The aim of our work here is to clarify deeply the optical Talbot effect and to understand the sensitivity of transverse shift inside this Talbot interferometer. First, we study the interference fringes or self-imaging at several distances z along the beam path and draw the optical carpet (Fig. 2). The result of this optical carpet is calculated by Eq (4). The sum is truncated at $n = \pm 25$ and this theoretical expectation is still fitted to the experimental result shown elsewhere [3].

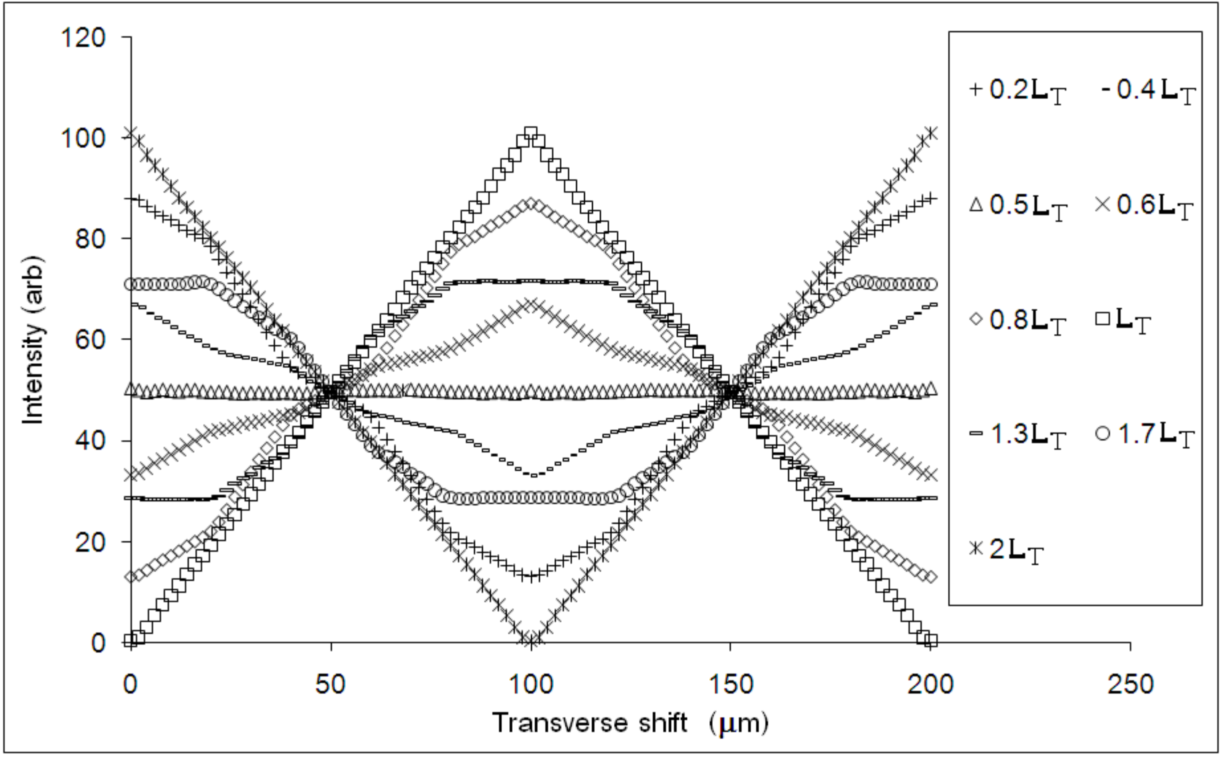

Figure 3. The simulation of intensity versus transverse shift (δ) with one period ($d = 200\ \mu m, f = 0.5$) and with the step of 2 μm for some longitudinal distances z (0.2 L_T to 2 L_T

The knowledge of how sensitive the intensity change with the transverse shift of the mask grating is revealed. Fig. 3 shows the simulation from Eq. (5) which is the sum of intensity along x-axis versus transverse shift of the second grating (δ) with one grating period ($d = 200\ \mu m, f = 0.5$) for some longitudinal distances z (0.2 L_T to 2 L_T). It shows that at a distance of multiple of Talbot length, the intensity change or slope is maximized and at half of Talbot length the slope is almost zero. Subsequently, we vary the parameters. i.e. grating constant (d), and opening fraction (f) at the constant longitudinal distance (z) of a single Talbot length. The sensitivity of the transverse shift, which is defined here as the slope of intensity change, is increased dramatically at smaller grating constants while no effect for different opening fractions (Fig. 4 and Fig. 5). Fig. 5 is a 3D plot of the sensitivity versus this grating constant and opening fraction. The sensitivity axis is normalized in order to compare for all parameters. With high S/N light source such as a laser source, one can obtain the sensitivity as good as in nanometer scale according to the data shown in Fig. 4 at the grating constant of 10 μm. For example, if the S/N is 1000 the resolution of the transverse shift can be below 100 nm.

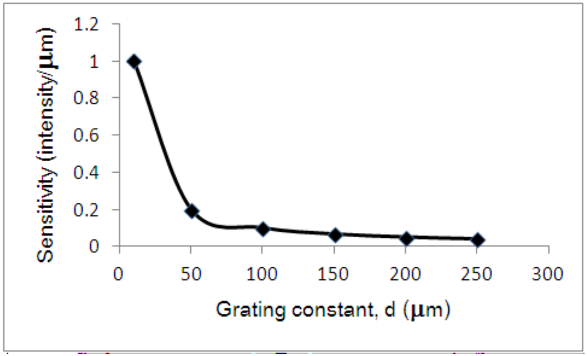

Figure 4. The sensitivity as a function of grating constant (d) at the opening fraction of 0.5. The simulation is done with the z distance of one Talbot length and with Eq. (5).

Conclusions

We study the optical near-field effect, namely Talbot effect. The effect represents an elegant interference pattern at the Talbot length which is similar to the grating itself. In addition, if the distance between the grating and the detection screen is shorter than the Talbot length, the patterns are relatively smaller than the grating period. We have also showed and described the term quantum carpets or carpets of light. Since the sum of intensity of interference patterns behind the mask grating is varied as a function of the transverse distance and very sensitive external perturbations such as vibrations, we propose the new idea for inventing a vibration sensor based on this Talbot effect. Our vibration sensor can be non-contact, low-cost, high sensitivity in nanometer scale, compact and portable because the Talbot distance is very small (mm to cm). In the near future, we will also pursue a matter-wave interferometric experiment of the near-field type because it accepts uncollimated beams, thus ensuring a high throughput when working with atoms and small molecules which tend to have a low flux compared to light beams.

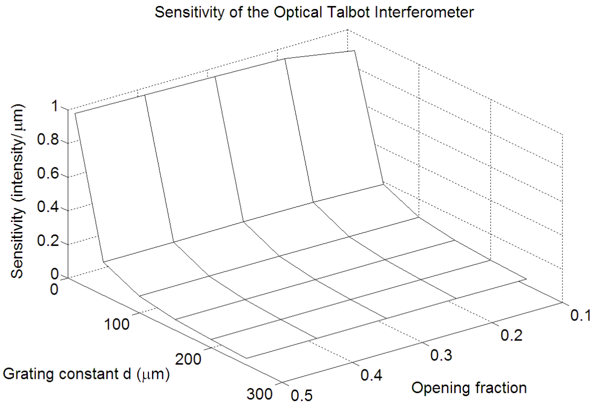

Figure 5. A 3-D plot of the sensitivity of the Talbot intererometry as a function of grating constant (d) and opening fraction (f). The simulation is done with the z distance of one Talbot length and with Eq (5).

Acknowledgments

S.D. acknowledges the support grant from the office of the higher education commission and the Thailand research fund (TRF) under contract number MRG5380264 and the National Electronics and Computer Technology Center, National Science and Technology Development Agency and Industry/University Cooperative Research Center (I/UCRC) in HDD Component, the Faculty of Engineering, Khon Kaen University and also Department of Physics, Faculty of Science, Burapha university. We also thank the Faculty of Science, Burapha University for financial support via the research funds.

References

1. H. F. Talbot, “Facts relating to optical science”, Philosophical Magazine series **9** (1836), 401.
2. M. Berry, I. Marzoli, and W. Schleich, “Quantum carpets, carpets of light”, Physics World **14** (2001), 1078.
3. W. B. Case, M. Tomand, S. Deachapunya, and M. Arndt, “Realization of Optical Carpets in the Talbot and Talbot-Lau Configurations”, Optics Express **17** (2009), 20966.
4. S. Mirza and C. Shakher, “Surface profiling using phase shifting Talbot interferometric technique,” Optical Engineering **44** (2004), 013,601.
5. P. Singh, M. Faridi, and C. Shakher, “Measurement of temperature of an axisymmetric flame using shearing interferometry and Fourier fringe analysis technique,” Opt. Eng. **43** (2004), 387.
6. G. Spagnolo, D. Ambrosini, and D. Paoletti, “Displacement measurement using the Talbot effect with a Ronchi grating,” J. Opt. A **4(6)** (2002), 376.
7. B. J. McMorran and A. D. Cronin, “An electron Talbot interferometer,” New J. Phys. **11** (2009), 033,021.
8. M. S. Chapman, C. R. Ekstrom, T. D. Hammond, J. Schmiedmayer, B. E. Tannian, S. Wehinger, and D. E. Pritchard, “Near-Field Imaging of Atom Diffraction Gratings: The Atomic Talbot Effect,” Phys. Rev. A **51** (1995), R14.
9. S. B. Cahn, A. Kumarakrishnan, U. Shim, T. Sleator, P. R. Berman, and B. Dubetsky, “Time-Domain de Broglie Wave Interferometry,” Phys. Rev. Lett. **79** (1997), 784.
10. B. Brezger, L. Hackermueller, S. Uttenthaler, J. Petschinka, M. Arndt, and A. Zeilinger, “Matter-Wave Interferometer for Large Molecules,” Phys. Rev. Lett. **88** (2002), 100,404.
11. S. Gerlich, L. Hackermueller, K. Hornberger, A. Stibor, H. Ulbricht, M. Gring, F. Goldfarb, T. Savas, M. Mueri, M. Mayor, and M. Arndt, “A Kapitza-Dirac-Talbot-Lau interferometer for highly polarizable molecules,” Nat. Phys. **3** (2007), 711.

Photonics and Optoelectronics

Prototype Microfluidic System for Fluorescence-based Chemical Sensing

S. Rujihan[1], P. Kittidachachan[1], and B. Damrongsak[2*]

[1]*Department of Physics, Faculty of Science, King Mongkut's Institute of Technology Ladkrabang, Bangkok, 10520, Thailand*
[2]*Engineering Physics Research Group, Department of Physics, Faculty of Science, Silpakorn University, Nakorn Pathom, 73000, Thailand*
[*]*Corresponding author. E-mail: badin@su.ac.th*

Abstract

In this paper, a prototype microfluidic system for fluorescence detection is presented. The system consists of several components, i.e., an excitation light source, a polymer-based microfluidic channel and an optical detector. Experiments are conducted to demonstrate use of the developed system for fluorescence detection in chemical applications. Three fluorescent dyes, i.e. Rhodamine 6G, Coumarin 153 and DCM, with different concentrations ranging from 100 nM to 5 mM are used as the analyte in the experiments. Relationship between the photoresponse of the microfluidic system and concentration of fluorescent dyes is investigated. The results are compared to that obtained from a bulk system where the analyte under test is dispensed into a standard-size cuvette. In the bulk system, we found a decrease in the fluorescence signal when dye concentration is higher than 10^{-5} for Rhodamine 6G and 10^{-4} M for Coumarin 153 and DCM. This is probably due to the re-absorption and self-quenching phenomena which result in low quantum yield of fluorescent dyes at high concentration. However, such problem is not found in the microfluidic system that has a low detection volume.

***Keywords*:** Fluorescence detection, lab-on-a-chip, chemical sensor, optical detection system.

Introduction

Fluorescence detection has been well known as a reliable and highly sensitive technique to measure toxic heavy metal contamination in ambient environment (e.g., mercury, cadmium and lead) [1-3]. Commercially available fluorescence systems are typically bulky and expensive; hence making it inconvenience for on-site measurement which requires small devices. For this reason, there has been much research to develop compact and low-cost fluorescence detection systems [4-6]. In recent decades, microfluidic systems have attracted much interest in various fields, e.g. biology, chemistry and physics, due to their miniaturization offering the ability to work with the small amount of volume/sample and portability. The fabrication of microfluidic devices is relatively simple and cheap; thus, making such devices an ideal choice for portable sensor system to detect toxic heavy metals.

In this paper, we present the development and characterization of a prototype microfluidic system for fluorescence detection. The diagram of the prototype microfluidic system is shown in Figure 1. A high power LED is used as a main light source instead of a tungsten lamp or a laser, thus making the system more compact and inexpensive. Theoretical model is also developed to investigate relationship between the photo-response of the microfluidic system and concentration of fluorescent dyes. Fabrication of a microfludic channel is described. Experiments are performed and results are then compared with the developed theoretical model.

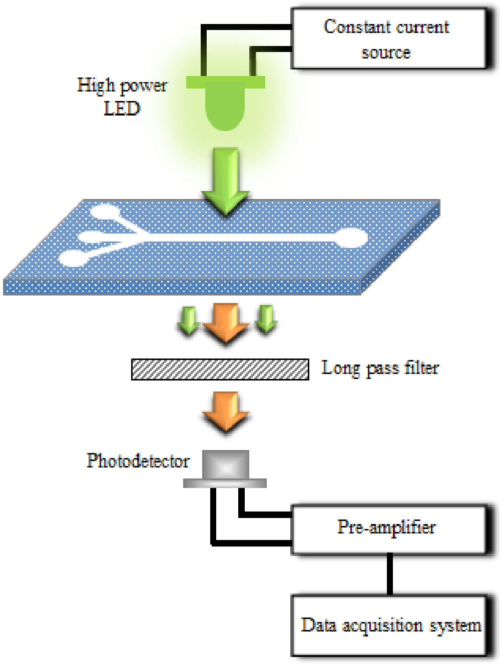

Figure 1. Diagram of a prototype microfluidic system for fluorescence detection.

Theoretical Background

A theoretical model based on Beer Lambert's law is developed in order to calculate the output of a prototype microfluidic system corresponding to different dye concentration. First, when the light with the excitation power P_0 travels through a microchannel containing dye solution, the transmitted power P_T can be expressed using Beer Lambert's law as

$$P_T = P_0 e^{-\alpha(\lambda)x} \tag{1}$$

where x is the optical path length through the dye solution and $\alpha(\lambda)$ is the absorption coefficient.

The power that is absorbed by fluorescence dye can then be calculated using Equation (2)

$$P_A = P_0 - P_T = P_0\left(1-e^{-\alpha(\lambda)x}\right) \tag{2}$$

where P_A is the absorbed power.

When a dye is illuminated by the excitation light, it emits photons at longer wavelength with a power P_F. The amount of emitted fluorescence power is proportional to the absorbed power and the fluorescence quantum yield ϕ_F, which can be given by

$$P_F = \phi_F P_A = \phi_F P_0\left(1-e^{-\alpha(\lambda)x}\right). \tag{3}$$

The fluorescence quantum yield is the ratio of the amount of emitted light over that of absorbed light.

In our microfluidic system, the emission light is observed through a long pass filter that suppresses the excitation wavelength. Therefore, only some emitted fluorescence can reach a photodetector. The output photocurrent I_{photo} is then proportional to the responsivity of the photodetector itself and the amount of emitted fluorescence reaching the photodetector, which can be given as

$$I_{photo} = R(\lambda) T_{filter} \phi_{CE} P_F \tag{4}$$

where $R(\lambda)$ is the wavelength dependent responsivity of the photodetector, T_{filter} is the transmittance of the long pass filter and ϕ_{CE} is the collection efficiency which is the ratio of the amount of collected fluorescence over total emission fluorescence.

Replacing the fluorescence emitted power from Equation (3) into (4), we have

$$I_{photo} = R(\lambda) T_{filter} \phi_{CE} \phi_F P_0\left(1-e^{-\alpha(\lambda)x}\right) \tag{5}$$

For the sake of simplification, some term is combined into a single lumped parameter K, called a K-factor. The K-factor depends on the responsivity of the photodetector, the filter transmittance, the collection efficiency of the system, the fluorescence quantum yield and the excitation power.

$$I_{photo} = K\left(1-e^{-\alpha(\lambda)x}\right) \tag{6}$$

where $K = R(\lambda) T_{filter} P_0 \phi_{CE} \phi_F$.

In chemistry, the absorption coefficient is proportional to the molar absorptivity $\varepsilon(\lambda)$ and the concentration c of a chemical species as

$$\alpha(\lambda) = \varepsilon(\lambda)c \tag{7}$$

Hence, the output photocurrent as a function of concentration can be written as

$$I_{photo}(c) = K\left(1-e^{-\varepsilon(\lambda)cx}\right) \tag{8}$$

Equation (8) is used for fitting experimental data for all experiments in this paper.

Experimental Method

Fabrication of microfluidic channels

Microfluidic channels used in this experiment were fabricated in house using the process flow described in [7]. First, the master mold of the desired pattern was fabricated using the printed circuit board technology. The next step, called replica molding, was done using poly-dimethysiloxane (PDMS) as a starting material. This PDMS part was used to create microfludic devices. The last step is PDMS-glass bonding. Prior to bonding, holes were drilled manually in PDMS for fluidic connections. Surface treatment using oxygen plasma was used to clean both PDMS and glass slide. Immediately after plasma treatment, PDMS is placed into contact with the glass slide and complete the bonding.

Experiment setup

Experiments were conducted to study the relationship between the photoresponse of the microfluidic system and concentration of fluorescent dyes. Three fluorescent dyes, i.e. Coumarin 153, DCM and Rhodamine 6G (Rh6G), with different concentrations ranging from 100 nM to 1 mM were used as the analyte in the experiments. In this study, a high power LED was used as the excitation light source. It was chosen in such a way that there is overlap between its peak wavelength and the absorption spectra of the fluorescence dyes. Therefore, UV LED with a peak wavelength of 396 nm was used as the excitation light for Coumarin 153, a blue LED with a peak wavelength of 451 nm for DCM dye and a green LED with a peak wavelength of 396 nm for Rh6G. Emission fluorescence was then observed by (1) a spectrophotometer (Avantes) in order to study the emitted spectra of fluorescence dyes and (2) a silicon photodetector (Roithner Laser) in order to study the corresponding photocurrent as a function of dye concentration.

Figure 2 and 3 show the diagram of the experimental setup for fluorescence spectroscopy measurement when sample is contained in a standard-size cuvette and a microfluidic channel, respectively. The investigation of the photocurrent in response to the variation of dye concentration was carried out using the experimental setup shown in Figure 1.

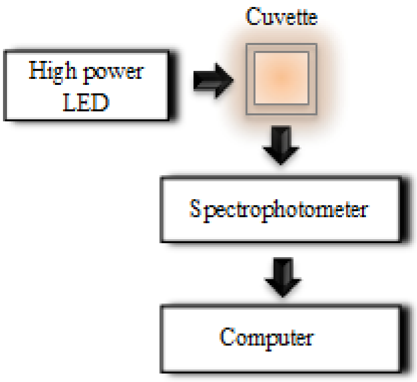

Figure 2. Diagram of the experimental setup for fluorescence spectroscopy measurement when sample is in a cuvette holder.

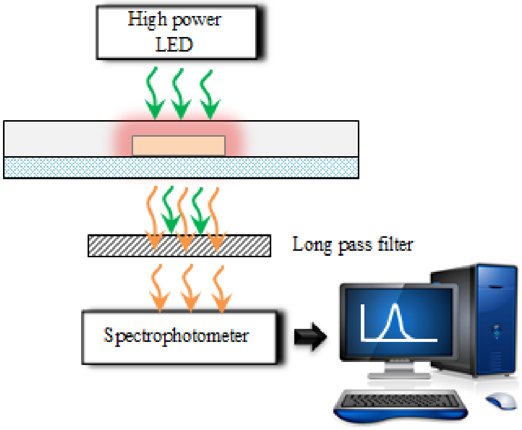

Figure 3. Diagram of the experimental setup for fluorescence spectroscopy measurement with a microfluidic channel.

Results and Discussion

The emission spectra of fluorescence dyes (Coumarin 153, DCM and Rh6G) corresponding to different dye concentration varying from 10^{-7} to 10^{-3} M are shown in Figure 3, 4 and 5, respectively. In the bulk system, we found a decrease in the fluorescence signal when dye concentration is about 1mM. This is probably due to the re-absorption and self-quenching phenomena which result in low quantum yield of fluorescent dyes at high concentration. However, such problem is not found in the microfluidic system that has a low detection volume; thus, making it has a dynamic range greater than the bulk system.

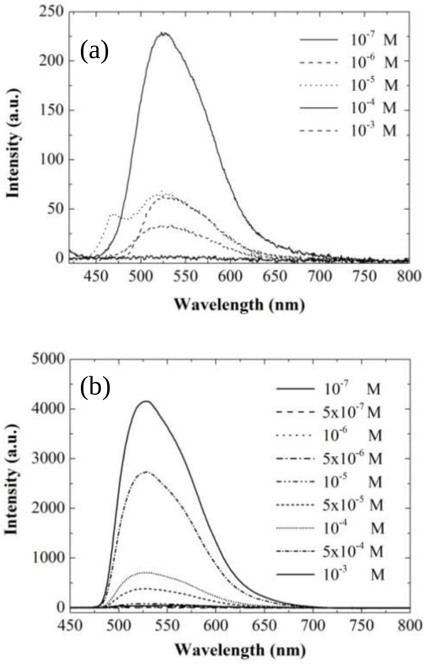

Figure 4. Fluorescence spectra of Coumarin 153 dyes in ethanol solution with different concentrations. The solution is contained in (a) a cuvette holder and (b) a microfluidic channel.

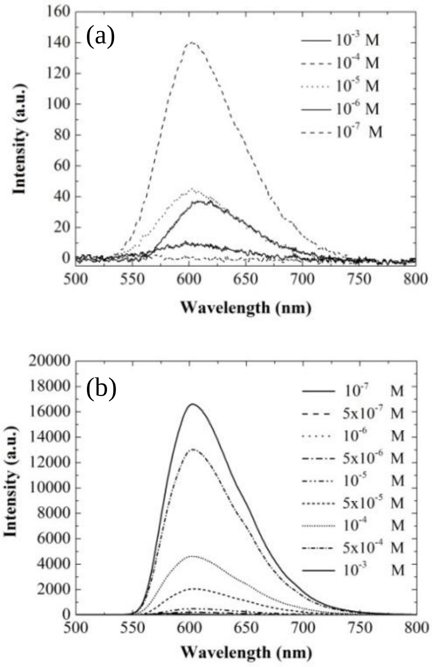

Figure 5. Fluorescence spectra of DCM dyes in ethanol solution with different concentrations The

solution is contained in (a) a cuvette holder and (b) a microfluidic channel.

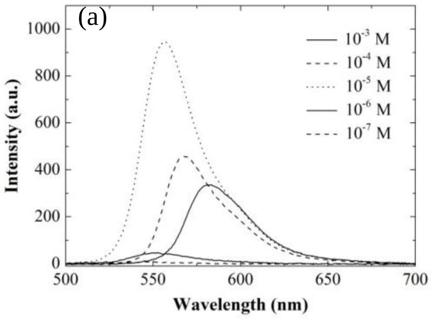

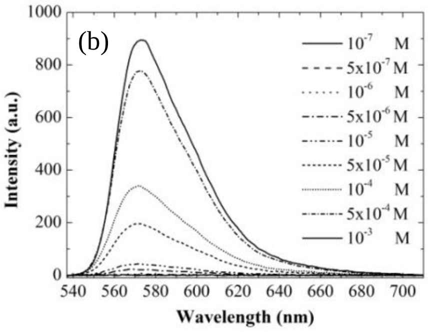

Figure 6. Fluorescence spectra of Rh6G dyes in ethanol solution with different concentrations. The solution is contained in (a) a cuvette holder and (b) a microfluidic channel.

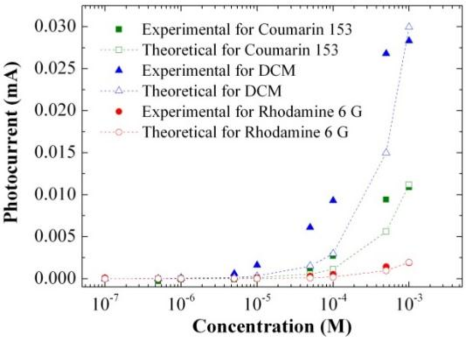

Figure 7. Experimental results and theoretical model of the photocurrent corresponding to different dye concentration.

Relationship between the output (photocurrent) of the prototype microfluidic system with regard to the variation of dye concentration was investigated using experimental setup shown in Figure 1. The experimental results for all three fluorescence dyes are shown in Figure 7. Then fitting a theoretical model using Equation (8) to experimental data was carried out. The optical path x is measured from the height of the microchannel, which is equal to 70 μm. The molar absorptivity $\varepsilon(\lambda)$ was taken from the standard value (the PhotochemCAD package version 2.1a) at the excitation wavelength. K-parameters were chosen in such a way that the R^2 value of the trend line is very close to 1. Fit parameters are shown in Table 1.

Table 1: Fit parameters for each fluorescence dyes

Dyes	**K**	ε **(× 10^5)**	**R^2**
Coumarin 153	8.00	1.16	0.89
DCM	10.20	2.00	0.81
Rh6G	0.24	4.20	0.91

Conclusions

The prototype microfluidic system for fluorescence-based heavy metal detection in ambient environment was developed and characterized. The results obtained from the prototype microfluidic system show higher dynamic range than that of the bulk system. This is due to the re-absorption and self-quenching found in the bulk system. In addition, the relationship between the photoresponse of the system corresponding to different dye concentration was modeled based on Beer Lambert's law. The measured results showed a good agreement to that of the theoretical model.

Acknowledgments

Authors gratefully acknowledge Dr.Sirapat Pratontep at College of Nanotechnology, KMITL for assistance with oxygen plasma treatment. We also would like to thank faculty of science, KMITL for financial support.

References

1. A. P. Demchenko, Introduction to Fluorescence Sensing, Springer, 2009.
2. L. Basabe-Desmonts, D. N. Reinhoudt and M. Crego-Calama, "Design of Fluorescent Materials for Chemical Sensing," Chem. Soc. Rev., **36** (2007), 993.
3. H. Liu, P. Yu, Dan Du, C. He, B. Qiu, X. Chen and G. Chen, "Rhodamin-based Ratiometric Fluorescence Sensing for the Detection of Mercury(II) in Aqueous Solution," Talanta **81** (2010), 433.
4. D. Zhang, L. Men and Q. Chen, "Microfabrication and Applications of Opto-Microfluidic Sensors," Sensors **11** (2011), 5360.
5. S. Kou, *et al.*, "Microfluidic Detection of Multiple Heavy Metal Ions Using Fluorescent Chemosensors," Bull. Korean Chem. Soc. **30** (2009) 1173.
6. A. Banerjee, Y. Shuai, R. Dixit, I. Papautsky and D. Klotzkin, "Concentration Dependence of Fluorescence Signal in a Microfludic Fluorescence Detector.
7. S. Rujihan, P. Kittidachachan and B. Damrongsak, "Low-cost Fabrication of Masters for Plastic-based Microfluidic Devices," 7th

annual conference of Thai Physics Society, SPC2012, May 9-12, 2012, Ayutthaya, Thailand.

Physics Teaching

A Development of the Demonstration Based-exercise Project

P. Leevongwat, S. Meeklin, W. Putchana, and A. Ratanavis *

Laser Physics Laboratory, Department of Industrial Physics and Medical Instrumentation, Faculty of Applied Science, King Mongkut's University of Technology North Bangkok, Bangkok 10800 Thailand
**Corresponding author. E-mail: amarinr@kmutnb.ac.th*

Abstract

It remains a challenge to perform real experiments in physics during large lectures. The demonstration based-exercise (DBE) project is proposed as an approach to support the interactive lecture demonstration (ILD) strategies. In particular, the DBE project focuses on a combination between free available softwares and low cost devices to perform a demonstration on a projection screen in large lecture halls. In the DBE approach, students make predictions, observations, explanations and calculations on problem exercises. In addition, a so called "Ticker" device is proposed to be used as a learning tool for the DBE project in the part of "hear-and-see" activities.

***Keywords*:** Interactive lecture demonstrations, Physics demonstrations**,** Light sensors

Introduction

It is a well-known problem on the insufficient learning of students on introductory university physics using traditional lectures [1]. The curriculum development based on physics education research has been proven as a great approach to mitigate this problem [2, 3, 4]. To support such a development, lecture demonstrations are desirable to enhance learning activities in physics. Demonstrations mean to gain student attention and participation during class lectures. Learning process can be improved by demonstrations which encourage student engagement [5]. However, several attempts on various demonstrations found difficulties on teaching large classes. The major drawback of lecture demonstrations is that the equipments are expensive and too bulky. Simulated experiments or virtual laboratories can be alternative approaches to allow simplicities of presentations [6, 7, 8]. However, real demonstrations promote students to encounter not only concepts in physics but also experimental setup procedures, errors, quantitative results as well as solving technical problems that may occur during demonstrations. The mentioned drawback of traditional demonstrations can be circumvented through technological advances in electronic devices. The interactive lecture demonstrations (ILDs) using microelectronics based laboratory (MBL) equipments have been proposed to serve as lecture demonstrations [9]. For the ILD procedures, students predict, observe and discuss the demonstration [9]. Despite apparent successes of improving student learning [10], the cost of ILDs based on MBL is relatively higher than traditional demonstrations. In addition, there is still room for further development of ILDs.

In this paper, we describe the demonstration based-exercise (DBE) project that has been proposed as an approach to support ILDs with the concentration on problem solving exercises based on demonstrations. In addition, we also explore possibility of using a so called device "Ticker" as a toolkit for the DBE project.

A development of the DBE project

The DBE project is being developed in the department of industrial physics and medical instrumentation, King Mongkut's University Technology of North Bangkok, Thailand. The aim of the DBE project is to create demonstration environments on a large projection screen combining features of a webcam, free available computer softwares and low cost physics equipments. The project also aims to provide supports for students with disabilities. By using this teaching approach, students can participate the demonstration by making predictions, observations, explanations and calculations. Several simple experiments described in general laboratory exercises and research articles have been adapted more or less to be applicable on the DBE strategies. To illustrate the DBE procedures, the demonstrations on beat frequency, diffraction and conservation of momentum and energy are described as examples.

Physics of sound

In recent years, there has been considerable interest in physics experiments involving the technique of the sound detection [11, 12]. Such experiments have used a free sound editor program called Audacity [13]. Audacity was used in observations of sound resonance phenomena and beat frequencies on a video sharing website [14]. The goal of this demonstration is to study the beat frequency between sound waves generated by a tuning fork and Audacity. In lecture halls, the beat frequency is mostly pictured as the mathematical description of the interference of two waves with different frequencies. To illustrate the shape of the beat wave experimentally, Audacity was used to create various sound frequencies. At the same time, the tuning fork was hit to produce the sound. An example of the beat frequencies is shown in Figure 1. In this demonstration, students can be asked to identify the beat frequency obtained by the demonstration.

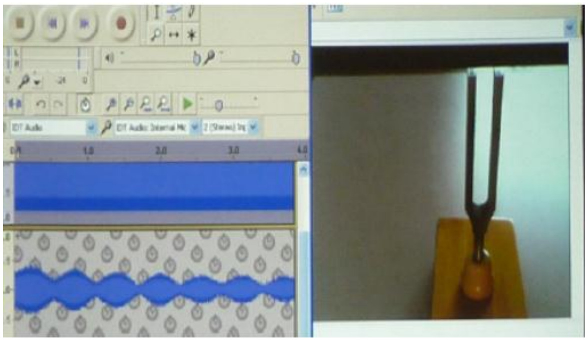

Figure 1. A demonstration of the beat frequency. The frequency of the tuning fork was 439 Hz while the frequency generated by a free sound editor program “Audacity” was 441 Hz.

Diffraction

The diffraction experiment based on a single slit is one of classic experiments in the introductory physics level. A simple diffraction experiment can be conducted on the DBE strategy (see Figure 2). Advances in diode or solid state laser technology offer low cost laser pointers acting as light sources. In addition, a vernier can be set as an apparatus to form a single slit. The appearance of the diffraction pattern on a detection screen can be captured by a webcam allowing a real-time exhibition on the projection screen.

The analysis of the diffraction pattern shown on the projection screen may need supports from additional programs. There are a number of available programs to serve on this purpose. In this investigation, a free program called Screenmarker [15] was used to mark the minima of the diffraction pattern. Furthermore, a free program called Screenruler [16] was used to measure the lengths between the marks on the projection screen (the length calibration of the Screen-ruler is required). According to this demonstration, students can determine the wavelength of the laser pointer using the information shown on the projection screen such as the width of the center maximum, distance between the minima, etc., associated to the slit width and the distance between the slit and the detection screen. In addition, the noteworthy advantage of this demonstration over the traditional exercise is the technique of the space calibration for students to gain experience.

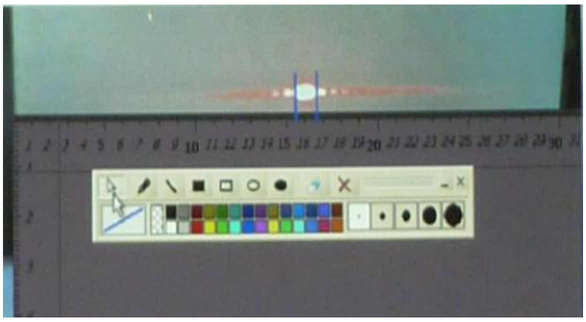

Figure 2. The diffraction of a red laser pointer on a single slit. A vernier served as a single slit with the width of 0.2 mm. The distance from the vernier to the diffraction screen was 1.9 m.

Conservation of momentum and energy

The relationship between the conservation of energy and the conservation momentum is still a challenge topic in physics teaching. The connection between the energy and momentum is truly essential for physics. An attractive treatment to reach the importance of such a topic is an experimental observation.

The DBE project handles this activity by choosing an example of the collision between two identical golf balls which can be approximated about an elastic collision. The two golf balls were attached to very light strings to form simple pendulums. The golf ball A was freely released from a height to collide the ball B sitting at rest.

Figure 3. Conservation of energy and momentum of collided golf balls. The maximum height of the ball B after collided by ball A describes the relationship between the conservation of energy and the conservation of momentum. The marked line refers to the released position of the ball A when it was released.

This demonstration was based on recording and analyzing videos. VirualDub [17] can be used to record and play the video of the experiment. The programs, Screenmarker and Screen-ruler, can be used to measure the height of the ball A and B during the experiment on the recorded video. The observation revealed that the ball B reached the maximum height at the same level as the ball A when it was thrown (see Figure 3). The result shows the relationship between the conservation of momentum and the conservation energy on the collided pendulums. Such a relationship points out that the velocity of the ball A before the collision was the same as the velocity of the ball B after the collision. From the results shown on the projection screen, students can be asked to calculate the velocities of the balls before and after the collision at various heights of throwing.

Ticker

The development of DBE project also aims toward "hear and see" activities. These demonstrations offer the interactive problem solving exercises. Students can appreciate the physics of experiments by solving problems using the information provided by demonstrations. In addition, such demonstrations can be used to support student with disabilities. We are seeking some demonstrations and suitable devices that will allow students with visual impairments to hear as well as students with hearing impairments to see the demonstrations. We have invented the Ticker device to fulfill these purposes. Ticker serves as the timing device which can generate the ticking sound. To illustrate Ticker applications, the experiments on simple pendulum and simple harmonics will be used as examples. Many conclusions obtained by such examples will be applied to promising physics experiments that could be performed by using Ticker.

A development of Ticker and its components

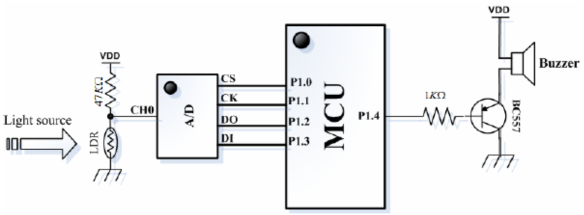

Figure 4. (a) LDR responds to the change of light intensity. An analog-to-digital converter (A/D) converts the voltage signal to a digital number and sends it forward to a microcontroller (MCU) being in command of the buzzer.

The primary concept of Ticker was concerned to durability, spectral response to available light sources and economic cost. Ticker consists of a light sensor, a simple circuit and a buzzer. The operating principle of Ticker is based on the change of intensity of a light source that incidents to its light sensor. As a consequence, the simple circuit will send the signal to turn on the buzzer that will generate the ticking sound. The circuit diagram of Ticker is shown in Figure 4. In this preliminary study of the Ticker, we use a light dependent resistor (LDR) as our light sensor due to its durability and low price. LDR is also attractive for its high responsivity in the range between 500 nm to 600 nm which can be used with current available light sources for example red and green laser pointers, and light emitting diodes (LEDs). However, the main drawback of the LDR is the slow rise time which is in the order of millisecond (ms). Therefore, the time resolution of ms should be an awareness of the LDR uses.

In addition, Ticker was also developed to provide the ability to connect a personal computer via a USB interface. With equipped Ticker program, the experimental data can be collected in a real time. Furthermore, the compact size of Ticker offers various practical adaptations and orientations for potential physics demonstrations. Figure 5 shows Ticker and its developed software.

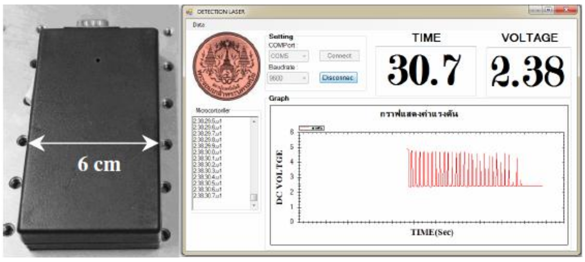

COMPort : COM5
Baudrate : 9600
TIME 30.7
VOLTAGE 2.38

Figure 5. Ticker and its software.

The use of Ticker can be alternatively approached by using free sound analysis programs such as Audacity and the sound card oscilloscope [18] reflecting the heightened technological benefits to users.

The applications of Ticker can be illustrated by using simple physics experiments such as a simple pendulum and a simple harmonic motion (SHM) of springs. The choice of these experiments was due to the time scale of these experiments which are in the order of hundred ms. In these demonstrations, Ticker serves a timing device with ms resolution replacing a classic stop watch. To emphasize the use of Ticker with free available softwares, the ticking sound was recorded by the sound card oscilloscope.

Simple pendulum

In this demonstration, a simple pendulum consisted of a small bob suspended by a cord (almost weightless compared to the bob). It can swing freely in the simple harmonic fashion. Figure 6 shows the demonstration.

The light source used in the demonstration was a HeNe laser. The Ticker was placed on the opposite side of the laser to receive the incident light. The bob cut the laser beam when it passed the aligned beam position. During such an event, Ticker created the ticking sound. The ticking sound was recorded by the sound card oscilloscope. In this demonstration, students can perform an exercise identifying the acceleration due to gravity on the surface of earth (g) from the observed oscillation period.

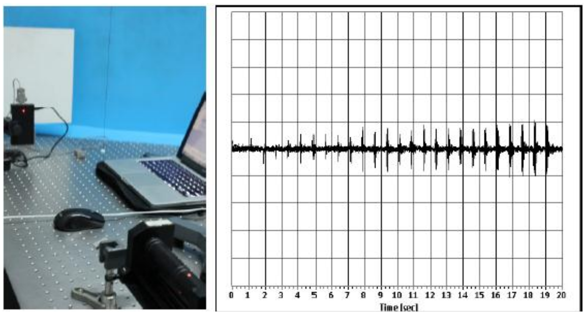

Figure 6. A demonstration on simple pendulum. The length of the cord was 56 cm.

SHM of a spring

A mass hanging on the end of a vertical spring is an excellent example of a system that will perform SHM. Figure 7 shows the SHM demonstration. A spring with attached mass was pulled away from its equilibrium and it was then released. The edge of the attached mass blocked the beam path when it oscillated. Again, Ticker generates its sound when the laser beam was terminated. In this demonstration, the calculation of the spring constant can be left as an exercise for students.

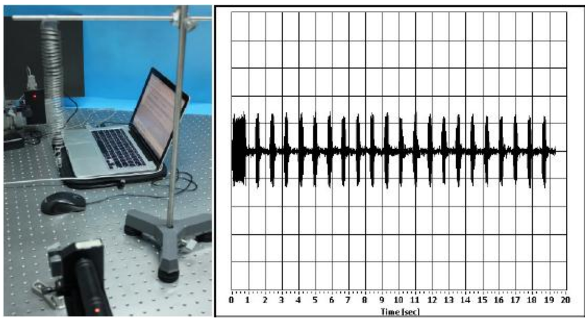

Figure 7. A 50 g-mass was hung on a vertical spring. The Ticker sound was recorded by the sound card oscilloscope.

Conclusions

The DBE project is being developed to perform real-time demonstrations in physics on large lecture halls via projection screens. The DBE project is seeking an economic solution for ILD strategies with providing problem solving exercises. The sound, diffraction, and collided pendulum experiments are excellent examples of the DBE project. The DBE project allows the old physics equipments sitting in warehouses, garages or boxes to be reused again. In addition, some materials or equipment can even be found in the normal household.

Ticker serves as a timing device for the DBE project. The examples of physics experiments such as simple pendulum and simple harmonics are presented to illustrate the use of Ticker. These experiments can be performed with simplicities of setup and detection with the error less than 5%. Ticker leaves a huge room for creativity on potential physics experiments and then benefits both students and instructors leading to a development of learning and teaching physics with low cost technological advances.

Acknowledgments

This research work is financially supported by the Office of the Higher Education Commission, and King Mongkut’s University of Technology North Bangkok.

References

1. L. McDermott and E. Redish, “Resource letter PER-1: physics education research”, Am. J. Phys. **67**(1999) 755.
2. E. Redish, “Teaching physics with physics suite”, Wiley (2003).
3. L. Keiner and T. Burns, “Interactive engagement: how much is enough?”, Phys. Teach. **48**(2010)108.
4. B. Spike and N. Finkelstein, “Preparing tutorial and recitation instructors: A pedagogical approach to focusing attention on content and student reasoning”, Am. J. Phys. **80**(2012)1020.
5. C. Crouch, A. Fagen, J. Callan and E. Mazur, “ Classroom demonstrations: Learning tools or entertainment?”, Am. J. Phys. **72**(2004)835.
6. M. Gonzalez, G. Arranz, R. Portales, M. Tamayo and A. Gonzalez, “Development of a virtual laboratory on the internet as support for physics laboratory training”, Eur. J. Phys. **23**(2002) 61
7. J. Anderson and M. Barnett, “Using video games to support pre-service elementary teachers learning of basic physics principles”, J. Sci. Educ. Technol. **20**(2011) 347.
8. V.Teodoro, “Playing newtonian games with Modellus”, Phys. Educ. **39**(2004)421.
9. D. Sokoloff and R. Thornton, “Using interactive lectue demonstration to creat an active learnig Environment”, Phys. Teach. **35**(1997) 340.
10. M. Sharma, I. Johnston , H. Johnston, K.Varvell, G. Robertson, A. Hopkins, C. Stewart, I. Cooper, and R. Thornton, “Use of interactive lecture demonstrations: A ten year study”, Phys. Rev. ST Physics Ed. Research **6**(2010) 020119.
11. J. White, A. Medina, F. Romn, and S. Velasco, “ A Measurement of g Listening to Falling Balls”, Phys. Teach. **45**(2007) 175.
12. J. Groppe J 2011 The hope of audacity (to teach acoustic) Phys. Teach. **49**(2011)99.
13. http://audacity.sourceforge.net
14. http://wwww.youtube.com
15. http://www.screenmarker.com

16. http://wonderwebware.com/screen-ruler/
17. http://www.virtualdub.org
18. http://www.zeitnitz.de/Christian/scope_en

A Worksheet for the Recovery of Students' Vector Understanding

U. Wutchana[1*]

Faculty of Education, Ramkhamkaeng University, Hua Mark, Bangkapi, Bangkok, 10241, Thailand
[*]Corresponding author. E-mail: peak_um@hotmail.com

Abstract

Lacking of understanding about vectors might cause serious problems in learning physics when the vector concepts are embedded in almost all physics concepts. Student might be unable to use vectors in solving problems about kinematical quantities, forces or fields. Many studies have shown students still hold misconception about vectors although they have studied it before. Based on students' misconception, the researcher intended to design a worksheet to recover their understanding of vector direction, magnitude, addition and subtraction before starting their initial physics topics. A 2-page worksheet was constructed and distributed to 36 high-school students in a large public school in Bangkok. Students took approximately 20 minutes to complete the worksheet. A seven-item diagnostic quiz was applied as a pre-post test in order to evaluate the effectiveness of the worksheet. Using paired-sample t-test ($p<0.000$), results from the diagnostic quiz showed that the students' average post-test score was significantly higher than their average pre-test score. In other words, the students' normalized learning gain was 0.53 which was considered a medium gain that might be reached by conducting classes with active learning activity only. It indicated that the worksheet was also effective as a well organized activity while taking a very short time. This might be used to reduce students' difficulty in learning physics caused by a lack of skills and understanding about vectors.

Keywords: Vectors; Basic vector concept; Vector addition; Vector subtraction; Vector teaching

Introduction

Beginning in about 1980, physics education research began to show that the traditional class left most students confused about the basic concepts of mechanics and other important areas including optics, heat and thermodynamics, electricity and magnetism and so on. Subsequently, a growing number of researchers began to design some effective instructional strategies to teach physics concepts. Some previous studies have shown that students' difficulty in learning physics is mainly caused by a lack of skills and understanding about mathematics, especially vectors [1-2]. Students require a good grasp of basic vector concepts to succeed in a physics course [3]. While understanding vector is necessary, physics education researchers also found that students still hold misconception about vectors although they have studied it before [4-7].

Vectors are component of mathematics which is an essential language for physics [4]. Normally, high-school students face vectors as the first topic when they start learning their first physics course. Even in general university physics textbooks, vector concepts are set as the first topic. Basically, the vector concepts are included in the introduction chapter of a physics textbook. Both at the high-school and university levels, students have to study a lesson of vectors. Lacking of understanding about vectors might cause many serious problems when the vector concepts are embedded in almost all physics concepts [8-9]. For example, student might be unable to use vectors in solving problems about kinematical quantities, forces or fields.

Based on the author's idea that recovering students' understanding of basic vector might reduce their difficulties in physics learning, this study intended to design an appropriate worksheet for the recovery of the students' understanding in order to reduce their difficulties in learning before starting their initial physics topics. It was also interesting to know how students who already completed their vector lesson understood the concepts of basic vector and what their difficulty was.

Thus, this article set out to explore 36 high-school students' understanding of basic vector concepts (vector magnitude, direction, addition and subtraction) and also to illustrate the preliminary results of the worksheet instruction.

Background

It might be deduced from previous studies that understanding of initial topics in physics requires the ability to reason about vectors [4-7]. Students require a good grasp of basic vector concepts to succeed in a physics course [2-3]. As the starting point, Knight [4] surveyed students' pre-understanding of vector concepts before starting calculus-based physics course using his *Vector Knowledge Test* focusing on algebraic aspects of vectors. The results from his study showed that less than half of those students had sufficient skills with vectors to read the text and solve typical problems although they had studied the concept of vectors before. In the years 2000-2001, for both fall and spring semesters, Nguyen and Meltzer [5] investigated 2,031 physics students' understanding of vector addition, magnitude, and direction for problems presented in graphical form. They administered a seven-item quiz, including free-response problems, in all introductory general physics courses at Iowa State as pre/post-test. Results showed that most of the students were unable to carry out two-dimensional vector addition after completing a physics course. Flores, Kanim and Kautz [6] described some of the procedural and reasoning difficulties they observed in students' use of vectors. Consistent with the work of Nguyen and Meltzer, students had difficulties performing basic vector operation. They found that many students were not able to add or subtract vectors graphically after traditional instruction, and could not answer qualitative questions about vector addition and subtraction. Shaffer and McDermott [7] investigated the ability of university students to treat velocity and acceleration as vectors in one- and two-dimensions. Some vector difficulties were identified among those students. Not only the introductory students but also many precollege teachers and even graduate students, vector operation difficulties were observed. Flores-Garc´ıa, Alfaro-Avena and Dena-Ornelas [1] concluded from the literatures that most students have difficulties with vector addition and subtraction for both with and without physics context.

In Thailand, also students still hold misconception especially in graphical vector addition for both one- and two-dimensions. The finding was presented by the work of Wutchana and Emarat [10] in 2011. By using the diagnostic quiz previously used by Nguyen and Meltzer and deeply analyzing student responses from two free-response problems of graphical vector addition in one- and two-dimensions, they found that there was a variety of student misunderstanding with vector properties and operation. Most students did not grasp the important concept about the vector direction and how a vector may be moved while its magnitude and direction are preserved. Many students were still confused about the tip to tail addition. These findings are consistent with the work of Knight [4] and also the work of Nguyen and Meltzer [5].

Methodology

Worksheet description

The findings of Wutchana and Emarat [10] in the year 2011 indicated that students' common misunderstanding about graphical vector addition in one- and two-dimensions comprised (1) missing the direction of resultant vector ($\vec{R}$), (2) giving a wrong direction of resultant vector ($\vec{R}$), (3) attaching two vectors in various ways and not giving resultant vector ($\vec{R}$), (4) connecting two original vectors without making an attachment, (5) making various triangles, and (6) connecting between two vector tips.

From the study, they suggested four important points that physics instructors should check to make sure that their students understand: 1) students realize that vector quantities comprise both magnitude and direction; 2) students understand that a vector can be moved and while moving a vector, its magnitude and direction must be preserved; 3) students know that when adding two vectors, one vector's tip must be attached to the other vector's tail and; 4) students are clear that the direction of the resultant vector points from the tail of the initial vector to the tip of the second vector.

Based on these suggestions, in this study, a worksheet was designed to resolve student difficulties in basic vector concepts. There were three parts in the worksheet. Part 1: vector quantities included suggestion points 1 and 2. For point 1, students were asked to draw a symbol and identify magnitude and direction of the given vectors. They might be aware that vector quantities should be composed of both magnitude and direction. For point 2, vector preserve, students were assigned to draw vectors that contained the same magnitude with the given one and the vectors with the same direction as well. An exercise on moving vectors to any point was successively given before they learned how to add vectors. The students were assured that vectors can be moved and they must also ensure that they preserve their magnitude and direction while moving them. Part 2: one-dimension vector addition and part 3: two-dimension vector addition included suggestion points 3 and 4. For point 3, the major problem was that students did not know the correct way to attach two vectors. They simply attached the vector tails together and then made the connection between the vector tips to form a resultant vector [10]. Many students added the vectors by creating a wrong triangle. Most of them thought that adding two vectors meant just attaching them to each other without knowing how to do it properly. To clarify their understanding that adding vectors meant connecting those vectors from tail to tip or tip to tail. The students were asked to add all given vectors in one- and two-dimensions starting with adding two and three vectors in one-dimension, then, two vectors in two dimensions and following with two vector subtraction in one- and two-dimensions. Consequently, the students were given an exercise of three vector addition and subtraction in two dimensions, to check their understanding. At the last point, resultant vector direction is also embedded in parts 2 and 3. During adding and subtracting vectors, students had to consider that direction of the resultant vector will point from the started vector tail to the final vector tip.

Data collection

As one group pretest-posttest design, data was collected from a class of 36 grade eleven students from a large public school in Bangkok during the 1st semester of 2012 academic year. The students previously took two physics courses which already contained the basic vector concepts. Those concepts are also embedded in other physics topics including kinematical quantities, forces and fields that they had studied before.

During the first meeting hour, a diagnostic quiz translated from the work of Nguyen and Meltzer [5] was administered to the students to measure their understanding of vector direction, magnitude, addition and subtraction presented in a graphical form. The diagnostic quiz includes problem #1: vector magnitude, problem #2: vector direction, problem 3: Qualitative vector addition, problem #4: One-dimensional vector addition, problem #5: Two-dimensional vector addition, problem #6: Two dimensional vector subtraction, and problem #7: Comparison of resultant magnitude. Students were asked to give a free response or to select multiple options from a list. Except for problems #3 and #7, the students were given possible choices. The students spent 20 minutes to complete the quiz. The designed worksheet, then, was distributed to the students individually. Taking approximately 20 minutes, the students recovered their vector understanding following the worksheet step accompanied with teacher guidance. After completing the worksheet, they have to study their first physics topic. A week later, the diagnostic quiz again was administered to the students as a post-test in order to evaluate effectiveness of the worksheet instruction. Like the pre-test, the students spent 20 minutes to complete.

Results and Discussion

The pre-test could establish a baseline for students' understanding before the instruction and post-test could represent students' understanding after the instruction. Differences between pre- and post-test could indicate effectiveness of the worksheet instruction.

Table 1: Class average pre- and post-test scores on the diagnostic quiz

Pre-test	**Post-test**	**Sig**	**<g>**
3.3	5.3	0.000*	0.53

* Significant 2-tailed

Table 1 shows the whole class's pre- and post-test average scores on the seven-item quiz (maximum score is 7). They are 3.3 for pre-test and 5.3 for post-test, respectively. The difference between pre- and post-test average scores is statistically significant using paired-sample t-test ($p<0.000$). It could be said that the students' understanding were improved or they recovered their understanding of basic vector concepts after the worksheet instruction. The whole class normalized learning gain is 0.53 which could be considered a medium gain ($0.3 \leq \langle g \rangle_{medium} < 0.7$) [12] that might be reached by conducting classes with active learning activity only.

Not only the pretest establishes a baseline for student understanding before the instruction but it also provides insights into the nature of specific difficulties. Although the students have studied basic vector concepts before, their average score on the pre-test is lower than a half of the maximum score. Considering their correct responses to the pre-test, low numbers were found in problems #7, #2, #6, and #5 as presented in table 2. It was interesting to know how these students understand each concept of the basic vector. To clarify this doubt, their conceptual learning gains in each problem were categorized.

Table 2: Number of the students' correct responses to the diagnostic quiz during pre- and post-test

Problems	**Pre-test**	**Post-test**	**<g>**
#1	23	29	0.46
#2	10	12	0.08
#3	26	30	0.40
#4	22	33	0.79
#5	19	34	0.88
#6	17	22	0.26
#7	6	31	0.83

According to the above presented results, it could be noted that the worksheet instruction could recover students' understanding of vector magnitude (#1). More students could identify the vectors that contained equal magnitude even when its direction differed. Their normalized gain for this problem was 0.46, considered to be a medium gain. Especially for graphical vector addition in one- (#4) and two-dimensions (#5), the students learned these concepts very well. Their conceptual learning gains were 0.79 and 0.88, respectively. These were considered as very high gains ($\langle g \rangle_{high} \geq 0.7$) that might be rarely reached by conducting classes even with active learning activity [12]. The worksheet instruction was also good for recovering understanding of the resultant vector direction (#3) and magnitude (#7) since a number of students' correct response reached 80% after the instruction. The normalized gains were 0.40 and 0.83. However, the worksheet needed to be reconstructed in the parts for the recovering of the concepts of vector direction (#2) and subtraction (#6). The normalized gains were 0.08 and 0.26, considered as low gain ($\langle g \rangle_{low} < 0.3$).

Problem #2 asks students to select vectors that have the same direction with the given one. Numbers of the students providing correct responses were very low both for pre- and post-test. It indicated that not only this worksheet instruction but also previous courses could not clarify the students' understanding of this particular topic. Deep analysis of the students' responses indicates that common student error is selecting a vector with its direction just closing to the given vector but not exactly the same as shown in figure 1.


2. จงพิจารณาเวกเตอร์ที่กำหนดให้ด้านล่าง เวกเตอร์ใดบ้างที่มี<u>ทิศทาง</u>เดียวกับเวกเตอร์ $\vec{A}$

ตอบ |A| ทิศเดียวกับ |F| ทิศเดียวกับ |G|

Figure 1. 61% of the students choose both $\vec{F}$ and $\vec{G}$.

Be vectors considered the same direction, its angle to vertical and horizontal lines should be the same. This revealed that the students might not be aware of these properties of vectors. For this worksheet, an exercise on vector direction should be added or modified.

Problem #6 is about vector subtraction in two dimensions. When looking back to vector addition in two dimensions, most students worked well on problem #5. The highest gain appeared there. It means common errors on vector subtraction might not be caused by lacking understanding of vector addition although subtracting vectors is adding with the opposite direction vectors. To be clear about students' difficulties and understand various algorithms that they used to subtract vectors, their post responses to problem #6 were analyzed. Their responses were categorized into five groups. There were 61% of the correct responses. Some students (11%) added the two given vectors ($\vec{A}$ and $\vec{R}$) to find $\vec{B}$ while 14% of them worked with correct subtraction algorithm but redrew $\vec{A}$ and $\vec{R}$ without preserving its magnitude and direction. Another 6% of the students connected two given vectors with different strategies and the last 8% provided no answer.

Considering percentages of each category, possible reasoning could be that students did not understand the correct strategy for subtracting vector. The worksheet may need a separate part for students to tract the subtraction strategy. A part asking students to draw vectors with the same magnitude but opposite direction might be added in order to ensure that students realize opposite direction vectors before starting the subtraction.

Conclusions

The most crucial thing is that spending 20 minutes with the 2-page worksheet could recover students' understanding of basic vector concepts. Conducting classes following these four suggested points, students could grasp all important vector concepts which might reduce some serious problems in learning kinematical quantities, forces, fields and so on. These can be confirmed by the students' post-test scores on the diagnostic quiz which is significantly higher than their pre-test scores. The post-test correct responses are higher than the pre-test in every problem as well. However, it is just a preliminary conducting of the worksheet instruction that needs a later study for validation.

Acknowledgments

The author would like to thank Ramkhamhaeng University for providing, in part, the support for the manuscript presentation at Siam Physics Congress SPC2013. Special thanks must go to Assoc. Prof. Ampai Kiatchai for her English grammatical check.

References

1. S. Flores-Garc´ıa, L. L. Alfaro-Avena, and O. Dena-Ornelas, Students' understanding of vectors in the context of forces. REVISTA MEXICANA DE FI´SICA E **54** (2008), 7.
2. G. Zavala, and P. Barniol, Students' understanding of the concepts of vector components and vector products. in Presentation given at Physic Education Research Conference PERC 2010. July 21-22, 2010. Portland, OR, USA.
3. H. D. Sheets, Communicating with Vectors. The Physics Teacher **33** (1998), 74.
4. R. D. Knight, The Vector Knowledge of Beginning Physics Students. The Physics Teacher **33** (1995), 74.
5. N. Nguyen, and D. E. Meltzer, Initial understanding of vector concepts among students in introductory physics course. American Journal of Physics **71** (2003), 630.
6. S. Flores, S. E. Kanim, and C. H. Kautz, Student use of vectors in introductory mechanics. American Journal of Physics **72** (2004), 460.
7. P. S. Shaffer, and L. C. McDermott, A research-based approach to improving student understanding of the vector nature of kinematical concepts. American Journal of Physics **73** (2005), 921.
8. J. M. Aguirre, Student Preconceptions about Vector Kinematics. The Physics Teacher **26** (1988), 212.
9. J. M. Aguirre and G. Rankin, College students' conceptions about vector kinematics. Physics Education **24** (1989), 290.
10. U. Wutchana, and N. Emarat, Students' Understanding of Graphical Vector Addition in One and Two Dimensions. Eurasian Journal of Physics and Chemistry **3** (2011), 102.
11. J. Roche, Introducing vectors. Physics Education **32** (1997), 339.
12. R. R. Hake, Interactive-engagement versus traditional methods: A six-thousand student survey of mechanics test for introductory physics course. American Journal of Physics **66** (1998),64

An Alternative Derivation Kinetic Theory of Gases

P. Khongrattna, P. Kessratikoon, and N. Choosiri*

Physics Department, Faculty of Science, Thaksin University,
Songkhla, 90000, Thailand
**Corresponding author. E-mail: nikom@tsu.ac.th*

Abstract

According to molecular model of an ideal gas, Bernoulli showed that the pressure that a gas exerted on the walls of its container was a consequence of the collisions of the gas molecules with the walls and he got the expression of pressure, $P = \frac{1}{3}(N/V)m\overline{v^2}$. In Bernoulli's model he used a cubical box as a container of gases and used Cartesian coordinates for his derivation. However in 1999 Peffer showed that by using spherical coordinates and a sphere as a container of gases the expression $P = \frac{1}{3}(N/V)m\overline{v^2}$ could be performed. In this paper, the cylindrical coordinates and a cylinder as a gas container were used to apply to molecular model of an ideal gas and the result showed that our pressure expression was the same as that obtained by Bernoulli and Peffer.

Keywords: Kinetic theory of gas, Molecular model of an ideal gas, Cubical box, Sphere, Cylinder

Introduction

Kinetic theory of gases was first introduced by Daniel Bernoulli in 1737[1], his theory showed that such large-scale properties of gases could be related to a description on a microscopic scale of gases, where gases were treated as a collection of molecules provided a reasonable description of thermodynamic process. In his model of gas behavior, called kinetic theory provides us with a physical basis for our understanding of the concept of temperature.

In developing a microscopic model of an ideal gas, Bernoulli made some assumptions[2] such as the number of molecules in the gas was large, and separation between them was large compared with their dimensions, the molecules obeyed Newton's law of motion but as a whole they moved randomly, etc.

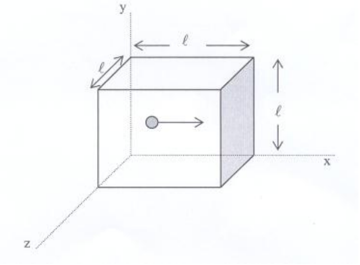

Figure 1. A cubical box with side of length ℓ containing an ideal gas.

For the first application of kinetic theory we shall derive an expression for the pressure of N molecules of an ideal gas in a container of volume V in term of microscopic quantities. The container is a cube with edges of length ℓ (Fig. 1). We shall first focus our attention on one of these molecules of mass m and assume that it is moving so that it component of $\vec{v}$ in the x direction as shown in Figure 1. As the molecule collides elastically with any wall, the change in x component of the momentum of the molecule is

$$\Delta p_x = -2mv_x \, .$$

Because the molecules obey Newton's law, we can apply the impulse-momentum theorem to the molecule to give us

$$\bar{F}_x \Delta t = -2mv_x \, ,$$

where $\bar{F}_x$ is the x component of the average force that the wall exerts on the molecule during the collision and Δt is the duration of the collision. The time interval between two collisions with the same wall is .

$$\Delta t = 2\ell / v_x \, .$$

Thus, we can rewrite the impulse-momentum theorem as

$$\bar{F}_x(on\ molecule) = -m\frac{v_x^2}{\ell} \, .$$

Now, by Newton's third law, the average x component of the force exerted by the molecule on the wall is

$$\overline{F}_x(on\ wall) = -(-m\tfrac{v_x^2}{\ell}) = m\tfrac{v_x^2}{\ell}\,.$$

The total average force exerted by the gas on the wall is found by adding the average force exerted by the individual molecules. We add terms such as that above for all molecules :

$$\overline{F}_x = \sum_{i=1}^{N} m\tfrac{v_{xi}^2}{\ell} = \frac{m}{\ell}\sum_{i=1}^{N} v_{xi}^2\,.$$

However for a very large number of molecules such as Avogadro’s number the average force given above is the same over any time interval. Thus, the constant force F on the wall due to the molecular collision is

$$\overline{F}_x = \frac{m}{\ell}\sum_{i=1}^{N} v_{xi}^2\,. \qquad (1)$$

By expressing the average value of the square of the x component of the velocity for molecules as :

$$\overline{v_x^2} = \frac{1}{N}\sum_{i=1}^{N} v_{xi}^2\,,$$

the total force on the wall can be written :

$$F_x = \frac{m}{\ell}N\overline{v_x^2}\,. \qquad (2)$$

Now let us focus again on the molecule with velocity component v_{xi}, v_{yi} and v_{zi}. The Pythagorian theorem relates the square of the speed of the molecule to the square of the velocity components :

$$v_i^2 = v_{xi}^2 + v_{yi}^2 + v_{zi}^2\,.$$

Hence, the average value of v^2 for all molecules in the container is related to the average of v_x^2, v_y^2 and v_z^2 according to the expression

$$\overline{v^2} = \overline{v_x^2} + \overline{v_y^2} + \overline{v_z^2}\,.$$

Because the motion is completely random, the average $\overline{v_x^2}, \overline{v_y^2}$ and $\overline{v_z^2}$ are equal to each other. Using this fact and the preceding equation, we find that

$$\overline{v^2} = 3\overline{v_x^2} = 3\overline{v_y^2} = 3\overline{v_z^2}\,. \qquad (3)$$

Thus from equation 2, we can find the total force on the wall is

$$F = \frac{m}{3\ell}N\overline{v^2}\,,$$

and we can find the total pressure exerted on the wall

$$P = \frac{F}{A} = \frac{F}{\ell^2} = \frac{1}{3}\left(\frac{N}{V}\right)m\overline{v^2}\,. \qquad (4)$$

Materials and Methods

Cylindrical Coordinates

In some physical situations it is convenient to use cylindrical coordinates for solving problems, such as in an electric field line problem when there is a constant charge density on an infinite straight wire. By the definition, cylindrical coordinates (ρ,φ,ρ) system relates to Cartesian coordinates system (x,y,z) as shown in Figure 2.

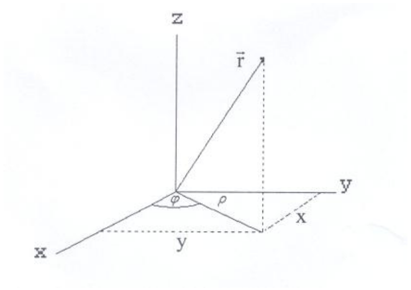

Figure 2. The relation between cylindrical coordinates and Cartesian coordinates.

From figure 2 we find that

$$\left.\begin{array}{l} x = \rho\cos\varphi \\ y = \rho\sin\varphi \\ z = z \end{array}\right\} \qquad (5)$$

where ρ is a projection of $\vec{r}$ on the xy plane.

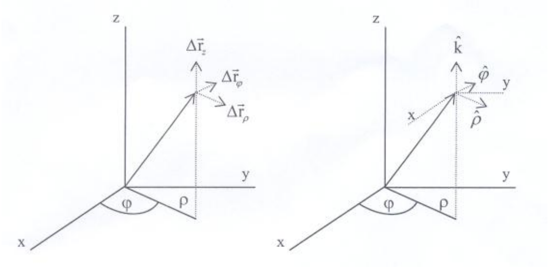

Figure 3. The increments of the components of a radius vector $\vec{r}$ in cylindrical coordinates system and the unit vectors .

By using cylindrical coordinates system, any vector can be written in the form

$$\vec{A} = A_\rho \hat{\rho} + A_\varphi \hat{\varphi} + A_z \hat{k} .$$

Similarly for the velocity, in cylindrical coordinates system, we have

$$\vec{v} = v_\rho \hat{\rho} + v_\varphi \hat{\varphi} + v_z \hat{k} . \qquad (6)$$

However, in Cartesian coordinates system equation 6 becomes

$$\vec{v} = v_x i + v_y j + v_z \hat{k} . \qquad (7)$$

From equation 6 and 7 we get

$$v_\rho \hat{\rho} + v_\varphi \hat{\varphi} = v_x \hat{i} + v_y \hat{j} ,$$

or in other words,

$$v_{\rho\varphi}^2 = v_\rho^2 + v_\varphi^2 = v_x^2 + v_y^2 = v_{xy}^2 . \qquad (8)$$

From equation 3 and equation 8 it is found that the average of $v_{\rho\varphi}^2$ can be written as

$$\overline{v_{\rho\varphi}^2} = \frac{2}{3} \overline{v^2} . \qquad (9)$$

Results and Discussion

The Derivation of a gas Pressure According to Kinetic Theory by Using a Cylinder as a Gas Container

In this section let us derive an expression for the pressure of N molecules in a cylinder of volume V with radius of length ρ and height of length h in terms of microscopic quantities. Consider the ith molecule with velocity $\vec{v}_i$ moving in a cylinder as shown in Figure 4.

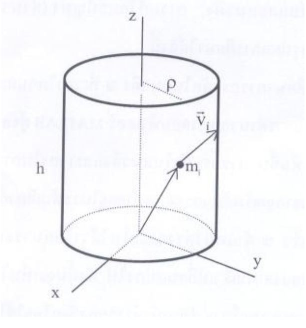

Figure 4. A cylinder containing an ideal gas, the molecule shown moves with velocity $\vec{v}_i$.

By considering the velocity of the ith molecule within the cylinder, the component of velocity in an xy plane is $\vec{v}_{\rho\varphi} = v_\rho \hat{\rho} + v_\varphi \hat{\varphi}$. This component of velocity is responsible for the pressure in $\hat{\rho}$ direction while the component of velocity in $\hat{k}$ direction leads to the pressure on the top and the bottom walls of the cylinder. However, from equation 4, for the pressure in $\hat{k}$ direction, we obtain

$$P = \frac{1}{3}\left(\frac{N}{V}\right) m\overline{v^2} .$$

Now we consider the pressure on the side wall of the cylinder due to the impulse in $\hat{\rho}$ direction.

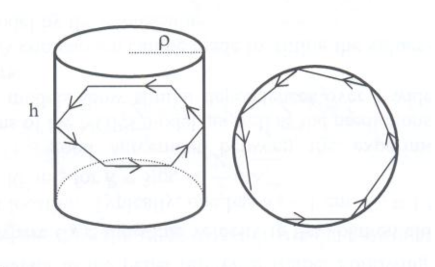

Figure 5. The direction of momentum in an xy plane after multiple of collisions.

Let us consider $\vec{v}_{\rho\varphi} = v_\rho \hat{\rho} + v_\varphi \hat{\varphi}$, this component of velocity leads to a sequence of collisions as shown in figure 5. However, according to Peffer's ideas[3]the path of motion of a gas molecule may be treated as a circular motion of radius ρ due to the centripetal force. For the ith molecule, it is written in the form

$$F_{ic} = \frac{m v_{i\rho\varphi}^2}{\rho} .$$

The surface area of the side wall of a cylinder is given by

$$A = 2\pi\rho h ,$$

and the pressure of a gas molecule exerts on a side wall is

$$P_i = \frac{F_{ic}}{A} = \frac{m v_{i\rho\varphi}^2}{2\pi\rho^2 h} = \frac{m v_{i\rho\varphi}^2}{2V} .$$

The total pressure exerted by the gas on the wall is found by adding the pressure exerted by the individual molecule, we obtain

$$P = \sum_{i=1}^{N} P_i = \frac{m}{2V} \sum_{i=1}^{N} v_{i\rho\varphi}^2 . \qquad (10)$$

However, the factor $\sum_{i=1}^{N} v_{i\rho\varphi}^2$ can be transformed into $N\overline{v_{\rho\varphi}^2}$,so that equation 10 becomes

$$P = \frac{m}{2V} N\overline{v_{\rho\varphi}^2} \,. \qquad (11)$$

However, from equation 9 we have $\overline{v_{\rho\varphi}^2} = \frac{2}{3}\overline{v^2}$,so that equation 11 can be rewritten as

$$P = \frac{1}{3}\left(\frac{N}{V}\right) m\overline{v^2} \,. \qquad (12)$$

It is the same form as that obtained by Bernoulli.

Conclusions

According to kinetic theory of an ideal gas, the pressure of a gas that exerts on the wall of its container is a consequence of the collisions of the gas molecule with the walls. From the molecular model of an ideal gas, Bernoulli used a cube as a gas container and used Newton’s law of motion to get the expression of the pressure in the form of equation 4. Here, we use a cylinder as a gas container and consider the pressure of a gas on the side wall of the cylinder, by using Peffer’ s ideas which treats the path of motion of a gas molecule in an xy plane as a circular motion due to a centripetal force from the wall, then we also get the pressure expression in the form of equation 4. From this study we can conclude that the mathematical formula of a gas pressure is independent of geometrical shape of a gas container.

References

1. D. H. Trevena, Statistical Mechanics an Introduction, Ellis Horwood, Chichester., 1993.
2. R. A. Serway and J.W. Jewett, (6th) Physics for Scientist and Engineers, Thomson/Cole © 2004, 2004.
3. J.I. Peffer, “An Alternative Derivation Kinetic Theory of Gas”, Physics Education **3**(1999) 237.

An Experimental Observation of Faraday's Law of Induction

Satina Srisuna[1,2], S. Boonduang[1], and S. Limsuwan[1*]

[1]*Department of Physics, Faculty of Science, King Mongkut's University of Technology Thonburi, Bangkok 10140, Thailand*
[2]*Saint Gabriel's College, 565 Samsen Rd., Bangkok 10300, Thailand*
[*]*Corresponding authors. E-mail: supanee.lim@kmutt.ac.th*

Abstract

A cylindrical magnet was dropped from rest through a coil which encircled a PVC pipe. The coil consisted of 100 turns of copper wire. The velocity of the magnet at the coil plane was varied by dropping the magnet from different heights. The voltage signal induced in the coil was recorded and measured using a digital storage oscilloscope. The results showed that the maximum induced voltage and magnetic flux were 3.42 V and 9.30 Vs, respectively.

Keywords: Electromagnetic induction, Faraday's law, magnetic flux

Introduction

Electromagnetic induction is a significant subject in high school and undergraduate physics courses and it is difficult for most students [1,2]. Because this subject involves more abstract concepts and mathematical sophistication far beyond what they have experienced [2,2]. Furthermore, almost all the quantities are invisible such as magnetic field, flux and potential. Unlike mechanics, where many situation involue familiar macroscopic objects. Furthermore, most important concepts, such as velocity and force are easily related to everyday experience [2,3].

In the past decades, various demonstrations and experiments on electromagnetic induction phenomena have been introduced to help students overcome their learning problems [1,4-9]. In this work, we investigate the electromagnetic induction phenomenon due to a magnet falling through a coil from different heights.

Materials and Methods

The magnets used are neodymium disk magnets. Each one has a diameter of 10 mm and 3 mm thick. For convenience to drop the magnet through the PVC pipe, six disk magnets were stacked up together to form a cylindrical magnet.

The PVC pipe with an inner diameter of 12 mm and 80 cm long was supported vertically by a steel rod and meter stick as shown in Figure 1. At the lower end of the PVC pipe, it was wound with 200 turns using #26 copper wires. The width of the coil was approximately 1 cm. The magnet was dropped from rest, with the north end up, above the coil from different heights of 20, 30, 40, 50, 60 and 70 cm.

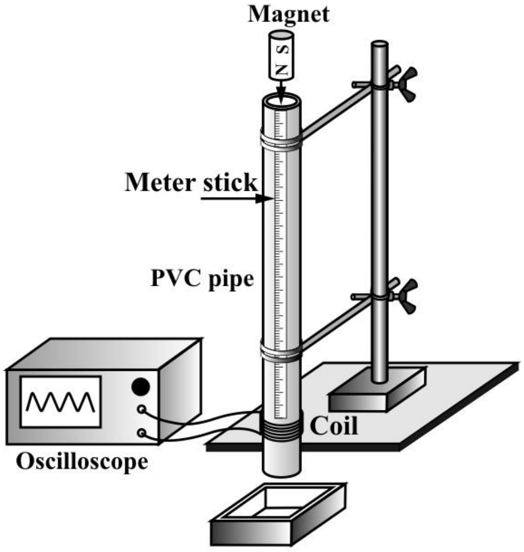

Figure 1. Experimental setup.

As it passes through the center of the coil, the speed of the magnet is given by $v = \sqrt{2gh}$, where g is the acceleration due to gravity and h is the distance from the magnet to the coil. Therefore, the velocities corresponding to the height of 20, 30, 40, 50, 60 and 70 cm were 2.0, 2.4, 2.8, 3.2, 3.5 and 3.7 m/s, respectively.

When the magnet is approaching the coil, the magnetic flux changes quickly, and therefore the induced voltage in the coil increases. After the magnet crosses the coil, the magnetic flux also changes quickly, but it now decreases, and so the induced voltage is high, but with a negative value. This induced voltage was recorded on a digital storage oscilloscope (Agilent, 54621 A).

Due to the small size of the magnet relative to the coil, it will be considered to behave as an ideal point magnetic dipole with a magnetic dipole moment $\vec{m}$ as shown in Figure 2.

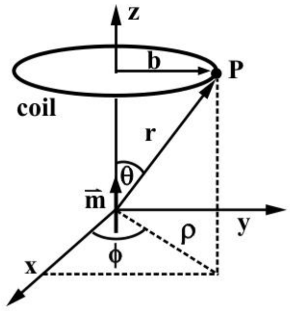

Figure 2. A magnetic dipole was put at the origin and it pointed in the z-direction.

The magnetic field at the point P is given by [10]

$$\vec{B} = \frac{\mu_0}{4\pi}\frac{m}{r^3}(2\cos\theta\hat{r} + \sin\theta\hat{\theta}) \qquad (1)$$

Since
$$\vec{m} = m\hat{k} = m\cos\theta\hat{r} - m\sin\theta\hat{\theta}$$
$$= (\vec{m}\cdot\hat{r})\hat{r} + (\vec{m}\cdot\hat{\theta})\hat{\theta} \qquad (2)$$

and
$$3(\vec{m}\cdot\hat{r})\hat{r} - \vec{m} = 3m\cos\theta\hat{r} - m\cos\hat{r} + m\sin\theta\hat{\theta}$$
$$= (2\cos\theta\hat{r} + \sin\theta\hat{\theta}) \qquad (3)$$

By substituting Eq.(3) into Eq.(1) we obtain

$$\vec{B} = \frac{\mu_0}{4\pi}\frac{1}{r^3}[3(\vec{m}\cdot\hat{r})\hat{r} - \vec{m}] \qquad (4)$$

It is convenient to express this magnetic field in cylindrical coordinates. Therefore, in this case

$$\vec{r} = \rho\cos\phi\hat{i} + \rho\sin\phi\hat{j} + z\hat{k} \qquad (5)$$

and as $\vec{m} = m\hat{k}$. The magnetic field $\vec{B}$ can be written as

$$\vec{B} = \frac{\mu_0 m}{4\pi(\rho^2 + z^2)^{5/2}} \times$$
$$[3z\rho\cos\phi\hat{i} + 3z\rho\sin\phi\hat{j} + (2z^2 - \rho^2)\hat{k}] \qquad (6)$$

In order to obtain magnetic flux through the coil at constant z, a flat surface limited by the coil which is perpendicular to the z axis is used. Taking into account that $d\vec{A} = dA\hat{k}$, where $dA = \rho d\rho d\phi$. Then, evaluation of the integral gives

$$\Phi = \int\vec{B}\cdot d\vec{A} = \int_0^{2\pi} d\phi\int_0^b d\rho\,\frac{\mu_0 m}{4\pi}\,\frac{2z^2\rho - \rho^3}{(\rho^2 + z^2)^{5/2}} \qquad (7)$$

where b is the radius of the circular coil. Solving the integral of Eq. (7), the equation for the magnetic flux is

$$\Phi = \frac{\mu_0 mN}{2}\,\frac{b^2}{(b^2 + z^2)^{3/2}} \qquad (8)$$

where N is the number of turns in the coil.

From Faraday's law of induction, the voltage generated as the magnet moves through the coil is given by

$$V = -\frac{d\Phi}{dt} = -\frac{d\Phi}{dz}\frac{dz}{dt} = -\frac{d\Phi}{dz}v$$
$$= \frac{3}{2}\mu_0 mNb^2\,\frac{zv}{(b^2 + z^2)^{5/2}} \qquad (9)$$

where v is the velocity of the magnet at the coil plane. The derivative of V with respect to z is

$$V' = \frac{dV}{dz} = \frac{3}{2}\mu_0 mNb^2 v\,\frac{(b^2 - 4z^2)}{(b^2 + z^2)^{7/2}} \qquad (10)$$

The extreme values of V occur when $V' = 0$ which leads to $z = \pm b/2$. These values are

$$V = \pm\frac{24\mu_0 mNv}{(5)^{5/2}b^2} \qquad (11)$$

From Eq.(1), the magnetic field of a magnetic dipole on axis is

$$B_z = \frac{\mu_0 m}{2\pi z^3} \qquad (12)$$

Results and Discussion

The magnetic field was measured along magnet axis (B_z) at a distance z from its center using a gauss/tesla meter (F.W. Bell, 5170). The values of B_z at different distances z are given in Table 1 and the plot between B_z and $1/z^3$ is shown in Figure 3.

Table 1: Magnetic field (B_z) at different distances (z)

z (cm)	B_z(mT)	$1/z^3(10^5/m^3)$
0.9	71	13.7
1.0	48	10.0
1.1	36	7.5
1.2	28	5.8
1.3	21	4.5
1.4	18	3.6
1.5	14	2.9
1.6	9	2.4
1.7	6	2.0
1.8	5	1.7
1.9	2	1.4

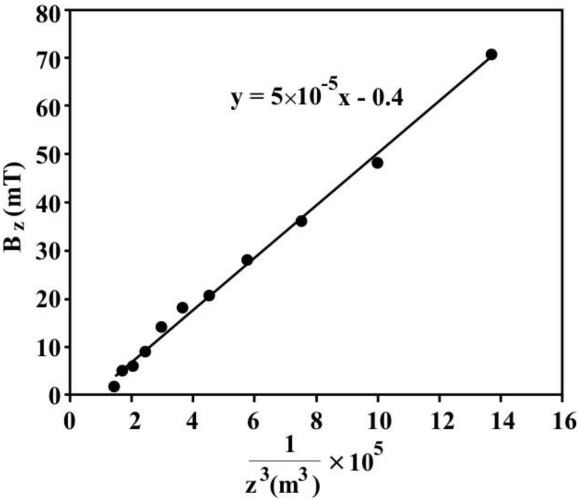

Figure 3. A graph of B_z and $1/z^3$.

From Eq. (12), $m = \frac{2\pi}{\mu_0}\frac{B_z}{z^3} = \frac{2\pi}{\mu_0}$ slope

$$= \frac{2\pi}{4\pi \times 10^{-7}} \times 5 \times 10^{-8} = 0.25\,\mathrm{Am}^2$$

where $\mu_0 = 4\pi \times 10^{-7}\,\mathrm{N/A}^2$

The induced voltage was recorded on a digital storage oscilloscope. Figure 4 shows a typical induced voltage waveform on the digital oscilloscope.

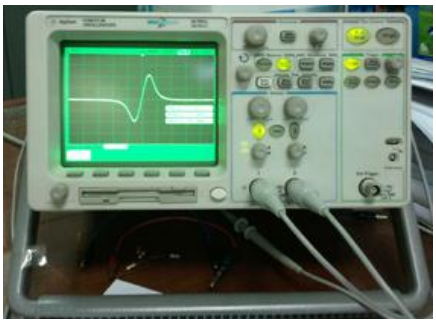

Figure 4. Showing the induced voltage pulse.

Figure 5 shows the printout of various induced voltages recorded on a digital storage oscilloscope when the magnet was dropped towards the coil at different heights. Figure 5 suggests that the peak of induced voltage pulse is higher and sharper for a magnet falling at a higher height (e.g. 70 cm) than that of the lower height.

As can be seen in Table 2, the magnetic flux measured during the magnet passed through the coil with various velocities was slightly different.

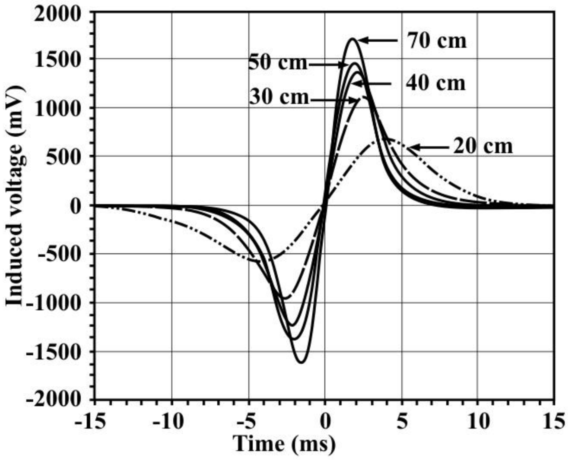

Figure 5. Measured induced voltage pulses for a magnet falling through a coil from different heights of 20, 30, 40, 50 and 70 cm

The peak to peak induced voltages (V_{PP}) in Figure 5 and root mean square voltage (V_{rms}) were also obtained from oscilloscope and the values of V_{PP} and V_{rms} are given in Table 2.

Table 2: Measured values of V_{PP}, $V_{(rms)}$ and flux (Φ)

z(cm)	V_{PP}(V)	V_{rms}(mV)	Flux(Vs)
20	1.99	483	9.01
30	2.38	528	8.92
40	2.74	568	8.98
50	3.00	595	8.91
60	3.22	621	9.30
70	3.42	637	8.97

The magnetic flux (Φ) was obtained experimentally by integrating V-t graph with time. That is, $\Phi(t) = -\int V dt$. The waveform of magnetic flux is shown in Figure 6. The values of magnetic flux are given in Table 2.

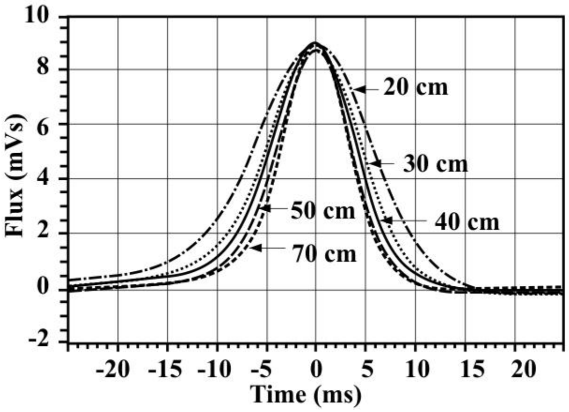

Figure 6. Measured magnetic flux waveforms.

The magnetic flux can be calculated using Eq.(8),

$$\Phi = \frac{\mu_0 mN}{z} \frac{b^2}{(b^2 + z^2)}$$

where m = 0.25 Am^2, b = 20 mm and N = 100 turns. At the coil plane, z = 0, by subsisting μ_0, m, N, b and z into Eq.(8) we obtained Φ = 7.9 Vs. It is seen that the calculated value is in good agreement with that of measured value.

It should be pointed out that the magnetic flux (Φ) of the magnet is independent on the magnet velocity. This conclusion is confirmed by the measured and the calculated values of magnetic flux. It is also observed from Eq.(8) that Φ is independent on the magnet velocity.

The induced voltage can be calculated using Eq.(9), $$V = \frac{3}{2}\mu_0 mNb^2 \frac{zv}{(b^2 + z^2)^{5/2}}$$

where m = 0.25, b = 20 mm and N = 100 turns. We calculated the induced voltage when the magnet arrive at the lower end of the coil, that is z = 1.0 cm from the top coil plane. By substituting μ_0, m, b, N and z into Eq.(9), we obtained the induced voltages as a function of magnet velocity. That is, V = 0.033 v volt = 33 mV. For v = 2.0, 2.4, 2.8, 3.2, 3.5 and 3.7 m/s, we obtained V = 66, 79.2, 92.4, 105.6 and 115.5 mV, respectively.

It is seen that the calculated induced voltage values are much lower than those of measured values (i.e. V_{rms}). Because we calculated the induced voltage only when the lower pole of the magnet arrive at the lower end of the coil (i.e. z = 1.0 cm). Actually, the induced voltage occurred throughout the moving magnet along the core of the coil. That is, the calculated induced voltage should be integrated from z = 0 to z = 1.0 cm.

Conclusions

In this work, a simple experiment for the observation of Faraday's law of induction was presented. A cylindrical magnet was dropped from rest at different heights along a PVC pipe and passed through a coil with 100 turns. The induced voltage was recorded and measured using a digital oscilloscope. It was found that the maximum induced voltage and magnetic flux were 3.42 V and 9.30 Vs, respectively. The calculated values of the induced voltage and magnetic flux were also presented. This experimental setup can help students to develop a deeper and more coherent conceptual understanding of the Faraday's law of electromagnetic induction.

Acknowledgments

This work was supported by Thailand Center of Excellent in Physics (ThEP) and King Mongkut's University of Technology Thonburi under The National Research University Project.

References

1. D. Wong, P. Lee, S.K. Foong, "A Datalogger Demonstration of Electromagnetic Induction with a Falling, Oscillating and Swinging Magnet", Physics Education **45** (2010) 394.
2. P. Onorato, A.D. Ambrosis, "Magnetic Damping: Quantitative Experiments with MBL Sensors", GIREP-ICPE-MPTL Conference 2010, Reims.
3. R. Chabay, B. Sherwood, "Restructuring the Introductory Electricity and Magnetism Course", American Journal of Physics **74 (**2006), 329.
4. R.C. Nicklin, "Faraday's Law-Quantitative Experiments" American Journal of Physics **54** (1986), 422.
5. J.A. Manzanares, "An Experiment on Magnetic Induction Pulses" American Journal of Physics **62** (1994), 422.
6. P. Carpena, "Velocity Measurements Through Magnetic Induction", American Journal of Physics **65** (1997), 135.
7. R. Kingman, S.C. Rowland, S. Popescu, "An Experimental Observation of Faraday's Law of Induction", American Journal of Physics **70** (2002), 595.
8. A. Singh, Y.N. Mohapatra, S. Kumar, "Electromagnetic Induction and Damping: Quantitative Experiments Using a PC Interface", American Journal of Physics **70** (2002), 424.
9. Y. Levin, F.L. da Silveira, F.B. Rizzato, "Electromagnetic Braking: A Simple Quantitative Model", American Journal of Physics **74** (2006), 815.
10. D.J. Griffiths, Introduction to Electrodynamics, 3rd ed., Prentice Hall, New Jersey (1909) 246.

Demonstration of Newton's Ring Experiment using a USB Camera

P. Kopatta[1*] and P. Limsuwan[2]

[1]*Division of Physics, Mahidol Wittayanusorn School, Puttamonthon, Nakhon Pathom 73170, Thailand*
[2]*King Mongkut's University of Technology Thonburi (KMUTT) Bangkok 10140, Thailand*
**Corresponding author. E-mail: pornchai_kopatta@yahoo.com*

Abstract

Newton's ring is one of the most well-known classic experiments of thin film interference. In the experimental setup, a convex lens is placed on an optical flat. The sodium (Na) lamp is generally used as a chromatic light source. The yellow light from Na lamp is reflected by 45° glass slide onto the top surface of convex lens. The light is then transmitted into the convex lens and finally the circular fringes are formed. In conventional experiment, the fringes are observed through the eyepiece of a travelling microscope. However, this method is very difficult for students to setup the experiment for observing circular fringes. Furthermore, the students in the classroom cannot observe the fringes at the same time. In this work, a USB camera was attached to the eyepiece of the travelling microscope for observing the circular fringes. The USB camera was connected to a computer notebook. The picture of circular fringes was then displayed on a computer screen and also on a large projector screen. Therefore, this technique can be used for the demonstration in the classroom and all the students can observe the Newton's ring at the same time.

***Keywords*:** *Newton's rings, USB Camera*

Introduction

Newton's rings are formed due to interference between the light waves reflected from the top and bottom surfaces of the air film formed between the convex lens and glass plate. The monochromatic light such as Na lamp is generally used as a light source. The yellow light from Na lamp is reflected by 45° glass slide onto the convex lens and glass plate to produce the interference as mentioned above and results in the formation of circular fringes. The central fringe is usually a dark fringe. The circular fringes can be observed by a microscope. The real diameter of the whole circular fringes that can be observed is only 1-2 mm. Therefore, it is difficult for student to setup the Newton's ring experiment to observe the circular fringes through the eyepiece of microscope. Moreover, this experiment is usually carried out in the dark room and the student can observe the fringes only one by one. Therefore, it is not possible to demonstrate Newton's ring experiment in the lecture room. In this work, the conventional Newton's ring experiment was modified by attaching a WebCam USB camera to the eyepiece of travelling microscope. Then, the circular fringes was recorded and displayed on a computer screen and also a large projector screen. Therefore, this technique can be used for the demonstration of Newton's ring experiment in the classroom and students in the whole class can observe the circular fringes at the same time.

Materials and Methods

Theory [1-3]

When a plano-convex lens with its convex surface is placed on a plane glass plate, an air film of gradually increasing thickness outward is formed between the lens and the glass plate as shown in Fig.1. The thickness of film at the point of contact is zero. If monochromatic light is allowed to fall normally on the lens, and the film is viewed in reflected light, alternate bright and dark concentric rings are seen around the point of contact. These rings were first discovered by Newton, that's why they are called Newton's rings

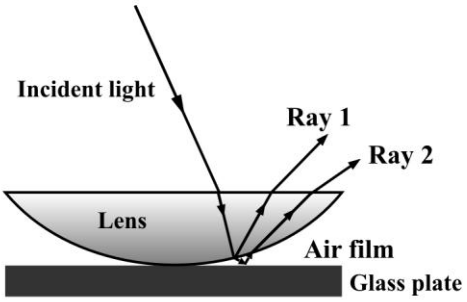

Figure 1. Experinental arrangement for Newton's rings

Newton's rings are formed due to interference between the light waves reflected from the top and bottom surfaces of the air film formed between the lens and glass plate as shown in Fig. 1.

The phenomenon of the formation of the Newton's rings can be explained on the basis of wave theory of light. An air film of varying thickness is formed between the lens and the glass plate. When a light ray is incident on the upper surface of the lens, it is reflected (ray 1) as well as refracted. When the refracted ray strikes the glass plate, it is reflected (ray 2) and undergo a phase change of 180°. Interference occurs between ray 1 and ray 2 which interfere constructively if path difference between them is (m+1/2)λ and destructively if □path difference between them is mλ producing alternate bright and dark rings as shown in Fig. 2.

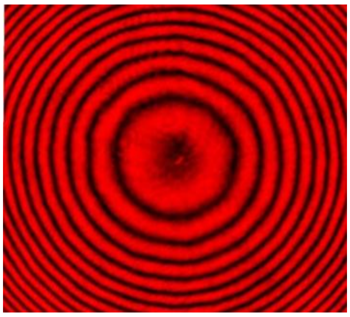

Figure 2. Newton's rings observed through a microscope.

Let the radius of curvature of the convex lens is **R** and the radius of ring is '**r**' as shown in Fig. 3. Consider light of wave length 'λ' falls on the lens. After refraction and reflection two rays **1** and **2** are obtained. These rays interfere each other producing alternate bright and dark rings. At the point of contact the thickness of air film is zero and the path difference is also zero and as a 180^{O} path difference occurs, so they cancel each other and a dark ring is obtained at the center.

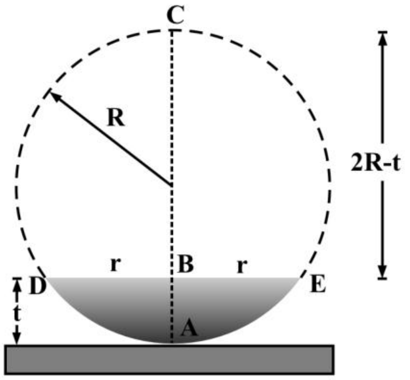

Figure 3. Showing the radius of curvature of lens.

As we move away from the central point , path difference is also changed and alternate dark and bright rings are obtained. Let us suppose that the thickness of air film is '**t**'. By using the theorem of geometry,

$$BD \times BE = AB \times BC$$

$$r \times r = t(2R - t)$$

$$r^2 = (2Rt - t^2)$$

where AB = t
BC = 2R-t
BD = r

Since 't' is very small as compared to 'r', therefore, neglecting 't^2'. Then,

$$r^2 = 2Rt \qquad (1)$$

In thin films, path difference for constructive and destructive interferences are

Bright 2nt = (m+1/2)□λ (2)
Dark 2nt = mλ (3)

where n= refractive index For air n = 1 Therefore,

Bright 2t = (m+1/2) λ (4)
Dark 2t = mλ (5)

where m = 0,1, 2, 3, …

For central dark ring	m = 0
For 1st dark ring	m = 1
For 2nd dark ring	m = 2

From Eq.(5) $t = \frac{m\lambda}{2}$ (6)

Putting the value of t in Eq.(1)

$$r^2 = 2R \cdot \frac{m\lambda}{2}$$

$$= mR\lambda$$

$$\left(\frac{D}{2}\right)^2 = mR\lambda$$

$$D^2 = 4mR\lambda \qquad (7)$$

where D is the diameter of the ring of order m.

Materials

1. A travelling microscope attached on the rail equipped with a veriner scale
2. A sodium light source, λ=5,893 nm
3. A convex lens and a glass plate
4. A Webcam USB camera

Methods

Figure 4 shows the diagram of Newton's ring experimental setup. It consists of travelling microscope a attached on a rail of stainless steel frame. A veriner scale is attached in parallel with the rail. Therefore, during the measurements of the ring diameter by travelling microscope, the distance or ring diameter is measured by veriner scale. At the eyepiece of travelling microscope, it is attached with a WebCam USB camera to record the Newton's rings and transmit to computer for the display on the screen.

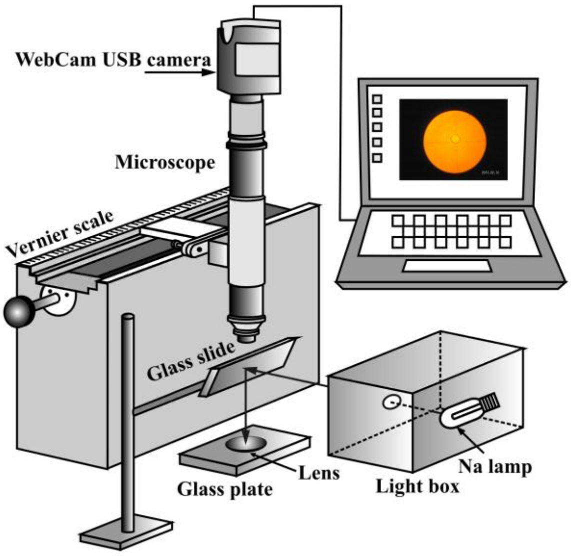

Figure 4. Diagram of Newton’s ring experimental setup.

Results and Discussion

Fig. 5 shows the photograph of Newton’s ring experimental setup.

The front view of Fig.5(a) shows the light box which contains the Na lamp. The 45° glass slide, convex lens and glass plate cannot be observed. The yellow light can pass through a hole on the light box to reflect at 45°glass slide.

From the side view of Fig.5(b), 45° glass slide can be observed. However, due to the yellow light of Na lamp which reflect from 45° glass slide onto the lens surface is to bright the convex lens and glass plate cannot be observed.

Fig.5(c) shows the WebCam USB camera attached on the eyepiece of travelling microscope and USB cable is connected to a notebook computer.

Fig.5(d) shows the appearance of Newton’s rings on the notebook computer screen

Fig.5(e) shows the large circular rings on the notebook computer screen.

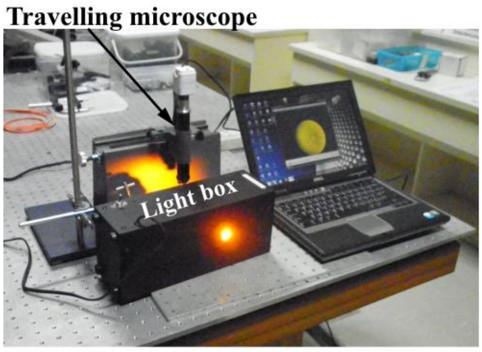

(a) Front view

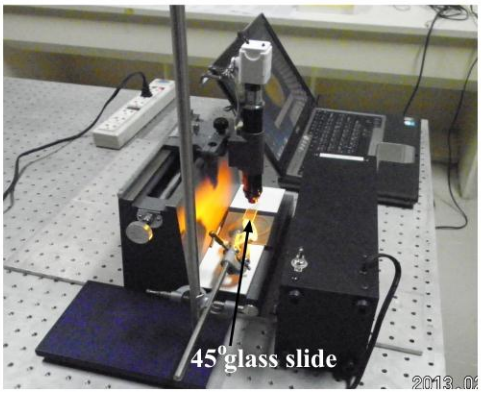

(b) Side view

(c) WebCam USB camera

(d) Newton’s rings were displayed on computer screen

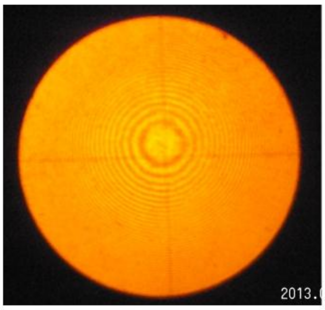

(e) Newton’s rings on computer screen

Figure 5. Photograph of Newton’s ring experimental setup.

Conclusions

In this work, a conventional Newton’s ring experimental setup was modified by the attachment of a WebCam USB camera to the eyepiece of travelling microscope. The circular fringes were recorded and transmitted to the computer to display on the computer screen. The circular fringes could be further displayed on a large projector screen. Therefore, by this method the teacher can demonstrate the interference from Newton’s experiment in the classroom and all students can observe the circular rings at the same time.

References

1. Serway, Jewett, 2004, Physics for scientists and engineers with modern physics, 6th ed., Singapore, Thomson Learning, pp. 1189-1193.
2. Young & freedman, 2000, University Physics with modern physics, Addison Wesley Longman, Inc. pp. 1149-1153
3. Halliday, David, Resnick, Jearl Walker, 2005, Fundamental of Physics,7th ed., New York, Johnwiley & Sons, pp. 972-977.

Determination of Refractive Index of Liquid by Newton's Ring Method

A. Boonyastitstaporn[1*] and P. Limsuwan[2]

[1]*Department of Physics, Mahidol Wittayanusorn School, Puttamonthon, Nakhon Pathom 73170, Thailand*
[2]*King Mongkut's University of Technology Thonburi, Bangkok 10140, Thailand*
**Corresponding author. E-mail: ampornkee@yahoo.com*

Abstract

In this work, the refractive indices of distilled water, green tea, and sugar solution were determined by Newton's ring method. The convex lens and glass slide were used as optical devices to construct the circular interference fringes. The Na lamp was used as a monochromatic light source. The circular fringes were observed through a travelling microscope equipped with a vernier scale. By measuring the diameter of circular dark rings for different order numbers when there is a liquid and without liquid, refractive index can be determined. It was found that the refractive indices of distilled water, green tea and 15% sugar solution were 1.33, 1.34 and 1.35, respectively.

***Keywords*:** Newton's rings, Interference, Circular fringes, Refractive index

Introduction

In the study of physical optics, such as interference of light, for high school students, it is difficult to understand due to the lack of experiment corresponding to those topics. Because each set of physical optics experiment is quite expensive compared with a limited school budget supported from the government. The refractive index of liquid can be generally determined using Abbe refractometer. However, it is not available in any high schools due to its high cost. Therefore, in this work an inexpensive the Newton's ring set was modified for the measurement of refractive index of liquid.

In recent years, various methods for refractive index of liquid measurement have been reported. Lee [1] reported the development of a simple apparatus for refractive index of liquid measurement using a laser pointer and the concept of refraction of laser light in liquid. Boonphuan [2] developed a demonstration apparatus for refractive index of liquid measurement using He-Ne laser and the concept of critical angle of liquid. Tharnrak [3] developed an experimental set for refractive index of liquid measurement using He-Ne laser and prism. Charerntantanakul and Jiranaphawiboon [4] constructed an experimental set for refractive index of liquid measurement using a convex lens.

Theory [5,6]

A thin film of air is formed between the two contact surfaces of lens or glass plate. For example, if an optical flat surface is placed in contact with a shallow convex spherical surface, a thin air film of varying thickness results (see Figure 1). This film is symmetrical about the point of contact. The localized interference fringes, which are the contours of the air film thickness, become concentric circles centred on the point of contact. These fringes were first observed by Newton and are know as Newton's rings.

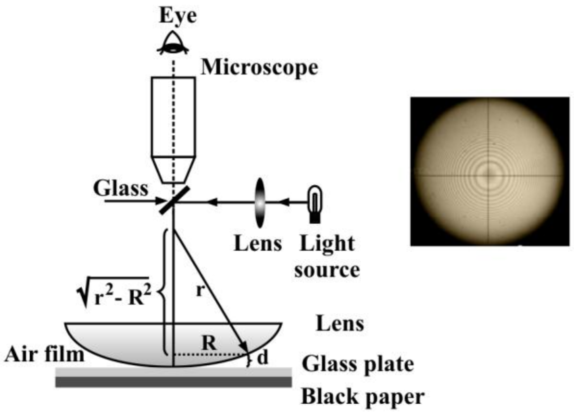

(a) Experimental setup (b) Ring patterns

Figure 1. Observation of Newton's rings.

Note that in this case there is no phase reversal of the light reflected from the upper surface of the film (which here is of smaller index than that of the medium in which the light is traveling before reflection), but the phase of the wave reflected from the lower surface is reversed.

Consider the case of reflected light, the centre of the pattern is dark. If r is the radius of curvature of the spherical surface and d is the thickness of the air film at a distance R from the point of contact, we find

$$r = \frac{R^2 + d^2}{2d}$$

If R is large $d^2 << R^2$, then

$$d = \frac{R^2}{2r} \qquad (1)$$

Because the film is thin, any departure from normal incidence can be ignored. Since film is of air, we have n = 1. There is a phase change of light at the lower surface, the condition for a maximum (bright) or minimum (dark) interferences are :

For a minimum $2d = m\lambda$ (2)

For a maximum $2d = (m + \frac{1}{2})\lambda$

Thus the radii of the bright and dark fringes are given by

(Dark) $R^2 = mr\lambda$

$$D^2 = 4mr\lambda \qquad (3)$$

(Bright) $R^2 = (m + \frac{1}{2})\, r\lambda$

$$D^2 = 4(m + \frac{1}{2})r\lambda \qquad (4)$$

where, m = 0, 1, 2, 3, …. = the number of rings.
D = the diameter of rings.
λ = the wavelength of the light
n = the refractive index of thin film

For liquid film with refractive index n, the dark ring is given by

$$2nd = m\lambda \qquad (5)$$

Then, the diameter of the dark ring becomes

$$n_{liquid} D^2_{liquid} = 4mr\lambda \qquad (6)$$

Dividing Eq. (6) by Eq.(3), we obtain

$$n_{liquid} = \frac{D^2_{air}}{D^2_{liquid}} \qquad (7)$$

Materials and Methods

Materials

1. A traveling microscope attacked with vernier scale
2. A sodium light with λ = 5,893 nm
3. A glass plate, a thin convex lens and a black paper
4. Distilled water, green tea and 15% sugar solution

Methods

1. Place the glass plate on the black paper.
2. Place the convex lens on the glass plate.
3. Set the Na light source as shown in Fig.1.
4. Place a glass plate at 45° to the Na light to reflect the light into convex lens.
5. Observe the circular fringes due to air films through the eyepiece of the travelling microscope.
6. Measure the diameter of the dark ring of different orders from m = 2 to 10. For each order, we repeat measurement for D three times and average diameter was obtained.
7. Plot between D^2 and m then from Eq.(3) the slope = $\frac{D^2}{m} = 4\, r\lambda$ was obtained.
8. Suck the distilled water and put a small drop at the contact point of lens and glass plate.
9. Observe the circular fringes due to water film.
10. Measure the diameter of the dark ring of different order from m = 2 to 10 and repeat measurements for three times
11. Plot between D_{water} and m then from Eq.(6) the slope = $\frac{D^2_{water}}{m} = \frac{4}{n_{water}} r\lambda$ was obtained
12. Divide the slope value from (11) by that from (7) we obtain $n_{water} = \frac{D^2_{air}}{D^2_{water}}$ (8)
13. Repeat the measurement for green tea and 15% sugar solution from 6 to 12

Then, we obtain

$$n_{green\ tea} = \frac{D^2_{air}}{D^2_{green\ tea}} \qquad (9)$$

and

$$n_{sugar} = \frac{D^2_{air}}{D^2_{sugar}} \qquad (10)$$

Results and Discussion

Tables 1-4 show the diameters of different dark rings of order m = 2,3,4,…., 10 for air, water, green tea and 15% sugar solution films, respectively. For each dark ring, the diameter (D) was measured three times and average diameter (D_{ave}) was obtained.

Table 1: Diameter of dark rings with various orders for air film.

m	Diameter (mm)				D^2 (mm^2)
	D(1)	D(2)	D(3)	D(ave)	
2	1.19	1.13	1.21	1.18	1.38
3	1.49	1.58	1.55	1.54	2.37
4	1.84	1.77	1.76	1.79	3.20
5	2.06	2.09	2.06	2.07	4.28
6	2.31	2.32	2.30	2.31	5.34
7	2.55	2.50	2.49	2.51	6.32
8	2.71	2.69	2.68	2.69	7.25
9	2.88	2.90	2.95	2.91	8.47
10	3.01	3.08	3.04	3.04	9.26
11	3.14	3.20	3.17	3.17	10.05
12	3.27	3.31	3.25	3.28	10.74

Table 2 : Diameter of dark rings with various orders for water film.

m	Diameter (mm)				D^2 (mm^2)
	D(1)	D(2)	D(3)	D(ave)	
2	1.05	1.16	1.06	1.09	1.19
3	1.42	1.41	1.43	1.42	2.02
4	1.58	1.62	1.62	1.61	2.58
5	1.75	1.85	1.80	1.80	3.24
6	1.95	2.06	1.97	1.99	3.97
7	2.14	2.25	2.16	2.18	4.77
8	2.31	2.42	2.32	2.35	5.52
9	2.47	2.55	2.51	2.51	6.30
10	2.62	2.68	2.63	2.64	6.99

Table 3 : Diameter of dark rings with various orders for green tea film.

m	Diameter (mm)				D^2 (mm^2)
	D(1)	D(2)	D(3)	D(ave)	
3	1.19	1.14	1.14	1.16	1.34
4	1.46	1.41	1.40	1.42	2.03
5	1.72	1.68	1.65	1.68	2.83
6	1.90	1.91	1.89	1.90	3.61
7	2.08	2.11	2.10	2.10	4.40
8	2.21	2.21	2.20	2.21	4.87
9	2.42	2.42	2.40	2.41	5.82
10	2.50	2.49	2.52	2.50	6.27

Table 4 : Diameter of dark rings with various orders for sugar solution film.

m	Diameter (mm)				D^2 (mm^2)
	D(1)	D(2)	D(3)	D(ave)	
3	1.59	1.60	1.61	1.60	2.56
4	1.82	1.81	1.81	1.81	3.29
5	1.96	1.98	1.97	1.97	3.88
6	2.15	2.19	2.14	2.16	4.67
7	2.35	2.36	2.33	2.35	5.51
8	2.48	2.48	2.47	2.48	6.13
9	2.60	2.63	2.60	2.61	6.81
10	2.72	2.76	2.73	2.74	7.49

The plots between D^2 and m for air film and all liquid films are shown in Fig. 2. From Fig. 2, the slope of air film, water, green tea and sugar solution are 0.963, 0.724, 0.719 and 0.711, respectively.

Therefore, the refractive index for water, green tea and sugar solution can be calculated from Eqs.(8-10). That is

$$n_{\text{water}} = \frac{0.963}{0.724} = 1.33$$

$$n_{\text{green tea}} = \frac{0.963}{0.719} = 1.34$$

$$n_{\text{sugarsolution}} = \frac{0.963}{0.711} = 1.35$$

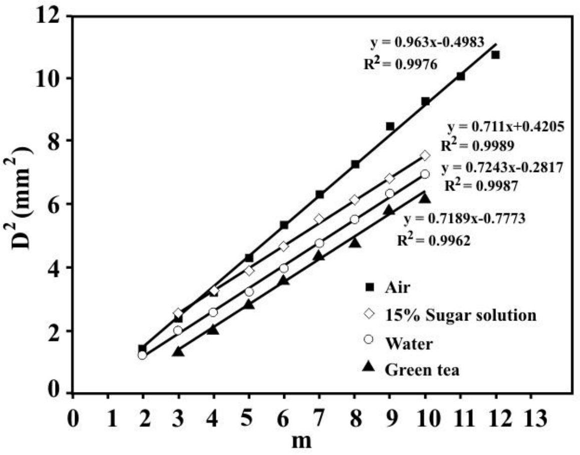

Figure 2. Relationship between D^2 and m.

5. Conclusions

The refractive indices of distilled water, green tea and 15% sugar solution were determined by Newton's ring method. The monochromatic light was obtained from a Na lamp. By measuring the diameter of circular dark rings of various order numbers from m = 2,3,4,… 10 for air film and all liquid films, then the refractive index of each liquid was determined. The results show that the refractive indices of distilled water, green tea and 15% sugar solution were 1.33, 1.34 and 1.35, respectively.

References

1. A.A. Lee, Can the Index of Refraction Determine the Concentration of Sugar in Water, USA., 2003.
2. Jaruda Boonphuan, Demonstration set for determination of refractive index of liquid using He-Ne laser, Master thesis, King Mongkut's University of Technology Thonburi, Thailand, 2009.
3. Paveena Tharnrak, Measurement of refractive index of liquid using laser, Master thesis, King Mongkut's University of Technology Thonburi, Thailand, 2008.
4. W. Charerntantanakul and A. Jiranaphawiboon, Determination of the Refractive Index of Liquid using Convex Lens, Mahidol Wittayanusorn School, Thailand, 2011.
5. R.S. Longhurst, Geometrical and Physical Optics, Hongkong, The Continental Printing Co.
6. Ltd., 1973.
7. R. Serway and J. Jewett, Physics for Scientists and Engineers with Modern Physics. 7th., Singapore, Thomson Learning, p.1190, 2004.

Developing Interactive Laboratory Sets in Mirrors and Lens Topics

C. Douangchid[1] and P. Wattanakasiwich[2*]

[1]Department of Physics and Materials Science, Chiang Mai University, Chiang Mai, 50000 Thailand
[2]Thailand Center of Excellence in Physics (ThEP), Commission on Higher Education, Bangkok 10400, Thailand
**Corresponding author. E-mail: pwattanakasiwich@gmail.com*

Abstract

The objectives of this study were (1) to develop geometrical optics conceptual evaluation about mirrors and lens in Lao language and determine its validity and reliability, (2) to build simple and low-cost laboratory equipments for demonstrating and conducting an experiment based on active-learning approach, (3) to study results of using interactive laboratory sets in mirrors and lens topics in terms of student understanding, and (4) to compare student understanding from learning in a lecture-based class versus a class taught by interactive laboratory sets. The main instrument used to collect data about student understanding was Light and Optic Conceptual Evaluation (LOCE) consisting of 25 multiple-choice questions. We also constructed low-cost laboratory equipments for mirrors and lens experiments. The setup consisted of an optical bench, an object made from LEDs as a letter "L", mirrors, lens and a paper screen. Participants were Grade 13 students in Paksong high school in Savannakhet province of Lao PDR. Students were separated into two groups –control and treatment group. The control group consisted of 68 students taught by lecturing only. The treatment group consisted of 80 students taught by demonstrating and conducting interactive laboratory. Data were collected from student responses on both pre- and post-tests of LOCE. As a result, we found that the treatment group did better on LOCE than the control group for most questions.

Keywords: Interactive laboratory sets, Geometrical Optics, Light and Optics Conceptual Evaluation

Introduction

To developing an effective curriculum, one has to get information about common misconceptions of students in that certain topic. Students with misconceptions intended to not change their way of thinking after a traditional instruction. Therefore over the past 30 years, many physics education research studies have developed an interactive teaching strategies based on an active-learning approach, so that students improved and constructed their understanding correctly [1, 2].

Several previous physics education studies had reported misconceptions found in a topic of geometrical optics [3-5]. These misconceptions related to conditions for a real-image formation, functions of optical components (lens, mirrors and a screen), and practical understanding of a ray diagram [4, 5]. In this study, we had developed an interactive laboratory sets based on these previous discovered misconceptions in geometrical optics. Also, Lao high school students at Paksong high school experienced hand-on experiments for the first time because of lacks of budgets to buy any laboratory equipments. The objectives of this study were (1) to develop geometrical optics conceptual evaluation about mirrors and lens in Lao language and determine its validity and reliability, (2) to build simple and low-cost laboratory equipments for demonstrating and conducting an experiment based on active-learning approach, (3) to study results of using interactive laboratory sets in mirrors and lens topics in terms of student understanding, and (4) to compare student understanding from learning in a lecture-based class versus a class taught by interactive laboratory sets.

Methodology

Sample groups

Sample groups were selected by using purposeful sampling of Grade 13 students in Paksong high school in Savannakhet province of Lao PDR. There were 148 students from four classrooms. Students were divided into a control group and a treatment group. The control group consisted of 68 students learning geometrical optics by lecturing only classrooms. The treatment group consisted of 80 students taught by lecturing and doing interactive laboratory sets in geometrical optics.

Conceptual test

The conceptual test for collecting data was Light and Optic Conceptual Evaluation (LOCE). The original LOCE consists of 34 multiple-choice questions, developed by David Sokoloff [6]. The LOCE was translated into Lao language by four Lao graduate students. The LOCE were administered to Lao students in October of 2011, but many students did poorly on questions about non-symmetric lens. Since this topic is not emphasized in Lao curriculum, we eliminated questions related to this topic. The LOCE was reduced to include 25 questions. Table 1 presents conceptual areas and question numbers that address each area in the reduced version of LOCE. The 25-item LOCE in Lao language was administered to a control and a treatment groups as a pre- and post-test. An example of questions in LOCE is included in an appendix.

Table 1: Conceptual areas and question numbers

Conceptual area	Question numbers
I. Image formation in spherical mirrors	1-5
II. Refraction	6-10
III. Image formation in lens (Thin lens equation)	11-15
IV. Image formation in lens (conceptual misconceptions)	16-25

Only student responses in the post-test were used to determine item analysis and overall analysis. Item analysis composed of three measures—item difficulty index, item discrimination index and point biserial coefficient. Overall analysis of the survey consisted of Kuder-Richardson reliability and Ferguson's delta [6].

1) *Item difficulty index (P)* is a measure of how difficult an item is. It is calculated as a ratio between the numbers of correct response over the total responses.

2) *Item discrimination index (D)* is a measure of the ability of a question to differentiate between competent and less competent students; in other words, those who scored well overall on the test from those who did not.

3) *Point biserial coefficient (PBI)* is a measure of correlation of each item to the whole test score. If the PBI is high, this indicates that students who answered this question correctly are most likely to have a high total score.

4) *Kuder-Richardson formula 20 (KR-20)* was used to measure the internal consistency of the whole survey. In an ideal situation, if the test is administered twice at different times to the same group of students, then two test scores should be highly correlated. However in the real world, students might remember questions on the survey and study for the test, so students are not the same group anymore. Therefore this method of measuring reliability is quite often referred to as re-test.

5) *Ferguson's Delta* (δ) measures the discriminating ability of the whole test via how broadly it spreads the distribution of scores.

Laboratory sets

The laboratory sets, constructed according to L. Dvořák's work [7] included simple optical bench and optical components (lens, mirrors and screen).

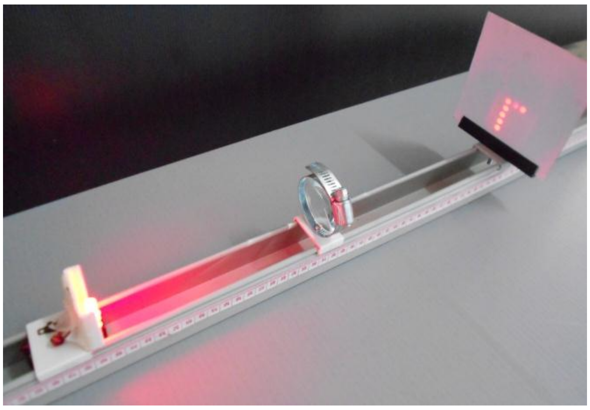

Figure 1. Laboratory sets consisted of a low-cost optical bench with LEDs connected in L-shape, converging lens, and a screen.

Experimental design

An experimental design for this study was a quasi-experimental design because the groups were not randomly selected. The quasi-independent variable in this study is the interactive laboratory sets based on the active-learning approach. In order to evaluate effectiveness of this interactive laboratory sets, we compared the pre- and post-test scores between the treatment group and the control group by using two methods of analysis:

1) Percentage of correct responses—we plotted percentage of correct responses between the pre- and post-test of each group (as shown in Figure 2 and 3).

2) A pair samples t-test of each group—we compared the mean of difference between the pre- and post-test scores of both groups. If the

Results and Discussion

Validity and reliability

The content validity is a judgment of how appropriate the items seem to a panel of experts [8]. The content validity of Thai LOCE was evaluated by two physics experts and three Lao physics teachers. The discussion involved reasonableness and appropriateness of each item and a whole test. The experts and Lao physics teachers agreed that the questions covered important topics on geometrical optics, so this represented the content validity of LOCE.

Item analysis and reliability

From Table 2, all three measures of item analysis of LOCE were higher than the desired values. The LOCE is considered to be a medium difficulty test and has satisfactory discrimination index and reliability for individual items. For the overall analysis, the LOCE has satisfactory discrimination ability but quite low reliability of the whole test.

Table 2: Item analysis and reliability of LOCE

Analysis	LOCE values	Desired values [6]
P-index	Average of 0.36	$0.30 \le P \le 0.90$
D-index	Average of 0.31	≥ 0.3
PBI	Average of 0.23	≥ 0.20
KR-20	0.65	≥ 0.70
δ	0.96	≥ 0.90

Interactive laboratory sets

The treatment groups were administered a 5-Likert scale questionnaire to provide their opinions on the interactive laboratory sets. The questionnaire consisted of 18 items. Most averaged students' opinions on each item were higher than 4.00, as presented in Table 3. This indicated that students had an overall positive attitude toward learning with an interactive laboratory sets.

Table 3: Averaged opinions on the questionnaire

Q.	Question	Ave.
Part 1: Materials covered in lectures and lab.		
1	Materials covered in lectures and laboratories are suitable and challenging.	4.03
2	Materials covered in lectures, worksheets and laboratories are related and suitable.	4.14
3	The laboratories are appropriated in terms of time and materials covered.	4.07
4	I learned skills in conducting physics experiments in the laboratories.	4.28
5	I understood geometrical optics better after doing the laboratories.	4.11
6	I understood image formation in lens and mirrors better after doing the laboratories.	4.40
Part 2: Quality of worksheets and laboratory sets		
7	Information sheet is well-written, clear and well put.	4.05
8	Questions in worksheet are well-written, clear and well put.	4.20
9	Questions in worksheet help me think and understand geometric optics better.	4.54
10	The laboratories are interesting and challenging for learning.	4.12
11	The laboratories are related to and suitable for materials covered in the lectures.	3.96
Part 3: Learning experience		
12	Answering the worksheets help me realize my misconceptions about image formations in lens and mirrors.	4.23
13	Overall activities help me relate physics principles in geometric optics, ray diagram for image formations in lens and mirrors, calculation of image locations, and experiments to locate a real-image position.	4.26
14	The laboratories help me develop skills in collecting and analyzing data.	4.03
15	The laboratory on image formations in mirrors helps me understand image formations in concave mirrors.	4.49
16	The laboratory on image formations in lens helps me understand image formations in converging lens.	4.48
17	I learned how to work as a team from doing the laboratories.	4.03
18	This laboratory is my first physics laboratory.	4.14

Overall understanding of the treatment group

From figure 2, the treatment group did better on the post-test than the pre-test, especially in the conceptual area IV. This area was about common misconceptions found in geometrical optics. Thus, most students taught by the interactive laboratory sets did correctly construct their understanding. However, the treatment group did poorly on questions 11-15, relating to a thin lens equation. In the interactive laboratory sets, we did not spend enough time with students to solve problems using a thin lens equation. This might be a reason that the treatment group did poorly in this area.

Comparison between both groups

From figure 2 and 3, the treatment group did better after the instruction than the control group. We then further analyzed by using the statistical analysis, in this case, the pair samples t-test.

A pair-samples t-test was conducted to compare pre- and post-test scores of control and treatment groups. For the control group, there was no significant difference in the pre-test scores ($\bar{x} = 5.10,\ SD = 2.166$) and the post-test scores

($\bar{x} = 4.56,\ SD = 2.208$); $t(67) = 1.578$, $p = 0.119$. For the treatment group, the pre-test scores ($\bar{x} = 6.01,\ SD = 1.984$) and the post-test scores ($\bar{x} = 8.84,\ SD = 2.563$) were significantly difference; $t(79) = -7.903$, $p=0.001$. This statistical analysis indicated that the treatment group did significantly better on LOCE. Therefore, this result suggests that students in the treatment group taught by interactive laboratory sets better understood than a control group taught by lecturing only.

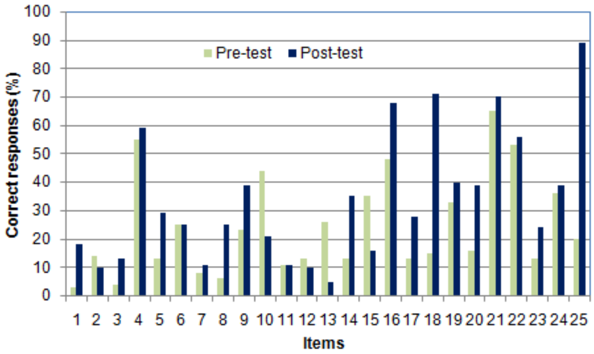

Figure 2. Percentages of correct responses on pre- and post-test of the treatment group

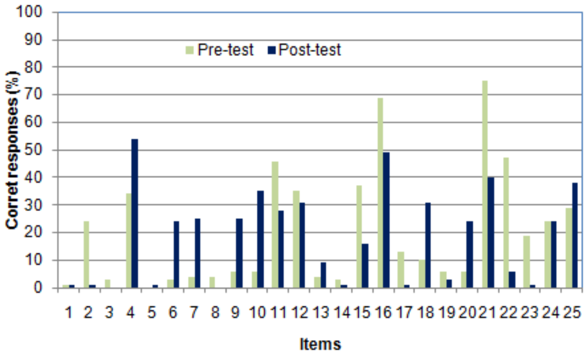

Figure 3. Percentages of correct responses on pre- and post-test of the control group

Conclusions

In this study, we accomplished four objectives. We developed geometrical optics conceptual evaluation or LOCE in Lao language and determined its validity and reliability. We also built simple and low-cost laboratory equipments for conducting lens and mirrors experiments. We also investigated student opinions from learning with our interactive laboratory sets. As a result, students had a positive attitude and learning experience from this new teaching approach. In comparison of student understanding, we found that students taught by the interactive laboratory sets did significantly better on LOCE than students taught by lecturing only. This work is the first physics education research emphasizing on an active-learning approach, conducted in Lao PDR. However, this interactive laboratory sets should be included more topics such as a thin lens equation, virtual image formation, and combination lens.

Acknowledgments

We would like to thank Thailand Center of Excellence in Physics (ThEP), Graduate school and Faculty of Science, Chiang Mai University, Thailand. We extend our appreciation to Child Dream foundation for supporting the first author in conducting this research in Lao PDR.

References

1. D. R. Sokoloff, “Active Learning in Optics and Photonics: Training Manual”, UNESCO, 2006.
2. B. Paosawatyanyong and P. Wattanakasiwich, “Implication of physics active- learning in Asia”, Latin American Journal of Physics Education **4** (2010)501.
3. S. Jongsala, “Using geometric optics kit (go-kit) to promote student’s learning in lenses and optical Instrument”, Veridian E-Journal SU 4(2011) 411.
4. F. M. Goldberg and L. C. McDermott, “An investigation of students’ understanding of the real image formed by a converging lens or concave mirror”, American Journal of Physics **55**(1987) 108.
5. I. Galili and A. Hazan, “Learners’ knowledge in optics: interpretation, structure and analysis”, International Journal of Science Education **22**(2000) 57.
6. L. Ding and R. Beichner, “Approaches to data analysis of multiple-choice questions”, Physical Review Special Topics—PER **5**(2009)020103-1.
7. L. Dvořák, “Apparatus for Teaching Physics”, The Physics Teacher **49**(2011)101.
8. P. Wattanakasiwich, P. Taleab, M. Sharma, and I. Johnston, “Construction and implementation of a conceptual survey in thermodynamics”, International Journal of Innovation in Science and Mathematics Education (In pressed).

Developing Learning Modules on Linear Motion using Guiding Questions

M. Suwansaweg[1], J. Tipparach[2], and U. Tipparach[1*]

[1]*Department of Physics, Faculty of Science, Ubon Ratchathani University, Warinchamrab,*
Ubon Ratchathani Province 34190 Thailand
[2]*Department of English, Faculty of Humanities and Social Sciences, Ubon Ratchathani Rajabhat*
University, Mueang District, Ubon Ratchathani Province 34190 Thailand
[*]*Corresponding author. E-mail: washington.1747@gmail.com*

Abstract

Learning modules on linear motion using guiding questions were developed to promote independent self-learning as supplementary text. The modules are composed of the concise concepts vectors, distance, displacement, speed, velocity, and acceleration and follow by guiding questions. To solve difficult problems, students should have understood the related concepts and should have solved previous questions. The results show that the students could not solve problems without guiding questions. Having answered the guiding questions, the students may solve the problems. The developed learning modules are very successful and demanded for other topics in Physics.

***Keywords*:** Guiding questions, teaching, learning module, self-learning, Physics Education

Introduction

The ability to self-control and regulate one's learning is vital to success in all academic careers. For effective self-regulation, learners must make use of either internally or externally generated feedback about their performance to self-evaluate progress towards their goals. If progress is evaluated to be inadequate, they must adjust their goals or performance to accomplish their tasks [1-2]. Accurate self-evaluations, therefore, become a critical guide to successful self-regulated learning. Unfortunately, many students are poor at evaluating their learning, which can lead to repeated experiences of failure.

Standard texts used in schools [3] and universities [4-5] do not provide enough feedbacks so students cannot evaluate their works. Some students rely on "handbooks" or supplementary books to enhance understanding and boost their scores. None of book provides good feedbacks and guidelines. Many researchers believe that good guidelines and well-designed learning module can help students learn by themselves effectively and independently [6-7]. In this work, the design and outcome of learning modules on linear motion using guiding questions will be discussed.

Materials and Methods

The design of learning modules

The chapter 2: Motion in one and two dimensions in the text written by the Institute for the Promotion of Teaching Science and Technology (IPST) [3] was selected to design lessons. The lesions are composted of 4 learning modules: vectors, speed and velocity, acceleration and motion with constant acceleration, relative velocity and inertia frame. Each module consists of definitions, concepts, examples and exercise. The problems or questions are asked systematically so that students have to understand step-by-step by as guided by the modules. The questions are made efforts to use the question-asking strategy as a key to monitor learners' steps. To compare the effectiveness of the guiding questions, we prepare 2 set of the problems: set A and set B. Examples of guiding questions (set A) on speed and velocity module are as follows:

Problem 1A an object moves in one dimension so that its position (s, in meter) as a function of time (t, in second) is, $s(t) = 10 + 20t - 5t^2$ for 4 seconds, guiding questions:

(a) Fine position at the beginning, ($t = 0$) and at the end $t = 4\,s$
(b) What is the displacement (vector)?
(c) What is the average velocity?
(d) Sketch the positions in one dimension at time $t = 0, 1, 2, 3, 4\,s.$
(e) What is the distance (scalar) of the object moving from beginning untilthe end of $t = 4\,s$?
(f) What is the average speed?

It is obvious that the answer of question (a) leads to answer question (b), then the answer (b) leads to obtain the average velocity (c) which is a vector quantity. Similarly, a student performing tasks in (d) and (e) will be able to answer (f).

Examples of traditional questions without guiding question (set B) on speed and velocity are given as follows:

Problem 1B an object moves in one dimension so that its position (s, in meter) as a function of time (t, in second) is, $s(t) = 10 + 20t - 5t^2$ for 4 seconds, without guiding questions

(a) What is the average velocity?
(b) What is the average speed?

The use of the modules and data collection

Twenty eight out of thirty eight Olympiad physics students attending the summer class in 2012 were purposively selected to examine the effectiveness of the guiding question modules. The students were supported by The Promotion of Academic Olympiad and Development of Science Education Foundation under the patronage of Her Royal Highness Princess Galyani Vadhana Krom Luang Naradhiwas Rajanagarindra, (POSN). The students were randomly divided into two groups equally. The pretest was given to probe students' background. Both groups were treated the same lecture at the same time. Group A was assigned the task with guiding questions (problem set A) while group B was assigned the task without guiding questions (problem set B). The total score was 40 and only important questions were graded. For example, problem 1A and 1B only questions what is the average velocity? and (a) what is the average speed? would be graded and scored.

Results and Discussion

Pre-test scores

The pretest scores and t-test independent were shown in table 1. The scores of group A and group B are 8.75 and 8.18 out of 40, respectively. Statistical t-test showed that there was no statistically significant difference at the level of .05 between the background scores of group A and group B.

Table 1: Pretest scores and t-test independent

statistics parameters	Group A	Group B
mean	8.5714	8.1429
variance	3.6484	3.0549
observations	14	14
df	23	
t stat	0.6193	
t critical two-tail, .05	2.0555	

Homework scores

The homework scores and t-test independent were shown in table 2. The scores of group A and group B are 34.64 and 27.14 out of 40, respectively. Statistical t-test showed that the average score of group A were greater than that of group B with statistical significance at the level of .05. This evident indicates that the guiding questions are useful to help the students for grasping main points and enhance the achievement scores.

Table 1: Homework scores and t-test independent

statistics parameters	Group A	Group B
mean	34.6429	27.1429
variance	22.2473	44.5934
observations	14	14
df	23	
t stat	3.4325*	
t critical one-tail, .05	1.7138	

The interviews reveal that the students were challenged to do the tasks. They said it was good to learn by their own pace and know how to move forward if they could answer previous guiding questions. The students could not solve many problems without guiding question. They said without guiding questions always lead them to think and realize what we needed to understand to find the solution to the problems. They also can regulate themselves. The learning modules were also used in high schools. The results show that the modules help the students learn how to solve physics problems effectively. The students considered the guiding modules as self-study modules. They demanded for other topics to provided guiding modules.

Conclusions

We have designed and investigate the effectiveness of learning modules with guiding questions. Scenarios of the design and strategy of the learning modules were dedicated to be self-study supplementary texts. The design was considered as a strategy of asking questions instead of the more common pattern of giving examples. The modules facilitate guided discovery learning and have a strong positive effect on learning outcome.

Acknowledgments

We would like to thank Department of Physics and Faculty of Science, Ubon Ratchathani University to give us an opportunity to work with POSN students and partially financial supports.

References

1. B. J. Zimmerman, "Investigating self-regulation and motivation: Historical background, methodological developments, and future prospects", American Educational Research Journal, 45(1), (2008), 166–183.
2. R. Phanikiran, H. Arrow, J. Sniezek, "Hoping, performing, learning, and predicting: Changes

in the accuracy of self-evaluations of performance”, Human Performance, **9(1)**, (1996). 23–32.

3. สถาบันส่งเสริมการสอนวิทยาศาสตร์และเทคโนโลยี, หนังสือเรียนสาระการเรียนรู้พื้นฐานและเพิ่มเติม ฟิสิกส์ เล่ม 1, โรงพิมพ์คุรุสภาลาดพร้าว, 2549.
4. Raymond A. Serway, John W. Jewett, Jr., Physics for Scientists and Engineers with Modern Physics, 8th Ed., (2010).
5. 5. Hugh D. Young, Roger A. Freedman, A. Lewis Ford, Sears and Zemansky’s University Physics: with modern physics, 13th Ed., Addison-Wesley, (2012).
6. G. Olshera, Itay-Danny Kantorb, “Asking Questions as a Key Strategy in Guiding a Novice Teacher: A self-study”, Studying Teacher Education, **8(2)**, (2012), 157-168.
7. Ryan D. Honomichl, Zhe Chen, “The role of guidance in children's discovery learning”, Wiley Interdisciplinary Reviews: Cognitive Science **3(6)**, (2012), 615–622.

Appendix

Problem 1A an object moves in one dimension so that its position (s, in meter) as a function of time (t, in second) is, $s(t) = 10 + 20t - 5t^2$ for 4 seconds, guiding questions:

(a) Fine position at the beginning, ($t = 0$) and at the end $t = 4\,s$

<u>Ans</u>

$s(0) = 10 + 20(0) - 5(0)^2 = 10$ m

$s(4) = 10 + 20(4) - 5(4)^2 = 10$ m

(b) What is the displacement (vector)?

<u>Ans</u>

Displacement d = s(4)-s(0) =10 – 10 =0.

(c) What is the average velocity?

$$\vec{v}_{ave} = \frac{\text{Displacement}}{\text{time}} = \frac{0}{4} = 0.$$

(d) Sketch the positions in one dimension at time $t = 0, 1, 2, 3, 4\,s$.

t(s)	0	1	2	3	4
s(m)	10	25	30	25	10

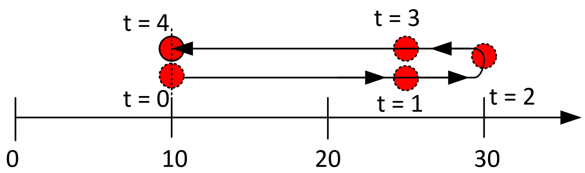

(e) What is the distance (scalar) of the object moving from beginning untilthe end of $t = 4\,s$?

<u>Ans</u> The distance = go (20 m) + back (20 m)

= 40 m.

(f) What is the average speed?

<u>Ans</u>

$$v_{ave} = \frac{\text{distance}}{\text{time}} = \frac{40\text{ m}}{4\text{ s}} = 10\text{ m/s}$$

Developing Simple Experiments for Teaching Concepts of the Radius of Gyration and Moment of Inertia

T. Saipin[1], S. Norrapoke[2], U. Srisakorn[2], G. Shuwunnasillp[3], and U. Tipparach[2*]

[1]*Department of Arts and Sciences, Ubon Ratchathani Technical College, Mueang District, Ubon Ratchathani Province 34000 Thailand*
[2]*Department of Physics, Ubon Ratchathani University, Ubon Ratchathani 34190 Thailand*
[3]*Chonradsadornumrung school, Mueang District, Chonburi Province, 20000 Thailand*
**Corresponding author. E-mail: udomt@hotmail.com*

Abstract

We have designed and constructed simple sets of apparatus for teaching on moment of inertia and radius of gyration for teachers' training courses and undergraduate courses. The goals of this work are two folds: (1) to probe in-service teachers' and undergraduate students' ideas about moment of inertia and radius of gyration of rotational objects and (2) to provide in-service teachers and students with opportunities for active, hand-on scientific investigation and gaining skills in inquiry pedagogy. Rolling objects down a plane was used as an experimental theme. The sets of apparatus used in rolling are composed of objects with different masses to investigate the effect of mass and with different radii to study the effect of radius. The results show that both in-service teachers and undergraduate students poorly understand the concepts. The teachers and students gained much better understanding the concepts of moment of inertial and radius of gyration. These learning activities also worked well with high school students.

Keywords**:** Moment of inertia, gyration, pedagogical content knowledge (PCK), laboratory design, inquiry

Introduction

Children have a natural curiosity about the world around them especially science. They enjoy practical science and explore new things. They may want to observe or measure things around them. Such practical activity is motivating and engaging, especially if there is a strong collaborative element. Working with a classmate ensures that there is someone to share ideas, acquire knowledge, and also promote social development as well as emotional growth. Students' curiosity is fuelled when they find out enough to know that there are still questions to ask and things to investigate. However, many teachers and professors in schools and universities have experienced with a large number of students in introductory classes. The courses are rich in contents. Thus, these courses often do not engage students in active, authentic scientific investigation, nor do they adequately concentrate on problem-solving process and inquiry skills required to further development. It has long been misunderstood that Physics has an image of being difficult, boring, and unfavorable [1-2]. Decreasing motivation and competence in Physics studies among students at different levels has also been an issue broadly discussed by educators, researchers, and politicians. Some researchers found that one of the big problems was laboratory scarcity [3]. Our research shows we can use simple tools to do simple experiments and integrate subject matter in Physics and Mathematics so that the students may learn more contents [4]. In this work, we present the design of simple sets of apparatus for teaching on moment of inertia and radius of gyration for teachers' training courses to show that the useful experiments do not require expensive apparatus. We use inquire method to challenge ability of new teacher generation and to use the integration of pedagogical and content knowledge (PCK) for teaching Physics. We will report the used of the experiment sets to demonstrate the concepts of the relationship between mass distribution of bodies and their moments of inertia through inquiry method in different levels such as high schools and universities.

Materials and Methods

The study is an action research involving 32 in-service teachers attending 2011summer class of Ubon Ratchathani University. The work was intended to provide the in-service teachers with both pedagogical and content knowledge (PCK) and teach the students about the concept of moment of inertia as well as develop attitude towards Physics and Physics learning method.

Pedagogical knowledge

A pre-survey, developed by the researchers, to probe the perception and concept of moment of inertia and how to introduce the concept to students was administered to the classes before the topic was taught. Inquiry method was used to encourage the classes to build their own ways to teach students, to find out solutions to the problems. Some of the questions were:

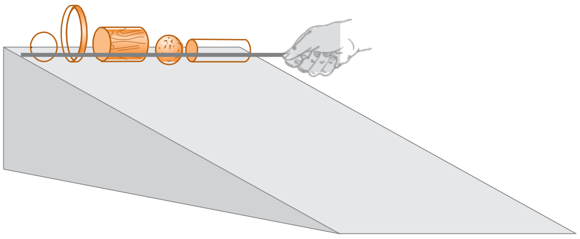

Figure 1. Bodies with different shapes roll down a ramp [5].

1. What is moment of inertia?
2. What is a radius of gyration of rotational body?
3. Given bodies with different shapes: solid sphere, cylinder, and hollow cylinder, if the bodies are released from the rest down an inclined plane where they are free to roll without slipping as shown in Fig. 1, what shape should a body have to reach the bottom of the incline first? or which body rolls down the incline fastest, and why?

To illustrate the inquiry method of learning, the researchers questioned the classes to lead the teachers as follows:

1. Does velocity of the bodies depends on mass?
2. Does velocity of the bodies depends on radius?
3. Does velocity of the bodies depends on shape?
4. How can we design an experiment to find out the solution to this problem?

The teachers were grouped in four to perform the inquiry experiments so that they can bring the experience to their teachings.

Content knowledge

After the class have discussed and designed the experiments as well as found the solution, the researchers provided the contents related to this problem.

1. Conservation of mechanical energy is used to get the velocity for high school students due to its simplicity [5,6].

The motion of a rolling body is combined the motion of the body is combined translational and rotational kinetic energies,

$$E_{\text{Potential}} = E_{\text{Translational}} + E_{\text{Rotational}}$$

$$\mathrm{Mgh} = \frac{1}{2}\mathrm{M}v_{\mathrm{c.m.}}^2 + \frac{1}{2}\mathrm{I}\omega^2 \qquad (1)$$

The moments of inertia (I) of a solid sphere, cylinder, and hollow cylinder are $\frac{2}{5}\mathrm{MR}^2$, $\frac{1}{2}\mathrm{MR}^2$, and MR^2, respectively. Using $v_{\mathrm{c.m}} = \omega R \rightarrow \omega = v_{\mathrm{c.m.}}/R$, we get the velocities for a solid sphere, cylinder, and hollow cylinder are $v_{\mathrm{sph}} = \sqrt{\frac{10}{7}gh}$, $v_{\mathrm{cyl}} = \sqrt{\frac{4}{3}gh}$, and $v_{\mathrm{hl\ sph}} = \sqrt{gh}$, respectively. The ratio of the velocities is,

$$v_{\mathrm{sph}} : v_{\mathrm{cyl}} : v_{\mathrm{hl\ sph}} = 1.42 : 1.33 : 1.00. \qquad (2)$$

2. Newton's second law of motion is applied to obtain the acceleration for first year undergraduate classes [7].
3. Lagrange equation with constraints is used to find out either velocity or acceleration for the teacher training class or graduate class [8].

Results and Discussion

Most of the teachers knew the concept of moment of inertia, but none of them had performed an inquiry-based experiment. Some of them understood physical meaning of the radius of gyration, the others did not. Almost teachers did not know the physical meaning of the radius of gyration. With the leading questions, the teachers have learned how to set up the experiments. The prepared equipment is shown in Fig. 2. From our observation, the teachers worked cooperatively and enthusiastically to solve the problem.

Figure 2. Prepared equipment for inquiry-based experiments.

1. To answer the question "does velocity of the bodies depends on mass?", the teachers used bodies with the same shape and same dimensions but have different densities. For example, they used the same dimension cylinders of metals; brass, steel, and aluminum. They did not observe the different velocity.

2. After they have learned that the velocity of the rolling body did not depend on its mass, the teachers used tubes regardless of their mass, but different

radius to answer the question "does velocity of the bodies depends on radius?", as shown in Fig. 3. They did not observe the different velocity.

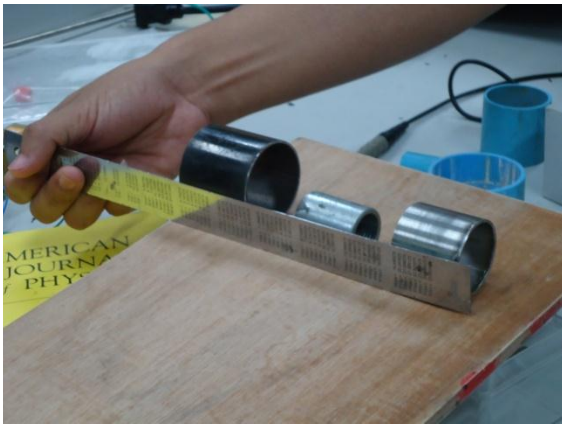

Figure 3. The experiment to inquire mass dependence to the velocity.

3. To answer the question "does velocity of the bodies depends on shape?", the teachers used tube with the same kind of materials, but different radius. They significantly observed the different velocity. They also have learned that the velocity of rolling bodies is independent with mass and radius. Then, they could use bodies with different masses or different radii, but different shapes. They found that with any mass, any radius, or any materials, the velocity would depend on the shape of rolling objects as predicted by theory they have learned from content knowledge in eq. (2). The fastest velocity was the body with sphere in shape as shown in Fig. 4. They said this was exciting and simple experiment and they would take to their classrooms. In addition, the teacher said that if they may use bamboo as a hollow cylinder or use sugar cane as a cylinder.

The tool kits and the same questions were also used to teach other levels. We asked the question "Given bodies with different shapes: solid sphere, cylinder, and hollow cylinder, if the bodies are released from the rest down an inclined plane where they are free to roll without slipping as shown in Fig. 1, what shape should a body have to reach the bottom of the incline first? or which body rolls down the incline fastest, and why?" Most of the students did not know exactly the way to think. After doing the experiments, they have thought over and over. Some of them asked for the mass. The others asked for radii, masses, and the height of the inclined plane. A few students could solve the problem. No one thought about the radius of the moment of inertia, gyration of the distribution of mass of rotational objects.

We also introduced the radius of gyration (K) for a rotational body in term of moment of inertia, $I = MK^2$ to the classes. We showed the radius of gyration, $K = \sqrt{I/M}$. The radius of gyration represents the distance from the axis of rotation at which all the mass of whole body could be concentrate without changing the moment of inertia. The radius of gyration is useful quantity because it can be determined for distribution of the entire body. The radii of a solid sphere, cylinder, and hollow cylinder are, $0.63R$, $0.70R$, and $1.0R$, respectively. Now, we showed them that a body with large K-body, hollow cylinder, seems that its mass is located at 1.0R.

Figure 4. Rolling down on an inclined plane of a solid sphere, cylinder, and hollow cylinder. The fastest is the ball (sphere) while the slowest is the thin-hollow cylinder.

It was obvious to see. More of their kinetic energy of large K-body is tied up in rotation and so less is available for translation. Thus, it rolls down an inclined plane slower than any other body as shown in Fig. 4. On the other hand, the solid sphere with (K = 0.63R) small K-body small-K body always goes faster than large-c body because less of its kinetic energy is tied up in rotation and so more is available for translation. Having learnt about physical meaning of the radius of gyration, the in-service teachers and students concluded that more compact bodies with small radius of gyration are easier to be rotated while large radius of gyration are more difficult to be rotated. This can be confirmed by rolling theme experiments.

Although the concept of the radius of gyration is important, it is not contained in new versions of well-know texts, e.g. Young and Freedman (2012) [5], and Serway and Jewett (2010) [7]. However, the concept is contained in the standard-classic texts, e.g. Alonso and Finn (1980) [9]. Many in-service teachers and student said that they should have learnt Physics this way since they started studying Physics. After having gone to teach their students, they reported us they had applied the inquiry-based experiments to their classroom. The experiments were very effective and drew much more students' attention.

Conclusions

We have successfully introduced inquiry-based experiments to enhance the understanding on the concepts of moment of inertia and the radius of gyration. This method of learning Physics provides the in-service teachers to emphasize on inquiry skills and contents required to teach students. The experiments confirm the theory and builds long-term understanding and memory. This pedagogical method not only promotes scientific skills, but also develops social skills. The results provided in-service teachers develop the needed skills and content knowledge to create effective and engaging Physics experiments for their students. Furthermore, this method helps the students learn Physics naturally and happily.

Acknowledgments

We would like to thank Faculty of Science, Ubon Ratchathani for financial and traveling supports.

References

1. R. Sillitto, L.M. MacKinnon, “Building a multimedia educational resource for physics learners”, Physics Education, 35(3), 325-331.
2. Rujira Karisook, Udom Tipparach, “The attitudes and expectations of students from Benchama Maharat School on learning Physics”, Proceedings in 36th Congress on Science and Technology of Thailand, 26-28 October 2010.
3. สุนีย์ คล้ายนิล, การศึกษาวิทยาศาสตร์ไทย: การพัฒนาและภาวะถดถอย, สถาบันส่งเสริมการสอนวิทยาศาสตร์และเทคโนโลยี, 2555.
4. ชลิตา ทักษิณกานนท์, อุดม ทิพราช, “การบูรณาการการเรียนวิชาคณิตศาสตร์และฟิสิกส์ในโรงเรียน”, Proceedings in Siam physics congress 2012 May 9-12, 2012, 266-268.
5. Hugh D. Young, Roger A. Freedman, A. Lewis Ford, Sears and Zemansky’s University Physics: with modern physics, 13th Ed., Addison-Wesley, 2012.
6. สถาบันส่งเสริมการสอนวิทยาศาสตร์และเทคโนโลยี, หนังสือเรียนสาระการเรียนรู้พื้นฐานและเพิ่มเติม ฟิสิกส์ เล่ม 1, โรงพิมพ์คุรุสภาลาดพร้าว, 2549.
7. Raymond A. Serway, John W. Jewett, Jr., Physics for Scientists and Engineers with Modern Physics, 8th Ed., 2010.
8. Herbert Goldstein, Classical Mechanics, Addison-Wesley, 1950.
9. Marcelo Alonso, Edward j. Finn, Fundamental University Physics, 2nd Ed., Addison-Wesley, 1980.

Fostering Primary School Students to Understand Electricity and Magnetism

N. Amorasin[1], G. Shuwunnasillp[2], T. Saipin[3], and U. Tipparach[1]*

[1]*Department of Physics, Ubon Ratchathani University, Ubon Ratchathani Province 34190 Thailand*
[2]*Department of Arts and Sciences, Ubon Ratchathani Technical College, Mueang District, Ubon Ratchathani Province 34000 Thailand*
[3]*Chonradsadornumrung school, Mueang District, Chonburi Province, 20000 Thailand*
**Corresponding author. E-mail: tipparach_u@yahoo.com*

Abstract

Simple electricity and magnetism experiments in conjunction with inquiry learning method were used to inspire and foster primary school students to learn science. The experiments consisted of conducting materials, simple series and parallel circuits and, magnetic generation. The pretest and posttest simple questions were used to evaluate the students' concepts on Electricity and Magnetism. 16 tenth grade students were used in this research. The results show that the experiments can effectively engage and motivate the students. The students' attitude towards electricity and magnetism was very positive. The students gained better understand electricity with high retention rate. The experiments can be also used for secondary school students with minor modification.

***Keywords*: ** Electricity and magnetism, experiment, retention rate, inquiry, Science Education

Introduction

Science is an important base of daily life and technology because it is concerned with natural phenomena and helps people understand the increasingly changing technological society. Due to the importance of Science, Thailand's Ministry of Education has emphasized its teaching and learning in schools by encouraging. This is the instruction for preparation of manuscripts for the SPC2013 Proceedings. Standard English or American spelling can be used but consistency should be maintained within a paper. The use of common or standard abbreviations is encouraged science teachers to teach students with active learning activities so that students are involved in learning process. However, the performance of students in science in Thailand for Ordinary National Educational Test (O-NET) organized by the National Institute of Educational Testing Service (NIETS) has been poor. Some students have performed extremely poorly on the O-NET tests. The scores in science for 6th grade students were even decreased and equaled 41.56 % and 40.82 % in 2010 and 2011, respectively [1].

Analysis of the results also indicates that the performance of higher levels (grade 9 and grade 12) is lower than that of grade 6. Many research works show that the students do not have enough scientific skills required to study science I advanced levels. The learn science by memorizing and reciting. Many science teachers say they do not have equipment or supplies to foster their student learn science or the apparatus and kits required to do experiments designed by the Institute for the Promotion of Teaching Science and Technology (IPST) are not available [2]. Some teachers teach students electricity and magnet without doing experiments. Students do not know how it can be used and they do not realize the need of science to their careers in future. There is therefore need to motivate students towards studying science so that the learners can perform and acquire knowledge and skills that will be relevant in future study and career. The teaching approach a teacher adopts is a strong factor that may affect the students' motivation towards learning, therefore affecting the achievement. Motivation can be enhanced through teaching methods that actively involve students.

Electricity and magnetism is seen as a central area of physics curricula at all levels of education: primary, secondary and university. However, it is one of the most difficult topics in teaching physics. Physics education research has shown that students have difficulties in understanding electricity and magnetism because of the abstract nature of the subject which is difficult to visualize and because the mathematical relationships can be complex [3-5]. Research on understanding electricity is focused on current, potential difference and especially brightness of bulbs in parallel or series dc circuits and deal with secondary schools and university levels [6-9]. It is common to say that many people misunderstood about electricity and magnetism even pre-service teachers [10]. In this work, we introduced how to build a set of simple electricity and magnetism experiments in conjunction with inquiry learning method were used to inspire and foster primary school students to learn science. The outcome of the use of the apparatus and the inquiry as a pedagogical method will be also discussed.

Materials and Methods

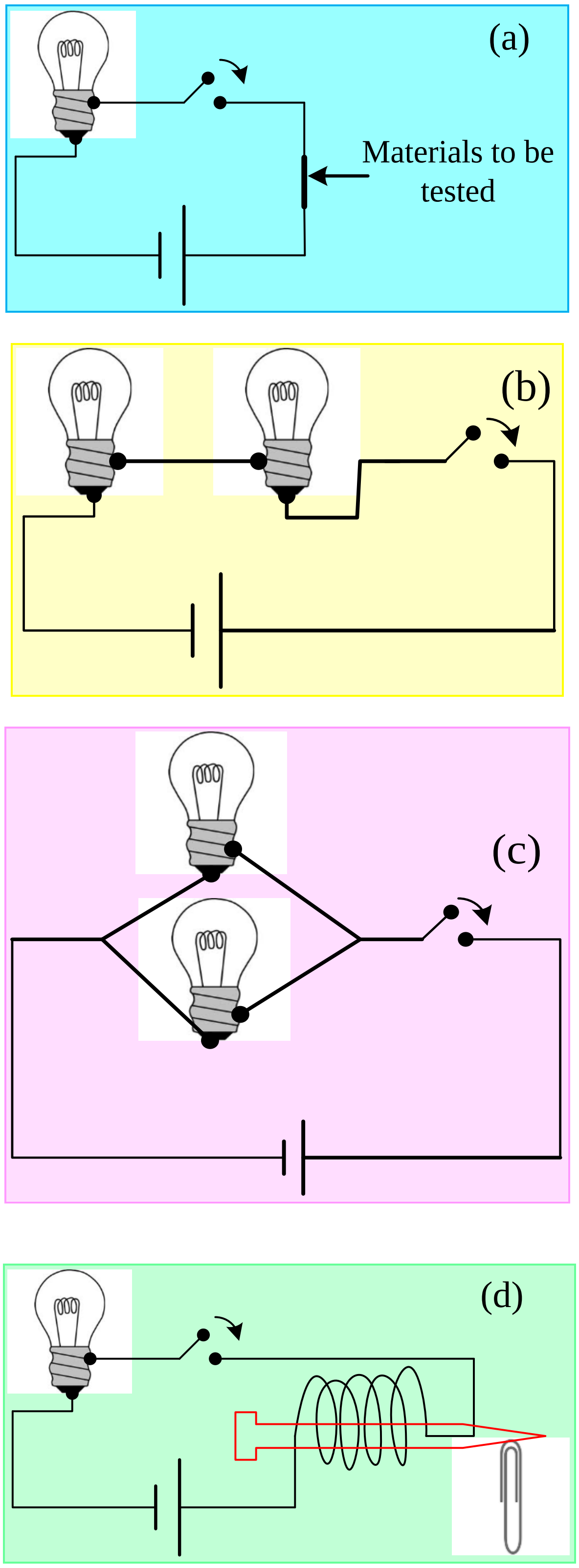

Figure 1. The schematic diagrams of the circuits.

The simple electricity circuits were built from materials available in local hardware stores. Each set of the circuits were composted of (1) a simple circuit, (2) serial circuit, and (3) parallel circuit with two light bulbs as well as (4) an experiment demonstrating the relation between electricity and magnetism. The schematic diagrams of the circuits are shown in Fig. 1.

The simple circuit Fig. 1(a) was used to learn how electricity circuit work. It was also used to inquire which materials can conduct electricity and how good materials conduct a current. Sixteen Grade 6 elementary students were used in this work and were divided in a group of four. The students were treated with an inquiry to do the experiments. They were asked how they know to carry out the experiments. For example, to do the first experiment, the students were questioned “Do you know which materials can conduct a current?” The researchers asked the students how we can make a magnet out of electricity current. The researchers also let the students investigate the relation between (1) a current and (2) the number of turn of the coils and the strength of a magnetic field.

The researchers observed and recorded students’ behavior. We also interviewed some of the students to investigate there attitude towards science on the topic of electricity and magnetism. Finally, the post-test were administered. One of the questions asked the students that “what happens with the light bulb 1 if points C and D are connected with a conducting wire” as shown in Fig. 2, or what happens with the light bulb 2 if points C and D are connected with a conducting wire”.

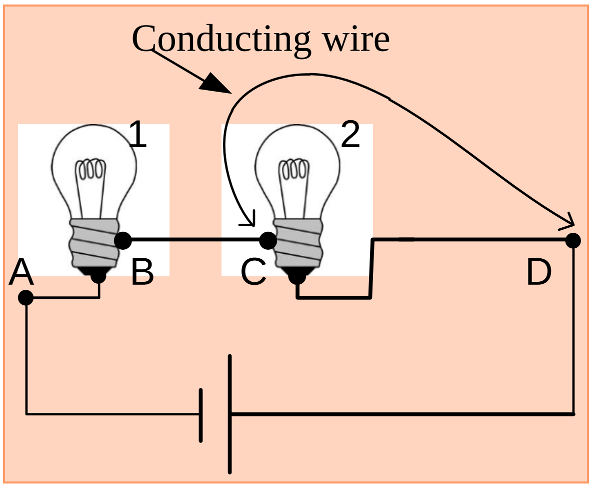

Figure 2. The schematic diagrams of some of the post-test questions.

Results and Discussion

The tool sets were built and used in the experiments students were very attractive. They draw much of students' attention. The students were excited about the equipment and the inquiry-based experiments. The students explore new experiments actively. Everybody enjoyed working together. They could build their own knowledge about a conductor and insulator without reciting the lists in the text. They also understood how to know witch materials are good conductors by observing the bright of the light bulb. They know that the copper wire can carry a current better than graphite. They were eager to learn about the circuits. When asked, the students said they loved to learn by doing and investigating by themselves.

Figure 3. Students' attention to the experiments and exploration (a) planning, (b) collaborating, and (c) resulting.

Amazingly, they could answer the questions as shown in the Fig. 2. In class, we asked the students that what happens with the light bulbs 1 and 2 if we connected an insulator wire, e.g. nylon or rubber, between the points A and B, we gave some time to allow the students think. The most students reply correctly, only 2 were wrong. Then we asked the students that what happens with the light bulbs 1 and 2 if we connected a conductor wire, e.g. copper or aluminum wire, between the points A and B, we gave some time to allow the students think. 10 students were correct, but 6 were wrong. Then, we provided the kits and let them explored the answer. We questioned, only a half of students gave correct reasons. Therefore, we had to explain.

In the post-test, we asked the students that "what happens with the light bulb 1 if points C and D are connected with a conducting wire" as shown in Fig. 2, or what happens with the light bulb 2 if points C and D are connected with a conducting wire", instead of points A and B are connected as in the classroom. The responses were very impressive because the most of students were correct.

The last experiment was the lab linking between electricity and magnetism. This experiment promoted the students learn by doing trough inquiry perfectly because the factors for inducing a magnetic field are the number of turn of a coil, amount of current, and type of materials core. In this experiment, the students tried to find out only first two factors. We also let this equipment use in secondary school students by just replacing a battery with a power supply. The results showed that all students liked the equipment and the inquiry method. Based on our observation and interviews, the students' attitude towards electricity and magnetism was very positive. The students also kept a good memory about the experiments and could get the same level post-test scores.

Conclusions

We have designed and built Simple electricity and magnetism experiments in conjunction with inquiry learning method were used to motivate and promote primary school students to learn science by active way. The teachers enjoyed teaching with home-made equipment available in their home town. The students were happy to learn by doing without reciting and memorizing. The students' attitude towards science on electricity was very positive. The retention rate of the students was very high.

Acknowledgments

We would like to thank the faculty of science, Ubon Ratchathani University for financial support through graduate research fund and travel fund.

References

1. The National Institute of Educational Testing Service (Public Organization) Thailand, The report on O-NET test, 2012.
2. สุนีย์ คล้ายนิล, การศึกษาวิทยาศาสตร์ไทย: การพัฒนาและภาวะถดถอย, สถาบันส่งเสริมการสอนวิทยาศาสตร์และเทคโนโลยี, 2555.
3. P. Brna, “Confronting misconceptions in the domain of simple electrical circuits”, Instructional Science **17**,(1988), 29-55.
4. B. Kibble, “How do you picture electricity?”, Physics Education **34**, 226-229 (1999).
5. B. A. Thacker, U Ganiel, and D. Boys, “Macroscopic phenomena and microscopic processes: Student understanding of transients in direct current electric circuits”, Phys. Educ. Res. **67**, (1999), 25-31.
6. H. Pardhan, and Y. Bano, Science, “teachers’ alternate conceptions about direct-currents”, Int. J. Sci. Educ. **23**, (2001), 301-318.
7. Y. Lee, and N. Law, “Explorations in promoting conceptual change in electrical concepts via ontological category shift”, Int. J. Sci. Educ. **23**, (2001), 111-149.
8. H. Küçüközer, and S. Kocakülah, “Secondary school students’ misconceptions about simple electric circuits”, Journal of Turkish Science Education **4**, (2007), 101-115.
9. H. Küçüközer, and Neset Demirci, “Pre-service and in-service physics teachers’ ideas about simple electric circuits”, Eurasia Journal of Mathematics, Science and Technology Education, **4(3)**, (2008), 303-311.
10. P. Loxley, Lyn Dawes, Linda Nicholls, and Babs Dore, Teaching Primary Science Promoting Enjoyment and Developing Understanding, Pearson Education Limited 2010.

Investigation of Freshmen Conceptual Understanding of Forces and Motions by using the Model Analysis Technique

S. Puttisanwimon*, S. Rakkapao, and T. Pengpan

Department of Physics, Faculty of Science, Prince of Songkla University,
Hatyai, Songkhla, 90112, Thailand
**Corresponding author. E-mail: choky13@gmail.com*

Abstract

To examine students' conceptual understanding of forces and motions, the Force and Motion Conceptual Evaluation (FMCE) test was administered to 420 freshmen (18% male) of faculty of Science, Prince of Songkla University (PSU) in year 2012. These students, enrolled in the fundamental physics I course, were asked to determine 43 items of the FMCE both at the beginning and the end of the conventional classes as pre-and post-tests, respectively. For the FMCE results, although it was displayed by the paired t-test at 0.05 significant level that the post-test mean score (13.05±7.44) was greater than the pre-test mean score (9.03±4.00), most students still held misunderstanding of forces and motions. To illustrate the overall improvement, we have calculated the average normalized gain ($\langle g \rangle$) and found the low learning gain (0.12±0.02) of these students. Moreover, the results have shown that these students had the lowest learning gain (0.06±0.02) on the cluster of the first and second laws of Newton. We then analyzed the characteristics of these students' mental models on that topic by using the model estimation of the model analysis technique. Based on the largest eigenvalue and its eigenvectors, as well as the model plot, it obviously revealed that both pre-and post-class model states of these students, taught by traditional lecture-based methods, were still in the misconception state. These preliminary findings indicated that a more active instructional approach is required for freshmen physics lecture classes.

Keywords: Conceptual understanding, misconception, forces and motions, normalized gain, model nnalysis

Introduction

The evaluation plays a significant role in Physics Education Research (PER) as it reveals the students' prior knowledge, as well as the students' improvement at the end of classes. Generally, class quantitative evaluation by using the research-based multiple-choice tests in PER is such statistical methods as t-test, and normalized gain.

T-test is a basic statistical method for comparing the difference of the two mean scores at any levels of significance. On the other hand, the normalized gain, developed by Richard Hake in 1998, can be calculated for demonstration the student's learning gain in a class or a given topic [1]. Both former methods do not show the students' mental model state of learning that will be of benefit to instructors in the views of guided information for developing proper teaching and learning processes for the learners.

The model analysis, founded by Lei Bao in 1999, has served this advantage [2]. It is a new evaluation technique in PER, which is based on the matrix mechanics of quantum physics. The model analysis consists of two algorithms; the concentration factor and the model estimation. The concentration factor is used for the test analysis by determining the distribution of students' responses from the multiple-choice instruments. The model estimation is used for investigation of students' mental models as the students' knowledge states.

In this study, we focus on the part of model estimation. Since several physics education researches have disclosed that numberless students have difficulties in identifying the correct answers when a similar concept is presented under different physical contexts [2-5]. Students' understanding depends on contexts of questions. The probability for a student to use a concept to solve a question is exposed by the model estimation of model analysis. The model estimation presents both the students' misconception and the students' mental model state of knowledge. Its results will introduce instructors in ways of plans and designs the instructional materials for classrooms. This method is useful in analyzing student's knowledge states in large classes with well designed multiple-choice questions.

To evaluate students' conceptual understanding on the topic of forces and motions, this study will utilize the model analysis technique. The collected data are from science freshmen at Prince of Songkla University by using the Force and Motion Conceptual Evaluation (FMCE) test.

Materials and Methods

1. Data collection

The data were collected both pre- and post-instruction from 420 complete responses of science freshmen (18% male), Prince of Songkla University, enrolling fundament physics I (332-101) course in the first semester of year 2012, by using Thai version of FMCE developed by the Physics Education Network of Thailand (PENThai) research group at Mahidol University. In the physics classes, these students were taught by using the traditional lecture-based method, including some physics animations from academic websites. The participants were asked to determine 43 items of the FMCE for 30 minutes. The FMCE is categorized into four-cluster contents, such as velocity, acceleration, the Newton’s first and second laws and the Newton’s third law [6]. Each item of FMCE is a multiple-choice single response question (A-H). If students consider that there is no correct choice, they can choose choice J.

2. T-test and Normalized gain (g)

In the study, we use t-test to compare the difference between pre-test and post-test mean scores. Because the pre-and post-test scores are from the same student, we select to calculate the paired-samples t-test as shown in the following equation:

$$t = \frac{\bar{d}}{\dfrac{S_d}{\sqrt{n}}} \qquad (1)$$

where $\bar{d}$ is the difference of average scores between pre- and post-classes; S_d is the standard deviation of difference scores; and n is number of samples.

The normalized gain is use to evaluate the effectiveness of the instructional tools by measuring the students’ learning gain. It is calculated from the ratio of the actual gain ($\langle G\rangle$) and the maximum possible gain ($\langle G\rangle_{\max}$) defined as:

$$\langle g\rangle = \frac{\%\langle G\rangle}{\%\langle G\rangle_{\max}} = \frac{\left(\%\langle S_f\rangle - \%\langle S_i\rangle\right)}{\left(100\% - \%\langle S_i\rangle\right)} \qquad (2)$$

where $\langle g\rangle$ is *average normalized gain* of a class; $\langle S_f\rangle$ and $\langle S_i\rangle$ are class average scores of post- and pre-tests as percentages, respectively. The interpretation of $\langle g\rangle$ values has been divided into 3 levels, namely high gain ($\langle g\rangle \geq 0.7$), medium gain ($0.3 \leq \langle g\rangle < 0.7$), and low gain ($\langle g\rangle < 0.3$), respectively. In general, an active learning method reinforces students’ learning gain into at least the middle level [1-2].

3. Model analysis

The theoretical framework of model analysis is based on the scientific researches of cognitive science, neuroscience and education [3-4]. It utilizes the qualitative researches to design the quantitative parameters. The part of model estimation of the model analysis aims to model students’ knowledge state for a given concept. Based on several previous researches, student understanding of a concept depends on the context [4]. It means that, for a given physics concept, students may apply a scientific concept to solve a question with one context, but they may use alternative concepts to answer other different context questions. Therefore, if we use a set of equivalent concept questions, designed for a particular physics concept to activate students understanding, the probability for students to apply different concepts in solving these questions can be measured by using the model estimation. Its diagram is shown in figure 1. When a student answers a question, the physical context of that question causes him/her to activate or create a certain model.

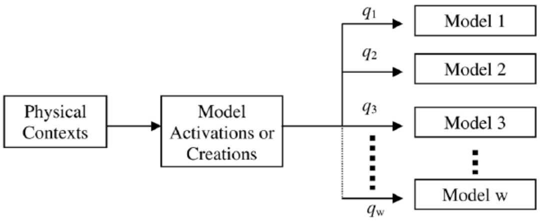

Figure 1. The diagram represents processes of model creations. There are a total of w common models in solving this problem (i.e., Model 1, Model 2,…, Model w). The q_1, q_2,…,q_w represent the probabilities for a student being triggered into activating the corresponding models [3].

This process is analogous to that of quantum measurement [2-3]. The different common models with context dependent defined as the mental model states. Each of common models is associated with an element of an orthonormal basis ($\hat{e}_w$) in a linear vector space. It can be shown mathematically as:

$$\hat{e}_1 = \begin{pmatrix} 1 \\ 0 \\ \vdots \\ 0 \end{pmatrix}, \quad \hat{e}_2 = \begin{pmatrix} 0 \\ 1 \\ \vdots \\ 0 \end{pmatrix}, \quad \ldots, \hat{e}_w = \begin{pmatrix} 0 \\ 0 \\ \vdots \\ 1 \end{pmatrix} \qquad (3)$$

where w is the total number of common models for a certain concept.

The responses from a single student to the research-based multiple-choice instruments are used to construct a student model state with a vector of unit length in the model space ($|u\rangle$). For example, for one concept with three common models, the model state for k^{th} student in a class is shown as:

$$\left|u_k\right\rangle = \frac{1}{\sqrt{m}}\begin{bmatrix}\sqrt{n_1^k}\\ \sqrt{n_2^k}\\ \sqrt{n_3^k}\end{bmatrix} \qquad (4)$$

where n_1^k, n_2^k and n_3^k represent the numbers of the k^{th} student answers corresponding with Model 1, Model 2 and Model 3, respectively. The *m* represents the total number of questions in that concept.

The individual student model state is used to construct a student density matrix (D_k), as show in the following.

$$D_k = u_k \otimes u_k^T = \left|u_k\right\rangle\left\langle u_k\right| = \frac{1}{m}\begin{bmatrix} n_1^k & \sqrt{n_1^k n_2^k} & \sqrt{n_1^k n_3^k}\\ \sqrt{n_2^k n_1^k} & n_2^k & \sqrt{n_2^k n_3^k}\\ \sqrt{n_3^k n_1^k} & \sqrt{n_3^k n_2^k} & n_3^k \end{bmatrix} \qquad (5)$$

For the entire class, we then sum the student density matrices and divide it by number of all students (N) called the class density matrix (D). It is the average of the individual students' model density matrices.

$$D = \frac{1}{N}\sum_{k=1}^{N} D_k = \frac{1}{N.m}\begin{bmatrix} n_1^k & \sqrt{n_1^k n_2^k} & \sqrt{n_1^k n_3^k}\\ \sqrt{n_2^k n_1^k} & n_2^k & \sqrt{n_2^k n_3^k}\\ \sqrt{n_3^k n_1^k} & \sqrt{n_3^k n_2^k} & n_3^k \end{bmatrix} \qquad (6)$$

Then eigenvalues and eigenvectors are computed to show the students' distribution in each common model.

For the presentation of these values, we will create the model plot. It is a two-dimensional graph to represent the class use of two models (correct and incorrect) [2]. It is displayed by using a large eigenvalue (> 0.65) which established the primary eigenvector to be represented as a point in a space of graph. The class model state is expressed by this point and shown in Figure 2. The primary vector, denoted by $v_\mu = \left(v_{1\mu}, v_{2\mu}, v_{3\mu}\right)^T$ with the large eigenvalue σ_μ^2 is a point on the model plot with a coordinate $\left(P_1, P_2\right)$, where $P_1 = \sigma_\mu^2 v_{1\mu}^2$ and $P_2 = \sigma_\mu^2 v_{2\mu}^2$ [3]. Each region in the model plot can give information about the class model state in each concept, which model 1 as correct model, model 2 as incorrect model, and the middle as mixed model state.

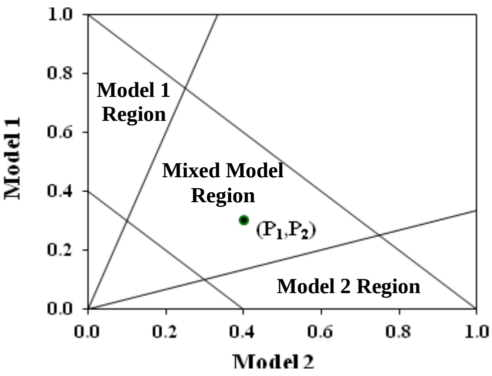

Figure 2. Model plot and model regions [3].

Results and Discussion

1. Results of T-test and Normalized Gain

The FMCE data were first calculated the paired t-test to compare the difference between pre-test and post-test mean scores. The results showed that the post-test mean score (13.05 ± 7.44) was greater than the pre-test mean score (9.03 ± 4.00) at 0.05 significant level. Hence, these students, learned by the traditional lecture-based approach, have knowledge increment.

Moreover, we have analyzed the percentage of these students in correct responses on pre-and post-tests, and improvement via the average normalized gain ($\langle g \rangle$) as shown in figure 3. It was displayed as overall data and the four-cluster concept. Total students' learning gain was in the low level ($\langle g \rangle$=0.12). Generally, the students' correct answers were less than 35% for post-test and 25% for pre-test, with the exception of the cluster concept of velocity. This means that these students have less problem on that topic. Its learning gain was in the middle level ($\langle g \rangle$=0.60). In contrast, these students had the lowest learning gain ($\langle g \rangle$=0.06) on the cluster concept of the first and second laws of Newton. There was merely 20% correction of these students in post-test. Therefore, we selected to focus on that topic by computing the model estimation.

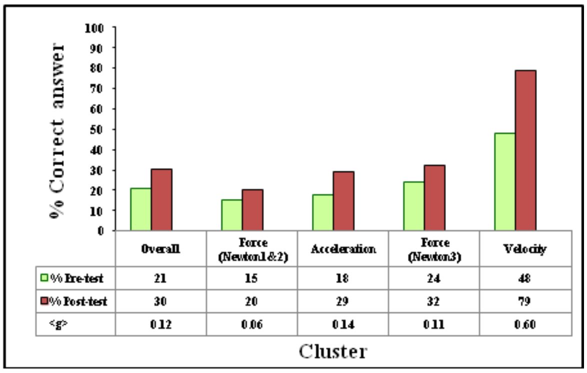

Figure 3. Average normalized gain ($\langle g \rangle$) and percentage of students' correct answers of FMCE pre- and post-tests categorized into overall and four-cluster concept.

2. Results of Model Analysis

This study has measured the model analysis only on the topic of the first and second laws of Newton's motion. Based on qualitative physics education researches, students' common models on this topic were classified as:

Model 1: It is necessary to have a force to maintain motion and there is no such a thing as a "force in the direction of motion." (Correct model);

Model 2: A force is needed to maintain motion. This model also includes the ideas that there is always a force in the direction of motion and that the force is directly related to the velocity of motion. (Incorrect model); and

Model 3: Other ideas and incomplete answers (Null model) [3].

We utilized question 2, 5, 11 and 12 of the FMCE as the typical items associated with the concept. Then the data were analyzed to find out a student model state, a student density matrix and a class density matrix, respectively. In this study, we calculated eigenvalues and eigenvectors by using the freeware program called ***Scilab*** [7]. The class density matrices, dominant eigenvalues and their primary eigenvectors were shown in the following table 1.

Eventually, the eigenvalues and the primary eigenvectors are constructed to be the class model state plotting on the model plot, as shown in figure 4.

Table1: Results of pre-and post class density matrices, dominant eigenvalues, primary eigenvectors, and components of the class model point.

Result	Pre-test	Post-test
Class density matrix	$\begin{bmatrix} 0.10 & 0.12 & 0.07 \\ 0.12 & 0.58 & 0.33 \\ 0.07 & 0.33 & 0.32 \end{bmatrix}$	$\begin{bmatrix} 0.21 & 0.23 & 0.06 \\ 0.23 & 0.66 & 0.15 \\ 0.06 & 0.15 & 0.13 \end{bmatrix}$
Dominant eigenvalue	0.84	0.79
Primary eigenvactor	$\begin{pmatrix} 0.19 \\ 0.82 \\ 0.55 \end{pmatrix}$	$\begin{pmatrix} 0.38 \\ 0.90 \\ 0.23 \end{pmatrix}$
Class model point		
A vertical component	$P_1=(0.84)(0.19)^2$ $=0.03$	$P_1=(0.79)(0.38)^2$ $=0.11$
A horizontal component	$P_2=(0.84)(0.82)^2$ $=0.56$	$P_2=(0.79)(0.90)^2$ $=0.64$

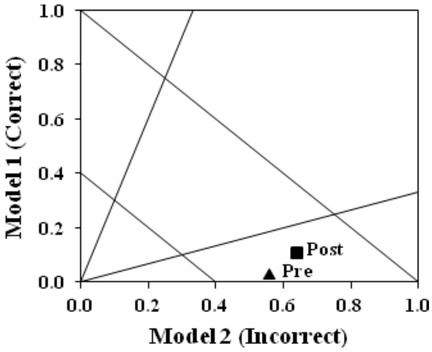

Figure 4. Model plot of freshmen class model states on the first and second laws of Newton concept from the FMCE data.

In the model plot, although a small shift of the post-class model points towards the correct model (model 1), both pre- and post-class model points were located in the incorrect model (model 2) region. This indicated that most students still have misconception about force and motion concept even after lecture class instruction. Thus, a more active instruction is necessary to use in physics classes to improve students' learning.

Conclusions

In this study, we have evaluated science freshmen understanding of forces and motions by using the FMCE. Both pre-and post-test data of the traditional lecture-based class were analyzed. Results have been revealed by the paired t-test at 0.05 significant level that the post-test mean score was greater than the pre-test mean score. Overall improvement of these students was in the low level acquired by calculating the average normalized gain. Moreover, the students' lowest learning gain was found in the first and second laws of Newton concept. Ultimately, the data of that concept were measured by the model estimation of the model analysis technique. It was shown by the model plot that both pre- and post-class model states of these freshmen were still in the misconception region. These findings have suggested the significant information that a more active instruction is desired for freshmen physics lecture classes.

Acknowledgments

This work was supported by the Graduate School and the Department of Physics, Prince of Songkla University. The authors would like to thanks all participating students, and also to show gratitude to the PENThai team at Mahidol university.

References

1. R. R. Hake, "Interactive-engagement versus traditional methods: A six-thousand-student survey of mechanics test data for introductory physics courses," Am. J. Phys. 66 (1), 64-74 (1998).
2. L. Bao, University of Maryland, 1999.
3. L. Bao and E. F. Redish, "Model analysis: Representing and assessing the dynamics of student learning," Physical Review Special Topics-Physics Eucation Research 2, 1-16 (2006).
4. K. Hogg L. Bao, and D. Zollman, "Model analysis of fine structures of student models: An example with Newton's third law," Am. J. Phys. 70, S766-S787 (2002).
5. P. Wattankasiwich and S. Anata, "Model Analysis: A Quantum Approach to Analyze Student Understanding," Chiang Mai J. Sci. 36 (1), 24-32 (2009).
6. T. I. Smith and M. C. Wittmann, "Applying a resources framework to analysis of the Force and Motion Conceptual Evaluation," Physical Review Special Topics-Physics Eucation Research 4 (020101), 1-12 (2008).
7. Scilab Enterprises S.A.S, "Scilab 5.3.3", (Claude Gomez, CEO, Versailles, France, 2001), Vol. 2013.

Physical Conception in High-school Chemistry textbooks; Electron Cloud Model

Y. Aramsri[1*], K. Arayathanitkul[2], and J. Tantirungrotechai[1]

[1]*Department of Chemistry, Faculty of Science, Mahidol University, Bangkok, Thailand.*
[2]*Department of Physics, Faculty of Science, Mahidol University, Bangkok, Thailand.*
[*]*Corresponding author. E-mail: y.aramsri@hotmail.com*

Abstract

This article presents physical conception in high-school Chemistry textbooks about electron cloud model. This research analyzed the contents of several Thai high-school Chemistry textbooks. Fifteen high-school Chemistry textbooks used in Thailand were analyzed. The books surveyed showed quotes, argument, or pictures are wrong and mismatch to popular chemistry textbook or popular physics textbook. For example, path of electron movement around the nucleus is a spherical shape, and probabilities of finding electron have certain boundary. Moreover, these explanations relate to student' misconception that had been explored already.

Keywords: Electron cloud model, sources of misconceptions, high-school chemistry textbooks

Introduction

Textbook is a source of knowledge for students. They can use textbooks for further reading, as additional source of information, and etc. In secondary school Chemistry, The Institute for promotion of Teaching Science and Technology' Chemistry textbook is recommended for students. Actually, students do not only use IPST Chemistry textbook but also use other textbooks such as Basis and additional Chemistry M.4. [1] It cannot be denied that textbooks have influences on student learning. Therefore, the content on these textbooks, must be checked, criticized, and developed in order to achieve the best results in student learning. If information in textbooks is wrong or uncertain, it will lead to students' misunderstanding. In the past, the study of Michael J. Sanger [2] showed that the texts and pictures in the book caused the students' misunderstanding, that relates to students misunderstand that had been explored already. Moreover, Georgios Tsaparlis and Georgios Paphotis [3] found that misunderstood the electron cloud model. They mistakenly perceived the electron cloud with a finite boundary because that was what was described in the book.

Therefore, this article aims to answer the question whether. The content, on the electron cloud model in textbooks is a source of students' misconception.

Materials and Methods

To answer to the question above, 15 Text books that had been printed between 1987 and 2008 were analyzed by considering the content, text, badly images or any information that will mismatch to popular chemistry textbook or popular physics textbook and will relate to student' misconception that had been explored already.

Results and Discussion

Form the analysis of the textbooks, we found...

First, Statements. In Textbooks have been written that the movement of electron has several type such as spherical shape, orbital shapes..

"The movement of the electrons around the nucleus has a spherical or other shape depending on the energy level of electrons"[1] [4]

"The movements of electron around the nucleus have several types and energy. There are orbital... may be s-orbital, p-orbital, d-orbital or f-orbital"[2] [5]

---

[1] In Thai, *"อิเล็กตรอนเคลื่อนที่ไปรอบ ๆ นิวเคลียสเป็นรูปทรงกลมและรูปอื่น ๆ ซึ่งจะเป็นรูปใดขึ้นอยู่กับระดับพลังงานของอิเล็กตรอน"* [4]

[2] In Thai, *"การเคลื่อนที่ของอิเล็กตรอนรอบ ๆ นิวเคลียสมีได้หลายแบบและมีพลังงานต่าง ๆ กันก็คือออร์บิทัล... อาจจะเป็น s-orbital, p-orbital, d-orbital หรือ f-orbital"* [8]

But in fact, we cannot tell about the types of the movement of electron. We only tell about probability of electron. In addition, orbital or orbital shapes are not the movement of electron but they are the area that finding electron. In Raymond Chang' textbook, popular chemistry textbook, explain orbital is wave function of electron. [6]

The statements in textbooks reflect that writer did not explain electrons by quantum mechanics. The statement, the movement of electron has spherical shape, supports student's misconception, that atoms have electrons circling them like planets around a star. [7]

Second, Argument. There has argument in textbook in order to conclude why we cannot tell certainly position of the electron. There have many premises in argument.

- The movement of electron has several types
- Electrons have small size
- Electrons move faster
- Electrons move around nucleus
- The movement of electron has not certainly position

The argument is not workable. In fact, we cannot tell certainly position of the electron. It's natural. Sometime electron likes wave and other time electron like particle. [6] Moreover, wave has equally amplitude. Therefore, we cannot tell certainly position of the electron. [8] Uncertainly position of the electron argument is not match with several types of electron motion and other in the textbooks.

The statements in textbooks reflect that writer did not explain electrons by quantum mechanics.

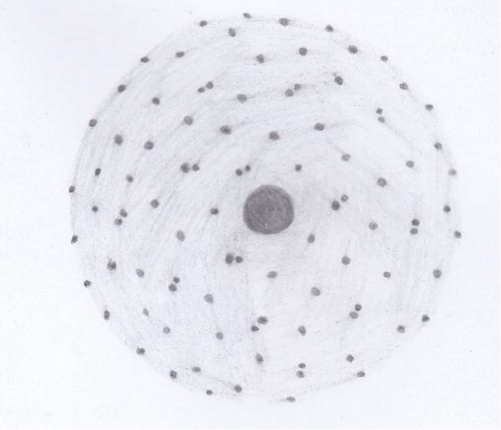

Figure 1. Pictures of Electron cloud model is a source of misconception. The probability picture looks like circle and has a certain boundary.

Finally, Electron cloud model. There has the picture of the electron cloud model with finite boundary in textbooks. As shown in figure 1, the probabilities of locating electron in any areas around the nucleus are equal. Additionally, the probability picture looks like circle and has a certain boundary. Or in other words, there are two locations, in and out of the circle. In the circle, there are dots or electron cloud to represent the probability of locating electrons of the circle, there is neither electron cloud nor the probability of locating electrons. In addition, dots may represent high probability of locating electron, and gray area may represent low probability of locating electron.

In the past, Georgios Tsaparlis and Georgios Papaphotis conducted research about Quantum-chemical concept by using student's tests. The interesting question was which was the picture that presented the probability of locating electron with a finite boundary? They found that only 11% of students gave the answer of the electron cloud model without the boundary. Moreover, some of students told them that both pictures are correct, because both picture appeared in textbook! [3]

Moreover, electron cloud model as shown in figure 1 looks like Thomson atomic model.[6] Thomson atomic model looks like circle and has pot that is negative charges in circle.

Conclusions

This article answers question whether. The content, on the electron cloud model in textbooks is a source of the students' misconception. Because, there have wrong statement, badly argument and wrong electron cloud model. Not only wrong but also relate to student' misconception that had been explored already. When student read this textbook, it tend to make theirs misunderstand and disadvantage for learning.

Suggestion

1. Should be checked, criticized, commented and developed textbooks and other source of knowledge.

2. Physicists and physics educator should concern this topic and other of physical knowledge in chemistry course. If students learn the same physical knowledge in chemistry before physics course, they may have misconception.

References

1. Ninpon. Basic and additional Chemistry M.4.
2. Bangkok: The Book. 2004.Michael J. Sanger. "An analysis of College Chemistry textbooks as sources of misconceptions and errors in

Electrochemistry" Journal of Chemical Education **76** (1999), 853-860.

3. Georgios Tsaparlis and Georgios Paphotis. "Quantum-chemical concept: Are they suitable for secondary student." Chemistry education: Research and practice in Europe **3** (2002), 129-144.
4. Sompong. Modern Academic Chemistry M.4 volume1. Bangkok: Hi-Ed publishing. 1978
5. Tawjunnong. Chemistry volume 1 Bangkok: Hi-Ed publishing.
6. Raymond Chang. Chemistry (Edition 10). New York:McGrawHill. 2010.
7. Chris Horton. (2001). Student Preconceptions and Misconceptions in Chemistry. [Online] Available : http://assessmentws.wikispaces.com/file/view/chemistry-misconceptions.pdf/30978619/chemistry-misconceptions.pdf (1 January 2013)
8. Chernchok, and other. Physics II (Edition 4). Bangkok: Mahidol University.

Student Understanding of Electric Field Related with the Inverse Square Law

T. Unyapoti[1], T. Sujarittham[2*], N. Emarat[1], and K. Arayathanitkul[1]

[1]*Department of physics, Faculty of Science, Mahidol University, Bangkok, 10400, Thailand*
[2]*Institute for Innovative Learning, Mahidol University, Nakhon Pathom, 73170, Thailand*
**Corresponding author. E-mail: terzo_san_trio@hotmail.com*

Abstract

One problem of learning electrostatics is that students often learn by using their common-sense beliefs about electric field. This study investigated 162 first-year university students' conceptual understanding of finding electric field from a point charge after learning introductory physics courses. We administered the Electrostatics Conceptual Evaluation Test to the students as pre and post tests. There were two questions of interest in this study. The first question was a comparison of the electric field from a point charge at two different positions, one being twice the distance of the other. The use of the inverse square law is required to find the electric field at the new position. It was found that 74.1 percents of the students answered correctly. The second question was a comparison of the electric field between charges that had the same size but with different Gaussian surfaces. 68.5 percents of the students answered this question correctly. In addition, 72.2 percents of the students who answered the first question with the idea that the electric field decreases as the distance increases, got the correct answer in the second question. This showed that most students were able to link the knowledge of the inverse square law and Gauss law in finding the electric field from a point charge.

***Keywords*:** Inverse square law, Student understanding, Electric field

บทนำ

ในการสำรวจความเข้าใจเรื่องไฟฟ้าสถิต โดยส่วนมากพบว่าผู้เรียน ยังคงมีความเข้าใจที่คลาดเคลื่อนอยู่มาก โดยเฉพาะในเรื่องสนามไฟฟ้า [Maloney et al.; Ding et al.; Singh] พบว่านักเรียนส่วนมาก ไม่สามารถเขียนเวกเตอร์แสดงสนามไฟฟ้าได้ เนื่องมาจากผู้เรียนยังคงมีความเข้าใจที่คลาดเคลื่อนเกี่ยวกับ ความสัมพันธ์ระหว่างขนาดสนามไฟฟ้ากับระยะห่างจากจุดประจุ อาทิเช่น ในเรื่องการหาสนามไฟฟ้าลัพธ์เนื่องจากจุดประจุหลายจุดประจุ นักเรียนส่วนมากมักจะรวมเพียงแค่ สนามไฟฟ้าลัพธ์เนื่องจากจุดประจุที่อยู่ใกล้ตำแหน่ง ที่สนใจหาสนามไฟฟ้าลัพธ์เท่านั้น เนื่องจากมีแนวคิดว่า ประจุที่อยู่ไกลออกไปจะไม่มีผลต่อทิศทางและขนาดของสนามไฟฟ้าลัพธ์ จากผลดังกล่าวแสดงให้เห็นชัดเจนว่า ผู้เรียนยังคงมีความเข้าใจที่คลาดเคลื่อนในการหาขนาดของสนามไฟฟ้า ซึ่งสัมพันธ์กับกฎกำลังสองผกผันของระยะทางซึ่งเป็นแนวคิดพื้นฐานของเรื่องนี้ [Bilal and Erol] ซึ่งจะส่งผลโดยตรงต่อนักศึกษาในระดับปริญญาตรีชั้นปีที่ 1 ที่จะต้องเรียนเรื่องการหาขนาดสนามไฟฟ้าโดยประยุกต์ใช้กฎของเกาส์ ซึ่งกฎดังกล่าวต้องมีเชื่อมโยงกับหลายแนวคิด ได้แก่ ฟลักซ์ไฟฟ้า สนามไฟฟ้า การหาปริพันธ์และผลคูณเชิงสเกลาร์ของเวกเตอร์ เป็นต้น จากผลการวิจัยเบื้องต้นของผู้วิจัยในปีที่ผ่านมาของผู้วิจัยพบว่า เมื่อบริบทของคำถามเปลี่ยนไปจากเดิม คือให้หาขนาดสนามไฟฟ้าเนื่องจากจุดประจุที่ตำแหน่งต่างๆ เป็นให้หาขนาดสนามไฟฟ้าที่ตำแหน่งหนึ่งบนผิวของเกาส์ ที่มีขนาดเปลี่ยนไป ผู้เรียนไม่สามารถตอบคำถามได้อย่างถูกต้อง ซึ่งแสดงให้เห็นว่า ผู้เรียนไม่มีความเข้าใจในพื้นฐานการหาขนาดของสนามไฟฟ้าซึ่งสัมพันธ์กับกฎกำลังสองผกผันของระยะทางอย่างแท้จริง

งานวิจัยนี้จะเป็นการสำรวจความเข้าใจในแนวคิด ของนักศึกษาชั้นปีที่ 1 เกี่ยวกับการหาสนามไฟฟ้าเนื่องจากจุดประจุ ที่สัมพันธ์กับแนวคิดตามกฎกำลังสองผกผัน และการเชื่อมโยงความรู้จากกฎกำลังสองผกผันกับกฎของเกาส์ในการหาขนาดของสนามไฟฟ้าเนื่องจากจุดประจุ

ระเบียบวิธีวิจัย

กลุ่มตัวอย่าง

นักศึกษาระดับปริญญาตรีชั้นปีที่ 1 คณะวิทยาศาสตร์ จำนวน 162 คน ที่เข้าเรียนในรายวิชาฟิสิกส์ทั่วไป ประจำปีการศึกษา 2555

เครื่องมือวัดผลและการเก็บข้อมูล

ในการศึกษาความเข้าใจ ของนักศึกษาในแนวคิดเกี่ยวกับการหาสนามไฟฟ้าเนื่องจากจุดประจุ ที่สัมพันธ์กับแนวคิดตามกฎกำลังสองผกผัน ผู้วิจัยใช้แบบสำรวจแนวคิดเชิงวิทยาศาสตร์เรื่องไฟฟ้าสถิต ที่ประยุกต์มาจากแบบทดสอบมาตรฐาน และตำราภาษาต่างประเทศ ฉบับแปลภาษาไทย [Young et al.; Knight] โดยให้นักศึกษาทำแบบทดสอบทั้งก่อนและหลังเรียน หัวข้อเรื่องไฟฟ้าสถิตในภาคเรียนที่สอง ซึ่งคำถามที่เลือกมาวิเคราะห์ในการศึกษานี้มีจำนวน 2 ข้อ ข้อแรกเป็นการเปรียบเทียบสนามไฟฟ้าจากจุดประจุ ณ ตำแหน่งที่มีระยะห่างเพิ่มเป็นสองเท่าของเดิม ซึ่งอาศัยกฎกำลังสองผกผัน ในการหาสนามไฟฟ้าที่ตำแหน่งใหม่ และข้อที่สองเป็นการเปรียบเทียบสนามไฟฟ้าเนื่องจากจุดประจุ 3 จุดประจุที่มีขนาดประจุเท่ากันแต่มีผิวของเกาส์ขนาดแตกต่างกัน โดยคำถามข้อที่หนึ่งเป็นแบบเลือกตอบ ส่วนคำถามข้อที่สองเป็นการเขียนตอบ แสดงการเปรียบเทียบขนาดของสนามไฟฟ้าและแสดงเหตุผลประกอบ คำถามที่อยู่ในแบบทดสอบเป็นดังนี้

ข้อ 1. อนุภาคที่มีประจุ +Q ถูกตรึงไว้ พบว่า สนามไฟฟ้าเนื่องจากอนุภาคนี้ที่ตำแหน่ง A มีขนาดเป็น E และมีทิศทางดังรูป ขนาดของสนามไฟฟ้าเนื่องจากอนุภาคดังกล่าว ที่ตำแหน่ง B มีค่าเท่าใด

ก) 4E ข) E ค) E/2 ง) E/4 จ) อื่นๆ ระบุ.......

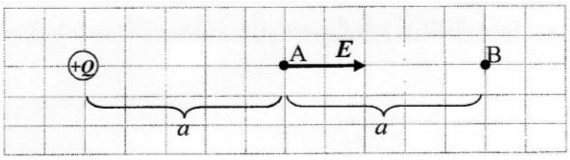

รูปที่ 1. ภาพประกอบที่ใช้สำหรับคำถามข้อ 1

ข้อ 2. ฉนวนทรงกลมตันมีขนาดเท่ากันสามอัน แต่ละอันมีประจุ +Q เท่ากันกระจายอยู่อย่างสม่ำเสมอ โดยทรงกลมตันทั้งสามถูกล้อมรอบด้วยผิวของเกาส์รูปทรงกลม ที่มีรัศมีต่างกันดังรูป จงเปรียบเทียบขนาดสนามไฟฟ้า (E_A, E_B, E_C) เนื่องจากทรงกลมตัน ณ จุดหนึ่งบนผิวเกาส์ในแต่ละแบบ พร้อมทั้งให้เหตุผลประกอบ

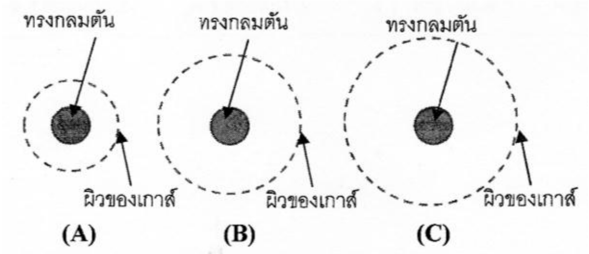

รูปที่ 2. ภาพประกอบที่ใช้สำหรับคำถามข้อ 2

ผลการวิจัยและอภิปรายผล

จากผลการสำรวจความเข้าใจของนักศึกษา ก่อนเรียนเรื่องไฟฟ้าสถิต พบว่านักศึกษาส่วนมากตอบผิดทั้งข้อ 1 และข้อ 2 เป็นจำนวนถึง 90 คน หรือคิดเป็นร้อยละ 55.6 ดังข้อมูลที่แสดงในตารางที่ 1 แสดงให้เห็นว่านักศึกษาในกลุ่มนี้มีความเข้าใจที่คลาดเคลื่อน กับการหาขนาดของสนามไฟฟ้าจากจุดประจุ อีกทั้งยังมีจำนวนนักศึกษาที่ตอบถูกทั้งข้อ 1 และข้อ 2 เพียง 13 คน ซึ่งเป็นสิ่งช่วยยืนยันได้ว่านักศึกษาส่วนมาก มีความเข้าใจที่คลาดเคลื่อนในการหาขนาดสนาม ไฟฟ้าจากจุดประจุอยู่

ตารางที่ 1: รูปแบบคำตอบของนักศึกษาในการทำแบบทดสอบก่อนเรียน

ข้อ 1	ข้อ 2	จำนวนนักศึกษา (คน)
✓	✓	13
✓	✗	36
✗	✓	23
✗	✗	90
รวม		162

✓ นักศึกษาตอบคำถามได้ถูกต้อง

✗ นักศึกษาตอบคำถามไม่ถูกต้อง

ผลจากการตอบแบบทดสอบก่อนเรียน เรื่องไฟฟ้าสถิตของนักศึกษา ผู้วิจัยพบว่านักศึกษาตอบถูกข้อ 1 จำนวน 49 คน คิดเป็นร้อยละ 30.2 ซึ่งยังไม่ถึงครึ่งแสดงให้เห็นว่านักศึกษาส่วนใหญ่ ยังไม่เข้าใจการหาขนาดสนามไฟฟ้าจากกฎกำลังสองผกผัน และตอบถูกข้อ 2 จำนวน 36 คน คิดเป็นร้อยละ 22.2 แสดงให้เห็นว่านักศึกษาส่วนใหญ่ไม่เข้าใจการหาขนาดของสนามไฟฟ้าจากกฎของเกาส์ได้ อีกทั้งพบว่านักศึกษาส่วนใหญ่ ไม่สามารถเลือกคำตอบที่ถูกต้องได้ เนื่องจากนักศึกษากลุ่มนี้ มีความเชื่อว่า “ถ้าเพิ่มระยะห่างเป็นสองเท่าสนามไฟฟ้าก็จะลดลงครึ่งหนึ่ง” หรือ “การเพิ่มระยะห่างไม่มีผลกับสนามไฟฟ้าที่เกิดขึ้น ณ ตำแหน่งใหม่” ซึ่งความเชื่อแบบนี้นั้นเป็นแนวคิดที่คลาดเคลื่อน เนื่องจากคำถามในข้อ 1 นี้ต้องอาศัยกฎกำลังสองผกผันในการหาสนามไฟฟ้าที่ตำแหน่งใหม่แทนการแปรผกผันที่นักศึกษาส่วนใหญ่เข้าใจ และสำหรับคำถามในข้อ 2 ต้องอาศัยกฎของเกาส์ในการหาคำตอบ ซึ่งมีแนวคิดที่มีความสัมพันธ์กับกฎกำลังสองผกผัน

ในกลุ่มที่ตอบถูกในข้อ 1 แต่กลับผิดในข้อ 2 มีจำนวนถึง 36 คน แม้ว่าจะเข้าใจเรื่องการหาสนามไฟฟ้าจากกฎกำลังสองผกผันแล้ว แต่นักศึกษากลุ่มนี้ก็ไม่สามารถเชื่อมโยงแนวคิดที่ถูกต้องกับกฎของเกาส์ได้ ในกลุ่มที่ตอบผิดในข้อ 1 แต่กลับตอบถูกในข้อ 2 นั้นส่วนใหญ่จะตอบข้อ 1 โดยมีแนวคิดว่า สนามไฟฟ้านั้นลดลงแบบผกผัน ทำให้สามารถเชื่อมโยงแนวคิดนี้กับข้อที่ 2 และสามารถที่จะเลือกคำตอบถูกได้ เนื่องมาจากข้อ 2 เป็นแค่การเปรียบเทียบขนาดของสนามไฟฟ้าจากผิวเกาส์ทรงกลมขนาดแตกต่างกัน ไม่ใช่การหาขนาดของสนามไฟฟ้า จึงทำให้นักศึกษาในกลุ่มนี้ยังสามารถตอบได้ถูกในข้อ 2

จากผลการสำรวจความเข้าใจ ของนักศึกษาหลังเรียนเรื่องไฟฟ้าสถิต พบว่านักศึกษาส่วนมากจะถูกทั้งข้อ 1 และข้อ 2 เป็นจำนวนถึง 90 คน หรือคิดเป็นร้อยละ 55.6 ดังข้อมูลที่แสดงในตารางที่ 2 แสดงให้เห็นว่านักศึกษาส่วนใหญ่มีความเข้าใจที่ถูกต้อง เกี่ยวกับการหาขนาดของสนามไฟฟ้าจากจุดประจุ และยังสามารถเชื่อมโยงระหว่างกฎกำลังสองผกผันกับกฎของเกาส์ ในการหาขนาดของสนามไฟฟ้าเนื่องจากจุดประจุได้ และพบว่านักศึกษามีความเข้าใจที่ถูกต้องมากกว่าก่อนเรียนที่มีนักศึกษาถูกทั้งสองข้อเพียง 13 คน อย่างชัดเจน แสดงให้เห็นว่านักศึกษาสามารถเข้าใจเนื้อหาเรื่องการหาสนามไฟฟ้าเนื่องจากจุดประจุได้

ตารางที่ 2: รูปแบบคำตอบของนักศึกษาในการทำแบบทดสอบหลังเรียน

ข้อ 1	ข้อ 2	จำนวนนักศึกษา (คน)
✓	✓	90
✓	✕	30
✕	✓	21
✕	✕	21
รวม		162

✓ นักศึกษาตอบคำถามได้ถูกต้อง

✕ นักศึกษาตอบคำถามไม่ถูกต้อง

ผลจากการตอบแบบทดสอบหลังเรียน เรื่องไฟฟ้าสถิตของนักศึกษา ผู้วิจัยพบว่านักศึกษาตอบถูกข้อ 1 จำนวนถึง 120 คน คิดเป็นร้อยละ 74.1 ซึ่งเป็นจำนวนถึงหนึ่งในสาม แสดงให้เห็นว่า นักศึกษาส่วนใหญ่เข้าใจการหาขนาดสนามไฟฟ้าจากกฎกำลังสองผกผัน และตอบถูกข้อ 2 จำนวน 111 คน คิดเป็นร้อยละ 68.5 และมีถึงจำนวน 99 คนที่ให้เหตุผลถูกด้วย แสดงให้เห็นว่านักศึกษาส่วนใหญ่เข้าใจการหาขนาดของสนามไฟฟ้าจากกฎของเกาส์

ในกลุ่มที่ตอบถูกข้อ 1 แต่ผิดข้อ 2 หรือกลุ่มที่ตอบถูกข้อ 2 แต่ผิดข้อ 1 มีจำนวนถึง 51 คน ที่ยังไม่สามารถเชื่อมโยงกฎกำลังสองผกผันกับ กฎของเกาส์ในการหาขนาดสนามไฟฟ้าเนื่องจากจุประจุได้ แม้ว่าจะผ่านการเรียนมาแล้วก็ตาม แต่ก็พบว่าในกลุ่มที่ตอบถูกข้อ 2 แต่ผิดข้อ 1 นั้นมีบางส่วนที่มีความเชื่อว่าสนามไฟฟ้าลดลงแบบแปรผกผัน ทำให้สามารถตอบถูกในข้อ 2 ได้ และก็ยังพบว่ามีนักศึกษาเป็นจำนวนหนึ่งที่ตอบผิดทั้งสองข้อ เพราะว่านักศึกษากลุ่มนี้ยังคงใช้ความเชื่อที่คลาดเคลื่อนในการเลือกคำตอบอยู่ แต่จำนวนของนักศึกษาในกลุ่มนี้ก็ลดลง เมื่อเทียบกับก่อนเรียนเรื่องไฟฟ้าสถิต แสดงให้เห็นว่านักศึกษาส่วนมากมีการพัฒนาความเข้าใจที่คลาดเคลื่อนให้ถูกต้องมากขึ้น

ผู้วิจัยยังพบอีกว่ามีนักศึกษาจำนวน 144 คน ที่ตอบ

คำถามข้อ 1 โดยมีแนวคิดว่าเมื่อระยะห่างเพิ่มมากขึ้น ขนาดของสนามไฟฟ้าจะลดลง สามารถเลือกคำตอบที่ถูกต้องในคำถามข้อ 2 ได้ถึง 104 คน คิดเป็นร้อยละ 72.2 เทียบกับผู้มีความเชื่อในรูปแบบนี้ แสดงให้เห็นว่านักศึกษาส่วนใหญ่สามารถเชื่อมโยงความสมพันธ์ระหว่างกฎกำลังสองผกผันกับกฎของเกาส์ในการหาสนามไฟฟ้าเนื่องจากจุประจุได้ ถึงแม้จะมีบางส่วนที่มีความเชื่อที่ไม่สมบูรณ์ แต่ก็ยังเลือกคำตอบที่ถูกในข้อ 2 ได้ดังที่ได้แสดงเหตุผลไว้ก่อนหน้านี้แล้ว

ในกลุ่มนักศึกษาที่ตอบคำถามข้อ 2 ผิด บางส่วนจะเข้าใจว่าสนามไฟฟ้าจะสัมพันธ์กับระยะทางแบบแปรผันตรง ซึ่งกลับกันกับความเป็นจริง บางส่วนก็เข้าใจว่าสนามไฟฟ้าขึ้นกับขนาดของประจุ ถ้าขนาดของประจุเท่ากันแล้วสนามไฟฟ้าก็จะเท่ากันด้วย

ข้อสรุปและข้อเสนอแนะ

จากผลการศึกษาในข้างต้น พบว่านักศึกษาสามารถเชื่อมโยงความสัมพันธ์ จากกฎกำลังสองผกผันและกฎของเกาส์ในการหาขนาดสนามไฟฟ้าเนื่องจากจุดประจุ ผู้วิจัยจึงมีความคาดหวังว่า ผลการศึกษานี้จะเป็นแรงผลักดันให้ครูอาจารย์ฟิสิกส์พัฒนาการจัดรูปแบบการเรียนการสอน ที่ช่วยส่งเสริมการเชื่อมโยงความสัมพันธ์ ของกฎกำลังสองผกผันให้เหมาะสมกับนักศึกษาได้

กิตติกรรมประกาศ

ขอขอบคุณกลุ่มวิจัยฟิสิกส์ศึกษา แห่งประเทศไทย (PENThai) ภาควิชาฟิสิกส์ คณะวิทยาศาสตร์ มหาวิทยาลัยมหิดล ที่ให้คำแนะนำที่ดี และขอขอบคุณคณะวิทยาศาสตร์ มหาวิทยาลัยมหิดลที่ให้ทุนสนับสนุนงานวิจัยในครั้งนี้

เอกสารอ้างอิง

1. Maloney, David P, et al. "Surveying Students' Conceptual Knowledge of Electricity and Magnetism." *American Journal of Physics* 69 (2001): S12.
2. Ding, Lin, et al. "Evaluating an Electricity and Magnetism Assessment Tool: Brief Electricity and Magnetism Assessment." *Physical Review Special Topics-Physics Education Research* 2.1 (2006): 010105.
3. Singh, Chandralekha. "Student Understanding of Symmetry and Gauss's Law of Electricity." *American Journal of Physics* 74 (2006): 923.
4. Bilal, Esra, and Mustafa Erol. "Investigating Students' Conceptions of Some Electricity Concepts." *Latin-American Journal of Physics Education* 3.2 (2009): 1.
5. Young, Hugh D., and Roger A. Freedman. *University Physics*. Addison Wesley, 2007.
6. Knight, R.D. *Physics for Scientists and Engineers with Modern Physics: A Strategic Approach*. Addison Wesley, 2004.

The Investigation of Student Concepts in Coulomb’s Law using *Concentration Factor* and *Model Analysis*

S. Phimsen and N. Suwonjandee [*]

Department of Physics, Faculty of Science, Chulalongkorn University,
Bangkok 10330 Thailand
**Corresponding author. E-mail: snarumon@gmail.com*

Abstract

The objective of this study is to investigate students’ basic understanding in the Coulomb's law concept under electromagnetism topic. We use two analysis methods called *concentration factor* and *model analysis* to analyze our data. The data are students’ responses in Coulomb's law concept on Brief Electricity and Magnetism Assessment (BEMA) standard test. There are 87 students’ samples in 2011 and 113 in 2012 from Faculty of Science, Chulalongkorn University. The results from both Concentration Factor and Model Analysis will be presented in this paper.

***Keywords*:** Concentration factor, model analysis, brief electricity and magnetism assessment (BEMA) standard test

Introduction

Coulomb's law is an important concept in physics that students have difficulties in understanding. They often understand this concept based on their experience. They could understand this concept intuitively when it makes sense to them and they often have different responses when it does not.

These problems are difficult to analyze with classical test theory, cluster analysis, or item response theory[1] because only correct responses from multiple choice tests would be interested. *Concentration factor* and *model analysis* are new approach to analyze multiple choice questions in which we can investigate misconceptions and alternative conceptions of students.

In this paper we use *concentration factor* and *model analysis* to investigate students’ responses in Coulomb’s law concept on three questions of Brief Electricity and Magnetism Assessment (BEMA) standard test [Appendix].

Materials and Methods

Concentration Factor

Concentration factor can be used to analyze the distribution of students’ responses which is determined as[2]:

$$C = \frac{\sqrt{m}}{\sqrt{m}-1}\left(\frac{\sqrt{\sum_{i=1}^{m} n_i^2}}{N} - \frac{1}{\sqrt{m}}\right) \qquad (1)$$

C has a value between 0 and 1 where n_i is the total number of student answering choice i. There are N students taking the test that have m choices.

Model analysis

L. Bao and E. F. Redish proposed that certain models of students are activated by context of questions[3]. They referred to a result of findings in fields of neuroscience, cognitive sciences, and education research. However, the process of model activation is complicated. So, only the probability of activating a certain model state could be obtained by investigating students’ responses in standard tests, as shown in Figure 1.

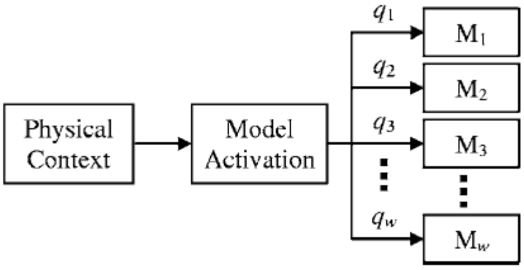

Figure 1. A diagram represents the process of model activation [3].

From the diagram, students have different certain models, $M_1, M_2,\ldots,M_w$ which the physical contexts (questions) trigger them to some models in which their probabilities are q_1, $q_2,\ldots, q_w$. This process could be treated as a process of quantum measurement. Firstly, physical models are defined in the model space as elements of an orthonormal basis in the vector space. Secondly, we construct a student model state as a vector in which physical models are elements of an orthonormal basis in vector space. We then construct a student model state of the k^{th} student by using students’ responses from the standard test as:

$$|u_k\rangle = \frac{1}{\sqrt{m}}\begin{bmatrix}\sqrt{n_{1k}}\\ \sqrt{n_{2k}}\\ \sqrt{n_{3k}}\end{bmatrix}, \qquad (2)$$

where n_{1k}, n_{2k} and n_{3k} are numbers of the k^{th} student answers corresponding with Model 1, Model 2 and Model 3, respectively. m is a total number of questions in a concept group. We construct a student density matrix of the k^{th} student as:

$$\mathcal{D}_k = |u_k\rangle\langle u_k| = \frac{1}{m}\begin{bmatrix} n_{1k} & \sqrt{n_{1k}n_{2k}} & \sqrt{n_{1k}n_{3k}} \\ \sqrt{n_{2k}n_{1k}} & n_{2k} & \sqrt{n_{2k}n_{3k}} \\ \sqrt{n_{3k}n_{1k}} & \sqrt{n_{3k}n_{2k}} & n_{3k}\end{bmatrix}. \qquad (3)$$

From student density matrix of all students, we construct class density matrix as:

$$\mathcal{D} = \frac{1}{N}\sum_{k=1}^{N}\mathcal{D}_k = \frac{1}{Nm}\sum_{k=1}^{N}\begin{bmatrix} n_{1k} & \sqrt{n_{1k}n_{2k}} & \sqrt{n_{1k}n_{3k}} \\ \sqrt{n_{2k}n_{1k}} & n_{2k} & \sqrt{n_{2k}n_{3k}} \\ \sqrt{n_{3k}n_{1k}} & \sqrt{n_{3k}n_{2k}} & n_{3k}\end{bmatrix}. (4)$$

Eigenvalues and eigenvectors will be obtained from class density matrix as:

$$\mathcal{D}|\mathbf{v}_\mu\rangle = \sigma_\mu^2|\mathbf{v}_\mu\rangle. \qquad (5)$$

σ_μ^2 is eigenvalue of eigenvector $|\mathbf{v}_\mu\rangle = [v_{1\mu} \quad v_{2\mu} \quad v_{3\mu}]^T$ where $v_{1\mu}$, $v_{2\mu}$ and $v_{3\mu}$ are components of $|\mathbf{v}_\mu\rangle$ corresponding with Model 1, Model 2 and Model 3, respectively and μ are numbers of eigenvalue according to numbers of model. If eigenvalue σ_μ^2 is larger than 0.65, then $|\mathbf{v}_\mu\rangle$ is dominant state. This dominant state is called *primary model state* which are often enough to represent the whole class[3].

Then, we obtain probabilities of the primary model state using Model 1 and Model 2 as $P_1 = \sigma_\mu^2 v_{1\mu}^2$ and $P_2 = \sigma_\mu^2 v_{2\mu}^2$, respectively. We can represent P_1 and P_2 as a point on the model plot, as shown in Figure 2.

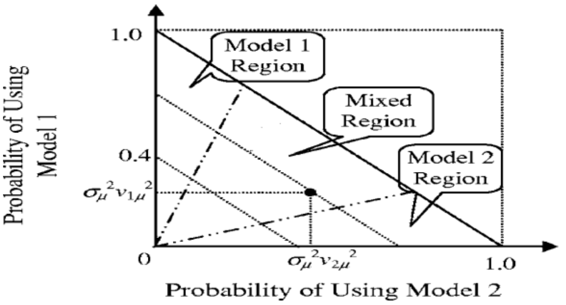

Figure 2. A model plot represents probabilities of using Model 1 and Model 2[3].

Data collection

The data are students' responses in Coulomb's law concept on Brief Electricity and Magnetism Assessment (BEMA) standard test. There are 87 students' samples in 2011 and 113 in 2012 from Faculty of Science, Chulalongkorn University.

Results and Discussion

Concentration factor

Results from *concentration factor* in 2011 and 2012 are summarized in Figure 3 and Figure 4.

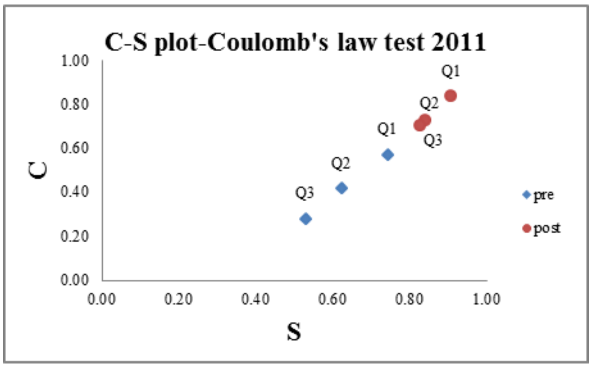

Figure 3. Plot of score versus concentration factor in 2011.

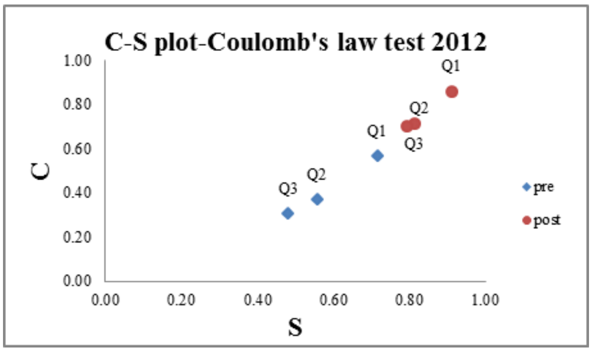

Figure 4. Plot of score versus concentration factor in 2012.

There is a similarity of C-S plots in 2011 and 2012. The plots show that students have improvement, but many of them have alternative conception. It can be seen that many students had correct model in Q1 (high score and high concentration factor), but they have incorrect models in Q2 and Q3 (low score and low concentration factor). Students' understanding can be analyzed in more detail by model analysis.

The Model Analysis

1. Identify physical models

We can identify physical models as:

Model 1: The correct model, the force between two point charges is directly proportional to the product of magnitude of each charge and inversely proportional to the square of distance between them.

Model 2: The incorrect model, the force between two point charges is not directly proportional to the product of magnitude of each charge and this force is not inversely proportional to the square of distance between them, but it depends on charges that are observed.

Model 3: Other ideas, students do not have the concept of Coulomb's law and answer choice “None of the above”.

2. Class density matrix

Results of class density matrix in 2011 and 2012 are shown in Table 1.

Table 1: Class Density Matrix in 2011 and 2012

Years	Pre	Post
2011	$\begin{bmatrix}0.62 & 0.13 & 0.18\\0.13 & 0.15 & 0.08\\0.18 & 0.08 & 0.23\end{bmatrix}$	$\begin{bmatrix}0.86 & 0.05 & 0.10\\0.05 & 0.06 & 0.02\\0.10 & 0.02 & 0.08\end{bmatrix}$
2012	$\begin{bmatrix}0.58 & 0.09 & 0.20\\0.09 & 0.11 & 0.07\\0.20 & 0.07 & 0.31\end{bmatrix}$	$\begin{bmatrix}0.84 & 0.05 & 0.07\\0.05 & 0.04 & 0.02\\0.07 & 0.02 & 0.12\end{bmatrix}$

L. Bao states that large off-diagonal elements of class density matrix indicated low consistency in using the physical models[4]. Table 1 shows the consistency of the post-tests which implies that most students have less alternative concept after instruction. We can obtain more detail by using eigenvalues and eigenvectors of class density matrix.

3. Eigenvectors and eigenvalues of class density matrix

From constructed class density matrices in Table 1, eigenvalues and eigenvectors of class density matrix can be obtained from (5). The results are shown in Table 2 and Table 3, respectively.

Table 2: Eigenvalues and Eigenvectors of Class Density Matrix in 2011

	σ_1^2 σ_2^2 σ_3^2	$\lvert v_1\rangle$	$\lvert v_2\rangle$	$\lvert v_3\rangle$
pre	0.20 0.80 0	$\begin{bmatrix}-0.55\\0.84\\0\end{bmatrix}$	$\begin{bmatrix}0.84\\0.55\\0\end{bmatrix}$	$\begin{bmatrix}0\\0\\1.00\end{bmatrix}$
post	0.11 0.88 0	$\begin{bmatrix}-0.18\\0.98\\0.05\end{bmatrix}$	$\begin{bmatrix}0.98\\0.18\\0\end{bmatrix}$	$\begin{bmatrix}0.01\\-0.05\\1.00\end{bmatrix}$

Table 3: Eigenvalues and Eigenvectors of Class Density Matrix in 2012

	σ_1^2 σ_2^2 σ_3^2	$\lvert v_1\rangle$	$\lvert v_2\rangle$	$\lvert v_3\rangle$
pre	0.22 0.76 0.02	$\begin{bmatrix}-0.58\\0.81\\0.06\end{bmatrix}$	$\begin{bmatrix}0.82\\0.58\\0.02\end{bmatrix}$	$\begin{bmatrix}0.02\\-0.06\\1.00\end{bmatrix}$
post	0.14 0.85 0.01	$\begin{bmatrix}-0.15\\0.99\\0.05\end{bmatrix}$	$\begin{bmatrix}0.99\\0.15\\0.01\end{bmatrix}$	$\begin{bmatrix}0\\-0.05\\1.00\end{bmatrix}$

The results show that $\lvert v_2\rangle$ is the primary model state because its eigenvalue is larger than 0.65[3]. We then plot the probabilities using Model 1 and 2 for $\lvert v_2\rangle$ state in 2011 and 2012 as shown in Figure 5.

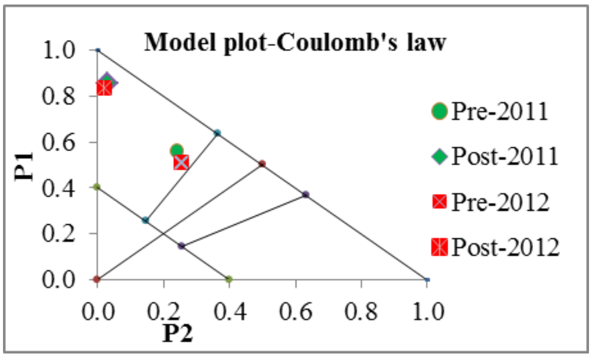

Figure 5. Model plot of pre-pest and post-test in 2011 and 2012.

From the model plot in Figure 5, all model points are located in the model 1 region. This indicates that most students in these two years have good understanding in the concept of Coulomb’ law prior instruction. Model points of post-tests move close to model 1 (correct model) axis and this indicates that students have more understanding after instruction.

Conclusions

From this investigation, the *concentration factor* shows that our students have improvement, but many of them have alternative conception while the *model analysis* could indicate in more detail. Class density matrices show the consistency of the post-tests which implies that most students have less alternative concept after instruction. The model plots in both 2011 and 2012 indicate that students have good concept in Coulomb’s law prior instruction and have improved their conceptual understanding after instruction. Moreover, the result shows that *concentration factor* and *model analysis* can be used to analyze students’ responses in more qualitative detail better than classical test theory, cluster analysis, or item response theory.

Acknowledgments

We would like to thank Department of Physics, Faculty of Science, Chulalongkorn University for financial support.

References

1. L. Ding and R. Beichner, Approaches to data analysis of multiple-choice questions, Phys. Rev. ST Physics Ed. Research 5, 020103 (2009)
2. L. Bao, and E. F. Redish, Concentration Analysis: A Quantitative Assessment of Student states, Am. J. Phys., 2001
3. L. Bao, and E. F. Redish, Model Analysis: Representing and Assessing the Dynamics of

Student Learning, Phys. Rev. ST Physics Ed. Research 2, 010103 (2006).

4. L. Bao, Dynamics of Student Modeling: A Theory, Algorithms, and Application to Quantum Mechanics, Ph.D. thesis, University of Maryland, 1999.

Appendix: Coulomb’s law concept on three questions of Brief Electricity and Magnetism Assessment (BEMA) standard test

Two small objects each with a net charge of +Q exert a force of magnitude F on each other:

We replace one of the objects with another whose net charge is +4Q:

Q1 The original magnitude of the force on the +Q charge was F; what is the magnitude of the force on the +Q charge now?

(a) 4F
(b) 5F/2
(c) 3F
(d) 2F
(e) F
(f) F/4
(g) None of the above

Q2 What is the magnitude of the force on the +4Q charge?

(a) 4F
(b) 5F/2
(c) 3F
(d) 2F
(e) F
(f) F/4
(g) None of the above

Next we move the +Q and +4Q charges to be 3 times as far apart as they were:

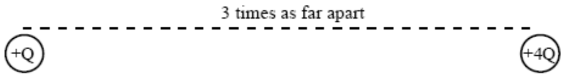

Q3 Now what is the magnitude of the force on the +4Q charge?

(a) 4F/3
(b) 4F/9
(c) F/3
(d) 5F/18
(e) 2F/9
(f) F/9
(g) F/36
(h) 4F
(i) None of the above

The Young's Modulus Measurement of Natural Thai Silk

O. Nookaew[1,2] an S. Limsuwan[1]*

[1]Department of Physics, Faculty of Science, King Mongkut's University
of Technology Thonburi, Bangkok 10140, Thailand
[2]Mahannoparam School, Bangkok 10170, Thailand
**Corresponding authors. E-mails: supanee.lim@kmutt.ac.th*

Abstract

A simple apparatus used for the Young's modulus measurements of silk fibers was designed and constructed. The silkworm (*Bombyx mori*) cocoons obtained from Ubonratchathani province were used in this study. The cocoons were cooked in boiling water for 60 min to remove serecin. Then, they were washed with flowing water for 5 min and dried in air for at least 24 h. It was found that silk fiber with a length of 700-1500 m was obtained from one cocoon. The silk fiber was cut into smaller segments with four different lengths of 20, 30, 40 and 50 cm. All the cut silk fibers were selected to obtain only the fiber with a diameter in the range of 0.15-0.17 mm. Moreover, for each length, 10 pieces of fiber were selected for the Young's modulus measurements. The results show that the Young's modulus values of the silk fiber obtained in this work varies within the range of 5-7 GPa.

Keywords: Silkworm fiber,tensile stress, Young's modulus

Introduction

Silkworm silk has long been recognized as a wonderful natural fiber due to its superior properties such as strength, elasticity, softness, luster, absorbency and affinity for dyes [1]. It has been utilized primarily as a textile fiber for about 5,000 years. The silkworm, *Bombyx mori*, silk consists of two type of proteins, fibroin and serecin. Fibroin is the protein that forms the filaments of silkworm silk and give silk its unique physical and chemical properties. Serecins are the group of gummy proteins which bind the fibroin filaments [1].

A silkworm caterpillar spins a lightweight and compact cocoon around itself by continuously moving its shape of either a figure 8 or an S and by cyclically bending and stretching its body. The construction of a cocoon needs approximately 3 days [2]. A cocoon is a natural polymeric composite shell made of a single continuous silk strand with a length in the range of 700-1,500 m and conglutinated by serecin [2,3].

Silkworm silk fiber is one of the most important materials extensively used in the textile industry. However, silk processing from cocoons to the finished clothing consists of a series of steps. Degumming is a key process during which serecin is removed by thermo-chemical treatment of the cocoon [4]. A simple process to remove serecin from the silk fiber is the cooking of the cocoons in boiling water. During the cooking, the silk fiber is reeled and finally a complete silk fiber is obtained [3].

In recent years, the structural, physical and mechanical properties of the silk fibers have been widely studied. Chen et al. [5] studied the structure and physical properties of silkworm cocoon. Reddy and Yang [6] studied the properties of cocoon and silk fibers produced by *Hyalophora cecropa*. Furthermore, the mechanical properties of silknworm cocoons were extensively studied by many researchers [2-4,7,8].

In present work, the silkworm (*Bombyx mori*) cocoons obtained from Ubonratchathani province were used for the Young's modulus measurements. A simple tensile stress apparatus was firstly designed and constructed for the Young's modus measurements.

Experimental

Materials preparation

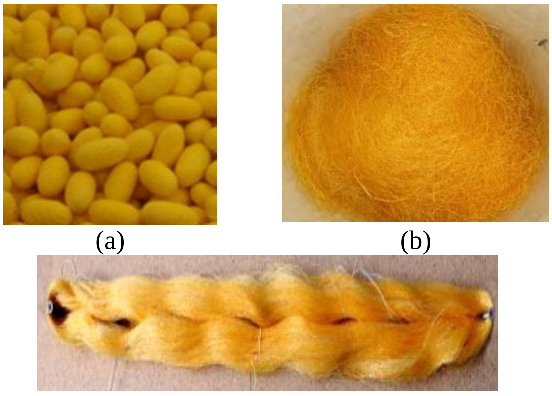
(a) (b)
(c)

Figure 1. Photographs showing:(a) silkworm cocoons, (b) silk fiber obtained from one cocoon after boiling and (c) silk fiber after reeling.

Figure 1 (a) shows the photograph of silkworm (*Bombyx mori*) cocoons used in this study. These cocoons obtained from Ubonratchathani province. To obtain the cocoon silk fiber, the following procedures were carried out. Firstly, the cocoons were cooked in boiling water for 60 min to remove serecin. Secondly, the cocoon silk fibers were washed with flowing water for about 5 min. Finally, the silk fibers were allowed to dry in air for at least 24 h. Figure 1(b) shows the silk fiber obtained from one cocoon after boiling. Figure 1(c) shows the silk fiber after reeling and we can get a complete fiber of 700-1500 m in length from each cocoon.

Each silk fiber was cut into smaller segments with four different lengths of 20, 30, 40 and 50 cm. The diameter of silk fiber was roughly measured by a micrometer to select the silk fiber with a diameter in the range of 0.15-0.17 mm. All the selected silk fibers, each length with 10 pieces, were used for the Young’s modulus measurements.

Young’s modulus measurements

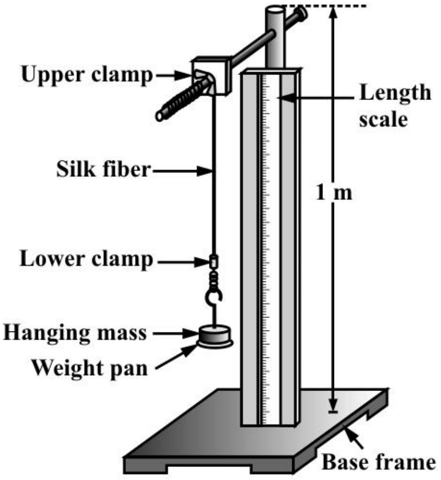

Figure 2. Experimental setup for the Young’s modulus measurements.

Figure 2 shows the experimental setup used for the Young’s modulus measurements of silk fibers. The silk fiber sample was clamped at both ends between upper and lower clamps. The lower clamp was hanged by a weight pan. A hanging mass, generally copper disk was used as a tensile force on the silk fiber.

Considering a silk fiber of cross-sectional area A and length L_0. When an external force, i.e. a copper disk was placed on the weight pan with a total mass m. As a result, the silk fiber was stretched to the length L. The tensile stress (σ) is defined by the ratio of the tensile force (F) to the cross-sectional area (A). Thus,

$$\sigma = \frac{F}{A} = \frac{mg}{A} \qquad \mathrm{N/m^2}\ \text{or Pa} \qquad (1)$$

The tensile strain (ε) is defined by the ratio of the change in length (ΔL) to the original length (L_0). Thus,

$$\varepsilon = \frac{L - L_0}{L_0} = \frac{\Delta L}{L_0} \qquad (2)$$

The Young’s modulus (Y) of material is defined by

$$Y = \frac{\sigma}{\varepsilon} = \frac{F/A}{\Delta L/L_0} = \frac{mg/A}{\Delta L/L_0} \qquad (3)$$

In this work, the mass of the lower clamp and weight pan are 0.65 and 20 g, respectively. It is seen that the mass of the lower clamp is small compared with that of the weight pan and it can be neglected. Therefore, the starting mass (m) was 20 g. Furthermore, the mass of each copper disk is 50 g and hence the increment of mass (Δm) is also 20 g. The corresponding increment of length (ΔL) can be observed on the length scale (accompanied with a vernier) as shown in Figure 2. The stretching of silk fiber was carried out by adding the copper disk until the silk fiber reached the breaking point. According to Eq.(3), area A (assumed to be constant) and L_0 were known while m and ΔL values were obtained from the experiments. Therefore, the Young’s modulus for each silk fiber was determined.

Results and Discussion

Silk fiber with an initial length (L_0)

The diameter of the 20 cm long silk fiber was carefully measured using an optical microscope (Meiji Techno, MT 5300 L) with optical lens of 4x magnifications. The diameter measurements were carried out on all 10 silk fibers. For each fiber, the diameter of the silk fiber was measured at three different positions on the silk fiber. Table 1 shows the results on the diameter of 10 silk fibers.

Table 1: Diameter of 10 silk fibers, each with a length of 20 cm

Silk fiber No.	Diameter (mm)			
	Position 1	Position 2	Position 3	Average
1	0.18	0.15	0.15	0.16
2	0.15	0.18	0.16	0.16
3	0.16	0.15	0.15	0.15
4	0.15	0.19	0.17	0.17
5	0.18	0.16	0.15	0.16
6	0.16	0.15	0.16	0.16
7	0.15	0.15	0.15	0.15
8	0.18	0.17	0.18	0.18
9	0.16	0.15	0.15	0.15
10	0.16	0.16	0.15	0.16
Average diameter				0.16

The silk fibers were further used for tensile testing. Each fiber was clamped on the vertical stand as shown in Figure 2. The initial known values are as follows.

Initial length (L_0) = 20 cm

Average diameter (D) = 0.16 mm
Cross-sectional area (A) = $\frac{\pi D^2}{4}$ = 0.02 mm^2
Mass of weight pan = 20 g
Mass of each copper disk = 20 g

The length (L) of each silk fiber was measured three times and the average value was obtained. Then, the ΔL was determined. Finally, the stress (σ) and strain (ε) were calculated. The typical results on the measured values are given in Table 2.

Table 2: Typical measured values of L and ΔL, and calculated values of σ and ε at various tensile forces for 20 cm long silk fiber

m (g)	F=mg (N)	L Ave. (mm)	ΔL (mm)	σ (N/mm^2)	ε
20	0.196	200.31	0.31	10.12	0.002
40	0.392	200.69	0.69	19.04	0.003
60	0.588	200.95	0.95	29.83	0.005
80	0.784	201.26	1.26	39.57	0.006
100	0.980	201.63	1.63	49.53	0.008
120	1.176	201.94	1.94	59.21	0.010
140	1.372	202.32	2.32	69.05	0.012
160	1.568	202.74	2.74	78.88	0.014
180	1.764	203.07	3.07	88.66	0.015
200	1.960	204.01	4.01	98.77	0.020
220	2.156	204.87	4.87	108.57	0.024
240	2.352	206.13	6.13	118.64	0.031
260	2.548	206.87	6.87	128.18	0.034
280	2.744	207.67	7.67	138.05	0.038
300	2.940	209.26	9.26	148.45	0.046
320	3.136	210.54	10.54	158.08	0.053
340	3.332	211.63	11.63	167.78	0.058
360	3.528	212.35	12.35	177.32	0.062
380	3.724	213.49	13.49	187.52	0.067
400	3.920	214.06	14.06	196.85	0.070
420	4.116	215.27	15.27	207.29	0.076
440	4.312	216.19	16.19	216.83	0.081
460	4.508	218.38	18.38	228.01	0.092
480	4.704	219.53	19.53	236.76	0.098
500	4.900	220.66	20.66	246.58	0.103

The plots between tensile force (F) and incremental length (ΔL) is shown in Figure 3.

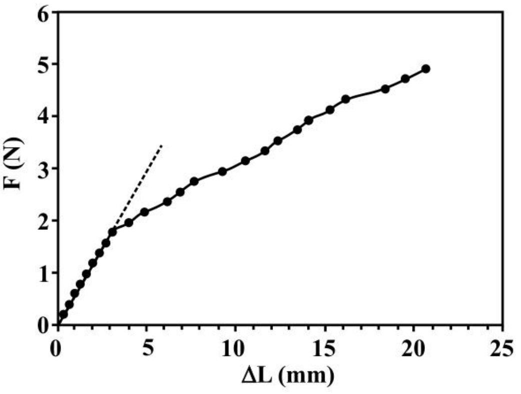

Figure 3. Variation of ΔL as a function of F.

The plot between stress and strain is shown in Figure 4.

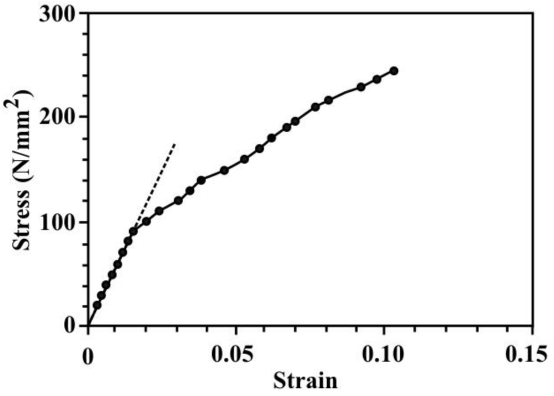

Figure 4: Variation of strain as a function of stress.

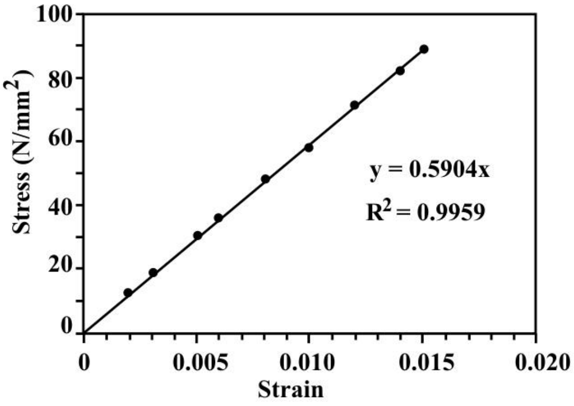

Figure 5. Linear relation between stress and strain.

It is seen from Figure 3 that ΔL is linearly dependent on the tensile force only in a small range from 0.196 to 1.764 N or mass (m) 20 to 180 g. As a result, the strain is also linearly dependent on the stress in a small range as shown in Figure 4. Therefore, the Young's modulus can be determined by fitting the straight line into stress-strain curve (Figure 4) and the result is shown in Figure 5.

The slope, i.e, Young's modules value was found to be 0.5904 N/mm^2 (5904 MPa).

The Young's modulus measurements were further carried out for the silk fibers with the length of 30, 40 and 50 cm. The obtained F-ΔL and stress-strain graphs were similar to those of Figure 3 and Figure 4, respectively. The Young's modulus values were then determined and the results are given in Table 3.

Table 3: Young's modulus values obtained from silk fiber of different lengths

Fiber length (cm)	Young's modulus (MPa)
20	5904
30	6599

40	6333
50	5600

It was observed that the Young's modulus value of the silk fiber obtained from silk fiber of various lengths are different. This result indicates that the silk fiber used in this study is not uniform throughout the fiber length. However, Zhao et al. [3] have collected the measured values of Young's modulus of *Bombyx mori* silk fiber reported in the literature. The Young's modulus varies within the range of 5-23 GPa. It is clearly seen that all these values show marked variability. In conclusion, the Young's modulus values of *Bombyx mori* silk fiber obtained in this study are in agreement with those reported in literature.

Conclusions

In this study, a simple apparatus used for the Young's modulus measurements of silk fibers was designed and constructed. The silkworm (*Bombyx mori*) cocoons used for the study were obtained from Ubonratchathani province. Before tensile testing, the cocoons were cooked in boiling water for 60 min to remove serecin. Then, they were washed with flowing water for 5 min and dried in air for at least 24 h. It was found that silk fiber with a length of 700-1500 m was obtained from one cocoon. The silk fiber was cut into smaller segments with four different lengths of 20, 30, 40 and 50 cm. All the cut silk fibers were selected to obtain only the fiber with a diameter in the range of 0.15-0.17 mm. Moreover, for each length, 10 pieces of fiber were selected for the Young's modulus measurements.

Acknowledgments

This work was supported by Thailand Center of Excellent in Physics (ThEP) and King Mongkut's University of Technology Thonburi under The National Research University Project.

References

1. S. Polymers, Materials Science and Biotechnology, D. Kaplan, W.W. Adams, B. Farmer and C. Viney, (eds.), Workshop on Silks: Biology, Structure, Properties and Genetics, Charlottesville, Va., 1993.
2. H.P. Zhao, X.Q. Feng, S.W. Yu, W.Z. Cui, F.Z. Zou,"Mechanical Properties of Silkworm Cocoons", Polymer **46** (2005) 9192.
3. H.P. Zhao, X.Q. Feng, H.J. Shi, "Variability in Mechanical Properties of *Bombyr Mori Silk*", Materials Science and Engineering C **27** (2007) 675.
4. P. Jiang, H. Liu, C. Wang, L.Wu, J. Hang, C. Guo, "Tensile Behavior and Morphology of Differently Degummed Silkworm (*Bombyx mori*) Cocoon Silk Fibres", Materials Letters **60** (2006) 919.
5. F. Chen, D. Porter, F. Vollrath, "Structure and Physical Properties of Silkworm Cocoons", Journal the Royal Society Interface (doi : 10. 1098/rsif. 2011.0887).
6. N. Reddy and Y. Yang, "Structure and Properties of Cocoons and Silk Fibers Produced by *Hyalophora Cecropia*", Journal of Materials Science **45** (2010) 4414.
7. J. Perez-Rigueiro, C. Viney, J. Florca, M. Elices, "Mechanical Properties of Silkworm Silk in Liquid Media", Polymer **41** (2000) 8433.
8. H.P. Zhao, X.Q. Feng, W.Z. Cui, F.Z. Zou, "Mechanical Properties of Silkworm Cocoon Pelades", Engineering Fracture Mechanics **74** (2007) 1953.

Statistical and Theoretical Physics

Emission of Gravitons from a Closed Nambu String

P. Viriyasrisuwattana, S. Charoenwong, and J. Yamdee*

Department of Physics, Faculty of science, Ramkhamhaeng University
Huamark, Bangkapi, Bangkok, 10240, Thailand
**Corresponding author. E-mail: Jitti-yamdee@hotmail.com*

Abstract

We present an interesting type of vibrating closed Nambu string that can produce the gravitons. The energy-momentum tensor of the vibrating closed Nambu string can be solved, and then the number of gravitons emitted from the vibrating closed string is solved in term of Gravitons Number Density (GND). The GND produced by the external energy-momentum tensor source also depend on the temperature.

Keywords: Gravitons, vibrating strings, gravitons number density

Introduction

We using the quantum viewpoint of gravitation; formalism is developed to compute the number density of gravitons, of specified energies, produced by an arbitrary external energy-momentum tensor source at any temperature. The formalism is applied to a simple Nambu string which is closed string arising from Nambu action, without making the usual assumption of a long wavelength approximation (L.W.A.), the exact result is derived and also is compared to the L.W.A. that exchange between two sources at finite temperature. We solved for solution of the field equation of Nambu string that associated to the boundaries which is a non-circular oscillating string.

Formalism for the number density

The vacuum-to-vacuum transition amplitude for a spin-two massless particle interacting with an external symmetric conserved tensor source is given by the well known expression:

$$\langle 0_+|0_-\rangle^s =$$

$$\exp\left[\frac{i}{2}\int (dx)(dx')S^{\mu\nu}(x)[g_{\mu\lambda}g_{\nu\sigma}-\frac{1}{2}g_{\mu\nu}g_{\rho\lambda}]\right.$$
$$\left.\times \mathrm{D}_+(x-x')S^{\rho\lambda}(x')\right] , \qquad (1)$$

where

$$\mathrm{D}_+(x-x') = \int \frac{d^3\vec{k}}{(2\pi)^3 2k^0} e^{ik(x-x')},$$

for $x^0 > x'^0, k^0 = |k|$

The probability density is given by

$$|\langle 0_+|0_-\rangle^s|^2 =$$

$$\exp\left[-\int d\omega_k S^{\mu\nu}(k)^* \left[g_{\mu\lambda}g_{\nu\sigma}-\frac{1}{2}g_{\mu\nu}g_{\rho\lambda}\right] S^{\rho\lambda}(k)\right],$$
(2)

we may rewrite the integrand in the exponent in (2) as($k^0 = |k|$):

$$\boldsymbol{S^{\mu\nu*}\left[g_{\mu\lambda}g_{\nu\sigma}-\frac{1}{2}g_{\mu\nu}g_{\rho\lambda}\right]S^{\rho\lambda} = S^{ab*}\Pi_{\mathrm{abcd}}S^{cd}},$$

$$\boldsymbol{= \widehat{S}^{ab*}\Pi_{\mathrm{abcd}}\widehat{S}^{cd}} ,$$

$$\boldsymbol{= \widehat{S}^{ij*}e^{ij}_{\lambda}e^{ab}_{\lambda}\widehat{S}^{ab}}. \qquad \textbf{(3)}$$

Hence we may write (3) as

$$\boldsymbol{|\langle 0_+|0_-\rangle^s|^2} =$$

$$\boldsymbol{\exp\left[-\int d\omega_k \sum_{\lambda=1,2} \left|\widehat{S}^{ij}e^{ij}_{\lambda}\right|^2\right]}, \qquad \textbf{(4)}$$

The energy-momentum tensor for matter$\boldsymbol{T_{\mu\nu}}$is identified by requiring that the expression in (1) leads to the Newtonian gravitational exchange energy between two widely separated static sources$\boldsymbol{T_1^{00}, T_2^{00}}$. as shown by Scwinger [3], this leads to the identifications

$$\boldsymbol{S_{\mu\nu} = \sqrt{8\pi G}T_{\mu\nu}} , \qquad \textbf{(5)}$$

where G is the universal gravitational constant.

To study graviton production, we write:

$\boldsymbol{S_{\mu\nu}(x) = S^1_{\mu\nu}(x) + S^2_{\mu\nu}(x)}$.Where$\boldsymbol{S^2_{\mu\nu}}$ is switched on after $\boldsymbol{S^1_{\mu\nu}}$is switched off. Then

$$\langle 0_+|0_-\rangle^s =$$

$$\langle 0_+|0_-\rangle^{s_2} \exp\left[\int d\omega_k \sum_{\lambda=1,2} i\hat{S}^{2*}_{ij}\, e^{ij}_\lambda i\hat{S}^1_{ab} e^{ab}_\lambda\right]$$

$$\times \langle 0_+|0_-\rangle^{s_1}. \qquad (6)$$

Temperature-Dependent Graviton Productionat finite temperature, we must first replace the amplitude $\langle 0_+|0_-\rangle$ by an amplitude$\langle N; N_1 N_2 \ldots | N; N_1 N_2 \ldots\rangle$. Involving an arbitrary number of N gravitons,$N_1$of which have energyω_1, N_2 energy ω_2 and so on.It is convenient to introduce a discrete notation for all possible energies. We then average this amplitude with the statistical factor $\prod_{i=1}^{\infty}(\exp - \beta k_i^0)^{N_i}$, and sum over N as well. This gives the thermal average ground state amplitude $\langle G_+|G_-\rangle$ containing an arbitrary number of gravitons of all possible energies.

$$\langle G_+|G_-\rangle^S =$$

$$\langle G_+|G_-\rangle^{S_2} \exp\left[\int d\omega_k \sum_{\lambda=1,2} i\hat{S}^{2*}_{ij}\, e^{ij}_\lambda \coth\left(\frac{\beta k^0}{2}\right) i\hat{S}^1_{ab} e^{ab}_\lambda\right]$$

$$\times \langle G_+|G_-\rangle^{S_1}, \qquad (7)$$

Giving for the average number of gravitons emitted by matter with energy-momentum tensor distribution$T_{\mu\nu}$

$$\langle N\rangle =$$

$$8\pi G \int \frac{d^3\vec{k}}{(2\pi)^3 2k^0} \sum_{\lambda=1,2} \left|\hat{T}^{ij}(k) e^{ij}_\lambda\right|^2 \coth\left(\frac{\beta k^0}{2}\right), (8)$$

A moment's reflection also show the amplitude $(8)$of stimulated emissions holds true for T≠0 with $s_r$in(5)) replaced by $s_r\sqrt{(\coth\beta k^0)}$.

$$\langle N\rangle =$$

$$\frac{4\pi G}{(2\pi)^3} \int_0^\infty \omega d\omega \int d\Omega \sum_{\lambda=1,2} \left|\hat{T}^{ij}(k) e^{ij}_\lambda\right|^2 \coth\left(\frac{\beta k^0}{2}\right), (9)$$

The expression for the density

To extract the expression for the density $\langle N(\omega)\rangle$ corresponding to theaverage number of gravitons emitted with energies within the interval $(\omega, \omega + d\omega)$, which is the object of interest in this work, we must establishthat the integrand in(2.89) is positive definite. To this end, the integrand, not containing the $\coth(\beta\omega/2)$factor which is itself positive, may be rewritten as

$$\frac{1}{2} T^*_{\mu\nu}[g^{\mu\sigma} g^{\nu\rho} + g^{\mu\rho} g^{\nu\sigma} - g^{\mu\nu} g^{\sigma\rho}] T_{\sigma\rho} =$$

$$\sum_{\lambda,\varepsilon=1,2} T^*_{\mu\nu} e^{\mu\nu}_{\lambda\varepsilon} e^{\sigma\rho}_{\lambda\varepsilon} T_{\sigma\rho} \equiv \sum_{\lambda,\varepsilon=1,2} \left|e^{\mu\nu}_{\lambda\varepsilon} T_{\mu\nu}\right|^2, \qquad (10)$$

$$g^{\mu\nu} = \sum_\lambda e^\mu_\lambda e^\nu_\lambda + \frac{k^\mu \bar{k}^\nu + \bar{k}^\mu k^\nu}{k\bar{k}}. \qquad (11)$$

In writing the expression on the right -hand side of (2.90)we have made useof the conservation $k^\mu T^{\mu\nu} = 0$. Accordingly, from (2.89) and (2.90) we have for density of the average number of gravitons of energy ω

$$\langle N(\omega)\rangle =$$

$$\frac{G\omega}{2\pi^2} \coth h\left(\frac{\beta\omega}{2}\right) \int d\Omega\, T^{\mu\nu *}(\omega, \vec{k})\, \pi^{\mu\nu\sigma\rho} T^{\sigma\rho}(\omega, \vec{k}), (12)$$

The long wavelength approximation

Fourier transform from momentum space becomes

$$\boldsymbol{T^{\mu\nu}(\omega, \vec{k}) = \int d^3x\, e^{-ikx} T^{ij}(x) \int dt\, e^{i\omega t},} \qquad (13)$$

$$\boldsymbol{\langle N(\omega)\rangle =}$$

$$\boldsymbol{\frac{G\omega}{2\pi^2} \coth h\left(\frac{\beta\omega}{2}\right) \int d\Omega \sum_{\lambda=1,2} \int dt d^3x\, e^{ik.x} e^{-i\omega t} \hat{T}^{*ij}(x)}$$

$$\boldsymbol{\times\, \pi^{\mu\nu\sigma\rho} \int dt' d^3x''' e^{-ik.x'} e^{i\omega t'} \hat{T}^{ij}(x'),} \qquad (14)$$

In passing, we obtain the long wavelength approximation of $\boldsymbol{(14)}$ forcompleteness. We choose $\boldsymbol{e^\mu_\lambda = (0, \vec{e}_\lambda)}$,is

$$\boldsymbol{T^{\mu\nu}(\omega, \vec{k}) = \int d^3x\, T^{ij}(x) \int dt\, e^{i\omega t}} \qquad (15)$$

Consider the terms

$$\int d\Omega\,\pi^{ijml} = \int \sum_{\lambda,\varepsilon=1}^{2} d\Omega\, e^{ij}_{\lambda\varepsilon} e^{ml}_{\lambda\varepsilon}$$

$$= \frac{4\pi}{5}\left(\delta^{im}\delta^{jl} + \delta^{il}\delta^{jm} - \frac{2}{3}\delta^{ij}\delta^{ml}\right) \qquad (16)$$

$$\langle N(\omega)\rangle_{\mathrm{L.W.A}} =$$

$$\frac{4G\omega}{5\pi}\coth h\left(\frac{\beta\omega}{2}\right)\left|\int dt\, e^{i\omega t}\int d^3x\,\hat{T}^{ij}(x)\right|^2, (17)$$

Using the formal identity

$$\int d^3x\,T^{ij}(x) = \frac{1}{2}\frac{\partial^2}{\partial t^2}\int d^3\vec{x}\,x^i x^j T^{00}(x) \quad (18)$$

Let

$$Q^{ij}(t) = \int d^3\vec{x}\left(x^i x^j - \frac{\delta^{ij}}{3}\vec{x}^2\right)T^{00}(x) \quad (19)$$

As a result of the conservation of energy-momentum tensor, give a final result

$$\langle N(\omega)\rangle_{\mathrm{L.W.A}} = \frac{G\omega}{5\pi}\coth h\left(\frac{\beta\omega}{2}\right)\left|\int_{-\infty}^{\infty} dt\,\ddot{Q}^{ij}(t)e^{i\omega t}\right|^2$$

(20)

The closedNambu string

The trajectory of the string is described by a vector function where σisparameterizes the string.The equations of motion of the closed Numbustring is

$$\frac{\partial^2\vec{X}}{dt^2} - \frac{\partial^2\vec{X}}{\partial\sigma^2} = 0\ . \qquad (21)$$

A general solution of the equation of motion is given by:

$$\vec{R}(\sigma,t) = \frac{1}{2m}[\,(cosm(\sigma+t), sinm(\sigma+t), 0)$$

$$+(cosm(\sigma-t), sinm(\sigma-t), 0)], \quad (22)$$

This is describe the closed string oscillate in circular shape. When the angular velocity of moving wave is reduced for example $cosmt \rightarrow cos\frac{m}{N}t$ where *N* is integers 2, 3... The string will oscillate in star shape. Then $\frac{m}{N} = 4\pi$, the string will oscillate in approximate straight line.

$$\vec{R}(\sigma,t) = \frac{1}{m}(cosm\sigma, sinm\sigma, 0)cos4\pi t, \qquad (23)$$

The general expression for the energy-momentum tensor of the string is given by

$$T^{\mu\nu}(x) =$$

$$\frac{\mathrm{m}^2}{2\pi}\int_0^{\frac{2\pi}{\omega}}\partial\sigma(\partial_t X^\mu\partial_t X^\nu - \partial_\sigma X^\mu\partial_\sigma X^\nu)\delta^3\left(\vec{\mathrm{x}} - \vec{X}(\sigma,t)\right),$$

(24)

$$T^{\mu\nu}(t,\vec{r}.z) =$$

$$\int\frac{dk^0}{2\pi}\int\frac{d^2p}{(2\pi)^2}\int\frac{dq}{2\pi}e^{i\vec{p}.r}e^{iq.z}e^{-ik^0t}T^{\mu\nu}(k^0,p,q), \quad (25)$$

$$T^{\mu\nu}(t,\vec{r}.z) =$$

$$\sum_{M=-\infty}^{\infty} e^{-iMmt}\int\frac{d\vec{p}}{(2\pi)^2}\int\frac{dq}{2\pi}e^{ip.r}e^{iq.z}B^{\mu\nu}(\vec{p},M), \quad (26)$$

$$T^{\mu\nu}(k^0,\vec{p},q) \equiv T^{\mu\nu}(k^0,\vec{p})$$

$$= 2\pi\sum_{M=-\infty}^{\infty}\delta(k^0 - mM)B^{\mu\nu}(\vec{p},M) \qquad (27)$$

Applications to the Nambu string

Our starting point is the expression for give in , we use the expression for with $k^0 = \omega$ as given in , to obtain substitute into

$$\langle N(\omega)\rangle =$$

$$= 2G \sum_{M,L=0}^{\infty} \delta(\omega - mM)\omega\coth\left(\beta\omega/2\right)\delta(\omega - mL)$$

$$B^{\sigma\rho}(\vec{\mathrm{p}},M)\left[g_{\mu\sigma}g_{\nu\rho} - \frac{1}{2}g_{\mu\nu}g_{\sigma\rho}\right]B^{\sigma\rho}(\vec{\mathrm{p}},L), (29)$$

To obtain for the average number of gravitons emitted with energies in the interval in a period (a cycle) of oscillation of length the expression

$$\langle N(\omega)\rangle_c = 2\pi mG \sum_{n=1}^{\infty} \delta(\omega - 2nm)\coth\left(\beta\omega/2\right)$$

$$B^{\mu\nu}(\vec{\mathrm{p}},M)\left[g_{\mu\sigma}g_{\nu\rho} - \frac{1}{2}g_{\mu\nu}g_{\sigma\rho}\right]B^{\sigma\rho}(\vec{\mathrm{p}},L)\,, \qquad (30)$$

we note that the average number of gravitons emit ted with an energy in the width

, during a period of length is then

$$\langle N(\omega)\rangle_{c,\mathrm{n}} = \frac{4\mathrm{G}m^2}{\hbar c}\coth(\beta nmc^2)U_n\,, \quad (31)$$

In particular, for gravitons emitted with the threshold energy we have

$$\langle N(\omega)\rangle_{c,1} = \frac{0.05\mathrm{G}m^2\pi}{\hbar c}\coth(\beta mc^2)\,, \qquad (32)$$

The high and low temperature limits of are, respectively,

$$\langle N(\omega)\rangle_{c,\mathrm{n};\tau\to\tilde{\infty}}\frac{4\mathrm{G}m\pi}{\hbar c}U_n k\tau \qquad (33)$$

$$\langle N(\omega)\rangle_{c,\mathrm{n};\tau\to\tilde{0}}\frac{4\mathrm{G}m\pi}{\hbar c}U_n (34)$$

For the long wavelength approximation in

$$Q^{ij}(\mathrm{t}) = \frac{1}{3}\frac{\sin^2 mt}{m}C^{ij} \qquad (35)$$

$$C^{ij} = \begin{bmatrix} \frac{1}{2} & 0 & 0 \\ 0 & \frac{1}{2} & 0 \\ 0 & 0 & -1 \end{bmatrix} \qquad (36)$$

$$\ddot{Q}^{ij} = \frac{d^2}{dt}\left(\frac{1}{3}\frac{\sin^2 mt}{m}C^{ij}\right) = \frac{2}{3}m\cos(2mt)C^{ij} \quad (37)$$

For graviton emissions during a period of length with energies within the width

, to the final expression

$$\langle N(\omega)\rangle_{L.W.A.c,n} = \frac{4\mathrm{G}m^2\pi}{15\hbar c}\coth(\beta mc^2)\delta_{n,1} \qquad (38)$$

Conclusions

The energy-momentum source propagate the gravitons, we solved the average number of gravitons propagating from the source by using the well-known vacuum to vacuum transition amplitude. Then the average number at finite temperature is derived by adding heating term from boson distribution equation, and the number density can be solved. So by taking the result from the number density at any temperature.nd the closed Nambustring can becomes many shape proportional to the angular velocity of moving wave.

References

1. Schwinger, J . (1976) .*Gen . Rel. Grav.* 7 , 251; (1969) . *Particles and Sources* (Gordon Breach, New York).
2. Manoukian, E. B. (1990) .*Hadronic J.* 1 3 , 375.
3. Misner, C. W., Thorne, K. S., and Wheeler, J. A.(1973). *Gravitation* (W. H. Freeman, San Francisco).
4. Manoukian,E.B.(1990) Temperature-Dependent Particle Production and Stimulated Emissions by External Sources
5. Schwinger, J.(1998).*Particles,Sources,and fields Vol.1*(late, University of California at Los Angeles).
6. Manoukian, E. B. and Sukkhasena,S. (2007), The graviton propagator with a non-conserved external generating source. Fortschr. Phys. 55, No. 11–12, 1281 – 1288
7. Manoukian, E. B. and Viriyasrisuwattana,P. (2007).Localization of photons and propagation in spacetime in quantum field theory. International Journal of Theoretical Physics 46(12):3247-3253.
8. L.D.Landau and E.M. Lifshitz (1975).The classical theory of fields (Fourth Revised English Edition) (Institute for Physic Problems,Academy of the U.S.S.R.)

Simulations on Attraction and Repulsion of Vortices by Square-shaped Defects

M. Sutthiopad and C. Luengviriya*

Department of Physics, Kasetsart University, 50 Phaholyothin Road, Jatujak, Bangkok 10900, Thailand

**Corresponding author. E-mail: fscicyl@ku.ac.th*

Abstract

Vortices play essential roles in many domains of physics, including fluid dynamics, catalytic waves, and condensed matter physics. In superconductors, pinning of vortices to defects is required to maintain the superconducting state. Such pinning and unpinning transitions are typical features of superfluid dynamics. In the heart, vortices of electrical excitation so-called spiral waves concern a class of physiologically arrhythmias which can last longer when the spiral waves are attracted and subsequently pinned to anatomical defects. In this article, we present a study on attraction and repulsion of spiral waves by square-shaped defects in a simulated reaction-diffusion system with the well-known Oregonator model for dynamics in excitable media. We placed a defect close to the spiral tip, the organizing center of the wave structures, which evolved around a circular core (diameter = 0.92 s.u.) and observed the motion of spiral tip. The defect size was varied between 0.1 and 2.0 s.u. The influence of the defect on the spiral wave depended on the initial position *P* of the spiral core center measured from the closest defect edge. The spiral tip was attracted and ultimately pinned to the defect when it was in the attraction region (i.e. points between the closest defect edge and the maximal *P* for attraction). The width of the attraction region was similar (2.5-2.7 s.u.) for all defect sizes. The tip was repulsed and drifted away when it located at larger *P*, however, in the repulsion region. The width of the repulsion region (i.e. points between the maximal *P* for attraction and the maximal *P* for repulsion) was 0.2-1.5 s.u., increased with the defect size. For *P* outside both regions of attraction and repulsion, the spiral tip rotated around the circular core as if no defect existed.

***Keywords*:** Spiral wave, excitable medium, Oregonator model, reaction-diffusion system.

Introduction

Vortices, also known as spiral waves, have been observed in many physical, chemical, and biological systems [1–8]. In superconductors, the motion of free vortices induces dissipation, so pinning is required to maintain the superconductor state [1]. As such, pinning and unpinning transitions are essential features of superfluid dynamics [2]. In the heart, such spiral forms of electrical excitation and their instabilities concern cardiac tachycardia and life-threatening fibrillations [9–11]. The tachycardia can last longer when the spiral waves are attracted and subsequently pinned to anatomical defects. It has been shown that a circular defect with a diameter of 0.7 s.u. either attracted or repulsed a spiral wave whose spiral core diameter was 0.9 s.u., depending on the distance of spiral core center and the defect [12].

In this article, we present an investigation on the effect of square-shaped defects with different width between 0.1 and 2.0 s.u. on the dynamics of spiral waves. We employed a reaction-diffusion system [13] with the Oregonator model [14] which wildly used for study dynamics in excitable media.

Materials and Methods

The reaction-diffusion system with the Oregonator model described the dynamics of the activator *u* and the inhibitor *v* in the system:

$$\frac{\partial u}{\partial t} = \frac{1}{\varepsilon}\left(u - u^2 - fv\frac{u-q}{u+q}\right) + D_u\nabla^2 u,$$

$$\frac{\partial v}{\partial t} = u - v + D_v\nabla^2 v. \qquad (1)$$

The system supported a spiral wave rotating rigidly around a circular core when the parameters were chosen as in refs. [15,16]: the diffusion coefficients $D_u = 1$ and $D_v = 0.6$, $\varepsilon = 0.01$, $q = 0.002$, and $f = 1.4$.

The simulations were performed using an explicit Euler method with a 9-point approximation of the two-dimensional Laplacian operator. The uniform grid space $\Delta x = \Delta y = 0.1$ s.u. and the time step $\Delta t = 0.003$ as required for numerical stability ($\Delta t \le (3/8)(\Delta x)^2$ [17]). The dimensionless size of the system was 40 × 40 s.u. (corresponding to 400 × 400 grid points). A completely unexcitable square was set as the defect. Therefore, the boundaries of both the medium and the obstacle had no-flux conditions.

To create a spiral wave, a planar wave was triggered by setting a 5-grid-point strip at an edge of the medium to an excited state (e.g. $u = 1.0$ and $v = 0$ for $0.0 \leq x \leq 0.5$). The wave front was allowed to propagate into the middle of the medium before half of the medium was reset to an excitable state (e.g. $u = 0$ and $v = 0$ for $0.0 \leq y \leq 20.0$) leading to a free-end wave front which subsequently curled to form a spiral wave.

Analysis of the spiral wave dynamics was done by traces of the spiral tip trajectories. The spiral tip was defined as the intersection of the contour $u = 0{:}15$ and $v = 0.0935$. This definition ensures that $\partial u/\partial t = 0$ on the spiral tip [18].

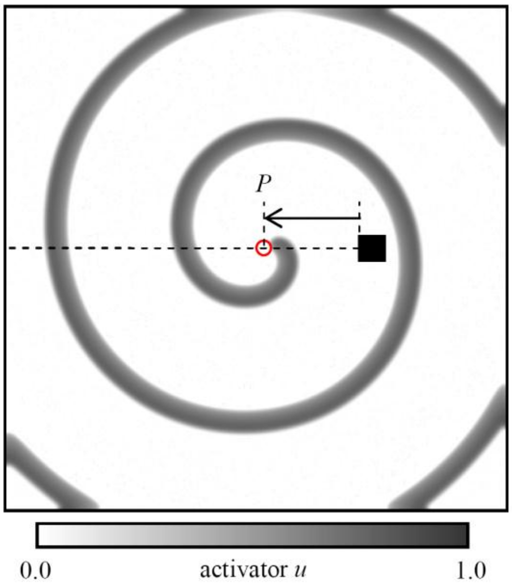

Figure 1. Position of a spiral wave and a squared-shaped defect. The field of the activator u was illustrated as a gray-scale image. The spiral tip rotated counter-clockwise around a circular core (diameter = 0.92 s.u.). The initial position P of the spiral core center was measured from the closest defect edge. The horizontal dashed line indicated the spatial region studied in our simulations.

Results and Discussion

In the absence of any defect, our simulated system supported a propagating spiral wave whose tip rotated around a circular core with a diameter of area 0.92 s.u., as shown in Fig. 1. The wave period was approximately 1.5 time unit (~500 time steps). The activator u in the system ranged between zero and one. Note that u changed very fast across the space as an overshoot of the action potential in physiological systems.

The effect of an unexcitable squared-shaped defect on the spiral wave depended on the initial position P of the spiral core center measured from the closest defect edge (see Fig. 1). We investigated the effect for different P along a horizontal line at the middle height of the defect.

Attraction of the spiral tip was found when the spiral core center was located close to the defect, i.e., P smaller than a threshold. The spiral tip moved towards the defect while the wave front was deformed when it passed the defect (Fig. 2a-b). In the initial phase of pinning (Fig. 2c), the front structure was anisotropic. However, the front became isotropic within about 9-10 wave periods (Fig. 2d). Note that the attraction was observed only when P was in a region close enough to the defect. We named it as the attraction region (Fig. 3a).

For the case of repulsion (Fig. 2e-f), the spiral tip slowly moved away from the defect and the wave front was also deformed (Fig. 2f) as for the attraction (Fig. 2b). The repulsion occurred only when the spiral core center was in the repulsion region (Fig. 3a) which located next to the attraction region. For the position P farer than both regions, the spiral tip simply rotated around a fixed circular core.

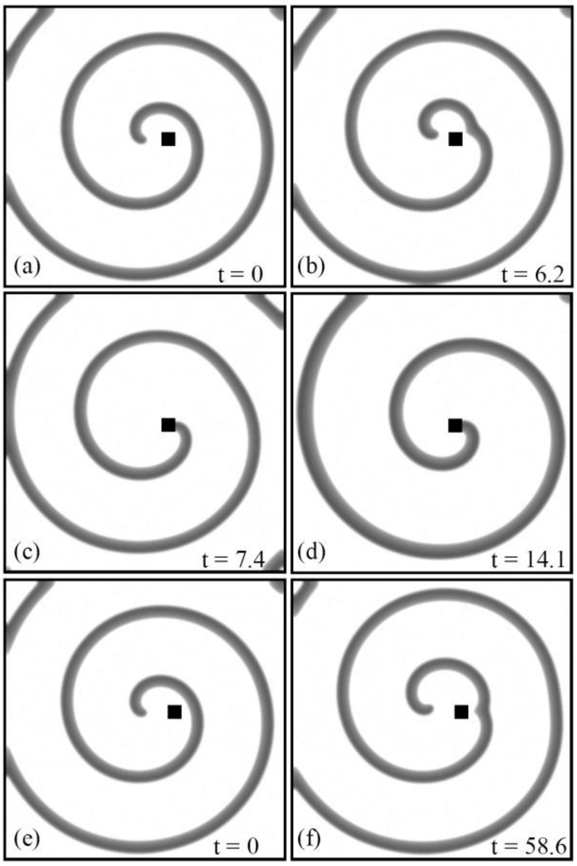

Figure 2. Attraction and repulsion of a spiral wave by a defect with a width of 2.0 s.u.: (a) The spiral wave located at the initial position P = 1.8 s.u. (b) moved towards the defect. (c-d) The tip was eventually pinned. (e) In contrast, the spiral wave located at P = 2.7 s.u. (f) moved away the defect. In both cases, the

wave front was also deformed when it passed the defect. The bottom right shows the time *t* for each illustration.

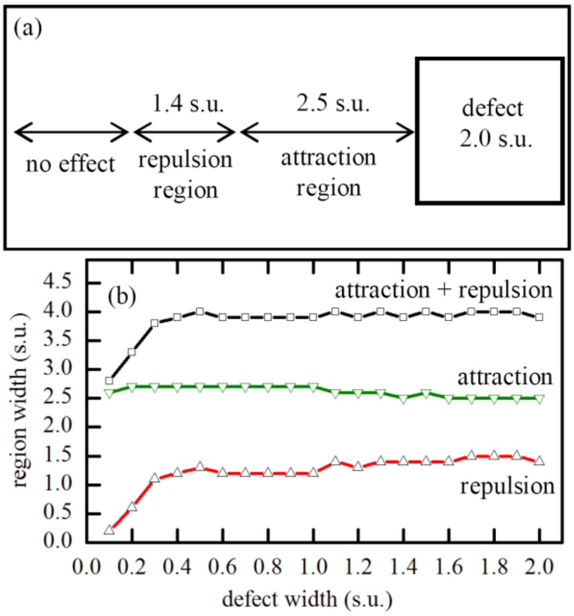

Figure 3. Attraction and repulsion regions of the defects. (a) An illustration of the regions for the defect width = 2.0 s.u. (b) The region width for different defect width of 0.1-2.0 s.u.

The mechanisms of such attraction and repulsion by a square-shaped defect in our study might be the same as in the case of a circular defect which has been proposed in [12]. Attraction and repulsion of the spiral tip originate from a deformation of the wave front close to the tip, as in Figs. 2b and 2f. Such deformations cause changes in curvature and wave velocity near the tip. Therefore, the tip drifts either towards or away the defect.

Attraction and repulsion of the spiral tip were studied for the defect width of 0.1-2.0 s.u. Figure 3b shows the width of regions. For attraction case, the variation of the width was very tiny. It ranged between 2.5 and 2.7 s.u. The width of repulsion evidently increased with the defect width of 0.1-0.3 s.u., however, it gradually increased for larger defect 0.4-2.0 s.u. We also calculated the sum of both widths of attraction and repulsion regions. These revealed the regions where the defects had impact on the spiral tip motion. As one can expected, the width of such impact region increased steeply for small defects 0.1-0.3 s.u., then it grew very slow as the defect width was enlarged.

In nature, the tip of a spiral wave often drifts due to anisotropic properties of the media, e.g., as found in cardiac cases [19]. The drift may force the spiral tip far from a defect to move across the repulsion region into the attraction one leading to a pinning phenomenon. Recently, theoretical and simulation studies [20] demonstrated that such forced pinning can occur in a system subjected to a gradient, however, the process might be complicated.Conclusions

We have investigated dynamics of a spiral wave whose circular core diameter was 0.92 s.u. in a simulated reaction-diffusion system with the Oregonator model in the presence of unexcitable square-shaped defects with a width of 0.1 and 2.0 s.u.

The influence of the defect on the spiral wave depended on the location of the spiral core center. In the attraction region, the spiral tip was attracted and ultimately pinned to the defect. The wave structure was also transiently deformed. The width of the attraction region was approximately independent on the defect width (2.5-2.7 s.u.).

In contrast, the spiral tip was repulsed and drifted away when it located in the repulsion region whose width increased from 0.2-1.5 s.u. with the defect width. For the case of outside both regions of attraction and repulsion, the spiral tip rotated around a nonmoving circular core.

Acknowledgments

We thank the Faculty of Science, the Research and Development Institute (KURDI), and the Center for Advanced Studies of Industrial Technology, Kasetsart University; and the Thailand Research Fund (grant no. MRG5480248) for financial support.

References

1. P.G. de Gennes, *Superconductivity of Metals and Alloys* (Benjamin, New York, 1966).
2. R. Blaauwgeers, V.B. Eitsov, M. Krusius, J.J. Ruohlo, R. Schanen, G.E. Volovik. Double-quantum vortex in superfluid 3He-A, *Nature* (London) **404**:471-473, 2000.
3. A.T. Winfree. Spiral waves of chemical activity. *Science*, **175**:634-636, 1972.
4. J. Lechleiter, S. Girard, E. Peralta, and D. Clapham. Spiral calcium wave propagation and annihilation in Xenopus laevis oocytes. *Science*, **252**:123-126, 1991.
5. F. Siegert and C.J. Weijer. Digital image processing of optical density wave propagation in Dictyostelium discoideum. *J. Cell Sci*, **93**:325-335, 1989.
6. S. Nettesheim, A. von Oertzen, H.H. Rotermund, and G. Ertl. Reaction-diffusion patterns in the catalytic CO-oxidation on Pt(110): Front propagation and spiral waves. *J. Chem. Phys.*, **98**:9977-9985, 1993.
7. M.A. Dahlem and S.C. Müller. Self-induced splitting of spiral-shaped spreading depression waves in chicken retina. *Exp. Brain Res.*, **115**:319-324, 1997.
8. S.C. Müller, T. Mair, and O. Steinbock. Traveling waves in yeast extract and in cultures of Dictyostelium discoideum. *Biophys. Chem.*, **72**:37-47, 1998.A.T. Winfree. Electrical

turbulence in three-dimensional heart muscle. *Science*, **266**:1003-1006, 1994.

9. R.A. Gray, A.M. Pertsov, and J. Jalife. Spatial and temporal organization during cardiac fibrillation. *Nature* (*London*), **392**:75-78, 1998.
10. F. Fenton, E.M. Cherry, H M. Hastings, and S.J. Evans. Multiple mechanisms of spiral wave breakup in a model of cardiac electrical activity. *Chaos*, **12**:852-892, 2002.
11. A.P. Munuzuri, V. Perez-Munuzuri, and V. Perez-Villar. Attraction and repulsion of spiral waves by localized inhomogeneities in excitable media. *Phys. Rev. E*, **58**:R2689, 1998.
12. A.M. Turing. The chemical basis of morphogenesis. *Phil. Trans. Roy. Soc. Lond. B*, **237**:37-72, 1952.
13. R.J. Field and R.M. Noyes. Oscillations in chemical systems. IV. Limit cycle behavior in a model of a real chemical reaction. *J. Chem. Phys*., **60**:1877-1884, 1974.
14. W. Jahnke, W.E. Skaggs, and A.T. Winfree. Chemical vortex dynamics in the Belousov-Zhabotinsky reaction and in the two-variable oregonator model. *J. Phys. Chem*., **93**:740-749, 1989.
15. B. Schmidt and S.C. Müller. Forced parallel drift of spiral waves in the Belousov-Zhabotinsky reaction. *Phys. Rev. E*, **55**:4390-4393, 1997.
16. M. Dowle, R. M. Mantel, and D. Barkley. Fast simulations of waves in three-dimensional excitable media. *Int. J. Bif. Chaos*, **7**:2529, 1997.
17. S. Alonso, F. Sagues, and A.S. Mikhailov. Negative tension instability of scroll waves and Winfree turbulence in the Oregonator model. *J. Phys.Chem. A*, **110**:12063-12071, 2006.
18. J. M. Davidenko, A. M. Pertsov, R. Salomonz, W. Baxter, and J. Jalife. Stationary and drifting spiral waves of excitation in isolated cardiac muscle. *Nature*, **335**:349-351, 1992.
19. C. W. Zemlin and A. M. Pertsov. Anchoring of drifting spiral and scroll waves to impermeable inclusions in excitable media. *Phys. Rev. Lett*, **109**: 038303, 2012.

Stability of Korteweg-de Vries-Burgers Solitons

S. Yothathitikun*, and M. A. Allen

Physics Department, Mahidol University, 272 Rama VI Road, Bangkok 10400, Thailand
**Corresponding author. E-mail: santirak_phy@hotmail.com*

Abstract

In this paper, we study the stability with respect to perturbations of Korteweg-de Vries-Burgers (KdVB) solitons which are kink solutions. We investigate their stability by solving the full equation numerically using a spectral method. We show numerically that arbitrary ‘step-down’ initial conditions of the KdVB equation will evolve into kink solutions of that equation. A stability criterion for the numerical solution of the equation using this method is also obtained.

***Keywords*:** Solitons, stability, KdVB equation

Introduction

The Korteweg-de Vries-Burgers (KdVB) equation is

$$u_t + \alpha u u_x - \beta u_{xx} + s u_{xxx} = 0 \tag{1}$$

where α, β, and s are real constants with $\alpha\beta s \neq 0$ and the subscripts denote partial differentiation. It can be used as a nonlinear wave equation [1] and has plasma physics applications [2]. It has the travelling wave solution

$$u(x,t) = \frac{V}{\alpha} + A[-2\tanh B(x-Vt) \\ +\operatorname{sech}^2 B(x-Vt) \tag{2}$$

where $A = 3\beta^2/25s$ and $B = \beta/10$. We can see that this solution is a kink. A kink is a kind of wave solution that tents to different values as $x \to \pm\infty$. The solution (2) can be rearranged to give

$$u(x,t) = \frac{V}{\alpha} + 2A - A(1+\tanh B(x-Vt))^2$$

from which it is clearly monotonic, and has only one parameter V , as pointed out in [3].

Numerical method

The methods we use for solving the KdVB equation numerically are the spectral method to find spatial derivatives and the well-known 4th-order Runge-Kutta method for the time derivatives. The spectral method is a way of transforming an equation expressed in continuous space into a discrete equation which can be solved numerically. The discrete Fourier transform can be used to find the derivatives much more accurately than the usual finite difference approximations since all the points in the x-direction are used to find ∂_x^r.

There are limitations of the spectral method which are that the function that we wish to find the derivative of must be periodic with a period equal to the length of the domain (l_x). Ideally, the function should also not have any discontinuities. For a pulse solution where the function u is not periodic but tends to the same value as $x \to \pm\infty$ we can simply treat it as being periodic by choosing to use a large domain such that $u(0) \simeq u(lx)$. This is particularly effective if u decays exponentially. Then we can either choose to integrate the equations in time until the region of interest approaches the boundary and then stop, or allow it to pass through the boundary and reappear at the other boundary.

The KdVB equations have a kink solution which tends to different values as $x \to \pm\infty$. There is a trick which will allow us to find $\partial_x^r u$. Define

$$v = \exp(\mathrm{i}Qu), \tag{3}$$

where

$$Q \equiv 2\pi/D \tag{4}$$

and

$$D = u(-\infty) - u(\infty) \neq 0, \quad \text{where } u \text{ is real} \tag{5}$$

but the derivatives at infinity are equal. Then v tends to the same value as $x \to \pm\infty$ and so $\partial_x^r v$ can be found spectrally. Differentiating (3) and rearranging leads to

$$u_x = \frac{1}{Q}[c \operatorname{Im} v_x - s \operatorname{Re} v_x],$$

$$u_{xx} = \frac{1}{Q}[2(c \operatorname{Re} v_x + s \operatorname{Im} v_x)(s \operatorname{Re} v_x - c \operatorname{Im} v_x) \\ + c \operatorname{Im} v_{xx} - s \operatorname{Re} v_{xx}],$$

$$u_{xxx} = \frac{1}{Q}[6(c \operatorname{Re} v_x + s \operatorname{Im} v_x)^2(c \operatorname{Im} v_x - s \operatorname{Re} v_x)$$

$$-2\left(c\,\mathrm{Im}\,v_x - s\,\mathrm{Re}\,v_x\right)^3 - 3\left(c^2 - s^2\right)$$

$$\left(\mathrm{Im}\,v_{xx}\,\mathrm{Re}\,v_x + \mathrm{Im}\,v_x\,\mathrm{Re}\,v_{xx}\right)$$

$$-(6cs)\left(\mathrm{Im}\,v_x\,\mathrm{Im}v_{xx} - \mathrm{Re}\,v_x\,\mathrm{Re}\,v_{xx}\right)$$

$$+\,c\,\mathrm{Im}v_{xxx} - s\,\mathrm{Re}\,v_{xxx}], \tag{6}$$

where $c \equiv \cos Qu$ and $s \equiv \sin Qu$. Now consider the KdVB equation (1)

$$u_t = -\alpha u u_x + \beta u_{xx} - s u_{xxx} = 0 \tag{7}$$

right hand side of equation (7) can be calculated by using equation (6) and then the solution (u) can be obtained by using the Runge-Kutta method.

The programs for these methods were written in C on Linux using the Numerical Recipes routines for the Runge-Kutta method and fast Fourier transform [4].

Testing the numerical method

If we use the solution (2) as the initial value and make $\alpha = 12$, $\beta = 10$, $s = 1$, and $V = 12$ then we obtain

$$u(x,0) = 1 - 2\tanh x + \mathrm{sech}^2\,x. \tag{8}$$

We can see that $u(-1,0) = 3$ and $u(1,0) = -1$ so from (5) and (4) we get $D = 4$. Using the numerical method gives the kink solution moving to the right as in Fig. 1. After the wave moves through the right boundary, it will pass through the left boundary and we use that as the new initial value. Then we still get the kink solution moving to the right with the same amplitude but different values at large and small x. In other words, the left value at the boundary will increase when some part of wave passes through the right boundary to keep the difference in boundary values the same. The new solution is

$$u(x,0) = 5 - 2\tanh x + \mathrm{sech}^2\,x.$$

One important thing is to find the stability of the methods. If we use too large a time step, this will make the method fail (see Fig. 2). When the step size is too small we waste time by using more time steps than necessary. If we choose a time step that is a little too large, it will give the wave but with small oscillations (see Fig. 3). The values of Δt and Δx we tried are shown in Table 1. If we make a log-log plot of the values of Δt and Δx when the integration just has no sign of instability we obtain a graph with a straight line with a slope of about 2.67 which means the stability condition is

$$\frac{\Delta t}{\Delta x^{2.67}} < 0.039$$

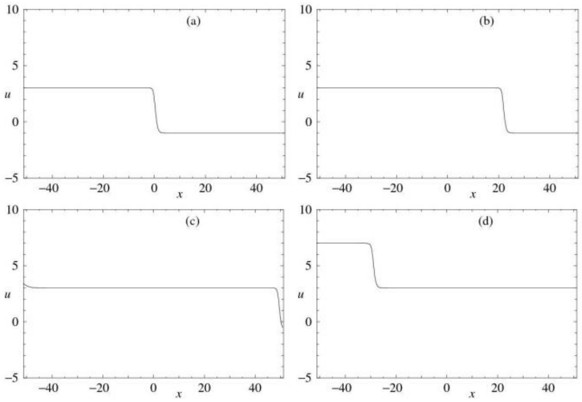

Figure 1. KdVB wave solution with (8) as initial condition: (a) $t = 0$, (b) $t = 1.8$, (c) $t = 4.1$, and (d) $t = 4.55$.

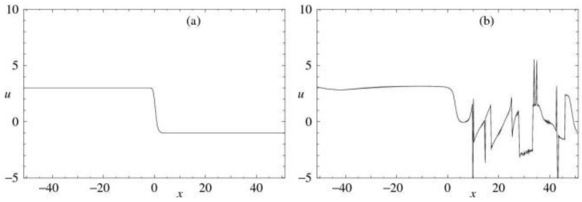

Figure 2. KdVB wave solution when $\Delta t = 0.00066$ and $\Delta x = 0.2$: (a) $t = 0$ and (b) $t = 0.264$.

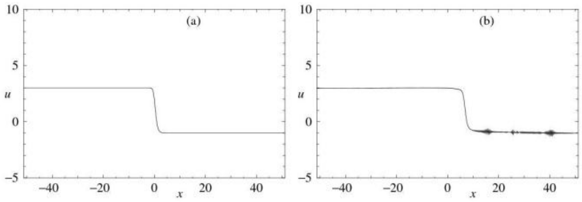

Figure 3. KdVB wave solution when $\Delta t = 0.00062$ and $\Delta x = 0.2$: (a) $t = 0$ and (b) $t = 0.59$.

Table 1: Testing the stability of the spectral method for integrating the KdVB equation.

Δx	Δt	Result
0.4	0.0043	N
0.4	0.0042	O
0.4	0.0037	O
0.4	0.0036	Y
0.3	0.0019	N
0.3	0.0018	O
0.3	0.0017	O
0.3	0.0016	Y
0.2	0.00066	N
0.2	0.00064	O
0.2	0.00059	O
0.2	0.00058	Y
0.1	0.000094	N
0.1	0.000093	O
0.1	0.000090	O
0.1	0.000089	Y

Y: Integrates without any sign of instability. N: Fails.
O: Integrates but shows small oscillation.

Investigating the behaviour of the KdVB equation

If we use the initial condition

$$u(x,0) = 1 - 2\tanh x \qquad (9)$$

then $D = 4$. This initial value gives the wave solution as shown in Fig. 4 which still gives the kink solution after a while.

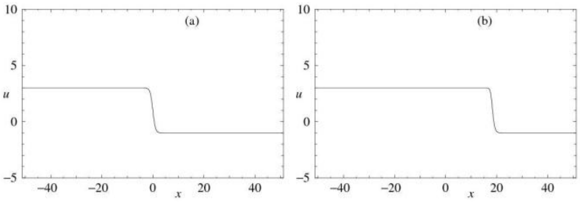

Figure 4. KdVB equation solution when using (9) as initial condition: (a) $t = 0$ and (b) $t = 1.54$.

If we use the initial condition

$$u(x,0) = 1 + 2\tanh x \qquad (10)$$

then $D = -4$. This results in a structure which gets wider without limit (Fig. 5).

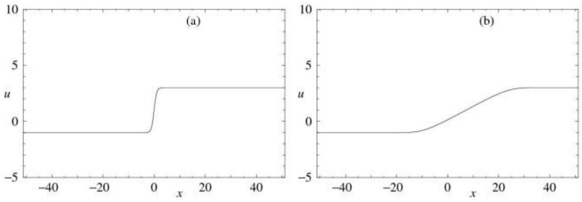

Figure 5. KdVB equation solution when using (10) as initial condition: (a) $t = 0$ and (b) $t = 0.605$.

If we add a small pulse to the solution by using the initial condition

$$u(x,0) = 1 + 2\tanh x + \operatorname{sech}^2 x + \operatorname{sech}^2(x-5) \qquad (11)$$

then we still have $D = 4$. This gives the solution in Fig. 6 which finally gives the kink solution.

If we move the position of the small pulse by using the initial condition

$$u(x,0) = 1 + 2\tanh x + \operatorname{sech}^2 x + \operatorname{sech}^2(x+5) \qquad (12)$$

then $D = 4$. This evolves as shown in Fig. 7 and finally changes into the kink solution.

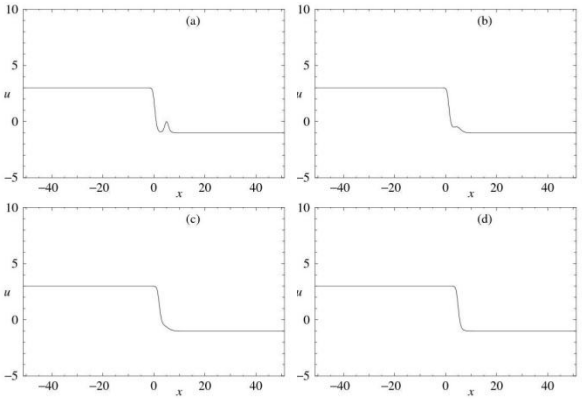

Figure 6. KdVB equation solution when using (11) as initial condition: (a) $t = 0$, (b) $t = 0.08$, (c) $t = 0.14$ and (d) $t = 0.34$.

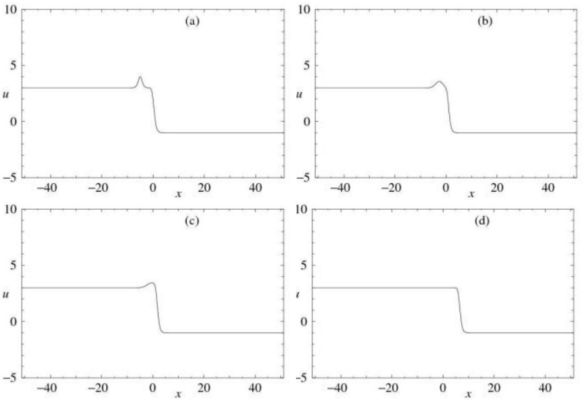

Figure 7. KdVB equation solution when using (12) as initial condition: (a) $t = 0$, (b) $t = 0.06$, (c) $t = 0.12$ and (d) $t = 0.48$.

It seems that we always get the kink solution when we start with a 'step-down' initial condition. From the solution (2) we have $u_\infty = u(\infty) = V/\alpha - 2A$ and $u_{-\infty} = u(-\infty) = V/\alpha + 2A$. Combining these two equations gives

$$V = \frac{1}{2}\alpha(u_\infty + u_{-\infty}),$$

and

$$A = \frac{1}{4}\alpha(u_{-\infty} - u_\infty).$$

If we use an initial condition where $u_\infty = u_{-\infty}$, then A = 0. This means that we will eventually get no wave. For any initial condition for which $u_\infty < u_{-\infty}$ it appears that we will eventually get the kink solution. This is similar to the behaviour of the Burgers equation.

Now consider the conserved quantity of the KdVB equation. We know that the solution (2) does not vanish as $x \to \pm\infty$ but its derivatives vanish. If we differentiate with respect to x and integrate (7) with respect to x over all space we obtain

$$\frac{\partial}{\partial t}\int_{-\infty}^{\infty} u_x \, dx = \left[-\frac{1}{2}\alpha(u^2)_x + \beta u_{xx} - s u_{xxx}\right]_{-\infty}^{\infty} = 0$$

This means that u_x does not change with time so this quantity is conserved. We can see from the numerical result that the integral of u_x is clearly conserved since the difference in boundary values does not change in the numerical method. If we differentiate the solution (8) and integrate this gives

$$\int_{-\infty}^{\infty} u_x \, \mathrm{d}x = [u(x)]_{-\infty}^{\infty} = D$$

since the difference in u at the boundaries is D.

Conclusions

We used the 4th order Runge-Kutta and spectral methods to investigate the KdVB equation. We gave the numerical results of the behaviour of the KdVB for various initial conditions. It seems that the kink solution is always stable to perturbations and any ‘step-down’ initial condition $u_0(x)$ with different values at as $x \rightarrow \pm\infty$ will eventually become a kink.

References

20. R. S. Johnson. A non-linear equation incorporating damping and dispersion. *J. Fluid Mech.*, 42(1):49–60, 1970.
21. W. M. Moslem. Dust-ion-acoustic solitons and shocks in dusty plasmas. *Chaos Soliton. Fract.*, 28(4):994–9, 2006.
22. I. Kourakis, S. Sultana, and F. Verheest. Note on the single-shock solutions of the Korteweg-de Vries-Burgers equation. *Astrophys. Space Sci.*, 338(2):245–249, 2012.
23. W. H. Press, B. P. Flannery, S. A. Teukolsky, and W. T. Vetterling. *Numerical Recipes in C*. Cambridge University Press, Cambridge, 1988.

Surface, Interface and Thin Films

Effects of Under-layers on Surface Morphology of Sputtered Co film

P. Manaviroj[1] and W. Rattanasakulthong[1*]

[1]*Department of Physics, Faculty of Science, Kasetsart University, 50 Ngam Wong Wan Ladyaow, Chatuchak, Bangkok, 10900, Thailand*
**Corresponding author. E-mail: fsciwrr@ku.ac.th*

Abstract

Structure, electrical resistance and surface morphology of Co films sputtered on Cr, Co, Cu Ag and Al under-layers have been studied. SEM indicates that the thickness of Co films is averaged about 85 nm with the electrical resistance range between 0.032 ohm to 25.7 ohm and the thickness of Cr, Co, Cu Ag and Al under-layers are 137, 69, 149, 317, and 108 nm, respectively. XRD result show that the Co film on under-layers is consisted Co (HCP) phase with (101) directions. AFM reveals that the surface morphology of Co film is strongly dependent on surface roughness and morphology of under-layers. The surface roughness (R_a) range over scan area of 1x1 μm^2 of the Co film is between 0.720 nm to 1.690 nm. The maximum and minimum roughness of Co film is observed on Ag and Cr under-layers, respectively. The grain size and distribution of Co film are affected by grain size and distribution of the under-layer film and the thickness of under-layers is indirect effect on the surface morphology of Co films. It is clearly show that the small grain size on surface area of the under-layer film give rises to the bigger grain size of Co film whereas, the big grain size of under-layer film give rises to the smaller grain size of Co film. All results confirm that the under-layer film plays important role on surface roughness of Co film. It can be concluded that the surface roughness of Co film can be modified by under-layers roughness and material.

***Keywords*:** Co films, Under-layers, Sputtering, Surface roughness, Thickness

Introduction

Thin films prepared on a various under-layers and substrates have attracted great interest because of their sensor and recording media applications. The effects of different metallic under-layers on the structural, magnetic and morphology of the magnetic thin films were studied by many groups of researcher. Lee et al [1] reported that a CrMn alloy improves the magnetic properties of sputtered CoCrPt film in comparison to the conventional Cr underlayer. Nguyen et al [2] reveals the effects of metallic Al under-layer and polymer substrate (PET) on morphology of magnetic property Co film prepared by sputtering. Moreover, morphology and structure the Co film on Cu and Cr under-layers investigated [3]. They found that the different microstructure and morphology strongly of under-layers strongly affected the properties of sputtered Co film and the difference in morphology of the under-layer result in the different structure of 20 nm Co film. Yang et al [4] studied the properties of Fe/Pt multilayer films with and without Al under-layer prepared by magnetron sputtering on SiO_2 substrate. They found that the Al under-layer can reduce the ordering temperature of Fe/Pt film and increase its coercive filed. Fu et al [5] investigated the morphology, structure and magnetic properties of FeCo thin film on Co under-layer with different thickness. They reported that the Co under-layer changed the preferred orientation and reduced the averaged the grain size and surface roughness of the FeCo films.

In this research work, surface morphology, structure and electrical resistance of Co film on different under-layers (Cr, Co, Cu, Ag and Al) prepared by RF-sputtering were investigated in order to study the effects of under-layers on the properties of sputtered Co film.

Materials and Methods

Co film was deposited on different under-layers (Cr, Co, Cu, Ag and Al) by RF-sputtering in argon atmosphere. The targets with a diameter of 3.00 inch and thickness of 0.250 inch were installed at a distance of about 4.5 cm away from the substrate in vacuum chamber under the base pressure of about $1x10^{-5}$ mbar. The argon pressure during the deposition process was 10^{-3} mbar. The glow discharge process was performed before the sputtering process to clean the target. The Co film was prepared at a constant sputtering power of 250 Watt for 1 hour. The under-layer of Cr, Cu, Ag, Al and Co films were sputtered at the power of 200 Watt for 10 min and 1 hour, respectively. The thickness of the sputtered films was measured by scanning electron microscope (SEM). Morphology and surface roughness of each film were investigated by atomic force microscopy (AFM). Crystal structure of the film was obtained using X-ray diffraction (XRD) with CuK_α radiation was used to identify the film crystal structure. Electrical resistance of films was measured by four-point-probe technique.

Results and Discussion

SEM images reveals the thickness and cross section of Co film on Cr, Co, Cu, Ag and Al under-layers shown in Figure 1. The SEM images show a smooth interface between Co film and under-layers. The average thickness of Co films on different under-layers and glass substrate estimated from SEM was between 72-93 nm and 85 nm, respectively. The thickness, electrical resistance and crystal structure of Co films on various under-layers was summarized in Table1. Additionally, the thickness of Cr, Co, Cu Ag and Al under-layers was about 137, 69, 149, 317, and 108 nm, respectively. The maximum and minimum thicknesses of Co film were observed on Cu and Cu under-layers, respectively. The difference of Co film thickness is may be due to the variance of the atomic interactions at an interface surface between of Co film and under-layers.

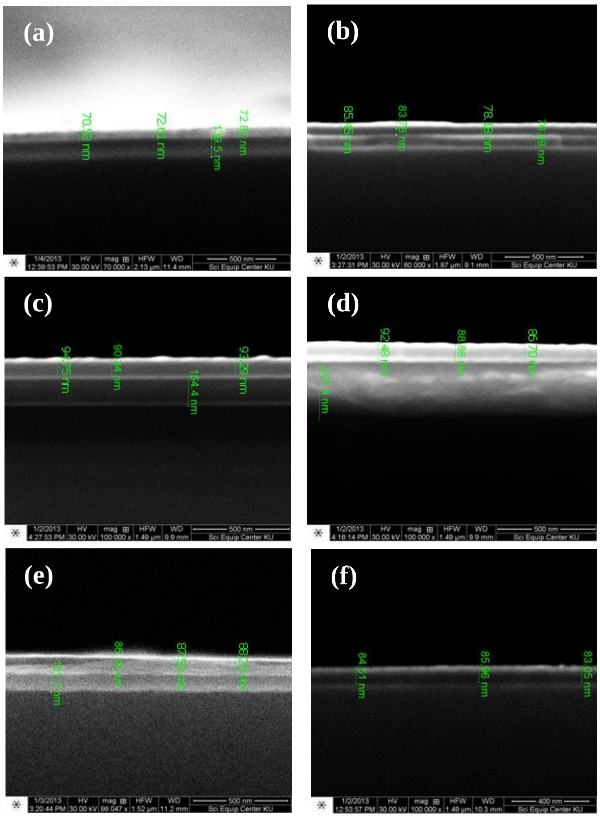

Figure 1. Cross section and thickness from SEM of Co film on (a) Cr (b) Co (c) Cu (d) Ag, (e) Al under-layers and (f) glass substrate.

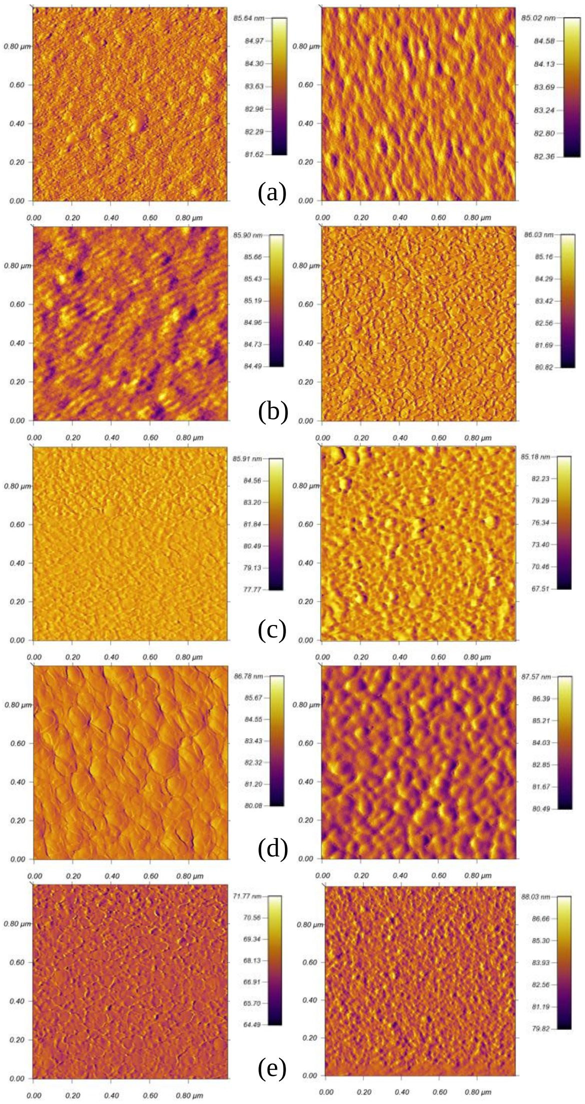

Figure 2. AFM images of under-layer (left) and Co film (right) on (a) Cr, (b) Co, (c) Cu, (d) Ag and (e) Al under-layers.

AFM result in Figure 2 shows the surface morphology of Co films on different under-layers over scan area of $1\mu m\times1\mu m$. The surface morphology of Co film reveals granular structure with different grain size, distribution and shape depending on under-layer materials. The fine granular size with regular size distribution was found in Co film on Al under-layer whereas the biggest granular size with regular distribution was observed in Co film on Al under-layer. It clearly shows that the surface morphology of Co film was affected by under-layer morphology. It can be described that the small grain size of under-layers gives rise to the bigger grain size of Co film shown in Figure 2 (a), (c) and (e). On the other hand, the big grain size of under-layers gives rise to the smaller grain size of Co film shown in Figure 2 (b) and (d). The Cr, Cu and Al under-layers with the layer thickness of 137, 143 and 108 nm, respectively, show a small grain size at the surface but, the Co and Ag under-layers with the layer thickness of 69 and 319 nm, respectively, exhibit the bigger grain size. It indicates the dependence of surface morphology on the thickness of the films. It can be described that the under-layer thickness directly effects on the surface morphology of under-layer films and, then it is indirect effect on the surface morphology and roughness of Co films.

Moreover, AFM result in 3D in Figure 3 also shows the different surface roughness of Co film on different under-layers. It is clearly revealed that all Co films on various under-layers show a columnar structure with the different size and distribution. The under-layer films possess a different structure at the surface depending on their type of material. The smoothest surface is observed in a Co/Cr film with a minimum surface roughness (R_a) of 0.72 nm. The maximum roughness of 1.69 nm is found in Co/Ag film. The correlation of under-layer material and roughness as a function of the surface roughness of sputtered Co film is shown as a column chart Figure 4. The chart indicates that the Co, Cu, Ag, Al under-layers and glass substrate gives rise to the higher surface roughness of Co films than that of the under-layers and the surface roughness of Co film is lower than that of the Cr under-layer.

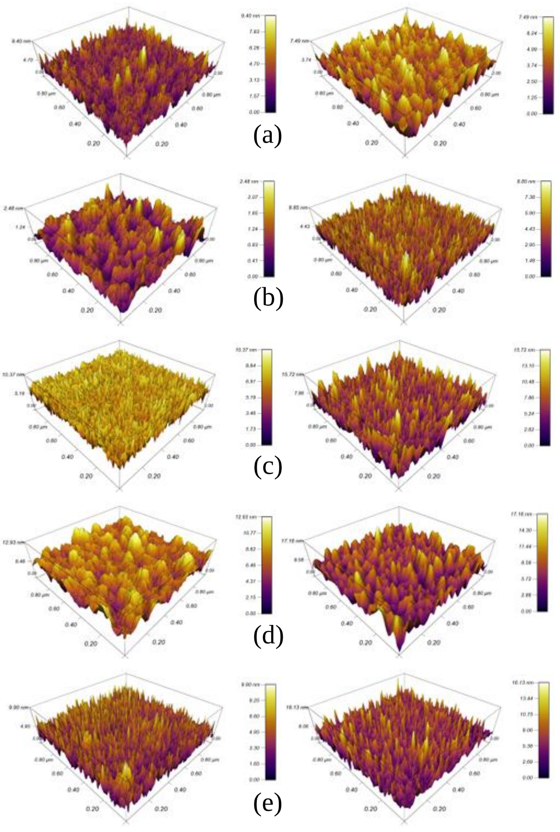
(a)
(b)
(c)
(d)
(e)

Figure 3. Surface roughness in 3D of under-layers (left) and Co film (right) on (a) Cr, (b) Co, (c) Cu, (d) Ag and (e) Al under-layers.

Crystal structures of sputtered Co films from XRD characterization are summarized as in Table 1. All sputtered Co films on various under-layer materials exhibits Co (HCP) phase in (101) preferred direction corresponding to 2-theta of 47.30 degree. The Cr under-layer shows Cr (BCC) phase with (110) direction. The Cu, Ag and Al under-layers are similar showing the FCC phase in a (111) direction. This result infers that the Co/Cr films possess a smoothest surface and regular grain size and distribution because of the BCC lattice of the Cr under-layer and the FCC-under-layers increase the roughness of Co film. It is attributed that the roughness of Co film is importantly affected by under-layer crystal structure.

Table 1: The thickness, electrical resistance and crystal structures of Co film on different under-layers.

Sample	**Thickness (nm)**	**Resistance (Ω)**	**Structure**
Co/Cr	72/138	16.917	Cr: BCC (110), Co: HCP (101)
Co/Co	83/69	0.9966	Co: HCP (101), Co: HCP (101)
Co/Cu	93/150	0.3794	Cu: FCC (111), Co: HCP (101)
Co/Ag	89/317	0.0327	Ag: FCC (111), Co: HCP (101)
Co/Al	87/108	25.695	Al: FCC (111), Co: HCP (101)
Co/Glass	85	46.363	Co: HCP (101)

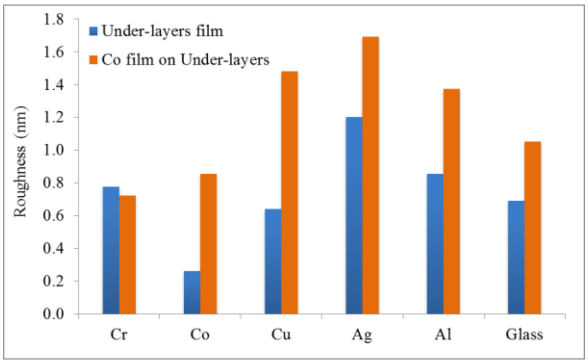

Figure 4. Correlation between surface roughness of under-layers and Co films

The electrical resistance of all samples in Table 1 shows that the Co/Ag film shows a minimum resistance because of the high conductivity of Ag elements and the highest resistance is found the Co film on glass substrate. All results confirm that the under-layer film plays important role on surface roughness of Co film because of its grain size, roughness and crystal structure. It can be concluded that the desirable surface roughness of Co film prepared by sputtering process can be strongly modified by under-layers roughness and material. Additionally, the BCC phase structure of the under-layer significantly reduces the surface roughness of the HCP-Co film.

Conclusions

Co film was deposited on different under-layers (Cr, Co, Cu, Ag and Al) by RF-sputtering. Co/Cr and Co/Ag films have the minimum and maximum surface roughness of 0.72 and 1.69 nm, respectively. The Cr, Cu and Al under-layers give rise to the bigger grain size of Co film. The Co and Ag under-layers give rise the the smaller grain size of Co film. The surface morphology and roughness of the sputtered Co films on various under-layer materials are strongly affected by the under-layers roughness, crystal structure and material.

Acknowledgments

This research work was financially supported by Department of Physics and Faculty of Science, Kasetsart University.

References

1. L. L. Lee, E. D. Laughlin and D. N. Lambeth, “CrMn Underlayers for CoCrPt thin film media”, IEEE Transactions on magnetic **34** (1998) 1561.
2. L. T. Nguyen, A. Lisfi and J. C. Lodder, “The effects of metallic underlayers on magnetic properties of obliquely sputtered Co thin films”, Journal of magnetism and Magnetic Materials **242-245** (2002) 374.
3. L.T. Nguyen and J. C. Lodder, “Properties of obliquely sputtered Co on different underlayers on polymer substrate” Journal of magnetism and Magnetic Materials **272-276** (2004) 2171.
4. F. J. Yang, H. Wang, H. B. Wang, B. Y. Wang, X. L. Wang, H. S. Gu and C. P. Yang, “Low-temperature ordering and enhanced coercivity of $L1_0$-FePt thin films with Al underlayer” , Applied Surface Science **257** (2011) 3216.
5. Y. Fu, T. Miyao, J. W. Cao, Z. Yang, M. Matsumoto, X. X. Liu, A. Morisako, “Effect of Co underlayer on soft magnetic properties and microstructure of FeCo thin films”, Journal of magnetism and Magnetic Materials **308** (2006) 165.

Investigation of Swift Heavy I-ion Irradiation Effects on Damage in Silicon Dioxide Thin Film

Saweat Intarasiri[1*], Duangkhae Bootkul[2], and Somsorn Singkarat[3]

[1]Science and Technology Research Institute, Chiang Mai University, Chiang Mai 50200, Thailand
[2]Department of General Science, Faculty of Science, Srinakharinwirot University,
Bangkok 10110, Thailand
[3]PBP Research Facility, Department of Physics and Materials Science, Faculty of Science,
Chiang Mai University, Chiang Mai 50200, Thailand
**Corresponding author. E-mail: saweat@gmail.com*

Abstract

Silicon dioxide (SiO_2) is considered as next generation dielectric material for semiconductor processing. Especially, thin film of a-SiO_2 on silicon wafers has many technological applications, e.g., in micro-electronics. However, a-SiO_2/Si structures can be severely degraded in radiation environments due to defect formation in SiO_2 and its interface. In the present study, irradiation induced defects of SiO_2 by swift I-ions were investigated. Thermally a-SiO_2 film was grown on Si wafer and subsequently irradiated with swift I-ions at energies of 10, 20, and 30 MeV at low or high fluences and at room or high temperatures. The effects of the irradiation were investigated following the changing of the infrared transmittance properties of the samples. From the measurements we concluded that the energy, fluence, and substrate temperature during irradiation had great effects on the defection of the film. It is noticed that the electronic energy loss mechanism of the tens-MeV I-ion irradiation of a-SiO_2/Si structure plays a major role in the structure destruction.

Keywords**:** Silicon dioxide, Thin film; Ion irradiation; Swift heavy ions; Infrared spectroscopy

Introduction

Thin film of amorphous SiO_2 on silicon wafers has many technological applications, especially in fabricating semiconductor devices. These applications includes [1] passivate the silicon surface for preventing uncontrolled potential fluctuations, act as a diffusion barrier against the diffusion of impurities, act as an insulating film between the metalization pattern, interconnecting devices, and the silicon substrate; and act as a dielectric, insulating the gate from the substrate in field effect devices. The effects of radiation on SiO_2/Si structures have been studied for many years. This steady interest reflects the importance of their practical applications. For example, Si integrated circuits can be severely degraded in nuclear radiation environments due to defect formation in SiO_2 and its interface [2]. Several studies have investigated the defects induced by γ- and x-rays, electron or proton irradiation of SiO_2/Si structures [3,4].

As far as ion irradiation is concerned, low-energy ($E < 1$ MeV/u) incident particles mainly transfer their kinetic energies to the target nuclei (nuclear stopping). The primary elastic knock-on collisions produce cascades of secondary atomic displacements, resulting in the creation of vacancy-interstitial pairs. In the high-energy range ($E > 1$ MeV/u), the incident ion collides with the target electrons and thus induces in its trail a localized high density of excited and ionized target atoms, also causing the emission of secondary electrons (electronic stopping). In most insulators, part of the energy transferred initially to the electrons is subsequently passed to the atoms, causing some anisotropic permanent damage (the so-called ion latent track). Large, high-energy accelerators dominated the early investigation of irradiation induced defects in SiO_2. However, heavy ions with energies below 1 MeV/u may deposit a high enough energy density to create continuous latent tracks of short length or at small depth, e.g. in thin films.

It is therefore important from both fundamental and application points of view to make a systematic study of radiation induced damages in thin films of SiO_2 by ions delivered from smaller accelerators. The main aim of this work is, thus, to investigate effects of such ions on the radiation damages of the SiO_2 thin film deposited on Si-substrate by thermal process. The experiments are limited by the investigation of irradiation induced defects of 10 – 30 MeV iodine ions (^{127}I-ions), which have the energy of about 0.08 – 0.25 MeV/u, in a-SiO_2.

Materials and Methods

Amorphous SiO_2 (a-SiO_2) films were thermally grown on (100) n-type silicon wafers of 525 µm thickness in a water vapor environment at 1050 °C. The thickness of the film was determined by the exposure time to be ~600 nm. After SiO_2 growth, the silicon wafers were cut into pieces with a size of ~1 x 1 cm^2 and subsequently treated by ion bombardment.

Irradiations of the samples were carried out in the irradiation facility at the Tandem Laboratory, Uppsala University. Heavy ions were delivered by a 5-MV NEC pelletron accelerator. The absolute ion fluence was determined from the irradiation time and the beam current, which was measured using a set of three Faraday cups with 1.0 cm^2 apertures located behind the sample holder. The irradiations were performed with an electrostatically rastered beam and the Faraday cups were thus used to measure the fluence homogeneity over the scanned area of 2 x 2 cm^2. The samples were bombarded at normal incidence with I-ions of 10, 20 or 30 MeV. The irradiations were done at room temperature (RT) or 800 ^{o}C (HT) to fluences of 1 x 10^{12} ions/cm^2 (low fluence = LF) or at 2 x 10^{12} ion/cm^2 (high fluence = HF), and at a pressure of ~10^{-6} mbar.

SRIM 2008 [5] simulation program was used to estimate the values of nuclear $(dE/dx)_n$ and electronic stopping power $(dE/dx)_e$, and the range (R_p) of the iodine ion in the SiO_2 substrate as summarized in Table 1. The density of SiO_2 was given from SRIM to be that of bulk vitreous silica (ρ = 2.20 g/cm^3 [6]). It is clear from the table that the iodine ions passed through the film and finally stopped deeply inside the silicon substrate.

Table 1: Parameters for the iodine ion irradiations: projected range (R_p), nuclear $(dE/dx)_n$ and electronic stopping power $(dE/dx)_e$ at the incident energy (E).

E (MeV)	R_p (µm)	$(dE/dx)_n$ (keV/nm)	$(dE/dx)_e$ (keV/nm)	$\frac{(dE/dx)_e}{(dE/dx)_n}$
10	3.9	0.46	2.5	5.4
20	6.3	0.28	4.7	16.8
30	8.0	0.21	6.3	30.0

Information about the vibronic and structural properties of the SiO_2 film on the Si-substrate can be obtained by measuring its infrared (IR) transmittance. The vibrations detected by IR spectroscopy are those that produce a change in a molecule's dipole moment [7]. Due to varied properties of the SiO_2 film, such as distortions in the film composition and differences in both the Si-O bond angle and the Si-O bond length, the frequency and the width of the IR absorption peak vary significantly. The information about SiO_2 film properties, therefore, can be obtained by analyzing the peak shape of the Si-O absorption mode and a narrower and stronger peak is considered here as an indicator of better crystallographic quality of SiO_2 [8]. In this study, the IR spectra were obtained using a Perkin Elmer FT-Infrared spectrometer in the range of 200-2000 cm^{-1} with a resolution of 4 cm^{-1}.

Results and Discussion

In the IR spectrum of as-prepared sample, three main vibrations of SiO_2 are clearly observed as strong peaks at 457, 817, 1095 cm^{-1}, which are ascribed to the vibrations of Si-O-Si bond rocking, O-Si-O bond bending and Si-O bond symmetric stretching modes, respectively [9,10]. The mode at 1095 cm^{-1} is the dominant mode observed in IR spectra of SiO_2. This vibration has been described as a rigid sublattice mode in which oxygen atoms and silicon atoms move in opposite directions [11]. The in-phase oxygen motion accompanied by silicon motion gives rise to the peak around 1095 cm^{-1} and the high-frequency shoulder is due to the out-of-phase oxygen motion, where there is very little associated silicon motion [12]. We noticed that the three peaks of SiO_2 showed the same trend of modification upon irradiation. Therefore, only the Si-O stretching mode at peak around 1095 cm^{-1} as shown in Figure 1 was fully characterized and summarized in Table 2.

As seen in Figure 1, it is obvious that energy, fluence, and substrate temperature during irradiation have great effects on the damage in the film. Chaudhari et al. [13] reported that when a SiO_2 matrix is irradiated with swift ions, the oxygen diffuses away from the ion tracks, leaving Si nanostructures whenever quenching of the melted zone is slower than the oxygen diffusion. The observed phenomena might be originated from a chemical reactions induced by high energy ion irradiation; $SiO_2 \rightarrow Si + 2O$. Oxygen molecule will be pumped out from the samples. Carlotti et al. [14] reported silicon bumps growth, induced by swift heavy ions at the silicon oxide-silicon interface. According to these authors' suggestions, the phase separation assists the Si bump growth at the SiO_2/Si interface, and consequently recrystallized silicon nanostructures can be generated inside the ion-irradiation damaged volume in the silicon-rich region close to the interface. The underlying silicon single crystal substrate is quickly rebuilt due to the intrinsic properties of that material: high thermal conduction and high diffusion of excited electrons. Then the structure of the silicon substrate and the near-interfacial silicon-rich oxide can provide favourable seeds for silicon nanostructure growth. Saint Martin et al. proposed that [15], for lower-energy swift irradiation where the track did not reach the SiO_2/Si interface, a Si local concentration increased into the track-damaged material region, associated with oxygen diffusion away from the ion track. Discontinuous silicon nanostructures may be growing inside SiO_2 tracks even for distances far away from the favourable site at the SiO_2/Si interface. This nanostructure should be responsible for the modification of the IR-peak characteristics ion our experiments.

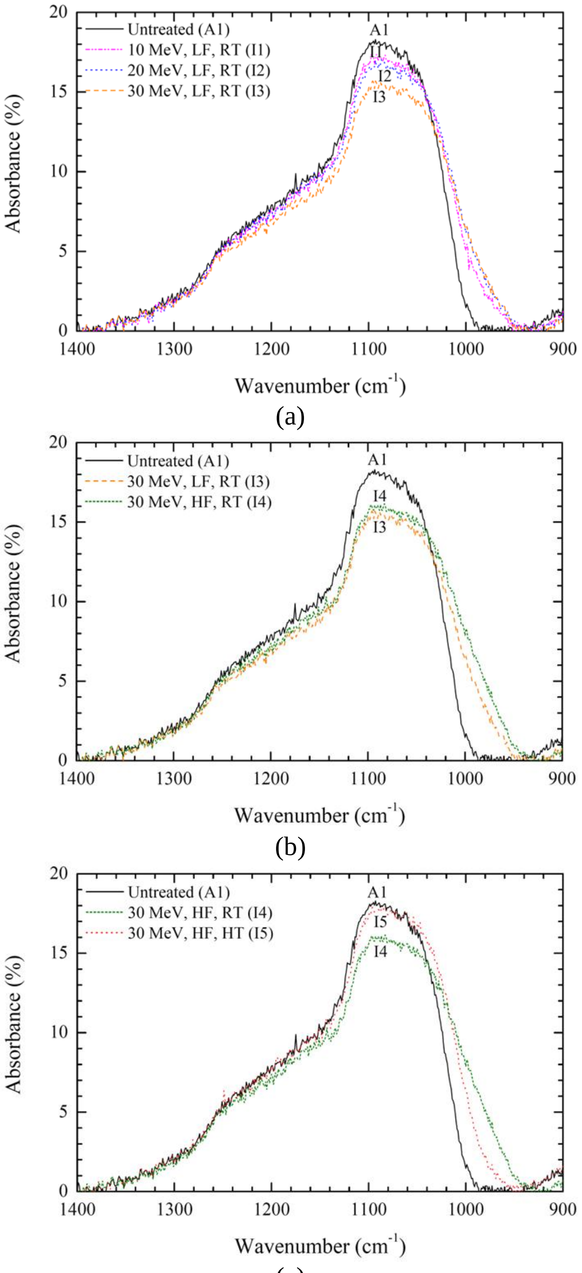

(a)

(b)

(c)

Figure 1. Deconvolution of the Si-O stretching mode of IR-spectra of all investigated samples; (a) energy dependence, (b) fluence dependence, and (c) substrate temperature dependence.

It is noticed from Figure 1 (a) that the ion energy shows strong effects on the damage of SiO_2. As observed from the figure, the peak height decreases while the peak width increases for increasing energy. When an energetic ion enters a solid it loses energy by two processes: (i) by elastic or nuclear collisions with the matrix atoms causing direct atom displacements and disorder; and (ii) by inelastic or electronic processes in which the electrons of the solid are excited [16]. In semiconductors, only elastic collisions usually generate lattice damage, whereas in insulators, both processes can induce atomic displacements [17]. The collisional or direct displacement processes which occur during the collision cascade take place in a very short time. After that the cascade is quenched and, if the resulting discrete defects are immobile and stable, disorder will be preserved. However, if defects such as vacancies and interstitials are mobile at the implantation temperature, then significant dynamic annealing and annihilation of damage can occur during implantation [18]. It is very interesting that in our case, the FWHM of IR-peak is linearly dependent to the electronics stopping power $(dE/dx)_e$ as seen in Figure 2.

Table 2: Samples details and their IR peak characteristics.

Samples	**Peak characteristics**			
	Posi-tion (cm^{-1})	**Height (a.u.)**	**FWHM (cm^{-1})**	**Area (a.u.)**
A1 *(untreated)*	1093	18.30	153	3083
I1 *(10, LF, RT)*	1097	17.45	163	3129
I2 *(20, LF, RT)*	1087	17.04	169	3158
I3 *(30, LF, RT)*	1093	15.70	176	2961
I4 *(30, HF, RT)*	1083	16.16	183	3174
I5 *(30, HF, HT)*	1083	17.90	172	3288

Note: 10, 20, 30 = ion energy in MeV; LF = low fluence; HF = high fluence; RT = room temperature; HT = high temperature

It is noticed from Figure 1 (b) that as the energy is kept constant at 30 MeV, the irradiation fluence shows strong effects on the damage of SiO_2. As observed from the figure, the peak height decreases while the peak width increases for increasing fluence. Thus, a higher fluence enhances the destruction of Si-O bonding. This observation is not difficult to understand, as, naturally, higher fluences cause heavier damage until the damage is saturated.

In comparison between irradiation temperatures Figure 1 (c), the IR peak height increases while the IR peak width decreases following the rise of the target temperature. This indicates that the amount of SiO_2 increases as increasing of the irradiation temperature, while the quality of the structure is preserved quite well. It seems that oxygen is more activated by higher temperatures to form Si oxide. It is known that oxidation can be achieved by annealing in dry oxygen at 800 °C [19]. Besides, Yano et al. [20] demonstrated that the damage of neutron irradiated crystalline and non-crystalline SiO_2 was 80-90 % recovered by subsequent annealing at the temperature of about 800 °C. They believed that the irradiation-induced thermal spike was responsible for the effects. Some parts of the spike regions were rapidly quenched, leaving a slightly denser and more disordered state than the original glass state. After annealing, dense and disordered portions were relaxed into ordinary state and restored to completely the same as the unirradiated one. Morover, Arnoldbik et al. [21] proposed the following model for the behavior of O in

SiO_2 under ~MeV/u. heavy ion irradiation: O_2 molecules are produced in and/or along the ion track in the SiO_2 film, via bond breaking and recombination, presumably by energetic electrons that are produced as a result of the passage of the ions. These molecules are considered as volatile but not inert, except in a perfect SiO_2 matrix. So, only in the beginning of irradiation O_2 can escape from the entire bulk of the film. Already at a low fluence, the irradiation brings about a structural change in the oxide. This structural change and/or the removal of O may bring oxygen trapping centers into existence causing the process of bulk loss of oxygen to be self-limiting. Only in the surface region O_2 molecules are able to desorb from a typical depth of 5 nm. So, a typical O_2 diffusion length of about 5 nm is deduced. Therefore, we believe that in our case, most of oxygen relieved from the irradiation sites is trapped and induced to bond back to silicon under high temperatures. This is because the pumping speed is slower than the bonding mechanism. Additionally, the residual oxygen in the vacuum chamber (even very low in quantity) is also induced to oxide the silicon surface at this temperature.

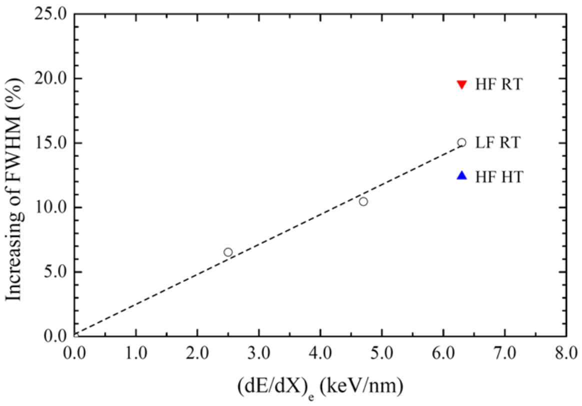

Figure 2. Increasing FWHMs after irradiation for selected Infrared bands as a function of electronic stopping power *(dE/dx)ₑ*. Trends are similar for all bands. The lines represent linear fits to the data.

Conclusions

Irradiation induced defects of SiO_2 by swift I-ions were investigated. Thermally a-SiO_2 film was grown on Si wafer and was subsequently irradiated with swift I-ions at energy of 10, 20, and 30 MeV at low or high fluence and at room or high temperature. The effects of the irradiation were investigated following the changing of the infrared transmittance properties of the samples. From the measurements we concluded that the energy, fluence, and substrate temperature during irradiation have great effects on the damage in the film. The higher energy and fluence irradiations induce more dissociation of the Si oxide and leave Si nanostructure growing in the ion tracks. The high irradiation temperature plays a compensatory effect to the high energy and fluence irradiation effects as relieved oxygen is activated to recombine silicon to form more Si oxide.

Acknowledgments

S. Intarasiri wishes to thank the International Science Program (ISP) of Uppsala University for supporting his research work at Uppsala University.

References

1 A. H. Van Ommen, Solid State Phenomena **1–2** (1988) 133.
2 T. P. Ma, and P. V. Dressendorfer, Ionizing Radiation Effects in MOS Devices and Circuits, Wiley Interscience, New York, 1989.
3 F. B. Mclean, IEEE Trans Nucl Sci **NS-27** (1980) 1651.
4 M. Antonini, P. Camagni, P. N. Gibson, and A. Manara, Radiat Eff **65** (1982) 41.
5 SRIM 2008 Program. Available from: www.research.ibm.com/ionbeams/srim/.
6 S. M. Sze, Physics of Semiconductor Devices, John Wiley and Sons, Inc, New York, 1981.
7 D. Lin-Vien, N. B. Colthup, W. G. Fateley, and J. G. Grasselli, The Handbook of Infrared and Raman Characteristic Frequencies of Organic Molecules, 1991, Academic Press, California, ISBN 0-12-451160-0, p. 1-7.
8 F. Ay, Ph.D. Thesis, Bilkent University, 2000.
9 P. K. Bhan, and R. Ashokan, J Appl Phys **71** (1992) 2387.
10 D. M. Wolfe, B. J. Hinds, F. Wang, G. Lucovsky, B. L. Ward, M. Xu, R. J. Nemanich, and D. M. Maher, J Vac Sci Technol **A 17** (1999) 2170.
11 F. L. Galeener, and G. Lucovsky, Phys Rev Lett **37** (1976) 1474.
12 P. G. Pai, S. S. Chao, V. Takagi, and G. Lucovsky, J Vac Sci Technol **A 4** (1986) 689.
13 P. S. Chaudhari, T. M. Bhave, D. Kanjilal, and S. B. Bhoraskar, J Appl Phys **93** (2003) 3486.
14 J. F. Carlotti, A. D. Touboul, M. Ramonda, M. Caussanel, C. Guasch, J. Bonnet, and J. Gasiot, Appl Phys Lett **88** (2006) 41906.
15 G. Saint Martin, O. A. Bernaola, G. Garcia Bermúdez, and M. Behar, Radiat Meas **42** (2007) 130.
16 G. Dearnaley, J. H. Freeman, R. S. Nelson, and J. Stephen, Ion Implantation, North-Holland, Amsterdam, 1973.
17 R. Kelly, Nucl Instrum Methods Phys Res **182-183** (1981) 351.
18 J. S. Williams, Rep Prog Phys **9** (1986) 491.
19 A. Ourmazd, J. A. Rentschler, and J. Bevk, Appl Phys Lett **53** (1988) 743.
20 T. Yano, K. Fukuda, M. Imai, and H. Miyazaki, J Nucl Mater **367-370** (2007) 730.

21 W. M. Arnoldbik, N. Tomozeiu, and F. H. P. M. Habraken, Nucl Instrum Methods Phys Res **B 219-220** (2004) 312.

Refining of Silicon from Thick Film Silicon Dioxide by Electro-deoxidation Technique

Alongkot Phothawan [1,*] and Sukum Eittsayeam[1, 2]

[1]Department of Physics and Materials, Faculty of Science, Chiang Mai University, Chiang Mai 50200, Thailand
[2]Materials Science Research Center, Faculty of Science, Chiang Mai, 50200, Thailand
**Corresponding author. E-mail :* hunsahorse@hotmail.com

Abstract

The SiO_2 films were prepared by a tape casting process. Then, electro-deoxidation was used to produce Si from the SiO_2 film in a molten $CaCl_2$ electrolyte in Ar atmosphere at 850 °C for 24 h at an applied potential range of 1.50 – 3.00V relative to a graphite anode. The results showed that the SiO_2 films transformed to Si by increasing applied voltage. The results of XRD and SEM confirmed that SiO_2 was electrochemically reduced to Si by applied potential of 2.50V and 2.75V. In addition, $CaSi_2$ alloy formation was observed at 3.00V.

Keywords: Electro-deoxidation, Silicon, Silicon dioxide

Introduction

Solar grade silicon (SOG-Si) is an important material for solar cells. The current cost of SOG-Si production is high. Industrial extraction of silicon is through the carbothermic reduction of SiO_2 raw material at high temperatures ~1700°C, resulting in large energy consumption of about 13 kWh/(kg-Si) with energy efficiency lower than 30% and serious carbon emissions greater than 3 for the mass ratio of CO_2:Si [1]. Then, silicon from the industrial process is improved to high purity silicon, which involves conversion into silane compounds (SiH_4, $SiHCl_3$, etc.) and transforming these compounds back to high purity silicon, making silicon solar cells very expensive [2-5].

The electro-deoxidation process is a direct electrolytic reduction in molten salt [4]. This process extracts metal from solid metal oxide (such as TiO_2, ZrO_2, etc.) or metal based glass (such as Zr-based glass, Fe based glass, etc.) in molten salt (such as $CaCl_2$, NaCl, etc.) [6-10]. This technique has also been used to extract silicon metal from SiO_2 raw materials [2-4]. Electrochemical deoxidizing of SiO_2 in molten salts requires three components, the conducting wire, SiO_2 and molten salts electrolyte. The total reaction is written as

$$SiO_2 + 4e^- \rightarrow Si + 2O^{2-} \qquad (1)$$

The O^{2-} ions diffuse into the molten salts electrolyte resulting in silicon layer formation [1-5]. There are several advantages of this process such as low energy consumption, less contamination, low or zero carbon emission and direct production of SOG-Si [1]. The new process has the advantages of simple purification process and low energy consumption applied to use.

In this study, SiO2 raw materials were prepared as SiO_2 films. Then, these films were converted to silicon by using the electro-deoxidation process in $CaCl_2$ molten salt at 850°C and with applied voltages in the range between 0 - 3 volt for a duration of 24 h. The influence of applied voltage on the properties of silicon converted from SiO_2 in the electro-deoxidation process was reported.

Materials and Methods

SiO_2 raw material from a quartz mine was ground into powder using a ball milling technique in ethanol. Then, SiO_2 slip was formed, again using a ball milling technique, from SiO_2 powder in a solution of dolapix PC 21, PVA, DI water and octanol. The composition and functions of the SiO_2 slip materials are listed in Table 1. Green tapes were prepared by a tape casting technique on polypropylene films. The casting rate and gap height were 1cm/s and 2 mm. After that, the green tapes were sintered at 1300 °C for 3 h with a heating rate of 2 °C/min to form SiO_2 films. $CaCl_2$ was the molten electrolyte solution. This salt was kept at 100 °C for 24 h in air to remove the moisture. An alumina crucible was used to hold the electrochemical cell for the electro-deoxidation process. The crucible was filled with $CaCl_2$ salt and placed inside a stainless steel chamber in a furnace. The anode electrode was graphite rods and SiO_2 film was attached to a nichrome wire frame for the cathode. The salt was melted at 850°C and the electrochemical process was held at this temperature under Ar atmosphere. Applied voltages were in the range between 0 – 3 volt for a total time of 24 h. After processing, the salts in the crucible were removed using DI water and samples were washed in DI water in an ultrasonic bath.

The SiO_2 films and deoxidised samples were investigated in terms of phase identification, weight loss, chemical composition and microstructure via X-ray diffraction (XRD: Bruker AXS D8 ADVANCE) and scanning electron microscopy (SEM: JSM-6335F).

Table 1: Function and composition of materials for SiO_2 slip preparation.

Materials	Function	Composition (wt%)
SiO_2 powder	Source component	55
Dolapix PC 21	Dispersant	1
polyvinyl alcohol : PVA (W_m=13,000 g/mol)	Binder	8
deionize *Water*	Solvent	35
Octanol	Defoamer	1

Results and Discussion

The appearance of samples which were prepared by electro-deoxidation for 24 h and with applied potentials of 1.50V, 2.00V, 2.25V, 2.50V, 2.75V and 3.00V are shown in Fig 1. From Fig 1., it can be seen that the color of the SiO_2 films changed from white to black and brown with increasing voltage. At voltages around 2.25V -2.75V, the samples were more brittle (Fig 1.(d-f)). In the case of 3.00V, the reaction proceeded considerably inside the film and it was transformed to powder (Fig 1.(g)). In another study [4], the electrochemical reduction was found to start at the contact zone between the SiO_2 films and metal wire, and spread in both surface and bulk directions. In both studies material reduced increased when applying higher potentials. The oxygen atom in SiO_2, which received electrons from the DC power supply, was converted to O^{2-} ion. Then O^{2-} diffused though the molten $CaCl_2$ to the graphite anode. This resulted in decreasing in the weight of the sample as shown in Fig 2. Similar results have been reported by K. Yasuda at el [4].

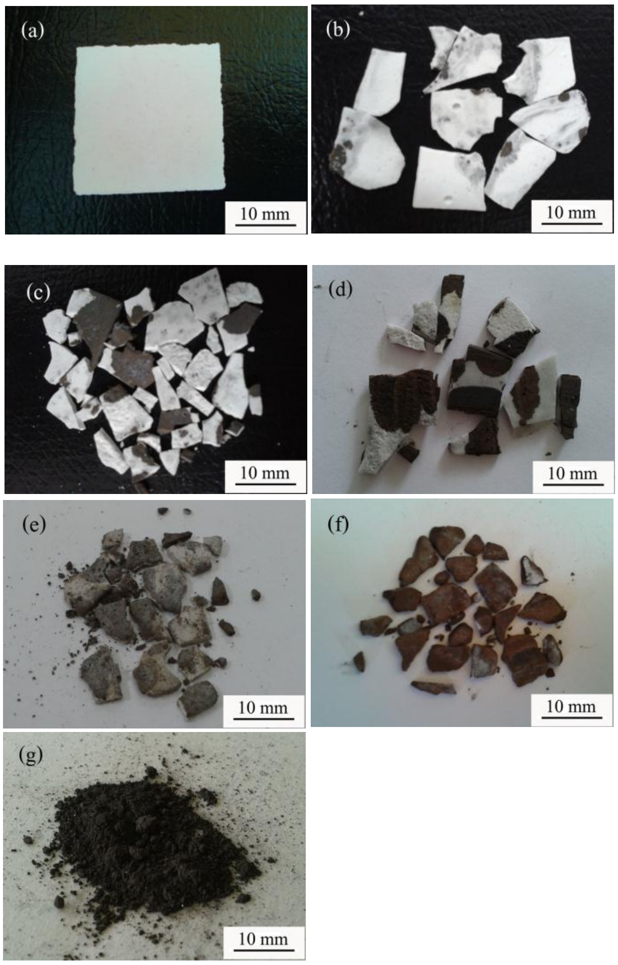

Fig 1. The appearance of obtained SiO_2 films from the electro-deoxidation process after applying different voltages for 24 h in molten $CaCl_2$ at 850 °C (a) no applied voltage, (b) 1.50V, (c) 2.00V, (d) 2.25V, (e) 2.50V, (f) 2.75V and (g) 3.00V.

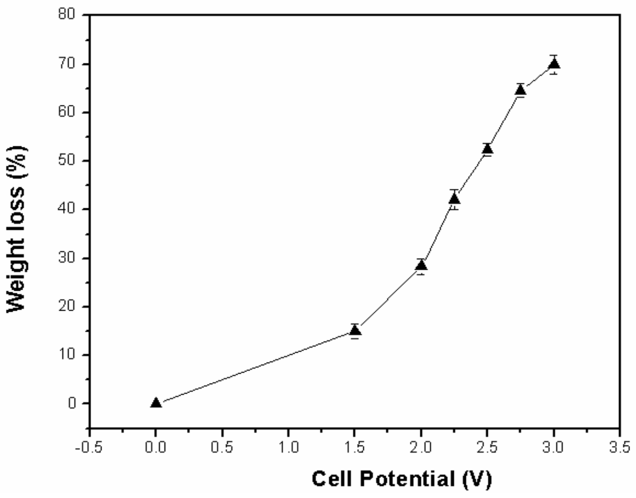

Fig 2. Weight loss versus applied potential for the electro-deoxidation of SiO_2 films.

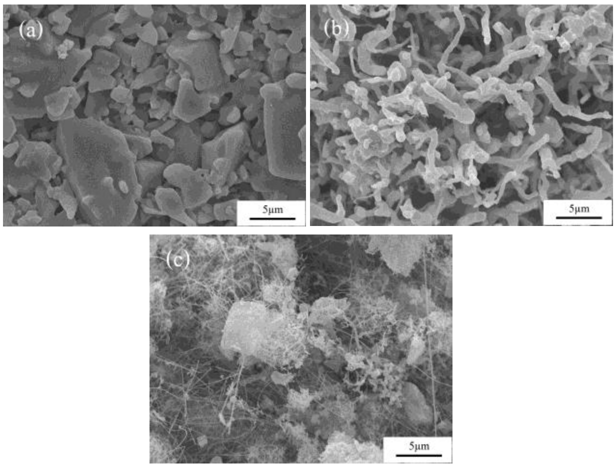

Fig 3. SEM images of the contact zone of SiO_2/Si samples from the electro-deoxidation process of 24 h in molten $CaCl_2$ at 850 °C at (a) no applied voltage, (b) 2.50V and (c) 3.00V.

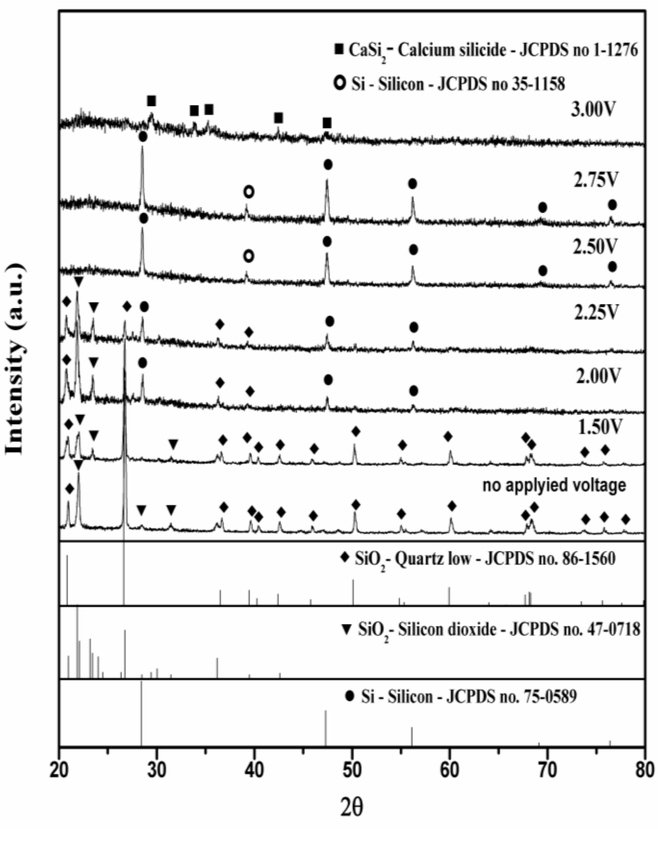

Fig 4. XRD patterns of SiO_2/Si samples from electro-deoxidation process with various applied voltages.

In Fig 3., the SEM micrographs show the microstructure of the sample at the contact point between the SiO_2 films and nichrome wire. The SiO_2 film with no applied voltage exhibited spherical crystal (Fig 3.(a)). After the electro-deoxidation process, the samples at 1.50 - 2.75V revealed columnar crystals (Fig 3.(b)). This is consistent with weight loss as shown in Fig 2. The sample at 3.00V showed a fibrous structure (Fig 3(c)).

Fig 4. shows the XRD patterns of all samples. For the samples at 1.50V - 2.25V, XRD showed mixing of phases between SiO_2-quartz low (JCPDS no 86-1560) and SiO_2 (JCPDS no 47-0718). The electrolysis time was chosen at 24 h to allow SiO_2 to Si conversion in the sample. For samples at 2.00V, 2.25V, 2.50V and 2.75V, XRD confirmed that SiO_2 was electrochemically reduced to Si. In the case of 3.00V, the sample was identified as $CaSi_2$ (JCPDS no 1-1276). This may be explained by excessive applied voltage in the reaction as mentioned by H. Nishihara at el [4]. The following reaction occurs at more than 3.00V.

$$2Si + Ca^{2+} + 2e \rightarrow CaSi_2 \tag{2}$$

In addition, these results corresponded to the report by P.C. Pistorius at el [11], which studied the cathodic polarization curve of the cathode. They found that the cathodic polarization curve was steep and constrained the voltage of the cathode close to the equilibrium voltage for silicon formation (and more positive than that for calcium silicide formation) so any increase in cell voltage largely went toward increased *IR* drop and anode overpotential, at least for cell voltages up to 2.75V.

Conclusion

The electro-deoxidation of SiO_2 films, which was performed in molten $CaCl_2$ at 850°C and various applied potentials has been investigated. The samples showed changes in color from white to black and brown with increasing potential. From the XRD, it was found that samples treated at low voltages (2.00V-2.25V) showed mixing between SiO_2 phase and Si phase. For samples at 2.50V and 2.75V, XRD confirmed that SiO_2 was electrochemically reduced to Si. At a higher potential of 3.00V, the reaction proceeded considerably inside and the film transformed to powder. The sample was identified as $CaSi_2$ and the film permanently broke into powder and so it was difficult to identified its composition. The electro-deoxidation refining silicon process, has promise to be an alternative processing technique for refining pure silicon in the future.

Acknowledgments

The authors would like to thank the NSTDA University Industry Research Collaboration (NUI-RC) under National Science and Technology Development Agency (NSTDA), Materials Technology Center (MTEC), Office of the Higher Education Commission (OHEC), the Graduate School and Faculty of Science, Chiang Mai University, Thailand for financial support.

References

1. W. Xiao, X. Jin, Y. Deng, D. Wang, and G. Z. Chen, “Rationalisation and optimisation of solid state electro-reduction of SiO_2 to Si in molten $CaCl_2$ in accordance with dynamic three-phase interlines based voltammetry”**,** Journal Electroanal Chem **639** (2010), 130-140.
2. K. Yasuda, T. Nohira, R. Hagiwara, and Y. H. Ogata, “Direct electrolytic reduction of solid SiO_2 in molten $CaCl_2$ for the production of solar grade silicon”, Electrochim Acta **53** (2007), 106–110.
3. E. Ergul, I. Karakaya, and M. Erdogan “Electrochemical decomposition of SiO_2 pellets to form silicon in molten salts”, Journal of Alloys and Compounds **509** (2011), 899–903.
4. K. Yasuda, T. Nohira, and Y. Ito, “Effect of electrolysis potential on reduction of solid silicon dioxide in molten $CaCl_2$”, Journal of Physics and Chemistry of Solids **66** (2005), 443–447.
5. E. Juzeliunas, A. Cox, and D. J. Fray, “Silicon surface texturing by electro-deoxidation of a thin silica layer in molten salt”, Electrochem Commun **12** (2010), 1270–1274.
6. I. Park, T. Abiko, and T. H. Okabe, “Production of titanium powder directly from TiO_2 in $CaCl_2$ through an electronically mediated reaction”, Journal of Physics and Chemistry of Solids **66** (2005), 410–413.
7. K. S. Mohandas, and D. J. Fray, “Electrochemical Deoxidation of Solid Zirconium Dioxide in Molten Calcium Chloride”, Metals & Materials Society and ASM International, 2009.
8. S. Bossuyt, S. V. Madge, G. Z. Chen, A. Castellero, S. Deledda , J. Eckert, D. J. Fray, and A. L. Greer, “Electrochemical removal of oxygen for processing glass-forming alloys”, Materials Science and Engineering A, **375–377** (2004), 240–243.
9. S. L. Wang, H. X. Li, Y. U. Jeong and S. Yi, “Effects of Electrolyte pH on the Electrochemical Behavior of Fe-Based Bulk Metallic Glass”, Met. Mater. Int., 2012.
10. S. Wang, S. Li, L. Wan, and C. Wang. “Electro-deoxidation of V_2O_3 in molten $CaCl_2$-NaCl-CaO”, International Journal of Mineral Processing **3** (2012) 212.
11. P. C. Pistorius, D. J. Fray, “Formation of silicon by electrodeoxidation, and implications for titanium metal production”, Journal of South American Earth Sciences, 2006.

Surface Modification of Polymethyl Methacrylate by Argon/Acetylene Plasma Jet for Dental Applications

P. Saikrueng[1]*, P. Yavirach[2] and D. Boonyawan[1]

[1] *Plasma-Bio and Clean Energy Laboratory, Department of Physics and Materials Science, Faculty of Science, Chiang Mai University, Suthep Road, Chiang Mai 50200, Thailand*
[2] *Department of Prosthodontic, Faculty of Dentistry, Chiang Mai University, Suthep Road, Chiang Mai 50200, Thailand*
**Corresponding author. E-mail: neung_31717504@hotmail.com*

Abstract

This research studies modified surface of polymethyl methacrylate (PMMA) with carbon films from acetylene by using plasma jet technique. It is to improve the adhesion between denture teeth, made from heat-curing PMMA and denture bases, made from self-curing PMMA. This process deposit carbon atoms from plasma on heat-curing PMMA at atmospheric pressure. By varying power of RF from 30, 40 and 50 watt and flow rate of argon : acetylene mixed gas with 200:1, 250:1 and 300:1 ratio and time deposited from 60, 90 and 120 second. As results of OES, CH species have the best association at the ratio of Ar : C_2H_2 equal to 250:1 which increase the contact angle from 27.86 to 61.82. As results from AFM, the roughness increase when operating time increases.

***Keywords*: Plasma jet, Acetylene, PMMA, Carbon films, Denture**

1. Introduction

Atmospheric pressure plasma jet (APPJ) was developed by Jeong et al. [1-6] (University of California, Los Angeles, CA) in collaboration with Park et al. (Los. Alamos National Laboratory) by the technique of the plasma jet is composed of bipolar electrodes. And a gas mixture of helium, oxygen or other gas to flow through the 13.56 MHz radio frequency and voltage between 100-250 volts supplied to the electrodes within. And the outer electrode is grounded. To be used as a raw material gas flow between the electrodes and the cylindrical electrode and within the nucleus. The electrodes are powered by radio frequency energy within. Which serves to accelerate free electrons. When the free electrons have enough energy to break away from the electrodes within the electrode to the outside. Gas on discharge was released. Ions and electrons are rapidly lost by recombination to occur and remain electrically neutral state.

Atmospheric pressure plasma jets have been established as suitable sources of low-temperature and non-equilibrium atmospheric pressure plasmas [7, 8]. The main distinctive features of this plasma tool is the remote operation and its scalable dimension which can be adjusted from several cm down to the sub-mm region, thus, allowing local treatment of 3D surfaces, e.g. inner walls, trenches or cavities [8]. Among other applications, the treatment of temperature-sensitive surfaces such as biological material is of interest, in particular the interaction of plasma with living cells, tissues and bacteria, e.g. for cultivation, deactivation or remedial treatment of diseases.

Present material denture made 2 types of poly methyl methacrylate or PMMA are denture teeth made from heat-curing PMMA in the solid state with denture base made from self-curing PMMA. PMMA is polymers which are composed mostly of carbon and hydrogen. This research has the idea that if we can make this 2 type of PMMA together with a strong bond between the molecule 2 PMMA species to be identified to better than the old method of sandblasting or silane coating. To make this bonding of 2 type PMMA layer between the 2 PMMA has to be this kind of elements carbon and hydrogen as well. Therefore a technique to create a plasma jet of hydrocarbon layer. By the breakdown of a gas mixture of argon and acetylene coating on heat-curing PMMA surface. In order to have an intermediate layer of carbon bonding between the 2 types PMMA.

2. Experimental Setting

The scheme of our plasma jet is shown in Figure. 1 used stainless steel capillary with outer and inner diameters of 1.5 and 0.9 mm is inserted into a quartz tube with outer and inner diameters of 5 and 3 mm. A gap of 0.75 mm is formed between the capillary and the tube in this way. The capillary is connected to a 300 KHz power supply through a matching network. The plasma jet control of the ambient atmosphere. Plasma source used argon 2, 2.5 and 3 slm flowed between the quartz tube with the capillary and C_2H_2 gas injected in the capillary flow of 10 SCCM and varies power 30, 40 and 50 watt and observe plasma chemistry by Optical emission spectroscopy (OES). After that, We used argon mixed with acetylene gas deposited on PMMA by varies time are 1, 1.5 and 2 minute with a source-substrate distance of 1 mm. Resulting have been analyzed surface roughness and thickness of the carbon film by Atomic force microcopy (AFM).

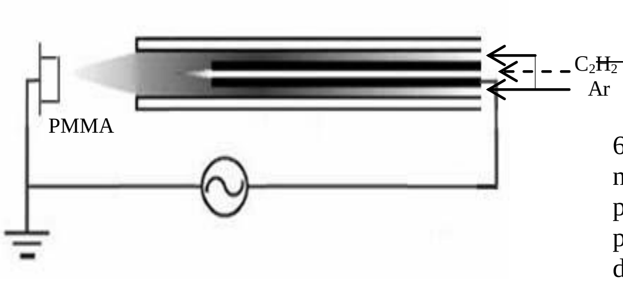

Figure 1. Schematic sketch of the experimental by plasma jet technique.

3. Results and Discussion

The study of Ar/C_2H_2 mixtures by OES is of great interest for the application of plasmas jet to organic C:H film growth. In a previous work, soft polymerlike C:H thin films were grown in this experimental setup using Ar/C_2H_2 mixtures.

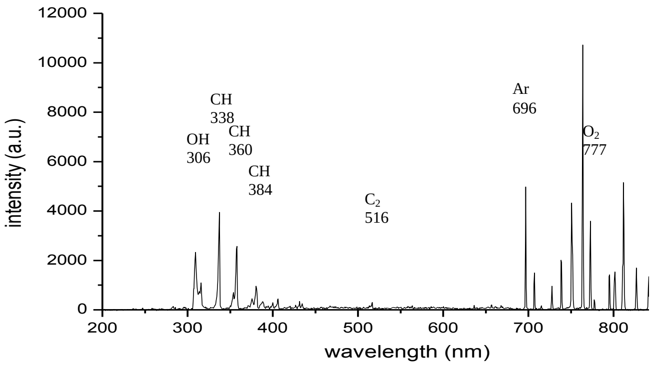

Figure. 2 OES spectra of Ar/C_2H_2 discharges for identical precursor concentrations C_2H_2 10 SCCM and Ar flow 2.5 slm by power 50 W.

In Figure. 2 typical spectra in the range of 200–900 nm are presented for Ar/C_2H_2 mixtures with precursor of 10 SCCM. The different bands detected apart from the Ar 4p→4s atomic emission lines and the OH band at 306 nm, the most important features correspond to the CH emission bands located at 338, 360, and 384 nm and the Swan band system of C_2. As in the case of the Ar plasmas, there is no evidence of CN or CO compounds that would come from the reaction of hydrocarbon radicals with N_2 and O_2 molecules from ambient air. The main species identified are summarized in Table 1. [9]

Table 1. The emitted species identified in the C_2H_2 and Ar plasma

Species System	Transition	Wavelength (nm)
C_2	$A^3\Pi \rightarrow X^3\Pi$, ground state	516
CH	$A^2\Delta \rightarrow X^2\Pi$, ground state	338
	$B^2\Pi^- \rightarrow X^2\Pi$, ground state	360
	$C^2\Pi^+ \rightarrow X^2\Pi$, ground state	384
OH	$A^2\Sigma^+ \rightarrow X^2\Pi$, ground state	306

In Figure. 3, the total intensities of the Ar 696 nm line, the CH 338 nm band, and the OH 306 nm emission band are

presented for Ar/C_2H_2 mixtures as a function of the precursor amount. In mixtures there is an important drop in the intensity of the Ar lines when the precursor is injected. This is a well known effect of the presence of molecular gases in a noble gas plasma, and it has been observed also when other molecular species are inserted in the plasma, while in Ar/C_2H_2 plasmas the CH band is the carbon-containing species with the highest intensity in the OES spectra. In Ar/ C_2H_2 plasmas, C_2 species are produced in a similar way from the parent C_2H_2 molecule. Therefore, it is likely that each species present higher intensities in their respective mixtures.

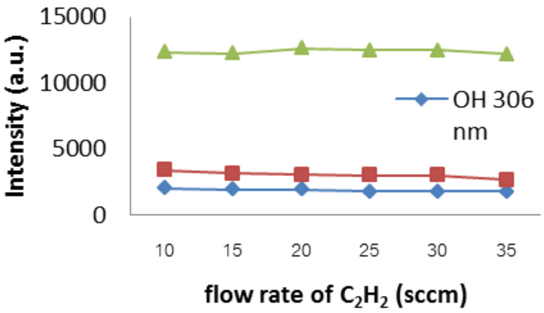

Figure. 3 Intensities of selected species detected by OES as a function of the amount of C_2H_2/Ar

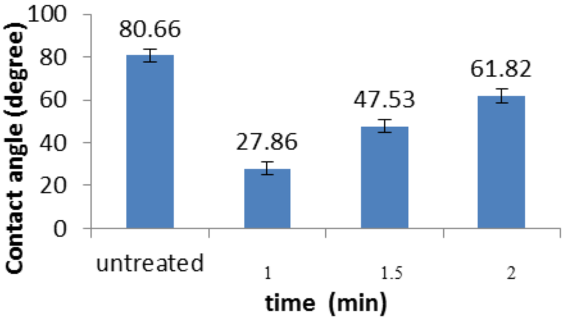

Figure. 4 Contact angle of C_2H_2/Ar treated on PMMA surface

From contact angle measurement as shown in Figure. 4. It show that the contact angle of native PMMA are about 80.66 degree. The surface of PMMA trend to be hydrophobic after plasma treatment the contact angle increase from 27.86 to 61.82 degree when the operate time increase from 1 to 2 minute because of amount of carbon increase with increasing time.

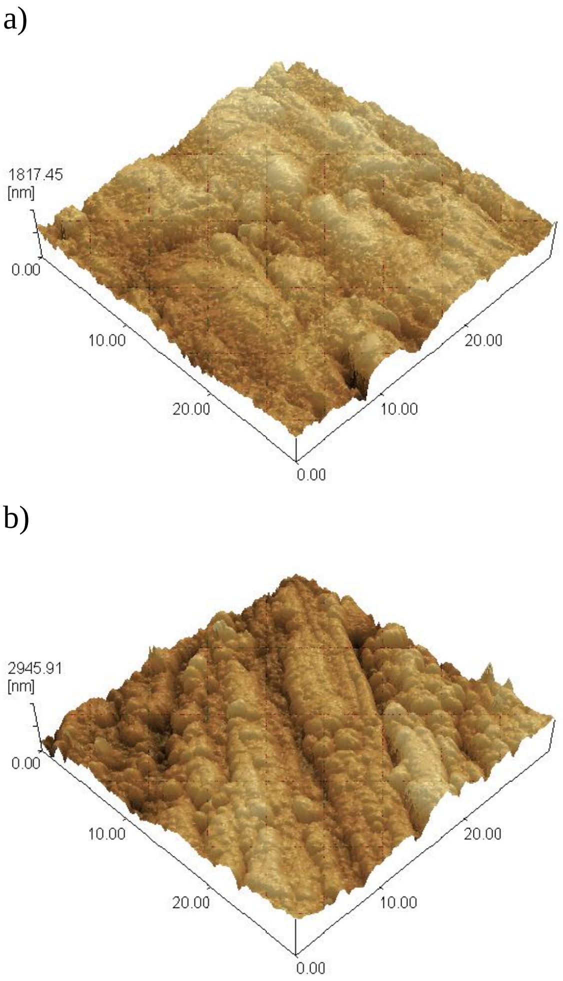

Figure. 5 AFM micrographs a) untreated PMMA b) treated Ar : C_2H_2 on PMMA for 2 minute.

Topologic changes of the surface of samples are investigated by AFM micrographs. They are shown in Figure. 5 just for 2 minutes treated Ar/C_2H_2 on samples RMS roughness increases with the time of treatment up to 2. By untreated sample RMS roughness about 267 nm and sample treatment for 2 minute RMS roughness about 385 nm. It is clear that CH species in plasma hit the surface. Range of energy is not influence on the surface topography. One expects that the roughness change has a direct impact on the surface properties, in particular on the wettability of the samples.

4. Conclusion

The study of Ar/C_2H_2 plasmas shows that CH emission bands located at 338, 360, and 384 nm. CO or CN species are not found inside the plasma. From the contact angle measurement contact angle increases from 27.86 to 61.82 degree when the operating time increases because of amount of carbon on the surface is depend on operating time. According to results from AFM that the roughness increases when operating time increase.

Acknowledgement

Thailand Center of Excellence in Physics (ThEP), Reesearch Center in Particle Beams and Plasma Physics (PBPP) and Plasma-Bio and Clean Energy Research Laboratory, Department of Physics and Materials Science, Faculty of Science, Chiang Mai University, and Department of Prosthodontics, Faculty of Dentistry, Chiang Mai University.

References

[1] A. Schutze, J. Y. Jeong, S. E. Babayan, J. Park, G. S. Selwyn and R.F. Hicks., IEEE Trans Plasma Sci.,1998, 1685-1694.
[2] J. Y. Jeong, S. E. Babayan, V. J. Tu, J. Park, I. Henins, R. F. Hicks and G. S. Selwyn., Plasma Sources Sci Technol., 1998, 282-285.
[3] H. W. Herrmann, I. Henins, J. Park and G. S. Selwyn., Physics of Plasmas., 1999, 2284-2289.
[4] J. Park, I. Henins, H. W. Hermann and G. S. Selwyn., J. Appl. Phy., 2001, 15-19.
[5] G. S. Selwyn, H. W. Herrmann, J. Park and I. Henins., Contrib Plasma Phys., 2001, 610-619.
[6] S. E. Babayan, J. Y. Jeong, A. Schutze, V. J. Tu, M. Moravej and G. S. Selwyn., Plasma Sources Sci Technol., 2001, 573-578.
[7]] E. Stoffels, A.J. Flikweert, W.W. Stoffels, G.M.W. Kroesen,Plasma needle: a non-destructive atmospheric plasma source for fine surface

treatment of (bio)materials, Plasma Sources Science and Technology 11 (2002) 383-388.

[8] R. Foest, Th. Bindemann, R. Brandenburg, E. Kindel, H. Lange, M. Stieber, K-D Weltmann, On the Vacuum Ultraviolet Radiation of a Miniaturized Non-thermal Atmospheric Pressure Plasma Jet, Plasma Processes and Polymers 4/0 (2007) S460-S464.

[9] A. Yanguas-Gill, K. Focke, J. Benedikt and A. von Keudell. “Optical and electrical characterization of an atmospheric pressure microplasma jet for Ar/CH_4 and Ar/C_2H_2 mixtures” J. Appl. Phy., 101: 103307, 2007

Surface Modification of Polymethyl Methacrylate by Hexamethyldisiloxane/Argon Plasma Jet for Dental Applications

P. Phanbunplook[1]*, P. Yavirach[2], and D. Boonyawan[1]

[1]Plasma-Bio and Clean Energy Laboratory, Department of Physics and Materials Science,
Faculty of Science, Chiang Mai University, Suthep Road, Chiang Mai 50200, Thailand
[2]Department of Prosthodontics, Faculty of Dentistry, Chiang Mai University,
Suthep Road, Chiang Mai 50200, Thailand
**Corresponding author. E-mail:pongrawee.trio@gmail.com*

Abstract

Polymethyl Methacrylate (PMMA) is used in dentistry as denture base material, restorative materials and prosthodontics. Generally, they use sandblasting method (mechanical locking) or using silane coupling agent to make bonding. This research proposes a Silicon Oxide deposition to enhance bonding strength between heat-curing and self-curing, Denture Base Acrylic Resin by using plasma jet. Hexamethyldisiloxane (HMDSO) is used as a precursor with Argon (Ar) as carrier gas. The rf power, gas flows rate and time for surface modification are varied to optimize the adhesion bonding strength of PMMA. The surface topography will be observed by Atomic Force Microscopy (AFM). The results revealed that the contact angle of the PMMA surface was improved from 76.0° to 107.5°, and the hydrophobic surface of PMMA, obtained at 2% of HMDSO flow rate and 50w RF power for a 1-min treatment time. According to the results, the increases of roughness from 133.23 to 422.58 nm are created by the reaction of HMDSO/Ar plasma jet. This experiment expects to perform better coupling between the two PMMA surfaces.

Keywords: Plasma jet, HMDSO, PMMA, Surface modification

Introduction

Atmospheric Pressure Plasma Jet: APPJ (non-thermal, glow-discharge plasma)is a type of plasma that operates at atmospheric pressure. APPJ are generates highly reactive ions, electrons and free radicals. The reactive species generated by APPJ, are directed onto a surface where chemical reaction occurs. APPJ devices generate plasma in surrounding air, so they are suitable for direct treatment of targets of any size. They are easy to construct because they do not need any vacuum system and can be operated with various feeding gases under a wide range of driving frequencies. Many different types of atmospheric pressure plasma jets were developed in a simple device with low cost. [1]. The plasma jet is commonly used in the industry for activating and cleaning plastic and metal prior to adhesive bonding and painting processes. Plasma treatment has proven to be a powerful tool for surface modification of polymeric materials. By using plasma treatment, interface properties can be introduced to a polymer surface without affecting the desired bulk properties of a material, such as strength, and roughness [2].

Polymethyl methacrylate (PMMA) is a lucid thermosetting, commonly known as acrylic glass. It is the synthetic polymer of methyl methacrylate. PMMA is an interesting polymer for mechanical and optical applications due to its easy possibility and high transparency in the visible range [3].PMMA is wildly used as an alternative to glass to produce in the dental industry, such as denture main material, restorative materials and prosthodontics. In the dental industry, heat-cured PMMA is used not only to attach acrylic teeth and resin together, but also (in extreme cases) to make a whole new tooth. Generally, there are two methods to make bonding which is sandblasting or silane coupling agent. However both are still inefficient.

Hexamethyldisiloxane, known as HMDSO, it is an organ silicon compound with the formula $O[Si(CH_3)_3]_2$. HMDSO is non-toxic and environmentally friendly material, commercially available, and has a high vapor pressure at room temperature [4].The bond energy of Si-O, Si-C, and C-H are 8.3eV, 4.6eV, and 3.5eV, respectively [5].The organosiloxane film also has the potential applications in biocompatible coating for medical implants, oxygen barrier coating on polymer for packing industry, low dielectric constant interlevel dielectrics in microcircuits, etc.

This research aims to study into Silicon Oxide films deposition so as to improve efficiency of adhesion bonding strength between heat-cured PMMA and self-curing PMMA using plasma jet. Reacting with polymer, plasma can be cleaned, etched, and chemically modified [6]. There are the different uses of plasma particles such as surface cleaning, degradation of polymer chains, removal of surface material, formation of radicals, and change of surface [7,8]. This combination results in a surface improvement of the adhesion properties.

In this paper, surface modifications of PMMA were exposed to HMDSO/Argon plasma jet at radio frequency (RF) power of 30, 40 and 50W for a treatment time up to 5 min under 1% up to 5% of HMDSO flow rate and 5L/min flow rate Argon is constant. The active species in HMDSO plasma are distinguished by optical emission spectrum (OES). After plasma treated, characterize silicon film on physical and chemical properties by Contact angle measurement was performed to characterize the surface energy and with that confirm hydrophobic and hydrophilic surface of modified PMMA. Surface smoothness and morphology of the surface were examined by Scanning electron microscope (SEM), and Atomic force microscope (AFM).

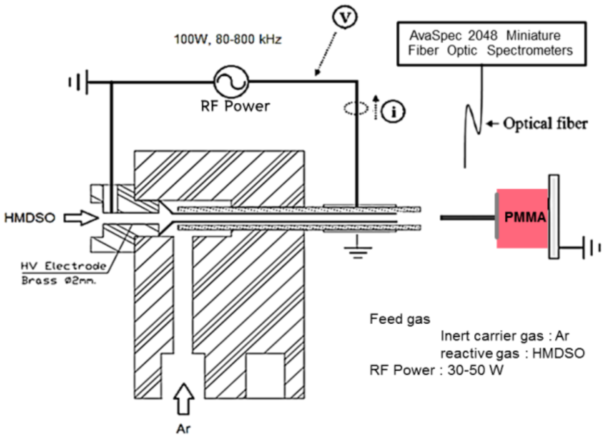

Figure 1.Configuration of the surface modification of PMMA by HMDSO/Argon plasma jet experiment.

Experimental details

Materials preparation

HMDSO (+98%) was purchased from Sigma Aldrich Inc. (St. Louis, USA). The PMMA samples (1.0 cm x 1.0 cm x 0.7 cm) were obtained from department of Prosthodontics, faculty of Dentistry, Chiang Mai University. These samples were cleaned in successive ultrasonic baths of ethanol for 10 min before HMDSO plasma modification.

Experimental arrangement

The plasma jet (Fig. 1) is driven by high voltage source (100W, 80-800 kHz). Designed by the Plasma and Clean Energy Laboratory, Department of Physics and Materials Science, Faculty of Science, Chiang Mai University.

In this experiment, surface modification of PMMA has been performed through a use of HMDSO/Argon plasma jet. HMDSO was used as a precursor mix with Argon, a silicon composition and inexpensive, and belongs to the same functional group of Silane. Silane is a toxic and extremely flammable chemical compound with a chemical formula SiH_4, and is used to couple the agents for composite materials. Argon starts flow at a rate of 5L/min while HMDSO grows at a rate from 1% up to 5%. The film depositions were done with the RF power of 30, 40 and 50W, respectively, for a treatment time ranging from 1 to 5 min. The 3 steps were set to generate HMDSO/Ar plasma jet and collected the data. STEP 1: To optimize the RF power, to find the RF power that make plasma decomposed while the flow rate of HMDSO/Ar gas is constant. STEP 2: To optimize the flow rate of HMDSO/Ar gas, to determine the most appropriate HMDSO ratio. STEP 3: To Apply HMDSO plasma jet on PMMA, to determine the most appropriate time.

Characterization techniques

After plasma was treated, Characterize silicon films on physical and chemical properties are analyzed by

Optical Emission Spectroscopy (OES) was used to analyze the species in the plasma. The spectrometer using in this work was an AvaSpec-2048 fiber optics spectrometer (Ocean Optics Inc., USA) with a wavelength range from 200 nm to 1100 nm.

Contact angle measurement was tested the surface hydrophobic, hydrophilic, and surface energy of modified by plasma. The device was designed by the Plasma and Clean Energy Laboratory, Department of Physics and Materials Science, Faculty of Science, Chiang Mai University.

Atomic force microscopy (AFM) was carried out to observe surface topography of the films on PMMA. The AFM used was a Nano-scope III (Digital Instrument, USA), operated in tapping mode. The images were collected at a fixed scan rate of 1 Hz.

Results and Discussion

Optical emission spectroscopy analysis

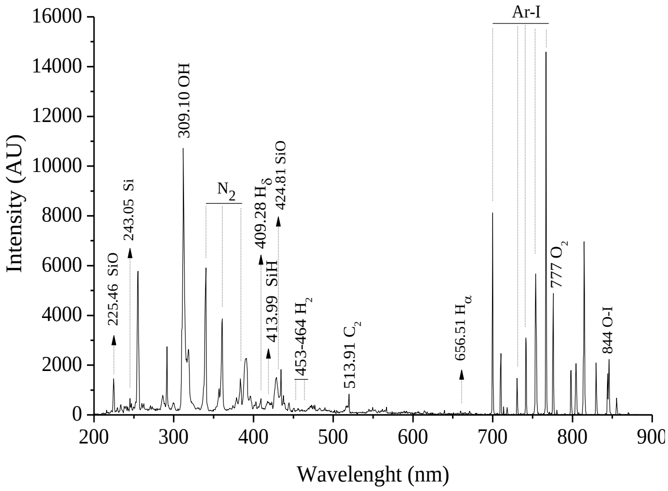

Figure 2. OES spectrum of 2%HMDSO plasma jet at RF power of 50 W.

Fig. 2 shows the emission spectra of 2% of HMDSO plasma jet at RF power of 50W. The light emitted by the plasma is collected by an optical fiber. The emitted species identified in HMDSO plasma are shown in Table 1 [4,8,9,14] with the corresponding wavelengths. It is clearly seen that HMDSO plasma includes N_2, Si, SiH, SiO, CO, H_2, O_2, C_2, and Ar emitted species. An amount of H_2, C_2 and O_2 fragments in the plasma are contained as a result from the dissociation of CH_3 functional group. The presence of SiO emission lines in the spectral range 216–293 nm indicated the fragmentation of Si-O-Si. We expected that species like SiO_x and $SiO_xC_yH_z$ played a role in increase adhesive bonding strength between the 2 types of PMMA. The emission spectrum of Ar, OH, O_2, and N line of HMDSO/Ar were highly intense, while the emission lines of Si, SiO, C_2 and H_2 were less significant. The best condition of dissociation is 2% of HMDSO plasma jet at RF power of 50W is clearly observed. The detected spectrum lines of HMDSO plasma tend to decrease dissociation when a % of HMDSO flow rate increase. In addition, weak lines of SiH and SiO fragments at 400–430 nm are direct evidence of the dissociation of Si-O-Si functional group. The emission line of O atom occurs due to the dissociation of O_2 or H_2O monomer in the atmosphere and depends upon the high-energy electron impact. It is clearly that the dissociation processes are highly dependent on the ratio of HMDSO in Ar and RF power. In particular, at 2% of HMDSO plasma, the intensity of Si and SiO are high, due to the dissociation of HMDSO, and are in line with an increase of RF power

The behavior depicted in Fig. 3 shows two different variation of Argon (Ar), hydroxyl (OH), Silicon (Si), Silicon Oxide (SiO), and Oxygen (O) line intensity as a function of %HMDSO in the gas mixture. The behavior of O, Ar and OH is similar to that reported by M.Goujon et al. and Y.Wang et al. [5,9].

Table 1: Emission lines of HMDSO plasma.

Species	**Wavelength (nm)**
Si	243
SiO	216-293 (main system)
SiH	414
Ar	700-800
H_α, H_β, H_δ	656, 486, 409
OH	281-309
H_2	453-464
C_2	512-516

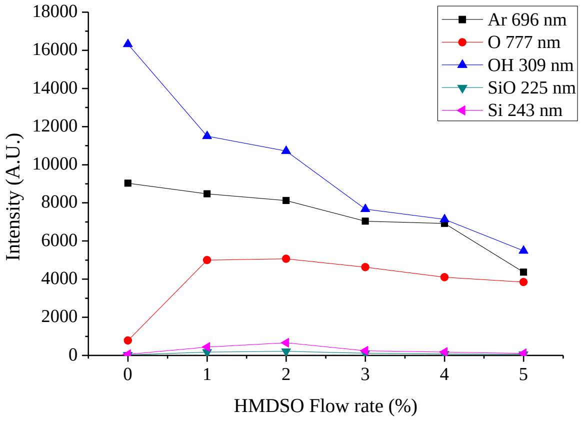

Figure 3. Variation of (a) Ar, O, OH, Si and SiO line intensity as a function of 2%HMDSO in the gas mixture at RF power of 50W.

In Fig.3 for a HMDSO flow rate, the intensity of the transition of atomic Ar at 696 nm, O at 777 nm, and OH at 309 nm decrease while immediately when the % of HMDSO increases the transition of Si and SiO increases with % of HMDSO. As confirmed later by FTIR measurements, Silicon and Silicon Oxide atoms, which are produced by electron impact in the plasma jet , are generate by the dissociation of HMDSO. According to Fig. 2, it can be seen that the most appropriate the atomic spectrum line of Si and SiO for plasma application is 2% of HMDSO plasma jet at RF power of 50W, thus corresponding to Fig. 2. Next the best condition (2% of HMDSO plasma jet at RF power of 50W) obtained is used to conduct modification on PMMA surface.

Contact angle analysis

To evaluate the water affinity on a PMMA surface, contact angle measurement was conducted using a drop water shape to analyze the degree of contact angle [2,10,11]. During each measurement, 2 micro liter of water was dispersed from a syringe to form a sessile drop which is, later, put on top of PMMA. As shown in Fig. 4, values for contact angles of PMMA surface treated by HMDSO plasma jet at RF power of 50W are varied in accordance with a % of HMDSO flow rate. The results indicate that the maximum degree of contact angle is related to the RF power, gas flow rate and treatment time for plasma application. At the 2% of HMDSO plasma jet at RF power of 50W, the contact angle with measurement for the modified PMMA surface increases rapidly to a maximum degree of 107.5, the hydrophobic surface of PMMA and a contact angle gradually decreases when the % of HMDSO flow rate increases for 1-min treatment. The increasing % of HMDSO flow rates of plasma treatment whiles the RF power constant result to contact angle decreasing.

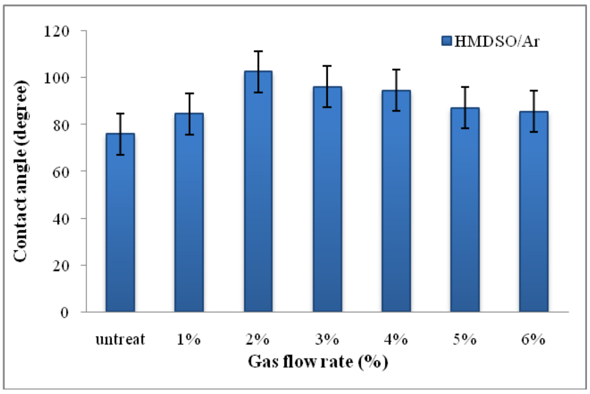

Figure 4. Contact angle of PMMA surface treated by HMDSO/Ar plasma jet at RF power of 60W for different treatment flow rate.

AFM analysis

After PMMA is treated by HMDSO plasma jet, it is, then, coated silicon film before to an analysis using AFM. Fig. 5 shows the surface rootmean-square (RMS) roughness between untreated PMMA and HMDSO plasma treatment on PMMA surface. The untreated PMMA is as smoothness as anticipated. The untreated PMMA sample exhibits a rough surface with RMS roughness value of 133.23 nm (Fig. 5 (a)). After 2% of HMDSO on PMMA surface is treated at 30W (Fig.5 (b)) and 50W (Fig.5 (c)), the value of RMS roughness are 296.84 nm and 422.58 nm, respectively. After the plasma treatment, the RMS roughness changes as a result from an increase in RF power of plasma application on PMMA surface [11,12,13] and occurred in the film deposited at 50 W. With 2% of HMDSO plasma jet at RF power of 50W (Fig.5 (c)), the surface RMS roughness increases clearly to the maximum value of 422.58 nm for 1-min PMMA sample treatment. With RF power 30W of treatment, the surface RMS roughness decreases to 125.74 nm from the maximum. HMDSO plasma treatment on PMMA surface, increases the roughness are created by the reaction of HMDSO/Ar plasma jet, when the level of roughness has increased, as the result to the surface area for activating and efficiency of adhesion of the PMMA increased. Which this in experiment expects to efficiency of adhesion between the two PMMA surfaces, which it will be confirmed later by pull-out test [8].

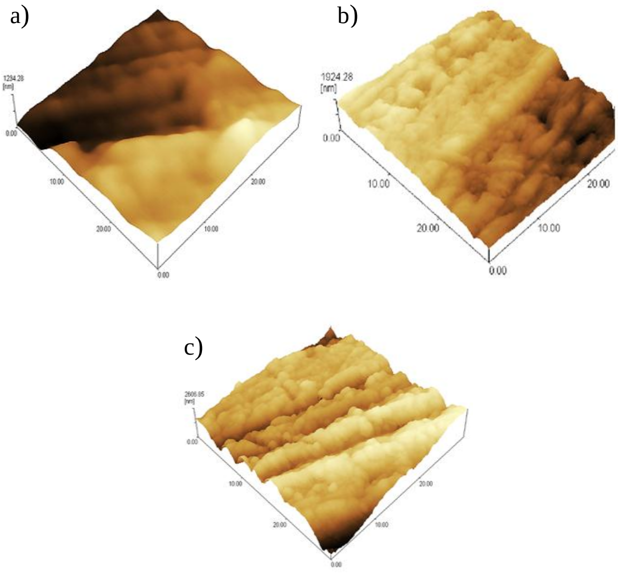

Figure 5. Surface RMS roughness of PMMA samples of (a) untreated and (b) treated2%HMDSO at 30W, (c)treated 2%HMDSO at 50Wfor 1-min treatment times.

Conclusions

In the process of plasma, HMDSO monomer is dissociated into smaller fragments as seen in the emission spectra of the plasmas. At the 2% of HMDSO plasma jet at RF power of 50W for 1-min treatment, the contact angle of PMMA surface is increases from 76.0 to 107.5 via the HMDSO plasma jet modification, the hydrophobic surface of PMMA and a contact angle gradually decreases when the % of HMDSO flow rate increases. These results point out that the characterize silicon film on physical and chemical properties depends on RF power, used to generate plasma, on an amount % of HMDSO flow rate in the gas mixture, and on treatment time for plasma application.

A Further work in this research will include an experiment to determine the best time for plasma treatment, to evaluate the efficiency and the adhesion of the PMMA by pull – out test, and to analyze the chemical bond and chemical structure by using Fourier transform infrared spectroscopy (FT-IR) and X-ray photoelectron spectroscopy (XPS).

Acknowledgments

Thailand Center of Excellence in Physics (ThEP) ,Research Center in Particle Beams and Plasma Physics (PBPP) and Plasma – Bio and Clean Energy Research Laboratory, Department of Physics and Materials Science, Faculty of Science, Chiang Mai University, and Department of Prosthodontics, Faculty of Dentistry, Chiang Mai University.

References

1. Hyun Woo Lee, Seoul Hee Nam, Abdel-Aleam H. Mohamed, Gyoo Cheon Kim, Jae Koo Lee, “Atmospheric Pressure Plasma Jet Composed of Three Electrodes: Application to Tooth Bleaching. Plasma Processes and Polymers”, **7** (2010) 274–280.
2. Song-Hua Gao, Ming-Kai Lei, Yang Liu, Li-Shi Wen, “CF4 radio frequency plasma surface modification of silicone rubber for use as outdoor insulations”, Applied Surface Science, **255** (2009) 6017–6023.
3. Amit Chatterjee, “Properties Improvement of PMMA Using Nano TiO2. Journal of Applied Polymer Science”, **118** (2010) 2890–2897.
4. C. Chaiwong , P. Rachtanapun, S. Sarapirom, D. Boonyawan, “Plasma polymerization of hexamethyldisiloxane: Investigation of the effect of carrier gas related to the film properties”, Surface & Coatings Technology, **xxx** (2012) xxx–xxx.
5. Ying Wang, Jing Zhang, Xinyuan Shan, “Surface structures tailoring of hexamethyldisiloxane films by pulse rf plasma polymerization”, Materials Chemistry and Physics, **96** (2006) 498-505.
6. Molitor, P., Barron, V. and Young, T, “Surface Treatment of Titanium for Adhesive Bonding to Polymer Composites: A Review”, International Journal of Adhesion and Adhesives, **20** (2001) 129–36.
7. Lommatzsch U, Pasedag D, Baalmann A, Ellinghorst G, Hans-Erich Wagner, “Atmospheric Pressure Plasma Jet Treatment of Polyethylene Surfaces for Adhesion Improvement”, Plasma Process of Polymer, **4** (2007) 1041–1045.
8. Yavirach P, Chaijareenont P, Boonyawan D, Pattamapun K, Tunma S, Takahashi H, “Effects of plasma treatment on the shear bond strength between fiber-reinforced composite posts and resin composite for core build-up”, Dental Materials Journal, **28(6)** (2009) 686–692.
9. Goujon M, Belmonte T, Henrion G, “OES and FTIR diagnostics of HMDSO/O2 gas mixture for SiOx deposition assisted by RF plasma”, Surface & Coatings Technology, **188-189** (2004) 756-761.
10. Ozden N, Akaltan F, Suzer S, Akovali G, “Time-related wettability characteristic of acrylic resin surfaces treated by glow discharge”, Journal of Prosthetic Dentistry, **82** (1999) 680-684.
11. Riccardia C, Barnia R, Sellib E, Mazzoneb G, Rosaria Massafrac M, Marcandallic B, Poletti G, “Surface modification of poly(ethylene terephthalate) fibers induced by radio frequency air plasma treatment”, Applied Surface Science, **211** (2003) 386–397.

12. Noeske M, Degenhardt J, Strudthoff S, Lommatzsch U, “Plasma jet treatment of five polymers at atmospheric pressure: surface modifications and the relevance for adhesion”, International Journal of Adhesion & Adhesives, **24** (2004) 171–177.
13. IA Rusu, G Borcia, SO Sayed, JL Sullivan, “Ar rf plasma effect on polymer surfaces”, 28th ICPIG, 2007.
14. Guangliang Chen, Shihua Chen, Wenran Feng,Wenxing Chen, Si-ze Yang, "Surface modification of the nanoparticles by an atmospheric room-temperature plasma fluidized bed", Applied Surface Science, **254** (2008) 3915–3920.

Synthesis of TiO_2 Films on Polymethyl Methacrylate by Filtered Cathodic Vacuum Arc Deposition for Dental Applications

T. Bunfong[1]*, P. Yavirach[2], S. Sansongsiri[1], and D. Boonyawan[1]

[1] *Plasma-Bio and Clean Energy Laboratory, Department of Physics and Materials Science, Faculty of Science, Chiang Mai University, Suthep Road, Chiang Mai 50200, Thailand*
[2] *Department of Prosthodontic, Faculty of Dentistry, Chiang Mai University, Suthep Road, Chiang Mai 50200, Thailand*
**Corresponding author. E-mail: the_skyphoenixbird@hotmail.com*

Abstract

Thin films of titanium dioxide have been deposited on polymethyl methacrylate (PMMA) that used in denture in order to act as interface to increase adhesion between heat-curing PMMA (Denture teeth) and self-curing PMMA (Denture base) by filtered cathodic vacuum arc deposition (FCVAD). The deposition process operated in pulsed mode with macro particle filter. Titanium was utilized as cathode at pulsed-DC voltage 240 volt and applied a DC bias at -50 volt and -80 volt to the substrate holder at oxygen gas (O_2) 4.6 x 10^{-3} mbar and the operating times is 60 min. The characteristic of films varied with change in the Ti^- energy (resulted by changing of substrate bias), amount of O_2 and operating times. The influences of these parameters on the treated substrates have been investigated. The surface topography and films thickness characterized by atomic force microscopy (AFM) shown that the roughness of PMMA samples increase from native PMMA and vary with applied bias. For the TiO_2 coated PMMA, the contact angle increase from native PMMA and contact angle results after UV irradiation reveal that oxygen vacancies are lesser at higher applied bias.

***Keywords*:** TiO_2 film, PMMA, FCVA deposition

Introduction

Surface Modification is the key to make the desired surface characteristics such as surface roughness, physical and chemical corrosion resistance, including surface preparation in a state ready to react with the other substance. Plasma treatment is the effective process to modify surface of various materials such as metal, glass, wood, polymer and biological materials. The use of plasma treatment to treat polymers has been known for more than 20 years. This allows polymer surface to be cleaned, etched or chemically modified [1].

TiO_2 has been extensively studied both in bulk and thin film forms because of its excellent properties such as biocompatibility, photocatalytic activity, photo-induct hydrophilicity, electron transport properties in solar cell application, gas sensing, opticall properties, corrosion resistance, mechanical strength and relatively low cost [2, 3]. At present it is used in various fields. One of them is application in thermoplastics such as polymethyl methacrylate (PMMA), poly- carbonate (PC), cyclic olefin copolymer (COC) or cyclic olefin polymer (COP) and elastomers such as polydimethylsiloxane (PDMS) [4]. Polymethylmethacrylate (PMMA) has been used in a wide range and also used in dental, it is importance materials used to fabricate dentures. The most common material used to fabricate the denture base is an acrylic resin made from a mixture of methylmethacrylate (MMA) and poly (methyl methacrylate) (PMMA) .This material possesses favorable working characteristics, polishability, stability in the oral environment, and excellent aesthetic appearance [5]. The importance process in producing dentures is bonding between denture teeth and denture base. The traditional processes of bonding are using of silane coupling agent [6] and sandblasting [7] but this research present the new way to make bonding between materials. It is the using of TiO_2 films as interface in order to make chemical bonding between them.

The cathodic arc is a low-voltage, high-current plasma discharge that take place between two metallic electrodes in vacuum. The plasma plume produced from the solid conducting material which is cathode. The metallic ions energy is ranging from 20 to 100 eV which is sufficient to bury the ions a few atomic layers beneath the substrate surface. The ion fraction from the arc source is found to be material dependent and could be as high as 100%. For the average energy of Ti^+ is around 40 eV [8] which can be increased by applying a negative bias to the substrate. The main effect of the deposited films is resulted by changing the negative substrate bias. The main disadvantage of cathodic arc is the occurring of macroparticles during the arc process, which affect the quality of the film. So that, the magnetic filtered was employed to reduce macroparticles [8, 9]. The generating of plasma by filtered cathodic vacuum arc deposition (FCVAD) is a good technique for deposition of oxides films because of the high degree of ionization and the high energy of the depositing species [10].

In this work, TiO_2 thin films were deposited onto PMMA by using FCVAD in order to let the one act as interface to increase adhesion between heat-curing PMMA (Denture teeth) and self-curing PMMA (Denture base). The varies high energy species such as ions, electrons, atoms and radicals could be interact with the surface to modify surface functionality and the surface morphology in a non equilibrium condition. Only the skin layer of the substrate is modified with no destruction of the bulk material [11].

Materials and Methods

Material

PMMA used in this experiment were divided into two types by curing. There are self-curing PMMA and heat-curing PMMA. In this research heat-curing PMMA surfaces were modified by plasma. They were received from Department of Prosthodontic, Faculty of Dentistry, Chiang Mai University with dimensions of 1.0 cm x 1.0 cm x 0.7 cm. They were cleaned by ultrasonic with dilute acetone and kept in dry cabinet before plasma treatment.

Filtered Cathodic Vacuum Arc Deposition (FCVA)

FCVA is plasma-based ion implantation known as plasma immersion implantation and deposition. In this technique, a high negative voltage can be applied to the sample being treated while it is immersed in plasma. Effect of applying negative voltage is increasing ionic energy to deposited on the surface that affect the film quality. High energy ions provide an additional benefit in the mixing of the substrate coating interface because high energy ions can bury themselves a few atomic layers beneath the surface of the growing film and provide some mobility for minor atomic rearrangements [9]. The principle of FCVA system as showed in Fig.1 is start by applying a high electric field to the trigger-cathode and anode-cathode [12]. The plasma expanding from cathode spots contains ions that are usually multiply charged and have a kinetic energy in the range 18–150 eV, depending on the cathode material [13]. The magnetic filtered was applied to the system to filter macroparticles out of plasma plume before it reach to the substrate.

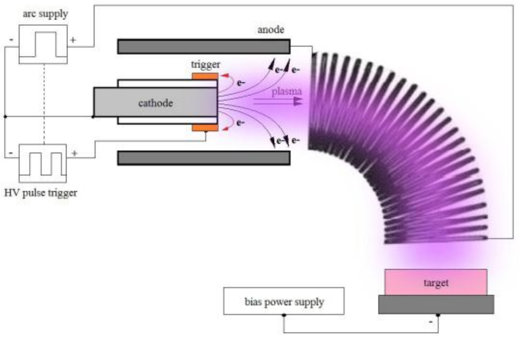

Fig.1. Schematic diagram of FCVA show the plasma expanding from cathode spots contains ions that are usually multiply charged to the substrate.

Synthesis of TiO_2 by FCVAD

TiO_2 thin films were deposited on to PMMA and silicon wafers substrates by using FCVAD. The base pressure of the system was maintained at 9.0 x 10^{-5} mbar. The deposition process operated in pulsed mode 1 pulsed/second with macro particle filter. Titanium was utilized as cathode at pulsed-DC voltage 240 volt and applied a DC bias at -50 volt and -80 volt to the substrate holder at oxygen gas (O_2) 4.6 x 10^{-3} mbar with flow rate 100 ml/min and the operating times was maintained at 60 min.

Surface characterization

The surfaces of TiO_2 coated PMMA and silicon wafers were characterized both of physical and chemical by many scientific instruments. TiO_2 coated silicon wafers were measure thickness and reflective index by ellipsometer. The surfaces topography were characterized by atomic force microscopy (AFM) in tapping mode. The contact angle of water droplet were measured by using camera to capture picture of liquid drop on the surface of sample and sent it to measured contact angle by program in computer as illustrated in Fig. 2. The surface free energies can be calculated from contact angle measurements [14].

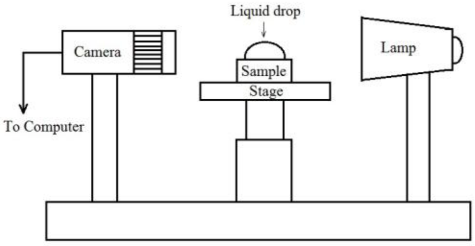

Fig. 2. Schematic diagram of contact angle measurement.

From the liquid drop on the surface and measuring of contact angle as showed in Fig. 3, the surface free energies can be calculated by using Young's equation as given by Eq. (1), where γ is the surface free energy and the subscripts 'S' and 'L' stand for solid and liquid, respectively [14].

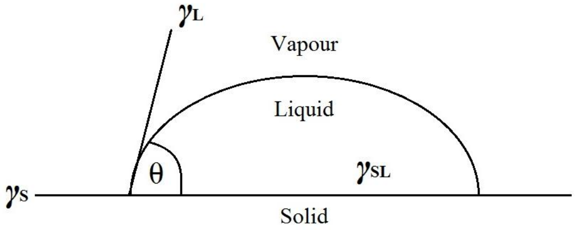

Fig. 3. Liquid drop on the surface and measuring of contact angle.

$$\gamma_S = \gamma_{SL} + \gamma_L \cos\theta \qquad (1)$$

From thermodynamic work of adhesion (W_{ad}) which Dupre proposed. It is the Dupre equation (Eq. (2)) which is the reversible work done in separation of unit area of a solid/liquid interface [14].

$$W_{ad} = \gamma_S + \gamma_L - \gamma_{SL} = \gamma_L(1 + \cos\theta) \qquad (2)$$

Results and Discussion

Characterization of TiO_2 films coated PMMA

Atomic force microscopy (AFM)

The topography of PMMA and TiO_2 coated PMMA surfaces as observed by AFM are illustrated in Fig. 4. The native PMMA surface has a mean rough -ness (Ra) and root-mean-square roughness (rms) values equal to 224.610 nm and 267.137 nm, respectively. After plasma treatment, the roughness increases because of formation of TiO_2 on the surface. The roughness (Ra) and root-mean-square roughness (rms) values of TiO_2 coated PMMA is 409.09 nm and 502.036 nm, respectively. When applied bias -50 V to the substrate, the roughness (Ra) and root-mean-square roughness (rms) values increases to 687.526 nm and 806.768 nm, respectively. But when increases bias to -80 V, the roughness (Ra) and root-mean-square roughness (rms) values decreases to 291.576 nm and 354.332 nm, respectively. This is due to the deposition rate decreases when substrate bias increases. The decreasing in the deposition rate has been attributed to the sputtering effect due to increasing ions bombardment and accumulation of ions on the substrate [10].

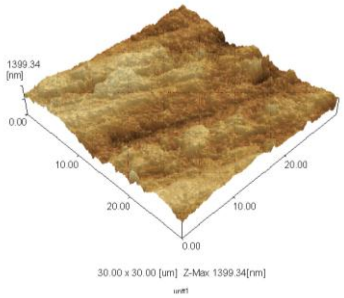

(a)

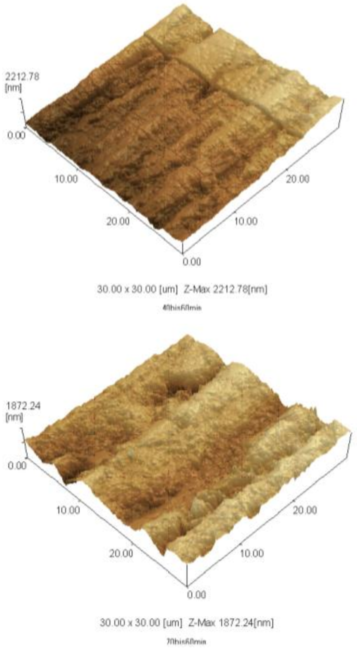

(b)

(c)

Fig. 4. AFM is illustrated surfaces of native PMMA (a), TiO_2 coated PMMA with bias -50 V (b) and -80 V (c).

Contact angle

The water contact angle of PMMA is about 78°. After deposition of TiO_2 films onto the surface, the contact angle increase to 85°, 92° and 82° for no bias, -50 V bias and -80 V bias, respectively, which are almost hydrophobic. But after UV light 240 min irradiation, the contact angle of all TiO_2 films decrease to 57°, 54° and 62° for no bias, -50 V bias and -80 V bias, respectively as illustrated in Fig 5, which are all hydrophilic. This phenomenon is known as the photo-induced hydrophilicity [15]. It is attributed to TiO_2 is a semiconductor with a bandgap energy of 3.2 eV which according to Plank's equation. When TiO_2 is irra- diated with UV light which $\lambda < 380$ nm, the electrons and holes are generated in conduction band and valence band, respectively. As see in (3)-(5), electrons can reduce Ti^{4+} cations to Ti^{3+} state and the holes oxidize the O^{2-} anions. So that, oxygen vacancies are generated on the surface which can absorb water molecules and produce –OH groups which are hydrophilic and can decrease the water contact angle [15, 16].

$$TiO_2 + h\upsilon \rightarrow TiO_2\,(e^-_{CB} + h^+_{VB}) \qquad (3)$$

$$Ti^{4+} + e^- \rightarrow Ti^{3+} \qquad (4)$$

$$O^{2-} + 2h^+ \rightarrow \frac{1}{2}O_2 \qquad (5)$$

Before UV irradiation.

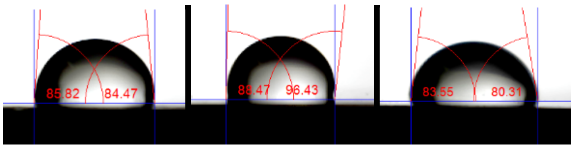

(a) no bias (b) -50 V bias (c) -80 V bias

After UV irradiation.

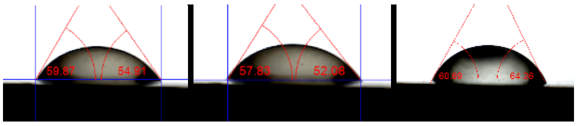

(d) no bias (e) -50 V bias (f) -80 V bias

Fig. 5. Contact angle of TiO_2 coated PMMA before (a), (b), (c) and after UV irradiation (d), (e), (f).

Conclusions

TiO_2 films have been synthesis on PMMA by FCVAD. The surface topography were characterized by AFM showed that the surfaces roughness of TiO_2 coated PMMA are increase from native PMMA because of deposition of TiO_2 films and the roughness of films depend on substrate bias, where bias -50 volt showed the highest roughness. The contact angle of TiO_2 coated PMMA increase from native PMMA because of TiO_2 is likely to be hydrophobic. After UV irradiation the contact angle de - crease because of TiO_2 has photo-induced hydrophilicity property and the hydrophilicity of TiO_2 is depend on substrate bias, where the bias -50 volt showed the highest and lowest contact angle before and after UV irradiation, respectively.

Acknowledgments

The author would like to thank S. Sansongsiri and D. Boonyawan for guiding in this research, Plasma and Clean Energy Laboratory, Department of Physics and Materials Science, Faculty of Science, Chiang Mai University for the support of cost of doing research.

References

1. P. Molitor, V. Barron, T. Yong, International Journal of Adhesion & adhesive 21 (2001) 129.
2. Jaroslaw Bienias, Barbara Surowska, Anna Stoch, Halina Matraszek, Mariusz Walczak, Dental Materials 25 (2009) 1128.
3. T.O. Kaariainen, S. Lehti, M.-L Kaariainen, D.C. Cameron, Surface & Coatings Technology 205 (2011) s475.
4. Hsih Yin Tan, Weng Keong Loke, Nam-Trung Nguyen, Sensors and Actuators B151 (2010) 133.
5. Natsuko Murakami, NoriyukiWakabayashi, RieMatsushima, Akio Kishida, Yoshimasa Igarashi, Jurnal of the Mechanical Behavier of Biomedical Materials 20 (2013) 98.
6. Tabassom Hooshmand, JukkaP.Matinlinna, Alireza Keshvad, Solmaz Eskandarion, Fereshteh Zamani, Jurnal of the Mechanical Behavier of Biomedical Materials 17 (2013) 327.
7. Takashi Nakamura DDS, PhD, Kazumichi Wakabayashi DDS, PhD, Chiaki Zaima DDS,Hisataka Nishida DDS, PhD, Soichiro Kinuta DDS, PhD, Hirofumi Yatani DDS, PhD, Journal of Prosthodontic Research 53 (2009) 116.
8. A. Bendavid, P.J. Martin, H. Takikawa, Thin Solid Films 360 (2000) 24.
9. M.M.M. Bilek, D.R. McKenzie, R.N. Tarrant, S.H.M. Lim, D.G. McCulloch, Surface and Coatings Technology 156 (2002) 136.
10. A. Bendavid, P.J. Martin, E.W. Preston, Thin Solid Films 517 (2008) 494.
11. Wenyue Su, Shichao Wang, Xuxu Wang, Xianzhi Fu, Jingning Weng, Surface and Coatings Technology 205 (2010) 465.
12. B.K. Tay, Z.W. Zhao, D.H.C. Chua, Materials Science and Engineering R 52 (2006) 1–48.
13. Andre Anders, Vacuum 67 (2002) 673–686.
14. B.C. Lim, N.L. Thomas, I. Sutherland, Progress in Organic Coatings 62 (2008) 123–128.
15. Junjie Xiong, Sachindra Nath Das, Sungyeon Kim, Jinhyong Lim, Hyun Choi, Jae-Min Myoung, Surface & Coatings Technology 204 (2010) 3436–3442
16. AKBAR ESHAGHI, MAHMOUD PAKSHIR and REZA MOZAFFARINIA, Bull. Mater. Sci., Vol. 33, No. 4, August 2010, pp. 365–369. © Indian Academy of Sciences

สมาคมฟิสิกส์ไทย
THAI PHYSICS SOCIETY

Gratefully Acknowledges Sponsorships

For

The 8th Siam Physics Congress 2013

Thai Physics Society on the Road to ASEAN Community

By

BARA SCIENTIFIC
Solution of Success

SCI/ED
THE SCIENCE AND EDUCATIONAL COMPANY LIMITED

S.M. CHEMICAL SUPPLIES CO., LTD.
S.M. CHEMICAL

www.extrad.co.th
we are the exclusive distributor of GATAN
gatan

CERNTEK

crest
One Company, One Mission

Hakuto

Marigold
Technologies Co.,Ltd.

SAENG VITH 2000

NATIONAL E-SCIENCE INFRASTRUCTURE CONSORTIUM

PONDPOL
Group of companies

iRCT

Next Generation
Products Company Limited

MR CENTER
Faculty of Science Chiang Mai University

Vittaya Amornkitbamrung
The President of Thai Physics Society

Extrad Instruments (Thailand) Co., Ltd.
www.extrad.co.th ☎ 02-2721498

Mini-SEM (SNE-4500M)

Features

- Max. 100,000x Magnification
- SE Detector (Option – BSE Detector)
- 5kV to 30kV Variable Accelerating Voltage
- Multi-Vacuum Mode – Standard / Charge Up Reduction
- Image Observation Ready within 2 min.
- 5-axis Strokes – X, Y, R, Z, T
- 4-Hole Variable Aperture (30 / 50 / 100 / 200 um)
- Options – EDX System, Cooling Stage, Low Vaccum Control

SEC

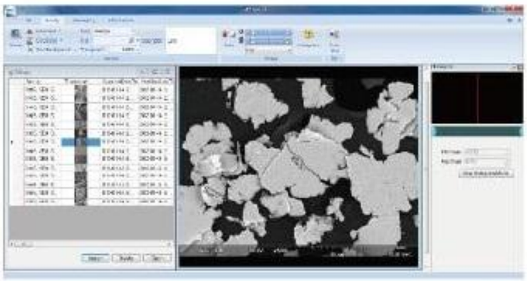

Image Database Manager - Measurement & Annotation

The Ion Mill You Know: Reborn

Low energy ion guns Cold stage Touch screen Automation and recipes
Live viewing and saving images in Gatan DigitalMicrograph®

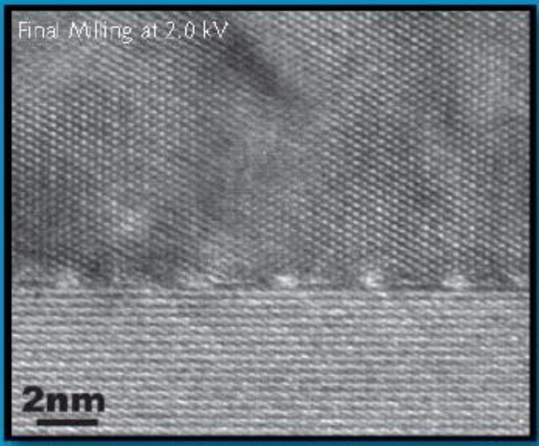

gatan

PIPS II

Solutions for High-Tech Research

S.M.CHEMICAL SUPPLIES CO.,LTD

More than 25 years of services to the scientific community

Life Science & Biochemicals
Cell Biology
Cell Culture
Custom Oligos
Epigenetics
Functional Genomics & RNAi
Molecular Biology
ZFN
Proteomics
Stem Cell Biology

Chemistry
Organics & Inorganics Chemical
Stable Isotopes
Materials Science
Flavors & Fragrances

Analytical/Chromatography
Analytica reagents
Analytical standards
GC / HPLC columns & accessories
SPE / SPME
Food safety
Air mornitoring
Microbiology
Trace Analysis
Titration

Tosoh Bioscience
EcoSEC GPC System
TSKgel HPLC Column
TOYOPEARL

Cerilliant
Certified reference materials
Drug standards
Environmental standards

Lipomed AG
Drug reference standards
Forensic reference standards

Zymo Research
The Epigenetic Company
DNA Mathylation kits
Enzymes for epigenetics
DNA Purification
Total RNA Purification

DUKSAN
High purity solvent
HPLC, Pesticide
GR Grade

Dedicated to Studies of Topoisomerase Enzymes

TopoGen
Topoisomerase Enzymes
Topoisomerase Assay Kits
Topoisomerase Antibodies

S.M. Chemical Supplies Co., Ltd.
☎ *Head Office: +662 1961013* ☎ *Chiangmai Branch: +6653 400812* ☎ *Khonkaen Branch: +6643 009030* ☎ *Had Yai Branch: +6674 348740*

Email : info@smchem.co.th | www.smchem.co.th

BARA SCIENTIFIC

Solution of Success

Bara Scientific
Solution of Success

Bara Scientific Co., Ltd.
968 Rama 4 Road Silom Bangrak
Bangkok 10500 Thailand
Telephone : +662-6324300
Fax : +662-6375496-7
Website : www.barascientific.com


Bic
Che
Phy
Sci


PHYWE
2008
PHYSICS


BEST SELLER


NEW
BEST SELLER


Cobra4 Wireless
PHYWE


BEST SELLER


PHYWE
CHEMISTRY
PHYWE
BIOLOGY
PHYWE
APPLIED SCIENCES

CERNTEK : YOUR CERTIFIED TECHNOLOGY

CERNTEK COMPANY LIMITED

AT CERNTEK, WE PROVIDE CERTIFIED TECHNOLOGY WITH HIGH-END TECHNIQUES

ADVANCED EQUIPMENTS	Field of Applications
BALANCE UNIT	Food/ Agriculture
UV-Visible Spectrometer	Forensic Science
Fluorescent Spectrometer	Material Science
Gas Chromatography	Environmental
High Performance Liquid Chromatography	Pharmaceutical
Auto Titration	Building materials
X-ray Fluorescence Spectrometer	Quality Control
Particle Size Analyzer	Quality Assurance
C/S and N/O Analyzer	Research and Development
Water Quality	Coating Technolgy
Mass Flow Controller	Vacuum Technology

OUR PARTNER :

EDWARDS HORIBA Explore the future Precisa Hitachi High-Technologies Corporation

CERNTEK Co.,LTD
ADDRESS :257 Soi Phetkasem 102/2 Bangkae Sub-district,, Bangkae District, Bangkok 10160, Thailand
Tel : (66)-2-8093050 FAX : (66)-2-8094118 www.cerntek.co.th

CERNTEK COMPANY LIMITED

COAX GROUP CORPORATION LTD.

1131/325,327,328 Nakornchaisri Road,
Kwang Thanon Nakornchaisri, Khet Dusit,
Bangkok 10300, Thailand

Tel : +662-668-2436
Fax : +662-243-7386
http://www.coax.co.th

Scanning Electron Microscopes

Hitachi High-Tech

TM3000

SU8000

HT7700

Tabletop Microscope Field Emission -Scanning Electron Microscope Transmission Electron Microscope

Atomic Force Microscopes

Park SYSTEMS

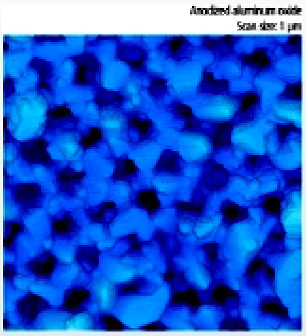

XE Technology & Innovation

- ✓ **Ultimate AFM Resolution by True Non-Contact Mode**
- ✓ **Decouple XY&Z Scanner**
- ✓ **Direct on-axis optics**
- ✓ **Non-invasive In-liquid by SICM**

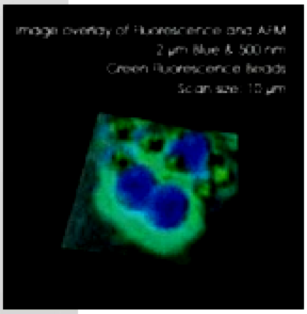

Park NX10
The World's Most Accurate AFM

XE-Bio
Non-Contract In-Liquid Imaging
and Ion Conductive Microscopy

PONDPOL
Group of companies

www.pondpol.com

10,12 M.6 Soi Pinklaonamchoke Sala-Thammasop, Thaweewattana Bangkok 10170 Tel 0-2431-7444 Fax 0-24317440

B&WTEK INC.

Your Photonics Partner

- > Spectrometers
- > Color Measurement
- > Spectrophotometers
- > Lasers
- > Raman Spectrometer System
- > Raman Accessories

HORIBA JOBIN YVON

- > Optical Spectroscopy
- > Fluorescence Spectroscopy
- > Raman Spectroscopy
- > Grating and OEM
- > Thin Film Analysis
- > Forensics
- > Surface Plasmon Resonance Imaging

FLIR

- > Airborne Systems
- > Maritime Systems
- > Land Systems
- > Tactical Vision
- > Unmanned Systems

OEM & Integration

eDAQ

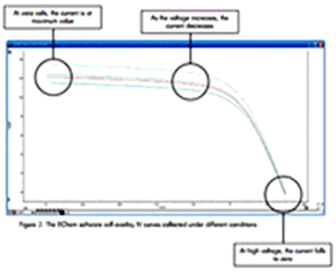

- > e-corder Units
- > Powerchrom Systems
- > Flow Analysis System
- > Contactless Conductivity Systems
- > pH, Temperature, Conductivity & Dissolved Oxygen
- > Potentiostats & Electrochemistry
- > Transducer and Accessories
- > Software for Data Aquisition & Analysis
- > Teaching Kits & Startup Systems

Quorum Technologies

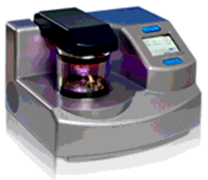

- > Cryo-SEM Preparation Systems
- > Sputter Coaters & SEM Carbon Coaters
- > Carbon Attachment & Consumables
- > Film Thickness Monitors
- > RF Plasma Etchers/Plasma Reactors
- > Freeze Dryers for Samples Preparation
- > Critical Point Dryer
- > Sputter Targets
- > Glow Discharge Systems
- > Bench-Top Vacuum Evaporators
- > Recirculating Heaters and Chillers
- > Feltier Cooling Stages for SEM

BiolinScientific

Qsense
- > Quartz Crytal Microbalance (QCM) with Dissipation Monitoring

KSV NIMA
- > Langmuir Trough
- > Langmuir-Blodgett Trough
- > Microscopy Trough
- > Interfacial Shear Rheometer
- > PM-IRRAS (FTIR)
- > Brewter Angle Microscope
- > Surface Potential Sensor
- > Dip Coaters

attension
- > Force Tensiometers
- > Optical Tensiometers
- > Bubble Tensiometers
- > Volumetric Tensiometers

AMETEK ORTEC

- > General Gamma Spectroscopy
- > Radiation Monitoring System
- > Gross Alpha/Beta Counting
- > Portable and Mobile Spectroscopy System
- > Electrical Coolers (replace LN)
- > Homeland Security
- > Software
- > General Alpha Spectroscopy
- > Counting Laboratory System
- > Chemical Weapons & Portable Nuclide Identification Sys.
- > Nuetron Detection Systems and Instruments
- > Digital Signal Processing Electronics
- > Whole Body Counting
- > Modular Electronics

Electron Microscopy Sciences

- > SEM Supplier
- > Chemical for Electron Microscopy, Light Microscopy & Histology
- > Equipment & Accessories
- > Material Science & Metrology

Agar SCIENTIFIC

- > Calibration specimens
- > Vacum Coating
- > Filaments
- > Apertures
- > Specimen preparation equipment
- > EM films

Hakuto (Thailand) Ltd.
2nd Floor, Regent House Building
183 Rajdamri Road, Lumpini, Patumwan, Bangkok, 10330 Tel. 0-2255-8910

PFEIFFER VACUUM TECHNOLOGY (Germany)

- Rotary Vane Pumps, Roots Pumps, Turbo Pumps,
- Dry-compressing Pumps
- Leak-Detectors
- Mass Spectrometers and Gas Analysis System
- Vacuum measurement and control units

HAMAMATSU (Japan)

- Electron Tube product

Example : Photomultiplier tube, Photomultiplier tube Module, Microchannel Plates, Image Intensifiers, Xenon lamp, D2 Lamp, Light Source Applied Product, Laser applied Products, Microfocus X-ray Sources, X-ray Imaging Device

- Image and Processing System

Example: Cameras/Image Processing Measuring Systems, X-ray Products, Life Science Systems, Medical Systems, Spectroscopic and Optical Measurement System

- Opto-semiconductors

Excample: Si Photodiode, APD, Photo IC, Image sensors, PSD, Infrared detectors, LED, Optical communication Devices, X-ray

Laser Power Meter

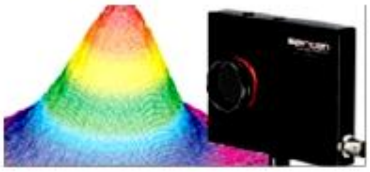

Laser Bearm Profiler

Scanning Slit prodiler